中 国 气 象 局 气 候 研 究 开 放 实 验 室

论 文 汇 编

第 十 六 卷

(2013)

LCS

气候研究开放实验室

中国气象局气候研究开放实验室

论文汇编

第 十 六 卷

(2013)

中国气象局气候研究开放实验室

内 容 简 介

本文集收录了2013年度中国气象局气候研究开放实验室在国内外核心期刊发表的学术论文59篇。内容涉及气候诊断、气候预测理论及方法、气候模式模拟、气候变化检测及影响评估等研究领域。

目　录

1. 海温异常对东亚夏季风影响机理的研究进展 …………………………………… 陈丽娟　袁　媛　杨明珠 等　(1)
2. 缓变下垫面对浅水方程的动力学订正 …………………………………… 达朝究　冯爱霞　龚志强　宋　健　(13)
3. 基于2009年初长江中下游地区持续阴雨过程的10—30天延伸期稳定分量的提取及配置分析 ………
……………………………………………………………………………… 封国林　孙树鹏　赵俊虎　郑志海　(19)
4. 动力—统计客观定量化汛期降水预测研究新进展 ………………………… 封国林　赵俊虎　支　蓉 等　(31)
5. 长江上游降水变化及其对径流的影响 ……………………… 冯亚文　任国玉　刘志雨　吴吉东　张　雷　(41)
6. Nitrogen dioxide measurement by cavity attenuated phase shift spectroscopy (CAPS) and implications in ozone production efficiency and nitrate formation in Beijing, China ……………………………………
………………………… Ge, B., Y. Sun, Y. Liu, H. Dong, D. Ji, Q. Jiang, J. Li, and Z. Wang　(50)
7. 2010年西北太平洋与南海热带气旋活动异常的成因分析 ………………………………… 龚振淞　陈丽娟　(61)
8. 基于多时间尺度的回归集成预测模型 ………………………………………… 胡娅敏　覃志年　陈丽娟 等　(72)
9. 利用海气耦合模式预测的大尺度环流进行热带气旋年频数的预测试验 ………… 贾小龙　陈丽娟 等　(80)
10. 浅谈极端气温事件研究中阈值确定方法 ……………………………………… 李　娇　任国玉　战云健　(90)
11. 我国冬季气温与影响因子关系的年代际变化 ……………………… 李维京　李　怡　陈丽娟　赵振国　(95)
12. A new statistical downscaling scheme for predicting winter precipitation in China …………………
…………………………………………………………………………………… Liu Y, Fan K, Yan Y-P　(107)
13. 基于CFS模式的中国站点夏季降水统计降尺度预测 …………………………… 刘　颖　范　可　张　颖　(112)
14. 我国强降雪气候特征及其变化 …………………………………… 刘玉莲　任国玉　于宏敏　康恒元　(122)
15. 东亚地区云垂直结构的CloudSat卫星观测研究 ……………………………… 彭　杰　张　华　沈新勇　(132)
16. 广西夏季降水的多时间尺度特征及影响因子 …………………………………… 覃志年　胡娅敏　陈丽娟　(142)
17. Recharge Oscillator Mechanisms in Two Types of ENSO …… Ren, Hong-Li, and Fei-Fei Jin　(153)
18. ENSO regime change since the late 1970s as manifested by two types of ENSO ……………………
…………………………… Ren, Hong-Li, Fei-Fei Jin, Malte F. Stuecker, and Ruihuang Xie　(171)
19. 中国东北地区冬季气温变化特征及其与大气环流异常的关系 ……………………………………………
…………………………………………………………………………… 沈志超　任国玉　李　娇　孙秀宝　(179)
20. Decadal Change in the Correlation Pattern between the Tibetan Plateau Winter Snow and the East Asian Summer Precipitation during 1979-2011 ……………………… Dong SI, Yihui DING　(187)
21. 江淮流域夏季降水对前冬持续时间长短的响应 ………………… 苏　涛　张世轩　支　蓉　陈丽娟　(200)
22. 风场变形误差对冬季降雪测量及其趋势估算的影响 …………… 孙秀宝　任国玉　任芝花　沈志超　(209)
23. 全球和中国区域近50年气候变化检测归因研究进展 ………………… 孙　颖　尹　红　田沁花 等　(218)
24. 2012/2013年东亚冬季风活动特征及其可能成因分析 ………………… 王东阡　周　兵　孙丞虎 等　(229)
25. Analysis of stable components in extended-range forecast for the coming 10-30 days in winter 2010 and 2011 ………………………………………………………………… Wang K, Feng G, et al　(237)

26. 2010 年夏季欧亚异常阻高演变过程及对天气气候的影响 ………………………… 王小玲　丁一汇　(245)
27. 中国冬季区域性极端低温事件分类及其与气候指数极端性的联系 ……………………………………
……………………………………………………………………… 王晓娟　沈柏竹　龚志强　封国林　(252)
28. Effect of non－spherical dust aerosol on its direct radiative forcing ……………………………………
……………………………………………………………………… Zhili Wang，Hua Zhang，et al　(263)
29. Radiative forcing and climate response due to the presence of black carbon in cloud droplets ……
……………………………………………………………………… Zhili Wang，Hua Zhang，et al　(278)
30. 气候信息交互显示与分析平台(CIPAS)设计与实现 …………… 吴焕萍　张永强　孙家民　邵鹏程　(292)
31. 一套格点化的中国区域逐日观测资料及与其它资料的对比 ………………………… 吴　佳　高学杰　(302)
32. Similar spatial patterns of climate responses to aerosol and greenhouse gas changes ………………
……………………………………………………… Xie，S.－P.，B. Lu(co－first author)，B. Xiang　(312)
33. 黑潮区海温对中国北方初霜冻日期的影响研究 …………………………… 杨明珠　陈丽娟　宋文玲　(317)
34. Spatial and temporal characteristics of Beijing urban heat island intensity …………………………
……………………………………………………………………… Yang，P.，G. Y. Ren，W. D. Liu　(325)
35. Can temperature extremes in China be calculated from reanalysis? …………………………………
Qinglong You，Klaus Fraedrich，Jinzhong Min，Shichang Kang，Xiuhua Zhu，Guoyu Ren，et al　(339)
36. Comparison of NCEP/NCAR and ERA－40 total cloud cover with surface observations over the Tibetan Plateau …………………………………………………………………………………………
……… Qinglong You，Yang Jiao，Houbo Lin，Jinzhong Min，Shichang Kang，Guoyu Ren，et al　(351)
37. Decadal variation of surface solar radiation in the Tibetan Plateau from observations，reanalysis and model simulations ………………… Qinglong You，Arturo Sanchez－Lorenzo，Martin Wild，et al　(360)
38. Variability of temperature in the Tibetan Plateau based on homogenized surface stations and reanalysis data ……………………………………………… Qinglong You,Klaus Fraedrich，Guoyu Ren，et al　(374)
39. Winter temperature extremes in China and their possible causes …………………………………
………………… Qinglong You，Guoyu Ren，Klaus Fraedrich，Shichang Kanga，Yuyu Ren，et al　(385)
40. Present and projected degree days in China from observation,reanalysis and simulations …………
………… Qinglong You，Klaus Fraedrich，Frank Sielmann，Jinzhong Min，Shichang Kang，et al　(397)
41. 黑龙江省大气边界层不同高度风速变化 ……………………………………… 于宏敏　任国玉　刘玉莲　(411)
42. 1951—2009 年东亚地区日降水趋势特征分析 ………………………… 战云健　任国玉　任玉玉 等　(424)
43. 北京中心商务区夏季近地面气温时空分布特征 ……………………… 张本志　任国玉　张子曰 等　(438)
44. Application and evaluation of McICA scheme with new radiation code in BCC_AGCM 2.0.1. Geosci
……………………………………………………………………… Zhang，H.，Jing，X. and Li，J　(447)
45. The features of cloud overlapping in Eastern Asia and their effect on cloud radiative forcing ……
……………………………………………… ZHANG Hua，PENG Jie，JING XianWen，LI JiangNan　(472)
46. 东亚地区云的垂直重叠特性及其对云辐射强迫的影响 ………………………… 张　华　彭　杰 等　(483)

47. Influence of changes in solar radiation on changes of surface temperature in China ………………
…………………………………………………………………………… Hua Zhang, Qing Yin, et al (496)
48. An updated estimation of radiative forcing due to CO_2 and its effect on global surface temperature change ……………………………………………………… Hua Zhang, Ruoyu Zhang, Guangyu Shi (507)
49. CH_4 和 N_2O 的辐射强迫与全球增温潜能 ……………………………… 张 华 张若玉 何金海 等 (515)
50. Effect of data homogenization on estimate of temperature trend: a case of Huairou station in Beijing Municipality ……… Zhang, L., G. Y. Ren, Y. Y. Ren, A. Y. Zhang, Z. Y. Chu, Y. Q. Zhou (525)
51. 长江中下游地区暴雨"积成效应" ……………………………………………… 张世轩 封国林 赵俊虎 (534)
52. 欧亚中高纬阻塞高压关键区高度场动力－统计跨季度预测实验 …… 赵俊虎 杨 杰 龚志强 等 (545)
53. 黑碳与非吸收性气溶胶的不同混合方式对其光学性质的影响 …………… 周 晨 张 华 王志立 (554)
54. Evaluation and Preprocess of Chinese Fengyun－3A Sea Surface Temperature Experimental Product for Data Assimilation …………………… ZHOU Wei, CHENG Yan－Jie, WANG Su－Juan, et al (566)
55. 基于三层嵌套网格的珠江口冬季盐度层化的数值模拟 ……………… 周 巍 王东晓 组婷婷 等 (571)
56. 2012 年冬春季高原积雪异常对亚洲夏季风的影响 ……………………… 竺夏英 陈丽娟 李 想 (583)
57. Representation of the Arctic Oscillation in the CMIP5 Models ……………………………………
……………………………………………………… ZUO Jin－Qing, LI Wei－Jing, REN Hong－Li (591)
58. Impact of the North Atlantic Sea Surface Temperature Tripole on the East Asian Summer Monsoon
…………………………………… Zuo Jinqing, Li Weijing, Sun Chenghu, Xu Li, Ren Hong－Li (599)
59. CMIP5 模式对北极涛动的模拟评估 ……………………………………… 左金清 李维京 任宏利 (613)

第 24 卷 第 5 期 应 用 气 象 学 报 Vol. 24, No. 5
2013 年 10 月 JOURNAL OF APPLIED METEOROLOGICAL SCIENCE October 2013

陈丽娟,袁媛,杨明珠,等. 海温异常对东亚夏季风影响机理的研究进展. 应用气象学报,2013,24(5):521-532.

海温异常对东亚夏季风影响机理的研究进展

陈丽娟* 袁 媛 杨明珠 左金清 李维京
(国家气候中心 中国气象局气候研究开放实验室,北京 100081)

摘 要

从短期气候预测关注的外强迫信号角度出发,回顾了国内外在海温异常对东亚夏季风和我国汛期降水影响机理方面的主要研究进展,重点评述了热带太平洋 ENSO 循环、热带印度洋全区一致型海温模态、热带印度洋海温异常偶极子、南印度洋偶极子和北大西洋海温三极子模态的年际变化及其对东亚夏季风年际变率的影响。从研究成果在短期气候预测业务中应用的角度,重点关注海温异常和东亚夏季风年际变率以及我国汛期降水多雨带位置的关系,总结了海温异常作为外强迫信号对我国汛期降水预测的指示意义以及汛期降水预测的难度。最后指出气候预测业务对东亚夏季风影响的机理研究和动力气候模式发展方面的需求。

关键词: 外强迫信号;海温异常;东亚夏季风;汛期降水

引 言

短期气候预测主要指月、季、年时间尺度的气候预测,与人类的生产生活关系密切。该时间尺度的预测既是初值问题,也是边值问题。随着预测时间尺度的延长,更多地表现为边值问题[1]。在我国短期气候预测的边值问题中,主要考虑的外强迫信号包括多海区的海温异常[2-8]、土壤湿度异常[9-11]、积雪覆盖异常[12-14]、极冰异常[15-17]、植被异常[18-19]等信息。利用这些外强迫信号的气候预测业务或试验性业务在国外从 19 世纪后期就存在了,我国于 20 世纪 50 年代正式发布气候展望[20]。在这些外强迫信号中,对东亚夏季风预测而言,海温异常是最强、最重要的因子,而土壤湿度、积雪覆盖、极冰、植被等信息受资料来源、异常持续时间长短、因子季节性变化等特征的限制,对东亚夏季风影响的不确定性更大,在我国短期气候预测业务中的应用也受到季节限制。长期的预测业务实践[21]、海气相互作用方面的理论研究进展[22]、气候系统模式的发展[23]均证实海洋异常在全球气候异常和海气相互作用方面作用重大。

本文以我国短期气候预测业务和服务中非常关注的东亚夏季风和我国夏季降水预测为目标,回顾了国内外全球主要海洋异常模态对东亚夏季风年际变率的影响机理,重点梳理了热带太平洋 ENSO 循环、热带印度洋全区一致型海温模态、热带印度洋海温异常偶极子、南印度洋偶极子、北大西洋海温三极子模态对东亚夏季风系统以及我国夏季降水多雨带分布的影响,从而有利于全面认识海温异常的年际信号在东亚夏季风和我国夏季降水预测中的应用能力。

1 热带太平洋 ENSO 循环对东亚夏季风的影响

作为年际气候变化中的最强信号,ENSO 现象很早就倍受气象学者关注。ENSO 不仅是造成全球气候异常的一个重要原因,也是导致亚洲季风异常和我国旱涝发生的关键因素。我国位于东亚季风区,东亚夏季风和冬季风异常直接导致我国气候异常,ENSO 通过大气环流以遥相关的形式影响东亚季风系统的每个关键成员,并由此间接影响中国的气候异常[22-24]。国际上在ENSO冷暖位相对全球

2013-04-08 收到, 2013-07-12 收到再改稿。
资助项目:国家重点基础研究发展计划(2013CB430203),国家自然科学基金项目(41275073,41005038),国家科技支撑项目(2009BAC51B05)
* email: chenlj@cma.gov.cn

降水和温度分布型的影响方面也开展了大量研究[25-27]，但是这些结果基本上未给出 ENSO 循环对东亚夏季风和中国区域的影响结果。本章着重回顾 ENSO 循环对东亚夏季风和我国夏季降水的影响机理，阐述菲律宾异常反气旋在 ENSO 循环对东亚夏季风影响中的桥梁作用，随着对 ENSO 循环复杂性的进一步认识，总结了不同分布型厄尔尼诺对东亚夏季风的影响。

1.1 ENSO 循环对东亚夏季风和我国夏季降水的影响

大量研究表明，ENSO 事件的不同阶段对我国夏季降水有不同影响[28]。厄尔尼诺发展期的夏季，西太平洋副热带高压偏弱、偏南，影响我国的西南气流偏弱，东亚夏季风偏弱，我国夏季主要季风雨带偏南，中南半岛和华南大部降水偏少，东南沿海偏多，夏季中期江淮流域多雨；厄尔尼诺衰减期的夏季，西太平洋副热带高压偏强、偏北，影响我国的西南气流偏强，东亚夏季风偏强，从而导致江淮流域降水偏少、洞庭湖和鄱阳湖流域出现洪涝灾害[4,28-30]。拉尼娜对东亚夏季风和我国夏季雨带的影响与厄尔尼诺大致相反，但拉尼娜影响没有厄尔尼诺影响显著。拉尼娜发展阶段的夏季对应着强的东亚夏季风，我国夏季华北和江南往往多雨；而拉尼娜衰减期的夏季则对应弱的东亚夏季风，我国夏季江淮多雨，华北、东北以及长江中游地区少雨[30-31]。

厄尔尼诺和拉尼娜对东亚夏季风和我国夏季雨带影响还可能与西太平洋暖池北部海温异常有关。Huang 等[32-34]研究指出，东亚夏季风的季节内变化受菲律宾附近对流活动影响。当菲律宾附近海域海温偏暖导致对流活动增强时，西北太平洋副热带高压在 6 月中上旬北跳明显，我国长江和淮河流域以及韩国、日本夏季降水偏弱；相反，当暖池附近海温偏冷、对流活动偏弱时，西太平洋副热带高压北跳不明显，长江流域和淮河流域以及韩国、日本等地的夏季降水偏强。曹杰等[35]从非线性动力学理论角度出发，研究了菲律宾附近对流活动强弱对西太平洋副热带高压影响的物理机制。

西太平洋暖池的热状态不仅强烈影响西太平洋副热带高压的季节内变化，还影响南海夏季风爆发的早晚[36]。当西太平洋暖池海水变暖时，则对流活动从中印半岛向菲律宾以东加强，且西太平洋副热带高压可能向北异常移动，在这种情况下，南海夏季风可能提前爆发；相反，当暖池处于冷状态时，则菲律宾的对流活动减弱，西太平洋副热带高压可能偏南、偏西，南海夏季风可能爆发偏晚。其主要原因可能是暖池热状态明显地影响着 Walker 环流与 Hadley 环流[37]。

1.2 ENSO 循环影响东亚气候异常的物理机制

研究表明，正是由于热带太平洋海温异常所产生的对流活动异常分布，使 ENSO 事件对热带西太平洋和东亚上空的季风环流有显著影响[38]。在厄尔尼诺成熟期，赤道中太平洋和以东地区对流活动加强，而在热带西太平洋海洋性大陆区对流活动偏弱，从而使赤道太平洋洋面上的对流活动异常形成了一个偶极子结构。热带西太平洋海洋性大陆上空的对流冷却使得热带大气在对流层低层产生 Rossby 波响应，从而在海洋性大陆以北的热带西太平洋和我国南海地区强迫出反气旋环流的异常。与此异常反气旋性环流相伴随的水汽输送异常使得东亚沿岸附近的水汽输送增强，并在我国华南沿岸附近产生异常辐合，导致了我国华南地区在厄尔尼诺盛期出现降水正异常[24,39-40]。Wang 等[22,41]也指出，在 ENSO 的极端位相时出现在海洋性大陆以北的反气旋异常(称为菲律宾异常反气旋)环流是连接 ENSO 暖位相和东亚冬季风的桥梁，这个反气旋异常可以持续到夏季，对东亚夏季风产生滞后影响。在厄尔尼诺达到成熟期之后的夏季，东北亚往往出现异常强的反气旋性环流，并且西太平洋副热带高压异常偏西，从而加强副热带东亚地区的季风环流，并使长江流域降水偏多，发生洪涝灾害。

1.3 不同分布型厄尔尼诺及其对气候影响

研究发现，20 世纪 80 年代后 ENSO 不同位相与次年夏季我国雨带的对应关系似乎较难成立[42-43]，例如 2002，2004，2006 年发生了 3 次厄尔尼诺事件，每次事件衰减年的夏季，我国的主要多雨带并未出现在长江流域而是位于淮河流域至黄淮地区[43]，这可能与 ENSO 事件成熟期分布类型的变化有关[44]。事实上，早期研究已经注意到厄尔尼诺事件的发生过程包括两类：一类主要在太平洋东部(秘鲁沿岸)增暖再向西扩展，另一类则主要在赤道中太平洋出现大范围增暖并自西向东扩展[45-48]。但人们注意到厄尔尼诺成熟期的海温分布特征在 20 世纪 90 年代以后发生了显著变化，最大海温正距平中心不同于传统的厄尔尼诺事件分布在赤道东太平洋秘鲁沿岸，而是向西移动到赤道中太平洋日界线附近。人们将这类事件称为中部型厄尔尼诺(或厄尔尼诺

Modoki),而将传统的厄尔尼诺事件称为东部型厄尔尼诺[49-54]。实际观测发现,20世纪90年代以后,中部型厄尔尼诺的发生频率和强度都呈现明显上升趋势[54],期间共发生了8次厄尔尼诺事件,其中5次为中部型,而另外3次则兼有中部型和东部型的共同特征,Kug等[52]称之为混合型厄尔尼诺[55]。

中部型厄尔尼诺事件不仅在发展演变机制上与东部型厄尔尼诺不同,其对全球大气环流[56]、西北太平洋台风和大西洋飓风活动[57-58]以及北美、澳大利亚和东亚的气温和降水[56,59-66]影响也表现出与东部型厄尔尼诺的显著差异。当中部型厄尔尼诺发生时,由于最大海温正距平中心位于赤道中太平洋日界线附近,对流活跃区较东部型厄尔尼诺偏西,在赤道太平洋上空地区会形成两个异常Walker环流圈,从而对南美、北美西海岸,甚至日本和新西兰气候的影响与东部型厄尔尼诺的影响可能完全相反[49,67]。由于海温偏高,赤道太平洋中部为相对偏湿的区域,由此会在西北太平洋上空对流层中层激发正位相的太平洋—日本(Pacific—Japan,PJ)波列,在西北太平洋—北美地区上空的对流层中层激发正位相的夏季太平洋—北美(Pacific—North American,PNA)型,从而导致西北太平洋夏季风偏强,东亚夏季风偏弱[61]。

前面提到,菲律宾异常反气旋性环流是联系ENSO与东亚气候异常的重要桥梁[22,24,40-41]。但当中部型厄尔尼诺发生时,菲律宾异常反气旋强度会显著减弱,持续时间会明显缩短,其位置则会西移到我国南海地区[68],由此而导致在中部型ENSO事件循环期,东亚南部的降水异常分布特征与东部型ENSO对应的情况几乎完全相反[56,62-64,66],该特征提示在使用ENSO信号进行气候预测时,不能仅考虑Niño指数,而要从热带海温分布型以及大气的垂直环流特征等多种角度看待ENSO循环的影响。

2　印度洋海温异常对东亚夏季风的影响

印度洋位于亚洲地区夏季季风气流上游,是亚洲夏季风各种能量及水汽的重要源地之一,也是亚澳季风系统活动的重要下垫面,Walker环流、横向季风环流和侧向季风辐散风环流均交汇于此,其中自西南印度洋指向东亚、南亚的侧向季风辐散风环流最强。因此,印度洋热力异常对作为“第二推动力”的海陆热力特性差异,对印度洋—太平洋海温配置,以及对大气环流和亚-澳季风的变异均具有十分重要的作用[69-70]。大量研究显示,热带印度洋海温异常模态和南印度洋偶极子模态对东亚夏季风和我国夏季降水有明显影响。

热带印度洋海温异常最主要的模态就是全区一致型海温变化,而热带印度洋秋季海温异常最主要模态是热带西印度洋和东南印度洋反相变化的偶极型海温模态[71-72]。南印度洋偶极子是指副热带西南印度洋和南热带中东印度洋SST异常呈反位相分布模态。

2.1　热带印度洋海温异常偶极子

热带印度洋偶极子(TIOD)具有两个相反的模态,通常将西印度洋偏暖、东南印度洋偏冷的模态称为正偶极子(或偶极子正位相),将西印度洋偏冷、东南印度洋偏暖的模态称为负偶极子(或偶极子负位相)。TIOD具有明显的季节位相锁定的特征,通常在春末夏初开始出现,秋季达到盛期,冬季快速衰亡。一般5—6月海温负距平最先出现在爪哇岛南部,同时赤道东南印度洋上出现东南风异常。7—8月海温负距平加强且沿着印度尼西亚海岸向赤道方向延伸,同时西印度洋开始出现海温正距平,赤道印度洋纬向东风距平也随之加强。9—10月上述特征迅速达到盛期,赤道印度洋偶极型海温模态与赤道印度洋东风距平相互耦合;11—12月偶极子快速衰减[71,73]。

研究表明,TIOD对我国夏季降水有显著影响。TIOD正偶极子发生的夏季,热带西印度洋偏暖、东南印度洋偏冷的海温异常分布型使得赤道印度洋盛行东风距平,从而使Walker环流减弱,同时菲律宾附近对流活动减弱,西太平洋副热带高压偏强、偏西、偏南,我国南方地区大气呈异常上升运动,为整层水汽的异常辐合区,从而有利于我国华南夏季降水偏多。而当TIOD负位相发生时,西太平洋副热带高压偏弱、偏东、偏北,华北处于异常辐合区,降水偏多,而南方降水偏少[74-76]。

尽管有些年份,TIOD正(负)位相刚好发生在厄尔尼诺(拉尼娜)发生年的夏、秋季节,使得TIOD对印度洋周边地区气候的影响在很大程度上被认为是ENSO的影响。但实际上,TIOD也有相对独立于ENSO的一面。百年尺度的海温资料清楚地揭示了热带印度洋偶极子和太平洋ENSO事件关系的年代际变化。在1948—1969年阶段,正(负)位相

的 TIOD 与暖(冷)ENSO 事件表现出较多的相对独立性,但在 1970—2000 年阶段,两者常同时发生。ENSO 影响偶极子的整个生命史,而偶极子反过来也会显著影响 ENSO 事件发展阶段的强度[77-78]。前面提到,2000 年以后中部型 ENSO 事件的发生频率和强度都显著增加,统计结果显示,当中部型 ENSO 事件发生时,热带印度洋海温和大气环流的响应均没有东部型 ENSO 事件发生时显著[51,68],TIOD 与 ENSO 的同位相关系在近 10 年是否发生变化值得进一步深入研究。

正是考虑到 TIOD 与 ENSO 显著的同位相关系,刘宣飞等[79]详细分析了偶极子独立发生年和偶极子与 ENSO 共同发生年我国夏季降水的特征。研究表明,TIOD 独立发生时,其正位相年,夏季江南西部到华南大部的降水偏多;TIOD 与 ENSO 同时发生时,正位相年,河套、华北地区夏季降水偏少,而东南沿海地区降水偏多。因此,ENSO 与偶极子对我国夏季降水关系的影响主要表现为在华南西部、江淮流域、河套及华北地区起抵消作用,而在东南沿海地区起协同作用。

2.2　热带印度洋全区一致海温模态

热带印度洋全区一致海温模态是热带印度洋海温变化的最主要模态,并没有特别显著的季节变化特征,但经常发生在 ENSO 事件成熟的冬季和次年春季[69]。早期研究已经揭示出热带印度洋全区一致增暖(变冷)模态对太平洋厄尔尼诺(拉尼娜)事件的滞后响应,而其中的物理机制包括印度尼西亚贯穿流[80]、大气桥[81-83]、南印度洋海洋 Rossby 波的传播等[84]。

然而,近几年的研究则更多强调热带印度洋海温在 ENSO 衰减年所起的重要“充电器”作用,正是因为热带印度洋全区一致海温增暖(变冷)在厄尔尼诺(拉尼娜)衰减时却发展到盛期,因此,通过改变对流活动和 Walker 环流异常以及激发向东传播的 Kelvin 波,印度洋海温像“充电器”一样延续了 ENSO 对大气环流和气候异常的影响[85-89]。例如,热带印度洋全区一致增暖(变冷)通过海气相互作用激发赤道印度洋—西太平洋异常 Walker 环流圈,加强(减弱)西太平洋副热带高压的强度,进而有利于南海夏季风爆发的推迟(提前)。由此可知,热带印度洋全区一致海温模态在维持 ENSO 对第 2 年南海夏季风爆发的影响方面起到了重要的传递作用[88]。

2.3　热带印度洋海温对菲律宾异常反气旋的影响

菲律宾异常反气旋被认为是联系 ENSO 与东亚季风环流的重要纽带。Zhang 等[39]最早提出了与厄尔尼诺盛期相伴随的热带西太平洋的对流异常减弱所造成的对流冷却异常,激发出大气 Rossby 波响应,导致菲律宾异常反气旋的产生。Wang 等[41]也对该反气旋的产生进行研究,认为热带西太平洋负海温异常使热带西太平洋的对流潜热释放减弱,从而激发冷的 Rossby 波在菲律宾海域附近形成菲律宾异常反气旋。另外,菲律宾异常反气旋的建立和维持还受到 ENSO 事件的遥强迫作用、热带—热带外大气的相互作用(来自北半球中高纬度地区的外强迫)以及季风-海洋间相互作用的共同影响。Chou[90]和 Chen 等[91]还提出了对菲律宾异常反气旋建立起作用的另一种过程。Chou[90]认为在厄尔尼诺情形下,菲律宾异常反气旋是印度洋生成的低层异常反气旋环流东移,秋末锁定在菲律宾海域称为菲律宾异常反气旋。在热带印度洋正偶极子发生的夏季,海气相互作用使热带西印度洋对流活动增强、异常上升运动发展,而东南印度洋对流活动减弱、为异常下沉运动控制。根据 Matsuno-Gill 响应原理[92-93],正偶极子会激发关于赤道对称的异常反气旋对。赤道北侧的异常反气旋比赤道南侧强,且随正偶极子的发展成熟不断加强并缓慢向东移动[68]。而这种东移是由东西湿度和温度的水平不对称以及强厄尔尼诺事件影响大尺度辐散异常所驱动[90-91,94]。

由于该异常反气旋环流能持续到厄尔尼诺衰减年的夏季,显著加强了西太平洋副热带高压并给我国夏季南方带来大量降水。Wang 等[22]认为,西太平洋局地海气相互作用的正反馈机制是菲律宾异常反气旋能够维持到厄尔尼诺次年夏季的重要原因。但 Watanabe 等[95]通过一系列的模拟试验发现,热带印度洋全区一致增暖模态强度不一定比西太平洋的异常冷水和中东太平洋的异常暖水强,而是通过激发东传的 Kelvin 波更加显著影响了菲律宾异常反气旋在厄尔尼诺次年夏季的维持。Xie 等[89]的统计分析和大气环流模式进一步证实了该观点。近期,Wu 等[96-97]再次对比分析了西太平洋局地海温和印度洋海温对菲律宾异常反气旋在厄尔尼诺衰减年的作用,认为在衰减年夏季(6—8 月),热带印度洋暖海温的作用不断增强,而西太平洋冷海温的作用则不断减弱。因此,当东部型厄尔尼诺事件发生

时,在其发展年的夏秋季热带印度洋有西暖东冷的正偶极子发生,而在其盛期至次年春季,热带印度洋全区一致海温增暖发展,共同导致菲律宾异常反气旋建立早、结束晚、强度强。而当中部型厄尔尼诺事件发生时,印度洋海温的响应变得不显著,由此导致菲律宾异常反气旋建立晚、结束早、强度弱[68]。

2.4 南印度洋偶极子

研究发现,印度洋除了上述热带印度洋海温异常一致型和热带印度洋偶极子(TIOD)模态外,在南印度洋副热带区域存在西南印度洋(西极子)和南热带中东印度洋(东极子)海温异常呈反位相分布的另一种偶极型海温差异现象,具有明显的年际和年代际尺度变化特征,称为南印度洋偶极子(SIOD)或南印度洋偶极模(SDP)[98-101]。本文定义当西极子为负异常海温、东极子为正异常海温时,为 SIOD(SDP)正位相,反之为 SIOD(SDP)负位相。研究表明,SIOD 现象主要出现在冬春季[100-102]。晏红明等[70]研究认为,印度洋副热带海温偶极差异的季节锁相出现在 1—3 月,而一些个例合成则显示 SIOD 在春季最为显著[101,103]。但大多研究表明,SIOD 在前期秋冬季开始出现,并能持续到次年夏、秋季。因此,SIOD 在区域和季节锁相上与 TIOD 不同,同时 SIOD 的持续性高于 TIOD。

大多研究认为,SIOD 的形成与大气环流异常有重要关系。由于赤道印度洋环流场异常(热带季风变化),激发出 Kelvin 波向南沿苏门答腊传播,之后通过 Rossby 波或耦合的 Rossby 波向西传播,快速地将海表高度异常、温跃层异常(或海温异常)由热带印度洋向西南副热带印度洋传播[104],并认为这种波的传播每年有 4 次。但 Xie 等[84]认为 SIOD 主要由 ENSO 强迫造成,杨明珠等[101]认为 SIOD 的形成是对前期秋冬季中高纬度环流场强迫(即对风应力)的响应。另外,海温-辐射-云反馈过程对区域海温变化的影响对于 SIOD 的维持具有重要作用[70,98]。有研究认为,SIOD 与 ENSO 是相互独立的[100];也有研究认为,SIOD 与 ENSO 事件具有密切的联系,SIOD 就像连接 ENSO 位相转换的一个中间环节,SIOD 事件前后期,ENSO 的位相刚好相反,SIOD 在 ENSO 事件中的作用不仅涉及海气相互作用的正负反馈过程,还与热带和副热带大气环流之间的相互作用有关,尤其东南印度洋海温变化所引起的异常纬向风由赤道印度洋向赤道太平洋传播,对后期赤道东太平洋海温异常变化具有重要影响[102]。还有研究认为,冬季 SIOD 能激发出极显著的南北半球环绕太平洋的波列结构[105],而南半球的这种环流结构对 ENSO 循环的年际变化有重要影响[106]。此外,SIOD 与西太平洋暖池海温异常呈显著的滞后相关关系,西太平洋暖池的热状况在联系 SIOD 与夏季我国东部地区降水异常的关系中起重要作用[100]。

SIOD 形成后,通过热力强迫影响并调整着局地大气环流。副热带中纬度南印度洋区域海温变化对邻近区域环流及降水具有显著影响[98-99,107-108]。亚洲夏季风的来源可以追溯到南半球中高纬度地区,马斯克林高压、索马里越赤道气流、孟加拉湾越赤道气流等季风环流系统正是以副热带印度洋区域作为其直接下垫面或源区[109],SIOD 对局地环流有影响,也间接影响着亚洲季风系统。SIOD 为正位相时,夏季马斯克林高压增强,进而使得索马里越赤道气流增强,在印度地区低空产生异常辐合、高层辐散,从而增强印度季风环流,使得印度季风降水偏多,印度季风偏强[101];SIOD 为负位相时,情况相反。另外,SIOD 海温异常分布型对南海夏季风建立早晚起重要作用[110-111],SIOD 通过加大(减弱)东亚和西太平洋区域的海陆热力差异以及增强(减弱)南海区域的对流活动对南海夏季风产生影响。前期 SIOD 为正(负)位相时,南海夏季风建立较早(晚)。SIOD 与马斯克林高压变化的关系明显,并通过马斯克林高压的影响,使得南半球中高纬度地区出现异常波列,再通过 Hadley 环流的变化,对北半球环流产生影响[70]。因此,SIOD 形成后通过热力强迫不仅影响局地大气环流,还对南北半球环流、亚洲季风系统产生影响,并影响我国夏季降水的分布。概括已有研究成果,SIOD 主要通过 3 种途径影响我国夏季降水:①通过影响当地马斯克林高压的强度而改变越赤道气流强度,进而影响印度夏季风对中国地区的西南水汽输送条件;②暖海温异常在热带中东印度洋和海洋大陆可以维持到秋季,影响当地对流以及来自印度洋和太平洋水汽输送通道上的量值和输送方向,从而改变进入东亚的水汽输送条件;③改变西北太平洋副热带高压的位置和强度,对我国夏季降水造成影响。

总之,春季 SIOD 可以通过影响南北半球环流系统和亚洲夏季风系统,进而对我国夏季降水产生影响。具体表现:SIOD 正位相年,黄河及其以北、以东区域、华南地区降水明显偏多,长江流域降水偏

少;SIOD负位相年,西南、江南、黄淮地区降水偏多[70,100,103]。

3 大西洋海温异常对东亚夏季风的影响

早在20世纪80年代就有研究指出,冬季北大西洋的海温异常能够引起欧亚环流的显著变化,并可进一步影响到同期冬季东亚的地表气候[112]。实际上,北大西洋海温异常对东亚夏季气候也存在显著影响,但这方面研究直到最近几年才受到人们的重视。Wu等[113]指出,在年际时间尺度上东亚夏季风的增强(减弱)与春—夏季北大西洋区域经向上呈现为"－＋－"("＋－＋")的三极子型海温异常(以下称为北大西洋海温三极子)显著相关。其中,显著负相关主要出现在北大西洋热带和副极地地区,而显著正相关主要出现在美国东部海域。在年代际时间尺度上,当长江中下游夏季梅雨降水偏少(多)时,前期冬季北大西洋的海温异常也呈现为一种"－＋－"("＋－＋")的三极子型[114]。观测分析和数值试验结果表明,夏季北大西洋海温三极子可以激发出一支跨越欧亚大陆的准正压的纬向遥相关波列,并通过该波列引起东亚夏季风的强弱变化[115]。其中,对应于北大西洋海温三极子的正位相("－＋－"),美国东部和西欧上空主要为显著的反气旋式环流异常,而副极地北大西洋和乌拉尔山地区上空为气旋式环流异常;反之亦然。由于乌拉尔山环流形势是影响东亚夏季风降水的关键环流系统[116],若乌拉尔山地区上空的位势高度场异常偏高(低),则该地区阻塞高压增强(减弱),有利于梅雨锋偏强(弱),使长江中下游梅雨降水偏多(少),东亚夏季风偏弱(强)。当夏季北大西洋海温三极子处于正(负)位相时,乌拉尔山地区上空主要为负(正)的高度异常所控制,因此,有利于长江中下游梅雨降水偏少(多)和东亚夏季风偏强(弱)。

北大西洋海温三极子的形成受局地上方北大西洋涛动(NAO)型的环流异常所控制[117-118]。由冬至夏,NAO的活动中心将会发生系统性北移[119],它所激发的海温三极子也随之北移。Zuo等[115]分析发现,对东亚夏季风存在显著影响的北大西洋海温三极子实际上是由前期春季的NAO异常激发形成的,而与同期夏季的NAO异常无明显联系。其中,夏季NAO异常所激发的海温三极子主要位于热带外北大西洋;而春季NAO异常所激发的海温三极子的位置较偏南,其低纬度异常中心出现在热带北大西洋。这也说明,东亚夏季风环流对北大西洋海温三极子的响应敏感于对后者的经向位置异常。研究还指出,东亚夏季风与北大西洋海温三极子的年际关系在20世纪70年代之前较弱,而之后明显增强,这种年代际不稳定性与NAO的影响有关[120]。

除了北大西洋外,南大西洋的海温异常对东亚夏季风和我国夏季降水也可能存在显著影响。例如,在年代际时间尺度上我国华北地区夏季降水与南大西洋海温异常之间存在显著负相关关系[121]。但南大西洋海温异常对我国夏季降水的影响机理尚不明确。此外,在厄尔尼诺事件成熟的次年夏季,热带大西洋海温往往高于其气候平均值;反之亦然[122]。耦合模式的试验结果显示,只有在考虑大西洋海温变化的情况下,模式才能够较好地再现ENSO成熟次年印度—东亚季风区大气环流异常的主要特征[123-124]。因此,与印度洋类似,热带大西洋海温异常在联系ENSO对东亚夏季风的影响中发挥着重要作用。

4 总结和展望

本文主要回顾了太平洋ENSO事件、印度洋海温、大西洋海温年际变率对东亚夏季风以及我国夏季降水的影响机理研究。需要指出的是,近几年关于不同分布型厄尔尼诺对东亚气候的不同影响、热带印度洋海温的作用、南印度洋偶极子的作用,菲律宾异常反气旋环流的发展演变特征及物理机制、大西洋海温异常型的作用等研究已经在气候异常诊断和短期预测业务中发挥了重要作用。

与厄尔尼诺的分布型及其气候影响的大量研究相比,拉尼娜的分类及气候影响的研究相对较少,有些研究认为拉尼娜事件的东部型和中部型特征非常相似,可能不存在不同的分布类型[52,125-126]。最新研究根据成熟期标准化的Niño3和Niño4指数及成熟期海温距平的空间分布特征,将1950年以来的14次拉尼娜事件分为了东部型和中部型,并指出热带大气对这两类不同分布型拉尼娜事件的响应特征具有显著差异[127-128]。值得注意的是,尽管拉尼娜事件的气候影响可能没有厄尔尼诺事件显著,但是拉尼娜事件的发展演变特征以及对东亚气候的影响却表现出与厄尔尼诺事件明显的非对称性。Zhang等[39]利用东亚沿岸对流层低层的经向风作为东亚

季风指数,分析了与 Niño3 区海面温度异常之间的关系,指出厄尔尼诺盛期时东亚季风异常显著,而拉尼娜期间东亚季风异常在统计上不显著,指出东亚季风对厄尔尼诺和拉尼娜响应的不对称性。还有研究表达了类似观点[129-131]。因此,鉴于拉尼娜影响的复杂性及其与厄尔尼诺影响的非对称性,关于拉尼娜的不同分布型及其对东亚季风和我国气候异常的影响更值得深入分析。

热带印度洋全区一致海温模态经常发生在 ENSO 事件成熟的冬季和次年春季,TIOD 也常发生在厄尔尼诺(拉尼娜)发生年的夏秋季,但反过来也会影响 ENSO 事件的强度。有研究表明[102],SIOD 事件就像连接正负 ENSO 位相转换的一个环节,不仅涉及海气相互作用的正负反馈过程,还与热带和副热带大气环流之间的相互作用有关。因此印度洋海气相互作用是全球海气相互作用的一部分,印度洋不同海温异常分布型与不同类型 ENSO 事件的相互联系及独立作用对于亚洲季风系统和我国气候的影响需要进一步探讨。另外,印度洋海气相互作用与南半球中高纬度大气环流之间的联系及影响、与青藏高原形成的南北海陆热力对比、与北半球中高纬度环流系统的多因子多尺度相互作用及对我国夏季气候的影响非常复杂,也是未来气候预测需要深入探索的方向。

热带外北大西洋海温的年际变率主要受大气环流控制,而前者对后者往往也存在显著的反馈作用[132]。在北大西洋海温三极子影响东亚夏季风强弱变化的过程中,虽然热带海温异常所引起的非绝热加热起主导作用,但是热带外海温异常的贡献仍需要在未来利用对大气内部变率有较好模拟能力的气候模式进行深入研究[115]。

在实际的气候预测业务中,需要面临的问题非常复杂,有的年份海温异常信号强且异常信息对东亚夏季风的影响比较一致,有利于预报员根据已有研究成果进行分析,但这种年份并不多;有的年份海温异常信号强,但是不同海域的异常信息对东亚夏季风的影响不一致甚至矛盾,因而很难判断采用哪个强信号;有的年份海温异常信号弱,根据强信号影响的研究成果对这些海温接近常年的特征不适用,使得预报员无所适从。因此,针对实际气候预测业务,海温的影响领域还有大量的研究工作要做。此外,本文主要回顾了各大洋独立的海温年际变化特征及其对东亚夏季风年际变率的影响,没有考虑各大洋海温异常对我国气候变异的综合影响、海温异常的年代际变化及其对东亚夏季风的影响以及海温异常的多时间尺度特征与东亚夏季风的联系。在这些领域已经有一些研究工作[133-135],值得进一步梳理和应用。

参考文献

[1] 李维京. 现代气候业务. 北京:气象出版社,2012:202-203.

[2] 刘永强,丁一汇. ENSO 事件对我国天气气候的影响. 应用气象学报,1992,3(4):473-481.

[3] 倪允琪,沈新勇. ENSO 动力学及其数值模拟的研究评述. 应用气象学报,1998,9(2):239-245.

[4] 金祖辉,陶诗言. ENSO 循环与中国东部地区夏季和冬季降水关系的研究. 大气科学,1999,23(6):663-672.

[5] 张人禾,李强. 热带海洋变异对东亚季风的影响. 气象,2004,30(12):22-26.

[6] 王蕾,张人禾. 不同区域海温异常对中国夏季旱涝影响的诊断研究和预测试验. 大气科学,2006,30(6):1147-1159.

[7] 张人禾,殷永红,李清泉,等. 利用 ARGO 资料改进 ENSO 和我国夏季降水气候预测. 应用气象学报,2006,17(5):538-547.

[8] 魏凤英. 我国短期气候预测的物理基础及其预测思路. 应用气象学报,2011,22(1):1-11.

[9] 王万秋. 土壤温湿异常对短期气候影响的数值模拟试验. 大气科学,1991,15(5):115-123.

[10] 李巧萍,丁一汇,董文杰. 土壤湿度异常对区域短期气候影响的数值模拟试验. 应用气象学报,2007,18(1):1-11.

[11] Zhang R H, Zuo Z Y. Impact of spring soil moisture on surface energy balance and summer monsoon circulation over East Asia and precipitation in East China. *J Climate*, 2011, 24:3309-3322.

[12] 陈烈庭,阎志新. 青藏高原冬春季积雪对大气环流和我国南方汛期降水的影响//中长期水文气象预报文集(第一集). 北京:水利电力出版社,1979:145-148.

[13] 韦志刚,罗四维,董文杰,等. 青藏高原积雪资料分析及其与我国夏季降水的关系. 应用气象学报,1998,9(增刊):39-46.

[14] Wu B Y, Yang K, Zhang R H. Eurasian snow cover variability and its association with summer rainfall in China. *Adv Atmos Sci*, 2009, 26(1):31-44, doi:10.1007/s00376-009-0031-2.

[15] Zhao P, Zhang X, Zhou X J, et al. Sea-ice extent anomaly in the North Pacific and impact on the East Asian summer monsoon rainfall. *J Climate*, 2004, 17:3434-3447.

[16] 王嘉,郭裕福. 北半球海冰强迫作用下大气可预报性研究. 应用气象学报,2004,15(3):291-305.

[17] Wu B, Zhang R, Wang B, et al. On the association between spring Arctic sea ice concentration and Chinese summer rainfall. *Geophys Res Lett*, 2009, 36, L09501, doi: 10.1029/2009GL037299.

[18] Zhang J Y, Dong W J, Fu C B, et al. The influence of vegetation cover on summer precipitation in China: A statistical a-

nalysis of NDVI and climate data. *Adv Atmos Sci*, 2003, 20(6): 1002-1006.

[19] Zuo Z Y, Zhang R H, Zhao P. The relation of vegetation over the Tibetan Plateau to rainfall in China during the boreal summer. *Clim Dyn*, 2011, 36: 1207-1219.

[20] 陈兴芳，赵振国. 中国汛期降水预测研究及应用. 北京：气象出版社，2000：191-194.

[21] 王绍武. 现代气候学研究进展. 北京：气象出版社，2001：304-326.

[22] Wang B, Wu R G, Fu X. Pacific-East Asian teleconnection: How does ENSO affect East Asian climate? *J Climate*, 2000, 13: 1517-1535.

[23] Wang B, Ding Q, Fu X, et al. Fundamental challenge in simulation and prediction of summer monsoon rainfall. *Geophys Res Lett*, 2005, 32, L15711, doi: 10.1029/2005GL022734.

[24] Zhang Renhe, Akimasa Sumi, Masahide Kinoto. A diagnostic study of the impact of El Nino on the precipitation in China. *Adv Atmos Sci*, 1999, 16(2): 229-241.

[25] Ropelewski C F, Halpert M S. Global and regional scale precipitation patterns associated with the El Niño/Southern Oscillation. *Mon Wea Rev*, 1987, 115: 1606-1626.

[26] Ropelewski C F, Halpert M S. Precipitation patterns associated with the high index phase of the Southern Oscillation. *J Climate*, 1989, 2: 268-284.

[27] Halpert M S, Ropelewski C F. Surface temperature patterns associated with the Southern Oscillation. *J Climate*, 1992, 5: 577-593.

[28] Huang R H, Wu Y F. The influence of ENSO on the summer climate change in China and its mechanism. *Adv Atmos Sci*, 1989, 6: 21-32.

[29] 符淙斌，腾星林. 我国夏季的气候异常与埃尔尼诺/南方涛动现象的关系. 大气科学，1988，12(增刊)：133-141.

[30] 陈文. El Nino 和 La Nina 事件对东亚冬、夏季风循环的影响. 大气科学，2002，26(5)：595-610.

[31] 倪东鸿，孙照渤，赵玉春. ENSO 循环在夏季的不同位相对东亚夏季风的影响. 南京气象学院学报，2000，23(1)：18-54.

[32] Huang R H, Li C Y. Influence of the Heat Source Anomaly over the Tropical Western Pacific on the Subtropical High over East Asia. Proceeding of the International Conference on the General Circulation of East Asia, 1987: 40-51.

[33] Huang R H, Sun F Y. Impact of the tropical western Pacific on the East Asian summer monsoon. *J Meteor Soc Japan*, 1992, 70: 243-256.

[34] Huang R H, Yin B Y, Liu A D. Intraseasonal Variability of the East Asian Summer Monsoon and Its Association with the Convective Activities in the Tropical Western Pacific // Ye Duzheng. Climate Variability. Beijing: Chinese Meteorological Press, 1992: 134-155.

[35] 曹杰，黄荣辉，谢应齐，等. 西太平洋副热带高压演变物理机制的研究. 中国科学：D 辑，2002，32：659-666.

[36] Huang R H, Wu S S. Impact of the Thermal State of the Tropical Western Pacific on the Onset of the South China Sea Summer Monsoon. Proceedings of the Third International Symposium on Asian Monsoon System (ISAM3), 2001: 8-21.

[37] 黄荣辉，陈文，丁一汇，等. 关于季风动力学以及季风与 ENSO 循环相互作用的研究. 大气科学，2003，27(4)：484-502.

[38] 黄荣辉，陈文. 关于亚洲季风与 ENSO 循环相互作用研究最近的进展. 气候与环境研究，2002，7(2)：146-159.

[39] Zhang R H, Sumi A, Kimoto M. Impact of El Nino on the East Asian monsoon: A diagnostic study of the '86/87 and '91/92 events. *J Meteor Soc Japan*, 1996, 74: 49-62.

[40] Zhang R H, Sumi A. Moisture circulation over East Asia during El Nino episode in northern winter, spring and summer. *J Meteor Soc Japan*, 2002, 80: 213-227.

[41] Wang B, Zhang Q. Pacific-East Asian teleconnection. Part II: How the Philippine Sea anomalous anticyclone is established during El Niño development? *J Climate*, 2002, 15: 3252-3265.

[42] 高辉，王永光. ENSO 对中国夏季降水可预测性变化的研究. 气象学报，2007，65(1)：131-137.

[43] 宗海峰，陈烈庭，张庆云. ENSO 与中国夏季降水年际变化关系的不稳定性特征. 大气科学，2010，34(1)：184-192.

[44] 袁媛，杨辉，李崇银. 不同分布型 El Nino 事件及对中国次年夏季降水的可能影响. 气象学报，2012，70(3)：467-478.

[45] Rasmusson E M, Wallace J M. Meteorological aspects of El Niño/Southern Oscillation. *Science*, 1983, 222: 1195-1202.

[46] Fu C B, Diaz H, Fletcher J. Characteristics of the response of sea surface temperature in the central Pacific associated with the warm episodes of the Southern Oscillation. *Mon Wea Rev*, 1986, 114: 1716-1738.

[47] Wang B. Interdecadal changes in El Niño onset in the last four decades. *J Climate*, 1995, 8: 267-285.

[48] 李崇银. 气候动力学引论. 北京：气象出版社，2000：240-260.

[49] Ashok K, Behera S K, Rao S A, et al. El Niño Modoki and its possible teleconnection. *J Geophys Res*, 2007, 112: C11007, doi: 10.1029/2006JC003798.

[50] Yu J Y, Kao H Y. Decadal changes of ENSO persistence barrier in SST and ocean heat content indices: 1958—2001. *J Geophys Res*, 2007, 112, D13106, doi: 10.1029/2006JD007654.

[51] Kao H Y, Yu J Y. Contrasting Eastern-Pacific and Central-Pacific types of ENSO. *J Climate*, 2009, 22: 615-632.

[52] Kug J S, Jin F F, An S I. Two types of El Niño events: Cold tongue El Niño and warm pool El Niño. *J Climate*, 2009, 22: 1499-1515.

[53] Yeh S W, Kug J S, Dewitte B, et al. El Niño in a changing climate. *Nature*, 2009, 461: 511-514.

[54] Lee T, McPhaden M J. Increasing intensity of El Niño in the central-equatorial Pacific. *Geophys Res Lett*, 2010, 37, L14603, doi: 10.1029/2010GL044007.

[55] 任福民，袁媛，孙丞虎，等. 近 30 年 ENSO 研究进展回顾. 气象科技进展，2012，2(3)：17-24.

[56] Yuan Y, Yang S. Impacts of different types of El Niño on the

East Asian climate:Focus on ENSO cycles. *J Climate*,2012,25:7702-7722,doi:10.1175/JCLI-D-11-00576.1.

[57] Kim H M,Webster P J,Curry J A. Impact of shifting patterns of Pacific Ocean warming on North Atlantic tropical cyclones. *Science*,2009,325:77-80,doi:10.1126/science.1174062.

[58] Chen G,Tam C. Different impacts of two kinds of Pacific Ocean warming on tropical cyclone frequency over the western North Pacific. *Geophys Res Lett*,2010,37,L01803,doi:10.1029/2009GL041708.

[59] Wang G,Hendon H H. Sensitivity of Australian rainfall to inter-El Niño variations. *J Climate*,2007,20:4211-4226.

[60] Taschetto A S,England M H. El Niño Modoki impacts on Australian rainfall. *J Climate*,2009,22:3167-3174.

[61] Weng H Y,Ashok K,Behera S K,et al. Impacts of recent El Niño Modoki on dry/wet conditions in the Pacific Rim during boreal summer. *Climate Dyn*,2007,29:113-129.

[62] Weng H,Behera S K,Yamagata T. Anomalous winter climate conditions in the Pacific rim during recent El Niño Modoki and El Niño events. *Climate Dynamics*,2009,32:663-674,doi:10.1007/s00382-008-0394-6.

[63] Weng H,Wu G X,Liu Y M,et al. Anomalous summer climate in China influenced by the tropical Indo-Pacific Oceans. *Climate Dynamics*,2011,36:769-782,doi:10.1007/s00382-009-0658-9.

[64] Feng J,Chen W,Tam C Y,et al. Different impacts of El Niño and El Niño Modoki on China rainfall in the decaying phases. *Int J Climatol*,2011,31(14):2091-2101,doi:10.1002/joc.2217.

[65] Feng J,Wang L,Chen W,et al. Different impacts of two types of Pacific Ocean warming on Southeast Asian rainfall during boreal winter. *J Geophys Res*,2010,115,D24122,doi:10.1029/2010JD014761.

[66] Feng J,Li J. Influence of El Niño on spring rainfall over south China. *J Geophys Res*,2011,116,D13102,doi:10.1029/2010JD015160.

[67] Larkin N K,Harrison D E. Global seasonal temperature and precipitation anomalies during El Niño autumn and winter. *Geophys Res Lett*,2005,32:L13705,doi:10.1029/2005GL022738.

[68] Yuan Y,Yang S,Zhang Z Q. Different evolutions of the Philippine Sea anticyclone between Eastern and Central Pacific El Niño:Effects of Indian Ocean SST. *J Climate*,2012,25:7867-7883,doi:10.1175/JCLI-D-12-00004.1.

[69] 袁媛.热带印度洋海温异常及其与 ENSO 事件的相互联系.北京:中国科学院研究生院,2008.

[70] 晏红明,袁媛.印度洋海温异常的特征及其影响.北京:气象出版社,2012.

[71] Saji N H,Goswami B N,Vinayachandran P N,et al. A dipole mode in the tropical Indian Ocean. *Nature*,1999,401:360-363.

[72] Webster P J,Moore A M,Loschnigg J P,et al. Coupled ocean-atmosphere dynamics in the Indian Ocean during 1997—98. *Nature*,1999,401:356-360.

[73] 肖莺,张祖强,何金海.印度洋偶极子研究进展综述.热带气象学报,2009,25(5):621-627.

[74] 肖子牛,晏红明,李崇银.印度洋地区异常海温的偶极振荡与中国降水及温度的关系.热带气象学报,2002,18(4):335-344.

[75] 唐卫亚,孙照渤.印度洋海温偶极振荡对东亚环流及降水影响.南京气象学院学报,2005,28(3):316-322.

[76] 钱玮,管兆勇.中国南方夏季降水与热带印度洋偶极型海温异常的联系.南京气象学院学报,2007,30(1):9-16.

[77] 袁媛,李崇银.热带印度洋偶极子与 ENSO 事件关系的年代际变化.科学通报,2008,53(12):1429-1436.

[78] Yuan Y,Li C Y. Decadal variability of the IOD-ENSO relationship. *Chinese Science Bulletin*,2008,53:1745-1752.

[79] 刘宣飞,袁慧珍,管兆勇. ENSO 对 IOD 与中国夏季降水关系的影响.热带气象学报,2008,24(5):502-506.

[80] Meyers G. Variation of Indonesian throughflow and El Niño/Southern Oscillation. *J Geophys Res*,1996,101:12255-12263.

[81] Klein S A,Soden B J,Lau N C. Remote sea surface temperature variations during ENSO:Evidence for a tropical atmospheric bridge. *J Climate*,1999,12:917-932.

[82] Lau N C,Nath M J. Impact of ENSO on the variability of the Asian-Australian monsoons as simulated in GCM experiments. *J Climate*,2000,13:4287-4309.

[83] Yang S,Ding X,Zheng D,et al. Time-frequency characteristics of the relationships between tropical Indo-Pacific SSTs. *Adv Atmos Sci*,2007,24:343-359.

[84] Xie S P,Annamalai H,Schott F A,et al. Structure and mechanism of south Indian Ocean climate variability. *J Climate*,2002,15:864-878.

[85] Wu R,Kirtman B. Understanding the impacts of the Indian Ocean on ENSO variability in a coupled GCM. *J Climate*,2004,17:4019-4031.

[86] Annamalai H,Xie S P,McCreary J P,et al. Impact of Indian Ocean sea surface temperature on developing El Niño. *J Climate*,2005,18:302-319.

[87] Yang J,Liu Q,Xie S P,et al. Impact of the Indian Ocean SST basin mode on the Asian summer monsoon. *Geophys Res Lett*,2007,34,L02708,doi:10.1029/2006GL028571.

[88] Yuan Y,Zhou W,Chan J C L,et al. Impacts of the basin-wide Indian Ocean SSTA on the South China Sea summer monsoon onset. *Int J Climatol*,2008,28:1579-1587.

[89] Xie S P,Hu K,Hafner J,et al. Indian Ocean capacitor effect on Indo-western Pacific climate during the summer following El Niño. *J Climate*,2009,22:730-747.

[90] Chou C. Establishment of the low-level wind anomalies over the western North Pacific during ENSO development. *J Climate*,2004,17:2195-2212.

[91] Chen J M,Li T,Shih J. Fall persistence barrier of sea surface temperature in the South China Sea associated with ENSO. *J*

Climate,2007,20:158-172.
[92] Matsuno T. Quasi-geostrophic motions in the equatorial area. *J Meteor Soc Japan*,1966,44:25-43.
[93] Gill A E. Some simple solutions for heat induced tropical circulation. *Quart J Roy Meteor Soc*,1980,106:447-462.
[94] 李琰,王亚非,朱伟军.热带太平洋、印度洋海温异常在菲律宾海异常反气旋建立过程中的作用.气象学报,2010,68(6):865-876.
[95] Watanabe M,Jin F F. Role of Indian Ocean warming in the development of Philippine Sea anticyclone during ENSO. *Geophys Res Lett*,2002,29,1478,doi:10.1029/2001GL014318.
[96] Wu B,Zhou T,Li T. Seasonally evolving dominant interannual variability mode over the East Asia. *J Climate*,2009,22:2992-3005.
[97] Wu B,Li T,Zhou T. Asymmetry of atmospheric circulation anomalies over the western north Pacific between El Niño and La Nina. *J Climate*,2010,15:4807-4822.
[98] Reason C J C. Warm and cold events in the southeast Atlantic/southwest Indian Ocean region and potential impacts on circulation and rainfall over southern Africa. *Meteor Atmos Phys*,1998,69:49-65.
[99] Behera S K,Yamagata T. Subtropical SST dipole in the southern Indian. *Geophys Res Lett*,2001,28(2):327-330.
[100] 贾小龙,李崇银.南印度洋海温偶极子型振荡及其气候影响.地球物理学报,2005,48(6):1238-1249.
[101] 杨明珠,丁一汇.印度洋海表温度的变化及其对印度夏季季风降水影响的诊断研究.海洋学报,2006,28(4):9-16.
[102] 晏红明,李崇银,周文.南印度洋副热带偶极模在ENSO事件中的作用.地球物理学报,2009,52(10):2436-2449.
[103] 杨明珠,丁一汇.中国夏季降水对南印度洋偶极子的响应研究.大气科学,2007,31(4):685-694.
[104] Schouten M W,de Ruijter W P M,van Leeuwen P J,et al. An oceanic teleconnection between the equatorial and southern Indian Ocean. *Geophys Res Lett*,2002,29(16),doi:10.1029/2001GL014542-59-1-4.
[105] 杨秋明.南印度洋副热带偶极子型海温异常与全球环流和我国降水变化的关系.海洋学报,2006,28(3):47-56.
[106] Ray G P,White W B. Slow oceanic teleconnections linking the Antactic circumpolar wave with the tropical El Niño-Southern Oscillation. *J Geophys Res*,1998,103(C11):24573-24583.
[107] Mason S J. Sea-surface temperature-South African rainfall associations,1910—1989. *Int J Climatol*,1995,15:119-135.
[108] Reason C J C. Interannual warm and cool events in the subtropical mid-latitude South Indian Ocean region. *Geophys Res Lett*,1999,26(2):215-218.
[109] 丁一汇.高等天气学(第二版).北京:气象出版社,2005:212-235.
[110] 梁肇宁,温之平,吴丽姬.印度洋海温异常和南海夏季风建立迟早的关系:I耦合分析.大气科学,2006,30(4):619-634.
[111] 温之平,梁肇宁,吴丽姬.印度洋海温异常和南海夏季风建立迟早的关系:II机理分析.大气科学,2006,30(6):1138-1146.
[112] Gambo K,Lu L,Li W J. Numerical simulation of Eurasian teleconnection pattern in atmospheric circulation during the Northern Hemisphere winter. *Adv Atmos Sci*,1987,4(4):385-394.
[113] Wu Z,Wang B,Li J,et al. An empirical seasonal prediction model of the East Asian summer monsoon using ENSO and NAO. *J Geophys Res*,2009,114,D18120,doi:10.1029/2009JD011733.
[114] Gu W,Li C Y,Wang X,et al. Linkage between Mei-yu precipitation and North Atlantic SST on the decadal time scale. *Adv Atmos Sci*,2009,26(1):101-108.
[115] Zuo J Q,Li W J,Sun C H,et al. The impact of North Atlantic sea surface temperature tripole on the East Asian summer monsoon. *Adv Atmos Sci*,2013,doi:10.1007/s00376-012-2125-5.
[116] 张庆云,陶诗言.亚洲中高纬度环流对东亚夏季降水的影响.气象学报,1998,56(2):199-211.
[117] Deser C,Timlin M. Atmosphere-ocean interaction on weekly timescales in the North Atlantic and Pacific. *J Clim*,1997,10:393-408.
[118] 周天军,宇如聪,郜永琪,等.北大西洋年际变率的海气耦合模式模拟.I:局地海气相互作用.气象学报,2006,64(1):1-17.
[119] Barnston A G,Livezey R E. Classification,seasonality and persistence of low-frequency atmospheric circulation patterns. *Mon Wea Rev*,1987,115:1083-1126.
[120] 左金清,李维京,任宏利,等.春季北大西洋涛动与东亚夏季风年际关系的转变及其可能成因分析.地球物理学报,2012,55:384-395.
[121] 陈文,康丽华,王玎.中国夏季降水与全球海温的耦合关系分析.气候与环境研究,2006,11:259-269.
[122] Saravanan R,Chang P. Interaction between tropical Atlantic variability and El Niño-Southern Oscillation. *J Clim*,2000,13:2177-2194.
[123] Lu R,Dong B. Impact of Atlantic sea surface temperature anomalies on the summer climate in the western North Pacific during 1997—1998. *J Geophys Res*,2005,110:D16102,doi:10.1029/2004JD005676.
[124] 容新尧,张人禾,Li Tim.大西洋海温异常在ENSO影响印度-东亚夏季风中的作用.科学通报,2010,55(14):1397-1408.
[125] Kug J S,Ham Y G. Are there two types of La Niña? *Geophys Res Lett*,2011,38:L16704,doi:10.1029/2011GL048237.
[126] Shinoda T,Hurlburt H E,Metzger E J. Anomalous tropical ocean circulation associated with La Niña Modoki. *J Geophys Res*,2011,116:C12001,doi:10.1029/2011JC007304.
[127] 袁媛,晏红明.不同分布型La Nina事件及热带大气的响应特征对比.科学通报,2012,57(34):3312-3322.

[128] Yuan Y, Yan H M. Different types of La Niña events and different responses of the tropical atmosphere. *Chinese Science Bulletin*, 2013, 58(3): 406-415, doi: 10.1007/s11434-012-5423-5.

[129] Hoerling M P, Kumar A, Zhong M. El Niño, La Niña and the nonlinearity of their teleconnections. *J Climate*, 1997, 10: 1769-1786.

[130] Wu B, Li T, Zhou T. Relative contributions of the Indian Ocean and local SST anomalies to the maintenance of the western North Pacific anomalous anticyclone during El Niño decaying summer. *J Climate*, 2010, 23: 2974-2986.

[131] Wang X, Wang D X, Zhou W, et al. Interdecadal modulation of the influence of La Niña events on Mei-yu rainfall over the Yangtze River Valley. *Adv Atmos Sci*, 2012, 29: 157-168, doi: 10.1007/s00376-011-1021-8.

[132] Peng S, Robinson W A, Li S. Mechanisms for the NAO responses to the North Atlantic SST tripole. *J Climate*, 2003, 16: 1987-2004.

[133] Xie S P, Du Y, Huang G, et al. Decadal shift in El Niño influences on Indo-western Pacific and East Asian climate in the 1970s. *J Climate*, 2010, 23: 3352-3368.

[134] 马音,陈文,冯瑞权,等.我国东部梅雨期降水的年际和年代际变化特征及其与大气环流和海温的关系.大气科学,2012,36(2):397-410.

[135] Chen W, Feng J, Wu R. Roles of ENSO and PDO in the link of the East Asian winter monsoon to the following summer monsoon. *J Climate*, 2013, 26: 622-635.

A Review of Physical Mechanisms of the Global SSTA Impact on EASM

Chen Lijuan　Yuan Yuan　Yang Mingzhu　Zuo Jinqing　Li Weijing

(*Laboratory of Climate Studies*, *National Climate Center*, *CMA*, *Beijing* 100081)

Abstract

The impact of global sea surface temperature anomaly (SSTA) on the East Asia Summer Monsoon (EASM) and summer precipitation in China is reviewed from the aspects of physical mechanisms, on the basis of key external forcing signals in short-term climate prediction. Focusing on El Niño-Southern Oscillation (ENSO) cycle in the tropical Pacific and the main SSTA modes in Indian and Atlantic Ocean, their inter-annual variability are further reviewed as well as their different impacts on the EASM, especially their relationship with the main summer rainfall belt in China.

During different phases of ENSO cycle, ENSO exerts different impacts on the EASM and the summer precipitation in China. In the developing summer of El Niño, the EASM tends to be weak and the main summer rainfall belt would shift southward in eastern China. However, in the decaying summer of El Niño, the EASM tends to be strong, and the summer precipitation would be below normal in the Yangtze-Huaihe Valley. The situations are approximately reverse for the impact of La Niña on the EASM and summer precipitation in China, although the impact of La Niña is not as significant. The influence of ENSO on the EASM and the summer rainfall belt in China is closely correlated with the SSTA in the western Pacific warm pool as well as the resulted convective activities in its northern part. Moreover, the Philippine Sea anticyclone also plays an important role. In recent years, different types of El Niño are widely discussed. It is revealed that the Central Pacific (CP) El Niño not only has different evolution mechanisms, but also shows different impacts on the global atmospheric circulation as compared with the Eastern Pacific (EP) El Niño or classical El Niño.

Indian Ocean SSTA modes also show significant influences on the EASM and the summer precipitation in China. For example, the basin-wide warming (cooling) mode in the tropical Indian Ocean would cause a late (an early) South China Sea summer monsoon (SCSSM) onset; in the summer of positive (negative) tropical Indian Ocean dipole phase, more precipitation would occur in South China (North China); during the positive (negative) phase of subtropical southern Indian Ocean dipole, Indian summer monsoon tends to be stronger (weaker), and SCSSM may establish earlier (later). The positive (negative) North Atlantic tri-pole mode would lead to a stronger (weaker) EASM through motivating quasi-barotropic zonal tele-connection wave train across the Eurasian continent.

SSTA is the important pre-signal on the prediction of summer precipitation anomaly in China. Because of the predictability of short-term climate prediction, it is still difficult to give high skill prediction for summer rainfall anomaly in China. Some advices and requirements on the physical mechanism research and dynamical model development are proposed in order to improve the prediction of the EASM and summer rainfall in China.

Key words: external forcing signal; SSTA; EASM; summer precipitation

《应用气象学报》征稿简则

《应用气象学报》(双月刊)是大气科学理论与应用研究的综合性学术期刊,主要刊登反映新理论与新技术在大气科学中的应用,以及大气科学理论与实践相结合,应用于各个有关领域的研究论文、业务系统和研究简报;国内外大气科学与应用气象科学发展中的新动态与新问题的探讨与评论;国内外重要学术会议或研究、业务活动的报道;气象书刊评介。

投稿要求和注意事项:

1. 论点明确、文字精炼。摘要请按文摘四要素(目的、方法、结果、结论)撰写,列出3~8个关键词,作者姓名请附汉语拼音,所在单位请附中、英文全名、地名、邮编。要求中文摘要为200~400字,英文摘要为500个单词左右(并请附对应的中文译文)。

2. 插图请插入文中适当位置,要求准确、清晰、美观。图中物理量、单位请勿遗漏,中、英文图题及说明写在插图下面。表格请采用三线表形式,并列出中、英文表题。

3. 参考文献请择主要的列入,并请按文中引用顺序标号。期刊书写格式:作者.文章题目.刊名,年,卷(期):起止页.专著书写格式:作者.书名.译编者.出版地:出版社,出版年:起止页.

4. 计量单位请按《中华人民共和国法定计量单位》列出,已废止的单位请换算成法定计量单位。

5. 科技术语和名词请使用全国自然科学名词审定委员会公布的名词。外国人名和地名,除常用者外请注原文。

6. **网上投稿(http://qk.cams.cma.gov.cn)请同时寄送全体作者签名的《承诺书》(请网上自行下载)。**稿件自收到之日起,将在6个月内决定刊用与否,来稿一经刊登,酌情收取版面费,并酌付稿酬。

7. 文中的数字及符号必须清楚无误,易混淆的外文字母、符号,请标注文种,大、小写,正、斜体,黑、白体,公式中的上、下标。

8. 本刊已加入"中国学术期刊(光盘版)"、"万方数据——数字化期刊群"和"中文科技期刊数据库"。本刊所付稿酬包含光盘稿酬和刊物内容上网服务报酬。凡向本刊投稿的作者(除事先声明外),本刊视为同意将其稿件纳入此两种版本进行交流。

欢迎投稿。投稿请登录 qk.cams.cma.gov.cn。

地址:中国气象科学研究院《应用气象学报》编辑部,邮政编码:100081;电话:(010)68407086,68408638;网址:qk.cams.cma.gov.cn;E-mail:yyqxxb@cams.cma.gov.cn,yyqxxb@163.com。

缓变下垫面对浅水方程的动力学订正*

达朝究[1)2)†] 冯爱霞[3)] 龚志强[3)] 宋健[4)]

1) (西北民族大学数学与计算机科学学院, 兰州 730030)

2) (兰州大学大气科学学院, 兰州 730000)

3) (国家气候中心气候研究开放实验室, 北京 100081)

4) (内蒙古工业大学理学院, 呼和浩特 010062)

(2012 年 7 月 4 日收到; 2012 年 9 月 7 日收到修改稿)

讨论了当下垫面随时间缓慢变化时浅水方程的形式. 从控制大气运动的连续性方程和动量方程出发, 将下垫面的缓慢变化作为一个小量叠加到固有下垫面函数上, 利用大气的上下边界条件, 得到改进的浅水方程. 在改进的浅水方程中, 由缓变局部水平体积散度, 订正了局部水平体积散度和流体局部厚度变化之间的平衡, 在此基础上得到包含下垫面缓变的涡度方程.

关键词: 下垫面, 全球变暖, 缓变, 浅水方程

PACS: 92.40.Cy, 92.60.Aa **DOI:** 10.7498/aps.62.039202

1 引 言

大气的下垫面指地球表面, 包括海洋、陆地及陆地上的高原、山地、平原、森林、草原、城市等等. 下垫面的性质和形状, 对大气的热量、水分、干洁度和运动状况有明显的影响; 在陆地上, 巨大的山地和高原对气候的形成与影响有着不可忽视的作用, 而在海洋上, 海平面的变化、海水成分的变化, 以及海洋环流的异常无疑会影响大气环流, 进而影响气候.

全球变暖对大气、海洋系统及社会经济体系具有深远的影响. 以全球气候变化为核心的全球变化问题, 引起各国政府、科学工作者的高度重视, 也是普通民众广泛关注的问题, 20 世纪 80 年代以来, 在全球范围内开展了全球气候变化及其影响的研究 [1−10].

全球变暖对陆地生态系统的影响及其反馈, 是全球变化研究的焦点, 全球变化对陆地生态系统的影响已经进行了大量的研究, 这主要体现在陆地结构、植被变化和气候变化的关联 [11−13], 这种关联的年际气候变化表现为区域增温和降水波动 [14], 对气候变暖的响应呈现出全球气候增暖的趋势 [15], 这势必对我国区域发展带来影响 [16,17], 但是陆地系统的变化对气候变化的影响还没有定量的研究; 全球变暖以后, 两极冰盖融化, 大量的淡水进入海洋, 造成海平面的上升, 这会影响到海水的物理结构, 在持续温暖的条件下, 海水的膨胀率也会增长. 这种变化是一种缓变性海洋灾害, 其长期的累积效应将加剧风暴潮、海岸侵蚀、海水入侵、土壤盐渍化和咸潮等海洋灾害的致灾程度 [18−23], 同样海平面的上升对气候变化的影响也没有定量的研究.

在全球变暖条件下, 就极端事件的发生和发展, 封国林, 侯威, 龚志强等做了系统的研究. 首先对于极端事件进行了理论研究, 给出了一种确定极端事件阈值的新方法 [24], 对于温度破纪录事件和温度极端事件也做了研究, 得到中国各地区极端温度变化幅度差异明显, 具有明显的区域特征 [25],

* 全球变化研究国家重大科学研究计划 (批准号: 2012CB955902)、国家自然科学基金 (批准号: 40930952, 41175067)、国家科技支撑计划 (批准号: 2009BAC51B04)、公益性行业 (气象) 科研专项 (批准号: GYHY201106016, GYHY201206009)、内蒙古自然科学基金 (批准号: 2011MS0112) 和中央高校基本科研业务费专项资金 (批准号: zyz2011079) 资助的课题.

† 通讯作者. E-mail: jtdcj@163.com

给出了温度突变的过程可能是极端温度事件由一个相对稳定状态向另一个稳定状态演变过程的结论[26], 气候变暖对中国极端暖月事件的变率有明显影响[27], 全球增暖与中国温度破纪录事件的时空分布有一定的关联, 随着全球变暖趋势的不断增强, 破纪录温度事件发生的频次呈现不断增加的特点[28,29].

综上所述, 可以知道在全球变暖和人类活动的双重影响下, 大气的下垫面会发生变化, 这种变化会对气候有反馈作用[30,31], 而气候的变化也会对社会经济发展产生影响[32]! 大气下垫面的变化对气候的反馈作用就是本文要解决的问题, 讨论正压均值流体在下垫面发生缓慢变化时, 浅水方程的形式, 以及对应涡度方程的变化.

2 缓变地形下的浅水方程

2.1 基础知识

2.1.1 连续性方程与运动方程

当流体内部无质量源、汇时, 连续性方程为[33]

$$\frac{\partial\rho}{\partial t}+\nabla\cdot\rho\boldsymbol{u}=0, \tag{1a}$$

这里 ρ 是密度, p 是压力, $\boldsymbol{u}$ 是速度矢量, 都是时间 t 和空间坐标 (x,y,z) 的函数. 上式用全导数形式还可写为

$$\frac{\mathrm{d}\rho}{\mathrm{d}t}+\rho\nabla\cdot\boldsymbol{u}=0, \tag{1b}$$

这里 $\dfrac{\mathrm{d}}{\mathrm{d}t}\equiv\dfrac{\partial}{\partial t}+\boldsymbol{u}\cdot\nabla$ 是全导数.

运动方程为[33]

$$\rho\frac{\mathrm{d}\boldsymbol{u}}{\mathrm{d}t}=-\nabla p+\rho\nabla\phi+\boldsymbol{F}(\boldsymbol{u}). \tag{2}$$

这里 ϕ 是保守彻体力 (the body force)[33,34] 的位势, 是已知量. 而 $\boldsymbol{F}(\boldsymbol{u})$ 是非保守力, 在本文中表示大气、海洋这样牛顿流体的摩擦力, $\boldsymbol{F}(\boldsymbol{u})$ 有如下的近似表示

$$\boldsymbol{F}(\boldsymbol{u})\approx\mu\Delta\boldsymbol{u}+\frac{\mu}{3}\nabla(\nabla\cdot\boldsymbol{u}). \tag{3}$$

假设 μ 和 ρ 是常数, 方程 (1) 与方程 (2) 就封闭[33], 未知的变量只有速度 $\boldsymbol{u}$ 与压力 p.

2.1.2 旋转坐标系中的运动方程

对于大气与海洋, 由于它们随地球旋转, 而运动方程 (2) 是在惯性坐标系中描述的, 以地球角速度 Ω 旋转的坐标系中描述大气海洋的运动方程 (2) 为[33]

$$\rho\left(\frac{\mathrm{d}\boldsymbol{u}}{\mathrm{d}t}+2\Omega\times\boldsymbol{u}\right)=-\nabla p+\rho\nabla\boldsymbol{\Phi}+\boldsymbol{F}, \tag{4}$$

这里 $\boldsymbol{u}$ 是地球上观测到的速度, 是相对速度, p 是压力, 而 $\boldsymbol{\Phi}$ 是位势函数 ϕ 与由于旋转而产生的向心加速度 $\Omega\times(\Omega\times\boldsymbol{r})$ 的位势函数 ϕ_c 之和; $\dfrac{\mathrm{d}\boldsymbol{u}}{\mathrm{d}t}$ 称为相对加速度, $2\Omega\times\boldsymbol{u}$ 是科氏加速度[33].

方程 (1) 在旋转坐标系中没有变化, 仍为

$$\frac{\mathrm{d}\rho}{\mathrm{d}t}+\rho\nabla\cdot\boldsymbol{u}=0. \tag{5}$$

2.2 缓变下垫面下的浅水方程

如图 1 所示, 具有均匀常值密度 ($\rho=\mathrm{const}$) 的一层流体, 自参考面 $z=0$ 算起, 流体的表面高度为 $h(x,y,t)$. 考虑到地球对大气、海洋的作用, 把由位势 $\boldsymbol{\Phi}$ 引起的彻体力模式化为一个矢量 $\boldsymbol{g}$, 其方向垂直于 $z=0$ 平面, 即 $\boldsymbol{\Omega}=k\Omega$, 与垂直坐标轴平行、方向相反[33−35]. 在我们的研究问题中, 流体的旋转

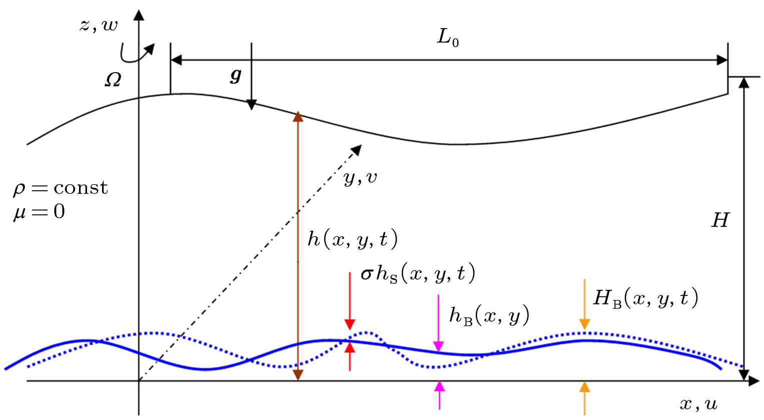

图 1 浅水模式

轴与 z 轴重合, 所以在此情况下, 科氏参数 f 就是 $2\Omega\sin\theta$ (Ω 是地转角速度, θ 为纬度). 由于全球变暖, 地球下垫面随时间会缓变, 将其细化为两部分: 大气海洋的固有下垫面和随时间缓慢变化部分, 记其形式为

$$z\equiv H_{\mathrm{B}}(x,y,t)=h_{\mathrm{B}}(x,y)+\sigma h_{\mathrm{S}}(x,y,t),\tag{6}$$

这里 $H_{\mathrm{B}}(x,y,t)$ 是大气海洋下垫面, $h_{\mathrm{B}}(x,y)$ 为大气海洋固有下垫面, 而 $h_{\mathrm{S}}(x,y,t)$ 为随时间缓慢变化的部分, 参数 σ 是刻画这种缓慢变化程度的一小量, 显然, 当参数 $\sigma=0$ 时, 问题就退化为大气下垫面没有缓变的情况; 平行于 x, y 和 z 轴的速度分量分别是 u, v, w; 施加在流体表面的压力可以是任意的, 在本文中取其为常数; 最后, 我们假设流体是无黏性, 即 $\mu=0$, 或者在讨论中流体的黏滞性不是太重要 [33–35].

显然, 流体的深度 $h(x,y,t)$-$H_{\mathrm{B}}(x,y,t)$ 随时间和空间变化的. 假设流体的深度特征量是已知量, 记其为 H. 同样, 假设存在一个运动的水平特征量, 记为 L_0. 表征浅水理论的基本参数条件是

$$\delta=H/L_0\ll 1,\tag{7}$$

δ 就是形态比, 是描述水平运动与垂直运动关系的一个量 [33–35]. 由于假设密度是常数, 所以连续性方程 (5) 简化为不可压缩条件

$$\frac{\partial u}{\partial x}+\frac{\partial v}{\partial y}+\frac{\partial w}{\partial z}=0,\tag{8}$$

为了研究方便, 将压力 $p(x,y,z,t)$ 写为 [33–35]

$$p(x,y,z,t)=-\rho gz+\tilde{p}(x,y,z,t),\tag{9}$$

上式右侧第一项将于单位质量流体所受的常值重力抵消. 假设无黏, 这时候运动方程 (4) 的分量形式有如下表示

$$\frac{\partial u}{\partial t}+u\frac{\partial u}{\partial x}+v\frac{\partial u}{\partial y}+w\frac{\partial u}{\partial z}-fv=-\frac{1}{\rho}\frac{\partial \tilde{p}}{\partial x},\tag{10a}$$

$$\frac{\partial v}{\partial t}+u\frac{\partial v}{\partial x}+v\frac{\partial v}{\partial y}+w\frac{\partial v}{\partial z}+fu=-\frac{1}{\rho}\frac{\partial \tilde{p}}{\partial y},\tag{10b}$$

$$\frac{\partial w}{\partial t}+u\frac{\partial w}{\partial x}+v\frac{\partial w}{\partial y}+w\frac{\partial w}{\partial z}=-\frac{1}{\rho}\frac{\partial \tilde{p}}{\partial z},\tag{10c}$$

在推导 (10a), (10b) 的过程中, $f=2\Omega\sin\theta$. 根据浅流体模式的定义, 用总压力 $p(x,y,z,t)$ 表示, 有

$$\frac{\partial p}{\partial z}=-\rho g+O(\delta^2),\tag{11}$$

上式就是静力近似 [33–35]. 关于 z 积分 (11) 式, 得

$$p(x,y,z,t)=-\rho gz+A(x,y,t),\tag{12}$$

这里 $A(x,y,t)$ 是积分常数, 由上、下边界条件来定. 为了讨论方便取上边界条件为

$$p(x,y,h,t)=p_0,\tag{13}$$

也就是施加在流体表面的压力为 p_0, 这里的 p_0 为常数. 所以

$$A(x,y,t)=p_0+\rho gh.\tag{14}$$

将 (14) 式代入 (12) 式, 得

$$p(x,y,z,t)=p_0+\rho g(h-z),\tag{15}$$

由 (15) 式知道: 水平压力梯度与 z 无关, 即

$$\frac{\partial p}{\partial x}=\rho g\frac{\partial h}{\partial x},\tag{16a}$$

$$\frac{\partial p}{\partial y}=\rho g\frac{\partial h}{\partial y}.\tag{16b}$$

所以水平加速度必然与 z 无关, 假设初始水平速度与 z 无关, 则在以后的运动中仍能够保持与 z 无关, 这样水平动量方程为

$$\frac{\partial u}{\partial t}+u\frac{\partial u}{\partial x}+v\frac{\partial u}{\partial y}-fv=-g\frac{\partial h}{\partial x},\tag{17a}$$

$$\frac{\partial v}{\partial t}+u\frac{\partial v}{\partial x}+v\frac{\partial v}{\partial y}+fu=-g\frac{\partial h}{\partial y}.\tag{17b}$$

由于水平速度 u, v 与 z 无关, 将 (8) 式关于 z 积分得

$$w(x,y,z,t)=-z\left(\frac{\partial u}{\partial x}+\frac{\partial v}{\partial y}\right)+\tilde{w}(x,y,t),\tag{18}$$

上式中的 $\tilde{w}(x,y,t)$ 为积分常数, 利用刚性地面 $z\equiv H_{\mathrm{B}}(x,y,t)=h_{\mathrm{B}}(x,y)+\sigma h_{\mathrm{S}}(x,y,t)$ 处法向速度为零的条件 [36], 有

$$\begin{aligned}&w(x,y,H_B(x,y,t),t)\\&=u\frac{\partial h_{\mathrm{B}}}{\partial x}+v\frac{\partial h_{\mathrm{B}}}{\partial y}+\sigma\left(u\frac{\partial h_{\mathrm{S}}}{\partial x}+v\frac{\partial h_{\mathrm{S}}}{\partial y}\right),\end{aligned}\tag{19}$$

得到

$$\begin{aligned}\tilde{w}(x,y,t)=&\left(u\frac{\partial h_{\mathrm{B}}}{\partial x}+v\frac{\partial h_{\mathrm{B}}}{\partial y}\right)+\sigma\left(u\frac{\partial h_{\mathrm{S}}}{\partial x}+v\frac{\partial h_{\mathrm{S}}}{\partial y}\right)\\&+\left[h_{\mathrm{B}}(x,y)+\sigma h_{\mathrm{S}}(x,y,t)\right]\\&\times\left(\frac{\partial u}{\partial x}+\frac{\partial v}{\partial y}\right),\end{aligned}\tag{20}$$

故有

$$\begin{aligned}w(x,y,z,t)=&\left[h_{\mathrm{B}}(x,y)+\sigma h_{\mathrm{S}}(x,y,t)-z\right]\\&\times\left(\frac{\partial u}{\partial x}+\frac{\partial v}{\partial y}\right)+u\frac{\partial h_{\mathrm{B}}}{\partial x}+v\frac{\partial h_{\mathrm{B}}}{\partial y}\\&+\sigma\left(u\frac{\partial h_{\mathrm{S}}}{\partial x}+v\frac{\partial h_{\mathrm{S}}}{\partial y}\right).\end{aligned}\tag{21}$$

在自由面 $z=h$ 上相应的运动学条件是 [36]

$$w=\frac{\partial h}{\partial t}+u\frac{\partial h}{\partial x}+v\frac{\partial h}{\partial y},\quad z=h(x,y,t),\tag{22}$$

由 (21) 与 (22) 式得到

$$\begin{aligned}&\frac{\partial h}{\partial t}+u\frac{\partial h}{\partial x}+v\frac{\partial h}{\partial y}-[h_{\mathrm{B}}(x,y)+\sigma h_{\mathrm{S}}(x,y,t)-h]\\&\times\left(\frac{\partial u}{\partial x}+\frac{\partial v}{\partial y}\right)-u\frac{\partial h_{\mathrm{B}}}{\partial x}-v\frac{\partial h_{\mathrm{B}}}{\partial y}\\&-\sigma\left(u\frac{\partial h_{\mathrm{S}}}{\partial x}+v\frac{\partial h_{\mathrm{S}}}{\partial y}\right)=0,\end{aligned}\tag{23a}$$

即

$$\begin{aligned}&\frac{\partial(h-h_{\mathrm{B}})}{\partial t}+\nabla_{\mathrm{H}}\cdot\boldsymbol{u}_{\mathrm{H}}(h-h_{\mathrm{B}})\\&-\sigma\nabla_{\mathrm{H}}\cdot\boldsymbol{u}_{\mathrm{H}}h_{\mathrm{S}}(x,y,t)=0,\end{aligned}\tag{23b}$$

这里 ∇_{H} 是水平梯度算子, $\boldsymbol{u}_{\mathrm{H}}$ 是水平速度, 这较之没有地形缓变的方程 [33]

$$\frac{\partial(h-h_{\mathrm{B}})}{\partial t}+\nabla_{\mathrm{H}}\cdot\boldsymbol{u}_{\mathrm{H}}(h-h_{\mathrm{B}})=0\tag{24}$$

来说, 方程左侧的第三项就是下垫面缓变的效应, 该效应受参数 σ 的制约. 比较方程 (23b) 和方程 (24), 从方程 (24) 知道, 下垫面没有缓变时, 局部水平体积散度 $\nabla_{\mathrm{H}}\cdot\boldsymbol{u}_{\mathrm{H}}(h-h_{\mathrm{B}})$ 和流体局部厚度变化两者之间建立了平衡关系; 从方程 (23d) 知道, 当下垫面有缓变时, 局部水平体积散度 $\nabla_{\mathrm{H}}\cdot\boldsymbol{u}_{\mathrm{H}}(h-h_{\mathrm{B}})$、流体局部厚度变化以及缓变局部水平体积散度之间三者保持平衡关系, 方程 (23d) 订正原有平衡关系 (24), 更真实地反映动力学关系; 还可以看到, 当下垫面没有缓变时, 即前文所说的 $\sigma=0$, 方程 (23b) 就退化为方程 (24), 这说明方程 (23b) 是方程 (24) 的推广, 方程 (24) 是方程 (23b) 的特殊情况. 方程 (17a), (17b), (23) 构成缓变下垫面条件下的改进浅水模式方程组.

2.3 缓变地形位涡方程

在笛卡尔坐标系中, 相对涡度的三个分量是

$$\omega_x=\frac{\partial w}{\partial y}-\frac{\partial v}{\partial z},\tag{25a}$$

$$\omega_y=\frac{\partial u}{\partial z}-\frac{\partial w}{\partial x},\tag{25b}$$

$$\omega_z=\frac{\partial v}{\partial x}-\frac{\partial u}{\partial y},\tag{25c}$$

由于假设 u, v 与 z 无关, 有

$$\omega_x=\frac{\partial w}{\partial y}=O\left(\frac{W}{L}\right)=O\left(\delta\frac{U}{L}\right),\tag{26a}$$

$$\omega_y=-\frac{\partial w}{\partial x}=O\left(\frac{W}{L}\right)=O\left(\delta\frac{U}{L}\right),\tag{26b}$$

$$\omega_z=\frac{\partial v}{\partial x}-\frac{\partial u}{\partial y}=O\left(\frac{U}{L}\right),\tag{26c}$$

所以, 相对涡度的水平分量是其垂直分量的 $O(\delta)$ 倍. 如果将方程 (17a) 对 y 求微商, 将方程 (17b) 对 x 求微商, 消去 h, 便得

$$\begin{aligned}\frac{\mathrm{d}\zeta}{\mathrm{d}t}&\equiv\frac{\partial\zeta}{\partial t}+u\frac{\partial\zeta}{\partial x}+v\frac{\partial\zeta}{\partial y}\\&=-(\zeta+f)\left(\frac{\partial u}{\partial x}+\frac{\partial v}{\partial y}\right),\end{aligned}\tag{27}$$

式中引进了记号

$$\zeta\equiv\omega_x.\tag{28}$$

利用 (24) 式, 可以把 (27) 式写为

$$\begin{aligned}&\frac{\mathrm{d}(h-h_{\mathrm{B}})}{\mathrm{d}t}+(h_{\mathrm{B}}-h)\left(\frac{1}{(\zeta+f)}\frac{\mathrm{d}\zeta}{\mathrm{d}t}\right)+\sigma\Bigg[h_S(x,y,t)\\&\times\left(\frac{1}{(\zeta+f)}\frac{\mathrm{d}\zeta}{\mathrm{d}t}\right)+\left(u\frac{\partial h_{\mathrm{S}}}{\partial x}+v\frac{\partial h_{\mathrm{S}}}{\partial y}\right)\Bigg]=0,\end{aligned}\tag{29}$$

上式就是改进的浅水流体的位涡方程, 可以作为大气与海洋大尺度运动中考虑了下垫面缓变的动力学模型. 同样当 $\sigma=0$, 方程 (29) 就退化为 [33]

$$\frac{\mathrm{d}(h-h_{\mathrm{B}})}{\mathrm{d}t}+(h_{\mathrm{B}}-h)\left(\frac{1}{(\zeta+f)}\frac{\mathrm{d}\zeta}{\mathrm{d}t}\right)=0.\tag{30}$$

3 结 论

在全球变暖的大背景和人类活动的直接影响下, 大气下垫面随时间会发生变化, 这种变化从某种意义上来说是缓慢变化, 这种缓慢变化对大气运动会产生影响, 涡度是描述空气微团旋转运动的强弱程度及其方向的一个物理量, 涡度方程定量地描述了这种变化. 本文基于大气运动基本方程, 采用了不可压缩和常值密度的假设, 将下垫面的缓变作为一个小量叠加于固有下垫面上, 利用大气的上下边界条件, 得到改进的浅水方程, 这个方程较之原始浅水方程来说, 很好地处理了下垫面条件, 下垫面的缓慢变化对浅水方程做了合理的动力学订正, 得到改进的位涡方程, 其更适合描述大气运动的真实状态.

[1] Tehart W J, Shenlelon G W, Giffiths D C 1990 *The IPCC Impacts Assessment* (Canberra: Australian Government Publishing Service)
[2] Perry J S 1993 *Understanding Our Own Planet*: *An Overview of Major International Scientific Activities* (Paris: ICSU Secretariat)
[3] IPCC 1998 *The Regional Impacts of Climate Change*: *An Assessment of Vulnerability* (Cambridge: Cambridge University Press)
[4] IPCC 2001 *Climate Change 2001*: *Impacts, Adaptation & Vulnerability* (Cambridge: Cambridge University Press)
[5] Zhang Z Q, Sun C Q 1999 *Chin. Sci. Bull.* **44** 464 (in Chinese) [张志强, 孙成权 1999 科学通报 **44** 464]
[6] Sha W Y, Shao X M, Huang M 2002 *Scientia Sinica Terrae* **32** 317 (in Chinese) [沙万英, 邵雪梅, 黄玫 2002 中国科学 (D 辑) **32** 317]
[7] Liu S Y, Ding Y J, Li J, Shangguan D H, Zhang Y 2006 *Quaternary Sciences* **26** 762 (in Chinese) [刘时银, 丁永建, 李晶, 上官冬辉, 张勇 2006 第四纪研究 **26** 762]
[8] Zhang S X, Zhang L, Sun S P, Feng G L 2011 *Plateau Meteor.* **30** 659 (in Chinese) [张世轩, 张璐, 孙树鹏, 封国林 2011 高原气象 **30** 659]
[9] Sun S P, Zhang L, Hou W, Feng G L 2011 *Acta Phys. Sin.* **60** 029201 (in Chinese) [孙树鹏, 张璐, 侯威, 封国林 2011 物理学报 **60** 029201]
[10] Zong X P, Li M H, Hu J G, Feng G L 2010 *Acta Phys. Sin.* **59** 8272 (in Chinese) [宗序平, 李明辉, 胡经国, 封国林 2010 物理学报 **59** 8272]
[11] Zhao M S, Neilson R P, Yan X D 2002 *Acta Geog. Sin.* **57** 28 (in Chinese) [赵茂盛, Ronald P. Neilson, 延晓东 2002 地理学报 **57** 28]
[12] Zhou G S, Zhang X S 1995 *Acta Phytoecologica Sinica* **20** 9 (in Chinese) [周广胜, 张新时 1995 植物生态学报 **20** 9]
[13] Zhou G S, Wang Y H 1999 *Journal of Natural Resources* **14** 318 (in Chinese) [周广胜, 王玉辉 1999 自然资源学报 **14** 318]
[14] Li X B, Chen Y H 2002 *Advances in Earth Science* **17** 254 (in Chinese) [李晓兵, 陈云浩 2002 地球科学进展 **17** 254]
[15] Wang C H, Dong W J, Wei Z G 2001 *Acta Geog. Sin.* **56** 523 (in Chinese) [王澄海, 董文杰, 韦志刚 2001 地理学报 **56** 523]
[16] Lü X M, Wu S H, Yang Q Y 2003 *Progress in Geography* **22** 260 (in Chinese) [吕新苗, 吴绍洪, 杨勤业 2003 地理科学进展 **22** 260]
[17] Yang G S, Shi Y F 1995 *Acta Geog. Sin.* **50** 302 (in Chinese) [杨桂山, 施雅风 1995 地理学报 **50** 302]
[18] Douglas B C 1991 *J. Geo. Phys. Research* **96** 6981
[19] Pirazzoli PA 1989 *Global and Planetary Change* **1** 241
[20] Yang G S, Zhu J W 1993 *Advances in Earth Science* **8** 70 (in Chinese) [杨桂山, 朱季文 1993 地球科学进展 **8** 70]
[21] Li J L, Zhang D F, Yang X P, Tong Y Q, Zhang R S 2005 *J. Catastrophology* **20** 49 (in Chinese) [李加林, 张殿发, 杨晓平, 童亿勤, 张忍顺 2005 灾害学 **20** 49]
[22] Shi Y F 1996 *Journal of Natural Disasters* **5** 106 (in Chinese) [施雅风 1996 自然灾害学报 **5** 106]
[23] Ji Z X, Jiang Z X, Zhu J W 1993 *Acta Geog. Sin.* **48** 516 (in Chinese) [季子修, 蒋自巽, 朱季文 1993 地理学报 **48** 516]
[24] Hou W, Zhang D Q, Zhou Y, Yang P 2011 *Acta Phys. Sin.* **60** 109202 (in Chinese) [侯威, 章大全, 周云, 杨萍 2011 物理学报 **60** 109202]
[25] Feng G L, Yang J, Wan S Q, Hou W, Zhi R 2009 *Acta Meteor. Sin.* **67** 61 (in Chinese) [封国林, 杨杰, 万仕全, 侯威, 支蓉 2009 气象学报 **67** 61]
[26] Gong Z Q, Wang X J, Zhi R, Feng G L 2009 *Acta Phys. Sin.* **58** 4342 (in Chinese) [龚志强, 王晓娟, 支蓉, 封国林 2009 物理学报 **58** 4342]
[27] Wan S Q, Wang L, Feng G L, He W P *Acta Phys. Sin.* **58** 5083 (in Chinese) [万仕全, 王令, 封国林, 何文平 2009 物理学报 **58** 5083]
[28] Xiong K G, Feng G L, Wang Q G, Hu J G 2009 *Acta Phys. Sin.* **58** 8107 (in Chinese) [熊开国, 封国林, 王启光, 胡经国 2009 物理学报 **58** 8107]
[29] Zhang D Q, Yang J, Wang Q G, Feng G L 2009 *Acta Phys. Sin.* **58** 4354 (in Chinese) [章大全, 杨杰, 王启光, 封国林 2009 物理学报 **58** 4354]
[30] Da C J, Chou J F 2008 *Acta Phys. Sin.* **57** 2595 (in Chinese) [达朝究, 丑纪范 2008 物理学报 **57** 2595]
[31] Da C J, Sun S P, Song J, Yang L G 2011 *Plateau Meteor.* **30** 349
[32] Dong W J, Chou J M, Feng G L 2007 *Adv. Atmos. Sci.* **24** 336
[33] Wang B, Weng H Y 1981 *Geophysical Fluid Dynamics* (Beijing: China Ocean Press) pp7–141 (in Chinese) [王斌, 翁衡毅 1981 地球物理流体动力学导论 (北京: 海洋出版社) 第 60—141 页]
[34] Joseph Pedlosky 1986 *Geophysical Fluid Dynamics* (New York: Springer Verlag) pp7–9
[35] Da C J 2005 *M. S. Dissertation* (Hohhot: Inner Mongolia University) (in Chinese) [达朝究 2005 硕士学位论文 (呼和浩特: 内蒙古大学)]
[36] Guo B R B 1990 *the Introduction of Linear and Nonlinear Wave Theory* (Beijing: China Meteorological Press) (in Chinese) [郭秉荣 1990 线性波与非线性波导论 (北京: 气象出版社)]

Dynamic modification of the shallow water equation on the slowly changing underlying surface condition*

Da Chao-Jiu[1)2)†] Feng Ai-Xia[3)] Gong Zhi-Qiang[3)] Song Jian[4)]

1) (*School of Mathematics and Computer Science Institute, Northwest University for Nationalities, Lanzhou* 730030, *China*)

2) (*College of Atmospheric Sciences, Lanzhou University, Lanzhou* 730000, *China*)

3) (*Laboratory for Climate Studies, National Climate Center, China Meteorological Administration, Beijing* 100081, *China*)

4) (*College of Science, Inner Mongolia University of Technology, Hohhot* 010062, *China*)

(Received 4 July 2012; revised manuscript received 7 September 2012)

Abstract

In this paper, the shallow water equation is discussed, when the underlying surface is slowly changing. From the continuity equation and the equation of motion controlling the movement of the atmosphere, the slowly changing of the underlying surface is superimposed on the topography function as a small quantity, using the upper and lower boundary conditions of the atmosphere, the modified shallow water equation is obtained. In the modified shallow water equation, the slowly changing local horizontal divergence modifies the equilibrium between the local horizontal divergence and the local change of the thickness of the atmosphere. On the basis of this, the vorticity equation is obtained, which contains the slowly changing underlying surface.

Keywords: underlying surface, global warming, slowly changing, shallow water equation

PACS: 92.40.Cy, 92.60.Aa **DOI:** 10.7498/aps.62.039202

* Project supported by the National Basic Research Program of China (Grant No. 2012CB955902), the National Natural Science Foundation of China (Grant Nos. 40930952, 41175067), the Key Technologies R & D Program of China (Grant No. 2009BAC51B04), the Meteorological Special Project of China (Grant Nos. GYHY201106016, GYHY201206009), the Natural Science Foundation of Inner Mongolia, China (Grant No. 2011MS0112) and the Fundamental Research Funds for the Central Universities, China (Grant No. zyz2011079).

† Corresponding author. E-mail: jtdcj@163.com

中国科学: 地球科学 2013 年 第 43 卷 第 5 期: 836 ~ 847
www.scichina.com earth.scichina.com
《中国科学》杂志社
SCIENCE CHINA PRESS

论 文

基于 2009 年初长江中下游地区持续阴雨过程的 10~30 天延伸期稳定分量的提取及配置分析

封国林[①②], 孙树鹏[②], 赵俊虎[①②*], 郑志海[①]

① 国家气候中心气候研究开放实验室, 北京 100081;
② 兰州大学大气科学学院, 兰州 730000
* 联系人, E-mail: huzi348637577@sina.com

收稿日期: 2012-04-23; 接受日期: 2012-07-18; 网络版发表日期: 2013-04-19
国家自然科学基金(批准号: 40930952)和国家重点基础研究发展计划(编号: 2012CB955902, 013CB430204)资助

摘要 2009 年 2 月中下旬至 3 月上旬, 中国长江中下游地区出现了持续阴雨天气, 这次持续性异常事件影响范围之广、持续时间之长为历史罕见. 本文利用 EOF 分解方法对相应时段 NCEP-DOE Reanalysis 2 逐日位势高度场距平资料进行分析, 定义了 10~30 天延伸期稳定分量, 并根据各 EOF 分量的贡献率的不同变化特征进一步定义了 10~30 天延伸期气候态稳定分量和异常型稳定分量. 气候态稳定分量主要解释气候平均信息对延伸期天气过程的影响, 而异常型稳定分量则侧重体现了持续性阴雨过程的“异常”特征. 研究发现, 稳定分量尤其是异常型稳定分量具有如下特征: (1) 时间尺度较长, 能维持较长时间(10 天以上)的稳定或者表现为月尺度的低频变化及超长波活动; (2) 空间活动范围较大, 表现为行星尺度的超长波活动, 且在垂直各层有稳定一致的配置关系; (3) 能够较好地反映中高纬大气环流的变化特征, 体现了指数循环和超长波的移动、调整活动; (4) 与地面持续性天气过程有较好的对应关系.

关键词
稳定分量
气候态稳定分量
异常型稳定分量
10~30 天延伸期预报

近年来, 10~30 天延伸期预报成为天气和气候业务预报发展的一个重要方向, 提高持续性异常极端事件的延伸期预报能力, 是我国气象部门目前面临的重大气象服务需求[1]. 金荣华等[2]对国内外延伸期预报业务现状和延伸期预报的发展做了详细介绍. 目前国内外 10~30 天延伸期的预报技巧普遍偏低, 重要的原因就是其预报时效接近和超过了目前普遍认可的逐日预报的理论可预报上限[3~12]. 但必须指出的是, 逐日天气预报的时效超过了 2 周的理论上限后, 并不意味着大气运动就没有可预报的分量. 一些行星尺度的大气活动中心(副高、极涡等), 特征时间尺度比天气尺度长得多, 另外大气中还存在准双周(10~20 天)振荡、季节内(30~60 天)振荡, 这些都能为 10~30 天延伸期提供可用的预报信息, 尤其对持续性异常事件的预报有重要的影响和潜在预报价值[13~17]. 观测研究表明, 大气演变中有一些变化较慢的过程

中文引用格式: 封国林, 孙树鹏, 赵俊虎, 等. 基于 2009 年初长江中下游地区持续阴雨过程的 10~30 天延伸期稳定分量的提取及配置分析. 中国科学: 地球科学, 2013, 43: 836–847
英文引用格式: Feng G L, Sun S P, Zhao J H, et al. Analysis of stable components for extended-range (10–30 days) weather forecast: A case study of continuous overcast-rainy process in early 2009 over the mid-lower reaches of the Yangtze River. Science China: Earth Sciences, 2013, doi: 10.1007/s11430-012-4527-8

存在于天气噪音水平之上，这些缓变过程是和大尺度大气运动相联系的，其时间尺度达数周，持续性比根据非线性流体动力学所估计的持续性要长得多，这表明在 10~30 天的时间尺度内，仍然存在一些可预报的气象场的特征[17,18]. 丑纪范等[19,20]基于同一时段不同气象场的特征具有不同的可预报性这一特征，提出在 10~30 天延伸期时间尺度内，将气象场一分为二：数值模式的状态变量=可预报的稳定分量+不可预报的混沌分量，然后针对大气系统的可预报分量和混沌分量采用不同的策略和方法进行延伸期预报. 在相同的初始特征和外源强迫特征的条件下，时空尺度较大的系统具有较大的可预报性. 对于不同时空尺度的大气或气候预测来说，应针对其稳定分量特别加以研究，抓住其稳定分量的主要特点可以提高对系统的认识和预测水平[19].

因此，针对 10~30 天的延伸期预报，提取和分析该时间尺度可预报的稳定分量，并基于稳定分量改进现有的全球预报模式，对研究 10~30 天延伸期可预报性是一个既面临挑战又具有原始创新研究的课题. 本文研究了 10~30 天延伸期稳定分量的定义、提取方法和变化特征，并结合 2009 年 2 月中下旬至 3 月上旬长江中下游持续阴雨天气过程，考虑到持续性异常事件的特殊性，将稳定分量进一步分为气候态稳定分量和异常型稳定分量. 气候态稳定分量主要体现气候信息对延伸期天气过程的影响，而异常型稳定分量则侧重体现了持续性阴雨过程的“异常”特征. 需要说明的是，本文中的稳定分量仅是从资料分析角度提取，与可预报的稳定分量存在一些不同，我们将在后续工作中对其可预报性进行分析，并进一步对可预报分量(可预报的稳定分量)进行分析，进而尝试对 10~30 天延伸期预报进行更进一步的探索.

1　资料和方法

1.1　资料

本文所用资料为 NCEP-DOE Reanalysis 2 (资料来源于 NOAA/OAR/ESRL PSD, Boulder, Colorado, USA, http://www.esrl.noaa.gov/psd) 1979~2009 年逐日资料，资料的水平分辨率为 2.5°×2.5°. 另外还用到了中国气象局国家气象信息中心提供的长江中下游地区 41 站逐日降水量资料，并绘制了 2009 年 2 月 14 日至 3 月 15 日 41 站平均日降水量演变图(图 1).

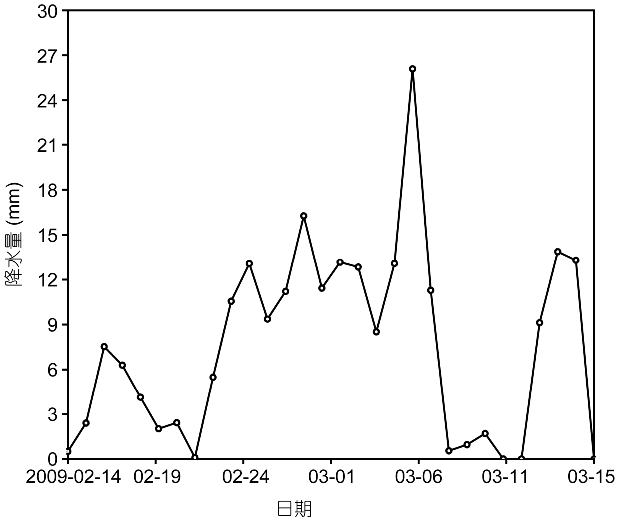

图 1　2009 年 2 月 14 日至 3 月 15 日长江中下游地区 41 站平均日降水量逐日演变图

2009 年 2 月中下旬至 3 月上旬长江中下游地区出现了持续时间历史罕见的连阴雨天气，本文基于此个例进行研究(以下简称个例). 罗小莉等[21]对这次过程作了较详尽的分析，将这次过程分为两个阶段：2 月 14 日至 20 日为第 1 阶段，其中 14~17 日，18~20 日各有一次冷空气活动；2 月 21 日至 3 月 9 日为第 2 阶段，期间不断有冷空气南下，其中 24~28 日降水非常明显，6 日起随着环流调整，雨区明显南压. 乌拉尔山阻塞高压的偏强和较长时间维持、西太平洋副热带高压异常偏北、青藏高原南缘的南支低槽系统活跃以及切变线在长江中下游一带摆动形成了此次过程的异常环流特征.

1.2　方法

本文主要采用了经验正交函数(EOF)分解方法[22]，其基本思想是把气象要素场分解为具有典型分布意义的空间特征向量场和对应时间权重系数的线性组合. 空间特征向量表征某一气候变量场的变率分布结构，其空间分布形式代表了该变量场的主体分布结构，时间系数反映空间分布形式与某时间点的实际分布形式相似或相反的程度：

$$X_{m\times n}=V_{m\times m}Z_{m\times n}. \tag{1}$$

利用 EOF 可以从近期历史气候资料中获取一组正交的空间特征向量基底，然后将个例过程的逐日要素场展开到相应基底上，得到一组对应的时间系数序列：

$$Z = V'X. \quad (2)$$

因为要素场的信息主要集中在前面一部分所占比重较大的空间特征向量基底上, 所以可以截取前面 p 个向量用来近似表征总体场的变化情况[23], 而且李志锦和纪立人[24]通过对 EOF 谱分量的研究发现, 随着 EOF 分量序号数的增大, 可预报性依次减小:

$$X_{m\times n} \approx V_{m\times p} Z_{p\times n}. \quad (3)$$

2 稳定分量的定义和提取方法

2.1 稳定分量的定义、分类及提取方法

穆穆等[25]与李建平和丑纪范[26]给出了稳定分量和混沌分量的确切含义.

当给定初始场 X_0 和外源强迫 F 的情况下, 空间尺度为 D(这里 D 为三维尺度)和时间尺度为 T 的气候可预报性时间 T_p 满足如下函数关系:

$$T_p=T_p(D\times T;\, X_0,\, F). \quad (4)$$

在相同初始特征和相同外源强迫特征条件下, 对于特定的预报时间 T_p, 对应一个临界尺度 D 满足式(4). 而系统的稳定分量是这样的一些分量, 其时空尺度为$(D_i\times T)$, 满足

$$D\leqslant D_i,\ T_p\leqslant(D_i\times T;\, X_0,\, F); \quad (5)$$

而系统的混沌分量是尺度为$(D_i\times T)$的那些分量, 它们满足

$$D_i\leqslant D,\ T_p(D_i\times T;\, X_0,\, F)\leqslant T_p. \quad (6)$$

以上表明, 对于特定的预测时间尺度而言, 系统的可预报的部分称为稳定分量, 而不可预报的部分为混沌分量. 对于不同时空尺度的大气或气候预测来说, 应针对其稳定分量特别加以研究, 抓住其稳定分量的主要特点可以提高对系统的认识和预测水平.

正如莫宁[27]指出: “只有当预报误差不超过预报量的平均气候变化时, 个别过程的预报才能给出超过统计(气候)描述所给的信息之外的补充信息, 相应的期限可以称为所研究的过程的可预报性期限. ”为进一步明确持续性异常事件中的特殊环流形势, 我们试图将稳定分量做如下处理:

$$(D_i\times T) = \overline{(D_i\times T)} + (D_i\times T)', \quad (7)$$

其中, $(D_i\times T)$(时空尺度为$(D_i\times T)$的分量, 简记为$(D_i\times T)$, 以下类同)代表 10~30 天延伸期的稳定分量; $\overline{(D_i\times T)}$ 代表多年气候平均的稳定分量; $(D_i\times T)'$ 为距平扰动稳定分量. 即10~30天延伸期的稳定分量可以看作多年气候平均的稳定分量叠加上一个距平扰动稳定分量构成, $\overline{(D_i\times T)}$ 主要体现 10~30 天延伸期的稳定分量中所包含的气候信息, 利用该部分分量可以解释个例中气候平均的影响, 而 $(D_i\times T)'$ 可以解释持续性异常过程中体现的“异常”稳定分量信息, 故将 $\overline{(D_i\times T)}$ 称为 10~30 天延伸期气候态稳定分量, $(D_i\times T)'$ 称为 10~30 天延伸期异常型稳定分量.

利用经验正交函数(EOF)分解方法可以通过多年气候资料场得到一组正交的空间特征向量基底, 然后将某时刻(或某段序列)的要素场展开到这组基底上, 从而将要素场的变化转化为空间特征向量对应时间系数的变化. 按照 EOF 分量对原始场的贡献率进行排序, EOF 分量序号越小代表该分量对应的空间分布型对原始场的贡献越大, 李志锦和纪立人[24]通过对 EOF 谱分量的研究发现, 随着 EOF 分量序号数的增大, 可预报性依次减小, 因此可以通过选取部分 EOF 序号数较大的分量来实现筛选稳定分量的目的. 一般而言, 多数情况下 EOF 分量序号与多年气候资料 EOF 所得空间特征值序号相近. 但在持续性异常过程中, 可能会出现一些例外, 某些贡献率排名靠后的 EOF 分量出现异常靠前并且维持相当长一段时间的情况. 通过进一步分析表明, 该部分分量在很大程度上可以解释持续性异常过程的气象要素的“异常”分布型, 我们将这类 EOF 分量定义为 10~30 天延伸期异常型稳定分量. 而将除此之外对原场贡献率较大的 EOF 分量定义为 10~30 天延伸期气候态稳定分量, 具体方法如下.

(1) 首先利用近 30 年历史同期气候资料进行 EOF 分解, 获取一组正交的空间特征向量基底. 本文取 1979~2008 年 2 月 14 日至 3 月 15 日共 30 年×30 天 500 hPa 逐日位势高度场, 对其距平场进行 EOF 分解得到一组空间特征向量正交基. 利用各 EOF 分量的空间特征向量与其对应时间系数的合成分量相对于总合成场(即距平场)的解释方差百分比, 作为考察该 EOF 分量对原场的影响指标, 并将其定义为该 EOF 分量的贡献率. 利用 30 年气候资料各 EOF 分量多年平均贡献率进行排序, 取累积贡献率前 85%的 EOF 分量进行研究(表 1).

(2) 将 2009 年 2 月 14 日至 3 月 15 日 500 hPa 逐日位势高度距平场序列展开到上述正交基上, 并根据各分量的贡献率进行排序, 同样取累积贡献率前 85%的 EOF 分量, 如表 2 所示.

表 1　多年平均累积贡献率前 85%的 EOF 分量

排序	贡献率(%)	累积贡献率(%)	原始序号	平均持续时间(天)
1	16.3	16.3	1	26
2	9.2	25.5	2	24
3	9.0	34.5	3	24
4	7.1	41.5	4	23
5	5.6	47.2	5	22
6	5.4	52.6	7	21
7	4.9	57.5	6	21
8	3.7	61.2	8	21
9	2.9	64.1	9	19
10	2.8	66.9	10	18
11	2.7	69.6	11	18
12	2.2	71.8	12	17
13	2.1	74.0	13	17
14	2.0	76.0	14	17
15	1.9	77.9	15	17
16	1.6	79.5	16	15
17	1.4	80.9	17	16
18	1.3	82.2	18	13
19	1.3	83.5	19	14
20	1.1	84.6	20	14

表 2　个例中累积贡献率前 85%的 EOF 分量

排序	贡献率(%)	累积贡献率(%)	原始序号	平均持续时间(天)
1	19.6	19.6	6	23
2	9.6	29.2	3	18
3	7.0	36.2	1	15
4	6.0	42.2	5	15
5	4.3	46.4	10	20
6	3.8	50.3	11	22
7	3.7	54.0	14	14
8	3.7	57.7	2	16
9	3.0	60.7	9	13
10	2.5	63.2	22	13
11	2.1	65.3	4	16
12	1.9	67.2	19	8
13	1.9	69.1	17	14
14	1.8	70.9	12	12
15	1.8	72.6	16	13
16	1.7	74.4	13	11
17	1.6	75.9	20	12
18	1.5	77.4	23	11
19	1.4	78.8	18	12
20	1.4	80.2	38	15
21	1.3	81.5	8	12
22	1.3	82.8	16	13
23	1.2	84.1	29	8
24	1.2	85.3	7	11

(3) 比较表 1 与表 2 可以发现有一些 EOF 分量的贡献率有了明显的增加, 这表明这些分量在个例中作用更加突出. 如表 1 中 EOF6 分量的多年平均贡献率为 4.9%, 排序第 7 位, 而在个例中其贡献率提升至 19.6%, 排序为第 1 位. 图 2 给出了 EOF6 分量的空间分布和贡献率的逐日变化情况, 可以发现该分量主要体现波数为 3 的超长波分布特征, 结合个例中对应时间系数的变化, 该分量在乌拉尔山地区为一正距平中心, 利于阻塞高压的形成和维持, 在东亚地区为一负距平中心, 这种形势十分有利于中高纬冷空气的南下, 而在中国南部的副热带地区则表现为正距平, 使得南下冷空气受阻同时正距平西北侧有利于暖湿气流的北上, 这样的形势在低层表现为切变线的维持, 从而造成了这次持续性阴雨过程. 在表 2 中选取类似 EOF6 分量, 将贡献率排序提升 5 位以上并且在累积贡献率前 85%内持续天数超过两周的 EOF 分量定义为 10~30 天延伸期异常型稳定分量, 而将与多年平均表现相近, 在累积贡献率前 85%内的其余 EOF 分量定义为 10~30 天延伸期气候态稳定分量. 在个例中对于距平场而言, 异常型稳定分量贡献率为 37.2%, 气候态稳定分量的贡献率为 48.1%, 可见异常型稳定分量所占比重相当高, 达到气候态稳定分量的量级, 故对整个延伸期的天气过程产生了较大的"异常"作用, 而其中 EOF6 的"异常"维持时间达两周以上, 其重要作用不言而喻.

2.2　稳定分量的演变情况

个例反映的是长江中下游地区的持续阴雨过程, 造成这次事件的主要原因是欧亚地区中高纬度大气环流经向度加大, 乌拉尔山阻塞高压维持, 同时西太平洋副热带高压异常偏北以及青藏高原南缘的南支低槽系统活跃, 利于西南暖湿气流北上与冷空气在长江中下游一带交汇产生降水. 图 3~5 分别为个例中北半球 500 hPa 位势高度距平场所得的 10~30 天延伸期异常型稳定分量、气候态稳定分量和二者叠加所得稳定分量间隔 5 天的日平均分布场.

由图 3 可见异常型稳定分量在个例前 21 天尤其前两周内一直维持着一个比较稳定的环流形势: 在欧洲东部维持一个较强的正距平, 在东北亚一带为较强的负距平, 在北太平洋上为较强的正距平中心, 受其影响我国华南地区以南均呈现正距平分布. 而图 4 气候态稳定分量的持续性不如异常型稳定分量

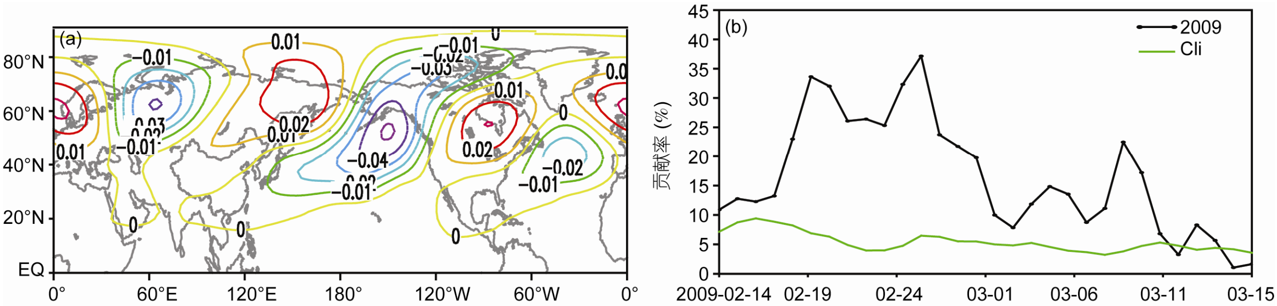

图 2　北半球 500 hPa 位势高度场 EOF6 空间分布(a)和贡献率(b)随时间的变化

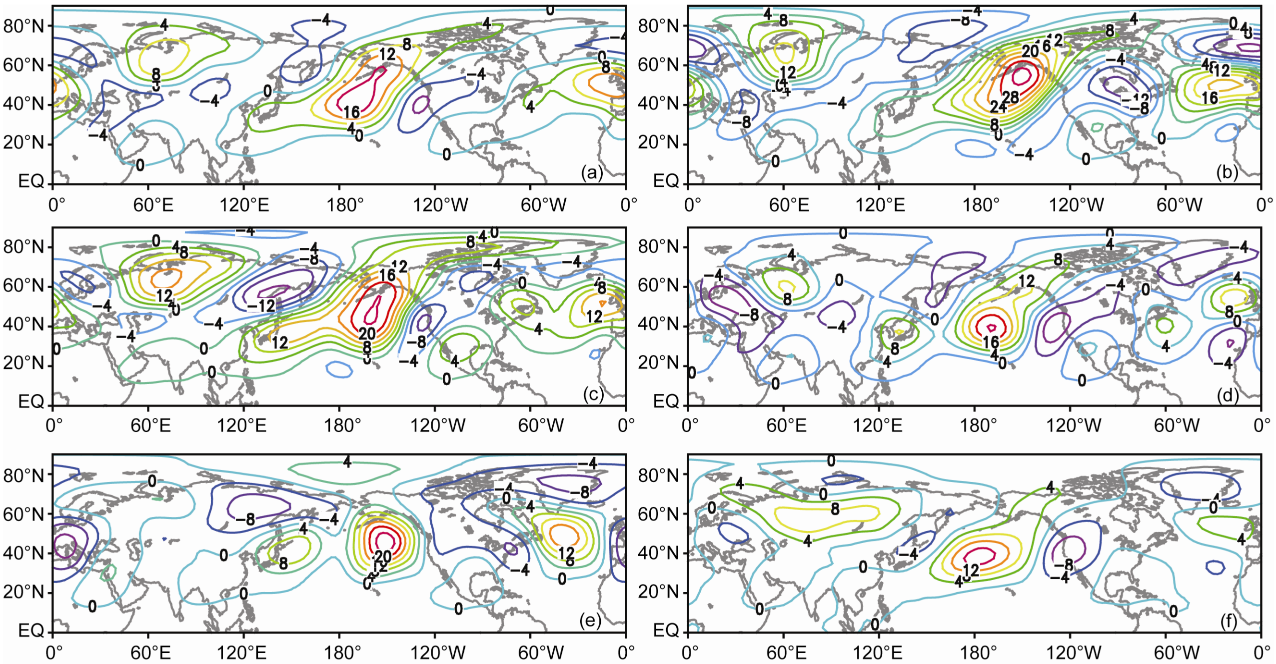

图 3　北半球 500 hPa 位势高度距平场异常型稳定分量的空间分布(单位: dagpm)

(a) 2 月 14 日; (b) 2 月 19 日; (c) 2 月 24 日; (d) 3 月 1 日; (e) 3 月 6 日; (f) 3 月 11 日

那么明显, 尤其在个例时段第 16 日(3 月 1 日)极涡的增强, 导致原本的槽脊形势减弱, 纬向环流特征有加强趋势, 对应长江中下游持续阴雨有所减弱, 但由于异常型稳定分量的异常强烈维持, 导致二者叠加所得稳定分量直至持续至第 21 天(3 月 6 日)时仍然呈现较强的经向环流特征(图 5), 形成了长江中下游地区的短期降水加强形势. 而在第 26 天(3 月 11 日)时纬向环流特征加强, 冷空气的南下形势减缓, 长江中下游的持续阴雨过程结束. 综上, 气候态稳定分量更多地体现了指数循环特征, 反映了中高纬的环流形势变化, 尤其是中高纬的超长波槽脊移动和调整, 而异常型稳定分量则集中反映了原场相对稳定的持续性形势, 中高纬的超长波槽区在东北亚的维持和脊区在欧亚大陆西部的维持形势, 这十分有利于中高纬冷空气的南下, 同时北太平洋脊区向西南延伸至我国华南, 使得南下的气流受到阻挡而堆积在长江一带, 形成了本次持续阴雨过程. 可见, 异常型稳定分量较清晰地反映了持续性的“异常”环流形势, 能够较好地解释这次个例过程的形成原因.

对比图 5 和图 3, 可以看出所提取的稳定分量尤其是异常型稳定分量较清楚地对应了乌拉尔山阻塞高压和东亚地区的低压形势, 同时副热带地区有高压中心维持在长江以南地区, 这种形势的维持与 2009 年 2 月 14 日至 3 月 9 日长江中下游地区连阴雨

过程有较好的对应关系，即所提取的异常型稳定分量达到了预期的效果，能够充分体现延伸期天气过程的形势变化.

将距平场所得异常型稳定分量和气候态稳定分量叠加上气候平均态，即可得到原场的稳定分量. 由此原始位势高度场(图 6)分为两部分：稳定分量(图 7)和混沌分量(图 8). 图 7 为稳定分量的空间分布随时间演变情况，对比图 6，可以发现稳定分量去除了变

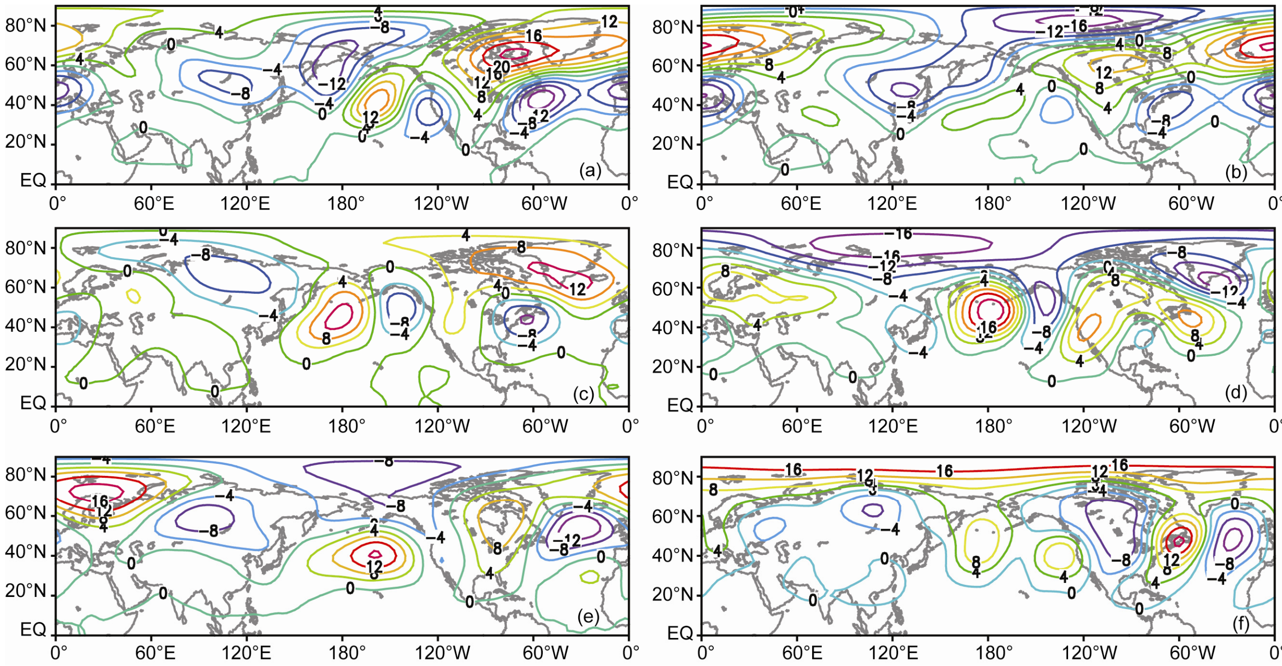

图 4　北半球 500 hPa 位势高度距平场气候态稳定分量的空间分布(单位: dagpm)

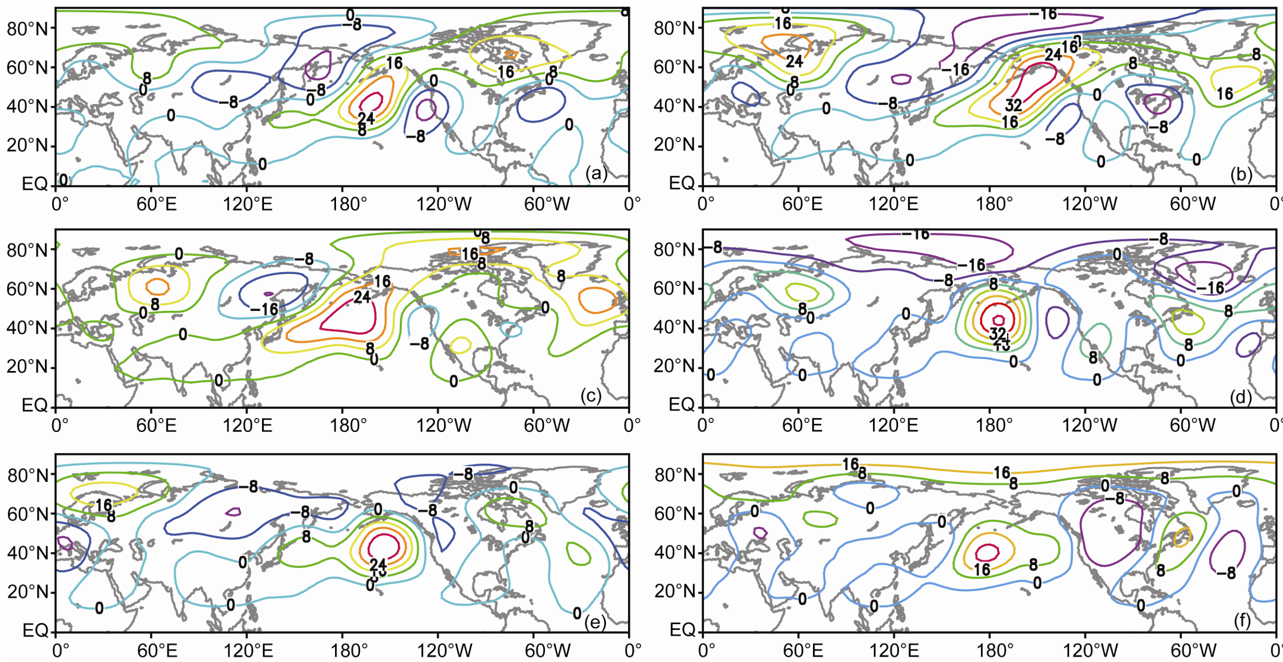

图 5　北半球 500 hPa 位势高度距平场稳定分量的空间分布(单位: dagpm)

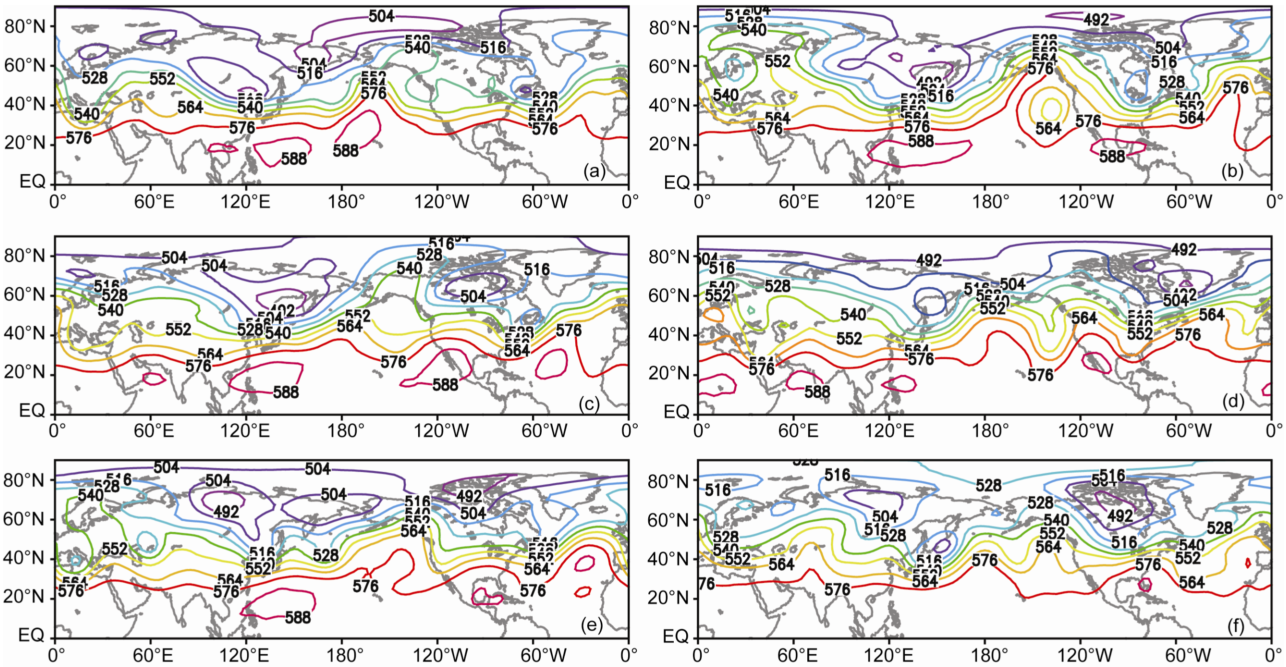

图 6　北半球 500 hPa 位势高度场的空间分布(单位: dagpm)

(a) 2 月 14 日; (b) 2 月 19 日; (c) 2 月 24 日; (d) 3 月 1 日; (e) 3 月 6 日; (f) 3 月 11 日

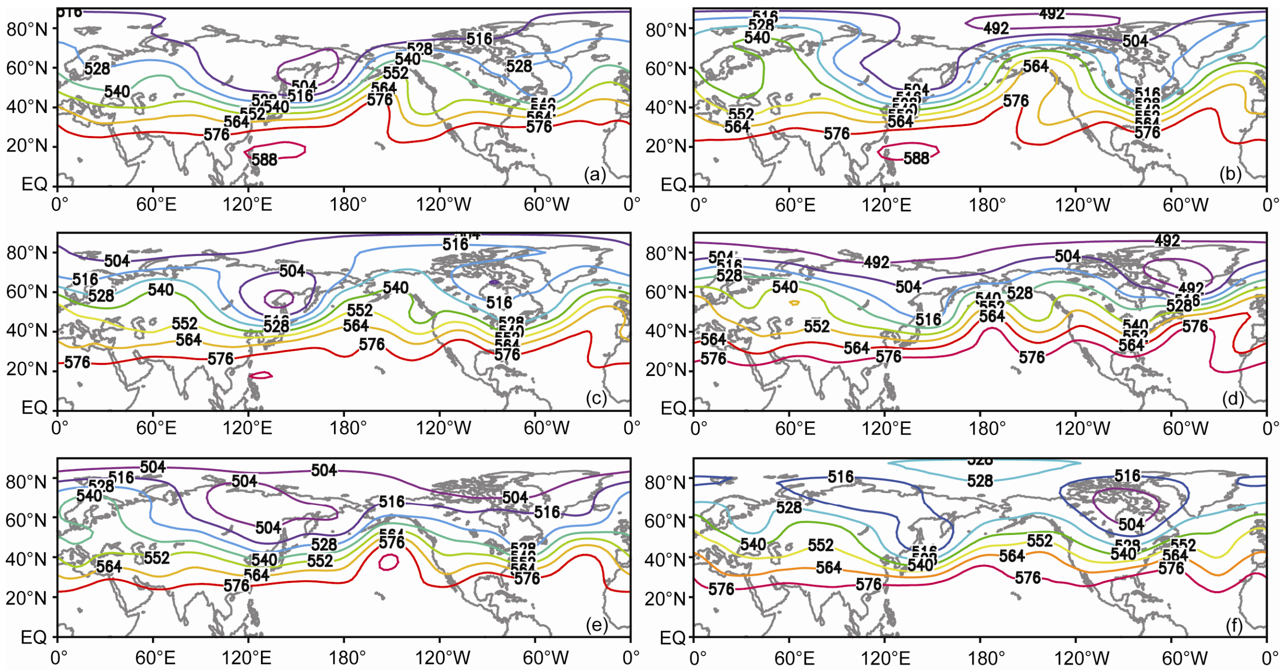

图 7　北半球 500 hPa 位势高度场稳定分量的空间分布(单位: dagpm)

化周期较短的小尺度波动, 从而更清晰地反映了延伸期内的大体形势变化, 在包含异常型稳定分量所反映异常稳定形势的同时, 其形势分布更贴近实际状况. 图 8 混沌分量中则包含了更多较小尺度的波动,

尤其其中周期为 5 天左右的天气波动在 10~30 天延伸期内进一步发展和增强, 对短期天气过程有重要的影响, 但总体而言由于其持续性较差, 变化周期较短, 给 10~30 天延伸期的预测带来困难, 故将其划分为混沌分量.

图 9(a)为稳定分量与原场间的距平相关系数(ACC)的逐日变化情况, 反映了所提取的稳定分量与原场有较好的相关关系, 尤其在持续阴雨的时段 ACC 值都在 0.8 以上. 从预报角度讲, 抓住了稳定分量的变化即可较为准确预测延伸期的天气过程. 而如果单独考察气候态稳定分量, 不考虑异常型稳定分量, 则 ACC 出现较大的振荡变化(图 9(b)), 尤其在第 5~15 天出现一个低谷, 从侧面反映了异常型稳定分量的持续性对于个例过程的重要性.

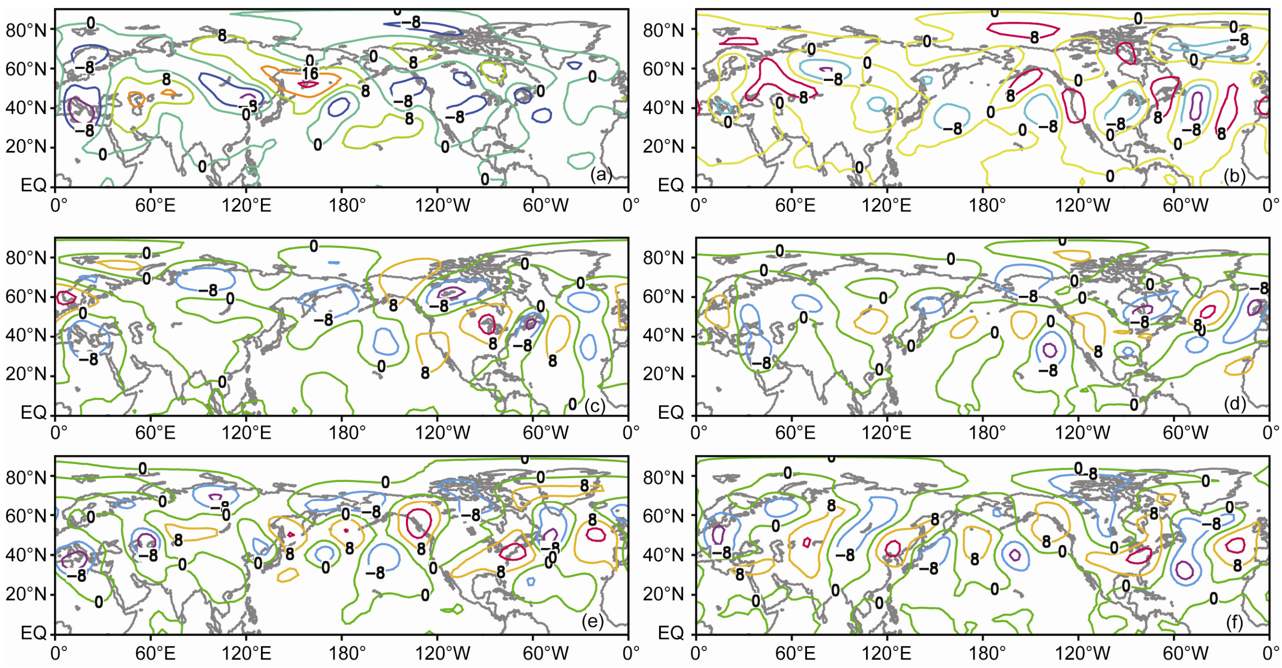

图 8　北半球 500 hPa 位势高度场混沌分量的空间分布(单位: dagpm)

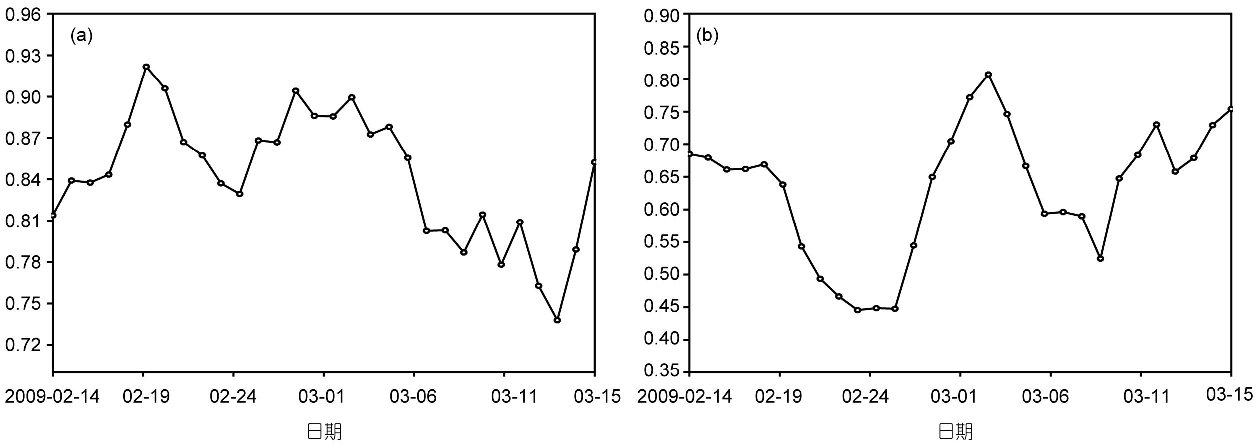

图 9　北半球 500 hPa 位势高度场稳定分量的 ACC 评分逐日变化曲线

(a) 包括异常型稳定分量; (b) 不包括异常型稳定分量

3 延伸期稳定分量的配置及演变

3.1 不同尺度滤波与延伸期天气变化

对变量场序列做距平处理, 实际上相当于去除了变量的年变化和季节循环等特征, 这与低通滤波有异曲同工之妙, 故上述对距平场提取稳定分量的做法同样适用于滤波分量, 而且通过对不同时间尺度滤波分量的分析, 可以使我们能更清楚地了解个例中不同尺度波动的变化和配置关系. 图 10(a)为 2009 年 2 月 22 日北半球 500 hPa 位势高度场 60 天以上低通滤波分量的空间分布, 图中欧亚大陆西部为一较强的高压脊区, 东部为东亚大槽控制区, 亚洲极涡的偏强使得东亚大槽呈现较强的形势, 这十分利于冷空气的大量南下影响我国中南部地区, 结合图 10(b)带通滤波分量在华南地区的脊区维持, 共同形成了个例的环流形势. 图 11(a)为 60 天以上低通滤波分量沿 30°N 的时间-经度剖面图, 由图可以发现在个例对应时段内 120°E 附近一直维持着一个槽区低值中心, 其中 2 月 25 日前后几天负值达到最强, 这与图 1 中长江中下游地区降水量峰值相对应. 而图 11(b)显示了 10~60 天带通滤波分量的演变形势, 其中 110°E~120°E 有几次较明显的低值中心变化过程, 这与长江中下游连阴雨的几次过程有较好的对应关系. 60 天以上低通滤波分量与 10~60 天带通滤波分量配合叠加形成 500 hPa 层次控制长江中下游地区连阴雨过程的槽区环流形势.

3.2 不同高度层次稳定分量的配置

对 200 和 850 hPa 两个层次重复上述稳定分量的提取操作, 即从垂直方向的空间分布进一步考察异常 EOF 分量的立体层次配置情况, 分别得到两个层次的异常型稳定分量. 结合 200, 500 和 850 hPa 三个层次的异常 EOF 分量的变化情况及其空间分布的对应情况, 对各层次的异常 EOF 分量进行删减修正, 最终得到各层异常 EOF 分量集合, 然后分别与各自对应时间系数进行合成, 得到异常型稳定分量的逐

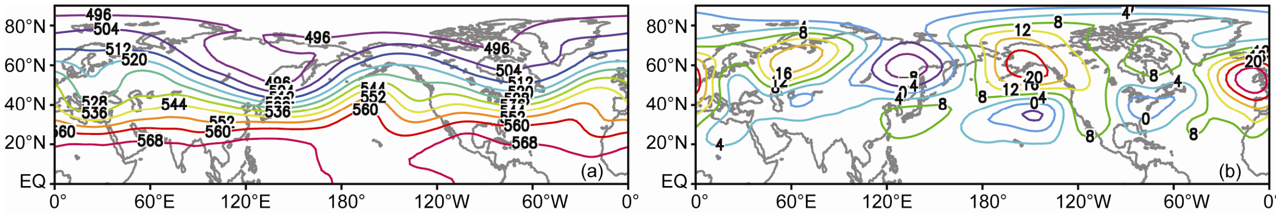

图 10 北半球 500 hPa 位势高度场不同滤波分量的空间分布(单位: dagpm)

(a) 60 天以上低通滤波; (b) 10~60 天带通滤波

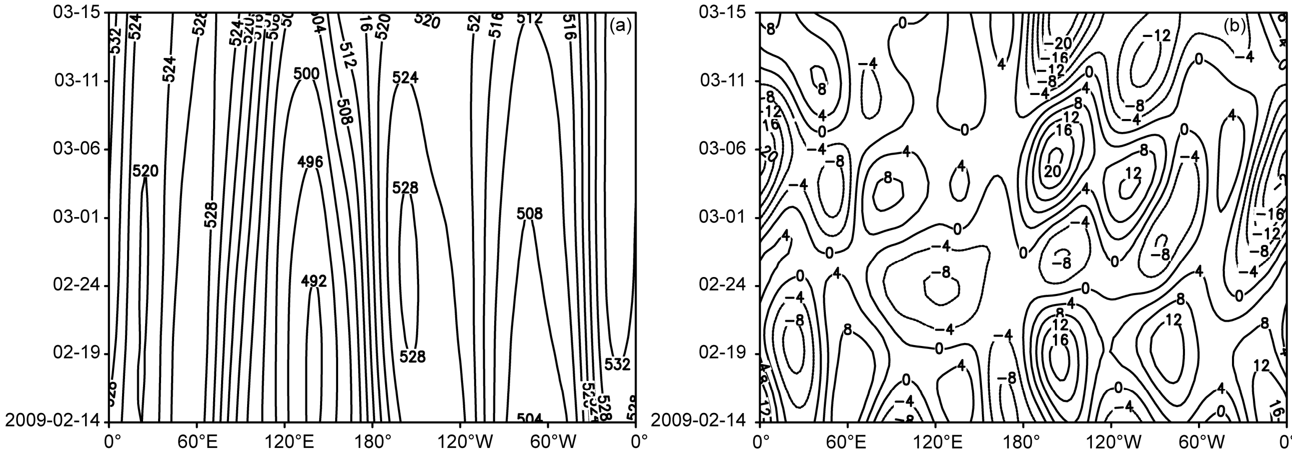

图 11 北半球 500 hPa 位势高度场不同滤波分量沿 30°N 的时间-经度剖面图(单位: dagpm)

(a) 60 天以上低通滤波; (b) 10~60 天带通滤波异常型稳定分量

日演变情况. 图 12 为个例第 21 天(3 月 6 日)三个层次的异常型稳定分量的空间分布图. 由图可见, 三个层次的异常型稳定分量的空间分布较为一致, 都是在亚洲东部维持了一个槽区而在欧亚大陆西部为脊区, 反映了异常型稳定分量所体现系统的深厚稳定. 三个层次的一致性, 也在一定程度说明了异常型稳定分量的提取过程是较为成功和可靠的.

3.3 不同变量场稳定分量的配置

持续性异常事件是各要素场相互配置共同影响所致, 对温度场和风场进行稳定分量的提取同样可以得到类似的结论. 在个例过程中, 温度场稳定分量与高度场有较好的配置关系, 在东亚槽区为低温中心, 乌拉尔山附近及副热带地区为温度正距平区域, 温压场的配置形成了长江中下游地区北方冷空气南下与南方暖湿气流北上的形势, 从而造成此次持续阴雨过程. 图 13 给出流场中稳定分量的空间分布和随时间的演变情况.

由图 13(a)~(e)可以发现在个例过程中欧亚大陆的西部一直维持着一个反气旋式的环流, 同时配合

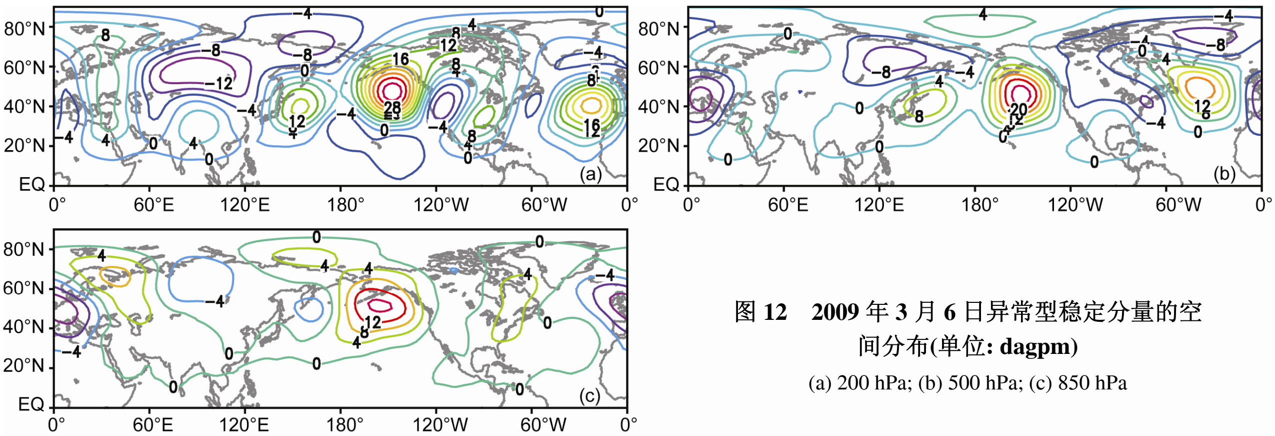

图 12　2009 年 3 月 6 日异常型稳定分量的空间分布(单位: dagpm)

(a) 200 hPa; (b) 500 hPa; (c) 850 hPa

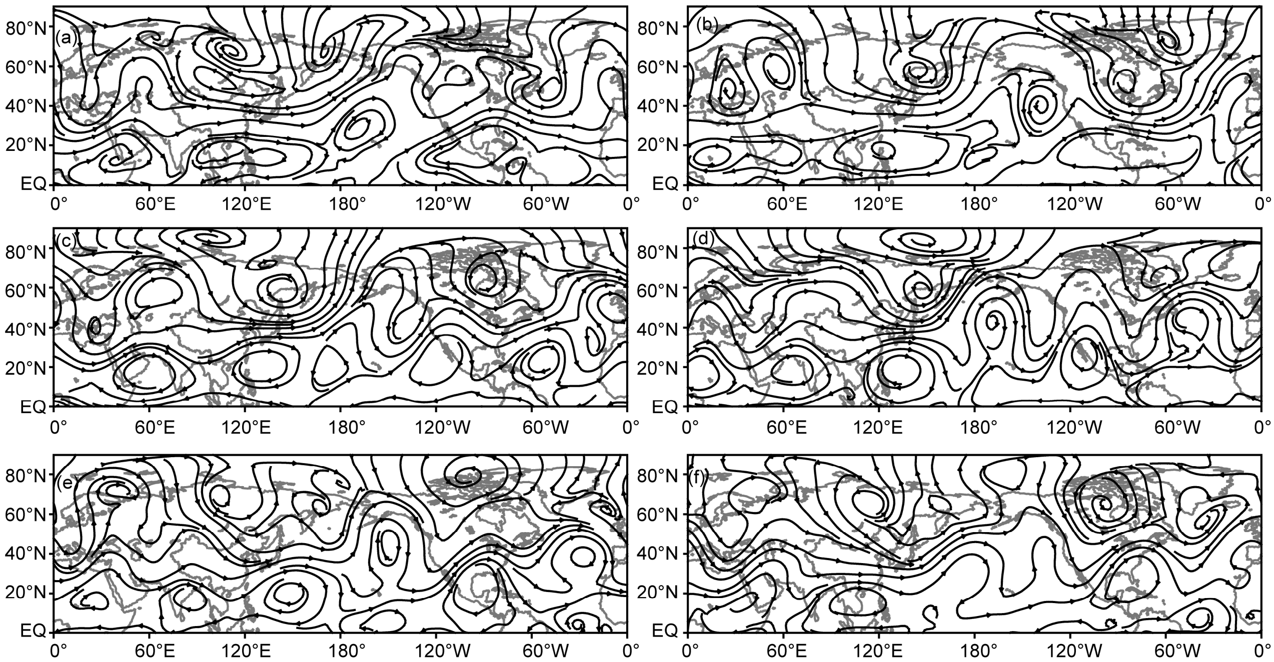

图 13　北半球 500 hPa 流场稳定分量的空间分布

(a) 2 月 14 日; (b) 2 月 19 日; (c) 2 月 24 日; (d) 3 月 1 日; (e) 3 月 6 日; (f) 3 月 11 日

亚洲东部的气旋式环流利于大量冷空气南下至东亚地区, 另一方面在西北太平洋上空则为维持着一个反气旋式环流, 利于暖湿气流北上, 冷暖空气在长江中下游地区交汇, 并在该地区上空形成一个较强的辐合形势, 有利于降水过程的发生和维持, 从而导致了这次持续阴雨过程. 尤其在图 13(c)和(d) (2 月 24 日~3 月 1 日)上, 在长江中下游地区出现较强的西风锋区, 流场呈现异常强的辐合形势, 这与个例时段较强的降水过程有较好的对应关系.

4 讨论和结论

基于 2009 年 2 月中下旬至 3 月上旬长江中下游地区的持续阴雨天气过程, 利用经验正交函数(EOF)分解方法对 200, 500, 850 hPa 三个位势高度场距平资料进行分析. 基于各 EOF 分量对原场贡献率的不同变化特征定义了 10~30 天延伸期稳定分量, 并进一步定义了气候态稳定分量和异常型稳定分量. 气候态稳定分量主要解释气候态对延伸期天气过程的影响, 而异常型稳定分量则重点体现了持续性阴雨过程的"异常"特征. 研究发现稳定分量(尤其异常型稳定分量)具有如下特征: (1) 时间尺度较长, 能维持较长时间(10 天以上)的稳定或者表现为月尺度的低频变化及超长波活动; (2) 空间活动范围较大, 表现为行星尺度的超长波活动, 且在垂直各层有稳定一致的配置关系; (3) 能够较好地反映中高纬环流的变化特征, 体现了指数循环特征和超长波的移动、调整活动; (4) 与地面持续性天气过程有较好的对应关系. 10~30 天延伸期稳定分量应该是在延伸期过程中占主导变化地位的、具有较大时空尺度的大气活动中心或遥相关型的配置, 它的活动变化受大气永久和半永久活动中心的影响, 甚至也可能是大气活动中心在延伸期尺度上的低频变化分量. 另一方面, 它不同于天气尺度的长波活动, 其更体现了超长波的移动和调整, 与西风带的指数循环有较为密切的联系.

本文工作主要是从已有的历史资料中进行分析, 在实际预报中, 如何提前确定稳定分量尤其是异常型稳定分量, 这方面的工作有待进一步探讨.

致谢 感谢审稿专家提出的宝贵意见.

参考文献

1 丁一汇, 梁萍. 基于 MJO 的延伸预报. 气象, 2010, 36: 111–122
2 金荣华, 马杰, 毕宝贵. 10~30d 延伸期预报研究进展和业务现状. 沙漠与绿洲气象, 2010, 4: 1–5
3 Lorenz E N. A study of the predictability of a 28-variable atmospheric model. Tellus,1965,17: 321–333
4 Lorenz E N. Atmospheric predictability as revealed by naturally occurring analogues. J Atmos Sci, 1969, 26: 636–646
5 Lorenz E N. Atmospheric predictability experiments with a large numerical model. Tellus, 1982, 34: 505–513
6 新田尚. 天气的可预报性. 赵其庚, 胡圣昌, 译. 北京: 气象出版社, 1988
7 Chou J F. Predictability of the atmosphere. Adv Atmos Sci, 1989, 6: 335–346
8 丁瑞强, 李建平. 天气可预报性的时空分布. 气象学报, 2009, 67: 343–354
9 陈宝花, 李建平, 丁瑞强. 非线性局部 Lyapunov 指数与大气可预报性研究. 中国科学 D 辑: 地球科学, 2006, 36: 1068–1076
10 李建平, 丁瑞强, 陈宝花. 大气可预报性研究的回顾与展望. 21 世纪初大气科学前沿与展望. 北京: 气象出版社, 2006
11 Ding R Q, Li J P. Nonlinear finite-time Lyapunov exponent and predictability. Phys Lett A, 2007, 364: 396–400
12 Li J P, Ding R Q. Temporal-spatial distribution of atmospheric predictability limit by local dynamical analogues. Mon Weather Rev, 2011, doi: 10.1175/MWR-D-10-05020.1
13 李崇银. 大气中的季节内振荡. 大气科学, 1990, 14: 32–44
14 张庆云, 陶诗言, 彭京备. 我国灾害性天气气候事件成因机理的研究进展. 大气科学, 2008, 32: 815–825
15 张庆云, 宣守丽, 彭京备. La Nina 年冬季亚洲中高纬环流与我国南方降雪异常关系. 气候与环境研究, 2008, 13: 385–394
16 王允, 张庆云, 彭京备. 东亚冬季环流季节内振荡与 2008 年初南方大雪关系. 气候与环境研究, 2008, 13: 459–467
17 孙国武, 信飞, 陈伯民, 等. 低频天气图预报方法. 高原气象, 2008, 27(增刊): 64–68
18 Hoskins B J, Pearce R. Large Scale Dynamical Processes in the Atmosphere. New York: Academic Press, 1983
19 丑纪范, 徐明. 短期气候数值预测的进展和前景. 科学通报, 2001, 46: 890–895
20 丑纪范, 郑志海, 孙树鹏. 10~30 天延伸期数值天气预报的策略思考——直面混沌. 气象科学, 2010, 30: 569–73

21　罗小莉, 王盘兴, 李丽平. 2009 年冬春之交长江中下游异常连阴雨过程分析. 气象研究与应用, 2010, 31: 11–15
22　施能. 气象统计预报. 北京: 气象出版社, 2009, 128–145
23　郑志海, 任宏利, 黄建平. 基于季节气候可预报分量的相似误差订正方法和数值试验. 物理学报, 2009, 58: 7359–7367
24　李志锦, 纪立人. 实际预报可预报性的时空依赖性分析. 大气科学, 1996, 20: 290–297
25　穆穆, 李建平, 段晚锁, 等. 气候系统可预报性理论研究. 气候与环境研究, 2002, 7: 227–35
26　李建平, 丑纪范. 非线性大气动力学的进展. 大气科学, 2003, 27: 653–673
27　莫宁, 著. 天气预报——一个物理学的课题. 林本达, 王绍武, 译. 北京: 气象出版社, 1981

封国林,赵俊虎,支蓉,等. 动力-统计客观定量化汛期降水预测研究新进展. 应用气象学报,2013,24(6):656-665.

动力-统计客观定量化汛期降水预测研究新进展

封国林* 赵俊虎 支 蓉 龚志强 郑志海 杨 杰 熊开国
(国家气候中心 中国气象局气候研究开放实验室,北京 100081)

摘 要

汛期降水预测是短期气候预测的重要内容之一,也是难点之一。近 20 年来,动力-统计相结合的预测方法在解决这一复杂的科学难题方面取得了一定进展。该文系统地介绍了近年来国家级气候预测业务中关于动力-统计客观定量化预测的原理、最优因子订正和异常因子订正两类预测方案,及动力-统计集成的中国季节降水预测系统(FODAS1.0)。2009—2012 年的汛期降水预测中,动力-统计客观定量化预测方法 4 年平均 PS 评分为 73,距平相关系数为 0.16,体现了较高的预报技巧。但该方法仍存在不足,需通过加强气候因子与降水之间关系的诊断分析、完善短期气候模式的物理过程、改进参数化方案及研发有针对性的区域气候模式等手段,进一步提高模式本身的预报技巧,使动力-统计预测方法在汛期降水预测中发挥更大作用。

关键词: 汛期预测; 动力-统计方法; 历史资料

引 言

我国的气候灾害发生频率较高,旱、涝灾害极大影响我国的经济建设和社会发展。据统计,每年气候灾害所造成的损失占我国国民生产总值的 2.7% 左右[1]。在近几十年全球气候变暖背景下,某些灾害性天气气候事件频繁发生,且随着经济发展,气象灾害造成的经济损失越来越严重[2]。因此,对月、季节时间尺度旱、涝气候,尤其是汛期旱、涝趋势的预测是我国大气科学工作者的一项重要课题[3]。

相关研究表明,动力-统计相结合是提高短期气候预测准确率的有效途径之一[4-6]。围绕两者如何有效结合的问题,国内外开展了广泛研究。其中,在气候模式预报基础上结合数理统计方法,利用历史资料信息对模式误差进行预报是引人注目的研究方向。早在 1958 年,顾震潮就提出将数值预报从初值问题改为演变问题[7],并指出了数值天气预报中使用历史资料的重要性和可行性[8]。丑纪范从理论上探讨了在长期预报中动力和统计如何结合的问题[9-12],在此基础上,众多气象工作者从不同角度建立相似-动力模式[13-19],发展适用于动力季节预测的相似误差订正方法,并进行预测试验,其结果显示该方法能有效提高热带降水和环流的预报技巧[20-25];近年来,人们利用国家气候中心(NCC)的实际业务模式-耦合全球环流模式(CGCM)[26-32]和较全面的历史资料,发展了利用相似年的模式误差信息实现对预报年气候模式预报误差预报的汛期降水动力-统计客观定量化预测方法,进一步有效改进模式预测结果。

本文简要回顾了动力-统计预测早期的研究成果,在此基础上,系统介绍了近年来国家级气候预测业务中关于动力-统计客观定量化预测的原理、流程和方案等方面的最新研究进展。

1 动力-统计预测早期研究回顾

数值模式本身不可避免地存在误差,目前主要从正面改进模式各个环节来减小模式误差,但进一步提高预报水平的难度越来越大。相比之下,如何

2013-04-08 收到, 2013-07-22 收到再改稿。
资助项目:国家自然科学基金项目(40930952,41105055),国家重点基础研究发展计划(2012CB955902,2013CB430204),公益性行业(气象)科研专项(GYHY201106016)
* email: fenggl@cma.gov.cn

使用数理统计学方法来提高动力模式的预报水平，实现动力和统计方法的有机结合，一直是倍受关注的科学问题。事实上，在使用动力模式的数值天气预报诞生不久，动力-统计相结合的思路就应运而生。

顾震潮在充分认识到模式只用初值的缺陷后，提出将数值预报从初值问题改变为演变问题，并指出天气数值预报中使用历史资料的重要性和可行性[7-8]。丑纪范将微分方程的定解问题变为等价的泛函极值问题[9]，通过引入广义解首次建立了多时刻预报模式。此后，基于不同原理使用大气近期演变数据的预报方法被创造性提出：郑庆林等[13]发展了使用多时刻观测资料的数值天气预报新模式；邱崇践等[14-16]基于求解反问题提出了模式识别和参数优化的新方法；通过将预报场视为叠加在历史相似上的一个小扰动来建立相似-动力模式[17-19]，对模式模拟结果进行 EOF 分解，确定支撑吸引子的缩减气候模式自由度的方法[33-34]；曹鸿兴[35-36]基于大气运动是不可逆过程，推导出了多时次观测的大气自记忆性方程，并建立了自记忆预报模式[37]，进而提出了包含多个时间层的回溯阶差分格式[38-39]，上述方法利用历史资料信息求解三类反问题[40]，属于动力-统计方法的内部结合，其数值试验表明预报技巧在旬、月尺度的预报中有显著提高[41]。

动力-统计相结合的另一种表现形式为外部结合，即两种方法相对独立，统计方法一般只作为模式预报的外围辅助或后处理。早期发展的 PP 法和 MOS 法用于将环流预报信息转换成地面的天气预报[42-43]，利用过去观测或预报数据建立环流场与地表要素场之间的统计关系，然后由模式输出环流场间接预报地面要素场。在此基础上，进一步发展起来降尺度技术[44-48]和模式结果后处理技术等[49]。特别是模式误差订正技术[50-51]，已成为改善模式预报不可或缺的重要手段。任宏利等[20-23]和郑志海等[24-25]分别发展了适用于动力季节预测的相似误差订正方法，并进行了预测试验，其结果显示该方法能有效提高热带降水和环流的预报技巧。2008 年以来，利用实际业务模式 CGCM 和历史资料发展了利用相似的模式误差信息实现对预报年气候模式预报误差预报的汛期降水动力-统计客观定量化预测方法，并在 2009—2012 年汛期降水预测中实现业务应用，并体现了较高的预报技巧。

2　动力-统计客观定量化预测原理、流程及方案

2.1　动力-统计客观定量化预测的基本原理

一般来讲，数值预报是作为偏微分方程的初值问题提出来的，长期业务预报的经验表明，在相似的初始场和边界条件下，大气状况演变在一定的时间尺度范围内也具有一定的相似性[12,20-22]。因此在相似动力模式中，可以将当前的预报场视为历史相似加上一个小扰动，引入历史相似对应的预报误差信息来估计当前的预报误差，从而减小数值模式误差，将数值模式预报问题转化为预报误差的估计问题[23-25]。

2.2　动力-统计客观定量化预测流程

基于动力-统计客观定量化预测的基本原理，以全国汛期降水预测为例，图 1 给出了动力-统计客观定量化预测的总体流程。总体的预测流程主要分为 5 步：①前期处理，通过历史降水资料（美国气候预报中心组合降水分析(CMAP)夏季降水数据和国家气候中心全球海气耦合模式 CGCM 生成的 1983—2009 年共 27 年回报和预报的夏季降水数据）与气候因子（主要采用国家气候中心整编的 74 项环流指数和 NOAA 的 40 项气候因子，简称 114 项因子）的相关性检验建立各区域预测因子集（区域划分参考文献[52]）；②预测方案选取，通过异常判别指标判断预测年前期的因子是否出现异常，如果出现异常，则采用异常因子订正方案，否则采用最优多因子组合订正方案；③误差预报，通过步骤②有针对性的预测方案选取预测年的相似误差，并进行区域集合形成全国模式预报误差；④降水预报，模式预报误差与模式原始预报结果相加，得到全国汛期降水距平百分率预测结果；⑤预测检验，通过计算 PS 评分和距平相关系数(ACC)检验预测效果（评分方法详见文献[53]）。

预测流程中步骤②和③为重点，步骤②采用了两种有针对性的预测方案：一为针对正常年份具有普适性的最优多因子组合订正方案，另一为针对前期因子异常年采用异常因子订正方案；而步骤③则为动力-统计预测的核心问题，即通过相似指标选取相似年和相似误差，其中相似年份数的选取需要进行敏感性试验。

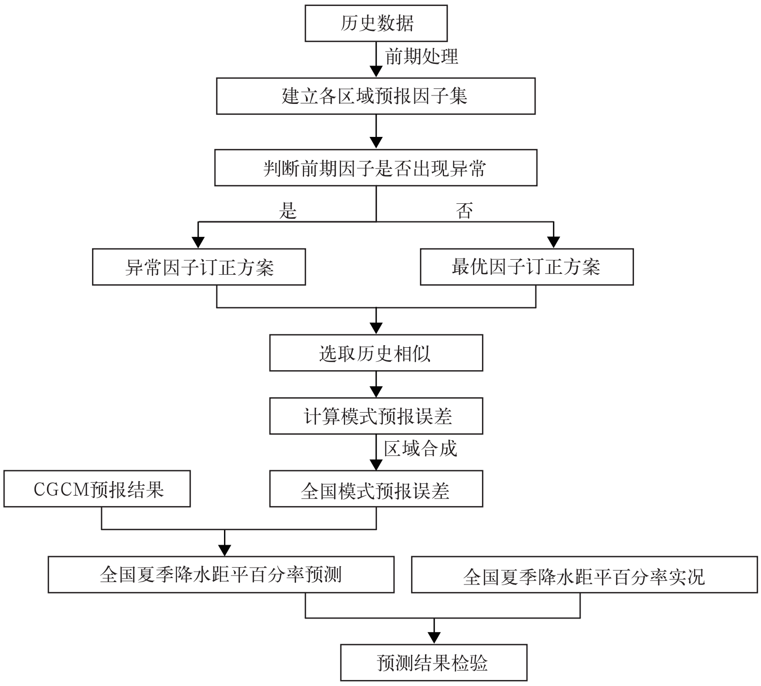

图 1　全国汛期降水动力-统计客观定量化预测流程

Fig. 1　The processes of Dynamical-Statistical Objective and Quantifiable Forecasting (DSOQF) of summer rainfall in China

2.3　动力-统计客观定量化预测方案

由于区域气候特征的不同及影响因素的差异，王启光等[26-27]、熊开国等[28-29]和杨杰等[30-31]基于动力-统计的基本原理，从不同角度分别构建了针对长江中下游地区、东北地区和华北地区汛期降水的多种预测方案，这些预测方案归纳起来大致分为两类：最优多因子组合订正方案和异常因子订正方案。

以长江中下游汛期降水预测为例，最优多因子组合订正方案的预测流程如图 2 所示。具体步骤如下[26]：①根据 CMAP 历年降水资料和历年模式回报结果得到汛期降水历年模式预报误差；②将 114 项因子在预测年(例如 2009 年)的 1 月因子和前一年(2008 年)的 2—12 月的因子作为预测年前期因子，利用各单因子以交叉检验的方式对模式结果进行相似误差订正，与 CMAP 降水资料对比，得到单因子相似误差订正时 26 年(1983—2008 年)ACC 平均排序；③选取 26 年 ACC 平均值大于 0.10 的因子进行优化组合，将其中 ACC 最大值因子作为组合的首因子，根据双因子对 1983—2008 年交叉检验的 ACC 平均值的大小判断第 2 个因子，依此类推得到前 11 个优化因子组合；④利用前 9 个、前 10 个和前 11 个优化因子共 3 种组合，对因子组采用 EOF 分解提取占 80%的主分量，利用欧氏距离对每种因子组合选取 4 个相似年，结合历年模式误差分别选取相似误差场；⑤将各相似年误差场根据重复出现的次数加权集合平均，结合 2009 年模式预测结果，得到 2009 年汛期降水预测结果。2003—2009 年 7 年的独立样本回报结果表明，基于最优多因子组合的动力-统计集成预测方案具有较高的预报技巧，ACC 平均值为 0.43，相比于系统误差订正的 7 年 ACC 平均值 0.28 有了明显提高[26]。

熊开国等[29]通过确定主导因子，应用演化相似及优化因子组合配置等途径，发展了最优多因子动态配置汛期降水相似动力预测新技术，并对我国东北地区汛期降水进行了预报试验，交叉检验及对 2005—2009 年进行独立样本检验的结果均表明该方法对东北汛期降水有一定预报技巧，表明了汛期降水预测中采用多因子动态配置的必要性，同时也证实了利用历史资料改进数值模式的另类途径是可行的，显示出业务预报应用的潜在能力。杨杰等[30]通过对前期因子进行单因子交叉检验筛选，建立适用于华北夏季降水的区域特点的普适性固定关键相似因子集，考虑到影响因子对区域汛期降水的年际或年代际变化导致在不同的研究时段内的最优多因子配置的动态变化，结合历史近期最优因子配置得到预报时段内稳定的最优关键因子组合，研发了动

态最优多因子组合的华北汛期降水模式误差估计及预报技术，改善华北地区夏季降水预报效果。

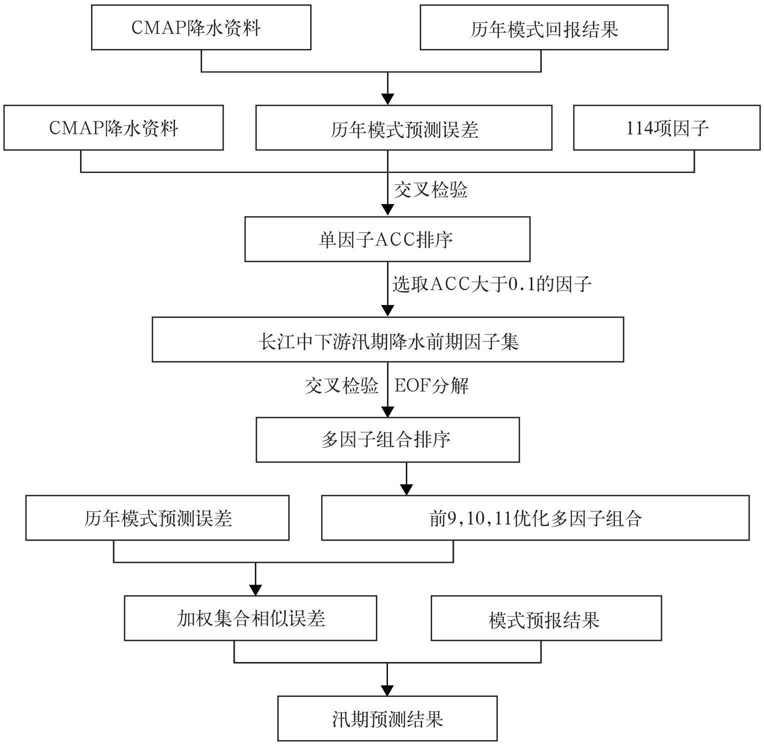

图 2　长江中下游地区汛期降水最优因子组合订正方案[26]

Fig. 2　The scheme for revising the forecasting of summer rainfall in the mid-lower reaches of the Yangtze based on optimal combination factors(from reference [26])

上述分别针对长江中下游地区、东北地区和华北地区的动力-统计集成预测方案、最优多因子动态配置预测方案和动态最优多因子组合预测方案，预测方法存在一定差异，但均属于针对正常年份具有普适性的最优多因子组合订正方案。另一类预测方案为针对前期因子年采用异常因子发生异常订正方案，预测流程如图 3 所示。

由图 3 可知，异常因子订正方案的预测流程主要包括 6 步[27,31]：①区域降水前期关键因子集建立，②因子异常级阈值判断，③判断是否存在关键性异常因子，④异常因子独立性判断及优化配置，⑤相似年选取及加权集合相似误差计算，⑥求取汛期预测结果。

王启光等[27]研究发现，114 项逐月因子在历年汛期前期总会出现部分因子异常的状况，其中 1985 年前期异常偏小的因子明显较多，而 1998 年和 1999 年前期异常偏大的因子明显多于往年，1983—2009 年 27 年因子异常偏小数量呈较明显的减小趋势，并提出了基于因子异常并压缩维度预报 NOFM 误差的方法，2005—2009 年 5 年独立样本回报结果表明，该方法可以将 5 年 ACC 平均值由系统误差订正的 0.22 提高到 0.47，提高了长江中下游地区汛期降水预报准确率。

此外，赵俊虎等[54]研究了西太平洋副热带高压（以下简称副高）指数的特征，将副高西伸脊点指数和脊线指数的距平投影于二维平面，对副高进行分类，并对其各种类型下我国夏季降水进行了合成分析，发现夏季副高西伸脊点和脊线不同配置下我国汛期降水的总体分布具有明显的规律性。在此基础上，杨杰等[55]基于动力-统计客观定量化预报原理，将模式误差动力-统计客观定量化预报方案应用于副高的客观定量化预测，并对 2003—2010 年的副高区域的 500 hPa 高度场进行了回报检验，结果显示该方案在数值模式预报结果基础上有进一步提高，显示出较好的预测水平。然后从高度场预测结果中提取出副高脊线与西伸脊点指数，将其投影于二维平面，与文献[54]中副高统计分类相结合，进而得到了预报年副高所属类型下我国汛期的可能雨型，检验结果表明：预测的投影类型所对应的降水合成分布与实况降水具有很好的一致性，达到了通过副高的定量化预测对汛

期的旱涝分布形势进行预测的目的,为进一步提高汛期降水预测水平提供一种可能的思路。

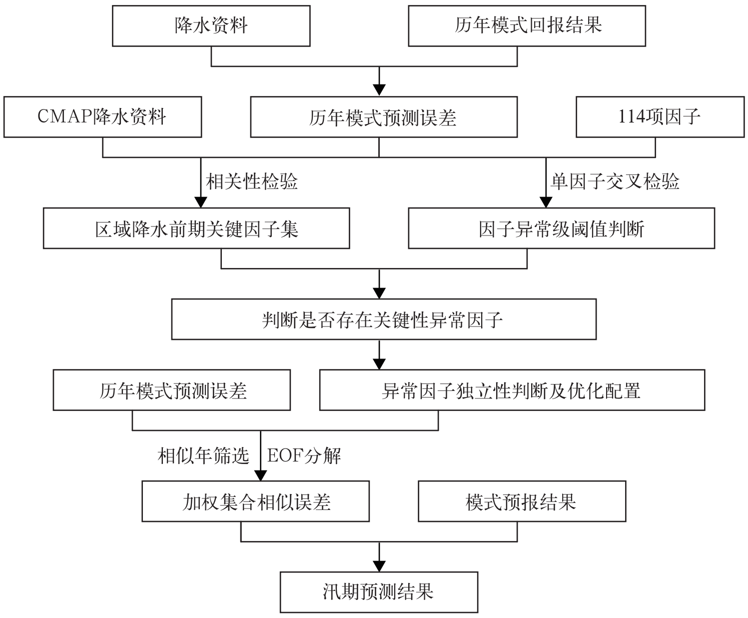

图 3　异常因子订正方案

Fig. 3　The scheme based on anomalistic factors

3　动力-统计集成的中国季节降水预测系统

利用国家气候中心业务预报模式 CGCM 和两类动力-统计预测方案,建立了动力与统计集成的季节降水预测系统(FODAS1.0)。该系统在动力-统计客观定量化预测理论和方法的基础上,充分借鉴国家气候中心和区域、省级气候中心现有科研和业务成果,尤其是预报员的诊断技术和预报经验,研制适合区域气候特点的预测方案。目前,FODAS1.0 已在国家气候中心、8 个区域气候中心和广西、山东等多省市气候中心实现准业务试用。

图 4 为 FODAS1.0 系统框架图。系统主要包括以下模块:实时数据接收模块、历史检索模块、相

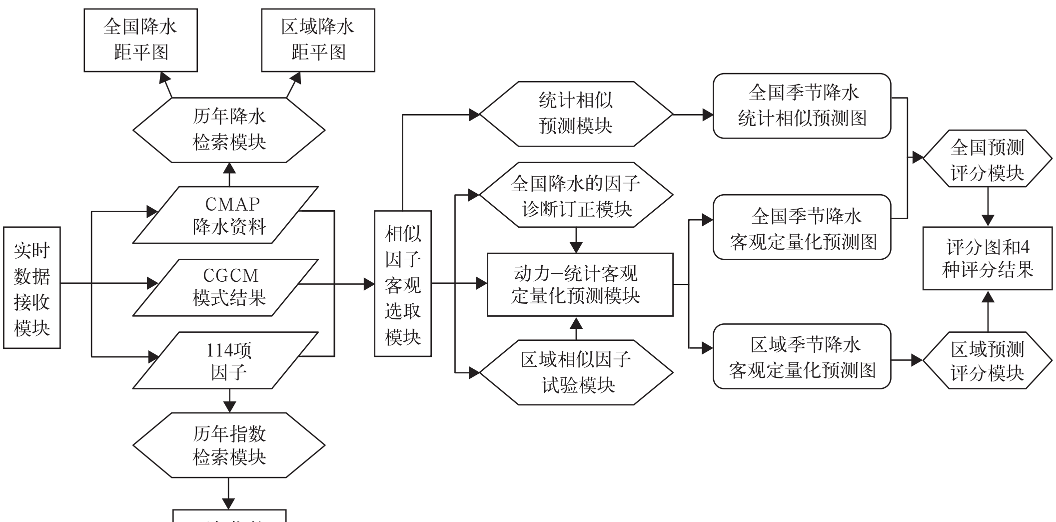

图 4　FODAS1.0 系统框架图

Fig. 4　The frame diagram for FODAS1.0

似因子客观选取模块、统计相似预测模块、全国降水因子诊断订正模块、区域相似因子订正模块、动力-统计客观定量化预测模块、预测评分模块。预报产品主要包括全国(或区域)季节降水的统计相似预测图、动力-统计客观定量化预测图以及预测产品的检验图形等。此外,该系统还可以检索历年降水距平百分率、因子演变曲线等,供预报员参考。FODAS1.0 的推广应用,为区域和省级气候中心进一步加强月-季节尺度降水等的客观定量化预报提供了有力支撑,使之更好地为国家和区域的防灾、减灾决策服务。

4　2009—2012 年汛期降水动力-统计客观定量化预测效果检验

围绕动力-统计客观定量化预测的基本原理,采用动力-统计客观定量化预测方法对 2009—2012 年我国汛期降水进行了实际预测,逐年情况具体如下。

2009 年我国夏季降水整体偏少,黄淮流域、长江下游、江南东部、东北北部和青藏高原东部等地区降水较常年偏多,其余大部分地区降水偏少(图 5a)。2009 年动力-统计客观定量化预测主雨带位于黄淮流域,华南东部至江南南部、青藏高原东部及东北北部降水偏多,西北至东北东南部的北方大部地区、西南地区、长江下游等地区降水偏少(图 5b)。其中东北北部、黄淮流域、青藏高原东部及江南东部的降水偏多的预测与实况相符,西北至东北东部及西南地区的降水偏少预测也与实况相符,而华南地区降水偏多的预测与实况不符,预测结果 PS 评分为 79,ACC 为 0.38。

2010 年全国夏季降水整体偏多,主雨带位于江汉至江南一带地区,西北西部、东北北部和南部、长江中下游及其以南地区降水较常年偏多,华北、西北东部及淮河流域等地区降水较常年偏少;动力-统计客观定量化预测全国降水偏多,预测除西北东部、华北南部及华南等少数地区外,其余大部地区降水偏多,全国降水偏多预测正确,但是北方降水偏多预测错误,预测结果 PS 评分为 72,ACC 为 0.10[56]。对此,赵俊虎等[56]在分析 2010 年夏季降水异常气候成因的基础上,进行降水动力统计-诊断回报,回报结果较初次预测有明显改进,回报结果 PS 评分为 75,ACC 为 0.26,从而验证了前冬海温和积雪的异常是导致 2010 年夏季降水异常分布的主要气候成因,并提出了改进优化多因子汛期降水客观定量化预测方法的可能途径。

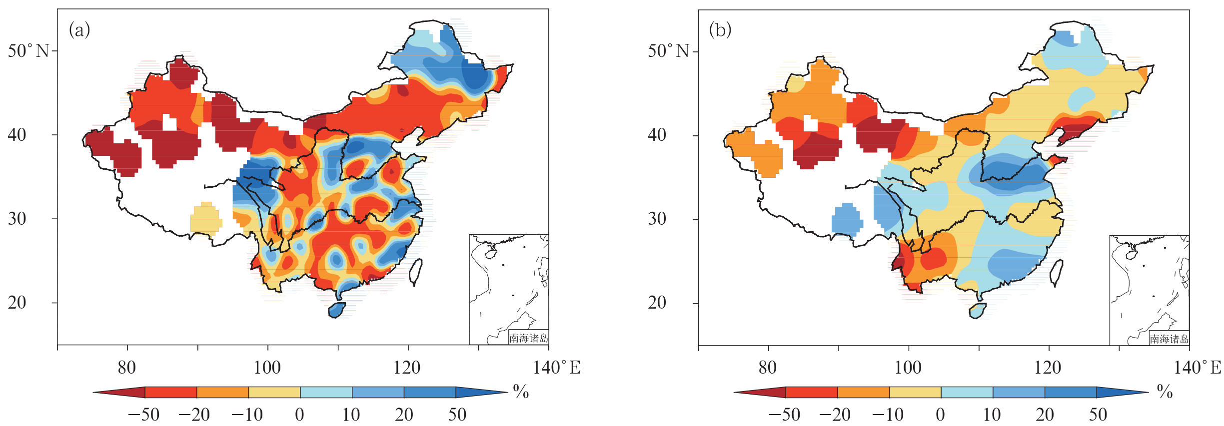

图 5　2009 年夏季降水距平百分率 (a)观测,(b)预测

Fig. 5　Distributions of observed(a) and predicted(b) summer rainfall anomaly percentages in 2009

2011 年夏季我国降水整体偏少,降水异常偏多的区域主要位于长江中下游地区,华北东部至东北西部、西藏西南部至陕南一带地区降水也偏多;南疆、内蒙古中部、东北东南部、华北南部及西南至江南南部大范围地区降水偏少[57]。动力-统计客观定量化预测[57]主雨带位于华北,华南东部至江南南部、西藏和西北中东部降水偏多,新疆经内蒙古至东北的北方一带、西南经江汉至长江下游一带地区降

水偏少;其中西南地区、南疆、内蒙古中西部及东北东部的干旱预测正确,西藏南部、西北东部、江淮部分地区以及华北沿渤海湾地区偏涝预测与实况相符;而黄淮流域及华南、江南等地区的预测结果与实况差异较大;预测结果PS评分为70,ACC为0.12。此外,在上述预测方法的基础上,进行了动力统计-诊断预测[57],预测主雨带位于江淮流域,新疆西部、西藏至黄河上游、黑龙江东北部及华南地区降水偏多;而新疆中东部经内蒙古至东北一带的北方地区及西南等地区降水偏少;其中对主雨带的预测接近实况,新疆东部、内蒙古大部、黄河中下游、东北东南部及西南地区的干旱预测与实况一致,而东北西北部、华南等地区预测与实况不符;预测结果PS评分为75,ACC为0.25。赵俊虎等[57]以长江中下游地区为例,对比说明了动力-统计客观定量化和动力统计-诊断两种预测方法选取因子的差异及后者预测结果有一定提高的原因,并指出2011年夏季主雨带偏南是中高纬度地区阻塞形势与低纬度地区副高的季节内异常振荡及二者逐月不同配置的产物,而中高纬度地区阻塞形势与低纬度地区副高的季节内异常振荡是由海温、积雪等外强迫及东亚环流系统内部成员相互作用共同所致。

2012年夏季我国降水整体偏多,大体呈北方涝、长江旱的分布,主雨带位于黄河流域及其以北,降水异常偏多的区域主要位于西北大部、内蒙古和环渤海湾,此外东北大部、西南北部、江南等地区降水偏多。黄淮、江淮、长江中游至广西北部及广东大部等地区降水偏少,其中江汉至淮河上游降水异常偏少(见文献[58]图3a)。2012年3月动力-统计客观定量化预测南北两条雨带,即河套地区经华北北部至黑龙江的北方多雨带和西南经华南至江南大部的南方多雨带,此外预测黄淮流域降水也偏多,而其他大部地方降水偏少(图略);其中北方和江南等地的降水偏多预报正确,华中地区降水偏少预报正确,西北大部地区降水偏少预测错误,广东、云南等地降水偏多预测与实况不符;预测结果PS评分为70,ACC为0.03。2012年5月动力-统计客观定量化预测主雨带位于北方地区,此外预测黄河下游和西南地区降水偏多,此外大部分地区降水偏少,广西至淮河流域一带大范围地区降水异常偏少(见文献[58]图3b);其中,北方多雨带预测和广西至淮河流域一带大范围地区降水偏少预测正确;内蒙古东部至辽宁、江南等地预测降水偏少,与实况不符;预测结果PS评分为76,ACC为0.16。

5 小 结

我国地处东亚季风区,地理自然条件复杂,区域气候差异较大,围绕以旱涝预测为焦点的月-季节尺度的短期气候预测,在我国区域经济发展、建设中起着重要作用,一直是国家和区域防灾减灾工作的重中之重[59]。近几年,在全球增暖的背景下,我国区域气候异常和极端事件频发[60-62],客观上增加了国家和区域对于提高月-季节气候预测准确率的需求。此外,由于全球增暖导致了影响短期气候的关键因子发生变化,即在全球变暖背景下年代际变化带来了统计相关不稳定的问题[63],更增加了预测的难度和不确定性。为了适应气候变化和预测的新需求,发展新的统计诊断与预测技术十分必要[64-65]。从国内外的研究进展来看,充分利用历史资料和数值模式,采用动力和统计相结合的思路进行短期气候预测,已成为提高客观预测水平的重要手段,有着广阔的发展前景[66-68]。动力学方法和数理统计学方法在天气预报和短期气候预测中各有所长,如何使动力与统计更有机的结合,是需要继续深入研究的一个重要课题。

近年来动力-统计客观定量化预测方法在短期气候预测领域取得了一定突破,该方法在近4年的全国汛期降水预测中表现出较高的预报技巧,这更说明了动力-统计相结合的短期气候预测思路的正确性。目前,动力-统计客观定量化预测方法已经从季节气候预测移植到月气候预测中,此外还从降水预测向气温和高度场预测[69]进行了拓展。但该方法仅是一种模式预报的外围辅助或后处理手段,也存在不足之处,如采用多因子选取相似年时,部分因子与降水之间的物理机制不清晰。目前只是进行月、季节尺度气候预测试验,今后还需要向年际、年代际气候预测方向拓展;预测结果对模式的预测能力依赖性强,若模式结果很差,动力-统计预测的提升空间也很有限。因此,需要通过加强因子与降水之间关系的诊断分析、完善模式物理过程、改进参数化方案及研发有针对性的区域气候模式等手段,进

一步提高模式本身的预报技巧,使动力-统计方法有更大的用武之地。

参考文献

[1] 黄荣辉,蔡榕硕,陈际龙,等. 我国旱涝气候灾害的年代际变化及其与东亚气候系统变化的关系. 大气科学,2006,30(5):730-742.

[2] 吴国雄,李建平,周天军,等. 影响我国短期气候异常的关键区:亚印太交汇区. 地球科学进展,2006,21(11):1109-1118.

[3] 丑纪范,徐明. 短期气候数值预测的进展和前景. 科学通报,2001,46(1):890-894.

[4] Barnett T P,Preisendorfer R W. Multifield analog prediction of short-term climate fluctuations using a climate state vector. *J Atmos Sci*,1978,35(10):1771-1787.

[5] Chao J P,Guo Y F,Xin R N. A theory and method of long-range numerical weather forecasts. *J Meteor Soc Japan*,1982,60:282-291.

[6] Van H M. Searching for analogues,how long must we wait? *Tellus*,1994,46A:314-324.

[7] 顾震潮. 作为初值问题的天气形势预报与地面天气历史演变作预报的等值性. 气象学报,1958,29(2):93-98.

[8] 顾震潮. 天气数值预报中过去资料的使用问题. 气象学报,1958,29(3):176-184.

[9] 丑纪范. 天气数值预报中使用过去资料的问题. 中国科学,1974,17(6):635-644.

[10] 丑纪范. 为什么要动力-统计相结合?——兼论如何结合. 高原气象,1986,5(4):367-372.

[11] 丑纪范. 短期气候预测的现状、问题与出路(一). 新疆气象,2003,26(1):1-4.

[12] 丑纪范,任宏利. 数值天气预报——另类途径的必要性和可行性. 应用气象学报,2006,17(2):240-244.

[13] 郑庆林,杜行远. 使用多时刻观测资料的数值天气预报新模式. 中国科学,1973,16(2):289-297.

[14] 邱崇践,丑纪范. 改进数值天气预报的一个新途径. 中国科学:B辑,1987,17(8):903-910.

[15] 邱崇践,丑纪范. 预报模式识别的扰动方法. 大气科学,1988,12(3):225-232.

[16] 邱崇践,丑纪范. 预报模式的参数优化方法. 中国科学:B辑,1990,20(2):218-224.

[17] 邱崇践,丑纪范. 天气预报的相似-动力方法. 大气科学,1989,57(2):131-142.

[18] 黄建平,王绍武. 相似-动力模式的季节预报试验. 中国科学:B辑,1991,35(2):216-224.

[19] Huang Jianping,Yi Yuhong,Chou Jifan. An analogue-dynamical long-range numerical weather prediction system incorporating historical evolution. *Quart J Roy Meteor Soc*,1993,119:547-565.

[20] 任宏利,丑纪范. 统计-动力相结合的相似误差订正法. 气象学报,2005,63(6):988-993.

[21] 任宏利,张培群,李维京,等. 基于多个参考态更新的动力相似预报方法及应用. 物理学报,2006, 55(8):4388-4396.

[22] 任宏利,丑纪范. 动力相似预报的策略和方法研究. 中国科学:D辑,2007,37(8):1101-1109.

[23] 任宏利,封国林,丑纪范. 论动力相似预报的物理基础问题. 地球科学进展,2007,22(10):1027-1035.

[24] 郑志海,封国林,丑纪范,等. 数值预报中自由度的压缩及误差相似性规律. 应用气象学报,2010,21(2):139-148.

[25] 郑志海,任宏利,黄建平. 基于季节气候可预报分量的相似误差订正方法和数值试验. 物理学报,2009,58(10):7359-7367.

[26] 王启光,封国林,郑志海,等. 长江中下游汛期降水优化多因子组合客观定量化预测研究. 大气科学,2011,35(2):287-297.

[27] 王启光,封国林,支蓉,等. 长江中下游汛期降水数值预报业务模式误差场预报研究. 气象学报,2012,70(4):789-796.

[28] Xiong Kaiguo,Feng Guolin,Huang Jianping,et al. Analogue-dynamical prediction of monsoon precipitation in Northeast China based on changeable configuration of optimal multi-predictor. *Acta Meteor Sinica*,2011,25(3):316-326.

[29] 熊开国,赵俊虎,封国林,等. 汛期降水相似动力预报——模式误差主分量相似预报方法. 物理学报,2012,61(14):149204, doi:10.7498/aps.61.149204.

[30] 杨杰,王启光,支蓉,等. 动态最优多因子组合的华北汛期降水模式误差估计及预报,物理学报,2011,60(2):029204.

[31] 杨杰,赵俊虎,郑志海,等. 华北汛期降水多因子相似订正方案与预报试验. 大气科学,2012,36(1):11-22.

[32] 李维京,张培群,李清泉,等. 动力气候模式预测系统业务化及其应用. 应用气象学报,2005,16(增刊):1-11.

[33] 张邦林,丑纪范. 经验正交函数在数值气候模拟中的应用. 中国科学:B辑,1991,21(4):442-448.

[34] 张培群,丑纪范. 改进月延伸预报的一种方法. 高原气象,1997,16(4):376-388.

[35] 曹鸿兴. 大气运动的自记忆方程. 中国科学:B辑,1993,23(1):104-112.

[36] 曹鸿兴. 大气自忆谱模式及其应用. 大气科学,1998,22(1):119-126.

[37] 曹鸿兴,谷湘潜. 自忆谱模式对中期环流预报的改进. 自然科学进展,2001,11(3):309-313.

[38] 封国林,曹鸿兴,魏凤英,等. 长江三角洲汛期预报模式的研究及其初步应用. 气象学报,2001,59(2):206-212.

[39] Feng G L,Cao H X,Dong W J,et al. A new differential scheme with multi-levels. *Chin Phys*,10:1004-1010.

[40] 范新岗,丑纪范. 提为反问题的数值预报方法与实验Ⅰ:三类反问题及数值解法. 大气科学,1999,23(5):543-550.

[41] 龚建东,丑纪范. 论过去资料在数值天气预报中使用的理论和方法. 高原气象,1999,18(3):392-399.

[42] Klein W H,Lewis B M,Enger I. Objective preciction of five-day mean temperatures during winter. *J Meteorology*,1959,16:672-682.

[43] Klein W H. Computer prediction of precipitation probability in the United States. *J Appl Met*,1971,10:903-915.

[44] Feddersen H,Uffe A. A method for statistical downscaling of seasonal ensemble predictions. *Tellus*,2005,57A:398-408.

[45] 李维京,陈丽娟.动力延伸预报产品释用方法的研究.气象学报,1999,57(3):338-345.

[46] 陈丽娟,李维京,张培群,等.降尺度技术在月降水预报中的应用.应用气象学报,2003,14(6):648-655.

[47] 魏凤英,黄嘉佑.我国东部夏季降水量统计降尺度的可预测性研究.热带气象学报,2010,26(4):483-488.

[48] 郭彦,李建平.一种分离时间尺度的统计降尺度模型的建立和应用——以华北汛期降水为例.大气科学,2012,36(2):385-396.

[49] Marzban C. Neural networks for postprocessing model output:ARPS. *Mon Wea Rev*,2003,131:1103-1111.

[50] Saha S. Response of the NMC MRF model to systematic error correction within integration. *Mon Wea Rev*,1992,120:345-360.

[51] 任宏利.动力相似预报的策略和方法.兰州:兰州大学,2006.

[52] 赵俊虎,封国林,张世轩,等.近48年中国的季节变化与极端温度事件的联系.物理学报,2011,60(9):099205.

[53] 陈桂英,赵振国.短期气候预测评估方法和业务初估.应用气象学报,1998,9(2):178-185.

[54] 赵俊虎,封国林,杨杰,等.夏季西太副高的不同类型下中国汛期大尺度旱涝分布.气象学报,2012,70(5):1021-1031.

[55] 杨杰,封国林,赵俊虎,等.夏季西太副高的客观定量化预测及其对汛期降水的指示.气象学报,2012,70(5):1032-1044.

[56] 赵俊虎,封国林,王启光,等.2010年我国夏季降水异常气候成因分析及预测.大气科学,2011,35(6):1069-1078.

[57] 赵俊虎,杨杰,封国林,等.2011年我国夏季降水动力统计预测与异常成因.应用气象学报,2013,24(1):43-54.

[58] 宋连春,肖风劲,李威.我国现代气候业务现状及未来发展趋势.应用气象学报,2013,24(5):513-520.

[59] 魏凤英.我国短期气候预测的物理基础及其预测思路.应用气象学报,2011,22(1):1-11.

[60] 任国玉,封国林,严中伟.中国极端气候变化观测研究回顾与展望.气候与环境研究,2010,15(4):337-353.

[61] 封国林,杨涵洧,张世轩,等.2011年春末夏初长江中下游地区旱涝急转成因初探.大气科学,2012,36(5):1009-1026.

[62] 杨萍,刘伟东,王启光,等.近40年我国极端温度的变化趋势和季节特征.应用气象学报,2010,21(1):29-36.

[63] 赵平,周秀骥.近40年我国东部降水持续时间和雨带移动的年代际变化.应用气象学报,2006,17(5):548-556.

[64] 魏凤英.气候统计诊断与预测方法研究进展——纪念中国气象科学研究院成立50周年.应用气象学报,2006,17(6):736-742.

[65] 范可,王会军,Choi Young-Jean.一个长江中下游夏季降水的物理统计预测模型.科学通报,2007,52(24):2900-2905.

[66] 黄建平,衣育红,王绍武.相似-动力模式的由夏季报冬季的季节预报试验.气象学报,1993,51(1):118-121.

[67] Wang H J,Fan K. A new scheme for improving the seasonal prediction of summer precipitation anomalies. *Wea Forecasting*,2009,24:548-554.

[68] 王会军,范可,郎咸梅,等.我国短期气候预测的新理论、新方法和新技术.北京:气象出版社,2012:147-159.

[69] 赵俊虎,杨杰,龚志强,等.欧亚中高纬阻塞高压关键区高度场动力-统计跨季度预测试验.物理学报,2013,62(9):099206,doi:10.7498/aps.62.099206.

Recent Progress on the Objective and Quantifiable Forecast of Summer Precipitation Based on Dynamical-statistical Method

Feng Guolin　Zhao Junhu　Zhi Rong　Gong Zhiqiang
Zheng Zhihai　Yang Jie　Xiong Kaiguo

(*Laboratory for Climate Studies*, *National Climate Center*, *CMA*, *Beijing* 100081)

Abstract

Short-term climatic prediction, which mainly aims at monthly, seasonal and annual time scales, is very important for the public and government decision making. The trend of summer flood and drought distribution is one of the most important contents in operational forecast. Generally, there are two types of forecasting methods, including statistical method and dynamical method, which both have advantages and disadvantages. Therefore, the general consensus is to let them learn from each other, merging and developing. During recent 50 years, the Dynamical-Statistical Integration Forecasting Method (DSIFM) has made great progresses in dealing with the complex scientific issue of summer precipitation forecasting in China and abroad.

The research results in early period and the development about DSIFM are briefly reviewed, as well as the two forms of dynamical-statistical integration forecasting method. And then, the principle, processes and programs of Dynamical-Statistical Objective Quantitative Forecasting (DSOQF) in recent operational forecast are systematically introduced. Based on the Coupled Global Circulation Model (CGCM) of National Climate Center and two types of prediction scheme of DSOQF, a dynamical-statistical integrated forecasting system for seasonal precipitation (FODAS1.0) is set up, which fully assimilates existing research and profession achievements, especially forecaster diagnostic techniques and forecasting experience from national, regional and provincial climate centers. Suitable regional climate characteristics prediction scheme is also developed based on the theory and methods of DSOQF. By now, FODAS1.0 achieves quasi-operational trial in National Climate Center, 8 regional climate centers and Guangxi, Shandong and other provincial climate centers.

Experimental predictions are carried out for the summer rainfall in China from 2009 to 2012 with the method of DSOQF. The predictive score (PS) from 2009 to 2012 are 79, 72, 70 and 70, respectively. The anomaly correlation coefficient (ACC) from 2009 to 2012 are 0.38, 0.10, 0.12 and 0.03. For abnormal years such as 2010 and 2011, diagnostic analysis is performed. Overall, the forecast results are ideal, but it still needs further improving.

The problems in DSIFM and the solutions are also discussed. The forecasting skills can be improved by strengthening diagnostic analysis of the relationship between precipitation and its main factors, improving the physics processes and parameterization scheme of short-term climate models, and developing the targeted regional climate models. The DSIFM will be more useful in the future.

Key words: forecasting of summer rainfall; dynamical-statistical method; historical data

资源科学 Resources Science
第35卷 第6期 2013年6月 2013,35(6):1268-1276 Vol.35,No.6 Jun.,2013

文章编号:1007-7588(2013)06-1268-09

长江上游降水变化及其对径流的影响

冯亚文[1,2],任国玉[1],刘志雨[3],吴吉东[4],张　雷[1]

(1. 中国气象局气候研究开放实验室,国家气候中心,北京100081;
2. 中国科学院地理科学与资源研究所,北京100101;3. 水利部水利信息中心,北京100053);
4. 北京师范大学环境演变与自然灾害教育部重点实验室,北京100875

摘　要:利用长江上游地区60个国家基本、基准站1960年-2009年的月降水量资料和干流区屏山、寸滩和宜昌3个水文控制站同期径流资料,分区域对长江上游地区的降水量、径流量变化趋势以及降水量和径流量的相关性进行了分析。主要结论如下:①年降水量呈上升和下降趋势的气象站点空间分布相对集中,分别分布在屏山站以上流域和屏山站以下流域;屏山站以下流域和整个长江上游地区年降水量近50年呈现下降趋势,屏山站以下流域秋季降水量的显著减少是长江上游年降水量减少的主要原因;②整个长江上游月降水量趋势从1月-7月以上升趋势为主逐渐转变到8月-12月以下降趋势为主,且月降水量变化趋势空间分布有从3月份至9份月由屏山站以下流域开始逐渐向长江源头过渡的趋势,到9月份整个长江上游基本呈减少趋势;③与降水量变化趋势基本一致,屏山站以下流域寸滩和宜昌站年径流下降趋势显著的主要原因是5月-11月径流的减少,且秋季下降显著,而屏山站春、夏、冬和年径流呈上升趋势,且春季和冬季上升趋势很显著;④整个上游地区面雨量与径流量具有很好的相关性,同期面雨量与径流量在月、季和年尺度上相关性都较显著。屏山以上流域隔月相关比同期相关性强。

关键词:长江上游;降水;径流;趋势;面雨量;气候变化

1 引言

长江上游流域,地形复杂,环境条件多样,不同地区降水差异相对较大。未来南水北调西线工程将从通天河、雅砻江、大渡河调水,这将改变长江流域宜宾以上的来水情况;三峡大坝竣工后,上游降水和径流的变化对其蓄水量和工程效益也有重要影响。了解长江上游区域降水和径流的变化趋势以及降水量对径流量的影响,对于三江源地区生态和环境建设、三峡大坝年度和季节性蓄水的调度和未来南水北调西线工程的建设与管理等,均具有重要现实意义[1-3]。

前人对长江流域的降水和径流变化已做了许多研究。如:任国玉等[4]利用1951年-1996年地面气象记录资料计算我国全年和季节降水量长期变化趋势特征指数,结果表明我国长江中下游地区年和夏季降水量呈现明显增加趋势;姜彤等[5]研究发现1961年-2000年整个长江流域夏季降水显著增加;沈浒英等[6]分析长江流域降水径流的年代际变化,结果表明1951年-2001年长江流域夏季降水有更加集中的趋势;Zhang等[7]研究发现近50年嘉陵江干流和乌江流域9月降水显著减少;Wang等[8]认为1958年-2008年长江流域降水的减少是寸滩、宜昌、汉口、大通站径流量减少的主要原因;王艳君等[9]研究发现1961年-2000年长江上游年和冬季降水显著增加。这些研究多侧重于整个流域年、季尺度降水和径流变化的分析,对上游单站月时间尺度的降水量和径流量变化分析以及把两者结合起来的研究较少。本文侧重于长江上游60个气象站的月降水量时空变化趋势分析,进而计算月、季和年度流域面雨量,并分析降水量对径流量变化的影响,以期为长江流域的水量调度、水资源保护、规划与管理提供科学依据。

收稿日期:2013-01-08;修订日期:2013-02-02
基金项目:国家公益性行业专项(编号:GYHY201206012);973项目(编号:2010CB428400)。
作者简介:冯亚文,女,甘肃会宁人,硕士,从事水文气象研究。E-mail:yawenf@163.com

2 数据来源与研究方法

2.1 数据来源

采用长江上游60个国家基本气象站和基准气候站观测资料。在这些站点中,大部分记录开始于20世纪60年代,为保证所有气象站点资料长度一致,统一采用1960年–2009年的月降水观测记录。中国气象局国家气象信息中心对资料进行了质量控制。部分站点个别月份存在缺测,由于上游站点分布较稀疏,再加上地形起伏相对较大,临近站点之间观测数据相关程度不高,采用临近站点资料进行空间插值并不理想,因此对个别月份缺测数据(占0.1%)的处理,均选用前后两年该月降水的平均值来插补,年降水数据则由月降水累加所得,以保证降水序列的完整和连续性。

水文资料选取长江上游屏山、寸滩和宜昌3个干流控制站1960年–2009年的月径流数据,资料来源于水利部水文信息中心。研究区及气象、水文站点分布见图1。

2.2 研究方法

线性倾向估计和Mann–Kendall秩次相关法是趋势分析最常用的方法[10–13],另外,还有累积距平、滑动平均、二次平滑、三次样条函数及小波分析等趋势分析方法[14],而线性倾向估计以其简洁易操作特点在国内水文气象趋势分析中多被采用[4,6,9,10,12]。

本文中降水量和径流量的趋势分析采用线性倾向估计法。若用 y_i 表示样本量为 n 的某一变量,用 x_i 表示 y_i 所对应的时间,建立 x_i 与 y_i 之间的一元线性回归方程[14]:

$$y_i = ax_i + b, \qquad i = 1,\ 2,\ \cdots,\ n \tag{1}$$

式中 a 为回归系数;b 为回归常数;$a\times10$ 称为气候变化速率或变化速率,即每10a 气象要素的趋势变化值,其值为正或负的绝对值大小即表示 y_i 随 x_i 上升或下降的快慢。变量 y 与时间 x 之间的相关系数 r 计算公式如下[14]:

$$r_{xy} = \frac{\sum_{i=1}^{n}\left(y_i-\bar{y}\right)\left(x_i-\bar{x}\right)}{\sqrt{\sum_{i=1}^{n}\left(y_i-\bar{y}\right)^2\sum_{i=1}^{n}\left(x_i-\bar{x}\right)^2}} \tag{2}$$

式中 n 为时间序号;$\bar{y}$ 和 $\bar{x}$ 分别为变量 y 和时间 x 的均值;r 为正(负)时,表示变量在该时间段内有线性增加(减少)的趋势;r 可称为趋势系数,给定显著性水平α,若 $|r| > r_a$,认为 y 的变化趋势是显著的。在 n =50的条件下,当 $|r|$ 的值不小于0.231、0.273和0.354时,表示变量 y 的线性趋势通过了信度为0.10、0.05和0.01的显著性检验,分别表示趋势变化较显著、显著和很显著。流域面雨量采用泰森多边

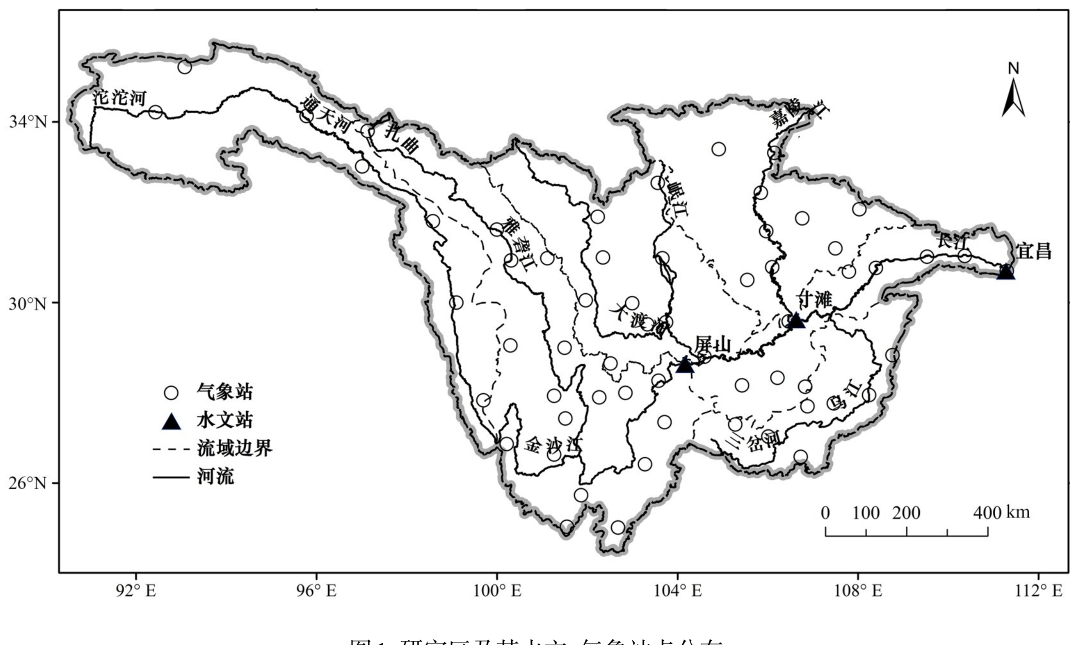

图1 研究区及其水文、气象站点分布

Fig.1 The study area and hydro–meteorological stations

形方法计算[15]：首先求得各测站的面积权重系数，然后用各测站雨量与该测站面积权重系数相乘后累加得到整个流域的面雨量 p：

$$p = f_1 p_1 + f_2 p_2 + ,\cdots, + f_n p_n \tag{3}$$

式中 p 为流域面雨量；f_1，f_2，…，f_n 分别为各测站的面积权重系数；p_1，p_2，…，p_n 分别为各测站同时期降雨量。

3 降水趋势分析

3.1 年降水量趋势空间分布特征

长江上游60个气象站近50年（1960年–2009年）年降水量趋势变化空间分布如图2所示。年降水量呈上升趋势的气象站有31个，主要分布在江源地区、金沙江以及雅砻江流域，即屏山水文站控制流域基本表现为上升趋势，其中上升趋势较显著的是江源地区的伍道梁站以及川西高原的康定站和小金站。具有下降趋势的气象站有29个，主要分布在屏山站以下流域（本文指屏山至宜昌段），其中宜宾、都江堰、峨眉山、乐山、昭通、略阳、广元和遵义8个气象站降水下降趋势较显著，宜宾、都江堰、峨眉山、乐山和昭通站的年降水下降幅度都超过–20mm/10a，形成一个降水量趋势性下降中心。

总体来说，长江上游年降水量下降和上升的区域分布都比较集中，即屏山水文站以上流域和以下流域降水变化趋势基本相反，这两个区域分别对应于竺可桢中国气候区划中的西藏类和云南高原类气候类型[16]，分别主要受高原大陆性气候和海洋性过渡气候的影响。这种趋势可能会导致局部地区洪涝或干旱发生的频率增加，但整个长江上游流域降水变化趋势具有升降互补性，可能在很大程度上平抑了三峡大坝以上流域面雨量长期趋势性变化。因此，以下分析面雨量变化时将长江上游划分为屏山站以上流域、屏山站以下流域以及整个上游流域分别进行讨论。

3.2 年、季面雨量变化趋势

长江上游流域年、季雨量趋势系数和趋势变化速率见表1。

屏山站以上流域：年面雨量呈上升趋势，变化速率为7.37mm/10a，但上升趋势不显著；春、夏和冬季三季面雨量均表现出上升趋势，变化速率分别为5.01mm/10a、2.06mm/10a和0.85mm/10a，其中，春季降水增加趋势很显著，冬季降水增加趋势显著；而秋季面雨量呈不显著下降趋势；说明冬季和春季降水增加是屏山站以上流域年降水增加的主要原因。

屏山站以下：年面雨量下降趋势显著，变化速率为–15.63mm/10a；除冬季面雨量呈上升趋势外，其它3个季节降水均表现出下降趋势，其中秋季面雨量减少趋势很显著，变化速率达–10.19mm/10a，

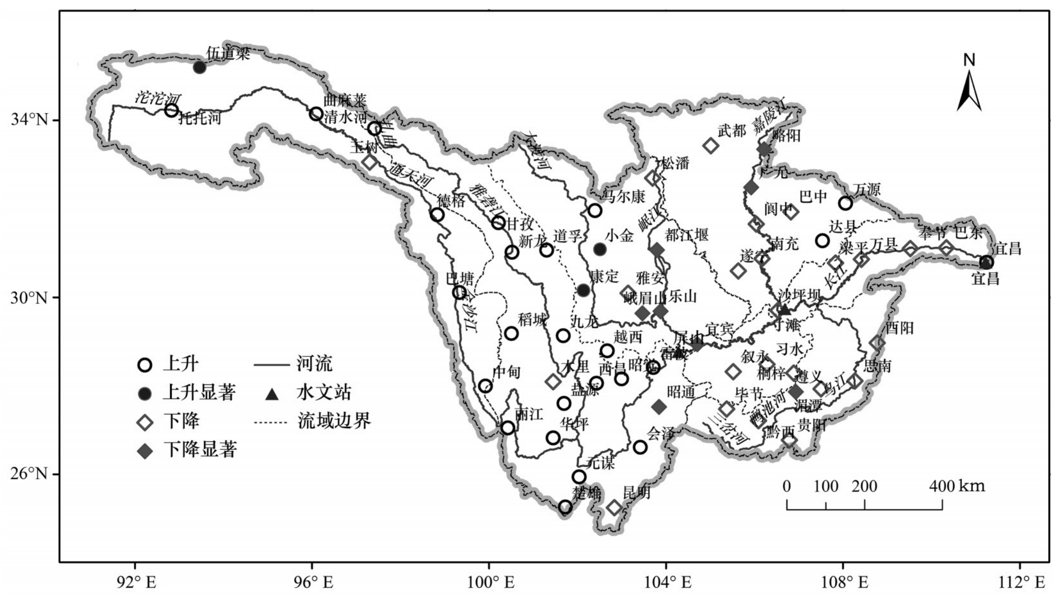

图2 1960年–2009年长江上游年降水量变化趋势空间分布（P<0.1）

Fig.2 Annual precipitation trends in the upper Yangtze River from 1960 to 2009

表1 1960年–2009年长江上游年、季节面雨量趋势系数及变化速率

Table 1 Seasonal and annual areal rainfall trends coefficient and change rate in the upper Yangtze River from 1960 to2009

	屏山站以上		屏山站以下		长江上游	
	趋势系数	变化速率（mm/10a）	趋势系数	变化速率（mm/10a）	趋势系数	变化速率（mm/10a）
年	0.227	7.37	–0.318**	–15.63	–0.152	–4.69
春	0.381***	5.01	–0.092	–1.44	0.040	0.61
夏	0.074	2.06	–0.047	–1.75	0.030	0.98
秋	–0.045	–0.58	–0.430***	–10.19	–0.430***	–7.08
冬	0.291**	0.85	0.129	0.59	0.190	0.79

注：*、**和***分别表示通过0.10、0.05和0.01的显著性检验。

说明秋季降水减少是年降水量下降的主要原因。

整个长江上游：年面雨量呈不显著下降趋势，这与文献[17]研究发现长江上游年降水量有降低趋势的研究结果一致；春、夏和冬季三季面雨量均表现出弱的上升趋势，但是变化不显著；秋季面雨量呈很显著下降趋势，变化速率为–7.08mm/10a；整个上游地区四季面雨量趋势变化与屏山站以上流域一致，且长江上游秋季面雨量变化趋势与年面雨量趋势相同，说明近50年来秋季降水，特别是屏山站以下流域秋季降水量减少是长江上游年降水量下降的主要原因。这与文献[18]认为长江流域大多数站点秋季面雨量呈显著下降趋势的研究结果一致。

3.3 月面雨量变化趋势

屏山站以上流域、屏山站以下流域和整个上游地区各月面雨量变化速率列于表2，趋势系数见图3。

屏山站以上流域：除了9月和12月份面雨量呈不显著下降趋势外，其余10个月面雨量呈增加趋势，且1月–5月份上升趋势较显著，其中1月和3月份面雨量上升趋势显著，3月–6月份的面雨量变化速率都在1mm/10a以上，5月份达到2.77mm/10a。

屏山站以下流域：1月、2月和6月份面雨量呈不显著上升趋势，其中6月份变化速率为1.99mm/10a，3月份无明显变化趋势；其余8个月均为下降趋势，其中9月份下降趋势很显著，变化速率达到–7.87mm/10a。

长江上游：1月–7月份，除了4月份表现出微弱的下降趋势外，其余6个月均呈上升趋势，其中1月上升趋势显著，变化速率为0.60 mm/10a；8月–12月份，连续5个月表现为下降趋势，其中9月份下降趋

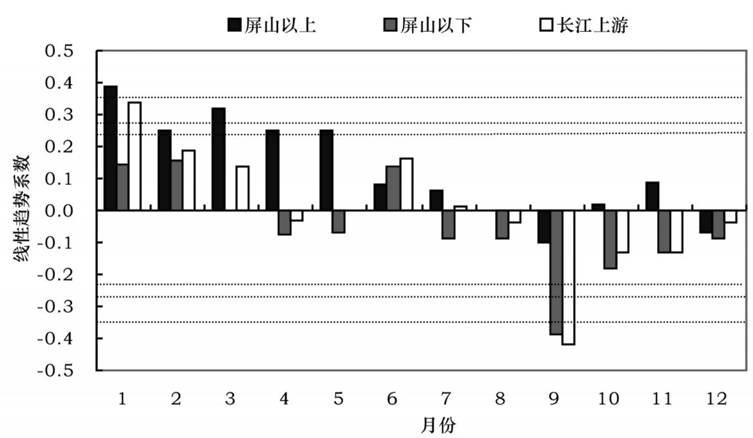

（虚线分别表示α=0.10、α=0.05和α=0.01的显著性水平临界值，图6、图7、图8同）

图3 1960年–2009年长江上游各月面雨量趋势系数

Fig.3 Trend coefficients of monthly mean areal rainfall in the upper Yangtze River from 1960 to 2009

表2 长江上游各月面雨量变化速率

Table 2 Monthly mean areal rainfall change rate in the upper Yangtze River （mm/10a）

	1月	2月	3月	4月	5月	6月	7月	8月	9月	10月	11月	12月
屏山以上	0.56	0.4	1.19	1.06	2.77	1.13	0.90	0.04	–0.99	0.13	0.28	–0.11
屏山以下	0.29	0.50	0.00	–0.64	–0.81	1.99	–1.83	–1.91	–7.87	–1.61	–0.72	–0.21
长江上游	0.60	0.53	0.59	–0.24	0.26	0.18	0.11	–0.93	–5.51	–0.97	–0.58	–0.34

势很显著,变化速率为-5.51mm/10a。

综上分析看出,屏山站以上流域、屏山站以下流域和整个上游地区面雨量在1月、2月、6月、9月和12月等5个月份趋势变化一致,1月、2月和6月均为上升趋势,9月和12月都为下降趋势;屏山站以上流域和整个上游地区在4月、8月、10月和11月份趋势变化不一致;屏山以下和整个上游地区在3月,5月和7月变化趋势不一致。整个上游地区呈上升趋势的月数与呈下降趋势的月数相等,但由于降水的季节分配不均,主要集中在夏秋季节,故整个上游地区年降水仍然为不显著下降趋势。其中对秋季降水量减少贡献最大的是9月降水量明显减少,对冬季降水量增加贡献最大的则是1月降水量的增加。

为对比月降水量上升或下降台站数的变化,图4给出了长江上游月降水量具有不同变化趋势与通过显著性检验的气象站数量百分比。从降水量呈上升趋势的气象站来看,1月-8月整个上游地区以上升趋势的气象站个数占优势,其中1月-3月平均在80%以上,4月-8月5个月都在50%以上;上升显著的气象站以1月和5月最多,约占参与统计气象站总数的20%。9月-12月以下降趋势的气象站占优势,下降趋势站点占60%以上,下降显著的气象站以9月最多,为参与统计气象站总数的25%。

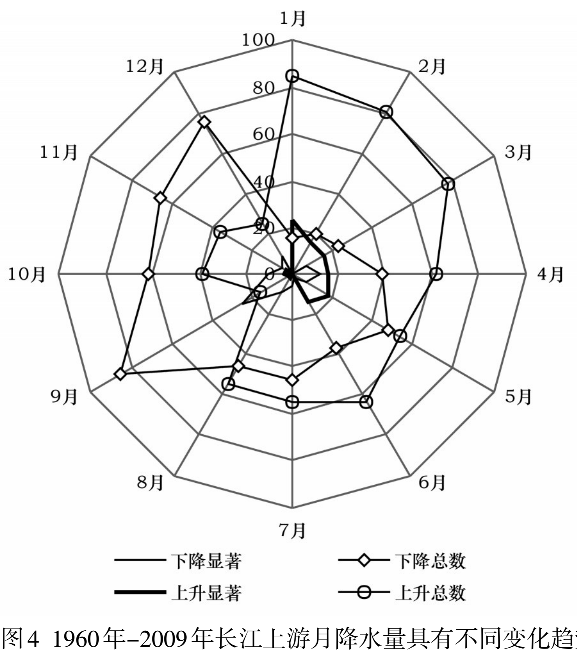

图4 1960年-2009年长江上游月降水量具有不同变化趋势与通过显著性检验(P<0.1)的气象站数量百分比(%)

Fig.4 Percentages of stations with monthly precipitation experiencing varied trends in the upper Yangtze River from 1960 to 2009(%)

为进一步分析各月降水趋势的空间分布特征,图5给出了长江上游各月降水量变化趋势空间分布情况。

1月-2月:整个上游地区绝大多数气象站表现为上升趋势,只有个别气象站表现为下降趋势,其中1月份具有下降趋势的气象站主要分布在嘉陵江上游以及下游偏西地区和泯沱江下游地区,上升趋势较显著的站点主要位于干流区及右岸;2月份呈下降趋势的站点主要在泯沱江流域西部,上升趋势显著的站点主要位于整个上游地区偏北部。

3月-4月:具有上升趋势的站点集中分布在屏山站以上地区和泯沱江流域,且上升趋势显著的站点主要分布在金沙江和雅砻江流域;4月份呈下降趋势的站点主要集中在嘉陵江流域和乌江流域,而3月份乌江流域为上升趋势。

5月-7月:呈现上升趋势的站点5月份主要分布在宜宾以上地区,6月份主要位于干流区、右岸流域和嘉陵江流域,7月份则分布比较凌乱,只有乌江全流域为上升趋势。

8月-12月:8月份上升趋势和下降趋势的站点分布亦较凌乱;9月份除了宜宾以上地区极少数台站(9个)出现上升趋势外,其余地区均为下降趋势;10月和11月具有上升趋势的站点仍然集中分布在宜宾以上地区,站点个数比9月份有所增加;12月份有15个气象站表现出上升趋势,但均未通过显著性检验,主要分布在江源地区和嘉陵江流域的偏东部地区。

4 径流趋势分析

4.1 年、季径流趋势

年径流序列受人类活动和气候变化等因素的影响,亦可表现出相应的随时间变化特征。这里对长江上游干流屏山、寸滩和宜昌三水文站的年、季径流序列进行趋势变化分析(表3),并检验其统计显著性。

从表3可以看出,屏山站除秋季表现出下降趋势外,其余季节都呈上升趋势,且冬季和春季径流上升趋势很显著,年径流也呈上升的趋势,但上升趋势不显著。寸滩站年径流下降趋势较显著,春、

夏和秋三季表现为下降趋势,其中秋季下降趋势显著,冬季为很显著上升趋势。宜昌站年径流呈较显著下降趋势,这与文献[19]、[20]研究发现长江上游径流量趋于减少的结论相似;春、冬季为上升趋势,夏、秋季为下降趋势,其中秋季下降趋势很显著,冬季上升趋势显著。可见,近50年长江上游径流的减少主要是由于屏山站以下流域秋季径流量减少所致,这也与上文屏山站以下流域1960年–2009年期间面雨量的年、季趋势变化基本一致。

4.2 月径流趋势

长江上游三水文站各月径流量变化趋势分析结果见图6。可以看出:屏山站近50年12个月中6月、8月、9月和10月表现为不显著下降趋势外,其余月份为上升趋势,其中1月–4月的径流增加趋势很显著,5月径流增加趋势显著。寸滩站5月–11月表现为下降趋势,其中9月、11月下降趋势较显著,

表3 长江上游干流水文站年和季节径流趋势系数

Table 3 Seasonal runoff trend coefficients in the upper Yangtze River

站名	春季	夏季	秋季	冬季	年
屏山	0.549***	0.014	–0.044	0.492***	0.076
寸滩	–0.020	–0.141	–0.356**	0.478***	–0. 271*
宜昌	0.073	–0.083	–0.434***	0.333**	–0.264*

注:同表1。

10月下降趋势很显著,1月–4月、12月为上升趋势,其中1月–3月上升趋势很显著。宜昌站除12月外,其余月份径流量变化趋势同寸滩站一致,但显著性有所差异。近50年整个长江上游地区三个水文站1月–4月份径流量均表现出增加的趋势,6月、8月、9月、10月径流量均表现出减少的趋势,5月、7月、11月屏山站流量变化趋势与寸滩和宜昌站相反,12月屏山站和寸滩站呈上升趋势,而宜昌站为下降趋势,但上升和下降趋势均不显著。

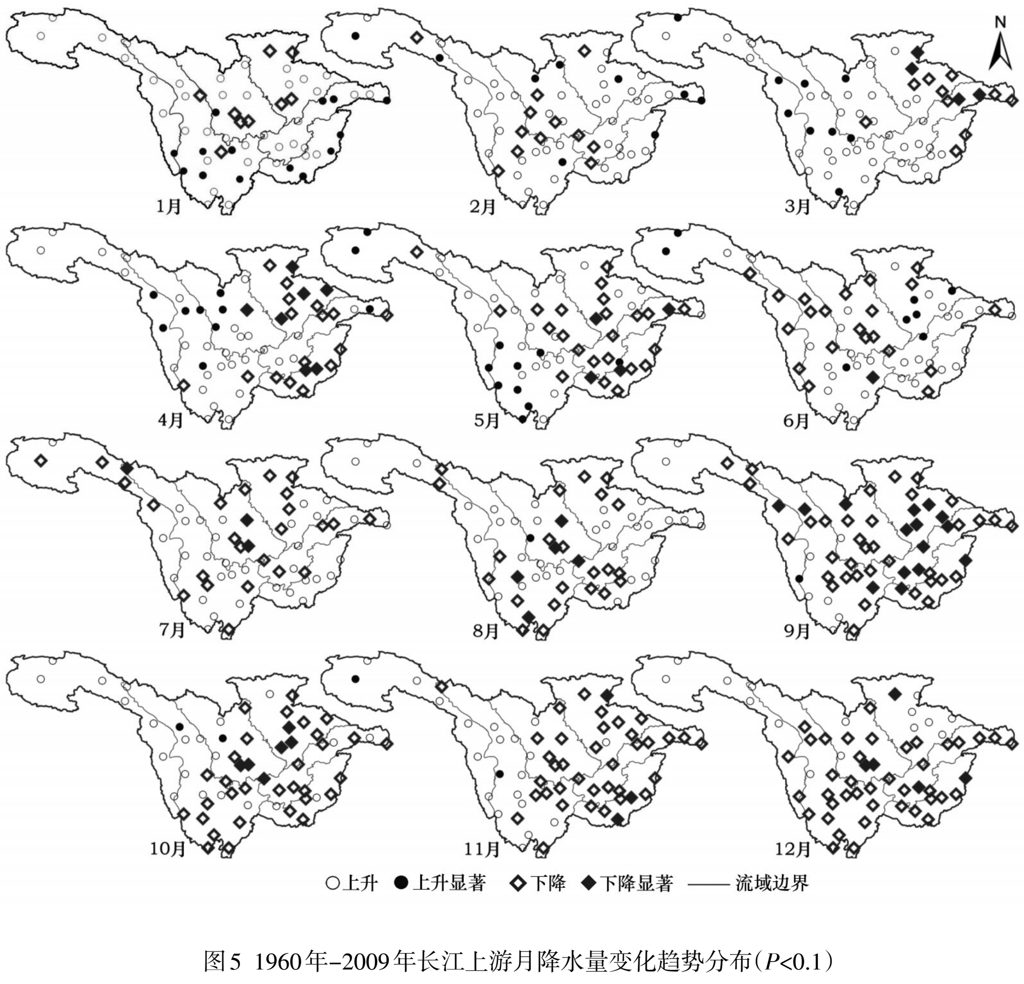

图5 1960年–2009年长江上游月降水量变化趋势分布(P<0.1)

Fig.5 Monthly precipitation trends by meterological stations in the upper Yangtze River from 1960 to 2009

5 面雨量与径流量相关性分析

长江上游径流补给来源分为冰雪融水和大气降水两种，但以大气降水为主。选取长江上游50年的径流、降水数据，对屏山以上流域面雨量与屏山站径流量、整个上游面雨量和宜昌站径流量分别做年、季和月相关性分析，同期和延时1个月相关性分析结果见图7，同期年和季节相关性分析结果见图8。

从屏山站以上流域面雨量与同期屏山站径流量的相关性看，12个月中5月–10月相关性显著，其中5月–8月和10月份相关性很显著，9月份相关性显著，2月和11月表现为负相关；四季面雨量和同期径流量除冬季表现为负相关外，春、夏和秋三季的正相关性都很显著；年面雨量和径流量相关性也很显著。

整个上游面雨量和同期宜昌站径流量有很好的正相关性。从月份来看，1月和12月为显著相关，2月为较显著相关，其余各月都表现为很显著相关；季、年面雨量与同期径流量亦具有很好的正相关性，除冬季为较显著外，其余都表现为很显著，年面雨量与径流量相关性也很显著。因此，长江上游流域多雨年与丰水年、少雨年与枯水年对应关系很好。这也说明，长江上游地区径流量年际变化主要取决于流域降水，人类活动的影响仍十分微弱。

由于长江上游流域面积大、流程长，径流对降水的响应可能具有滞后性，故对当月面雨量与下月径流量的相关性也做了分析。结果表明：屏山站以上流域，2月–6月、8月–9月、11月8个月延时相关性比同期相关性强；整个上游地区1月–3月、9月–10月和12月共6个月的延时相关性比同期相关性强，最高的延时相关出现在2月、3月和8月，但6月的降水对7月径流的影响相对比较弱。陈正洪等[21]也指出长江上游6月降水与7月宜昌站径

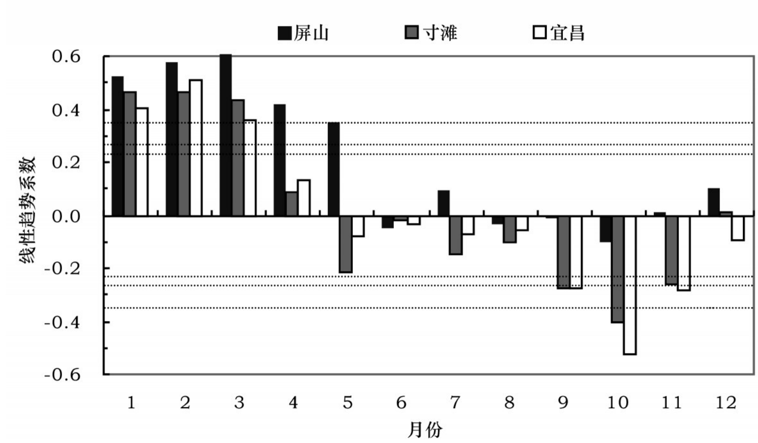

图6 长江上游三水文站月径流量线性趋势系数

Fig.6 Monthly runoff linear trends coefficient in three hydrological stations of the upper Yangtze River

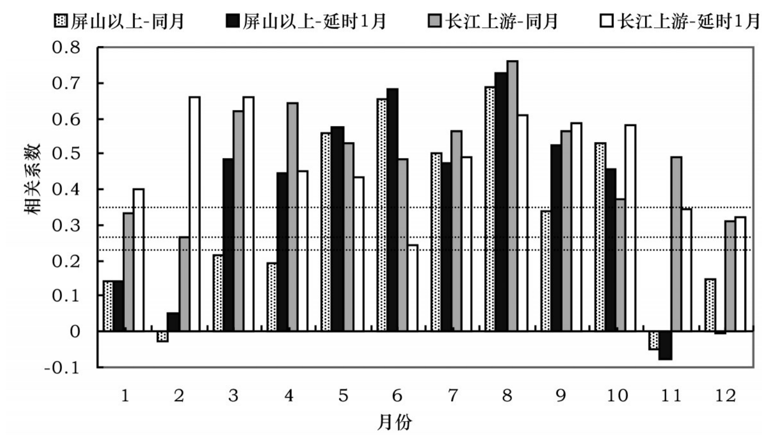

图7 1960年–2009年长江上游面雨量与径流量同月和延时1月相关系数

Fig.7 Correlation coefficients between areal rainfall and runoff at different hydro stations from 1960 to 2009

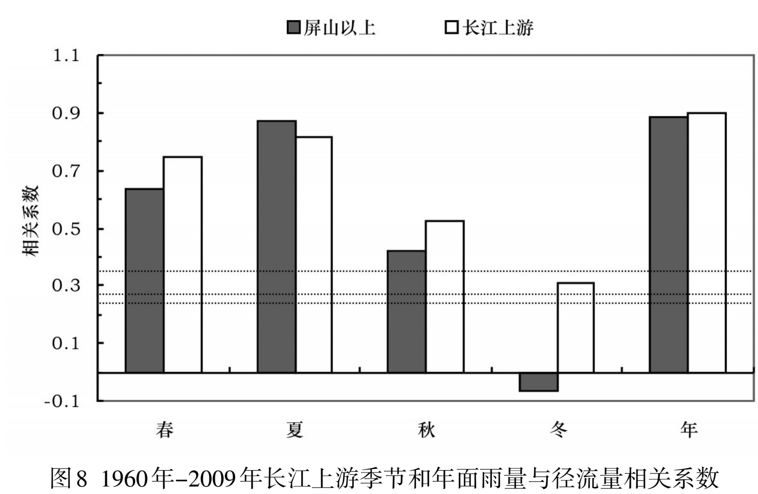

图8 1960年–2009年长江上游季节和年面雨量与径流量相关系数

Fig.8 Correlation coefficients between areal rainfall and runoff at different hydro stations from 1960 to 2009

流关系较弱。造成这一现象的原因可能与上游冰雪融水贡献增大、屏山站以下到宜昌流程短等因素有关。

6 结论与讨论

利用长江上游60个气象站的降水资料和3个水文站的径流资料,对长江上游地区降水和径流变化趋势及相关性进行了分析,得出以下结论:

(1)整个长江上游地区年降水量近50年呈现下降趋势,秋季降水的显著减少是年降水减少的主要原因,特别是9月份降水下降趋势极显著,对整个上游地区降水量的下降起关键作用;同时,年降水量上升和下降的气象站点空间分布相对集中,分别分布在屏山站以上流域和屏山站以下流域,屏山站以下降水量的减少对整个长江上游地区年降水量下降的贡献最大。

(2)从月降水量变化趋势来看,整个长江上游地区1月-8月以上升为主,9月-12月以下降趋势为主,而且从1月-12月,降水从以上升趋势为主逐渐转变,并在9月转为以下降趋势为主,持续至12月份,到1月再转为上升趋势。从月降水趋势的空间分布来看,屏山站以上流域大部分气象站点多数月份表现出上升的趋势,其中1月-5月上升趋势较显著;而屏山站以下流域和整个上游地区月降水趋势基本一致,8月-12月表现为下降趋势,9月份月降水量下降趋势很显著;同时从3月-9月,月降水趋势空间变化有从屏山站以下流域向长江源头逐渐过渡,到9月整个长江上游基本呈减少趋势的变化规律。

(3)不同区域径流量趋势变化不一致。从年径流来看,寸滩站和宜昌站下降趋势较显著,而屏山站呈不显著上升趋势;屏山站春、夏和冬三季径流量均呈上升趋势,且春季和冬季上升趋势很显著,而寸滩站春、夏和秋三季表现为下降趋势,且秋季下降趋势很显著。从月径流来看,屏山站与寸滩、宜昌站表现不一致,屏山站12个月中除了6月、8月-10月表现为下降趋势,其余月份均为上升趋势,而寸滩、宜昌站5月-11月呈下降趋势。

(4)整个上游地区面雨量与径流量具有很好的相关性。屏山以上流域有8个月延时1个月相关比同期相关性强;整个上游地区同期面雨量与径流量有很好正相关性,12个月的同期面雨量与径流量相关性都较显著;季、年面雨量与径流量亦具有很好的正相关性,除冬季外其余季节都表现为很显著。

本文仅仅研究了长江上游降水和径流的相互关系,未考虑气温、蒸发、人类活动等其它因素对径流的影响,而径流变化是气候变化因素与人类活动对下垫面的改造共同作用的结果。因此,今后在分析降水、径流演变规律时,还应全面考虑气候条件、流域下垫面改变和人类活动等因素的综合影响。但是,本文分析表明,目前引起长江上游地区径流年际和趋势变化的主要因子仍然是降水。了解降水量年际和趋势变化的规律和原因,对于长江上游径流和洪水监测、预测,并进而对三峡大坝等重大水利工程的运行、管理具有一定实际意义。

参考文献(References):

[1] 秦大河. 中国气候与环境演变(上卷)[M]. 北京:科学出版社, 2005.

[2] 辛文. 三峡工程与长江上游经济社会发展研究[M]. 成都:西南财经大学出版社,2000.

[3] 张建云,王国庆. 气候变化对水文水资源影响研究[M]. 北京:科学出版社,2007.

[4] 任国玉,吴虹,陈正洪. 我国降水变化趋势的空间特征[J]. 应用气象学报,2000,11(3):322-329.

[5] 姜彤,苏布达,王艳君,等. 四十年来长江流域气温、降水与径流变化趋势[J]. 气候变化研究进展,2005,1(2):65-68.

[6] 沈浒英. 长江流域降水径流的年代际变化分析[J]. 湖泊科学, 2003,15(S1):90-96.

[7] Zhang Nan, Xia Ziqiang, Zhang Shaofeng, et al. Temporal and spatial characteristics of precipitation and droughts in the upper reaches of the Yangtze river basin (China) in recent five decades [J]. *Journal of Hydroinformatics*, 2012, 14(1):22-235.

[8] Wang Yan, Ding YongJian, Ye BaiSheng, et al. Contributions of climate and human activities to changes in runoff of the Yellow and Yangtze rivers from 1950 to 2008[J]. *Science China Earth Sciences*, 2012, doi:10.1007/s11430-012-4505-1.

[9] 王艳君,姜彤,施雅风. 长江上游流域1961-2000年气候及径流变化趋势[J]. 冰川冻土,2005,27(5):709-714.

[10] Gemmer M., Becker S., Jiang T. Observed monthly precipitation trends in China 1951-2002[J]. *Theoretical and Applied Climatology*, 2004, 77:39-45.

[11] Guo Jing, Chen Hua, Xu Chong-Yu, et al. Prediction of variability of precipitation in the Yangtze River Basin under the climate change conditions based on automated statistical downscaling[J]. *Stochastic Environmental Research and Risk Assessment*, 2012, 26

(2):157-176.

[12] Su B. D., Jiang T., Jin W. B. Recent trends in observed temperature and precipitation extremes in the Yangtze River basin, China[J]. *Theoretical and Applied Climatology*, 2006, 83: 139-151.

[13] Yao Cai, Yang Song, Qian Weihong, et al. Regional summer precipitation events in Asia and their changes in the past decades [J]. *Journal of Geophysical Research*, 2008, 113, D17107, doi: 101029/2007JD009603.

[14] 魏凤英. 现代气候统计诊断与预测技术[M]. 北京:气象出版社, 2007.

[15] 徐晶,林建,姚学祥,等. 七大江河流域面雨量计算方法及应用[J]. 气象,2001,27(11):13-16.

[16] 刘明光. 中国自然地理图集[M]. 北京:中国地图出版社,1998.

[17] 孙甲岚,雷晓辉,蒋云钟,等. 长江流域上游气温、降水及径流变化趋势分析[J]. 水电能源科学,2012,30(5):1-5.

[18] 任国玉,陈正洪,杨宏青. 长江流域近50年降水变化及其对干流洪水的影响[J]. 湖泊科学,2003,15(S1):49-55.

[19] 王顺久. 长江上游川江段气温、降水及径流变化趋势分析[J]. 资源科学,2009,31(7):1142-1149.

[20] 王渺林,易瑜. 长江上游径流变化趋势分析[J]. 人民长江, 2009,40(19):68-69.

[21] 陈正洪,杨洪清,任国玉,等. 长江流域面雨量变化趋势及对干流流量影响[J]. 人民长江,2005,36(1):22-23.

Rainfall and Runoff Trends in the Upper Yangtze River

FENG Yawen[1,2], REN Guoyu[1], LIU Zhiyu[3], WU Jidong[4], ZHANG Lei[1]

(*1. Laboratory for Climate Studies, National Climate Center, CMA, Beijing* 100081, *China*;

2. Institute of Geographic Sciences and Natural Resources Research, Chinese Academy of Sciences, Beijing 100101, *China*;

3. Hydrological Information Center, Ministry of Water Resources, Beijing 100053, *China*;

4. Key Laboratory of Environmental Change and Natural Disaster, MOE, Beijing Normal University, Beijing 100875, *China*)

Abstract: Spatiotemporal monthly rainfall-runoff analysis is the foundation of water regulation, water resource protection and management, and drought and flood hazard prediction. Previous studies of the Yangtze River have mainly focused on the whole river basin and seasonal or yearly rainfall and runoff analysis. Here, rainfall records from 60 national basic and reference stations, and hydrological data from three control stations of the upper Yangtze River were used to analyze rainfall and runoff characteristics across the upper Yangtze River. First, the spatial distribution of weather stations with upward and downward trends for precipitation were comparatively concentrated. Weather stations with an upward trend were located in the Sichuan Basin above the Pingshan Hydro station (PA region), while weather stations with a downward trend were mainly located in the rest of the upper Yangtze River (PR region). Annual precipitation in the upper Yangtze River has declined in the last 50 years. Second, monthly precipitation trends show that more than half of weather stations experienced upward trends in eight months (Jan-Aug). The spatial distribution of monthly rainfall shows a transition from the PA region to PR region between Mar-Sep. Runoff shows a similar trend to rainfall and an indistinctively upward trend in Pingshan station, and a downward trend in Cuntan and Yichang stations. The decrease in runoff in the PR region from May-Nov is the main reason for the runoff drop seen at the Cuntan and Yichang stations. Runoff in the PA region shows an upward trend in all seasons except autumn, especially in spring and winter. A good correlation was found between area rainfall and runoff in the upper Yangtze River.

Key words: Upper Yangtze River; Areal rainfall; Runoff; Trend; Precipitation; Climate change

JOURNAL OF GEOPHYSICAL RESEARCH: ATMOSPHERES, VOL. 118, 1–11, doi:10.1002/jgrd.50757, 2013

Nitrogen dioxide measurement by cavity attenuated phase shift spectroscopy (CAPS) and implications in ozone production efficiency and nitrate formation in Beijing, China

Baozhu Ge,[1,2] Yele Sun,[1] Ying Liu,[3] Huabin Dong,[1] Dongsheng Ji,[1] Qi Jiang,[1,4] Jie Li,[1] and Zifa Wang[1]

Received 25 April 2013; revised 16 July 2013; accepted 10 August 2013.

[1] Nitrogen dioxide (NO_2) is a key species in studying photochemical smog and formation mechanisms of nitrate in fine particles. However, the conventional commercially available chemiluminescence (CL)-based method often has uncertainties in measuring NO_2 because of interferences with other reactive nitrogen species. In this study, an Aerodyne Cavity Attenuated Phase Shift Spectroscopy (CAPS) NO_2 monitor that essentially has no interferences with nitrogen containing species was deployed in Beijing for the first time during August 2012. The CAPS NO_2 monitor is highly sensitive with a detection limit (3σ) of 46.6 ppt for 1 min integration. The NO_2 measured by CAPS shows overall agreement with that from CL, yet large differences up to 20% were also observed in the afternoon. Further, the discrepancies of NO_2 measurements between CAPS and CL appear to be NO_z dependent with larger differences at higher NO_z concentrations (e.g., > 14 ppb). As a result, the ozone production efficiency of NO_x (OPE_x) derived from the correlations of O_x-NO_z with the CL NO_2 can be overestimated by 19–37% in Beijing. The daily OPE_x calculated with the CAPS NO_2 ranges from 1.0 to 6.8 ppb/ppb with an average ($\pm 1\sigma$) of 2.6 ($\pm$1.3) for the entire study. The relatively low OPE_x and the relationship between OPE_x and NO_x suggest that ozone production chemistry is VOC sensitive during summer in Beijing. Two case studies further show that high concentrations of NO_x can significantly enhance the formation of nitrate in fine particles in the presence of high O_3 and favorable meteorological conditions.

Citation: Ge, B., Y. Sun, Y. Liu, H. Dong, D. Ji, Q. Jiang, J. Li, and Z. Wang (2013), Nitrogen dioxide measurement by cavity attenuated phase shift spectroscopy (CAPS) and implications in ozone production efficiency and nitrate formation in Beijing, China, *J. Geophys. Res. Atmos.*, *118*, doi:10.1002/jgrd.50757.

1. Introduction

[2] Air pollution is a great concern in China in recent years. The roles of megacities in regional air pollution, such as photochemical smog and haze, have been extensively investigated in previous works [*Guttikunda et al.*, 2003, 2005; *Kanakidou et al.*, 2011; *Lawrence et al.*, 2007; *Madronich*, 2006; *Molina et al.*, 2010; *Molina and Molina*, 2004; *Ran et al.*, 2012]. Beijing, one of the largest cities in China and one of the top 25 world megacities, has a resident population of more than 20 million in 2012 (http://www.bjstats.gov.cn/nj/main/2012-tjnj/index.htm). The dense population and rapid economic growth have resulted in a substantial increase of anthropogenic pollutants in Beijing and regions in its vicinity, which contributes significantly to the air pollution in Beijing [*Hao et al.*, 2005; *Shao et al.*, 2006; *Wang et al.*, 2006]. It was estimated that ~74% of the ground level NO_x in Beijing is due to vehicular emissions, whereas power plants and industrial sources contribute only 2% and 13%, respectively [*Hao et al.*, 2005]. Although photochemical smog is a major air pollution issue in Beijing, the mechanisms of the formation of surface O_3 are not well known for this area; specifically with respect to the formation mechanisms of O_3 in urban versus rural areas of Beijing. *Wang et al.* [2006] found that O_3 formation in a mountainous area in the north of Beijing was limited by NO_x; however, a VOC-controlled ozone formation mechanism was dominant at the urban sites in Beijing [*Wang et al.*, 2010b]. Similarly, *Chou et al.* [2009] found that reduction of NO_x emission appeared not to be effective toward reducing O_3 concentration at an urban site in Beijing.

[1]State Key Laboratory of Atmospheric Boundary Layer Physics and Atmospheric Chemistry, Chinese Academy of Sciences, Institute of Atmospheric Physics, Beijing, China.
[2]Research Center for Environmental Changes, Academia Sinica, Taipei, Taiwan, ROC.
[3]Laboratory for Climate Studies National Climate Center, China Meteorological Administration, Beijing, China.
[4]Key Laboratory for Aerosol-Cloud-Precipitation of China Meteorological Administration, Nanjing University of Information Science and Technology, Nanjing, China.

Corresponding author: Y. Sun, State Key Laboratory of Atmospheric Boundary Layer Physics and Atmospheric Chemistry, Institute of Atmospheric Physics, Chinese Academy of Sciences, Beijing 100029, China. (sunyele@mail.iap.ac.cn)

2169-897X/13/10.1002/jgrd.50757

[3] Previous studies [*Chameides et al.*, 1992; *Kleinman et al.*, 1994, 2000; *Sillman*, 1999] have shown that the surface O_3 is primarily formed from photochemical reactions of VOCs and NO_x. NO_x not only plays the role of catalyst in the chain reactions for O_3 production but also is a major terminator of free radicals, which has the potential to limit the formation of O_3 in the atmosphere [*Sillman*, 1999; *Roberts et al.*, 1995; *Seinfeld and Pandis*, 2006]. Since the oxidants of NO_x can be removed from the O_3-production-reaction system, *Liu et al.* [1987] defined the number of molecules of O_3 formed per NO_x as O_3 production efficiency of NO_x (OPE_x), which has been used as an important indicator in studying O_3 chemistry. *Trainer et al.* [1993] and *Kleinman et al.* [1994] found better correlations between O_3 and the oxidation products of NO_x, i.e., NO_z (= NO_y − NO_x) than the sum of reactive nitrogen species, NO_y, in the photochemically aged air, based on which the OPE_x was revised as $\Delta[O_3 + NO_2] / \Delta[NO_z]$. Therefore, accurate measurements of NO_y and NO_x are of importance to understand the formation mechanism of O_3 production, and hence to make the corresponding control strategies for mitigation of photochemical smog. Because of interferences of reactive nitrogen species, the OPE_x derived from the commercially standard chemiluminescence-based (called CL hereafter) instruments often has large uncertainties and represents an upper limit, especially in the photochemically aged air [*Ge et al.*, 2010]. For example, *Dunlea et al.* [2007] reported an overestimation of 22% of NO_2 measured by the CL monitors compared with the collocated spectroscopic measurements in Mexico City. Such uncertainties are expected to be enlarged in the downwind areas of megacities where the production of NO_z, such as PAN and HNO_3, in the total reactive nitrogen species is more significant in comparison to urban cities.

[4] To improve the accuracy of NO_2 measurements, a NO_2 monitor utilizing Cavity Attenuated Phase Shift Spectroscopy (CAPS) was recently developed [*Kebabian et al.*, 2005, 2008]. The CAPS NO_2 monitor directly measures the absorption of NO_2 at the wavelength of 450 nm and requires no conversion of NO_2 to other species. Compared to the standard commercially available CL-based NO_x analyzer, the CAPS NO_2 monitor shows much enhanced performance in terms of sensitivity, accuracy, and baseline stability [*Kebabian et al.*, 2005]. In particular, the CAPS NO_2 has essentially no interferences from other nitro containing species, although small spectral interferences from 1,2-dicarbonyl compounds, such as glyoxal and methylglyoxal, are possible due to the ±20 nm band-pass centered at 440 nm [*Kebabian, et al.*, 2008]. Commercially available CL analyzers are the standard type of instrument employed at surface monitoring network stations for ambient measurements of atmospheric NO_2. Ambient NO_2 analyzers employing the same CL detection scheme, yet utilizing UV photolysis with high power LEDs to convert NO_2 to NO prior to CL detection, are also commonly utilized in field research. Similar to the Aerodyne CAPS instrument, photolysis-chemiluminescence (P-CL) instruments have higher sensitivity and chemical selectivity for NO_2 than the standard commercially available NO_2 CL analyzer [*Ryerson et al.*, 2000; *Pollack et al.*, 2010; *Sadanaga et al.*, 2010]. These P-CL systems are the current recommended standard for ambient measurements of NO_2 by the Global Atmospheric Watch (GAW). Considering the above mentioned advantages of the commercially available Aerodyne CAPS NO_2 monitor compared to the standard commercial CL analyzer, evaluation of the Aerodyne CAPS NO_2 instrument as a potential resource for future NO_2 measurements has significant implications for future surface monitoring networks, especially for monitoring sites with low concentrations of NO_2 and/or where photochemical production of NO_z is intense.

[5] In this work, an Aerodyne CAPS NO_2 monitor was first deployed at an urban site in Beijing, China for in situ measurement of ambient gaseous NO_2. Here we report the results from 1 month measurement campaign during August 2012. We first evaluate the performance of the CAPS NO_2 monitor by comparing with a standard, commercial CL-based NO_x analyzer (Thermo Scientific, Model 42i). Then, we explore the impact of NO_2 measurement on the derivation of OPE_x. Further, the implications of OPE_x in O_3-NO_x-VOCs chemistry and the strategies for ozone pollution control in Beijing are discussed. Finally, two high-O_3 episodes are used to elucidate the roles of O_3 and NO_2 in the formation of secondary particulate nitrate.

2. Experimental

2.1. Sampling Site and Meteorology

[6] The ambient gaseous NO_2 was measured in situ by an Aerodyne CAPS NO_2 monitor [*Kebabian et al.*, 2005, 2008] from 1 to 29 August 2012 at the Institute of Atmospheric Physics (IAP), Chinese Academy of Sciences (39°58′ 28″N, 116°22′16″E), which is located between the north 3rd and 4th Ring Road in Beijing. We have two sampling sites in this study, named site A and site B, which are approximately 50 m apart. The CAPS NO_2 monitor was deployed on the roof of a two story building (~8 m above the ground) at site A. Collocated gaseous species including NO, NO_y, and O_3 were simultaneously measured by a NO/NO_y analyzer (Thermo Scientific, 42CY) and an Ozone Analyzer (Thermo Scientific, 49C), respectively. In addition, NO, NO_2, and NO_x were measured by a CL NO/NO_2/NO_x analyzer (Thermo Electron Corporation, 42CTL) at site B. The detailed descriptions of the sampling sites are given in *Sun et al.* [2012]. The meteorological variables including temperature (T), relative humidity (RH), precipitation, solar radiation (SR), wind speed (WS) and wind direction (WD) were obtained from the meteorology tower of IAP, which is approximately 30 m away from site A and ~20 m from site B.

2.2. Cavity Attenuated Phase Shift Spectroscopy NO_2 Monitor

[7] The CAPS NO_2 monitor determines NO_2 by directly measuring optical absorption of NO_2 at 450 nm in the blue region of electromagnetic spectrum [*Kebabian et al.*, 2005, 2008]. Unlike standard CL monitors, the CAPS measures the average time that the light spends within the sample cell and requires no conversion of NO_2 to other species, and thus is not sensitive to other nitro containing species (such as HNO_3, nitrate, PAN, etc.). The CAPS NO_2 system contains three major parts including a blue light emitting diode (LED) as the light source, a sample cell with two high reflectivity mirrors centered at 450 nm, and a vacuum photodiode detector. The detailed principles of the CAPS system have been described elsewhere [*Kebabian et al.*, 2005, 2008]. In brief, a square wave modulated LED light is input into

the first reflected mirror, after passing through the absorption cell, the light appears to be a distorted waveform which is characterized by a phase shift in comparison to the initial modulation. By measuring the amount of the phase shift (ϑ), the concentration of NO_2 (χ) can be determined using the following formula:

$$\cot\vartheta = \cot\vartheta_0 + \frac{c}{2\pi f}\alpha_{NO_2}(T,P)\chi \qquad (1)$$

where c is the speed of light, f is the LED modulation frequency, T and P are the sample temperature and pressure respectively, a_{NO2} is the absorption coefficient of nitrogen dioxide at the measured T and P, and ϑ_0 is the sensor response of NO_2-free air. Although the measurement of NO_2 theoretically requires no calibration, the CAPS NO_2 monitor was calibrated using a gas mixture with the known concentration of NO_2 before the deployment because of the nonmonochromatic light source.

2.3. Instrument Operations

[8] Ambient air was drawn into the instrument via 9.525 mm Teflon tubing at a flow rate of 0.85 L/min and passed through a disposable filter cartridge to remove particulates and prevent mirror contamination prior to being introduced to the detector. In order to measure NO_2 baseline, a zero air generator that consists of a particle filter followed by a silica gel dryer, two cartridges filled by charcoal, and the mixture of charcoal and hydroquinone, respectively was used to generate NO_2-free air. During this study, the NO_2 was measured at a time resolution of 1 s. Every hour, the ambient air flow was automatically switched to NO_2-free air to conduct baseline measurements. The cell/mirror was first flushed for 45 s and then the baseline was measured for the next 90 s. Figure 1 shows the time series of NO_2 baseline measured for the entire study. Overall, the baseline was rather stable throughout the study with more than 80% of data points falling within ±0.2 ppb and is well represented by a Gaussian distribution. The detection limit, defined as three times of one standard deviation (3σ), is 0.361 ppb for 1 s time resolution, which is equivalent to 46.6 ppt for 1 min integration. The linear response range of CAPS NO_2 instrument is 15 ppt–1 ppm. In comparison to the commercial CL-based NO_x analyzer, e.g., $NO/NO_2/NO_x$ Analyzer (Model 42i, TE) and NO_x Analyzer (Model 42i-D, TE), the sensitivity of the CAPS NO_2 exceeds the CL analyzer by nearly an order of magnitude.

[9] The CL-based gas monitors were calibrated during this study. Daily zero/span checks were automatically done using dynamic gas calibrators (Model 146C) combined with zero air suppliers (Model 111) and standard gas mixtures for NO. The multipoint calibrations of NO_x 42CTL, and NO_y 42CY analyzers were made on 20 August using the standard gases, which were compared with National Institute of Standards and Technology (NIST) traceable standards (Scott Specialty Gases, USA). An O_3 calibrator (49CPS) was used to calibrate the O_3 analyzers at the site A. The calibrator is traceable to the Standard Reference Photometer maintained by World Meteorological Organization (WMO) World Calibration Centre in Switzerland. All the gaseous species above were recorded at a time resolution of 1 min, yet 5 min averaged data were presented in this study.

[10] In addition to the gaseous species measurements, an Aerodyne Aerosol Chemical Speciation Monitor (ACSM) was used to measure the mass concentration and chemical composition of nonrefractory submicron aerosol species including organics, sulfate, nitrate, ammonium, and chloride at a time resolution of ~15 min at the site A. The detailed descriptions of ACSM measurements can be found in *Sun et al*. [2012, 2013]. In addition, all the data in this study are reported at Beijing local time which equals Coordinated Universal Time (UTC) plus 8 h.

3. Result and Discussion

3.1. Intercomparison

[11] A time series of NO and NO_2 measured by the CAPS and CL instruments is presented in Figure 2. The NO measured by 42CY at site A and 42CTL at site B track each other well (r^2 = 0.94, Figure 3a). However, the regression slope of 0.91 suggests that the NO measured at site A appears to be systematically lower than that observed at site B, which is likely due to the calibration errors. Also, note that the differences at the two sites are larger at low ambient levels (< 1 ppb). For example, while the minimum of NO at site A is approximately 0.4 ppb, which is close to the detection limit of 0.4 ppb for 1 min average, the NO at site B however can go down to 0.2 ppb.

[12] The NO_2 measured by the CAPS NO_2 monitor also tracks tightly with that measured by the CL-based analyzers (r^2 = 0.91, slope = 0.999, Figure 3b), yet noticeable differences in particular during afternoon were observed. Figure 3b shows that the differences between the CAPS and CL appear to be NO_z dependent. While the discrepancies are within ~10% when NO_z is below 8 ppb, large differences up to ~30% at high NO_z levels (> 14 ppb, Figure 3c) were observed between CAPS and CL because of the interferences of other reactive nitrogen species on CL NO_2 measurement. This is due to the well known sensitivity of the CL-based NO_2 measurements to organic nitrates and HNO_3, which depends upon inlet configuration and thermal operation range of a molybdenum or stainless steel converter [*Winer et al*., 1974; *Parrish et al*., 1990; *Murphy et al*., 2007; *Kebabian et al*., 2008; *Steinbacher et al*., 2007]. At low NO_z levels (< 2 ppb), the CAPS NO_2 shows slightly higher values than that from CL. Although the band of 440 nm is essentially interference free, the 1,2-dicarbonyl compounds, e.g., glyoxal and methyl glyoxal can affect the accuracy of CAPS NO_2 measurements by absorbing in the same spectral region. Such interferences might be significant when the ratio of glyoxal to NO_2 is high. However, based on previous measurements of glyoxal and NO_2 at both urban and rural sites [*Volkamer et al*., 2005; *Li et al*., 2013], the interferences of glyoxal on the measurement of ambient NO_2 are generally less than 10%.

[13] Figure 4b shows the diurnal variation of NO_2 measured by the CAPS and CL for the entire study. While the NO_2 from two methods agree reasonably with each other at nighttime, large differences up to 20% were observed during daytime, mostly between 12:00 and 16:00. The large discrepancies in the afternoon are likely due to the overestimation of CL NO_2 because of the interferences of abundant reactive nitrogen species. In addition, the different sampling sites might also contribute to the observed differences in NO_2

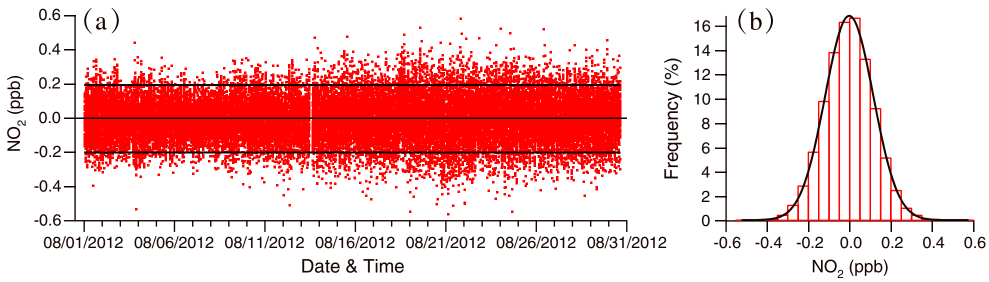

Figure 1. (a) Time series of NO_2 concentration (1 s data) measured from NO_2-free air every 1 h for the entire study, (b) Gaussian distribution of NO_2 in Figure 1a. The two solid lines in Figure 1a indicate the 10th and 90th percentiles of the data points.

measurements. We also note that the CAPS NO_2 sometimes shows higher concentration than the CL NO_2 at nighttime, which might be due to the interferences of some nitrogen containing species, e.g., peroxyacyl nitrates (PANs) and N_2O_5, which are not thermally stable and can decompose to NO_2 in the CAPS system [*Kebabian et al.*, 2008]. However, the discrepancies at nighttime (3.7%) are much smaller compared to those observed during daytime (17.4%).

3.2. Time Series and Diurnal Variations

[14] The time series of NO, NO_2, NO_y, NO_z, O_x, and particulate NO_3^-, as well as the solar radiation during the observation period is shown in Figure 2. The NO shows regular and prominent peaks in the early morning due to the traffic emissions in the morning rush hour. This is evident from the diurnal cycle of NO (Figure 4a), which shows a pronounced morning peak. The NO concentration peaks between 7:00 and 8:00 (~17 ppb) and then gradually decreases to a low ambient level (~ 1 ppb) due to the titration of NO by O_3, and also the rising boundary layer during the daytime [*Lin et al.*, 2008, 2011].

[15] The gaseous NO_2 also presents a pronounced diurnal cycle, yet the highest concentration occurs in the early morning and the lowest values appear between 14:00 and 15:00 (Figure 4b). The low concentration of NO_2 in the afternoon is due to the deep boundary layer [*Quan et al.*, 2013] and also the oxidation to NO_z, e.g., nitric acid, PAN, etc., consistent with the pronounced NO_z peak in the afternoon (Figure 5).

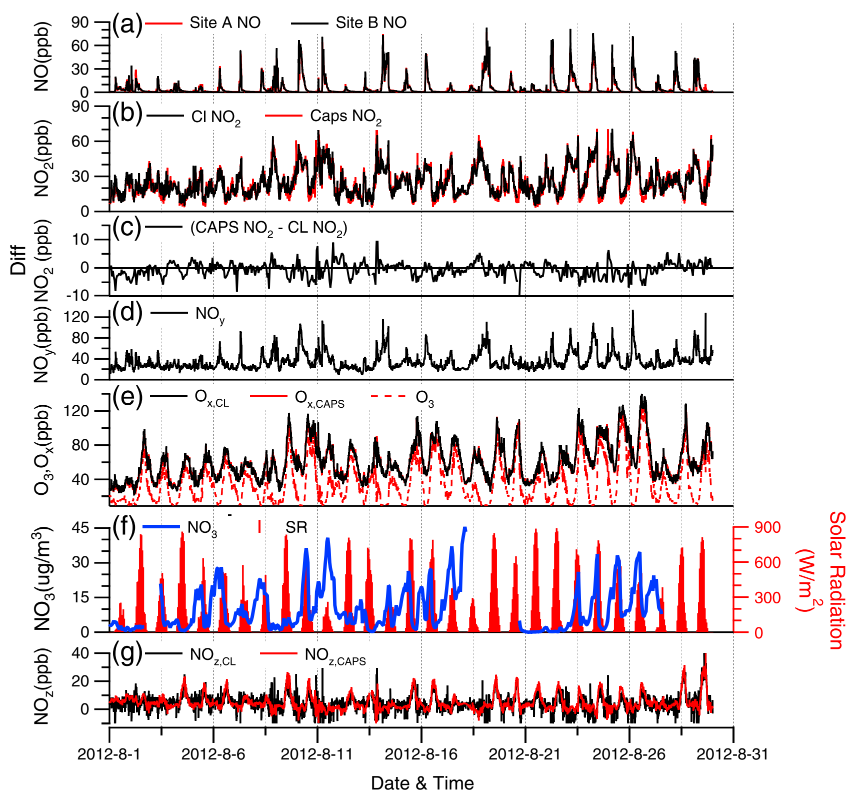

Figure 2. Time series of gaseous NO, NO_2, NO_y, O_3, O_x, and NO_z, particulate NO_3^- in submicron aerosols, and solar radiation (SR). The $NO_{z,CL}$ and $O_{x,CL}$ are $[NO_y] - [NO] -$ CL $[NO_2]$ and $[O_3] +$ CL $[NO_2]$, respectively, while The $NO_{z,CAPS}$ and $O_{x,CAPS}$ are $[NO_y] - [NO] -$ CAPS $[NO_2]$ and $[O_3] +$ CAPS $[NO_2]$, respectively.

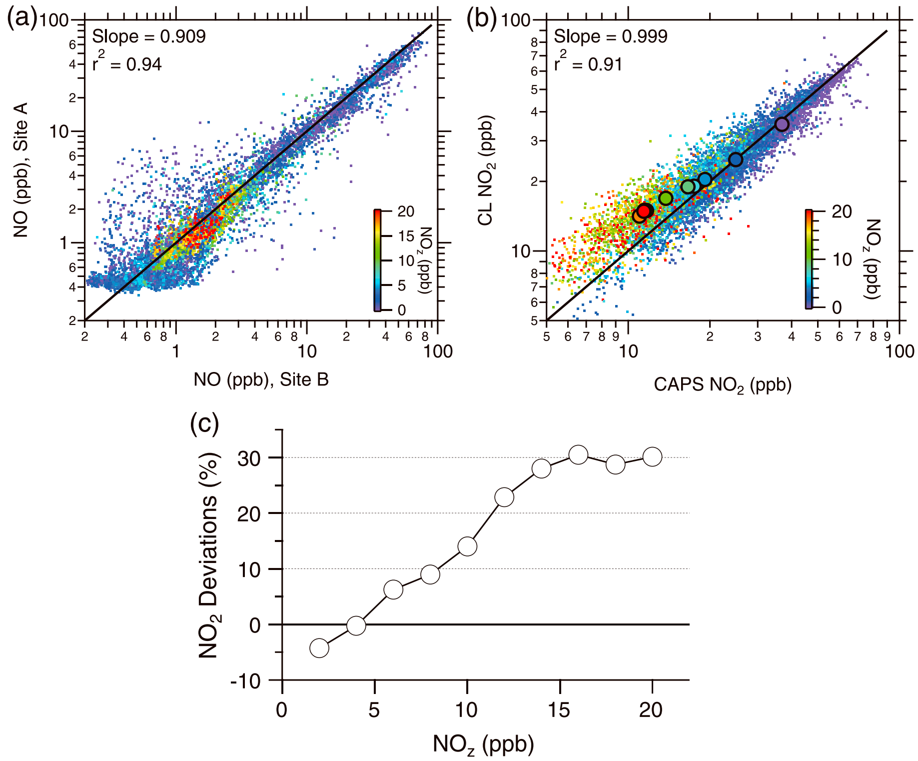

Figure 3. (a) Comparison of NO measured at site A and B; (b) Comparison of NO_2 measured by the CL NO_x analyzer at Site B and the CAPS NO_2 monitor at Site A; (c) NO_2 deviation between CAPS and CL versus NO_z. The data points are color coded with the NO_z concentration in Figures 3a and 3b. Also, the data points in Figure 3b are averaged according to NO_z concentration with 2 ppb increment (solid circles).

Figure 4c shows the diurnal cycles of NO_x and NO_y. Again, the diurnal profile of NO_x and NO_y shows a large gap during daytime with the max difference of ~15ppb at ~14:00, clearly indicating the photochemical production of NO_z. The photochemical formation of NO_z is strongly associated with solar radiation and O_3 mixing ratio. For example, the high O_3 pollution episodes, e.g., 9–10, 15–16, 19–26, and 28–29 August, show evident noon peaks, indicating the photochemical production of NO_z. However, the days with weak solar radiation (< 300 W m^{-2}) and low O_3, e.g., 1, 7–8, 12, 17–18, and 27 August, show correspondingly low production of NO_z. The relationship between O_x and NO_z will be further discussed in section 3.2

[16] Figure 5 shows the diurnal variations of $O_{x,CAPS}$ (= $[O_3]$ + CAPS $[NO_2]$) and $NO_{z,CAPS}$ (= $[NO_y]$ − [NO] − CAPS [NO_2]), as well as the $O_{x,CL}$ (= $[O_3]$ + CL $[NO_2]$) and $NO_{z,CL}$ (= $[NO_y]$ − [NO] − CL [NO_2]). The diurnal cycle of O_x is similar to NO_z with higher values appearing during the afternoon and lower ones at night and early morning. In addition to the photochemical production, regional transport might be another reason for the daytime peaks. For example, *Wang et al.* [2010b] found that regional pollution sources could contribute ~34–88% to the peak ozone at the urban site in Beijing. In this study, the average concentration of O_x for the second peak (15:00–18:00) was 79.4 and 54.4 ppb, respectively, from the air masses in the east-southwest and northeast. If assuming that the O_x from clean regions in the northeast represents a background level, the regional transport could contribute ~32% of O_x peak when the air masses are from the east-southwest, overall consistent with the results from *Wang et al.* [2010b].

3.3. Ozone Production Efficiency (OPE_x)

[17] The OPE_x is an important indicator to evaluate O_3-NO_x-VOCs sensitivity and to make effective O_3 control strategies in urban areas [*Couach et al.*, 2004; *Rickard et al.*, 2002; *Shiu et al.*, 2007; *Sillman*, 1999; *Xu et al.*, 2009; *Zaveri et al.*, 2003]. The OPE_x can be derived from the regression slopes of correlations between O_x and NO_z [*Kleinman et al.*, 1994; *Trainer et al.*, 1993]. Therefore, the accuracy of NO_2 measurement plays an important role in the calculation of OPE_x by influencing the quantification of O_x and NO_z. Using the same approach, the $OPE_{x,CAPS}$ and $OPE_{x,CL}$ were obtained from the correlation analysis of $[O_{x,CAPS}]$ versus $[NO_{z,CAPS}]$ and $[O_{x,CL}]$ versus $[NO_{z,CL}]$, respectively in this study. Hourly averaged data between 7:00 and 17:00 are used for the correlation analysis. In addition, only slopes with correlation coefficients R > 0.6 (significant level at 95%) and intercept > 0 (the background O_x concentration) are considered to be effective daily $OPE_{x,CAPS}$/$OPE_{x,CL}$ for this study. Given the general overestimation of CL NO_2 [*Steinbacher et al.*, 2007], the $OPE_{x,CL}$ calculated from the NO_y and NO_x measured by 42CTL analyzer would represent an upper limit of OPE_x, especially in the photochemically aged air [*Ge et al.*, 2010].

[18] Figure 6 shows the calculated daily $OPE_{x,CAPS}$ and $OPE_{x,CL}$ using 1 h average data for the entire study. It should be noted that some OPE_x values were missed in Figure 6 because the correlations of O_x versus NO_z in these days did

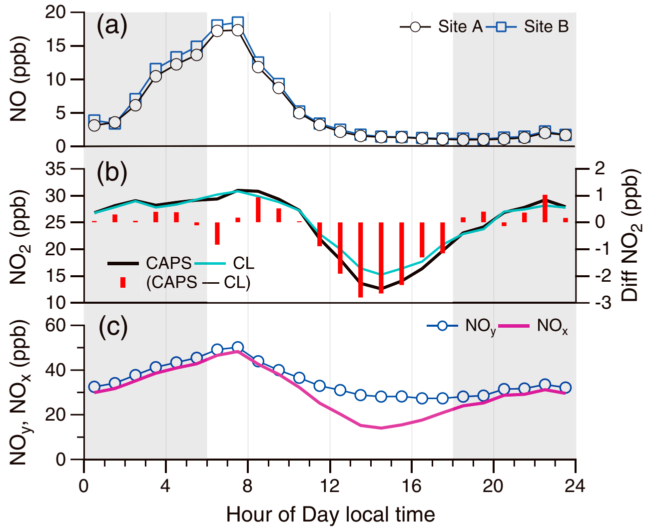

Figure 4. Mean diurnal cycles of (a) NO, (b) NO_2, and (c) NO_x and NO_y based on the entire measurement period.

not meet the requirements for calculation of OPE_x in this study. The daily $OPE_{x,CAPS}$ varies from 1.0 to 6.8 ppb/ppb with an average ($\pm 1\sigma$) of 2.6 ($\pm$1.3) for the entire study. As a comparison, the $OPE_{x,CL}$ is generally higher than $OPE_{x,CAPS}$, ranging from 0.9 to 8.1. The average of $OPE_{x,CL}$ for the entire study is 3.4, which is ~30% higher than that of $OPE_{x,CAPS}$. The higher $OPE_{x,CL}$ is primarily due to the overestimation of the CL NO_2, leading to an over prediction of $[O_{x,CL}]$, and further a corresponding underestimation of $[NO_{z,CL}]$. As a result, the $OPE_{x,CL}$ calculated from the relationship between $[O_{x,CL}]$ and $[NO_{z,CL}]$ is overestimated. The discrepancies between $OPE_{x,CAPS}$ and $OPE_{x,CL}$ vary day by day, and the overestimation of $OPE_{x,CL}$ ranges from 19–37% depending on photochemical production of NO_z and the differences of NO_2 between CAPS and CL. Our results suggest that the previously reported OPE_x calculated from the CL measurements [*Xu et al.*, 2009; *Ge et al.*, 2012] might have been overestimated by 30% on average.

[19] Despite this, the $OPE_{x,CAPS}$ in this study overall falls within the OPE_x range previously reported in summer in Beijing (Table 1), for example, 3–6 [*Wang et al.*, 2006, 2010b] and 2.7–8.7 at the urban sites in Beijing[*Chou et al.*, 2009]. Also, the $OPE_{x,CAPS}$ in this study is close to those reported in other cities, e.g., 2.5–4 for Nashville urban plume [*Nunnermacker et al.*, 1998], 2.2–4.2 in New York City [*Kleinman et al.*, 2000], and slightly lower than the range of 3.9–4.7 observed in Los Angeles, California [*Pollack et al.*, 2012]. However, the OPE_x in Beijing during summertime is observed to be higher by a factor of 2.4 compared to wintertime [*Lin et al.*, 2011], indicating higher ozone production efficiency in summer than winter. It should be noted that the OPE_x in this study is generally lower than the values observed during Olympics 2008 [*Sun et al.*, 2011; *Chou et al.*, 2011]. One explanation for the higher OPE_x during the Olympic Games in 2008 is the different VOCs-NO_x-O_3 sensitivity. During the 2008 Olympics, the NO_x emission was reduced by 47% due to the strict controlling strategy [*Wang et al.*, 2010a]. The O_3 formation was likely shifted from VOC sensitive to NO_x sensitive [*Chou et al.*, 2011; *Sun et al.*, 2011]. Also, the low NO_x concentration generally would lead to the high OPE_x values (Figure 8). Another reason might be related to the well-known phenomenon commonly referred to as the "weekend ozone effect" or "holiday effect" [*Fujita et al.*, 2003; *Pollack et al.*, 2012; *Yarwood et al.*, 2003]. In these cases, *Chou et al.* [2011] and *Sun et al.* [2011] observed that enhancements in ozone are caused by reductions in NO_x emissions on weekends that lead to enhancements in VOC/NO_x ratio and ozone production efficiency. Although the high OPE_x values observed during the 2008 Olympics also coincided with weekends, the observed enhancements likely reflect changes in ozone precursors due to the short-term, but strict control policies implemented for this event. Note that the OPE_x varies differently among different O_3 episodes. Figure 7 shows the correlations of $[O_x]$ versus $[NO_z]$ during four O_3 episodes (hourly maximum $O_3 > 100$ ppb), i.e., 9–10, 15–16, 19–20, and 23–26 August. Although the daily OPE_x during every episode is similar, the average OPE_x for four episodes is quite different, for example, the highest OPE_x of 3.6 ppb/ppb is observed during the episode of 23–26 August, which is more than twice higher than 1.5 ppb/ppb during the episode of 15–16 August.

[20] The daily OPE_x in this study is always lower than the value suggested for O_3-VOC sensitivity ($OPE_x < 7$, [*Sillman*, 1995]), indicating that the ozone production in summer in Beijing is VOC-limited. Therefore, measures to control VOC emissions in Beijing would be effective to reduce O_3 levels. To further support this, we plot the daily OPE_x versus the peak of NO_x in early morning ($[NO_x]_0$, a surrogate of NO_x emissions from local traffic) in Figure 8. Similar to that reported by *Chou et al.* [2009] during the CAREBeijing-2006 campaign, the daily OPE_x presents a negative relationship with $[NO_x]_0$, suggesting that reduction of NO_x emissions appears not to be helpful for mitigation of O_3 pollution. The decrease of OPE_x as a function of $[NO_x]_0$ also supports the potential O_3-VOC sensitivity under the current ambient level of NO_x in Beijing. This is because that increase of $\Delta[NO_z]$ will not result in a corresponding increase of O_3 since high $[NO_x]_0$ is associated with high value of $\Delta[NO_z]$. $[NO_z]$/$[NO_y]$ is used to indicate the photochemical age by a number of studies [e.g., *Dommen et al.*, 1999; *Ge et al.*, 2012; *Kleinman et al.*, 2000; *Nunnermacker et al.*, 1998; *Olszyna et al.*, 1994]. The variations of daily OPE_x as a function of $[NO_z]$/$[NO_y]$ are shown in Figure 8b. The OPE_x shows a

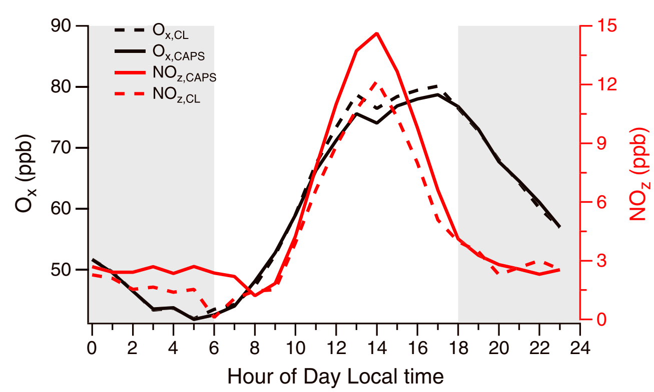

Figure 5. Mean diurnal cycles of $O_{x,CAPS}$, $O_{x,CL}$, $NO_{z,CAPS}$, and $NO_{z,CL}$ for the entire study. The shaded areas in the figure refer to nighttime.

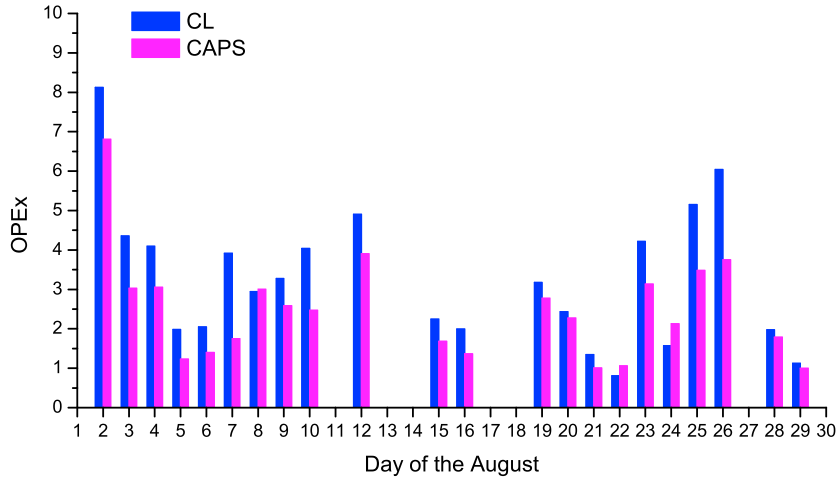

Figure 6. Time series of daily $OPE_{x,CAPS}$ and $OPE_{x,CL}$ derived from the correlations of $O_{x,CAPS}$ versus $NO_{z,CAPS}$, and $O_{x,CL}$ versus $NO_{z,CL}$, respectively.

positive correlation with $[NO_z]/[NO_y]$ ($r^2 = 0.38$, $p < 0.05$)), indicating that the OPE_x at the urban site of Beijing increases simultaneously with the aging of air parcels. This result is consistent with that observed at Peking University (near 4th North Ring of Beijing) during CAREBeijing-2006 [*Chou et al.*, 2009] and also in agreement with those at various urban sites, e.g., Houston and Tennessee, USA [*Daum et al.*, 2003; *Zaveri et al.*, 2003]. However, the correlation between OPE_x and $[NO_z]/[NO_y]$ is contrary to that observed at a rural site (SDZ) in Beijing, where ~75% of O_3 pollution is from regional transport rather than local photochemical production [*Ge et al.*, 2012].

3.4. Case Studies

[21] Our previous study frequently observed high concentration of nitrate in summer, which played an important role in particulate matter pollution in Beijing [*Sun et al.*, 2012]. Similarly, several episodes with high concentration of nitrate were also observed in this study (Figure 2). The formation of nitrate is mainly driven by three different processes, i.e., daytime photochemical production (R1), gas-particle partitioning (R2), and nighttime heterogeneous reactions (R3–R5). It appears that high concentration of NO_3^- is closely linked to the high O_3 and NO_2, which are two key precursors in the formation of nitrate particles. Here two high-O_3 episodes were chosen to further elucidate the roles of precursors of O_3 and NO_2 in the nitrate formation.

$$NO_2 + OH + M \rightarrow HNO_3(g) + M \qquad (R1)$$

$$HNO_3(g) + NH_3(g) \Leftrightarrow NH_4NO_3(s) \qquad (R2)$$

$$NO_2 + O_3 \rightarrow NO_3 + O_2 \qquad (R3)$$

$$NO_2 + NO_3 + M \rightarrow N_2O_5 + M \qquad (R4)$$

$$N_2O_5 + H_2O\ (aq) \rightarrow 2\ HNO_3 \qquad (R5)$$

[22] The first high-O_3 episode (Ep1) occurred between 9–10 August (Figure 9). The daily maximum of O_3 showed a large enhancement from ~60 ppb on 8 August to ~100 ppb on 9–10 August, indicating the strong photochemical processing during the 2 days. Although the OPE_x values were similar, 2.6 and 2.5 ppb/ppb, respectively, the variations of nitrate in aerosol particles were quite different. The concentration of NO_3^- remained consistently low (< 7 μg m^{-3}) on 9 August, yet exhibited a large enhancement associated with a pronounced diurnal cycle on 10 August. The increase of NO_3^- on 10 August showed a corresponding decrease of NO_y and NO. While the NO_3^- concentration was enhanced by a factor of more than 6 from ~6 μg m^{-3} to 38 μg m^{-3} in 6 h (6:00–12:00), the NO_y and NO decreased by ~53% and

Table 1. A Summary of the OPE_x Reported in Beijing and Surrounding Regions[a]

Location	OPE_x	Method	NO_2 Instrument	Date	References
Beijing, Mountain area	3–6	$[O_3]$ versus $[NO_y]$	P-CL	July 2005	*Wang et al.* [2006]
Beijing, Mountain area	3.0	$[O_x]$ versus $[NO_z]$	P-CL	Olympics, 2008	*Wang et al.* [2010b]
Beijing, Urban	1.1	$[O_x]$ versus $[NO_z]$	CL	Winter 2007	*Lin et al.* [2011]
Beijing, Urban	3.7–9.7	$[O_x]+[NO_z]$ versus $[NO_z]$	P-CL	Summer 2008	*Chou et al.* [2009]
Beijing, Urban	4–22	$[O_x]$ versus $[NO_z]$	P-CL	Olympics, 2008	*Sun et al.* [2011]
Beijing, Urban	8	$[O_x]+[NO_z]$ versus $[NO_z]$	P-CL	Olympics, 2008	*Chou et al.* [2011]
Beijing, Urban	1–6.8	$[O_x]$ versus $[NO_z]$	CAPS	Summer 2012	This study
Beijing, Rural area					
Urban plume	4.0	$[O_x]$ versus $[NO_z]$	CL	Summer 2008	*Ge et al.* [2012]
Rural plume	5.3	$[O_x]$ versus $[NO_z]$	CL	Summer 2008	*Ge et al.* [2012]
Nashville, Urban plume	2.5–4	$[O_x]$ versus $[NO_z]$	P-CL	July 1995	*Nunnermacker et al.* [1998]
New York, Urban	2.2–4.2	$[O_3]$ versus $[NO_z]$	P-CL	July 1996	*Kleinman et al.* [2000]
Los Angeles, California	3.9–4.7	$[O_x]$ versus $[NO_z]$	P-CL	May–June 2010	*Pollack et al.* [2012]

[a]P-CL represents the photolysis-chemiluninescence instruments.

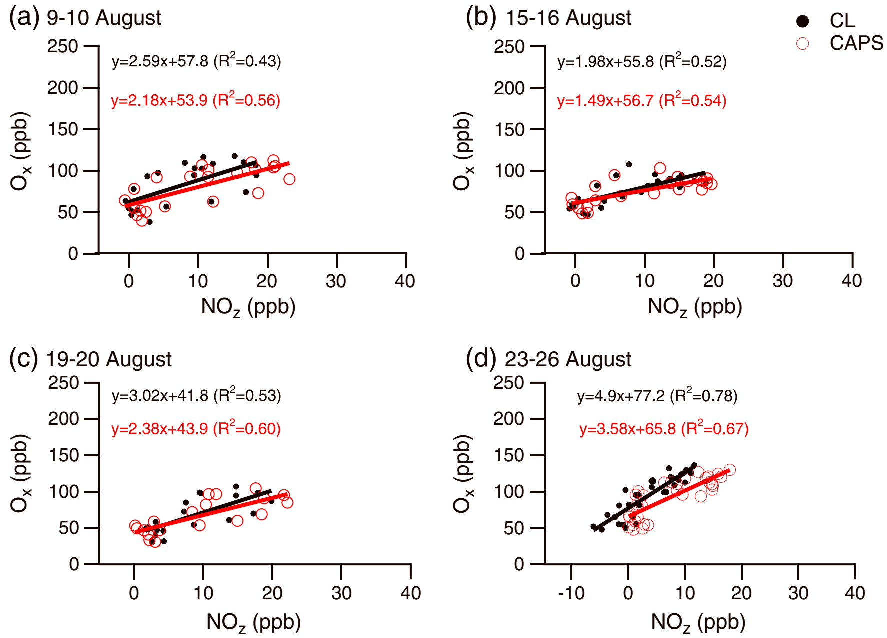

Figure 7. Correlations between $O_{x,CAPS}$ and $NO_{z,CAPS}$ (red dots), and $O_{x,CL}$ and $NO_{z,CL}$ (black dots) during four high-O_3 episodes: (a) 9–10 August, (b)14–15 August, (c)19–20 August, and (d) 23–26 August. The regression slopes refer to the average $OPE_{x,CAPS}$ (red dots) and $OPE_{x,CL}$ (black dots) determined for each episode.

85% to 47 and 9 ppb, respectively. It is very likely that the NO_3^- plume was due to the rapid photochemical production from the reactions of NO_2 and OH, followed by the formation of nitrate particles. In addition, the relatively low ambient temperature and high RH also facilitates the partitioning of HNO_3 to nitrate particles. After 12:00, the NO_3^- started to decrease rapidly mainly because of the evaporative loss of NH_4NO_3 at high ambient temperature, and also the deeper PBL. Although the variations of O_3 and meteorological variables were similar, the concentration of nitrate however was much lower on 9 August than on 10 August, which was likely due to the consistently low levels of NO_2 limiting the daytime photochemical production of nitrate from the reaction of NO_2 with OH.

[23] Beijing experienced another high-O_3 episode during 23–26 August (Ep2, Figure 10). During the 4 day episode, the variations of wind, RH and temperature were rather similar day by day, and the precursors of O_3 and NO_2 remained at high levels. The average OPE_x of 3.4 ppb/ppb is among the highest values throughout this study, suggesting the strong photochemical processing during this episode. Indeed, the daily maximum of O_3 is up to 130 ppb, which is the highest value observed in this study. To better elucidate the formation of nitrate, we calculate the photochemical production rate of HNO_3 using $NO_2 \times UV$ as a surrogate during daytime and the equilibrium constant of K_p for the reaction R2 (higher K_p indicates more stable NH_4NO_3) [*Seinfeld and Pandis*, 2006]. The time series of $NO_2 \times UV$ and K_p is shown in Figure 11.

[24] The NO_3^- presented two peaks occurring in the early morning and around noon, and it appeared that the evolution of NO_3^- was separated into two stages, i.e., from midnight to ~3:00–4:00, and from ~5:00–6:00 to noon. During the first stage, the increase of NO_3^- was associated with a synchronous increase of NO_2 and a corresponding decrease of O_3.

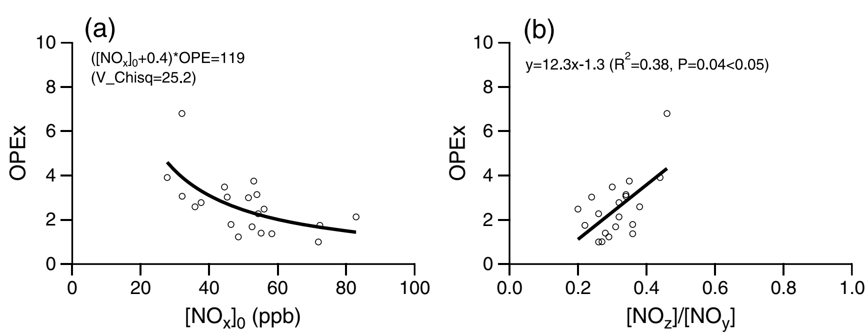

Figure 8. Correlations of (a) OPE_x versus $[NO_x]_0$, and (b) OPE_x versus $[NO_z]/[NO_y]$. $[NO_x]_0$ is the maximum of NO_x in early morning representing the relative traffic emission of 1 day. $[NO_z]/[NO_y]$ indicates the photochemical age of the air, and higher values suggest more aged air.

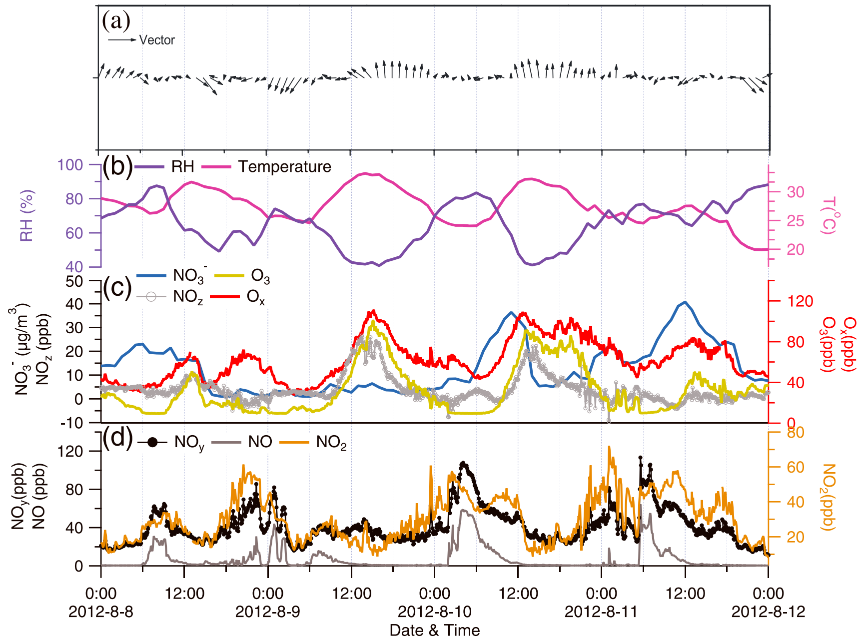

Figure 9. Time series of (a) wind vector, (b) RH and temperature , (c) particulate NO_3^-, NO_z, O_3, and O_x, (d) NO, NO_2, and NO_y during 8–11 August.

While the NO was low, the NO_2 and O_3 remained at a considerable level, which facilitated the formation of the NO_3 radical and dinitrogen pentoxide (R3–R4), and hence the heterogeneous formation of HNO_3 under high RH conditions. This is consistent with the continuous increase of the equilibrium constant of K_p for ammonium nitrate formation. Although the low boundary layer height might have played a role in the enhancement of NO_3^- concentration, the first peak at ~3:00–4:00 was more likely due to the heterogeneous reaction associated with the removal of NO_x at nighttime. The formation of NO_3 was then slowed down because the precursor of O_3 was almost completely consumed during this period. The NO_3^- started to increase again at ~5:00–6:00 and peaked between ~10:00–12:00. The increase of NO_3^-

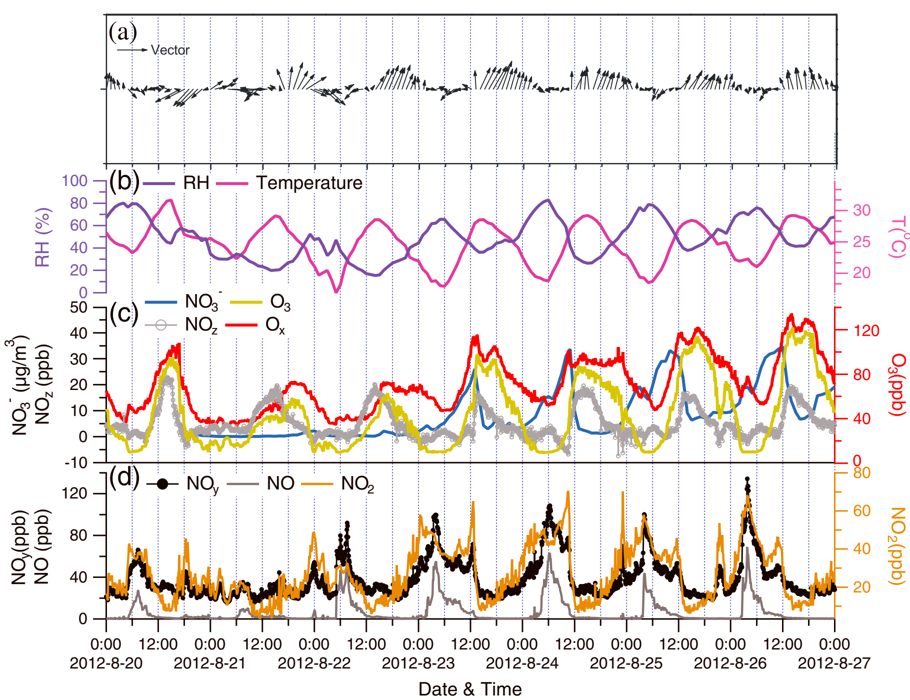

Figure 10. Same as Figure 9, but during 20–26 August.

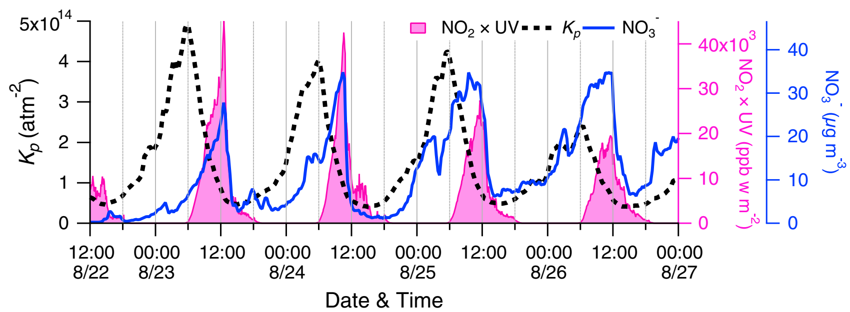

Figure 11. Time series of particulate NO_3^-, equilibrium constant of K_p for ammonium nitrate formation, and $NO_2 \times UV$, a surrogate of photochemical production rate of HNO_3 during daytime.

exactly corresponded to the start of daytime photochemical processing ($NO_2 \times UV$ in Figure 11). Meanwhile, the K_p gradually decreased counteracting the formation of nitrate. Therefore, the second increase of NO_3^- suggests the photochemical production dominates over the evaporative loss processes during this stage. The photochemical production reached a maximum at noon time when the NO_3^- concentration peaked as well. After that, the NO_3^- rapidly decreased to the lowest level of the day in ~2–3 h, due to the reduced photochemical production rate and significantly enhanced evaporative loss.

4. Conclusions

[25] The ambient nitrogen dioxide (NO_2) was measured in situ by an Aerodyne Cavity Attenuated Phase Shift NO_2 monitor in August 2012 at an urban site in Beijing. The CAPS is highly sensitive with the detection limit an order of magnitude lower than the standard, commercially available CL-based NO_x analyzer, and also a wide linear response range of 15 ppt–1 ppm. The NO_2 measured by the CAPS and CL shows overall agreement; however, large discrepancies up to ~20%, in particular during the afternoon, were also observed due to the interferences with reactive nitrogen species on CL measurements. The discrepancies therefore were NO_z dependent with larger differences associated at higher NO_z levels.

[26] The daily OPE_x was derived from the correlation of O_x versus NO_z. The average OPE_x for the entire study was 2.6 (1–6.8) ppb/ppb, which is comparable to the values previously reported in Beijing. Our results showed that the OPE_x derived from the CL NO_2 can be overestimated by 19–37% due to the interferences with reactive nitrogen species. The overestimation is expected to be more significant in rural and remote areas where the contribution of NO_z to the total NO_y is much higher than urban cities. The generally low OPE_x and the negative correlation between OPE_x and $[NO_x]_0$ implied the VOC-limited ozone production in summer in Beijing. In addition, the OPE_x increased as a function of photochemical age, $[NO_z]/[NO_y]$, which is in contrast to that observed at rural sites, indicating the different sources and photochemical processing of O_3 between urban and rural areas in and around Beijing.

[27] Two case studies during 9–10 August and 23–26 August 2012 revealed that high concentrations of precursors of O_3 and NO_2 are of importance for the formation of nitrate particles. A detailed analysis of the evolution of gaseous species, nitrate, and meteorological conditions suggest that the variations of nitrate in fine particles are caused by the competing effects of different formation mechanisms, including daytime photochemical production, gas-particle partitioning equilibrium, and nighttime heterogeneous reactions. Overall, high concentrations of NO_2 and O_3 with favorable meteorological conditions, e.g., high RH and low temperature, will greatly facilitate the formation of nitrate particles and increase the air pollution levels in the cities.

[28] **Acknowledgments.** This work was supported by the National Natural Science Foundation of China (41175108 & 41225019), the National Key Project of Basic Research (2013CB955801), and the Strategic Priority Research Program (B) of the Chinese Academy of Sciences (grant XDB05020501 & grant XDB05030203). This work was also partly supported by Academia Sinica through grants AS-102-SS-A10. We thank the Technical and Service Center, Institute of Atmospheric Physics, Chinese Academy of Sciences for providing the meteorology data.

References

Chameides, W. L., et al. (1992), Ozone precursor relationships in the ambient atmosphere, *J. Geophys. Res.*, *97*, 6037–6055.

Chou, C. C. K., C. Y. Tsai, C. J. Shiu, S. C. Liu, and T. Zhu (2009), Measurement of NO_y during Campaign of Air Quality Research in Beijing 2006 (CAREBeijing-2006): Implications for the ozone production efficiency of NO_x, *J. Geophys. Res.*, *114*, D00G01, doi:10.1029/2008JD010446.

Chou, C. C. K., C. Y. Tsai, C. C. Chang, P. H. Lin, S. C. Liu, and T. Zhu (2011), Photochemical production of ozone in Beijing during the 2008 Olympic Games, *Atmos. Chem. Phys.*, *11*(18), 9825–9837.

Couach, O., F. Kirchner, R. Jimenez, I. Balin, S. Perego, and H. van den Bergh (2004), A development of ozone abatement strategies for the Grenoble area using modeling and indicators, *Atmos. Environ.*, *38*(10), 1425–1436, doi:10.1016/j.atmosenv.2003.12.001.

Daum, P. H., L. I. Kleinman, S. R. Springston, L. J. Nunnermacker, Y. N. Lee, J. Weinstein-Lloyd, J. Zheng, and C. M. Berkowitz (2003), A comparative study of O_3 formation in the Houston urban and industrial plumes during the 2000 Texas Air Quality Study, *J. Geophys. Res.*, *108*(D23), 4715, doi:10.1029/2003jd003552.

Dommen, J., A. S. H. Prévôt, A. M. Hering, T. Staffelbach, and G. L. Kok (1999), Photochemical production and aging of an urban air mass, *J. Geophys. Res.*, *104*, 5493–5506.

Dunlea, E. J., et al. (2007), Evaluation of nitrogen dioxide chemiluminescence monitors in a polluted urban environment, *Atmos. Chem. Phys.*, *7*(10), 2691–2704.

Fujita, E. M., W. R. Stockwell, D. E. Campbell, R. E. Keislar, and D. R. Lawson (2003), Evolution of the magnitude and spatial extent of the weekend ozone effect in California's South Coast Air Basin, 1981–2000, *J. Air Waste Manage.*, *53*(7), 802–815.

Ge, B., X. Xu, W. Lin, and Y. Wang (2010), Observational study of ozone production efficiency at the Shangdianzi Regional Background Station (in Chinese with English abstract), *Environ. Sci.*, *31*(7), 1444–1450.

Ge, B. Z., X. B. Xu, W. L. Lin, J. Lie, and Z. F. Wang (2012), Impact of the regional transport of urban Beijing pollutants on downwind areas in summer: Ozone production efficiency analysis, *Tellus B*, *64*, 17,348–17,351, doi:10.3402/tellusb.v64i0.17348.

Guttikunda, S. K., G. R. Carmichael, G. Calori, C. Eck, and J. H. Woo (2003), The contribution of megacities to regional sulfur pollution in Asia, *Atmos. Environ.*, *37*(1), 11–22.

Guttikunda, S. K., Y. H. Tang, G. R. Carmichael, G. Kurata, L. Pan, D. G. Streets, J. H. Woo, N. Thongboonchoo, and A. Fried (2005), Impacts of Asian megacity emissions on regional air quality during spring 2001, *J. Geophys. Res.*, *110*, D20301, doi:10.1029/2004JD004921.

Hao, J. M., L. T. Wang, L. Li, J. N. Hu, and X. C. Yu (2005), Air pollutants contribution and control strategies of energy-use related sources in Beijing, *Sci. China Ser. D*, *48*, 138–146.

Kanakidou, M., et al. (2011), Megacities as hot spots of air pollution in the East Mediterranean, *Atmos. Environ.*, *45*(6), 1223–1235.

Kebabian, P. L., S. C. Herndon, and A. Freedman (2005), Detection of nitrogen dioxide by cavity attenuated phase shift spectroscopy, *Anal. Chem.*, *77*(2), 724–728.

Kebabian, P. L., E. C. Wood, S. C. Herndon, and A. Freedman (2008), A practical alternative to chemiluminescence-based detection of nitrogen dioxide: Cavity attenuated phase shift spectroscopy, *Environ. Sci. Technol.*, *42*(16), 6040–6045.

Kleinman, L., et al. (1994), Ozone formation at a rural site in the southeastern United States, *J. Geophys. Res.*, *99*, 3469–3482.

Kleinman, L. I., P. H. Daum, D. G. Imre, J. H. Lee, Y.-N. Lee, L. J. Nunnermacker, S. R. Springston, J. Weinstein-Lloyd, and L. Newman (2000), Ozone production in the New York City urban plume, *J. Geophys. Res.*, *105*, 14,495–14,511.

Lawrence, M. G., T. M. Butler, J. Steinkamp, B. R. Gurjar, and J. Lelieveld (2007), Regional pollution potentials of megacities and other major population centers, *Atmos. Chem. Phys.*, *7*(14), 3969–3987.

Li, X., T. Brauers, A. Hofzumahaus, K. Lu, Y. P. Li, M. Shao, T. Wagner, and A. Wahner (2013), MAX-DOAS measurements of NO_2, HCHO and CHOCHO at a rural site in Southern China, *Atmos. Chem. Phys.*, *13*(4), 2133–2151.

Lin, W., X. Xu, X. Zhang, and J. Tang (2008), Contributions of pollutants from North China Plain to surface ozone at the Shangdianzi GAW Station, *Atmos. Chem. Phys.*, *8*, 5889–5898.

Lin, W., X. Xu, B. Ge, and X. Liu (2011), Gaseous pollutants in Beijing urban area during the heating period 2007–2008: Variability, sources, meteorological, and chemical impacts, *Atmos. Chem. Phys.*, *11*(15), 8157–8170, doi:10.5194/acp-11-8157-2011.

Liu, S. C., M. Trainer, F. C. Fehsenfeld, D. D. Parrish, E. J. Williams, D. W. Fahey, G. Hubler, and P. C. Murphy (1987), Ozone production in the rural troposphere and the implications for regional and global ozone distributions, *J. Geophys. Res.*, *92*(D4), 4191–4207.

Madronich, S. (2006), Chemical evolution of gaseous air pollutants downwind of tropical megacities: Mexico City case study, *Atmos. Environ.*, *40*(31), 6012–6018.

Molina, M. J., and L. T. Molina (2004), Megacities and atmospheric pollution, *J. Air Waste Manage.*, *54*(6), 644–680.

Molina, L. T., et al. (2010), An overview of the MILAGRO 2006 Campaign: Mexico City emissions and their transport and transformation, *Atmos. Chem. Phys.*, *10*(18), 8697–8760.

Murphy, J. G., D. A. Day, P. A. Cleary, P. J. Wooldridge, D. B. Millet, A. H. Goldstein, and R. C. Cohen (2007), The weekend effect within and downwind of Sacramento. Part 1: Observations of ozone, nitrogen oxides, and VOC reactivity, *Atmos. Chem. Phys.*, *7*(20), 5327–5339.

Nunnermacker, L. J., et al. (1998), Characterization of the Nashville urban plume on July 3 and July 18, 1995, *J. Geophys. Res.*, *103*, 28,129–28,148.

Olszyna, K. J., E. M. Bailey, R. Simonaitis, and J. F. Meagher (1994), O_3 and NO_y relationships at a rural site, *J. Geophys. Res.*, *99*(D7), 14,557–14,563.

Parrish, D. D., et al. (1990), Systematic variations in the concentration of NO_x (NO Plus NO_2) at Niwot-Ridge, Colorado, *J. Geophys. Res.*, *95*(D2), 1817–1836.

Pollack, I. B., B. M. Lerner, and T. B. Ryerson (2010), Evaluation of ultraviolet light-emitting diodes for detection of atmospheric NO_2 by photolysis-chemiluminescence, *J. Atmos. Chem.*, *65*, 111–125.

Pollack, I. B., et al. (2012), Airborne and ground-based observations of a weekend effect in ozone, precursors, and oxidation products in the California South Coast Air Basin, *J. Geophys. Res.*, *117*, D00V05, doi:10.1029/2011JD016772.

Quan, J. N., Y. Gao, Q. Zhang, X. X. Tie, J. J. Cao, S. Q. Han, J. W. Meng, P. F. Chen, and D. L. Zhao (2013), Evolution of planetary boundary layer under different weather conditions, and its impact on aerosol concentrations, *Particuology*, *11*(1), 34–40.

Ran, L., et al. (2012), Ozone production in summer in the megacities of Tianjin and Shanghai, China: A comparative study, *Atmos. Chem. Phys.*, *12*(16), 7531–7542.

Rickard, A. R., G. Salisbury, P. S. Monks, A. C. Lewis, S. Baugitte, B. J. Bandy, K. C. Clemitshaw, and S. A. Penkett (2002), Comparison of measured ozone production efficiencies in the marine boundary layer at two European coastal sites under different pollution regimes, *J. Atmos. Chem.*, *43*, 107–134.

Roberts, J. M., et al. (1995), Relationships between Pan and ozone at sites in eastern North America, *J. Geophys. Res.*, *100*(D11), 22,821–22,830.

Ryerson, T. B., E. J. Williams, and F. C. Fehsenfeld (2000), An efficient photolysis system for fast-response NO_2 measurements, *J. Geophys. Res.*, *105*(D21), 26,447–26,461.

Sadanaga, Y., Y. Fukumori, T. Kobashi, M. Nagata, N. Takenaka, and H. Bandow (2010), Development of a selective light-emitting diode photolytic NO_2 converter for continuously measuring NO_2 in the atmosphere, *Anal. Chem.*, *82*(22), 9234–9239.

Seinfeld, J. H., and S. N. Pandis (2006), *Atmospheric Chemistry and Physics: From Air Pollution to Climate Change*, 1203 pp., Wiley, New York.

Shao, M., X. Tang, Y. Zhang, and W. Li (2006), City clusters in China: Air and surface water pollution, *Front. Ecol. Environ.*, *4*(7), 353–361.

Shiu, C. J., S. C. Liu, C. C. Chang, J. P. Chen, C. C. K. Chou, C. Y. Lin, and C. Y. Young (2007), Photochemical production of ozone and control strategy for Southern Taiwan, *Atmos. Environ.*, *41*(40), 9324–9340, doi:10.1016/j.atmosenv.2007.09.014.

Sillman, S. (1995), The use of NO_y, H_2O_2 and HNO_3 as indicators for ozone-NO_x -hydrocarbon sensitivity in urban locations, *J. Geophys. Res.*, *100*, 14,175–14,188.

Sillman, S. (1999), The relation between ozone, NO_x and hydrocarbons in urban and polluted rural environments, *Atmos. Environ.*, *33*(12), 1,821–1,845.

Steinbacher, M., C. Zellweger, B. Schwarzenbach, S. Bugmann, B. Buchmann, C. Ordonez, A. S. H. Prevot, and C. Hueglin (2007), Nitrogen oxide measurements at rural sites in Switzerland: Bias of conventional measurement techniques, *J. Geophys. Res.*, *112*, D11307, doi:10.1029/2006JD007971.

Sun, Y., L. L. Wang, Y. S. Wang, L. Quan, and Z. R. Liu (2011), In situ measurements of SO_2, NO_x, NO_y, and O_3 in Beijing, China during August 2008, *Sci. Total Environ.*, *409*(5), 933–940.

Sun, Y. L., Z. F. Wang, H. B. Dong, T. Yang, J. Li, X. L. Pan, P. Chen, and J. T. Jayne (2012), Characterization of summer organic and inorganic aerosols in Beijing, China with an Aerosol Chemical Speciation Monitor, *Atmos. Environ.*, *51*, 250–259.

Sun, Y. L., Z. F. Wang, P. Q. Fu, T. Yang, Q. Jiang, H. B. Dong, J. Li, and J. J. Jia (2013), Aerosol composition, sources and processes during wintertime in Beijing, China, *Atmos. Chem. Phys.*, *13*, 4577–4592, doi:10.5194/acp-13-4577-2013.

Trainer, M., et al. (1993), Correlation of ozone with NO_y in photochemically aged air, *J. Geophys. Res.*, *98*(D2), 2917–2925.

Volkamer, R., L. T. Molina, M. J. Molina, T. Shirley, and W. H. Brune (2005), DOAS measurement of glyoxal as an indicator for fast VOC chemistry in urban air, *Geophys. Res. Lett.*, *32*, L08806, doi:10.1029/2005GL022616.

Wang, T., A. Ding, J. Gao, and W. S. Wu (2006), Strong ozone production in urban plumes from Beijing, China, *Geophys. Res. Lett.*, *33*, L21806, doi:10.1029/2006GL027689.

Wang, S. X., M. Zhao, J. Xing, Y. Wu, Y. Zhou, Y. Lei, K. B. He, L. X. Fu, and J. M. Hao (2010a), Quantifying the air pollutants emission reduction during the 2008 Olympic Games in Beijing, *Environ. Sci. Technol.*, *44*(7), 2490–2496.

Wang, T., et al. (2010b), Air quality during the 2008 Beijing Olympics: Secondary pollutants and regional impact, *Atmos. Chem. Phys.*, *10*(16), 7,603–7,615, doi:10.5194/acp-10-7603-2010.

Winer, A. M., J. W. Peters, J. P. Smith, and J. N. Pitts Jr (1974), Response of commercial chemiluminescent nitric oxide-nitrogen dioxide analyzers to other nitrogen-containing compounds, *Environ. Sci. Technol.*, *8*, 1118–1121.

Xu, X. B., B. Z. Ge, and W. L. Lin (2009), Progresses in research of Ozone Production Efficiency (OPE), *Adv. Earth Sci.*, *24*(8), 845–853.

Yarwood, G., T. E. Stoeckenius, J. G. Heiken, and A. M. Dunker (2003), Modeling weekday/weekend Los Angeles region for 1997, *J. Air Waste Manage.*, *53*(7), 864–875.

Zaveri, R. A., C. M. Berkowitz, L. I. Kleinman, S. R. Springston, P. V. Doskey, W. A. Lonneman, and C. W. Spicer (2003), Ozone production efficiency and NO_x depletion in an urban plume: Interpretation of field observations and implications for evaluating O_3-NO_x-VOC sensitivity, *J. Geophys. Res.*, *108*(D14), 4436, doi:10.1029/2002jd003144.

龚振淞, 陈丽娟. 2013. 2010 年西北太平洋与南海热带气旋活动异常的成因分析 [J]. 气候与环境研究，18（3）：342–352，doi: 10.3878/j.issn.1006-9585.2012.11063. Gong Zhensong, Chen Lijuan. 2013. Analysis of anomalous tropical cyclone activities over the western North Pacific and the South China Sea in 2010 [J]. Climatic and Environmental Research (in Chinese), 18 (3): 342–352.

2010 年西北太平洋与南海热带气旋活动异常的成因分析

龚振淞 陈丽娟

国家气候中心中国气象局气候研究开放实验室，北京 100081

摘　要　利用中国气象局热带气旋（TC）资料、NCEP/NCAR 再分析资料和美国 NOAA 向外长波辐射（OLR）等资料，分析了 2010 年西北太平洋（WNP）及南海（SCS）热带气旋活动异常的可能成因，讨论了同期大气环流配置和海温外强迫对 TC 生成和登陆的动力和热力条件的影响。结果表明，2010 年生成 TC 频数明显偏少，生成源地显著偏西，而登陆 TC 频数与常年持平。导致 7～10 月 TC 频数明显偏少的大尺度环境场特征为：副热带高压较常年异常偏强、西伸脊点偏西，季风槽位置异常偏西，弱垂直风切变带位置也较常年偏西且范围偏小，南亚高压异常偏强，贝加尔湖附近对流层低高层均为反气旋距平环流，这些关键环流因子的特征和配置都不利于 TC 在 WNP 的东部生成。影响 TC 活动的外强迫场特征为：2010 年热带太平洋经历了 El Niño 事件于春末夏初消亡、La Niña 事件于 7 月形成的转换；7～10 月，WNP 海表温度维持正距平，140°E 以东为负距平且对流活动受到抑制；暖池次表层海温异常偏暖，对应上空 850 hPa 为东风距平，有利于季风槽偏西和 TC 在 WNP 的西北侧海域生成。WNP 海表温度和暖池次表层海温的特征是 2010 年 TC 生成频数偏少、生成源地异常偏西的重要外强迫信号。有利于 7～10 月热带气旋西行和登陆的 500 hPa 风场特征为：北太平洋为反气旋环流距平，其南侧为东风异常，该东风异常南缘可到 25°N，并向西扩展至中国大陆地区；南海和西北太平洋地区 15°N 以南的低纬也为东风异常；在这样的风场分布型下，TC 容易受偏东气流引导西行并登陆我国沿海地区。这是 2010 年生成 TC 偏少但登陆 TC 并不少的重要环流条件。

关键词　热带气旋　西太平洋副高　季风槽　垂直风切变　次表层海温

文章编号　1006–9585（2013）03–0342–11　　**中图分类号**　P457.8　　**文献标识码**　A

doi:10.3878/j.issn.1006-9585.2012.11063

Analysis of Anomalous Tropical Cyclone Activities over the Western North Pacific and the South China Sea in 2010

GONG Zhensong and CHEN Lijuan

Laboratory for Climate Studies of China Meteorological Administration, National Climate Center, Beijing 100081

Abstract　The possible reasons for anomalous tropical cyclone (TC) activity over the western North Pacific (WNP) and South China Sea (SCS) were studied, and the possible effects of dynamic conditions and the thermal state on the frequency of TC genesis and landfall, derived from circulation patterns and boundary forcing, were analyzed using TC data from the China Meteorological Administration, NCEP/NACR reanalysis data, and the outgoing long-wave radiation data from the US NOAA. The results showed that TC genesis was much less frequent than normal but that TC landfall

---

收稿日期　2011–04–26 收到，2013–01–23 收到修定稿

资助项目　科技部科技支撑项目 2009BAC51B05，公益性行业（气象）科研专项 GYHY200906015，中国气象局气候预测创新团队项目

作者简介　龚振淞，女，1977 年出生，高工，主要从事气候异常诊断和气候预测研究与应用工作。E-mail: gongzs@cma.gov.cn

通讯作者　陈丽娟，E-mail：chenlj@cma.gov.cn

was near normal in 2010. The TC genesis locations were west of the usual genesis longitudes. The circulation patterns leading to fewer TCs were characterized as strong western North Pacific subtropical highs and South Asia highs, westward monsoon troughs, and vertical wind shear, anticyclone anomalies at low and high levels of the troposphere over Lake Baikal. Each of these features does not favor the genesis of TC in the eastern part of the WNP. Boundary forcing showed that the tropical Pacific experienced an El Niño event that ended in the late spring and early summer 2010 while a new La Niña event formed that July. From July to October, there was a positive sea surface temperature (SST) anomaly over the WNP west of 140°E while convection was suppressed east of 140°E. The subsurface temperature over the warm pool was much higher than normal, corresponding to an 850 hPa easterly wind anomaly. This thermal state led to the monsoon trough moving west of its average position and TC genesis in the eastern WNP. The SST and subsurface temperature features in the warm pool were the key thermal factors in the lower frequency of TCs in the western WNP in 2010. Further analysis showed that there was an anticyclone 500 hPa wind anomaly over the middle latitudes of the North Pacific from July to October 2010. The easterly anomaly to the south of the anticyclone was accompanied by another in the west of the WNP and SCS. The easterly anomaly extended southward to 25°N and westward to mainland China and the western anomaly extended northward to 15°N. Such a wind anomaly pattern favors the westward movement of TCs and then making landfall in mainland China. These are, therefore, the circulation conditions required for much less frequent TC genesis and almost normal TC landfall.

Keywords Tropical cyclone, Western Pacific subtropical high, Monsoon trough, Vertical wind shear, Subsurface sea temperature

1 引言

每年在热带西北太平洋都会生成数十个热带气旋，占全球热带洋面上热带气旋年生成总数的1/3，从而使得我国成为受热带气旋影响最为严重的国家之一，我国东南部沿海地区都有可能有热带气旋登陆，平均每年大概有 7 个左右（苏振生，1949～1988，1989～2004；吴晓鹏，2005～2008）。热带气旋带来的大风、暴雨严重威胁人民的生命财产安全。近几年因热带气旋造成的年平均直接经济损失达到 200 多亿元，平均每年死亡人数超过 500 人。因此，研究生成热带气旋的条件和异常成因对热带气旋活动趋势预测非常重要，有利于为防灾减灾提供服务。

陈联寿和丁一汇（1979）、Gray（1979）把热带气旋形成的条件分为：热力条件、动力条件和环境条件，并指出西北太平洋季风槽的位置对热带气旋活动的分布有很大的影响。王慧等（2004）的研究工作证明了季风槽活动影响热带气旋的生成，当季风槽加强并向东扩展使得季风加强时，热带气旋数明显增多。Chen et al.（1998）和 Chan（2000）等的研究也指出，ENSO 循环中的季风槽加强东伸或减弱西退显著影响热带气旋的生成位置。并且，季风槽又与西太平洋副热带高压的演变紧密相关 (Wang and Wu, 1997)。大气涛动或遥相关型对热带气旋的活动也有显著的影响。西北太平洋热带气旋生成频次的年际变化与 6～9 月的南极涛动之间存在显著的负相关关系（王会军和范可，2006），同时也与冬春季节北太平洋海冰呈显著的反相关；而冬春季北太平洋海冰通过北太平洋涛动（NPO）影响西太平洋热带气旋生成的热力和动力环境（范可，2007a, 2007b；王会军等，2007）。夏季亚洲—太平洋涛动（APO）和西北太平洋热带气旋频数多寡之间具有显著正相关关系（周波涛等，2008），而春季 Hadley 环流偏强（弱），夏季西北太平洋热带气旋频数减少（增多）（Zhou and Cui, 2008）。这些影响热带气旋活动的物理机制分析都有助于全面认识影响热带气旋活动的因子。

除了对热带气旋生成进行物理诊断分析之外，我国学者还发展了热带气旋的气候预测方法，包括动力统计相结合的预测试验（王会军等，2006），具有物理意义的统计预报模型（范可，2007b），显示了对热带气旋预测研究的应用前景。

事实上，每年热带气旋的生成和登陆预测都是一个非常复杂的问题，影响每年热带气旋活动的主导因子不尽相同，热带气旋的年代际尺度、年际尺度、季节内振荡等信息的共同作用增加了气候预测的难度。因此认识每年热带气旋活动的异常特征及成因是我们加深对热带气旋活动认识、提高预测能力的重要环节。已经有不少学者在这方面做了大量有意义的工作（刘舸等，2007；王瑾等，2009）。2010 年热带气旋活动的特殊性及其形成原因也非常值得分析。

2 资料与方法

本文采用的大气和海洋资料来自NCEP的再分析资料（Kalnay et al.，1996）。大气资料的长度为1948～2010 年，分辨率为 2.5°（纬度）×2.5°（经度）；海洋资料的分辨率为 2.0°（纬度）×2.0°（经度），气候平均值选取 1971～2000 年 30 年平均。

次表层海温资料来自美国Godas全球逐月次表层海温（GODAS）资料，资料的长度为 1980～2010 年，水平分辨率为 1.0°（纬度）×0.333°（经度），气候平均值选取 1981～2010 年 30 年平均。

向外长波辐射（OLR）资料来自 NOAA，资料的长度为 1979～2010 年，气候平均值选取 1981～2010 年 30 年平均。

本文使用的热带气旋频数及生成位置的历史资料来自中国气象局编制的《热带气旋年鉴》（苏振生，1949～1988，1989～2004；吴晓鹏，2005～2008），2009～2010 年热带气旋实况资料来自中国气象局中央气象台。这些资料中，热带气旋定义为在西北太平洋和南海生成、中心附近的平均风力达到 8 级（17 m/s）或以上的热带气旋（TC），包括热带风暴、强热带风暴、台风、强台风、超强台风5 个级别。气候平均值选取 1971～2000 年 30 年平均。

3 西北太平洋和南海热带气旋活动特征

3.1 生成热带气旋频数异常偏少，登陆频数与常年持平

2010 年在西北太平洋和南海共生成 14 个热带气旋，较 1971～2000 年平均值（27 个）偏少 13 个，与 1998 年并列为 1951 年以来生成热带气旋最少的年份。热带气旋的生成时段主要集中在 7～10 月，在这 4 个月中共有 13 个热带气旋生成，占全年总数的 93%，但较常年同期偏少 7 个。除了 3 月生成热带气旋数高于多年平均值，其余的月份均低于多年平均（图 1a）。虽然 2010 年与 1998 年生成的热带气旋数都为历史最少，只有 14 个，但 2010 年有7 个在我国沿海地区登陆，与多年平均持平（图 1b），登陆与生成频数比达到 50%，为 1951 年以来最高。而 1998 年只有 4 个登陆，表现为生成少、登陆也少的特征，符合一般热带气旋生成频次与登陆频次成正比的活动规律。相比 1998 年生成异常少、登陆也异常少的特征，2010 年热带气旋活动表现为生成异常少、登陆并不少。因此 2010 年热带气旋活动表现得更加复杂。

3.2 生成源地异常偏西

参考美国联合热带气旋监测中心(Joint Typhoon Warning Center, JTWC) 对热带气旋生成源地的划分办法(http://www.usno.navy.mil/JTWC/ [2011-04-26])，将西北太平洋和南海地区热带气旋生成源地分为 3 个主要的区域（表 1）：120°E 以西、120°E～145°E 区域、145°E～180°E，平均每年生成热带气旋数分别为 4、12、12，即 120°E 以东为热带气旋生成的主要源地。2010 年在 120°E 以西生成TC 3 个，120°E～145°E 区域生成 11 个，在 145°E以东没有编号热带气旋（第 12 号热带气旋为热带低压时在 146.4°E，但达到热带风暴的编号级别时位于 144.9°E）。这是造成 2010 年热带气旋总数异常偏少的直接原因。

1998 年生成 TC 与 2010 年的情况类似：在120°E 以西生成 6 个，120°E～145°E 范围内生成 8个，而在 145°E 以东没有热带气旋生成。所不同的是 1998 年只有 4 个热带气旋登陆，登陆时间分布

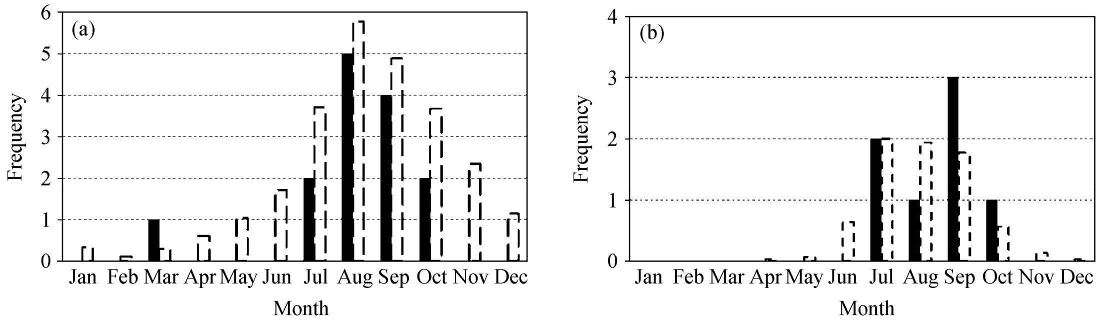

图 1 2010 年逐月（a）生成和（b）登陆热带气旋频数（黑色：2010 年实况，空白：1971～2000 年平均）

Fig. 1 The monthly frequency of tropical cyclone (TC) (a) genesis and (b) landfall in 2010 (dark columns indicate 2010 and white columns stand for the average from 1971 to 2000)

是 7 月 1 个、8 月 2 个、9 月 1 个（表 2）。而 2010 年有 7 个热带气旋登陆，其中 9 月 3 个、10 月 1 个。即 2010 年 9～10 月登陆台风比 1998 年多 3 个，表现为秋季异常活跃的特点。此外，对比登陆热带气旋的路径：1998 年的登陆地点均在广东珠江口以北地区，而 2010 年有 2 个 TC 到珠江口以西地区登陆，即 2010 年西行热带气旋明显偏多。

表 1　不同 TC 生成源地的频数

Table 1　The frequency of TC genesis in different positions

	120°E 以西	120°E～145°E	145°E 以东
1971～2000 年平均	4	12	12
1998 年	6	8	0
2010 年	3	11	0

表 2　7～10 月登陆 TC 频数

Table 2　The frequency of TC landfall from July to October

	7 月	8 月	9 月	10 月
1971～2000 年平均	2	2	1.5	0.5
1998 年	1	2	1	0
2010 年	2	1	3	1

是什么原因导致 2010 年热带气旋生成源地异常偏西，生成的总频次异常偏少但是登陆数却不少？下面我们将从大尺度环流特征和外强迫信号的角度进行详细的分析。

4　影响热带气旋活动的大气环流特征

4.1　西太平洋副热带高压

已有的研究表明，副热带高压的演变可通过影响季风槽的经纬向位置进而影响热带气旋的形成位置（Wang and Wu, 1997）。当副高从南海东撤到菲律宾附近海域时，季风槽南侧西风东进，有利于热带气旋在西北太平洋东侧生成。

2010 年 7～10 月，500 hPa 高度距平场（图 2）显示，西太平洋副热带高压异常强大，面积远远大于气候值，西伸脊点较常年异常偏西，7～9 月西伸至 110°E 以西，脊线异常偏北。从副高强度、西伸

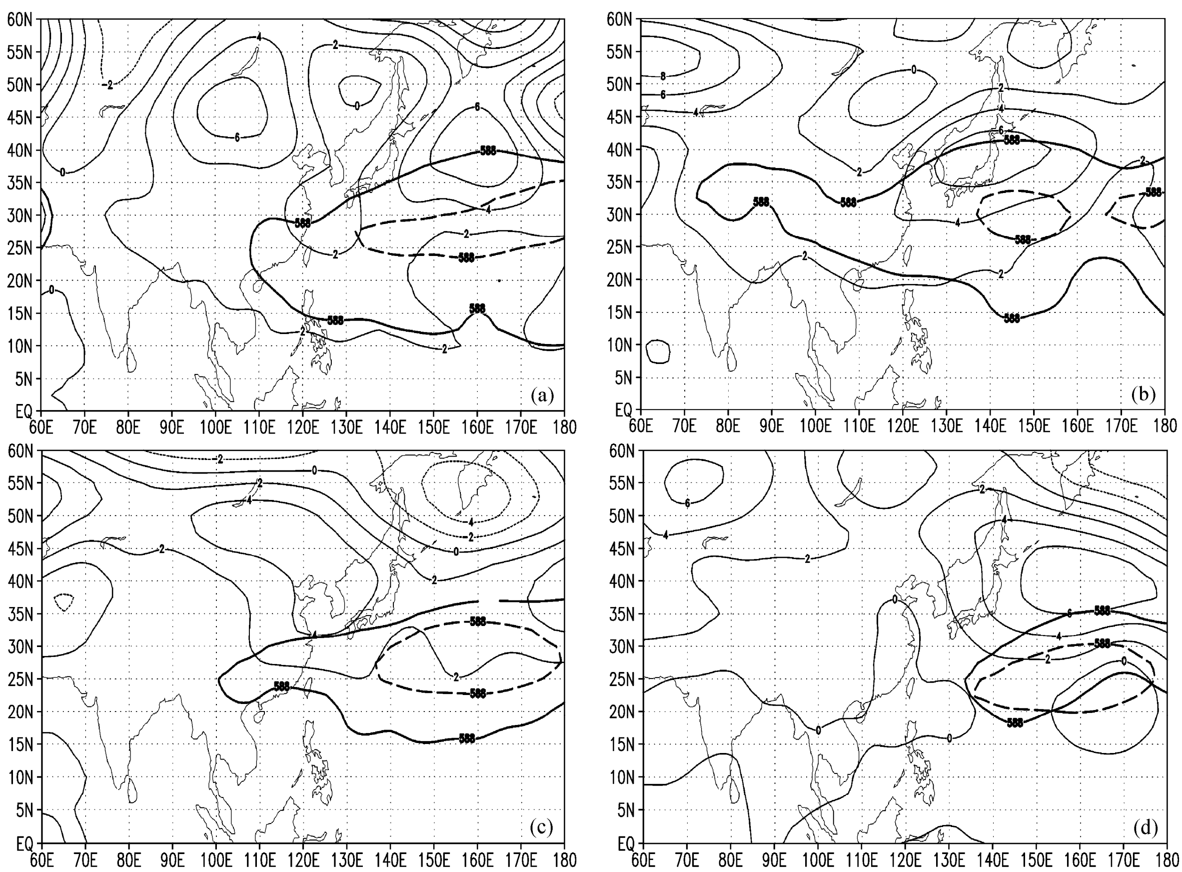

图 2　2010 年（a）7 月、（b）8 月、（c）9 月、（d）10 月 500 hPa 高度距平场（单位：dagpm）（粗实线：2010 年 588 dagpm 等值线，粗虚线：1971～2000 年平均 588 dagpm 等值线）

Fig. 2　The 500-hPa geopotential height anomalies (dagpm) in (a) Jul, (b) Aug, (c) Sep, and (d) Oct in 2010 (the thick solid line represent 588-dagpm isoline in 2010 and thick dashed line represent that averaged from 1971 to 2000)

脊点及脊线指数[定义见赵振国（1999）]的逐月演变显示：2010 年 1～9 月西太平洋副热带高压强度较常年偏强，尤其是 7 月和 8 月强度为 1951 年以来最强值，10 月副高开始有所减弱；6～8 月西伸脊点的偏西程度也为 1951 年以来的历史第 1 位，平均在 90°E 附近，9 月西伸脊点位置在 100°E 附近，10 月才东撤至 135°E 左右；副高脊线位置在 6 月偏南，7 月接近常年，8～10 月均异常偏北。

由于 2010 年的 6～8 月副高体异常强大，副高的西伸脊点可至 90°E 附近，且夏初副高脊线偏南。在这种强大的副高体控制下，季风槽很难加强东伸，季风槽南侧的西风也无法向东推进。热带气旋的主要生成区域（5°N～25°N，120°E～170°E）基本被副高所控制，以下沉气流为主（图 3），抑制了该地区对流的发展，不利于热带气旋的生成。因此在 2010 年 6 月没有热带气旋活动，7 月也只有 2 个生成。随着 8 月西太平洋副热带高压北跳，热带气旋才开始活跃起来。

4.2 季风槽和垂直风切变

季风槽是北半球夏季西南季风和副热带高压脊南侧之信风合成的低压带，为热带气旋生成提供有利的动力学条件。丁一汇和 Wright（1983）指出热带气旋偏多年和偏少年，低层季风槽的分布显著不同，当西北太平洋季风槽增强并向东扩展使季风加强时，有利于热带气旋的生成，而且热带气旋生成的位置也偏东；当季风槽弱时不利于热带气旋生成且生成位置偏西。一般情况下，7～10 月季风槽经历从南往北推进，然后又撤退的过程。从季风槽的东西向气候特征看，其位置也会随季节向东伸展，最东端一般位于 150°E 附近。

影响热带气旋形成的另外一个关键环境因素是垂直风切变。垂直风切变较大会抑制对流的发展，从而抑制暖心和涡旋的形成（Demaria,1996）。垂直风切变较小可以使得初始扰动的对流凝结所释放的潜热能集中在一个有限的空间范围，热能量可在对流层中上层集中，形成暖心结构，促使初始扰动的气压不断下降，有利于热带气旋的形成。正常年份弱的垂直风切变（纬向风切变小于 10 m/s）位于西太平洋东部，可延伸至日界线附近。季风槽东段的大部分位于宽阔的太平洋洋面，暖池附近。暖的海温加上活跃的对流活动，且高低层风垂直切变小，对流层上下空气相对运动很小，形成有利于热带气旋发生、发展的条件。

2010 年的季风槽活动出现异常（图 4），季风槽位置异常偏西。7～10 月季风槽的东端都在 120°E 附近，与正常年相比，2010 年季风槽东端位置较常年偏西 30 个经度。此外，沿着东伸季风槽分布的弱垂直风切变带位置也较常年偏西，且范围偏小，这是造成 2010 年热带气旋生成位置异常偏西的主要动力条件。由于季风槽东端只延伸到 120°E 附近，使得在热带气旋生成重要源地之一的 145°E

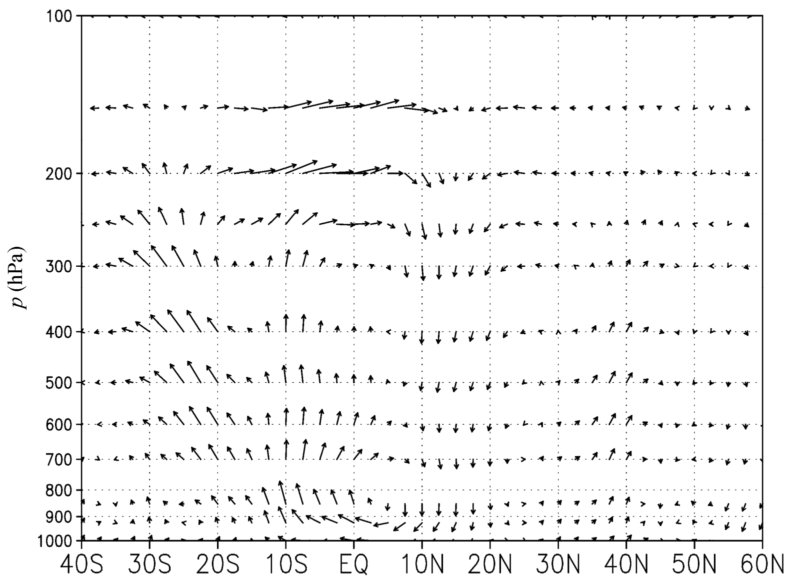

图 3 2010 年 7～10 月 120°E～170°E 平均经圈环流的气压—纬度剖面图（经向风和垂直速度单位：m/s）

Fig. 3 The pressure–latitude section of average meridional circulation (units: m/s for the meridional wind and vertical velocity) over 120°E–170°E from Jul to Oct in 2010

以东太平洋地区缺乏初始扰动生成和热带气旋发展的动力条件，因此 2010 年在该区域没有热带气旋生成。

4.3　南亚高压及中高纬度环流

作为东亚季风系统的重要成员，南亚高压和中高纬度环流特征也会影响热带气旋的运动（陶诗言等，1962；陈联寿，1965；丁一汇和 Wright，1983）。南亚高压是北半球夏季出现在青藏高原及邻近地区上空对流层上部最强大、最稳定的反气旋环流系统。南亚高压位置及强弱的变化对南亚和东亚大范围地区环流和天气气候有重要影响，也对热带气旋的活动产生影响。热带气旋生成偏多的年份，对应高层 100 hPa 高度场上孟加拉湾西南气流偏强，在高原上空形成气旋性环流，削弱了南亚高压的强度；而在热带气旋生成偏少的年份，高原上空以东北气流为主，使得南亚高压强度加强。进一步分析 7～10 月热带气旋偏少年与偏多年的 100 hPa 高度场差值图（图 5a），青藏高原上空为显著正值，这与丁一汇和 Wright (1983) 对 500 hPa 高度场的分析一致，说明南亚高压深厚强大时，热带气旋活动偏

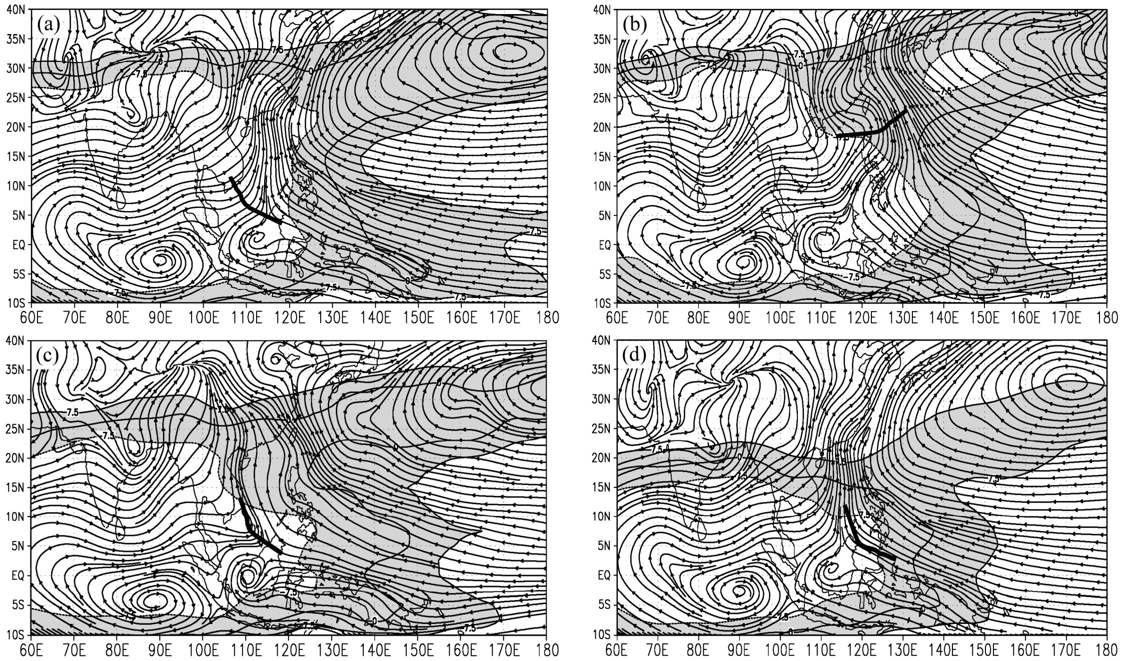

图 4　2010 年（a）7 月、（b）8 月、（c）9 月、（d）10 月平均 850 hPa 流场和季风槽（粗线）。阴影区表示高低层风速垂直切变<10 m/s

Fig. 4　850-hPa stream line and monsoon trough (broad-brush line) in (a) Jul, (b) Aug, (c) Sep, and (d) Oct in 2010 (the shaded regions stand for vertical wind shear <10 m/s)

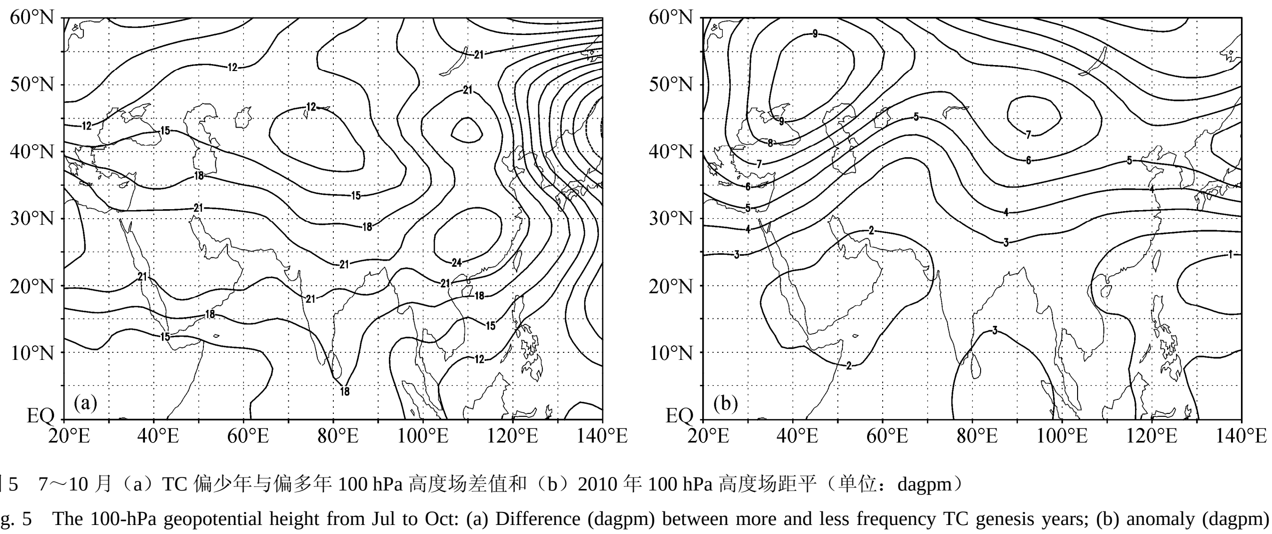

图 5　7～10 月（a）TC 偏少年与偏多年 100 hPa 高度场差值和（b）2010 年 100 hPa 高度场距平（单位：dagpm）

Fig. 5　The 100-hPa geopotential height from Jul to Oct: (a) Difference (dagpm) between more and less frequency TC genesis years; (b) anomaly (dagpm) in 2010

弱。2010 年 7～10 月 100 hPa 高度场距平（图 5b）显示整个青藏高原及其周边地区高度场异常偏高，说明南亚高压偏强。

850 hPa 风场上，孟加拉湾为东风距平，表示西南风偏弱（图 6a），因而不利于季风槽形成并向东伸展，造成热带气旋生成的动力条件不足。

2010 年 7～10 月，西北太平洋（20°N～40°N，120°E～180°E）区域的对流层上层为东风距平，表明西风急流偏弱。由于西风减弱，在该区域南侧形成异常气旋环流，其北侧形成异常反气旋环流（图 6b）。南侧异常气旋环流对应的对流层低层（图 6a）为较强东风距平和弱的反气旋性环流距平特征，该东风距平一直向西延伸至孟加拉湾。这样的高低层纬向风异常配置使得高低层纬向风垂直切变幅度显著增大，从而不利于涡旋系统生成，也不利于季风槽形成和东伸，即热带气旋生成的动力条件不足。这与王会军等（2007）的研究结论一致。此外，在贝加尔湖西南地区，无论是在高层（200 hPa）还是在低层（850 hPa）都存在一个异常反气旋。异常反气旋东侧的偏北气流异常偏强，850 hPa 上偏北风距平一直向南延伸到 20°N 附近，使得夏季风很难向北推进，造成 2010 年夏季风明显偏弱（贾小龙等，2011），因此季风槽也偏弱，不利于热带气旋的生成。

除北半球环流系统对热带气旋活动有直接影响外，南半球中高纬度的环流对热带气旋的生成也会造成影响（王会军等，2006）。热带气旋活跃季节的南极涛动（AAO）和西北太平洋热带气旋生成频次具有显著的反相关关系。2010 年 6～10 月 AAO 处于异常正位相，西北太平洋地区纬向风的垂直切变幅度加大，有利于对流层低层为异常反气旋环流（图 6a），高层为异常气旋环流（图 6b），这些特征均不利于热带气旋的生成和发展。2010 年的 AAO 与热带气旋的关系完全符合王会军等（2006）的研究结果。

5　造成大气环流异常的外强迫特征

5.1　海表温度

2010 年经历了从 El Niño 事件向 La Niña 事件的转换，一次中等强度的 El Niño 事件在 2009 年底达到峰值后，于 2010 年春末夏初迅速消亡，并于 2010 年 7 月转为 La Niña 事件。2010 年后半年，赤道中东太平洋为异常冷水，西太平洋地区为异常暖水。因此该年热带气旋生成源地偏西的特征也主要体现了 La Niña 事件海温分布型对热带气旋活动的影响（Chan，2000）。

从西北太平洋局地海温来看，2010 年上半年由于处于 El Niño 的衰减期，热带西太平洋海温为负距平，该地的对流活动受到抑制，不利于扰动产生。2010 年 6～10 月，随着 La Niña 事件的发展，热带西太平洋海温维持正距平，而 140°E 以东的中太平洋海温则为负距平。由于低纬的海气相互作用，使得 140°E 以东对流活动总体受到抑制（图 7），而 140°E 以西至 100°E 的对流则明显加强，因此有利于热带气旋在该海域生成。2010 年热带气旋在夏秋季的活动经历了从不活跃到相对活跃的演变过程。对比 1998 年 6～10 月热带海温距平分布，西太平洋海温为正距平，中太平洋海温为负距平，而东太平洋海温为正距平。中西太平洋的空间分布与 2010 年相似（东太平洋海温距平不同，但是对热带气旋活动的直接影响很小）。这说明 1998 年的 140°E 以东的热带中太平洋海温场分布特征也是非常不利于热带气旋活动的。

5.2　次表层海温

还有一些学者研究了西北太平洋暖池对热带气旋活动的影响，结果发现暖池地区次表层海温与生成的热带气旋个数具有显著相关（陈光华和黄荣辉，2006）。作为 ENSO 事件前期信号的暖池

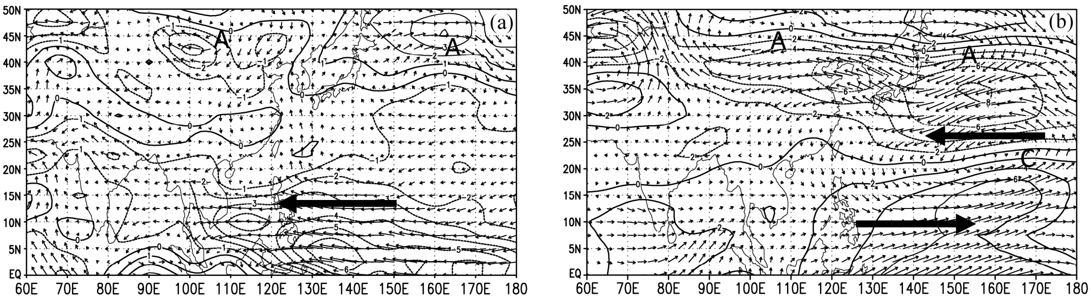

图 6　2010 年 7～10 月（a）850 hPa 和（b）200 hPa 风场距平（箭头）分布和纬向风距平（等值线，单位：m/s）分布

Fig. 6　The (a) 850-hPa and (b) 200-hPa wind anomalies (vector) and zonal wind anomalies (isoline, units: m/s) from Jul to Oct in 2010

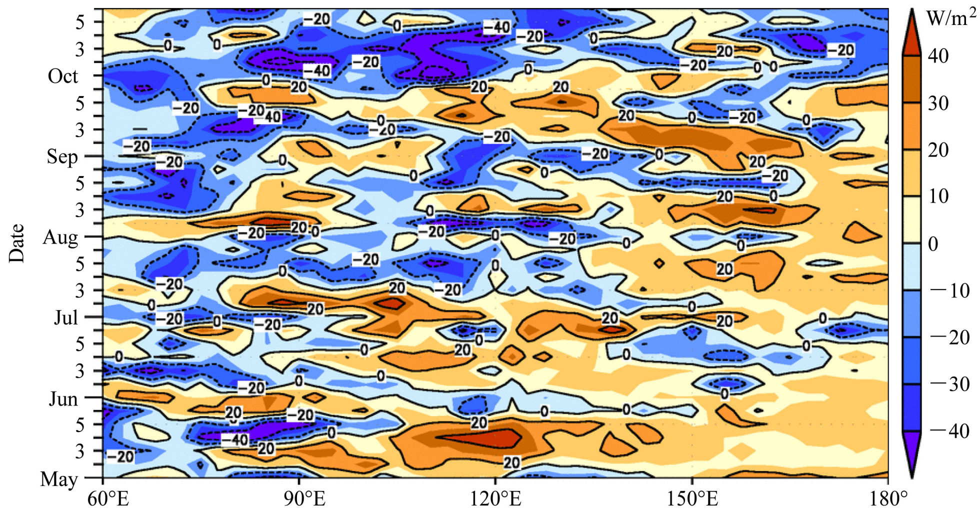

图 7　2010 年 5～10 月 10°N～20°N 平均 OLR 距平的时间—经度剖面

Fig. 7　The time–longitude section of OLR anomaly over 10°N–20°N from May to Oct in 2010

热状况将直接影响到上空的对流活动和大气环流，从而对西北太平洋热带气旋的生成与移动产生影响。当西太平洋暖池次表层偏暖，季风槽位置偏西北，TC 易在西北太平洋的偏西北位置（即 150°E 以西，10°N 以北）生成，这种状况下 TC 易往西北方向移动，因而造成登陆我国的 TC 增多；相反，当热带西太平洋暖池次表层处于冷状态、季风槽位置偏东南，TC 易在 150°E 以东和 10°N 以南的区域生成，这造成西北太平洋 TC 移动路径易于在日本东南部转向东北方向，造成登陆我国 TC 偏少。

2010 年 7～10 月，西太平洋暖池次表层海温异常偏暖，对应上空 850 hPa 为异常东风（图 6a）控制，这一异常强的东风向西一直延伸到阿拉伯海，不利于季风槽向东南延伸，这也解释了前面 2010 年 7～9 月季风槽偏弱、位置偏西特征的热力强迫成因。同时在高层（图 6b），与低层相对应的热带西太平洋一直维持异常西风距平，这种高低层的配置不利于低层西风气流进一步向东伸展，所以季风槽明显偏西。对应热带气旋生成源地 200 hPa 高层为散度负距平，对流上升支位于西北太平洋的西北侧，因而有利于热带气旋在该区域活跃。

2010 年 7～10 月，西北太平洋海表温度和次表层海温的特征是 2010 年 TC 生成频数偏少、生成源地异常偏西的重要外强迫信号。

6　影响 TC 移动路径和登陆的重要环流特征

西太平洋热带气旋的移动主要受到副热带高压和西风带环流的影响（朱乾根和林景瑞，1992）。西太平洋地区的中层风场对登陆我国的热带气旋移动路径也产生显著的引导作用，王磊等（2009）认为副高位置偏东时，西北太平洋副高西南侧的东南气流有利于引导 TC 登陆厦门以北区域；反之，副高脊点偏西导致副高西北侧为西风异常，从而使得登陆厦门以北的 TC 个数偏少。而 2010 年 7～10 月西太平洋副热带高压西伸至我国内陆地区，且副高体庞大，控制了我国南方的大部分地区和东海海域。这种特征一般是不利于热带气旋生成和登陆我国的，究竟是什么原因造成在 2010 年生成热带气旋异常偏少的情况下登陆我国的热带气旋并不少呢？

图 8a 为 2010 年 7～10 月的 500 hPa 风矢量距平场和 588 dagpm 等值线，在南海和西北太平洋地区，15°N 以南的低纬和 25°N 以北的中纬度地区都存在明显东风异常。值得关注的是在副热带中太平洋 150°E～180°E 区域为气旋式环流距平，其北侧为东风异常，而日本及其以东地区为明显的反气旋环流距平，中心位置在（40°N，155°E）附近，其南侧为东风异常，该东风异常南缘可到 25°N，并向西扩展至中国大陆地区，在这种异常东风气流的引导下，热带气旋容易西行和西北行并登陆我国沿海地区。2010 年登陆热带气旋路径也显示了西行和西北行路径占优势的特点。相比之下，1998 年 500 hPa 距平风场显示（图 8b），副热带 150°E～180°区域为气旋式环流距平，日本以东的反气旋环流中心位置在（45°N，180°E）附近，较 2010 年明显偏北偏

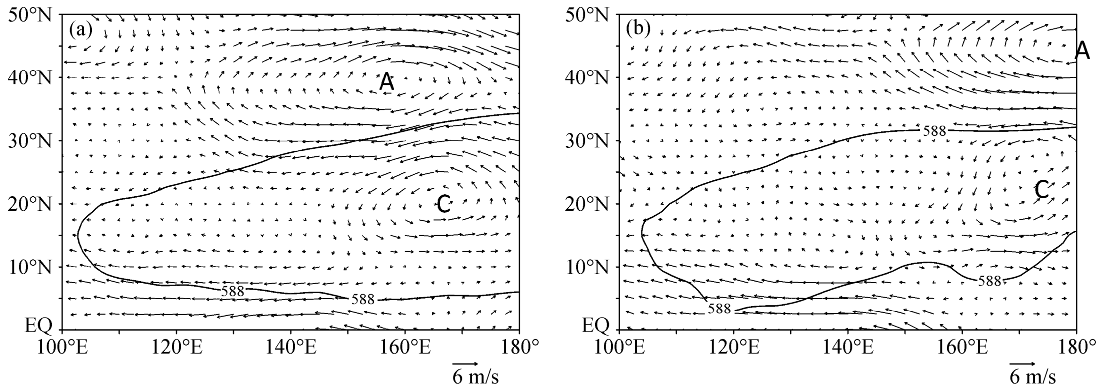

图 8 （a）2010 年和（b）1998 年 7～10 月 500 hPa 风场距平（箭头）和 588 dagpm 线（等值线）

Fig. 8 The wind anomalies (vector) for 500 hPa and 588-dagpm isolines from Jul to Oct in (a) 2010 and (b) 1998

东，其南侧的东风异常南缘最多到 30°N，且东风异常向西只延伸到 150°E，较 2010 年的东风异常伸展区域明显偏北、偏东。因此 1998 年生成的 TC 不易被引导至我国沿海地区。

进一步合成热带气旋登陆达到 7 个以上年份的 500 hPa 距平风场（图略），环流特征与 2010 年相似，在副热带中太平洋 155°E～180°区域为气旋式环流距平，在日本以东地区为反气旋环流距平，中心位置在（43°N，165°E）附近，其南侧为东风异常，其南缘可到 20°N，向西扩展可至中国东部近海地区，热带西太平洋地区的东风异常在 5°N 以南。可见北太平洋地区的反气旋环流强弱和影响范围与 TC 的移动路径和登陆密切相关。2010 年 7～10 月，500 hPa 西太平洋副高异常强大和日本以东异常反气旋距平环流导致中纬度东风气流增强的共同影响是生成 TC 异常偏少却有利于西行登陆我国的重要原因。

7 小结

本文分析了 2010 年西北太平洋热带气旋活动的异常特征和大尺度环流条件及海洋外强迫特征，主要结论如下：

（1）2010 年生成热带气旋频数异常偏少，生成源地偏西，登陆热带气旋数与常年持平，登陆热带气旋数与生成热带气旋数的比例为 1951 年以来历史最高值。而 1998 年生成和登陆热带气旋均偏少，相比之下，2010 年的热带气旋活动更加复杂。

（2）热带气旋活动异常是大气环流异常的直接结果。2010 年 7～10 月，副热带高压较常年异常偏强、西伸脊点偏西；季风槽位置异常偏西，其东端仅延伸到 120°E 附近，较常年偏西 30 个纬度；沿着季风槽分布的弱垂直风切变带位置也较常年偏西，且范围偏小；南亚高压异常偏强；贝加尔湖附近对流层中高层均为反气旋距平环流；这些关键环流因子的特征和配置都不利于 TC 的生成。

（3）环流异常受到海温异常演变的明显影响。2010 年上半年由于处于 El Niño 的衰减期，热带西太平洋海温为负距平且对流活动受到抑制，不利于扰动产生。2010 年上半年，随着 La Niña 事件的发展，热带西太平洋海温维持正距平，140°E 以西至 100°E 的对流明显加强，因此有利于热带气旋在该海域生成。2010 年热带气旋在夏秋季经历了从不活跃到相对活跃的演变过程。2010 年 7～10 月海表温度分布形态使得对流在热带西太平洋东部（140°E 以东）受到抑制而在西太平洋西部（140°E 以西）加强，有利于热带气旋在西北太平洋西北部海域生成。西太平洋暖池处于暖状态直接影响其上空的大气环流，使得低层盛行异常东风，高层盛行异常西风，抑制了季风槽向东南延伸，使得季风槽明显偏西。西北太平洋海表温度和暖池次表层海温的特征是 2010 年 TC 生成频数偏少、生成源地异常偏西的重要外强迫信号。1998 年的热带中西太平洋海温距平分布型与 2010 年相似，二者具有相似的影响热带气旋生成的外强迫条件。

（4）2010 年热带气旋移动和登陆频次受到中纬度环流的显著影响。2010 年 7～10 月 500 hPa 距平风场特征显示中纬度日本及其以东地区为反气旋环流，其南侧为东风异常，该东风异常南缘可到 25°N，并向西扩展至中国大陆地区；南海和西北太平洋地区 15°N 以南的低纬也为东风异常；在这样的风场分布型下，热带气旋容易受偏东气流引导西

行并登陆我国沿海地区。这是 2010 年生成 TC 异常偏少但登陆 TC 并不少的重要环流条件。而 1998 年的 500 hPa 风矢量距平场显示在中纬度地区与 2010 年有很大差异，日本以东的反气旋环流中心较 2010 年明显偏北、偏东，其南侧的东风异常南缘最多到 30°N，且东风异常向西只延伸到 150°E，较 2010 年的东风异常伸展区域明显偏北、偏东。因此 1998 年生成的 TC 不易被引导至我国沿海地区。

初步分析显示，2010 年 TC 的生成数量和源地受到热带地区动力和热力条件的显著影响，而 TC 的移动路径和登陆频次则受到中纬度环流系统的明显作用。关于中纬度环流特征的成因还需要深入研究。

参考文献（References）

陈光华, 黄荣辉. 2006. 西北太平洋暖池热状态对热带气旋活动的影响 [J]. 热带气象学报, 22 (6): 527–532. Chen Guanghua, Huang Ronghui. 2006. The effect of warm pool thermal states on tropical cyclone in West Northwest Pacific [J]. Journal of Tropical Meteorology (in Chinese), 22 (6): 527–532.

陈联寿. 1965. 盛夏亚洲中高纬度流型与西太平洋台风路径的关系 [J]. 气象学报, 35 (4): 476–485. Chen Lianshou. 1965. Flow patterns in westerlies in relation to the East–Asia typhoon tracks [J]. Acta Meteorologica Sinica (in Chinese), 35 (4): 476–485.

Chan J C L. 2000. Tropical cyclone activity over the western North Pacific associated with EL Niño and La Niña events [J]. J. Climate, 13: 2960–2972.

陈联寿, 丁一汇. 1979. 西太平洋台风概论 [M]. 北京: 科学出版社, 109pp. Chen Lianshou, Ding Yihui. 1979. Introduction to Typhoon of Western Pacific (in Chinese) [M]. Beijing: Science Press, 109pp.

Chen T C, Weng S P, Yamazaki N, et al. 1998. Interannual variation in the tropical cyclone formation over the western North Pacific [J]. Mon. Wea. Rev., 126: 1080–1090.

Demaria M. 1996. The effect of vertical on tropical cyclone intensity change [J]. J. Atmos. Sci., 53 (14): 2076–2087.

丁一汇, Wright E R. 1983. 影响西太平洋台风形成的大尺度环流条件 [J]. 海洋学报, 5 (5): 561–574. Ding Yihui, Wright E R. 1983. The large scale circulation condition for the western Pacific typhoon genesis [J]. Acta Oceanologica Sinica (in Chinese), 5 (5): 561–574.

范可. 2007a. 北太平洋海冰，一个西北太平洋台风生成频次的预测因子？[J]. 中国科学 (D 辑), 37 (6): 851–856. Fan Ke. 2007a. North Pacific sea ice cover, a predictor for the western North Pacific typhoon frequency? [J]. Science in China (Ser. D) (in Chinese), 37 (6): 851–856.

范可. 2007b. 西北太平洋台风生成频次的新预测因子和新预测模型 [J]. 中国科学 (D 辑), 37 (9): 1260–1266. Fan Ke. 2007b. New predictors and new prediction model for the typhoon frequency over western North Pacific [J]. Science in China (Ser. D) (in Chinese), 37 (9): 1260–1266.

Gray W M. 1979. Hurricanes: Their formation, structure and likely role in the tropical circulation [J]. Meteorology over the Tropical Oceans: 155–218.

贾小龙, 陈丽娟, 龚振淞, 等. 2011. 2010 年海洋和大气环流异常及对中国气候的影响 [J]. 气象, 37 (4): 446–453. Jia Xiaolong, Chen Lijuan, Gong Zhensong, et al. 2011. Anomalies of ocean and atmospheric circulation in 2010 and their impacts on climate in China [J]. Meteorological Monthly (in Chinese), 37 (4): 446–453.

Kalnay E, Kanamistu M, Kistler R, et al. 1996. NCEP/NCAR 40-year reanalysis project [J]. Bull. Amer. Meteor. Soc., 77: 437–471.

刘舸, 张庆云, 孙淑清. 2007. 2006 年夏季西太平洋热带气旋活动的初步研究 [J]. 气候与环境研究, 12 (6): 738–750. Liu Ge, Zhang Qingyun, Sun Shuqing. 2007. A preliminary study on activities of tropical cyclones over the western North Pacific during the summer in 2006 [J]. Climatic and Environmental Research (in Chinese), 12 (6): 738–750.

苏振生. 1949–1988. 台风年鉴 [G]. 北京: 气象出版社. Su Zhensheng. 1949–1988. Typhoon year book (in Chinese) [G]. Beijing: China Meteorological Press.

苏振生. 1989–2004. 热带气旋年鉴 [G]. 北京: 气象出版社. Su Zhensheng. 1989–2004. Year book of Tropical Cyclone (in Chinese) [G]. Beijing: China Meteorological Press.

陶诗言, 徐淑英, 郭其蕴. 1962. 夏季东亚热带和副热带地区经向和纬向环流型的特征 [J]. 气象学报, 32 (1): 91–103. Tao Shiyan, Xu Shuying, Guo Qiyun. 1962. The characteristics of the zonal and meridional circulation over tropical and subtropical regions in eastern Asia in summer [J]. Acta Meteorologica Sinica (in Chinese), 32 (1): 91–103.

Wang B, Wu R R. 1997. Peculiar temporal structure of the South China Sea summer monsoon [J]. Advances in Atmospheric Sciences, 14: 177–194.

王慧, 丁一汇, 何金海. 2004. 西北太平洋夏季风的变化对台风生成的影响 [J]. 气象学报, 63 (4): 418–430. Wang Hui, Ding Yihui, He Jinghai. 2004. Influence of Western North Pacific summer monsoon changes on typhoon genesis [J]. Acta Meteorologica Sinica (in Chinese), 63 (4): 418–430.

王会军, 范可. 2006. 西北太平洋台风生成频次与南极涛动的关系 [J]. 科学通报, 51 (24): 2901–2914. Wang Huijun, Fan Ke. 2006. Relationship between the Antarctic oscillation and in the Western North Pacific typhoon frequency [J]. Chinese Science Bulletin (in Chinese), 51 (24): 2901–2914.

王会军, 孙建奇, 范可. 2007. 北太平洋涛动与台风和飓风频次的关系研究 [J]. 中国科学 (D 辑), 37 (7): 966–973. Wang Huijun, Sun Jianqi, Fan Ke. 2007. Relationship between the North Pacific oscillation and the typhoon/hurricane frequencies [J]. Science in China (Ser. D) (in Chinese), 37 (7): 966–973.

王会军, 郎咸梅, 范可, 等. 2006. 关于 2006 年西太平洋台风活动频次的气候预测试验 [J]. 气候与环境研究, 11 (2): 133–137. Wang Huijun, Lang Xianmei, Fan Ke, et al. 2006. Real-time climatic prediction experiment for the typhoon frequency in the Western North Pacific for 2006 [J]. Climatic and Environmental Research (in Chinese), 11 (2): 133–137.

王瑾, 柯宗建, 江吉喜. 2009. 2008 年西北太平洋热带气旋活动特征分析

[J]. 气象, 35 (12): 44–50. Wang Jin, Ke Zongjian, Jiang Jixi. 2009. Analysis of tropical cyclone over Western North Pacific in 2008 [J]. Meteorological Monthly (in Chinese), 35 (12): 44–50.

王磊, 陈光华, 黄荣辉, 等. 2009. 影响登陆我国不同区域热带气旋活动的大尺度环流定量分析 [J]. 大气科学, 33 (5): 916–922. Wang Lei, Chen Guanghua, Huang Ronghui, et al. 2009. Quantitative analysis on large scale circulation system modulating landfalling tropical cyclone activities in the diverse Chinese regions [J]. Chinese Journal of Atmospheric Sciences (in Chinese), 33 (5): 916–922.

吴晓鹏. 2005–2008. 热带气旋年鉴 [G]. 北京: 气象出版社. Wu Xiaopeng. 2005–2008. Yearbook of Tropical Cyclone (in Chinese) [G]. Beijing: China Meteorological Press.

赵振国. 1999. 中国夏季旱涝及环境场 [M]. 北京: 气象出版社. Zhao Zhenguo. 1999. Summer Drought and Environmental Field in China (in Chinese) [M]. Beijing: China Meteorological Press.

Zhou B T, Cui X. 2008. Hadley circulation signal in the tropical cyclone frequency over the western North Pacific [J]. J. Geophys. Res., 113, D16107, doi: 10. 1029/2007JD009156.

周波涛, 崔绚, 赵平. 2008. 亚洲—太平洋涛动与西北太平洋热带气旋频数的关系 [J]. 中国科学 (D 辑), 38 (1): 118–123. Zhou Botao, Cui Xuan, Zhao Ping. 2008. Relationship between the Asia–Pacific oscillation and tropical cyclone frequency in the western North Pacific [J]. Science in China (Ser. D) (in Chinese), 38 (1): 118–123.

朱乾根, 林景瑞. 1992. 天气学原理与方法 [M]. 北京: 气象出版社, 748. Zhu Qiangen, Lin Jingrui. 1992. Principles and Methods of Weather (in Chinese) [M]. Beijing: China Meteorological Press, 748.

胡娅敏，覃志年，陈丽娟，等. 2013. 基于多时间尺度的回归集成预测模型. 气象，39(9)：1182-1189.

基于多时间尺度的回归集成预测模型[*]

胡娅敏[1,2]　覃志年[3]　陈丽娟[4]　罗晓玲[2]

1 广东省气候中心，广州 510080
2 广州市气候与农业气象中心，广州 510080
3 广西自治区气候中心，南宁 530022
4 国家气候中心中国气象局气候研究开放实验室，北京 100081

提　要： 引入能够将非线性、非平稳过程的数据进行线性化和平稳化处理的 EMD 方法，对广东降水的时间序列进行时间尺度分离，从复杂的非平稳信号中提取相对简单以不同时间尺度振荡的准周期信号，选取能较好描述降水周期特征的 IMF 分量作为建模备选因子，然后以均生回归、均生相关、韵律拟合误差和拟合误差 4 种方法构建预测模型，结果得到采用多尺度因子构建的 4 种单预测模型近 10 年 *Ps* 评分和降水距平符号同号率平均分在 68～73 分和 50%～58%之间，而采用 4 种模型构建的回归集成模型两种评分方法的平均分分别高达 79.8 和 68.8%，较单一预测模型评分分别提高了近 10 分和 10%以上。将具有降水指示信号的前冬赤道东太平洋海温因子耦合到回归集成预测模型，其 *Ps* 评分结果与纯降水集成模型相当，但同号率评分略高 3.1%。从而，提取要素序列的多种时间尺度特征，并采用多模型的集成预报，均能有效提高短期气候预测水平。

关键词： 多时间尺度，经验模态分解，回归集成

中图分类号： P456　　　**文献标志码：** A　　　**doi：** 10.7519/j.issn.1000-0526.2013.09.014

The Regression Ensemble Predication Model Based on Multi-Time Scale

HU Yamin[1,2]　QIN Zhinian[3]　CHEN Lijuan[4]　LUO Xiaoling[2]

1 Guangdong Climate Centre, Guangzhou 510080
2 Guangzhou Climate and Agricultural Meteorology Centre, Guangzhou 510080
3 Guangxi Climate Centre, Nanning 530022
4 Laboratory for Climate Studies, CMA, National Climate Centre, Beijing 100081

Abstract: The empirical mode decomposition (EMD) method has the advantage of dealing with the nonlinear and nonstationary data, making them linearized and stationary. So EMD is adopted to analyze the precipitation data based on the multi-time scale viewpoint, and the relatively simple semi-period signal with different oscillations are decomposed from the complex nonstationary and nonlinear signal. Then the characteristic intrinsic mode functions (IMFs) are chosen to construct the regression ensemble prediction model (REPM), which is based on the mean generation regression (MGR) method, the mean generation correlation (MGC) method, the rhythm fitting error (RFE) method and the fitting error (FE) method. The results show that the average score of the *Ps* and the same symbol ratio (SSR) are 68−73 and 50%−58%, respectively, among the four kinds of single models during rainy period in Guangdong for the recent 10 years. However, in the REPM, the average *Ps* and SSR scores have reached 79.8 and 68.8%, respectively, increasing 10 scores and 10% or so compared with one of the four kinds of single models. Meanwhile,

* 国家自然科学基金青年基金项目(40905043)、广州市科技计划项目(2010Y1-C031)、广东省气象局课题(2011B04)、中国气象局气候预测创新团队、中英瑞适应气候变化项目(ACCC/2010527) 和中国气象局气候变化专项(CCSF2011-25)共同资助
2012 年 12 月 17 日收稿；　2013 年 3 月 6 日收修定稿
第一作者：胡娅敏，主要从事短期气候预测研究. Email：huyamin_1978@sohu.com

if the SST signals in tropical East Pacific in the previous winter are coupled into the REPM, the *Ps* and SSR scores have improved, but the SSR scores, 3.1% higher than the former. Therefore, both the multi-time scale information extracting from the meteorological elements and the ensemble model construction can improve the accuracy of short-term climate prediction.

Key words: multi-time scale, empirical mode decomposition (EMD), regression ensemble prediction model

引　言

目前,提高短期气候预测水平的常用方法有两种:一是对数值模式结果进行统计降尺度或动力降尺度应用,其预报效果的好坏依赖于数值模式预测结果的优劣。二是依靠改进统计方法,虽然统计方法存在着某些局限性和不稳定性,比如历史样本的有限性,统计方法无法对历史上没有出现过的气候异常强度和分布做出预测,历史资料得到的统计关系随着气候的长期变化也在不断的改变,甚至很多关系目前已经变得不如当初发现它们时显著。但是,由于数值预报水平发展仍有待提高,研究和发展新的统计方法仍是提高省(市)短期气候预测水平的有效途径之一。

短期气候预测中引入的经典数学方法大多是针对线性和平稳时间序列进行分析的,而气象问题本质上都是非线性的,因而对于气象要素序列中很多非平稳和非线性过程不能较好地提取出有用的信息。经验模态分解(Empirical Mode Decomposition,EMD),即逐级进行平稳化处理,把不同周期的波动从原信号中分离出来,且该波动是平稳的,称该波动为本征模态函数(Intrinsic Mode Function,IMF),不同的 IMF 分量是平稳信号,具有非线性特征和缓变波包的特征。另外,EMD 方法依据数据自身的时间尺度特征来进行信号分解,无须预先设定任何基函数,这一点与建立在先验性的谐波基函数和小波基函数上的傅里叶分解与小波分解方法具有本质性的差别。因此,EMD 方法在处理非平稳及非线性数据上,具有非常明显的优势(张明阳等,2007)。EMD 方法及相应的 Hilbert 变换正成为处理非线性、非平稳时间序列的有力手段,并已在生物、海洋、大气科学、天文学和工程技术等领域中得到了初步应用(林振山等,2004;郑祖光等,2010)。许多气象学家开展了基于 EMD 方法对各种气象资料时间序列的分析工作,主要包括:MJO(Love et al,2008)、降水(McMahon et al,2008)、气温(方仕全等,2005;邹明玮,2007;玄兆燕等,2008a;2008b)、降水日数(毕硕本等,2010)、副热带大气系统(侯威等,2006)、成灾面积(刘莉红等,2008)、海平面高度(刘莉红等,2010b)、大气边界层高度(刘莉红等,2010a)和海水温度(杨周等,2010)。但是把这种方法初步应用到预测的研究主要有:万仕全等(2005)和邹明玮(2007)以扬州 530 年(1470—1999 年)旱涝级别序列和北半球 1995 年(1—1995 年)树木年轮序列为例,采用 EMD 方法、均生函数和最优子集回归方法构建了一个新的预测模型,结果表明,特征 IMF 分量有较高的可预测性,它对原序列趋势的预测有重要指示意义。玄兆燕等(2008b)采用 EMD 和神经网络方法相结合对石家庄的气温和降水进行预测,结果得到 EMD 方法降低了被预测信号中的非平稳性,其预测精度比直接用神经网络预测的预测精度有较明显的提高。这些研究(万仕全等,2005;邹明玮,2007;玄兆燕等,2008a;2008b)采用实例数据在预测方面做了初步尝试,这为气候预测开辟一条新的有效途径。

另一方面,随着科技的发展,集成方法已经成为当前气候预测中的关键技术,尤其是气候模式发展的重要方向(陈法敬等,2011;尤凤春等,2009;狄靖月等,2013;纪永明等,2011)。然而,目前大部分气象部门预测方案都是采用单一的数理方法来构建模型,由于使用的预测手段不同,考虑影响气象要素的物理因素不同,各种预报方法得到的预报结果也不尽相同或存在很大差异,但都能在一定程度上提供一些有用的信息。因此,若采用一种客观方法将各种预报结果加以集成,可提高对气象变量的短期气候预测准确率(魏凤英,2007;2011)。雷向杰(2011)基于多元回归预测法、月际持续性预测法、年际持续性预测法和基于 EOF 的 Downscaling 法共 4 种方法建立了集成预测模型,结果得到集成预测方法的效果明显优于单一预测方法。毕硕本等(2012)采用 EMD 对广西 2 月气温序列进行分解,然后对得到的 IMF 分量构建集成预报成员,用均生函数逐步回归法对各集成成员进行预测,结果表明加入 EMD 算

法和集成预报技术的方法比单一预测方法具有更好的预测能力。从而可见，集成方法的引入可有效改进短期气候预测效果。

本文引入 EMD 方法对广东降水时间序列进行多时间尺度分离，将复杂的非平稳信号简化为相对简单的不同时间尺度振荡的准周期信号，选取能较好描述降水周期特征的 IMF 分量作为预测模型的备选因子，然后分别采用均生回归、均生相关、韵律拟合误差和拟合误差 4 种方法对选取的备选因子构建预测模型。最后，参照雷向杰(2011)的研究方法，再以这 4 种预测模型为备选因子，采用多元线性回归方法构建集成预测模型。与毕硕本等(2012)研究不同的是，他们是对 IMF 分量构建集合序列，即考虑了初值的集合，本文是对预测方法进行集成，即考虑了预测模型的集成。本研究期望引入 EMD 方法和回归集成预测模型能提高广东降水的短期气候预测水平，为政府决策部门提前做出准确的指导。

1 资料和方法

1.1 资料处理

降水和气温数据是由广东省气候中心提供的 1961—2011 年广东 86 个台站的逐月降水和气温观测资料，以 1981—2010 年作为气候平均值。

用于降水和气温检验的方法为 2010 年中国气象局国家气候中心《短期气候预测质量分级检验办法》中的 Ps 六级评分方法。

1.2 研究方法

本文采用相关分析、经验正交函数（EOF）、EMD、均生回归、均生相关、韵律拟合误差、拟合误差、多元线性回归和回归集成等方法对资料进行处理、多时间尺度分离和模型构建。其中，均值生成函数（魏凤英等，1990）（Mean Generating Function，MGF），提出了视 MGF 为原序列生成的、具有周期性的基函数的新构思，设一时间序列 $x(t)$：

$$x(t) = \{x(1), x(2), \cdots, x(n)\} \tag{1}$$

式中，n 为样本量。

$x(t)$的均值为：

$$\overline{x} = \frac{1}{n}\sum_{i=1}^{n} x(i) \tag{2}$$

对于式(1)定义均值生成函数：

$$\overline{x}_l(i) = \frac{1}{n_l}\sum_{j=0}^{n_l-1} x(i+jl) \quad (i = 1, \cdots, l, 1 \leqslant l \leqslant m) \tag{3}$$

式中 $n_l = \mathrm{INT}(n/l)$，$m = \mathrm{INT}(n/2)$ 或 $\mathrm{INT}(n/3)$，INT 表示取整数。根据式(3)，可以得到 m 个均生函数，将均生函数定义域延拓到整个数轴上，即作周期性延拓，构造均生函数延拓矩阵。而均生回归法，即先把降水序列作均生延拓，对得到的所有均值生成函数因子，采用多元线性回归方法（魏凤英，2007；吴诚鸥等，2007；黄嘉佑，2004）建立预测模型。另外，均生相关法，即先把降水序列作均生延拓，再对延拓结果与原序列计算相关，取 2～7、7～15 和 15～N/2 年间（N 为序列长度）的延拓序列高相关的 3 个因子，即找到长、中、短 3 个不同尺度因子，采用多元线性回归方法建立预测模型。韵律拟合误差法参见魏淑秋（1985）工作。拟合误差法参见谢小康（1994）工作。本文主要采用 EMD（郑祖光等，2010）方法对各月、季降水序列进行多时间尺度分离，分别采用均生回归、均生相关、韵律拟合误差和拟合误差 4 种方法对基于 EMD 得到的 IMF 分量构建月、季降水预测模型。

2 基于 EMD 算法的多时间尺度信息提取及集成模型构建

2.1 基于 EMD 算法的多时间尺度信息提取

长时间的降水序列本身蕴含了其多重周期演变特性，但由于影响降水系统的复杂性，使该序列包含了许多非平稳和非线性信息，如何从中提取出具有预测指示意义的周期特征，是众多研究者关注的重点之一，EMD 工作在尺度分离工作中的优势已被一些学者证明。

对广东各月或季降水序列进行标准化，然后用 EMD 方法分解，通常能得到 5～6 个 IMF 分量和 1 个趋势项，计算各 IMF 分量与原序列的相关系数，以及 IMF 分量所占方差贡献，选取相关系数高、方差贡献大的 IMF 因子作为 2.2 节建模的备选因子。

选取广东汛期（4—9 月）降水为例进行 EMD 分析。首先，对 1961—2011 年广东汛期降水进行 EMD，得到 4 个 IMF 分量和 1 个趋势项（图 1）。在构成广东汛期降水量变化的 4 个不同时间尺度的波频中，IMF1 与原序列相关系数为 0.78，其周期分别

表现为 4 a,而 IMF2、IMF3 和 IMF4 的相关系数分别为 0.25、0.22 和 0.16,周期分别为 7、12 和 25 a,最后一项 IMF5 为趋势项,与原序列相关系数为 0.07,表现为自 20 世纪 60 年代中期以来广东汛期降水一直呈现上升趋势,但近 5 年增加趋势不明显。

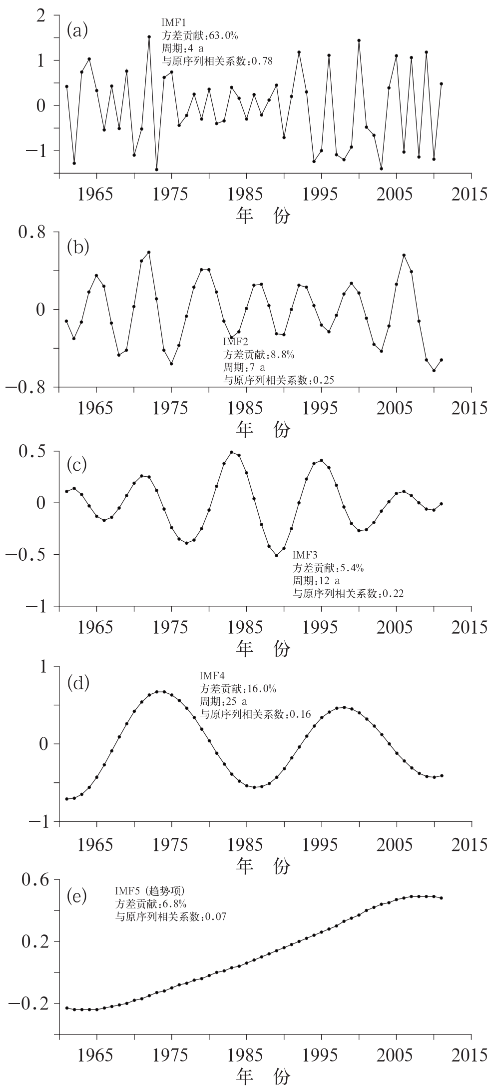

图 1　1961—2011 年广东汛期降水量的 IMF1～IMF5 分量

Fig. 1　The IMF1 to IMF5 components of Guangdong precipitation during rainy peroid from 1961 to 2011

计算各 IMF 分量的方差贡献得到,IMF1 占方差的贡献达 63.0%,比较 IMF1 分量与原序列(图 2a),可以看出 IMF1 基本能拟合出原序列,说明汛期降水主要以 4 a 振荡为主。IMF1 和 IMF4 这 2 个分量累积方差贡献达 79%,取这两个 IMF 分量合成与原序列曲线的对比(图 2b),可以看出合成曲线基本包含了原序列信息,与原序列相关系数高达 0.88,即在 IMF1 分量中加入 25 a 长周期的 IMF4 分量,其合成效果较图 2a 更好。若取 IMF1～IMF4,则累积方差贡献达 93.2%,与原序列相关系数高达 0.97,其重构值与原值非常接近,可见 EMD 方法分离出多时间尺度信息基本能重构原信息的特征。

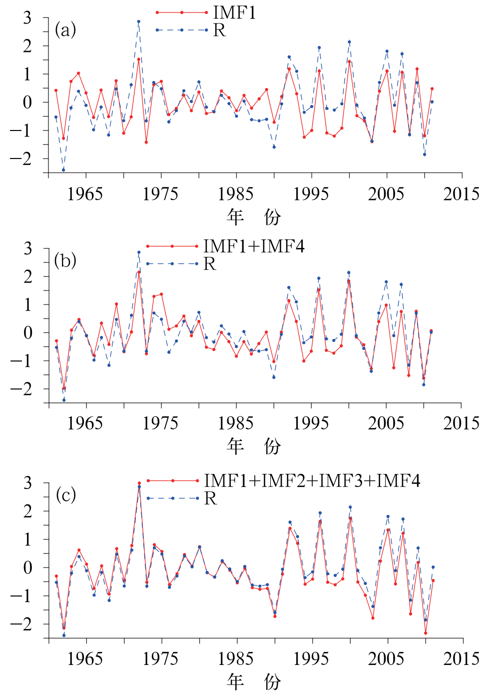

图 2　汛期降水量与 IMF1 分量(a)、IMF1+IMF4(b)和 IMF1+IMF2+IMF3+IMF4 重构序列(c)的对比

(虚线:原序列,实线:IMF 分量合成)

Fig. 2　The comparison between the precipitation and the first component (a), the composition from the first and the fourth components (b) and the composition from the first, the second, the third, the fourth components (c) during rainy peroid in Guangdong

(The dashed line is the precipitation and the solid line is the IMF components)

2.2　基于多尺度信息的统计模型构建

对基于 EMD 方法得到具有较高相关系数和较大方差贡献的 IMF 分量,分别采用均生相关法、均生回归法、韵律误差法和拟合误差法构建降水的预测模型,建模年份为 1961 年至预测前一年,回报检

验时采用逐年向前滚动检验法。其预报结果如表 1 和表 2，可以看出 4 种预测方法对近 10 年广东汛期降水的 Ps 评分平均值在 68～73 分之间，而降水距平同号率评分的平均值在 50%～58%。与原降水序列构建模型相比（表略），多时间尺度各单一预测模型均有不同程度的提高，Ps 评分增加了 3 分，同号率评分增加了 5%，可以看出若剔除了原序列中的噪音，在一定程度上能有效改进预报效果。

表 1 基于 EMD 多时间尺度的预测模型广东汛期降水 *Ps* 评分

Table 1 The *Ps* score of Guangdong precipitation from April to September during 2002－2011 based on the multi-time sacle prediction model from EMD

年份	均生相关	均生回归	韵律	拟合误差	回归集成
2002	69.2	72.3	68.3	69.8	80.2
2003	72.8	74.4	68.0	76.6	85.3
2004	70.0	74.1	71.0	67.8	78.3
2005	74.4	72.8	70.2	70.5	81.3
2006	72.1	72.2	62.2	76.7	78.4
2007	70.9	73.8	70.3	71.4	80.7
2008	74.5	71.9	67.0	72.4	77.9
2009	57.4	67.1	69.5	64.7	77.9
2010	66.4	73.8	72.2	70.9	78.1
2011	74.1	76.7	64.4	70.9	80.3
平均	70.2	72.9	68.3	71.2	79.8
大于 60 的年份	9	10	10	10	10

表 2 基于 EMD 多时间尺度的预测模型广东汛期降水距平符号的同号率评分(单位:%)

Table 2 The anomaly sign consistency rate between the hindcast and the observed precipitation in Guangdong from April to September during 2002－2011 based on the multi-time sacle prediction model from EMD (unit: %)

年份	均生相关	均生回归	韵律	拟合误差	回归集成
2002	46.5	50.0	47.7	45.3	67.4
2003	55.8	55.8	44.2	61.6	70.9
2004	52.3	59.3	55.8	47.7	65.1
2005	59.3	53.5	51.2	53.5	69.8
2006	66.3	66.3	46.5	68.6	72.1
2007	51.2	52.3	48.8	50.0	66.3
2008	68.6	61.6	52.3	67.4	69.8
2009	38.4	50.0	52.3	44.2	66.3
2010	45.3	53.5	53.5	51.2	61.6
2011	69.8	74.4	52.3	60.5	79.1
平均	55.3	57.7	50.5	55	68.8
大于 50 的年份	7	10	6	7	10

2.3 基于回归方法的集成预测模型构建

集成预报的基本含义是将两个以上模型的预报结果用统计方法集成为单一的预报结果。集成预报的关键是如何确定权重系数。通常采用简单的算术平均或根据各种方法事先人为设定历史预报技巧或用回归系数给各种预报方法不同的权重。在预报样本量不是足够大的情况下，算术平均通常不能得到最优集成预报。在有限样本情况下，回归系数可以保证在最小方差意义下得到最优集成拟合（魏凤英，2007），因此本文选取回归集成法（朱伯承，1981）构建预测模型。回归集成法将 n 种原始预报模型 y_1，y_2，…，y_n 作为新的预报因子，求预报量实况值 y 的回归方程：

$$p = a_0 + a_1 y_1 + a_2 y_2 + a_3 y_3 + a_4 y_4 \tag{4}$$

其系数满足如下线性方程组

$$\begin{cases} s_{11}a_1 + s_{12}a_2 + \cdots + s_{1n}a_n = s_{1y} \\ s_{21}a_1 + s_{22}a_2 + \cdots + s_{2n}a_n = s_{2y} \\ \vdots \\ s_{n1}a_1 + s_{n2}a_2 + \cdots + s_{nn}a_n = s_{ny} \\ a_0 = \overline{y} - (a_1\overline{y}_1 + a_2\overline{y}_2 + \cdots + a_n\overline{y}_n) \end{cases} \tag{5}$$

$$s_{ij} = \sum_{k=1}^{M}(y_{ik} - \overline{y}_i)(y_{jk} - \overline{y}_j)$$

其中：

$$s_{iy} = \sum_{k=1}^{M}(y_{ik} - \overline{y}_i)(y_k - \overline{y}_j)$$

式中，M 为预报次数，y_{ik} 为第 i 种原始预报方法所作的第 k 次预报值，y_k 为第 k 次实况值。将式(5)的解代入式(4)便得回归集成预报方程。

本文选取均生相关 y_1、均生回归 y_2、韵律误差 y_3 和拟合误差 y_4 共 4 种预报模型作为集成成员的备选因子，采用多元线性回归方法构建如式(4)的集成预测模型。取 4 种单预测模型预测年份前 10 年的回报值代入式(5)，得到 a_0，a_1，a_2，a_3 和 a_4 5 个系数的解，代入式(4)即得到回归集成预测模型。该集成预测模型是动态的，各台站的回归系数随预测对

表 3 以汛期降水 5 个台站为例得到的集成模型的回归系数

Table 3 The ensemble model regression coefficients for precipitation at five stations of Guangdong from April to September

台站	a_0	a_1	a_2	a_3	a_4
阳山	−1.7	0.41	0.0	0.98	−0.65
广州	16.5	−1.71	2.57	0.58	−1.06
饶平	−22.1	0.28	−2.74	0.71	1.19
台山	−0.2	0.0	1.00	0.55	−0.80
中山	−5.2	0.18	0.0	−0.47	−0.42

象(降水或气温等)、预测年和预测时段(季、月及旬等)的变化而动态改变。以汛期降水为例，取2002—2011年86个台站近10年4种单预测模型的回报值代入式(5)，分别计算得到各台站的5个回归系数，表3列出任意5个台站的 a_0，a_1，a_2，a_3 和 a_4 回归系数，可以看出在不同的台站预测过程中各种预测模型发挥着不同的作用，效果各有优劣。

对回归集成方法近10年广东汛期进行回报(表1和表2)，可以看出回归集成的效果明显优于各单独预测模型，Ps 评分的平均值上升到79.8分，较单一模型中最优的均生回归法增加了6.9分，降水距平符号同号率平均值为68.8%，较单预测模型增加了10%以上。较原降水序列回归集成模型(表略)，其 Ps 评分和同号率评分分别增加了10分和10%以上，说明开展物理模型的集成预测，能有效提高短期气候预测水平。

进一步分析各预测模型的空间预测效果，以2012年汛期为例，对广东86站降水进行EMD分解后，选取特征IMF分量，分别采用均生相关法、均生回归法、韵律拟合误差法和拟合误差法构建模型进行预测，得到如图3所示结果，实况的分布为广东省大部分降水偏少，各单预测模型也均预测出降水偏少的形势，其 Ps 评分在67.4～74.2分之间。对这4种预测方法进行回归集成，得到的预测结果与实况最为接近，其 Ps 评分在77.2分，可以看出，回归集成较其他单一预测模型在空间分布和量级的预测上较单一预测模型更优。

3　前冬海温对广东汛期降水的影响及其与序列方法的集成

虽然降水序列本身包括了很多重要信息，但降

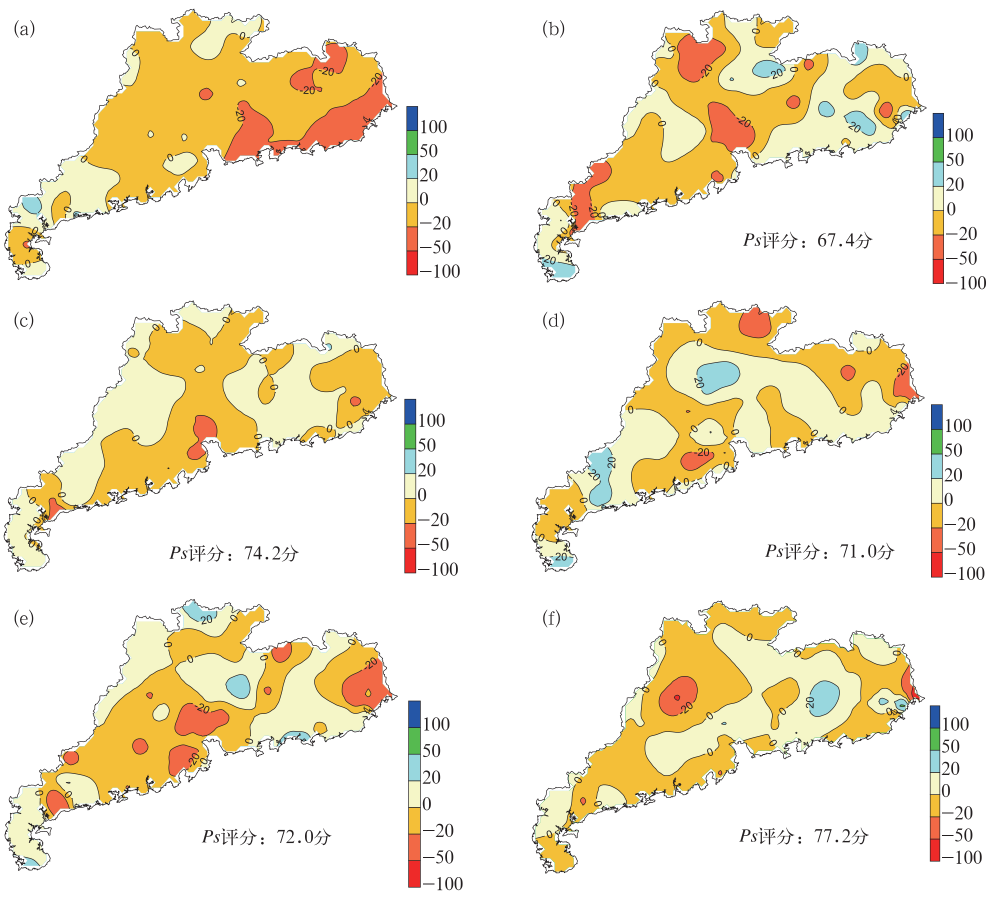

图3　2012年汛期广东降水预测实况及各种预测结果

(a)实况，(b)均生相关，(c)均生回归，(d)韵律拟合误差法，(e) 拟合误差，(f)回归集成

Fig. 3　The precipitation observation (a) and prediction results from the methods of mean generation correlation (b), mean generation regression (c), rhythm fitting error (d), fitting error (e) and regression ensemble (f)

水本身只是一个事后信息，更有效的提高短期气候预测的方法是分析影响降水的物理系统，由于影响降水系统的复杂性，这种信息具有非线性和非平稳性。众所周知，降水的成因很复杂，因而降水预测是目前短期气候预测的难点和重点。降水不仅受自身变化规律的影响，同时受到外强迫和大气环流影响。随着全球气候变暖变“乱”，仅用降水时间序列本身预测一方面不稳定，另一方面预测不出异常等级。因此，有必要考虑对降水预测具有指示意义的外强迫信号和环流因子。然而，考虑到环流因子是一个相对的快变量，很容易遗忘前期信号对降水的指示，另一方面大气的混沌性会限制季节尺度的预报性。因此，下面开展海温外强迫因子与降水自身规律结合构建预测系统。

将广东 86 站汛期降水量进行 EOF 展开，取能表述其平均特征的第一特征向量对应的时间系数与前期不同时期全球海温(SST)计算相关，结果得到前冬(12 月到次年 2 月)赤道东太平洋地区有一正高相关中心(图略)，对该区域海温序列进行 EMD 展开，取前 3 个 IMF 分量作为预测备选因子构建逐步回归方程。对 2002—2011 年海温模型进行回报检验(表 4)，近 10 年平均 Ps 和同号率分别为 68.3 分和 52.8%，与降水单预测模型结果相当。进一步将海温因子耦合到回归集成预测模型，其 Ps 评分结果与纯降水集成模型相当，但同号率评分略高 3.1%。海温因子对降水的可能影响：当冬季赤道东太平洋海温偏高，有利西太平洋副热带高压偏南，易出现南方类雨型(陈兴芳等，2003)。

表 4 采用前冬 SST 信号预测及其与降水序列预测的集成结果对比

Table 4 The comparison between the prediction from SST signal of previons winter and the results with the SST coupled into the precipitation ensemble prediction model

年份	前冬 SST 模型		序列+SST 集成	
	同号率/%	Ps	同号率/%	Ps
2002	32.6	61.0	70.9	82.3
2003	70.9	79.5	66.3	79.3
2004	80.2	79.0	62.8	74.0
2005	27.9	60.7	70.9	79.7
2006	30.2	54.3	83.7	84.8
2007	50.0	70.0	75.6	82.4
2008	10.5	38.8	83.7	80.7
2009	68.6	77.0	70.9	80.5
2010	69.8	80.1	65.1	80.3
2011	87.2	82.1	68.8	75.1
平均	52.8	68.3	71.9	79.9
大于 50 的年份	6	9	10	10

4 结论和讨论

本文引入能够将非线性、非平稳过程的数据进行线性化和平稳化处理的 EMD 方法，对广东降水和影响降水的海温因子的时间序列进行时间尺度分离，从复杂的非平稳信号提取出相对简单的不同时间尺度振荡的准周期信号，选取能较好描述降水周期特征的关键备选因子，然后以均生回归、均生相关、韵律拟合误差和拟合误差 4 种方法构建集成预测模型。结果得到：

(1) EMD 方法能提取降水序列不同尺度的周期特征，广东汛期降水主要呈现为 4、7、12 和 25 a 周期，其中以 4 a 周期为主，占总方差贡献的 63.0%，其次是 25 a 长周期，它和 4 a 短周期占方差贡献的 79%，与原序列相关高达 0.88，4 和 25 a 周期的重构值基本能包含汛期降水的绝大部分信息。

(2) 采用均生相关、均生回归、韵律拟合误差法和拟合误差预测方法对近 10 年广东汛期进行回报，结果得到各单一预测模型的 Ps 评分的平均分为 68～73 分，同号率评分的平均分为 50%～58%，而回归集成 Ps 评分和同号率的平均值分别达到 79.8 分和 68.8%，较单一预测模型的评分分别偏高了 10 分和 10%以上。同时，回归集成也较好地模拟出降水的偏多空间分布型。从而开展物理模型的集成预测，能有效提高短期气候预测水平。

(3) 将具有降水指示信号的前冬赤道东太平洋海温因子耦合到回归集成预测模型，其 Ps 评分结果与纯降水集成模型相当，但同号率评分略高 3.1%。可见，寻找对降水预测具有指示意义的外强迫信号和环流因子可一定程度上提高降水预报的准确率。

本文采用 EMD 方法提取能较好描述降水周期特征的关键备选因子，并分别采用均生回归、均生相关、韵律拟合误差和拟合误差 4 种方法构建预测模型，接着采用回归方法对 4 种模型进行集成，研究得到引入 EMD 和回归集成方法能有效提高短期气候预测效果。同时，将具有降水指示信号的前冬赤道东太平洋海温因子耦合到回归集成预测模型，其 Ps 评分结果与纯降水集成模型相当，但同号率评分略高 3.1%。寻找对降水预测具有指示意义的外强迫信号和环流因子可一定程度上提高降水预报的准确

率。但是由于影响降水因子的复杂性,且外强迫因子和环流因子均是和降水序列作前期相关来寻找关键区,而这种相关关系并不十分稳定,且这种信息易受非线性作用的干扰,因而如何提取影响降水系统中可识别的具有可预报性的物理因子,是今后将进一步深入开展的工作。

参考文献

毕硕本,陈譞,覃志年,等. 2012. 基于 EMD 和集合预报技术的气候预测方法. 热带气象学报,28(2):283-288.

狄靖月,赵琳娜,张国平,等. 2013. 降水集合预报集成方法研究. 气象,39(6):691-698.

陈法敬,矫梅艳,陈静. 2011. 一种温度集合预报产品释用方法的初步研究. 气象,37(1):14-20.

陈兴芳,赵振国. 2003. 中国汛期降水预测研究及应用. 北京:气象出版社.

侯威,封国林,董文杰,等. 2006. 利用排列熵检测近 40 年华北地区气温突变的研究. 物理学报,55(5):2663-2268.

黄嘉佑. 2004. 气象统计分析与预报方法(第 3 版). 北京:气象出版社,58-70.

雷向杰. 2011. 月平均气温集成预测方法研究. 气象,37(12):1560-1565.

纪永明,陈静,矫梅燕,等. 2011. 基于多中心 TIGGE 资料的区域 GRAPES 集合预报初步试验. 气象,37(4):392-402.

林振山,汪曙光. 2004. 近四百年北半球气温变化的分析:EMD 方法的应用. 热带气象学报,20(1):90-96.

刘莉红,翟盘茂,郑祖光. 2008. 中国北方夏半年最长连续无降水日数的变化特征. 气象学报,66(3):474-477.

刘莉红,翟盘茂,郑祖光. 2010a. 中国北方夏半年极端干期的时空变化特征. 高原气象, 29(2):403-411.

刘莉红,郑祖光,琚建华,等. 2010b. 夏季副热带大气系统的多尺度振荡分析. 高原气象,29(1):115-127.

万仕全,封国林,周国华,等. 2005. 基于 EMD 方法的观测数据信息提取与预测研究. 气象学报,63(4):516-525.

魏凤英. 2007. 现代气候统计诊断与预测技术(第 2 版). 北京:气象出版社,182,222.

魏凤英. 2011. 我国短期气候预测的物理基础及其预测思路. 应用气象学报,22(1):1-11.

魏凤英,曹鸿兴. 1990. 建立长期预测模型的新方案及其应用. 科学通报,35(10):777-780.

魏淑秋. 1985. 农业气象统计. 福建:科学技术出版社.

吴诚鸥,秦伟良. 2007. 近代实用多元统计分析. 北京:气象出版社.

谢小康. 1994. 用拟合误差分析寻找周期作七月雨量预报. 贵州气象,18(3):13-14.

玄兆燕,杨公训. 2008a. 经验模态分解法在大气时间序列预测中的应用. 自动化学报,34(1):97-101.

玄兆燕,杨公训. 2008b. EMD 在地面气温预测中的应用. 微计算机信息,24(7):516-525.

尤凤春,魏东,王雨. 2009. 北京奥运期间多模式降水检验及集成试验. 气象,35(11):3-8.

张明阳,王克林,刘会玉,等. 2007. 基于 EMD 的洪涝灾害成灾面积波动的多时间尺度分析——以湖南省为例. 中国生态农业学报,15(1):131-134.

郑祖光,刘莉红. 2010. 经验模态分析与小波分析及其应用. 北京:气象出版社,32.

朱伯承. 1981. 统计天气预报. 上海:科技出版社,373.

邹明玮. 2007. 基于非线性时间序列分析方法的非线性系统特性研究. 扬州:扬州大学.

Love B S, Matthews A J, Janacek G J. 2008. Real-time extraction of the Madden-Julian oscillation using empirical mode decomposition and statistical forecasting with a VARMA model. J Cli, 21(20):5318-5335.

McMahon T A, Kiem A S, Peel M C, et al. 2008. A new approach to stochastically generating six-monthly rainfall sequence based on empirical mode decomposition. J Hydrometeoro, 9(6):1377-1389.

贾小龙，陈丽娟，LUO Jing-jia. 利用海气耦合模式预测的大尺度环流进行热带气旋年频数的预测试验[J]. 热带气象学报，2013，29(1): 37-46.

文章编号：1004-4965(2013)01-0037-10

利用海气耦合模式预测的大尺度环流进行热带气旋年频数的预测试验

贾小龙[1]，陈丽娟[1]，LUO Jing-jia[2]

(1. 国家气候中心/中国气象局气候研究开放实验室，北京 100081；　2. Climate Variation Predictability and Applicability Research Program, Research Institute for Global Change，Japan Agency for Marine-Earth Science and Technology，Japan)

摘　　要：基于对热带气旋生成频数和大尺度环流相关关系的分析，利用 SINTEX-F 海气耦合模式预测的大尺度大气环流信息，通过提取模式预测较好与热带气旋生成密切相关的有用信息，建立了一个基于动力模式预测结果的南海和西太平洋热带气旋年频数预测模型，并对 1982—2010 年的热带气旋生成频数进行预测试验与检验。SINTEX-F 海气耦合模式能够较好预测部分与热带气旋生成密切相关的大尺度环流特征，其中包括热带气旋活动区域的海平面气压、对流层风垂直切变、850 hPa 热带辐合带和 850 hPa 90 ℃E 附近的越赤道气流。利用这些大尺度环流建立的预测因子与热带气旋生成频数有很好的相关关系，利用这些预测因子建立的多元回归预测模型对热带气旋频数的拟合率为 0.8(相关系数，超过 99.9%的信度检验)。预测模型的交叉检验结果表明模型整体预测效果较好。交叉检验预测结果与实况热带气旋频数的相关为 0.71(超过了 99.9%的信度检验)，距平同号率为 82.8%。但模型对热带气旋异常年的预测误差较大。

关　键　词：CGCM；大尺度环流；热带气旋；气候预测

中图分类号：P435　　　**文献标识码**：A　　　**Doi**：10.3969/j.issn.1004-4965.2013.01.005

1　引　　言

我国是受热带气旋危害最严重的国家之一，尤其是登陆热带气旋，除了带来丰沛的降水外，还经常引起严重的灾害，造成重大的经济损失和人员伤亡。影响我国的热带气旋主要来自西北太平洋和南海，对西北太平洋和南海地区热带气旋频数的预测是国家气候中心的一项重要业务。台风的发生频率、强度和路径受大尺度大气环流的影响，影响热带气旋生成和发展的主要大尺度环流条件包括：热带海温、热带大气对流条件、高低空大气辐散辐合条件、风的垂直切变等，国内外很早就有较多研究[1−11]，近年来新的研究指出，西北太平洋热带气旋频次与北太平洋涛动[12]、北太平洋海冰面积[13]、澳大利亚东侧的环流[14]以及南极涛动[15]都有密切的关系。这些研究为热带气旋的预测提供了很好的理论基础。

在热带气旋的季节预测方面，统计方法得到广泛使用[1, 16−19]。最近，Fan等[20]基于多个气候因子建立了一个西北太平洋热带气旋年频数的统计预测模型，预测效果较好。统计预报方法也是国外进行热带气旋个数预测的主要方法。Nicholls[16]利用南方涛动指数进行澳大利亚台风个数的季节预测。Klotzbach等[18−19]利用大气前期信号建立统计预测模型进行大西洋飓风频数预测。目前国家气候中心热带气旋预测的客观方法较少，主要包

收稿日期：2011-04-07；**修订日期**：2012-06-18
资助项目：公益性行业科研专项(GYHY200906015)；科技部科技支撑项目(2007BAC29B04、2009BAC51B05)；联合重点基金(U0833602)共同资助
通讯作者：贾小龙，男，山东省人，副研究员，博士，研究方向：气候预测研究和应用。E-mail: jiaxl@cma.gov.cn

括最优子集和均生函数方法，而且都是基于物理统计分析进行的，物理统计预报由于在很多方面无法考虑大气内部的自身变化，而热带气旋的活动与同期的大尺度环流的异常密切联系，因此，热带气旋活动规律的预测需要预测这些与热带气旋生成有密切关系的热带大气大尺度环流的异常，动力模式无疑体现出优越性。因此可以利用动力模式的大尺度变量开展热带气旋的预测。2006年王会军等[21]首次提出并利用气候模式对我国2006年夏季西太平洋地区热带气旋活动频次进行实时气候预测，预测与实况比较一致。朗咸梅等[22]利用中科院大气物理研究所9层模式进一步考察了模式对与热带气旋密切联系的大尺度环流异常的预测能力，指出模式有能力在一定程度上实现西北太平洋热带气旋活动的气候预测。这些新的研究表明，利用动力模式，基于观测结果的分析，开展热带气旋频数的预测是可行的。目前国家气候中心的热带气旋预测业务中还没有使用基于动力模式的热带气旋频数统计预测模型，这主要是由于相关模式对与热带气旋有关的环流异常的预测能力还不高。

SINTEX-F耦合模式是在欧洲-日本合作计划下建立的SINTEX模式的基础上发展的[23−26]。分析表明，SINTEX-F GCM对热带大气的大尺度环流特征有较好的模拟和预测能力[27]，因此本文将尝试基于观测结果以及 SINTEX-F GCM对大尺度环流异常的预测结果分析，提取有较高预测技巧的与热带气旋生成有关的大尺度环流场，建立一个客观的南海和西太平洋地区年热带气旋频数的统计预报模型，进行预测试验和效果检验。

2 模式、资料和方法

SINTEX-F 耦合模式是在欧洲-日本合作计划下建立的 SINTEX 模式的基础上发展的。大气模式部分是 ECHAM4 最新的高分辨率版本[28]。水平分辨率为 T_{106}，垂直 19 层。全球海洋模式是具有 OCRA2 结构的 Océan Parallélisé的 Version 8.2 版本[26]。模式水平分辨率为 2 °×2 °，在近赤道地区分辨率提高到 0.5 °，垂直方向有 31 层。模式耦合场(SST、地表动量通量、热通量和水汽通量等)以内插获得，海气交换通过海洋-大气-海冰-土壤耦合器每 2 小时交换一次[30]，耦合模式没有进行任何通量订正，仅在 OCGCM 的海冰覆盖区向观测的月气候海冰值适应。大气的初值条件是模式在观测月气候 SST 强迫下积分一年获取。模式集合预报方案包括 9 个集合成员，来源于三组不同的耦合物理过程(相当于三组不同的模式)和三组初值形成方案，两两组合，共计 9 组预报方案，模式的详细介绍见文献[28－30]。SINTEX-F 模式对 ENSO、IOD 和亚洲季风均有很高的预测技巧[31−36]。在近几年的实时预测试验中展现了良好的预测性能[37]，见 http://www.jamstec.go.jp/frcgc/research/d1/iod/index.html)。

本文利用该模式的资料为 SINTEX-F GCM 逐年 3 月 1 日起报的 1982—2010 年 5—10 月环流场，包括海平面气压，850 hPa 和 200 hPa 纬向风，850 hPa 经向风。西北太平洋和南海热带气旋频数资料来自中国气象局出版的《台风年鉴》，本文所指热带气旋为中心附近风力≥8 级的热带气旋。使用的观测资料为 NCEP/NCAR 发布的水平格点分辨率为 2.5 °×2.5 °的月平均全球再分析资料[38]，变量包括海平面气压、向外长波辐射(OLR)、1 000 hPa 和 200 hPa 纬向风、850 hPa 纬向风和经向风。

本文首先通过热带气旋年频数与 NCEP 大气环流资料的相关分析确定了影响热带气旋活动的主要大尺度环流条件；然后通过相关分析提取模式有较高预测技巧且与热带气旋生成有密切关系的大尺度环流场，建立关键区预报因子，利用 SINTEX-F 模式预测的大尺度环流因子通过多元回归分析建立热带气旋年频数的统计预测模型，并对预测模型预测效果进行交叉检验和预测试验。

3　热带气旋频数和大尺度大气环流的关系

热带气旋的生成和大尺度环流有密切的关系，很多研究分析了不同大尺度环流和热带气旋频数的关系。国家气候中心的年度台风预测是针对全年台风个数，而南海和西太平洋的台风也主要生成在夏半年(5—10 月)，5—10 月台风生成个数占全年总个数的 80%，5—10 月台风个数序列和全年台风个数序列的相关达到 0.94，而且 1—4 月每月生成的台风个数多年平均都不超过 1 个。因此，为了针对业务预报需要建立针对全年台风频数的预测，考虑 5—10 月台风频数和全年台风频数的上述关系，同时又考虑到环流的冬夏差异，所以使用全年台风频数和夏半年的环流建立统计关系。图 1 给出了热带气旋年频数和 5—10 月平均的大尺度环流的相关，包括海平面气压(SLP)、1 000 hPa 和 200 hPa 的散度、850 hPa 的涡度、200 hPa 和 850 hPa 的纬向风垂直切变($|U_{200\ \mathrm{hPa}}-U_{850\ \mathrm{hPa}}|$)和 850 hPa 经向风。图 1a 反映了热带气旋年频数和南海-西太平洋地区 SLP 呈显著的负相关，热带气旋主要活动区海平面气压偏低则热带气旋易活跃，反之亦然，其物理意义也很清楚。图 1b～1d 反映了热带辐合带与热带气旋频数的关系，低层辐合(图 1b)偏强、高层辐散偏强(图 1c)、850 hPa 涡度偏强(图 1d)，都有利于生成热带气旋数偏多，其中的物理意义也容易理解。图 1e 反映了热带气旋频数和对流层高低层风切变的关系，很多研究也都指出热带气旋源区的风垂直切变对热带气旋的生成有重要的影响，风垂直切变越大越不利于热带气旋的生成，在 140 °E～160 °W，10～20 °N 宽广的范围内为显著的负相关，与前人的研究一致。另外，也注意到，在这一区域的西面也存在一个大范围显著的正相关区，与东面的负相关区形成一个明显的偶极型分布。这种相关分布同时也反映了东亚副热带季风环流异常对热带气旋频数的影响，因为从印度洋到西太平洋的副热带地区夏季由于受季风的影响，一般低层为西风，高层为东风，高低层风切变越大实际也反映了整个季风环流偏强，导致季风槽偏强，也就越有利于热带气旋的生成。在孙淑清等[14]的研究中也强调了西太平洋(125～150 °E)以西的上游赤道西风(西面)异常对热带气旋生成频数的影响。因此，图 1e 上这一区域的正相关也有内在的物理意义，而研究也指出，当 90 °E 附近的越赤道气流强时，125～150 °E，5～15 °N 范围内的西风也随之加强，从而使菲律宾以东对流活动加强，西太平洋热带气旋频数增高。因此，热带气旋生成频数也与 90 °E 附近的越赤道气流有很好的关系，这在图 1f 所示的热带气旋频数与 850 hPa 经向风的相关上也可以看到，最大相关也超过了 0.4(超过 99%的信度)。考虑到 1970 年代中期以前的热带气旋序列可能存在问题，用 1975—2008 年的资料重新计算了相关分布，结果和使用 1951—2008 年的资料计算的相关，主要的显著相关区仍然存在(图略)，说明以上分析的相关关系比较稳定。

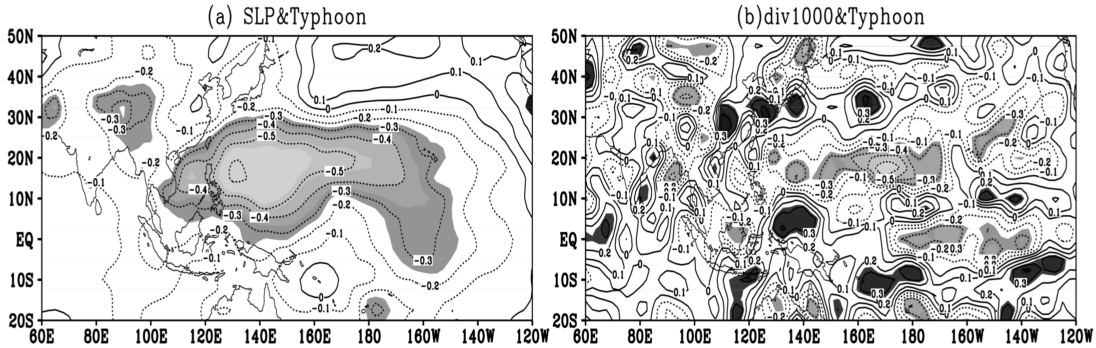

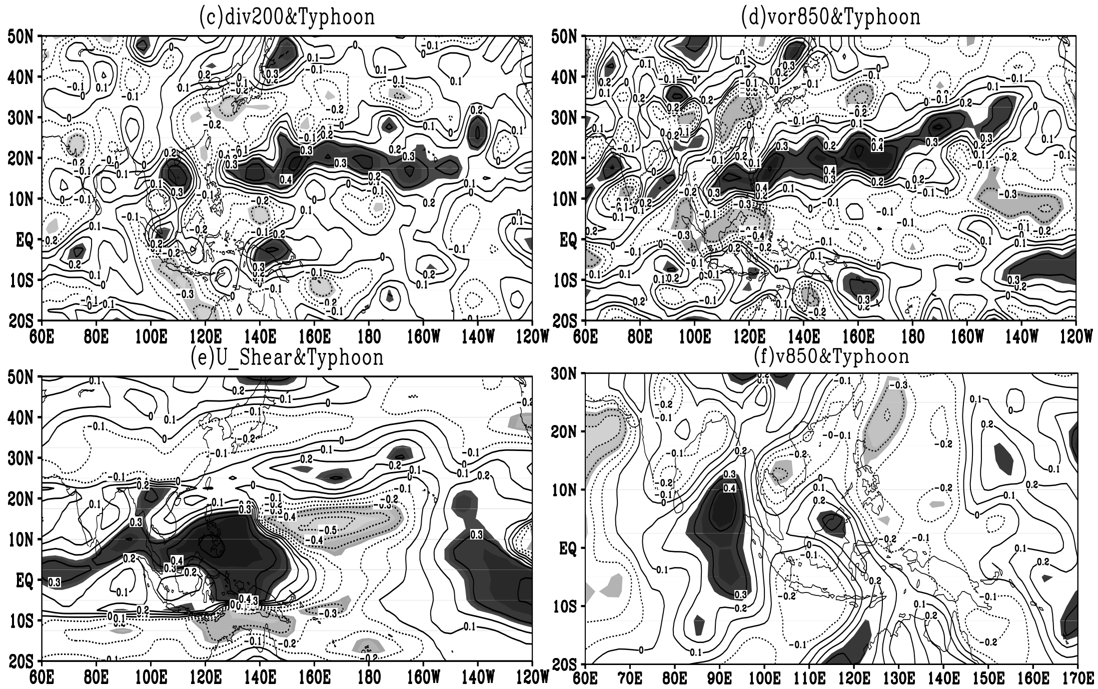

图 1 热带气旋年频数和 5—10 月平均的大尺度环流的相关 阴影区为通过 95%信度检验的区域。a. 海平面气压(SLP)；b. 1 000 hPa 散度；c. 200 hPa 散度；d. 850 hPa 涡度；e. 纬向风垂直切变($|U_{200\ \mathrm{hPa}}-U_{850\ \mathrm{hPa}}|$)；f. 850 hPa 经向风。

基于以上的相关分析，可以从其中构建 6 个关键区指数作为预测因子，表 1 是 6 个指数构建的计算方法和区域。这些指数都很好地反映了图 1 所给出的相关特征。图 2 是构建的 6 个关键区指数和热带气旋频数的时间序列。6 个指数和热带气旋频数的相关分别为−0.63、−0.65、0.61、0.61、0.57、0.38，都超过 99.9%的信度检验。两条时间序列如果存在显著的线性趋势，那么高相关就有可能是由趋势造成的，而本文台风的年际预测更关心序列年际之间的相关，为此，对热带气旋和大气序列都去除线性趋势，然后重新计算了相关，分别为−0.65、−0.64、0.57、0.66、0.54、0.33，两条序列的高相关仍然存在，说明建立的关键区因子和台风的确有密切的联系。利用这 6 个指数建立热带气旋频数的多元回归方程：

$$y(t)=-0.078-0.18\times x_1(t)-0.47\times x_2(t)+0.29\times x_3(t)+0.33\times x_4(t)-0.57\times x_5(t)+0.18\times x_6(t),$$

图 3 给出了建立的多元回归方程对热带气旋频数序列的拟合，可以看到利用这 6 个指数建立的回归方程对热带气旋频数序列可以进行很好的拟合，重建的热带气旋序列和观测的热带气旋频数序列的相关系数达到 0.73，远远超过了 99.99%的信度检验，而且都大大超过了每个指数序列与热带气旋频数序列的相关系数。如果环流模式能够较好预测这些与热带气旋生成有密切关系的大尺度环境场异常，就可以通过利用模式预测的大尺度环流建立热带气旋频数的预测模型。下一节将在分析 SINTEX-F GCM 模式对与热带气旋生成有密切关系的大尺度环流异常的预测能力的基础上，利用模式输出信息，建立一个客观的南海和西太平洋地区年热带气旋频数的统计预报模型，进行预测试验和效果检验。

表 1 NCEP 资料关键区指数的计算

环流因子	关键区及指数计算
海平面气压(SLP)	125 ~ 155 °E，10 ~ 22.5 °N 平均的标准化 SLP 距平
1 000 hPa 散度(div1000)	160 ~ 180 °E，15 ~ 22.5 °N 平均的标准化 1 000 hPa 散度距平
200 hPa 散度(div200)	150 ~ 180 °E，17.5 ~ 22.5 °N 平均的标准化 200 hPa 散度距平
850 hPa 涡度(Vor850)	140 ~ 170 °E，15 ~ 25 °N 平均的标准化 850 hPa 涡度距平
高低层纬向风切变(*US*) $US=\lvert U_{200\ \mathrm{hPa}}-U_{850\ \mathrm{hPa}}\rvert$	标准化的 117.5 ~ 137.5 °E，5 ~ 15 °N 平均与 152.5 ~ 177.5 °E，10 ~ 17.5 °N 平均的风切变(*US*)差
850 hPa 越赤道气流(*V*850)	87.5 ~ 92.5 °E，7.5 °S ~ 7.5 °N 平均的标准化 850 hPa 经向风距平

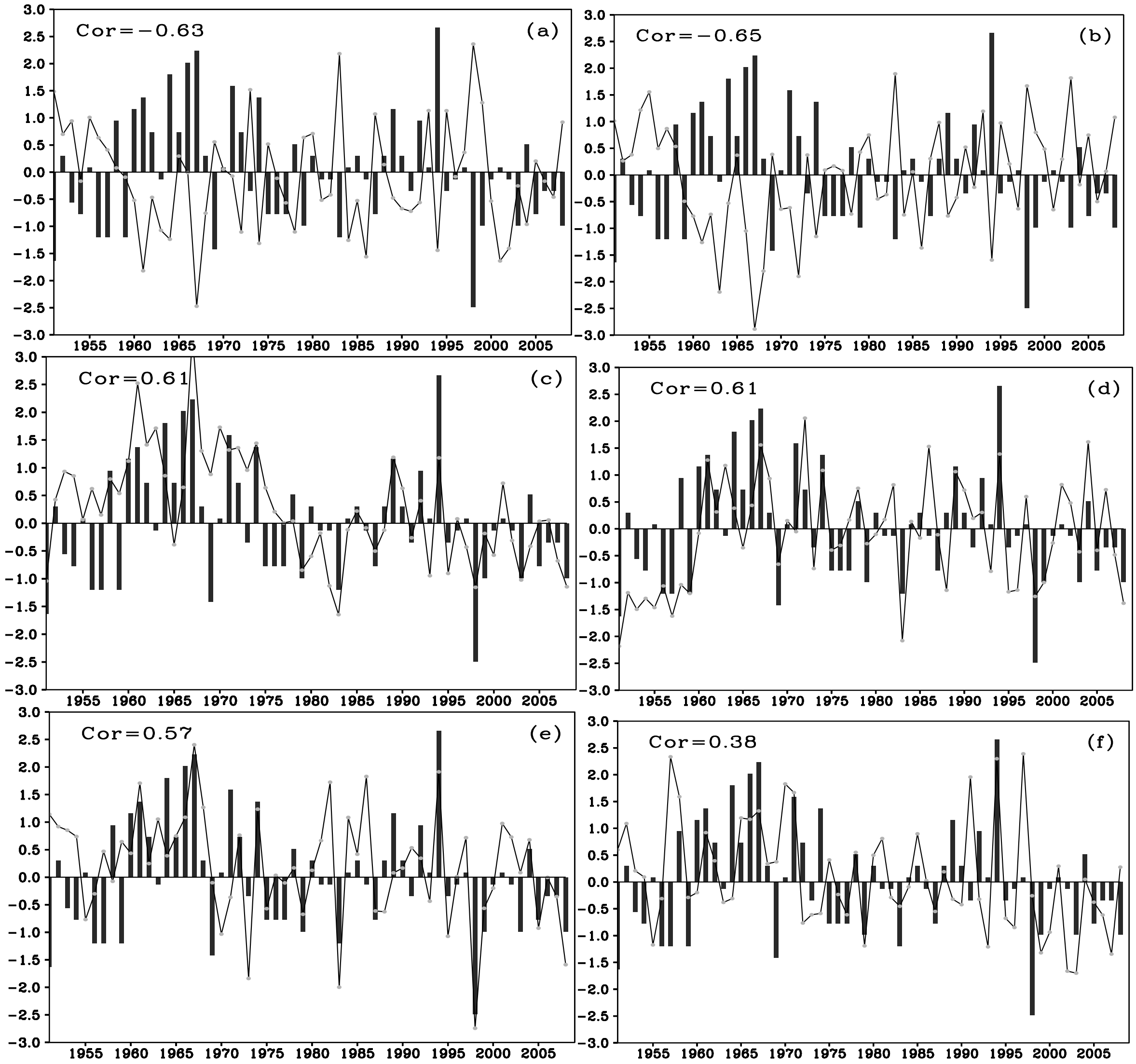

图 2　6 个关键区指数(实线)和热带气旋频数(柱状图)的标准化时间序列(曲线左上角为两序列的相关系数)

a. 海平面气压(SLP)；b. 1 000 hPa 散度；c. 200 hPa 散度；d. 850 hPa 涡度；

e. 纬向风垂直切变(|$U_{200\ \mathrm{hPa}}$−$U_{850\ \mathrm{hPa}}$|)；f. 850 hPa 经向风。　横坐标为年份。

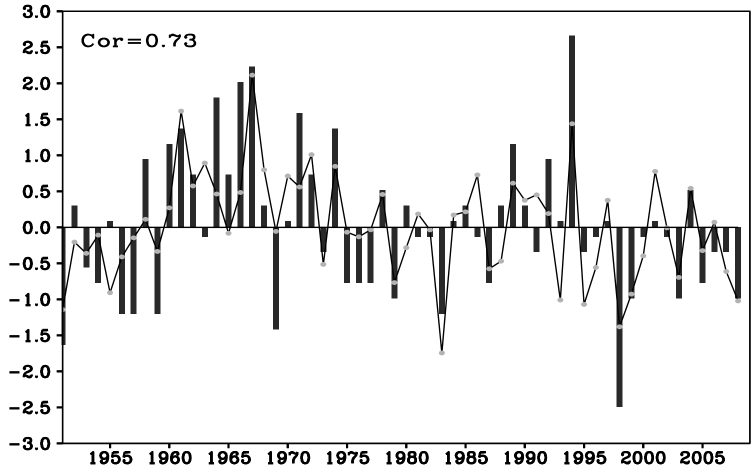

图 3　6 个关键区指数建立的多元回归方程对热带气旋频数序列的拟合(曲线)

和热带气旋频数序列实况(柱状)　　序列都为标准化序列，左上角为两序列的相关系数。

4 基于 SINTEX-F GCM 的预报模型及检验

基于前文对观测结果的分析，首先对 SINTEX-F GCM 模式对前面这些热带气旋频数和大尺度环流相关关系的模拟能力进行检查。同前文分析，计算了热带气旋年频数与模式预测的 5—10 月的环流场的相关，相关分析显示，前文的 6 个大尺度环境场中，热带气旋频数与其中 4 个环境场的相关关系在模式的预测结果中有较好的体现，包括 SLP、对流层风垂直切变、850 hPa 的越赤道气流和 850 hPa 涡度。图 4 是年热带气旋频数与模式预测的 4 个环流的相关，可看到该模式能够再现观测的主要相关分布特征，热带气旋频数与预测的SLP的相关较观测的分布有一定的系统性的东移，但整体的相关性还是很显著的(图 4a)。与对流层风切变的相关分布与观测的特征也很一致，但也存在一定差异，比如在北太平洋和南半球的相关明显强于观测结果(图 4b)。与 850 hPa 经向风(图 4c)和 850 hPa 涡度(图 4d)的相关尽管与观测结果也存在一定的系统偏差，但主要的物理特征与观测还是一致的。基于这些相关分布，同样可以类似前文定义模式的 4 个关键区指数。表 2 给出了 4 个关键区指数的定义。图 5 是 4 个关键区指数序列，4 个关键区指数序列和热带气旋频数的相关分别为-0.7、0.79、0.53、0.64，都超过 99%的信度检验。去除台风序列和大气序列的线性趋势后的相关为 0.65、0.75、0.63、0.60，显著的相关性仍然存在。

表 2 模式资料关键区指数的计算

预报因子	关键区及指数计算
海平面气压(SLP)	170 °E～140 °W，7.5～22.5 °N 平均的标准化 SLP 距平
高低层纬向风切变(US) $US=\|U_{200\ \mathrm{hPa}}-U_{850\ \mathrm{hPa}}\|$	标准化的 110～140 °E，2.5～15.0 °N 平均与 155～175 °E，2.5～15.0 °N 平均的风切变(US)差
850 hPa 越赤道气流(V850)	82.5～90 °E，10.0 °S～2.5 °N 平均的标准化 850 hPa 经向风距平
850 hPa 涡度(Vor850)	140～170 °E，10.0～17.5 °N 平均的标准化 850 hPa 涡度距平

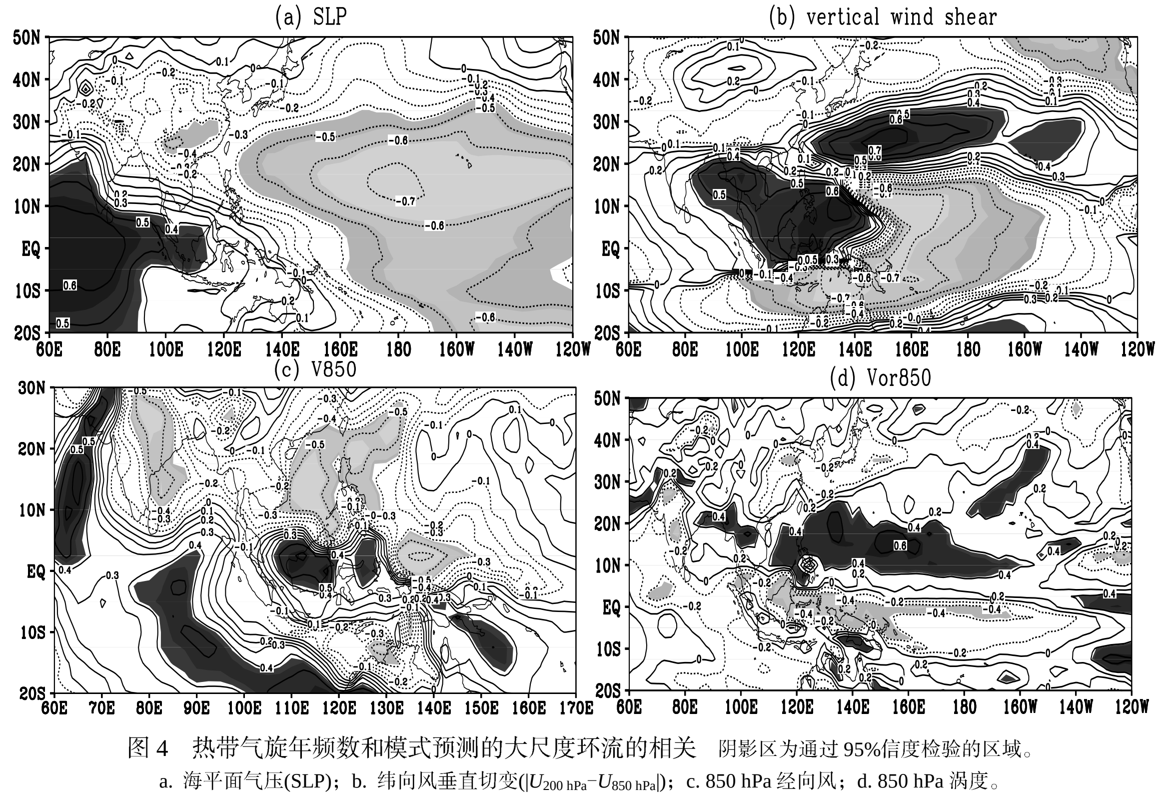

图 4 热带气旋年频数和模式预测的大尺度环流的相关 阴影区为通过 95%信度检验的区域。
a. 海平面气压(SLP)；b. 纬向风垂直切变($|U_{200\ \mathrm{hPa}}-U_{850\ \mathrm{hPa}}|$)；c. 850 hPa 经向风；d. 850 hPa 涡度。

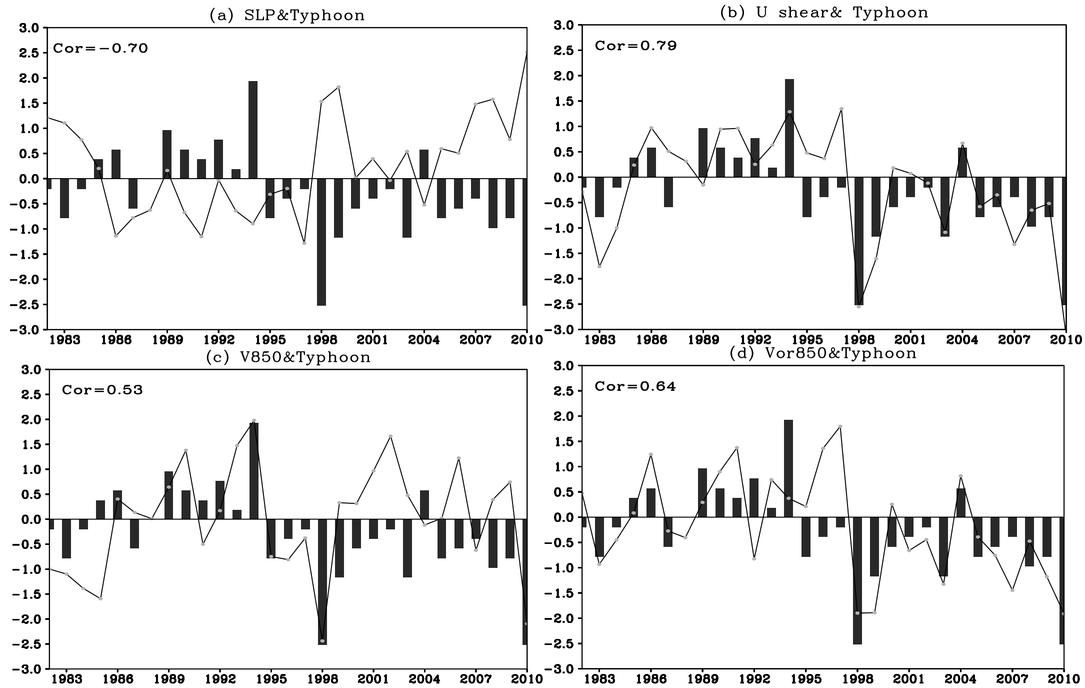

图 5　模式预测的 4 个关键区指数(实线)和热带气旋频数(柱状图)的标准化时间序列

曲线左上角为两序列的相关系数。其它说明同图 4。

以这 4 个关键区指数作为预报因子，建立热带气旋年频数的多元回归方程：

$$y(t) = -0.19 + 0.16\times x_1(t) + 0.74\times x_2(t) + 0.12\times x_1(t) - 0.0018\times x_4(t)$$ 。

图 6 是预测模型拟合的 1982—2010 年热带气旋频数距平和观测的热带气旋频数距平，两者的相关系数为 0.8，距平同号率为 86%。

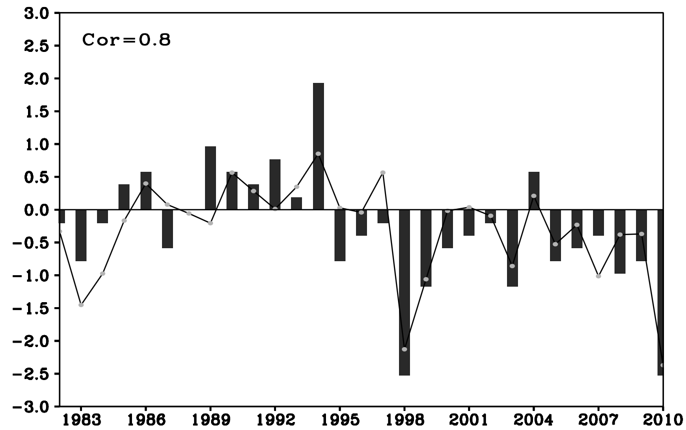

图 6　模式预测的 4 个关键区指数建立的多元回归方程对热带气旋频数序列的拟合(曲线)和热带气旋频数序列实况(柱状)　序列都为标准化序列，左上角为两序列的相关系数。横坐标为年份。

利用交叉检验的方法对该预测模型的预测效果进行进一步检验。具体做法是，每次模型预报方程由所有可用资料(本文为 1982—2010 年共 29 年资料)中去掉第 M(M 依次取 1，2，……，29)年的资料建立，然后用保留的第 M 年的因子资料作为因子观测值进行预报，而保留的第 M 年的预报对象资料作为实况。重复以上过程，使 M 取遍所有可能的取值(本文 M 可取 1, 2，……, 29)，可以得到预报值序列，这样得到的预报因为当年的预报因子并没有参与预报模型的建立，因此得到的预报可以认为是独立样本的预报。按照这种做法，预报检验的结果接近实际预报情况，而非事后预报。图 7 给出了交叉检验得到的热带气旋频数的标准化距平，与实况热带气旋频数的相关为 0.71，超过了 99.9%的信度检验。表 3 进一步给出了预报模型交叉检验方法预报的各年热带气旋频数，以及对历年预报效果的统计。29 年的交叉检验结果中，预测与实况距平符号一致的有 24 年，同号率为 82.8%，绝对预报误差在±2 个之间的年数为 16 年，占总年数的 65.5%。预报误差比较大的是 1994 年和 1989 年，这两年生成热带气旋数异常偏多，分别为 37 个和 32 个，为 1951 年以来最多的一年，预测分别为 30 个和 25 个，相对预报误差也分别达到−18.9%和−21.9%。对极

端少的 1998 年(14 个)和 2010 年(14 个)，模型分别预报 17 个和 15 个，1998 年的相对预报误差较大(21.4%)。可见，对极端的情况预报误差相对较大。1994 年和 1998 年是台风异常多和异常少的年份，属于很极端的情况，对于本文基于统计方法的预测模型来说，由于主要预测信息都来自历史资料，所以对历史资料中非常极端的情况很难较好预测。极端事件本身也很难用一般的统计预报方法进行预测。另外，本文主要是利用大尺度环流场进行建模预测，但对于台风来说大尺度环境场只是影响台风生成的因素之一，尤其是对比较极端的情况而言，不能完全用大尺度环境场解释，这可能也是模型对热带气旋异常多和异常少年预测误差较大的可能原因。

表 3　预测模型对 1982—2010 年热带气旋年频数预测的交叉检验结果

年份	实况热带气旋年频数	交叉检验预测的热带气旋年频数	距平正确与否(1971—2000 年气候平均 27 个)	预测绝对误差	预测相对误差/%
1982	26	25	Y	−1	−3.8
1983	23	19	Y	−4	−17.4
1984	26	22	Y	−4	−15.4
1985	29	25	N	−4	−13.8
1986	30	29	Y	−1	−3.3
1987	24	27	Y	3	12.5
1988	27	27	Y	0	0
1989	32	25	N	−7	−21.9
1990	30	30	Y	0	0
1991	29	28	Y	−1	−3.4
1992	31	26	N	−5	−16.1
1993	28	29	Y	1	3.6
1994	37	30	Y	−7	−18.9
1995	23	27	Y	4	17.4
1996	25	27	Y	2	8.0
1997	26	31	N	5	19.2
1998	14	17	Y	3	21.4
1999	21	21	Y	0	0
2000	24	27	Y	3	12.5
2001	25	27	N	2	8.0
2002	26	26	Y	0	0
2003	21	23	Y	2	9.5
2004	30	28	Y	−2	−6.7
2005	23	24	Y	1	4.3
2006	24	26	Y	2	8.3
2007	25	22	Y	−3	−12.0
2008	22	26	Y	4	18.1
2009	23	25	Y	2	8.7
2010	14	15	Y	1	7.1

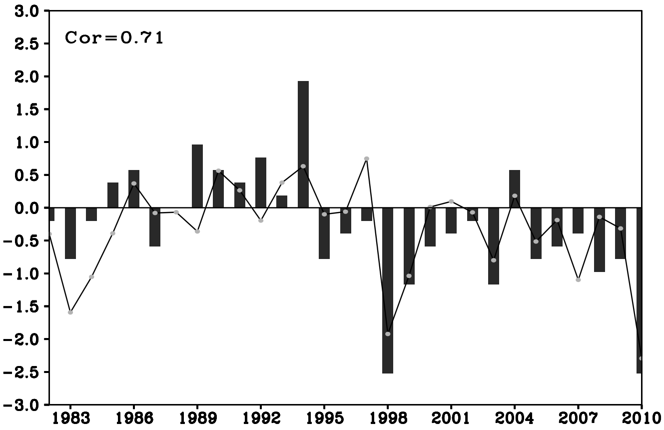

图 7　利用模式预测的关键区指数建立的多元回归方程预测的热带气旋频数序列(交叉检验结果)(曲线)和热带气旋频数序列实况(柱状)

序列都为标准化序列，左上角为两序列的相关系数。

5 结　论

基于对热带气旋生成频数和大尺度环流相关关系的分析，利用 SINTEX-F 海气耦合模式输出的大尺度环流信息，通过提取模式有较好预测能力，且与热带气旋生成密切相关的有用信息，建立了一个基于动力模式预测结果的热带气旋频数统计预测模型，并进行了预测试验与检验。

(1) 热带气旋的生成与大尺度的环流有密切关系。这些大尺度环流不仅包括热带气旋源区的对流、高低层的风切变、高低层的辐合辐散、热带辐合带异常，还包括热带气旋源区上游(西面)的副热带季风以及越赤道气流。利用 NCEP 资料建立的 6 个大尺度环流关键区因子建立的预测模型对热带气旋年频数的拟合率达到 0.73(相关系数)。

(2) SINTEX-F 海气耦合模式能够较好预测部分与热带气旋生成密切相关的大尺度环流特征，其中包括热带气旋活动区域的海平面气压、对流层风垂直切变、850 hPa 热带辐合带的涡度和 850 hPa 90 °E 附近的越赤道气流。利用这 4 个大尺度环流建立的 4 个预测因子与热带气旋生成频数有很好的相关关系，利用 4 个预测因子建立的多元回归预测模型对热带气旋频数的拟合率为 0.8(相关系数，超过 99.9%的信度检验)。

(3) 对利用 SINTEX-F 海气耦合模式输出信息建立的预测模型的预测效果进行交叉检验，表明模型整体预测效果较好。交叉检验预测结果与实况热带气旋频数的相关为 0.71(超过 99.9%的信度检验)，预测距平同号率为 82.8%。预测模型对热带气旋极端年的预测误差最大。除大尺度环流外，模型需要在引入能反映台风较为极端情况的因子方面进行改进，以提高对对极端台风多寡的预测能力。

参　考　文　献：

[1] 丁一汇. 影响西太平洋台风形成的大尺度环流条件[J]. 海洋学报，1983，5(5)：561-574.

[2] 李崇银. 厄尔尼诺影响西太平洋台风活动的研究[J]. 气象学报,1987,45：229-236.

[3] 董克勤，钟铚. 赤道东太平洋海温与南海热带风暴频数的相关关系[J]. 热带气象学报，1989，5(4)：335-350.

[4] 陈联寿, 罗哲贤. 影响热带气旋结构和运动的两类因子的数值研究[J]. 气象学报, 1996,54： 409-415.

[5] 雷小途. 热带气旋频数预测的研究进展和业务预测水平[J]. 大气科学研究与应用,1998,1：196-202.

[6] 宋文玲，何敏. 热带太平洋对流活动与西北太平洋台风活动关系的探讨[J]. 应用气象学报，1998(增刊)：109-118.

[7] 陈光华, 黄荣辉. 西北太平洋暖池热状态对热带气旋活动的影响[J]. 热带气象学报, 2006, 22(6): 527-532.

[8] 吴迪生，白毅平，张红梅，等. 赤道西太平洋暖池次表层水温变化对热带气旋的影响[J]. 热带气象学报，2003，19(3): 253-259.

[9] 林惠娟，张耀存. 影响我国热带气旋活动的气候特征及其与太平洋海温的关系[J]. 热带气象学报，2004，20(2)：218-224.

[10] 李春晖，刘春霞，程正泉. 近 50 年南海热带气旋时空分布特征及其海洋影响因子[J]. 热带气象学报，2007, 23(4)：341-347.

[11] 王咏梅，李维京，任福民，等. 影响中国台风的气候特征及其与环境场关系的研究[J]. 热带气象学报，2007，23(6)：538-544.

[12] 王会军, 孙建奇, 范可. 北太平洋涛动与台风和飓风频次的关系研究[J]. 中国科学D 辑: 地球科学, 2007, 37(7): 966-973.

[13] 范可. 北太平洋海冰,一个西北太平洋台风生成频次的预测因子[J]. 中国科学 D 辑: 地球科学,2007,37(6): 851-856.

[14] 孙淑清，刘舸，张庆云. 南半球环流异常对夏季西太平洋热带气旋生成的影响及其机理[J]. 大气科学，2007, 31(6)：1 189-1 200.

[15] 王会军, 范可. 西北太平洋台风生成频次与南极涛动的关系[J]. 科学通报, 2006, 51(24): 2 910-2 914.

[16] NICHOLLS N. Recent performance of a method for forecasting Australian season tropical cyclone activity[J]. Aust Meteor Mag, 1992, 40: 105–110.

[17] 蒋国荣, 沙文钰. 用赤道东太平洋海温预报西太平洋热带气旋年际变化的探讨[J]. 热带气象学报,1993,9(3): 221-228.

[18] KLOTZBACH P J, GRAY W M. Twenty-five years of Atlantic basin seasonal hurricane forecasts (1984–2008)[J]. Geophys Res Lett, 2009, 36, L09711, doi:10.1029/2009GL037580.

[19] KLOTZBACH P J, GRAY W M. Extended range forecast of Atlantic seasonal hurricane activity and landfall strike probability for 2010. [Available online at http://hurricane.atmos.colostate.edu.].

[20] FAN Ke, WANG Hui Jun. A new approach to forecasting typhoon frequency over the western North pacific[J]. Weather and Forecasting, 2009, doi:10.1175/2009WAF2222194.1.(On line)

[21] 王会军，郎咸梅，范可，等. 关于2006年西太平洋台风活动频次的气候预测试验[J]. 气候与环境研究，2006，11(2)：133-137.

[22] 郎咸梅，王会军. 利用气候模式能够预测西北太平洋台风活动的气候背景吗？[J]. 科学通报，2008, 53(14)：1 702-1 708.

[23] GUALDI S, NAVARRA A, GUILYARDI E, et al. Assessment of the tropical Indo-Pacific climate in the SINTEX CGCM[J]. Ann Geophys, 2003, 46(1)：1-26.

[24] GUILYARDI E, DELECLUSE P, GUALDI S, et al. Mechanism for ENSO phase change in a coupled GCM[J]. J Climate, 2003, 16(8)：1 141-1 158.

[25] LUO J J, MASSON S, BEHERA S, et al. South Pacific origin of the decadal ENSO-like variation as simulated by a coupled GCM[J]. Geophys Res Lett, 2003, 30：2250, doi:10.029/2003GL018649.

[26] LUO J J, ROECKNER E, MADEC G, et al. Reducing climatology bias in an ocean-atmosphere CGCM with improved coupling physics[J]. J Climate, 2005, 18(13)：2 344-2 360.

[27] 陈丽娟. 基于海气耦合模式的季节气候可预报性分析和解释应用[D]. 博士学位论文，2008,中国科学院研究生院.

[28] ROECKNER E, COAUTHORS. The atmospheric general circulation model ECHAM-4: Model description and simulation of present-day climate [M]. 1996, Max-Planck-Institut für Meteorologie Rep. 218, Hamburg, Germany, 90 pp.

[29] MADEC G, DELECLUSE P, IMBARD M, et al. OPA 8.1 ocean general circulation model reference manual[M]. 1998, LODYC/IPSL Tech. Rep. Note 11, Paris, France, 91.

[30] VALCKE S, TERRAY L, PIACENTINI A. The OASIS coupler user guide version 2.4. 2000, CERFACE Tech. Rep. TR/CGMC/00-10, 85.
[31] LUO J J, MASSON S, BEHERA S, et al. Seasonal climate predictability in a coupled OAGCM using a different approach for ensemble forecasts [J]. J Climate, 2005, 18(21): 4 474–4 497.
[32] LUO J J, MASSON S, BEHERA S, et al. Extended ENSO predictions using a fully coupled ocean–atmosphere model[J]. J Climate, 2008, 21(1): 84-93.
[33] LUO J J, ZHANG R, BEHERA S, et al. Interaction between El Niño and extreme Indian Ocean Dipole[J]. J Climate, 2010, 23(3): 726-742.
[34] LUO J J, MASSON S, BEHERA S, et al. Experimental forecasts of the Indian Ocean Dipole using a coupled OAGCM[J]. J Climate, 2007, 20 (10): 2 178-2 190.
[35] JIN E K, COAUTHORs. Current status of ENSO prediction skill in coupled ocean–atmosphere models[J]. Climate Dyn., 2008, 31: 647-664.
[36] WANG B, LEE J Y, KANG I S, et al. How accurately do coupled climate models predict the Asian-Australia monsoon interannual variability?[J]. Climate Dyn, 2008, 31: 605-619.
[37] LUO J J, BEHERA S, MASUMOTO Y, et al. Successful prediction of the consecutive IOD in 2006 and 2007[J]. Geophys Res Lett, 2008, 35, L14S02, doi:10.1029/2007GL032793.
[38] KALNEY E, KANAMITSU M, KISTLER R, et al. The NCEP/NCAR 40-year reanalysis project[J]. Bull Amer Meteor Soc, 1996, 77(3): 437-471.

CLIMATE PREDICTION EXPERIMENT FOR TROPICAL CYCLONE FREQUENCY USINGTHE LARGE SCALE CIRCULATION FORECAST BY A CGCM

JIA Xiao-long[1], CHEN Li-Juan[1], LUO Jing-jia[2]

(1. National Climate Center, Laboratory for Climate Studies, China Meteorological Administration, Beijing 100081, China;
2. Climate Variation Predictability and Applicability Research Program, Research Institute for Global Change，
Japan Agency for Marine-Earth Science and Technology，Japan)

Abstract：Based on an analysis of the relationship between the tropical cyclone frequency and large scale circulation anomaly in NCEP reanalysis, large scale atmosphere circulation information forecast by JAMSTEC SINTEX-F coupled model is used to build a statistical model to predict the tropical cyclone frequency over the South China Sea and the western North Pacific. The SINTEX-F coupled model has relatively good prediction skill for some circulation features associated with the tropical cyclone frequency including sea level pressure (SLP), wind vertical shear, tropical convergence belt and cross-equatorial air flow. Predictors derived from these large scale circulations have good relationships with the tropical cyclone frequency over the South China Sea and the western North Pacific. A multivariate linear regression (MLR) model is further designed using these predictors. This model shows good prediction skill with the anomaly correlation coefficient reaching, based on the cross validation, 0.71 between the observed and predicted tropical cyclone frequency. However, it also shows relatively large prediction errors in extreme tropical cyclone years (1994 and 1998, for example).

Key words: CGCM; large scale circulation; tropical cyclone; climate prediction

浅谈极端气温事件研究中阈值确定方法

李娇[1, 2]　任国玉[2]　战云健[2, 3]

（1 辽宁省铁岭市气象局，铁岭 112000；2 中国气象局气候研究开放实验室，北京 100081；
3 中国气象科学研究院，中国气象局，北京 100081）

摘要：比较了极端气温事件研究中，绝对阈值和相对阈值指数的适用范围。归纳总结了近年来国内外在陆地极端气温事件研究中，相对阈值百分位选取、修订以及资料和计算方法的异同，评价了不同计算方法的优缺点和适用范围，讨论了参考期选取的影响。综合已有研究结论发现，采用不同的相对阈值计算方法检测出的极端气温事件长期趋势以及变异性特征差异极小。为了增强极端气温事件趋势变化分析的统计意义，以及对不同研究和不同区域分析结果进行比较，在资料选择和处理、阈值计算方法、气候基准期的确定等方面还需要进一步完善和规范。

关键词：极端气温事件，绝对阈值，相对阈值，计算方法，气候参考期

DOI：10.3969/j.issn.2095-1973.2013.05.006

Discussion on Threshold Determination in Defining Extreme Temperature Indices

Li Jiao[1, 2], Ren Guoyu[2], Zhan Yunjian[2, 3]

(1 Tieling Meteorological Service, Liaoning Province, Tieling 112000 2 Laboratory for Climate Studies, China Meteorological Administration, Beijing 100081 3 Chinese Academy of Meteorological Sciences, China Meteorological Administration, Beijing 100081)

Abstract: In this paper, the application scope of fixed threshold and percentile threshold index is compared during extreme temperature events. Also, the determination of percentile thresholds for defining extreme temperature indices in studies of long-term change of extreme temperature events is briefly summarized, and the differences of data and calculation methods used in different studies are compared. The effect of reference-period selection on percentile threshold values and the results of analyses are discussed. It is clear from the overview that both advantages and disadvantages exist for different methods of percentile threshold determination. It is found that the long-term trends of extreme temperature events detected are almost the same when different methods of calculation are used. In order to enhance the significance of the statistical analysis of extreme events, trends and to compare the analyses among different studies and different regions, however, it is necessary to further improve the methods of data selection, data processing, threshold calculation methods and the usage of climate baseline period. It is advisable to consistently use the uniform methods for determining percentile thresholds.

Keywords: extreme temperature events, fixed threshold, percentile threshold, methods of calculation, climate baseline period

1　引言

气候变化伴随着极端天气、气候事件频率和强度的变化。了解全球和区域极端气候事件长期变化规律，是当前气候变化监测、检测和预估研究的重要方面，对于气候变化影响和适应性评价也有帮助。

极端气温事件是极端天气与气候事件中的一类，其定义方法有很多[1-3]。目前国际上主要采用极端气温指数来研究极端气温事件。由于各国、各地区极端指数定义不一，研究方法不同，气候变化检测、监测和指数专家小组选取了16个极端气温指数（14个常用指数见表1），用于区域或全球极端气温事件变化的分析。这些极端气温指数是基于简单的数学统计，除去反映季节或年内最大、最小值的极值指数外，都是采用阈值指标来度量的。超过阈值的值被认为是极值，该事件称为极端事件。阈值又分为绝对阈值和相对阈值。

本文比较了绝对阈值和相对阈值指数的适用范围，重点讨论相对阈值的确定方法。不同研究者对相对阈值的选择、修订、样本选取、样本容量和计算方法不尽相同，导致计算的阈值有所差别；同时参考期

收稿日期：2012 年 6 月 20 日；修回日期：2013 年 5 月 15 日
第一作者：李娇（1986—），Email: lijiaostu@163.com
通信作者：任国玉，Email: guoyoo@cma.gov.cn
资助信息：国家科技支撑计划（2007BAC29B02）；公益性（气象）行业科研专项（201206024）

表1 常用的极端气温指数

序号	代码	名称	定义	单位
1	FD0	霜冻日数	日最低气温（TN）<0℃的全部日数	d
2	SU25	夏季日数	日最高气温（TX）>25℃的全部日数	d
3	ID0	结冰日数	日最高气温（TX）<0℃的全部日数	d
4	TR20	炎热夜数	日最低气温（TN）>20℃的全部日数	d
5	TXx	月极端最高气温	每月内日最高气温的最大值	℃
6	TNx	月最低气温极大值	每月内日最低气温的最大值	℃
7	TXn	月最高气温极小值	每月内日最高气温的最小值	℃
8	TNn	月极端最低气温	每月内日最低气温的最小值	℃
9	TN10p	冷夜日数	日最低气温（TN）<10%分位值的日数	d
10	TX10p	冷昼日数	日最高气温（TX）<10%分位值的日数	d
11	TN90p	暖夜日数	日最低气温（TN）>90%分位值的日数	d
12	TX90p	暖昼日数	日最高气温（TN）>90%分位值的日数	d
13	WSDI	热日持续指数	每年至少连续6天日最高气温（TX）>90%分位值的日数	d
14	CSDI	冷日持续指数	每年至少连续6天日最低气温（TX）<10%分位值的日数	d

的选择不同也提出了相对阈值的代表性问题。本文主要针对这些问题进行简要总结与讨论。

2 绝对阈值指数

绝对阈值指数是选取某个影响人类或生物的界限气象要素值来定义的指数。例如：将日最高气温高于35℃的日数作为高温日数（事件），将日最低气温低于0℃的日数作为霜冻日数（事件）。绝对阈值指数定义的极端事件较为直观，计算简单。绝对阈值气温指数由于基于固定值，在全球各地的适用性有所差别，在估算线性趋势时要慎重。Zhou等[4]在中国大陆绝对气温指数趋势变化分析时做如下处理，认为在研究时段的2/3年份未出现某项极端事件记录，则估算该站该指数的线性趋势是不可信的。绝对阈值指数适用于空间变率较小的地区，当研究区域气候差异较大时，通常采用相对阈值指数来表征。

3 相对阈值指数

3.1 相对阈值的定义方法

相对阈值指数是相对于当地气候态的百分位临界值定义的，即从概率分布角度统计的小概率事件。这种定义方法考虑了不同地区气候的差异性，避免了极端气温事件绝对强度随区域不同，难以用同一标准做比较的问题[5]。百分位阈值是相对阈值的代表，它是基于气候重现期的思想[6]。重现期反映了小概率事件平均发生的时间间隔或年数，重现期越长表明发生概率越小，类似事件越是稀有。具体的重现期计算与选取的百分位数值和样本容量有关。目前相对阈值的应用较为广泛。

例如：冷（暖）日和冷（暖）夜指数是根据当地日最高、最低气温分布中最冷和最暖的某一分位数值，估计出一年或年内特定时段内极端气温事件发生的频次。将某站参考气候期内同日的最高气温资料按升序排列，得到该日第x（$100-x$）个百分位值，这样依次得到366个值，将其作为逐日的极端高温事件的上（下）阈值。当某日最高气温大于等于（小于等于）此阈值时，认为该日发生了暖（冷）昼事件。暖（冷）夜事件则以逐日最低气温为研究对象，定义同上。

具体百分位数的选择取决于业务和研究需要。一般来说，气候变化研究中的极值不宜取的太极端，典型重现期不能太长，这样可以确保每一年都检测出足够数量的极端事件，使得气候变化分析更具统计意义。一般极端气温事件的百分位数值多取为90%（10%）或95%（5%），也有人分别取99%和1%[7, 8]，将此概率所对应的气温临界值定义为极端气温事件的阈值。

3.2 相对阈值的修订

为了去除逐日阈值曲线中包含的天气尺度扰动，得到光滑的逐日阈值曲线，需对其进行低通滤波处理。黄丹青等[9]认为滤去8d以下波动的逐日阈值修订方法，能够更合理地检测极端气温事件；张雷等[10]参考前人工作，将气温百分位阈值采用5日滑动平均处理，使得逐日阈值更加连续。不同的研究对极端气温阈值的修订方法不同，也有研究未对逐日阈值进行滤波。总体来说，这对检测出的极端事件的频率及趋势变化影响很小。

4 相对阈值研究中存在的问题

4.1 资料问题

对极端气温事件的研究主要采用逐日最高、最低气温观测资料。例如，有研究以日最高（低）气温第95（5）百分位定义的阈值，用来检测特定季节高温热浪和寒潮事件[11]。也有研究[9, 12]以日平均气温资料

来选取百分位阈值，分析相对高、低温事件。按照极端事件的统计学定义，第一种样本的概率分布双尾侧分别对应日间和夜间的相对暖、冷事件；日平均气温反映逐日气温的平均状态，以日平均气温为研究对象可以检测出全天平均状态下的暖、冷事件。因为最低和最高气温在很多台站呈现出非对称性趋势，利用两种资料检测出的极端气温事件频次趋势变化可能有所差别。实际研究中，究竟采用哪种资料作为样本，要依照研究目的和资料可获得性等进行选择。

黄丹青等[9]以日平均气温资料为研究对象，确定了以90%（10%）为标准的日、旬、月和季四种不同时间尺度的极端高（低）温事件阈值。将相对阈值的定义方法分别应用于逐日、逐旬、逐月和逐季尺度，这样一年中分别得到365，36，12和4个阈值。不同时间尺度的阈值随时间的分布形势基本一致，但研究时段内逐日超过高阈值日数的时间分布具有不同特点。超过日尺度高阈值的日数分布均匀，为3～5d；超过旬尺度高阈值的日数在0～14d；而基于月阈值和季阈值得到的日数取值范围更广。因此，基于逐日时长的资料（样本）选取方式检测极端气温事件更为合理。

但是，逐日气温阈值的定义表明，这种方法可供使用的样本量有限，只有30个。为了增加概率分布参数估计的稳定性，Folland等[13]提出增加额外的数据来扩充样本量的思想。增加的数据要相对独立，并能够准确代表该日的概率分布特征。Jones等[14]完善了这种做法，采用某日及前后间隔各5d的5个数据作为样本（5SD）。最近国外的研究中多是采用连续5d的资料，即以某日为中心，补充前后2d的资料（5CD）。这样在标准气候期中，有5×30个样本来反映当日的气候分布。国内研究多未详细说明是否增加以及如何扩充样本量。

4.2 计算方法不同

百分位阈值的主要计算方法有三种：（1）针对不同气候要素采用不同分布型的边缘值来确定阈值；（2）采用经验公式计算某个百分位值作为极端事件的阈值；（3）累积频率法（CDF）。第一种参数化方法，计算较为复杂，同时参数估计和选取的概率分布类型会增加阈值的不确定性。第二种经验公式方法计算简单，不受错误值干扰，但是当数据结构不服从正态分布时，用经验公式法求得的阈值同样具有不确定性。第三种累积频率法同样不需要了解气象要素的具体统计模型，但是，当确定的组数较少时，求算阈值的精确性较差。

*不同分布型的边缘值方法。*该方法要考虑气象要素的概率分布特征，然而不同的气象要素概率分布函数有所不同。在实际确定某一分布时，通常用极大似然方法根据均值μ、方差2σ和变化系数来确定。但参数估计和选取的概率分布类型会增加阈值的不确定性。气温要素的概率分布一般都服从正态分布，但大多数情况下，并非严格正态。特别是台站气温的月（年）平均值，在一定程度上近似为正态或偏度很小的铃型分布。总体来说，月平均气温、平均最高和最低气温等，是否基本符合正态分布，常因地区、季节而略有差异[6]。

Folland等[13]提出计算百分位阈值的三个步骤。首先计算逐日的30年气候平均值，然后逐日去除30年的均值（即计算距平值）以消除年际变化；最后对逐日的距平值选择一个合适的概率分布函数进行拟合来计算某个百分位的阈值。

Jones等[14]进一步给出了估算阈值的详细步骤，介绍了逐日基准气候值的算法。例如1月1日的平均气温是30年基准气候期内1月1日气温的平均；在非闰年2月29日的值由2月28日和3月1日平均算出。由于这366个值不能产生一个光滑的日平均温度的年际序列，需要进行平滑。文中采用11点的二项式滤波，滤去8.8d以下的天气变化。同样以距平值拟合气象要素的概率分布函数，来求算百分位值。

*经验排序公式法。*经验排序公式法根据顺序统计量的累积概率与数据排序后的位置建立相关联系，估计百分位值。经验公式方法计算简单，不受错误值干扰，近年来广泛用于极端事件百分位阈值的估计。

方法1：设某个气温变量有n个值，将这n个记录按升序排列，得到x_1，x_2，…，x_n，则百分位值为[15]：

$$x_0 = (1-a)\,x_j + a x_{j+1} \qquad (1)$$

式中：$j=[p(n+1)]$，$a=p(n+1)-j$。j为气温记录按大小升序排列后的序号；p为百分位值对应的概率；方括号表示数值取整；n为序列样本容量。

方法2：如果某个气温变量有n个值，将这n个记录按升序排列x_1，x_2，…，x_n，某个值小于或等于序号为m对应的事件出现概率为[16]：

$$p = (m-0.31)/(n+0.38) \qquad (2)$$

式中：m为x_m的序号，n为某个气温变量记录的个数。如果有30个值，那么第95个百分位值为排序后的x_{29}（$p=94.4$）和x_{30}（$p=97.7$）的线性插值。

需要注意的是：只有当分析的数据服从或近似服从正态分布时，这两个经验公式才能得到较准确的结果[17]。但对于不同地区和不同季节的气温序列，正态分布存在不同程度的偏态性质，因此采用以上两个公

式确定的百分位值会有一定偏差。周云等[17]以偏态分布下的累积概率分布函数，通过理论推导和数值模拟建立新的经验百分位值估计公式，丰富了非正态分布条件下经验公式的选择。Folland等[18]则列举了满足其他分布（潜在正态分布、Gamma分布和指数分布）的经验公式。

累积频率法（CDF）。李庆祥等[19, 20]和黄丹青等[9, 21-23]根据气温要素的实际样本频率分布作为实际概率分布的近似，确定样本频率分布的组数，求得变量的频率分布后，利用累积频率分布确定百分位阈值。例如将第90百分位与按分组后各组的累积频率值相比较，落入某两组的累积频率值时，采用线性插值求取第90百分位值。

该方法不需要了解气象要素的具体统计模型，因此避免了任何分布假设。但是，当确定的组数较少时，求算阈值的精确度较差。李庆祥[19]认为根据最高气温的实际样本频率分布作为实际概率分布的近似，在极端高温阈值的选择上较前两种经验公式效果要好。

不同方法计算的阈值具有一定差别，因而检测出的极端气温事件的日数也有差别，但对极端气温事件频率和强度的趋势变化影响很小。Zhang等[24]采用经验公式和高斯分布函数分别获得百分位阈值方法，计算得到的极端气温日数比率（大于阈值日数与总日数的比值）差别很小。Bonsal等[16]认为采用经验公式（方法2）和Gamma分布函数检测出的极端气温事件频率长期趋势以及年际变率几乎相同。

4.3 参考期选择

由于各个国家、各个台站建站时间不同，为了更好地比较不同站点、不同研究时段的极端气温事件，国外文献多以世界气象组织规定的某一30年基准气候期作为气候参照时段，在基准气候期内确定阈值作为极端气温事件的标准，来评估极端气温事件频率和强度相对于该时期的变化程度。在基准气候期选择的阈值具有相对稳定性和可比性，因此可以沿用到未来一段时间，不同站点间也可以进行比较。也有文献在整个研究时段选取阈值[13, 25, 26]，用以研究整个时段内的极端气温事件的总体变化情况。近几年，国内研究多在基准气候期内选取阈值[27-30]来分析极端气温事件的变化。

以整个研究时段作为参考期，选取气温相对阈值的一个主要问题是，计算获得的台站极端气温指数的气候平均值和平均重现期相同[8, 12]。例如，文献[12]给出的各个代表站极端低温指数T10%和极端高温指数T90%的40年平均值是相同的，都为36d，平均重现期都为10d（表2）。因为对于某一天，40年中日平均气温低于T10%阈值的天数都是4d，全年按照365个历日计算，极端低温日数共有1460d，40a平均每年36.5d。在这种情况下，进行区域之间极端气温事件的气候学比较就很困难。

表2 各代表站极端低温、高温日数的多年（1961—2000年）平均值

代表站名	乌鲁木齐	沈阳	兰州	成都	南京	福州
T10%/d	36（10）	36（10）	36（10）	36（10）	36（10）	36（10）
T90%/d	36（10）	36（10）	36（10）	36（10）	36（10）	36（10）

注：此表据文献[12]改制，括号内为平均重现期

在基准参考期计算相对阈值的方法也存在问题。Zhang等[24]采用蒙特卡罗模拟试验发现：基准气候期内确定的极端气温百分位阈值指标，由于抽样的不确定性，阈值在基准气候期前后存在非均一性，当许多站点求算平均时，这种非均一性更加明显。因此估计的极端事件频数在趋势分析时会产生错误结论。Zhang等[24]对该问题进行了处理，bootstrapping方法的提出和应用减少或消除了有关极端气温指数趋势估计中的可能偏差。

对于参考期的选择，Jones等[14]认为：当两个时期的平均气温相差不大时，选择不同的参考期对极端气温事件的检测结果不是很敏感。他们分别采用1931—1960年和1961—1990年作为参考期，得到的极端冷、暖事件日数相差不大，因为这两个时段的平均气温几乎没有差异。他指出，如果极端气温事件阈值在一个变化的参考期内确定，则可能会得到有所不同的结论。

气候状态的改变影响极端事件概率的情况有3种可能情况：气候要素均值发生变化，气候要素变率（标准差）发生变化，变率和均值同时变化。气候状态的不同变化对极端事件的影响是不同的。有研究表明[31]，平均值的很小变化会导致极端事件频率发生很大变化；标准差变化对极端事件频率的影响要大于均值变化的影响。参考期的选择一般对极端气温阈值本身和极端气温事件的气候学特征分析有影响，然而在全球气候变暖的背景下，随着气候参考期（目前为1981—2010年）不断调整，参考期的选择对于极端气温事件的长期趋势变化的影响还有待于进一步研究。

5 结论与讨论

本文归纳总结了近年来国内外在陆地极端气温事件研究中，绝对阈值和相对阈值指数的适用范围。重点评述了相对（百分位）阈值选取、修订以及样本和

计算方法的异同，评价了不同计算方法的优缺点和适用范围，讨论了参考期选取对分析结果的影响。

已有研究对相对阈值选择、修订、样本选取、样本容量和计算方法不尽相同，导致计算的极端气温事件阈值有所差别，检测出逐年的和各个年代极端气温事件的频数也略有不同，但总体来说，不同计算方法一般只对阈值本身和极端气温事件年际、年代际变化分析结果具有影响，而对于极端气温事件长期趋势研究结果几乎没有影响。对极端气温事件气候变化分析结果影响比较大的主要是资料选取和处理方法，需要今后给予足够重视。不同的参考期选取对于极端气温事件的长期趋势变化的影响还有待于进一步研究。

但是，为了增强极端气温事件趋势变化分析的统计意义，同时为了增加不同研究和不同区域分析结果之间的可比性，在极端气温事件阈值定义、计算方法和气候基准期选择等方面，确实需要进一步完善和规范。

参考文献

[1] 马柱国, 符淙斌, 任小波, 等. 中国北方年极端温度的变化趋势与区域增暖的联系.地理学报, 2003, 58(增刊): 11-20.

[2] Andrew F, David E, Bryan W. Climate variability and the frequency of extreme temperature events for nine sites across Canada: implications for power usage. Journal of Climate, 1999, 12(7): 2490-2502.

[3] 章大全, 钱忠华. 利用中值检测方法研究近50年中国极端气温变化趋势. 物理学报, 2008, 57(7): 4634-4640.

[4] Zhou Y Q, Ren G Y. Change in extreme temperature event frequency over mainland China, 1961-2008. Climate Research, 2011, 50: 125-139.

[5] 封国林, 侯威, 支蓉, 等. 极端气候事件的检测、诊断与可预测性研究. 北京: 科学出版社, 2012: 3-6.

[6] 丁裕国, 江志红. 极端气候研究方法导论. 北京: 气象出版社, 2009: 79-80, 54-55.

[7] Griffiths G M, Chambers L E, Haylock M R, et al. Change in mean temperature as a predictor of extreme temperature change in the Asia-Pacific region. International Journal of Climatology, 2005, 25: 1301-1330.

[8] KleinTank A M G, KÖnnen G P, Trends in indices of daily temperature and precipitation extremes in Europe, 1946-99. Journal of Climate, 2003, 16: 3665-3680.

[9] 黄丹青, 钱永甫. 我国极端温度事件的定义和趋势分析.中山大学学报, 2008, 47(3): 112-116.

[10] 张雷, 任国玉, 刘江, 等. 城市化对北京气象站极端值气温指数趋势变化的影响. 地球物理学报, 2011,54(5): 1150-1159.

[11] 潘晓华, 翟盘茂. 气温极端值的选取与分析. 气象, 2002, 28(10): 28-31.

[12] 刘学华, 季致建, 吴洪宝, 等. 中国近40年极端气温和降水的分布特征及年代际差异. 热带气象学报, 2006, 22(6): 618-624.

[13] Folland C, Miller C, Bader D, et al. Workshop on indices and indicators for climate extremes, Asheville, NC, USA, 3-6 June 1997. Breakout Group C: Temperature indices for climate extremes. Climatic Change, 1999, 42: 31-43.

[14] Jones P D, Horton E B, Folland C K, et al. The use of indices to identify changes in climatic extremes. Climatic Change, 1999, 42: 131-149.

[15] Frich P, Alexander L V, Della-Marta P, et al. Observed coherent changes in climatic extremes during the second half of the twentieth century. Climate Research, 2002, 19: 193-212.

[16] Bonsal B R, Zhang X, Vincent L, et al. Characteristics of daily and extreme temperatures over Canada. Journal of Climate, 2001, 14: 1959-1976.

[17] 周云, 侯威, 钱忠华, 等. 基于偏态分布的百分位估计公式的建立. 物理学报, 2011, 60(8): 089201-1-089201-9.

[18] Folland C, Anderson C. Estimating changing extremes using empirical rangking methods. Journal of Climate, 2002, 15: 2954-2960.

[19] 李庆祥, 黄嘉佑. 对我国极端高温事件阈值的探讨. 应用气象学报, 2011, 22(2): 138-144.

[20] 李庆祥, 黄嘉佑. 北京极端低温事件的长期变化趋势. 高原气象, 2012, 31(4): 1145-1150.

[21] 黄丹青, 钱永甫. 极端温度事件区域性的分析方法及其结果. 南京大学学报, 2009, 45(6): 715-723.

[22] Huang D Q, Qian Y F, Zhu J. Trends of temperature extremes in China and their relationship with global temperature anomalies. Advances in Atmospheric Sciences, 2010, 27(4): 937-946.

[23] 黄丹青, 钱永甫. Community Climate Model 3模拟夏季极端降水的初步分析.南京大学学报, 2007, 43(3): 238-248.

[24] Zhang X, Gabriele H, Francis W Z, et al. Avoiding inhomogeneity in percentile-based indices of temperature extremes. Journal of Climate, 2005, 18: 1641-1651.

[25] 游庆龙, 康世昌, 李潮流, 等. 三江源地区1961—2005年气温极端事件变化. 长江流域资源与环境, 2008, 17(2): 232-236.

[26] 张宁, 孙照渤, 曾刚. 1955—2005年中国极端气温的变化. 南京气象学院学报, 2008, 31(1): 123-128.

[27] 翟盘茂, 潘晓华. 中国北方近50年温度和降水极端事件变化. 地理学报, 2003, 58(增刊): 001-010.

[28] 周雅清, 任国玉. 中国大陆1956—2008年极端气温事件变化特征分析.气候与环境研究, 2010, 15(4): 405-417.

[29] 任玉玉, 任国玉. 1960—2008年江西省极端降水变化趋势. 气候与环境研究, 2010, 15 (4): 462-469.

[30] 杨金虎, 江志红, 王鹏祥, 等. 西北地区东部夏季极端降水量非均匀性特征. 应用气象学报, 2008, 19(1): 111-115.

[31] 丁裕国, 申红艳, 江志红, 等. 气候概率分布理论及其应用新进展. 气象科技, 2009, 37(3): 257-262.

李维京,李怡,陈丽娟,等. 我国冬季气温与影响因子关系的年代际变化. 应用气象学报,2013,24(4):385-396.

我国冬季气温与影响因子关系的年代际变化

李维京[1)*] 李 怡[2)] 陈丽娟[1)] 赵振国[1)]

[1)](国家气候中心 中国气象局气候研究开放实验室,北京 100081)

[2)](中国气象科学研究院,北京 100081)

摘 要

利用 1951—2012 年冬季全国 160 个站月平均气温以及 NCEP/NACR 再分析资料和海温、北极海冰等资料,分析了我国冬季气温及其关键影响因子的年代际变化特征,重点研究了关键影响因子对我国冬季气温影响关系的年代际变化。研究表明:我国冬季气温在 1985 年之前处于冷期,之后为暖期;我国冬季气温异常与影响因子的关系发生了显著的年代际变化,而且影响因子之间的关系也发生了显著的年代际变化。针对这种年代际变化的基本事实,提出针对冷期和暖期中不同影响因子与冬季气温的关系分时段建立冬季气温的多因子回归预测模型,可以反映冬季气温及其影响因子关系的年代际变化特征。正确的预测策略是利用相同年代际背景下预测对象与预测因子的时间序列资料建立预测模型,以确保预测模型中反映的预测对象与预测因子关系的稳定性,进而保持较高的拟合及预测水平。

关键词: 冬季气温; 影响因子; 东亚冬季风; 年代际变化

引 言

在全球变暖背景下,我国冬季气温表现出了显著的年代际变化特征,1985 年以来经历了 16 个暖冬,而从 2004 年之后又出现偏冷特征,特别是 2008 年以来,冬季极端冷事件明显增多。正确认识冬季气温年代际变化的成因对于有效地预测冬季气温异常非常重要。

研究表明:近百年来,我国不同地区的年平均气温均反映出 20 世纪 20 年代初和 80 年代中期的两次增暖[1]。我国气温变暖存在较强的区域性和季节性特征,以北方地区增暖强度最大且在冬季增暖最显著[2]。影响我国冬季气温年际气候异常的大气环流因子主要有东亚冬季风、西伯利亚高压、北极涛动、西太平洋副热带高压和青藏高原高度场等[3-6],外强迫信号主要有 ENSO 循环[7-8]、北极海冰[9]、热带印度洋海温和黑潮海温异常[10-11]等信号,这些影响因子也存在年代际变化。在年代际时间尺度上,东亚冬季风 1987 年以后持续减弱[12];西伯利亚高压从 20 世纪 70 年代开始减弱直到 90 年代末,在近 20 年表现出增强趋势[13];北极涛动在 80 年代之前多处于负位相,之后出现正位相频次增加[14];冬季喀拉海和巴伦支海的海冰存在 10 年变化周期[15];赤道东太平洋海温也在 1977 年之后较前一阶段增暖 0.5℃,而西北太平洋的海温降低达0.6℃[16],El Niño 事件在 20 世纪 80 年代之前多为东部型,而之后多为中部型[17],这两种海温模态对我国冬季气候的影响也不同;热带印度洋海表温度发生了由冷到暖的年代际变化,20 世纪 50—60 年代为偏冷期,80—90 年代为偏暖期[18];黑潮区海温在 20 世纪 90 年代后期呈现出升高趋势[19]。

大量研究表明,近几十年我国冬季气温不仅发生了明显的年代际变化,其影响因子也发生了年代际变化,更重要的是我国冬季气温异常与关键影响因子的关系也可能发生了变化。近期有研究认为,ENSO 和东亚冬季风的关系在 20 世纪 70 年代中期以后减弱,由显著负相关变为相关不显著[20],这说明影响我国冬季气温异常的各关键因子之间的相互关系也可能发生了变化,增加了对冬季气候预测的难度。

2013-03-20 收到, 2013-05-27 收到再改稿。

资助项目:国家重点基础研究发展计划项目(2013CB430203),科技部科技支撑项目(2009BAC51B05),国家自然科学基金项目(41275073)

* email: liwj@cma.gov.cn

本文旨在研究我国冬季气温及其影响因子年代际变化的基础上,重点揭示冬季气温与关键影响因子关系发生年代际变化的基本事实,以及在短期气候预测中如何正确利用这种变化关系来建立预测模型,从而探索我国冬季气温异常的预测方法。

1 资料与方法

本文所用的资料包括国家气候中心整编的全国160个站1951—2012年逐月气温,取当年12月与次年1月和2月的气温平均值作为当年的冬季平均气温,气候平均态采用1951—2011年平均值。NCEP/NCAR提供的1951—2012年2.5°×2.5°的月平均再分析资料[21];Hadley中心提供的同时段月平均全球海平面气压资料HadSLP2[22]和英国大气数据中心(BADC, http://badc.nerc.ac.uk/data/hadisst/)同时段的1°×1°北极海冰密集度(SIC)资料,以及美国国家海洋大气局同时段的2.0°×2.0°的月平均海温资料和逐月ENSO指数(ONI)序列资料[23]。

本文所用的大气环流指数资料包括:利用冬季西伯利亚中心区域平均海平面气压定义的西伯利亚高压指数[24],可反映东亚大槽及相关冷空气活动强弱的冬季风指数[20],美国气候预测中心(CPC)提供的北极涛动(AO)指数,西太平洋副热带高压面积指数[25]和青藏高原高度场指数[26]。

此外,还考虑外强迫因子(印度洋海温、黑潮海温和北极海冰)对我国冬季气温的影响,热带印度洋全区一致海温模态(IOBW)定义为热带印度洋20°S～20°N,40°～110°E区域平均的海温距平;黑潮海温指数定义为15.5°～32.5°N,120.5°～150.5°E区域平均的海温距平[27];北极海冰指数定义为北冰洋区域76.5°～83.5°N,60.5°～149.5°E海冰密集度平均值[28]。

利用相关分析获得两个序列之间协同变化的关系,采用滑动t检验方法确定冬季气温序列的气候突变时间,利用多元线性回归建立拟合模型。

2 冬季气温及关键影响因子的年代际变化

2.1 冬季气温的年代际变化特征

1885年以来,我国气温变化存在3个显著增温期,前两次变暖分别为1885—1900年和1910—1940年[29],第3次变暖从20世纪80年代中期开始,滞后于北半球的增暖时间[30]。通过计算我国冬季气温1951—2011年的线性变化趋势,得出近61年来增暖率为0.3℃/10 a。为了准确定义我国冬季气温冷期和暖期的分界线,利用滑动t检验得出我国冬季气温在1985年发生由冷到暖的突变(图1断线所示)。在1985年之前为冷期,平均气温为−0.5℃;而1985年之后为暖期,平均气温为0.7℃,较之前上升了1.2℃。丁一汇等[31]对我国7个地区冬季地表气温序列用同样的方法进行突变检验发现,全国7个地区冬季气温也普遍在1985年之后发生突变。

由于季节内变化特征的影响,有的冬季表现为持续偏冷或偏暖,有的冬季表现为冷暖交替。为详细了解冬季冷暖的变化,定义我国冬季(月)平均气温距平不大于-2σ(σ为标准差,相当于气温距平不大于−3.5℃)作为异常冷季(月)阈值,概率为40年一遇;冬季(月)平均气温距平不大于-1.29σ且大于-2σ(即气温距平不大于−2℃且大于−3.5℃)作为冷季(月)阈值,其发生概率为10年1次;冬季(月)平均气温距平不大于-0.43σ且大于-1.29σ(即气温距平不大于−1℃且大于−2℃)作为偏冷季(月)阈值,其发生的概率是几年1次。类似地,定义异常暖季(月)平均气温距平不小于2σ,暖季(月)平均气温距平不小于1.29σ且小于2σ,偏暖季(月)平均气温距平不小于0.43σ且小于1.29σ。由图1可知,在1985年之前的冷期,有11年冬季偏冷、4年冷和2年异常冷,共17年;而只有2年冬季偏暖。1985年之后的暖期,有13年冬季偏暖,2年为暖,2年为异常暖,共17年,而在暖期中仅有1年冬季偏冷。在2000年之后,我国冬季气温虽在暖期中,但并未保持持续升温趋势,尤其在2008年低温雨雪冰冻发生之后,我国冬季气温总体趋势明显下降,出现偏冷的月份增加。

在1951—1985年冷期,冬季3个月出现偏冷月21次、冷月7次、异常冷月4次、偏暖月13次,没有出现暖月和异常暖月(图2);在1986—2011年暖期,偏暖月出现18次、暖月7次,异常暖月2次。值得关注的是1986—2003年中,偏冷月仅出现1次,未出现冷月和异常冷月;而在2004—2011年,偏冷月出现5次,冷月1次,7年中有5年出现了偏冷月,出现偏冷月的概率较1986—2003年明显增大,我国冬季气温是否进入了由暖转冷的阶段值得关注和进一步研究。

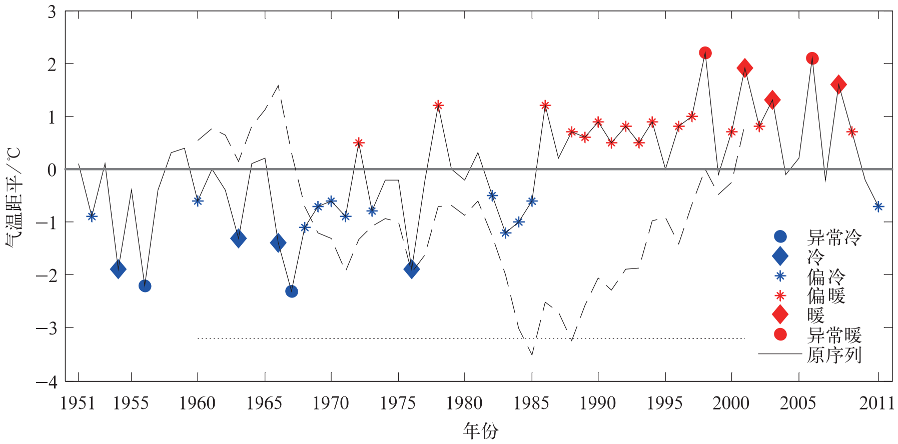

图 1　1951—2011 年全国冬季月平均气温距平演变

（断线为气温距平滑动 t 统计量，横点线为滑动 t 检验量 0.01 显著性水平临界值）

Fig. 1　Anomalies of the winter temperature in China from 1951 to 2011

(dashed line: moving t-test statistic value;

straight dotted line: 0.01 significant level critical value)

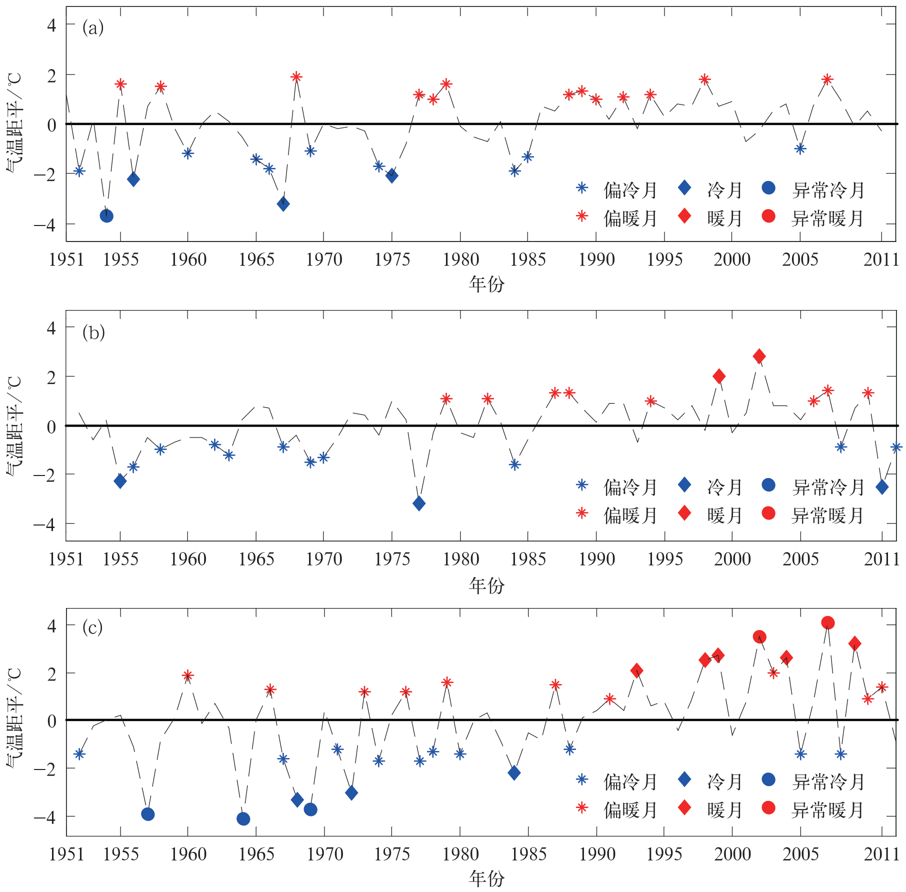

图 2　1951—2012 年全国平均冬季 12 月(a)、1 月(b)、2 月(c)气温距平演变

Fig. 2　Anomalies of the temperature in December(a),

January(b) and February(c) over China

2.2 影响冬季气温异常关键因子的年代际变化

我国冬季气温具有非常显著的年代际变化特征，影响冬季气温异常的关键因子是否也具有类似的年代际变化特征值得探讨。首先，我国冬季冷暖变化与欧亚地区的大气环流型密切相关。1951—1985年冷期的500 hPa高度距平场(图3a)显示欧亚地区呈北高南低的距平分布，大西洋—西欧—乌拉尔山至东亚北部地区为“＋－＋－”的典型欧亚型(EU)波列分布，乌拉尔山高压脊强且东亚大槽较深，东亚高纬度地区偏北气流较强，盛行经向环流，冷空气活动较强，东亚冬季风偏强，同时西太平洋副热带高压偏弱，这种环流配置有利于冷空气南下入侵我国，我国冬季容易发生寒潮或大范围持续偏冷的情况。1986—2011年暖期的500 hPa高度距平场(图3b)与冷期(图3a)的环流型相反，大西洋至东亚为“－＋－＋”的波列分布，欧亚地区呈北低南高的距平分布，乌拉尔山为负距平区且东亚大槽较浅，东亚西风带盛行纬向环流，冬季风偏弱，不利于冷空气南下影响我国，同时西太平洋副热带高压偏强，有利于我国大部分地区气温偏高。可见，1985年前后的冬季冷期阶段和暖期阶段，欧亚地区大气环流型基本呈相反的分布特征。

由1951—2011年冬季60°～70°E经度范围内500 hPa位势高度距平随纬度的时间变化(图4)可

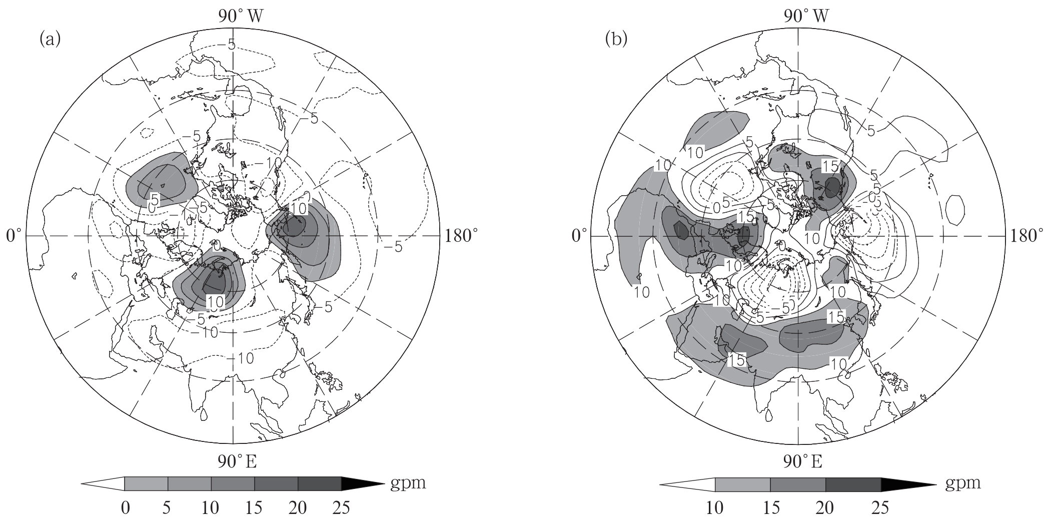

图3　冷期(a)和暖期(b)冬季500 hPa位势高度场距平

Fig.3　Average anomalies of geo-potential height at 500 hPa during cold episodes(a) and warm episodes(b) in winter

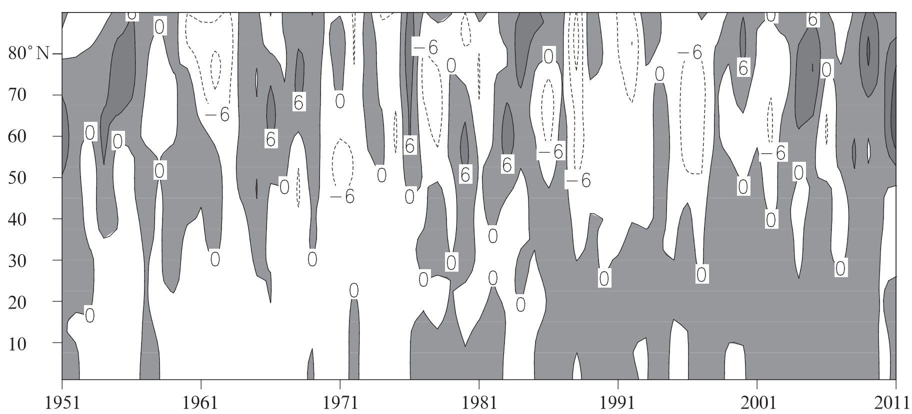

图4　1951—2011年冬季60°—70°E区域平均500 hPa位势高度距平的时间-纬度剖面图(单位：dagpm)

Fig.4　Latitude-time section of 60°—70°E average anomalies at 500 hPa in winter from 1951 to 2011(unit：dagpm)

以看出，冷期（1951—1985 年）500 hPa 高度场从赤道到 40°N 附近地区持续为负距平，40°N 以北的中高纬度地区多为正距平；表明乌拉尔山地区高度场距平呈北高南低的分布，脊强槽深，有利于我国大部地区气温偏低。暖期（1986—2011 年）500 hPa 高度场在 40°N 以南的中低纬度地区为正距平，中高纬度地区多为负距平，乌拉尔山地区高度场距平呈北低南高的分布，弱脊浅槽，有利于我国大部地区气温偏高。

进一步分析影响我国冬季气温关键因子的指数累积距平演变（图 5）可知，这些关键影响因子也发生了显著的年代际变化。由图 5 可知，西伯利亚高压从 20 世纪 50—60 年代末期持续增强，70 年代开始持续减弱，直至 21 世纪进入平稳期；而冬季风指数显示从 20 世纪 50 年代持续增强至 80 年代初，然后持续减弱至 21 世纪初；AO 的年代际变化与西伯利亚高压和冬季风指数变化有所不同，20 世纪 50—80 年代末期有准 10 年左右的周期振荡，但从 20 世纪 90 年代开始至 21 世纪持续向正位相转换。西伯利亚高压、冬季风指数和 AO 3 个影响因子的年代际变化与我国冬季气温的年代际变化具有较好的一致性。图 5 还反映了中低纬度大气环流因子的年代际变化，西太平洋副热带高压（以下简称副高）面积和强度以及青藏高原高度场（以下简称高原高度场）大约在 1976 年前后发生了从负位相到正位相的突变。由图 5 可以看出，Niño3 区海温和 9 月北极海冰都发生了明显的年代际变化。Niño3 区海温突变时间为 1976 年和 2008 年，海温指数经历了降低、升高、又在波动中降低的过程。9 月北极海冰在 20 世纪 80 年代之前累积距平持续增加；1982 年开始累积距平值出现转折性下降，表明海冰明显减少，尤其在 2004 年之后累积距平直线下降。由图 5 也可以看出，热带印度洋全区一致海温模态（IOBW）在 20 世纪 50—70 年代均处于负位相，1976 年开始经历了近 10 年的冷暖交替变化，80 年代中期进入暖位相，气候突变点为 1986 年。而黑潮海温与 IOBW 海温变化相似，1986 年有短暂回升，之后在 20 世纪 90 年代中期进入正位相。

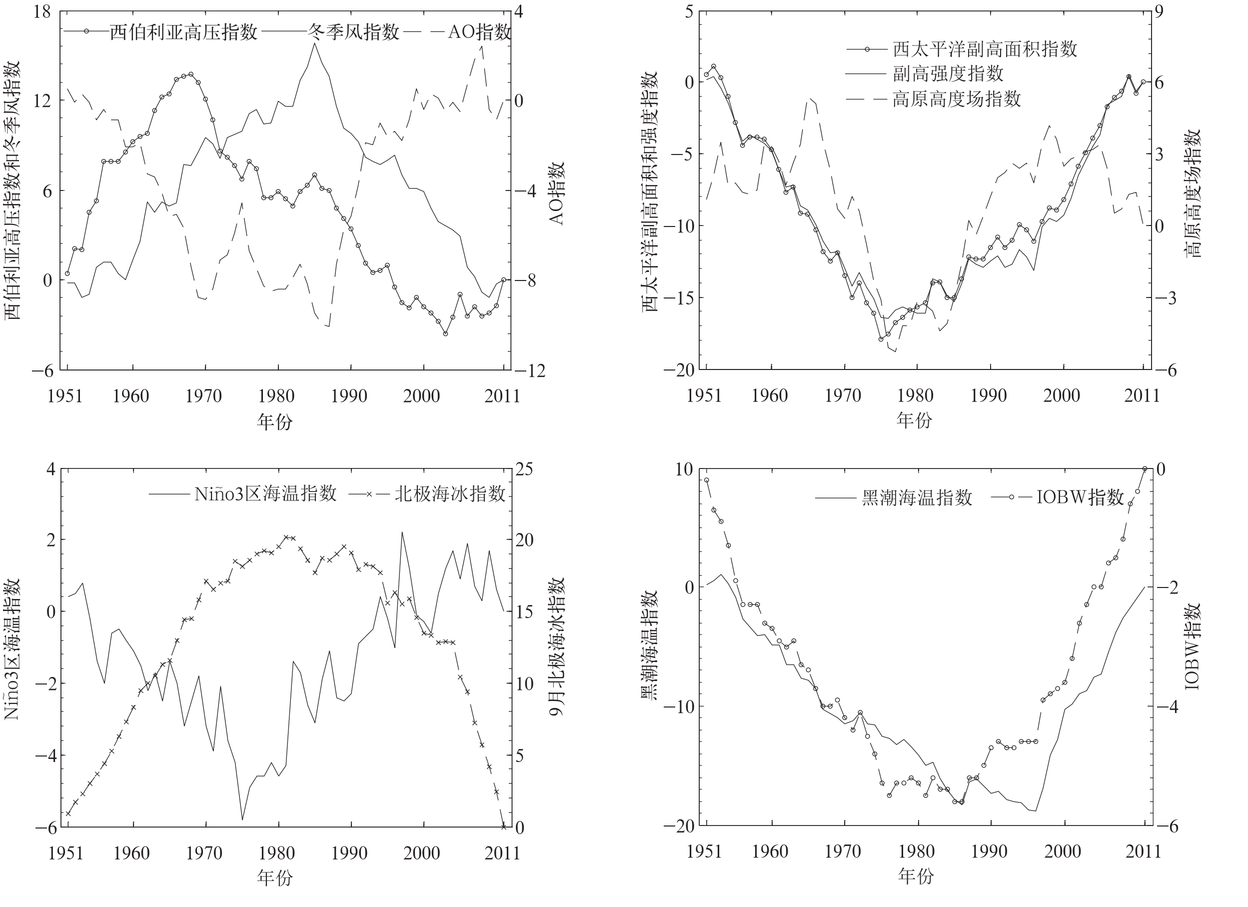

图 5　我国冬季气温的关键影响因子累积距平曲线

Fig. 5　Cumulative anomalies of the key affecting factors of winter temperature in China

综上所述,影响我国冬季气温异常的关键因子发生了显著的年代际变化,多数因子的年代际变化超前于冬季气温变化。其中 Niño3 区的海温距平的年代际变化超前于冬季气温变化大约有 10 年,9 月北极海冰距平超前大约 3～4 年,西太平洋副高强度、面积和高原高度场超前大约 8～10 年,而西伯利亚高压、冬季风指数、AO 和 IOBW 超前大约 1～2 年,而黑潮海温的年代际变化较冬季气温变化略有滞后。需要指出的是,这些影响因子年代际转型的时间与我国冬季气温的年代际转型时间并不完全一致,多数外强迫信号和大气环流因子的转型时间超前,影响因子与我国冬季气温的年代际变化之间必然存在某种内在的物理联系,正是这些影响因子年代际和年际变化的影响决定了我国冬季气温年代际和年际变化特征,其机制有待深入探究。

3 冬季气温与影响因子关系的年代际变化

3.1 时间域的年代际变化特征

从全时段(1951—2011 年)、冷期(1951—1985 年)和暖期(1986—2011 年)我国冬季气温与前期和同期的大气外强迫因子、大气环流因子的相关系数(表 1)发现,海温指数和北极海冰指数与我国冬季气温相关关系发生了显著的年代际变化,尤其是冬季黑潮区海温和 IOBW 指数与我国冬季气温相关关系在冷期比暖期更为显著,但 9 月北极海冰与我国冬季气温相关关系在暖期比冷期更为显著。即我国冬季气温与同期黑潮区海温、赤道印度洋海温的相关关系发生了年代际减弱、而与 9 月北极海冰指数的相关关系发生了年代际增强的特征。同期大气环流因子对我国冬季气温不同时段的影响不完全相同,冬季风指数、西伯利亚高压以及西太平洋副高面积指数等在整个时段均显著影响我国冬季气温,但是它们在暖期中与冬季气温的相关关系较冷期更为显著,它们与我国冬季气温的关系发生了年代际的增强。高原高度场指数在整个时段均显著影响我国冬季气温,但它在冷期与冬季气温的相关更为显著,说明青藏高原的热力作用与我国冬季气温的关系出现年代际减弱的趋势。另外,AO 指数在全时段与冬季气温相关不显著,但是分阶段之后(冷期和暖期)相关关系略有增强。AO 指数在全时段与我国冬季气温相关不显著的主要原因是它对全国不同区域冬季气温的影响不同所致。

表 1 大气外强迫因子和环流因子与我国冬季气温的相关系数

Table 1 The correlation coefficients of winter temperature to external forcing and circulation factors

因子	时间	秋季	冬季
黑潮海温	全时段	0.10	0.36*
	冷期	0.20	0.53*
	暖期	0.04	0.12
IOBW	全时段	0.10	0.28*
	冷期	0.15	0.33*
	暖期	0.20	0.18
北极海冰	全时段	0.33*(9月)	0.20
	冷期	0.03(9月)	0.06
	暖期	0.61*(9月)	0.38*
冬季风	全时段	−0.30*	−0.58*
	冷期	−0.15	−0.52*
	暖期	0.08	−0.67*
西伯利亚高压	全时段	−0.07	−0.59*
	冷期	−0.24	−0.50*
	暖期	0.20	−0.76*
副高面积	全时段	0.21	0.34*
	冷期	0.29	0.31*
	暖期	0.10	0.40*
高原高度场	全时段	0.15	0.49*
	冷期	0.19	0.55*
	暖期	0.07	0.37
AO	全时段	−0.04	0.19
	冷期	−0.03	0.16
	暖期	−0.07	0.19

注:*表示相关系数达到 0.05 显著性水平。

3.2　空间域的年代际变化特征

在我国冬季气温经历了冷暖期交替之后，冬季气温与其影响因子之间相关关系不仅在时间尺度上发生了改变，在空间分布上也发生了变化。图 6 给出了冬季风指数、冬季 AO 指数、9 月北极海冰指数与冷期和暖期冬季气温的相关系数分布图。冷期冬季风指数与我国气温在大部分地区呈显著负相关，高相关区中心位于东北南部、华南大部；而暖期两者显著相关的区域增加，尤其是新疆和东北大部相关度增加。这说明冬季风在冷期和暖期对全国冬季气温影响范围和强度的显著性发生了改变。AO 与我国冬季气温分别在冷期和暖期的相关关系的空间分布变化显示，AO 由负位相转正位相过程中，在东北、华北和新疆地区的正相关区域变化不大，但与我国中部至南部地区呈负相关，尤其与云南地区的负相关显著增强。该现象值得进一步研究。而 9 月北极海冰和我国冬季气温相关在冷期并不显著，在进入暖期后则呈显著正相关，尤其是西北东部到西南地区相关尤为显著。

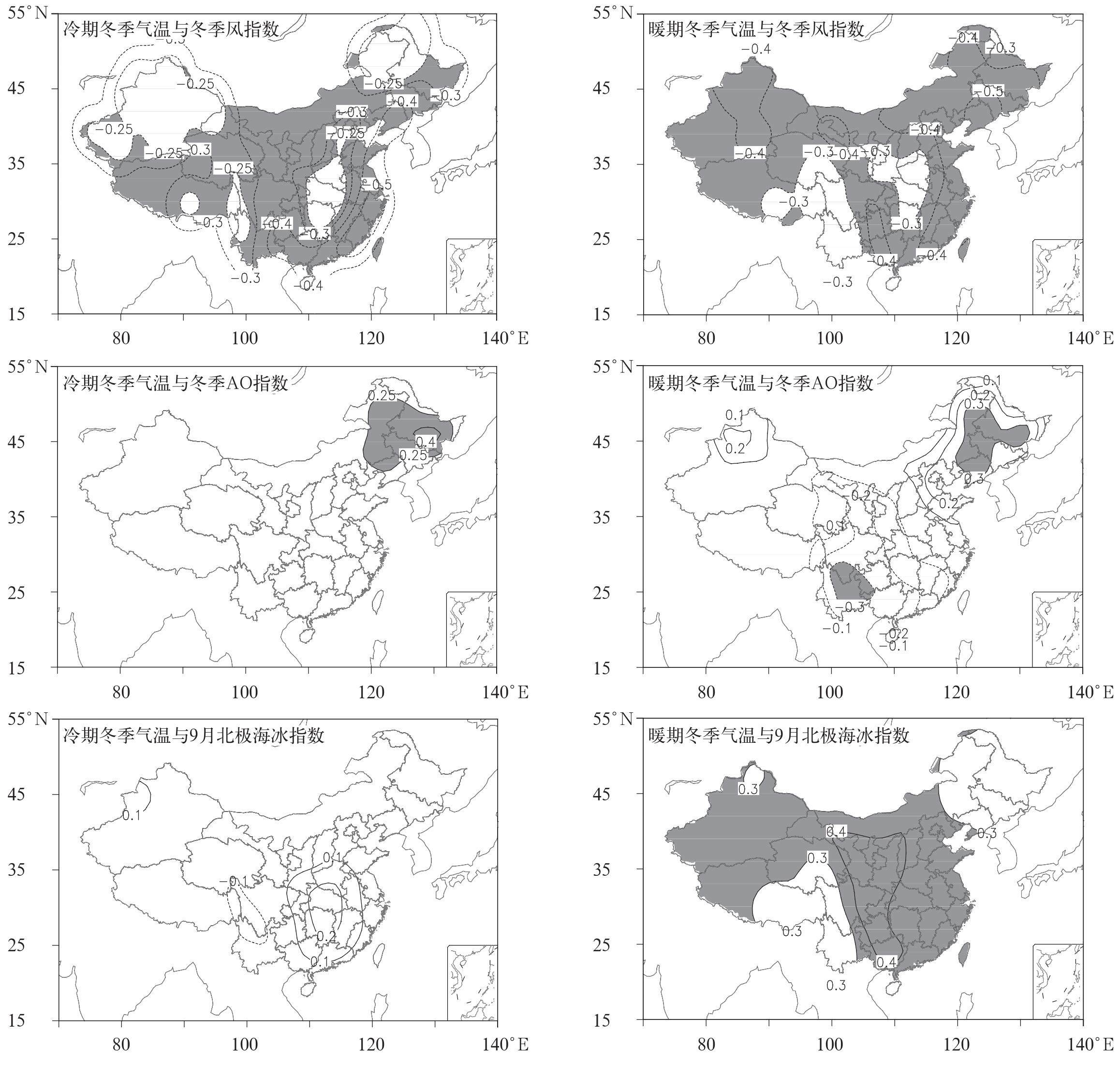

图 6　我国冬季气温与关键影响因子相关分布(阴影表示达到 0.05 显著性水平区域)

Fig.6　The correlation coefficients between winter temperature and key affecting factors (shaded areas denote passing the test of 0.05 level)

不仅我国冬季气温异常与影响因子的关系发生了年代际变化，同时影响因子之间的关系也发生了年代际变化。从东亚冬季风时间序列与同期全球海温的相关系数分布(图 7)可以看出，冷期(图 7a)东

亚冬季风与中东太平洋、印度洋以及西太平洋暖池和日本海等海区呈负相关，与赤道中太平洋南北两侧中纬度海区呈正相关，这种相关的空间分布是典型的ENSO分布型。也就是在La Niña年的冬季东亚冬季风较强，相应地，我国冬季气温偏低，El Niño年的冬季则相反。而暖期(图7b)冬季风指数与全球海区几乎没有达到显著性水平的相关区域，说明冬季风指数与冬季海温相关关系呈现出显著的年代际减弱特征。

由以上分析可见，不仅我国冬季气温异常与影响因子的时空关系发生了显著的年代际变化，而且影响因子之间的相互关系也发生了显著的年代际变化。

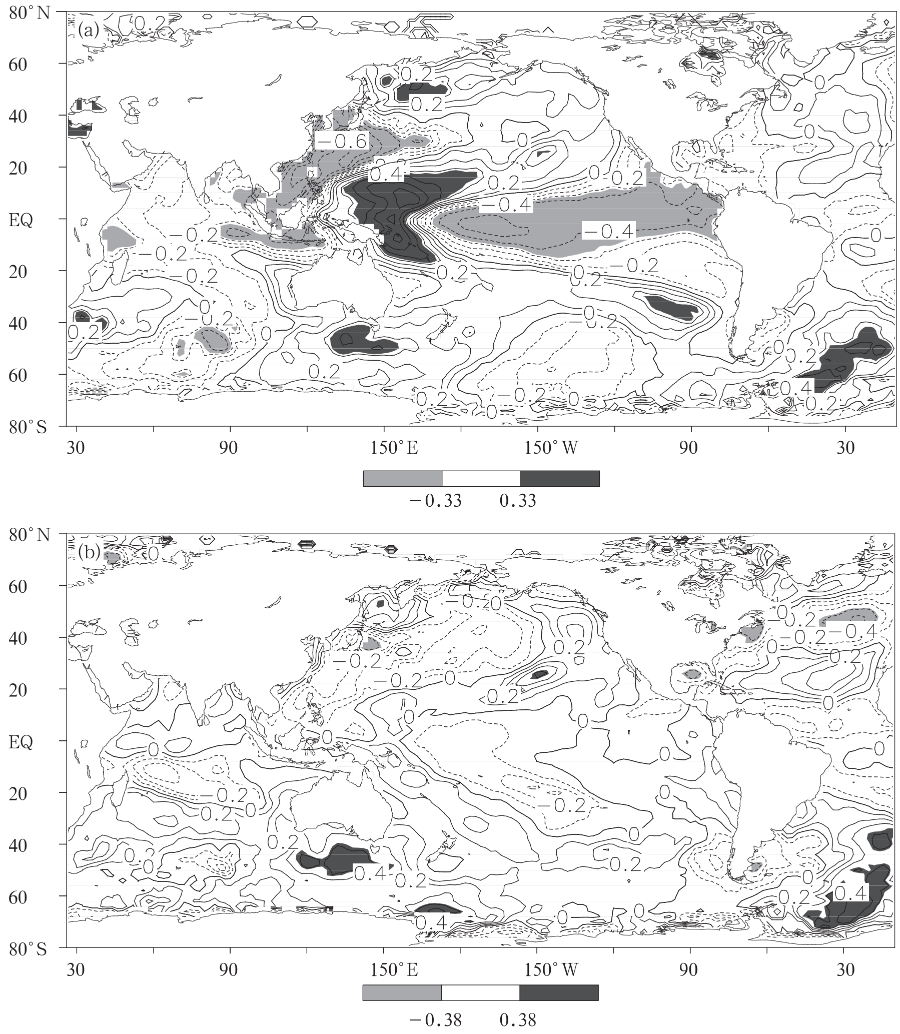

图7 冷期(a)和暖期(b)冬季风指数与同期海温相关图

(阴影区相关系数达到0.05显著性水平)

Fig.7 The correlation coefficients between winter monsoon index and simultaneous SSTs in cold episodes(a) and warm episodes(b)

(shaded areas denote passing the test of 0.05 level)

4 冬季气温预测方法的探讨

统计预测方法依然是目前短期气候预测业务的主要方法之一，但该方法的缺陷是利用历史资料建立的统计预测模型有很高的历史回报拟合率，但在实际气候预测时技巧比较低。主要因为预测对象和影响因子之间虽然具有显著的统计关系，但缺乏明确的物理联系，造成所建立的预测模型不能正确反映两者真实的物理机制；另外，影响因子与预测对象的关系已经发生了变化，而统计预测模型没有正确反映两者之间变化的关系，从而导致统计预测结果

不正确。

前面分析指出,我国冬季气温及其影响因子具有显著的年代际变化特征,冬季气温与关键影响因子的关系以及不同影响因子之间的时空关系也出现了显著的年代际变化。正确的预测方法和策略应该是在同样的年代际背景下,利用预测对象与预测因子的关系建立预测模型,以确保预测技巧的稳定性和有效性。

为了证明这种策略的有效性,根据表 1 给出的全时段、冷期和暖期的前期外强迫因子和同期大气环流因子与我国冬季气温的相关关系,分别建立全时段、冷期和暖期的冬季气温回归模型。该模型中使用了同期外强迫因子和大气环流因子,并不具有实际预测的能力,但可用于比较 3 种不同建模策略的差异。为直观比较各因子对冬季气温的贡献大小,对冬季气温和影响因子序列分别进行标准化处理。

试验 1:利用与冬季气温在全时段显著相关的外强迫因子和大气环流因子以及多元线性回归方法,进行冬季气温(Y)的拟合试验,线性回归方程为

$$Y = 0.023X_1 - 0.048X_2 + 0.425X_3 - 0.647X_4 + 0.017X_5 - 0.106X_6 + 0.471X_7 - 0.327。\quad (1)$$

式(1)中,X_1 表示冬季黑潮海温指数,X_2 表示 IOBW 指数,X_3 表示 9 月北极海冰指数,X_4 表示西伯利亚高压,X_5 表示冬季风指数,X_6 表示冬季西太平洋副高面积指数,X_7 表示冬季高原高度场指数的贡献。可以看出,在全时段中北极海冰、西伯利亚高压、高原高度场的贡献较大。

试验 2:利用与冬季气温在冷期显著相关的外强迫因子和大气环流因子以及多元线性回归方法,进行冬季气温(Y)的拟合试验,线性回归方程为

$$Y = -0.111X_1 - 0.099X_2 - 0.592X_4 - 0.045X_5 + 0.102X_6 + 0.367X_7 - 0.447。\quad (2)$$

式(2)中,X_1 表示冬季黑潮海温指数,X_2 表示 IOBW 指数,X_4 表示西伯利亚高压指数,X_5 表示冬季风指数,X_6 表示冬季西太平洋副高面积指数,X_7 表示冬季高原高度场指数。可以看出,在冷期西伯利亚高压和高原高度场的贡献较大。

试验 3:利用与冬季气温在暖期显著相关的外强迫因子和大气环流因子以及多元线性回归方法,进行冬季气温(Y)的拟合试验,线性回归方程为

$$Y = 0.117X_3 - 0.615X_4 + 0.255X_5 + 0.261X_6 + 0.567。\quad (3)$$

式(3)中,X_3 表示 9 月北极海冰指数,X_4 表示西伯利亚高压指数,X_5 表示冬季风指数,X_6 表示冬季西太平洋副高面积指数。根据回归系数可见,暖期北极海冰、西伯利亚高压、冬季风、西太平洋副高的贡献较为均衡,其中西伯利亚高压的影响更突出些。在不同时段,主要影响因子有所不同,其原因也值得进一步分析。

图 8 给出了 3 个模拟试验的拟合气温与冬季气温时间序列。试验1中,全时段拟合的冬季气温与观

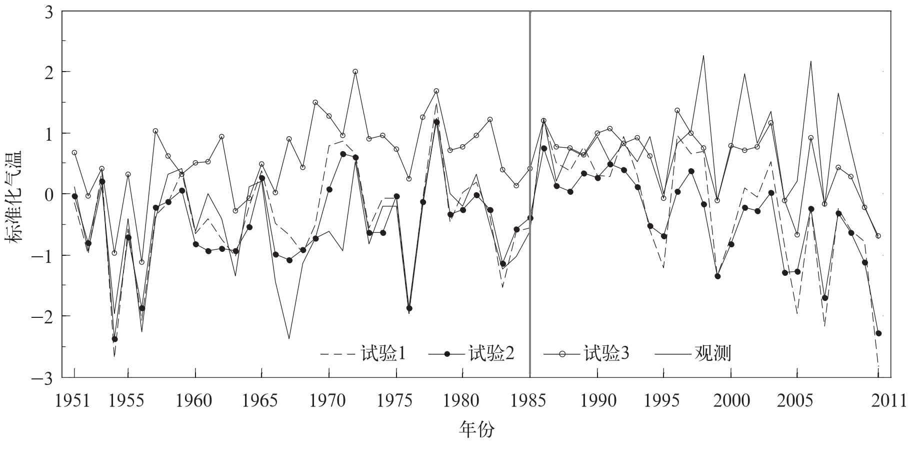

图 8　试验 1 模型拟合、试验 2 模型拟合、试验 3 模型拟合和观测的冬季气温标准化时间序列

Fig. 8　The hindcast winter temperature by Test 1, Test 2, Test 3 and the time series of standardized observed temperature

测值在冷期的相关系数为0.77,均方根误差为0.58;在暖期的相关系数为0.62,均方根误差为1.27。试验2中,冷期显著因子拟合的冬季气温与观测值在冷期的相关系数为0.80,均方根误差为0.50;在暖期的相关系数为0.60,均方根误差为1.32。试验3中,暖期显著因子拟合的冬季气温,与观测值在冷期的相关系数为0.56,均方根误差为1.35;在暖期的相关系数为0.66,均方根误差为0.60。

可见,利用冷期影响因子建立的模型拟合冷期气温时,均方根误差最小,相关系数最大,拟合效果最佳,但该模型拟合暖期气温效果最差。利用暖期的影响因子建立模型拟合暖期气温时,均方根误差最小,相关系数最大,拟合效果最佳,而该模型用于冷期的气温拟合效果最差。全时段模型对冷期的拟合效果较冷期因子建立的模型拟合差,对暖期的拟合效果较暖期因子建立的模型拟合差。3组拟合试验说明,不能笼统地用全时段影响因子建立统计预测模型,更不能用冷期的影响因子建模来预测暖期的冬季气温,或用暖期的影响因子建模来预测冷期的冬季气温。不同年代际背景下应选取不同的关键影响因子对气温进行预测,这样才可能提高预测准确率。

5 结论和讨论

本文分析了我国冬季气温及其影响因子的年代际变化特征,揭示了多个影响因子与我国冬季气温时空关系发生了显著的年代际变化,提出采用正确的建模策略才能够有效地利用统计预测方法提高冬季气温的预测技巧。主要结论如下:

1)我国冬季气温及其关键影响因子均具有显著的年代际变化特征。1985年冬季之前为冷期,之后为暖期,其中2004—2011年冬季暖的范围和程度明显减弱。影响我国冬季温度异常的关键因子也具有显著的年代际变化,且大多超前于我国冬季气温的变化。

2)我国冬季气温及其影响因子的时空关系发生了年代际变化,冬季气温与热带印度洋、黑潮海温、高原高度场的相关关系发生了显著的年代际减弱,与9月北极海冰指数、冬季风指数、西伯利亚高压以及西太平洋副高面积指数的相关关系发生了年代际增强;影响因子之间的关系也发生了年代际变化,冬季风指数与冬季海温的关系也发生了显著的年代际变化,呈减弱趋势。

3)针对我国冬季气温与其影响因子的时空关系发生了年代际变化的事实,提出了考虑冷期和暖期不同影响因子对冬季气温的影响,分时段建立预测模型的策略。这样可以适应冬季气温及其影响因子关系发生年代际变化的事实,对提高预测准确率极其重要。

本文仅仅揭示了我国冬季气温与影响因子及其关系年代际变化的一些基本事实,对于我国冬季气温和影响因子关系年代际变化的机理以及对冬季气温预测方法的应用还需要深入研究。本文提出了分时段建立统计预测模型的策略,但在使用统计预测模型对未来状态进行预测时,要求预测时段与建立统计模型所使用的资料序列处于同一个年代际变化背景下,即假设模型结构在建模和预测期间保持不变,若遇到预测时段内发生年代际突变时仍存在不确定性,需要进一步对年代际变化趋势进行预测。关于预报对象和预报因子之间年际关系的年代际变化机理和预测应用问题还需深入研究。

参考文献

[1] 王绍武,叶瑾琳,龚道溢,等.近百年中国气温序列的建立.应用气象学报,1998,9(4):392-401.

[2] 陈隆勋,邵永宁,张清芬,等.近四十年我国气候变化的初步分析.应用气象学报,1991,2(2):164-174.

[3] 郭其蕴.东亚冬季风的变化与中国气温异常的关系.应用气象学报,1994,5(2):218-225.

[4] 刘实,布和朝鲁,陶诗言,等.东亚冬季风强度的统计预测方法研究.大气科学,2010,34(1):35-44.

[5] 孙林海,赵振国.我国暖冬气候及其成因分析.气象,2005,30(12):57-60.

[6] 汤懋苍,安林.高原地区月平均海平面气压图的绘制方法及初步分析结果.高原气象,1985,4(4):372-381.

[7] Li Chongyin. Interaction between anomalous winter monsoon in East Asia and El Nino events. *Adv Atmos Sci*,1990,7(1):36-46.

[8] Zhang R,Sumi A,Kimoto M. Impact of El Niño on the East Asian monsoon:A diagnostic study of the '86/87 and '91/92 events. *J Meteorol Soc Japan*,1996,74(1):49-62.

[9] 武炳义,黄荣辉.冬季北极喀拉海巴伦支海海冰面积变化对东亚冬季风的影响.大气科学,1999,23(3):267-275.

[10] 谭言科，张人禾，何金海，等. 热带印度洋海温的年际变化与ENSO. 气象学报，2004，62(6)：831-840.

[11] 朱伟军，孙照渤. 冬季黑潮区域海温异常对北太平洋风暴轴的影响. 应用气象学报，2000，11(2)：145-153.

[12] Wang L，Huang R H，Gu L，et al. Interdecadal variations of the East Asian winter monsoon and their association with quasi-stationary planetary wave activity. *J Climate*，2009，22(18)：4860-4872.

[13] Jeong J H，Ou T，Linderholm H W，et al. Recent recovery of the Siberian High intensity. *J Geophys Res*，2011，116，D23102，DOI：10.1029/2011JD015904.

[14] Watanabe M，Nitta T. Decadal changes in the atmosphere circulation and associated surface climate variation in the Northern Hemisphere winter. *J Climate*，1999，12(2)：494-510.

[15] 武炳义，高登义，黄荣辉. 冬春季节北极海冰的年际和年代际变化. 气候与环境研究，2000，5(3)：249-258.

[16] 朱亚芬，钱维宏. 全球海温异常的年代际变化. 海洋预报，1998，15(4)：1-7.

[17] Kug J S，Jin F F，An S I. Two types of El Nino events：Cold tongue El Nino and warm pool El Nino. *J Climate*，2009，22(6)：1499-1515.

[18] 晏红明，肖子牛，谢应齐. 近 50 年热带印度洋海温距平场的时空特征分析. 气候与环境研究，2000，5(2)：180-188.

[19] 赵斐苗，朱鑫君，李飞，等. 黑潮区域海温异常与我国冬季气温和降水的关系. 气象与环境科学，2007，30：28-31.

[20] 王会军，贺圣平. ENSO 和东亚冬季风之关系在 20 世纪 70 年代中期之后的减弱. 科学通报，2012，57(19)：1713-1718.

[21] Kalnay E，Kanamitsu M，Kistler R，et al. The NCEP/NCAR 40-year reanalysis project. *Bull Amer Meteor Soc*，1996，77(3)：437-471.

[22] Allan R，Ansell T. A new globally complete monthly historical gridded mean sea level pressure dataset (HadSLP2)：1850—2004. *J Climate*，2006，19(22)：5816-5842.

[23] Smith T M，Reynolds R W，Peterson T C，et al. Improvements to NOAA's historical merged land-ocean surface temperature analysis (1880—2006). *J Climate*，2008，21：2283-2296.

[24] Gong D Y，Ho C H. The Siberian High and climate change over middle to high latitude Asia. *Theor Appl Climatol*，2002，72(1-2)：1-9.

[25] 刘芸芸，李维京，艾𬟽秀，等. 月尺度西太平洋副热带高压指数的重建与应用. 应用气象学报，2012，23(4)：414-423.

[26] 白虎志，马振锋，董文杰. 青藏高原地区季风特征及与我国气候异常的联系. 应用气象学报，2005，16(4)：484-491.

[27] 朱伟军，孙照渤，彭加毅. 冬季太平洋 SST 异常对风暴轴和急流的影响. 南京气象学院学报，1999，22(4)：575-581.

[28] 武炳义，苏京志，张人禾. 秋-冬季节北极海冰对冬季西伯利亚高压的影响. 科学通报，2011，56(27)：2335-2343.

[29] 秦大河. 中国气候与环境演变：2012 第一卷科学基础. 北京：气象出版社，2012.

[30] 陈隆勋，周秀骥，李维亮，等. 中国近 80 年来气候变化特征及其形成机制. 气象学报，2004，62(5)：635-646.

[31] 丁一汇，张莉. 青藏高原与中国其他地区气候突变时间的比较. 大气科学，2008，32(4)：794-805.

Inter-decadal Variability of the Relationship Between Winter Temperature in China and Its Impact Factors

Li Weijing[1)] Li Yi[2)] Chen Lijuan[1)] Zhao Zhenguo[1)]

[1)] (*Laboratory for Climate Studies, National Climate Center, CMA, Beijing* 100081)

[2)] (*Chinese Academy of Meteorological Sciences, Beijing* 100081)

Abstract

The inter-decadal variation characteristics of winter temperature in China and its key impact factors are analyzed by using monthly temperature data of 160 stations in China, NCEP/NACR reanalysis data, extended reconstructed sea surface temperatures data, and Arctic sea ice extent data from 1951 to 2012, focusing on the inter-decadal changes of the relationship between key influencing factors and winter temperature in China. Results show that the winter temperature in China before 1985 is in a cold period, and then a warm period follows. A significant inter-decadal variability has occurred for winter temperature anomalies. The scope and intensity of warming tendency has weakened significantly from 2004 to 2011.

The main diagnostic analysis conclusions are summarized as follows. The majority of impact factors of winter temperature anomalies in China shows significant inter-decadal shift from 1970s to 1980s, most of which changes ahead of that of winter temperatures in China, such as Arctic Oscillation (AO), the East Asian winter monsoon (EAWM), Western Pacific subtropical high (WPSN), Arctic sea ice cover in September, and Niño3 SST index. But the inter-decadal variability of Siberian High (SH) and the basin-wide SSTA variation in the tropical Indian Ocean (IOBW) has the same pace with that of the winter temperature. The inter-decadal variability of relationship between winter temperature and its impact factors have changed on temporal and spatial scales. On temporal scale, the relationship between the winter temperature and IOBW index has weakened significantly from cold to warm period. But the influences of EAWM index, SH index and the WPSH area index on winter temperature have strengthened. On spatial scales, distributions of correlations between winter temperatures and affecting factors have changed from cold to warm period. The high correlation coefficient regions between EAWM and winter temperature have enlarged significantly. The correlation coefficient between AO index and winter temperature is negative in central-southern China in warm period. The inter-decadal variability of relationship between the impact factors has changed, the relationship between EAWM index and tropical SSTA in winter are significantly weakened from cold to warm period.

Based on the basic facts of inter-decadal variations, a multi-factor regression prediction model of winter temperature can be established respectively in cold and warm period. This regression prediction model can reflect inter-decadal characteristics of relationship between the winter temperature and its impact factors. Such strategy may keep the stability and effectiveness of the prediction skill for winter temperature in China.

Key words: winter temperature; impact factors; East Asian winter monsoon; inter-decadal variability

ATMOSPHERIC AND OCEANIC SCIENCE LETTERS, 2013, VOL. 6, NO. 5, 332–336

A New Statistical Downscaling Scheme for Predicting Winter Precipitation in China

LIU Ying[1,2], FAN Ke[2], and YAN Yu-Ping[1]

[1] *Laboratory for Climate Studies, National Climate Center, China Meteorological Administration, Beijing 100081, China*
[2] *Institute of Atmospheric Physics, Chinese Academy of Sciences, Beijing 100029, China*

Received 17 January 2013; revised 30 January 2013; accepted 1 February 2013; published 16 September 2013

Abstract An effective statistical downscaling scheme was developed on the basis of singular value decomposition to predict boreal winter (December-January-February) precipitation over China. The variable geopotential height at 500 hPa (GH5) over East Asia, which was obtained from National Centers for Environmental Prediction's Coupled Forecast System (NCEP CFS), was used as one predictor for the scheme. The preceding sea ice concentration (SIC) signal obtained from observed data over high latitudes of the Northern Hemisphere was chosen as an additional predictor. This downscaling scheme showed significantly improvement in predictability over the original CFS general circulation model (GCM) output in cross validation. The multi-year average spatial anomaly correlation coefficient increased from –0.03 to 0.31, and the downscaling temporal root-mean-square-error (RMSE) decreased significantly over that of the original CFS GCM for most China stations. Furthermore, large precipitation anomaly centers were reproduced with greater accuracy in the downscaling scheme than those in the original CFS GCM, and the anomaly correlation coefficient between the observation and downscaling results reached ~ 0.6 in the winter of 2008.

Keywords: statistical downscaling, winter precipitation, China, Coupled Forecast System

Citation: Liu, Y., K. Fan, and Y.-P. Yan, 2013: A new statistical downscaling scheme for predicting winter precipitation in China, **6**, 332–336, doi:10.3878/j.issn.1674-2834.13.0008.

1 Introduction

Climate change is critical in the fields of industry and agriculture, particularly for the production of food and energy and water resources, which are directly related to the sustainable development of society. With consideration of climate change, seasonal prediction and improvements in accuracy have become important scientific research targets.

The East Asian Winter Monsoon (EAWM), prevalent over China during boreal winter (December-January-February), causes cold waves, gales, snowstorms, and other disastrous weather-related events. For example, central and southern China experienced an anomalously heavy snowfall during the winter of 2007–2008, and northern China endured a persistent storm during the winter of 2009. Such winter disasters have caused substantial losses in lives and property. Many researches have focused on anomalous winter weather and climate events (Tao and Wei, 2008; Gao, 2009; Sun et al., 2009; Wang et al., 2011). The study of Wang (2003a, b) has shown that winter anomalies in 2002 and 2003 at high latitudes in the Northern Hemisphere are mainly attributed to interannual variability in atmospheric circulation anomalies, and the changes in the Ural and North Pacific blocking high led to variability of the atmospheric systems over East Asia (Geng et al., 2001). Considering the influence of these large-scale variables, heavy winter snow activity in northeastern China and North China's surface temperature can be predicted effectively by statistical models with a year-to-year increment prediction approach (Fan, 2011; Fan and Tian, 2012). Hindcast results of the nine-level atmospheric general circulation model developed at the Institute of Atmospheric Physics (IAP9L-AGCM) indicate that the predictability of winter precipitation is relatively small over China (Lang et al., 2003). The prediction capability of region-average winter precipitation in eastern China can be improved by using prediction schemes established on the basis of dynamical and statistical information (Lang, 2011). Furthermore, Wang and Fan (2009) indicated that consideration of both GCM tropical information and the previous signal can increase the summer rainfall predictability over East Asia.

Several studies have focused on the prediction of region-average winter precipitation. Even though some statistical downscaling schemes were developed for precipitation over stations (Kang et al., 2011; Chen et al., 2012), few compared model prediction with data from 160 stations in China. Therefore, large-scale variables are used in this study to predict the winter precipitation over these stations; similar statistical downscaling research in spring and autumn precipitation over China stations has been reported by Liu and Fan (2012a, b). The synchronous predictor from the GCM prediction and preceding signal from observation are considered simultaneously. The chosen current predictor is accurate and closely related to China winter precipitation, while the previous predictor represents the delayed effect of climate on subsequent precipitation.

2 Data and method

2.1 Data

The GCM hindcast was used from the Coupled Fore-

Corresponding author: YAN Yu-Ping, yanyp@cma.gov.cn

cast System (CFS) of the National Centers for Environmental Prediction (NCEP). CFS is a fully coupled dynamical prediction system that has been an important component of the monthly to seasonal prediction system of the NCEP's Climate Prediction Center (CPC) since it became operational in 2004 (Saha et al., 2006). Here, geopotential height at 500 hPa (GH5) during 1982–2012 winters was used to define the current predictor. To facilitate the assurance and effectiveness of winter simulations, the CFS GCM datasets used in this study were initialized on 1 October. The joint reanalysis data of the NCEP and National Centers for Atmospheric Research (Kalnay et al., 1996) were compiled on a 2.5°×2.5° regular latitude-longitude grid. We used the GH5 in the reanalysis dataset to estimate the prediction skill of CFS GCM.

The sea ice concentration (SIC) data used in this study as the preceding predictor in the downscaling scheme covered the period of 1982–2012 and used Met Office Hadley Centre's sea ice and sea surface temperature data set version 1 (HadISST1) (Rayner et al., 2003), which includes globally complete monthly fields on a 1°×1° latitude-longitude grid. Monthly precipitation at the 160 stations for 1982–2011 was obtained from the National Climate Center of the China Meteorological Administration. This long-term monthly precipitation dataset was used to establish and validate the downscaling model. The present study used winter precipitation data at 160 stations over China as the predictand.

2.2 Method

Because the length of the CFS GCM data period is limited, a method known as one-year-out cross validation was used. One year of predictor and predict data are excluded from the respective data set, and the data from the residual years were used in the training period. Next, a prediction based on the training period was made for the remaining years (Michaelsen, 1987). This cross-validated procedure was performed 30 times to produce precipitation predictions from 1982 to 2011 for the validation. Finally, this downscaling method was conducted for real-time prediction of winter precipitation in 2012.

The singular value decomposition (SVD) of the cross-covariance matrix (Bretherton et al., 1992; Uvo et al., 2001), which statistically describes the link between precipitation and its predictors, was used to downscale the China winter precipitation. We chose this linear method to objectively determine coupled anomaly patterns in the predictor and predict and fields. Before SVD analysis was performed, the predictors and predictand were reconstructed by using the respective empirical orthogonal functions (EOFs) and principal components to filter the noise during the training period. The specific procedure for the downscaling method can be found in Liu and Fan (2012a). The criterion of the retained EOF modes refers to Kaiser's rule (Wilks, 2006):

$$\lambda_m > \frac{T}{K}\sum_{k=1}^{K} s_{k,k} \ , \tag{1}$$

where λ_m represents the mth retained eigenvalue of EOF (m=1,…,K, K is the total number of the eigenvalue of EOF), $s_{k,k}$ is the variance of the kth element of the variable field, and T is a threshold parameter, here T=0.7 (Jolliffe, 1972, 2002). On the basis of Eq. (1), the first nine, two, and three EOF modes were retained for the predictand (precipitation), GH5, and SIC, respectively.

In this study, the root-mean-square-error (RMSE) skill score indicated the difference between the RMSE of the original CFS GCM and that of the downscaling models through division of the former output. The formula for the RMSE skill score is

$$\mathrm{RMSE}_{\text{skill score}} = \frac{\mathrm{RMSE}_{\mathrm{GCM}} - \mathrm{RMSE}_{\mathrm{SD}}}{\mathrm{RMSE}_{\mathrm{GCM}}} \times 100\% \ , \tag{2}$$

where $\mathrm{RMSE}_{\mathrm{GCM}}$ and $\mathrm{RMSE}_{\mathrm{SD}}$ indicate the RMSE of the original CFS GCM and downscaling output, respectively. A positive $\mathrm{RMSE}_{\text{skill score}}$ indicated an improved prediction skill.

3 Results

3.1 Predictors

Statistical downscaling used long-term general circulation variables and regional variables to derive a robust relationship between the predictors and the predictand. Local changes in meteorological parameters in mid-latitudes, including precipitation, are mainly controlled by atmospheric circulation (Parker et al., 1994; Steinberger and Gazit-Yaari, 1996). Therefore, the GH5 during the 1982–2012 winters was considered for the 20–60°N, 70–180°E (East Asia) region, which covers Baikal, the western North Pacific, the EAWM, and the Somali jet, among other areas. These related and important atmospheric systems strongly influence the precipitation over China (Chen and Zhao, 2000; Wang, 2001). Moreover, the spatial correlation coefficient of GH5 between the reanalysis and CFS GCM data over this region can reach 0.97.

Summer Arctic sea ice was reduced under the scenario of global warming; this trend became more rapid after the late 1990s (Comiso et al., 2008). Decreases in autumn Arctic sea ice have affected climate variation in winter the Northern Hemisphere atmospheric circulation (Honda et al., 2009). Such recent declines in Arctic sea ice have led to a weakened EAWM system, which has resulted in recent cold and snowy winters (Liu et al., 2012; Ma et al., 2012). A weak EAWM is characterized by southerly wind anomalies, including a weakened Siberian High with warm surface air temperature and increased precipitation over China, and vice versa (Wang and Jiang, 2004; Gao, 2007). Therefore, September-October SIC over the 50°N region poleward during 1982–2012 was selected from observed data as the preceding predictor. Table 1 shows specific characteristics of the two predictors.

Table 1 Description of the predictors used in this study.

Predictors	Period	Datasets	Domains
GH5	1982–2012 winter	CFS	20–60°N, 70–180°E
SIC	1982–2012 Sep-Oct	HadISST1	50–90°N, 0–359°E

3.2 Cross validation and real-time forecast of SD

A downscaling model was established that involved the two aforementioned predictors and validation of the downscaling result compared with the original CFS GCM output was performed. The spatial anomaly correlation coefficient (ACC) between observation and original CFS GCM, or the downscaling result in the cross validation for 1982–2011, is shown in Fig. 1. With regard to the original CFS GCM, the ACC passed the 95% confidence level during 17% years from 1982 to 2011 and more than 66% years for the downscaling ACC in the counterpart. The multi-year average of ACC improved from –0.03 of the original CFS GCM result to 0.31 of the statistical downscaling. Moreover, the multi-year average of the spatial RMSE skill score of winter precipitation over China reached 75.9% (figure not shown). To provide a better understanding, we estimated the improvement of the downscaling scheme over the original CFS result, or the R_{RMSE}, which is defined by the ratio of $\mathrm{RMSE}_{\mathrm{GCM}}$ to the $\mathrm{RMSE}_{\mathrm{SD}}$. Figure 2 shows the spatial pattern of temporal R_{RMSE} during 1982–2011. The downscaling over northern China (i.e., 3–10) performed better than that of southern China (i.e., 1–3). For most stations in China, the R_{RMSE} was larger than 1, with the exception of two stations denoted by yellow points in the figure. This result demonstrates that the value of winter precipitation from downscaling is closer to observation than that of the original CFS GCM.

Snow storms and freezing rain occurred in southern China in the winter of 2008 (Fig. 3a), which caused significant economic losses and disrupted highway and railway transport, energy support systems, communication, agriculture, and the lives of residents (Wei et al., 2008). We used the downscaling method to determine whether it could improve the performance of the original CFS GCM hindcast during 2008 winter. The observational scenario, CFS hindcast, and downscaling results are shown in Fig. 3. A large positive precipitation anomaly was centered on

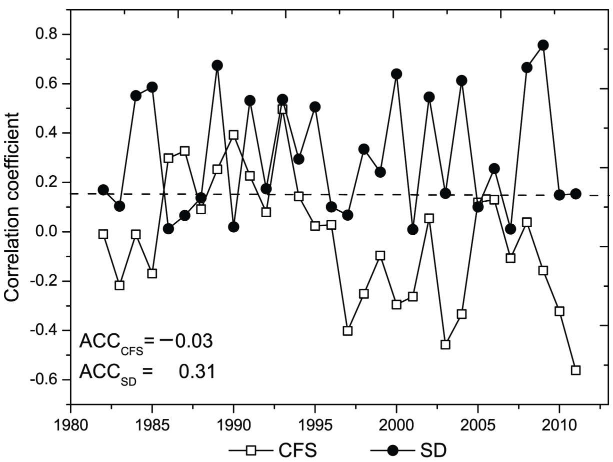

Figure 1 Spatial anomaly correlation coefficient of winter precipitation among the observation, CFS GCM output, and downscaling result. The hollow rectangle and solid circle represent original CFS and downscaling results, respectively. The multi-year average of the anomaly correlation coefficient is given at the left bottom of the panel. The dashed line represents the correlation coefficient at the 95% confidence level.

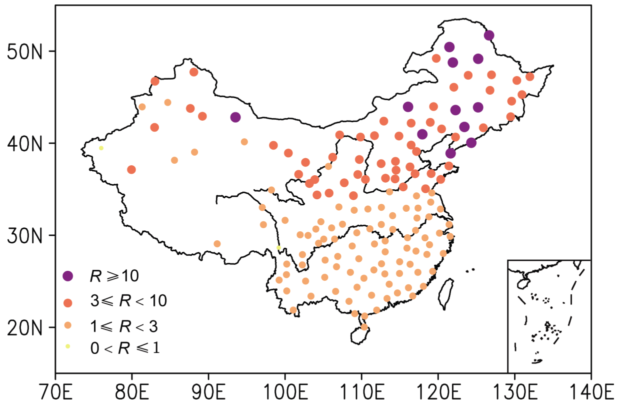

Figure 2 Improvement of the downscaling scheme over the original CFS result (R_{RMSE}) during 1982–2011. The purple, red, orange, and yellow solid circles represent the different thresholds of R_{RMSE}, respectively.

Jianghuai and the Yangtze River Valley, and other parts of China experienced relatively less precipitation (Fig. 3a). For the original CFS GCM, most parts of China experienced positive precipitation anomalies, except for parts of northwestern China, and a significantly larger positive precipitation anomaly region than that recorded in observations moved to southwestern China (Fig. 3b). Figure 3c shows the hindcast of 2008 winter obtained from the downscaling result. The downscaling scheme predicted the locations of the positive precipitation anomaly center over southern China and negative precipitation anomalies over most parts of China, except for northeastern China. Moreover, the magnitude of winter precipitation obtained from the downscaling results is comparable to that of observation. Furthermore, the ACC between observation and downscaling was 0.66, compared with 0.04 from the original CFS GCM (Fig. 1).

For all prediction models, hindcast was used to evaluate the average performance. However, our final objective was to apply the predictive models in the forecasting of future climate variation. By applying the downscaling scheme in this study, a real-time predicted precipitation anomaly pattern appeared in the 2012 winter (Fig. 4). This large positive precipitation anomaly was centralized mainly in Jianghuai Valley, South China, northern Inner Mongolia, and North China; northeastern China and western China were relatively dry. It should be noted that the first principal component of SIC in 2012 September-October, which explains 40% of the total variance, showed conditions similar to those of September-October 2008 (figure not shown); therefore, southern China is likely to experience increased precipitation this winter.

4 Conclusion and discussion

In this study, statistical downscaling based on CFS GCM output and observational data of large-scale circulation variables was used to predict winter precipitation over stations in China. In particular, GH5 from global CFS GCM and SIC from observational records were used as predictors. Downscaling outperformed the original CFS GCM considerably in predicting winter precipitation

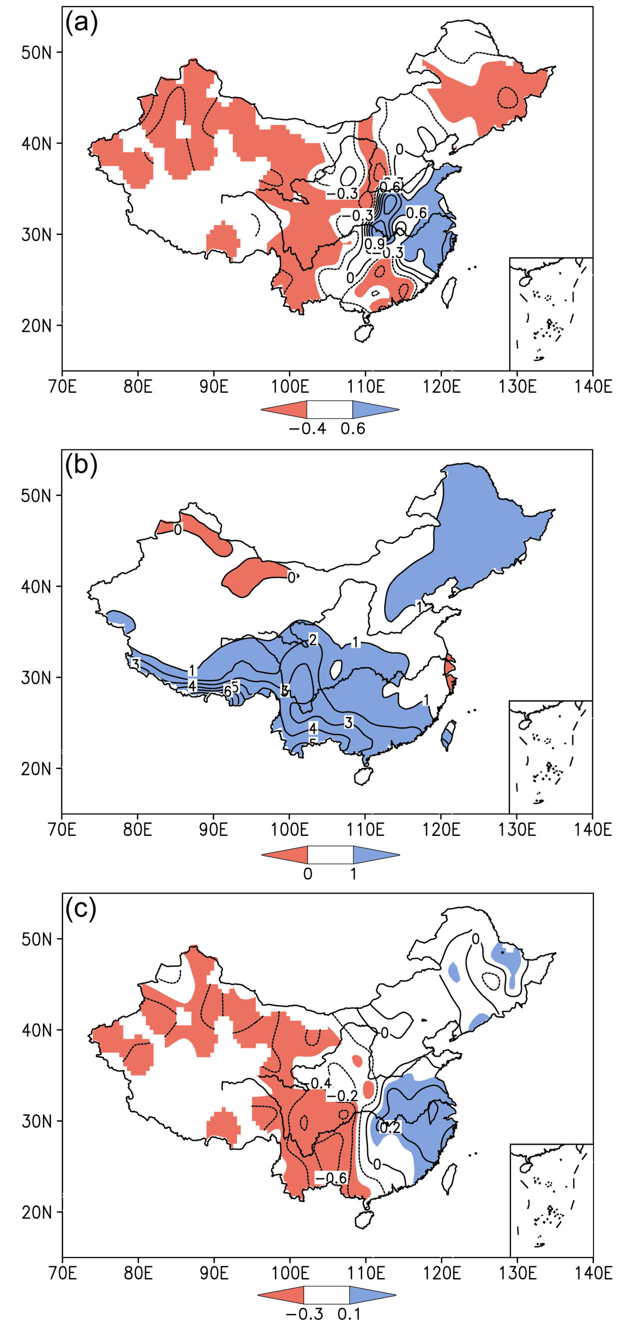

Figure 3 The spatial patterns of precipitation anomaly in the winter of 2008. (a), (b), and (c) indicate observation, CFS GCM prediction, and downscaling results, respectively. Units: mm d^{-1}. The red (blue) represents the negative (positive) precipitation anomaly region.

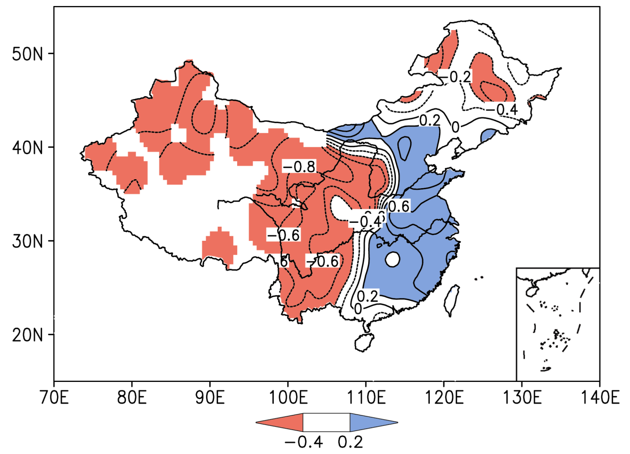

Figure 4 Pattern of 2012 winter precipitation anomaly obtained from downscaling. Units: mm d^{-1}. The red (blue) represents the negative (positive) precipitation anomaly region.

in the cross-validation experiment. Real-time prediction in precipitation over China stations has been implemented for the winter of 2012.

In the cross validation for 1982–2011, the multi-year average spatial ACC improved significantly from –0.03 to 0.31. The downscaling temporal RMSE decreased significantly compared with that of the original CFS GCM over most China stations. Furthermore, the precipitation pattern of observation in 2008 winter reproduced by the downscaling scheme was more accurate than that of the original CFS GCM. The main precipitation centers were reproduced by the statistical downscaling model. Moreover, the ACC between the observation and downscaling result reached ~ 0.6; in the counterpart of original CFS GCM, the ACC was 0.04. In general, the circulation-based approach successfully conveyed information from the large-scale atmosphere to the local regions.

Because the previous predictor SIC had a stable relationship with circulation in the mid-high latitudes of the Northern Hemisphere (Wu et al., 2011), autumn SIC accounted for deficiency of the GCM prediction of the circulation in mid-high latitudes to some extent, and the predictive skill in precipitation over East Asia was improved over with the original GCM output. Therefore, the combination of both GCM and observational information is an effective method for improving the prediction capability of the downscaling scheme. Additional stations have been erected in China; therefore, more observed information can be used to establish and validate the predictability of the downscaling method. More detailed prediction of month-by-month precipitation in winter is an objective for future research.

Acknowledgements. This research was jointly supported by the China Meteorological Special Project (GYHY201206016), the National Basic Research Program of China (2010CB950304), and the Innovation Key Program of the Chinese Academy of Sciences (KZCX2-YW-QN202).

References

Bretherton, C. S., C. Smith, and J. M. Wallace, 1992: An intercomparison of methods for finding coupled patterns in climate data, *J. Climate*, **5**, 541–560.

Chen, H. P., J. Q. Sun, and H. J. Wang, 2012: A statistical downscaling model for forecasting summer rainfall in China from DEMETER hindcast datasets, *Wea. Forecasting*, **27**, 608–628.

Chen, X. F., and Z. G. Zhao, 2000: *Study and Application on Prediction of Rainfall over China in Flood Season* (in Chinese), Meteorology Press, Beijing, 241pp.

Comiso, J. C., C. L. Parkinson, R. Gersten, et al., 2008: Accelerated decline in the Arctic sea ice cover, *Geophys. Res. Lett.*, **35**, L01703, doi:10.1029/2007GL031972.

Fan, K., 2011: A statistical scheme for the seasonal forecasting of North China's surface air temperature during winter, *Atmos.*

Oceanic Sci. Lett., **4**, 81–85.

Fan, K., and B. Q. Tian, 2013: Prediction of wintertime heavy snow activity in northeast China, *Chinese Sci. Bull.*, **58**, 1420–1426, doi:10.1007/ s11434-012-5502-7.

Gao, H., 2007: Comparison of four East Asian Winter Monsoon indices, *Acta Meteor. Sinica* (in Chinese), **65**, 272–279.

Gao, H., 2009: China's snow disaster in 2008: Who is the principal player? *Int. J. Climatol*., **29**, 2191–2196.

Geng, S. Q., Y. L. Wang, and S. Bai, 2001: The affection of the variation of the atmospheric general circulation in the Northern Hemisphere in the winter 2000/2001 on the climate and sea ice in the Bohai Sea, *Mar. Forecasts* (in Chinese), **18**, 25–33.

Honda, M., J. Inoue, and S. Yamane, 2009: Influence of low Arctic sea-ice minima on anomalously cold Eurasian winters, *Geophys. Res. Lett.*, **36**, L08707, doi:10.1029/2008GL037079.

Jolliffe, I. T., 1972: Discarding variables in a principal component analysis. I: Artificial data, *Appl. Stat.*, **21**, 160–173.

Jolliffe, I. T., 2002: *Principal Component Analysis* (2nd ed.), Springer, Berlin, 487pp.

Kalnay, E., M. Kanamitsu, R. Kistler, et al., 1996: The NCEP/NCAR 40-year reanalysis project, *Bull. Amer. Meteor. Soc.*, **77**, 437– 471.

Kang, H. W., C. W. Zhu, Z. Y. Zuo, et al., 2011: Statistical downscaling of pattern projection using multi-model output variables as predictors, *Acta Meteor. Sinica*, **25**(3), 293–302.

Lang, X. M., 2011: A hybrid dynamical-statistical approach for predicting winter precipitation over eastern China, *Acta Meteor. Sinica*, **25**(3), 272–282.

Lang, X. M., H. J. Wang, and D. Jiang, 2003: Extraseasonal ensemble numerical prediction of winter climate over China, *Chinese Sci. Bull.*, **48**(19), 2121–2125.

Liu, J. P., J. A. Curry, H. J. Wang, et al., 2012: Impact of declining Arctic sea ice on winter snowfall, *PANS*, **109**, 4074–4079.

Liu, Y., and K. Fan, 2012a: A new statistical downscaling model for autumn precipitation in China, *Int. J. Climatol.*, **33**, 1321–1336, doi:10.1002/joc. 3514.

Liu, Y., and K. Fan, 2012b: Prediction of spring precipitation in China using a downscaling approach, *Meteor. Atmos. Phys.*, **118**, 79–93.

Ma, J. H., H. J. Wang, and Y. Zhang, 2012: Will boreal winter precipitation over China increase in the future? An AGCM simulation under summer "ice-free Arctic" conditions, *Chinese Sci. Bull.*, **57**, 921–926, doi:10.1007/s11434-011-4925-x.

Michaelsen, J., 1987: Cross-validation in statistical climate forecast models, *J. Appl. Meteor. Sci.*, **26**(11), 1589–1600.

Parker, D. E., P. D. Jones, C. K. Folland, et al., 1994: Interdecadal changes of surface temperature since the late nineteenth century, *J. Geophys. Res.*, **99**, 14373–14399.

Rayner, N. A., D. E. Parker, E. B. Horton, et al., 2003: Global analyses of sea surface temperature, sea ice, and night marine air temperature since the late nineteenth century, *J. Geophys. Res.*, **108**, 4407, doi:10.1029/2002JD002670.

Saha, S., S Nadiga, C Thiaw, et al., 2006: The NCEP Climate Forecast System, *J. Climate*, **19**, 3483–3517.

Steinberger, E. H., and N. Gazit-Yaari, 1996: Recent changes in the spatial distribution of annual precipitation in Israel, *J. Climate*, **9**, 3328–3336.

Sun, J. Q., H. J. Wang, and W. Yuan, 2009: A preliminary investigation on causes of the catastrophic snowstorm in March, 2007 in the northeastern parts of China, *Acta Meteor. Sinica*, **67**(3), 469–477.

Tao, S. Y., and J. Wei, 2008: Severe snow and freezing rain in January 2008 in the Southern China, *Climatic Environ. Res.* (in Chinese), **13**(4), 337–349.

Uvo, C. B., J. Olsson, O. Morita , et al. 2001: Statistical atmospheric downscaling for rainfall estimation in Kyushu Island, Japan, *Hydrol. Earth Syst. Sci.*, **5**(2), 259–271.

Wang, H. J., 2003a: The extra-strong warm winter event in North Asia and its accompanying anomalous atmospheric circulation, *Chinese Sci. Bull.*, **48**(10), 1031–1033.

Wang, H. J., 2003b: 2003 vs. 2002: A large scale amplitude wintertime temperature anomaly reversion event and its anomalous atmospheric circulation, *Chinese Sci. Bull.*, **48** (Suppl. II), 1–4.

Wang, H. J., and K. Fan, 2009: A new scheme for improving the seasonal prediction of summer precipitation anomalies, *Wea. Forecasting*, **24**(2), 548–554.

Wang, H. J., and D. B. Jiang, 2004: A new East Asian winter monsoon intensity index and atmospheric circulation comparison between strong and weak composite, *Quat. Sci.* (in Chinese), **24**, 19–27.

Wang, H. J., E. T. Yu, and S. Yang, 2011: An exceptionally heavy snowfall in northeast China: Large-scale circulation anomalies and hindcast of the NCAR WRF model, *Meteor. Atmos. Phys.*, **113**, 11–25.

Wang, S. W., 2001: *Progress of Modern Climate Research (Chapter 11)* (in Chinese), China Meteorology Press, Beijing, 8pp.

Wei, J., S. Y. Tao, and L. N. Zhao, 2008: Predictability of snow storm and freezing rain disaster in southern China in January 2008, *Climatic Environ. Res.* (in Chinese), **13**(4), 520–530.

Wilks, D. S., 2006: *Statistical Methods in the Atmospheric Sciences* (2nd ed.), Academic Press, New York, 627pp.

Wu, B. Y., J. Z. Su, and R. H. Zhang, 2011: Effects of autumn-winter Arctic sea ice on winter Siberian High, *Chinese Sci. Bull.*, **56**, 3220–3228, doi:10.1007/s11434-011-4696-4.

刘颖, 范可, 张颖. 2013. 基于 CFS 模式的中国站点夏季降水统计降尺度预测 [J]. 大气科学, 37 (6): 1287–1296, doi: 10.3878/j.issn.1006-9895.2012.12143. Liu Ying, Fan Ke, Zhang Ying. 2013. A statistical downscaling model for summer rainfall over China stations based on the Climate Forecast System [J]. Chinese Journal of Atmospheric Sciences (in Chinese), 37 (6): 1287–1296.

基于 CFS 模式的中国站点夏季降水统计降尺度预测

刘颖[1,2]　范可[2]　张颖[2]

1 国家气候中心中国气象局气候研究开放实验室，北京 100081
2 中国科学院大气物理研究所，北京 100029

摘　要　本研究针对中国夏季站点降水，研制建立了基于 Climate Forecast System（CFS）实时预测数值产品及观测资料的统计降尺度预测系统。此预测系统选取了 CFS 模式中当年夏季 500 hPa 高度场和观测资料中前一年秋、冬季海表面温度场作为预测因子，两因子的关键区分别为泛东亚地区和热带太平洋地区。统计降尺度模型对 1982～2011 年中国夏季降水的回报效果较 CFS 模式原始结果显著提高，空间距平相关系数由 0.03 提高到 0.31，时间相关系数在中国大部分地区显著提高，最大可达 0.6。均方根误差较 CFS 模式原始结果明显降低，同时，此降尺度模型较好的回报出 2011 年汛期降水的距平百分率的空间分布型。

关键词　CFS　中国　夏季降水　统计降尺度

文章编号　1006–9895(2013)06–1287–10　　**中图分类号**　P446　　**文献标识码**　A

doi:10.3878/j.issn.1006-9895.2012.12143

A Statistical Downscaling Model for Summer Rainfall over China Stations Based on the Climate Forecast System

LIU Ying[1,2], FAN Ke[2], and ZHANG Ying[2]

1 *Laboratory for Climate Studies*, *National Climate Center*, *China Meteorological Administration*, *Beijing* 100081
2 *Institute of Atmospheric Physics*, *Chinese Academy of Sciences*, *Beijing* 100029

Abstract　A statistical downscaling system for forecasting summer precipitation at stations in China has been established in this study on the basis of real-time prediction of numerical products from the Climate Forecast System (CFS) and observational data. The summer 500-hPa geopotential height in the current year from CFS and the previous autumn–winter sea surface temperature from observations were selected as the two predictors, with corresponding key regions of Pan–East–Asia and the tropical Pacific, respectively. The statistical downscaling hindcast on the 1982–2001 summer precipitation over China improved the performance of the prediction compared with that of the original CFS. The spatial anomaly correlation coefficients increased from 0.03 to 0.31, and the temporal correlation coefficients over most parts of China also increased significantly by the downscaling scheme with a maximum of 0.6. The root mean square error decreased in comparison with the output of the original CFS. Furthermore, we successfully created a hindcast on the 2011 summer precipitation anomaly pattern in China by using this statistical downscaling scheme.

Keywords　CFS, China, Summer precipitation, Statistical downscaling

---

收稿日期　2012–09–03，2012–11–07 收修定稿

资助项目　全球变化研究国家重大科学研究计划 2010CB950304，国家自然科学基金（Granted）41175071，公益性行业（气象）科研专项 GYHY200906018，中国科学院知识创新工程重要方向项目青年人才类（Grant）KZCX2-YW-QN202，公益性行业（气象）科研专项 GYHY201206016（部分资助）

作者简介　刘颖，女，1982 年生，博士，从事短期气候预测研究。E-mail: liuying@cma.gov.cn

1 引言

在全球变暖背景下，气候变化成为科学界的研究热点之一，气候的形成和变化不仅是大气内部状态和过程的反映，也是陆地、海洋、冰雪圈以及生物圈等与大气相互作用的结果（曾庆存等，2003）。王会军（1997）指出，气候异常变化对全球各方面都会产生重要影响，因此，气候预测成为当今人类社会面临的一个重大课题。由于影响气候短期变化的因子众多，且因子间又有复杂的相互作用，我们尚未对其中的这些预测因子的详细物理过程及其影响有清晰的科学认识。对于中国来讲，夏季降水占全年比重较大，在北方地区占 50%以上，南方地区占 40%左右（图 1），因此，夏季降水预测对我国的国民经济以及现代化建设有着非常重要的作用。但是，由于中国地处东亚季风区，自然条件复杂，剧烈变化的气候影响着东亚季风系统等因素，导致中国夏季降水的短期气候预测业务平均水平一直不高。

短期气候预测方法主要分为数值模式方法和物理统计方法，对于大尺度环流模式（GCM）而言，其对热带地区以及大尺度环流具有较高预测能力，但对东亚地区的降水几乎没有预测能力，那么，降尺度方法的提出有效利用了 GCM 的高预测性能对局地变量进行预测。近年来，我国学者已在夏季降水短期气候预测以及降尺度方面取得诸多成果。如提出了年际增量的预测方法并将其应用到我国夏季降水、台风等预测中（范可等，2007；范可等，2008；Fan and Wang, 2009）。Zhu et al.（2008）利用经验正交分解和奇异值分解相结合的方法对亚太地区的夏季风降水做了降尺度预报，提高了本区域夏季风降水的距平相关系数，同时均方根误差显著降低。Wang and Fan（2009）利用模式对热带地区较好的可预测性对东亚地区降水进行降尺度预测，研究证明，这种方法能够提高东亚乃至中国夏季降水的预测能力。Lang and Wang（2010）对中国 6 个区域进行了研究，将模式输出资料与观测资料相结合，针对不同区域选取影响因子，研究结果显示，新的预测方法对各区域夏季降水距平符号、量值以及年际变化上优于模式本身的预报。Gu et al.（2011）利用中国气象局国家气候中心的大尺度海—气耦合模式（CGCM–NCC）对中国不同区域夏季降水进行了统计降尺度研究，降尺度结果较模式原始结果提高了中国区域夏季降水的预测技巧。Chen et al.（2012）和 Sun and Chen（2012）分别针对中国站点以及全球的夏季降水从 GCM 的大尺度环流变量中选取最优预测因子，降尺度模型结果的距平相关系数以及均方根误差均较 GCM 模式原始结果分别有显著的提高和降低。

美国国家环境预报中心（National Centers for Environmental Prediction, NCEP）的气候预测系统 (Climate Forecast System, CFS) 可以为全球提供最新的多时间尺度预测资料（Saha et al., 2006）。此预测系统的第一代从 2004 年 8 月开始业务运行，同时，对 1981～2004 年共 24 年进行了历史回报。第二代在 2011 年 3 月开始进行业务实时预测，并提供了 1982～2010 年的回报试验结果。已经有许多利用 CFS 模式资料展开的研究。Yang et al.（2008）对亚洲季风区的气候、主要降水区的年际变化以及大尺度环流系统做了细致分析。陈官军等（2010）也对此模式系统不同初始场资料对东亚夏季的预报效能进行了检验评估。Yuan and Liang（2011）针对美国降水，利用 WRF (Weather Research and Forecasting) 模式对 CFS 模式资料进行了动力降尺度回报。Gao et al.（2011）评估了 CFS 模式资料对梅雨带的预测能力。然而，现阶段利用 CFS 模式资料对中国地区站点夏季降水进行统计降尺度预测的研究还很少。因此，我们利用此资料对中国夏季降水进行预测。

2 数据

降水资料来源于中国气象局国家气候中心 1982～2011 年的 160 站点月平均数据。大气资料为 NCEP/NCAR 再分析资料（1982～2011 年）中的 500 hPa 高度场（GH5），水平分辨率为 2.5°×2.5°（Kalnay et al., 1996）。海温资料为 1981～2011 年秋、冬季 NOAA 的海表面温度 (Sea Surface Temperature, SST) 资料，水平分辨率为 2°×2°（Smith et al., 2008）。

CFS 模式有两个版本（CFSv1 和 CFSv2），本研究使用 CFSv2 版本的月平均资料，起始时间为 1982 年，资料更新至今。其中 1982～2010 年的结果取自回报试验。各月每隔 5 天分别从 0、6、12 和 18 UTC 开始积分，积分时间为 9 个月，即回报当月数据并对未来 1～9 个月进行预报。2011 和 2012 年的 CFS 资料取自实时预测，每天都从上述 4 个时

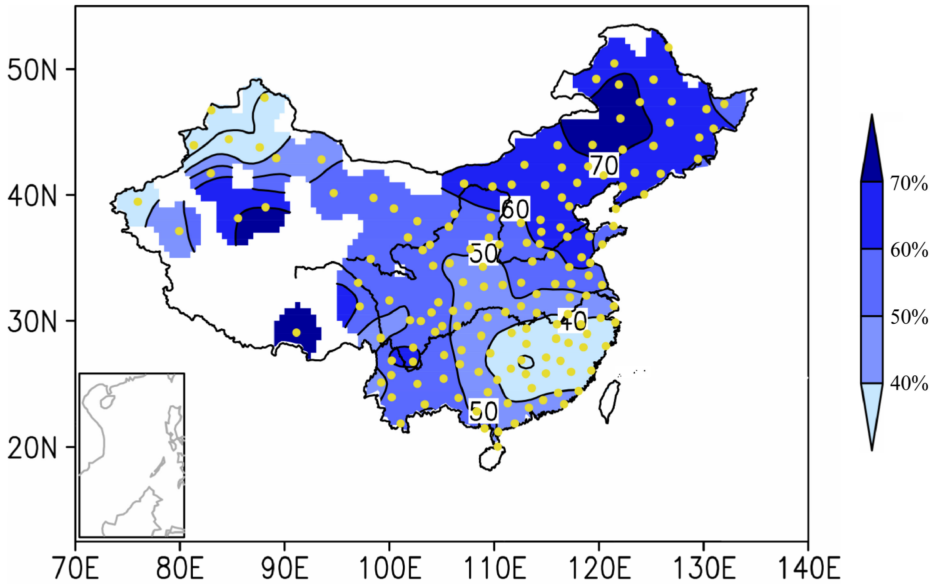

图 1 1982～2011 年夏季降水量占全年降水的百分率空间分布以及中国 160 站分布情况。黄色圆点代表 160 站位置

Fig. 1 The percentage pattern of the summer precipitation in annual mean during 1982–2011 and the 160 station locations in China. Yellow dots represent the locations of 160 stations

次开始积分，积分时间同为 9 个月。在本研究中，对每个月中所有不同初值的积分进行集合平均，并利用双线性插值方法将集合结果插值到 2.5°×2.5°水平网格上。为了保证资料完整性并及时参加国家气象局的汛期会商，我们选取 2 月份起报的 6、7、8 月 GH5 高度场资料。

3 方法

本文使用场信息耦合型方法建立统计降尺度预测模型。此方法的优点在于，能够针对预测因子和预测量空间场的主要信息，通过提取两变量场的最优耦合变化型建立模型。具体步骤为：

首先，在建模的拟合时段 t 内，利用 EOF（Empirical Orthogonal Function）分析，分别对预测因子和预测量变量场进行分解，基于 Kaiser's 标准（Wilks，2006）保留主模态进而将预测因子和预测量回算到原始变量场形式。此步骤能够将变量场中多余的噪音去除，达到滤波目的。Kaiser's 标准公式为

$$\lambda_m > \frac{T}{K}\sum_{k=1}^{K} s_{k,k}, \tag{1}$$

其中，λ_m 表示保留的 EOF 特征值，$s_{k,k}$ 为所分解变量的第 k 个方差，T 为阈值参数，这里取 T=0.7（Jolliffe，1972；2002）。

其次，将滤波之后的预测因子和预测量利用 SVD（Singular Value Decomposition）分解，提取两变量场之间的耦合变化型。

最后，利用得到的预测因子和预测量的 SVD 模态对、对应的时间系数以及预测时间段 t+1 预测因子场，利用多元线性回归方法，做出统计降尺度预测（Liu and Fan，2012a，2012b），建模过程如图 2 所示。

4 预测因子选取

500 hPa 高度场代表着对流层中层的无辐散层，可以很好地体现高空大尺度环流波动（例如，槽脊移动、阻塞系统等）的情况。由于天气系统的斜压性以及上下游效应，从 GH5 中可以抓住大尺度环流背景场的变化，从高低空系统的配置关系我们就可以推知低空系统的变化，从而对地面天气的未来发展形势做出预测预报。因此，我们选取来自于 CFS 模式资料的同期因子夏季 GH5 为预测因子，其关键区为 30°S～60°N，70°E～180°E，以下称泛东亚地区。图 3 为 1982～2011 年 NCEP 再分析资料与 CFS 资料之间的 GH5 相关场。可以看到，显著的正相关区集中在低纬度地区，相关系数最大可达到 0.6 以上，东亚及周围地区上空也存在显著的正相关区。同时，1982～2011 年 NCEP 再分析资料与 CFS 模式资料中泛东亚地区 GH5 的空间相关系数能够达到 0.97 以上。观测与 CFS 模式资料中 GH5 的 EOF 第一模态主成分，都显示出了随时间下降的趋势，两者之间的相关系数可以达到 0.46（图略）。

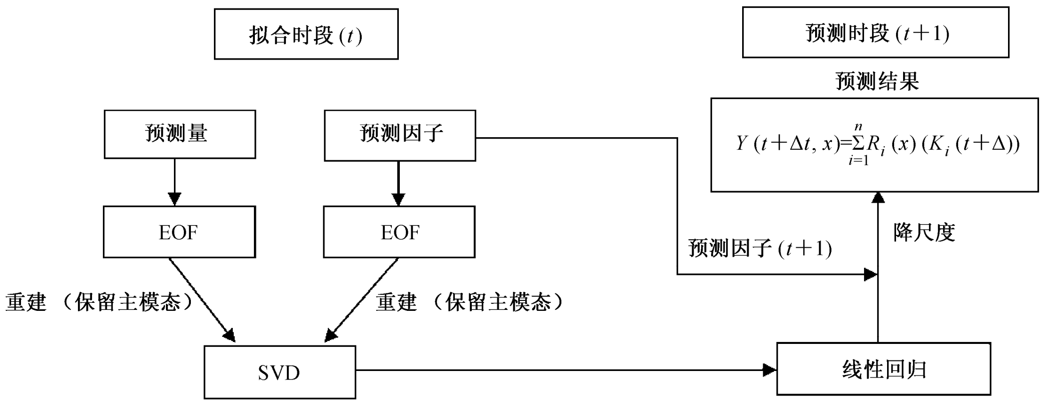

图 2　场信息耦合型统计降尺度方法示意图 $Y(t+\Delta t)$ 为预报年的降水值，$R_i(x)$ 为降水的 SVD 空间模态，$\hat{K}(t+\Delta t)$ 为预报年的 SVD 时间系数。
Fig. 2　The sketch map of the field information coupled patterns statistical downscaling method

因此，CFS 模式对 1982～2011 年夏季 500 hPa 高度场的回报能力较好，本研究将考虑利用夏季 GH5 为预测因子，建立统计降尺度模型。

中国夏季降水与泛东亚地区 GH5 的 SVD 第一模态空间分布以及对应的时间系数由图 4 给出。对于观测情形，由图 4c 可以看出，GH5 场在泛东亚地区中高纬为代表冷空气活动的高度异常场；在日本—中太平洋上空存在着一个异常的 PJ（Pacific–Japan）波列（Nitta, 1987；Nitta and Hu, 1996）。PJ 遥相关分布型与中国的气候变化有着密切的联系，例如，影响西太平洋副热带高压和中国降水（Huang and Li，1987；Kosaka and Nakamura，2006）。而热带及其以南地区则代表了南半球通过越赤道气流等系统的作用，对中国降水产生影响。降水场中，中国的东部地区大体呈现出南北多中间少（南北少中间多）的中国降水典型空间分布特征（图 4e）。相对于观测情形，在 CFS 中 GH5 的 SVD 模态空间分布场中，其热带地区大片带状负值区分裂为两块，而存在于东亚东北部地区的正值中心消失，取而代之的是在偏东的地方出现了一个负值的高值中心（图 4c、d）。而相应的降水场中，CFS 回报出了除东北地区的中国东部大部分地区的异常降水型（图 4a、b）。在观测与 CFS 中 SVD 第一模态对应的时间系数之间相关都超过了 0.8（图 4e、f）。

ENSO（El Niño–La Niña）存在于热带太平洋，是海气相互作用的重要系统。它是全球天气和气候年际变化的重要原动力之一（Kiladis and Diaz, 1989），影响着全球气候的年际变化（Webster et al., 1998），也是短期气候预测一个重要的基础。虽然 ENSO 与东亚夏季风之间的关系在长期变化中显示出不稳定特征（Wang,　2002），但它仍然是引起中国降水变化的主要外强迫因子之一。一般来讲，El Niño 易于导致弱的夏季风，而 La Niña 易于导致强的夏季风（Wang et al., 1999）。当发生 El Niño 时，纬向 Walker 环流的上升支东移，西太平洋副热带高压偏强，东亚季风偏弱，容易导致中国南方地区降水偏多，北方偏少；而发生 La Niña 时，情况相反（Bjerknes，1966，1969；臧恒范和王绍武，1984；任富民等，2012）。许多学者利用 ENSO 信号对降水进行预测预报（Ropelewski and Halpert, 1987; Jain and Lall, 2001；Maity and Kumar, 2006）。1982～2011 年中国夏季降水 EOF 第一模态的时间系数与 1981～2010 年秋、冬季 SST 的 EOF 第一模态的时间系数的相关系数可以达到 0.52（超过 99%信度检验水平）。

1982～2011 年夏季降水与 1981～2010 秋冬季 SST 的 SVD 第一模态由图 5 给出。可以看到，SST 的 SVD 第一模态为 ENSO 的典型分布型，表现为热带中东太平洋和热带西太平洋呈现相反的变化趋势（图 5b），而对应此 ENSO 型分布的中国夏季降水为北方大部分地区和华南、长江下游之间相反的降水趋势，且雨带呈现东北—西南走向，而不是经典的准东西走向的“三明治”雨带分布特征。降水与 SST 的 SVD 第一模态对应的时间系数之间的相关系数为 0.85。同时，可以看到，在 2000 年前后，时间系数出现了一个转型期。Zhu et al.（2011）指出，中国东部雨带在 2000 年前后出现了转型，其原因在于：太平洋年代际涛动（Pacific Decadal Oscillation, PDO）在 2000 年前后同样出现了转型，这就影响了西风急流以及中高纬环流，从而导致中

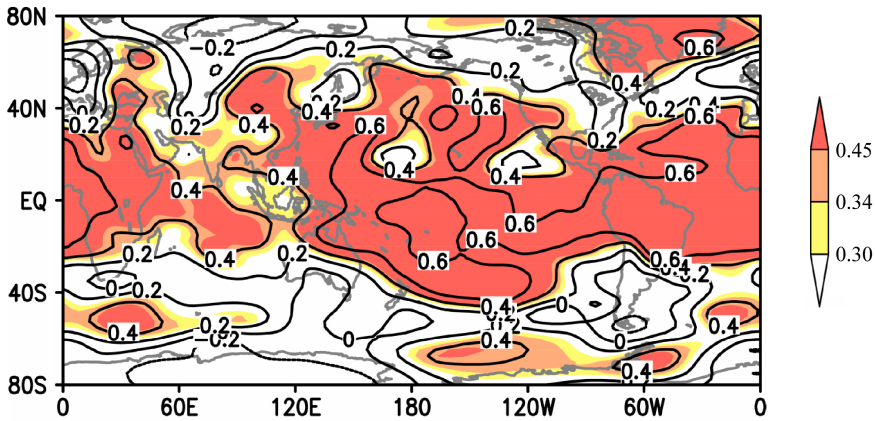

图 3 1982～2011 年 CFS 模式与观测的夏季 GH5 相关场。阴影区颜色由浅到深分别代表 90%、95%以及 99%的信度检验水平

Fig. 3 The correlation coefficients for summer 500 hPa geopotential height between the reanalysis data (NCEP) and Climate Forecast System output during 1982–2011. The shaded areas (from light to dark) correspond to 90%, 95%, and 99% confidence levels, respectively

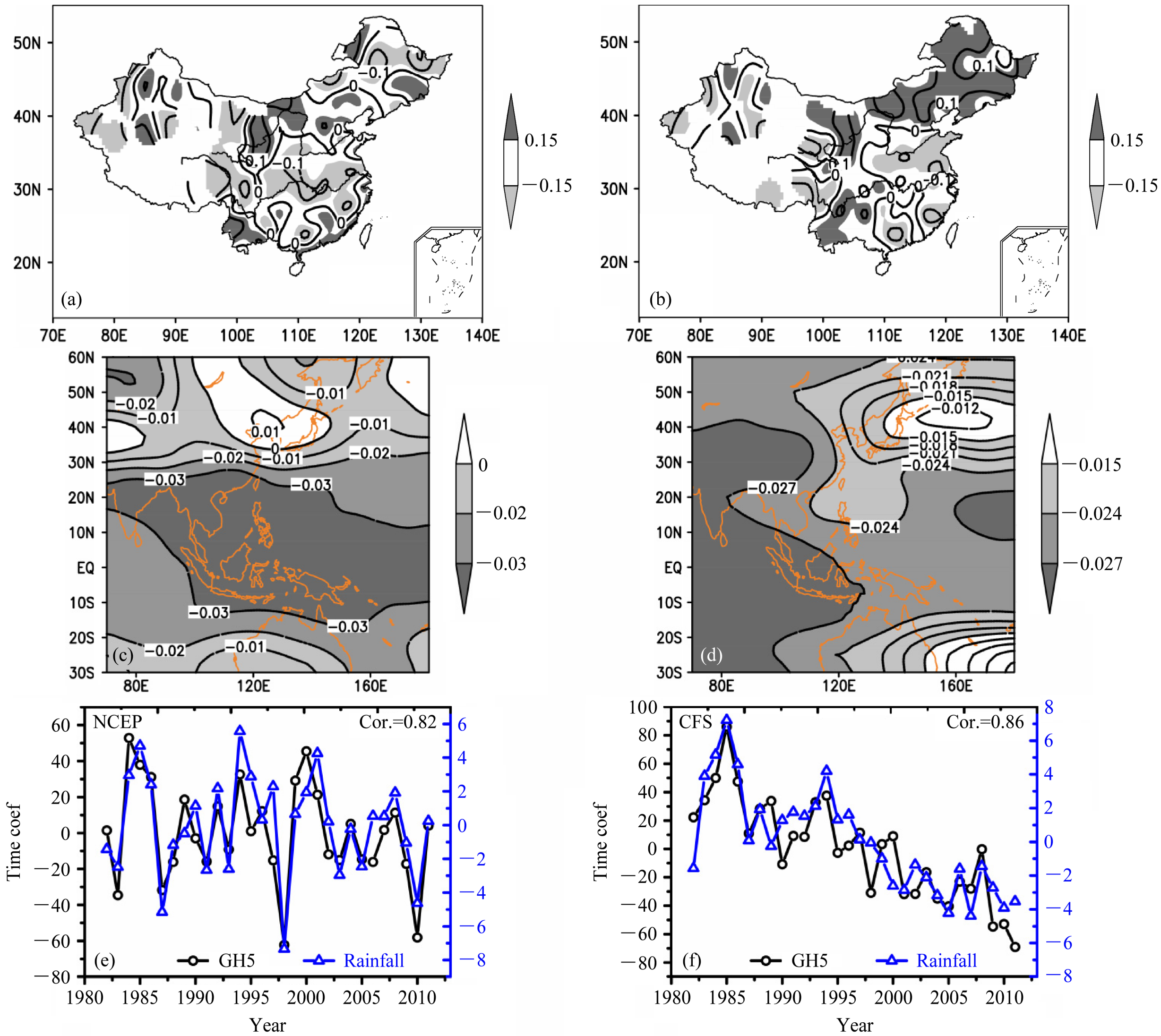

图 4 1982～2011 夏季（a，b）中国观测站点降水、（c，d）泛东亚地区 GH5 的 SVD 第一模态空间分布型以及（e，f）对应的时间系数。（a、c、e）基于 NCEP 资料，（b、d、f）基于 CFS 模式资料

Fig. 4 The first leading SVD modes for the observed rainfall in China and the GH5 over Pan-East Asia, and the corresponding time coefficients during 1982–2011 summers. (a, c, e) Based on the NCEP dataset; (b, d, f) based on the CFS GCMoutput

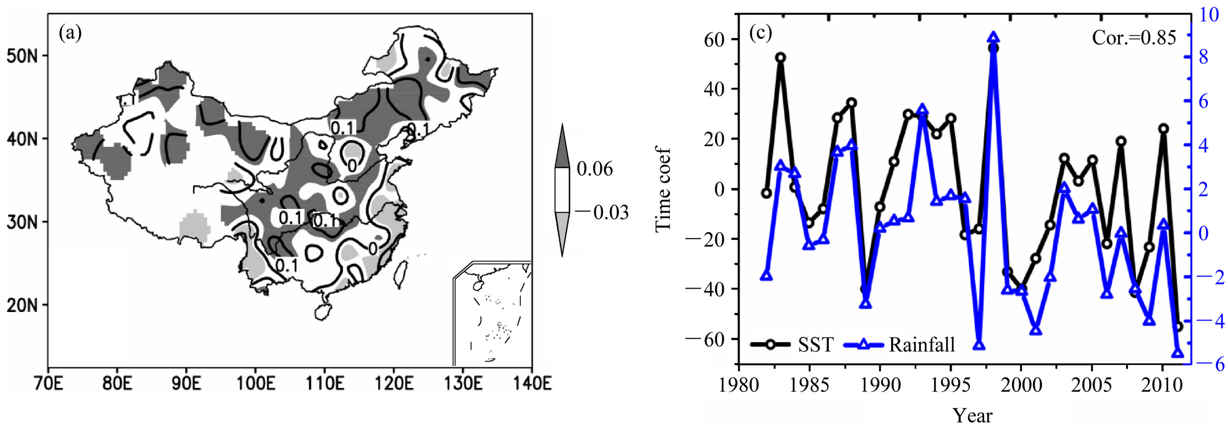

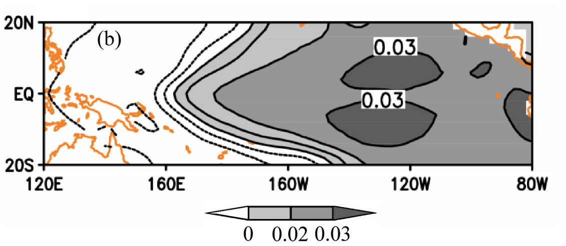

图 5 1982～2011 夏季中国观测站点降水（a）与 1981～2010 年秋冬热带太平洋 SST（b）的 SVD 第一模态空间分布型以及对应的时间系数（c）

Fig. 5 The first leading SVD modes of the (a) observed rainfall in China during 1982–2011 summers and (b) 1982–2010 autumn–winter SST over the tropical Pacific, and (c) the corresponding time coefficients

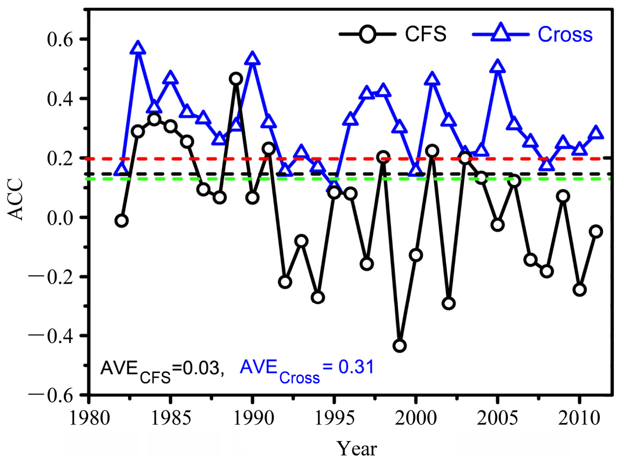

图 6 1982～2011 年观测数据与 CFS 模式原始数据（黑色）以及降尺度结果（蓝色）夏季降水空间距平相关系数。AVE 为多年平均值，Cross 代表交叉检验降尺度结果。绿色、黑色和红色虚线分别代表了 90%、95%和 99%的信度检验水平。

Fig. 6 The spatial anomaly correlation coefficients of summer precipitation between the observations and the CFS GCM output as well as the downscaling result. AVE and Cross represent the multi-year average and the cross validation results of downscaling. The green, black, and red dashed lines correspond to the 90%, 95%, and 99% confidence levels

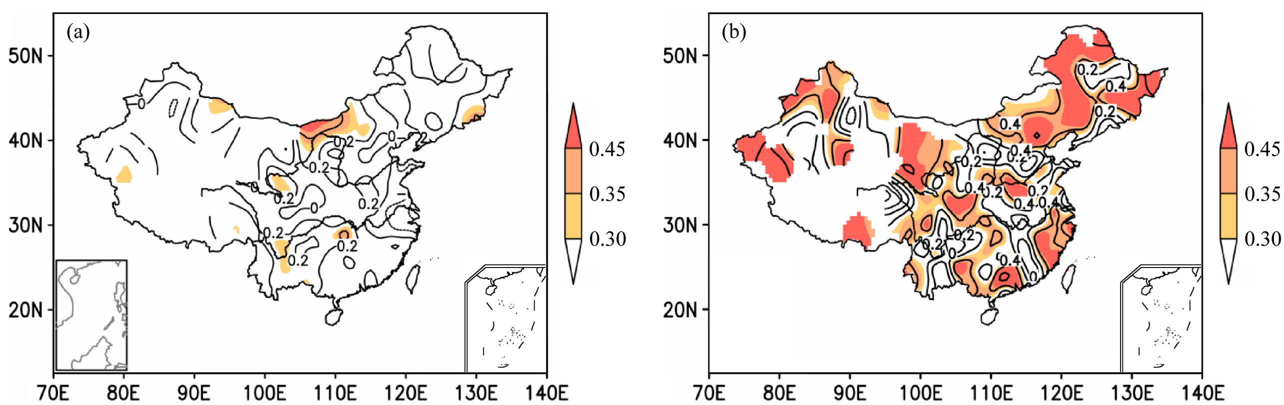

图 7 观测与 CFS 模式原始结果（a）以及降尺度结果（b）夏季降水的时间距平相关系数的空间分布。阴影区颜色由浅到深分别代表 90%、95%以及 99% 的信度检验水平

Fig. 7 The anomaly correlation coefficients of summer precipitation between the observation and (a) the original CFS output, (b) the downscaling result. The shaded areas (from light to dark) correspond to 90%, 95%, and 99% confidence levels, respectively

国雨带的变化。

5 统计降尺度预测结果

由于建模和检验的时段为 1982～2011 年，因此我们采用去掉一年的交叉检验方法来对降尺度模型进行检验。图 6 给出了观测与模式结果以及降尺度结果的降水量之间的空间距平相关系数 ACC（Anomaly Correlation Coefficient）。降尺度模型将 30 年平均的 ACC 从模式原始结果的 0.03 提高到 0.31，且在 97%年中降尺度结果的 ACC 都超过了 95%的信度检验水平，在 80%的年份中 ACC 超过了 99%的信度检验水平（图 6），最大值可以达到 0.6。同时，对于 30 年的时间距平相关系数 TCC 的空间场来讲，CFS 模式原始结果的 TCC 只有在内蒙古的部分地区，相关系数通过了显著性检验，其他大部分地区的相关系数均小于 0.3（图 7a）。而降尺度结果与观测数据之间在中国的西北、东北大部、黄淮、华南以及西南地区都具有显著的相关系数，最大值可以达到 0.6（图 7b）。因此，降尺度模型显著提高了 1982～2011 年中国夏季降水的时间 TCC 和空间 ACC。

那么，我们又比较了降尺度结果的均方根误差（RMSE, Root Mean Square Error）与模式原始结果 RMSE 之间的差异。P_{RMSE}（RMSE 的降低百分率）的表达式为：

$$P_{\mathrm{RMSE}}=\frac{E_{\mathrm{GCM}}-E_{\mathrm{SD}}}{E_{\mathrm{GCM}}}\times 100\%\,, \qquad (2)$$

其中，E_{GCM} 和 E_{SD} 分别代表模式原始结果和降尺度结果的 R_{MSE}，P_{RMSE} 大于零且绝对值越大，说明降尺度结果越接近于观测值。

图 8 为 1982～2011 年 P_{RMSE} 空间分布情况，对于全国的 160 个站来讲，除个别站点之外，大多数站点的 P_{RMSE} 都大于零。降尺度结果的 RMSE 比模式原始结果的 RMSE 最多可减小 40%以上。因此，此降尺度模型回报的 1982～2011 年夏季降水在量级上较 CFS 模式原始结果更加接近观测数据。

由前面的分析可以看到，此降尺度模型夏季降水预测能力在 1982～2011 年的总体（平均）水平较高，那么，对具体年份的预测效能如何呢？1982～1983 年发生了较强的 El Niño 事件，而中国地区的长江流域在 1983 年夏季出现洪涝，华北及华南地区普遍干旱（图 9a）。实际预测业务中，1983 年的夏季降水预报评分（PS 评分）不到 45 分。而

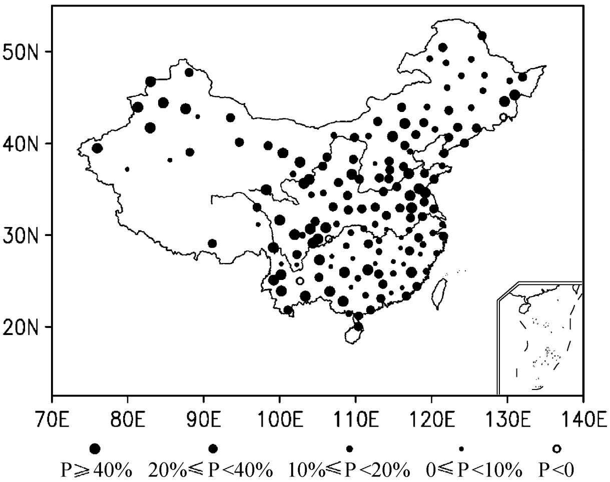

图 8 1982～2011 年 P_{RMSE}

Fig. 8 The decreased percentage of RMSE (P_{RMSE}) during 1982–2001

CFS 模式将中国东部大部分地区回报了降水正距平（图 9b），与实际降水型相差较大。经过降尺度之后，此降尺度模型大体回报出了“＋－＋”的降水距平空间分布型（图 9c），PS 评分提高到了 87 分。同样，此模型对于 2006 年夏季降水的预测较 CFS 模式原始结果，以及历史实际业务预测都有显著提高。此模型回报出了中国东部地区“－＋－”的降水距平空间分型（图 9d、f），PS 评分也从 67 分提高到 85 分。1982 年（2005 年）秋冬季，赤道中东太平洋地区出现了显著的海温异常偏高（偏低）现象，使得亚洲季风环流减弱（增强）（Wang et al.，1999），最终导致雨带的偏南（偏北）。因此，赤道太平洋地区的海温是夏季降水预测的重要因素之一。

我们又对 2011 年夏季的降水距平百分率做了检验，公式为：

$$P=\frac{R-\bar{R}}{\bar{R}}\times 100\%\,, \qquad (3)$$

其中，P 代表降水距平百分率，R 为某一站点的某年降水量，$\bar{R}$ 为某站点降水量的气候平均态，这里为 1982～2011 年。P 大于 13%表示降水偏多，P 小于－13%表示降水偏少（王绍武等，1999），P 介于两者之间表示降水正常。

图 10 为 2011 年夏季降水距平百分率的情况。2011 年夏季东北大部分地区降水偏少，同时在西南地区以及华南也出现了较严重的干旱现象，而在长江下游地区的降水偏多，西北地区大部分地区降水偏多（图 10a）。图 10b 为回报的 2011 年汛期降水情况。东北地区的偏旱，以及长江下游地区的降水

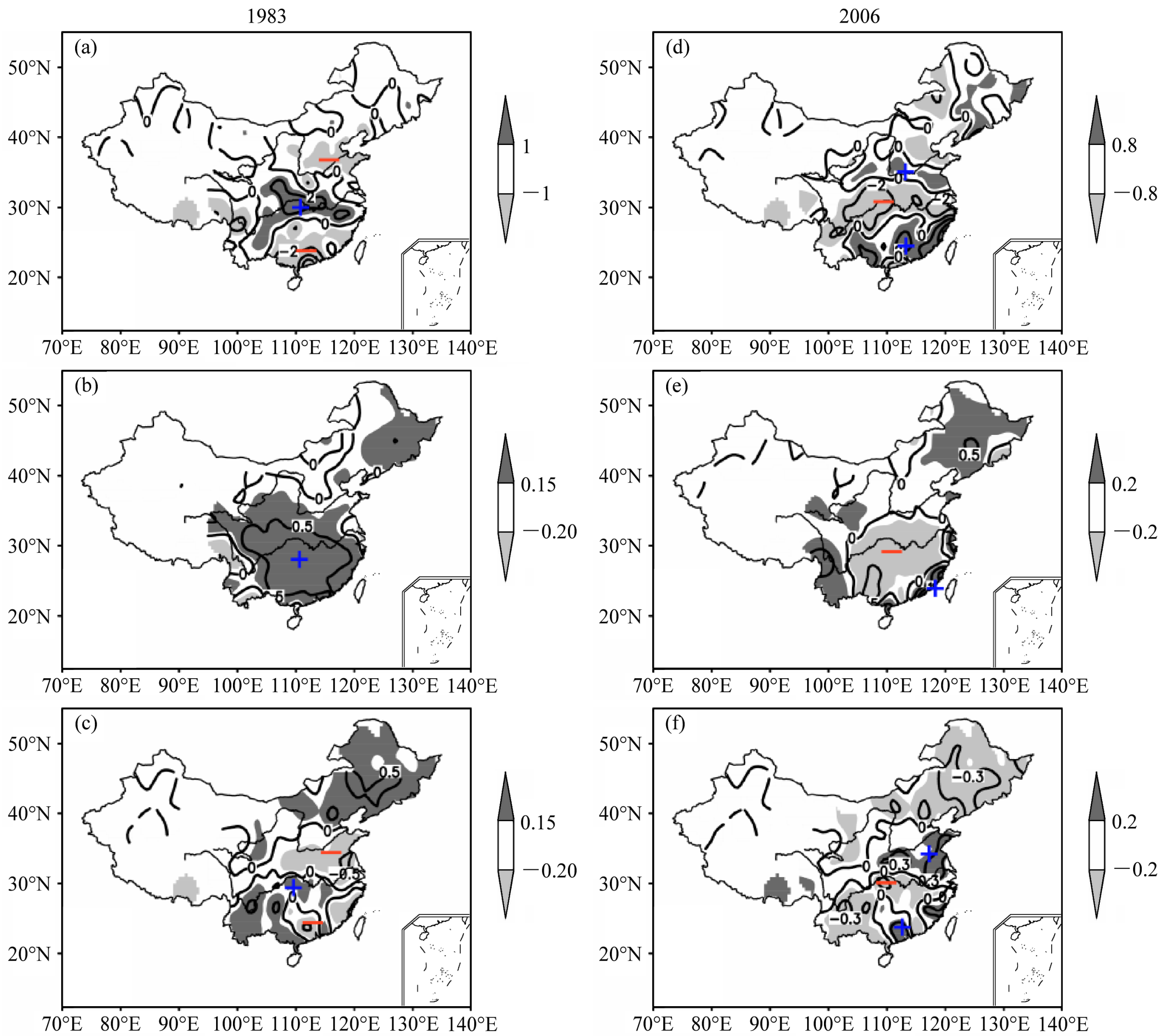

图 9 （a、b、c）1983 年和（d、e、f）2006 年夏季降水距平空间分布型：（a、d）观测数据，（b、e）CFS 模式原始结果，（c、f）降尺度结果。单位：mm d^{-1}

Fig. 9 The spatial patterns of summer precipitation anomalies in (a, b, c) 1983 and (d, e, f) 2006. (a, d), (b, e), and (c, f) represent observations, CFS output, and the downscaling result, respectively. Units: mm d^{-1}

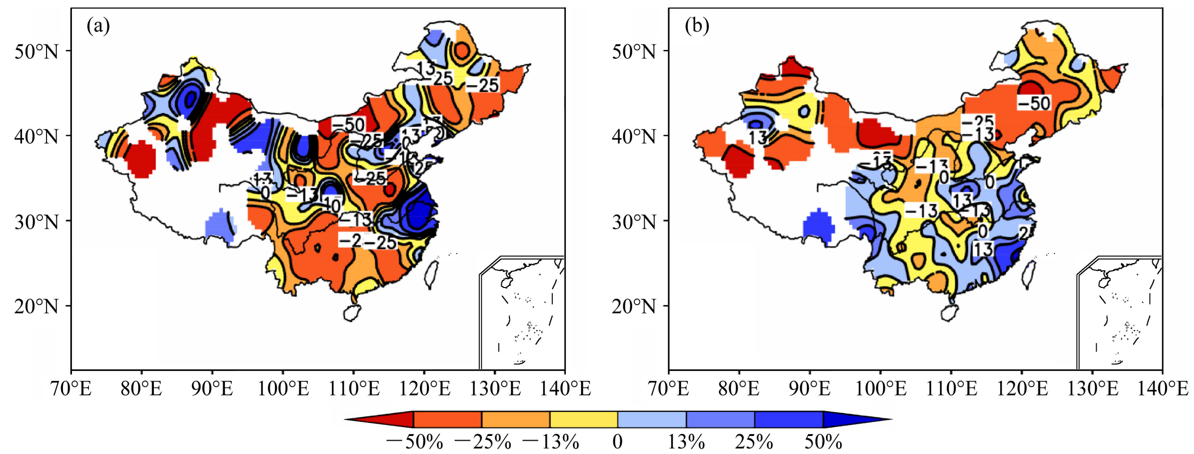

图 10 2011 年夏季降水距平百分率空间分布型：（a）观测数据；（b）降尺度结果

Fig. 10 The patterns of the 2011 summer precipitation anomaly percent from (a) observations and (b) downscaling result

偏多都较好的回报了出来，然而对于西南地区干旱，预测的结果偏弱，而华南地区的降水偏少没有回报出来，回报结果与观测之间的 ACC 为 0.28。总体来讲，此预测模型回报出了 2011 年汛期主要的降水区。

基于前面对此预测模型的回报检验，我们利用 1982～2012 年每年 2 月起报的 GH5 的 CFS 模式资料以及 1981～2011 年秋冬季 SST 建立预测模型，对 2012 年夏季降水进行预测（图略）。2012 年汛期预测结果显示，在东北地区、内蒙古地区以及长江中游的小部分地区降水偏少，在黄淮、长江下游以及华南地区降水偏多。

6 结论

本文利用同期夏季 CFS 实时预测模式资料以及前期秋、冬季观测资料，针对中国 1982～2011 年夏季站点降水建立了以场信息耦合型为建模方法的统计降尺度预测模型。此降尺度模型引入的两个预测因子，分别为泛东亚地区 CFS 模式资料的 GH5 和热带太平洋地区观测资料的 SST。文中分析了预测因子与预测量之间的 SVD 第一模态对，结果显示，两预测因子与预测量之间不仅有明晰的物理过程，而且具有显著的统计关系。

此降尺度模型对 1982～2011 年中国夏季降水的回报效果较 CFS 模式原始结果显著提高，表现为距平相关系数（ACC）的提高和均方根误差（RMSE）的降低。此模型较好回报出了 1983 年和 2006 年中国夏季降水距平的空间分布型，说明 ENSO 信号是影响中国夏季降水的重要因素之一。同时，该模型较好的回报出了 2011 年汛期降水的距平百分率的空间分布型，空间距平相关系数可以达到 0.28。因此，此降尺度模型有效结合前期因子与同期因子的综合作用，能够获取天气系统更多的同期和滞后效应，从而影响中国夏季降水，为夏季降水的预测提供有价值的信号。

参考文献（References）

Bjerknes J. 1966. A possible response of the atmospheric Hadley circulation to equatorial anomalies of ocean temperature [J]. Tellus, 18: 820–829.

Bjerknes J. 1969. Atmospheric teleconnections from the equatorial Pacific [J]. Mon. Wea. Rev., 97: 163–172.

陈官军, 魏凤英, 巩远发. 2010. NCEP/CFS 模式对东亚夏季延伸预报的检验评估 [J]. 应用气象学报, 21 (6): 659–670. Chen G J, Wei F Y, Gong Y F. 2010. Assessing the extended range forecast error of NCEP/CFS in the summer of East Asia [J]. Journal of Applied Meteorological Science (in Chinese), 21 (6): 659–670.

Chen H P, Sun J Q, Wang H J. 2012. A statistical downscaling model for forecasting summer rainfall in China from DEMETER hindcast datasets [J]. Wea. Forecasting, 27: 608–628.

Fan K, Wang H J. 2009. A new approach to forecasting typhoon frequency over the western North Pacific [J]. Wea. Forecasting, 24 (4): 974–978.

范可, 王会军, Choi Young-Jean. 2007. 一个长江中下游夏季降水的物理统计预测模型 [J]. 科学通报, 52 (24): 2900–2905. Fan K, Wang H J, Choi Y J. 2008. A physically-based statistical forecast model for the middle-lower reaches of the Yangtze River valley summer rainfall [J]. Chinese Science Bulletin, 53 (4): 602–609.

范可, 林美静, 高煜中. 2008. 用年际增量方法预测华北汛期降水 [J]. 中国科学 D 辑（地球科学）, 38 (11): 1452–1459. Fan K, Lin M J, Gao Y Z. 2009. Forecasting the summer rainfall in North China using the year-to-year increment approach [J]. Science in China Series D-Earth Sciences, 52 (4): 532–539.

Gao H, Yang S, Kumar A, et al. 2011. Variations of the East Asian Meiyu and simulation and prediction by the NCEP Climate Forecast System [J]. J. Climate, 24: 94–108.

Gu W Z, Chen L J, Li W J, et al. 2011. Development of a downscaling method in China regional summer precipitation prediction [J]. Acta Meteorologica Sinica, 25 (3): 303–315.

Huang R H, Li W J. 1987. Influence of the heat source anomaly over the western tropical Pacific on the subtropical high over East Asia [C]// Proc. International Conference on the General Circulation of East Asia, 40–51.

Jain S, Lall U. 2001. Floods in a changing climate: Does the past represent the future? [J] Water Resour. Res., 37: 3193–3205.

Jolliffe I T. 1972. Discarding variables in a principal component analysis. I: Artificial data [J]. Applied Statistics, 21: 160–173.

Jolliffe I T. 2002. Principal Component Analysis (2nd ed.) [M]. New York: Springer, 487pp.

Kalnay E, Kanamitsu M, Kistler R, et al. 1996. The NCEP/NCAR 40-year reanalysis project [J]. Bull. Amer. Meteor. Soc., 77: 437–471.

Kiladis G N, Diaz H F. 1989. Global climatic anomalies associated with extremes in the Southern Oscillation [J]. J. Climate, 2: 1069–1090.

Kosaka Y, Nakamura H. 2006. Structure and dynamics of the summertime Pacific–Japan teleconnection pattern [J]. Quart. J. Roy. Meteor. Soc., 132: 2009–2030.

Lang X M, Wang H J. 2010. Improving extraseasonal summer rainfall prediction by merging information from GCMs and observations [J]. Wea. Forecasting, 25: 1263–1274.

Liu Y, Fan K. 2012a. A new statistical downscaling model for autumn precipitation in China [J]. Int. J. Climat., doi: 10. 1002/joc. 3514.

Liu Y, Fan K. 2012b. Prediction of spring precipitation in China using a downscaling approach [J]. Meteor. Atmos. Phys., 118: 79–93.

Maity R, Kumar D N. 2006. Bayesian dynamic modeling for monthly Indian summer monsoon rainfall using El Niño–Southern Oscillation (ENSO) and Equatorial Indian Ocean Oscillation (EQUINOO) [J]. J. Geophys. Res., 111: D07104.

Nitta T. 1987. Convective activities in the tropical western Pacific and their impact on the Northern Hemisphere summer circulation [J]. J. Meteor. Soc. Japan, 65: 373–390.

Nitta T, Hu Z Z. 1996. Summer climate variability in China and its association with 500-hPa height and tropical convection [J]. J. Meteor. Soc. Japan, 74: 425–445.

任富民, 袁媛, 孙丞虎, 等. 2012. 近30年ENSO研究进展回顾 [J]. 气象科技进展, 2 (3): 17–23. Ren F M, Yuan Y, Sun C H, et al. 2012. Review of progress of ENSO studies in the past three decades [J]. Advances in Meteorological Science and Technology, 2 (3): 17–23.

Ropelewski C F, Halpert M S. 1987. Global and regional scale precipitation patterns associated with the El Niño/Southern Oscillation [J]. Mon. Wea. Rev., 115: 1606–1626.

Saha S, Nadiga S, Thiaw C, et al. 2006. The NCEP climate forecast system [J]. J. Climate, 19: 3483–3517.

Smith T M, Richard W R, Thomas C P, et al. 2008. Improvements to NOAA's historical merged land–ocean surface temperature analysis (1880–2006) [J]. J. Climate, 21: 2283–2296.

Sun J Q, Chen H P. 2012. A statistical downscaling scheme to improve global precipitation forecasting [J]. Meteor. Atmos. Phys., 117: 87–102.

王会军. 1997. 试论短期气候预测的不确定性 [J]. 气候与环境研究, 2 (4): 333–338. Wang H J. 1997. A preliminary study on the uncertainty of short-term climate prediction [J]. Climatic and Environmental Research, (in Chinese), 2 (4): 333–338.

Wang H J. 2002. The instability of the East Asian summer monsoon ENSO relations [J]. Adv. Atmos. Sci., 19: 1–11.

Wang H J, Fan K. 2009. A new scheme for improving the seasonal prediction of summer precipitation anomalies [J]. Wea. Forecasting, 24 (2): 548–554.

Wang H J, Zhang R H, Julie C, et al. 1999. El Niño and the related phenomenon Southern Oscillation (ENSO): The largest signal in interannual climate variation [J]. Proc. Natl. Acad. Sci. USA, 96: 11071–11072.

王绍武, 龚道溢, 陈振华. 1999. 近百年来中国的严重气候灾害 [J]. 应用气象学报, 10: 43–53. Wang S W, Gong D Y, Chen Z H. 1999. Serious climatic disasters of China during the past 100 years [J]. Quart. J. Appl. Meteor. (in Chinese), 10: 43–53.

Webster P J, Magana V O, Palmer T N, et al. 1998. Monsoons: Processes, predictability, and the prospects for prediction [J]. J. Geophys. Res., 103: 14451–14510.

Wilks D S. 2006. Statistical Methods in the Atmospheric Sciences (2nd ed.) [M]. New York: Wiley, 627pp.

Yang S, Zhang Z, Kousky V E, et al. 2008. Simulations and seasonal prediction of the Asian summer monsoon in the NCEP Climate Forecast System [J]. J. Climate, 21: 3755–3775.

Yuan X, Liang X Z. 2011. Improving cold season precipitation prediction by the nested CWRF–CFS system [J]. Geophys. Res. Lett., 38: L02706.

臧恒范, 王绍武. 1984. 赤道东太平洋水温对低纬大气环流的影响 [J]. 海洋学报, 6: 16–24. Zang H F, Wang S W.1984. The impact on atmospheric circulation at low latitude by sea surface temperature over tropical eastern Pacific [J]. Acta Oceanologica Sinica (in Chinese), 6: 16–24.

曾庆存, 王会军, 林朝晖, 等. 2003. 气候动力学与气候预测理论的研究 [J]. 大气科学, 27 (4): 468–483. Zeng Q C, Wang H J, Lin Z H, et al. 2003. A study of the climate dynamics and climate prediction theory [J]. Chinese Journal of Atmospheric Sciences (in Chinese), 2 (4): 333–338.

Zhu C W, Park C K, Lee W S, et al. 2008. Statistical downscaling for multi-model ensemble prediction of summer monsoon rainfall in the Asia–Pacific region using geopotential height field [J]. Adv. Atmos. Sci., 25 (5): 867–884.

Zhu Y L, Wang H J, Zhou W, et al. 2011. Recent changes in the summer precipitation pattern in East China and the background circulation [J]. Climate Dyn., 36: 1463–1473.

第 24 卷 第 3 期 应用气象学报 Vol. 24, No. 3
2013 年 6 月 JOURNAL OF APPLIED METEOROLOGICAL SCIENCE June 2013

刘玉莲,任国玉,于宏敏,等. 我国强降雪气候特征及其变化. 应用气象学报,2013,24(3):304-313.

我国强降雪气候特征及其变化

刘玉莲[1)] 任国玉[2)*] 于宏敏[1)] 康恒元[3)]

[1)](黑龙江省气候中心,哈尔滨 150030)

[2)](国家气候中心 中国气象局气候研究开放实验室,北京 100081) [3)](黑龙江省防雷中心,哈尔滨 150030)

摘 要

基于全国气象台站逐日地面降雪观测数据,对我国 25°N 以北不同气候区强降雪事件的地理分布和年内旬、月变化等气候特征进行分析,并探讨 1961—2008 年其时间序列演变特征,及 1961—2008 年和 1981—2008 年(气候变暖后)气候变化趋势。结果表明:强降雪量和强降雪日数在青藏高原东部、新疆和东北北部最多;强降雪强度高值中心出现在云南。东北北部、华北、西北、青藏高原东部强降雪事件多发生于初冬和初春,年内分布呈双峰型;新疆和黄淮地区年内分布呈单峰型,前者多发生在隆冬时节,后者多发生于晚冬;1961—2008 年东北北部、新疆、青藏高原东部平均强降雪量和强降雪日数呈明显增加趋势;气候变暖后我国大部年强降雪量增多,强降雪日数增加,强降雪强度增强。

关键词: 强降雪量; 强降雪日数; 强降雪强度; 气候特征

引 言

伴随着全球气候变暖,部分地区极端气候事件的强度和频率发生了相应变化,北半球中高纬度地区极端强降水事件频率增加[1],冬季降雪量和暴雪发生频率也有所增加[2-3]。一般认为,全球气候变暖会导致海面和地面蒸发能力增强,包括强降雪事件的强降水事件频率可能增加[4]。了解全球陆地和较大区域范围强降雪事件频率和强度的真实情况,有助于理解全球和区域气候变化的机理。此外,强降雪事件是气候学意义上的小概率事件,对自然和社会系统具有很大影响。因此,研究全球陆地和区域性强降雪事件,对于检测气候变化信号、减轻区域气象灾害影响均具有重要意义。

近年来,国内学者对降水事件分析较多[5-12],而对降雪特别是强降雪的分析较少[13-15]。已有关于强降雪事件研究,多是从天气学和短期气候异常监测、预测角度进行强降雪过程诊断分析。也有研究探讨了我国各个区域强降雪事件的空间分布和年内分配特征,如臧海佳[16]分析了中国降雪的时空分布,指出我国各级别降雪天气现象主要发生在 25°N 以北地区;邹进上等[17]、韦志刚等[18]和丁永红等[19]分别研究了青藏高原和宁夏等地区多年强降雪事件频率或积雪日数的气候学特征;杨秀春等[20]利用遥感技术探讨了我国北方草原地带积雪和强降雪事件监测问题。但是,利用完整的地面气象观测资料,开展全国性强降雪事件气候特征及其变化分析的工作,目前还很少。

本文利用最新的逐日地面降雪观测资料,研究了我国 25°N 以北地区强降雪量、强降雪日数和强度的主要气候特征及其变化,包括空间的地理分布差异、强降雪量和强降雪日数的季节性变化(旬、月)特征、强降雪量、强降雪日数和降雪强度的时间演变以及气候变化趋势。

1 资料和方法

资料来源于国家气象信息中心资料室提供的全国 740 个测站 1951—2009 年的逐日降水量、降雪资

2012-09-21 收到, 2013-03-18 收到再改稿。

资助项目:公益性行业(气象)科研专项(GYHY201106013,GYHY201206024)

* 通信作者,email: guoyoo@cma.gov.cn

料，这些站绝大部分属于国家基准气候站和基本气象站，个别为一般气象站。在所用资料中，20 世纪 50 年代初站点较少；其后站点数量增长迅速，到 1960 年站点数量已经接近 650 个；1960 年以后直到现在，各年的站点数量变化不大，基本上维持在 650～700 之间。

气候基准期选择 1971—2000 年，该时段内资料连续无缺测的站点数量为 629 个。研究区域选择有降雪的 25°N 以北我国大陆地区（图 1），该地区拥有的气象台站数量为 564 个。本文利用 564 个站点 1961—2008 年资料分析我国强降雪事件变化，台站的分布情况见图 1，其中Ⅰ区为东北北部，Ⅱ区为华北地区，Ⅲ区为黄淮地区，Ⅳ区为西北地区，Ⅴ区为新疆，Ⅵ区为青藏高原东部，Ⅶ区为东南地区。考虑到降水要素资料的时间序列对于台站位置变动等影响没有温度和风速敏感，本文选取资料连续无缺测站点，没有对日降水资料进行均一化订正。

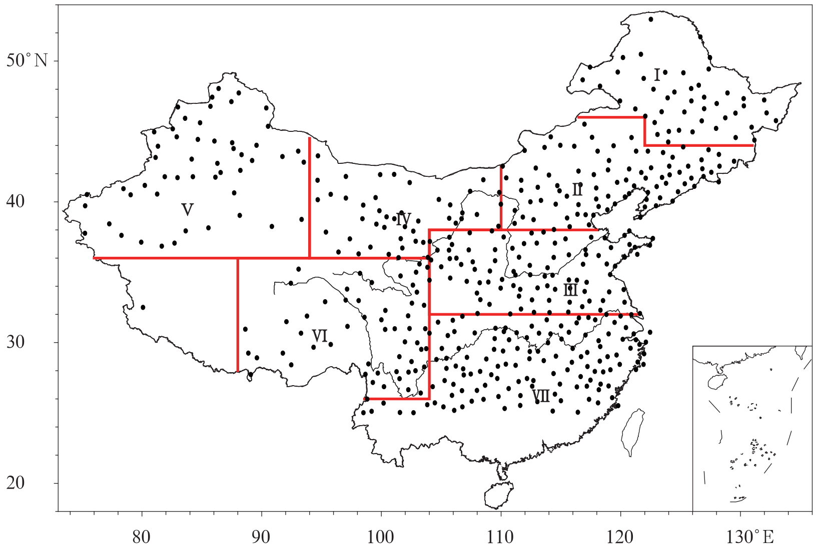

图 1　研究区站点分布及降雪气候分区

Fig. 1　The distribution of meteorological stations and snowfall regionalization

由于 REOF 方法[21-22]能够清晰显示气候变量场不同的地理区域特征，而被广泛用于气候变量场分区研究中，本文采用 REOF 方法，根据 1971—2000 年降雪日数资料对研究区域的降雪变异性进行分区。分区的临界相关系数确定为 0.4（资料序列长度为 30 年，$\alpha=0.05$），即将 REOF 载荷向量值大于 0.4 的区域划为一个降雪气候区[23]。青藏高原西北部缺少观测站点，插值结果可能存在虚假现象，故本文不讨论西藏西部区域。

本文对降雪年和雪季等定义见表 1。降雪年是指从当年 7 月 1 日至下一年 6 月 30 日的 1 年时间，例如 2000 年降雪年为 2000 年 7 月 1 日—2001 年 6 月 30 日。雪季是指按天气现象统计降雪年内第 1 日出现固态降水天气现象日期和最后 1 日出现固态降水天气现象日期之间的时间间隔。统计时剔除了有液态降水出现的降雪日，由于出现固、液混合态降水时，难以计算出当日的降雪量，同时考虑到雨、雪交加的日子地面气温不会过低，难以形成明显积雪，不会对农业生产和社会生活造成重要影响。

目前对极端降水（雪）或强降水（雪）事件的定义方法很多。有些研究选取某个固定的日降水（雪）量值作为阈值，判定出现大于该阈值的降水（雪）即为极端降水（雪）。例如，就降雪而言，我国通常将日降雪量超过 10 mm 的降雪事件称为暴雪，日降雪量超过 5 mm 的降雪事件称为大雪。事实上，在我国气候的地域差异十分明显，不同地区降水和降雪差异很大，因此用绝对阈值定义日强降雪事件，在各个地区之间缺乏可比性。目前在气候极值变化研究中经常选择某个百分位值作为阈值定义极端气候事件[24-25]。设某个气象要素值有 n 个值，将这些值按升序排列，取累积频率为某个百分位的观测值作为阈值，大于该阈值的即为极端气候事件。

本文定义雪季内日（24 h）降雪量超过气候基准期 80％分位值的全部降雪日数和总降雪量为强降

雪事件频率和强降雪量的指标；强降雪强度(年)是指雪季内强降雪量与强降雪日数的比值。选取80%百分位是因为有些台站降雪频次较少，为了保证各个分区内每年有足够的观测记录数据，以便使强降雪事件的统计和区域间比较具有意义。

表 1　降雪和强降雪指标定义

Tabel 1　Definition of indices of snowfall and intense snowfall used in this paper

指标	定义
降雪年	从当年 7 月 1 日至下一年 6 月 30 日
雪季	降雪年内第 1 日和最后 1 日出现固态降水天气现象的时间间隔(单位：d)
年降雪量	降雪年内降雪量总和
强降雪日数和强降雪量	雪季内日(24 h)降雪量超过气候基准期内 80%分位值的总降雪日数(单位：d)和总降雪量(单位：mm)
强降雪强度	雪季内强降雪量与强降雪日数的比值(单位：mm・d^{-1})

在计算各个分区和全国平均气候时间序列时，采用 Jones 等[26]提出的计算区域平均时间序列的方法。该方法是将每个分区按经纬度划分网格，求取每个网格区的平均距平值，然后采用面积加权平均法，得到区域平均的要素距平时间序列。本文采用 2°×2°的经纬度网格，面积加权平均采用每个网格中点纬度的余弦作为权重系数。

2　强降雪气候特征

2.1　强降雪事件地理分布

图 2 为我国多年平均强降雪量、强降雪日数和强降雪强度的地理分布情况。总体上看，强降雪量和强降雪日数具有大体一致的空间分布特征：东北北部、北疆和青藏高原东南部为 3 个高值区域；东北南部、内蒙古东部、华北和黄土高原、江淮流域强降雪日数和降雪量相对较高。我国多年平均强降雪量和强降雪日数较少区域主要分布在江南地区、西北地区的南疆和内蒙古西部。江南地区主要因为气温高，强降雪事件频率和降雪量比较少；西北内陆干燥区域主要因为水汽匮乏，雪季降水稀少，强降雪事件频率和降雪量很低。

强降雪强度的地理分布与强降雪量、强降雪日数有很大差异，强降雪强度高值中心出现在强降雪频率很低的南方地区。云贵高原、长江中下游和东南沿海地区强降雪强度最高，而强降雪频率很高的东北北部和青藏高原东南部强降雪强度则较低，强降雪强度最低值出现在四川盆地、南疆北部和内蒙古西部。

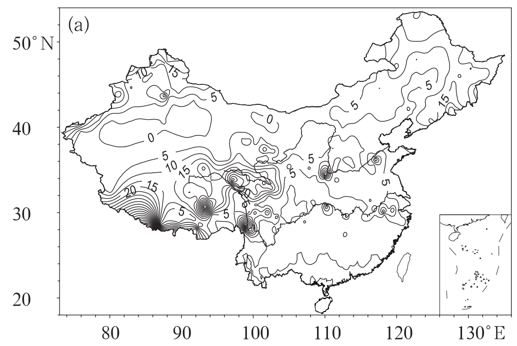

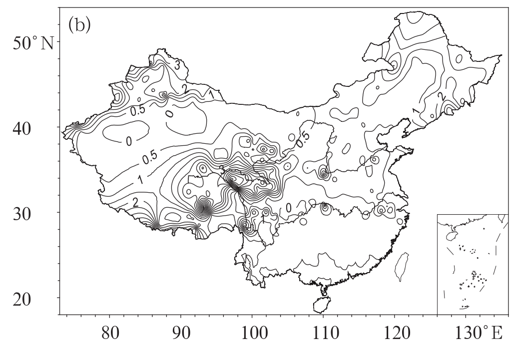

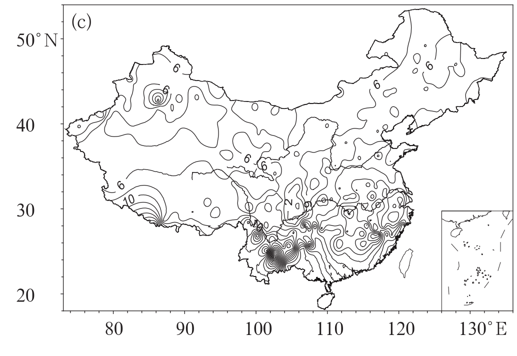

图 2　多年平均强降雪量(单位：mm)(a)、强降雪日数(单位：d)(b)及强降雪强度(单位：mm・d^{-1})(c)空间分布

Fig. 2　The distributions of annual intense snowfall(unit：mm)(a), the number of intense snow days(unit：d)(b) and intense snow intensity(unit：mm・d^{-1})(c)

从局地分布特点来看,中部的华山、青藏高原东部的梅里和玉龙雪山以及青藏高原西南侧山地等地点强降雪量较大(图 2a),年平均强降雪量最多出现在喜马拉雅山脉北麓,中心位于西藏聂拉尔(122.2 mm)、西藏嘉黎(67.6 mm)和云南德钦(53.7 mm)。年平均强降雪日数分布(图 2b)与强降雪量分布基本相同,华山、梅里、玉龙雪山、青藏高原西侧等高海拔地区强降雪日数较多,但强降雪日数最多发生在西藏嘉黎(7.3 d),而不在强降雪量最多的聂拉尔(5.3 d),其次是青海青水河(6.9 d)和四川石渠(2.4 d)。年平均强降雪强度分布(图 2c)最大中心出现在云南玉溪(36.2 mm·d^{-1})、云南昆明(27.3 mm·d^{-1})和云南丽江(24.1 mm·d^{-1})。这些地区均位于我国西南水汽通量最大区域。

表 2 给出各个分区多年强降雪量和强降雪日数。由于东南地区强降雪频次和降水量很小,故未做区域平均统计(下同)。青藏高原东部强降雪日数最多,其次是东北北部、新疆;西北地区、黄淮地区和华北地区;强降雪量最多也是出现在青藏高原东部,其次为新疆和东北北部,西北地区、黄淮地区和华北地区强降雪量最小。

表 2　1971—2000 年不同区域累积强降雪量和强降雪日数

Table 2　Accamulated intense snowfall amounts and the number of intense snowfall days in different sub-regions from 1971 to 2000

地区	强降雪量/mm	强降雪日数/d
东北北部	316.9	50.43
华北	221.2	31.57
黄淮	221.9	26.58
西北	149.2	28.15
新疆	321.1	48.89
青藏高原东部	511.7	70.79

2.2　强降雪事件年内变化

强降雪日数和强降雪量的年内各月分布基本一致(表 3 和表 4)。北方各地区和青藏高原东部年内各月变化呈现双峰型,黄淮地区呈现单峰分布特点。东北北部区强降雪量和强降雪日数最多均出现在 3 月和 10—11 月;华北地区强降雪量最多出现在 11 月,其次是 3 月和 1 月,而强降雪日数与强降雪量略有不同,最多是 3 月,其次是 11 月和 1 月;西北地区强降雪量和强降雪日数最多均出现在 3—4 月和11月;新疆强降雪量最多出现在11—12月和2

表 3　1971—2000 年不同区域平均强降雪量月变化(单位:mm)

Table 3　Monthly mean intense snowfall in different regions(unit: mm)

月份	东北北部	华北地区	黄淮地区	西北地区	新疆	青藏高原东部
7	0.0	0.0	0.0	0.0	0.0	2.7
8	0.0	0.0	0.0	0.7	0.0	2.1
9	0.7	0.1	0.0	0.7	0.5	19.0
10	61.5	14.1	4.1	20.3	20.0	79.0
11	67.4	46.8	27.4	19.3	63.3	37.3
12	35.0	31.9	32.7	4.7	76.2	16.8
1	16.2	34.7	48.0	5.5	51.7	23.4
2	17.9	31.6	46.2	10.0	53.4	47.9
3	79.9	45.4	51.5	39.0	40.2	105.8
4	35.5	15.2	10.6	33.5	14.7	94.8
5	2.8	1.3	1.3	15.2	1.2	64.9
6	0.0	0.0	0.0	0.4	0.0	18.0

表 4　1971—2000 年不同区域平均强降雪日数月变化(单位:d)

Table 4　The number of monthly mean intense snow days in different regions(unit: d)

月份	东北北部	华北地区	黄淮地区	西北地区	新疆	青藏高原东部
7	0.00	0.00	0.00	0.00	0.00	0.50
8	0.00	0.00	0.00	0.05	0.00	0.32
9	0.10	0.03	0.00	0.15	0.11	3.14
10	8.07	1.77	0.60	3.85	3.00	9.93
11	11.43	6.55	3.23	3.95	9.68	4.57
12	5.83	4.72	4.09	1.15	11.84	2.61
1	2.73	4.91	5.53	1.35	8.21	3.68
2	3.33	4.49	5.63	2.35	7.74	6.93
3	13.03	6.92	6.02	7.35	6.26	13.40
4	5.40	2.01	1.32	5.90	1.84	13.00
5	0.50	0.17	0.14	2.00	0.21	9.93
6	0.00	0.00	0.00	0.05	0.00	2.79

月，而强降雪日数最多出现在 11—12 月和 1 月；青藏高原东部强降雪量和强降雪日数最多出现在 3—4 月，其次出现 10 月和 5 月。单峰型分布型强降雪量和日数峰值出现在隆冬和晚冬，黄淮地区强降雪量和强降雪日数最多均出现在 1—3 月。

图 3 为我国各个区域强降雪量和强降雪日数年内各旬之间的变化特征。各个区域强降雪量和强降雪日数的旬际变化规律与月际变化相似，但可以更精确地反映年内变化情况。总体上看，强降雪量和强降雪日数年内变化基本相近，东北北部、西北、青藏高原东部和新疆等地双峰分布特点更明显，黄淮地区呈现单峰型分布，华北地区则表现出不明显的双峰型，实则属于单峰型与双峰型之间的过渡类型。

具体地说，东北北部强降雪量和强降雪日数最多的时间都出现在 10 月下旬、3 月中旬和 3 月下旬；华北地区强降雪量最多出现在 1 月上旬、3 月中旬和 11 月上旬，强降雪日数最多则出现在 3 月中旬，其次是 1 月上旬和 11 月上旬；黄淮地区强降雪量和强降雪日数最多均出现在 3 月上旬，强降雪量次多出现在 2 月下旬和 1 月上旬，强降雪日数次多出现在 1 月上旬和 2 月中、下旬；西北地区强降雪量和强降雪日数最多出现在 3 月下旬和 10 月上旬，强降雪量次多出现在 3 月中旬，强降雪日数次多出现在 4 月上旬；新疆强降雪量和强降雪日数峰值均出现在 12 月上旬，强降雪量次多出现在 11 月中旬和 1 月上旬，强降雪日数次多出现在 1 月上旬和 11 月中旬；青藏高原东部强降雪量和强降雪日数最多均出现在 3 月下旬、10 月中旬和 4 月中旬。

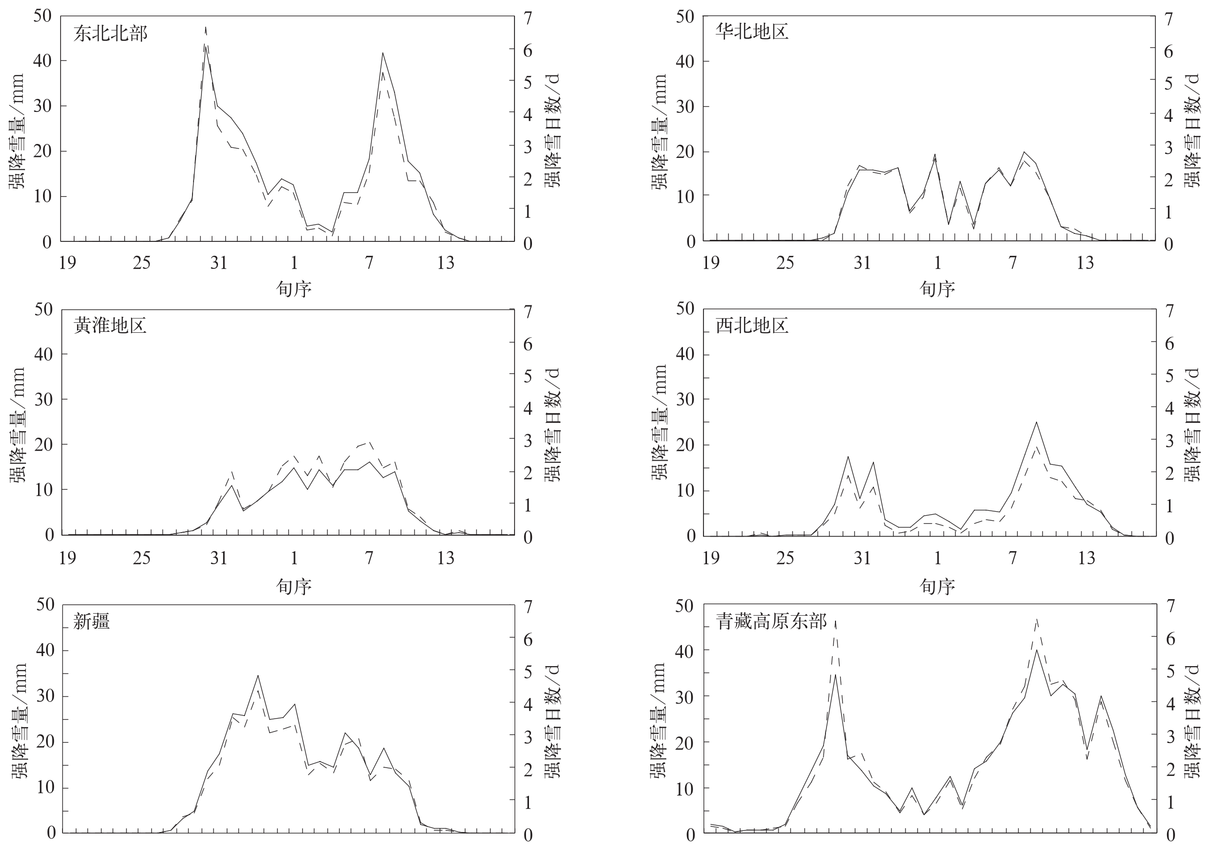

图 3　1971—2000 年不同区域强降雪量(虚线)和强降雪日数(实线)年内变化

Fig. 3　The changes of ten-day average intense snowfall(dashed line) and the number of intense snow days(solid line) in different regions from 1971 to 2000

2.3 时间序列演变

对我国 1961—2008 年强降雪量、强降雪日数和降雪强度分区平均，分析各区平均的强降雪量、强降雪日数和强降雪强度的逐年演变特征（图略）。

东北北部强降雪量增加趋势明显（达到 0.05 显著性水平），在 20 世纪 80 年代前以偏少为主，强降雪量最少的年份为 1971 年；80 年代以后转为偏多，强降雪量最多年份为 2006 年，次多年为 1980 年。华北地区强降雪量没有明显的年代际变化，但年际波动较大，强降雪量最少年份为 1967 年，最多为 2006 年。黄淮地区强降雪量阶段性变化比较明显，有 4 个偏多期，分别是 60 年代后期、80 年代初期、80 年代末 90 年代初期和 21 世纪初期，近几年为偏少时期，强降雪量最多和最少的年份分别为 1988 年和 1976 年。西北地区的强降雪量在 70 年代中期前以偏少为主，仅 1965 年和 1966 年超过气候平均值，而 1966 年的强降雪量是分析时段内最多的年份，70 年代中期以后到 80 年代末，强降雪量偏多，90 年代以来偏少为主，只 2000 年和 2006 年多于气候平均值，1998 年是强雪量最少的年份。新疆强降雪量增加趋势明显，80 年代中期以前以偏少为主，而分析时段内强降雪量最多的年份 1968 年和最少的年份 1964 年都出现在这个偏少的背景里，90 年代中期以后，强降雪量以偏多为主，2000 年是强降雪量次多的年份。青藏高原东部强降雪量增加趋势明显，强降雪量 70 年代以前明显偏少，最少年份为 1964 年，70 年代和 80 年代在平均值附近年际变化不大，90 年代出现了分析时段内降雪量最多的 1995 年，此后呈波动减少，2001 年后又呈波动增加。

各地区强降雪日数演变曲线与强降雪量演变趋势和阶段性变化大体一致。东北北部、华北地区强降雪强度年际和年代际变化均不大，只是在 2006 年华北地区出现 1 个降雪强度极值。黄淮地区降雪强度在 20 世纪 70 年代中期前和 80 年代中期到 90 年代中期偏大；70 年代中期到 80 年代中期和 90 年代中期以来，强降雪强度偏小。西北地区 70 年代中期以前强降雪强度偏小，80 年代偏大。新疆最强降雪强度出现在 80 年代中期，最小为 2006 年。青藏高原东部强降雪强度 80 年代以前波动性较大，80 年代和 90 年代较稳定，2000 年前后的几年较小，近年略有增加。

2.4 变化趋势

对我国强降雪量、降雪日数和降雪强度进行变化趋势分析，图 4 是 1961—2008 年和 1981—2008 年强降雪量、降雪日数和降雪强度的变化趋势系数空间分布图。趋势系数是要素序列与自然数 1，2，3，…，n 的相差系数，相差系数正负表示要素序列趋势的增加或减少，该值为正（负）时，表示该要素在 n 年内呈线性增加（减少）的趋势。

1961—2008 年我国大部分地区强降雪量没有明显变化趋势，增加趋势较明显地区为黑龙江省东北部、新疆北部、河西走廊中段和青藏高原东北部（达到 0.05 显著性水平），减少趋势明显地区为河套平原东南部、松嫩平原西部、燕山山脉西部、山东北部、长白山区南部；强降雪日数的趋势变化空间分布与强降雪量变化空间分布基本一致；强降雪强度变化趋势全国大部均不显著，增加趋势明显地区为柴达木盆地东北部，减小趋势明显地区为松嫩平原西部、燕山山脉西部、黄土高原西部。

考虑 20 世纪 80 年代以后全球变暖明显，分析 1981—2008 年我国强降雪变化，结果显示从 20 世纪 80 年代以来的 28 年中，我国大部地区强降雪量无明显变化趋势，增加较明显地区为新疆西部和北部、呼伦贝尔草原、长白山脉北部，减小较明显地区为东北地区中西部、黄河源区南部、河套平原东南部；强降雪日数变化趋势空间分布与强降雪量基本一致；强降雪强度变化趋势全国大部不显著，增加趋势明显地区主要为新疆西部、长白山脉北麓，减小趋势明显地区为阿尔山西南、黄河源区南部。

我国大范围气候变暖主要发生在 20 世纪 80 年代初以后，为了解气候变暖前后我国强降雪事件的变化，分别分析和比较了全国及各个区域 1961—1980 年和 1981—2008 年平均强降雪量、强降雪日数和强降雪强度（表 5）。由表 5 可见，气候变暖后全国大部年强降雪量增多，强降雪日数增加，强降雪强度增强。强降雪量增多最大地区为青藏高原东部，其次为新疆，华北区强降雪量没有增多，反而表现出减少；强降雪日数增加最多的地区为青藏高原东部，其次为新疆，华北地区强降雪日数减少；强降雪强度增强最明显地区为黄准地区，其次为西北地区，东北北部和华北地区强降雪强度减弱，华北地区较东北北部减弱更多。

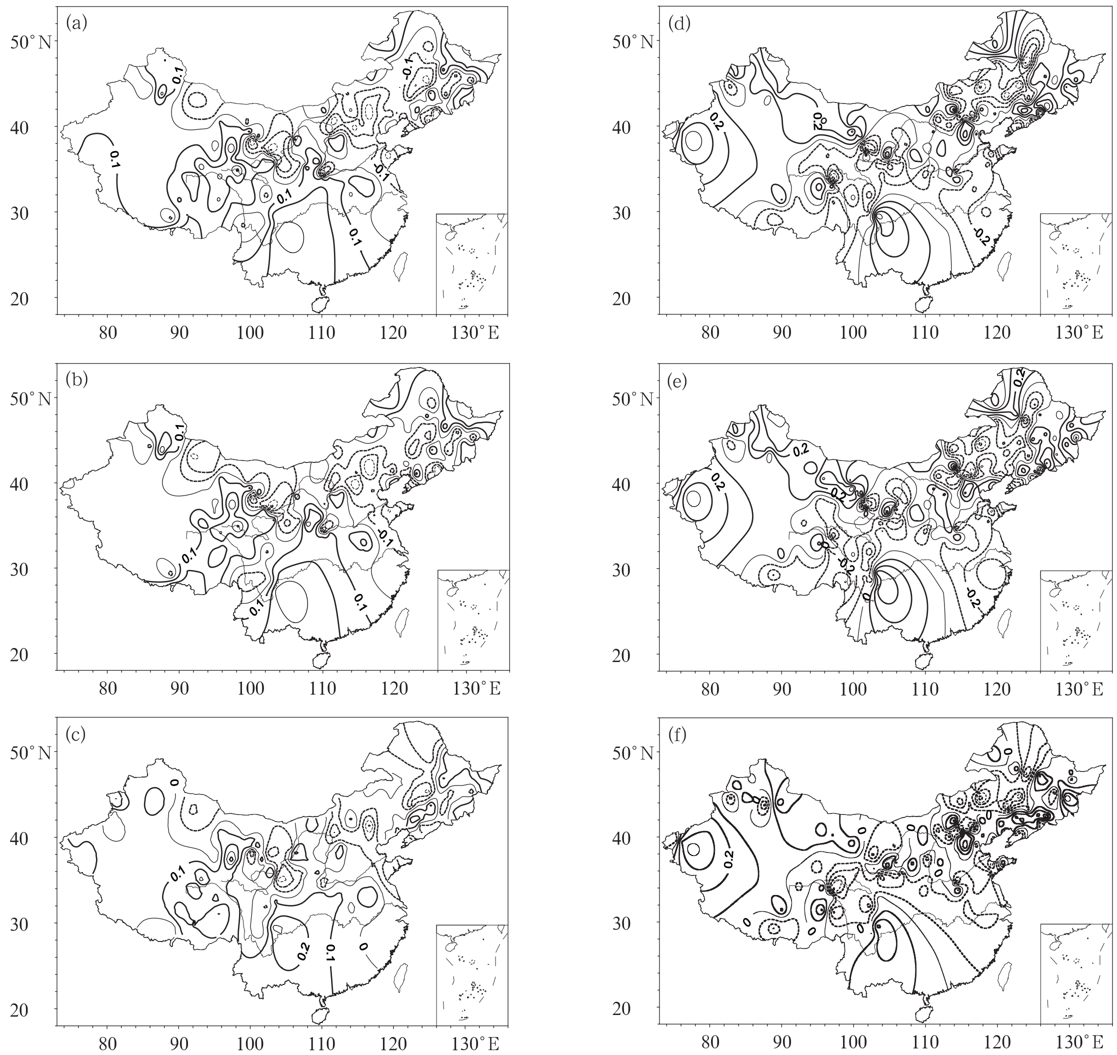

图4 1961—2008年强降雪量(a)、强降雪日数(b)、强降雪强度(c)和
1981—2008年强降雪量(d)、强降雪日数(e)、强降雪强度(f)变化趋势系数空间分布
Fig.4 Spatial distribution of the intense snowfall(a), the number of intense snow days(b), intense snow intensity(c) change trends during 1961—2008, and the intense snowfall(d), the number of intense snow days(e), intense snow intensity(f) change trends during 1981—2008

表5 1961—1980年和1981—2008年不同区域平均年强降雪量、年强降雪日数和年强降雪强度比较

Table 5 Comparison of annual mean intense snowfall amounts, the number of intense snow days and intense snow intensity between 1981—2008 and 1961—1980 for different sub-regions

要素	时段	东北北部	华北	黄淮	西北	新疆	青藏高原东部
强降雪量/mm	1961—1980年	9.5	7.8	7.0	4.3	9.1	13.0
	1981—2008年	10.9	7.3	7.3	5.0	11.3	17.1
强降雪日数/d	1961—1980年	1.48	1.06	0.86	0.86	1.42	1.84
	1981—2008年	1.73	1.01	0.87	0.96	1.72	2.35
强降雪强度/(mm·d^{-1})	1961—1980年	6.4	7.4	8.1	5.0	6.4	7.1
	1981—2008年	6.3	7.2	8.4	5.2	6.6	7.3

3 结论和讨论

本文利用地面观测站逐日降雪资料，研究了我国25°N以北地区强降雪量、强降雪日数和强降雪强度的气候空间分布，强降雪量和强降雪日数的月、旬变化特征，强降雪量、强降雪日数和强降雪强度的时间演变和空间趋势变化，得到以下主要结论：

1）我国强降雪量和强降雪日数在青藏高原东部、新疆和东北北部最多；强降雪强度中心出现在云南，超过 20 $mm \cdot d^{-1}$。

2）强降雪量和强降雪日数年内变化基本相近，东北北部、西北地区、青藏高原东部和新疆等地区双峰分布特点更清楚，黄淮地区呈单峰型分布，华北地区则表现出不明显的双峰型，实则属于单峰型与双峰型之间的过渡类型。

3）1961—2008 年我国强降雪量和强降雪日数在东北北部、新疆、青藏高原东部均呈明显增加趋势，其他地区变化不明显；强降雪强度各地区均无明显变化趋势。气候变暖后全国大部年强降雪量增多，强降雪日数增加，强降雪强度增强。

气象站的降水观测资料是研究强降雪事件气候特征的基础，因此单站降水观测资料的精度直接影响计算和分析结果。降雪量是利用符合一定标准的容器，将收集到的雪融化后测得的量值。由于风对雨、雪进入雨量器的干扰（动力损失）、雨量器承水器和储水瓶（筒）内壁对部分降水的吸附湿润损失和降水停止到观测时刻以及降水间歇期内雨量器储水瓶（筒）中雨（雪）水的蒸发（蒸发损失），使雨量器的观测值比实际降水量系统偏小，其中动力损失或风速导致的偏差最为严重，液态降水时的最大测量误差值可达实际降水量的 10%，固态降水时更可达 50%，甚至为 100%[27-29]。因此，降雪受近地面风速影响较大，近些年地面风速减弱明显[30-32]，对降雪观测的影响不仅表现在测量值的误差上，还表现为风速改变，影响到降雪测量误差的改变[33]。

目前，还没有全国经过降水动力损失误差订正的日观测资料，因此无法获得真实的雪季日降雪量和强降雪量估计值。根据最近的区域性研究结果，降水量或降雪量测量的绝对误差在降水量多的低纬度地区较大；而相对误差在高纬度地区，特别是内蒙古东部较大[33]。考虑降雪测量误差，本文对我国东北、内蒙古、新疆和青藏高原等地区的多年平均强降雪量和降雪强度估计结果可能偏低 10%以上，在北方平均风速较强的春季，强降雪量和降雪强度估计偏低会更多；文献[31]指出近地面风速变化呈明显的减小趋势，本文对强降雪量和降雪强度的气候变化分析可能增加的趋势偏大，减小的趋势偏小。但是，由于平均风速减弱引起的降雪测量误差变化，主要影响降雪和强降雪事件气候变化分析，对本文的气候特征分析影响很小。

参 考 文 献

[1] Groisman P, Kerl T, Easterling D, et al. Changes in the probability of extreme precipitation important indicators of climate change. *Climatic Change*, 1999, 42: 243-283.

[2] Obasi G O P. Reducing Vulnerability to Weather and Climate Extremes. Information and Public Affairs Office, WMO, 2002.

[3] IPCC. Climate Change 2007: The Physical Science Basis. Cambridge: Cambridge University Press, 2007.

[4] 秦大河. 中国西部环境演变评估：中国西部环境演变评估综合报告. 北京：科学出版社，2002.

[5] 翟盘茂，潘晓华. 中国北方近 50 年温度和降水极端事件变化. 地理学报，2003，58(增刊)：1-10.

[6] 刘海文，丁一汇. 华北夏季降水的年代际变化. 应用气象学报，2011，22(2)：129-137.

[7] 裴浩，郝璐，韩经纬. 近 40 年内蒙古候降水变化趋势. 应用气象学报，2012，23(5)：543-550.

[8] 魏维，张人禾，温敏. 南亚高压的南北偏移与我国夏季降水的关系. 应用气象学报，2012，23(6)：650-659.

[9] 孙娴，魏娜，肖科丽. 陕西秋季降水变化特征. 应用气象学报，2010，21(3)：360-365.

[10] 陈波，史瑞琴，陈正洪. 近 45 年华中地区不同级别强降水事件变化趋势. 应用气象学报，2010，21(1)：47-54.

[11] 张天宇，程炳岩，刘晓冉. 近 45 年长江中下流地区汛期极端强降水事件分析. 气象，2007，33(1)：80-87.

[12] 杨金虎，江志红，王鹏祥，等. 中国西北极端降水事件年内非均匀性特征分析. 中国沙漠，2008，28(1)：178-184.

[13] 仪清菊，刘延英，许晨海. 北京 1980—1994 年降雪的天气气候分析. 应用气象学报，1999，10(2)：249-254.

[14] 江毅，钱维宏. 内蒙古大(暴)雪的区域特征. 地理学报，2003，58(增刊)：38-48.

[15] 杨莲梅，杨涛，贾丽红，等. 新疆大～暴雪气候特征及其水汽分析. 冰川冻土，2005，27(3)：389-396.

[16] 臧海佳. 近 52 年我国各强度降雪的时空分布特征. 安徽农业科学，2009，37(13)：6064-6066.

[17] 邹进上，曹彩珠. 青藏高原降雪的气候学分析. 大气科学，1989，13(4)：400-409.

[18] 韦志刚，黄荣辉，陈文. 青藏高原地面站积雪的空间分布和年代际变化特征. 大气科学，2002，26(4)：496-508.

[19] 丁永红，冯建民，赵蔚，等. 1961—2009 年宁夏大到暴雪气候特征和变化规律. 冰川冻土，2011，33(6)：1399-1406.

[20] 杨秀春，曹云刚，徐斌，等. 我国北方草原区积雪遥感监测. 地理研究，2008，27(5)：1109-1117.

[21] 黄嘉佑. 转动主分量分析在天气气候分析中的应用. 气象，1988，14(9)：47-51.

[22] 魏凤英.现代气候统计诊断预测技术(第2版).北京:气象出版社,2007:105-125.
[23] 刘玉莲,任国玉,于宏敏.中国降雪气候学特征.地理科学,2012,32(10):1176-1185.
[24] Manton M J,Della-Marta P,Haylock M,et al. Trends in extreme daily rainfall and temperature in southeast Asia and the South Pacific:1961—1998. *IntJClimatol*,2001,21:269-284.
[25] Frich P,Alexander L V,Della-Marta P,et al. Observev coherent changes in climatic during the second half of the Twentieth century. *Climate Res*,2002,19:193-212.
[26] Jones P D,Hulme M. Calculating regional climatic time series for temperature and precipitation: Methodsand illustrations. *Int J Climatol*,1996,16:361-377.
[27] Sevruk B. Correction of Precipitation Measurements: SummaryReport. Instrument& Observing Methods Reports,No. 25, WMO,1985.
[28] WMO. International Organizing Committee for WMO Solid Precipitation Measurement intercomparison,Final Report. 1985.
[29] 杨大庆,施雅风,康尔泗,等.天山乌鲁木齐河流域雨量器对比观测降水实验结果分析.水文,1991(3):26-32.
[30] 李艳,王元,汤剑平.中国近地层风能资源的时空变化特征.南京大学学报:自然科学版,2007,43(3):280-291.
[31] 任国玉,郭军,徐铭志,等.近50年中国地面气候变化基本特征.气象学报,2005,63(6):948-952.
[32] Jiang Y,Luo Y,Zhao Z,et al. Changes in wind speed over China during 1956—2004. *Theor Appl Climatol*,2010,99:421-430.
[33] 孙秀宝,任国玉,任芝花,等.风场变形误差对冬季降雪测量及其趋势估算的影响.气候与环境研究,2013,18(2):178-196.

Climatic Characteristics of Intense Snowfall in China with Its Variation

Liu Yulian[1)] Ren Guoyu[2)] Yu Hongmin[1)] Kang Hengyuan[3)]

[1)] (*Heilongjiang Provincial Climate Center*, *Harbin* 150030)

[2)] (*Laboratory for Climate Studies*, *National Climate Center*, *CMA*, *Beijing* 100081)

[3)] (*Heilongjiang Provincial Lightning Protection Center*, *Harbin* 150030)

Abstract

Based on daily ground snowfall observations of national meteorological stations, climatic zonation is carried out according to the snowfall variability with the REOF method to the north of 25°N in China. The main climatic characteristics and variation of intense snowfall events in different climate zones are analyzed, including the spacial distribution difference, the changing characteristics of intense snowfall and the number of snow days of the month, ten-day, spatial changes and temporal evolutions in the trend of intense snowfall, the number of snow days and intensity, and the climate change trends of the 1961—2008 and 1981—2008 (considering climate warming) are calculated, respectively.

It shows that the east of Tibet Plateau, Xinjiang and the north of Northeast China have the highest amount and frequency of intense snowfall. The maximum intense snow intensity centers in Yunnan. The percentage of intense snow days to total snowfall days is generally low in North China, followed by the north of Northeast China and Xinjiang, and the largest percentage occurs in the Huang-Huai River Areas. In the north of Northeast China, North China, Northwest China and the east of Tibet Plateau, the high-frequency periods of intense snow events are generally in spring and early winter. It comes to mid-winter in Xinjiang, and to late winter in the Huang-Huai River Areas. In the north of Northeast China, Xinjiang and the east of Tibet Plateau, the intense snowfall and snow days obviously increased over the last 48 years. With climate warming, the intense snowfall and snow days increase, and meanwhile the intense snow intensity strengthens in most regions of China.

Due to the snowfall measurement error, the estimation results of the mean intense snowfall and snow intensity in the north of China may be low, in the spring, the mean wind speed is strong, and the intense snowfall and snow intensity estimation is lower. Because the wind speed near the ground is in decreasing trend, the analysis of climate change on intense snowfall and snow intensity may be that the increasing trend is overestimated, while the decreasing trend is underestimated. The snowfall measurement error change caused by the average wind speed decreasing mainly affects the analysis of intense snowfall events of climate change, while has few impacts on the research of climatic characteristics.

Key words: intense snowfall; intense snow days; intense snow intensity; climatic characteristics

《应用气象学报》征稿简则

《应用气象学报》(双月刊)是大气科学理论与应用研究的综合性学术期刊,主要刊登反映新理论与新技术在大气科学中的应用,以及大气科学理论与实践相结合,应用于各个有关领域的研究论文、业务系统和研究简报;国内外大气科学与应用气象科学发展中的新动态与新问题的探讨与评论;国内外重要学术会议或研究、业务活动的报道;气象书刊评介。

投稿要求和注意事项:

1. 论点明确、文字精炼。摘要请按文摘四要素(目的、方法、结果、结论)撰写,列出 3～8 个关键词,作者姓名请附汉语拼音,所在单位请附中、英文全名、地名、邮编。要求中文摘要为 200～400 字,英文摘要为 500 个单词左右(并请附对应的中文译文)。

2. 插图请插入文中适当位置,要求准确、清晰、美观。图中物理量、单位请勿遗漏,中、英文图题及说明写在插图下面。表格请采用三线表形式,并列出中、英文表题。

3. 参考文献请择主要的列入,并请按文中引用顺序标号。期刊书写格式:作者. 文章题目. 刊名,年,卷(期):起止页. 专著书写格式:作者. 书名. 译编者. 出版地:出版社,出版年:起止页.

4. 计量单位请按《中华人民共和国法定计量单位》列出,已废止的单位请换算成法定计量单位。

5. 科技术语和名词请使用全国自然科学名词审定委员会公布的名词。外国人名和地名,除常用者外请注原文。

6. **网上投稿(http://qk.cams.cma.gov.cn)请同时寄送全体作者签名的《承诺书》(请网上自行下载)。**稿件自收到之日起,将在 6 个月内决定刊用与否,来稿一经刊登,酌情收取版面费,并酌付稿酬。

7. 文中的数字及符号必须清楚无误,易混淆的外文字母、符号,请标注文种,大、小写,正、斜体,黑、白体,公式中的上、下标。

8. 本刊已加入“中国学术期刊(光盘版)”、“万方数据——数字化期刊群”和“中文科技期刊数据库”。本刊所付稿酬包含光盘稿酬和刊物内容上网服务报酬。凡向本刊投稿的作者(除事先声明外),本刊视为同意将其稿件纳入此两种版本进行交流。

欢迎投稿。投稿请登录 qk.cams.cma.gov.cn。

地址:中国气象科学研究院《应用气象学报》编辑部,邮政编码:100081;电话:(010)68407086,68408638;网址:qk.cams.cma.gov.cn;E-mail:yyqxxb@cams.cma.gov.cn, yyqxxb@163.com。

彭杰, 张华, 沈新勇. 2013. 东亚地区云垂直结构的 CloudSat 卫星观测研究 [J]. 大气科学, 37 (1): 91−100, doi:10.3878/j.issn.1006-9895.2012.11188.
Peng Jie, Zhang Hua, Shen Xinyong. 2013. Analysis of vertical structure of clouds in East Asia with CloudSat data [J]. Chinese Journal of Atmospheric Sciences (in Chinese), 37 (1): 91−100.

东亚地区云垂直结构的 CloudSat 卫星观测研究

彭杰[1,2] 张华[3] 沈新勇[1]

1 南京信息工程大学气象灾害省部共建教育部重点实验室，南京 210044
2 中国气象科学研究院，北京 100081
3 中国气象局气候研究开放实验室，国家气候中心，北京 100081

摘　要　本文利用卫星 CloudSat 同时结合了与其同轨道的卫星 CALIPSO（Cloud-Aerosol Lidar and Infrared Pathfinder Satellite Observations）2007 至 2009 年 3 年的观测资料，将东亚地区划分为六个研究区域，着重研究了东亚地区云垂直分布的统计特征。结果表明：东亚地区不同高度的云量之和具有明显的季节变化趋势，夏季最大，春秋次之，冬季最小。海洋上空的单层云量最大值出现在冬季，而在陆地上空则出现在夏季。从云出现概率来看，东亚地区单层云出现的概率在春、夏、秋、冬季节依次为 52.2%，48.1%，49.2%和 51.9%，而多层（2 层和 2 层以上）云出现的概率在春、夏、秋、冬季节分别为 24.2%，31.0%，19.7%，15.8%。云出现的总概率和多层云出现的概率，在六个区域都呈现出夏季最大，冬季最小；对 4 个季节都呈现出东亚南部比东亚北部大，海洋上空比陆地上空大的特点，表明云出现的总概率的季节变化主要由多层云出现的概率的变化决定。东亚地区云系统中最高层云云顶的高度，在夏季最高，为 15.9 km，在冬季最低，为 8.2 km；在东亚南部和海洋上空较高，平均为 15.1 km；在东亚北部较低，平均为 12.1 km，且呈现东亚南北部之间差异较大的特点。东亚地区云系统的云层厚度基本位于 1 km 到 3 km 之间，且夏季大，冬季小；对同一季节，不同区域的云层厚度差别较小；当多层云系统中的云层数目增加时，云层的平均厚度减少，且较高层的云层平均厚度大于较低层的。云层间距的概率分布基本呈单峰分布，出现峰值范围的云层间距在 1 到 3 km 之间，各区域之间没有明显差别，季节变化也不大。本文的研究为在气候模式中精确描述云的垂直结构提供了有用的参数化依据。

关键词　云垂直结构　云量　CloudSat　云观测卫星
文章编号　1006-9895(2013)01−0091−10　　**中图分类号**　P426　　**文献标识码**　A
doi:10.3878/j.issn.1006-9895.2012.11188

Analysis of Vertical Structure of Clouds in East Asia with CloudSat Data

PENG Jie[1,2], ZHANG Hua[3], and SHEN Xinyong[1]

1 *Key Laboratory of Meteorological Disaster of Ministry of Education*, *Nanjing University of Information Science and Technology*, *Nanjing* 210044
2 *Chinese Academy of Meteorological Sciences*, *Beijing* 100081
3 *Laboratory for Climate Studies*, *China Meteorological Administration, National Climate Center*, *Beijing* 100081

Abstract　Statistical characteristics of the vertical structure of clouds over East Asia are obtained by dividing the area into six regions and analyzing the 2007, 2008, and 2009 datasets from the cloud observing satellite CloudSat and Cloud-Aerosol Lidar and Infrared Pathfinder Satellite Observations (CALIPSO). Results indicate that the total cloud

收稿日期　2011-10-13，2012-06-29 收修定稿
资助项目　国家重点基础研究计划项目 2011CB403405，国家自然科学基金项目 41075056 和科技部公益性行业（气象）科研专项项目 GYHY201106022
作者简介　彭杰，男，博士研究生，主要从事卫星遥感资料分析、云－辐射相互作用研究。E-mail：pjay163@163.com
通讯作者　张华，E-mail：huazhang@cma.gov.cn

amount exhibits a distinct tendency of seasonal change at various altitudes, reaching a maximum in summer and minimum in winter. The maximum value of single-layer cloud amount appears in winter above the ocean and in summer above land. The frequency of occurrence of single-layer clouds in East Asia is 52.2%, 48.1%, 49.2%, and 51.9% for spring, summer, autumn, and winter, respectively; that for multilayer clouds is 24.2%, 31.0%, 19.7%, and 15.8%, respectively. For all six regions, the frequency of occurrence for both types of clouds is highest in summer and lowest in winter. In all four seasons, cloud frequency in the southern region of East Asia is higher than that in the northern region and is greater above the ocean than that above land. These results indicate that variance in the frequency of occurrence for total clouds is decided by that of multilayer clouds. Cloud top height of the highest cloud layer in East Asia reaches a maximum in summer and minimum in winter at 15.1 km and 8.2 km, respectively. The difference in levels is higher in the southern region above the ocean than in the northern region above land at 15.1 km and 12.1 km, respectively. In addition, the thickness of the cloud layer ranges from 1 km–3 km and is largest in summer and smallest in winter; little difference appears among the regions. Moreover, when the number of cloud layers in the multilayer cloud system increases, the mean cloud thickness decreases, and the mean thickness of the higher cloud layer is larger than that of the lower. The intervals among cloud layers show single peak distribution with the peak value appearing between 1 km and 3 km; differences among regions and seasons are minimal. This work supplies useful information for accurate parameterization of vertical cloud structures.

Keywords Cloud vertical structure, Cloud amount, CloudSat, Cloud observing satellite

1 引言

到目前为止，云仍然是气候模拟和气候变化研究中最大的不确定因子之一。首先，云本身在地气系统辐射平衡中扮演着双重角色，一方面，云将到达大气层顶的太阳短波辐射反射回太空，对地气系统起冷却作用，另外一方面，地表受到太阳辐射加热后放射出的长波辐射又被大气中的云截获，对地气系统起加热作用；其次云和气溶胶之间的相互作用导致的直接和间接辐射强迫的气候效应十分明显，但目前对于此作用的科学理解水平还很低（Forster et al.，2007）。因此，准确模拟云在气候变化中的作用是目前大尺度天气气候模式中的难点和热点问题，而这其中的重点之一是如何准确模拟云在辐射收支方面的作用及其对气候的影响。对于云对气候的反馈作用模拟的差异，主要取决于对云辐射强迫模拟的差异，是导致不同的大气环流模式之间模拟结果差异的重要原因之一（Cess et al.，1989，1990）。云的辐射强迫为某一给定大气的净太阳辐射通量（向下通量减去向上通量）与假定云不存在时同一大气的净太阳辐射通量之差（石广玉，2007），其值表征云对于地球气候系统能量收支平衡的影响，提高对云辐射过程和云的辐射强迫模拟的准确度成为提高气候模式模拟精度的关键。国内外在该领域已经开展了多年的研究（Arking，1991；赵高祥和汪宏七，1994；Wielicki et al.，1995；刘玉芝等，2007）。由于对于云结构的精确描述目前仍然是大尺度气候模式中的难点，因此在气候模式描述云辐射过程中，云的垂直分布的不确定性是研究云对气候影响的最大障碍之一（Barker et al.，1999）。地表观测表明，云层常常是重叠的（Wang et al.，2000）。多层云的重叠问题对大气和地表的辐射加热（或冷却）率有很大影响。而云的加热率不仅影响云的发展，也对大气和地表的辐射收支平衡产生重要影响（荆现文等，2009；张华和荆现文，2010）。例如，到达地面的辐射通量在晴空大气环流模式（General circulation model）之间的差别仅为几 W m^{-2}，而有云大气在大气环流模式之间的差别却高达 100 W m^{-2}（Barker et al.，1999）。

在气候模式中，处理云在垂直方向上的重叠时采取了不同的假设，如最大重叠，随机重叠以及最大／随机重叠和指数衰减重叠。而 Liang and Wang（1997）提出了一个处理多层云重叠的“马赛克”（MOASAIC）方法，在大气环流模式辐射参数化中显式地考虑云的垂直相关，结果表明，大气环流模式对云的垂直重叠的处理非常敏感，与假定随机云重叠的结果相比，显式处理云相关的大气环流模式结果具有非常不同的大气辐射加热率分布，所导致的气候影响非常大：热带和副热带对流层的中高层大气在全年变暖超过 3℃，两极夜间北半球平流层变得更暖，最大超过 15℃。

为了在大气环流模式中给出准确描述云的重叠的参数化方案，就需要用观测资料提供云的空间分布特征作为基础和验证。研究表明：云的垂直结

构（Cloud Vertical Structures）是非常重要的云宏观特征（Slingo and Slingo，1988；Randall et al.，1989；Wang and Rossow，1998），这一结构主要包含云层数目和间距，以及它们的高度分布等。以往的卫星和地面观测提供的云量垂直分布的信息非常有限（Wang et al.，2000），而在 2006 年 4 月美国航天航空局（NASA）成功发射了太阳极轨云观测卫星 CloudSat，其上所搭载的 94 GHz 毫米波云观测雷达垂直分辨率非常高，为我们研究云的垂直结构提供了丰富的观测资料。

CloudSat 资料已经被用于研究东亚地区的云垂直结构。比如：Luo et al.（2009）采用 14 个月的 CloudSat 观测资料对比分析了东亚地区和印度季风区的云量和云垂直结构及其季节变化；汪会等（2011）采用 3 年（2006 年 9 月至 2009 年 8 月）的 CloudSat 资料进一步对比分析了东亚季风区、印度季风区、西北太平洋季风区和青藏高原地区的云量和云垂直结构及其季节变化特征，还进一步分析了亚洲季风区低云量的分布及其与对流层低层稳定性的相关。

本文运用统计的方法，对 CloudSat 卫星观测资料加以分析和研究，不仅将东亚地区作为一个整体进行研究，而且将东亚地区分为 5 个子区域分别进行分析，在 Luo et al.（2009）和汪会等（2011）研究结果的基础上进一步细化了对东亚地区云的垂直分布特征的理解，为今后在气候模式中精确描述该地区云的垂直结构提供一定的参考依据。

2 卫星观测数据描述与处理

本文采用了 CloudSat 所搭载的 94 GHz 毫米波云廓线雷达（CPR）提供的观测资料，分析了 2007～2009 年 3 年的资料，用 3 月、4 月和 5 月份的平均结果表征春季，6 月、7 月和 8 月表征夏季，9 月、10 月和 11 月表征秋季，12 月、1 月和 2 月表征冬季。CloudSat 卫星是 2006 年 4 月 28 日（UTC）由美国航天航空管理局（NASA）成功发射入太空的太阳极轨气象观测卫星，几周后开始获得相关数据。CloudSat 每根轨道运行时间约为 2 小时，进行约 37081 次扫描，扫描星下点为 1.1 km（沿轨道运行方向）×1.3 km（垂直轨道运行方向）的区域，垂直方向扫描 30 km，并分为厚度为 0.24 km 的 125 层，扫描信息以 1.1 km×1.3 km×0.24 km 的扫描格点为单位储存，目前已经反演出多种 2 级产品（参见 http://www.cloudsat.cira.colostate.edu/cloudsat_documentation/CloudSat_Data_Users_Handbook.pdf.[2012-01-09]）。

本文工作主要使用了二级产品中 2B-GEOPROF 和 2B-GROPROF-Lidar（参见网站 http://cloudsat.cira.colostate.edu/dataSpecs.php.[2012-01-04]），前者信息来自于 CloudSat 卫星上搭载的 94 GHz 毫米波雷达，后者信息同时整合了 CloudSat 搭载的毫米波雷达的信息和与 CloudSat 同轨道，运行时差只有 15 秒的 CALIPSO 卫星搭载的激光雷达的信息，结合两者可同时发挥毫米波雷达和激光雷达的优点。在判断扫描格点中是否存在云时，我们用到了 2B-GEOPROF 产品中的 CPR_Cloud_mask 和 Radar_Reflectivity 数据以及 2B-GEOPROF-Lidar 中的 CloudFraction 数据。其中，CPR_Cloud_mask 的数据说明见表 1。而 Radar_Reflectivity 中所含的信息是雷达的反射率因子的对数表现值，单位是 dB*Z*，CPR 的最小可探测信号大约为－30 dB*Z*；CloudFraction 所包含的数据是经过激光雷达订正过的扫描格点中存在云的部分的百分比。Luo et al.（2009）和 Barker（2008a）在各自工作中对于确定扫描格点中是否存在云同样使用了上述 3 部分数据，但是使用了不同的阈值法。前者在满足 Radar_Reflectivity ≥－28 dB*Z* 的前提下，将扫描格点的信息整合为厚度为 1 km 的垂直层，假如组成 1 km 的雷达扫描格点中格点满足 CPR_Cloud_mask≥20，即认为扫描格点云量为 100%，否则扫描格点的云量等同于 CloudFraction 的值；后者则在满足 Radar_Reflectivity ≥－30 dB*Z* 的前提下，采用只有同时满足 CPR_Cloud_mask≥20 和 CloudFraction≥99%时，才认定该扫描格点云量为 100%，否则云量为 0。两者比较，前者的方法认为只要 CloudSat 上搭载的毫米波雷达和 CALIPSO 搭载的激光雷

表 1　CPR_Cloud_mask 数据值说明

Table 1　Values assigned to Cloud_mask Field of CloudSat data

值	含义
0	没有探测到云
1	损坏的数据
5	地面噪音
5～10	弱探测信号
20～40	探测到有云存在，值越大，探测越准

达二者有其一探测到存在云，就认为扫描格点存在云，而后者认为只有毫米波雷达和激光雷达同时探测到云才认为扫描格点存在云，前者会比后者高估云存在的概率，而本文在两种方法的基础上选取了折中的阈值法，即，当每个扫描格点的数据满足 Radar_Reflectivity ≥－30 dBZ 和 CPR_Cloud_ask≥20；或者 Radar_ Reflectivity≥－30 dBZ 和 CPR_Cloud_mask ≤20 和 CloudFraction ≥99%时，我们认为该扫描格点有云存在，否则扫描格点无云存在。

3 研究方法

图 1 给出的是本文研究的区域的示意图。我们研究了图 1 所示的整个东亚地区（记为 Total），同时因为东亚地区属季风气候，不同区域具有不同的气候特征。为了比较细致的研究它们之的差别，我们参照 1995 年版《中国自然地理》（赵济，1995）中的划分方法，按照图 1 所示将东亚的主要区域划分为西北地区（以下简称 Nw）、青藏高原区（以下简称 Tibet）、北方地区（以下简称 North）、南方地区（以下简称 South）和东部海域（以下简称 E.O）5 个部分，分别进行研究。综合一共得到 6 个区域的结果。

下面以 Tibet 和 2007 年 1 月为例说明本文的计算思路。CloudSat 的资料是以轨道为单位储存，因此本文首先选取出 2007 年 1 月中运行的所有轨道，接着根据扫描廓线的经纬度依次提取出这些轨道经过 Tibet 的部分，并将此部分以 50 根廓线为单位划分为子区域（下文简称子域），然后判断出子域中的每个扫描格点是否存在云。接着计算出每个子域内不同高度上存在云的格点数据与这一高度扫描格点总数（50）的比值，近似的认为此值为该子域在不同高度上的云量。需要特别说明的是，这里的近似是因为气候研究中通常定义的云量是指某一时刻观测到的天空中存在云的面积与天空面积的比值，是单一时刻的观测量，而由于 CloudSat 每 0.16 秒完成一次单根廓线的扫描，因而将此处由 50 根廓线所组成的子域中存在云的扫描格点与全部扫描格点的比值近似为云量，也就是将 50 个时刻观测到的值近似为单个时刻观测到的值，但是由于完成 50 根廓线的扫描只需要 8 秒钟，因此这里的近似处理相当于将 8 秒内 50 个时刻的观测数据近似为只观测了单个时刻，而该单个观测过程需要 8 秒时间。其次，以月为单位计算出经过 Tibet 所有子域不同高度云量的算术平均值，这一平均值就代表 Tibet 区域在 2007 年 1 月不同高度上的云量平均值。然后，我们计算出 2007 年 1 月经过 Tibet 的所有廓线中单层云和多层云（2 层及 2 层以上）的数目（廓线中存在云的扫描格点在垂直方向连续的层数定义为此廓线中的云层的数目），同样以月为单

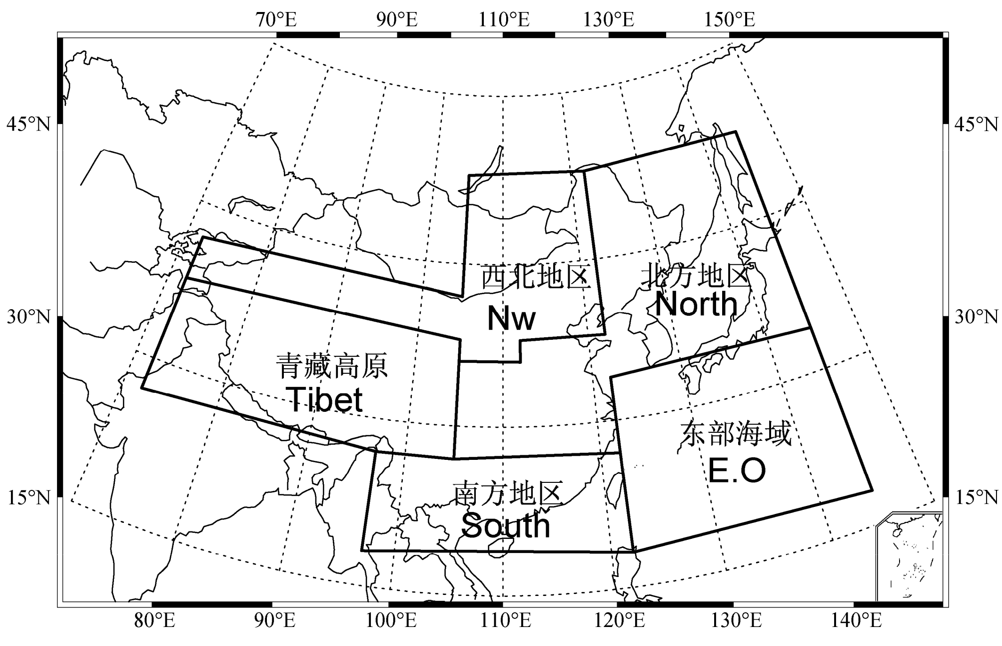

图 1　研究区域划分示意图

Fig. 1　The schematic of regional divisions in this work

位计算出这些值与扫描廓线总数的比值，这一比值在本文就代表 Tibet 区域在 2007 年 1 月中的单层云和多层云的出现概率；最后计算出每个廓线中云层的云顶/云低高度，同样以月为单位计算出这些值与扫描廓线总数的比值，这一比值在本文就代表 Tibet 区域在 2007 年 1 月中平均的云顶/底高度最后，计算出所有区域在 3 年共 36 个月中的平均值之后，再平均出春夏秋冬 4 个季节的结果，其中春季为 2007 年至 2009 年 3 月、4 月和 5 月共 9 个月的平均值，夏季为 6、7 和 8 月的平均值，秋季为 9、10 和 11 月的平均值，冬季为 12、1 和 2 月的平均值，同时计算了每 9 个月平均值组成的集合的标准差。表 2 给出了 6 个区域 4 个季节统计的扫描廓线数。

表 2　6 个区域 4 个季节统计的扫描廓线数
Table 2　The number of calculated pixels in 6 regions for four seasons

	Total	Nw	North	South	Tibet	E.O
春季	5103483	982104	713878	663855	699305	1044010
夏季	5637991	1071109	779817	714631	763817	1170591
秋季	5518669	1055143	779995	713529	744365	1159807
冬季	4888235	911190	676144	617947	650407	994643

4　结果分析与讨论

4.1　云量的垂直分布及其季节变化

图 2（见文后彩图）分别给出 6 个研究区域 4 个季节不同高度的平均云量，误差棒表示该高度上的标准差。从垂直方向上云量峰值的季节分布来看，E.O 区域与其他 5 个以陆地下垫面为主的区域有着明显的差别，E.O 垂直方向上面云量峰值的最大值出现在冬季，达到了 0.31，春秋季次之，最小值出现在夏季，为 0.21；而其他 5 个区域的云量峰值的最大值都出现在夏季，分别为 Total：0.23；Nw：0.23；North：0.24；South：0.24；Tibet：0.35。Total 区域、North 区域和 South 区域峰值的最小值都出现在秋季，依次为 0.16、0.19 和 0.18；而 Nw 区域和 Tibet 区域的最小值都出现在冬季，依次为 0.16 和 0.19。从误差棒表示的标准差可以看出，总体而言，图中所示季节的平均值对于 3 年 9 个月的平均状态有较好的代表性，但不同区域 9 个月的变化幅度各不相同，Tibet、North 和 E.O 变化相对比较大，标准差最大值依次达到了 0.1、0.06 和 0.06，而其他 3 个区域变化较小，标准差分别为 Total：0.03，NW：0.05 和 South：0.04。

4.2　东亚地区云垂直结构参数的统计

Wang and Rossow（1998）通过在戈达德空间研究所（Goddard Institute of Space Studies）的大气环流模式（GISS GCM）中的 13 个试验，总结出了几个重要的云垂直结构参数：（1）云是否重叠（即有无多层云）；（2）多层云系统中云层之间的距离；（3）最上层云顶位置高度。我们通过对 CloudSat 卫星资料的分析，统计了东亚地区的上述三个云垂直结构参数。图 3 分别给出四个季节在 6 个研究区域发生多层云的平均概率，误差棒同样表示标准差。因为在统计的过程发现云层数目超过 5 层的概率非常小，基本在 0.001 左右，因此，图中只给出了存在云的总概率和 1 至 4 层云出现的概率。整体而言，东亚地区单层云出现的概率在春夏秋冬分别为 52.2%、48.1%、49.2%和 51.9%，在冬春季最大，秋季次之，夏秋最小，而多层（2 层和 2 层以上）云出现的概率在春夏秋冬分别为 24.2%、31.0%、19.7%和 15.8%，在夏季最大，春秋季次之，冬季最小，与出现云的总概率一致，与汪会等（2011）的研究结果中对东亚季风区的研究结果相符。

从存在云的总概率来看，4 个季节的区域差异都一致地呈现出 South 区域最大，春夏秋冬依次为 84.5%、89.3%、81.6%和 78.5%，Total 和 E.O 次之，而后是 North 区域，最小的是 Nw 区域，春夏秋冬分别为 70.3%、68.6%、55.5%和 65.6%。反映出南方地区出现云的概率大，而北方地区则相对较小；海洋上空出现云的概率大，而陆地上空出现云的概率小的特点。由于 Tibet 区域的情况比较特殊，夏季作为热源，加上季风带来的充足水气，存在云的概率超过了 E.O，仅次于 South 区域，而秋冬季又小于 E.O 地区和 Total 区域，在春季与两者持平。比较不同季节之间的差异，除了 Nw 之外的 5 个区域出现云的总概率都呈现出在夏季最大，春秋季次之，冬季最小的特征。

以上结果表明，东亚地区南方的多层云比北方多，海洋上空的多层云比陆地上空的多；且与之前的研究（Luo et al.，2009；汪会等，2011）结果相一致地表现出夏季多云、冬季少云，夏季多云主要是因为多层云的概率增加所致。

为了研究整个东亚地区以及 5 个子区域的云层高度和厚度，对本文得到的 CloudSat 卫星的观测数据进行统计分析，分别按照 6 个研究区域和 4 个季

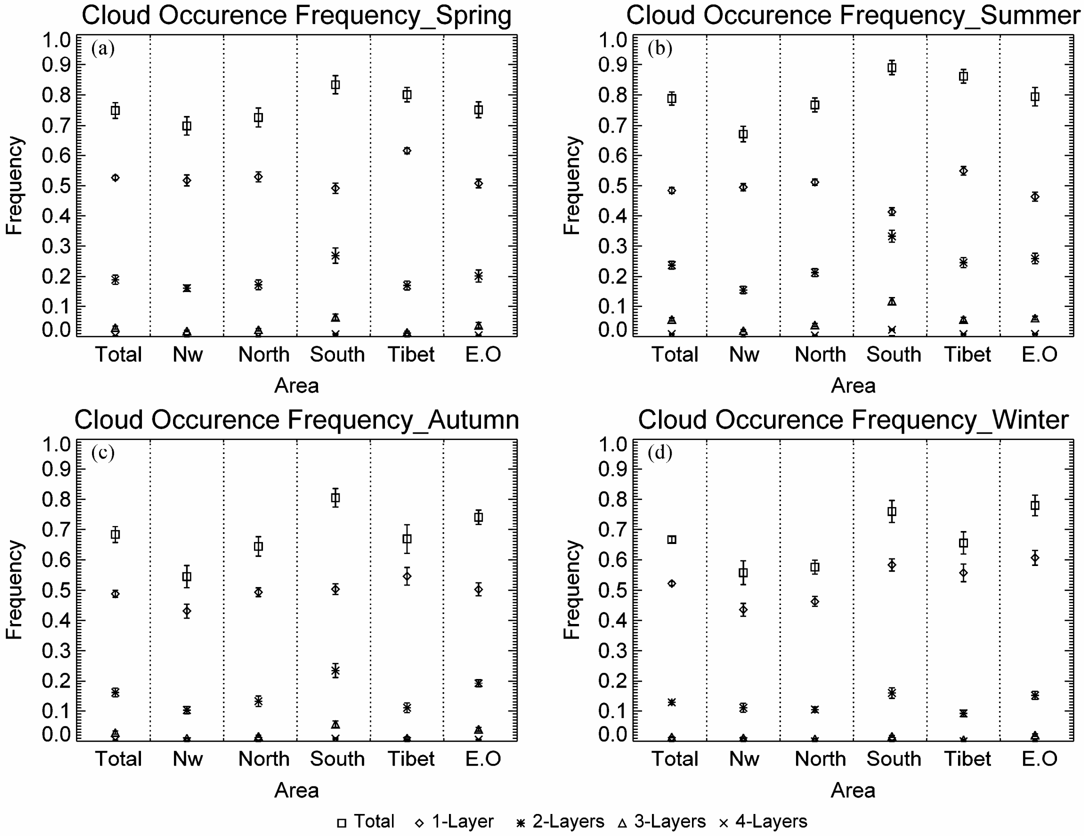

图 3 6 个区域发生多层云的季节平均概率:（a）春季;（b）夏季;（c）秋季;（d）冬季

Fig. 3 Seasonal averaged probability of multilayer cloud occurrence in six regions: (a) Spring; (b) summer; (c) autumn; (d) winter

节进行研究，同时，在多层云出现的情况下，再按照云层出现数目的不同区分，分别计算出不同区域、不同季节在不同云系统情况下的云顶高度和云底高度的平均值。图 4（见文后彩图）分别给出整个东亚地区中 6 个研究区域，1 层云、2 层云、3 层云和 4 层云系统中各层云的云顶和云底高的平均值。先看单层云系统的平均云顶高，对比 4 个季节，Nw 平均云顶高最大值出现在春季，其他 5 个区域平均云顶高最大值都出现在夏季。夏季的 6 个区域之间比较，平均云顶最高的区域是 South 区域，为 10.3 km，平均云顶最低的区域是 North 区域，为 7.6 km；春秋季的平均云顶高低于夏季，春季平均云顶高位于 Nw 区域的 8.3 km 和 E.O 区域的 8.0 km 之间；秋季的平均云顶高位于 South 区域的 5.9 km 和 Tibet 区域的 7.4 km 之间，除了 Nw 区域和 Tibet 区域冬季云顶高略高于秋季外，其他区域的平均云顶高都是冬季最低；冬季，平均云顶最高的区域是 Nw 区域，为 7.3 km，平均云顶最低的区域是 E.O 区域，为 3.9 km。从云的平均厚度来看，4 个季节对比，夏季的平均云厚度最大，6 个区域平均厚度最大的是 South 区域，为 4.6 km，最小的是 Nw 区域，为 3.0 km；春秋次之，平均厚度的范围分别是 2.6 km 到 3.1 km 之间和 2.1 km 和 3.0 km 之间；冬季最小，6 个区域平均厚度最大是发生在 Nw 区域为 2.3 km，平均厚度最小的是 South 区域，为 1.7 km。对 2 层、3 层和 4 层云系统，最高层云云顶高的平均值除了个别地区之外，同样是夏季最高，春秋次之，冬季最小。下面分春夏秋冬四个季节给予具体描述。对春秋两季，2 层、3 层和 4 层云系统中第二，第三和第四层云的平均云顶高最大的都是发生在 South 区域，分别为 11.0 km、12.6 km 和 14.3 km，和 11.8 km、14.2 km 和 15.4 km，最小的则都是发生在 North 区域，分别为 9.3 km、10.3 km 和 10.7 km，和 8.8 km、9.9 km 和 10.7 km。夏季，2 层和 3 层云系统中第二层和第三层云的平均云顶高最大的都是在 South 区域，分别为 14.2 km 和 15.6 km，最小的都是在 Nw 区域，分别为 10.0 km 和 10.8 km；而 4 层云系统中第四层云的平均云顶高最大的则发生在 Tibet 区域，为 15.9 km，最小的也是在 Nw 区域，为 11.4 km。冬季，2 层、3 层和 4 层云系统中

第二，第三和第四层云的平均云顶高最大的都是发生在 E.O 区域，分别为 9.4 km、12.2 km 和 13.4 km，最小的分别发生在 North，North 和 Tibet 区域，值分别为 8.2 km、9.0 km 和 8.3 km。不同研究区域之间的差别体现出，位于东亚南部地区和海洋下垫面上空的云层比较高，而位于东亚北部的云层比较低，且东亚南北部之间差别比较大。观察云层厚度的变化，平均云层厚度大部分位于 1 km 到 3 km 之间，且不同区域的云层厚度差别较小，随季节变化也不大。一个明显趋势是当多层云系统中的云层数目增加时，云层的平均厚度减少，验证了 Luo et al.（2009）对于东亚和南亚地区的研究结论，此外较高层的云层平均厚度大于较低层的云层平均厚度。

许多研究表明，多层云系统中云层之间的距离也是重要的云垂直结构参数之一（Barker，2008a，2008b），因此，本文对云层的间距参数也进行了分析。表 3 给出 6 个研究区域 4 个季节不同云系统下云层间距的平均值。结果表明：东亚地区云层间距的季节平均值位于 5.7 km 到 1.1 km 之间，同一区域间距的季节变化不大，秋季和夏季略为偏高，春季和冬季略为偏低。North 和 Nw 区域的云层间距最小，South 区域和 E.O 区域云层间距最大，说明海洋为主的下垫面区域的云层间距大于以陆地为主的下垫面区域的云层间距，处于较低纬的 South 区域和 E.O 区域的云层间距大于处于较高纬的 North 区域和 Nw 区域的云层间距，另一个明显的趋势是随着云系统中云层数目的增加，云层间距逐渐缩小。本文的研究结果表明，6 个区域云层间距的概率分布基本呈单峰分布，概率峰值出现在 0.08～0.3 之间，且云层数越多，概率越大。出现峰值范围的云层间距在 1～3 km 之间，各区域之间没有大的区别，季节的变化也不大，这与李积明等（2009）的研究结果是一致的。因此，在此只给出夏季 6 个研究区域 2 层、3 层和 4 层云系统情况下云层间距的概率分布（见图 5）。

5 讨论和结论

本文利用 CloudSat 提供的 2007~2009 年三整年的卫星观测资料，详细分析了东亚不同区域云的分布的统计特征，得出以下结论：

（1）东亚地区单层云出现的概率在春夏秋冬分别为 52.2%、48.1%、49.2%和 51.9%，而多层（2 层和 2 层以上）云出现的概率在春夏秋冬分别为 24.2%、31.0%、19.7%和 15.8%。出现单层云的概率远高于多层云出现的概率。

（2）东亚地区不同高度的云量之和具有明显的季节变化趋势：夏季最大，春秋次之，冬季最小。海洋上空的单层云量最大值出现在冬季，而在陆地上空则出现在夏季。

（3）从存在云的总概率的统计结果得出，东亚

表 3 6 个区域 4 个季节不同云系统下云层间距的平均值（单位：km）

Table 3 The mean values of intervals between cloud layers in different cloud systems in six regions for four seasons (units: km)

		Nw				North				South			
		春	夏	秋	冬	春	夏	秋	冬	春	夏	秋	冬
2LS*	L2-L1**	3.45	3.82	3.69	3.26	3.17	3.78	3.28	2.77	4.59	5.56	5.16	2.36
3LS	L2-L1	2.45	2.67	2.74	2.60	2.37	2.47	2.36	2.30	3.02	3.61	3.46	2.75
	L3-L2	2.46	2.79	2.48	2.05	2.10	2.79	2.19	1.69	3.30	3.58	3.58	4.15
4LS	L2-L1	1.87	1.97	2.07	2.21	1.72	1.82	1.87	1.81	2.14	2.60	2.62	1.87
	L3-L2	1.97	2.10	2.16	1.80	1.91	1.94	1.52	1.51	2.75	2.78	2.79	2.69
	L4-L3	1.86	2.20	1.88	1.36	1.62	2.27	1.69	1.13	2.49	2.56	2.63	2.68

		Tibet				E.O				Total			
		春	夏	秋	冬	春	夏	秋	冬	春	夏	秋	冬
2LS	L2-L1	3.41	4.96	4.08	3.41	4.23	5.71	4.79	4.35	4.44	5.60	5.08	4.10
3LS	L2-L1	2.39	3.44	2.83	2.21	2.84	3.78	3.68	3.07	3.13	3.88	3.83	3.04
	L3-L2	2.65	3.53	3.17	2.73	2.90	3.44	2.86	3.48	3.12	3.40	3.31	3.41
4LS	L2-L1	1.95	2.37	2.05	1.47	2.04	2.67	2.39	2.10	2.20	2.79	2.96	2.15
	L3-L2	2.03	3.08	2.66	1.35	2.31	2.75	2.77	2.73	2.63	2.84	2.96	2.83
	L4-L3	2.17	2.52	2.30	1.69	2.35	2.55	2.09	2.50	2.39	2.57	2.56	2.50

*第一列中 2LS、3LS 和 4LS 分别表示两层云、三层云和四层云系统。

**第二列中 L2-L1、L3-L2 和 L4-L3 分别表示第 2 层云与第 1 层云的间距、第 3 层云与第 2 层云的间距和第 4 层云与第 3 层云的间距。

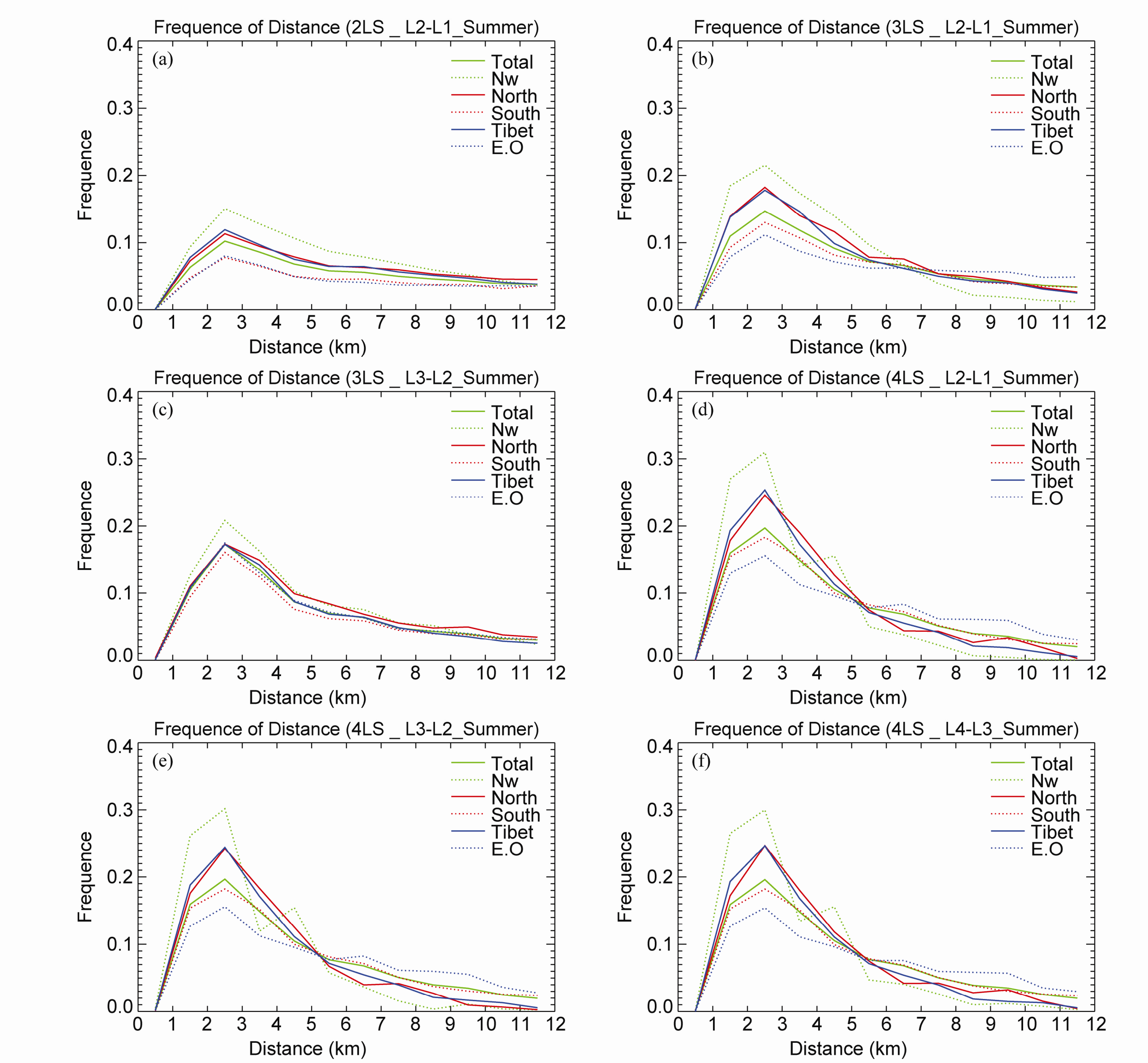

图 5 6 个区域夏季的云层间距的分布概率：(a) 双层云系统中第二层与第一层云的间距；(b) 三层云系统中第二层与第一层云的间距；(c) 三层云系统中第三层与第二层云的间距；(d) 四层云系统中第二层与第一层云的间距；(e) 四层云系统中第三层与第二层云的间距；(f) 四层云系统中第四层与第三层云的间距

Fig. 5 The occurrence probability distribution of intervals among cloud layers at summer in six regions: (a) For the intervals between the 1st and 2nd layers in two-layer cloud system; (b) for the intervals between the 1st and 2nd layers in three-layer cloud system; (c) for the intervals between the 2nd and 3rd layers in three-layer cloud system; (d) for the intervals between the 1st and 2nd layers in four-layer cloud system; (e) for the intervals between the 2nd and 3rd layers in four-layer cloud system; (f) for the intervals between the 4th and 3rd layers in four-layer cloud system

地区具有南方云多，北方云少；海洋上空云多，陆地上空云少的特点。季节变化表明，夏季存在云的总概率最大，冬季最小，而存在单层云的概率反而是夏季最小，春冬季最大，表明云出现的总概率的变化趋势主要由多层云出现概率的变化趋势决定。

（4）季节平均的云层高度结果表明：位于东亚南部地区和海洋下垫面上空的云层比较高，而位于东亚北部的云层比较低，且东亚南北部之间差别比较大。观察云层厚度的变化，平均云层厚度大部分位于 1 km 到 3 km 之间，且不同区域的云层厚度差别较小。一个明显趋势是当多层云系统中的云层数目增加时，云层的平均厚度减少，且较高层的云层平均厚度大于较低层的云层平均厚度。

（5）分析多层云系统中云层间距的概率分布表明：出现峰值概率的云层间距在 1～3 km 之间，各区域之间没有大的区别，季节的变化也不大。而云

层间距出现的概率的极大值在 0.8～0.3 之间，且云层越多，概率越大。

以上研究结果是本文利用最新发射的云观测卫星 CloudSat 同时结合了与其同轨道的激光雷达观测卫星CALIPSO 2007～2009年3年的观测资料，经过处理和分析得到的。目前其他的观测手段尚无法获取如此高垂直分辨率的云的结构信息。因此，本文的结果对于理解东亚地区及其 5 个子区域云的垂直结构，并在气候模式中精确描述该地区云的结构提供了可供参考的定量信息，具有十分重要的意义。

致谢 本文所用的资料来自美国宇航局（NASA）的 CloudSat 项目，在此表示感谢。

参考文献（References）

Arking A. 1991. The radiative effects of clouds and their impact on climate [J]. Bull. Amer. Meteor. Soc., 72: 795–813.

Barker H W. 2008a. Overlap of fractional cloud for radiation calculations in GCMs: A global analysis using CloudSat and CALIPSO data [J]. J. Geophys. Res., 113: D00A01, doi: 10.1029/2207JD009677.

Barker H W. 2008b. Representing cloud overlap with an effective decorrelation length: An assessment using CloudSat and CALIPSO data [J]. J. Geophys. Res., 113: D24205, doi: 10.1029/2008JD010391.

Barker H W, Stephens G L, Fu Q. 1999. The sensitivity of domain-averaged solar fluxes to assumptions about cloud geometry [J]. Quart. J. Roy. Meteor. Soc., 125: 2127–2152.

Cess R D, Potter G L, Blanchet J P, et al. 1989. Interpretation of cloud-climate feedback as produced by 14 atmospheric general circulation models [J]. Science, 245: 513–516.

Cess R D, Potter G L, Blanchet J P, et al. 1990. Intercomparison and interpretation of climate feedback processes in 19 atmospheric general circulation models [J]. J. Geophys. Res., 95: 16601–16615.

Forster P, Ramaswamy V, Artaxo P, et al. 2007. Changes in atmospheric constituents and in radiative forcing [M]// Solomon S, Qin D, Manning M, et al, Eds. Climate Change 2007: The Physical Science Basis. Contribution of Working Group I to the Fourth Assessment Report of the Inter- governmental Panel on Climate Change. Cambridge, United Kingdom and New York: Cambridge University Press.

石广玉. 2007. 大气辐射学 [M]. 北京：科学出版社，302–318. Shi Guangyu. 2007. Atmospheric Radiation (in Chinese) [M]. Beijing: Science Press, 302–318.

荆现文, 张华, 郭品文. 2009. 气候模式中云的次网格结构对全球辐射影响的研究 [J]. 气象学报, 67 (6): 1058–1068. Jing Xianwen, Zhang Hua, Guo Pinwen. 2009. A study of the effect of sub-grid cloud structure on global radiation in climate models [J]. Acta Meteorologica Sinica (in Chinese), 67 (6): 1058–1068.

李积明, 黄建平, 衣育红, 等. 2009. 利用星载激光雷达资料研究东亚地区云垂直分布的统计特征 [J]. 大气科学, 33 (4): 698–707. Li Jiming, Huang Jianping, Yi Yuhong, et al. 2009. Analysis of vertical distribution of cloud in East Asia by space-based lidar data [J]. Chinese Journal of Atmospheric Sciences (in Chinese), 33 (4): 698–707.

Liang X Z, Wang W C. 1997. Cloud overlap effects on general circulation model climate simulations [J]. J. Geophys. Res., 102: 11039–11047.

刘玉芝, 石广玉, 赵剑琦. 2007. 一维辐射对流模式对云辐射强迫的数值模拟研究 [J]. 大气科学, 31 (3): 486–494. Liu Yuzhi, Shi Guangyu, Zhao Jianqi. 2007. A study of the radiative forcing of clouds by using a one-dimensional radiative-convective model [J]. Chinese Journal of Atmospheric Sciences (in Chinese), 31 (3): 486–494.

Luo Y L, Zhang R H, Wang H. 2009. Comparing occurrences and vertical structures of hydrometeors between eastern China and the Indian monsoon region using CloudSat CALIPSO data [J]. J. Climate, 22: 1052–1064.

Randall D A, Harshvardhan, Dazlich D A. 1989. Interactions among radiation, convection, and large-scale dynamics in a general circulation model [J]. J. Atmos. Sci., 46: 1943–1970.

Slingo A, Slingo J M. 1988. The response of a general circulation model to cloud longwave radiative forcing. Part I: Introduction and initial experiments [J]. Quart. J. Roy. Meteor. Soc., 114: 1027–1062.

汪会, 罗亚丽, 张人禾. 2011. 用 CloudSat/CALIPSO 资料分析亚洲季风区和青藏高原地区云的季节变化特征 [J]. 大气科学, 35 (6): 1117–1131. Wang Hui, Luo Yali, Zhang Renhe. 2011. Analyzing seasonal variation of clouds over the Asian monsoon regions and the Tibetan Plateau region using CloudSat/CALIPSO data [J]. Chinese Journal of Atmospheric Sciences (in Chinese), 35 (6): 1117–1131.

Wang J H, Rossow W B. 1998. Effects of cloud vertical structure on atmospheric circulation in the GISS GCM [J]. J. Climate, 11: 3010–3029.

Wang J H, Rossow W B, Zhang Y C. 2000. Cloud vertical structure and its variations from a 20-yr global rawinsonde dataset [J]. J. Climate, 13: 3041–3056.

Wielicki B A, Harrison E F, Cess R D, et al. 1995. Mission to planet Earth: Role of clouds and radiation in climate [J]. Bull. Amer. Meteor. Soc., 76: 2125–2153.

张华, 荆现文. 2010. 气候模式中云的垂直重叠假定对模拟的地—气辐射的影响研究 [J]. 大气科学, 34 (3): 520–532. Zhang Hua, Jing Xianwen. 2010. Effect of cloud overlap assumptions in climate models on modeled earth‐atmosphere radiative fields [J]. Chinese Journal of Atmospheric Sciences (in Chinese), 34 (3): 520–532.

赵高祥, 汪宏七. 1994. 云和辐射(Ⅱ): 环流模式中的云和云辐射参数化 [J]. 大气科学, 18 (增刊): 933–958. Zhao Gaoxiang, Wang Hongqi. 1994. Cloud and radiation—Ⅱ: Cloud and cloud radiation parameterizations in general circulation models[J]. Chinese Journal of Atmospheric Sciences (Scientia Atmospherica Sinica) (in Chinese), 18 (Suppl.): 933–958.

赵济. 1995. 中国自然地理（3 版）[M]. 北京：高等教育出版社, 180–187. Zhao Ji. 1995. Chinese Nature Geography (in Chinese) [M]. 3rd ed. Beijing: Higher Education Press, 180–187.

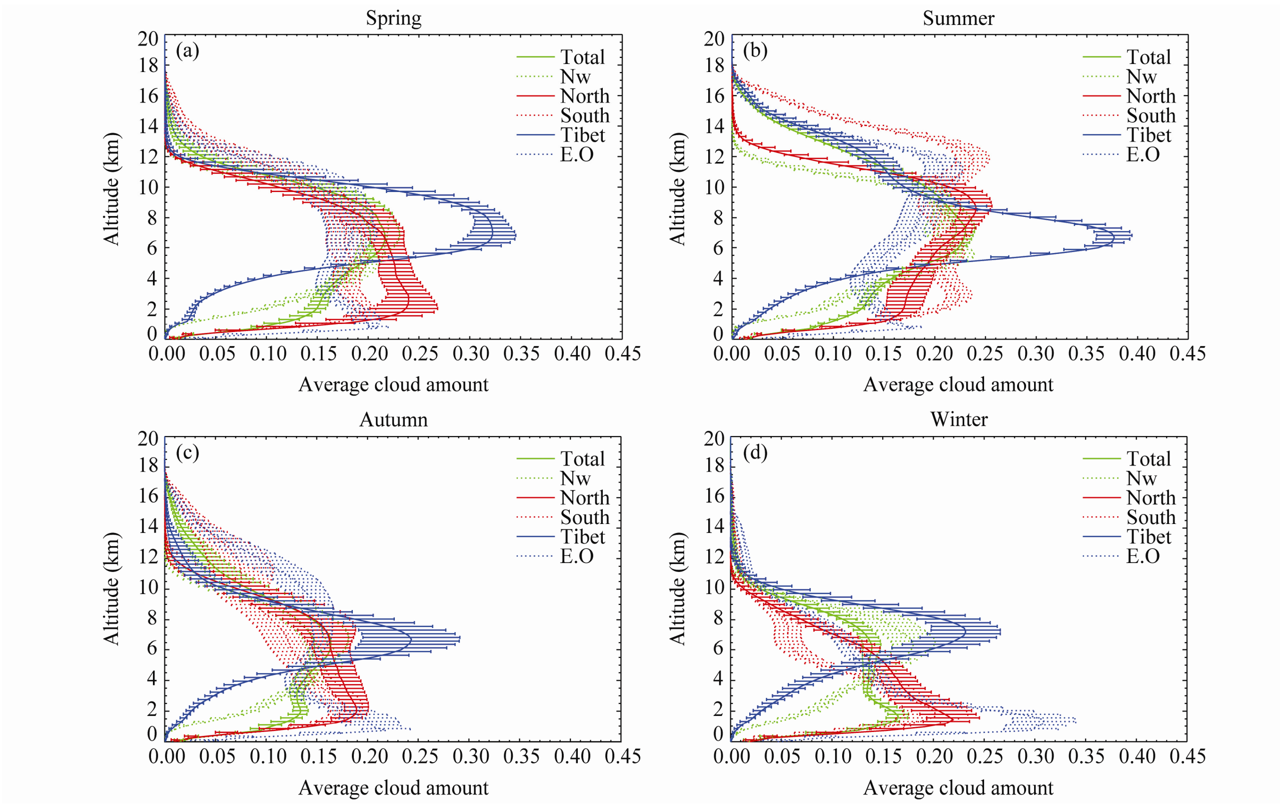

图 2　6 个区域季节平均的云量随高度的变化:（a）春季;（b）夏季;（c）秋季;（d）冬季

Fig. 2　Variation of seasonal averaged cloud amount with height in six regions: (a) Spring; (b) summer; (c) autumn; (d) winter

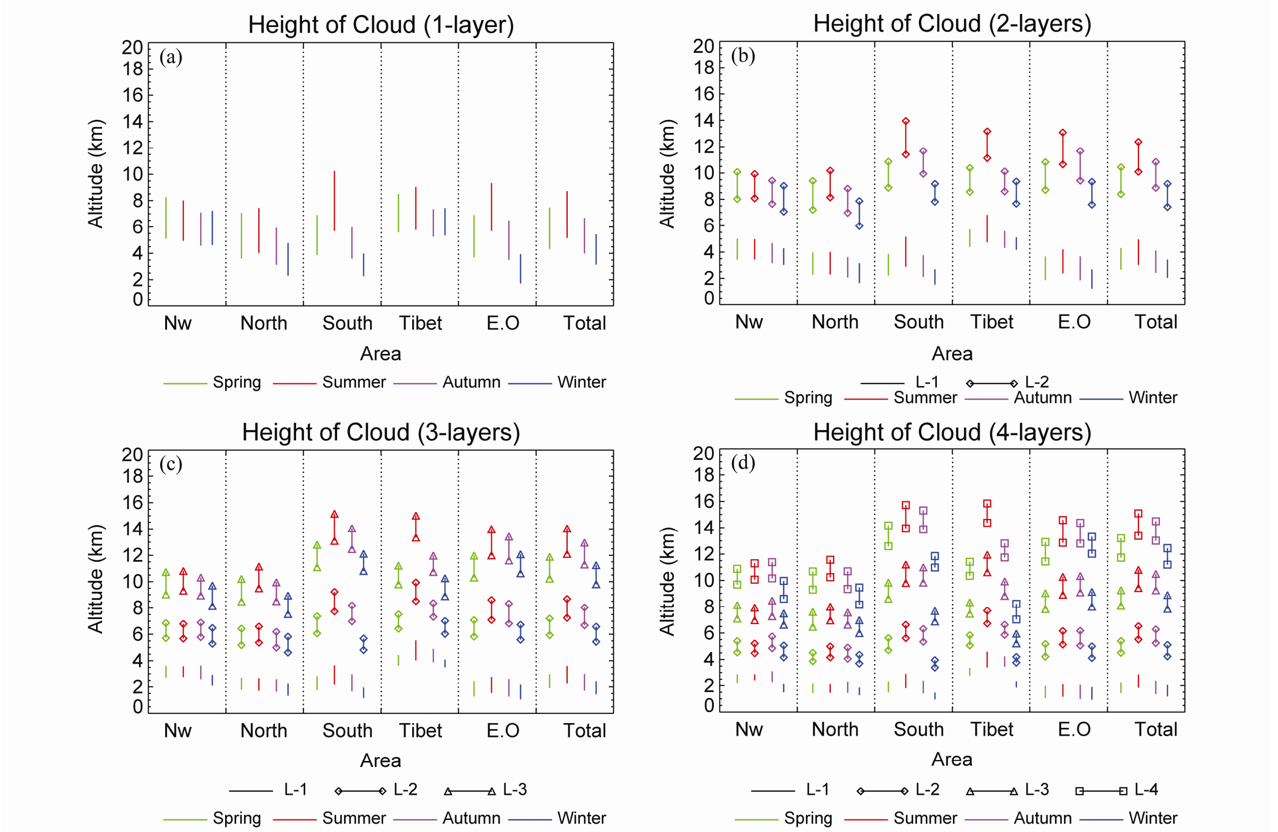

图 4　4 个季节 6 个区域平均云层高度和厚度:（a）单层云系统;（b）双层云系统;（c）三层云系统;（d）四层云系统

Fig. 4　The mean level and thickness of clouds in six regions for four seasons: (a) Single-layer cloud system; (b) two-layer cloud system; (c) three-layer cloud system; (d) four-layer cloud system

覃志年,胡娅敏,陈丽娟. 广西夏季降水的多时间尺度特征及影响因子. 应用气象学报,2013,24(5):565-575.

广西夏季降水的多时间尺度特征及影响因子

覃志年[1)]　胡娅敏[2)3)]*　陈丽娟[4)]

[1)](广西壮族自治区气候中心, 南宁 530022)　[2)](广东省气候中心, 广州 510080)

[3)](广东省广州市气候与农业气象中心, 广州 510080)

[4)](国家气候中心 中国气象局气候研究开放实验室,北京 100081)

摘　要

利用1951—2011年广西夏季降水站点资料和NCEP/NACR等多种再分析资料,通过相关分析、经验模态分解、统计检验分析了广西夏季降水的多时间尺度特征及其影响因子,利用多元线性回归方法对夏季降水进行拟合和预测试验。结果显示:广西夏季降水具有多时间尺度特征,不同时间尺度对应着环流因子不同时间尺度的分量;在准2年尺度上,主要影响因子为季风槽、低空急流、高空急流、贝加尔湖高度场、南印度洋东部海温。利用对广西夏季降水影响显著的环流因子本征模态函数分量和多元线性回归方法拟合夏季降水,相关系数为0.73,表明广西夏季降水是环流因子多时间尺度共同作用的结果。利用前期冬季南印度洋东部海温异常本征模态函数作为前兆因子预报广西夏季降水,6个独立样本检验显示预测与实况趋势一致,该工作可供利用多时间尺度信息进行区域气候预测参考。

关键词: 夏季降水; 多时间尺度; 经验模态分解; 本征模态函数

引　言

夏季降水异常会导致区域性干旱或洪涝等自然灾害发生,因而政府和公众极为关注夏季各地降水量的预测。广西位于旱涝灾害频发的华南地区,其夏季降水量占年降水量的47.5%,开展广西夏季降水量研究有重要的应用价值。近10年,很多学者从降水异常成因、旱涝分布规律与环流特征、客观预报方法等多方面对广西夏季降水量异常进行预测研究[1-4],这些研究多基于降水序列本身或平滑后的新序列进行。而气象要素序列多具有非平稳和非线性特征,因此需要对其具有的多时间尺度特征进行分析和再应用,该领域已取得一系列进展,其中经验模态分解(empirical mode decomposition, EMD)能有效提取气象要素序列非平稳和非线性过程中的有用信息,使其平稳化。EMD方法应用范围较广,包括气温[5-12]、降水[12-13]、降水日数[14-15]、波流相互作用[16]、季节内振荡[17]、海平面高度[18]、海表温度[19-20]、成灾面积[21-22]等等,首先基于EMD方法进行多时间尺度分离,然后对要素序列进行周期分析或趋势分析。万仕全等[23]、邹明玮[24]、玄兆燕等[5,25]和毕硕本等[26]进一步将该方法应用到预测研究中,结果表明,经过EMD分解后的本征模态函数主分量有较高的可预测性,它对原序列趋势的预测有重要指示意义。玄兆燕等[5,25]采用EMD和神经网络方法相结合对石家庄的气温和降水进行预测,结果显示:EMD方法降低了被预测信号中的非平稳性,预测精度较直接用神经网络有明显提高。这些尝试为气候预测开辟了一条有效途径。

已有研究主要是对要素序列尺度分离后,进行周期和趋势分析,或基于分离后的本征模态函数分量,采用数理统计方法进行拟合或预测。事实上,深入了解预测对象的影响因子和影响机制,对于提高预报对象的准确率更具实际意义,有利于深入认识造成不同时间尺度气象要素异常的物理机制。本文

2012-12-06收到, 2013-04-02收到再改稿。

资助项目:国家自然科学基金青年基金项目(40905043),广州市科技计划项目(2010Y1-C031),广西自然科学基金项目(2011GXNSFA018002),国家重点基础研究发展计划项目(2013CB430203),中国气象局气候预测创新团队项目

* 通信作者,email: huyamin_1978@sohu.com

基于 EMD 方法对广西夏季降水进行尺度分离，着重分析可能引起降水不同时间尺度变化的环流因子和外强迫因子，并从多时间尺度角度来研究导致广西夏季降水异常的可能物理机制，建立相应的预测模型，以提高广西夏季降水的短期气候预测能力。

1 资料和方法

本文所用资料包括广西气候中心提供的 1951—2011 年夏季(6—8 月)广西 88 个气象站降水量资料；NCEP/NCAR 1951 年 1 月—2011 年 12 月逐日再分析资料[27]，水平分辨率为 2.5°×2.5°；ERSST.v3(extended reconstructed sea surface temperatures version 3)1951 年 1 月—2011 年 12 月海温资料，水平分辨率为 2°×2°；NOAA-CIRES 20th century reanalysis version 2 1951 年 1 月—2010 年 12 月逐日积雪资料(高斯格点)；CPC soil moisture version 2 1951 年 1 月—2010 年 12 月逐月土壤湿度资料，水平分辨率为 1°×1°。

此外，根据文章分析需要，采纳已有研究成果和相关分析等方法定义了几个影响夏季降水的关键环流因子。包括西太平洋副热带高压(简称副高)脊线位置[28]；贝加尔湖阻高强度指数，为 45°～55°N，110°～130°E 区域 500 hPa 平均位势高度；季风槽指数，为 15°～20°N，80°～90°E 区域 850 hPa 风场平均风速；低空急流指数，为 18°～25°N，110°～120°E 区域 850 hPa 风场平均风速；副高南侧偏东气流指数为副高南侧 18°～25°N，110°～120°E 区域 850 hPa 风场平均风速；高空急流指数是 20°～25°N，90°～110°E 区域 200 hPa 风场平均风速；海温指数取 20°～30°S，95°～110°E 区域平均海表温度；后 6 个指数的选取方法见第 3 章，指数在使用时均进行了标准化处理，气候值均选取 1981—2010 年平均。

本文采用相关分析、合成分析、功率谱、带通滤波、突变检验、统计显著性检验、经验正交函数分析(EOF)、EMD 等方法[29]对资料进行处理和多时间尺度分离。其中 EMD 方法可对非线性非平稳信号逐级进行平稳化处理，即可将不同周期的波动从原信号中分离出来，并且该波动是平稳的，不同尺度的波动被定义成为本征模态函数(Intrinsic Mode Function，IMF)，不同的 IMF 分量是平稳信号，具有显著的缓变波包特性[29]。以下分别用 IMFn 表示第 n 个本征模态函数。

2 广西夏季降水的多时间尺度特征

首先对 1951—2011 年广西夏季站点降水资料进行 EOF 分析，空间第 1 模态为全区一致型，解释了总方差的 45.8%，而桂北和桂南地区呈现相反符号的第 2 模态仅解释总方差的 10.4%，反映了广西地区降水变化具有显著的全区一致性特征。将第 1 模态对应的时间系数与原降水做相关计算，得到相关系数为 0.98，因此将广西地区的夏季降水作为一个整体考虑比较合理。

本文取全区夏季降水的累积距平百分率作为降水指数，计算方法如下：

$$R_j = \sum_{i=1}^{88}\left(\frac{r_{ji}-\bar{r}_i}{\bar{r}_i}\right)\times 100。\quad (1)$$

式(1)中，R_j 为 j 年全区累积降水距平百分率；j 为年份序号，即 1951，1952，……，2011，r_{ji} 为第 i 个站 j 年夏季降水量，$\bar{r}_i$ 为第 i 个站 1981—2010 年夏季平均降水量，i=1，2，3，……，88，共计 88 个站。

对 1951—2011 年的广西累积降水距平百分率进行 EMD 分解，得到 5 个 IMF 分量和 1 个趋势项，IMF1～IMF5 各分量通过 0.05 显著性水平的周期分别为 2 年、7.6 年、12.7 年、19 年和 38 年，这些周期与江淮梅雨的 2～3 年、6～8 年、12～15 年和 18～20 年周期特征相近[30]。其中 IMF1～IMF4 分量方差贡献分别为 55%，18%，12%，12%。计算 IMF 各分量与原序列相关系数，并利用功率谱进行周期分析(红噪音标准谱的显著性水平为 0.05)，IMF1 与原序列相关系数为 0.71，前 3 个 IMF 分量合成与原序列相关高达 0.92，即在 IMF1 分量中加入 7.6 年和 12.7 年周期的 IMF2 和 IMF3 分量，合成效果更好，多时间尺度合成信息将更接近于原序列。

3 影响广西夏季降水的环流因子和外强迫信号

广西(22°～26°N，105°～112°E)为中高纬度环流和低纬度环流、西太平洋和印度洋水汽输送、东南季风和西南季风交汇的过渡区，因而广西降水的影响因子复杂，其中，导致降水异常的直接原因是同期大气环流异常。分别计算夏季降水与对流层低层(以 850 hPa 风场为代表)、中层(以 500 hPa 高度场

为代表)和高层(以 200 hPa 风场为代表)的相关(图 1),可以看到,降水与 850 hPa 风场的正相关区主要位于阿拉伯海—孟加拉湾—南海北部的低纬度地区,与 500 hPa 高度场的正相关区主要位于贝加尔湖附近的中纬度地区,与 200 hPa 风场的负相关区主要位于华南—中南半岛北部的低纬度地区。夏季 850 hPa 南亚季风槽偏强、孟加拉湾低空急流偏强、副高南侧的偏东气流偏强,同时 500 hPa 贝加尔湖高度场为正距平,200 hPa 华南上空的东风急流偏强,则广西夏季降水易偏多;反之亦然。

选取通过 0.05 显著性水平的区域平均特征作为环流因子,主要包括 850 hPa 季风槽区(15°～20°N,80°～90°E)可表征孟加拉湾水汽输送特征;低空急流区(18°～25°N,110°～120°E)可表征华南水汽输送特征;副高南侧偏东气流区(18°～25°N,110°～120°E)可表征西太平洋水汽输送特征;500 hPa 贝加尔湖阻塞高压区(45°～55°N,110°～130°E)可表征中纬度环流经向度及冷空气活动条件;200 hPa 华南高空急流区(20°～25°N,90°～110°E)可表征对流层辐合系统的深厚性。

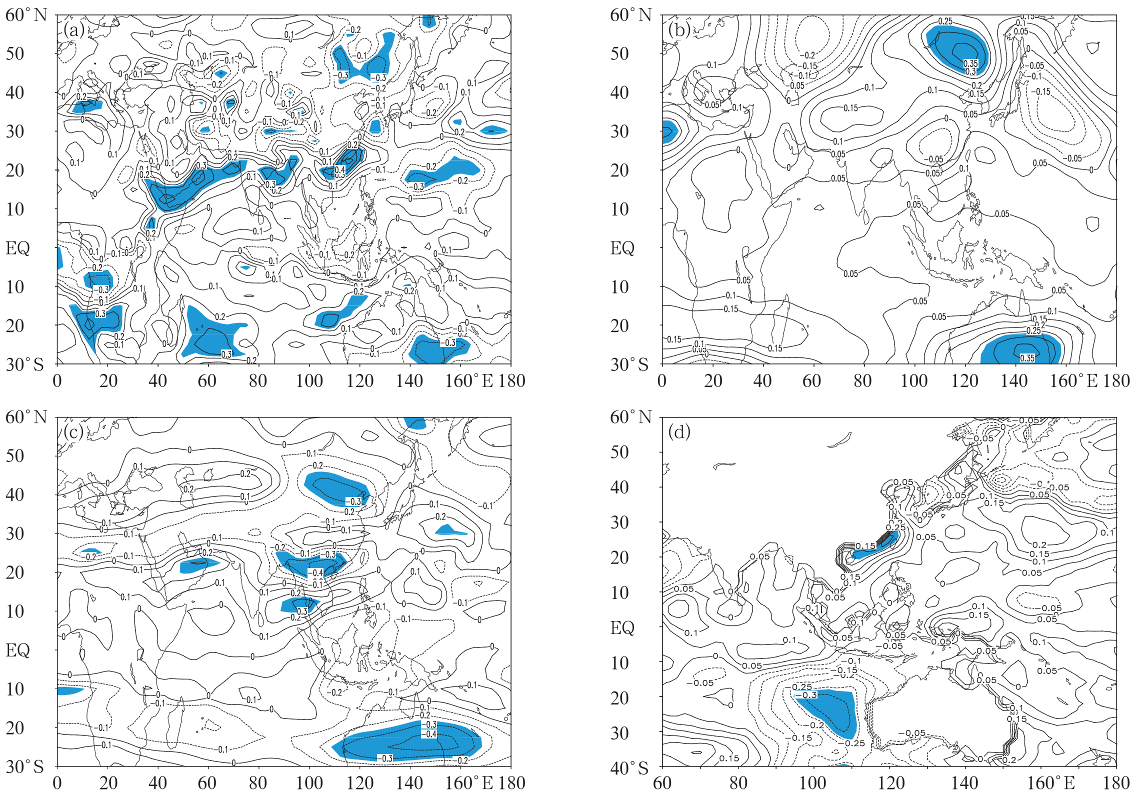

图 1　广西夏季降水与同期 850 hPa 风场(a)、500 hPa 高度场(b)、200 hPa 风场(c)和 2 月海温(d)的相关分布
(阴影区显示达到 0.05 显著性水平)

Fig. 1　The correlation coefficients of Guangxi summer precipitation to 850 hPa wind field(a), 500 hPa geopotential height(b), 200 hPa wind field(c) and SST in February(d)(the shaded denotes passing the test of 0.05 level)

降水除受到大气环流变率的直接影响外,外强迫因子的变化也会造成大气环流和降水异常。分别计算广西夏季降水指数与前期冬春季及同期夏季海温、土壤湿度、青藏高原积雪等的相关,寻找影响广西夏季降水的前兆信号。

广西夏季降水与前期 2 月海温相关场中,在南印度洋东部、澳大利亚西部海域呈显著负相关(图 1d),根据文献[31]可知,春季南半球中纬度印度洋区域海温偏低,南半球马斯克林高压和澳大利亚高压环流增强,会导致南半球越赤道气流加强,南亚夏季风增强,水汽输送增强,从而有利于广西降水偏多。选择通过 0.05 显著性水平检验的相关区(30°～20°S,95°～110°E)作为海温指数。

广西夏季降水与前期春季(3～5 月)华南地区土壤湿度为负相关,但未通过显著性检验,与夏季(6～8 月)土壤湿度为正相关,通过显著性检验(图

略)。这说明春季土壤湿度对夏季降水的影响比较复杂,而夏季降水偏多与土壤偏湿的关系很明显,因此土壤湿度很难作为广西夏季降水异常的先兆信号。

广西夏季降水与上一年 12 月青藏高原雪盖为负相关,但未通过显著性检验。与欧亚中纬度局部地区雪盖呈弱正相关(图略),研究指出[32]:冬季欧亚积雪异常偏多时,副热带高压脊线北跳偏迟,广西地区 6 月处在副热带高压北侧,易多雨;7 月受副热带高压脊控制,易少雨;8 月副热带高压北跳,又处于其南侧,受季风槽和热带辐合带影响,局地易有洪涝。但本文的相关分析显示积雪异常信号并未通过显著性检验,说明积雪对广西夏季降水的影响还存在较大不确定性。

初步分析表明,由于积雪、土壤湿度和热带太平洋海温异常对广西夏季降水异常影响不显著,而南印度洋东部海温异常的影响比较显著,因此可利用该区域海温信息作为预测因子进行应用分析。

4 广西夏季降水和影响因子的多时间尺度特征

4.1 年代际尺度特征

对广西夏季降水距平百分率采用滑动 t 检验、Mann-Kendall 方法和 Yamamoto 方法进行突变检验,得到广西夏季降水在 20 世纪 80 年代初、90 年代初分别发生 1 次突变。选取 1983—1992 年作为广西夏季降水偏少期,1993—2002 年为降水偏多期,两者相减得到广西夏季降水的年代际变化[33-34]信息。

多雨期与少雨期夏季 500 hPa 高度场差值图(图2a)表明,在欧亚中高纬度地区为西低东高形势,

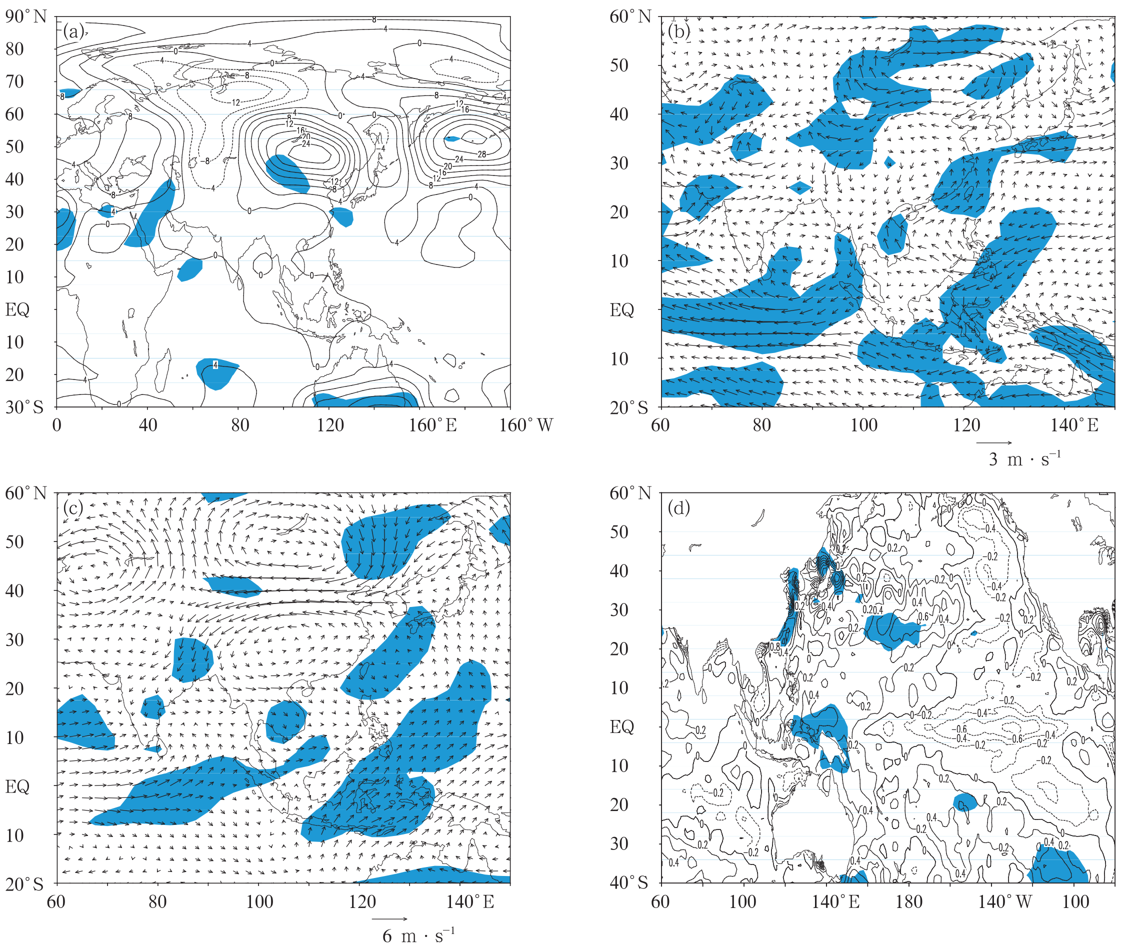

图 2 多雨期与少雨期夏季 500 hPa 位势高度场(单位:dagpm)(a)、850 hPa 风场(b)、200 hPa 风场(c)、2 月海温场(单位:℃)(d)差值距平(阴影区表示达到 0.05 显著性水平)

Fig. 2 The difference between the rich rain period and the poor rain period in summer for 500 hPa geopotential height(unit:dagpm)(a), 850 hPa wind field(b), 200 hPa wind field(c) and SST in February(unit:℃)(the shaded denotes passing the test of 0.05 level)

在乌拉尔山地区为深槽,贝加尔湖地区为强高压控制,这种环流型有利于冷空气在乌拉尔山堆积,同时贝加尔湖阻塞高压易导致西风带气流分支,副热带锋区南压,在 850 hPa 风场中(图 2b),广西上空为气旋式辐合区,来自于南海和中南半岛的水汽输送路径清晰;在 200 hPa 风场中(图 2c),广西处于青藏高原东部到西南气旋式辐合区的东南部,与低层的西南水汽输送路径一致,表现出相当正压结构,这种配置有利于广西夏季降水偏多。

多雨期与少雨期海温差值场表现为 2 月和春季(图略)赤道中东太平洋和南印度洋东部海温偏低,而我国东部沿海地区、菲律宾以南的热带西太平洋地区海温偏高。已有研究表明[35-36],菲律宾地区海温偏高,对流偏强,有利于夏季副高北跳偏早,江淮降水偏少;而菲律宾以南对流偏强时,副高偏南偏西,有利于长江以南降水偏多,而广西受副高引导的西太平洋水汽条件的影响,夏季降水易处于偏多期。

4.2　年际尺度特征

计算广西夏季降水距平的标准化值,选取 1 个标准差作为多雨年和少雨年的标准,则多雨年有 1993,1994,1998,2001,2002,2008 年,少雨年有 1983,1984,1985,1989,1990,1992 年,选取年份与文献[31]一致。用多雨年降水量减去少雨年降水量,得到降水的年际变化[33-34]信息,分析多雨年和少雨年差值的环流合成。

500 hPa 差值合成距平图(图3a)显示,在中高

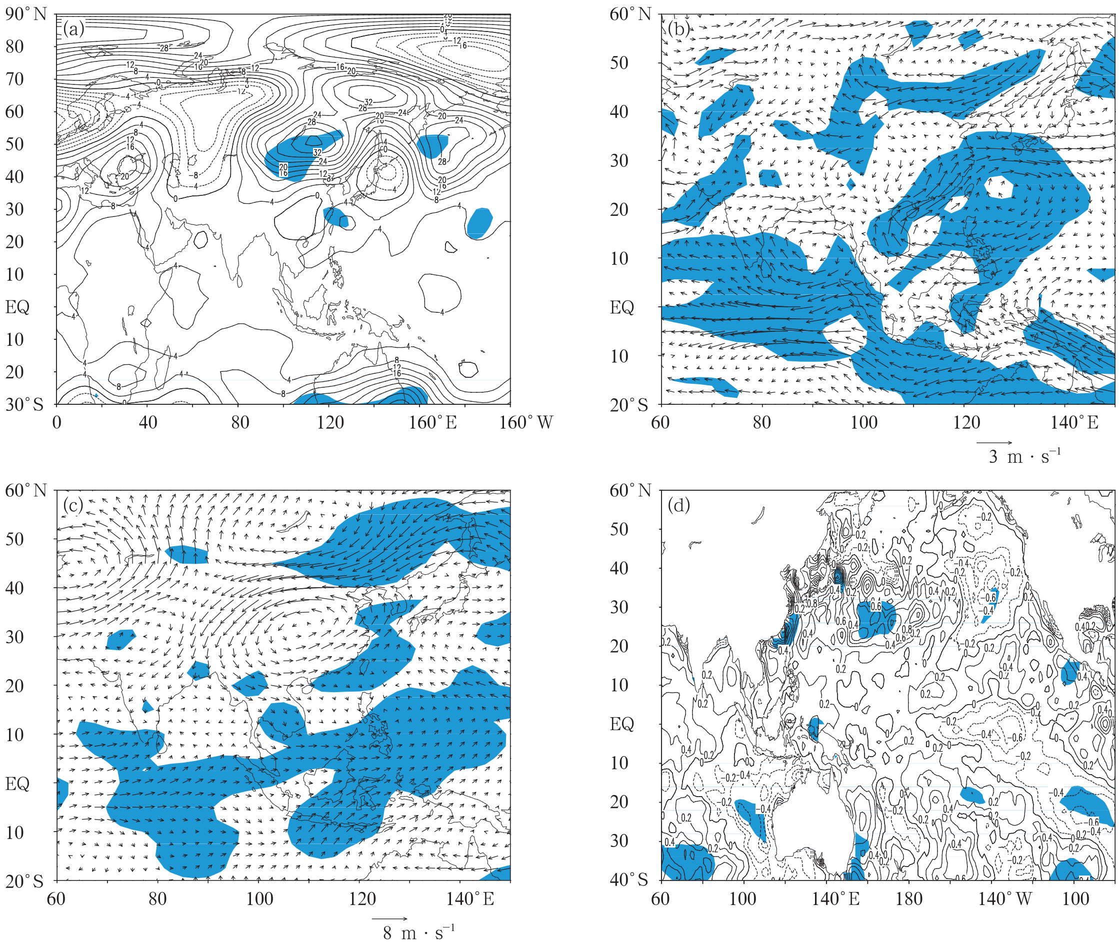

图 3　多雨年与少雨年年际尺度大气环流和外强迫距平分布场(阴影区表示达到 0.05 显著性水平)
(a)夏季 500 hPa 高度场(单位:gpm),(b)夏季 850 hPa 风场,
(c)夏季 200 hPa 风场,(d)2 月海温场(单位:℃)

Fig. 3　The circulation and SST anomaly fields between the rich rain year and the poor rain year for 500 hPa geopotential height(unit: gpm)(a), 850 hPa wind field(b), 200 hPa wind field(c), SST in February(unit:℃)(d)(the shaded denotes passing the test of 0.05 level)

纬度地区乌拉尔山为负距平，贝加尔湖地区为正距平，多雨年为西低东高分布，贝加尔湖以南的大范围地区达到0.05显著性水平，表明贝加尔湖地区位势高度场偏强，阻止了冷空气东移，有利于冷空气在乌拉尔山堆积，中高纬度地区以经向型分布为主，冷空气易南下影响广西。由850 hPa水平风场(图3b)可知，广西上空为气旋式环流，其东南侧为强西南风距平，孟加拉湾地区为异常反气旋性环流，其东侧为偏南风分量。西太平洋为反气旋式环流，有利于副高西伸加强。对应的200 hPa风场(图3c)，青藏高原东部至华南为显著的气旋式环流，广西处于气旋环流的东南侧，西南风偏强。高、中、低层的这种环流配置有利于广西夏季降水偏多，而少雨年的几个关键环流系统配置相反。

由多雨年与少雨年的春季海温差值场(图3d)可知，在热带太平洋没有显著的信息，在我国东部近海地区为正距平，南印度洋东部为显著负距平。这说明ENSO的年际变化对广西夏季降水的影响较为复杂，印度洋可能存在较显著的年际先兆信号。

4.3 年际和年代际时间尺度影响因子的异同

对比图2与图3可知，引起广西夏季降水异常的年际信号和年代际信号在850 hPa和200 hPa风场的关键环流区域比较一致，季风槽指数、低空急流指数、副高南侧偏东气流指数等的年际和年代际尺度信息接近。500 hPa高度场上，贝加尔湖阻塞高压强度指数和副高脊线位置的年际和年代际尺度的环流分布型略有差异，主要表现在年际信号更显著。海温的年际信号和年代际信号呈现明显不同的特征，年代际显著信号在西太平洋暖池区，而年际显著信号在南印度洋东部地区。

上面从年际和年代际尺度初步分析了广西夏季降水异常所对应的环流和外强迫信号，这些因子在不同尺度上对广西夏季降水异常的相对贡献有待研究，因此挑选与广西夏季降水相关关系达到0.05显著性水平的指数(表1)进行分析。另外增加了实际业务中经常使用的西太平洋副热带高压脊线[28]指数。首先对夏季降水和各指数进行2～9年和10～30年带通滤波，然后计算相关系数，分析它们在年际及年代际尺度上的关联性。可以看出，无论年际尺度还是年代际尺度，有些因子的相关值并不是很高，甚至低于原序列，说明仅有年际和年代际尺度信息还不足以解释广西夏季降水异常。

表1 各指数与广西夏季降水量的相关系数

Table 1 The correlation coefficients between each index and Guangxi summer precipitation

指数	原始资料	年际相关	年代际相关
季风槽指数	0.31	0.55	0.35
低空急流指数	0.41	0.49	0.54
副高南侧偏东气流指数	−0.31	−0.24	−0.24
贝加尔湖阻塞高压强度指数	0.30	0.21	0.15
西太平洋副热带高压脊线指数	−0.14	−0.52	−0.47
高空急流指数	−0.41	−0.53	−0.67
海温指数	−0.34	−0.24	−0.34

注:若相关系数绝对值大于0.25，表明该相关超过0.05显著性水平。下同。

4.4 广西夏季降水影响因子的多时间尺度特征

上面分析指出仅保留影响因子的年际和年代际信号还不足以代表影响广西夏季降水异常信息，这里利用EMD方法对6种夏季环流指数和2月海温指数进行展开，进而分析各指数的IMF分量与夏季降水各IMF分量间的关系。计算得到多数指数的IMF1均有2～4年周期振荡，这与占方差贡献50%以上的夏季降水的高频振荡相一致，广西夏季降水中第2到第4本征模态与这些指数的同一尺度的模态有着相近的周期(5～8年、9～13年和19年)。因此，广西夏季降水可能受到这些指数多尺度振荡的影响。

为了进一步探讨各因子与广西夏季降水在多时间尺度上的关系，分别计算各指数的IMF分量与降水IMF分量的相关系数，并将达到0.05显著性水平的高相关因子分量列于表2，选取方差贡献达10%以上的IMF1～IMF4进行分析。

影响夏季降水第1个本征模态(IMF1)变化的因子较多，与850 hPa的季风槽、低空急流和500 hPa贝加尔湖阻塞高压呈显著正相关，与200 hPa高空急流、副高南侧气流和东印度洋海温呈负相关，同期5个环流因子的合成与夏季降水的IMF1的相关系数为0.64，这说明夏季降水的IMF1在同期受到多种指数相同或相近尺度信息的影响。对比5种环流

指数 IMF1 分量合成与夏季降水的 IMF1 分量(图 4a),两者大致吻合。因此,造成夏季降水高频(即主频)变化的直接因子可能是 850 hPa 的季风槽、低空急流、副高南侧偏东气流和 500 hPa 贝加尔湖阻塞高压强度,以及 200 hPa 高空急流的高频振荡。即夏季 850 hPa 季风槽、低空急流和副高南侧的偏东气流偏强(弱),500 hPa 贝加尔湖阻塞高压偏强(弱),200 hPa 华南上空的东风急流偏强(弱),广西夏季降水易偏多(少),与 4.2 节的环流分析一致。另外,若春季南印度洋东部海温偏高,有利于夏季广西降水偏多,这可能与该处海温异常对越赤道气流强弱的影响有关。

表 2 各指数的 IMF1～IMF4 分量与广西夏季降水相应 IMF 分量的相关系数

Table 2 The correlation coefficients between IMF components of each index and that of Guangxi summer precipitation

指数	IMF1	IMF2	IMF3	IMF4
季风槽指数	0.33			0.50
低空急流指数	0.49			0.57
副高南侧偏东气流指数	−0.32		−0.49	−0.47
贝加尔湖阻塞高压强度指数	0.34			
西太平洋副热带高压脊线指数		0.33		
高空急流指数	−0.25		−0.39	−0.77
海温指数	−0.28		−0.49	−0.43

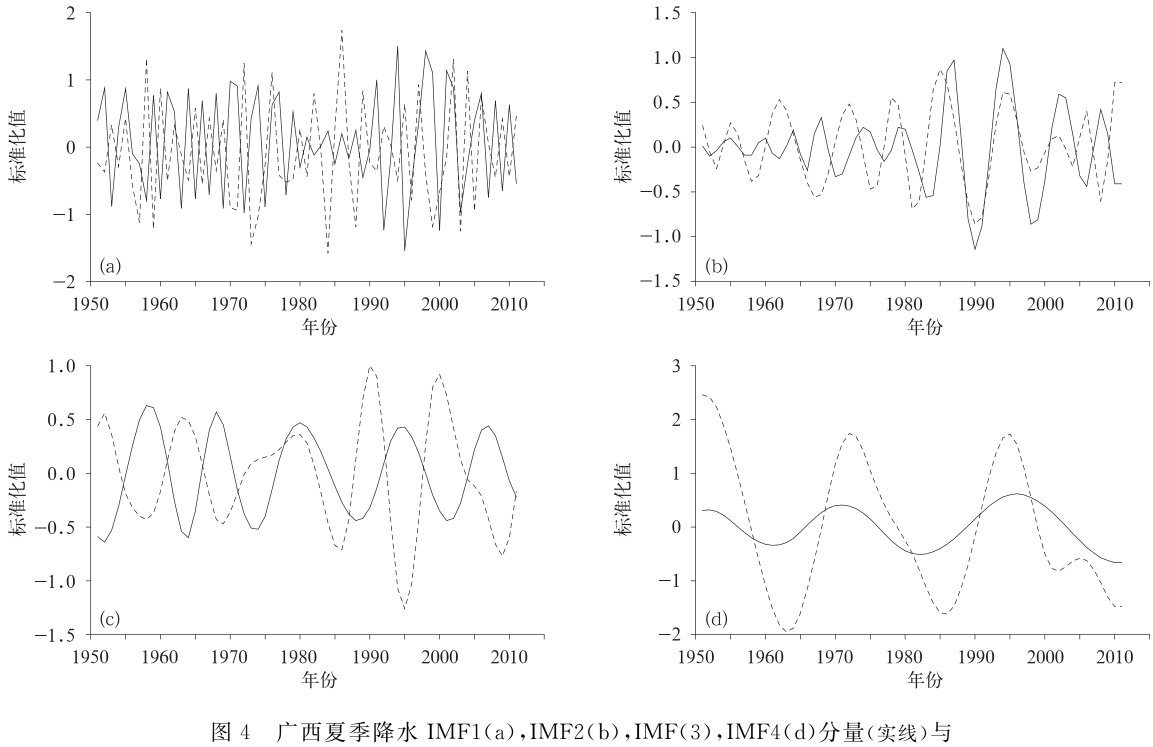

图 4 广西夏季降水 IMF1(a),IMF2(b),IMF(3),IMF4(d)分量(实线)与各显著影响环流因子 IMF 分量合成(虚线)对比

Fig. 4 The comparisons between IMF1(a),IMF2(b),IMF3(c),IMF4(d) of Guangxi summer precipitation(solid line) and their prominent index(dashed line)

影响夏季降水第 2 本征模态 IMF2 变化的因子主要为副高脊线的 IMF2(图 4b)。而副高脊线原序列与夏季降水原序列的相关系数仅为−0.14,这说明副高脊线的 IMF2 分量对夏季降水的 IMF2 分量有较大影响,其 IMF1 和 IMF3 与夏季降水相应的 IMF 分量周期变化并不同步。表明在 6～8 年的时间尺度上,夏季副高脊线偏北(南),广西夏季降水易偏多(少)。

影响夏季降水第 3 本征模态 IMF3 变化的因子有副高南侧偏东气流、高空急流和南印度洋东部海温,这说明夏季降水的 IMF3 分量主要受到同期高空急流和 850 hPa 副高南侧气流的 IMF3 调制,两

者相关系数达−0.55。图4c是副高南侧偏东气流和高空急流的IMF3合成与夏季降水的IMF3分量对比图,可见两者呈反位相关系,尤其是在20世纪70年代初以前和80代年末至21世纪初的反位相关系非常明显。这表明夏季高层东风急流和低层副高南侧偏东气流偏强(弱)时,广西夏季降水易偏多(少)。另外,春季南印度洋东部海温的偏低,有利于后期广西夏季降水偏多,这与4.1节的年代际尺度分析一致。

影响广西夏季降水第4个本征模态IMF4变化的因子主要有季风槽、低空急流、副高南侧偏东气流、高空急流和南印度洋东部海温,其中同期环流因子合成的相关系数均超过0.45。图4d是4种环流指数IMF4分量合成与夏季降水IMF4的对比,二者位相上基本吻合,但量值有差异。表示在准20年尺度上,夏季季风槽、低空急流和副高南侧偏东气流偏强(弱),华南上空的东风急流偏强(弱),有利于广西夏季降水偏多(少)。印度洋海温信号也表现出对降水的显著影响。

上述分析显示,增加6~8年、准20年尺度信息使广西夏季降水异常的影响因子信息更加全面,各时间尺度上影响因子的IMF分量拟合更接近于降水序列的分量。

5 利用影响因子对广西夏季降水的预测试验

利用环流指数的IMF分量和多元线性回归方程,进行广西夏季降水的拟合和预测试验(所有变量进行了标准化处理),拟合降水和实况的复相关系数达到0.73,夏季降水的线性回归方程为

$$Y=-0.04+0.20X_{11}+0.45X_{21}-0.10X_{31}+0.39X_{41}-0.04X_{51}+0.07X_{62}-0.34X_{33}-0.89X_{53}-0.31X_{14}-0.18X_{24}-1.65X_{34}-0.84X_{54}。\tag{2}$$

其中,X_{1n}表示季风槽指数IMFn分量的贡献,X_{2n}表示低空急流指数IMFn分量的贡献,X_{3n}表示副高南侧偏东气流指数IMFn分量的贡献,X_{4n}表示贝加尔湖阻塞高压强度指数IMFn分量的贡献,X_{5n}表示高空急流指数IMFn分量的贡献,X_{6n}表示副高脊线指数IMFn分量的贡献。

在0.05显著性水平下,分子自由度为12,分母自由度为48时,$F_{0.05}=1.92$,统计量值[37] $F=4.61>F_{0.05}$,上述回归方程是显著的。拟合值与实况值非常吻合(图5),说明这些因子是通过多时间尺度的叠加影响广西夏季降水。分别计算广西夏季降水与各影响因子的偏相关系数,达到0.05显著性水平的偏相关因子有低空急流指数IMF1分量(相关系数为0.45)、贝加尔湖阻塞高压强度指数IMF1分量(相关系数为0.37)、季风槽指数IMF1分量(相关系数为0.25)、高空急流指数IMF3分量(相关系数为−0.42),高空急流指数IMF4分量(相关系数为−0.35),说明850 hPa的低空急流、季风槽和500 hPa贝加尔湖阻塞高压的准2年周期影响以及高空急流的年代际变化对夏季降水的影响更为显著。该方程表明所选同期环流因子对广西夏季降水有显著影响。

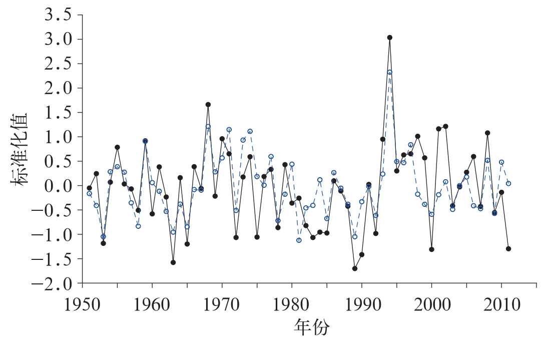

图5 采用环流指数因子的IMF分量的线性回归拟合值(虚线)与广西夏季降水(实线)的对比

Fig.5 The fitness value from the linear regression of IMF components from different indexes (dashed line) and Guangxi summer rainfall (solid line)

此外,利用前期2月南印度洋东部海温指数来构建广西夏季降水的预测模型,采用海温指数的IMF1~IMF4分量与广西夏季降水建立($n=55$)多元线性回归方程,其复相关系数为0.43,广西夏季降水预测的线性回归方程为

$$Y=-0.52-7.53X_1-10.81X_2-37.92X_3-3.02X_4。\tag{3}$$

式(3)中,$X_1\sim X_4$分别代表海温指数的IMF1~IMF4分量的贡献。在0.05显著性水平下,分子自由度为4,分母自由度为50时,统计量值[37] $F>F_{0.05}$,上述回归方程是显著的(图6),拟合与实况非常吻合。利用该方程对2006—2011年夏季降水进行了独立样本检验,2006—2011年的预测值(标准化后)分别为18.9,−4.9,3.3,−3.9,−11.9,−28.8;而相应的实况值(标准化后)为12.9,−9.3,23.4,−12,−3,−30.4。即近6年的预测结果与实况同号率完全一致,可见在多时间尺度上,南印度洋

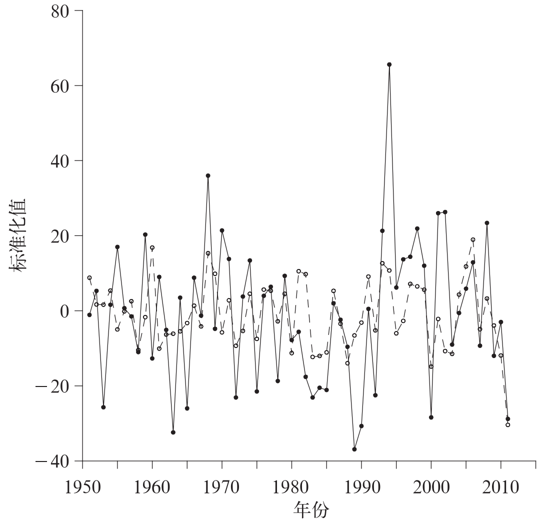

图6 采用海温指数因子的IMF分量线性回归拟合值(虚线)与广西夏季降水(实线)的对比

Fig. 6 The fitness value from the linear regression of SST IMF components(dashed line) and Guangxi summer rainfall(solid line)

东部海温因子可以作为一个显著的前兆信号预测广西夏季降水。

6 结论和讨论

本文利用广西站点资料和多种再分析格点资料,从年际和年代际尺度出发,获得影响广西夏季降水异常的7个关键指数,由于它们无法从两个时间尺度诠释造成降水异常的全部信息,进而采用EMD方法对指数进行尺度分离,从多时间尺度的角度分析了影响广西夏季降水的主要环流因子和外强迫因子,并尝试利用影响因子的本征模态函数进行广西夏季降水的拟合和预测试验。主要结论如下:

1) 广西夏季降水表现为准2年、7.6年、12.7年、19年和38年的周期特征,即广西夏季降水表现出多时间尺度的特征。

2) 在年际和年代际尺度上,影响广西夏季降水异常的环流型比较一致,即夏季850 hPa季风槽、低空急流和副高南侧的偏东气流偏强(弱),500 hPa贝加尔湖阻塞高压偏强(弱),副高脊线偏北(南),200 hPa华南上空的东风急流偏强(弱)时,广西夏季降水易偏多(少)。前期海温异常信号在年际尺度上位于冬季南印度洋东部,在年代际尺度上位于菲律宾以南的西太平洋暖池区。

3) 影响因子的年际和年代际尺度信息不能解释广西夏季降水异常的全部,对影响因子的进行EMD分解显示各因子的本征模态函数(IMF)在不同时间尺度上影响广西夏季降水,影响因子的多时间尺度特征分析有利于理解造成降水异常的因子分量来源。

4) 用影响夏季降水的同期环流因子对应的IMF分量和多元线性回归方程拟合夏季降水,拟合和实况夏季降水的复相关系数高达0.73,说明夏季降水确实受到多种因子的多时间尺度的共同影响。用前期冬季南印度洋东部海温的IMF分量和多元线性回归方法构建广西夏季降水的预测模型,对2006—2011年的独立样本检验表明:预测模型的同号率达100%,说明南印度洋东部海温因子可以作为广西夏季降水预测的前兆信号。

本文利用EMD方法从多时间尺度角度寻找了影响广西夏季降水的同期环流因子及前期外强迫因子,并分析引起降水异常的环流配置。该工作仅为初步诊断分析,还需深入研究广西夏季降水的影响因子的物理演变过程及其对外强迫的响应机制,此外,可以利用动力气候模式对环流预测的高技巧信息[38-39],从动力与统计相结合的角度[40-42]进一步提高夏季降水预测能力。利用印度洋海温指数的预测试验也只是单因子影响结果,而实际大气受到多因子非线性的作用,因此预测模型也需进一步完善。

致 谢:感谢国家气候中心刘芸芸高级工程师提供西太平洋副热带高压监测资料。

参考文献

[1] 覃志年,覃峥嵘.广西2002年夏季多雨成因分析.广西气象,2002(3):28-29.

[2] 吴洪宝,王盘兴,林开平.广西夏季降水量潜在可预报性估计.应用气象学报,2005,16(4):445-452.

[3] 覃志年,金龙,何慧.广西夏季异常降水量的前馈网络预报模型.灾害学,2005,20(4):23-28.

[4] 周文志.蒋丽娟.吴松/广西夏季旱涝分布规律及同期500 hPa环流特征.自然灾害学报,2009,18(4):132-137.

[5] 玄兆燕,杨公训.EMD在地面气温预测中的应用.微计算机信息,2008,24(7):516-525.

[6] 侯威,封国林,董文杰,等.利用排列熵检测近40年华北地区气温突变的研究.物理学报,2006,55(5):2663-2668.

[7] 林振山,汪曙光.近四百年北半球气温变化的分析:EMD方法的应用.热带气象学报,2004,20(1):90-96.

[8] 王兵,李晓东.基于EEMD分解的欧洲温度序列的多尺度分析.北京大学学报:自然科学版,2011,47(4):627-635.

[9] 杨周,林振山.北半球过去2000年气温变化的多尺度分析.地理科学,2010,30(2):295-299.

［10］ 秦旭,张讲社,延晓冬.基于改进的EMD的运城市持续极端气温的初步分析.大气科学学报,2009,32(5):645-651.

［11］ 孙娴,林振山.经验模态分解下中国气温变化趋势的区域特征.地理学报,2007,62(11):1132-1141.

［12］ 申倩倩,束炯,王行恒.上海地区近136年气温和降水量变化的多尺度分析.自然资源学报,2011,26(4):644-654.

［13］ McMahon T A,Kiem A S, Peel M C,et al. A new approach to stochastically generating six-monthly rainfall sequence based on empirical mode decomposition. *J Hydrometeoro*, 2008,9(6):1377-1389.

［14］ 刘莉红,翟盘茂,郑祖光.中国北方夏半年最长连续无降水日数的变化特征.气象学报,2008,66(3):474-477.

［15］ 王兆礼,覃杰香,陈晓宏.东江流域枯水期最长连续无降水日数的变化特征.地理研究,2011,30(9):1693-1701.

［16］ 刘莉红,郑祖光,琚建华,等.夏季副热带大气系统的多尺度振荡分析.高原气象,2010,29(1):115-127.

［17］ Love B S,Matthews A J,Janacek G J. Real-time extraction of the Madden-Julian oscillation using empirical mode decomposition and statistical forecasting with a VARMA model. *J Climate*,2008,21(20):5318-5335.

［18］ 顾小丽,李培良,谭海涛,等.基于RBF神经网络的EMD方法在海平面分析中的应用.海洋与湖泊,2009,40(5):532-539.

［19］ 卢晓亭,孙勇,笪良龙,等.基于EMD的BP神经网络海水温度时间序列预测研究.海洋技术,2009,28(3):79-82.

［20］ 王勤,陈显尧,王秀红.德雷克海峡上层海洋温度的年代际变化.海洋科学进展,2009,27(4):426-433.

［21］ 杜建丽,林振山,张真真.基于EMD的我国受旱面积波动的多时间尺度的分析.干旱区资源与环境,2009,23(5):90-93.

［22］ 张明阳,王克林,刘会玉,等.基于EMD的洪涝灾害成灾面积波动的多时间尺度分析——以湖南省为例.中国生态农业学报,2007,15(1):131-134.

［23］ 万仕全,封国林,周国华,等.基于EMD方法的观测数据信息提取与预测研究.气象学报,2005,63(4):516-525.

［24］ 邹明玮.基于非线性时间序列分析方法的非线性系统特性研究.扬州:扬州大学,2007.

［25］ 玄兆燕,杨公训.经验模态分解法在大气时间序列预测中的应用.自动化学报,2008(1):97-101.

［26］ 毕硕本,陈譞,覃志年,等.基于EMD和集合预报技术的气候预测方法.热带气象学报,2012,28(2):283-288.

［27］ Kalnay E,Kanamitsu M,Kistler R,et al. The NCEP/NCAR 40-year reanalysis project. *Bull Amer Meteor Soc*, 1996, 77(3):437-471.

［28］ 刘芸芸,李维京,艾孑兑秀,等.月尺度西太平洋副热带高压指数的重建与应用.应用气象学报,2012,23(4):414-423.

［29］ 郑祖光,刘莉红.经验模态分析与小波分析及其应用.北京:气象出版社,2010.

［30］ 胡娅敏,丁一汇.江淮地区梅雨的新定义及其气候特征.大气科学,2008,32(1):101-112.

［31］ 况雪源,黄梅丽,林振敏,等.广西前汛期降水年代际变化与南半球印度洋海温的关系.热带气象学报,2008,24(6):279-284.

［32］ 何慧,张健,黄莉.北半球冬季雪盖对南宁地区盛夏降水的影响.广西气象,2002,23(4):35-38.

［33］ 陆日宇.华北汛期降水量变化中年代际和年际尺度的分离.大气科学,2002,26(3):611-623.

［34］ 陆日宇.华北汛期降水量年代际和年际变化之间的线性关系.科学通报,2003,48(7):718-722.

［35］ 曹杰,黄荣辉,谢应齐,等.西太平洋副热带高压演变物理机制的研究.中国科学:D辑,2002,32:659-666.

［36］ Huang Ronghui,Sun Fengying. Impact of the tropical western Pacific on the East Asian summer monsoon. *J Meteor Soc Japan*,1992,70(1):243-256.

［37］ 魏凤英.现代气候统计诊断与预测技术.北京:气象出版社,2007.

［38］ 魏凤英.我国短期气候预测的物理基础及其预测思路.应用气象学报,2011,22(1):1-11.

［39］ 张婷,魏凤英,韩雪.华南汛期降水与南半球关键系统低频演变特征.应用气象学报,2011,22(3):265-274.

［40］ 陈丽娟,李维京.月动力延伸预报产品的评估和解释应用.应用气象学报,1999,10(4):486-490.

［41］ 顾伟宗,陈丽娟,张培群,等.月动力延伸预报最优信息提取和对中国降水的降尺度应用.气象学报,2009,67(2):280-287.

［42］ 覃志年,陈丽娟,唐红玉,等.月尺度动力模式产品解释应用系统及预测技巧.应用气象学报,2010,21(5):614-620.

The Multi-timescale Features for Guangxi Summer Precipitation and the Related Predictors

Qin Zhinian[1)]　Hu Yamin[2)3)]　Chen Lijuan[4)]

[1)] (*Guangxi Climate Center*, *Nanning* 530022)　[2)] (*Guangdong Provincial Climate Center*, *Guangzhou* 510080)

[3)] (*Guangzhou Climate and Agricultural Meteorology Center of Guangdong Province*, *Guangzhou* 510080)

[4)] (*Laboratory for Climate Studies*, *National Climate Center*, *CMA*, *Beijing* 100081)

Abstract

Based on NCEP/NACR reanalysis data and Guangxi summer precipitation (GSP) station data, using the correlation analysis, composite analysis, empirical orthogonal function (EOF), empirical mode decomposition (EMD), abrupt change test and the statistic significant test methods, GSP multi-timescale characteristics and their related circulation as well as the external forcing features are analyzed. According to the diagnostic analysis, the fitting and the prediction equation of GSP are proposed by the multivariate linear regression method.

GSP is mainly influenced by the mid-latitude height field anomaly in Lake Baikal region, the subtropical high and monsoon trough (MonTr) in the subtropical region, the low level jet (LLJ) and upper level jet (ULJ) in the same season, as well as the sea surface temperature (SST) anomaly in the eastern of the South Indian Ocean in the pre-winter and pre-spring.

The possible physical concept model for GSP is that, when MonTr, LLJ, and the easterly to the south of the subtropical high (ESTH) occur at 850 hPa wind field, the blocking high (BH) over Lake Baikal at 500 hPa potential height, as well as ULJ over South China at 200 hPa wind field are stronger (weaker) than normal, and the subtropical high ridge location is northward (southward) to its normal position, the rainfall is more. The influences of circulation may impact summer rainfall anomaly through the multi-timescale features.

Using EMD method, there are 5 principle modes for the summer rainfall. The variance contributions from the first to the fourth intrinsic mode function (IMF1—IMF4) are 55%, 18%, 12% and 12%, respectively. The periods over the statistic significant test are quasi-2 years, 7.6 years, 12.7 years and 19 years. On the scale of quasi-2 years, the summer rainfall is affected by the corresponding IMF1 components of the MonTr, LLJ, ULJ, BH over Lake Baikal, SST anomaly in the east of the South Indian Ocean. The summer rainfall has high relationship with the other influenced indexes on the different time scales.

Using IMF1—IMF4 components of circulation factors and the multivariate linear regression method, the summer precipitation equation is fitted. The results show that the multiple correlation coefficients reach 0.73 with the significant level over 0.05. The tests verify that the summer precipitation is really influenced by the multi-timescale components of different factors.

Furthermore, based on the IMFs of SST anomaly in the east of southern Indian in winter, the prediction model of the summer precipitation is constructed by the multivariate linear regression method. The trends of the 6 independent sample tests are accord with that of the observation. This method provides an idea in the regional climate prediction based on the multi-timescale features of predictant and predictor.

Key words: the summer precipitation; multi-timescale features; empirical mode decomposition (EMD); intrinsic mode function (IMF)

Recharge Oscillator Mechanisms in Two Types of ENSO

HONG-LI REN

Department of Meteorology, School of Ocean and Earth Sciences and Technology, University of Hawaii at Manoa, Honolulu, Hawaii, and Laboratory for Climate Studies, National Climate Center, China Meteorological Administration, Beijing, China

FEI-FEI JIN

Department of Meteorology, School of Ocean and Earth Sciences and Technology, University of Hawaii at Manoa, Honolulu, Hawaii

(Manuscript received 13 August 2012, in final form 26 February 2013)

ABSTRACT

The El Niño–Southern Oscillation (ENSO) tends to behave arguably as two different ''types'' or ''flavors'' in recent decades. One is the canonical cold-tongue-type ENSO with major sea surface temperature anomalies (SSTA) positioned over the eastern Pacific. The other is a warm-pool-type ENSO with SSTA centered in the central Pacific near the edge of the warm pool. In this study, the basic features and main feedback processes of these two types of ENSO are examined. It is shown that the interannual variability of upper-ocean heat content exhibits recharge–discharge processes throughout the life cycles of both the cold tongue (CT) and warm pool (WP) ENSO types. Through a heat budget analysis with focus on the interannual frequency band, the authors further demonstrate that the thermocline feedback plays a dominant role in contributing to the growth and phase transitions of both ENSO types, whereas the zonal advective feedback contributes mainly to their phase transitions. The westward shift of the SSTA center of the WP ENSO and the presence of significant surface easterly wind anomalies over the far eastern equatorial Pacific during its mature warm phase are the two main factors that lead to a reduced positive feedback for the eastern Pacific SSTA. Nevertheless, both the WP and CT ENSO can be understood to a large extent by the recharge oscillator mechanism.

1. Introduction

The phenomena of El Niño–Southern Oscillation (ENSO) are recognized to play a crucial role in global climate variability (Rasmusson and Carpenter 1982; Ropelewski and Halpert 1987; Mason and Goddard 2001). In general, the canonical El Niño has its major center of sea surface temperatures anomalies (SSTAs) in the equatorial Pacific cold-tongue (CT) region. Recently, a number of studies reported that, in addition to this canonical El Niño type, a different type of El Niño with its major SSTA center shifted to the central Pacific by the warm-pool (WP) edge region, is becoming a common occurrence during the past 20 years (Larkin and Harrison 2005a,b; Ashok et al. 2007; Kao and Yu 2009; Kug et al. 2009). There is evidence that this ENSO type may emerge even more frequently in a warming climate as projected by the Intergovernmental Panel on Climate Change (IPCC) Fourth Assessment Report (AR4) simulations (Yeh et al. 2009). This El Niño type is accompanied by a distinct tropical atmospheric circulation pattern (Ashok and Yamagata 2009) and exhibits significantly different global climate impacts compared to CT El Niños through tropical–extratropical teleconnections (e.g., Weng et al. 2007, 2009; Kim et al. 2009; Zhang et al. 2011, 2012). So far, various definitions and nomenclatures, such as date line El Niño (Larkin and Harrison 2005a,b), El Niño Modoki (Ashok et al. 2007), central Pacific ENSO (Kao and Yu 2009; Yeh et al. 2009), and WP El Niño (Kug et al. 2009; Ren and Jin 2011, hereafter RJ11), have been given to this type of ENSO. We adopt the terminology of WP and CT El Niño/ENSO in this study to highlight the fact that the WP and CT ENSO SSTAs overlay over very different climatological background sea surface temperatures.

A number of attempts have been made to examine the dynamical processes responsible for the generation and

Corresponding author address: Dr. Hong-Li Ren, School of Ocean and Earth Sciences and Technology, University of Hawaii at Manoa, 2525 Correa Rd. HIG350, Honolulu, HI 96822.
E-mail: honglir@hawaii.edu

DOI: 10.1175/JCLI-D-12-00601.1

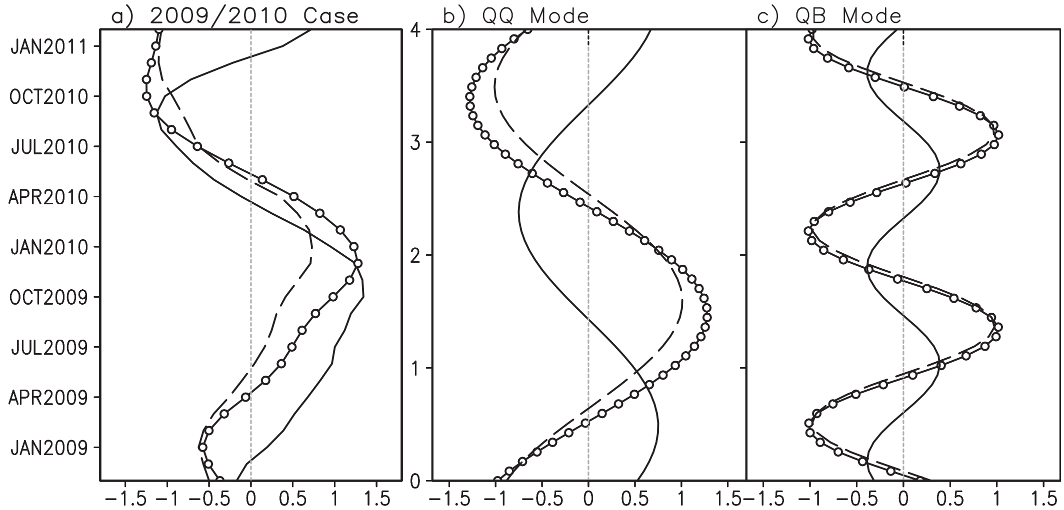

FIG. 1. (a) Zonal-mean equatorial indices of SSTA (line with circles, K) and SSHA (solid line, 0.025 m) and recharge oscillkator index (RDI) (dashed line, 1×10^{-8}) for the 2009–10 case. The indices are generated over 5°S–5°N. The SSTA index is averaged over 160°E–110°W and the SSHA index over 120°E–110°W. RDI is defined as the average of zonal gradient of SSHA over 120°E–90°W, positively proportional to meridional geostrophic current and represents the intensity of recharge–discharge of equatorial upper-ocean heat content. SSH is from the GODAS data and the climatology is defined in 1980–2010. (b),(c) As in (a) but for the QQ and QB modes, based on Fig. 5 of Bejarano and Jin (2008), where the green and blue lines are thermocline depth anomaly index (unit: 10 m) and its derived RDI (unit: 2.5×10^{-6}) that are averaged over 140°E–90°W and the SSTA indices over 180°–90°W.

maintenance of the WP El Niño type. Ashok et al. (2007) stressed the important role of wind-induced tropical Pacific thermocline variability in the evolution of WP El Niño events. Kug et al. (2009) accentuated that the zonal-current-driven advective feedback plays a key role in the developing phase of the WP El Niño type, whereas the thermocline feedback may be of less importance. Kao and Yu (2009) reported that phase reversal signatures are unclear for WP El Niños, whereas Yu et al. (2009, 2010) emphasized initial extratropical triggers or preconditions for the generation of the WP-type ENSO events. Further, Yu and Kim (2010a) suggested that there are three possible phase transition pathways for this El Niño type under different preconditions. However, most WP El Niño events occurred in the early 1990s and in the 2000s when the tropical Pacific decadal variability was in warm phases. This decadal modulation of the background state might have interfered, to some extent, with the basic characteristics of the WP ENSO in all previous studies. Kug et al. (2010), based on model output analyses, indicated that the dynamical feedbacks may not be crucial for the phase transition of the WP El Niño owing to a weak discharge of equatorial heat content so that a WP El Niño event is rarely followed by a cold (La Niña) event. However, most coupled general circulation models still fail to simulate both ENSO types due to relatively large model biases (Yu and Kim 2010b; Ham and Kug 2012). The basic features and dynamical processes associated with the WP ENSO flavor remain elusive and need to be further studied.

Bejarano and Jin (2008), in their theoretical study of the ENSO regime dependence on climate mean state changes, showed that there are two leading ENSO-like modes coexisting under the current climate conditions. One of the modes, termed the quasi-quadrennial (QQ) mode, has its SSTA pattern centered over the eastern equatorial Pacific (see their Fig. 7i), similar to the observed SSTA pattern of CT ENSO. The other mode, termed the quasi-biennial (QB) mode, has its SSTA center shifted westward (see their Fig. 8i), which is similar to the observed SSTA pattern of WP ENSO. Although the zonal advective feedback plays a more important role in the phase transition for the second mode, the dynamics of the two modes can be both understood to some extent by the recharge oscillator mechanism (Jin 1996, 1997a; Jin and An 1999).

Motivated by the study of Bejarano and Jin (2008), we give evidence that the 2009–10 event, the strongest WP El Niño event in recorded history, is reminiscent to their QB mode (Fig. 1). As seen in Fig. 1, this WP El Niño event exhibits a clear recharge–discharge process of upper-ocean heat content [referred to as the recharge–discharge index (RDI), defined as the zonal-mean zonal gradient of equatorial thermocline anomalies] and a fast phase transition indicated by the zonal-mean thermocline variability. In this study, we will examine the recharge oscillator mechanisms for the two ENSO types and the associated dynamical feedback in depth.

To capture the basic spatiotemporal features of the two ENSO types, we will utilize the so-called WP Niño index (WPI) and CT Niño index (CTI) developed in our recent study (RJ11). By removing the decadal signal, we will focus on interannual variability features of the two ENSO types and examine the dynamical feedback processes to determine their contributions to growth and phase transitions. This paper will be organized as follows. The utilized datasets are described in section 2. The indices and patterns for the two ENSO types are given in section 3. We examine the recharge–discharge processes of upper-ocean heat content associated with both ENSO types in section 4 and compare contributions of the different dynamical feedback processes to the growth and phase transitions in section 5. We conclude with a summary and discussion in section 6.

2. Data and ENSO indices

We use the improved extended reconstructed SST version 3b (ERSST V3b) (Smith et al. 2008) dataset from the National Climate Data Center of the National Oceanic and Atmospheric Administration. This SST data consists of monthly 2° spatial superobservations, which are defined as individual observations averaged onto a 2° horizontal grid. We will examine the period from January 1950 to February 2011.

The interior ocean temperature, current, and sea surface height variables are primarily taken from the Simple Ocean Data Assimilation (SODA) reanalysis version 2.2.4 (Giese and Ray 2011) for the period from January 1871 to December 2008. The ocean model in the data assimilation system is based on the Parallel Ocean Program (POP) version 2.0.1 (Smith et al. 1992) with a horizontal resolution of 0.25° latitude by 0.4° longitude. There are 40 vertical levels with a resolution of about 10 m in the upper 100 m. This global ocean model is forced by an extended atmospheric forcing field from a new NOAA reanalysis dataset [the Twentieth-Century reanalysis, version 2 (20CRv2)] (Whitaker et al. 2004; Compo et al. 2006) for the period 1871–2008.

In addition, the assimilation products generated from the Global Ocean Data Assimilation System (GODAS) (Behringer and Xue 2004) from the National Centers for Environmental Prediction (NCEP) are used for comparison with the SODA-data-based results. The GODAS analysis is available at a $\frac{1}{3}° \times \frac{1}{3}°$ horizontal resolution in the tropics for the period from January 1980 to February 2011.

Traditional Niño-3 and Niño-4 indices from January 1950 to February 2011 are directly obtained online (http://www.cpc.noaa.gov/data/indices/sstoi.indices) from the NOAA/Climate Prediction Center: the indices are defined as SSTA averages over the Niño-3 region (5°S–5°N, 150°–90°W) and Niño-4 region (5°S–5°N, 160°E–150°W). In this study, we remove the long-term linear trend from all indices before further analyses.

The two traditional Niño indices, Niño-3 and Niño-4, have been extensively used to quantify the ENSO phenomenon. A combination of these two, the Niño-3.4 index defined by the SSTA averaged in the Niño-3.4 region (5°S–5°N, 170°–120°W) (Trenberth 1997), is widely used in ENSO research and operational climate monitoring. Since the SSTA patterns of the ENSO types are highly correlated, neither of the two traditional indices alone can characterize the WP ENSO independently. All three indices capture the broad-scale nature of the ENSO-related SSTA and, thus, exhibit the main signals of the different ENSO types. Therefore, based on a transformation of Niño-3 and Niño-4 indices, RJ11 proposed WPI and CTI (refer to the appendix for details) to describe the two different ENSO types. These two indices can be used effectively to delineate time evolutions and extract characteristic patterns for both ENSO types.

We also utilize other indices proposed previously to represent the different ENSO flavors. One is the El Niño Modoki index (EMI) proposed by Ashok et al. (2007) to replicate the second empirical orthogonal function (EOF) of tropical Pacific SSTAs, which is defined as $[\mathrm{SSTA}]_\mathrm{C} - 0.5[\mathrm{SSTA}]_\mathrm{E} - 0.5[\mathrm{SSTA}]_\mathrm{W}$, where brackets denote spatial averages in the central (C: 165°E–140°W, 10°S–10°N), eastern (E: 110°–70°W, 15°S–5°N), and western (W: 125°–145°E, 10°S–20°N) areas, respectively. This index is somewhat similar to the trans-Niño index proposed by Trenberth and Stepaniak (2001). Another is the central Pacific ENSO index (CPI) proposed by Kao and Yu (2009), who realized that the second SSTA EOF is not quite adequate to describe the main features of the different ENSO flavors independently and devised a somewhat more complicated index. CPI is also based on an EOF decomposition of data with SSTA related to the Niño-1+2 index, which is defined at (10°S–0°, 80°–90°W), linearly removed. Similarly, an eastern Pacific ENSO index (EPI) is defined by linearly removing the Niño-4-index-related SSTA. All of these somewhat related indices utilize SSTA beyond the Niño-3 and Niño-4 regions. Overall all these new indices, despite being derived from different definitions, are essentially describing the same phenomenon.

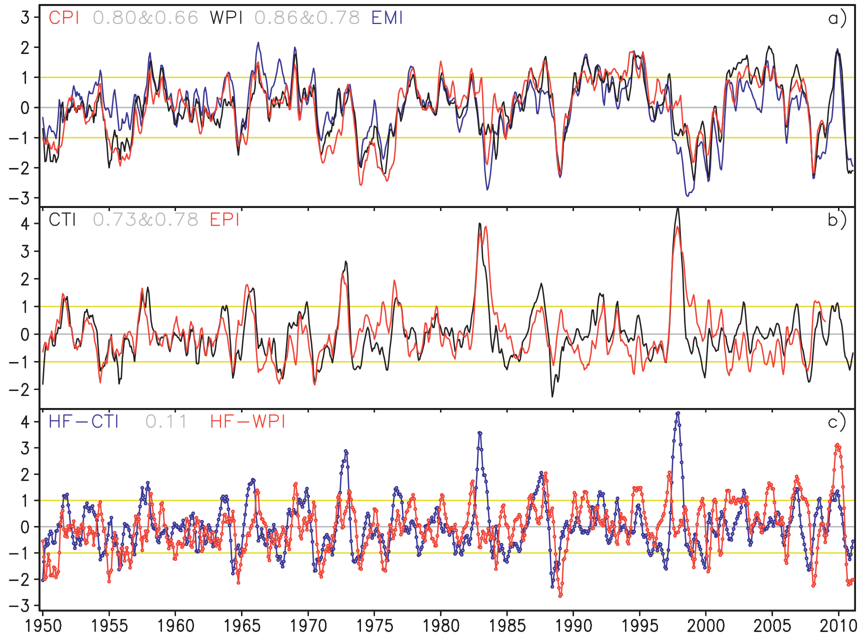

FIG. 2. Normalized indices: (a) CPI, WPI, and EMI; (b) CTI and EPI; and (c) HF CTI and WPI. All indices are subject to 3-month running mean after the normalization. Yellow lines correspond to one standard deviation of the indices. Gray number pairs in (a) or (b) are correlation coefficients between the indices with and without the decadal, respectively, while the gray number in (c) is correlation between the detrended indices. All of correlations are obtained by using the indices before the running mean.

3. Removal of the decadal signal from the ENSO indices

Figure 2a shows time evolutions of the normalized WPI, EMI, and CPI. All of these indices represent the temporal characteristics of the WP ENSO type and exhibit more or less the same characteristics in the last six decades. The correlation between WPI and EMI amounts to 0.86 and to 0.80 between WPI and CPI. These indices exhibit strong interannual and decadal variability besides a weak long-term linear trend. Their spectral coherence seems to be partly due to the decadal variability. Another main common feature found among the indices is the clear interannual variability superimposed on the slower-varying decadal signal. Weng et al. (2007) have noted that EMI is dominated by decadal time-scale variability, whereas Kao and Yu (2009) reported that the CP ENSO shows a dominant period near the 2-yr band. The considerable divergence of these conclusions reflects that the SSTA in the tropical central Pacific exhibit multi-time-scale characteristics. Therefore, to solely focus on the interannual variability of the WP ENSO type, we filtered out the decadal signals from our indices. We first produce low-pass filtered (LPF) WPI and CTI with a Gaussian filter, where the spectrum cutoff is chosen at 6 yr for WPI and 8 yr for CTI, and then subtract the LPF indices from the original indices to obtain high-frequency (HF) WP and CT indices (Fig. 2c).

In Fig. 2c, both HF WPI and HF CTI clearly feature variability on interannual time scales without any background decadal signal. Their correlation amounts to 0.11, indicating that WPI and CTI are independent from each other on interannual time scales. Furthermore, the correlations between HF WPI, HF CPI, and HF EMI are calculated (the second elements of gray number pairs in Figs. 2a,b). Their differences relative to the first elements reflect the impact of the decadal signals on the correlations. That is, the good coherence between the nonfiltered indices (Fig. 2a) is partly attributed to the decadal signal. This implies that the classification of CT El Niño, WP El Niño, and La Niña events directly based on unfiltered indices are subject to large interference from the decadal signal. In contrast, the decadal signal exhibits little impact on the canonical ENSO. Hence, we will use HF WPI and HF CTI to examine features and dynamical processes for the two types of ENSO in the present study. Compared with the SSTA pattern regressed upon WPI, the regressed SSTA pattern upon HF WPI displays weakened anomalies in the central Pacific and subtropics where the SSTAs are also related to the decadal variability (not shown).

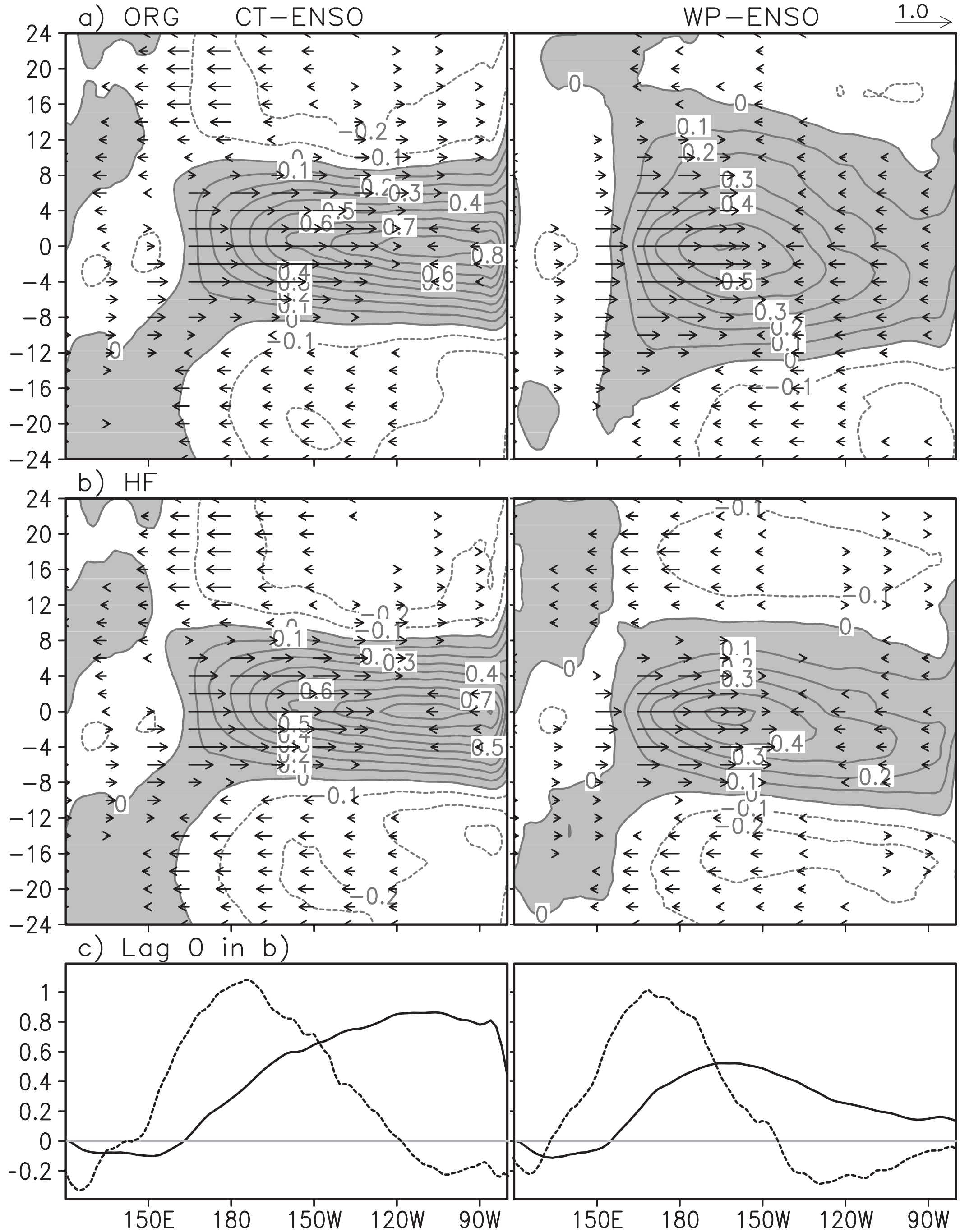

FIG. 3. Evolution of SSTA (K) (shading) and zonal wind stress anomalies (vectors, $0.01\,\mathrm{N\,m^{-2}}$) regressed (top) upon the detrended original (left) CTI and (right) WPI and (middle) by their HF indices. Both fields are averaged over 5°S–5°N. Ordinates are from lead 24 months to lag 24 months to event peak. Vectors smaller than 10% of the reference size are masked out. (bottom) SSTA (solid lines) and zonal wind stress anomalies (dashed lines) at lag 0 from the middle panels are shown. SODA data are used for wind stress.

Figure 3 shows the life cycles of the two ENSO types, where the differences between the patterns with and without the decadal signal are compared by using the original and HF indices. Clearly, the WPI-regressed pattern features a longer duration than the CTI-regressed one, an eastward extension in the developing phase, and a westward retreat in the decaying phase. In contrast, with the decadal signal removed, the WP ENSO exhibits a much reduced duration and evolves in a similar way to the CT ENSO, where the SSTAs diminish in the western Pacific but show almost no change in the eastern Pacific. It is evident that the distinct phase transition characteristics of the WP ENSO type have become much clearer after filtering out the decadal variability. To examine atmospheric wind responses to the SSTA, the regression patterns of anomalous zonal wind stress are computed (Fig. 3). For the CT ENSO type, the surface westerly wind anomalies dominate over the central Pacific during the mature positive ENSO phase and only weak anomalous easterly winds are found in the far eastern Pacific. In contrast, for the WP ENSO type, the center of the westerly wind anomalies shifts to the west of the date line and significant easterly wind anomalies occur over the eastern Pacific east of 150°W during the peak ENSO phase. These features are highlighted in Fig. 3c. The westward displacements of SSTA and wind stress patterns are the primary features of the WP ENSO type. Later, we will show that the westward shift of the SSTA pattern center and the presence of large easterly wind anomalies in the eastern Pacific are crucial for the reduction of SSTA growth in the eastern Pacific during WP ENSO events.

4. Recharge oscillator mechanisms of the two ENSO types

For the canonical ENSO cycle, the recharge oscillator mechanism that depicts the recharge and discharge of the equatorial upper-oceanic heat content (HC) has been proposed to be responsible for the transition process between warm and cold ENSO phases (Jin 1997a,b). This recharge mechanism was further extended to include two key dynamical feedbacks (Jin and An 1999): that is, one is the so-called zonal advective feedback that represents the zonal advection process of climate-mean temperature by anomalous zonal geostrophic current (e.g., Picaut et al. 1997) and the other is the so-called thermocline feedback that represents the vertical advection process of subsurface temperature anomalies by climate-mean upwelling (Suarez and Schopf 1988; Battisti and Hirst 1989; Jin 1997a,b). The two feedbacks can be linked dynamically through the geostrophic balance between thermocline depth and ocean current and contribute positively to the growth and phase transition of ENSO (Jin and An 1999; An and Jin 2001). The recharge (discharge) of equatorial HC during La Niña (El Niño) phase, which corresponds to a convergence (divergence) of the meridional geostrophic current, forms a zonally uniform positive (negative) excursion of the equatorial thermocline leading the following El Niño (La Niña) by a phase of 90°, which is accompanied by an eastward (westward) equatorial zonal geostrophic current. This typical characteristic of the recharge oscillator mechanism involving the zonal advective and thermocline feedback processes was demonstrated to operate for both the QQ and QB modes by Bejarano and Jin (2008), as also seen in Fig. 1. Following Bejarano and Jin, here we examine the typical characteristics of the recharge oscillation and the roles of these two dynamical feedbacks in the WP ENSO evolution compared to the CT ENSO.

In the first-order approximation, the thermocline variations can be well represented by sea surface height anomalies (SSHAs) or the upper-ocean HC that is defined by vertically integrated ocean temperature through the upper 300 m. Here, SSHAs are used to represent the thermocline variation and, following the approach of Jin and An (1999), anomalous zonal and meridional geostrophic currents (U_g and V_g) are estimated from the meridional and zonal gradients of SSHAs, respectively. A positive (negative) zonal gradient of SSHA can lead to a poleward (equatorward) heat transport by the divergence (convergence) of the meridional geostrophic current (Meinen and McPhaden 2000). Figures 4 and 5 show time evolutions of anomalous SSH, U_g, and V_g regressed upon the CT and WP ENSO indices. The former is the time–longitude cross section of the equatorial-mean SSHA and U_g, thereby examining the zonal ocean heat (or warm water) exchange between the east and west Pacific and the latter is the time–latitude cross section of zonal-mean SSHA and V_g, thereby examining the meridional heat exchange between the equatorial and off-equatorial regions.

The CT ENSO case (Figs. 4a and 5a) shows a typical recharge–discharge process of upper-ocean HC: that is, a basinwide meridional heat exchange between the equatorial and off-equatorial regions and an accompanied basin-scale zonal heat transport between the western and eastern equatorial Pacific. Notably, V_g is poleward (equatorward) with a positive (negative) zonal gradient of SSHA and U_g is eastward (westward) when the equatorial SSHA are greater (less) than the off-equatorial SSHA. In particular, V_g (U_g) reaches a maximum when the zonal (meridional) contrast of SSHA is the largest. We observe that U_g becomes uniformly eastward when the equatorial SSHA are larger than the off-equatorial SSHA with about a 12-month lead time to event peak. About 4 months later, V_g switches from an equatorward to a poleward current as the zonal gradient of the SSHA changes from negative to positive sign, indicating the beginning of the discharge process of equatorial HC. Then, U_g reaches its maximum when the zonal-mean equatorial SSHA reach a maximum at around a 4-month lead time to event peak and V_g reaches its peak poleward velocities at lag 0 month. Afterward, U_g reverses its sign

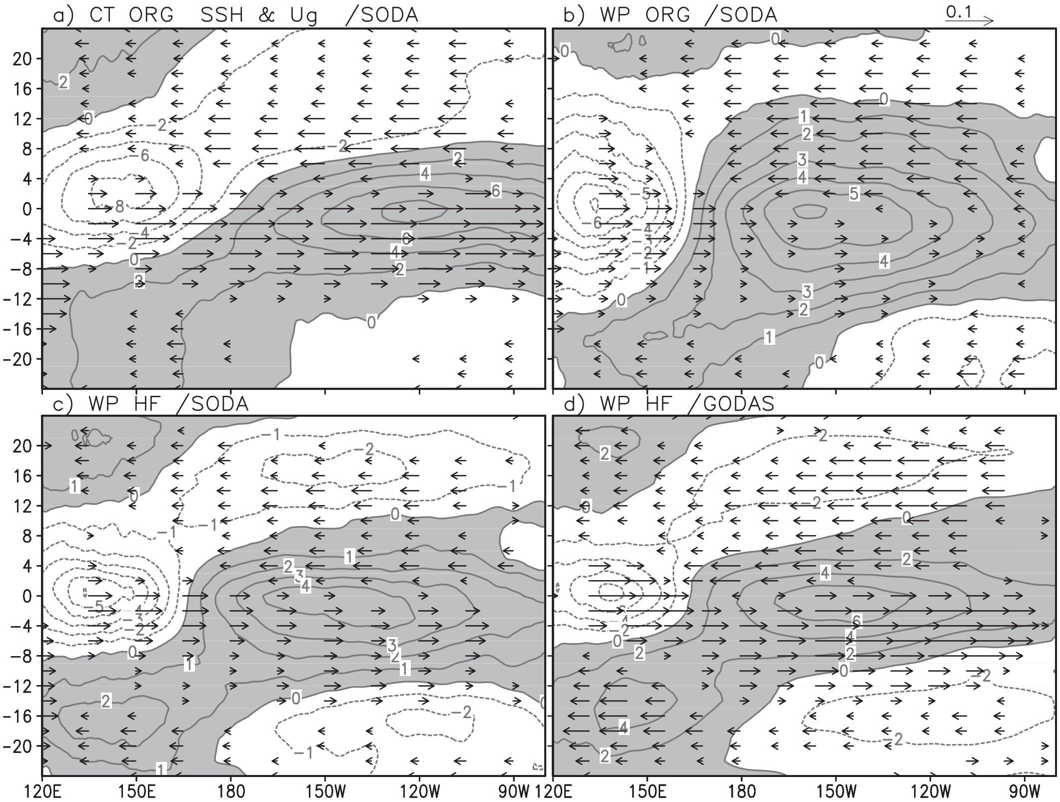

FIG. 4. Regressions of SSHA (shading, 5×10^{-3} m) and U_g anomalies (vectors, 5×10^{-3} m s^{-1}) upon the detrended (a) CTI; (b) WPI; and (c),(d) HF WPI, where (a)–(c) are made by using SODA data and (d) GODAS data. An average over 5°S–5°N is used. Vectors smaller than 10% of the reference size are masked out; ordinates are lag months.

at about lag 4 months to event peak. Then, for lag 10 months, V_g reverses its sign when the recharge process of equatorial HC begins, and U_g also reaches the peak westward velocity at this time. Almost the same regressed patterns are obtained using HF CTI (not shown).

The patterns for the WP ENSO evolution (Figs. 4b and 5b) based on the original nonfiltered WPI appear to be quite different from those of the CT ENSO type (Figs. 4a and 5a). The zonal contrast pattern of SSHA exhibits a long duration, which yields a weak phase transition. Interestingly, the discharge process in terms of the poleward zonal-mean V_g can still be clearly observed during the warm phase. It is overall difficult to see a clear phase transition signature and an accompanying recharge–discharge process because the ENSO signal is obscured by strong decadal variability. In contrast, the HF-WPI-regressed patterns (Figs. 4c and 5c) are very similar to the CT ENSO patterns (Figs. 4a and 5a), but quite different from the unfiltered WP ENSO patterns (Figs. 4b and 5b). It suggests that the influence of the decadal signal on the WP ENSO features may be greater than the distinctness between the two ENSO types. The largest feature in the distinctness is the westward shift of the positive SSHA center for the WP ENSO.

In Figs. 4c and 5c, the timings of the SSHA and current changes are also identified. The eastward U_g (poleward V_g) is set up when the meridional (zonal) contrast of the equatorial SSHA reverses at around lead 14 (10) months to event peak, then reaches its peak amplitude when the equatorial SSHA reach a maximum in the meridional (zonal) direction at lead 4 (0) months, and afterward reverses when the equatorial SSHA reverses again the sign of its meridional (zonal) contrast at about lag 2 (14) months. Then, U_g reaches its maximum westward amplitude at around lead of 16 month. Further, these results for the major features of the WP ENSO have been reconfirmed using the GODAS dataset (Figs. 4d and 5d). In addition, the meridional asymmetry of mass exchange represented by the zonal-mean SSHA and V_g, mentioned by Kug et al. (2003), are likewise apparent during the WP ENSO evolution.

Figure 6, similar to Fig. 1, highlights the major features of the recharge oscillation for the two ENSO types: that is, the clear recharge–discharge processes of HC as

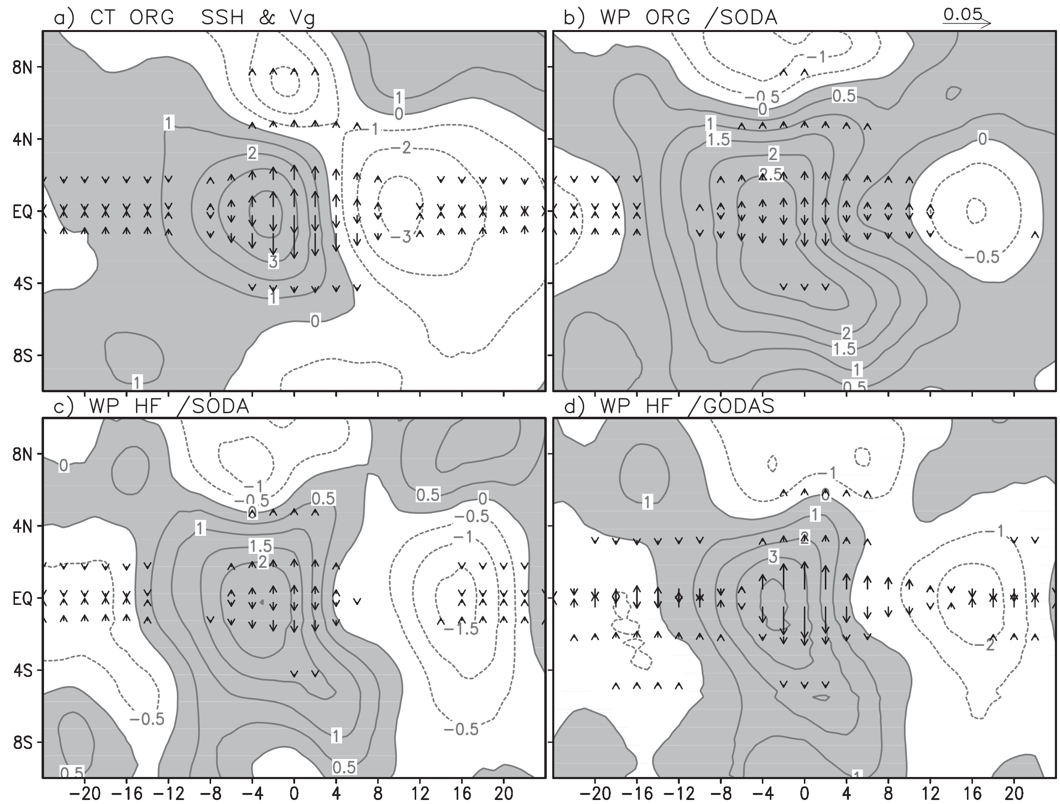

FIG. 5. As in Fig. 4 but for SSHA (shading, 5×10^{-3} m) and V_g anomalies (vectors, 5×10^{-3} m s^{-1}), where a zonal-mean over 130°E–90°W is used. Abscissas are lag months.

measured by RDI or V_g and the leading zonal-mean equatorial thermocline variations as expressed by the SSHA indices, which only are approximations of the real zonally uniform-distributed thermocline variations that lead strictly in quadrature (90° phase shift) to the SSTA indices (Jin 1997a; Meinen and McPhaden 2000). Overall, the intensity of the recharge–discharge process (measured by RDI or V_g) during the WP ENSO evolution is evidently smaller compared to the CT ENSO evolution. This weakening, on one hand, is because the climatological variance of SSHA is smaller in the central Pacific than in the eastern Pacific (not shown). On the other hand, since the center of the recharge–discharge process shifts to the west for the WP ENSO evolution, a weak additional recharge–discharge process of opposite sign occurs in the far eastern Pacific and acts to partly cancel the zonal-mean meridional exchange of HC, as also noted by Kug et al. (2010).

The above results suggest that the recharge oscillator mechanism operates for the WP ENSO type. To further contrast the WP and CT ENSO life cycles, we sample the regressed patterns of SSTA, SSHA, and anomalous geostrophic currents upon the HF WP and HF CT indices at the different lag months relative to event peak (Fig. 7), where an empirical constant factor is applied to amplify the magnitude of the patterns at large lag times. Based on the ENSO durations in Fig. 3, we approximate an e-folding time scale of 20 months and define the amplification factor as $e^{i/M}$, where i is the lead/lag month and $M = 20$.

Overall, the WP ENSO and CT ENSO types exhibit similar spatial patterns during their transition phases but different patterns during their peak phases as the former exhibits the westward-shifted SSTA center and the stronger easterlies in the far eastern Pacific compared to the latter. During the negative (positive) ENSO phases, the recharge (discharge) of basinwide equatorial ocean HC is clearly captured as represented by the convergence (divergence) of the near-equatorial V_g. As a result, the zonally uniform positive (negative) equatorial thermocline excursions and accompanied U_g on the equator are formed, which lead the observed SSTA peak. These are typical features of the recharge oscillator mechanism. For the WP ENSO type, a variation of this mechanism is clearly visible with a westward-shifted recharge–discharge process center relative to the CT ENSO type, which is probably a consequence of the strong equatorial wind stress anomalies over the far

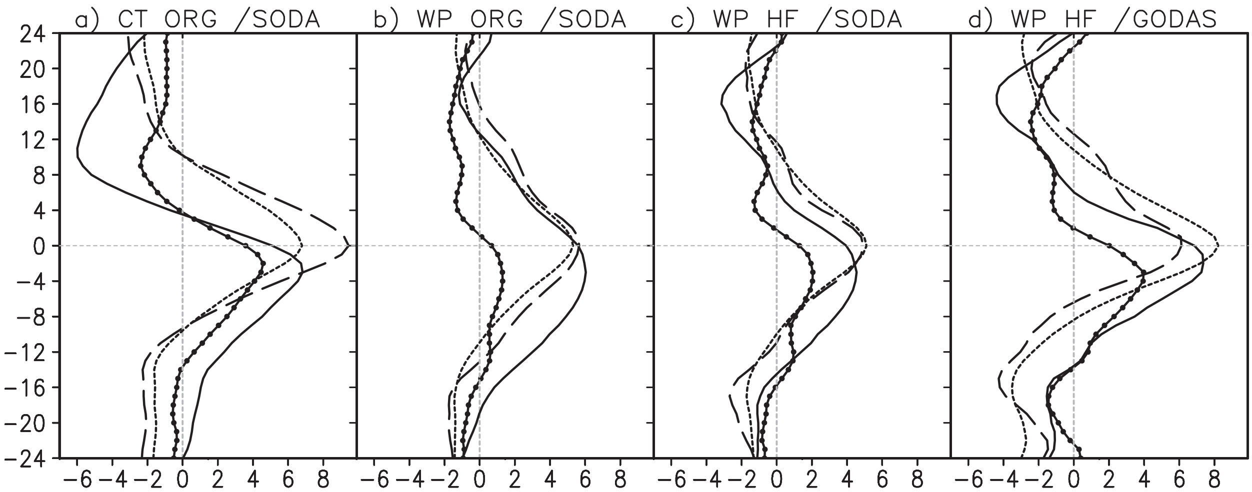

FIG. 6. Time evolutions of the zonal-mean SSHA (solid lines, 2×10^{-3} m), anomalous U_g (solid dotted lines, $1 \times 10^{-4}\,\mathrm{m\,s^{-1}}$) and V_g (dot–dashed lines, $2 \times 10^{-5}\,\mathrm{m\,s^{-1}}$) indices, RDIs (dashed lines, 0.5×10^{-9}). (a)–(d) correspond to those in Figs. 4 and 5, respectively. All indices are calculated from 5°S–5°N, 130°E–90°W, where V_g indices are obtained by subtracting the south from north of equator. Ordinates are lag months.

eastern Pacific during the peak ENSO phases. In other words, the westward-shifted SSHA center can be dynamically balanced by the strong surface wind anomalies in the equatorial eastern Pacific.

5. Heat budget analysis

Relative contributions of different physical processes to the SST thermodynamics associated with ENSO have been examined through ocean mixed layer heat budget analysis using model outputs and oceanic analysis datasets (e.g., An et al. 1999; Kang et al. 2001; Jin et al. 2006; Zhang et al. 2007; Kug et al. 2009, 2010). In this study, heat budget analyses, based on the two oceanic reanalysis datasets, are performed to investigate the relative importance of different dynamical feedbacks in the SSTA evolution for the two different types of ENSO.

The mixed layer averaged temperature tendency equation can be generally expressed as

$$\frac{\partial T'}{\partial t} = -\overline{u}\frac{\partial T'}{\partial x} - u'\frac{\partial \overline{T}}{\partial x} - u'\frac{\partial T'}{\partial x} - \overline{v}\frac{\partial T'}{\partial y} - v'\frac{\partial \overline{T}}{\partial y} - v'\frac{\partial T'}{\partial y} - \overline{w}\frac{\partial T'}{\partial z} - w'\frac{\partial \overline{T}}{\partial z} - w'\frac{\partial T'}{\partial z} + Q + R, \quad (1)$$

where an overbar denotes a climatological mean and a prime its departure from it (anomaly); T, u, v, and w denote oceanic temperature, zonal current, meridional current, and vertical velocity, respectively. The last terms, Q and R, denote the thermal forcing and residual terms, which are not considered in this study. The mean upwelling advection in Eq. (1) can be further decomposed in an approximation following (Jin and Neelin (1993); An et al. 1999; Zhang et al. 2007):

$$-\overline{w}\frac{\partial T'}{\partial z} \approx \overline{w}\frac{T'_{\mathrm{sub}}}{H} - \overline{w}\frac{T'}{H}, \quad (2)$$

where H is the effective mean mixed layer depth for the vertical advection (constant 50 m in this study). Subscript ''sub'' denotes a subsurface-layer average between 50 and 100 m. The first term in Eq. (2) is often referred to as the thermocline feedback (Jin and An 1999). All dynamical terms in Eq. (1) are first estimated using the monthly reanalysis datasets and then their evolution patterns from 24-month lead to 24-month lag are obtained by regressing them upon the HF WP and CT indices.

Following Jin et al. (2006), we regroup these terms into six feedback terms as follows:

$$\frac{\partial T'}{\partial t} = \mathrm{MC} + \mathrm{ZA} + \mathrm{EK} + \mathrm{TH} + \mathrm{NDH} + \mathrm{TD} + R, \quad (3)$$

where

$$\mathrm{MC} = -\overline{u}\frac{\partial T'}{\partial x} - \overline{v}\frac{\partial T'}{\partial y} - \overline{w}\frac{T'}{H}, \quad (4)$$

$$\mathrm{ZA} = -u'\frac{\partial \overline{T}}{\partial x}, \quad (5)$$

$$\mathrm{EK} = -v'\frac{\partial \overline{T}}{\partial y} - w'\frac{\partial \overline{T}}{\partial z}, \quad (6)$$

$$\mathrm{TH} = \overline{w}\frac{T'_{\mathrm{sub}}}{H}, \quad (7)$$

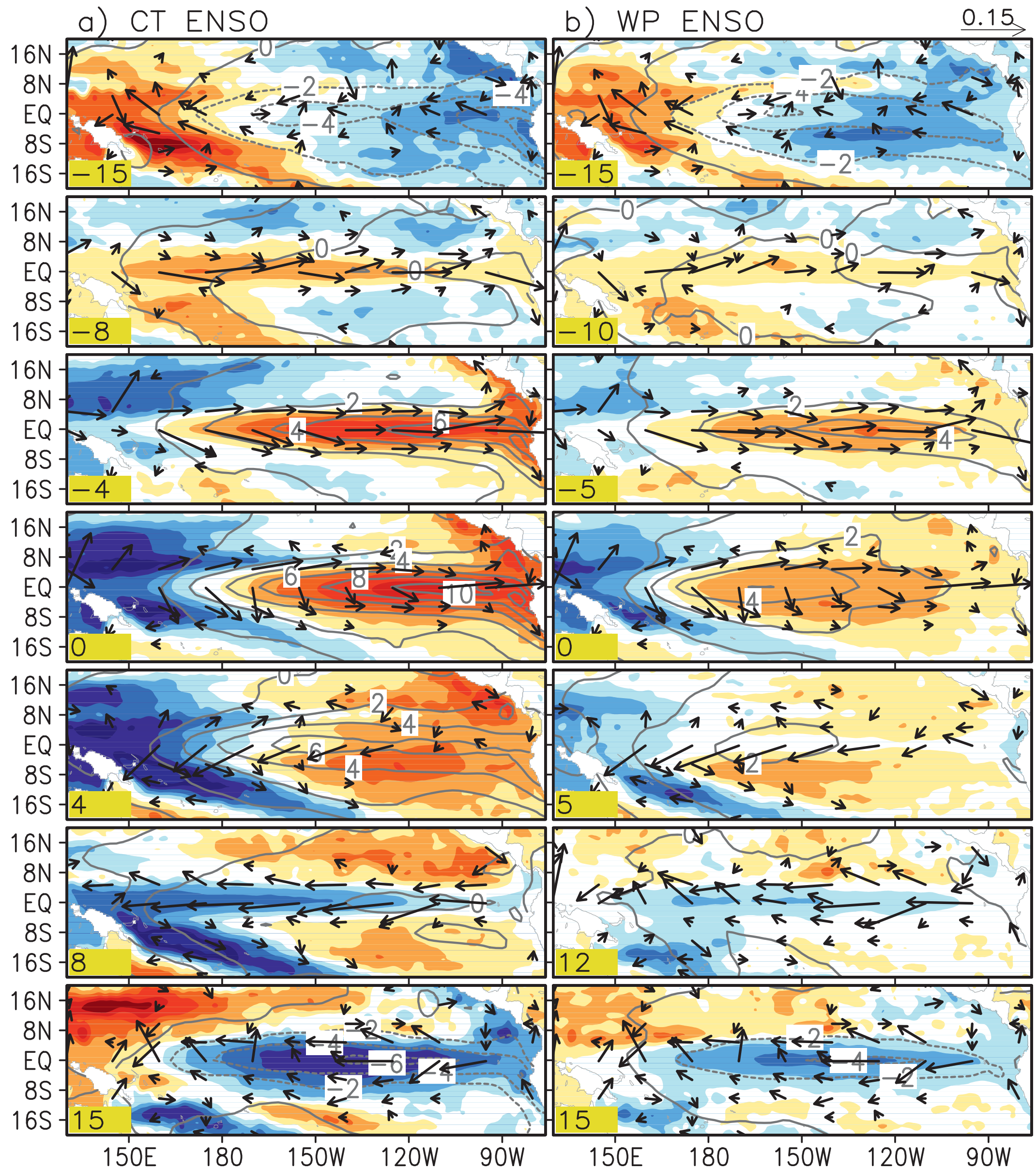

FIG. 7. Phase evolutions of the regressed SSTA (contours, 0.1 K), SSHA (shading, 5×10^{-3} m) and geostrophic current anomalies (black vectors; U_g 5×10^{-3} m s^{-1}, V_g 2.5×10^{-3} m s^{-1}) at eight different lag months for (a) CT ENSO and (b) WP ENSO by using the detrended HF CTI and HF WPI, respectively. Amplification factors are used to recover amplitude of fields at different lags with *e*-folding time of 20 months for CT and WP ENSOs. SODA data are used.

$$\mathrm{NDH} = -u'\frac{\partial T'}{\partial x} - v'\frac{\partial T'}{\partial y} - w'\frac{\partial T'}{\partial z}, \qquad (8)$$

$$\mathrm{TD} = Q. \qquad (9)$$

Here, MC denotes the effect of mean circulation, ZA the zonal advective feedback, EK the Ekman pumping feedback, TH the thermocline feedback, NDH the nonlinear dynamical heating, and TD denotes the thermodynamical damping. The ZA, EK, and TH terms, as the three major dynamical feedbacks (cf., Jin and Neelin 1993; Jin and An 1999), all tend to make positive contributions to the growth of ENSO with TH being the largest term (Jin et al. 2006). The NDH term acts to generate an asymmetry (skewness) of SSTA amplitude between El Niño and La Niña (Jin et al. 2003; An and Jin 2004).

In this study, we focus on the first four linear terms and examine their contributions to the growth and phase transitions of the two types of ENSO. We note that the WPI-related tendency patterns are not confined to the western equatorial Pacific. To fully understand the WP ENSO evolution through heat budget analysis, we need to examine the SSTA tendency patterns across the entire equatorial Pacific.

In Fig. 8, the MC terms, which are overall negative during ENSO peak phase, generally serve as a negative feedback for both ENSO types. The EK terms are relatively small and appear less important, although they also show a weak positive feedback to the growth of the two types of ENSO. Overall, the features of the MC and EK terms are nearly the same in the two datasets, except that the mature-phase EK term patterns in the eastern Pacific are slightly different for the WP ENSO type. The ZA and TH are the two most robust terms, serving in the phase transitions of both ENSO types. The ZA term exhibits a clear 90° phase shift in both CT and WP ENSO cycles relative to the SSTA peak, indicating that it contributes to the phase transition. In the GODAS dataset, the ZA term seems to be somewhat stronger for the WP ENSO type than in the SODA dataset. This difference reflects the common problem that the ocean advection estimation in reanalysis datasets is still associated with large uncertainties. The contributions of the ZA term to the growth rate of both CT and WP ENSO types seem to be small in both datasets. The TH term is the dominant term and leads the peak time by less than 90° during both CT and WP ENSO evolution, indicating that it contributes largest to both ENSO growth and phase transition.

To compare directly the roles of the ZA with the TH terms in contributing to the growth of ENSO, we examine zonal distributions of the equatorial tendency averaged at peak phase. As shown in Fig. 9, the ZA terms are much less important for the growth of ENSO than the TH terms owing to their relatively small amplitude, independent of the sign difference between the two datasets. The TH term dominates not only in the growth of the CT ENSO but also in that of the WP ENSO in both datasets. The tendency pattern of the WP ENSO type, relative to the CT ENSO type, shifts to the west and its eastern part is largely suppressed over the eastern equatorial Pacific region because of the eastern Pacific easterly wind anomalies.

To more clearly depict the contributions of the ZA and TH terms to the growth and phase transition of the two ENSO types, we decompose the tendency patterns, which evolve with lag time in Fig. 8 into symmetric and asymmetric parts with respect to 0 lag. These two parts represent the contributions of the feedback terms to the growth and phase transition of ENSO, respectively. Figure 10 shows these two parts of the tendencies as a function of lag time to event peak. All of the asymmetric curves, averaged over either the Niño-3 or Niño-4 region, exhibit a positive peak before 0 lag and a negative peak after, indicating clearly that both ZA and TH terms contribute to the phase transition for both ENSO types. However, only the TH-related symmetric parts show a positive contribution to their growths. In particular, the amplitude of such a contribution is almost equal in the two Niño regions for the WP ENSO type but quite different for the CT ENSO type. This reflects that the TH term serves for the WP ENSO growth identically in both Niño-3 and Niño-4 regions. In contrast, the symmetric curves of the ZA terms exhibit less amplitude.

Overall, the TH term makes dominant contributions to the growth and phase transitions for both ENSO types, while the ZA term plays a significant role in their phase transitions. In addition, the results of a heat budget analysis as shown in Figs. 8–10 are consistent with those in Figs. 3–7, such as the westward-shifted SSHA center and the westward tendency centers in the mature phase for the WP ENSO compared to the CT ENSO, as well as the coincident signs of the zonal geostrophic current anomalies and the ZA tendencies estimated from ocean currents.

6. Summary and discussion

Evidence exists to support the hypothesis that two different types of ENSO coexist in our climate regime: the cold-tongue (CT) ENSO with maximum SSTA variability located in the eastern equatorial Pacific and the warm-pool (WP) ENSO with major SSTA variability located in the central Pacific at the edge of the WP. A number of studies have revealed that this WP ENSO type exhibits some distinct spatiotemporal features and dynamics from the CT ENSO. In this study, motivated by the study of Bejarano and Jin (2008) in which they found two leading ENSO-like coupled modes coexisting under current climate condition and the striking similarity of the two modes to the observed ENSO types, we examined the observed features and physical processes associated with the recharge oscillator mechanisms for the two ENSO types.

To contrast the observed features, we compared the indices for the two ENSO types and found that all indices for the WP ENSO show strong decadal variability besides the interannual variability that ENSO dominates. To focus on the interannual variability, we first removed the decadal signal and then examined the spatiotemporal characteristics and dynamics for the two ENSO types. We showed a clear recharge–discharge process of ocean heat content throughout the life cycle for the WP ENSO. The mixed layer heat budget analyses further indicated that both thermocline feedback and zonal advective feedback

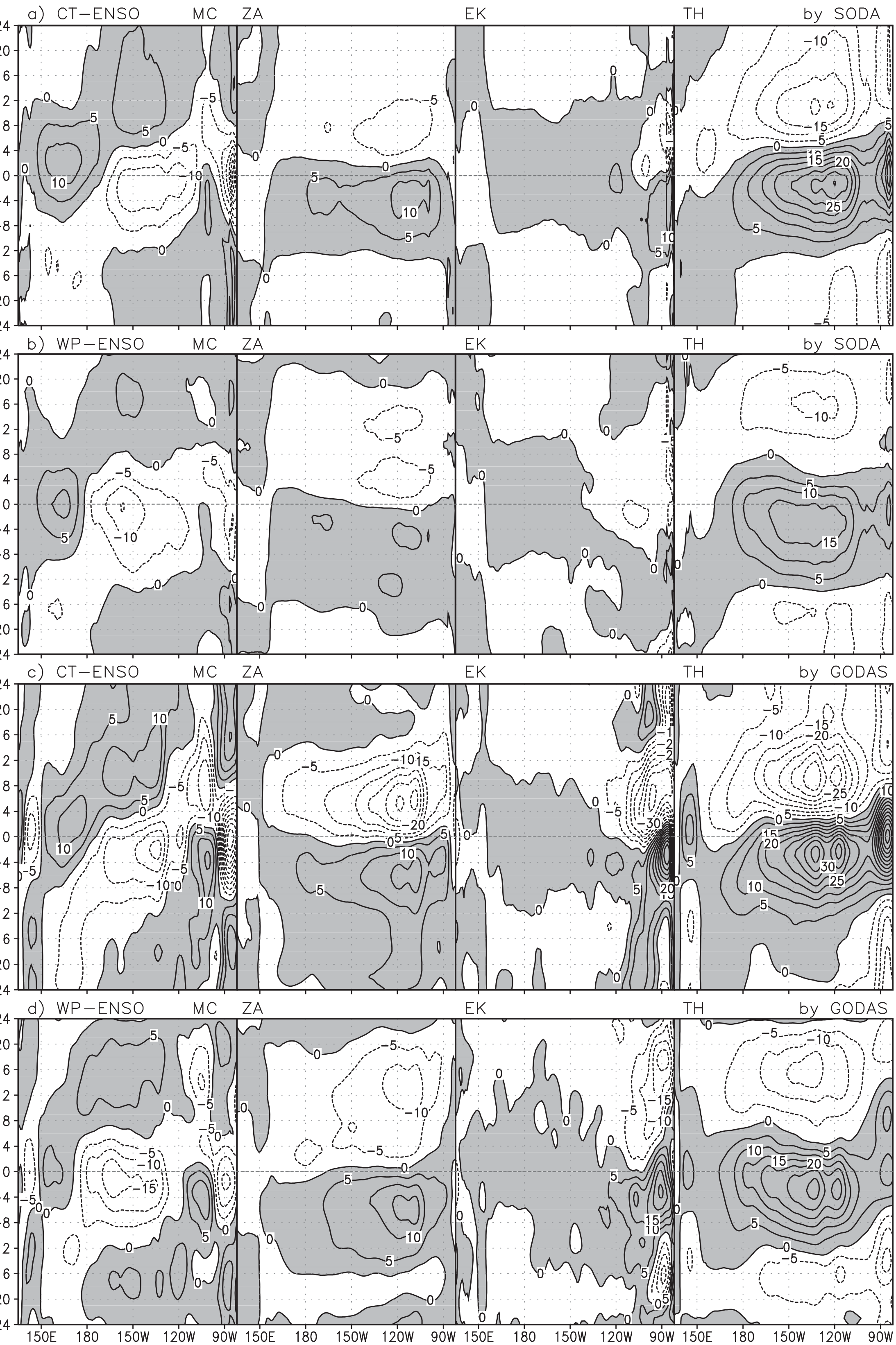

FIG. 8. Evolution of temperature tendency (0.01 K $month^{-1}$) of the four dynamical feedback terms for (a),(c) CT ENSO and (b),(d) WP ENSO by using (a),(b) SODA and (c),(d) GODAS datasets. Fields are averaged over 5°S–5°N. Ordinates denote lag months. A zonal 31 (5) point running mean is used for SODA (GODAS) data.

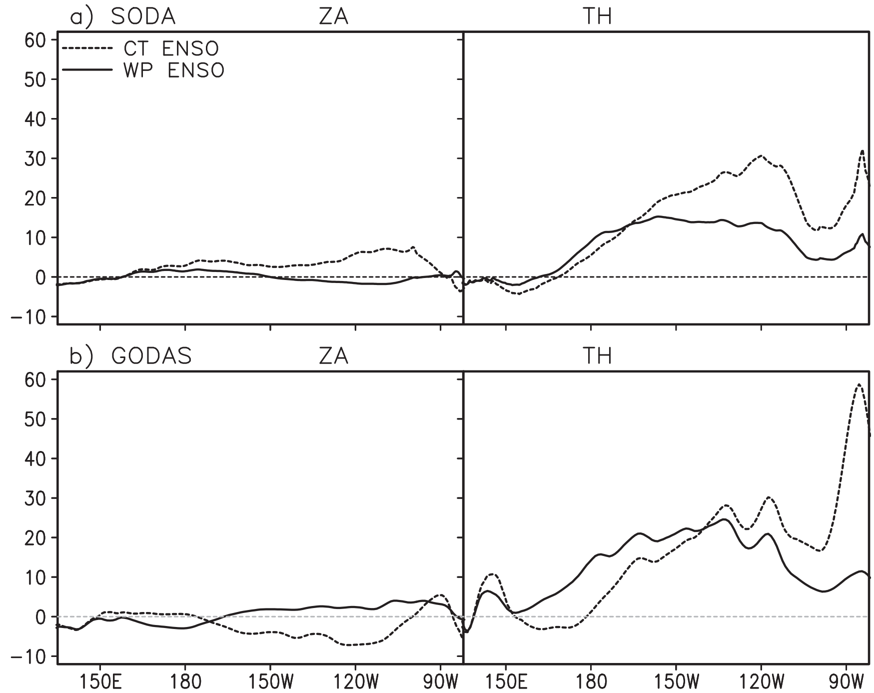

FIG. 9. Zonal distributions of (left) ZA and (right) TH feedback terms (0.01 K $month^{-1}$) at the peak phase averaged from lag −2 to 2 months in Fig. 8 for CT ENSO (dashed lines) and WP ENSO (solid lines) based on the (a) SODA and (b) GODAS datasets.

play important roles in the phase transitions of both ENSO types, where the former is the dominant contributor to the growth rate for both ENSO types and the latter contributes little to the growth rate. Regrettably, the oceanic reanalysis is known for poor estimates of oceanic currents, which may add an uncertainty to our conclusions regarding the zonal advective feedback.

To test the sensitivity of our conclusions regarding the applicability of the recharge oscillator to the WP ENSO type, we conducted additional analyses using other indices (HF EMI and HF CPI) and a composite analysis sampling typical WP El Niño events. All of these results (not shown) are quite similar to those above, indicating well that our main conclusions are not dependent on the definitions of the indices used and the contributions of the La Niña phase. Also, a natural question is why the recharge oscillation for the WP ENSO has not been detected in the previous studies (e.g., Kug et al. 2009). Our current study shows that the strong background decadal signal has interfered with, apparently, the recharge–discharge process and hence biased their conclusion.

The results in this study indicate that the WP ENSO can be understood to a large extent by a variation of the recharge oscillator theory. Recent studies showed indirect evidence in support of this conclusion. For example, McPhaden (2012) recently pointed out that the zonal-mean warm water volume (WWV) index that is based on the recharge oscillator mechanism is becoming less leading the Niño-3.4 SSTA index since 2000 when the WP El Niño events occurred frequently. Dewitte et al. (2012) also showed that the total WWV index corresponding to the first two oceanic baroclinic waves of the equatorial Pacific significantly lead the modified Niño-4 index for the WP type of events. Based on the results in this study that the ZA and TH terms play similar roles between the two ENSO types, except for the zonally different center positions of the SSTA pattern and associated zonal wind patterns, a conceptual diagram for delineating the recharge oscillator mechanism of the WP ENSO along with the original recharge oscillator model is shown in Fig. 11. Figures 11a–d display the four phases for the CT ENSO evolution, based on the recharge oscillator diagram of Jin and An (1999). Noting that the ZA term exhibits an uncertain contribution to the growth of ENSO during its peak phases, we thus express the zonal (geostrophic) current anomalies by dashed arrows (Figs. 11a,c).

The recharge oscillator model for the WP ENSO type is similar to that for the CT ENSO. The schematic diagram (Figs. 11e–h) exhibits the westward shift of SSTA, surface wind anomalies, and thermocline variation patterns during the peak phases and the presence of strong surface wind anomalies over the far eastern equatorial Pacific. The shifted SSTA and wind patterns are crucial for the reduction of SSTA growth in the eastern Pacific

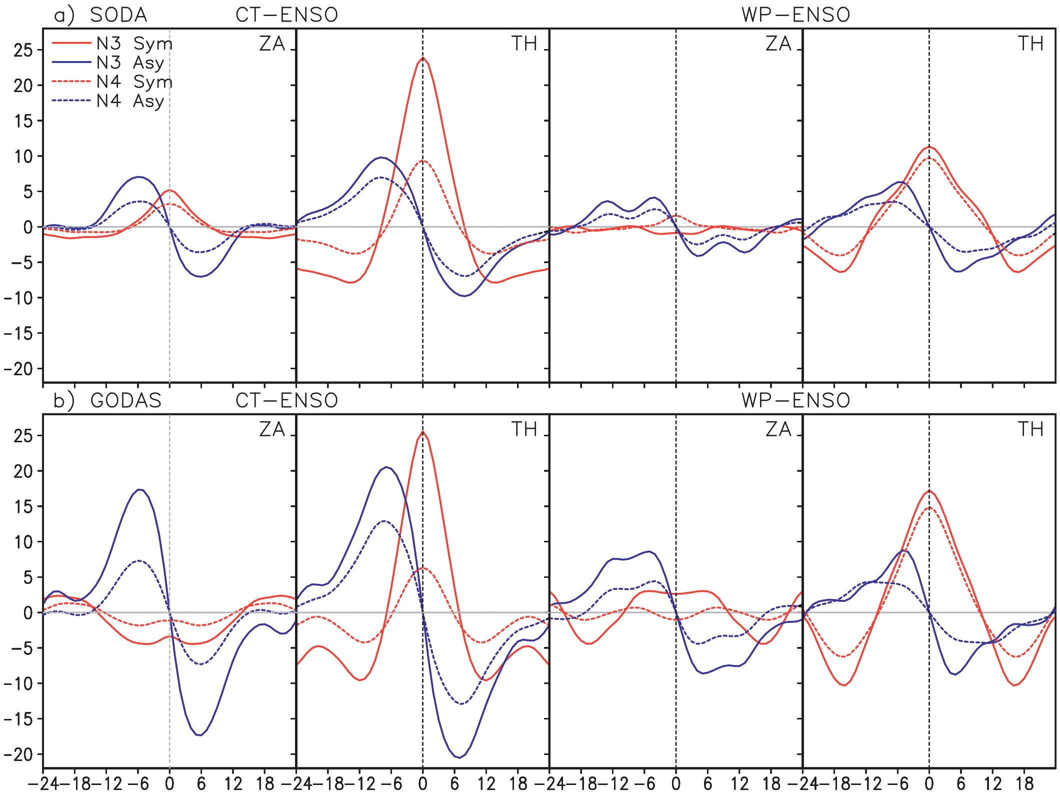

FIG. 10. Time evolution of symmetric (red lines) and asymmetric (blue lines) tendency parts of ZA and TH feedback terms (0.01 K month^{-1}) averaged over the Niño-3 (solid lines) and Niño-4 (dashed lines) regions in Fig. 8 for (left) CT ENSO and (right) WP ENSO based on the (a) SODA and (b) GODAS datasets. Abscissas are lag months.

and, hence, maintain the characteristic WP ENSO pattern. This is the main factor that makes the WP ENSO different from the CT ENSO.

Our results on the roles of the ZA term in contributing to the growth and phase transition during the entire ENSO life cycle are consistent with previous studies. For example, Wang and McPhaden (2001), in an observational analysis, showed that the anomalous zonal advection term is of particular importance in the onset and development phases of ENSO. Zhang et al. (2007) found that the ZA term prefers to act as a transition driver and that the TH term contributes to both the growth and phase transition of ENSO. Kug et al. (2009), as shown in their Fig. 10, also found that the ZA term plays an important role in the development phase of the WP El Niño. However, the role of the ZA term in driving the SSTA growing at the peak phase is still unclear for both the WP and CT ENSO, based on the results obtained from the model simulations and reanalysis datasets (e.g., Zhang et al. 2007; this study). Moreover, the importance of the TH term for the WP ENSO, as revealed in this study, appears to be different from that by Kug et al. (2009, 2010). The major reason is that the TH term here has a different definition from their studies in which it was directly defined as the vertical advection of mixed layer temperature anomalies by mean upwelling. Their definition actually underestimated the TH term because it involves the negative feedback by the mean upwelling damping ($-\overline{w}T'/H$).

This study has suggested that the WP ENSO operates as a variation of the classical recharge oscillator mechanism in the sense that both ZA and TH terms contribute to the growth and phase transition as for the CT ENSO. Either of the two ENSO types will have a tendency to emerge under the particular initial values, preconditions, or background states, which needs to be studied in the future. The theoretical results of Bejarano and Jin (2008) suggest that the two independent but similar modes, with likeness of the CT and WP ENSO, can coexist under current climate conditions. Thus, we contend that both CT and WP ENSO may be named as a different type of interannual modes of variability.

Our current focus is only on understanding how the recharge oscillator mechanism (Jin 1997a,b; Jin and An 1999) operates for the WP ENSO. Indeed, there are other dynamical mechanisms in the literature depicting

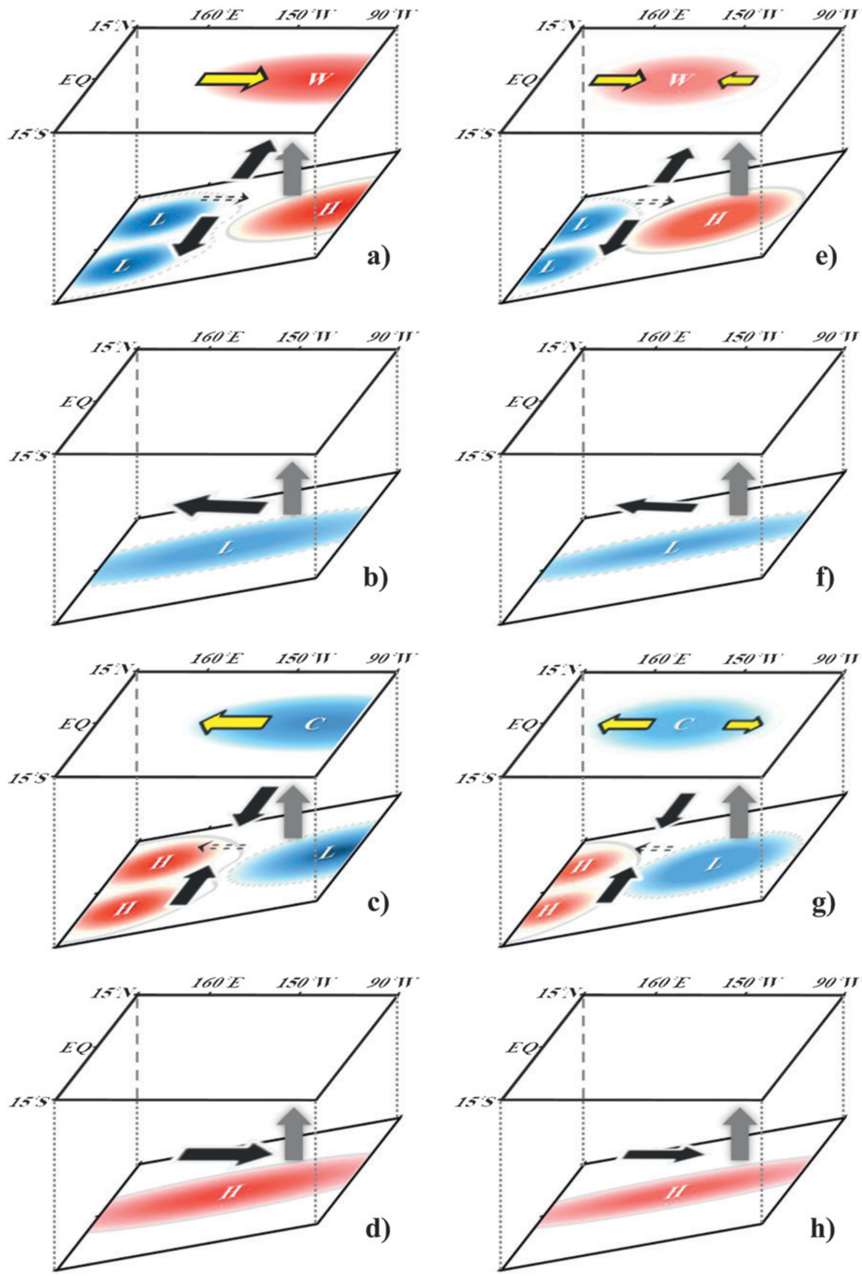

FIG. 11. Schematic diagrams for (a)–(d) CT ENSO and (e)–(h) WP ENSO recharge oscillator mechanisms in the (a),(e) warm, (b),(f) warm-to-cold, (c),(h) cold, and (d),(g) cold-to-warm phases. The red (blue) shadings on the top planes representing the sea surface denote positive (negative) SST anomalies, and those on the inclined planes representing the climatic thermocline denote positive (negative) subsurface temperature anomalies. The dark gray arrows denote mean upwelling,; the black arrows represent the zonal and meridional upper-ocean geostrophic current anomalies, and the solid yellow arrows stand for wind stress anomalies: W, C, H, and L denote warm, cold, high, and low, respectively.

the different paradigms for ENSO: for example, the delayed oscillator (Suarez and Schopf 1988; Battisti and Hirst 1989), the coupled wave oscillator (Cane et al. 1990), the advective–reflective oscillator (Picaut et al. 1997), and the western Pacific oscillator (Weisberg and Wang 1997). For the WP ENSO, besides the apparent difference of wind anomalies over the eastern Pacific, differences also exist over the western Pacific as well as the eastern and western boundaries, indicating the possibility that the other dynamical oscillator mechanisms may play roles in WP ENSO, which will be addressed in future studies.

Acknowledgments. This work is jointly supported by National Science Foundation (NSF) Grants ATM 1034798, the 973 Program of China (2010CB950404), DOE Grant DE-SC0005110, NOAA Grant NA10OAR4310200, NSF of China (NSFC) Grant 40805028, and the China Meteorological Special Project (GYHY201206016 and GYHY200906015). The authors especially appreciate M. F. Stuecker, W. Zhang, A. Levine, and J. Boucharel for their careful reading and revising of the manuscript.

APPENDIX

Definitions of Two Niño Indices for CT and WP ENSO

By using a coordinate transform in the Niño-3–Niño-4 phase space, RJ11 defined the CT Niño index and WP Niño index (N_{CT} and N_{WP}) as follows:

$$\begin{cases} N_{CT} = N_3 - \alpha N_4 \\ N_{WP} = N_4 - \alpha N_3 , \end{cases} \quad \alpha = \begin{cases} 2/5, & N_3 N_4 > 0 \\ 0, & \text{otherwise}. \end{cases} \tag{A1}$$

Indices N_3 and N_4 denote Niño-3 and Niño-4 indices, respectively, and N_{CT} and N_{WP} are a piecewise linear combination of N_3 and N_4 conditioned by the ENSO phase. The transformation parameter α can be determined by minimizing a cost function defined by the total metrics of N_{CT} over the WP El Niño time and N_{WP} over the CT El Niño time. However, one key question is how to determine a priori the time of occurrence of the WP/CT El Niño. This is discussed here in terms of different schemes. RJ11 has directly used a method of cluster analysis designed initially by Kug et al. (2009) to identify the WP (CT) El Niño month once N_4 (N_3) of this month is greater than the other and both greater than 0.5°C. The cost function for this minimization scheme is written as

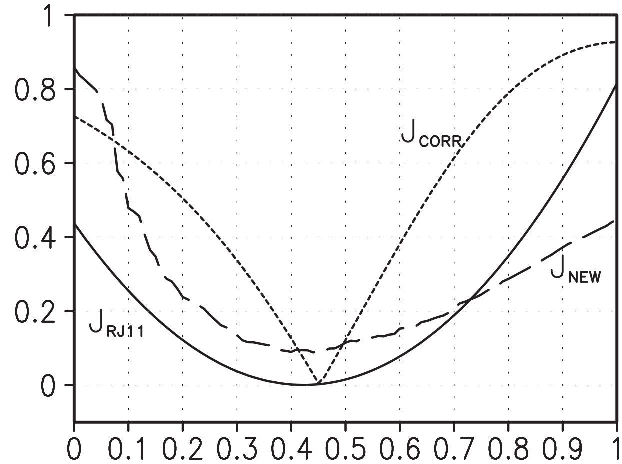

FIG. A1. Metrics as a function of α (abscissa) for defining the CT and WP indices using three kinds of unified cost functions (ordinate).

$$J(\alpha) = [N_{CT}]^2_{WPEN} + [N_{WP}]^2_{CTEN} , \tag{A2}$$

where the timing of WPEN and CTEN is always fixed with α changed. One can search α in a broad parameter domain to make

$$J(\alpha^*) \rightarrow \text{min when } \alpha = \alpha^* . \tag{A3}$$

Here α^* is the optimal. Figure A1 presents the J (RJ11) as a function of α, where $\alpha^* \approx 0.42$. In this study, the training period for determining α is January 1951–February 2011.

To test the impacts of different schemes on valuing α^*, a dynamic scheme is designed in contrast to the static scheme of RJ11. That is, with α changed, we redetermine the timing of the WPEN and CTEN by taking one standard deviation of the newly generated indices from Eq. (A1) as the criterion for identification. The new J curve is also plotted in Fig. A1 as a contrast, where $\alpha^* \approx 0.41$. So far, only the signatures of the determination of the two types of El Niño have been utilized for valuing α^*. This is because a natural separation has

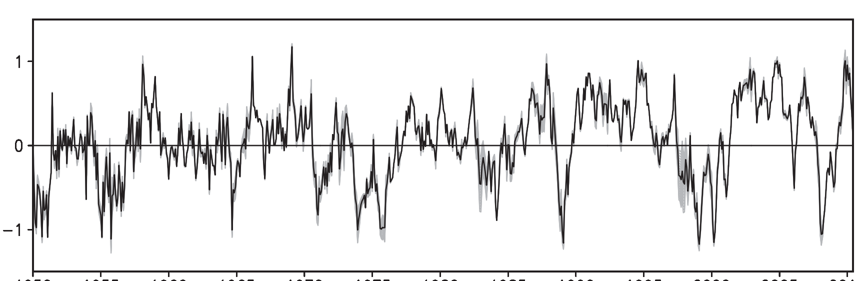

FIG. A2. WP indices (gray lines) and their mean (black line) using different α with an internal of 0.01 from 0.3 to 0.5.

been observed between the two clusters in N_3–N_4 phase space that correspond to the two types of El Niño, as shown in Fig. 1a of RJ11, whereas no such separation exists for the La Niña case. This is also why La Niña is difficult to separate into two clear types even though the transformation in Eq. (A1) is used. A question is whether there is a possibility to separate both the El Niño and La Niña through varying α. Therefore, we simply take the correlation between N_{WP} and N_{CT} as the cost function of α. When these two indices are irrelevant (viz., zero correlation), $\alpha^* = 0.45$ is easily obtained by the J curve (J_{CORR}) in Fig. A1. However, in this case, the separation makes it difficult to represent exactly some observed El Niño events despite the fact that La Niña is not well separated yet (not shown).

Based on this comparison, it appears that the dynamic scheme is much simpler and more effective. Figure A2 further tests the sensitivity of transformed indices to α. It is clear that the WP index is not sensitive to α, indicating that the transformed indices can be widely applied.

REFERENCES

An, S.-I., and F.-F. Jin, 2001: Collective role of thermocline and zonal advective feedbacks in the ENSO mode. *J. Climate,* **14,** 3421–3432.

——, and ——, 2004: Nonlinearity and asymmetry of ENSO. *J. Climate,* **17,** 2399–2412.

——, ——, and I.-S. Kang, 1999: The role of zonal advection feedback in phase transition and growth of ENSO in the Cane-Zebiak model. *J. Meteor. Soc. Japan,* **77,** 1151–1160.

Ashok, H., and T. Yamagata, 2009: Climate change: The El Niño with a difference. *Nature,* **461,** 481–484, doi:10.1038/461481a.

Ashok, K., S. K. Behera, S. A. Rao, H. Weng, and T. Yamagata, 2007: El Niño Modoki and its possible teleconnection. *J. Geophys. Res.,* **112,** C11007, doi:10.1029/2006JC003798.

Battisti, D. S., and A. C. Hirst, 1989: Interannual variability in a tropical atmosphere–ocean model: Influence of the basic state, ocean geometry, and nonlinearity. *J. Atmos. Sci.,* **46,** 1687–1712.

Behringer, D. W., and Y. Xue, 2004: Evaluation of the global ocean data assimilation system at NCEP: The Pacific Ocean. Preprints, *Eighth Symp. on Integrated Observing and Assimilation Systems for Atmosphere, Oceans, and Land Surface,* Seattle, WA, Amer. Meteor. Soc., 2.3. [Available online at https://ams.confex.com/ams/pdfpapers/70720.pdf.]

Bejarano, L., and F.-F. Jin, 2008: Coexistence of equatorial coupled modes of ENSO. *J. Climate,* **21,** 3051–3067.

Cane, M. A., M. Münnich, and S. E. Zebiak, 1990: A study of self-excited oscillations of the tropical ocean–atmosphere system. Part I: Linear analysis. *J. Atmos. Sci.,* **47,** 1562–1577.

Compo, G. P., J. S. Whitaker, and P. D. Sardeshmukh, 2006: Feasibility of a 100-year reanalysis using only surface pressure data. *Bull. Amer. Meteor. Soc.,* **87,** 175–190.

Dewitte, B., J. Choi, S.-I. An, and S. Thual, 2012: Vertical structure variability and equatorial waves during central Pacific and eastern Pacific El Niños in a coupled general circulation model. *Climate Dyn.,* **38,** 2275–2289, doi:10.1007/s00382-011-1215-x.

Giese, B. S., and S. Ray, 2011: El Niño variability in simple ocean data assimilation (SODA), 1871–2008. *J. Geophys. Res.,* **116,** C02024, doi:10.1029/2010JC006695.

Ham, Y.-G., and J.-S. Kug, 2012: How well do current climate models simulate two types of El Niño? *Climate Dyn.,* **39,** 383–398, doi:10.1007/s00382-011-1157-3.

Jin, F.-F., 1996: Tropical ocean-atmosphere interaction, the Pacific cold tongue, and the El Niño-Southern Oscillation. *Science,* **274,** 76–78.

——, 1997a: An equatorial ocean recharge paradigm for ENSO. Part I: Conceptual model. *J. Atmos. Sci.,* **54,** 811–829.

——, 1997b: An equatorial ocean recharge paradigm for ENSO. Part II: A stripped-down coupled model. *J. Atmos. Sci.,* **54,** 830–847.

——, and J. D. Neelin, 1993: Modes of interannual tropical ocean-atmosphere interaction—A unified view. Part I: Numerical results. *J. Atmos. Sci.,* **50,** 3477–3503.

——, and S.-I. An, 1999: Thermocline and zonal advective feedbacks within the equatorial ocean recharge oscillator model for ENSO. *Geophys. Res. Lett.,* **26,** 2989–2992.

——, ——, A. Timmermann, and J. Zhao, 2003: Strong El Niño events and nonlinear dynamical heating. *Geophys. Res. Lett.,* **30,** 1120, doi:10.1029/2002GL016356.

——, S. T. Kim, and L. Bejarano, 2006: A coupled-stability index for ENSO. *Geophys. Res. Lett.,* **33,** L23708, doi:10.1029/2006GL027221.

Kang, I.-S., S.-I. An, and F.-F. Jin, 2001: The role of zonal advection feedback in phase transition and growth of ENSO in the Cane-Zebiak model. *J. Meteor. Soc. Japan,* **79,** 1–10.

Kao, H.-Y., and J.-Y. Yu, 2009: Contrasting eastern-Pacific and central-Pacific types of El Niño. *J. Climate,* **22,** 615–632.

Kim, H.-M., P. J. Webster, and J. A. Curry, 2009: Impact of shifting patterns of Pacific Ocean warming on North Atlantic tropical cyclones. *Science,* **325,** 77–80, doi:10.1126/science.1174062.

Kug, J.-S., I.-S. Kang, and S.-I. An, 2003: Symmetric and antisymmetric mass exchanges between the equatorial and off-equatorial Pacific associated with ENSO. *J. Geophys. Res.,* **108,** 3284, doi:10.1029/2002JC001671.

——, F.-F. Jin, and S.-I. An, 2009: Two types of El Niño events: Cold tongue El Niño and warm pool El Niño. *J. Climate,* **22,** 1499–1515.

——, J. Choi, S.-I. An, F.-F. Jin, and A. T. Wittenberg, 2010: Warm pool and cold tongue El Niño events as simulated by the GFDL 2.1 coupled GCM. *J. Climate,* **23,** 1226–1239.

Larkin, N. K., and D. E. Harrison, 2005a: On the definition of El Niño and associated seasonal average U.S. weather anomalies. *Geophys. Res. Lett.,* **32,** L13705, doi:10.1029/2005GL022738.

——, and ——, 2005b: Global seasonal temperature and precipitation anomalies during El Nino autumn and winter. *Geophys. Res. Lett.,* **32,** L16705, doi:10.1029/2005GL022860.

Mason, S. J., and L. Goddard, 2001: Probabilistic precipitation anomalies associated with ENSO. *Bull. Amer. Meteor. Soc.,* **82,** 619–638.

McPhaden, M. J., 2012: A 21st century shift in the relationship between ENSO SST and warm water volume anomalies. *Geophys. Res. Lett.,* **39,** L09706, doi:10.1029/2012GL051826.

Meinen, C. S., and M. J. McPhaden, 2000: Observations of warm water volume changes in the equatorial Pacific and their relationship to El Niño and La Niña. *J. Climate,* **13,** 3551–3559.

Picaut, J., F. Masia, and Y. du Penhoat, 1997: An advective-reflective conceptual model for the oscillatory nature of ENSO. *Science,* **277,** 663–666.

Rasmusson, E. M., and T. H. Carpenter, 1982: Variations in tropical sea surface temperature and surface wind fields associated with the Southern Oscillation/El Niño. *Mon. Wea. Rev.,* **110,** 354–384.

Ren, H.-L., and F.-F. Jin, 2011: Niño indices for two types of ENSO. *Geophys. Res. Lett.,* **38,** L04704, doi:10.1029/2010GL046031.

Ropelewski, C. F., and M. S. Halpert, 1987: Global and regional scale precipitation associated with El Niño/Southern Oscillation. *Mon. Wea. Rev.,* **115,** 1606–1626.

Smith, R. D., J. K. Dukowicz, and R. C. Malone, 1992: Parallel ocean general circulation modeling. *Physica D,* **60,** 38–61, doi:10.1016/0167-2789(92)90225-C.

Smith, T. M., R. W. Reynolds, T. C. Peterson, and J. Lawrimore, 2008: Improvements to NOAA's historical merged land–ocean surface temperature analysis (1880–2006). *J. Climate,* **21,** 2283–2296.

Suarez, M. J., and P. S. Schopf, 1988: A delayed action oscillator for ENSO. *J. Atmos. Sci.,* **45,** 3283–3287.

Trenberth, K. E., 1997: The definition of El Niño. *Bull. Amer. Meteor. Soc.,* **78,** 2771–2777.

——, and D. P. Stepaniak, 2001: Indices of El Niño evolution. *J. Climate,* **14,** 1697–1701.

Wang, W., and M. J. McPhaden, 2001: Surface layer temperature balance in the equatorial Pacific during the 1997–98 El Niño and 1998–99 La Niña. *J. Climate,* **14,** 3393–3407.

Weisberg, R. H., and C. Wang, 1997: A western Pacific oscillator paradigm for the El Niño-Southern Oscillation. *Geophys. Res. Lett.,* **24,** 779–782.

Weng, H., K. Ashok, S. Behera, A. S. Rao, and T. Yamagata, 2007: Impacts of recent El Niño Modoki on dry/wet conditions in the Pacific Rim during boreal summer. *Climate Dyn.,* **29,** 113–129, doi:10.1007/s00382-007-0234-0.

——, S. K. Behera, and T. Yamagata, 2009: Anomalous winter climate conditions in the Pacific Rim during recent El Niño Modoki and El Niño events. *Climate Dyn.,* **32,** 663–674, doi:10.1007/s00382-008-0394-6.

Whitaker, J. S., G. P. Compo, X. Wei, and T. M. Hamill, 2004: Reanalysis without radiosondes using ensemble data assimilation. *Mon. Wea. Rev.,* **132,** 1190–1200.

Yeh, S.-W., J.-S. Kug, B. Dewitte, M.-H. Kwon, B. P. Kirtman, and F.-F. Jin, 2009: El Niño in a changing climate. *Nature,* **461,** 511–514, doi:10.1038/nature08316.

Yu, J.-Y., and S. T. Kim, 2010a: Three evolution patterns of central-Pacific El Niño. *Geophys. Res. Lett.,* **37,** L08706, doi:10.1029/2010GL042810.

——, and ——, 2010b: Identification of central-Pacific and eastern-Pacific types of ENSO in CMIP3 models. *Geophys. Res. Lett.,* **37,** L15705, doi:10.1029/2010GL044082.

——, F. Sun, and H.-Y. Kao, 2009: Contributions of Indian Ocean and monsoon biases to the excessive biennial ENSO in CCSM3. *J. Climate,* **22,** 1850–1858.

——, H.-Y. Kao, and T. Lee, 2010: Subtropics-related interannual sea surface temperature variability in the equatorial central Pacific. *J. Climate,* **23,** 2869–2884.

Zhang, Q., A. Kumar, Y. Xue, W. Wang, and F.-F. Jin, 2007: Analysis of the ENSO cycle in the NCEP coupled forecast model. *J. Climate,* **20,** 1265–1284.

Zhang, W., F.-F. Jin, J. Li, and H.-L. Ren, 2011: Contrasting impacts of two-type El Niño over the western north Pacific during boreal autumn. *J. Meteor. Soc. Japan,* **89,** 563–569.

——, ——, H.-L. Ren, J. Li, and J.-X. Zhao, 2012: Differences in teleconnection over the North Pacific and rainfall shift over the USA associated with two types of El Niño during boreal autumn. *J. Meteor. Soc. Japan,* **90,** 535–552.

Journal of the Meteorological Society of Japan, Vol. 91, No. 6, pp. 835–842, 2013
DOI:10.2151/jmsj.2013-608

NOTES AND CORRESPONDENCE

ENSO Regime Change since the Late 1970s as Manifested by Two Types of ENSO

Hong-Li REN

Department of Meteorology, School of Ocean and Earth Sciences and Technology, University of Hawaii, Honolulu, Hawaii, USA
Laboratory for Climate Studies, National Climate Center, China Meteorological Administration, Beijing, China

Fei-Fei JIN, Malte F. STUECKER

Department of Meteorology, School of Ocean and Earth Sciences and Technology, University of Hawaii, Honolulu, Hawaii, USA

and

Ruihuang XIE

Department of Marine Meteorology, Ocean University of China, Qingdao, China

(Manuscript received 3 April 2013, in final form 27 June 2013)

Abstract

During the late 1970s, the El Niño-Southern Oscillation (ENSO) experienced a notable regime change, manifested by a change in amplitude, dominant ENSO period, and sea surface temperature anomaly (SSTA) propagation characteristics. The present study shows that these features of the ENSO regime change are associated with property changes of the canonical ENSO, i.e., cold-tongue (CT) type ENSO. Another signature of the ENSO regime change is manifested in the frequent occurrence of a warm-pool (WP) type ENSO that accompanies SSTAs centered over the central Pacific near the WP edge and exhibits characteristics differing from those of the CT ENSO. The distinct manifestations of the two types of ENSO detected in this ENSO regime change are clearly identifiable with the removal of the strong background decadal signal. Since the late 1970s, the WP ENSO has featured a weak eastward (westward) propagation of the SSTA center in the developing (decaying) phase, which makes no net contribution to the observed eastward propagation, and a 2–3 yr period compared to the 4–5 yr period of the CT ENSO. Observations strongly suggest that the WP and CT ENSO are independent quasi-biennial and quasi-quadrennial modes, respectively, of the tropical Pacific climate variability. Our observations also suggest that these two ENSO modes have coexisted actively since the late 1970s when either El Niño or La Niña can be separated into the two types.

Keywords ENSO regime change; warm-pool ENSO; cold-tongue ENSO

Corresponding author: Hong-Li Ren, School of Ocean and Earth Sciences and Technology, University of Hawaii, Honolulu, Hawaii 96822, USA
E-mail: honglir@hawaii.edu; renhl@cma.gov.cn

1. Introduction

The El Niño-Southern Oscillation (ENSO) is the dominant mode of natural climate variability in the tropical Pacific, occurring on interannual timescales.

In the late 1970s, the ENSO regime experienced a major change (An and Wang 2000; An and Jin 2000; Fedorov and Philander 2000; Wang and An 2001). The dominant period of the ENSO cycle changed from a high-frequency regime during 1960s–1970s to a low-frequency regime during 1980s–1990s. The ENSO amplitude increased, which was accompanied by significant changes to the spatiotemporal structure of the ENSO. Before the late 1970s, the warm equatorial-Pacific SSTAs propagated westward (Rasmusson and Carpenter 1982); after 1980, the warm SSTAs propagated eastward or were nearly stationary with little propagation (Wallace et al. 1998). This feature of the ENSO regime change was illustrated clearly in terms of ENSO zonal propagation changes by Trenberth and Stepaniak (2001), and more precisely, in terms of zonal propagation changes of only the El Niño phase by other researchers (McPhaden and Zhang 2009; Ren and Jin 2011). These changes in the ENSO properties concurred with the prominent climate shift in the North Pacific, the cause of which is still a subject of research (Trenberth and Hurrel 1994; Meehl et al. 2009).

In recent years, the notion of ENSO regime change is being reflected in an increasing number of studies suggesting that, in addition to the canonical cold-tongue (CT) type El Niño, there is a different type of El Niño/ENSO named “Dateline El Niño” (Larkin and Harrison 2005a, b), “El Niño Modoki” (Ashok et al. 2007; Weng et al. 2007), “Central-Pacific ENSO/El Niño” (Kao and Yu 2009; Yeh et al. 2009), and “Warm-pool El Niño/ENSO” (Kug et al. 2009; Ren and Jin 2011). Despite using different names, these studies more or less described the same phenomenon. In this paper, we use the terminology “Warm-pool (WP) ENSO”. The WP ENSO, with different teleconnections and climate impacts from the CT type (Weng et al. 2007; Kim et al. 2009; Zhang et al. 2012), has occurred frequently in the past 30 years (Kug et al. 2009) and may continue to do so in a warming climate (Yeh et al. 2009).

In the ENSO regime after the late 1970s, both CT and WP ENSO types have been actively coexisting (Ren and Jin 2011; Takahashi et al. 2011; McPhaden et al. 2011), reminiscent of the two leading ENSO-like modes coexisting under current climate conditions. Bejarano and Jin (2008), in their theoretical study of the ENSO regime dependence on climate mean-state changes, showed that the so-called quasi-quadrennial (QQ) mode has its SSTA pattern centered in the eastern equatorial Pacific, while the so-called quasi-biennial (QB) mode has its SSTA center shifted westward (see their Fig. 5). They are similar to the observed SSTA patterns of the CT and WP ENSO, respectively. In this study, we differentiate the contributions of the two ENSO types to the ENSO regime change in the late 1970s and examine the correspondence between the two types and the two modes.

2. Data

The sea surface temperature (SST) dataset used was the improved Extended Reconstructed SST version 3b (Smith et al. 2008) from the National Climate Data Center at the National Oceanic and Atmospheric Administration (NOAA). This study focused on the period of Jan 1950–Feb 2011. Traditional Niño3 and Niño4 SSTA indices (N3I and N4I) were obtained from the Climate Prediction Center/NOAA. To effectively capture the spatiotemporal features of the two types of ENSO, Ren and Jin (2011) defined the WP and CT Niño indices (WPI and CTI) by introducing a transformation of N3I and N4I. As seen in Fig. 1, WPI has a strong decadal timescale (~8–16 year period) in its spectra besides the interannual timescales, compared to CTI. This feature can also be seen in the spectra of the El Niño Modoki index (EMI) devised by Ashok et al. (2007) and in the central Pacific ENSO index (CPI) of Kao and Yu (2009). This is consistent with the result of Weng et al. (2007). Furthermore, two statistically significant (90% confidence level) peaks were visible on interannual timescales (2–3 and 4–5 yr periods). Kao and Yu (2009) noted a near 2 yr period peak in their CPI. We argue here that the strong background decadal variability, evident in these indices, may have biased previous analyses of both the WP ENSO and the ENSO regime change, which was first noted by Ren and Jin (2013) in examining the mechanism of WP ENSO. To focus solely on the interannual variability, this study used high-frequency (HF) indices created by removing the decadal timescale (above 6 years). It can be roughly seen in Fig. 1 that HF-WPI depicted a period shortening since the late 1970s, with the HF-CTI quite similar to the CTI.

3. Results

The zonal phase propagation changes of SSTAs along the equator are an important indicator of the ENSO regime change (Trenberth and Stepaniak 2001). Trenberth and Stepaniak calculated lag correlations using Niño3.4 and trans-Niño indices to reveal the nature of different ENSO propagation directions and capture the ENSO regime change in the late 1970s. Following this approach, Ren and Jin (2011) used CTI and WPI to represent the dramatic regime change and

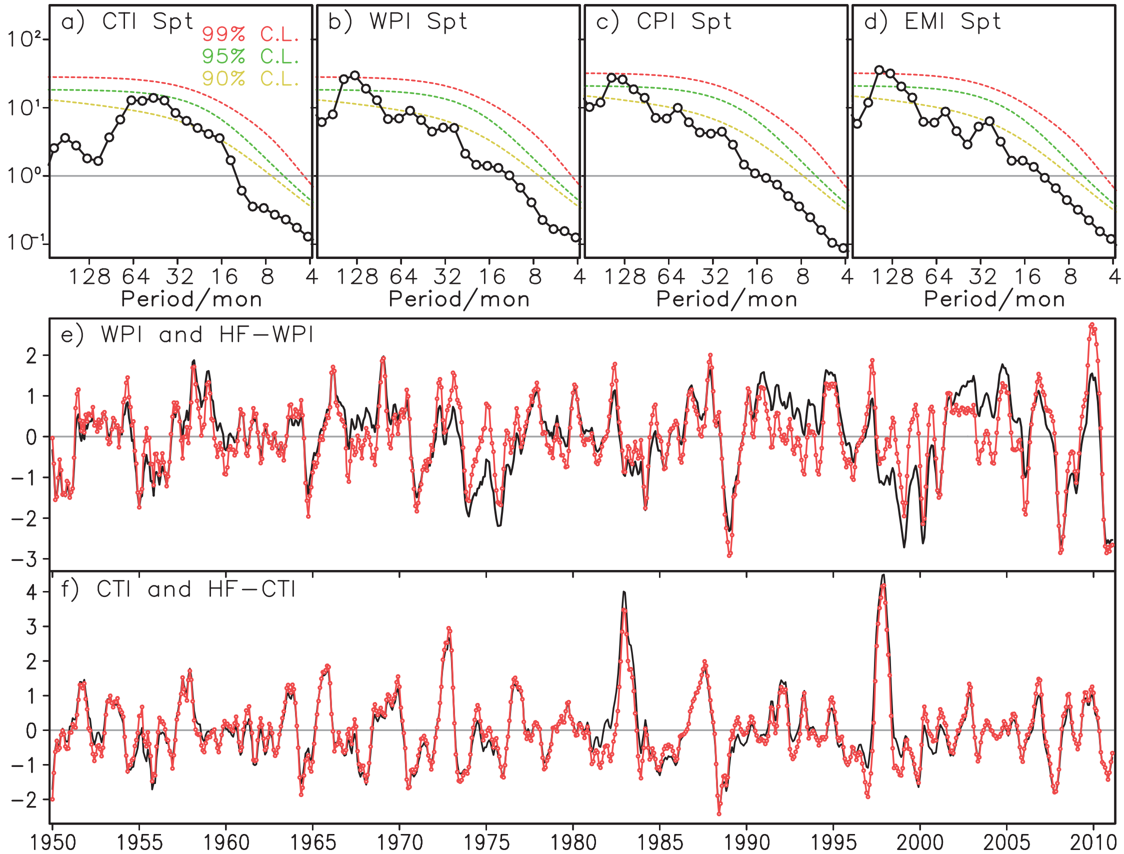

Fig. 1. Wavelet power spectra for CTI (a), WPI (b), CPI (c), and EMI (d), divided by their variances. Normalized WPI (black) and HF-WPI (red) in (e) and CTI (black) and HF-CTI (red) in (f), which are linearly detrended, with a 3 month running mean. The yellow, green, and red dashed lines correspond to 90%, 95%, and 99% confidence levels, respectively, of a χ^2 test for a red-noise process with a lag-1 autocorrelation of 0.72 (Torrence and Compo 1998).

confirmed the asymmetry in propagation direction changes between El Niño and La Niña phases; i.e., only El Niño changed from a westward to eastward propagation, while La Niña propagated westward (McPhaden and Zhang 2009). Here we reexamine the El Niño phase propagation change using HF-CTI and HF-WPI.

Figure 2a shows a similar but more robust ENSO regime change relative to Fig. 4b of Ren and Jin (2011). The HF-CTI leads the HF-WPI by approximately 4–5 months, with high positive correlations before the late 1970s, capturing the well-known westward propagation of El Niño SSTAs (Rasmusson and Carpenter 1982). These significant correlations, however, disappeared sharply in the late 1970s. Instead, positive correlations appeared at an 8–10 month lag after the late 1970s, which reflects a clear but weak eastward propagation. In contrast, a westward propagation has dominated the La Niña phase for the past 6 decades (not shown). This indicates that one major feature of the ENSO regime change in the late 1970s is the observed propagation change of El Niño from westward to eastward.

The overall low correlation in Fig. 2a, at almost all lags after the late 1970s, clearly suggests the potential independence of the two ENSO types. This was also discussed by Ashok et al. (2007). It is confirmed by the contrast between the situations before 1980 and after 1980 (Figs. 2b and 2c); either the El Niño or La Niña states since 1980 tend to be separated into the two groups that correspond to the positive or negative phase of the two different ENSO types. It is also apparent that two major features indicate the ENSO regime change (see the colored number pairs). The first is that WP El Niño has been occurring more frequently than CT El Niño since 1980, with a slight increase in

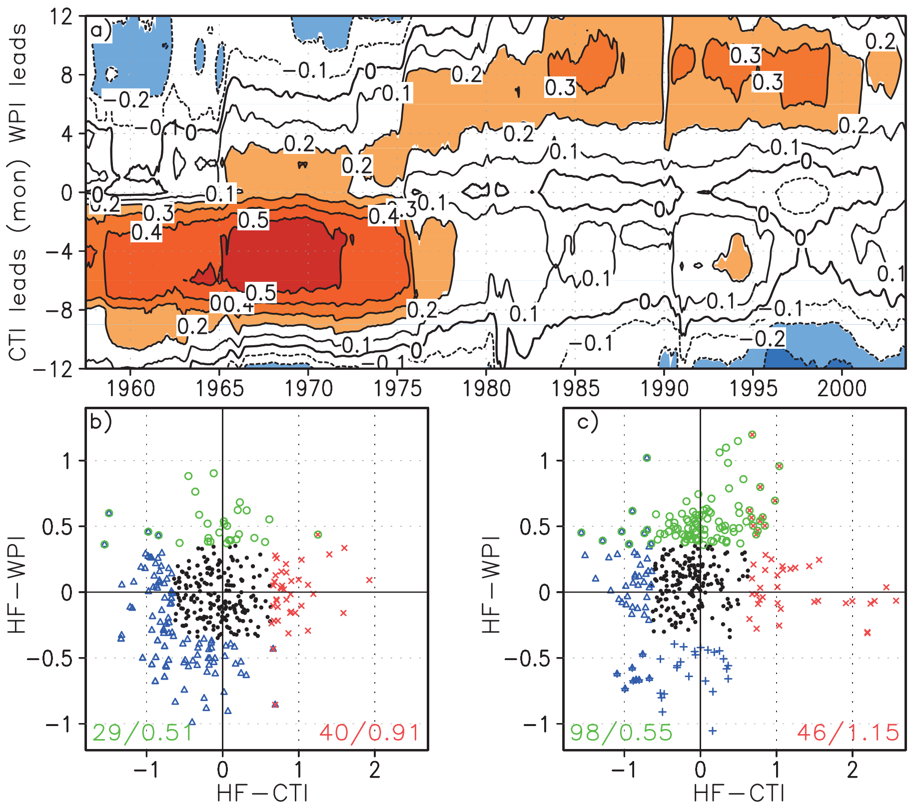

Fig. 2. Lead-lag partial correlations for the positive phases of HF-CTI and HF-WPI, using a 15 yr running window in (a), where the duration of the positive phases of these indices are determined by the leading index. Shading denotes the 95% confidence level of a student's *t*-test, with a degree of freedom of about 60. Scatter plots for HF-CTI and HF-WPI before 1980 (b) and after 1980 (c), where the green, red, blue, and black denote WP El Niño, CT El Niño, La Niña (the two kinds of blue marks in (c) denote the separation of two types of La Niña), and near neutral states, respectively, as defined by the criterion of one standard deviation of either index in the whole period. Colored number pairs represent the numbers of the colored dots and their averaged values.

amplitude (Lee and McPhaden 2010). The second is that CT El Niño became much stronger after 1980. These features motivated us to focus on the distinct contributions of the two ENSO types to the regime change.

Figure 3 depicts the evolution of the equatorial SSTAs to clarify typical characteristics and changes of the El Niño phase propagation in terms of the two different ENSO types. In Fig. 3a, the WP El Niño features a short duration and a weak eastward propagation of positive SSTAs during its developing phase. The figure also clearly illustrates that the maximum remains near the central Pacific, notwithstanding the extension of the warming slightly eastward during the mature stage, as is observed in some cases during boreal winter (Ashok et al. 2007). After removing the two strongest CT El Niño events (1982/83 and 1997/98), a weak westward propagation of WP El Niño after 1980 is visible, significantly so during its decaying phase (not shown). Due to the approximate symmetry between the eastward and westward propagations with respect to lag 0, the pure WP El Niño makes no net contribution to the observed eastward propagation of El Niño since 1980 (Fig. 2a). Before 1980, the HF-WPI-related positive SSTAs initiated in the eastern Pacific, propagated westward, and matured near the dateline (Fig. 3b). The CT El Niño shows a similar westward propagation before 1980 (Fig. 3d), but an eastward propagation, with an associated amplitude increase, after 1980 (Fig. 3c). These results suggest that El Niño propagation and amplitude changes occurring in the late 1970s are

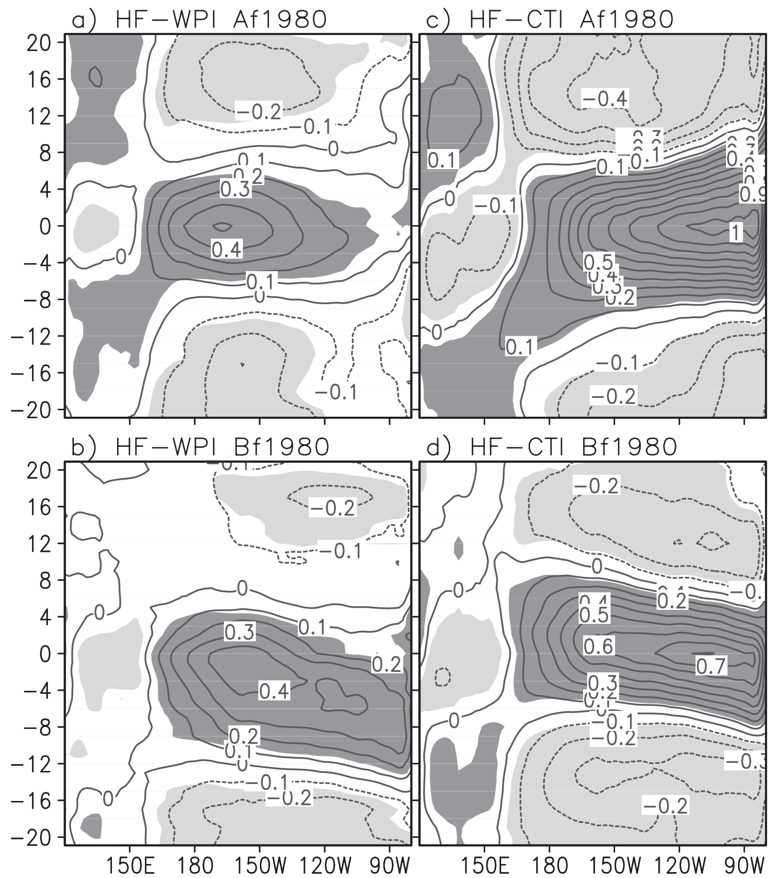

Fig. 3. Lead-lag partial regressions of the equatorial SSTAs (contours, unit: K) averaged from [5°S, 5°N], upon (a) the positive-phase HF-WPI after 1980, (b) the same as (a) but before 1980, (c) the positive-phase HF-CTI, and (d) the same as (c) but before 1980. Shading denotes the 95% confidence levels of a student's *t*-test. Ordinates are lag months.

primarily due to the CT El Niño property change. The similarity between the patterns in Figs. 3b and 3d reflects the strong westward propagation of ENSO, as seen in Fig. 2a, and thus the predominance of the CT type before 1980, notwithstanding during the time, a few WP El Niño-like events might have occurred (Kug et al. 2009; Yu and Kim 2010).

Another apparent feature in Fig. 3 is the change in duration of positive SSTAs. After 1980, the WP El Niño persisted for a shorter period and the CT El Niño for a longer period (which is quantitatively presented in Fig. 4), compared to pre-1980, when the El Niño SSTAs had similar durations irrespective of the type. This may indicate a similar change in ENSO periodicity, which is confirmed by power spectrum analyses, as shown in Fig. 4. In this study, the period bands are assumed significant simply if they have a spectral change of more than 100%, instead of based on a statistical test. The most significant feature of the CT ENSO is the intensification of the power spectrum and the increase of the interannual timescale from a 3–4 yr period before 1980 to a 4–5 yr period after 1980. Furthermore, it is clear that the WPI has a dominant interannual scale spectral peak at a 2–3 yr period after 1980. This is even more pronounced after 1990 when more WP El Niño events occurred (McPhaden et al. 2011), compared to the 4–5 yr period before 1980. Such a significant ENSO periodicity change strongly indicates the correspondence between the two observed ENSO types and the two leading ENSO modes, QQ and QB, suggested theoretically by Bejarano and Jin (2008). That is, the QQ mode dominated before the late 1970s, which mostly occurred as the CT ENSO (note that it remains controversial whether the WP ENSO existed at that time). After the late 1970s, the QB mode emerged as

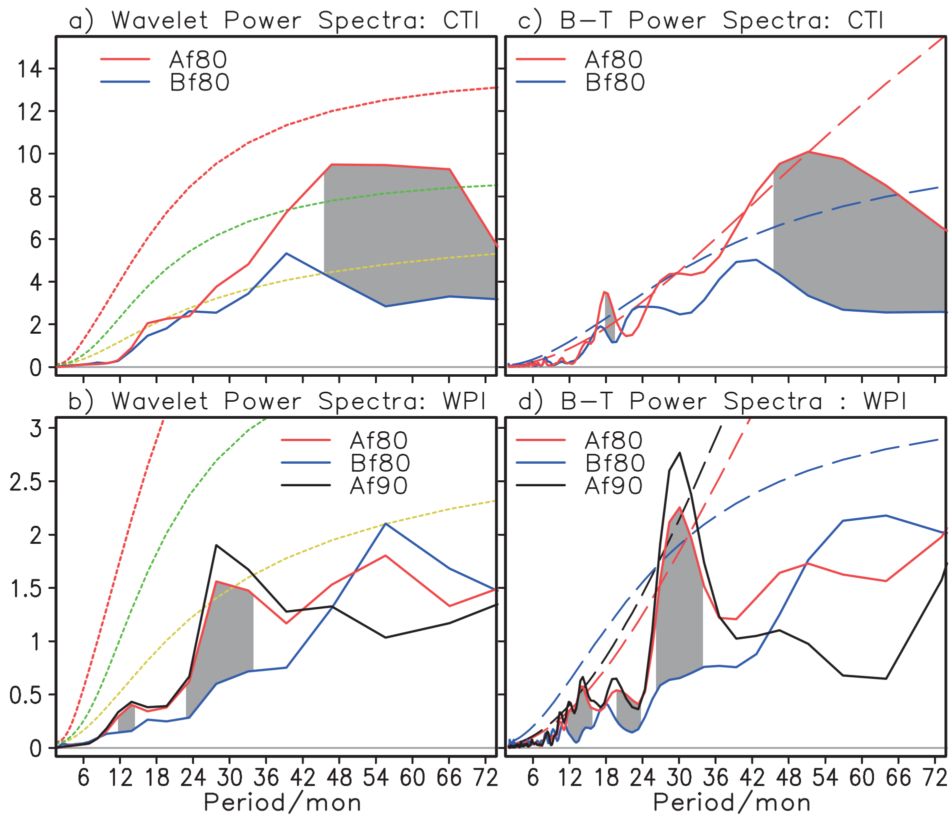

Fig. 4. Wavelet power spectra of CTI (a) and WPI (b) for the different periods, where the confidence levels are as per Fig. 1 and the shadings denote that the values of the red lines are 100% greater than those in the blue lines. Panels (c) and (d) are the same as panels (a) and (b), but for the B-T power spectra (c.f., Ghil et al. 2002), with the 95% confidence level represented by dashed lines.

the WP ENSO type with increasing occurrences, coexisting with the QQ mode that appears as the stronger CT ENSO type, with a slightly longer period than it previously had.

4. Summary and concluding remarks

As stated in the introduction, many studies have revealed changes in ENSO properties occurring in the late 1970s and an increasing number of studies suggest that a different ENSO type (WP ENSO), in addition to the canonical CT ENSO, has occurred frequently in the past 30 years. These studies appear to reveal the same phenomenon: The ENSO regime change in the late 1970s was not only a change in ENSO properties but also in the dominant ENSO modes. We have demonstrated in this study that the ENSO regime change since the late 1970s is predominantly manifested by the two types of ENSO: The dramatic changes of the CT ENSO properties, which are consistent with previous studies (e.g., An and Wang 2000), and the frequent occurrence of WP ENSO events, which demonstrates the emergence of an independent mode coexisting actively with the CT ENSO in the tropical Pacific.

This study has clarified the roles of the two ENSO types in manifesting the ENSO regime change by removing the decadal variability, which is strong enough in the central Pacific to obscure certain characteristics of the WP ENSO. The CT ENSO was mainly manifested by changes in the properties including the intensification of the amplitude, lengthening of the period, and a tendency of eastward propagation after the late 1970s. The typical WP El Niño has a clear extension of SSTAs to the east during its mature phase, with a westward-shifted SSTA center (relative to CT events) that propagates weakly eastward in the developing phase and westward in the damping phase, and hence makes no net contribution to the observed eastward propagation since the late 1970s. Moreover, the WP ENSO typically features a 2–3 yr period with an increasing significance and the CT ENSO features an enhanced QQ period, confirming the active coexistence of the QB and QQ modes that correspond to the two types of ENSO in the observation. It may be suggested that a complete definition of the different ENSO types must incorporate information not only on the spatial patterns, but also on the timescales. Also, it is proved that La Niña, similar to El Niño, appears to be separated into two types since 1980.

This study aimed to develop a deep understanding of the ENSO regime change in the late 1970s by linking new observational evidence with previous studies, not only regarding the change in ENSO properties, but also the change in ENSO types (or ENSO mode stability). The observed ENSO periodicity changes in the late 1970s reflect the sensitivity of ENSO modes that occur in the neighborhood of codimension-2 degeneracy to climate mean state changes (Jin and Neelin 1993; Jin 1997; Bejarano and Jin 2008). It is suggested that the essential change of the ENSO regime is likely in the stability of the two ENSO modes. Furthermore, the demonstration that the ENSO regime change in the late 1970s can be understood in terms of the WP and CT ENSO types and that the theoretical QB and QQ modes can be used to interpret the two ENSO types needs to be further validated in future studies by experiments based on the model of Bejarano and Jin (2008).

Still, questions remain as to what caused the ENSO regime change, how the change relates to changing background conditions (e.g., Ashok et al. 2007; Kim and An 2011), and whether the current ENSO regime will persist or be altered in a changing climate (e.g., McPhaden et al. 2011). A recent study has reported the weakened interannual variability in the tropical Pacific Ocean since 2000 (Hu et al. 2013). This is conceivable if WP ENSO events keep occurring actively but CT ENSO becomes inactive under the current climate conditions, and thus the total ENSO period might be shortening since 2000 (refer to the indices in Fig. 1). These results may imply the emergence of another ENSO regime change, which is worthy of further study. Moreover, it should be stressed that decadal signals need to be removed from data when clarifying the typical WP ENSO features and related issues that may be biased by the background decadal variability (Ren and Jin 2013).

Acknowledgments

This work is jointly supported by U. S. DOE grant DE-SC0005110, China Meteorological Special Project (GYHY201206016), the 973 Program of China (2010 CB950404), U. S. National Science Foundation grants ATM 1034798, and NOAA grand NA10OAR 4310200. Authors thank Axel Timmermann for valuable comments.

References

An, S.-I., and F.-F. Jin, 2000: An eigen analysis of the interdecadal changes in the structure and frequency of ENSO mode. *Geophys. Res. Lett.*, **27**, 2573–2576, doi: 10.1029/1999GL011090.

An, S.-I., and B. Wang, 2000: Interdecadal change of the structure of the ENSO mode and its impact on the ENSO frequency. *J. Climate*, **13**, 2044–2055.

Ashok, K., S. K. Behera, S. A. Rao, H. Weng, and T. Yamagata, 2007: El Niño Modoki and its possible teleconnection. *J. Geophys. Res.*, **112**, C11007, doi: 10.1029/2006JC003798.

Bejarano, L., and F.-F. Jin, 2008: Coexistence of equatorial coupled modes of ENSO*. *J. Climate*, **21**, 3051–3067.

Fedorov, A. V., and S. G. Philander, 2000: Is El Niño changing? *Science*, **288**, 1997–2002.

Ghil, M., R. M. Allen, M. D. Dettinger, K. Ide, D. Kondrashov, M. E. Mann, A. Robertson, A. Saunders, Y. Tian, F. Varadi, and P. Yiou, 2002: Advanced spectral methods for climatic time series. *Rev. Geophys.*, **40**, 1003, doi: 10.1029/2000RG000092.

Hu, Z.-Z., A. Kumar, H.-L. Ren, H. Wang, M. L'Heureux, and F.-F. Jin, 2013: Weakened interannual variability in the tropical Pacific Ocean since 2000. *J. Climate*, **26**, 2601–2613.

Jin, F.-F., and J. D. Neelin, 1993: Modes of interannual tropical ocean-atmosphere inter-action—a unified view. Part I: Numerical results. *J. Atmos. Sci.*, **50**, 3477–3503.

Jin, F.-F., 1997: An equatorial ocean recharge paradigm for ENSO. Part II: A stripped-down coupled model. *J. Atmos. Sci.*, **54**, 830–847.

Kao, H.-Y., and J.-Y. Yu, 2009: Contrasting eastern-Pacific and central-Pacific types of El Niño. *J. Climate*, **22**, 615–632.

Kim, B.-M., and S.-I. An, 2011: Understanding ENSO regime behavior upon an increase in the warm-pool temperature using a simple ENSO model. *J. Climate*, **24**, 1438–1450.

Kim, H.-M., P. J. Webster, and J. A. Curry, 2009: Impact of shifting patterns of Pacific Ocean warming on north Atlantic tropical cyclones. *Science*, **325**, 77–80.

Kug, J.-S., F.-F. Jin, and S.-I. An, 2009: Two types of El Niño events: Cold tongue El Niño and warm pool El Niño. *J. Climate*, **22**, 1499–1515.

Larkin, N. K., and D. E. Harrison, 2005a: On the definition of El Niño and associated seasonal average U. S. weather anomalies. *Geophys. Res. Lett.*, **32**, L13705, doi: 10.1029/2005GL022738.

Larkin, N. K., and D. E. Harrison, 2005b: Global seasonal temperature and precipitation anomalies during El Niño autumn and winter. *Geophys*. *Res*. *Lett*., **32**, L16705, doi:10.1029/2005GL022860.

Lee, T., and M. J. McPhaden, 2010: Increasing intensity of El Niño in the central-equatorial Pacific. *Geophys*. *Res*. *Lett*., **37**, L14603, doi:10.1029/2010GL044007.

McPhaden, M. J., and X. Zhang, 2009: Asymmetry in zonal phase propagation of ENSO sea surface temperature anomalies. *Geophys*. *Res*. *Lett*., **36**, L13703, doi: 10.1029/2009GL038774.

McPhaden, M. J., T. Lee, and D. McClurg, 2011: El Niño and its relationship to changing background conditions in the tropical Pacific Ocean. *Geophys*. *Res*. *Lett*., **38**, L15709, doi:10.1029/2011GL048275.

Ren, H.-L., and F.-F. Jin, 2011: Niño indices for two types of ENSO. *Geophys*. *Res*. *Lett*., **38**, L04704, doi: 10.1029/2010GL046031.

Ren, H.-L., and F.-F. Jin, 2013: Recharge oscillator mechanisms in two types of ENSO. *J*. *Climate*, **26**, 6506 –6523.

Smith, T. M., R. W. Reynolds, T. C. Peterson, and J. Lawrimore, 2008: Improvements to NOAA's historical merged land-ocean surface temperature analysis (1880–2006). *J*. *Climate*, **21**, 2283–2296.

Takahashi, K., A. Montecinos, K. Goubanova, and B. Dewitte, 2011: ENSO regime: Reprinting the canonical and Modoki El Niño. *Geophys*. *Res*. *Lett*., **38**, L10704, doi: 10.1029/2011GL047364.

Torrence, C., and G. P. Compo, 1998: A practical guide to wavelet analysis. *Bull*. *Amer*. *Meteor*. *Soc*., **79**, 61–78.

Trenberth, K. E., and D. P. Stepaniak, 2001: Indices of El Niño evolution. *J*. *Climate*, **14**, 1697–1701.

Wallace, J. M., E. M. Rasmusson, T. P. Mitchell, V. E. Kousky, E. S. Sarachik, and H. von Storch, 1998: On the structure and evolution of ENSO-related climate variability in the tropical Pacific: Lessons from TOGA. *J*. *Geophys*. *Res*., **103**, 14241–14259, doi:10.1029/97JC02905.

Wang, B., and S.-I. An, 2001: Why the properties of El Niño changed during the late 1970s. *Geophys*. *Res*. *Lett*., **28**, 3709–3712, doi:10.1029/2001GL012862.

Weng, H., K. Ashok, S. Behera, A. S. Rao, and T. Yamagata, 2007: Impacts of recent El Niño Modoki on dry/wet conditions in the Pacific rim during boreal summer. *Climate Dyn*., **29**, 113–129.

Yeh, S.-W., J.-S. Kug, B. Dewitte, M.-H. Kwon, B. P. Kirtman, and F.-F. Jin, 2009: El Niño in a changing climate. *Nature*, **461**, 511–514.

Yu, J.-Y., and S. T. Kim, 2010: Three evolution patterns of Central-Pacific El Niño. *Geophys*. *Res*. *Lett*., **37**, L08706, doi:10.1029/2010GL042810.

Zhang, W., F.-F. Jin, H.-L. Ren, J. Li, and J.-X. Zhao, 2012: Differences in teleconnection over the North Pacific and rainfall shift over the USA associated with two types of El Niño during boreal autumn. *J*. *Meteor*. *Soc*. *Japan*, **90**, 535–552.

沈志超,任国玉,李娇,等. 中国东北地区冬季气温变化特征及其与大气环流异常的关系[J]. 气象与环境学报,2013,29(1):47－54.
SHEN Zhi-chao,REN Guo-yu,LI Jiao,et al. Winter temperature variability and its relationship with atmospheric circulation anomalies in Northeast China[J]. Journal of Meteorology and Environment,2013,29(1):47－54.

中国东北地区冬季气温变化特征及其与大气环流异常的关系

沈志超[1,2]　任国玉[2]　李娇[1,3]　孙秀宝[1,2]

(1. 南京信息工程大学大气科学学院,江苏 南京 210044; 2. 中国气象局气候研究开放实验室,国家气候中心,北京 100081; 3. 铁岭市气象局,辽宁 铁岭 112000)

摘　要: 利用1957—2010年冬季中国东北地区90个站气温资料,应用REOF和聚类分析方法将东北地区划分为南、北两个冬季气温变化子区,分析讨论其冬季气温变化趋势和冷暖异常特征,及其与主要环流指数之间的同期和滞后关系。使用向后去除变量选择法,选取最优预测因子,并建立了全区和各子区的回归统计模型。结果表明:中国东北地区冬季增温较明显,平均上升速率为0.45 ℃/10 a,北部略高;与同期欧亚纬向环流指数之间存在着较显著相关;前期8月东太平洋副热带高压面积指数、前期10月亚洲区极涡面积指数和前期8月北半球极涡面积指数与中国东北地区冬季气温存在着显著相关,复相关系数为0.70,并且是回归方程最关键预测因子。在对冷、暖冬预测时,可以将选定时段和区域副热带高压和极涡面积指数作为重要的影响因素,且误报率较低。

关键词: 东北地区;冬季气温;旋转主分量分析;环流指数;相关;预测

中图分类号: P468.0+21/P434　　**文献标识码:** A　　doi:10.3969/j.issn.1673-503X.2013.01.008

引言

中国东北地区位于北半球中高纬度地带,是全球陆地气候增暖最明显的区域之一,冬季地面气温升高速率明显高出中国平均值和全球平均值。王绍武[1－2]指出,在近百年全球气候变暖的背景下,中国东北地区冬季升温趋势十分明显。任国玉等[3]研究表明,中国现今增暖最明显的地区包括东北、华北、西北和青藏高原北部,最显著变暖季节在冬季。李春和方之芳[4]指出,东北地区气温最大升温超过了0.7 ℃/10 a。平均升高0.5 ℃/10 a以上。

在冬季总体气候变暖的背景下,影响东北地区的寒潮频数也显著下降,暖冬年份明显增多[5]。但是,最近几年,冬季极端严寒事件又时有发生[6]。影响东北冬季平均和极端气温变化的因素很复杂,除了台站附近观测环境变化引起的资料序列偏差和大气中温室气体浓度增加的可能影响外,气候系统内部的年际到年代以上尺度变异性显然也是不可忽视的。丁一汇等[7]指出,对气候系统内部的过程与机理缺乏足够的认识,气候模式的可靠性还不高等。研究冬季温度变化有助于理解气候增暖本质,对于理解东北地区冬季气温的可预测性具有重要意义。这方面的研究已有不少。孙凤华等[8]指出,气候变暖增加了冬季气候变率,即增加气候异常事件的发生概率和强度,不仅引发暖冬事件,如在2004—2005年东北的冬季气温达到了偏冷标准,且没有得到准确的预报,因此,如何找出其影响因子和强信号来更好地预测也就显得更为重要。陈佩燕等[9]指出,影响中国东部地区冬季温度异常的关键海区,前期夏、秋季赤道印度洋、赤道东太平洋海温异常与中国东部地区冬季温度异常有较好的相关关系,对预测中国东部地区冬季温度异常有一定的前兆意义[10]。杨素英等[11]指出,在对流层中层,亚洲极涡(特别是极涡面积)、贝加尔湖高压脊和东亚大槽是影响中国东北冬季气温异常的关键同期因子。已有研究一般集中在对海温[12]、雪盖[13]、海冰[14－15]、高原热力异常[16]、西伯利亚高压[17]、北大西洋涛动(NAO)[18]、北极涛动(AO)[19]和极涡[20－21]等因子的探讨。

本文利用近53 a东北地区90站冬季气温资料,在划分为南、北个冬季气温变化子区的基础上,分析讨论东北地区冬季气温变化趋势和冷暖异常的时空特征,进一步研究这种时空变化与主要环流指数之

收稿日期: 2011－10－14;**修订日期:** 2011－12－11。
基金项目: 国家科技支撑项目(2007BAC29B02,2007BAC03A01)资助。
作者简介: 沈志超,男,1985年生,在读硕士研究生,主要从事短期气候预测及气候变化的研究,E-mail:szcsds@163.com。

间的同期和滞后关系,以及各环流因子对不同子区的作用情况,寻找最关键的预测因子和强信号,并探讨对东北冬季气温的可预报性。

1　资料与方法

1.1　资料来源

所用国家气象信息中心气象资料室整编的中国756个基本基准站地面月气温数据集资料。资料经过均一化处理。为使资料序列长度尽可能一致,选取1957年及以前建站的站点,排除了1957年以后建站的测站资料序列。观测资料序列长度为1957—2010年。其中黑龙江省泰来站只缺少1957年12月记录,用附近3个站当月资料对该站该月缺测值进行插补。全部入选台站数为90个(图1)。这些台站空间分布基本均匀,可以满足东北地区冬季长期气候变化分析的需要。

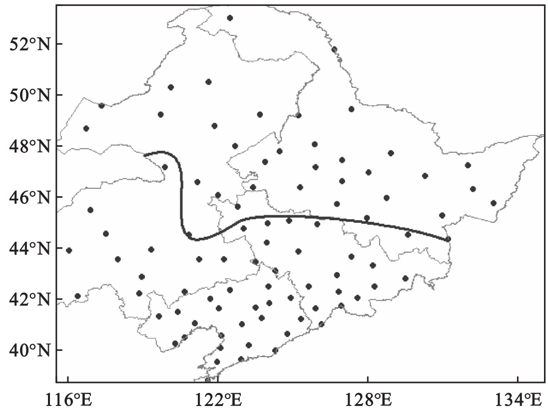

图1　中国东北90个气象站的位置与分区界限

Fig.1　The selected 90 weather stations in the northeast China in this paper and the boundary line of two subregions of the study area

定义冬季为当年12月和翌年1—2月。冬季年份用12月所在的年份表示,如1957年12月和1958年1—2月则记为1957年冬季,因此分析时期为1957—2009年共53个冬季。74项环流指数来源于国家气候中心气候系统诊断室。

1.2　分析方法

采用旋转经验正交分解(REOF)方法识别冬季平均气温变异的空间差异性[22]。EOF分析方法是在分析气象要素的时空分布时,将资料序列分解成空间和时间两部分,且分解具有正交性。分解结果得到多个荷载分布场及相应的时间变化系数,主要空间模式反映气象要素的主要空间特征。REOF则是通过因子轴的转动,能够分解出要素场中不同地理区域变化的特征。

为了准确合理地分区,采用聚类分析方法,对已分的各区边界加以鉴定。Pearson相关系数聚类分析方法用来衡量两个数据集合是否在一条线上面。其计算公式:

$$r=\frac{\sum xy-\frac{\sum x\sum y}{N}}{\sqrt{\left(\sum X^2-\frac{(\sum X)^2}{N}\right)\left(\sum Y^2-\frac{(\sum Y)^2}{N}\right)}} \tag{1}$$

环流因子初选。用前一年1月至前一年11月的74项环流指数,计算了持续时间分别为1个月、2个月、3个月30种月季组合,共得到备选环流指数因子数2220(74×30)个。求其与东北各区冬季平均气温距平序列之间的相关,选取超过0.001显著性水平的相关因子。

向后去除变量选择方法。在回归分析中一种变量的选择过程中,将所有变量输入到方程中,然后按顺序移去。考虑将与因变量之间的部分相关性最小的变量第一个移去(部分相关:对于因变量与某个自变量,当已移去模型中的其他自变量对该自变量的线性效应之后,因变量与该自变量之间的相关性。当变量添加到方程时,它与R方的更改有关。可称为半部分相关)。如果它满足消除条件,则将其移去。移去第一个变量之后,考虑下一个将方程的剩余变量中具有最小的部分相关性的变量移去。直到方程中没有满足消除条件的变量,过程结束。这与逐步回归建立的回归方程不同[24]。

网格面积加权法。在建立各区域平均时间序列时,采用Jones等[23]提出的计算区域平均气候时间序列的方法。首先将东北整个区域按经纬度划分网格,网格尺寸为2°×2°,共40个网格。然后将每个网格里所有站点数据进行算术平均,得到各网格平均值。最后应用面积加权法计算所有网格点的平均值,获得各区冬季平均温度时间序列。计算全部网格面积加权平均值的公式:

$$Y_k=\frac{\sum_{i=1}^{m}(\cos\theta_i)\times Y_{ik}}{\sum_{i=1}^{m}(\cos\theta_i)} \tag{2}$$

式(2)中,Y_k为第k年全国平均值,$i=1,2,\cdots,m$,(m为网格数),Y_{ik}为第i个网格中第k年的平均值,θ_i为第i个网格中心的纬度。

本文采用逐步回归、线性拟合等统计分析方法。其中多元回归方程采用F检验,$F_{0.01}(3,40)=4.31$。相关系数的显著性检验采用t检验[22]。本文中$N=53$,则$r_{0.001}=0.44$,$r_{0.01}=0.35$,$r_{0.05}=0.27$。

1.3　区域划分结果

由于地理环境的差异,东北不同地区冬季气温变化有一定的差异。对东北冬季气温距平场进行REOF分解计算,可以较好地揭示出差异性。由表1

可知,前两个特征向量的方差贡献分别为46% 和37%,前3 个特征向量的累计方差贡献达到87%。

表1　中国东北冬季气温距平场 REOF 分解前3 个特征向量的方差贡献和累计方差贡献

Table 1　Variance contribution and accumulated variance contribution of the first three eigenvectors of REOF components for winter temperature anomalies over the northeast China

旋转后特征向量序号	1	2	3
旋转后方差贡献	0.462	0.370	0.039
累计方差贡献	0.462	0.832	0.872

图2a 至图2c 给出东北冬季气温距平 REOF 分解的前3 个特征向量载荷的空间分布。第1 特征向量均为正值,且由北向南逐渐增大,以辽宁省营口为大值中心,为0.93。第2 特征向量均为负值,但负值绝对值由北向南减小,黑龙江省黑河、齐齐哈尔一带为低值中心,为 -0.89。第3 特征向量体现出东西部地区的差异变化,高值中心出现在大兴安岭以西,向东逐步减小。

前2 个特征量中心特征值的绝对值均在0.8 以上,构成以中国辽宁、黑龙江省为中心的2 个主要的局地变化区域。第3 个特征量的中心出现在蒙古国境内,中国境内只有两个站的特征值超过0.6,其方差贡献很小,不作为单独分区依据。

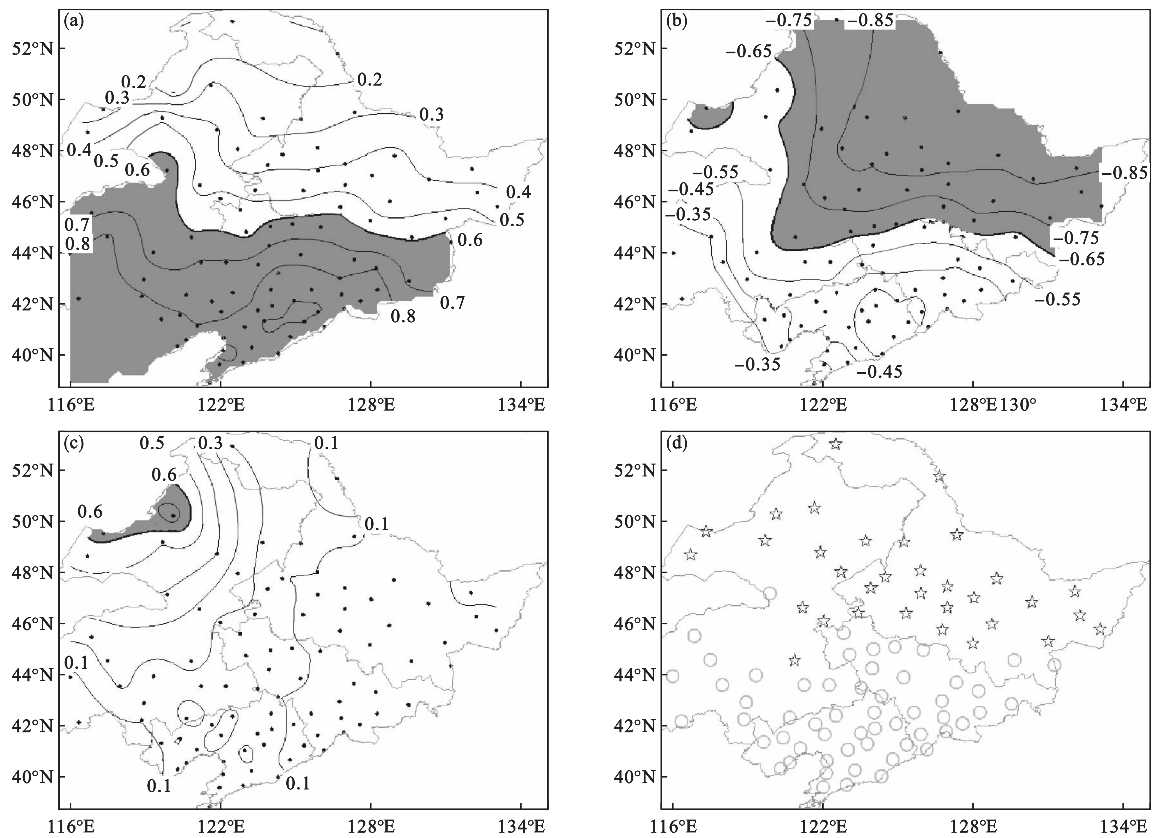

图2　中国东北冬季气温距平 REOF 的第1(a)、第2(b)、第3(c)特征量分布和聚类分析(d)

Fig.2　The distributions of the first(a), second(b) and third(c) eigenvectors of REOF components for winter temperature anomalies in northeast China and its cluster analysis(d)

根据以上分析结果,将东北地区划分出以辽宁西南和黑龙江北部为中心的两个局地变化区域(图2阴影区),第1 特征向量0.6 的载荷线与第2 特征向量0.65 的载荷线比较接近,为此使用聚类分析方法,发现使用第1 特征向量0.6 的载荷线分区更接近聚类分析。最终确定如图1 所示的东北南区和北区2 个子区。北区共有35 个站,南区有55 个站。

2　结果分析

2.1　冬季气温主要特征及异常年的划分

采用网格面积加权法得到各区域时间序列,用5 点滑动平均和一元线性趋势分析全区以及各分区温度变化趋势(图3)。从图3 可以看出,1957—2009 年东北冬季气温上升趋势非常明显,全区升温趋势为0.45 ℃/10 a,北区为0.47 ℃/10 a,南区为0.44 ℃/10 a;与文献[25]中国1951—2001 年冬季温度上升趋势,增温速率高为0.36 ℃/ 10 a 比较吻合。近53 a 东北冬季平均气温上升了约2.43 ℃。增温主要是自1980 年代开始。1980 年代以前,气温

在较小的范围内上下波动,而从20世纪80年代初

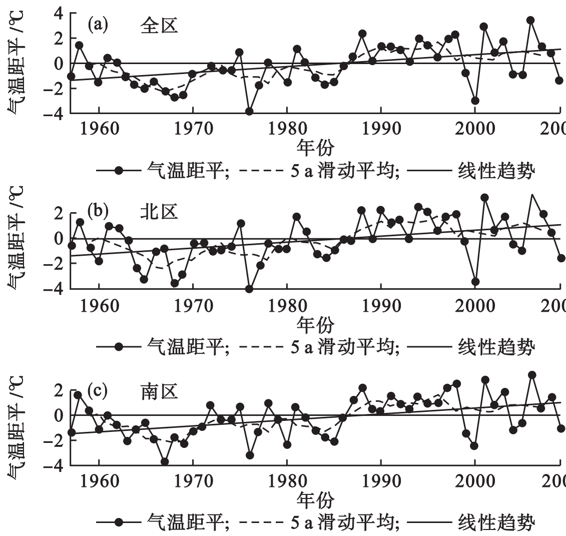

图3 1957—2009年全区(a)和北区(b)及南区(c)气温距平变化趋势

Fig. 3 The trends of air temperature anomalies in the study area(a),the north subregion(b) and the south subregion(c) from 1957 to 2009

开始,气温呈不断上升趋势。

从偏暖年份看,20世纪80年代中期以后的年份也明显增多。80年代以前,没有距平超过1个标准差的暖年;而以后却出现了8个距平超过1个标准差的偏暖年份,而且温暖程度也越来越大。记录中最暖的2006年温度距平值为2.3倍标准差。最近20 a为东北冬季最暖,其中2006年冬季最暖。

图4给出了东北地区冬季气温的线性倾向率的

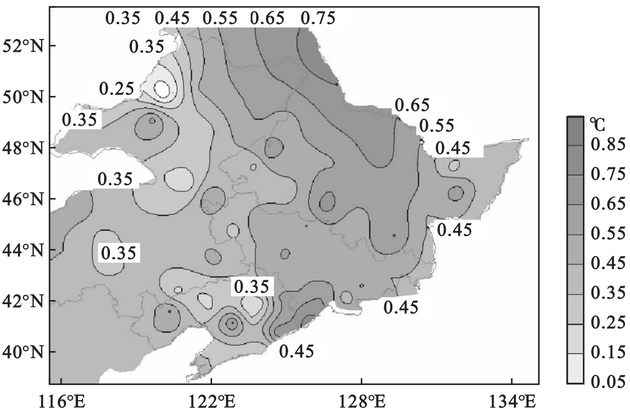

图4 中国东北冬季气温线性倾向率的等值线分布

Fig. 4 Contour distribution of liner tendency ratio of winter air temperature over the northeast China

等值线分布。1957—2009年黑龙江省东北部地区增长趋势最为显著,达到0.8 ℃/10 a,而西部增长相对较慢,东北地区气温平均升高了0.45 ℃/10 a(或)以上。与王绍武[2]中国1951—2001年年平均气温变化趋势,东北最大升温达到了0.8/10 a和李春等[4]指出东北地区气温最大升温超过了0.7/10 a,平均升高0.5/10 a或以上,比较一致。

为减少区域平均时人为因素的影响,使用全区、南、北子区EOF第1特征向量对应的时间系数标准化值为对应区域冬季平均气温距平序列,用来反映冬季平均气温的冷暖异常变化。考虑到所用资料为53 a,冷暖冬年的气候概率不宜过大,也不宜太小,以冬季平均气温距平大于(小于)1.0(-1.0)倍标准差作为确定冬季冷暖的标准。

表2表明,东北南、北两子区的冷、暖冬年有较

表2 中国东北各区异常冷暖冬年

Table 2 Abnormal cold and warm winter years in the different regions of the northeast China

北区		南区		全区	
冷冬年	暖冬年	冷冬年	暖冬年	冷冬年	暖冬年
1964	1988	1966	1958	1967	1988
1965	1990	1967	1988	1968	1991
1968	1994	1969	1991	1969	1994
1969	1995	1976	1994	1976	1997
1976	1997	1980	1997	1980	1998
1977	1998	1984	1998	1985	2001
2000	2001	1985	2001	2000	2003
–	2003	2000	2003	–	2006
–	2006	–	2006	–	–
–	2007	–	2008	–	–

大的不同。1957—2009年两者共同的冷冬年只有3 a,暖冬年有7 a,共同异常冷暖冬年份约占全部年份的50%。冷冬年集中发生在20世纪60—70年代,暖冬年集中发生在90年代以后,且暖冬年发生强度和频率有显著增加趋势,冷冬年发生强度和频率则显著减小。这一结果与前人研究获得的东北地区冬季气候明显变暖的结论完全一致[5]。

2.2 冬季平均气温与环流指数的相关性

2.2.1 与同期和前期环流指数的关系

用东北各区冬季平均气温距平序列与同期经向纬向环流指数进行相关,发现中国东北冬季气温和欧亚纬向环流指数、亚洲纬向环流指数呈正相关。其中与欧亚纬向环流指数相关最强,南区相关系数最高为0.69,显著性水平$\alpha<0.001$(表3),因此,欧

表3 中国东北冬季气温与环流指数的相关关系

Table 3 The correlation coefficient between winter air temperature and circulation index over the northeast China

项目	北区	南区	全区	显著性水平α
欧亚纬向环流指数(IZ,0°—150°E)	0.555	0.691	0.668	0.001
亚洲纬向环流指数(IZ,60°—150°E)	0.435	0.648	0.594	0.01
东亚槽位置(CW)	0.354	0.367	0.377	0.01
东亚槽强度(CQ)	0.464	0.289	0.368	0.05

亚纬向环流的强弱是影响冬季中国东北地区气温高低的重要因子,其中对南部影响最为显著。在异常发展的纬向型环流控制下,东亚大槽偏浅,西风带波动振幅不大且快速东移,高空西风气流强盛,中国东北地区冬季气温异常偏高。

图5给出了欧亚纬向环流指数与中国东北90站冬季平均气温的同期相关系数。同样可以看出,大部分站点具有显著的正相关,南部地区相关系数高达 0.75,北部地区相关较低,但多数台站也通过了 $\alpha<0.01$ 的显著性水平检验,表明东北地区冬季平均气温与欧亚纬向环流指数有较高的正相关性。

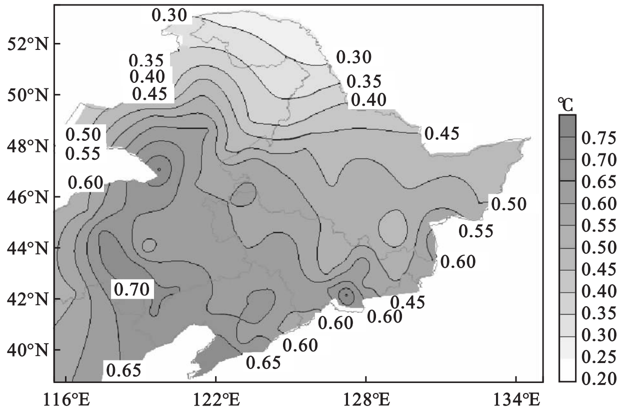

图 5　欧亚纬向环流指数与中国东北 90 站冬季气温同期相关系数分布

Fig. 5　The distribution of correlation coefficient between the simultaneous Eura-Asian zonal circulation index and winter air temperature from 90 weather stations over the northeast China

用前一年 1 月至前一年 11 月的 74 项环流指数,计算持续时间分别为 1 个月、2 个月、3 个月 30 种月季组合,共得到备选环流指数因子数 2220(74 × 30)个。求其与东北各区冬季平均气温距平序列之间相关发现,东北冬季气温与前期 10 个副热带高压面积指数呈现较显著正相关关系(表 4),与前期 5 个极涡面积指数呈现较显著负相关关系(表 5)。相关性在不同区域存在较大差异以及较大的月季差别。

其中前期 8 月东太平洋副热带高压面积指数、前期 7—8 月北美大西洋副热带高压面积指数与中国东北冬季气温相关最好,超过0.55(显著性水平 $\alpha<0.001$)。前期夏季 6—8 月北半球副热带高压面积指数、北美大西洋副热带高压面积指数、北美副热带高压面积指数和太平洋副热带高压面积指数相关均较好,最大相关系数超过 0.5(显著性水平 $\alpha<0.001$)。总体来说,中国东北北区相关性好于南

表 4　中国东北冬季气温与前期夏季副热带高压指数的相关关系

Table 4　The correlation coefficient between winter air temperature and summer subtropical high index over the northeast China

副热带高压指数	前期夏季 6—8 月			前期 7—8 月			前期 8 月			显著性水平 α
	北区	南区	全区	北区	南区	全区	北区	南区	全区	
北半球副热带高压面积指数(5°E—360°)	0.505	0.481	0.511	0.538	0.502	0.537	0.556	0.477	0.528	0.001
北非副热带高压面积指数(20°W—60°E)	0.214	0.312	0.287	0.247	0.321	0.306	0.303	0.310	0.320	0.050
北非大西洋北美副热带高压面积指数(110°W—60°E)	0.448	0.465	0.478	0.478	0.486	0.503	0.494	0.433	0.475	0.010
西太平洋副热带高压面积指数(110°E—180°)	0.456	0.415	0.449	0.464	0.402	0.444	0.427	0.343	0.391	0.050
东太平洋副热带高压面积指数(175°W—115°W)	0.472	0.416	0.456	0.514	0.458	0.499	0.553	0.476	0.526	0.001
北美副热带高压面积指数(110°W—60°W)	0.544	0.500	0.539	0.560	0.529	0.563	0.536	0.446	0.500	0.001
大西洋副热带高压面积指数(55°W—25°W)	0.428	0.410	0.433	0.519	0.459	0.502	0.426	0.328	0.379	0.010
南海副热带高压面积指数(100°E—120°E)	0.362	0.401	0.403	0.413	0.444	0.451	0.385	0.401	0.412	0.010
北美大西洋副热带高压面积指数(110°W—20°W)	0.541	0.502	0.538	0.583	0.541	0.580	0.560	0.456	0.515	0.001
太平洋副热带高压面积指数(110°E—115°W)	0.483	0.432	0.471	0.512	0.451	0.494	0.535	0.448	0.501	0.001

表 5　中国东北冬季气温与前期极涡指数的相关关系

Table 5　The correlation coefficient between winter air temperature and polar vortex index over the northeast China

极涡指数	前期 8 月			前期 10 月		
	北区	南区	全区	北区	南区	全区
亚洲区极涡面积指数(1 区,60°E—150°E)	−0.413	−0.358	−0.395	−0.533	−0.485	−0.525
太平洋区极涡面积指数(2 区,150°E—120°W)	−0.428	−0.350	−0.396	−0.337	−0.310	−0.334
北美区极涡面积指数(3 区,120°W—30°W)	−0.294	−0.208	−0.250	−0.095	−0.063	−0.078
大西洋欧洲区极涡面积指数(4 区,30°W—60°E)	−0.302	−0.296	−0.311	−0.129	−0.078	−0.100
北半球极涡面积指数(5 区,0°—360°)	−0.535	−0.456	−0.506	−0.375	−0.313	−0.351

区,7—8 月好于夏季。8 月东太平洋副热带高压面积指数相关性达到最高。

中国东北冬季气温与前期 10 月亚洲区极涡面积指数、前期 8 月北半球极涡面积指数相关最好,最大相关系数绝对值均超过 0.5,显著性水平达到 $\alpha<0.001$,其中中国东北北区相关性又好于南区。中国东北冬季气温与前期其他区域极涡面积指数相关性一般不高,仅与前期 8 月太平洋区极涡面积指数呈现较显著的负相关关系。

2.2.2 主要前期影响因子的选取与预测

根据以上冬季气温与前期副热带高压和极涡面积指数的相关分析结果,选取超过 0.001 显著性水平的相关因子,并用多元回归方法计算最优预测因子,得到关键因子:前期 8 月东太平洋副热带高压面积指数(175°—115°W)X_1,前期 10 月亚洲区极涡面积指数(1 区,60°E—150°E)X_2,前期 8 月北半球极涡面积指数(5 区,0°—360°)X_3,建立中国东北回归预测方程。

全区:$Y=0.243X_1-0.301X_2-0.323X_3 \quad R=0.67 \quad F=13.33$

北区:$Y=0.267X_1-0.290X_2-0.346X_3 \quad R=0.70 \quad F=15.52$

南区:$Y=0.242X_1-0.292X_2-0.225X_3 \quad R=0.61 \quad F=9.69$

以上各式均通过了显著性水平为 0.01 的 F 检验,$F \gg F_{0.01}(3,40)=4.31$。复相关系数分别为 0.67、0.70、0.61。北区和全区冬季平均气温与所选取的前期环流因子复相关系数较高。

图 6 给出关键因子多元回归值(图 6 中折线)与

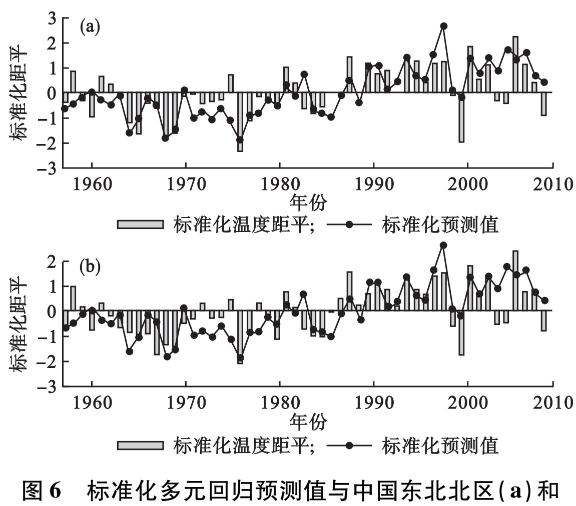

图 6 标准化多元回归预测值与中国东北北区(a)和全区(b)冬季气温标准化距平的比较

Fig. 6 Comparison of standardized predicted values by multi-variable regression and standardized anomalies of winter air temperature in the north subregion(a) and the whole study area(b)

冬季平均气温距平序列的关系。可见,两者对应关系较好。

表6分别列出各个区域冷冬年、暖冬年及对应

表 6 中国东北冷暖冬年及对应的预测值

Table 6 The cold and warm winter years and their corresponding forecast values over the northeast China

北区				全区			
冷年	预测值	暖年	预测值	冷年	预测值	暖年	预测值
1964*	−1.6268	1988	0.5448	1967	−0.4332	1988	0.5292
1965*	−1.1224	1990*	1.0328	1968*	−1.8564	1991*	1.1225
1968*	−1.8578	1994*	1.3950	1969*	−1.5474	1994*	1.4078
1969*	−1.5153	1995	0.6905	1976*	−1.9021	1997*	1.5904
1976*	−1.8682	1997*	1.5459	1980	−0.5676	1998*	2.6322
1977#	−0.9383	1998*	2.6359	1985#	−0.8696	2001*	1.3906
2000	−0.1575	2001*	1.4347	2000	−0.2344	2003*	1.3657
–	–	2003*	1.3843	–	–	2006*	1.4102
–	–	2006*	1.3911	–	–	–	–
–	–	2007*	1.5750	–	–	–	–

注:* 为大于(小于)1.0(−1.0);#为接近 1.0(−1.0)。

的模型预测值。根据大于(小于)1.0(−1.0)倍标准差作为确定冬季冷暖的标准,1957—2009 年,北区 80% 的暖冬年和 80% 冷冬年可以预测出,全区 87% 的暖冬年能够预测出来,而冷冬年仅有 50% 能预测出来。因此,本文所建立的统计预测模型对东北地区冷、暖冬年具有一定预测能力,尤其是暖冬年,误报率较低。

图7给出利用后10 a独立样本资料计算获得的

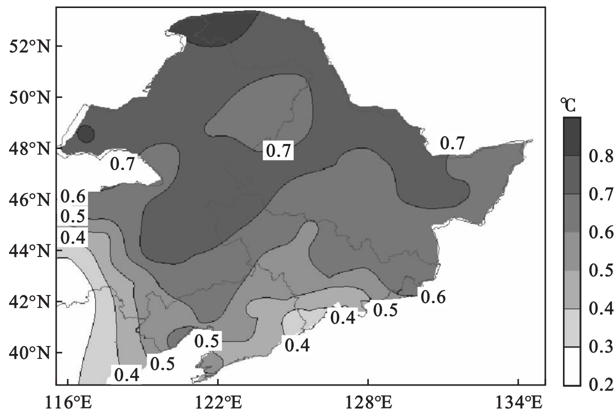

图 7 冷暖冬年模型预报值与观测值相关系数空间分布

Fig. 7 The spatial distribution of correlation coefficient between forecast values and observational values of cold and warm winter years

各站预测值与实际观测值之间的相关系数分布情况。平均相关系数 $r=0.61$,大部分区域在 0.60 以上,北区大部超过 0.70。由于 10 a 独立样本试验容量不大,有相当大的随机性。仅有的 2000 年和 2009 年两个冷冬年均成功地预测出来,2001 年和 2006 年两个暖冬预测出一个。除了 2005 年,距平超过 0.5

倍标准差的冷暖年份趋势均报对。说明其具有一定的预测能力。

2.3　冷暖冬年同期环流异常特征与成因

合成冷,暖冬年的同期 500 hPa 高度场和海平面气压距平场(图略)。在暖冬年,欧亚大陆的中纬度地区是大面积的正距平,欧亚大陆的高纬度地区为负距平。这种北低南高的位势高度距平场的配置使得欧亚纬向环流占优势,极涡在亚洲的活动范围减小,强度减弱。西风带波动振幅不大且快速东移,高空西风气流强盛,气流北侧靠近高纬度地面气压为负距平。在气流南侧气压为正距平。距平场的上述特征,抑制了冷暖气团的经向交换,加上高纬度空气持续冷却,中纬度增温稳定维持,最终在高纬度出现气温负距平,中纬度出现气温正距平,中国东北地区出现暖冬年。冷冬年的位势高度距平场分布与暖冬年基本呈现出相反分布,欧亚大陆的中纬度地区为负距平控制,高纬度表现为正距平,使得冷冬年在中高纬度地区盛行经向环流。在这样的环流形势背景中,极地的冷空气在西风带的偏北气流引导下,源源不断地向南入侵,造成中纬度的中国东北地区气温异常偏低,出现冷冬年。

从表 4—表 5 可以看出,极涡与东北气温呈显著负相关,副热带高压与东北气温呈正相关关系,如果 8 月和 10 月极涡面积显著收缩,通常后期冬季中国的大部分地区气温上升;反之,若当年 8 月和 10 月的极涡面积显著扩展,那么冬季中国东北地区气温有下降趋势;尤其是当前期亚洲区极涡面积扩大(缩小),冬季气温显著下降(上升)。从夏季同期 500 hPa高度距平场可以看出,当极涡面积异常偏大(偏小),反映副热带高压的 588 线主体也偏小(偏大)、偏南(偏北),即北半球副热带高压面积偏小(偏大)。

3　结论与讨论

(1)根据 REOF 分析,东北地区气温分布可分为两个区域:以辽宁渤海湾为中心的南部地区,以黑龙江北部为中心的北部地区。

(2)各分区冬季气温变化的特征,表现为一致的上升趋势,上升的幅度以北部地区为最大,其次是南部地区,西部地区温度上升最缓慢。冷冬年发生在 20 世纪 80 年代以前,暖冬年发生在 90 年代以后,南北区冷暖差异较明显。

(3)用前一年 1 月至前一年 11 月的 74 项环流指数,分别计算了持续时间为 1 个月、2 个月、3 个月 30 种月季组合,共 2220 个备选因子数。选取超过 0.001 显著性水平的相关因子,建立“最优”回归方程,得到两个极涡面积指数和一个副热带高压面积指数为中国东北冬季气温的最优预测因子;冷、暖冬年预测可以将选定时段和区域的极涡和副热带高压面积指数作为一个重要的影响因素,且误报率较低。

参考文献

[1]　王绍武. 现代气候学研究进展[M]. 北京:气象出版社,2001:80 - 87.

[2]　王绍武,蔡静宁,朱锦红,等. 中国气候变化的研究[J]. 气候与环境研究,2002,(2):137 - 145.

[3]　任国玉,初子莹,周雅清. 中国气温变化研究最新进展[J]. 气候与环境研究,2005(4):701 - 716.

[4]　李春,方之芳. 北极涛动与东北冬季温度的联系[J]. 高原气象,2005,24(6):927 - 934.

[5]　陈峪,任国玉,王凌,等. 近 56 年我国暖冬气候事件变化[J]. 应用气象学报,2009,20(5):539 - 545.

[6]　周雅清,任国玉. 中国大陆 1956—2008 年极端气温事件变化特征分析[J]. 气候与环境研究,2010,15(4):405 - 417.

[7]　丁一汇,任国玉,石广玉,等. 气候变化国家评估报告(Ⅰ):中国气候变化的历史和未来趋势[J]. 气候变化研究进展,2006,2(1):3 - 8.

[8]　孙凤华,袁天翊. 东北冬季气温异常与全球前期海温的关系及可预测性分析[J]. 安徽农业科学,2009,37(35):17806 - 17809.

[9]　陈佩燕,倪允琪,殷永红. 近 50 年来全球海温异常对我国东部地区冬季温度异常影响的诊断研究[J]. 热带气象学报,2001,17(4):371 - 380.

[10]　张卫青,钱永甫. 全球海气相互作用关键区及区内气候特征分析[J]. 热带气象学报,2001,17(1):23 - 33.

[11]　杨素英,王谦谦,孙凤华. 中国东北南部冬季气温异常及其大气环流特征变化[J]. 应用气象学报,2005(3):334 - 344.

[12]　侯伟芬,王谦谦,刘燕. 江南地区夏季气温异常与全球海温异常的相关关系[J]. 南京气象学院学报,2004,27(4):539 - 544.

[13]　王光宇,曾群柱. 北半球雪盖与我国夏季气温的相关分析[J]. 冰川冻土,1994,16(1):49 - 52.

[14]　陈寅生,陈隆勋. 北极冰盖对我国气温和降水的影响[J]. 南京气象学院学报,1994,17(1):51 - 57.

[15]　陈明轩,管兆勇,徐海明. 冬春季格陵兰海冰变化与初夏中国气温、降水关系的初步分析[J]. 高原气象,2003,22(1):7 - 13.

[16]　许利,毕云,钱永甫. 青藏、伊朗高原春夏季高层热力异常与我国夏季气温的关系[J]. 高原气象,2004,23(3):323 - 329.

[17]　龚道溢,朱锦红,王绍武. 西伯利亚高压对亚洲大陆的气候影响分析[J]. 高原气象,2002,21(1):8 - 14.

[18]　王永波,施能. 夏季北大西洋涛动异常与我国天气气

候的关系[J]. 气象科学,2001,21(3):271 -278.
[19] 何春,何金海. 冬季北极涛动和华北冬季气温变化关系研究[J]. 南京气象学院学报,2003,26(1):1 -7.
[20] Bretherton C S,Smith C,Wallace J M. An intercomparison of methods for finding coup led patterns in climate data[J]. Journal of Climate,5(6):541 -560.
[21] Wallace J M,Smith C,Brethert on C S. Singular value decomposition of wintertime sea surface temperature and 500-mb height anomalies[J]. Journal of Climate,1992,5(6):561 -576. 17806 -17809.
[22] 魏凤英. 现在气候统计诊断预测技术[M]. 北京:气象出版社,1999:128 -134.
[23] Jones P D,Hulme M. Calculating regional climatic time series for temperature and precipitation:methods and illust rations[J]. International Journal of Climatology,1996,16(4):361 -377.
[24] 阮桂海. SPSS 实用教程[M]. 北京:电子工业出版社,2000:143 -146.
[25] 任国玉,郭军,徐铭志,等. 近50年中国地面气候变化基本特征[J]. 气象学报,2005,63(6):942 -956.
[26] 马开玉,丁裕国,屠其璞,等. 气候统计原理与方法[M]. 北京:气象出版社,1993:146 -165.

Winter temperature variability and its relationship with atmospheric circulation anomalies in Northeast China

SHEN Zhi-chao[1,2] REN Guo-yu[2] LI Jiao[1,3] SUN Xiu-bao[1,2]
(1. College of Atmospheric Sciences, Nanjing University of Information Science and Technology, Nanjing 210044, China; 2. Laboratory for Climate Studies of China Meteorological Administration, National Climate Center, Beijing 100081, China; 3. Tieling Meteorological Service, Tieling 112000, China)

Abstract: Based on air temperature data from 90 metrological stations in winter from 1957 to 2010 in the northeast China, the study area was divided into the south and north subregions in terms of winter air temperature using methods of a rotated empirical orthogonal function (REOF) and a cluster analysis. The variation trends of winter air temperature and warm and cold winter were analyzed, and their relationships with main circulation indexes were discussed. The optimum forecast factor was selected by a back-method, and regression models were built in the whole study area and two subregions. The results indicate that winter air temperature increases obviously in the northeast China, and the ratio reaches 0.45 ℃/10 a, especially in the north area. The correlation between winter air temperature and the simultaneous Euro-Asian zonal circulation indexes is significant. The subtropical high area index in August in the east Pacific Ocean, polar vortex area index in October in the Asia area and polar vortex area index in August in the north hemisphere are in the significantly positive correlations with winter air temperature, and their multiple correlation coefficients all reach 0.70. The above three factors are the key forecast factors in regression equations. If the subtropical high and polar area indexes are used as the important influencing factors when it forecast cold winter and warm winter, the forecast effect is good.

Key words: Northeast China; Winter air temperature; Rotated empirical orthogonal function (REOF); Circulation index; Correlation; Forecast

Decadal Change in the Correlation Pattern between the Tibetan Plateau Winter Snow and the East Asian Summer Precipitation during 1979–2011

DONG SI AND YIHUI DING

National Climate Center and Laboratory for Climate Studies, China Meteorological Administration, Beijing, China

(Manuscript received 7 August 2012, in final form 21 March 2013)

ABSTRACT

Observational evidence indicates that the correlation between Tibetan Plateau (TP) winter snow and East Asian (EA) summer precipitation changed in the late 1990s. During the period 1979–99, the positive correlation between the TP winter snow and the summer precipitation along the Yangtze River valley (YRV) and southern Japan was disrupted by the decadal climate shift. In contrast, the summer precipitation over the Huaihe River valley (HRV) and the Korean Peninsula showed a strong positive correlation with the preceding winter snow over the TP during the period 2000–11.

The radiosonde temperature measurements over the TP show a pronounced warming since the late 1990s. This warming is associated with the significant increase in surface sensible heat flux and longwave radiation into atmosphere. The latter is closely related to the decrease of surface albedo and the soil hydrological effect of melting snow due to the decadal decrease in the preceding winter and spring snow over the TP. The TP warming induced by the decrease in winter snow, together with the cooling of the sea surface temperature in the tropical central and eastern Pacific, intensifies the land–sea thermal contrast in the subsequent spring and summer over EA, thus causing a northward advance of the EA summer monsoon. Accompanying the northward migration of the summer monsoon, the summer precipitation belt over EA shifts northward. Consequently, the high summer precipitation region over EA correlating with the preceding winter snow over the TP has shifted northward from the YRV and southern Japan to the HRV and the Korean Peninsula since the late 1990s.

1. Introduction

The Tibetan Plateau (TP), which has an average altitude of approximately 4 km, is one of the earth's most complex geographical features. The TP serves not only as a physical barrier but also as an elevated heat source that establishes a thermal contrast between the plateau and surrounding cooler air in the summer (Ding 1992). The combination of these two significant effects appears to be a central factor influencing the large-scale monsoon circulation over East Asia (EA) (e.g., Flohn 1957; Li and Yanai 1996). The seasonal cycle and interannual variation in the EA summer monsoon rainfall are known to be closely related to variations in TP heating (Ye and Gao 1979; Tao and Ding 1981; Hsu and Liu 2003; Wu and Qian 2003; Zhao et al. 2007). Zhang et al. (2004) and Ding et al. (2009) examined the relationship between winter and spring snow cover over the TP and the decadal variations of the EA summer monsoon rainfall based on the observed data for the period from the 1960s to 1990s. Correlation analysis documented that the TP winter snow has a significant positive correlation with the subsequent summer precipitation along the Yangtze River valley (YRV; 28°–31°N, 110°–120°E) in China. It is proposed that an increase in the winter snow cover over the TP is closely related to a significant reduction in surface sensible heat flux and a subsequent cooling over the TP and its surrounding atmosphere. The cooling is caused by the surface albedo and soil hydrological effect of melting snow owing to the snow increase over the TP. TP cooling thus reduces the land–sea thermal contrast during summer over EA, leading to a weak EA summer monsoon, which brings more precipitation to the YRV (Ding et al. 2009).

Recently, Si et al. (2009) found that summer precipitation in EA exhibited a decadal shift in the late 1990s. During the 1980s and 1990s summer precipitation was mainly concentrated along the YRV. Since the late 1990s the precipitation belt has shifted northward to the

Corresponding author address: Dr. Dong Si, National Climate Center, China Meteorological Administration, No. 46 Zhongguancun South Street, Haidian District, Beijing, 100081, China.
E-mail: sidong@cma.gov.cn

DOI: 10.1175/JCLI-D-12-00587.1

Huaihe River valley (HRV; 31°–33°N, 110°–120°E), which has an average distance of 200–300 km from the YRV. However, the winter snow cover over the TP has shown a significant decreasing trend since the late 1990s. That is to say, both the TP winter snow and the EA summer precipitation have undergone a decadal change in the late 1990s, which naturally raises questions as to whether the TP snow–EA precipitation correlation pattern also experienced a similar change in the late 1990s and, if so, what new correlation pattern between the TP winter snow and the subsequent summer precipitation over EA has been established. With these questions in mind, we will examine the decadal change in the correlation between the TP winter snow and the EA summer precipitation in the last decade. Additionally, a physical mechanism responsible for the change in the TP snow–EA precipitation correlation in the last decadal period is discussed.

This paper is arranged as follows. Section 2 describes the datasets used in this study. In section 3, we document the decadal decreases in the winter and spring snow over the TP, while in section 4 we examine the decadal changes in summer precipitation over EA in the last decade. In section 5, we compare the correlation patterns of the winter snow cover over the TP with summer precipitation in EA between the two periods of 1979–99 and 2000–11. Plausible causes for these changes are discussed in section 6. A summary is provided in section 7.

2. Data

The main observational data analyzed in this study include the following products.

1) The daily surface-observed snow depth, wind speed, air temperature, soil temperature, and pressure data used in this study are from the National Meteorological Information Center (NMIC) of the China Meteorological Administration (CMA). The monthly data are derived from daily data. Because surface observing stations in the western TP begin providing operational observations since the late 1970s, our research is performed using data records starting from 1979 to add more observations in the western TP. In this study, 72 stations (Fig. 1) located where there is good temporal continuity in meteorological observations are used. The quality control of this dataset was made by the NMIC of the CMA.
2) Monthly station rainfall data include 160 stations in China, 11 stations in southern Japan, and 8 stations in South Korea. The Chinese station data are provided by the National Climate Center of the CMA included information from 160 stations, of which we chose 46 stations located in east China. Station data in southern Japan and South Korea are derived from the Global Historical Climate Network (GHCN) of the National Climate Data Center (NCDC) of the National Oceanic and Atmospheric Administration (NOAA).

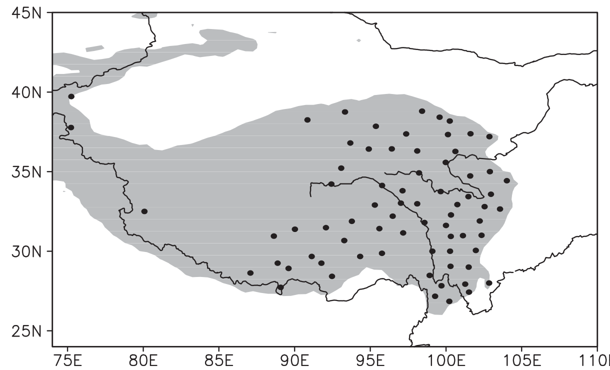

FIG. 1. Distribution of the 72 surface-observing stations (black dots) over the Tibetan Plateau. The shaded area (gray) indicates regions with an altitude above 2500 m.

3) Radiosonde temperature data (Guo and Ding 2009) are provided by the NMIC of the CMA. Twice-daily observational data at 0000 and 1200 UTC are combined into a merged daily radiosonde temperature dataset. The quality control of this dataset also was done by the NMIC of the CMA recently.
4) The National Aeronautics and Space Administration (NASA) Global Energy and Water Cycle Experiment (GEWEX) Surface Radiation Budget (SRB) release 3.1 dataset (Cox et al. 2006; Gupta et al. 2006) also is used in this study. This dataset uses International Satellite Cloud Climatology Project (ISCCP) clouds and radiance and other inputs to produce monthly mean upward and downward longwave radiative flux on a 1° latitude × 1° longitude resolution. The current release 3.1 covers the period from July 1983 through December 2007.
5) The atmospheric data are derived from the National Centers for Environmental Prediction (NCEP)–National Center for Atmospheric Research (NCAR) reanalysis dataset (Kalnay et al. 1996).
6) Monthly mean sea surface temperature (SST) data used are the optimum interpolated SST (OISST) dataset (Reynolds and Smith 1994) provided by NOAA at a 2° latitude × 2° longitude resolution.

3. Observed decreasing trend in the TP winter and spring snow

An examination of the observed snow depth data reveals that a prominent reduction in the winter and spring snow depth occurred throughout the TP during the last decade. Figure 2 depicts the time series of snow depths

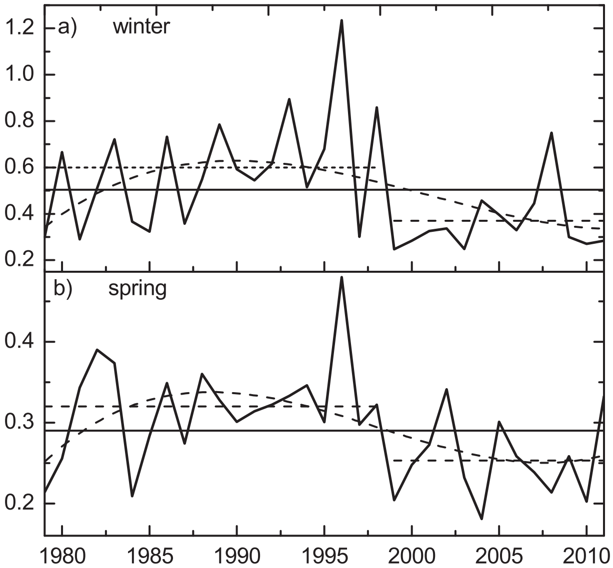

FIG. 2. Time series of (a) winter and (b) spring snow depth (cm day^{-1}) over the Tibetan Plateau, averaged for the 72 stations from 1979 to 2011. The dashed curve indicates the third-order polynomial fit. The horizontal dashed lines indicate averaged values for the two decadal periods 1979–99 and 2000–11. The horizontal solid lines indicate averaged values for the period 1979–2011.

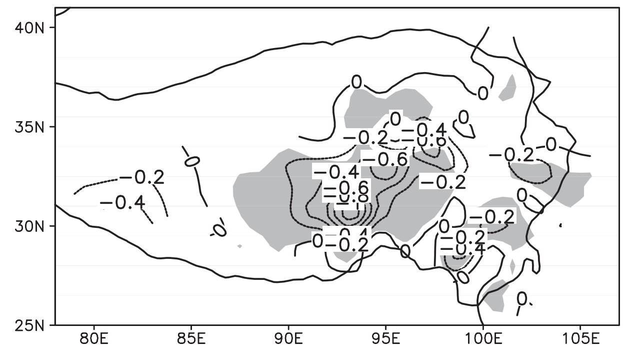

FIG. 3. Changes (2000–11 mean minus 1980–99 mean) in winter snow depth (cm day^{-1}) over the Tibetan Plateau based on the surface-observed data. The shaded areas are statistically significant at the 95% confidence level according to a Student's *t* test.

over the TP averaged for the 72 stations in winter and spring during the period 1979–2011. It can be seen that the winter and spring snow depth over the TP experienced a distinct decadal change in the late 1990s. This decadal change point is further confirmed by the Yamamoto method and Mann–Kendall method. The snow depth increases greatly from 1979 to 1996 and then decreases abruptly from 1996 to 1999. Since 1999 snow depth remains low except in winter 2008, possibly due to interannual variation. The average winter snow depth is 0.6 cm day^{-1} during 1979–99, but it drops to an average of 0.37 cm day^{-1} for the period 2000–11. The average spring snow depth is 0.32 cm day^{-1} during 1979–99, but it drops to an average of 0.25 cm day^{-1} for the period of 2000–11. Figure 3 presents the decadal change (2000–11 mean minus the 1979–99 mean, as below) in the winter snow depth over the TP. The regions experiencing significant snow reduction cover the majority of the TP.

4. Summer precipitation changes in East Asia

In tandem with a reduction in winter and spring snow throughout the TP, the precipitation and large-scale atmospheric circulation in EA have experienced considerable changes. Recently, Si et al. (2009) found that the summer precipitation in east China exhibited a substantial decadal shift in the late 1990s. Before 1999, the main precipitation belt was located along the YRV; subsequently, it has steadily shifted northward to the HRV.

Figure 4 displays the difference in summer precipitation patterns between 2000–11 and 1979–99 in east China. The most notable features are the two coherent zonal bands of precipitation anomalies, with opposite signs, over the YRV and HRV. One zonal area of negative anomalies is found along the YRV. Across the HRV, large precipitation anomalies with opposite signs are also observed. This pattern resembles the second leading mode of the empirical orthogonal function (EOF) analysis for the summer precipitation in east China in Si et al. (2009). Si et al. analyzed the spatial and temporal variation of the summer precipitation over the YRV and HRV and found that the second leading mode accounted for 21% of the total variance. This mode was characterized by a seesaw between the YRV and HRV (see Si et al. 2009, Fig. 1d). The time coefficients of the second leading mode also displayed an abrupt phase transition from negative to positive in the late 1990s (see Si et al. 2009, Fig. 1e). This change indicates that the summer precipitation has increased over the HRV but decreased over the YRV since the late 1990s.

Figure 5 shows the spatial pattern of contemporaneous correlation between the time series of summer precipitation averaged over the YRV/HRV and summer precipitation series of each of the 65 stations in EA. The most striking feature revealed by this figure is that the precipitation variations over southern Japan and Korean Peninsula are in phase with precipitation over YRV/HRV, showing a positive relationship. This correlation pattern also agrees with the results of Ninomiya and Akiyama (1992) and Ding and Chan (2005), who found that the mean summer precipitation belt over EA is normally elongated and narrow, extending from east China to southern Japan.

Therefore, the decadal change in the summer precipitation over east China in the late 1990s is not a local phenomenon but is connected to the shift in the large-scale

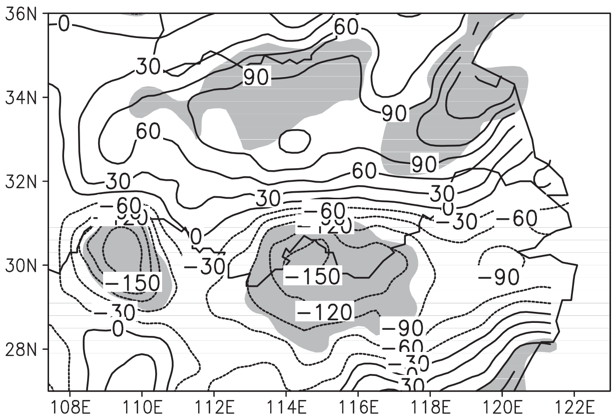

FIG. 4. Changes (2000–11 mean minus 1980–99 mean) in total summer precipitation (mm) over east China. The shaded areas are statistically significant at the 95% confidence level according to a Student's *t* test.

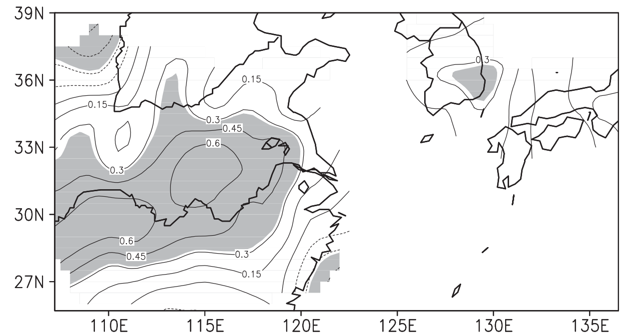

FIG. 5. Correlation map between the summer precipitation over the Yangtze River and Huaihe River valleys averaged for the 46 stations and summertime precipitation over East Asia for 1979–2011. The shaded areas are statistically significant at the 95% confidence level.

precipitation regime over EA. For southern Japan, the precipitation is also relatively high during the 1980s and 1990s, but relatively low during the 2000s. In contrast, the summer precipitation levels on Korean Peninsula are relatively low during the 1980s and 1990s but are comparatively high during the 2000s (not shown). This trend implies that the primary summer precipitation belt, indeed, shifted northward throughout EA in the late 1990s.

The changes in summer precipitation patterns throughout EA are revealed by EOF analysis. The normalized observed summer [June–August (JJA)] precipitation in EA is used in the EOF analysis. The first EOF mode, which accounts for 16.6% of the total variance, displays a pattern of an elongated band of positive precipitation anomalies along the YRV, southern Japan, and southern South Korea and negative precipitation anomalies over other EA regions (Fig. 6a). The first EOF mode clearly indicates that the main precipitation belt extends from the YRV to southern Japan, and its time coefficient show a declining trend (Fig. 6b). The second EOF mode accounts for 14.2% of the total variance. The spatial pattern corresponds to coherent variations over HRV and the Korean Peninsula and opposite variations in YRV and the area south of YRV (Fig. 6c). Figure 6d illustrates the time coefficient of the second EOF mode, which shows an abrupt decadal change in the late 1990s. Moreover, the period from the early 1980s to 1990s is mainly in the negative phase of time coefficient, implying that it is wet in the YRV, the area south of YRV, and southern Japan but dry over the HRV and Korean Peninsula. Since the late 1990s the phase abruptly turns positive. This change implies the decadal northward shift of the precipitation belt. For the earlier decade (1979–99), the average value of absolute time coefficient of the first EOF mode is 2.51, while the average value of absolute time coefficient of the second EOF mode is 2.26. This result indicates that the YRV–southern Japan mode is the leading mode during 1979 to 1999. For the later decade (2000–11), the average value of absolute time coefficient of the first EOF mode is 2.09, while the average value of the second EOF mode is 2.82. The first leading EA summer precipitation mode distinctly changes from a YRV–southern Japan mode during 1979–99 to an HRV–Korean Peninsula mode in the last decade (2000–11), indicating a decadal northward shift in the summer precipitation belt in EA.

All of these results reveal that the summer precipitation patterns in East China and EA have both demonstrated a decadal change in the late 1990s. This decadal change is opposite to the previous one in the late 1970s. The decadal change in precipitation over EA occurred in the late 1970s with more precipitation in the YRV and southern Japan and less in the HRV and the Korean Peninsula since then (e.g., Hu 1997; Chang et al. 2000; Huang 2001; Wang 2001; Gong and Ho. 2002; Yu et al. 2004; Ding et al. 2009; Zhou et al. 2009).

5. Decadal change in the TP snow–EA precipitation correlation

The above analysis reveals that both TP winter snow and the ensuing EA summer precipitation underwent a dramatic decadal change in the late 1990s. In this section, we will examine whether the correlation between TP winter snow and the following summer precipitation in EA changed in the late 1990s.

To elaborate on the relationship between the above two elements for the time periods of 1979–99 and 2000–11, a correlation analysis is applied to the winter snow depth over the TP and the following summer precipitation in EA.

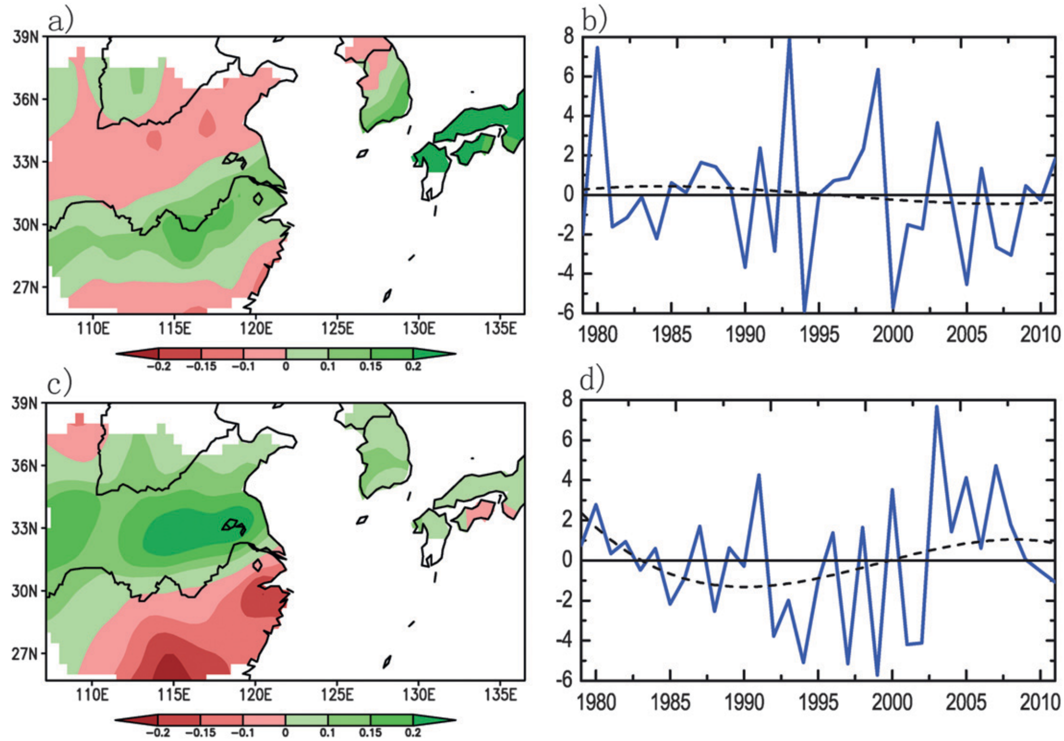

FIG. 6. Spatial pattern of (a) EOF1 and (c) EOF2 for summer precipitation and (b),(d) their corresponding time coefficient during 1979–2011. The dashed curves in (b),(d) indicate a third-order polynomial fit.

For the period 1979–99, the correlation map between the TP winter snow series (Fig. 2) and the summer rainfall in EA indicate a significant positive zonal band along the YRV and southern Japan (Fig. 7a). The correlation pattern obtained from the analysis implies that an above normal TP winter snow will be followed by increased precipitation along the YRV and southern Japan during the subsequent summer and vice versa.

However, for the period 2000–11 the correlation pattern changes radically and differs from the first period's pattern. The positive correlation shift northward from the YRV and southern Japan to the HRV and the Korean Peninsula, while a negative correlation along the YRV and southern Japan is detected (Fig. 7b). The result suggests that an above normal TP winter snow favors increased summer precipitation along the YHR–Korean Peninsula and decreased summer precipitation along YRV–southern Japan. This change implies a decadal change in the correlation pattern between the TP snow and the EA summer precipitation in the late 1990s.

6. Causes of the decadal change in the TP snow–EA precipitation correlation

We present a brief description in this section of why the regions of high correlation between the TP winter snow and the subsequent summer precipitation over East Asia have shifted northward from the YRV to the HRV. This may be closely related to the decadal reduction in the snow over the TP since the late 1990s. It is known that an anomalous preceding winter snow cover may affect the surface albedo and influence soil hydrology, which may further alter the soil moisture and surface and atmosphere temperature during the subsequent summer, thus leading to variations in the ensuing large-scale atmospheric circulation and the Asian summer monsoon (Liu and Yanai. 2002). Shukla (1984) and Shukla and Mooley (1987) pointed out that the memory of a winter snow anomaly in the climate system resides in the wetness of the subsurface soil as snow melts during spring and summer, which influences the soil and air temperature in the following summer and affects the regional monsoon circulation. Figure 8a illustrates the lagging effect of winter snow depth on the summer thermal condition over the TP by using a lead–lag correlation. We denote the high snow depth as year 0 and the following year as year 1. For the winter snow depth over the TP, the high snow depth peaks during January–February (1) and persists to early spring. Snow melting (Fig. 8a, red curve) begins to develop a significantly positive correlation with snow depth in March (1), which persists to April (1). Snow melting is a sink for latent heat;

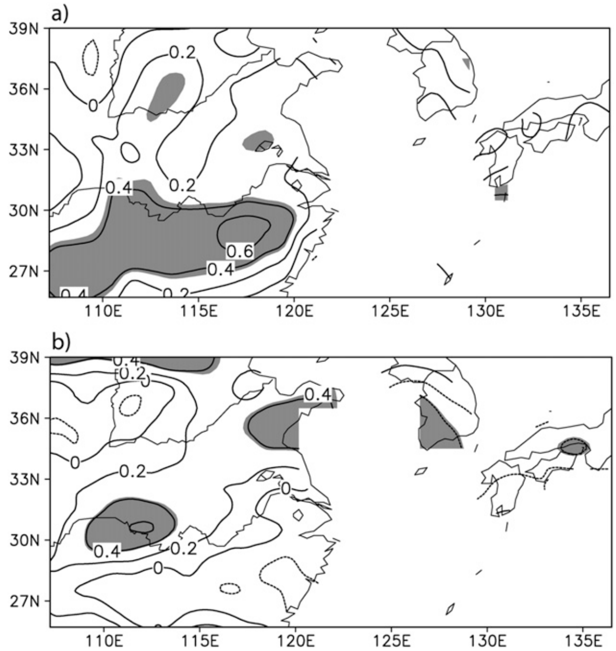

FIG. 7. Correlation between the winter snow depth over the Tibetan Plateau averaged for the 72 stations and the observed summer precipitation over East Asia for the period (a) 1979–99 and (b) 2000–11. Shaded areas are statistically significant at the 95% confidence level.

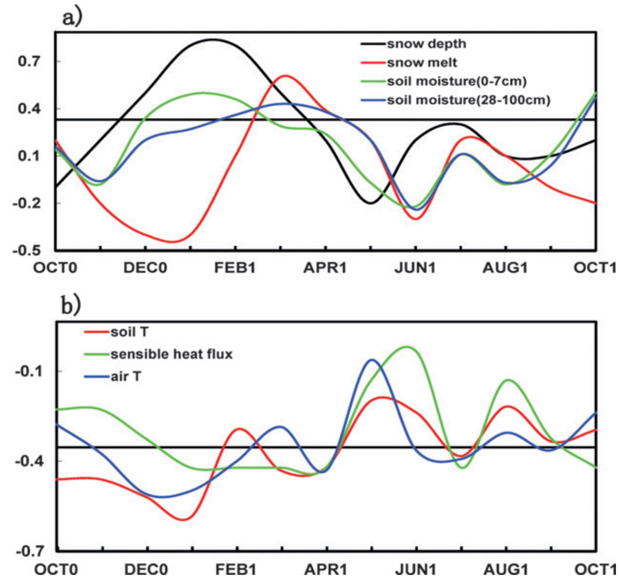

FIG. 8. (a) Correlation of the TP snow depth with the TP snowmelt (change of monthly snow depth, red curve), 0–7-cm-deep volumetric soil moisture (green curve), and 28–100-cm-deep volumetric soil moisture (blue curve) of the ECMWF Interim Re-Analysis for December (0)–February (1) at the 72 stations (29°–35°N, 90°–104°E) for the period 1979–2011. Note that the high snow-depth year designated as year 0 and following year as year 1. The black solid curve is for the autocorrelation of the TP snow depth with its December–February (DJF) values. (b). Correlation of the TP snow depth with the TP soil temperature (red curve), sensible heat flux (green curve), and air temperature (blue curve) for December (0)–February (1) at the 72 stations for the period 1979–2011.

snow melts to water that is available for evaporation, runoff, and to increase soil moisture by diffusion and gravitational transport (Vernekar et al. 1995). The top layer (0–7 cm) soil moisture (Fig. 8a, green curve) anomalies have a moderate persistence from winter to mid spring. High persistence is seen in the middle layer (28–100 cm) soil moisture (Fig. 8a, blue curve) and persists to late spring. This result is consistent with a longer persistence of soil moisture for the middle layer than the top layer in an earlier analysis of a numerical simulation by Wang et al. (2009). A significantly negative correlation with soil temperature (Fig. 8b, red curve), sensible heat flux (Fig. 8b, green curve), and air temperature (Fig. 8b, blue curve) persists from December (0) to March (1). This is largely because of the snow albedo effect. When snow is present on the ground, the soil and air temperature is colder than without snow. After March (1), a large amount of snow melts and effectively decreases the snowpack and the albedo effect. Snowmelt water increases not only the soil moisture but also the heat capacity of the soil. The air temperature retains a high negative correlation long after all of the snow is melted because of the large heat capacity of the wetter surface. However, air temperature is not significantly correlated with the winter snow depth in May (1) when most of the snow over the TP has melted. In summary, the air temperature over the TP is low because of the snow albedo effect in winter, heat loss energy used in melting snowpack, and the larger heat capacity of the wetter soil from spring and summer.

The anomalous snow condition over the TP may significantly affect the TP heating field. Based on previous estimates of heat sources and sinks over the TP in summer, the surface sensible heat flux is a dominant component of atmospheric heating field over the TP, especially over the western part of the TP (Ye and Gao 1979; Nitta 1981; Murakami and Ding 1982; Luo and Yanai 1984). Ye and Gao (1979) computed various components of long-term mean heat balanced over the TP and their seasonal variations, and pointed out that the sensible heating is the primary factor in atmospheric heating sources over the entire TP until the rainy season occurs.

We have estimated sensible heat flux by using the 72 station observed data. The sensible heat (H) is calculated by

$$H = \rho c_p C_H U (T_s - T_a), \tag{1}$$

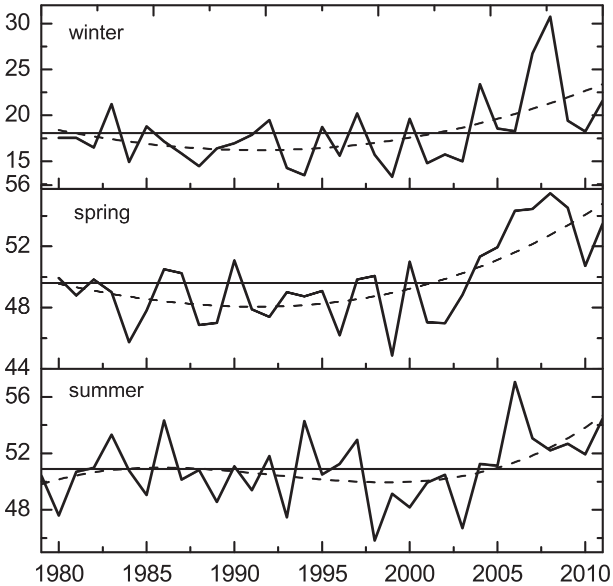

FIG. 9. Seasonal-mean sensible heat fluxes (W m^{-2}) over the TP averaged for the 72 stations for (a) winter, (b) spring, and (c) summer. The dashed curve indicates a third-order polynomial fit; horizontal solid lines indicate averaged values for the period of 1979–2011.

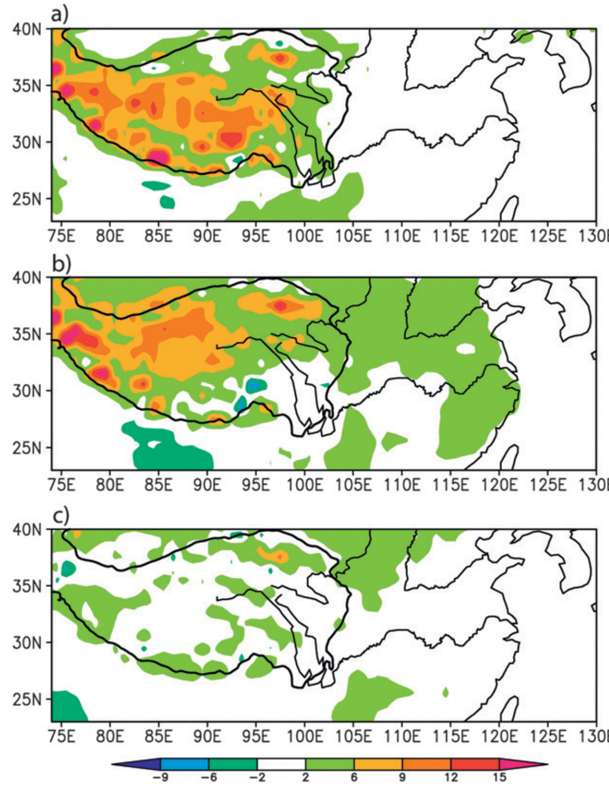

FIG. 10. Changes (2000–07 mean minus 1984–99 mean) in the surface longwave radiation ratio (%) (upward flux/downward flux) in (a) winter, (b) spring, and (c) summer.

where ρ is air density, C_p the specific heat at a constant pressure, U the wind speed, T_s the soil temperature, T_a is near-surface air temperature, and

$$C_H = 0.0012 + 0.01/U \tag{2}$$

(Chen and Wong 1984).

Figure 9 shows the seasonal mean sensible heat fluxes over the TP averaged for the 72 station during the period 1979–2011. Significant increasing trends in sensible heat flux, derived by using a third-order polynomial fit, are obvious in all three seasons since the late 1990s. The trend in summer is 0.6% decade^{-1}. It is in winter when the trend is most notable, 1.6% decade^{-1}. The trend in spring is comparably strong, 1.5% decade^{-1}.

Additionally, TP warming is an important factor driving the Asian summer monsoon. The seasonal variation in TP heating is closely associated with the anomalous reversal of the zonal thermal contrast in the Asian monsoon region. This variation, therefore, may influence the large-scale atmospheric circulation and summer monsoon in EA (Flohn 1957; Yanai et al. 1992; Li and Yanai 1996; Wu and Zhang 1998; Wang et al. 2008). Figure 10 shows the decadal changes in surface longwave radiation ratio (surface longwave upward flux/downward flux) over the TP. For winter, the decadal difference in surface longwave radiation ratio is positive over the entire plateau; that is, it represents the TP warming over most of the TP in the later decade, with surface longwave radiation ratio increasing by 2%–9%—even by 9%–15% in a few regions. A similar difference between the two periods, but with a relative smaller warming tendency, also appears in spring and summer.

We also examine the temperature series mostly in the central and eastern TP averaged for the 15 stations (Fig. 11a) at five levels from 1979 to 2011 (Figs. 11b,c). A remarkable feature is that the radiosonde temperature exhibits a prominent decadal change in the late 1990s. A distinctive tropospheric (from 500 to 200 hPa) warming trend and stratospheric (100 hPa) cooling trend are found over the TP in spring. The warming trend is most prominent in the upper troposphere and around 300 hPa. For summer, warming also occurs in the troposphere, with the amplitude of the warming tending to strengthen with increasing altitude, shifting to a cooling trend above 200 hPa. The tropospheric warming trend over the TP is notably more pronounced in summer than in spring.

Augmented atmospheric warming in the spring and summer over the TP since the late 1990s may, in turn, influence the land–sea thermal contrast in the EA monsoon region. Previous research revealed a positive correlation between TP snow and oceanic forcing (SST

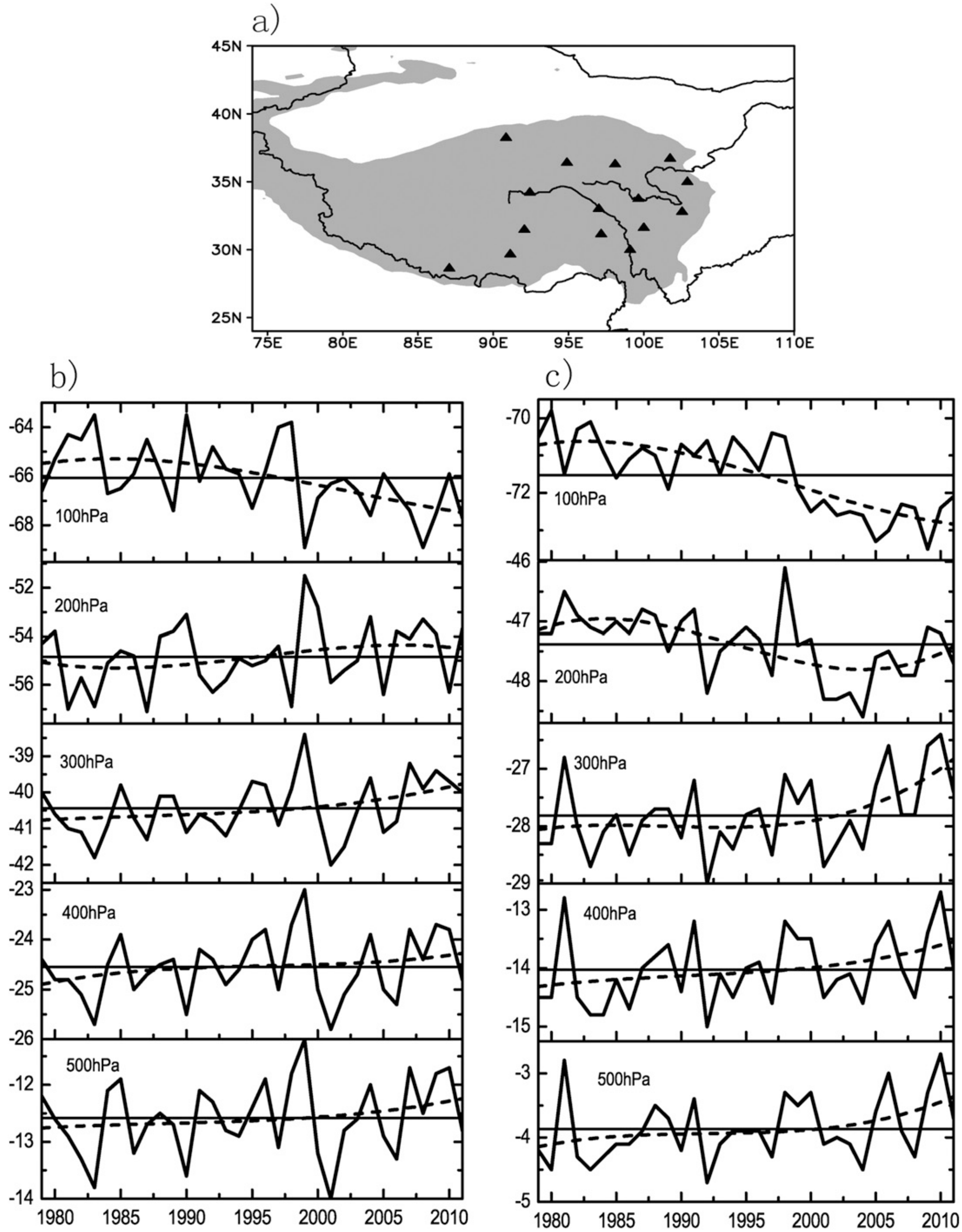

FIG. 11. (a) Distribution of the 15 radiosonde stations over the Tibetan Plateau and (b) spring and (c) summer temperature (°C) over the TP averaged for the 15 stations from 500 to 100 hPa. The horizontal solid lines indicate averaged values for the period of 1999–2011; Dashed curves indicate a third-order polynomial fits.

anomalies in the tropical central and eastern Pacific), and both factors had a high negative correlation with the land–sea thermal contrast in the EA monsoon region (Ding et al. 2009). This result implies that, if the TP has below normal (above normal) snow in the preceding winter and the tropical central and eastern Pacific anomalously cools down (warms up), the land–sea thermal contrast in the EA monsoon region will intensify during the subsequent spring and summer. Based on the computational methods discussed by Yanai et al. (1992), the vertically integrated (surface to 200 hPa) apparent heat source Q_1 is estimated by using the NCEP–NCAR

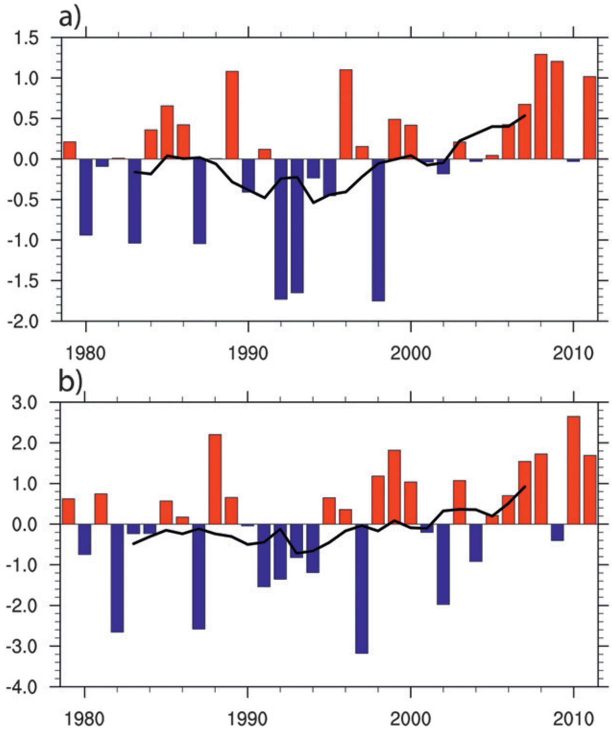

FIG. 12. Time series of the difference between the normalized vertically integrated (from surface to 200 hPa) apparent heat source Q_1 ($\mathrm{W\,m^{-2}}$) averaged over the Tibetan Plateau (28°–43°N, 70°–105°E) and the tropical central and eastern Pacific (10°S–10°N, 180°–120°W) for (a) spring and (b) summer. The solid lines denote 9-yr running mean curves.

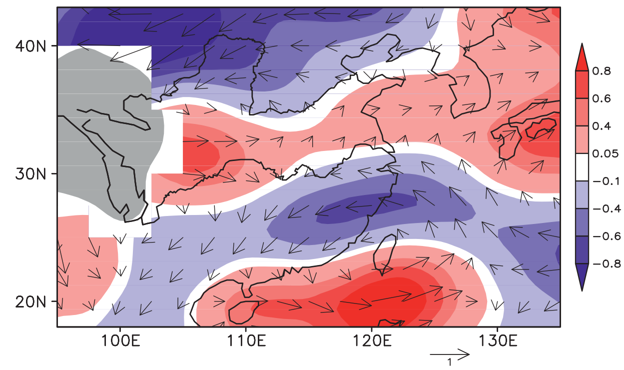

FIG. 13. Changes (2000–11 mean minus 1980–99 mean) in 850-hPa zonal components (red shading denotes westerly components and blue shading denotes easterly components, $\mathrm{m\,s^{-1}}$) and 850-hPa winds (vectors, $\mathrm{m\,s^{-1}}$) in summer. The shaded area (gray) indicates altitudes above 2500 m.

reanalysis dataset. Here, the difference of Q_1 between the TP and the tropical central and eastern Pacific is defined as the land–sea thermal contrast index. The higher the thermal contrast index, the more amplified the land–sea thermal contrast. The time series of the land–sea thermal contrast index for 1979–2011 is depicted in Fig. 12, which shows a distinct rising trend and a change in sign from negative to positive since the late 1990s, indicating an augmented land–sea thermal contrast in the EA monsoon region.

As the land–sea thermal contrast increases, the large-scale atmospheric circulation changes over the EA monsoon region during the subsequent spring and summer. Under the above forcing of the heightened land–sea thermal contrast, the northern boundary of the EA summer monsoon migrates northward. As seen from Fig. 13, anomalous low-level westerly winds decrease along the YRV, and anomalous westerly winds simultaneously increase along the HRV, indicating the northward migration of the northern boundary of the summer monsoon over EA. The anomalous cyclonic circulation strengthens over the HRV while it weakens over the YRV. Thus, the precipitation belt is located along the HRV but departs from the YRV (Fig. 4). Accompanying the northward advance of the summer monsoon, the EA monsoon subsystems also shift northward.

Because the westerly subtropical jet marks the poleward limit of the Hadley cell, a systematic northward shift of the jet implies that the Hadley cell expands northward in the Northern Hemisphere. Figure 14a illustrates the change in outgoing longwave radiation (OLR) in the summer. Enhanced convection is obtained in the climatological tropical western North Pacific intertropical convergence zone (ITCZ) and areas to its north, where the climatological OLR values are less than 220 $\mathrm{W\,m^{-2}}$ along 0°–13°N, implying that the tropical western Pacific ITCZ is enhanced and displaced northward. However, convection is suppressed to the north of the climatological western North Pacific subtropical high (WNPSH) where the climatological OLR values are greater than 250 $\mathrm{W\,m^{-2}}$ along 20°–30°N, implying that the WNPSH is enhanced and displaced northward as well. The change in the WNPSH is more evident in the 500-hPa geopotential height difference for the 2000–11 mean minus 1980–99 mean. As seen from Fig. 14b, geopotential height is raised in an extensive area to the north of the climatological WNPSH, where the climatological 500-hPa geopotential height values are greater than 5880 gpm, whereas it drops in the extensive area to the south of the climatological WNPSH, further verifying the northward displacement of the WNPSH. Because the locations of the ITCZ and WNPSH are considered as rising and subsiding branches of the Hadley cell, respectively, an enhancement and northward displacement of the ITCZ and the WNPSH implies that the local Hadley cell in EA intensified and expanded northward during the last decade. Because subsidence causes adiabatic heating and suppresses convection, this northward expansion leads to midlatitude (near 30°N) tropospheric warming

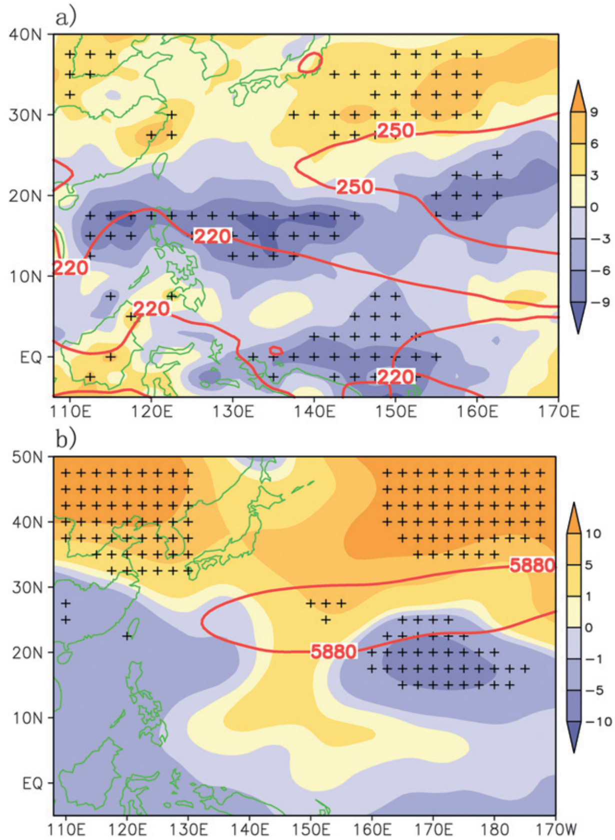

FIG. 14. (a) Changes (2000–11 mean minus 1980–99 mean) in outgoing longwave radiation ($W\,m^{-2}$) in summer. The red thick contours indicate the climatological outgoing longwave radiation distribution averaged for summer in 1981–2010. Values exceeding the 95% confidence level according to a Student's *t* test are stippled. (b) Changes (2000–11 mean minus 1980–99 mean) in 500-hPa geopotential height (gpm) in summer. The red thick contours indicate the climatological 500-hPa geopotential height distribution averaged for summer in 1981–2010. Values exceeding the 95% confidence level according to a Student's *t* test are stippled.

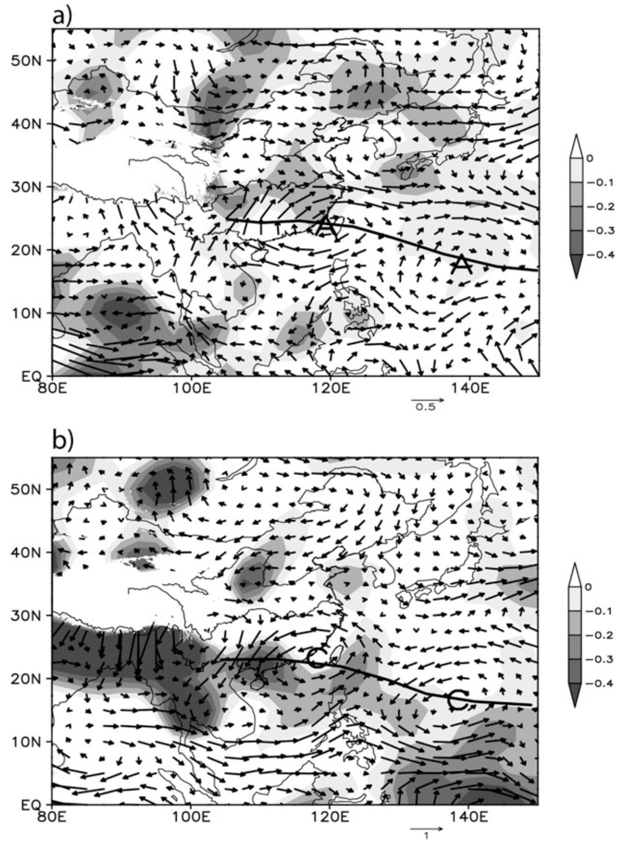

FIG. 15. Anomalous 850-hPa water vapor transport ($kg\,m^{-1}\,s^{-1}$) in summer for the period (a) 1979–99 and (b) 2000–11. The divergence of water vapor transports is plotted in shading; A (C) mark the centers of the anomalous anticyclone (cyclone); the dashed curves indicate the anomalous anticyclone (cyclone) ridge (trough).

and a broadening of subtropical dry zones (near 30°N) (Fu et al. 2006; Hu and Fu 2007), which would contribute to a decrease in summer precipitation along the YRV and southern Japan, but an increase summer precipitation along the HRV and Korean Peninsula.

As previously noted, water vapor transport is one of the most important components of the EA monsoon system. Anomalous precipitation is directly related to water vapor transport. Here, an analysis is made to examine the differences in water vapor transport over the EA monsoon region between the periods 1979–99 and 2000–11.

Figure 15 displays the anomalous composite field of the 850-hPa water vapor transport for 1979–99 and 2000–11. The shaded areas indicate the convergence of the anomalous water vapor. During 1979–99 the tropical southwest water vapor transport converges with the northwest midlatitude water vapor transport above the main rain belt along the YRV and southern Japan. This anomalous water vapor transport is associated with a southward displacement of the WNPSH and a southward migration of the northern boundary of the EA summer monsoon. During 2000–11, in contrast, the water vapor convergence zone moves northward to the HRV and Korean Peninsula. The origin of the anomalous convergence is from the subtropical southeast water vapor transport and the northeast midlatitude water vapor transport. The subtropical southeast branch originates from the East China Sea. This anomalous water vapor transport is associated with a northward displacement of the WNPSH and a northward migration of the northern boundary of the EA summer monsoon, which is favorable for a heavier rain belt along the HRV (Zhou and Yu, 2005) and Korean Peninsula.

Another phenomenon in the anomalous water vapor transport pattern worth discussion is the ENSO signal

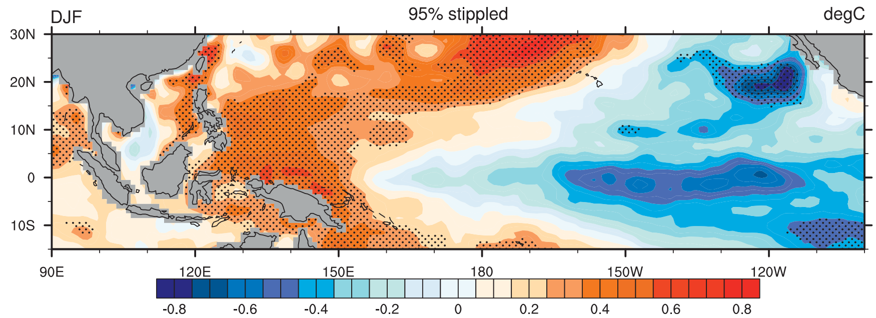

FIG. 16. Changes (2000–11 mean minus 1982–99 mean) in observed winter sea surface temperature (°C) based on the NOAA OISST data. Values exceeding the 95% confidence level according to a Student's t test are stippled.

from the tropical central and eastern Pacific. Throughout the period 1979–99, the circulation anomalies at low latitudes are dominated by an elongated anticyclonic ridge extending from the southeast coast of China to the western Pacific. This ridge has two centers at 22°N, 120°E and 20°N, 140°E. This anomalous anticyclonic ridge conveys, in part, the impacts of warm tropical central and eastern Pacific SSTs to the EA climate through the Pacific–East Asia teleconnection (Wang et al. 2000; Wang and Zhang 2002), which leads to a higher water vapor supply to the YRV and southern Japan. During the later period of 2000–11, the anomalous circulation change occurs at the low latitudes of EA and the former anticyclonic ridge is replaced by a cyclonic trough. This decadal shift results from the decadal change in the remote forcing produced by the tropical central and eastern Pacific SST anomaly. During the 1980s and 1990s, the SST over the tropical central and eastern Pacific is relatively high. Since the late 1990s, the central and eastern Pacific experiences a high La Niña event period, leading to a corresponding cold SST over the tropical central and eastern Pacific during the 2000s (Fig. 16).

Overall, the northward migration of the northern boundary of the summer monsoon, the subtropical westerly jet, the WNPSH and the local Hadley cell over EA results in the northward shift of the summer precipitation belt from the YRV and southern Japan to the HRV and Korean Peninsula. These results suggest that the connection between the northward shifts in the high summer precipitation throughout EA with the TP winter snow may be closely related to the significant decadal reduction in snow depth over the TP since the late 1990s.

7. Summary

A significant trend in the decline of winter and spring snow over the TP since the late 1990s is confirmed based on weather station observational data. This trend may exert some considerable influence on the precipitation and large-scale atmospheric circulation over the TP and its surrounding areas, including the displacement of the primary summer precipitation belt and the northern boundary of the summer monsoon over EA. It is verified that the summer precipitation belt over EA experienced a decadal shift in the late 1990s. There is a remarkable difference between the periods prior to and following the late 1990s, with the summer precipitation belt chiefly located along the YRV and southern Japan before the late 1990s, subsequently shifting northward to the HRV and Korean Peninsula.

In addition, the correlation between the TP winter snow and the following summer precipitation in EA changed in the late 1990s. For the period from the 1980s to the 1990s, the correlation analysis reveals a strong positive correlation between the TP winter snow and the subsequent summer precipitation along the YRV and southern Japan. Since the late 1990s, however, the areas of strong positive correlation between the TP winter snow and summer precipitation over EA shift northward from the YRV and southern Japan to the HRV and Korean Peninsula, thus leading to a negative correlation along the YRV and southern Japan. An above normal winter TP snow favors increased precipitation along the HRV and the Korean Peninsula but decreased precipitation along the YRV and southern Japan in the subsequent summer.

Further analysis suggests that this change in correlation patterns is closely associated with the decadal decrease in snow over the TP since the late 1990s. The increase in TP heating, mainly owing to the decrease in winter snow, together with the decrease in SST in the tropical central and eastern Pacific, possibly enhances the land–sea thermal contrast over EA in the subsequent spring and summer. Thus, the northern boundary of the EA summer monsoon and the summer precipitation belt migrate northward. Correspondingly, the WNPSH and the local Hadley cell advance northward over East Asia, and the water vapor convergence zone moves northward from the YRV and southern Japan to the HRV and Korean Peninsula. These changes led to an increase in precipitation over the HRV and Korean Peninsula and a decrease over the YRV and southern Japan in the subsequent summer. Thus, the decadal northward shift of the high correlation region over EA between the TP snow depth and the monsoonal precipitation in the late 1990s is closely related to the decrease in winter and spring snow over the TP. However, it is not apparent why the TP winter and spring snow has experienced a decadal-scale decrease.

For a long time period, the TP role, especially on the interannual time scale, in regional climate change is still an open question whether it plays an active role. This work provides evidence indicating the close relationship between decadal variations of the TP snow and that of the rainfall pattern in EA, but it does not mean logically that the rainfall anomaly pattern in EA is dominated completely by the TP snow variations as this relationship may be an indicator of, and is probably affected by, the external large-scale forcing from the interdecadal variation of SST in the Indian, Pacific, and even Atlantic Oceans, as well as polar ice concentration.

Acknowledgments. This work is jointly supported by the National Basic Research Program of China (2010CB950404, 2012CB955203, and 2013CB430202), the National Natural Science Foundation of China (41130960), and the CMA Special Public Welfare Research Fund (GYHY201006009). We thank the three anonymous reviewers and the editor for providing very useful critical comments on the paper.

REFERENCES

Chang, C.-P., Y. Zhang, and T. Li, 2000: Interannual and interdecadal variations of the East Asian summer monsoon and tropical Pacific SSTs. Part I: Roles of the subtropical ridge. *J. Climate,* **13,** 4310–4325.

Chen, W., and D. Wong, 1984: A preliminary study on the computational method of 10-day mean sensible heat and latent heat on the Tibetan Plateau. *Collected Works of the Qinghai-Xizang Plateau Meteorological Experiment* (in Chinese), Vol. 2, Science Press, 35–45.

Cox, S. J., P. W. Stackhouse, S. K. Gupta, J. C. Mikovitz, T. Zhang, L. M. Hinkelman, M. Wild, and A. Ohmura 2006: The NASA/GEWEX Surface Radiation Budget project: Overview and analysis. *Extended Abstracts, 12th Conf. on Atmospheric Radiation,* Madison, WI, Amer. Meteor. Soc., 10.1. [Available online at https://ams.confex.com/ams/pdfpapers/112990.pdf.]

Ding, Y., 1992: Effects of the Qinghai–Xizang (Tibetan) Plateau on the circulation features over the plateau and its surrounding areas. *Adv. Atmos. Sci.,* **9,** 113–130.

——, and J. C. L. Chan, 2005: The East Asian summer monsoon: An overview. *Meteor. Atmos. Phys.,* **89,** 117–142.

——, Y. Sun, Z. Wang, Y. Zhu, and Y. Song, 2009: Inter-decadal variation of the summer precipitation in China and its association with decreasing Asian summer monsoon. Part II: Possible causes. *Int. J. Climatol.,* **29,** 1926–1944, doi:10.1002/joc.1759.

Flohn, H., 1957: Large-scale aspects of the summer monsoon in South and East Asia. *J. Meteor. Soc. Japan,* **75,** 180–186.

Fu, Q., C. M. Johanson, J. M. Wallace, and T. Reichler, 2006: Enhanced mid-latitude tropospheric warming in satellite measurements. *Science,* **312,** 1179, doi:10.1126/science.1125566.

Gong, D.-Y., and C.-H. Ho, 2002: Shift in the summer rainfall over the Yangtze River valley in the late 1970s. *Geophys. Res. Lett.,* **29** (10), doi:10.1029/2001GL014523.

Guo, Y., and Y. Ding, 2009: Long-term free-atmosphere temperature trends in China derived from homogenized in situ radiosonde temperature series. *J. Climate,* **22,** 1037–1051.

Gupta, S. K., P. W. Stackhouse, S. J. Cox, J. C. Mikovitz, and T. Zhang, 2006: Surface Radiation Budget Project completes 22-year data set. *GEWEX News,* Vol. 16, No. 4, International GEWEX Project Office, Silver Spring, MD, 12–13.

Hsu, H.-H., and X. Liu, 2003: Relationship between the Tibetan Plateau heating and East Asian summer monsoon rainfall. *Geophys. Res. Lett.,* **30,** 2066, doi:10.1029/2003GL017909.

Hu, Y., and Q. Fu, 2007: Observed poleward expansion of the Hadley circulation since 1979. *Atmos. Chem. Phys.,* **7,** 5229–5236.

Hu, Z.-Z., 1997: Interdecadal variability of summer climate over East Asia and its association with 500 hPa height and global sea surface temperature. *J. Geophys. Res.,* **102,** 19 403–19 412.

Huang, R., 2001: Decadal variability of the summer monsoon rainfall in East Asia and its association with the SST anomalies in the tropical Pacific. CLIVAR Exchanges, No. 6, International CLIVAR Project Office, Southampton, United Kingdom, 7–8.

Kalnay, E., and Coauthors, 1996: The NCEP/NCAR 40-Year Reanalysis Project. *Bull. Amer. Meteor. Soc.,* **77,** 437–471.

Li, C., and M. Yanai, 1996: The onset and interannual variability of the Asian summer monsoon in relation to land–sea thermal contrast. *J. Climate,* **9,** 358–375.

Liu, X., and M. Yanai, 2002: Influence of Eurasian spring snow cover on Asian summer rainfall. *Int. J. Climatol.,* **22,** 1075–1089.

Luo, H., and M. Yanai, 1984: The large-scale circulation and heat sources over the Tibetan Plateau and surrounding areas during the early summer of 1979. Part II: Heat and moisture budgets. *Mon. Wea. Rev.,* **112,** 966–989.

Murakami, T., and Y. Ding, 1982: Wind and temperature changes over Eurasia during the early summer of 1979. *J. Meteor. Soc. Japan,* **60,** 183–196.

Ninomiya, K., and T. Akiyama, 1992: Multi-scale features of Baiu, the summer monsoon over Japan and the East Asia. *J. Meteor. Soc. Japan,* **70,** 467–495.

Nitta, T., 1981: Observational study of heat sources over the eastern Tibetan Plateau during the summer monsoon. *J. Meteor. Soc. Japan,* **59,** 590–605.

Reynolds, R. W., and T. M. Smith, 1994: Improved global sea surface temperature analyses using optimum interpolation. *J. Climate,* **7,** 929–948.

Shukla, J., 1984: Predictability of time averages. Part II: The influence of the boundary forcing. *Problems and Prospects in Long and Medium Range Weather Forecasting,* D. M. Burridge and E. Kallen, Eds., Springer-Verlag, 155–206.

——, and D. A. Mooley, 1987: Empirical prediction of the summer monsoon rainfall over India. *Mon. Wea. Rev.,* **115,** 695–704.

Si, D., Y. Ding, and Y. Liu, 2009: Decadal northward shift of the Meiyu belt and the possible cause. *Chin. Sci. Bull.,* **54,** 4742–4748.

Tao, S., and Y. Ding, 1981: Observational evidence of the influence of the Qinghai–Xizang (Tibet) Plateau on the occurrence of heavy rain and severe convective storms in China. *Bull. Amer. Meteor. Soc.,* **62,** 23–30.

Vernekar, A. D., J. Zhou, and J. Shukla, 1995: The effect of Eurasian snow cover on the Indian monsoon. *J. Climate,* **8,** 248–266.

Wang, B., and Q. Zhang, 2002: Pacific–East Asian teleconnection. Part II: How the Philippine Sea anomalous anticyclone is established during El Niño development. *J. Climate,* **15,** 3252–3265.

——, R. Wu, and X. Fu, 2000: Pacific–East Asian teleconnection: How does ENSO affect East Asian climate? *J. Climate,* **13,** 1517–1536.

——, Q. Bao, B. Hoskins, G. Wu, and Y. Liu, 2008: Tibetan Plateau warming and precipitation changes in East Asia. *Geophys. Res. Lett.,* **35,** L14702, doi:10.1029/2008GL034330.

Wang, H., 2001: The weakening of the Asian monsoon circulation after the end of 1970s. *Adv. Atmos. Sci.,* **18,** 376–386.

Wang, R., W. Li, X. Liu, and L. Wang, 2009: Simulation of the impact of spring soil moisture over the Tibetan Plateau on summer precipitation in China (in Chinese). *Plateau Meteor.,* **28,** 1233–1241.

Wu, G., and Y. Zhang, 1998: Tibetan Plateau forcing and the timing of the monsoon onset over South Asia and the South China Sea. *Mon. Wea. Rev.,* **126,** 913–927.

Wu, T., and Z. Qian, 2003: The relation between the Tibetan winter snow and the Asian summer monsoon and rainfall: An observational investigation. *J. Climate,* **16,** 2038–2051.

Yanai, M., C. Li, and Z. Song, 1992: Seasonal heating of the Tibetan Plateau and its effects on the evolution of the Asian summer monsoon. *J. Meteor. Soc. Japan,* **70,** 319–351.

Ye, D., and Y. Gao, 1979: *The Meteorology of Qinghai–Xizang (Tibet) Plateau* (in Chinese). Science Press, 278 pp.

Yu, R., B. Wang, and T. Zhou, 2004: Tropospheric cooling and summer monsoon weakening trend over East Asia. *Geophys. Res. Lett.,* **31,** L22212, doi:10.1029/2004GL021270.

Zhang, Y., T. Li, and B. Wang, 2004: Decadal change of the spring snow depth over the Tibetan Plateau: The associated circulation and influence on the East Asian summer monsoon. *J. Climate,* **17,** 2780–2793.

Zhao, P., Z. Zhou, and J. Liu, 2007: Variability of Tibetan spring snow and its associations with the hemispheric extratropical circulation and East Asian summer monsoon rainfall: An observational investigation. *J. Climate,* **20,** 3942–3955.

Zhou, T., and R. Yu, 2005: Atmospheric water vapor transport associated with typical anomalous summer rainfall patterns in China. *J. Geophys. Res.,* **110,** D08104, doi:10.1029/2004JD005413.

——, D. Gong, J. Li, and B. Li, 2009: Detecting and understanding the multi-decadal variability of the East Asian summer monsoon—Recent progress and state of affairs. *Meteor. Z.,* **18,** 455–467.

江淮流域夏季降水对前冬持续时间长短的响应*

苏涛1) 张世轩1)2) 支蓉2)† 陈丽娟2)

1) (兰州大学大气科学学院, 兰州 730000)

2) (国家气候中心, 中国气象局气候研究开放实验室, 北京 100081)

(2012 年 10 月 19 日 收到; 2012 年 11 月 1 日 收到修改稿)

利用 NCEP/NCAR 再分析资料计算得到江淮流域 1961—2011 年前冬持续时间, 分析其时空变化特征, 并进一步探究它与后期江淮流域夏季降水的关系. 结果表明, 江淮流域前冬持续时间存在着明显的年际和年代际变化, 前冬持续时间显著偏长年份比偏短年份的前冬温度低、气压高、北风强, 表明温度、气压、经向风可能是反映江淮流域前冬持续时间的关键因子, 且不同区域各气象要素对季节长度的影响存在一定差异; 1961—2011 年江淮流域前冬持续时间与该区域夏季降水呈显著正相关关系; 统计分析亦发现, 前冬持续时间显著偏长 (偏短) 的代表年份中, 夏季降水以偏多 (偏少) 为主; 对典型代表年份环流场进行合成分析发现, 前冬持续时间显著偏长时, 乌拉尔山与鄂霍次克海地区夏季易形成阻塞形势, 进而会对江淮流域夏季降水产生影响; 最后利用奇异值分解从空间场相关的角度探讨了两者的联系, 发现江淮流域夏季降水与前冬持续时间存在非常显著的关系.

关键词: 江淮流域, 季节划分, 前冬持续时间, 夏季降水

PACS: 92.60.Wc **DOI:** 10.7498/aps.62.069203

1 引 言

江淮流域地处中国东部, 受夏季风的影响, 夏季降水年际变率大, 易发生旱涝灾害, 如 1954 年、1991 年、1998 年的洪涝, 以及 1959 年、1961 年、1978 年的干旱, 都给该地区人民生产和生活造成了非常严重的损失. 因此, 探寻江淮流域夏季旱涝异常的前期信号, 并对夏季降水进行预测具有十分重要的意义.

以往的研究主要集中于从不同的角度揭示江淮流域夏季降水的成因, 例如早在 1962 年, 陶诗言等 [1] 就指出, 江淮流域持久性旱涝与 500 毫巴高度场流型的持续性异常有密切联系; 宣守丽等 [2] 的研究也表明, 夏季各月东亚高空急流位置、强度以及急流扰动的异常与我国淮河流域降水异常密切相关, 环流型的异常会影响江淮流域上空冷暖气流的强度, 进而影响该地区降水; 赵亮等 [3,4] 发现厄尔尼诺 - 南方涛动 (ENSO) 循环可以通过影响东亚夏季风环流异常的范围而使雨带位置发生变化, 而东亚夏季风强弱会使雨量发生变化; 赵勇和钱永甫 [5] 则指出青藏高原东部和其以北区域的大尺度热力差异对江淮流域夏季降水有很好的指示性; 司东等 [6] 的研究发现, 20 世纪 90 年代末由于江淮梅雨期东亚中纬度地区对流层明显增暖, 东亚副热带大气扩张, 导致东亚副热带急流北移, Hadley 环流圈拓宽北伸和中纬度西风带北移, 使得梅雨雨带向北移动, 导致长江以南降水减少, 长江以北降水增多.

综上可见, 以往的研究多从环流型的持续性异常、ENSO 循环、青藏高原的热力作用、水汽输送 [7] 等角度揭示了江淮流域夏季降水的成因, 研究的影响因子多为同期要素, 缺少预测意义. 近来, 张世轩等 [8] 利用多要素相似度量季节划分方法研究了中国东部地区前冬季节来临早晚与我国夏季雨带的联系, 发现前冬来临早晚与夏季雨型具有一定的对应关系. 而事实上, 夏季季节的长短决定了雨季的长短, 因而仅使用冬季季节来临时间不能

* 国家自然科学基金 (批准号: 41175067, 41105055, 41275073)、国家重点基础研究发展计划 (批准号: 2012CB955902) 和公益性行业 (气象) 科研专项 (批准号: GYHY200806005, GYHY201106016) 资助的课题.

† 通讯作者. E-mail: zhirong@cma.gov.cn

全面地把握冬季特征对夏季降水的影响, 而使用冬季季节持续时间作为指标, 既包含了冬季来临时间也包含了结束时间, 能够更为全面地代表前冬季节长短与夏季降水的关系. 因此, 本文利用季节划分方法计算江淮流域冬季持续时间, 并进一步探讨了江淮流域夏季降水对前期冬季持续时间长短的响应, 然后利用奇异值分解从空间场相关的角度探讨了两者的联系, 结果显示二者关系密切, 江淮流域前冬持续时间是其夏季降水多寡的一个显著前期信号.

2 资料和方法

2.1 分区与资料

根据王遵娅[9]提出的气候分区方法, 本文江淮流域的选取范围为 (27.5—35°N, 107.5—122.5°E). 使用的资料主要包括:

1) NCEP/NCAR 提供的 1960—2011 年日平均再分析资料, 主要包括地面温度、气压、相对湿度、经向风和纬向风; 1961—2011 年月平均再分析资料, 主要包括高度场、比湿、地面气压、经向风和纬向风等, 分辨率均为 2.5° × 2.5°; 其中位于江淮流域 (27.5—35°N, 107.5—122.5°E) 的共有 28 (7×4) 个格点;

2) 中国气象局气象信息中心资料室提供的 1961—2011 年中国 160 站月平均降水资料, 选取江淮流域范围内的 34 个站点.

2.2 季节划分方法

张世轩等[8]将利用多要素构造气候状态变量的观点[10,11]应用于相似性度量季节划分方法上, 提出一种多要素相似度量季节划分方法. 本文主要根据此季节划分方法计算江淮流域前冬的起始、结束以及持续时间. 具体步骤简介如下.

将日平均温度、气压、相对湿度和风速 (分别用 $P, T, R_{\mathrm{H}}, U, V$ 表示) 资料进行候平均 (以 5 天为一候) 处理, 得到各个要素的候平均资料序列; 然后利用上述要素在空间上构造一个气候态变量 $\boldsymbol{F}(t)$, 其表达式如下:

$$\boldsymbol{F}(t) = (P, T, R_{\mathrm{H}}, U, V), \tag{1}$$

取 1 月和 7 月的平均场分别作为冬季和夏季的典型气候状态场 (分别记为 $\boldsymbol{F}_{\mathrm{w}}$ 和 $\boldsymbol{F}_{\mathrm{s}}$), 消去其两者的公共部分 $\boldsymbol{F}^* = 1/2(\boldsymbol{F}_{\mathrm{w}} + \boldsymbol{F}_{\mathrm{s}})$, 得到偏差量 $\boldsymbol{F}'_{\mathrm{w}}$ 和 $\boldsymbol{F}'_{\mathrm{s}}$); 然后计算各候气候变量 $\boldsymbol{F}(t)$ 的偏差量 $\boldsymbol{F}'(t)$ ($\boldsymbol{F}(t)' = \boldsymbol{F}(t) - \boldsymbol{F}^*$). 并进一步计算各个时段偏差量 $\boldsymbol{F}'(t)$ 与 $\boldsymbol{F}'_{\mathrm{w}}$ (或 $\boldsymbol{F}'_{\mathrm{s}}$) 的相似系数 $R(t)$:

$$R(t) \equiv (\boldsymbol{F}'(t), \boldsymbol{F}'_{\mathrm{w}})/[||\boldsymbol{F}'(t)|| \cdot ||\boldsymbol{F}'_{\mathrm{w}}||], \tag{2}$$

上式右端各变量均为矢量, $R(t)$ 就可以表征某一候实际场与典型的冬季 (或夏季) 场的相似程度, 当实际场与典型场达到一定的相似度时 (即 $R(t)$ 达到一定量值), 便可将这一时间点 t 定义为季节的开始时间.

最后, 根据 $R(t)$ 的投影角 $\phi(t) = \arccos R(t)$ 给出四季的划分标准: 本文选取当 $0 \leqslant \phi(t) < \pi/4$ 为冬季开始, $3\pi/4 < \phi(t) \leqslant \pi$ 为夏季开始, $\pi/4 \leqslant \phi(t) \leqslant 3\pi/4$ 为春季或秋季开始, 各季节的终止日期即为下一个季节起始日期的前一天.

从构造的气候态变量的定义 $\boldsymbol{F}(t) = (P, T, R_{\mathrm{H}}, U, V)$ 可以看出, 这一气候态变量综合考虑了气压、温度、湿度和风等气象要素, 这些气象要素能够全面地表征一定地点和特定时刻大气的基本特征, 因而能够比较准确地刻画各地区一年四季的演变.

3 江淮流域前冬持续时间与夏季降水的变化特征分析

3.1 江淮流域前冬持续时间与夏季降水的变化特征

利用第 2.2 节的季节划分方法计算得到 1961—2011 年江淮流域前冬平均持续时间序列 (图 1(a)); 图 1(b) 为 1961—2011 年江淮流域夏季降水距平百分率序列.

由图 1(a) 可见, 近 50 年江淮流域前冬平均持续时间约为 122 d, 前冬持续时间最长的年份是 1998 年, 为 140 d; 最短的年份是 1973 年, 仅为 106 d, 两者相差 34 d, 表明前冬持续时间的年际变率很大. 此外, 由前冬持续时间的标准化距平累加量曲线可以看到, 江淮流域前冬持续时间也同时具有非常明显的年代际变化: 1961—1980 年前冬持续时间存在逐渐缩短的趋势, 1980—2001 年左右则又逐渐增长, 2001 年之后逐渐变短. 而由图 1(b) 可见, 1961—2011 年江淮流域夏季降水距平百分率最大值为 32.5% (1998 年), 最小值为 −39.5% (1978 年),

表明江淮流域夏季降水的强度也存在很强的年际变化; 由夏季降水距平百分率的标准化距平累加量曲线可见, 江淮流域夏季降水在 1961—1979 年都是以偏少为主, 1980 年之后降水逐渐增多, 特别是 90 年代中期之后降水量增大趋势最为明显.

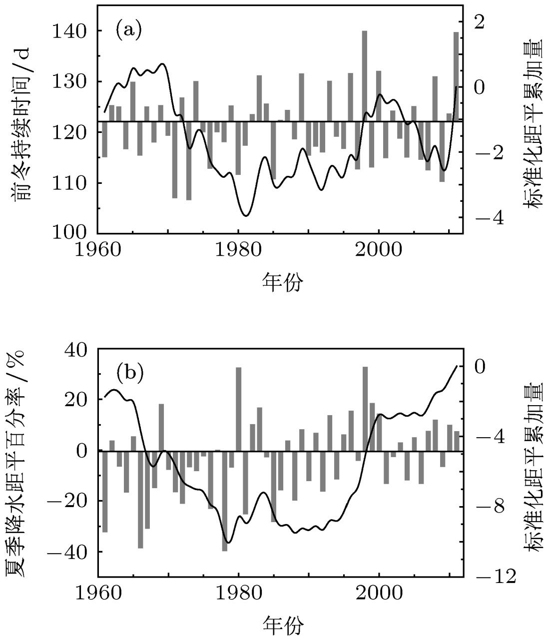

图 1 1961—2011 年江淮流域前冬持续时间 (a) 与夏季降水距平百分率; (b) 序列变化 (曲线为标准化距平累加量)

江淮流域 1961—2011 年前冬持续时间与夏季降水距平百分率的相关系数为 0.445, 置信水平达到 99%, 表明近 50 年江淮流域前冬持续时间与夏季降水存在显著的正相关关系.

3.2 江淮流域前冬持续时间与中国夏季降水的相关性分析

为了探究江淮流域前冬季节持续时间与夏季降水之间的联系, 本文计算了 1961—2011 年前冬持续时间序列与中国 160 站夏季降水距平百分率的相关分布, 得到时滞相关系数空间分布, 如图 2.

由图 2 可以看出, 江淮流域 1961—2011 年前冬持续时间与中国 160 站降水的相关系数在江淮流域存在明显的高值区, 大部分区域置信水平都达到 95%, 表明江淮流域前冬持续时间与夏季降水存在显著的正相关, 即前冬持续时间显著偏长 (偏短) 时, 夏季降水偏多 (偏少).

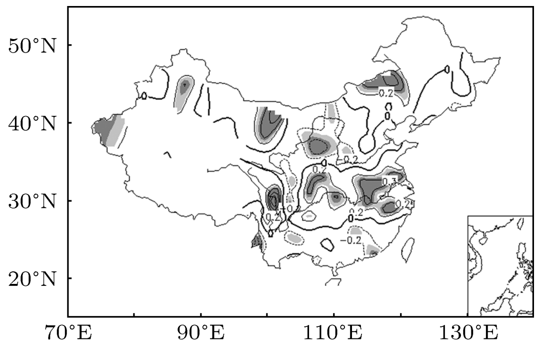

图 2 1961—2011 年江淮流域前冬持续时间与全国 160 站夏季 (6—8 月) 降水量相关系数分布图 (阴影区分别为置信水平达到 90%, 95%的区域)

3.3 江淮流域前冬持续时间与夏季降水的统计分析

江淮流域 1961—2011 年前冬持续时间的标准偏差约为 8.0, 本文以此作为标准选取江淮流域前冬持续时间显著偏长与偏短年份作为典型代表年份, 并研究这些典型年份对应的夏季降水特征. 前冬平均持续时间距平 (PWLA, preceding winter lengths anomalies, 单位: d) 与夏季降水距平百分率 (SRAP, summer rainfall anomalies percentage, 单位:%) 的对应关系见表 1.

由表 1 可见, 在前冬持续时间显著偏长的 8 年中, 除 1974 年 SRAP 为负值外, 其余年份 SRAP 均为正值, 即夏季降水偏多, 表明江淮流域前冬持续时间显著偏长时, 夏季降水易偏多; 而在前冬持续时间显著偏短的 9 年中, 1980, 1999, 2007 年 SRAP 为负值, 占 3/9, 其余年份 SRAP 均为负值, 占 6/9; 表明当江淮流域前冬持续时间显著偏短时, 夏季降水以偏少为主.

表 1 江淮流域前冬持续时间显著偏长与偏短年份对应的夏季降水距平百分率

偏长	1974	1983	1989	1996	1998	2000	2008	2011	
PWLA	8.6	9.7	10.1	10.2	18.5	10.6	9.5	18.2	
SRAP	−7.9	16.5	8.0	15.3	32.5	14.1	11.7	7.2	
偏短	1971	1973	1976	1980	1985	1997	1999	2007	2009
PWLA	−14.2	−14.6	−8.4	−9.6	−10.5	−8.5	−8.1	−8.6	−11.0
SRAP	−16.3	−6.5	−22.9	32.3	−28.1	−3.9	18.3	7.3	−6.4

3.4 江淮流域前冬持续时间显著偏长与偏短年份对应的气象特征分析

本文采用的季节划分方法是基于日平均温度、气压、相对湿度和风场来确定一年四季的起始与结束时间, 并进而划定四季的长度, 因此接下来分析江淮流域前冬持续时间显著偏长与偏短年份对应的日平均温度、气压、相对湿度和风场的差异, 探究造成前冬持续时间长度出现差异的原因. 为了得到有统计意义的结果, 分别对上述气象要素进行统计假设检验 [12−14]. 此处为了便于分析, 图 3 中计算前冬各气象要素差值时取的是前一年 12 月与当年 1, 2 月的平均值.

由图 3(a) 可以看出, 前冬持续时间显著偏长与偏短年份温度的差值在整个江淮流域均为负值, 除东北部分地区外, 其余地区置信水平均达到 95%, 即江淮流域前冬持续时间显著偏长年份比偏短年份温度低. 由图 3(b), 江淮流域前冬持续时间显著偏长年份比偏短年份气压高, 除西部与东南部分地区外, 其余地区置信水平均达到 95%. 图 3(c) 是相对湿度的差值分布, 可以发现整个江淮流域均未通过显著性检验, 在西北与东南地区差值为正值, 其余地区则为负值, 表明江淮流域前冬持续时间显著偏长与偏短年份, 相对湿度的差异并不明显, 相对湿度对前冬持续时间的影响可能比较小. 图 3(d) 是风场的差值分布, 可以看到江淮流域中部与东部沿海地区置信水平均达到 95%, 并且整个区域均为异常偏北风控制, 说明江淮流域前期冬季持续时间显著偏长年份北风比偏短年份的强.

根据以上分析, 江淮流域前冬持续时间显著偏长年份比偏短年份温度低、气压高、北风强, 而相对湿度的差异不是特别明显, 表明温度、气压、经向风可能是影响江淮流域前冬持续时间的关键因子, 而相对湿度的影响可能较小, 并且在不同的区域各个气象要素对季节长度的影响也可能存在差异.

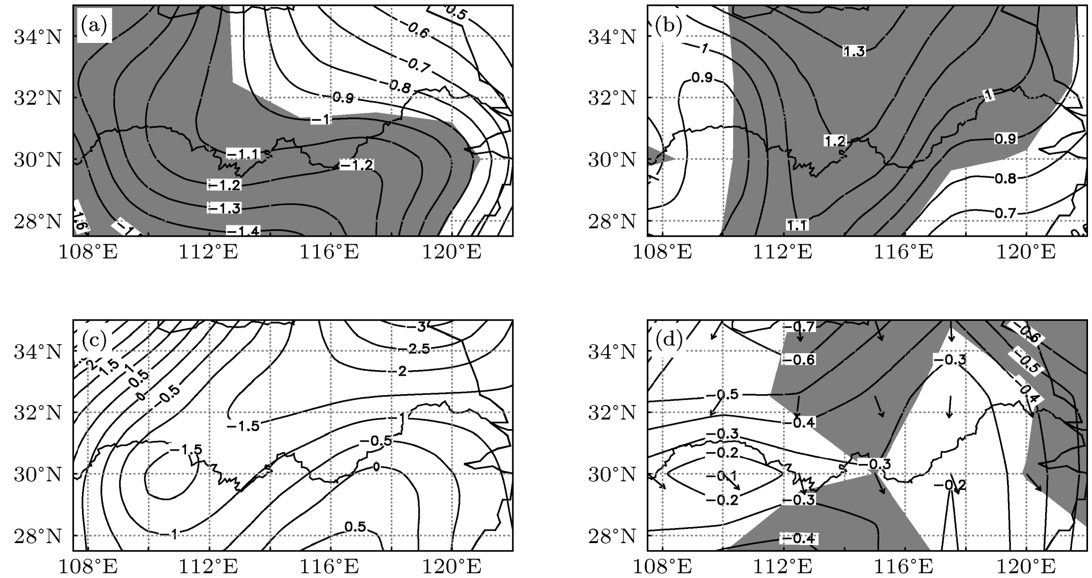

图 3 持续时间显著偏长与偏短年份冬季 (前一年 12 月与当年 1, 2 月平均) 地面温度 (a), 单位 °C, 气压 (b), 单位 hPa; 相对湿度 (c), 单位%; 经向风和纬向风 (d), 单位 m/s 的差值分布 (阴影区为置信水平达到 95%的区域)

4 江淮流域前冬持续时间显著偏长与偏短年份夏季大气环流场和水汽输送场分析

江淮流域夏季降水与全球 500 hPa 环流形势关系紧密 [15], 同时, 夏季东亚地区上空夏季风水汽输送通量与江淮流域降水也密切相关, 水汽输送最大中心与最大降水中心有很好的对应, 并且在水汽辐合带附近能够产生大量降水 [16−20], 所以本文接下来利用合成分析研究江淮流域前冬持续时间显著偏长与偏短年份夏季大气环流场与水汽输送通量场的异同, 并进一步分析造成江淮流域夏季降水产生差异的原因.

4.1 前冬持续时间显著偏长与偏短年份对应的夏季环流场分析

首先, 分别对前冬持续时间显著偏长与偏短年份的夏季 500 hPa 高度场, 850 hPa 风场进行合成分

析, 得到结果如图 4 所示.

由图 4(a), 前冬持续时间显著偏长时, 欧亚大陆中高纬度 500 hPa 高度场距平由西向东均呈现 “+, −, +” 的分布特点, 乌拉尔山、鄂霍次克海附近位势高度偏高, 贝加尔湖北部地区位势高度偏低, 江淮流域上空形成一个西风槽. 乌拉尔山、鄂霍次克海附近 850 hPa 风场各形成一个明显的反气旋式环流, 而贝加尔湖北部则形成了一个气旋性涡旋, 这种环流形势有利于欧亚大陆的偏冷空气向南输送, 导致江淮流域北部易受异常偏北风影响. 同时, 江淮流域南部则为异常偏南风, 南北气流在江淮流域上空形成了一条明显的切变线.

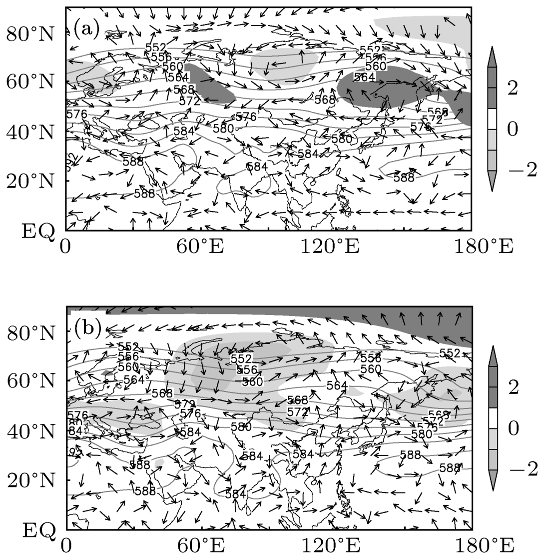

图 4 前冬持续时间显著偏长年份 (a) 与偏短年份 (b) 对应的夏季 500 hPa 高度场与 850 hPa 距平风场的合成分布 (阴影区为位势高度距平值, 等值线为位势高度, 单位 dagpm; 矢量线为距平风场, 单位 m/s)

当前冬持续时间显著偏短时 (图 4(b)), 乌拉尔山、鄂霍次克海附近地区 500 hPa 高度场位势高度偏低, 江淮流域西风带平稳. 同时, 乌拉尔山、鄂霍次克海附近地区 850 hPa 风场分别形成气旋性涡旋, 欧亚大陆上空的冷空气向江淮流域输送的强度比较弱, 江淮流域受异常偏南气流控制.

4.2 江淮流域前冬持续时间显著偏长与偏短年份夏季 500 hPa 高度场差值分析

由于 500 hPa 环流形势对江淮流域夏季降水能够产生很大的影响, 因此为了研究江淮流域前冬持续时间显著偏长与偏短年份夏季 500 hPa 高度场的差异, 本文接下来对它们的差值进行合成分析.

如图 5 所示, 江淮流域前冬持续时间显著偏长与偏短年份夏季 500 hPa 高度场的差值分布, 在乌拉尔山与鄂霍次克海地区置信水平均达到 95%, 表明前冬持续时间显著偏长年份比偏短年份夏季乌拉尔山与鄂霍次克海地区 500 hPa 位势高度显著偏高, 因此乌拉尔山与鄂霍次克海地区易形成阻塞环流形势. 而相关研究也表明 [21−23], 夏季乌拉尔山与鄂霍次克海地区的阻塞高压对江淮地区降水有很大影响, 陆日宇和黄荣辉 [23] 就指出阻塞高压日数多的年份基本上都是江淮地区的涝年, 而阻塞高压日数少的年份则都是江淮地区的旱年. 因此, 可能正是 500 hPa 环流形势的这种显著性差异造成了江淮流域夏季降水的多寡.

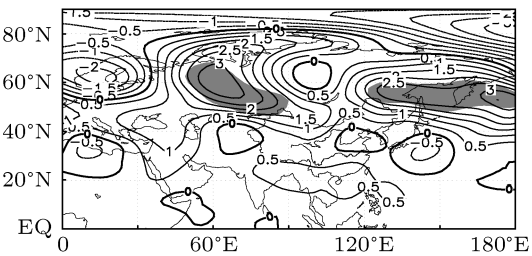

图 5 前冬持续时间显著偏长与偏短年份对应的夏季 500 hPa 高度场差值分布 (等值线为高度场差值, 单位 dagpm; 阴影区为置信水平达到 95%的区域)

4.3 前冬持续时间显著偏短与偏短年份对应的夏季水汽输送场分析

江淮流域夏季降水同时受很多因子的共同影响, 而水汽条件始终是其中一个重要的因子. 江淮流域夏季降水的强度与水汽输送形势密切相关, 水汽输送的强弱、路径以及辐合辐散能够直接影响降水的强度与范围. 图 6 是江淮流域前冬持续时间显著偏长与偏短年份分别对应的水汽输送场, 它们明显存在着很大的差异.

我国夏季降水的水汽源地主要位于孟加拉湾、南海以及西太平洋等地区 [19]. 当江淮流域前冬持续时间显著偏长时 (图 6(a)), 江淮流域主要是受异常偏南的水汽输送控制, 图 6(a) 阴影区显示, 由南海向江淮流域的水汽输送明显异常偏强, 而来自孟加拉湾与西太平洋地区水汽输送则比较弱. 同时, 江淮流域北部则主要是异常偏北水汽输送, 南北暖湿、干冷空气在江淮流域交绥, 形成了一条明显的切变线, 进而形成锋区, 因而导致江淮流域降水偏多. 图 6(a) 中江淮流域大部分地区水汽输送通量距平散度均为负值, 也表明该地区存在异常水汽输送辐合. 前冬持续时间显著偏短时 (图 6(b)), 江淮流域受异常偏南水汽输送控制, 南海与西太平洋等地区

的南方暖湿水汽输送较强, 而来自欧亚大陆的北方干冷空气活动比较弱, 冷暖空气难以在江淮流域辐合, 导致江淮流域降水相对偏少. 图 6(b) 中, 江淮流域大部分地区水汽输送通量距平散度均为正值, 也表明该地区水汽输送存在异常辐散, 因而不利于在该区域形成降水. 此外, 根据 4.1 节的分析, 水汽输送形势与 500 hPa 高度场和 850 hPa 风场也存在很好的对应关系, 说明大气环流形势与水汽输送存在非常紧密的联系.

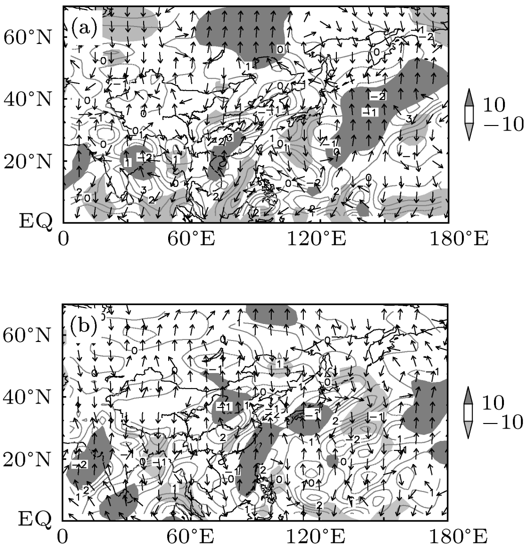

图 6　前冬持续时间显著偏长年份 (a) 与偏短年份 (b) 对应的夏季整层 (垂直积分从地面气压至 300 hPa) 水汽输送通量场的合成分布 (阴影区为经向水汽通量距平, 正值表示异常向北, 负值表示异常向南, 单位 kg/s; 矢量线为水汽输送通量距平, 单位 kg/s; 等值线为水汽输送通量距平散度, 单位 10^{-5} kg/m·s^{-1})

5 江淮流域前冬持续时间与夏季降水的奇异值分解

奇异值分解是对两个场交叉协方差矩阵进行广义对角化运算, 它能同时在时间和空间上考虑两个要素场的相互关系, 并得到两要素场数对相关的空间分布, 而且这种空间分布能最大解释要素场的方差 [24,25]. 为了研究江淮流域前冬持续时间与夏季降水之间相关场的空间结构, 揭示两个场关系密切的地域分布, 本文接下来利用奇异值分解探讨它们的联系.

根据采用的奇异值分解方法及分析的需要, 以江淮流域 1961—2011 年 28 个格点的前冬持续时间为左场, 34 个站点夏季降水距平百分率为右场, 对它们进行 SVD 分解, 得到奇异值和左、右奇异向量, 这两个向量分别对应于江淮流域前冬持续时间和夏季降水场的空间分布型.

表 2 给出了江淮流域前冬持续时间与夏季降水场前 4 对奇异向量协方差占总方差的百分比、相应模态的相关系数、左右奇异向量对各自场的方差贡献率等指标. 从表 2 中看出, 前 4 对空间分布型可以解释总方差的 65.34%, 这说明前 4 对奇异向量能表示出前冬持续时间与夏季降水场耦合作用的大部分特征, 研究这 4 对奇异向量的对应关系, 即可以较真实地反映前冬持续时间与夏季降水场的对应关系和特征, 因此以下只分析前 4 对空间分布型的特征.

空间分布型在一定程度上反映了两个场的遥相关特征, 每一对奇异向量分别对应于前冬持续时间和夏季降水场的一种空间分布型, 成对空间分布型清晰地展示出两个场相关的空间结构. 第一对奇异向量解释总方差的 22.38%, 首先分析第一对空间分布型的特征即同性相关系数分布.

表 2　江淮流域前冬持续时间与夏季降水奇异值分解结果

奇异向量	第 1 对	第 2 对	第 3 对	第 4 对
协方差百分比/%	22.38	16.83	15.25	10.88
相关系数	0.60	0.52	0.54	0.64
PWLA 方差百分比/%	11.22	15.99	17.67	7.00
SRAP 方差百分比/%	9.47	6.73	4.98	6.54

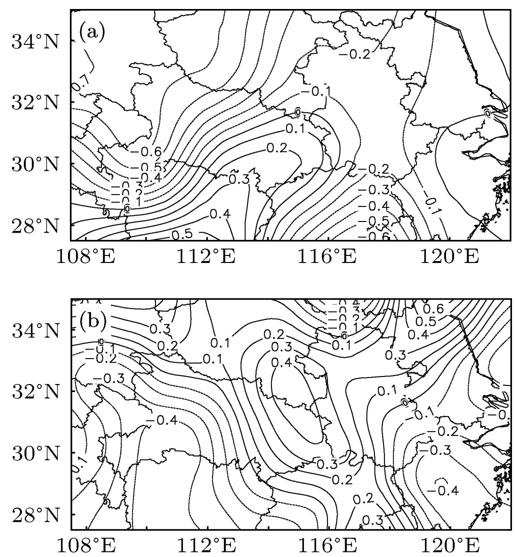

图 7　江淮流域前冬持续时间 (a) 与夏季降水 (b) 第一空间分布型

图 7 为第一对空间分布型, 从图 7(a) 右奇异向量分布型看出, 江淮流域除西南部分地区外, 其余大部分地区都为负值区, 西北大部分地区和江西省北部地区相关系数都小于 −0.3, 置信水平达到 95% ($\alpha_{0.05} = 0.271$), 部分地区相关系数甚至小于 −0.7.

右奇异向量 (图 7(b)) 的空间分布型表现为江淮流域西南、东南大部分地区是负值区, 西北、东北部分地区以及中部是正值区, 大部分地区置信水平都达到 95%.

图 8 为第二对空间分布型, 解释总方差的 16.83%. 由左奇异向量 (图 8(a)) 其空间分布型可以看出, 江淮流域整个区域均为正值区, 这是全区域一致性分布型态, 并且绝大部分地区相关系数都在 0.4 以上, 置信水平达到 99% ($\alpha_{0.01} = 0.351$). 而从夏季降水场奇异向量 (图 8(b)) 来看, 江淮流域西北、东南以及中部地区是正值区, 西南部以及江西省北部地区为负值区, 并且整个江淮流域绝大部分地区均是正值区, 这表明当江淮流域前冬持续时间偏长时, 江淮流域夏季降水整体上是偏少的.

图 9 为第三对空间分布型, 解释总方差的 15.25%. 左奇异向量 (图 9(a)) 与第二对左奇异向量 (图 7(a)) 分布型比较一致, 均表现为全区域一致性正值区的分布型态, 高值区位于江淮流域中北部, 正值中心位于湖北北部和安徽北部, 可解释其原始场方差的 17.67%. 夏季降水场奇异向量 (图 9(b)) 表现为江淮流域全区大部分地区均为正值区, 正值中心分别位于北部和南部地区. 而湖北省大部分地区与浙江省北部地区则是负值区, 负值中心分别位于湖北省西部和浙江省东部.

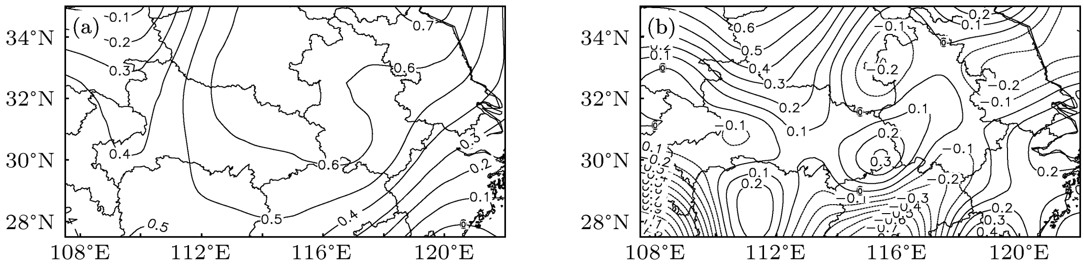

图 8 江淮流域前冬持续时间 (a) 与夏季降水 (b) 第二空间分布型

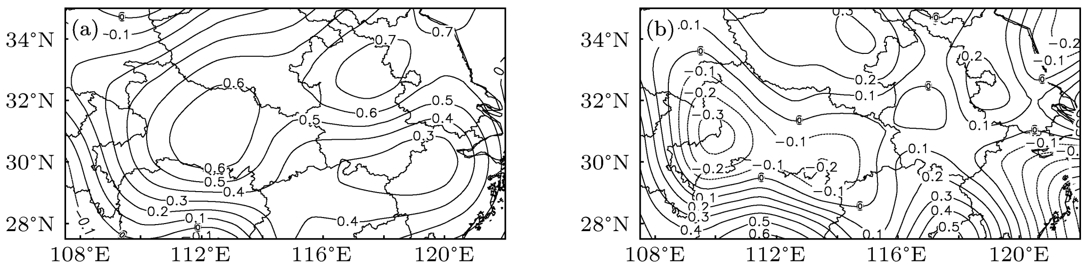

图 9 江淮流域前冬持续时间 (a) 与夏季降水 (b) 第三空间分布型

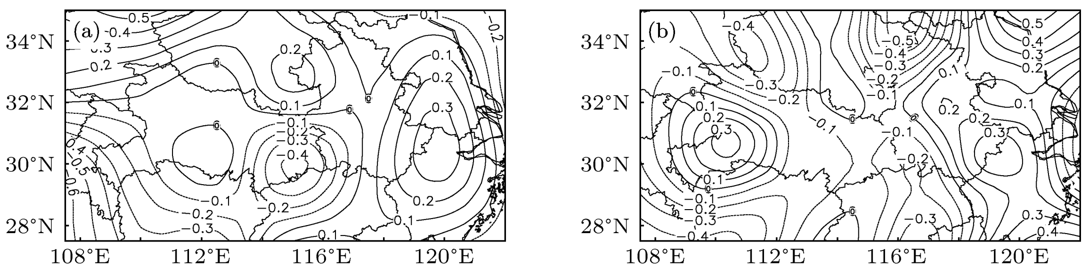

图 10 江淮流域前冬持续时间 (a) 与夏季降水 (b) 第四空间分布型

图 10 为第四对空间分布型, 解释总方差的 10.88%. 前冬持续时间奇异向量 (图 10(a)) 表现为江淮流域西南部为负值区, 而西北与东南部则为正值区. 夏季降水场奇异向量 (图 10(b)) 在湖北省西部与江苏、浙江省大部地区是正值区, 其余部分则为负值区, 正值区位于湖北西部和江苏、浙江交界处, 负值中心位于河南西南部、安徽北部以及湖南中南部.

上述奇异值分解表明: 江淮流域前冬持续时间与夏季降水存在明显的遥相关, 由前四对奇异向量可以发现, 江淮流域夏季降水与前冬持续时间呈现显著的正相关. 本节利用奇异值分解得到的江淮流域前冬持续时间与夏季降水的空间分布型与 3, 4 节根据统计、合成分析得到的结果也比较一致.

6 结 论

中国大部分地区位于中纬度, 季节变化明显, 受太阳辐射的驱动, 造成地面温度、降水、大气环流等发生调整, 导致一年内春、夏、秋、冬四季的更替, 因而四季的转变实际上反映的是气象要素和气候现象状态的变化 [26−30]. 本文利用多要素相似度量季节划分方法研究了江淮流域前冬持续时间的变化特征, 并且进一步利用统计、合成分析与奇异值分解等方法分析了江淮流域夏季降水对前冬持续时间长短的响应, 发现二者确实存在着一定的遥相关关系. 主要结论如下:

1) 江淮流域前冬持续时间的年际变率很大, 并且具有明显的年代际变化, 1961—1980 年前冬持续时间存在逐渐缩短的趋势, 1980—2001 年左右则又逐渐变长, 2001 年之后逐渐变短. 此外, 根据典型代表年份的合成分析可以发现, 江淮流域前冬持续时间显著偏长年份比偏短年份温度低、气压高、北风强, 而相对湿度的差异不是特别明显, 表明温度、气压、经向风可能是影响江淮流域前冬持续时间的关键因子, 并且在不同的区域各个气象要素对季节长度的影响也可能存在差异.

2) 1961—2011 年江淮流域前冬持续时间与夏季降水指数的相关系数为 0.445, 置信水平达到 99%, 说明近 50 年江淮流域前冬持续时间与夏季降水指数存在显著的正相关关系. 通过分析发现, 前冬持续时间显著偏长年份比偏短年份夏季乌拉尔山与鄂霍次克海地区 500 hPa 位势高度高, 而当乌拉尔山与鄂霍次克海地区形成阻塞形势时, 易造成江淮流域夏季降水偏多.

3) 江淮流域前冬持续时间与夏季降水的奇异值分解表明, 江淮流域前冬持续时间与夏季降水存在明显的遥相关. 由前四对奇异向量可以发现, 江淮流域夏季降水与前冬持续时间呈现显著的正相关关系.

以上为江淮夏季降水对前冬持续时间长短响应的初步结论, 江淮流域位于东亚季风区, 其夏季降水同时受夏季风、西太平洋副热带高压、极涡、阻塞形势、青藏高原的动力与热力作用等因素的共同影响 [31−35], 并且各个因子之间的相互作用也很复杂, 因此仅从其前冬持续时间依然是难以准确地确定其夏季降水的强度. 本文的工作也仅是为江淮流域夏季降水的预报提供一定的参考, 而如何合理利用这些结果预报我国夏季降水还需要更加深入的研究.

[1] Tao S Y, Xu S Y 1962 *Acta Meteor. Sin.* **32** 1 (in Chinese) [陶诗言, 徐淑英 1962 气象学报 **32** 1]

[2] Xuan S L, Zhang Q Y, Sun S Q 2011 *Climat. Environ. Res.* **16** 231 (in Chinese) [宣守丽, 张庆云, 孙淑清 2011 气候与环境研究 **16** 231]

[3] Zhao L, Zou L, Wang C L, Yin H B 2006 *J. Tropical Meteorol.* **22** 360 (in Chinese) [赵亮, 邹力, 王成林, 尹洪波 2006 热带气象学报 **22** 360]

[4] Zhao L, Zou L, Wang E H 2007 *Sci. Meteorol. Sin.* **27** 618 (in Chinese) [赵亮, 邹力, 王恩华 2007 气象科学 **27** 618]

[5] Zhao Y, Qian Y F 2007 *Chin. J. Atmos. Sci.* **37** 154 (in Chinese) [赵勇, 钱永甫 2007 大气科学 **37** 154]

[6] Si D, Ding Y H, Liu Y J 2010 *Chin. Sci. Bull.* **55** 68 (in Chinese) [司东, 丁一汇, 柳艳菊 2010 科学通报 **55** 68]

[7] Jiang Z H, Liang Z R, Liu Z Y, Zhu Y L 2011 *Chin. J. Atmos. Sci.* **35** 361 (in Chinese) [江志红, 梁卓然, 刘征宇, 朱云来 2011 大气科学 **35** 361]

[8] Zhang S X, Zhi R, Feng G L, Shen B Z 2012 *Chinese J. Atmos. Sci.* **36** 564 (in Chinese) [张世轩, 支蓉, 封国林, 沈柏竹 2012 大气科学 **36** 564]

[9] Wang Z Y 2004 *M.S. Dissertation* (Nanjing: Nanjing Institute of Meteorology) (in Chinese) [王遵娅 2004 硕士学位论文 (南京: 南京气象学院)]

[10] Hou W, Sun S P, Zhang S X, Zhao J H, Feng G L 2011 *Acta Phys. Sin.* **60** 109201 (in Chinese) [侯威, 孙树鹏, 张世轩, 赵俊虎, 封国林 2011 物理学报 **60** 109201]

[11] Sun S P, Zhang L, Hou W, Feng G L 2011 *Acta Phys. Sin.* **60** 029201 (in Chinese) [孙树鹏, 张璐, 侯威, 封国林 2011 物理学报 **60** 029201]

[12] Shi N, Gu W B 1993 *Meteorological Monthly* **19** 32 (in Chinese) [施能, 古文保 1993 气象 **19** 32]

[13] Wu Z W, Li J P, Jiang Z H, Ma T T 2012 *J. Climate* **25** 2481

[14] Shi N, Gu J Q, Huang X X, Liu J X, Gu Z 2004 *Chin. J. Atmos. Sci.* **28** 950 (in Chinese) [施能, 顾骏强, 黄先香, 刘锦绣, 顾泽 2004 大气科学 **28** 950]

[15] Chen L T, Wu R G 1998 *Chin. J. Atmos. Sci.* **22** 849 (in Chinese) [陈烈庭, 吴仁广 1998 大气科学 **22** 849]

[16] Huang R H, Chen J L, Huang G, Zhang Q L 2006 *Chin. J. Atmos. Sci.* **30** 545 (in Chinese) [黄荣辉, 陈际龙, 黄刚, 张启龙 2006 大气科学 **30** 545]

[17] Shen L L, He J H, Zhou X J, Chen L X, Zhu C W 2010 *Acta Meteor. Sin.* **68** 918 (in Chinese) [申乐琳, 何金海, 周秀骥, 陈隆勋, 祝从文 2010 气象学报 **68** 918]

[18] Shi X Y, Shi X H, Mao J F 2009 *Acta Geograph. Sin.* **64** 861 (in

Chinese) [施小英, 施晓晖, 毛嘉富 2009 地理学报 **64** 861]

[19] Zhou X X, Ding Y H, Wang P X 2008 *Acta Meteor. Sin.* **66** 59 (in Chinese) [周晓霞, 丁一汇, 王盘兴 2008 气象学报 **66** 59]

[20] Dai X G, Wang P, Zhang K J 2012 *Chin. Phys.* B **21** 119201

[21] Zhang Q Y, Tao S Y 1998 *Acta Meteor. Sin.* **56** 199 (in Chinese) [张庆云, 陶诗言 1998 气象学报 **56** 199]

[22] Zhang C J, Song L C, Li Y H 2004 *Acta Meteor. Sin.* **62** 119 (in Chinese) [张存杰, 宋连春, 李耀辉 2004 气象学报 **62** 119]

[23] Lu R Y, Huang R H 1999 *Chin. J. Atmos. Sci.* **23** 533 (in Chinese) [陆日宇, 黄荣辉 1999 大气科学 **23** 533]

[24] Wei F Y, Cao H X 1997 *Plateau Meteorology* **16** 174 (in Chinese) [魏凤英, 曹鸿兴 1997 高原气象 **16** 174]

[25] Wei D M, Li C Y, Tan Y K 2011 *Climat. Environ. Res.* **16** 255 (in Chinese) [韦道明, 李崇银, 谭言科 2011 气候与环境研究 **16** 255]

[26] Zhao J H, Feng G L, Zhang S X, Sun S P 2011 *Acta Phys. Sin.* **60** 099205 (in Chinese) [赵俊虎, 封国林, 张世轩, 孙树鹏 2011 物理学报 **60** 099205]

[27] Dong W J, Jiang Y D, Yang S 2010 *Climatic Change* **99** 81

[28] Thomson D J 2009 *Climatic Change* **22** 391

[29] Choi G Y, Robinson D A, Kang S Y 2010 *Journal of Climate* **23** 5305

[30] Trenberth K E 1983 *Bulletin American Meteorological Society* **64** 1276

[31] Wang Z Y, Ding Y H 2009 *Chin. J. Geophys.* **52** 20 (in Chinese) [王遵娅, 丁一汇 2009 地球物理学报 **52** 20]

[32] Huang J Y, Gao S T 2003 *Progress in Natural Science* **13** 206 (in Chinese) [黄嘉佑, 高守亭 2003 自然科学进展 **13** 206]

[33] Zhang D Q, Feng G L, Hu J G 2008 *Chin. Phys.* B **17** 0736

[34] Li F, Ding Y H 2004 *Acta Meteor. Sin.* **62** 347 (in Chinese) [李峰, 丁一汇 2004 气象学报 **62** 347]

[35] Shen B Z, Zhang S X, Yang H W, Wang K, Feng G L 2012 *Acta Phys. Sin.* **61** 109202 (in Chinese) [沈柏竹, 张世轩, 杨涵洧, 王阔, 封国林 2012 物理学报 **61** 109202]

Summer precipitation response to the length of the preceding winter over yangtze-huaihe river valley*

Su Tao[1)] Zhang Shi-Xuan[1)2)] Zhi Rong[2)†] Chen Li-Juan[2)]

1) (*College of Atmospheric Sciences, Lanzhou University, Lanzhou* 730000*, China*)

2) (*National Climate Center, Laboratory for Climate Studies of China Meteorological Administration, Beijing* 100081*, China*)

(Received 19 October 2012; revised manuscript received 1 November 2012)

Abstract

By using NCEP/NCAR reanalysis datasets, the length of preceding winter (LPW) in the Yangtze-Huaihe River valley (YHRV) from 1961 to 2011 is derived. We investigate the variation of LPW and the relationship between LPW and following summer precipitation, and the results indicate that LPW clearly displays interannual and decadal changes in the period of 1961–2011. The variation of LPW is closely related to temperature, pressure and meridional wind speed, statistical analysis indicates that a longer LPW corresponds to a lower temperature, a higher pressure and a stronger meridional wind, which shows that temperature, pressure, meridional wind are probably the key factors of adjusting the LPW. These characteristics also vary from region to region. There is significantly positive correlation between the summer precipitation and LPW. The statistical analysis also indicates that the longer (shorter) the LPW, the more (less) the summer precipitation in YHRV is. The comprehensive analysis of the circulation field indicates that when LPW is significantly longer than climatic status, a blocking situation is formed easily in the region of Ural Mountains and the Sea of Okhotsk in the summer, which will affect the summer rainfall in YHRV. By using singular value decomposition method, it is found that the relationship between summer precipitation and LPW is also very significant.

Keywords: Yangtze-Huaihe river valley, season division, lengths of the preceding winter, summer flood season precipitation

PACS: 92.60.Wc **DOI:** 10.7498/aps.62.069203

* Project supported by the National Natural Science Foundation of China (Grant Nos. 41175067, 41105055, 41275073), the National Basic Research Program of China (Grant No. 2012CB955902), Special Scientific Research Fund of Meteorological Public Welfare Profession of China (Grant Nos. GYHY200806005, GYHY201106016).

† Corresponding author. E-mail: zhirong@cma.gov.cn

第 18 卷 第 2 期
2013 年 3 月

气 候 与 环 境 研 究
Climatic and Environmental Research

Vol. 18, No. 2
Mar. 2013

孙秀宝, 任国玉, 任芝花, 等. 2013. 风场变形误差对冬季降雪测量及其趋势估算的影响 [J]. 气候与环境研究，18（2）：178–186，doi: 10.3878/j.issn. 1006-9585.2012.11133. Sun Xiubao, Ren Guoyu, Ren Zhihua, et al. 2013. Effects of wind-induced errors on winter snowfall and its trends [J]. Climatic and Environmental Research (in Chinese), 18 (2): 178–186.

风场变形误差对冬季降雪测量及其趋势估算的影响

孙秀宝 [1,2] 任国玉 [2] 任芝花 [3] 沈志超 [1,2]

1 南京信息工程大学大气科学学院，南京 210044

2 中国气象局气候研究开放实验室，国家气候中心，北京 100081

3 国家气象信息中心，北京 100081

摘 要 利用 71 个气象站 1960～2009 年共 50 年的冬季逐日降水、风速和天气现象资料，以及 3 个站降水对比观测试验数据，对东北地区降雪测量记录的风场变形误差进行了评价和订正，并在此基础上分析了风场变形误差对研究区降雪量变化趋势估算结果的影响。结果如下：1）东北地区冬季降雪量台站观测记录普遍被低估，全区观测的冬季平均降雪量为 15.1 mm，而风场变形误差订正后冬季平均降雪量为 22.5 mm。各站绝对误差介于 1.1～19.4 mm，平均绝对误差为 7.5 mm，各站相对误差介于 11.8%～50.8%，平均相对误差为 34.1%。2）主要由于受气象台站观测环境改变导致的风速减弱现象影响，东北地区大部分台站雨量计对降雪的捕获率有所增加，冬季降水观测中的风场变形误差减小，引起实测的降雪量变化趋势估算值被高估。风场变形误差订正前，东北地区近 50 年的冬季降雪量变化趋势为 0.4 mm·$(10\ \mathrm{a})^{-1}$，而风场变形误差订正后，冬季降雪量变化趋势为 0.1 mm·$(10\ \mathrm{a})^{-1}$。3）东北南部地区台站受风场变形误差影响尤其明显，冬季实测的降雪量变化趋势偏高更大，订正后和订正前趋势差值为－1 mm·$(10\ \mathrm{a})^{-1}$，即订正前冬季降雪量变化趋势被高估程度达到了 64.3%。

关键词 降雪 降水量 风速 误差 气候变化 中国东北

文章编号 1006–9585（2013）02–0178–09 **中图分类号** P467 **文献标识号** A

doi:10.3878/j.issn.1006-9585.2012.11133

Effects of Wind-Induced Errors on Winter Snowfall and Its Trends

SUN Xiubao[1,2], REN Guoyu[2], REN Zhihua[3], and SHEN Zhichao[1,2]

1 *School of Atmospheric Sciences*, *Nanjing University of Information Science and Technology*, *Nanjing* 210044

2 *Laboratory for Climate Studies*, *China Meteorological Administration*, *National Climate Center*, *Beijing* 100081

3 *National Meteorological Information Center*, *Beijing* 100081

Abstract Datasets of daily precipitation, wind speed, and weather phenomena of 71 stations during 1960–2009 and experimental observations of precipitation from three stations are used to estimate wind-induced errors in winter snowfall records over northeastern China, and to analyze the effects of wind-induced under-catch on long-term winter snowfall trends. The results show that winter snowfall is generally undervalued. Although the region's average annual snowfall was measured at 15.1 mm, the corrected snowfall was 22.5 mm, which indicates an average error of 7.5 mm, or relative error of approximately 34.1%. In recent years, the gauge catch rate has increased due to the weakening of surface wind speed resulting from urbanization and micro-environmental change surrounding the stations, which have led to an overestimate of winter snowfall trends in the study region. This analysis shows a 50-year linear trend of winter snowfall of 0.4 mm/10 a when original precipitation data are included and a long-term trend of winter snowfall at 0.1 mm/10 a when adjusted data are used. The effect of wind-induced error on the estimates of winter snowfall trends is particularly

收稿日期 2011–08–16 收到，2012–12–28 收到修定稿

资助项目 国家科技部公益性行业（气象）科研专项 GYHY201206012

作者简介 孙秀宝，男，1986 年出生，硕士，从事气候变化研究。E-mail: sun_2005009@126.com

通讯作者 任国玉，E-mail: guoyoo@cma.gov.cn

significant in the southern part of the study region, with an overestimate for long-term trends reaching −1 mm/10 a, or approximately 64.3% in terms of relative bias.

Keywords Snowfall, Precipitation, Wind speed, Error, Climate change, Northeast China

1 引言

降水是表征一个地区气候特征和气候变化的重要参数。降水观测资料广泛应用于气候变化分析、气候预测和陆地水循环等研究中。因此，气象台站降水观测资料的准确性和代表性问题就是开展相关研究、业务首先需要解决的。

导致降水观测误差的原因是多方面的，其中风场变形误差是降水误差中最主要的原因之一。由于雨量计器口上方风场的改变引起的雨滴（雪花）下落轨迹的偏移，以及雨量计摆放或设计上的缺陷，现有气象观测站测量的降水量普遍比实际降水量偏低。风场变形误差在中高纬度地区冬季降雪情况下更为明显（Yang et al., 1998, 1999）。

降水测量的风场变形误差很早以前就引起了研究者的关注，但由于各国雨量计型号、安装高度和观测规范的差异，这个问题始终没有得到很好的解决。通过对比观测试验，一些研究者获得了针对不同国家和地区的不同型号雨量计在不同风速下的捕获率，并发展了降水风场变形误差的订正方法 (Sevruk, 1985; Goodison et al., 1998)。近年来，国内学者也通过对比观测试验，试图了解我国降水观测误差并寻求找到解决我国降水观测误差的方法（杨大庆等，1988，1989，1990；任芝花等，2003，2007；Ren and Li，2007）。这些先期研究为深入评价全球陆地和中国地区降水观测误差及其对现有降水气候学和气候变化分析结果的影响奠定了良好的基础。

近年来，随着对近地面风速观测资料分析的深入，发现 20 世纪中期以来中国大陆地区国家基准气候站和基本气象站记录的平均风速和大风频率呈显著下降趋势（任国玉等，2005；Guo et al., 2010；Jiang et al., 2010）；全球陆地平均风速也呈现明显下降趋势（Vautard et al., 2010; 赵宗慈等，2011）。根据 Ding et al.（2007）和叶柏生等（2008）前期分析，如果地面风速随时间减小，会导致普通雨量计的捕获率提高，进而引起实际观测的降水量出现一定变化。因此，至少在中国大陆以及全球其他陆地区域，大部分气象台站观测的近地面平均风速普遍下降趋势可能已经引起气象台站雨量计捕获率增加，降水测量中的风场变形误差减小，并进而影响对降水量特别是冬季降雪量长期趋势变化的估计（Førland and Hanssen-Bauer, 2000; Ding et al., 2007; 叶柏生等，2008；任国玉等，2010）。

近年研究还发现，近地面平均风速的大幅下降在很大程度上与人为因素造成的局地观测环境改变和城市化影响有关（刘学锋等，2009；张爱英等，2009）。因此，风速导致的降水量变化趋势估计偏差，尽管可能与大尺度大气环流演化有一定联系，但更主要的原因还是人为因素引起的一种观测资料系统性偏差。但不论是自然还是人为因素影响，从气候变化研究的角度来看，近地面平均风速下降引起的降水量测量误差变化都是“虚假”现象，需要加以客观评价和订正（任国玉等，2010）。

现有对我国降水观测误差的评价和订正研究，主要是基于天山乌鲁木齐河源对比观测试验结果（Ye et al., 2004; Ding et al., 2007; 叶柏生等，2007，2008）以及全国 30 个标准雨量站对比观测结果（任芝花等，2003；Ren and Li, 2007）开展的。虽然乌鲁木齐河流域对比观测试验考虑了多种天气现象，对于天山高山区域甚至西北其他山地区域具有较好的代表性，但试验数据不一定完全适合中国其他地区，应用据此获得的订正方法到我国其他地区可能会产生一定误差。20 世纪 90 年代，中国气象局曾在全国 30 个台站开展了普通雨量计与坑式雨量计的对比观测试验，获得了多年连续试验数据。这些工作为今后系统评价和订正我国风速等因素引起的降水观测误差奠定了基础。

本文运用东北地区 1992～1998 年 3 个站的对比观测试验结果，发展了一个新的适应于东北地区的冬季降雪量风场变形误差的订正方法，订正了全区 71 个站冬季日降雪量资料，并在此基础上进一步分析了风场变形误差对冬季区域降雪测量及其变化趋势估计的影响。

2 资料和方法

2.1 研究区域和资料

本文选取的是中国气象局组织的全国降水对比观测试验数据中的东北地区海伦、长春、宽甸 3 个站降水对比观测资料（对比观测试验站点分布见

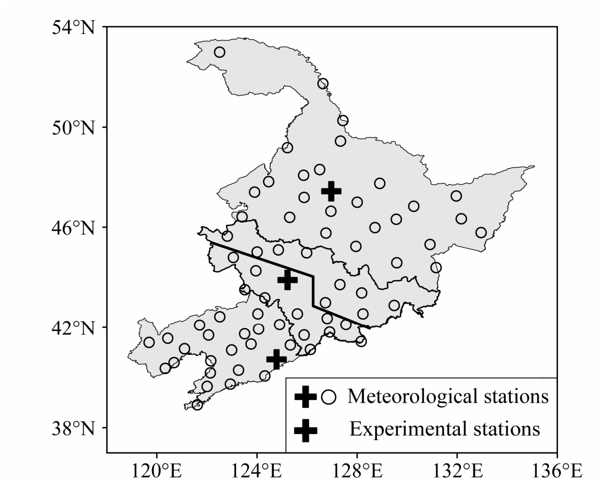

图1 研究区域、对比试验站点和气象站点分布以及分区界限

Fig. 1 Locations of study area, experimental stations, meteorological stations, and the two sub-regions classified based on varimax-rotated empirical orthogonal function (REOF) method

图 1）。资料来自国家气象信息中心保存的《中国降水测量误差及其订正资料集》（黎明琴等，2000）。降水对比试验站采用 1 台坑式雨量计和 2 台台站用普通雨量计进行平行观测。坑式雨量计与其中 1 台普通雨量计间的安装距离约为 5 m，2 台普通雨量计间的距离在 10～15 m 之间。坑式雨量计器口与地表面齐平，周围是标准化设计的防溅网。试验中两台普通雨量计的使用可降低随机误差的影响（任芝花等，2003；Ren and Li，2007）。观测试验资料长度为 1992～1998 年共 7 年。试验观测获得的日降雪资料经过质量控制，包括剔除缺测记录以及剔除吹雪、雨夹雪等天气现象时的记录。

区域常规气象观测资料，在全国 560 站 1960～2009 年近 50 年逐日降水、风速和天气现象记录资料中，根据序列长度不少于 50 年，缺测不超过 5% 的原则，并根据天气现象资料，剔除了雨夹雪、降雨和雾凇等非降雪的记录，最终选取东北地区 71 个台站（分布情况见图 1）。

考虑到东北区域内不同地区的降雪量变化趋势可能存在差异。为了更好地了解风场变形误差对各地区降雪量变化趋势的影响，参考孙秀忠等（2010）对东北地区降雪的区划方法，对全国冬季原始降雪观测资料做旋转经验正交函数（EOF）分析，根据各站与载荷高值中心站相关程度并结合地理因素，将东北地区分为北区和南区 2 个子区域（分区界限见图 1）。

2.2 风场变形误差形成原理和误差订正方法

降水观测误差包括微量损失、蒸发误差、沾湿误差以及风场变形误差。风场变形误差又称动力损失，是造成降水观测误差的最重要原因之一。

目前，对于降水测量中的风场变形误差的形成原理已经有较深入研究。在国内，任芝花等（2003）根据 Mk2 雨量计风洞实验结果（Sevruk and Klemm, 1989），分析风场变形误差形成原理主要为：雨量计器口上方的风速显著大于周围环境场风速，并且随着风速的增加风速的增量也加大。风速偏大导致了雨滴或者雪花下落时与地面的夹角变小，雨滴或雪花呈飘逸状态，或呈发散状下落，从而引起雨量计收集到的降水量低于周围环境中的降水量。由于坑式雨量计器口与地面高度一致，在最大程度上避免了仪器本身引起的风场结构变化，可以认为其不受风场变形误差影响，能够准确测量到各种风速条件下的降水量。

降水观测误差的基本订正方程为（Sevruk, 1985; Yang et al., 1999, 2001）：

$$P_c=K(P_g+\Delta P_w+\Delta P_e+\Delta P_t), \quad (1)$$

其中，P_c 为订正后的降水，P_g 为雨量计观测到的降水量，ΔP_w 和 ΔP_e 分别代表沾湿和蒸发损失，K 为订正系数，ΔP_t 为微量降水。

由于本文只研究动力损失项即风场变形误差对降水的影响，则订正方程可简化为：

$$P_c=K\ P_g, \quad (2)$$

其中订正系数 K=1/CR，此处 CR 是指普通雨量计降水捕获率，降水捕获率是指气象台站现用雨量计测得降水量与对比观测期间坑式雨量计测得的“真实”降水量的比值。由于普通雨量计收集到的降水量较“真实”值偏低，所以降水捕获率 CR≤100%，K 则大于或等于 1。当风速为 0 时 K=1，当风速大于 0 时 K＞1。近几十年来，由于风速存在明显趋势变化（任国玉等，2005），K 也将随时间改变。如果风速随时间变弱，则 K 随时间变小，反之则 K 随时间变大。K 随时间的变化必然会影响 P_c 的趋势。

获得风场变形误差的订正方法只需确定降水捕获率 CR 与风速的关系。降水捕获率与观测场附近风速和降水类型、雨量计类型等相关（Yang et al., 1995; 叶柏生等, 2007），可以直接利用对比观测试验数据，获得普通雨量计降水捕获率与风速之间的关系。

Yang et al. (1999) 指出，通常情况下通过试验结果获得风速与捕获率之间的关系时，降雪量较小

的降雪事件会对结果产生虚假影响。所以本文在确定东北地区风速和降雪捕获率的关系时，采用试验中 78 次降雪量大于或等于 1.0 mm 的降雪事件记录，剔除了降雪量小于 1.0 mm 的降雪记录。图 2 表示 3 个对比观测站 1992～1998 年降雪量所对应的 10 m 高度日平均风速与普通雨量计降雪捕获率的关系。

根据试验数据拟合，得到冬季普通雨量计降雪捕获率与降雪日平均风速的关系式为

$$CR_{snow}=\exp(-0.12W_s)\times 100，P_s\geqslant 1.0\ \text{mm}, \quad W_s<6.5\ \text{m/s}，n=78，R^2=0.50 \tag{3}$$

其中，CR_{snow} 为普通雨量计相对于坑式雨量计的降雪捕获率；P_s 为普通雨量计观测到的降雪量；W_s 为 10 m 高度日平均风速；n 为统计样本数，R 为相关系数。

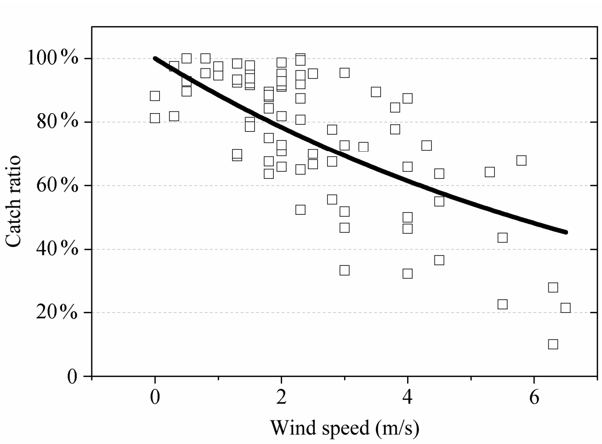

图 2　日平均风速与普通雨量计捕获率之间的关系(降雪量大于 1.0 mm)

Fig. 2　The relationship between daily wind speed and the gauge catch rates of snow (snowfall more than 1.0 mm)

2.3　统计分析方法

本文在降雪量测量误差订正的基础上，进一步对比分析了东北地区全区和分区情况下订正后与订正前冬季平均降雪量的长期趋势变化。东北地区降雪量及其误差的区域平均值是 71 个站的简单算术平均，其线性趋势则根据各自时间序列的一元线性回归方程斜率获得。线性趋势的显著性采用的是 t 检验（魏凤英，2009）。

3　结果分析

3.1　风场变形误差对降雪测量的影响

利用 2.2 节中所述订正方法对近 50 年东北地区 71 站冬季逐日降雪资料进行了订正。根据订正前后的资料比较，分析了东北地区台站观测降雪量的风场变形误差。降雪的绝对误差是指订正前（实测）降雪量与订正后降雪量差值的绝对值，相对误差是指绝对误差与订正后降雪量的百分比值。

从图 3a 中可以看出，绝对误差的大值区主要位于黑龙江东部和辽宁的东南部地区，对应冬季降雪量较大区域。图 3b 显示的是相对误差的空间分布，相对误差较大的区域集中在黑龙江省东北部和辽东半岛南部，从整个区域来看多数台站相对误差均大于 20%，说明东北地区冬季降雪量观测记录受风场变形影响产生的相对误差非常明显。

对东北地区冬季以及逐月降雪量误差大小的统计结果见表 1。整个区域订正后和实测的冬季平均降雪量分别为 22.5 mm 和 15.1 mm。但各站降雪的绝对

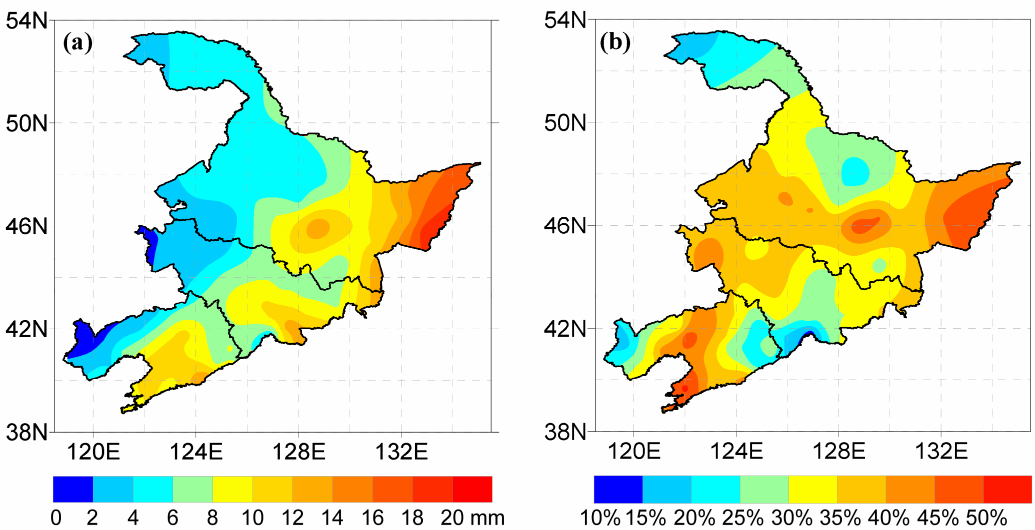

图 3　东北地区冬季实测降雪量（a）绝对误差和（b）相对误差的空间分布

Fig. 3　Spatial distributions of the absolute errors and relative errors of winter snowfall measurements in Northeast China

误差差异较大，冬季平均误差从 1.1～19.4 mm 不等，平均值为 7.5 mm；相对误差各站也不尽相同，最大的可达 50.8%，均值达到了 34.1%。从各月平均的绝对和相对误差来看，各月比较一致，月份之间差异较小。

表 1　东北地区近 50 年订正前后降雪量以及风场变形误差

Table 1　Snowfall amount and wind induced error in recent 50 years in Northeast China

	实测平均降雪量（mm）	订后平均降雪量（mm）	绝对误差范围（mm）	相对误差范围	平均绝对误差（mm）	平均相对误差
12 月	5.8	8.5	0.2～6.5	9.7%～49.4%	2.7	32.7%
1 月	4.7	7.0	0.8～11.0	10.3%～53.8%	2.3	33.2%
2 月	4.6	7.0	0.6～7.1	14.1%～52.1%	2.5	36.4%
冬季	15.1	22.5	1.1～19.4	11.8%～50.8%	7.5	34.1%

3.2　风场变形误差对降雪量变化趋势的影响

根据订正前后的降雪资料，进一步分析评价了风场变形误差对东北地区冬季降雪量变化趋势估计值的影响。方法是：分别计算风场变形误差订正前后 1960～2009 年冬季降雪量序列的线性趋势值，获得订正后减订正前降雪量线性趋势的差值，分析订正前（即实际测量）降雪量变化趋势被高估或低估的程度。趋势偏差是指订正后与订正前趋势差值的绝对值与订正后趋势绝对值的百分比值。

图 4 是订正前后冬季降雪量线性变化趋势差值（订正后减订正前）的空间分布情况。趋势差值大于 0 表示该区域实际观测的降雪量变化趋势被低估了，反之则被高估。从图 4 中可以看出趋势差值大于 0 的台站主要位于黑龙江北部地区，其中黑龙江东北部较大，达到了 1 mm • (10 a)$^{-1}$ 以上；另一方面，辽宁、吉林和黑龙江中部等地区实测的降雪量变化趋势被高估，订正后变化趋势有所减小，其中辽宁的大部分地区和吉林东南部订正前的降雪趋势被高估程度较大，绝对值一般也可达 1 mm • (10 a)$^{-1}$ 以上。

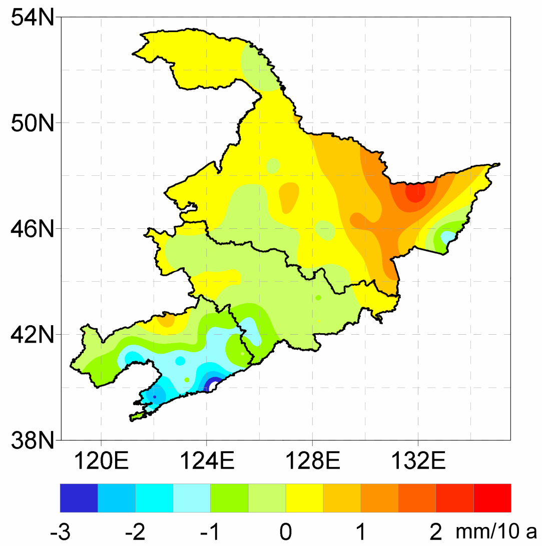

图 4　东北地区降雪量趋势差值的空间分布

Fig. 4　Spatial distribution of snowfall trend differences in Northeast China

从图 5a–c 可以看出，所有区域订正后的冬季降雪量都高于订正前降雪量，即订正后的气候均值增大了；近 50 年来北区的实测降雪量变化趋势被低估，但低估程度不明显；南区和整个区域冬季实测降雪量的变化趋势被高估，即整个区域的上升趋势被高估，南区的下降趋势绝对值被低估，其中南区下降趋势绝对值被低估程度较大；从整个区域来看实测降雪量有上升趋势，而订正后降雪量变化趋势趋于平缓，接近于 0。

从图 5 d–f 中可以看出 12 月订正前后趋势基本保持一致；1 月实测降雪量变化趋势在一定程度上被低估，但低估程度不明显；2 月订正后降雪量下降趋势明显大于实测的降雪量下降趋势，实测的降雪量下降趋势被高估程度较明显。

表 2 给出了东北各区域以及各月订正前后降雪量变化趋势以及趋势差值和偏差的大小。整个分析时期北区冬季实测降雪量变化趋势为 1.2 mm •(10 a)$^{-1}$，但订正后降雪量变化趋势为 1.4 mm •(10 a)$^{-1}$，订正后趋势值略有增加，相对增加量为 14.3%；南区冬季实测降雪量变化趋势为−0.6 mm • (10 a)$^{-1}$，订正后降雪量变化趋势为−1.6 mm • (10 a)$^{-1}$，比实测趋势下降 1 mm • (10 a)$^{-1}$，相对减少量为 64.3%；从整个区域来看，冬季实测降雪量变化趋势为 0.4 mm • (10 a)$^{-1}$，订正后的趋势为 0.1 mm • (10 a)$^{-1}$，

表 2　各区域以及各月降雪量变化趋势以及趋势差值和趋势偏差

Table 2　The linear trends of snowfall amounts for regions and months and the trend differences between aft-corrected and original data and relative bias

	实测趋势 [mm•(10 a)$^{-1}$]	订正后趋势 [mm•(10 a)$^{-1}$]	订正后与订正前趋势差值 [mm•(10 a)$^{-1}$]	趋势偏差
冬季全区	0.36	0.07	−0.29	414.3%
冬季北区	1.2**	1.4*	0.2	14.3%
冬季南区	−0.56	−1.57	−1.01	64.3%
全区 12 月	0.20	0.16	−0.04	25.0%
全区 1 月	0.45	0.57	0.12	21.1%
全区 2 月	−0.29	−0.66	−0.37	56.1%

*为通过 0.1 的显著性检验，**为通过了 0.05 的显著性检验。

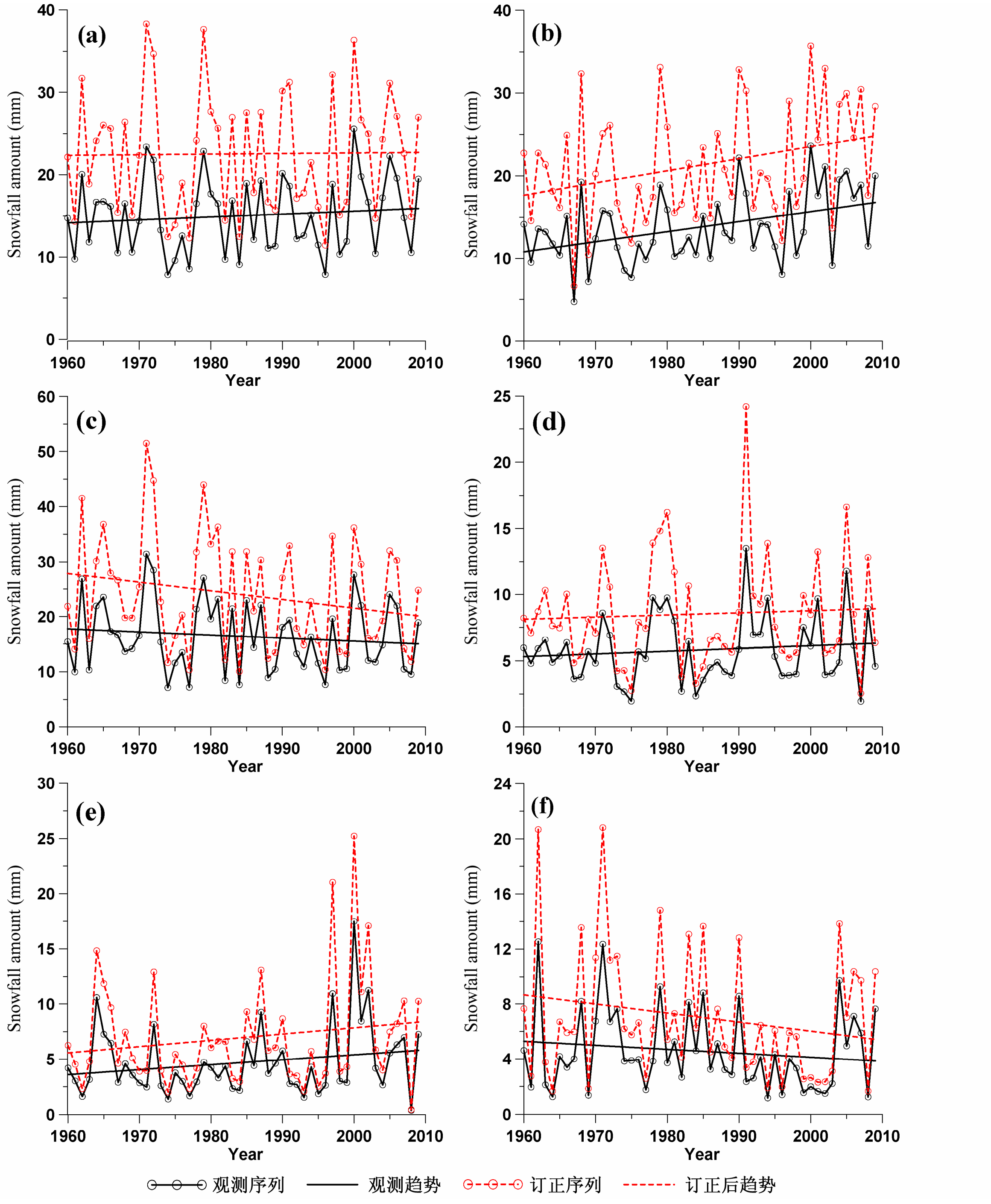

图5　东北地区订正前后降雪量时间序列及其线性趋势：（a）全区；（b）北区；（c）南区；（d）12月；（e）1月；（f）2月

Fig. 5　Winter snowfall amount and the linear trends of the aft-corrected data (red) and original data (black): (a) All regions; (b) northern part; (c) southern part; (d) Dec; (e) Jan; (f) Feb

趋势估计值减少了 0.3 mm•(10 a)$^{-1}$，订正后降雪量的长期上升趋势变得更微弱。

表 2 也给出了风场变形误差对东北逐月降雪量变化趋势估计的影响。从逐月的统计来看，各月存在一定的差异。对于整个区域，12 月和 2 月实测的降雪量变化趋势被高估，而 1 月的实测趋势被低估，其中 2 月的实测趋势被高估程度最为明显，趋势的偏差达到了 56.1%。

4　讨论

我国现有的降水资料风场变形误差订正方法

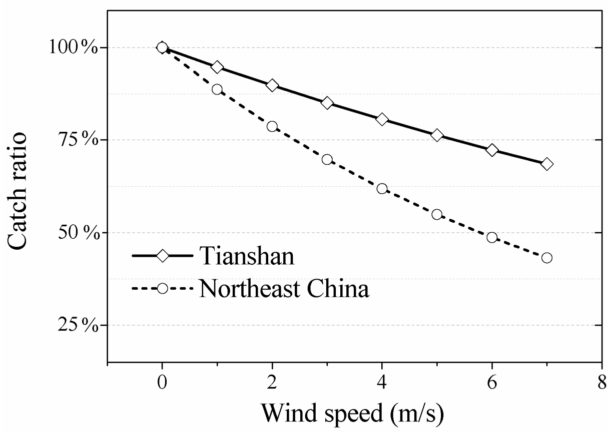

图 6 天山乌鲁木齐河源对比观测试验与东北地区对比观测试验结果中风速与普通雨量计捕获率关系曲线

Fig. 6 Relationships of the gauge catch rates and daily wind speeds for Northeast China and Tianshan Urumqi River

是在天山乌鲁木齐河源对比观测试验基础上发展的（杨大庆等，1989，1990）。本文通过分析东北地区 3 个地点对比观测试验结果，得到了日平均风速与普通雨量计捕获率的统计关系。对于降雪量较大的降雪事件，本文获得的日平均风速与普通雨量计降雪量捕获率的关系与杨大庆等（1990）得到的结果相近，但在数值上有一定差别。

通过两处对比观测试验发展的风速与普通雨量计捕获率关系曲线比较发现：东北地区试验得到的结果随日平均风速增加，冬季普通雨量计降雪捕获率下降更快；在同样风速情况下，本文得到的降雪捕获率一般更低（图 6）。造成这一差异的主要原因，除了样本数量和试验区域的差异以外，用于得到风速与捕获率关系的降雪量数据最小值取值不同，以及观测仪器的差异可能也是重要的。

本文所用的 3 个对比观测站资料相比于天山乌鲁木齐河源对比观测试验资料，站点数和试验时间长度都有所增加。东北地区 3 个对比观测站分别位于黑龙江、吉林和辽宁省，其中 2 个处在平原地区，1 个在东部山地，对全区地形和气候特征具有较好的代表性。对比试验观测资料长达 7 年，基本满足了针对整个区域的研究需要。因此，本文获得的分析结果是有一定说服力的。但是，由于对比观测试验站点数仍然偏少，对比试验观测长度也还有限，目前无法逐站开展针对当地特点的风场变形误差订正。今后还需要开展更多、更长时间的对比观测试验和深入的科学研究。

本文对降水测量记录的订正只考虑了风场变形误差，并未考虑沾湿损失、蒸发损失和微量损失对降雪测量的影响。已有的基于对比观测试验的误差分析表明，我国全国平均的降水量蒸发误差可认定为 0，风场变形误差则达到 10.97%，沾湿误差为 6.79%（任芝花等，2003；Ren and Li，2007）。尽管风场变形误差是最大的观测误差，但沾湿误差也不容忽视。特别是对于水资源评价，降雪或降水观测的沾湿误差应该得到进一步重视。但本文的主要目的不是单纯确定冬季降雪测量的误差，而是分析评价降雪观 测误差对冬季降雪量长期变化趋势估计的系统影响。虽然沾湿误差的影响也较大，但其随时间的变化较小，不像风场变形误差那样随时间出现显著系统变化，因而也不会对降雪量变化趋势估计值造成明显影响。

本文关于风场变形误差对降雪量变化趋势估算影响分析结果表明，东北地区特别是东北南部区域，由于过去 50 年内多数台站近地面平均风速明显减小（任国玉等，2005；Jiang et al., 2010），风速引起的冬季降雪观测误差持续降低，导致台站实际观测记录的降雪量变化趋势被高估了，即观测的长期正趋势偏大，负趋势绝对值偏小。这一现象在 Ding et al.（2007）的研究中已经被指出。但东北北部区域风场变形误差订正前后降雪量变化趋势的差异并不明显，虽然订正前实测降雪量变化趋势有被低估的问题，但低估程度却并不明显。因此，进行风场变形误差订正后，东北地区冬季降雪量变化趋势比原来有较明显的降低。过去利用未订正资料研究东北地区冬季降雪量变化，其获得的趋势估算值普遍有偏高现象。

5 结论

本文利用降雪对比观测试验结果，得到了针对东北地区降雪资料风场变形误差的订正方法，并在此基础上分析风场变形误差对降雪量气候均值和长期气候变化趋势估计值的影响，得到以下结论：

（1）东北地区冬季降雪量台站实测观测记录普遍被低估，全区目前实测的冬季平均降雪量为 15.1 mm，而风场变形误差订正后冬季平均降雪量为 22.5 mm。各站绝对误差介于 1.1～19.4 mm，平均绝对误差为 7.5 mm；各站相对误差介于 11.8%～50.8%，平均相对误差为 34.1%。冬季各月的绝对和相对误差比较平均，月份之间差异较小。

（2）对实测和订正后降雪量长期变化趋势对比分析表明，主要由于受气象台站附近观测环境改变导致的地面风速减弱趋势影响，东北地区大部分台站雨量计对降雪的捕获率有所增加，冬季降水量观测中的风场变形误差减小，引起降雪量的长期变化趋势估算值偏高。东北地区近 50 年实测的冬季降雪量变化趋势为 0.4 mm•$(10\ \mathrm{a})^{-1}$，而风场变形误差订正后全区平均冬季降雪量变化趋势为 0.1 mm•$(10\ \mathrm{a})^{-1}$。

（3）东北南部地区台站平均地面风速减小尤其明显，冬季降雪量变化趋势估算值偏高更大，订正后和订正前趋势差值达到了－1 mm•$(10\ \mathrm{a})^{-1}$，实测的变化趋势被高估程度达到 64.3%。而北部地区变化趋势则被低估，由于订正前后趋势差异并不明显，因而被低估程度较小。

（4）从逐月的分析结果来看，冬季各月风场变形误差对实测降雪变化趋势估计的影响有一定差异。从整个区域来看，12 月和 2 月实测降雪量变化趋势被高估，1 月被低估，其中 2 月的实测趋势被高估程度最为明显。

因此，在开展降水特别是中高纬度地区冬季降雪气候变化分析时，需要十分重视风场变形误差随时间变化对分析结果的影响，要应用风场变形误差订正后的资料开展研究。

参考文献（References）

Ding Y J, Yang D Q, Ye B S, et al. 2007. Effects of bias correction on precipitation trend over China [J]. J. Geophys. Res., 112, D13116, doi:10.1029/2006JD007938.

Førland E J, Hanssen-Bauer I. 2000. Increased precipitation in the Norwegian Arctic: True or false? [J]. Climate Change, 46: 485–509.

Goodison B E, Louie, Yang D. 1998. WMO solid precipitation measurement intercomparison, final report? [R]. WMO/TD-NO.872, 212pp.

Guo H, Xu M, Qi H. 2010. Changes in near-surface wind speed in China: 1969–2005 [J]. Int. J. Climatol., 31 (3): 349–358.

Jiang Y, Luo Y, Zhao Z C, et al. 2010. Changes in wind speed over China during 1956–2004 [J]. Theor. Appl. Climatol., 99: 421–430.

黎明琴, 任芝花, 邹耀芳, 等. 2000. 中国降水测量误差及其订正资料集, 1～7 册 [M]. 北京: 中国气象局. Li Mingqin, Ren Zhihua, Zou Yaofang, et al. 2000. Dataset of Precipitation Measurement Error and Its Adjustment, Vol. 1–7 (in Chinese) [M]. Beijing: China Meteorological Administration.

刘学锋, 江滢, 任国玉, 等. 2009. 河北城市化和观测环境改变对地面风速观测资料序列的影响 [J]. 高原气象, 28 (2): 433–439. Liu Xuefeng, Jiang Ying, Ren Guoyu, et al. 2009. Effect of urbanization and observation environment change on wind speed trend in Hebei Province, China [J]. Plateau Meteorology (in Chinese), 28 (2): 433–439.

任国玉, 郭军, 徐铭志, 等. 2005. 近 50 年中国地面气候变化基本特征 [J]. 气象学报, 63 (6): 942–956. Ren Guoyu, Guo Jun, Xu Mingzhi, et al. 2005. Climate changes of China's mainland over the past half century [J]. Acta Meteorologica Sinica (in Chinese), 63 (6): 942–956.

Ren Z H, Li M Q. 2007. Errors and correction of precipitation measurements in China [J]. Advances in Atmospheric Sciences, 24 (3): 449–458.

任国玉, 封国林, 严中伟. 2010. 中国极端气候变化观测研究回顾与展望 [J]. 气候与环境研究, 15 (4): 337–353. Ren Guoyu, Feng Guolin, Yan Zhongwei. 2010. Progresses in observation studies of climate extremes and changes in mainland China [J]. Climatic and Environmental Research (in Chinese), 15 (4): 337–353.

任芝花, 王改利, 邹凤玲, 等. 2003. 中国降水测量误差的研究 [J]. 气象学报, 61 (5): 621–627. Ren Zhihua, Wang Gaili, Zou Fengling, et al. 2003. The research of precipitation measurement errors in China [J]. Acta Meteorologica Sinica (in Chinese), 61 (5): 621–627.

任芝花, 李伟, 雷勇, 等. 2007. 降水测量对比试验及其主要结果 [J]. 气象, 33 (10): 96–101. Ren Zhihua, Li Wei, Lei Yong, et al. 2007. A comparison experiment of solid precipitation measurement and its primary results [J]. Meteorological Monthly (in Chinese), 33 (10): 96–101.

孙秀忠, 罗勇, 张霞, 等. 2010. 近 46 年来我国降雪变化特征分析 [J]. 高原气象, 29 (6): 1594–1601. Sun Xiuzhong, Luo Yong, Zhang Xia, et al. 2010. Analysis on snowfall change characteristic of China in recent 46 years [J]. Plateau Meteorology (in Chinese), 29 (6): 1594–1601.

Sevruk B. 1985. Correction of precipitation measurements [R]. WMO/ TD-NO.104, 13–23.

Sevruk B, Klemm S. 1989. Instruments and observing methods report, No. 39 [R]. WMO/ TD-NO.313,16–18.

Vautard R, Cattiaux J, Yiou P, et al. 2010. Northern Hemisphere atmospheric stilling partly attributed to an increase in surface roughness [J]. Nature Geoscience, 3: 756–761.

魏凤英. 2009. 现代气候统计诊断与预测技术 [M]. 北京: 气象出版社, 296pp. Wei Fengying. 2009. Diagnosis and Forecasting Methods of Modern Climatic Statistics [M] (in Chinese). Beijing: China Meteorological Press, 296pp.

Yang D Q, Goodison B E, et al. 1995. Accuracy of Tretyakov precipitation gauge: Results of WMO intercomparison [J]. Hydrol. Processes, 9 (8): 877–895.

Yang D Q, Goodison B E, Benson C, et al. 1998. Adjustment of daily precipitation at 10 climate stations in Alaska: Application of WMO inter comparison results [J]. Water Resour. Res., 34 (2): 241–256.

杨大庆, 姜彤, 张寅生, 等. 1988. 天山乌鲁木齐河源降水观测误差分析及其改正 [J]. 冰川冻土, 10 (4): 384–400. Yang Daqing, Jiang Tong, Zhang Yinsheng, et al. 1988. Analysis and correction of errors in precipitation measurement at the head of Urumqi River, Tianshan [J]. Journal of Glaciology and Geocryology (in Chinese), 10 (4): 384–400.

杨大庆, 康尔泗, 张寅生, 等. 1989. 天山乌鲁木齐河源夏季降水观测中的动力损失及其修正 [J]. 气象, 15 (1): 22–27. Yang Daqing, Kang Ersi, Zhang Yingsheng, et al. 1989. Analysis and correction of wind effects on precipitation measurements at the head of Urumqi River during summer

[J]. Meteorological Monthly (in Chinese), 15 (1): 22–27.

杨大庆, 施雅风, 康尔泗, 等. 1990. 天山乌鲁木齐河源高山区固态降水对比测量的主要结果 [J]. 科学通报, 35 (22): 1734–1736. Yang Daqing, Shi Yafeng, Kang Ersi, et al. 1990. Results of solid precipitation measurement intercomparison in the alpine area of Urumqi River basin [J]. Chinese Science Bulletin (in Chinese), 35 (22): 1734–1736.

Yang D Q, Ishida S, Goodison B E, et al. 1999. Bias correction of daily precipitation measurements for Greenland [J]. J. Geophys. Res., 105 (D6): 6171–6182.

Yang D Q, Goodison B E, Metcalfe J, et al. 2001. Compatibility evaluation of national precipitation gage measurements [J]. J. Geophys. Res., 106 (D2): 1481–1492.

Ye B S, Yang D Q, Ding Y J, et al. 2004. A bias-corrected precipitation climatology for China [J]. J. Hydrometeor., 5 (6): 1147–1160.

叶柏生, 杨大庆, 丁永健, 等. 2007. 中国降水观测误差分析及其修正 [J]. 地理学报, 62 (1): 1–13. Ye Baisheng, Yang Daqing, Ding Yongjian, et al. 2007. A Bias-corrected precipitation climatology for China [J]. Acta Geographica Sinica (in Chinese), 62 (1): 1–13.

叶柏生, 成鹏, 杨大庆, 等. 2008. 降水观测误差修正对降水变化趋势的影响 [J]. 冰川冻土, 30 (5): 717–725. Ye Baisheng, Cheng Peng, Yang Daqing, et al. 2008. Effects of the bias-correction on changing tendency of precipitation over China [J]. Journal of Glaciology and Geocryology (in Chinese), 30 (5): 717–725.

张爱英, 任国玉, 郭军, 等. 2009. 1980～2006 年我国高空风速变化趋势分析 [J]. 高原气象, 28 (3): 680–687. Zhang Aiying, Ren Guoyu, Guo Jun, et al. 2009. Analyses of change trend of upper air wind speed over China during 1980–2006 [J]. Plateau Meteorology (in Chinese), 28 (3): 680–687.

赵宗慈, 罗勇, 江莹. 2011. 全球大风在减少吗? [J]. 气候变化研究进展, 7 (2): 149–151. Zhao Zongci, Luo Yong, Jiang Ying. 2011. Is global strong wind declining? [J]. Advances in Climate Change Research (in Chinese), 7 (2): 149–151.

第9卷 第4期
2013年7月

气候变化研究进展
PROGRESSUS INQUISITIONES DE MUTATIONE CLIMATIS

Vol. 9 No. 4
July 2013

doi:10.3969/j.issn.1673-1719.2013.04.001
孙颖，尹红，田沁花，等. 全球和中国区域近50年气候变化检测归因研究进展 [J]. 气候变化研究进展，2013, 9 (4): 235-245

全球和中国区域近50年气候变化检测归因研究进展

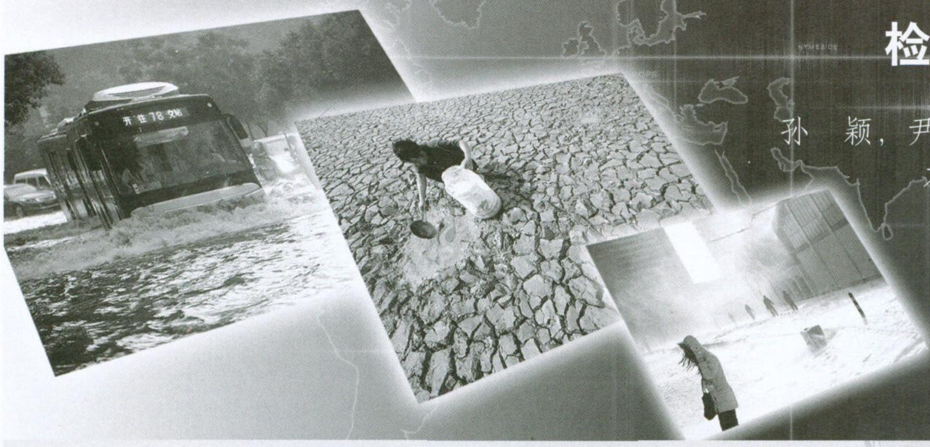

孙 颖，尹 红，田沁花，胡 婷，石 英，刘洪滨，周波涛

中国气象局国家气候中心，北京 100081

摘 要：回顾了近年来国内外对全球和中国区域气候变化的检测归因研究，主要集中在对20世纪中期以来温度、降水和主要极端事件变化的检测归因研究进展，而不涉及更长时间尺度历史气候变化的检测归因。分析表明，国际上近年来在气候变化检测归因研究领域发展迅速，从全球尺度气温变化的检测归因发展到区域尺度和多变量的检测归因。但在中国，虽然也有一些研究探讨了中国东部南涝北旱等发生的原因，但在以数理统计推断方法为基础的气候变化事实归因领域的研究仍然亟待加强。一些重要的问题，如中国不同区域的变暖、不同区域的变干或变湿的归因分析，以及这些因子和引起全球气候变化因子的异同等，都是迫切需要回答的科学问题。

关键词：检测归因；气候变化；全球尺度；区域尺度

引 言

气候变化的检测归因是识别人为和自然因子对气候变化相对贡献的核心研究内容，是回答"气候变化在多大程度上是由人类活动引起的"这一科学问题的重要科学基础。自20世纪90年代以来，检测归因研究迅速成为气候变化研究的一个热点问题，从研究如何给出检测和归因研究的主要气候变量指标、主要参照物，到具体的检测归因分析的主要方法以及分析影响20世纪气候变化的可能因子，研究内容十分广泛[1]。20世纪80年代以来，由于对全球气候变暖原因的争议不断，气候变暖的归因研究一直是国际上的热点和焦点问题[2]。

气候变化检测归因的主导思想是利用不同工具分辨各种因子的作用，然后给出影响明显的因子。气候变化的检测和原因判别有多种方法，如简单的指标和序列法、最优指纹法和贝叶斯方法等，其主要工具是数理统计方法(如指纹法和贝叶斯分析等)和气候模式（简单和复杂模式）[1]。从20世纪90年代以来，检测归因领域的研究在不断发展和深化。研究对象从全球平均气温发展到降水、极端事件以及一些中小尺度的现象，如台风等。研究的空间尺度从全球平均发展到大陆和洋盆尺度，乃至区域尺度的细化过程。研究方法从最初的简洁直观的单步归因发展到多步归因，其目的是为了解决除温度以外的其他变量的归因问题[3]。而一些具体的研究方法，

收稿日期：2013-01-10；**修回日期**：2013-03-25
资助项目：气候变化专项（CCSF 201342）；973项目（2012CB417205）；中国气象局气候研究开放实验室2012/2013年度开放青年基金
作者简介：孙颖，女，研究员，主要从事气候和气候变化研究，sunying@cma.gov.cn

如最优检测法等也在发展，从使用一般的最小二乘到总体最小二乘，或者贝叶斯方法[4]。随着这些研究的不断深入，观测资料的不断完善和气候模式的快速发展，对引起气候变化原因的科学认识也在不断深化。越来越多的证据表明，尽管观测资料和气候模式仍然存在不确定性，但是对20世纪50年代以来的气候变化，人类活动对全球变暖的影响是非常可能的[2,5]。可辨别的人类活动影响扩展到了气候的其他方面，包括海洋变暖、大陆尺度的平均温度、温度极值以及风场[5]。而自政府间气候变化专门委员会（IPCC）发布第四次评估报告（AR4）以来，检测归因领域的研究已经发展到对其他变量，如降水[6]和极端事件的归因分析[7]，而对台风等一些变量变化的归因研究也在进行[8]，虽然目前只能得出低信度的结论，但这反映了国际上在这一领域的快速发展趋势。

近年来，随着对气候变化原因认识的深化，气候变化检测归因从对气候变化基本观测事实的归因扩展到气候变化影响领域的归因，也就是要对气候变化产生的影响进行归因分析。这使得传统的检测归因从定义到方法学的研究均有很大的扩展。2009年9月，IPCC第一和第二工作组联合召开“气候变化检测与归因”专家研讨会，讨论了检测和归因的定义、评价方法、资料与要求等，在此基础上形成了覆盖检测与归因不同研究领域，包括气候变化观测事实和影响等的指导性文件[3]，并综合了4种检测归因方法，包括对外强迫的单步归因、多步归因、联合归因以及对观测到的气候条件变化的归因，囊括了目前研究这一因果链采用的不同途径。并指出，不管采用哪一领域的哪种方法，作者都要明确所研究的问题是归因于气候或环境条件变化还是其他外强迫或外驱动因素的变化。对于研究结果要从使用的数据、模式、方法、混淆因子等方面存在的问题给出可信度评价。

从上面这些研究进展可以看到，国际上检测归因的研究发展很快，研究领域已经从对气候变化观测事实的归因扩展到了气候变化影响等领域的归因分析。本文将从20世纪50年代以来气候变化事实检测归因的角度出发，针对国内外科学界近年来在该领域的研究进行回顾，但不包括对古气候和气候变化影响检测归因的研究分析。主要从国际和国内在气温、降水和主要极端事件变化的研究进展几个方面，总结和回顾相关的研究，并对我国在该领域的发展方向作出思考和探讨。

1 检测归因的定义和主要方法

1.1 检测归因的定义

2009年IPCC统一了不同领域的检测归因定义。在其发布的指导性文件中明确指出，气候变化的检测是在某种给定的统计意义上展现气候或受气候影响的系统发生变化的过程，而不提供该变化的原因。如果观测到的某种变化单独由于内部变率本身随机发生的可能性很小，如<10%，则可以说这种变化被检测到了。归因定义为以某种给定的信度，估算多种因子对某种变化或某个事件变化的相对贡献的过程。归因的过程需要观测到的变化必须能够检测到。与过去的定义相比，强调了多种因子的变化。

和上述检测归因的定义相一致，近年来，关于检测归因的方法研究有了很大的进展。从数学原理上发展了检测、归因技术，还发展了针对气候系统特点的检测方法，以期寻找气候变化的指纹。这些检测、归因技术大体上可分为多元分析和贝叶斯推断两大类，前者包括回归法、样式（pattern）相关法等，后者因能包容不同来源的数据而备受重视，应该说这些方法各有优劣。下面对常用的方法进行介绍。

1.2 最优指纹法

20世纪70年代末，Hasselmann提出一种定量化鉴别人为气候变化信号并作归因分析的方法，这就是最优指纹（OFP）法。最优指纹法是一种增强人为气候变化信号特征使之排除低频自然变率噪声干扰的技术方法，一般用在定量化鉴别人为气候变化的研究中。它比任意选择的某一气候指标（如全球平均气温）作为检测变量，更有说服力。但是，由于它必须对气候信噪比极大化，因而需要知道气候信号与噪声两者的空间－时间结构。这种方法不仅对早期的外部强迫检测有用，而且也可用于区分不同

的强迫机制来进行归因分析[9]。研究表明，最优指纹法是与其他一些最佳平均或滤波方法十分接近的方法，在噪声背景下它可以最佳地估计出气候变化振幅，当然，这种方法也类似于其他领域的一些信号处理方法。

最优指纹法可以用多元回归来实现，即把观察的气候变化y看作是外部气候强迫$\boldsymbol{X}$的线性结合，再加上内部气候变化u，即$y = \boldsymbol{XA} + u$[9]。其中y是经过滤波的观测资料，使其能够充分反映观测气候的时空变化，矩阵$\boldsymbol{X}$包括对外部强迫响应模态，$\boldsymbol{A}$为对应这些模态的标量因子矢量，u为内部气候变率。矩阵$\boldsymbol{X}$的信号来自耦合模式（CGCM）、大气模式(AGCM)或简化气候模式如能量平衡模式（EBM）。拟合多元回归模式，需要估计自然内部变率。观测资料序列太短，而且还包括外强迫因子的影响，因此不适合用来计算内部变率。一般用CGCM的控制试验计算内部变率。

1.3 格兰杰因果检验

该方法既考察变量间的相互关系又考虑其自身变化。两个时序变量之间的因果关系检验是由Clive W. J. Granger提出的，称为格兰杰因果性分析法[10]。格兰杰的基本着眼点是两个变量$\boldsymbol{X}$与$\boldsymbol{Y}$呈高度相关，并不能说明两者之间一定存在因果关系，须对相关变量进行因果关系检验。利用概率或分布函数来表示：在所有其他事件固定不变的条件下，如果一个事件A的发生或不发生对于另一个事件B的发生概率有影响，并且两个事件在时间上又有先后顺序（A前B后），则可说A是B的原因。格兰杰因果检验主要适用于时间序列数据模型的因果性检验，其结论只是统计意义上的因果性，需要从物理角度加以审慎考察，必要时需要用数值模拟加以验证。

设两个时间序列为$\boldsymbol{X} \equiv \{x_t\}$与$\boldsymbol{Y} \equiv \{y_t\}$，$t = 1, 2, \cdots, N$（$N$为样本量）。格兰杰检验可以判断变量$\boldsymbol{X}$是否能预测变量$\boldsymbol{Y}$，若不能，则认为$\boldsymbol{X}$不能导致$\boldsymbol{Y}$，反之亦然。检验方法是判断$F$统计量的临界值是否大于$F$分布的标准值，若临界值概率$p<\alpha$，则$\boldsymbol{X}$不能导致$\boldsymbol{Y}$的零假设不成立，即$\boldsymbol{X}$能导致$\boldsymbol{Y}$。要严格确定因果关系，必须考虑到完整的信息集，也就是说，要得出结论：A是B的原因，必须全面考虑论域中所有的事件。因此，格兰杰早期提出的因果关系定义是建立在完整信息集以及发生时间先后顺序基础上的，根据条件分布函数来判断。由于用量测样本来估计分布函数是否相等是相当困难的，于是退而求其次，只验证变量的数学期望E是否相等。

2 全球尺度的气候变化检测归因

2.1 地表气温

对全球气温变化的归因分析主要是将全球气温归因为人为外部强迫（主要包括CO_2等温室气体和气溶胶辐射强迫）、自然强迫（如火山活动和太阳活动）和内部变率（如ENSO、NAO、PDO等）3部分的影响。目前对全球气温变化的归因研究结果较多，IPCC第一次评估报告表明，人类活动产生的各种排放正在使大气中的温室气体浓度显著增加，这将增强温室效应，从而使地表升温[11]。IPCC第二次评估报告表明，人类活动已经对全球气候系统造成了“可以辨别”的影响[12]。IPCC第三次评估报告表明，20世纪50年代以来观测到的大部分增暖“可能”（≥66%）归因于人类活动造成的温室气体浓度上升[13]。IPCC AR4表明，近半个世纪以来的全球变暖“很可能”（≥90%）是由人为温室气体浓度增加导致（图1）。

自IPCC AR4以来，一些新的研究进一步深化了对气温变化的归因认识。新一代气候模式（CMIP5）的结果进一步支持了温室气体强迫对气温变化的影响，对模式不确定性对归因结果的影响有了更深入的研究，对其他因子的贡献有了进一步的认识。Huber等[14]基于全球能量方法，对观测到的全球表面温度变化的贡献因子进行估计，20世纪中叶以来由温室气体增加导致的全球气候变暖约为0.85 ℃，其中大约一半被气溶胶的冷却作用抵消后，与全球观测到的变暖相当，因此观测到的温度变化趋势极不可能由自然变率引起。Stott等[15]用HadGEM2-ES模式检测出了温室气体强迫的影响。但是，他们发现有些模式和观测振幅存在不一致的现象，如CanESM2模式可能高估了温室气体的影响。Santer

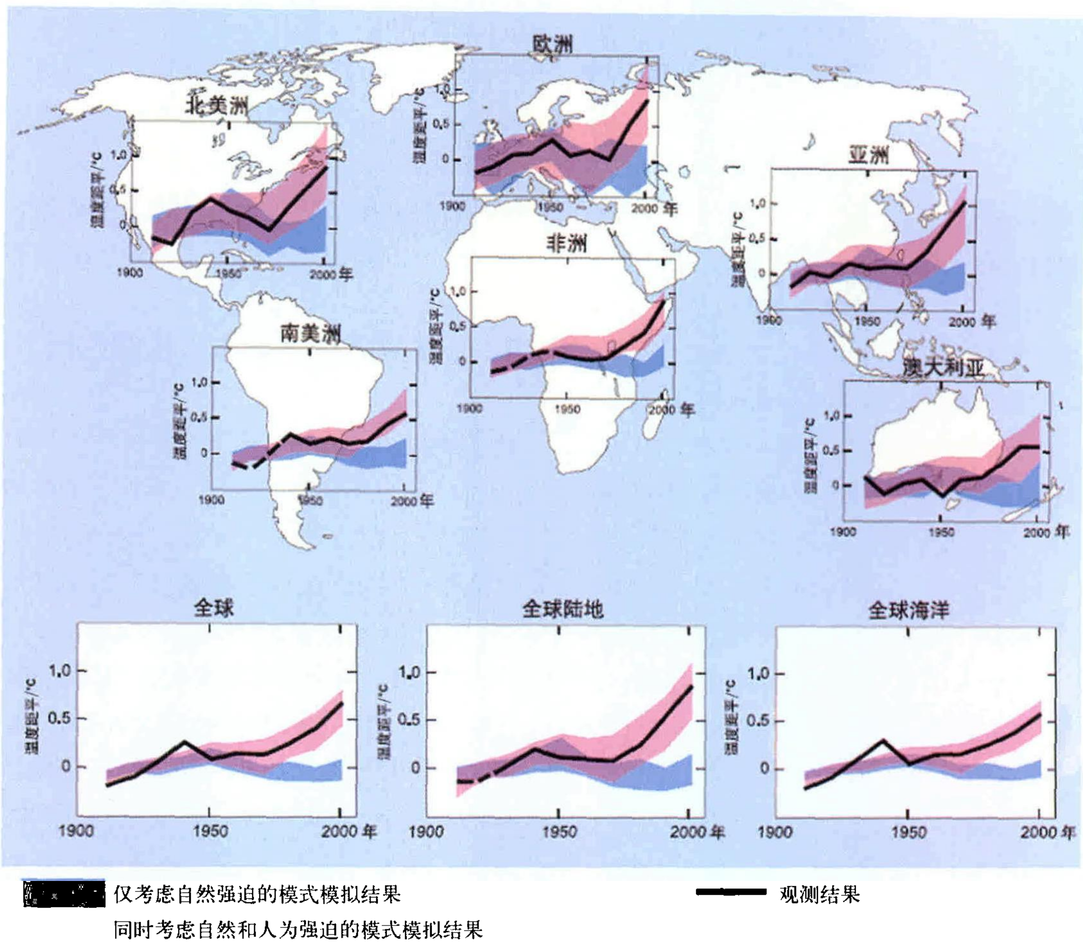

图1 观测到的大陆与全球尺度地表温度与使用自然和人为强迫的气候模式模拟结果的对比（相对于1901—1950年相应平均值，1906—2005年观测到的年代际平均值用黑线绘于年代中心，其虚线部分表示空间覆盖率低于50%。蓝色阴影表示仅使用太阳活动与火山自然强迫的5个气候模式19个模拟试验结果的5%～95%置信区间。红色阴影表示同时使用自然强迫和人为强迫的14个气候模式58个模拟试验结果的5%～95%置信区间）[5]

Fig. 1 Comparison of observed continental- and global-scale changes in surface temperature with results simulated by climate models using natural and anthropogenic forcings. Decadal averages of observations are shown for the period 1906–2005 (black line) plotted against the center of the decade and relative to the corresponding average for 1901–1950. Lines are dashed where spatial coverage is less than 50%. Blue shaded bands show the 5%–95% range for 19 simulations from 5 climate models using only the natural forcings due to solar activity and volcanoes. Red shaded bands show the 5%–95% range for 58 simulations from 14 climate models using both natural and anthropogenic forcings [5]

等[16]通过CMIP5的20个模式与卫星数据的分析发现了人类影响大气上层温度的明显证据。Jones等[17]基于HadGEM1模式对最近温度记录的分析表明，黑碳气溶胶（矿石燃料和生物燃料）的影响可以被检测出来，但黑碳气溶胶的影响比温室气体作用小。Jones等[18]利用1900—1999年HadCM3模式和5个不同观测数据得出的最优检测分析结果表明，温室气体和气溶胶的检测结论对数据的选择不敏感，回归系数是广泛一致的。然而，不同数据集的最优估计回归系数是变化的，这相当于与内部气候变率有关的不确定性。

2.2 降水

相对于地表气温的检测归因，降水的归因要困难得多。因为降水仅在陆地区域有长期的观测值，而在覆盖范围以及均一性方面，降水数据存在很大的问题。因此，由于数据问题、模式模拟结果的不一致以及降水的低信噪比，无法进行有意义的对比分

析。国际检测归因特设小组（IDAG）[19]指出，由于缺少充足的证据以及模式的不确定性，因此难以检测出人类影响下降水的变化。尽管大部分大气模式在外强迫驱动下能够较好地模拟出全球和区域的地表气温变化，但是却难以合理再现全球及区域降水变化，特别是亚洲季风区的陆地降水变化。近年来，虽然大量的多模式集合较大地提高了对温度的检测归因结论的信度，但对于降水而言，仍然难以区分各模式结果中常见的系统误差与降水变化信号，对降水的检测归因仍然是很大的挑战[20-21]。

早期对于降水的检测归因，不同研究结论间的一致性较低，甚至互相矛盾。例如，Allen 等[20]的研究显示，考虑了人类强迫和自然强迫的全球平均降水的模式模拟值与观测数据较为一致，但是Lambert 等[22]认为该一致性很可能是由于降水对自然强迫的响应。近年来，Wentz 等[23]基于 1987—2006 年观测数据的研究结果认为全球降水是依据 Clausius-Clapeyron 方程增加的，但是有研究显示，20年的研究时段不足以判断降水对全球变暖的响应的模式模拟与观测值是否一致。相比于仅有长波强迫的模拟结果，人类影响和自然强迫叠加作用下的模拟值更加接近全球平均的陆地降水观测值[24]。模拟结果显示，人为强迫可能导致全球平均降水量的增加以及降水型的经向变化，即高纬度地区降水增加，而亚热带地区的降水减少[25]，并可能通过改变热带辐合带或太平洋上沃克环流的位置从而改变热带地区的降水分布。Zhang 等[6]和Stott 等[26]的研究均表明，人为强迫对于北半球中纬地区的降水增加、北半球亚热带和热带地区的降水减少，以及南半球亚热带和热带地区的降水略增影响显著。

2.3　极端地表气温

确定极端气候变化的原因涉及一些独特问题。观测资料的数量和质量都有限，使得对过去变化的估算结果具有不确定性；许多变量的信噪比较低，资料数量不足，无法检测这类微弱的信号。此外，全球气候模式（GCM）在模拟极端值方面存在问题，降尺度技术也只能部分地规避这些问题。但是，由于极端事件检测的重要性，近年来对极端温度变化的研究大幅增加。很多研究显示，近几十年极端温度的变化中可以检测到人类活动的信号[27]。

Hegerl 等[28]指出，极端地面温度有可能受到人为强迫的影响。这一评估是基于全球多个极端温度资料集，包括对这一尺度上极暖事件数量增加和极冷事件数量减少的报告。他们同时指出人为强迫可能已使极端温度的风险大大增加，还使2003 年欧洲热浪的风险大大增加。Stott 等[29]利用单步归因理论得出，已经观测到的夏季高温频率增加的趋势在北半球以外的较多地区也均可被直接归因于人类活动的影响。

Christidis等[30]通过最优指纹法对比了观测和模拟的极端温度分布时变区域参数，首次尝试将外部动力因子和自然因子对观测到极端暖日变化的归因进行分离，并对观测到的可能引起极端温度变化的因子变化进行部分的归因，可以看出，人为因子对极端暖夜强度增加和极端冷日、冷夜强度减少存在显著影响。Zwiers 等[31]也对全球尺度及大陆和次大陆尺度上极端温度的影响进行了人类活动强迫及自然强迫分离研究，都指出了人类活动在其中的影响。

2.4　极端降水

对极端降水的检测归因研究相对较少，一方面是由于日平均降水观测资料较缺乏，另一方面是由于气候模式对降水模拟的不确定性很大，特别是在热带等受对流参数化影响较显著的地区[7]。但是，由于极端降水事件可能产生极为严重的影响，近几年在极端降水的检测与归因方面有了一些新进展。目前在做此方面研究工作时，一般首先选定几种极端降水指数，在检验模式模拟性能的基础上，基于气候模式不同强迫试验下的模拟结果，对极端降水进行检测并作归因分析。

全球气候模式集合平均的分析结果显示，在全球和半球尺度上，可以检测到人类活动对极端降水的影响。Hegerl 等[28]指出，人类活动很可能对全球20 世纪前 50 年的强降水发生频率的增长趋势是有贡献的，但是外部强迫与极端降水之间直接的影响和反馈还很难建立。Allan等[32]使用卫星观测数据和模式模拟结果检测了热带地区在自然因子驱动下，

降水与地表气温和大气含水量的反馈关系，结果表明，降水一般在暖位相期间将增加，冷位相期间将减少，且观测的极端降水幅度比模式预估结果大。Stott等[26]指出，人类活动的影响在全球水循环的不同方面都已经被检测到，而水循环与极端降水的变化直接相关。Min等[7]基于CMIP3中模式的模拟结果，使用最优指纹法对最大日降水量（RX1D）和连续5天最大降水量（RX5D）进行了分析，结果表明人类活动导致的全球变暖对北半球20世纪下半叶2/3的陆地区域上强降水事件的增加是有贡献的（图2）。

由于噪音的增加和不确定性以及其他一些因子的影响，在小的空间尺度上人类活动的检测是比较困难的。Fowler等[33]的研究表明，到目前为止，人类活动对英国冬季极端降水的影响仅可以检测出50%，而在其他季节检测出人类活动影响的可能性更小。Pall等[34]基于HadAM3-N144季节预测模式在

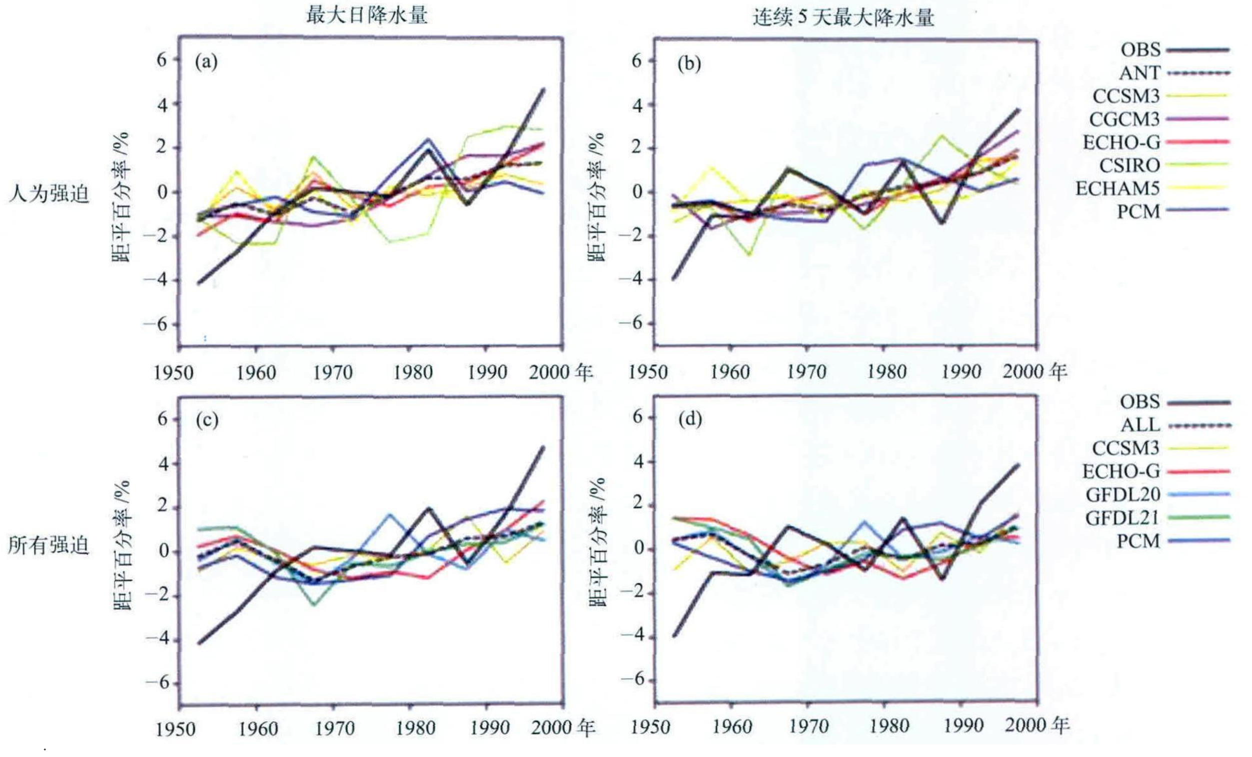

图2 1951—1999年北半球区域平均的极端降水指数距平百分率（OBS：观测；ANT：人为强迫；ALL：所有强迫）[7]
Fig. 2 Time series of five-year mean area-averaged probability-based index anomalies over Northern Hemisphere land during 1951–1999 (OBS: observation; ANT: anthropogenic forcing; ALL: anthropogenic plus natural forcing) [7]

两种不同排放情景（实际排放和假定20世纪人为温室气体排放没有发生）下的结果，使用多步归因方法对英格兰和威尔士2000年秋季洪水进行了分析，结果表明全球人为温室气体的排放对2000年秋季洪水的发生是有贡献的。

3 中国区域的气候变化检测归因

在全球范围内，人类活动影响气候变化已经得到大量的检测结果。然而，对陆地和更小尺度气候变化的检测和归因的研究要比全球尺度的研究更困难[26,28]。首先，对于小尺度的变化，内部变率比强迫响应的相对贡献要大，因为在大尺度范围内部变率的空间差异被平均掉了。其次，气候强迫响应的模式往往是大尺度的，当我们的注意力集中在全球区域范围内时，有较少的空间信息帮助区分不同强迫响应之间的差别。第三，在一些全球气候模式模拟中忽略的强迫或许在区域尺度上是重要的，例如土地利用变化或者黑碳气溶胶等。最后，模拟的内部变化和强迫响应的可靠性在小尺度比全球尺度要低，

虽然网格单元格变化通常在模式中没有被低估[35]。

鉴于上述原因，区域尺度检测归因的研究起步相对要晚。而在中国，这一领域的研究相对也比较少。针对中国区域的气温变化，一些研究利用简单或复杂的气候模式，考虑自然强迫（如太阳活动、火山活动）以及人类活动（如温室气体排放、硫酸盐气溶胶的直接和间接效应等）研究了气温变化的原因。也有试验考虑全球气候系统中圈层之间的相互作用，如考虑海温或ENSO的作用，以检测东亚温度和降水变化的原因。大多数气候模式模拟20世纪的全球气候变化，也有些模式模拟1000年中国的气候变化。下面本文将从地表气温、降水和极端事件3个方面回顾在该领域的研究成果。

3.1　地表气温和降水

在气候增暖的检测归因方面，中国学者从观测分析到数值模拟开展了大量工作，而对降水的检测归因则多与季风的变化联系在一起。在对气温的归因方面，利用全球和区域气候模式，多数研究的共识是，20世纪东亚和中国变暖，除了气候的自然变化，人类活动可能起了一定作用，尤以20世纪50年代以来最明显[1,36]。Zhou等[37]检验了参加IPCC AR4的19个耦合模式对20世纪全球和中国气温变化的模拟，其中对全球地表平均温度的模拟效果较好，但是对20世纪中国气温演变的耦合模式模拟效果要差。外强迫解释了20世纪中国年平均气温变化的32.5%，而内部变率（噪音）的贡献则高达67.5%，信噪比仅为0.69。这意味着对区域尺度的气温变化而言，强迫机制较之全球平均情况要复杂得多。Duan等[38]利用海气耦合模式对青藏高原20世纪气候的模拟发现，全球温室气体浓度增加对青藏高原变暖有贡献，而且由于高原上空臭氧浓度下降，温室气体浓度的增加对青藏高原的影响可能比其他地区更重要。满文敏等[39]基于气候系统模式FGOALS_g1对20世纪气温变化的模拟表明，对中国地区而言，20世纪早期的气温变化受自然变率影响，但20世纪后期的变暖主要是温室气体增加的结果。在自然和人为因子共同作用下，模式能够再现20世纪50年代以来中国东部气温变化冬、春两季增暖的特征，但没有模拟出夏季长江中下游地区及淮河流域的降温趋势。关于气溶胶对中国气候变冷的影响，周秀骥等[40]在区域气候模式中考虑了气溶胶的影响，模拟结果显示中国大陆地区的地面气温均有所下降。Menon等[41]研究认为中国黑碳气溶胶对区域气候变冷作用具有显著影响；另外，硫酸盐气溶胶的辐射影响具有明显的季节变化和地理分布特征，大量的模拟研究显示，夏季硫酸盐气溶胶对中国东部区域气温变冷具有显著贡献[42]。

对于20世纪70年代以来中国东部地区“南冷北暖”“南涝北旱”的气候变化，姜大膀等[43]基于6套全球海气耦合气候模式的数值模拟结果，指出20世纪后期东亚夏季风的年代际减弱（对应降水的“南涝北旱”现象）与同期人类活动引发的全球变暖之间没有明显的联系；如果21世纪温室效应在20世纪后期的基础上进一步加剧，东亚夏季风系统可能会受此影响而趋于增强。周天军等[44]基于大气环流模式特别是区域气候模式的数值试验表明，夏季硫酸盐气溶胶的负辐射效应超过了温室气体的增暖效应，从而对变冷产生贡献。但现有的数值模拟证据不足以说明气溶胶增加对“南涝北旱”型降水异常有贡献。

3.2　极端事件

在极端事件的归因方面，中国的研究相对较少。龚道溢等[45]指出北极涛动（AO）对中国大部分地区冬季气温有一定影响，通过最高和最低气温计算得来的冬季极端温度指数（暖日、冷日、暖夜和冷夜）也必将受到同期AO的影响。冬季AO对这些地区的冬季极端温度指标有显著的影响。龚志强等[46]研究表明，中国温度升高及极端温度出现频数变化的原因可能在于3个方面：(1) 全球范围内的温室效应的增强；(2) 经济发达地区、人口密集地区的城市热岛效应乃至区域热岛效应的加强；(3) 火山活动等各种外强迫的加强。杨萍等[47]的研究表明，20世纪90年代以来夏季显著的热岛效应，是城区极端高温事件发生频次明显高于其他地区的重要原因；但城区极端低温事件的发生频次有可能发生了与热岛效应无关的突变过程。中国科学家利用近百年资料和分辨率较高的区域气候模式对极端天气事件进行的分析

和模拟表明，温室效应将使中国区域的日最高和最低气温明显升高，而日较差减小。模拟得到的年平均日最高气温的显著增加区基本位于中国南部，而最低气温在黄河以北和长江以南的增加更显著。

4 气候变化检测归因研究的不确定性

目前，气候变化检测归因研究主要基于观测资料和气候模式模拟结果，使用各种统计方法进行。在这个过程中，主要存在两个方面的不确定性：一是模式的不确定性，二是观测资料的不确定性[3]。其中模式的不确定性主要来源于模式本身物理、化学、生物过程的不完善，如气溶胶－云－辐射的耦合、生态系统对气候变化的响应与反馈等；另一方面是辐射强迫的不确定性，对于充分混合的温室气体来说，辐射强迫的不确定性较小，但是对于一些其他类型的辐射强迫，如气溶胶、森林变农田的陆面变化的辐射强迫非常大。同时，阶段性的火山活动和太阳释放总能量的变化也存在不确定性，如20世纪之前火山强迫有很大的不确定性，而卫星时代以前太阳辐射强迫的估计存在很大的不确定性。

用于检验气候模式结果的观测资料不足及观测资料本身的限制等原因，观测资料也存在一定的不确定性。以气温为例，在观测网络覆盖范围、经纬度单元格内数据源分布状况、不同年代际温度记录数量的差异、温度序列长度、站点气温观测连续性、站点的城乡分布、城乡温度差异、城市热岛效应等方面都存在着一定的差异[48]，降水的观测更加复杂，不确定性更大。如城市化对地面气温记录的影响难以完全分离，现有的全球和区域陆面气温序列中还不同程度地保留着城市热岛效应增强因素的影响，在一些发展迅速、城乡差别悬殊的国家和地区，城市化的影响尤为突出。

5 结语和未来展望

总的来说，随着最近几年观测资料的增加，检测归因方法和技术的进一步完善，以及国际上大规模气候模式比较计划的实施与开展，气候变化的检测归因研究在国际上取得了较大的进展。如表 1 所示，现在对全球和大陆尺度地表气温变化的归因有了很好的认识。对人为信号的识别扩展到了气候的很多方面，包括海洋变暖、大陆尺度的平均温度、温度极值以及风场。同时，对其他变量的归因研究也开始推进，包括大气高层的温度、降水和北极海冰等。开始对一些复杂的科学问题，如气候极端事件与气候变化的关系，不同时间尺度气候变化的成因或机理等问题进行研究。这些研究结果的出现，极大地深化了对引起气候变化原因这一科学问题的认识，推进了相关领域的研究进展。从未来的发展来

表 1 IPCC 第一工作组 4 次评估报告关于气温和降水变化检测归因的研究结论[5,11-13]

Table 1 Conclusions of detection and attribution of temperature and precipitation changes in the four assessment reports by Intergovermental Panel on Climate Change (IPCC) working group I (WGI)

IPCC 评估报告	关于气温的主要结论	关于降水的主要结论
第一次（1990 年）	人类活动产生的各种排放正在使大气中的温室气体浓度显著增加，这将增强温室效应，从而使地表升温	观测到陆地部分区域的降水变化，海洋上的降水由于缺少数据难以得到其趋势。没有关于人为强迫对降水影响的相关内容
第二次（1995 年）	人类活动已经对全球气候系统造成了“可以辨别”的影响	降水的变化与地球表面正在变暖的气候是一致的（如更活跃的水循环、更多的严重降水事件和降水时间的改变）
第三次（2001 年）	20 世纪 50 年代以来观测到的大部分增暖“可能”归因于人类活动造成的温室气体浓度上升	观测到的北半球高纬度降水变化与模式对人类强迫响应的模拟结果间存在定性的一致性
第四次（2007 年）	20 世纪 50 年代以来的全球变暖“很可能”是由人为温室气体浓度增加所导致。可辨别的人类活动影响扩展到了气候的其他方面，包括海洋变暖、大陆尺度的平均温度、温度极值以及风场	可辨别的人类活动影响尚未能够扩展到降水变化。但有研究表明：考虑人为影响和自然变率的模式模拟陆地降水与观测值相关显著

看，虽然观测资料和气候模式的不确定性对检测归因的研究结果有较大影响，但仍可预期，随着科技的进步和资料、模式等的发展，检测归因研究还将取得更大的进展。

而从中国现阶段的情况来看，由于我国在检测归因领域的起步很晚，在这一领域仍然缺乏强有力的科技支撑，因此需要加强这一领域的工作，提升我国在气候变化检测归因领域的影响力，深化对东亚地区人为或自然气候变化的机理认识，为我国参与气候变化国际合作和国际谈判提供科学基础。未来我们将可能在以下几个方面加强研究：

(1) 针对中国的气候变化问题，需要加强基于数理统计方法的气候变化检测归因研究。在我国，虽然一些工作揭示了温室气体或气溶胶在东亚地区温度和降水变化中的作用，但是，这些工作所应用的方法基本都是一致性检验的方法，即使用不同强迫因子驱动气候模式所得到的结果和观测进行对比，没有进一步应用数理统计方法(如最优检测法等)对这些结果进行统计分析和推断，而这些统计推断方法正是检测归因分析的核心内容。因此，我们需要针对一些重要的科学问题，如人为和自然因子对中国区域气候变化的不同贡献做出研究，尤其是对一些关键变量，如温度、降水、极端事件以及对东亚地区有着重要影响的季风等大尺度环流的归因等，要加强研究。

(2) 对检测归因分析中的一些关于观测资料和模式的关键科学技术方法需要加强研究。观测资料的选取以及不同观测资料的差异对归因结果可能存在什么样的影响，明确如何选取有代表性的观测资料是进行检测归因研究的必要工作之一。同时，东亚地区由于其特殊的地理位置和复杂的气候过程，大部分气候模式对东亚气候的模拟性能较差，如何挑选有意义的气候指标，如何最大程度地在区域尺度上使信噪比最大化，如何合理地使用统计方法理解模式的结果和不确定性，都是在东亚地区的检测归因研究中的关键技术问题。

(3) 加快与国际接轨，加强对区域尺度和不同变量气候变化的归因研究。从目前的科学认识水平来看，虽然对于区域尺度气候变化的检测归因仍然被认为是一个很复杂的问题，但国际上已经开始在相关领域进行了很多的工作。而随着国际上大规模气候模式比较计划的开展，气候模式分辨率的提高以及模式性能的加强，未来对区域尺度上不同变量变化趋势的检测与归因将会有较大进展。因此，对于东亚区域而言，未来需要加强不同变量变化趋势的检测与归因研究，以满足对理解区域气候变化原因认识的不同需求。■

参考文献

[1] 《气候变化国家评估报告》编写委员会. 气候变化国家评估报告 [M]. 北京: 科学出版社, 2007: 80-105

[2] 王绍武, 罗勇, 赵宗慈, 等. 气候变暖的归因研究 [J]. 气候变化研究进展, 2012, 8 (4): 308-312

[3] Hergerl G C, Hoegh-Guldberg O, Casassa G, *et al*. Good practice guidance paper on detection and attribution related to anthropogenic climate change [R/OL]. 2010 [2012-12-20]. http://www.ipcc.ch/pdf/supporting-material

[4] Zwiers F W, Hergerl G C. Climate change: attributing cause and effect [J]. Nature, 2008, 453: 296-297

[5] IPCC. Climate change 2007: the physical science basis [M]. Cambridge: Cambridge University Press, 2007

[6] Zhang X B, Zwiers F W, Hegerl G C, *et al*. Detection of human influence on twentieth-century precipitation trends [J]. Nature, 2007, 448: 461-465

[7] Min S K, Zhang X B, Zwiers F W, *et al*. Human contribution to more intense precipitation extremes [J]. Nature, 2011, 470: 378-381

[8] Hergerl G C, Zwiers F. Use of models in detection and attribution of climate change [J]. WIREs Climate Change, 2011 2 (1): 570-591

[9] Hasselmann K. Conventional and Bayesian approach to climate-change detection and attribution [J]. Quart J R Met Soc, 1998, 124: 2541-2565

[10] 曹永福. 格兰杰因果性检验评述 [J]. 世界经济统计研究, 2005 (52): 16-21

[11] IPCC. Climate change 1990: the IPCC scientific assessment [M]. Cambridge: Cambridge University Press, 1990

[12] IPCC. Climate change 1995: the science of climate change [M]. Cambridge: Cambridge University Press, 1996

[13] IPCC. Climate change 2001: the scientific basis [M]. Cambridge: Cambridge University Press, 2001

[14] Huber M, Knutti R. Anthropogenic and natural warming inferred from changes in Earth's energy balance [J]. Nature Geoscience, 2012, 5: 31-36

[15] Stott P A, Jones G S. Observed 21st century temperatures further constrain likely rates of future warming [J]. Atmosphere Science Letter, 2012, 13: 151-156

[16] Santer B D, Painter J F, Mears C A, *et al*. Dentifying human influences on atmospheric temperature [J]. PNAS, 2013, 110 (1): 26-33

[17] Jones G S, Christidis N, Stott P A. Detecting the influence of fossil fuel and bio-fuel black carbon aerosols on near surface temperature changes [J]. Atmospheric Chemistry Physics, 2011, 11: 799-816
[18] Jones G S, Stott P A. Sensitivity of the attribution of near surface temperature warming to the choice of observational dataset [J]. Geophysical Research Letters, 2011, 38, L21702, doi: 10.1029/2011GL049324
[19] The International Ad Hoc Detection and Attribution Group (IDAG). Detecting and attributing external influences on the climate system: a review of recent advances [J]. Journal of Climate, 2005, 18: 1291-1314
[20] Allen M R, Ingram W J. Constraints on future changes in climate and the hydrologic cycle [J]. Nature, 2002, 419: 224-232
[21] Hergerl G C, Zwiers F W, Stott P A, *et al.* Detectability of anthropogenic changes in annual temperature and precipitation extremes [J]. Journal of Climate, 2004, 17: 3683-3700
[22] Lambert F H, Stott P A, Allen M R, *et al.* Detection and attribution of changes in 20th century land precipitation [J]. Geophysical Research Letters, 2004, 31, L10203, dio:10.1029/2004GL019545
[23] Wentz F J, Ricciardulli L, Hilburn K, *et al.* How much more rain will global warming bring? [J]. Science, 2007, 317: 233-235, doi: 10.1126/science. 1140746
[24] Lambert F H, Allen M R. Are changes in global precipitation constrained by the tropospheric energy budget? [J]. Journal of Climate, 2009, 23: 499-517
[25] Held I M, Soden B J. Robust responses of the hydrological cycle to global warming [J]. Journal of Climate, 2006, 19: 5686-5699
[26] Stott P A, Gillett N P, Hegerl G C, *et al.* Detection and attribution of climate change: a regional perspective [J]. Wiley Interdisciplinary Reviews: Climate Change, 2010, 1: 192-211
[27] IPCC. Managing the risks of extreme events and disasters to advance climate change adaptation [M]. Cambridge: Cambridge University Press, 2012: 1-582
[28] Hegerl G C, Zwiers F W, Braconnot P, *et al.* Understanding and attributing climate change [M]//IPCC. Climate change 2007: the physical science basis. Cambridge: Cambridge University Press, 2007
[29] Stott P A, Jones G S, Christidis N, *et al.* Single-step attribution of increasing frequencies of very warm regional temperatures to human influence [J]. Atmospheric Science Letters, 2011, 12: 220-227
[30] Christidis N, Stott P A, Brown S J. The role of human activity in the recent warming of extremely warm daytime temperatures [J]. Journal of Climate, 2011, 24: 1922-1930
[31] Zwiers F W, Zhang X, Feng Y, Anthropogenic influence on long return period daily temperature extremes at regional scales [J]. Journal of Climate, 2011, doi: 10.1175/2010JCLI3908.1
[32] Allan P R, Soden J B. Atmospheric warming and the amplification of precipitation extremes [J]. Science, 2008, 321: 1481-1484
[33] Fowler H J, Wilby R L. Detecting changes in seasonal precipitation extremes using regional climate model projections: implications for managing fluvial flood risk [J]. Water Resources Research, 2010, 46, W0525, doi: 10.1029/2008WR007636
[34] Pall P, Allen M R, Stone D A. Testing the Clausius-Clapeyron constraint on changes in extreme precipitation under CO_2 warming [J]. Climate Dynamics, 2007, 28: 353-361
[35] Wu Q G, Karoly D J. Implications of changes in the atmospheric circulation on the detection of regional surface air temperature trends [J]. Geophysical Research Letters, 2007, 34, L08703, doi: 10.1029/2006GL028502
[36] 周天军，赵宗慈．20 世纪中国气候变暖的归因分析 [J]. 气候变化研究进展，2006, 2 (1): 28-31
[37] Zhou T J, Yu R C. Twentieth century surface air temperature over China and the globe simulated by coupled climate models [J]. Journal of Climate, 2006, 19 (22) : 5843-5858
[38] Duan A M, Wu G X, Zhang Q, *et al.* New proofs of the recent climate warming over the Tibetan Plateau as a result of the increasing greenhouse gases emissions [J]. Chinese Science Bulletin, 2006, 51 (11): 1396-1400
[39] 满文敏，周天军，张丽霞，等．20 世纪温度变化中自然变率和人为因素的影响：基于耦合气候模式的归因模拟 [J]. 地球物理学报，2012, 55 (2): 372-383
[40] 周秀骥，李维亮，罗云峰．中国地区大气气溶胶辐射强迫及区域气候效应的数值模拟 [J]. 大气科学，1998, 22 (4): 418-427
[41] Menon S, Hansen J, Najarenko L, *et al.* Climate effects of black carbon aerosols in China and India [J]. Science, 2002, 297: 2250-2252
[42] Huang Y, Chameides W L, Dickinson R E. Direct and indirect effects of anthropogenic aerosols on regional precipitation over East Asia [J]. Journal Geophysical Research, 2007, 112, D03212, doi: 10. 1029/ 2006JD007114
[43] 姜大膀，王会军. 20世纪后期东亚夏季风年代际减弱的自然属性 [J]. 科学通报，2005, 50 (20): 2256-2262
[44] 周天军，李立娟，李红梅，等．气候变化的归因和预估模拟研究 [J]. 大气科学，2008, 2 (4) : 906-922
[45] 龚道溢，王绍武．近百年北极涛动对中国冬季气候的影响 [J]. 地理学报，2003, 58 (4): 559- 568
[46] 龚志强，王晓娟，支蓉，等．中国近 58 年温度极端事件的区域特征及其与气候突变的联系 [J]. 物理学报，2009, 58 (6): 4342-4353
[47] 杨萍，刘伟东，侯威．北京地区极端温度事件的变化趋势和年代际演变特征 [J]. 灾害学，2011, 26 (1): 60-64
[48] 王芳，葛全胜，陈泮勤．IPCC 评估报告气温变化观测数据的不确定性分析 [J]. 地理学报．2009, 64 (7): 828-838

Recent Progress in Studies of Climate Change Detection and Attribution in the Globe and China in the Past 50 Years

Sun Ying, Yin Hong, Tian Qinhua, Hu Ting, Shi Ying, Liu Hongbin, Zhou Botao

National Climate Center, China Meteorological Administration, Beijing 100081, *China*

Abstract: We reviewed recent studies about detection and attribution of climate change in the globe and China, with focus on the detection and attribution of temperature, precipitation and major extreme events changes since 1950s. The detection and attribution of historical climate change at a longer time scale are not considered in the paper. The investigation shows that there are very quick advance in the international field of detection and attribution. Many studies cover the field from the detection and attribution of temperature at global scale to regional scale, and from temperature to multi-variables. However, in China, the relevant study is still at an initial stage. Although some studies explore the physical reasons behind the dry North China and wet South China since 1970s, the detection and attribution studies based on statistical inference methods are still very little and need to be strengthened. Many important issues, such as the reasons for regional climate change, the contribution from various factors and their difference with those at global scale, are needed to answer.

Key words: detection and attribution; climate change; global scale; regional scale

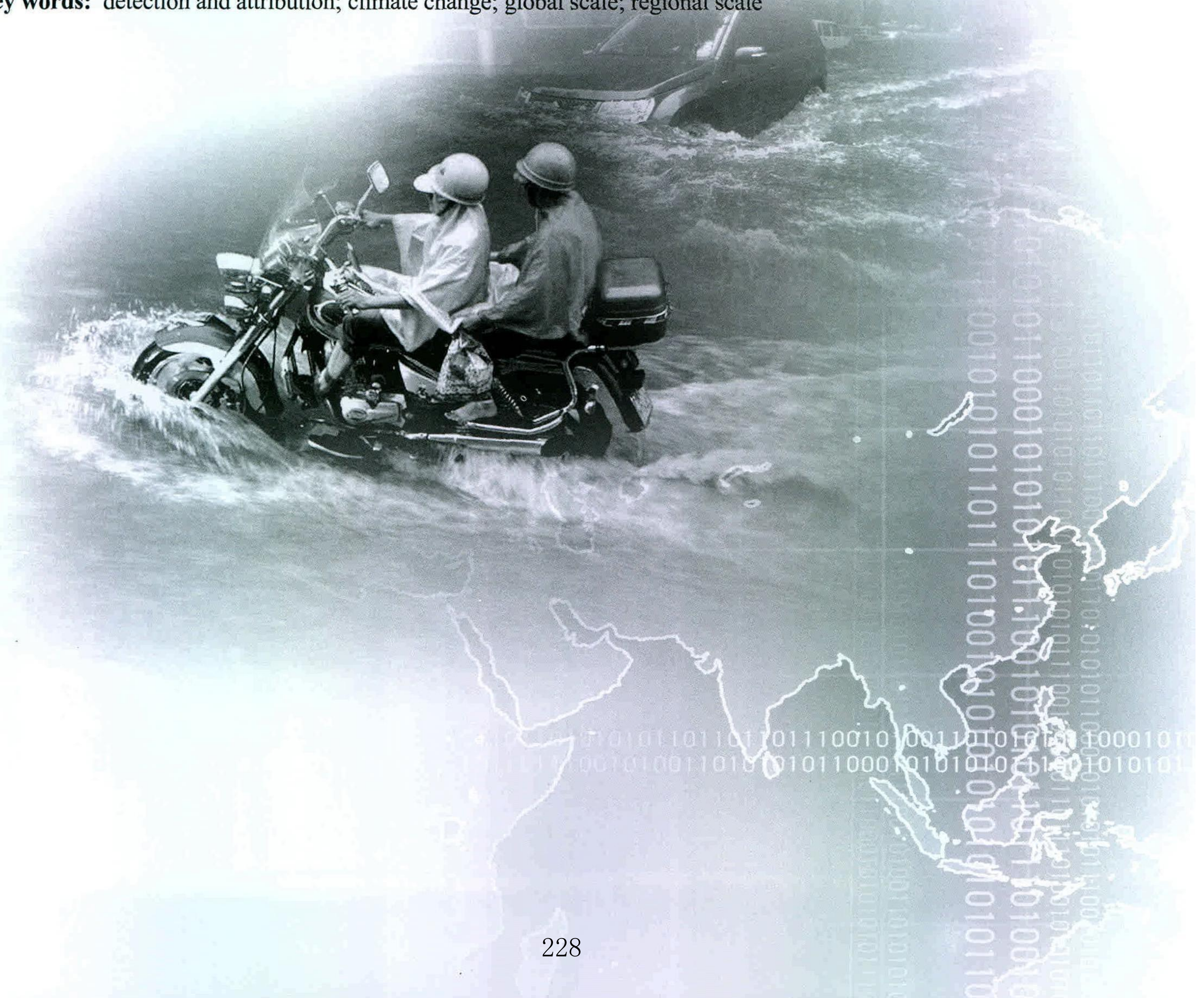

王东阡，周兵，孙丞虎，等.2013.2012/2013年东亚冬季风活动特征及其可能成因分析.气象，39(7)：930-937.

2012/2013年东亚冬季风活动特征及其可能成因分析*

王东阡[1,2] 周 兵[1] 孙丞虎[1] 袁 媛[1] 柳艳菊[1] 王朋岭[1]

1 国家气候中心，北京 100081

2 中国气象局气候研究开放实验室，北京 100081

提 要：东亚冬季风目前处于年代际偏强的气候背景下，2012/2013年东亚冬季风强度指数(EAWM)为0.83，连续第六年强度偏强。2012/2013年冬季，北极涛动(AO)指数维持负位相，导致全国平均气温较常年同期略偏低。季内，西伯利亚高压强度变化显著，与之相对应，我国气温季内阶段性变化大，前冬冷、后冬暖。进一步研究表明，前秋北极海冰的大幅偏少是造成东亚冬季风偏强的重要原因，前期海冰范围的减少有利于冬季欧亚大陆北部的海平面气压出现正异常，致使西伯利亚高压的偏强，有利于冷空气南下我国。而西伯利亚高压和东亚冬季风季内变化主要是受平流层环流异常信号影响，1月中旬前后，北半球高纬地区平流层位势高度出现明显正异常并迅速下传影响对流层中低层，造成西伯利亚高压和冬季风季内阶段性偏弱。

关键词：东亚冬季风，西伯利亚高压，北极涛动，北极海冰

中图分类号：P461 **文献标志码**：A **doi**：10.7519/j.issn.1000-0526.2013.07.014

Features and Possible Causes for East Asian Winter Monsoon in 2012/2013

WANG Dongqian[1,2] ZHOU Bing[1] SUN Chenghu[1] YUAN Yuan[1] LIU Yanju[1] WANG Pengling[1]

1 National Climate Centre, Beijing 100081

2 Laboratory for Climate Studies, CMA, Beijing 100081

Abstract: The East Asian winter monsoon (EAWM) was in the phase stronger than normal in the interdecadal variation, and the EAWM index was 0.83 in winter 2012/2013, which was the 6th consecutive year with strong intensity. During the winter from December 2012 to February 2013, the daily Arctic Oscillation index was negative, leading to a colder than normal situation over China. While the Siberian High (SH) exhibited strong intra-seasonal variations, the temperature over China had two-stage variations last winter, warmer in the early winter and colder in the late winter. Further research indicated that the reduced Arctic sea ice extent in the last autumn was responsible for the positive sea level pressure (SLP) in the Northern Eurasia in winter, resulting in the strengthening of Siberian High which was favorable for cold front to move southward into China. The intra-seasonal variation of the SH and EAWM was mainly affected by the downward propagation of positive geopotential height anomalies in stratosphere. The positive stratospheric anomalies over the high-latitude areas in Northern Hemisphere in mid-January had an

* 国家自然科学基金项目(41205042)、国家重大科学研究计划(2012CB955901)、中国气象局气象关键技术集成与应用项目(CMAGJ2013Z08)和中国气象局气候研究开放实验室2012/2013年度开放青年基金资助项目共同资助

2013年4月17日收稿； 2013年5月10日收修定稿

第一作者：王东阡，主要从事气候监测诊断工作.Email：wangdq@cma.gov.cn

evident influence on the mid and low levels of troposphere, causing the periodical weakening of SH and EAWM.

Key words: East Asian winter monsoon (EAWM), Siberian high, Arctic Oscillation, Arctic sea ice

引　言

东亚冬季风是东亚季风系统中重要的组成部分，是北半球冬季最活跃的大气环流系统之一，东亚冬季风的异常直接影响东亚地区冬季天气气候特征。当东亚冬季风偏强时，低层西伯利亚高压和阿留申低压偏强，中层东亚大槽偏深，造成副热带北风气流偏强，东亚副热带地区气温偏低（Lan et al，1984；陈隽等，1999；高辉，2007）。东亚冬季风系统与我国冬季气候异常也有着密切的关系，研究表明，东亚冬季风强度与我国各地冬季气温均为负相关，偏强的东亚冬季风会导致冷空气和寒潮活动频繁影响我国地区，造成低温冷害等灾害性天气频发（Chang et al，1982；Ding et al，1987；Zhang et al，1997；郭其蕴，1994；孙丞虎等，2012）。统计分析发现（吴尚森等，2000），异常偏强的东亚冬季风还会造成我国华南地区冬季异常冷月的出现。同时，东亚冬季风的发展变化也与我国春季和夏季的气候异常有一定的关系。

2012/2013 年冬季，东亚冬季风强度较常年同期略偏强，季风强度季内变化显著，与之相对应，我国冬季平均气温－3.7℃，较常年同期（－3.4℃）偏低 0.3℃，季内，我国气温变化呈现前冬冷、后冬暖的阶段性变化特征。前冬东北、华北地区气温均创近 40 年新低，低温雨雪天气导致新疆北部、内蒙古中东部及黑龙江东北部等地遭受不同程度雪灾，对部分地区交通安全、物流运输和电力供应造成不利影响（黄威，2013；花丛，2013）；而在后冬，全国除东北和内蒙古东部偏冷外，其余大部地区气温以偏暖为主（关月等，2013；安林昌等，2013）。由此可见，东亚冬季风强度的季内变化与我国冬季天气气候异常有密切的联系，那么，影响东亚冬季风系统的主要外强迫因子是什么？造成东亚冬季风强度季内变化的原因又是什么？本文将针对上述问题加以分析，并试图给出初步的解释。

1　资料和方法

本文使用的主要资料包括：国家气象信息中心提供的 1951 年以来中国 2286 站温度资料，美国气象环境预报中心（NCEP）和美国国家大气研究中心（NCAR）提供的 NCEP/NCAR 再分析数据集（Kalnay et al，1996），以及美国国家海洋和大气管理局（NOAA）提供的 IMS 海冰积雪范围数据集（Helfrich et al，2007）。本文使用的气候平均值为 1981—2010 年。

为表征东亚冬季风活动特征，本文还计算东亚冬季风指数（朱艳峰，2008）和西伯利亚指数，具体定义为：

东亚冬季风指数：

$$I_{\mathrm{EAWM}} = U_{500}(25^\circ \sim 35^\circ\mathrm{N}, 80^\circ \sim 120^\circ\mathrm{E}) - U_{500}(50^\circ \sim 60^\circ\mathrm{N}, 80^\circ \sim 120^\circ\mathrm{E})$$

西伯利亚高压指数：

$$I_{\mathrm{SH}} = SLP(40^\circ \sim 60^\circ\mathrm{N}, 80^\circ \sim 120^\circ\mathrm{E})$$

2　2012/2013 年冬季东亚冬季风活动及其影响

2.1　东亚冬季风活动特征

2012/2013 年冬季，东亚冬季风强度指数为 0.83，较常年同期略偏强（图 1）。从其年代际变化特征上看，东亚冬季风目前处于年代际偏强的阶段，已连续 6 年强度偏强。季内，冬季风强度变化显著，前冬冬季风偏强，后冬冬季风偏弱，2 月上旬出现低频尺度的偏强阶段（图2）。西伯利亚高压同样处于

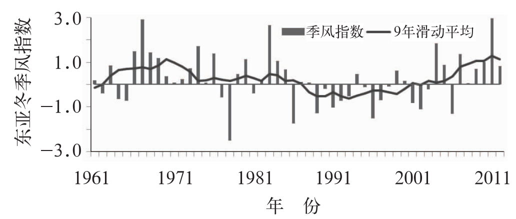

图 1　1961—2012 年东亚冬季风标准化强度指数（EAWM）演变

Fig. 1　Variation of standardized East Asian winter monsoon (EAWM) index during 1961－2012

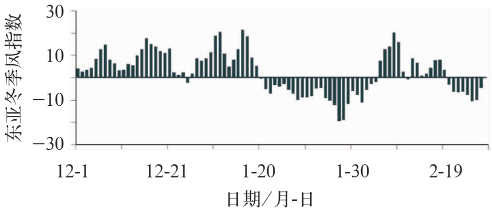

图2 2012/2013年东亚冬季风强度指数(EAWM)逐日演变

Fig. 2 Daily variation of East Asian winter monsoon (EAWM) index in 2012/2013

偏强的年代际背景下，但2012/2013年冬季西伯利亚总体强度呈现正常略偏弱的特征(图3)；逐日监测表明，西伯利亚高压强度表现出与东亚冬季风相对应的季内变化特征(图4)。

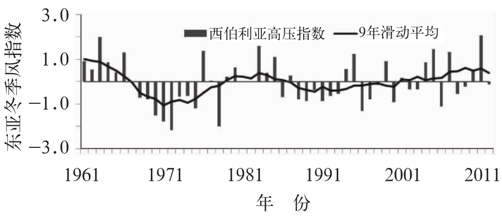

图3 1961—2012年冬季标准化西伯利亚高压强度指数(SH)演变

Fig. 3 Variation of standardized Siberian High (SH) intensity index in winters of 1961—2012

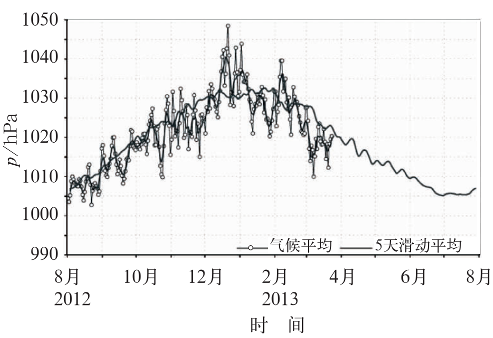

图4 2012/2013年冬季西伯利亚高压强度逐日演变(单位：hPa)

Fig. 4 Daily variation of Siberian High (SH) intensity index in winter 2012/2013 (unit: hPa)

2.2 我国冬季气温异常特征

2012/2013年冬季，全国平均气温−3.7℃，较常年同期(−3.4℃)偏低0.3℃(图5)。与常年同期相比，东北大部、内蒙古东部、华北大部、华东大部、华中大部、新疆北部和中部、西藏西部部分地区气温偏低，其中东北大部、内蒙古东部、华北东北部、新疆北部和西藏西部局部地区偏低2～4℃，局部偏低4℃以上；其余大部地区气温接近正常或偏高，其中云南大部和青海南部气温偏高1～2℃(图6)。季内，我国气温变化呈现前冬冷、后冬暖的阶段性变化特征，其中2012年12月上旬至2013年1月上旬，全国除西南地区略偏暖外，北方和中东大部气温偏低2～4℃，部分地区偏低达4℃以上。2013年1月上旬至2月下旬，全国除东北大部和内蒙古东部偏冷外，其余大部地区气温以偏暖为主(图7)。

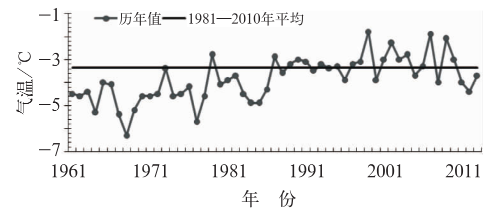

图5 冬季全国平均气温(单位：℃)历年变化

Fig. 5 Variation of the winter mena temperatures over China during 1961—2011 (unit: ℃)

2.3 我国极端事件特征

2012/2013年冬季，共有9次冷空气过程影响我国，受冷空气活动影响，我国主要发生了极端低温、极端日降温和极端连续降温事件。全国共有128站的日最低气温达极端低温事件监测标准，主要分布在华北北部、西南东北部和新疆等地，其中西藏狮泉河(−36.7℃)等6站的日最低气温突破历史极值(图8)。同期，全国共有141站发生极端日降温事件，主要发生在东北南部、华南和青海、西藏等地，普遍降温幅度达10℃以上，其中18站的降温幅度突破历史极值(图9)。另外，黑龙江、青海和西藏等地共45站的连续降温幅度达极端事件监测标准，其中3站的连续降温幅度突破历史纪录。

3 2012/2013年冬季大尺度环流异常特征

3.1 北极涛动

北极涛动(AO)作为高纬地区大气环流异常的

重要组成部分,与欧亚中高纬地区表面气温和海平面气压变化都有密切联系,并通过影响西伯利亚高压影响东亚冬季风的强度变化(Thompson et al, 1998; 2000; Wallace, 2000; Wang et al, 2000)。2012/2013 年冬季,AO 指数持续维持负位相,有利于极地的冷空气向南侵袭影响我国。图 10 给出冬季 AO 指数与表面气温和 200 hPa 纬向风场的相关关系。可见,欧亚地区中高纬大部分地区为显著的正相关区域,表明AO位于负位相时,对应欧亚中高

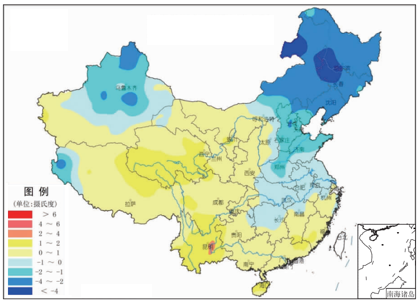

图 6　2012/2013 年冬季全国平均气温距平(单位:℃)

Fig. 6　Mean temperature anomalies of China in winter 2012/2013 (unit: ℃)

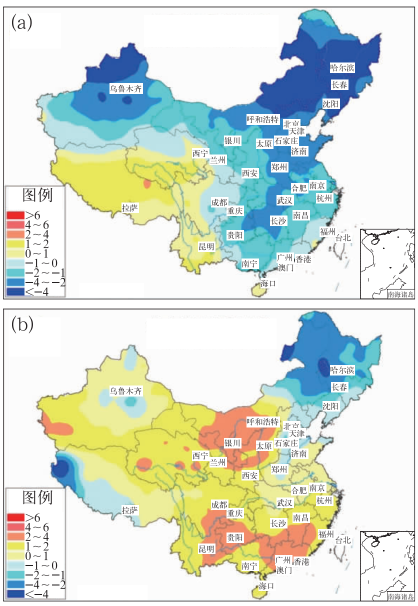

图 7　全国平均气温距平(单位:℃)
(a)12 月 1 日至 1 月 10 日平均,
(b)1 月 11 日至 2 月 28 日平均

Fig. 7　Mean temperature anomalies of China (unit: ℃)
(a) 1 December to 10 January,
(b) 11 January to 28 February

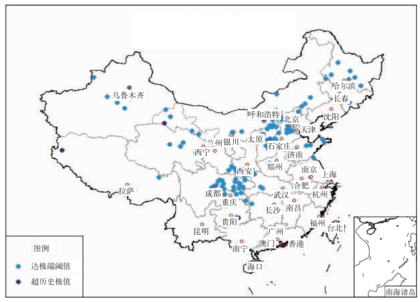

图 8　2012/2013 年冬季(2012 年 12 月 1 日至 2013 年 2 月 28 日)全国极端低温事件站点分布

Fig. 8　Station distribution of extreme daily minimum temperatures (DMT) from 1 December 2012 to 28 February 2013

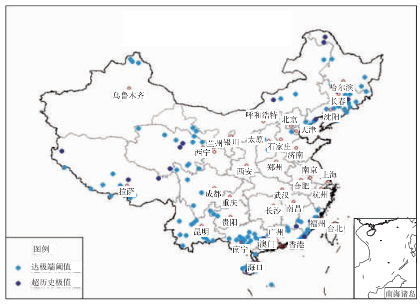

图 9　2012/2013 年冬季(2012 年 12 月 1 日至 2013 年 2 月 28 日)全国极端日降温事件站点分布

Fig. 9　Station distribution of extreme daily temperature drop (DTD) from 1 December 2012 to 28 February 2013

纬地区表面气温负异常(图 10a)。一方面,中高纬地区气温的偏低减弱了该地区与极区的经向温度梯度,从而不利于纬向西风的加强,如图 10b 所示,欧亚大陆 50°~80°N 区域为 AO 指数与 200 hPa 纬向风正相关区域,表明 AO 负位相时该区域纬向西风减弱;另一方面,减弱的纬向基本流有利于中高纬地区环流经向度加大,槽脊活动增多,引导极地的冷空气南下影响欧亚中高纬地区,造成该地区表面气温偏低。

3.2　高低层环流特征

根据上节的分析,北极涛动(AO)持续负位相有利于欧亚中高纬地区环流经向度加大,图 11a 给出 2012/2013 年冬季对流层 500 hPa 高度及其异常场

分布，分析表明，在 500 hPa 高度场上，欧亚大陆中高纬环流呈“两槽一脊”的环流形势，乌拉尔山的高压脊持续偏强，而东亚槽也异常偏强，有利于冷空气沿高空槽南下。此外，东亚中纬地区，位势高度距平场上为“北低南高”异常分布型，导致我国东部长江以北地区的东北、华北、内蒙古东部以及黄淮地区气温偏低，而长江以南的大部分地区气温偏高。而从海平面气压异常场分布来看（图 11b），欧亚地区表现为“北高南低”的海平面气压异常分布，有利于欧亚大陆中高地区气温的偏低和低纬地区气温的偏高。进一步分析表面，2012/2013 年冬季我国气温异常、500 hPa 高度场异常和海平面气压场异常的分布，与 Wang 等（2010）研究中东亚地区冬季气温 EOF 分解第一模态及其对应的环流场相一致，受这种大尺度环流分布型影响，我国东南部地区为低层异常南风控制，整体表现出现东北冷、西南暖的温度异常分布特征。值得指出的是，2012/2013 年冬季海平面气压场异常分布表现出对应 AO 持续负位相的分布特征，而不是典型的东亚冬季风和西伯利亚

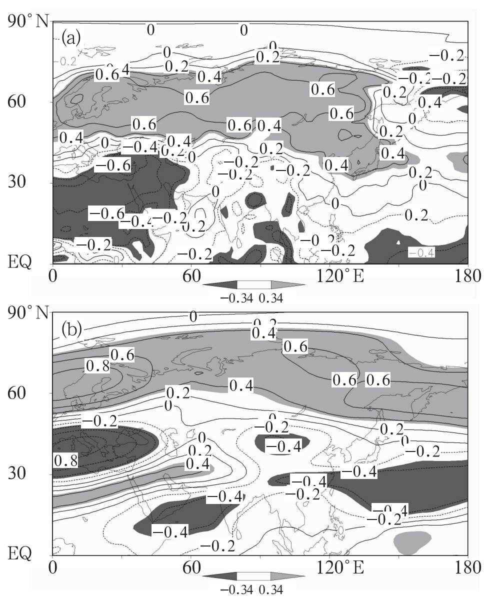

图 10 1981—2012 年北极涛动（AO）指数与冬季表面气温（SAT）（a）及 200 hPa（b）纬向风场的相关分布
（阴影为通过 $\alpha=0.05$ 显著性水平检验）

Fig. 10 Correlation of Arctic Oscillation index with (a) SAT, (b) 200 hPa zonal wind during 1981−2012
(Values significantly exceeding $\alpha=0.05$ significance level of test are shaded)

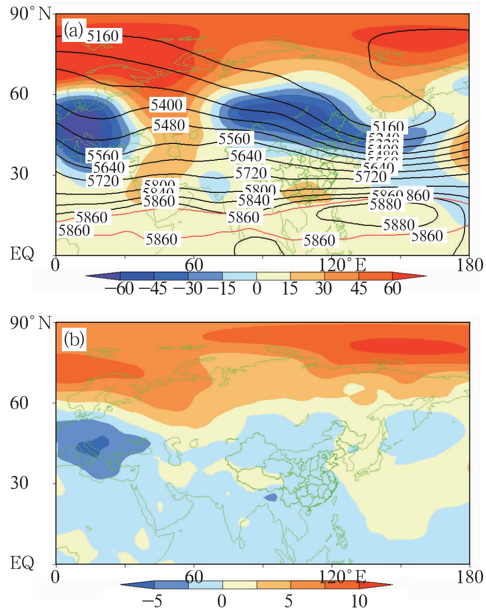

图 11 2012/2013 年冬季 500 hPa 位势高度及距平场（a，单位：gpm）和海平面气压距平场（b，单位：hPa）分布

Fig. 11 Distribution of 500 hPa geopotential height anomaly (a, unit: gpm) and sea level pressure (SLP) anomaly (b, unit: hPa) in winter 2012/2013

高压偏强的特征，这也是西伯利亚高压强度在季节尺度上略偏弱的重要原因。

4 东亚冬季风异常的可能原因

4.1 北极海冰的影响

前期研究表明，9 月海冰范围与后期冬季大尺度大气环流异常有着密切联系，海冰的减少会导致北极地区增暖，并通过与大气的正/负反馈作用影响遥远区域的气候变异（Honda et al，1999；2009；Alexander et al，2004；Screen et al，2010；Kumar et al，2010；Wu et al，2011）。观测结果也显示，冬季巴伦支海—喀拉海海冰偏少时，东亚冬季风会偏强。自 2012 年夏季开始，北极海冰覆盖范围持续异常偏小，偏小幅度超过气候态两倍标准差，这一状况一直持续到 2012/2013 年冬季（图略）；其中 8 月中旬至 10 月中旬，海冰覆盖面积持续低于自有观测资料以来年海冰覆盖面积的最小纪录——2007 年同期海冰覆盖面积。而从海冰范围距平分布来看（图

12)，秋季北极大部分地区海冰范围较常年明显偏少，巴伦支海北部、喀拉海、拉普捷夫海、楚科奇海、波弗特海和巴芬湾等海域海冰范围较常年同期偏低 20％～60％，其中喀拉海北部和波弗特海偏低 60％以上。图 13 给出 9 月北极地区海冰范围与冬季海平面气压的相关系数分布，分析可以发现，自欧洲东部到西伯利亚地区为显著的负相关区域，表明前期海冰范围的减少有利于冬季欧亚大陆北部的海平面气压出现正异常，致使西伯利亚高压的偏强，有利于冷空气南下我国。另一方面，前期秋季北极海冰偏少使得北极地区温度较常年同期偏高，导致极区与欧亚大陆之间的温差较常年同期偏小，减弱了欧亚

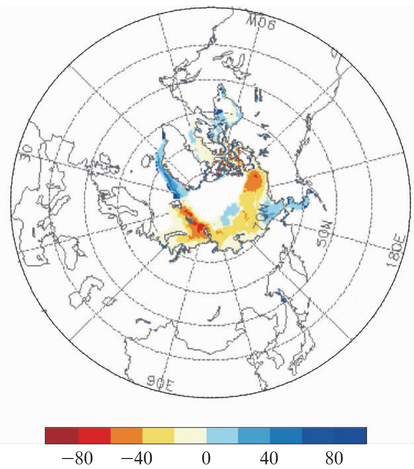

图 12　2012 年秋季北极海冰范围距平分布

Fig. 12　Distribution of sea ice extend anomalies in autumn 2012

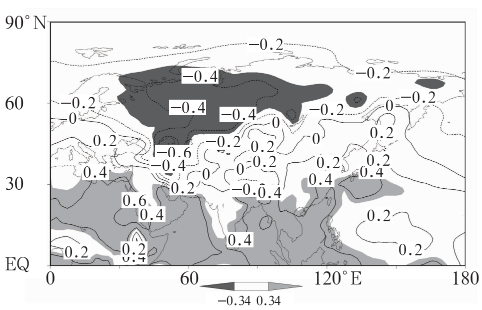

图 13　9 月北极海冰范围(ASI)指数与冬季海平面气压场(SLP)的相关分布

(阴影为通过 $\alpha=0.05$ 显著性水平检验)

Fig. 13　Correlation of September negative Arctic Oscillation index with winter sea level pressure

(Values significantly exceeding $\alpha=0.05$ significance level of test are shaded)

北部的西风急流，有利于欧亚地区高纬的冷空气南下影响我国，最终导致今年冬季我国东北、内蒙古东部、华北、华东等地大范围低温的出现。

4.2　平流层环流异常下传的影响

4.1 节的分析显示，北极海冰异常偏少作为相对持续和稳定的外强迫因子，有利于冬季西伯利亚高压的偏强，这与 2012/2013 年冬季西伯利亚高压略偏弱的事实并不完全吻合，进一步研究发现，西伯利亚高压强度表现出明显的季内变化特征，在 12 月初至 1 月上旬和 2 月上中旬明显偏强，而在冬季的其他时段偏弱，西伯利亚高压强度的这种阶段性减弱受平流层位势高度异常下传影响。

图 14 给出 2012/2013 年冬季平流层大气环流演变特征，分析发现，在2013年1月上中旬，平流层

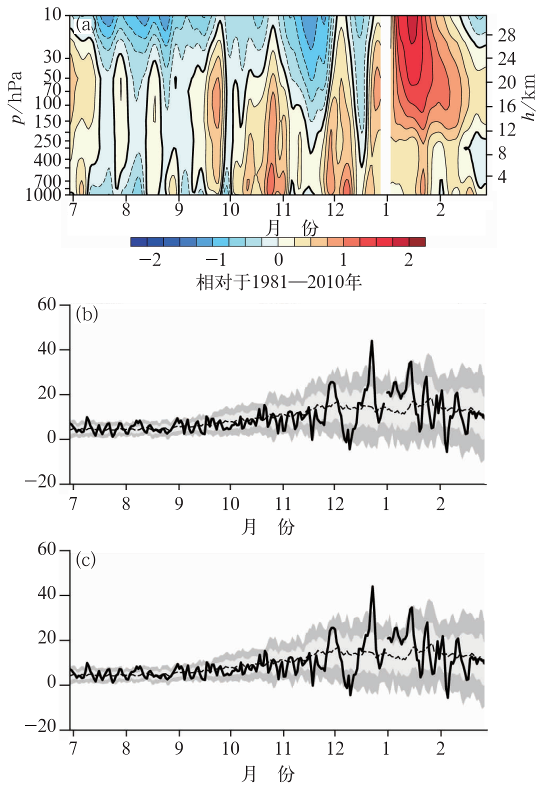

图 14　(a)北半球高纬标准化高度距平(单位：hPa)，(b)150 hPa 上传波动热通量[单位：℃・(m・s)$^{-1}$]，(c)20 hPa 纬向风(单位：m・s^{-1})演变

Fig. 14　(a) Variations of standardized geopotential height anomaly in Northern Hemisphere (unit: hPa), (b) 150 hPa outgoing heat flux (unit: ℃・m・s^{-1}) and (c) 20 hPa zonal wind (unit: m・s^{-1})

10 hPa 等压面出现明显的位势高度正异常(图 14a),并伴随着一次平流层爆发性增温过程(图略),平流层位势高度正异常出现后迅速下传并在 1 月中下旬开始影响对流层中低层。从 150 hPa 上传波动热通量和 20 hPa 纬向风场的演变特征来看(图 14b 和 14c),在这一次平流层位势高度正异常下传过程中,首先,在 2012 年 12 月中旬至 2013 年 1 月上中旬,整个平流层有异常强的上传波动热通量,这种异常强的上传波动热通量在平流层辐合,从而引起平流层的纬向基本流的减速;伴随着纬向西风减速作用,平流层极涡强度大大减弱,减弱的幅度在 1 月中旬前后达到最强,西风环流逆转为东风环流,形成暖的极区,导致平流层爆发性增温现象;在极区建立起来的东风环流不利于波动热通量的上传,从而抑制对流层能量的向上频散;在这种情况下,平流层大气环流在非绝热过程的调整下向辐射平衡发展,产生西风加速,从而逐渐恢复西风环流。在整个过程大约 50 d 的时间里,纬向基本流的偏弱一直在中高纬度维持(图 14c),从而形成弱的绕极涡旋,有利于 AO 负位相的维持,这也是北极涛动在 2012/2013 年冬季持续维持负位相的原因之一。同时,根据陈文等(2009)的研究,平流层位势高度正异常下传至对流层中低层后的 1 个月左右时段内,会导致西伯利亚地区海平面气压的降低,是造成西伯利亚高压季内变化的重要原因。

5 小 结

(1) 2012/2013 年冬季,东亚冬季风强度较常年同期略偏强,季内冬季风强弱转换阶段性特征明显。

(2) 2012/2013 年冬季,我国气温主要表现为东北冷,西南暖的异常分布,全国平均气温－3.7℃,较常年同期(－3.4℃)偏低 0.3℃,季内,我国气温变化呈现前冬冷、后冬暖的阶段性变化特征。

(3) 2012/2013 年冬季,北极涛动持续位于负位相,欧亚中高纬地区高层纬向西风减弱,环流经向度加大,在 500 hPa 高度场上,欧亚大陆中高纬环流呈"两槽一脊"的环流形势,乌拉尔山的高压脊持续偏强,而东亚槽也异常偏强,有利于极地的冷空气南下影响欧亚中高纬地区,是造成我国北方地区气温偏低的重要原因。

(4) 自 2012 年夏季开始持续偏低的北极海冰覆盖,有利于 2012/2013 年冬季西伯利亚地区海平面气压偏高,致使西伯利亚高压和东亚冬季风偏强,而 2013 年 1 月中旬前后平流层位势高度正异常下传并影响对流层中低层,是导致西伯利亚高压和冬季风出现显著季节内变化的重要原因。

参考文献

安林昌,张芳华. 2013. 2013 年 2 月大气环流和天气分析. 气象,39(5):659-664.

陈隽,孙淑清. 1999. 东亚冬季风异常与全球大气环流变 Ⅰ. 强弱冬季风影响的对比研究. 大气科学,23(1):101-111.

陈文,魏科. 2009. 大气准定常行星波异常传播及其在平流层影响东亚冬季气候中的作用. 地球科学进展,24(3):272-285.

高辉. 2007. 东亚冬季风指数及其对东亚大气环流异常的表现. 气象学报,65(2):272-279.

关月,何立富. 2013. 2013 年 1 月大气环流和天气分析. 气象,39(4):531-536.

郭其蕴. 1994. 东亚冬季风的变化与中国气温异常的关系. 应用气象学报,5(2):218-224.

花丛. 2013. 2012 年 12 月大气环流和天气分析. 气象,39(3):394-400.

黄威. 2013. 2012 年 11 月大气环流和天气分析. 气象,39(2):259-264.

孙丞虎,任福民,周兵,等. 2012. 2011/2012 年冬季我国异常低温特征及其可能成因分析. 气象,38(7):884-889.

吴尚森,梁建茵. 2000. 华南冬季异常冷月预测概念模型 Ⅱ——大气环流、极冰、积雪等物理因子特征. 热带气象学报,16(4):289-296.

朱艳峰. 2008. 一个适用于描述中国大陆冬季气温变化的东亚冬季风指数. 气象学报,66(5):781-788.

Alexander M A, Bhatt U S, Walsh J E. 2004. The atmospheric response to realistic sea ice anomalies in an AGCM during winter. J Clim, 17(5):890-905.

Chang C P, Lun K M. 1982. Short term planetary scale interaction over the tropics and the mid-latitudes during northern winter. Part Ⅰ: Contrast between active and inactive periods. Mon Wea Rev, 110(8):933-946.

Ding Y H, Krishnamurti T N. 1987. Heat budget of the Siberian High and the winter monsoon. Mon Wea Rev, 115(10):2428-2499.

Helfrich S R, McNamara D, Ramsay B H, et al. 2007. Enhancements to, and forthcoming developments in the Interactive Multisensor Snow and Ice Mapping System (IMS). Hydrol Process, 21(12):1576-1586.

Honda M, Inous J, Yamane S. 2009. Influence of low Arctic sea-ice minima on anomalously cold Eurasian winters. Geophys Res Lett, 36(8):L08707.

Honda M, Yamazaki K, Nakamura H, et al. 1999. Dynamic and thermodynamic characteristics of atmospheric response to anomalous sea-ice extent in the Sea of Okhotsk. J Clim, 12(12): 3347-3358.

Kalnay E, Kanamitsu M, Kistler R, et al. 1996. The NCEP/NCAR 40-Year Reanalysis Project. Bull Amer Meteor Soc, 77(3):437-471.

Kumar A, Perlwitz J, Eischeid J, et al. 2010. Contribution of sea ice loss to Arctic amplification. Geophys Res Lett, 37(21): L21701.

Lan K M, Li M T. 1984. The monsoon of East Asia and its global associations A survey. Bull Amer Meteor Soc, 65(2):114-125.

Screen J A, Simmonds I. 2010. The central role of diminishing sea ice in recent Arctic temperature amplification. Nature, 464: 1334-1337.

Thompson D W J, Wallace J M. 1998. The Arctic Oscillation signature in the wintertime geopotential height and temperature fields. Geophy Res Lett, 25(9):1297-1300.

Thompson D W J, Wallace J M. 2000. Annular modes in the extratropical circulation, Part I: month-to-month variability. J Clim, 13(5):1000-1016.

Wallace J M. 2000. North Atlantic Oscillation/annual Mode: Two paradigmsone phenomenon. Quart J Royal Met Soc, 126(564): 791-805.

Wang B, Wu Z W, Chang C P, et al. 2010. Another look at interannual-to-interdecadal variations of the East Asian winter monsoon: The northern and southern temperature modes. J Clim, 23(6):1495-1512.

Wang J, Ikeda M. 2000. Arctic Oscillation and Arctic sea ice oscillation. Geophys Res Lett, 27(9):1287-1290.

Wu B Y, Su J Z, Zhang R H. 2011. Effects of autumn-winter Arctic sea ice on winter Siberian High. Chinese Sci Bull, 56(30), doi: 10.1007/s11434-011-4696-4.

Zhang Y, Sperber K, Boyle J. 1997. Climatology and interannual variation of the East Asian winter monsoon: Results from the 1979-95 NCEP/NCAR reanalysis. Mon Wea Rev, 125(10): 2605-2619.

Analysis of stable components in extended-range forecast for the coming 10–30 days in winter 2010 and 2011*

Wang Kuo(王 阔)[a), Feng Guo-Lin(封国林)[b), Zeng Yu-Xing(曾宇星)[a), and Wang Xu-Jia(汪栩加)[a)†]

[a)] *College of Atmospheric Sciences, Lanzhou University, Lanzhou* 730000, *China*

[b)] *Laboratory for Climate Studies, National Climate Center, China Meteorological Administration, Beijing* 100081, *China*

(Received 29 March 2013; revised manuscript received 10 May 2013)

In this paper we try to extract stable components in extended-range forecast for the coming 10–30 days by using empirical orthogonal function (EOF) analysis, similarity coefficient and some other methods based on the National Center for Environmental Prediction (NCEP)/National Center for Atmospheric Research (NCAR) reanalysis daily data. The comparisons of the coefficient of variance of climatological background field and truth data in winter between 2010 and 2011 are made. The method of extracting stable components and climatological background field can be helpful to increase the forecast skill. The skill improvement of air temperature is better than geopotential height at 500 hPa. Moreover, this method improves the predictability better in the Pacific Ocean. In China, the forecast in winter in Northeast China is more uncertain than in the other parts.

Keywords: stable components, climatological background, coefficient of variance

PACS: 92.60.Wc **DOI:** 10.1088/1674-1056/22/12/000001

1. Introduction

In recent years, the standards of the extended-range forecast in the coming 10–30 days have been improving greatly. Because the atmosphere is a forced dissipative nonlinear system, its predictability is sensitive to initial condition. It has long been recognized that the upper limit of weather predictability for the synoptic and larger scales is about 2 weeks.[1–6] However, it is well established that some components in the climate system are more predictable than others. For instance, large-scale structures tend to be more predictable than small-scale structures and numerical evidence supports the hypothesis that the climate state is predictable beyond 2 weeks.[7,8] Studies show that some low-frequency atmosphere system can be observed. For example, as the Madden–Julian oscillation (MJO) is found,[9,10] research results support that MJO influences the weather significantly in China.[11–13] These studies strengthen our confidence to improve the extended-range forecast in the coming 10–30 days.

The extended-range forecast in the coming 10–30 days is gradually becoming a hot study direction in weather forecast. Chen *et at.*,[14] and Ding and Li[15] introduced a new approach using the nonlinear local Lyapunov exponent (NLLE) to study the atmospheric predictability from the view of nonlinear error growth dynamics. The spatiotemporal distributions of predictability limit of monthly and seasonal mean geopotential height and temperature fields were investigated.[16,17] Moreover, Mu[18] established a novel concept of nonlinear singular vector (NSV) and nonlinear singular vector value (NSVA) and improved the technique of conditional nonlinear optimal perturbations (CNOPs). These study results were used widely in the study of predictability, ensemble forecast and many other fields.[19,20]

The interannual variability of a climate mean consists of both climate signal and noise. The climate signals are those variations forced by the slowly varying anomalous boundary conditions external to the climate system.[21–24] A climate anomaly may display a certain degree of predictability if the percentage of climate signal in its total variability is large enough to overcome the destructive effect of the noise.[25] Many observations and studies showed that there is a strong relationship between the stable component and atmospheric oscillation,[26–29] and the stable components can be forecasted objectively on a 10–30 day time scale.[30–34] Therefore, some work extracted stable components in extended-range forecast for the coming 10–30 days by using empirical orthogonal function (EOF) analysis and some other methods during the snow storm event in the winter 2010 and 2011.[35–37] The stable components in extended-range forecast for the coming 10–30 days can be divided objectively into two parts, i.e., climatic stable components and abnormal stable components, by analyzing the contribution rate, similarity coefficient, etc. We combine climatic stable components and low-pass filter components to obtain the climatological background field and to investigate the 10–30 day component background. In this paper, the coefficient of variance is calculated to examine the predictability between true atmosphere and climatological back-

*Project supported by the National Basic Research Program of China (Grant No. 2013CB430204), the National Natural Science Foundation of China (Grant No. 40930952 and 41105070), and the State Key Development Program for Basic Research of China (Grant No. 2012CB955902).

†Corresponding author. E-mail: fenggl@cma.gov.cn

ground field in last two winters. These results can deepen our understanding of the predictability of extended range forecast for the coming 10–30 days and provide a new way to think and solve the problem of extended range forecast for the coming 10–30 days.

2. Data and method

2.1. Data

This study is based on the data reanalyzed by the National Center for Environmental Prediction/ National Center for Atmospheric Research (NCEP/NCAR)[38] for the period January 1980–April 2012. The dataset has a $2.5^\circ \times 2.5^\circ$ horizontal resolution and extends from 1000 hPa to 10 hPa, with 17 vertical pressure levels. The data of February 29 in leap year are omitted to keep it consistent.

2.2. Method

In this paper extracted are the components in extended-range forecast for the coming 10–30 days by the Butterworth Band-pass Filter on a month timescale. There we just extract stable components in extended-range forecast for the coming 10–30 days in December of 2010 for example. The basic function of climate state can be extracted by EOF analysis based on the NCEP/NCAR reanalysis daily data of geopotential height from 1981 to 2010 in December from the following equation:

$$X_{m\times n} = V_{m\times m} T_{m\times n}, \tag{1}$$

where $X_{m\times n}$ is the sequence of meteorological elements, $X_{m\times m}$ is the space characteristic vector, $T_{m\times n}$ is time coefficient. And then we calculate the daily data of geopotential height in December of 2010 by the Butterworth Band-pass Filter. Based on Eq. (1), contribution rate can be obtained by combining the space characteristic vectors of EOF and the corresponding time coefficients, the time coefficients can be calculated from the following equation:

$$T = V'X. \tag{2}$$

The contribution rate is used to check how to influence original field and explain the elements which influence this weather process in view of 10–30 days. When the explained variance of one component keeps at top twenty for more than fifteen days in one month, we define this component as stable component in extended-range forecast for the coming 10–30 days.

There are three big circulation systems at 500 hPa: subtropical high system in low latitudes, westerly belt system in middle latitudes, and polar vortex system in high latitude. The active degrees of these three circulation systems are different in different seasons. For example, westerly belt system shows three strong troughs in winter and four weak troughs in summer instead. The anomalies of three big circulation systems can lead to the anomaly of atmospheric circulation. Experiences show that atmospheric circulations are different in different seasons and different sectors. If the daily contribution rates of top 50 eigenvetors in December 2010 correspond to these in climate perfectly, the change of weather system would be similar to its historical change. Because they are different (Fig. 1), many extreme weather events happen every year. Therefore, it is an interesting thing to study the change of explained variances of eigenvetors.

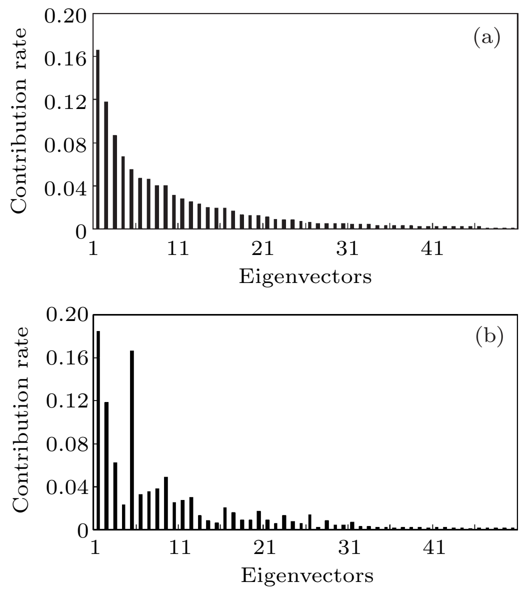

Fig. 1. December contribution rate: (a) climate and (b) 2010.

Y is defined as a threshold to separate climatic stable component from abnormal stable component. If one stable component, whose sequence of explained variance in climate minus its sequence of explained variance of a case is less than Y in absolute value, is called climatic stable component. Moreover, if one stable component, whose sequence of explained variance in climate minus its sequence of explained variance of a case is equal or more than Y in absolute value, is called abnormal stable component. There we assign the numbers from one to fifteen to Y and obtain the corresponding climatic stable components. The similarity coefficient (Eq. (3)) between climatic stable components in 1981 to 2010 is calculated and climatic stable component of a case.

$$\cos(\theta) = \frac{\sum\limits_{i=1}^{m} x_i y_i}{\sqrt{\sum\limits_{i=1}^{m} x_i^2}\sqrt{\sum\limits_{i=1}^{m} y_i^2}}, \tag{3}$$

where $\cos(\theta)$ represents the similarity coefficient, x and y are different metrorological elements, and m is sample size.

The flowchart of the objective separation of stable components is shown in Fig. 2. First, according to the 1980–2010

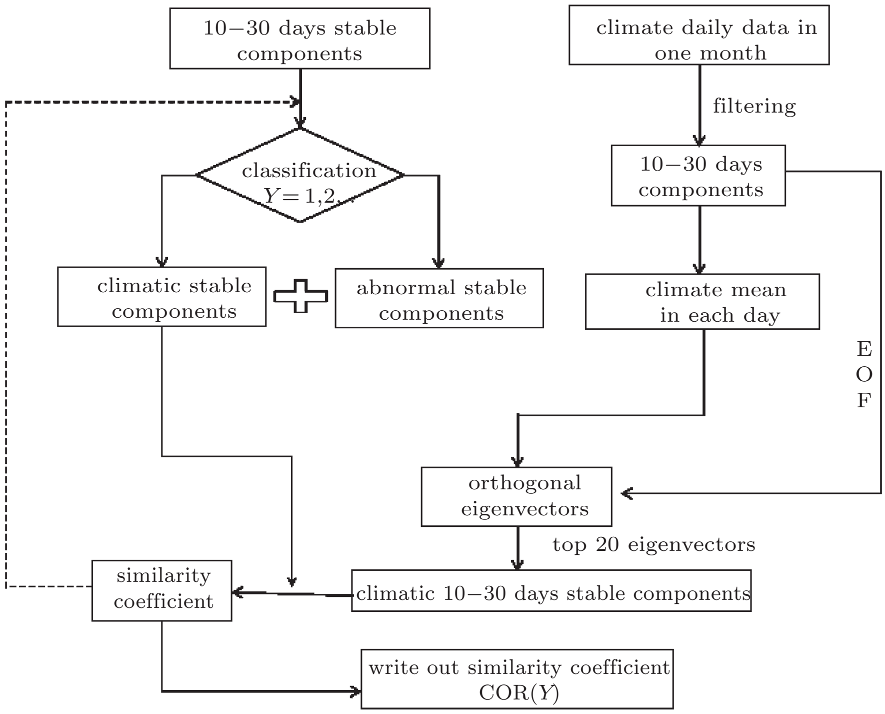

Fig. 2. Flowchart of the objective separation of stable components.

NCEP/NCAR data in December, the 10–30 days components are obtained. Subsequently, climatic mean 10–30 day components in each day are multiplied by orthogonal eigenvetors. Top 20 eigenvetors are selected to obtain climatic 10–30 day stable components, and the similarity coefficient is calculated with climatic stable components. We consider that when the similarity coefficient reaches extremum, Y is the right threshold that we want (Fig. 3). At this time, the climatic stable components and abnormal stable components can be ascertained objectively. For example in this case the geopotential height data in December 2010 at 500-hPa level, 2 is a reasonable threshold for Y. We combine climatic stable components and low-pass filter components to obtain climatological background field.

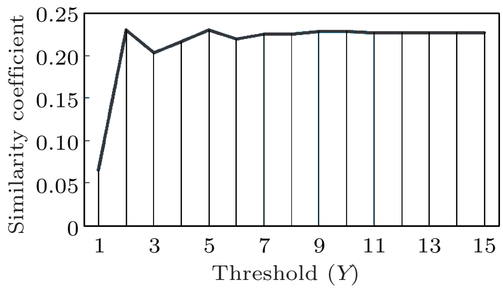

Fig. 3. Similarity coefficient between climatic 10–30 day stable component and climatic stable component when the threshold is in a range from 1–15.

The standard deviation is

$$S_x = \sqrt{\frac{1}{n}\sum_{t=1}^{n}(x_t-\bar{x})^2}, \tag{4}$$

where x is the meteorological time series; $\bar{x}$ is average; n is sample size. Standard deviation represents the average level of the variable change around average. So it can reflect the level of difficulty in predicting the variable. Of course, it is easier to predict a variable with lower S_x than with higher S_x. However, if there are two variables with different magnitudes, each changes according to its own percentage, we can obtain that their standard deviations are not equal. The larger magnitude variable has a higher standard deviation and the smaller magnitude variable has a lower standard deviation. In order to avoid this relative error and to compare the 500 hPa geopotential height and the climatological background field, we calculate their coefficient of variance (CV) from the following formula:

$$CV = \frac{1}{\bar{x}}\sqrt{\frac{1}{n}\sum_{t=1}^{n}(x_t-\bar{x})^2} \tag{5}$$

to compare their predictabilities.

3. Geopotential field and temperature field at 500 hPa in winter 2010

3.1. Geopotential field at 500 hPa

3.1.1. The *CV* analysis of truth field

Figure 4 shows the CVs of truth field at 500-hPa level in the Northern Hemisphere in winter 2010. The CVs reach their minima in the equator and increase along the direction of latitude increasing. It is in accordance with Li and Wang's studies.[39] In December 2010, the CVs are below 0.005 in south of 20° north latitude. They are lower in Southwest China

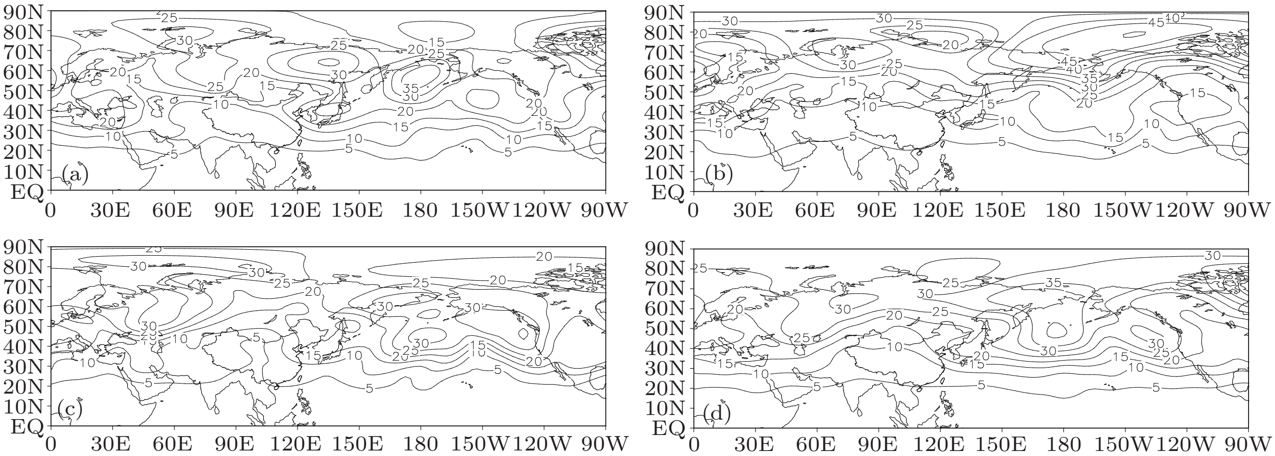

Fig. 4. The CVs of geopotential truth field at 500-hPa level in the Northern Hemisphere in (a) December 2010, (b) January 2011, (c) February 2011, and (d) Winter 2010. December, January, and February (DJF) ($\times 10^{-3}$).

and higher in Northeast China. There is a closed-isoline in the Japan Sea, with values exceeding 0.025. In January 2011, the CVs in China are similar except in Northeast China. The isolines become dense in high latitudes. In February 2011, they change a little but turn a closed-isoline in the North Pacific Ocean. The CV isolines become dense in mid-latitudes of the Pacific Ocean and the uncertainty of prediction increases. According to Fig. 4(d), the CVs are higher in Northeast China than in the other parts of China in winter 2010. Moreover, the isolines are dense in the North Pacific Ocean.

3.1.2. The CV analysis of climatological background field

From the CVs of geopotential climatological background field at 500-hPa level in the Northern Hemisphere in Fig. 5, we can obtain the information similar to that in Fig. 4. The CVs of climatological background field in Eurasia during December 2010 have two closed-isolines, and the west one is stronger than the other. In January 2011, there is a high closed-isoline in Northeast China and the Japan Sea, while the 0.005 isoline moves toward north which means that in this section the forecast skills are higher than December 2010. From Fig. 5 we can see that in high latitudes the CVs are higher than those in low latitudes, at the same time they show zonal distribution. In winter 2010 (Fig. 5(d)), the CVs are higher in Northeast China than in the other parts of China too. Especially, a comparison of Fig. 4 with Fig. 5 shows that the CVs of climatological background field are obviously less than the CVs of truth field in both Asia and the Pacific Ocean. It means that the climatological background field is easier to predict than the truth field at 500-hPa level. Therefore, the method of extracting stable components and obtaining climatological background field is helpful to increase the forecast skills. Moreover, the values in both truth field and climatological background field are higher in Northeast China than in the other parts. We may explain that in China the forecast of geopotential field at 500 hPa in winter in Northeast China is more uncertain.

3.2. Temperature field at 500 hPa

3.2.1. The CV analysis of truth field

From the CVs of truth field at 500-hPa level in the Northern Hemisphere (Fig. 6) we can see that the CVs are very low in low-latitudes and increase along the direction of increasing latitude. The CVs are low in Southwest China while high in

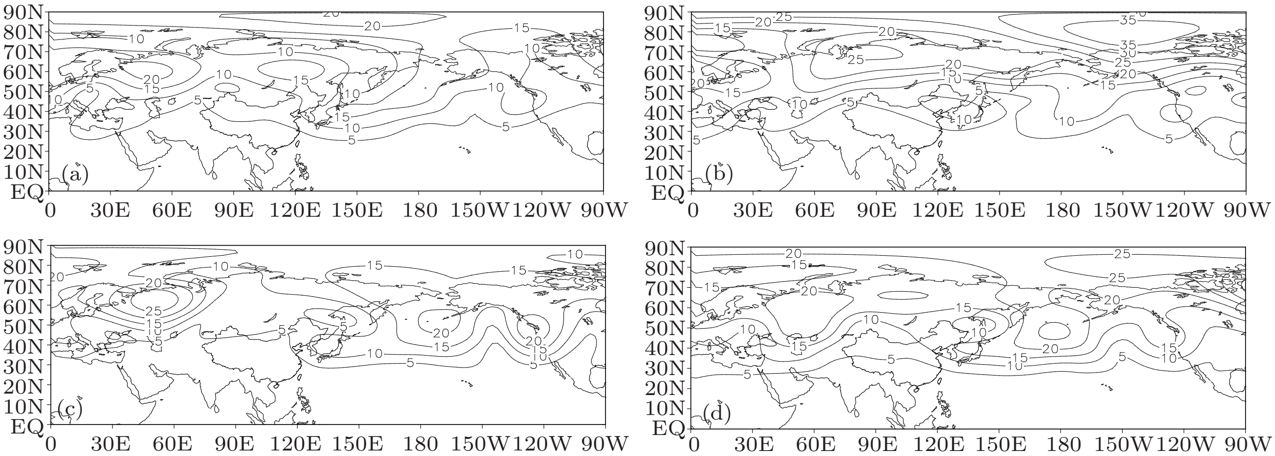

Fig. 5. The CVs of geopotential climatological background field at 500-hPa level in the Northern Hemisphere in (a) December 2010, (b) January 2011, (c) February 2011, and (d) Winter 2010. (DJF) ($\times 10^{-3}$).

Northeast China. In January 2011, the CVs of truth field are flat in south of 40° north latitude. They are lower in Southwest China while higher in Northeast China. With the time going on, there is a high closed-isoline which influences most of the Northwest Pacific Ocean at 500 hPa in February 2011. The 0.015 isoline moves to south in China which makes CVs in Northeast China and North China higher. Figure 6 shows that there is a high closed-isoline exceeding 0.025 in the North Pacific Ocean in winter 2010. The CVs of temperature truth field of China reach their maxima in Northeast China.

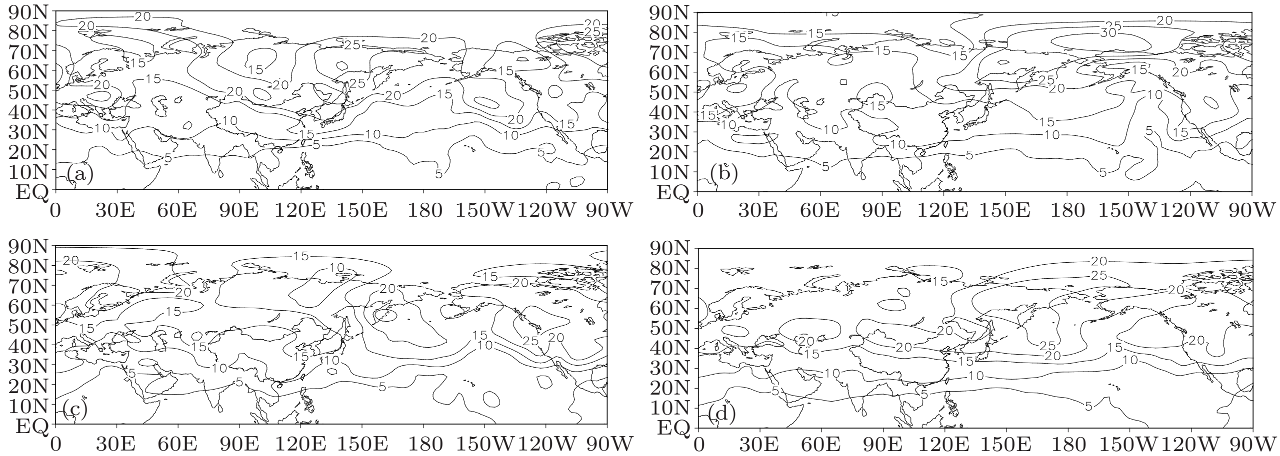

Fig. 6. The CVs of temperature truth field at 500-hPa level in the Northern Hemisphere in (a) December 2010, (b) January 2011, (c) February 2011, and (d) Winter 2010. (DJF) ($\times 10^{-3}$).

3.2.2. The CV analysis of climatological background field

Figure 7 shows the CVs of temperature climatological background field at 500-hPa level in the Northern Hemisphere. It displays the zonal distribution in December 2010 and changes little in the south of 20 °N. The isolines become dense in the section of juncture of Eurasia and the Pacific Ocean. In January 2011 there are two high closed-isolines in Northeast China and Okhotsk, which influence the change of temperature at 500 hPa together. The CVs of climatological background field at 500 hPa are sparse in February 2011 and show a high closed-isoline in the Central Pacific Ocean which influences East China especially some coastal areas.

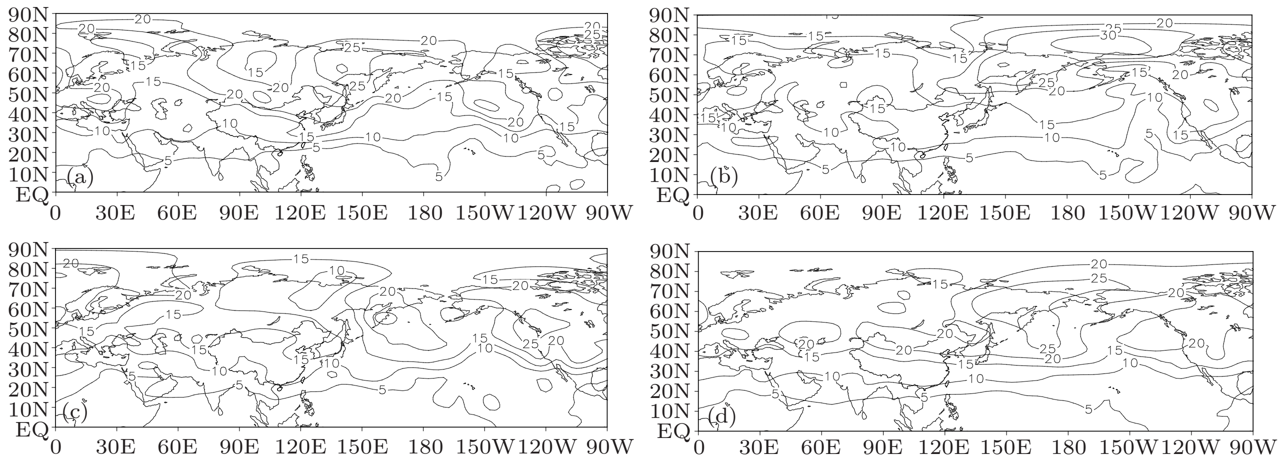

Fig. 7. The CVs of temperature climatological background field at 500-hPa level in the Northern Hemisphere in (a) December 2010, (b) January 2011, (c) February 2011, and (d) Winter 2010. (DJF) ($\times 10^{-3}$).

From the CVs of temperature climatological background field at 500-hPa level in the Northern Hemisphere in winter 2010 we can see that there is a strong high center in the Northwest Pacific Ocean which makes the isolines in Northeast China dense. We consider that the predictability in Northeast China is influenced mainly by the Northwest Pacific Ocean at 500-hPa level. Comparing Fig. 6 with Fig. 7, the CVs of temperature climatological background field are more stable than that of truth field.

4. Geopotential field and temperature field at 500 hPa in winter 2011

4.1. Geopotential field at 500 hPa

4.1.1. The CV analysis of truth field

Figure 8 shows the CVs of geopotential truth field at 500-hPa level in the Northern Hemisphere in winter 2011. The predictability in low latitudes is better than in other latitudes. In December 2011 and February 2012, there is a high closed-isoline exceeding 0.030 in the East Pacific Ocean. While in January 2012 the high closed-isoline appears in Aleutian area, which influences East Siberia obviously. From winter 2011 we can see that there are two closed-isolines in the North Pacific Ocean and the East Pacific Ocean and the CVs in the West Pacific Ocean are sparse. The CVs in Northeast China are higher than in the other parts in China, which means that the predictability limit in Northeast China is higher too. Comparing with Fig. 4, the source region of weather system influencing the distribution of CVs in China can be distinguished as two parts by time sequence: In former winter, the source region is in Siberia of North Eurasia, while in later winter, the source region is the Pacific Ocean.

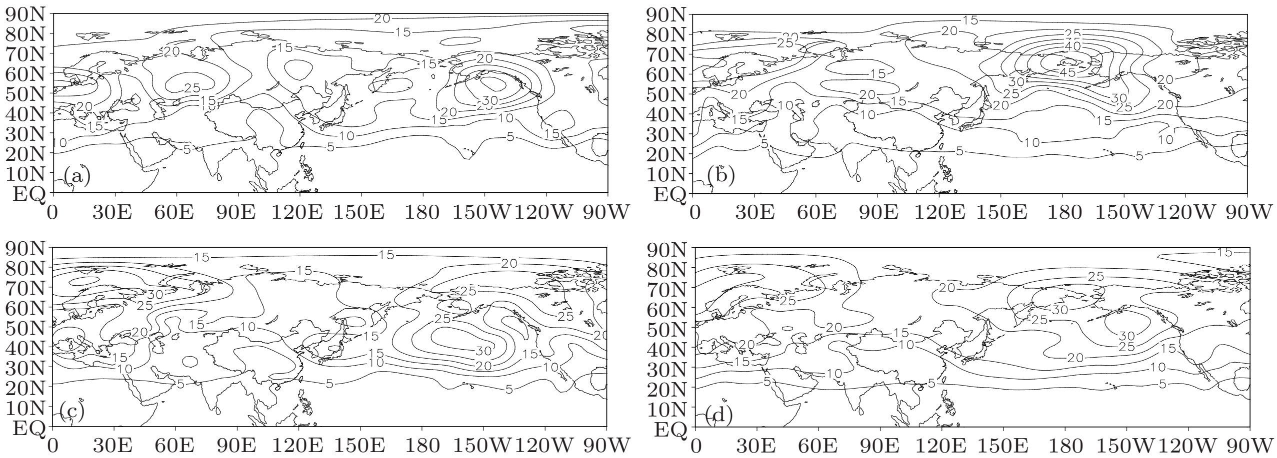

Fig. 8. The CVs of geopotential truth field at 500-hPa level in the Northern Hemisphere in (a) December 2011, (b) January 2012, (c) February 2012, and (d) Winter 2011. (DJF) ($\times 10^{-3}$).

4.1.2. The CV analysis of climatological background field

Comparing Fig. 8 with Fig. 9, we can see that the CVs of climatological background field we extracted are lower than those of truth field in the same areas. Moreover, the patterns in two fields are very similar, which means that the climatological background field can grasp the main circulation systems in truth field. Although just calculating low-pass filtering may also show some improvement, it is not clear whether separating climate signal from noise can lose some useful information. Obviously, the method we put forward is better than the simple low-pass filtering.

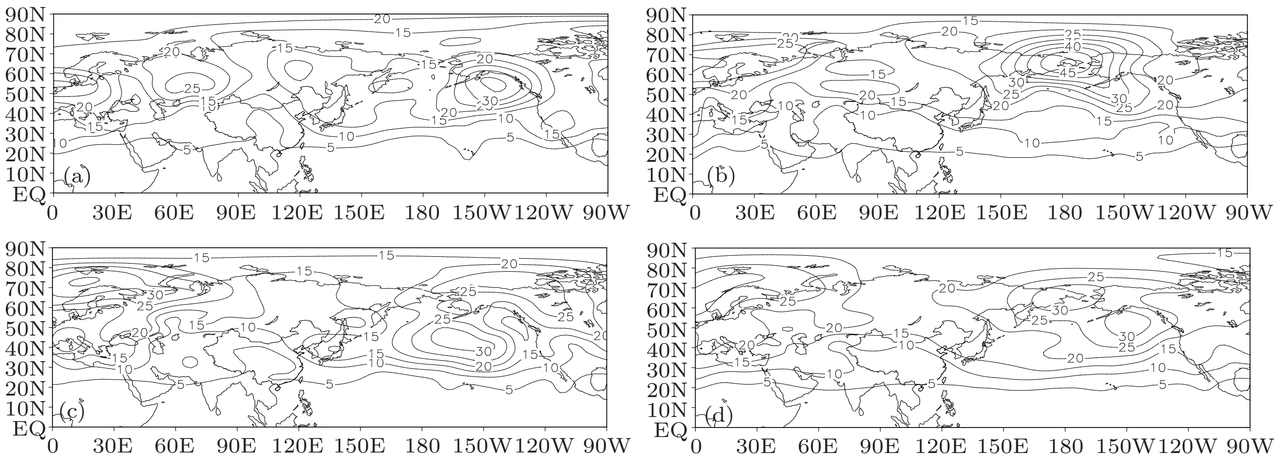

Fig. 9. The CVs of geopotential climatological background field at 500-hPa level in the Northern Hemisphere in (a) December 2011. (b) January 2012. (c) February 2012 , and (d) Winter 2011. (DJF) ($\times 10^{-3}$).

4.2. Temperature field at 500 hPa

4.2.1. The CV analysis of truth field

Figure 10 shows the CVs of temperature truth field at 500-hPa level in the Northern Hemisphere. In December 2011 and January 2012, high closed-isolines are in the North Pacific Ocean and the section of juncture of America and the Northeast Pacific Ocean. Then the high closed-isoline moves to the Center Pacific Ocean in February 2012. The CVs of truth field in winter 2011 (Fig. 10(d)) shows that they change little in the same latitudes. The predictability of North China is lower than in the other parts, this phenomenon is similar to that in winter 2010.

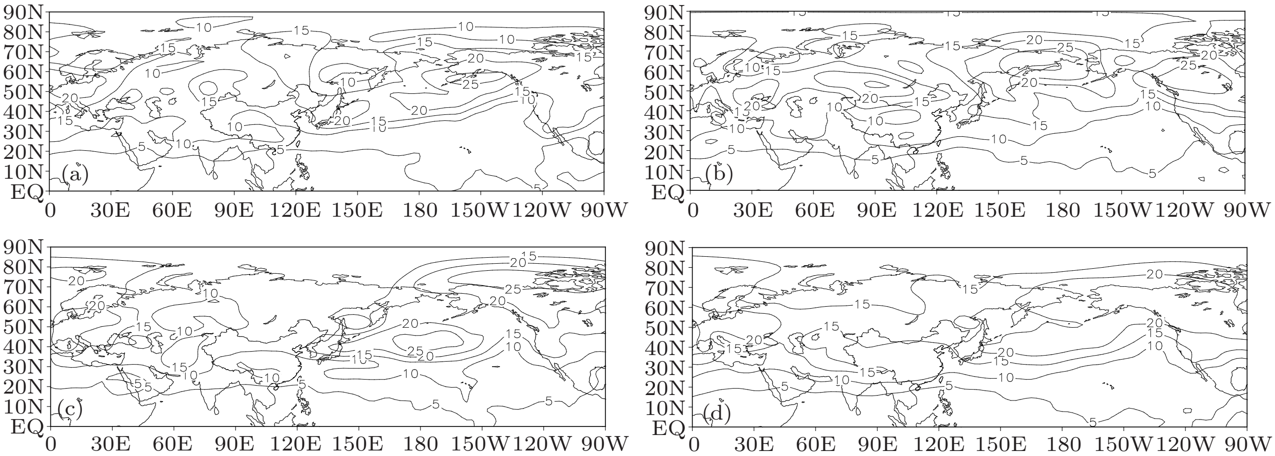

Fig. 10. The CVs of temperature truth field at 500-hPa level in the Northern Hemisphere in (a) December 2011, (b) January 2012, (c) February 2012, and (d) Winter 2011. (DJF) ($\times 10^{-3}$).

4.2.2. The CV analysis of climatological background field

Figure 11 shows the CVs of temperature climatological background field at 500-hPa level in the Northern Hemisphere. Comparing with Fig. 7, it is obvious to find that the CVs are very sparse and different from month to month. The CVs in China become lower and lower with the time going on and they are almost below 0.004 in February 2012. The predictability is better in the south of 30° north latitude with the CVs below 0.005 in winter. Moreover, figure 11 shows the temperature CVs in Northeast China are mainly influenced by the North Pacific Ocean and the predictability in the East Pacific Ocean is better than that in the West Pacific Ocean.

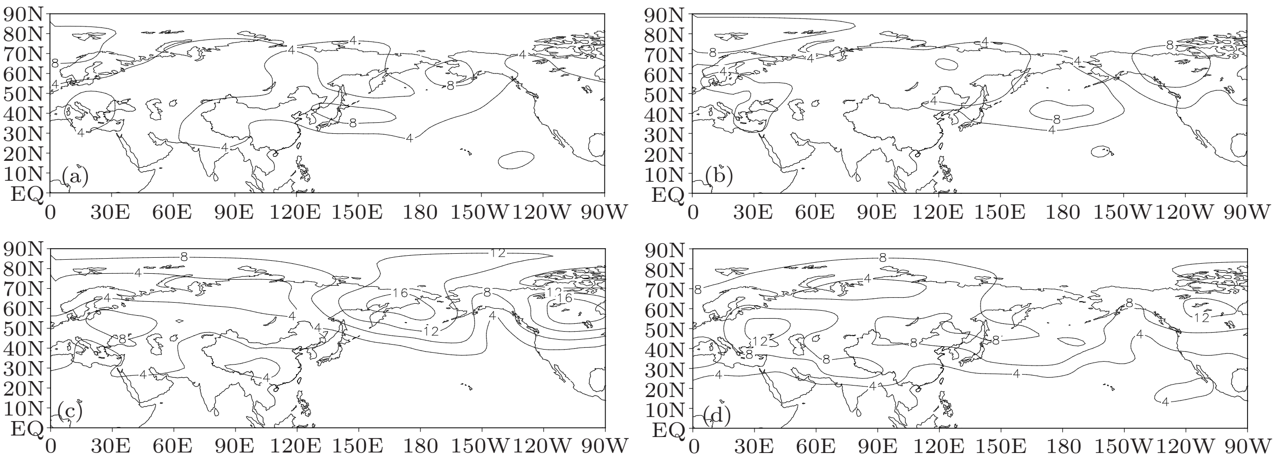

Fig. 11. The CVs of temperature climatological background field at 500-hPa level in the Northern Hemisphere in (a) December 2011, (b) January 2012, (c) February 2012, and (d) Winter 2011. (DJF) ($\times 10^{-3}$).

5. Conclusion and discussion

In this paper, we try to extract the stable components in extended-range forecast for the coming 10–30 days by using empirical orthogonal function analysis, similarity coefficient and some other methods based on the NCEP/NCAR reanalyzed daily data. The CVs of climatological background field and truth field in the winter 2010 and 2011 are compared to obtain some results.

The method of extracting stable components and climatological background field can be helpful to increase the forecast skill. The improvement on air temperature is better than geopotential height at 500 hPa. It is meaningful for extended-range forecast for the coming 10–30 days.

From the distribution of CVs in winter 2010 and 2011 we can see that the predictability decreases along the direction of increasing latitude. Moreover, this method improves the predictability obviously in the Pacific Ocean. The forecast in winter in Northeast China is more uncertain than in the other parts of China. The predictability of air temperature in Northeast China is influenced by the North Pacific Ocean mainly at 500 hPa.

In this paper developed is a new method of separating climate signal from noise to solve the difficulty in extended-range forecast for the coming 10–30 days based on some comprehensive studies. The results seem encouraging. However, the relevant studies need to be continued to combine this method with model results for weather forecast. Moreover, how to combine with boundary condition, for example, ENSO, also needs to be investigated.

References

[1] Lorenz E N 1965 *Tellus* **17** 321
[2] Lorenz E N 1969 *J. Atmos. Sci.* **26** 636
[3] Xie T, Zou G H, William P, Kuang H L and Chen W 2010 *Chin. Phys. B* **19** 059201
[4] Jiang H, Yang X X, Lin M M, Shi Y R and Duan W S 2011 *Chin. Phys. B* **20** 019401
[5] Feng G L, Dai X G, Wang A H and Chou J F 2001 *Acta Phys. Sin.* **50** 606 (in Chinese)
[6] Zhang Z S, Gong Z Q, Zhi R, Feng G L and Hu J G 2011 *Chin. Phys. B* **20** 019201
[7] Shukla J 1981 *J. Atmos. Sci.* **38** 2547
[8] Shukla J 1998 *Science* **282** 728
[9] Madden R A and Julian P R 1971 *J. Atmos. Sci.* **28** 702
[10] Madden R A and Julian P R 1972 *J. Atmos. Sci.* **29** 1109
[11] Wang B and Liu F 2011 *J. Atmos. Sci.* **68** 2524
[12] Jia X, Chen L J, Ren F M and Li C Y 2011 *Adv. Atmos. Sci.* **28** 521
[13] Li C Y and Zhou Y P 1994 *Chin. J. Geophys.* **37** 213 (in Chinese)
[14] Chen B H, Li J P and Ding R Q 2006 *Sci. China Ser. D* **49** 1111
[15] Ding R Q and Li J P 2007 *Phys. Lett. A* **364** 396
[16] Ding R Q, Li J P and Ha K J 2008 *J. Geophys. Res.* **113** D24112
[17] Ding R Q, Li J P and Seo K H 2011 *Mon. Wea. Rev.* **139** 2421
[18] Mu M 2000 *Sci. China Ser. D* **43** 375
[19] Mu M, Duan W S, Xu H and Wang B 2006 *Adv. Atmos. Sci.* **6** 992
[20] Zhou F F and Mu M 2012 *Adv. Atmos. Sci.* **29** 705
[21] Yang S, Zhang Z, Kousky V E, Higgins R W, Yoo S H, Liang J and Fan Y 2008 *J. Climate* **21** 3755
[22] Qian Z H, Hu J G, Feng G L and Cao Y Z 2012 *Chin. Phys. B* **21** 109203
[23] Horel J D and Wallace J M 1981 *Mon. Wea. Rev.* **109** 813
[24] Blackmon M L, Geisler J E and Pitcher E J 1983 *J. Atmos. Sci.* **40** 1410
[25] Chen W Y and Van den Dool H M 1996 *J. Climate* **10** 1236
[26] Plaut G and Vautard R 1994*J. Atmos. Sci.***51** 210
[27] Li C Y and Pan J 2006 *Adv. Atmos. Sci.* **23** 925
[28] Wang X J, Zhi R, He W P and Gong Z Q 2012 *Chin. Phys. B* **21** 029201
[29] Gong Z Q, Wang X J, Zhi R and Feng A X 2011 *Chin. Phys. B* **20** 079201
[30] Blackmon M L, Lee Y H, Wallace J M and Hsu H H 1984 *J. Atmos. Sci.* **41** 981
[31] Barnett T P and Preisendorfer R 1987 *Mon. Wea. Rev.***115** 1825
[32] DelSole T and Tippett M K 2008 *J. Atmos. Sci.* **65** 1666
[33] Chou J F 2011 *Advances in Meteorological Science and Technology* **1** 11 (in Chinese)
[34] Chou J F 2012 *Chin. J. Geophys.* **55** 1433 (in Chinese)
[35] Wang K, Feng G L, Sun S P and Zheng Z H 2012 *Acta phys. Sin.* **61** 109201 (in Chinese)
[36] Wang K., Feng G L, Sun S P and Zheng Z H 2012 *Acta phys. Sin.* **61** 209201 (in Chinese)
[37] Zheng Z H, Huang J P, Feng G L and Chou J F 2012 *Sci. China Earth Sci.*
[38] Kalnay E and Coauthors 1996 *Meteor. Soc.* **77** 437
[39] Li F and Wang H J 2012 *Adv. Atmos. Sci.* **29** 441

王小玲，丁一汇. 2013. 2010 年夏季欧亚异常阻高演变过程及对天气气候的影响. 气象，39(9)：1089-1095.

2010 年夏季欧亚异常阻高演变过程及对天气气候的影响*

王小玲[1,2,3] 丁一汇[3]

1 中国科学院大气物理研究所，北京 100029
2 中国科学院大学，北京 100049
3 国家气候中心，中国气象局气候研究开放实验室，北京 100081

提 要：2010 年 6—8 月，北半球存在欧亚遥相关，异常最早出现在北大西洋高空急流出口区，为负扰动，扰动沿遥相关波列向下游传播，造成莫斯科地区的高温热浪以及巴基斯坦与中国西北和东北部的暴雨洪涝。遥相关分析表明，急流出口区的负扰动首先引起俄罗斯西部的正扰动，阻塞高压发展，造成持续高温干旱；之后引起西亚北部的负扰动，造成冷空气频繁南下，与北上和西进的印度季风交汇在巴基斯坦北部，造成极严重的洪涝；8 月初扰动沿高空急流继续向下游传播，在我国西北、东北以及朝鲜半岛造成洪涝，甘肃舟曲突发性大暴雨和泥石流以及松花江暴雨就发生在这个时期。由于 2010 年夏季整个欧亚地区经向型环流异常发展，高空急流经向分量很大，这导致高、低纬冷暖空气在不同地区持续相互作用，不仅使阻塞高压在中高纬俄罗斯西部异常发展、强大和持续，而且使低纬巴基斯坦发生严重洪涝，以及我国中纬度地区的强烈暴雨。季风活动在引发上述暴雨洪涝起着十分关键的作用，分别表现为来自低纬阿拉伯海和孟加拉湾的两支暖湿气流与沿着阻高东侧南下的冷空气在巴基斯坦北部上空交汇；来自印度洋、太平洋的暖湿气流和中纬度西风带的水汽在我国东北以及朝鲜半岛上空交汇。

关键词：2010 年夏季，欧亚环流，阻高，遥相关，热浪，洪水
中图分类号：P461 **文献标志码**：A **doi**：10.7519/j.issn.1000-0526.2013.09.001

Evolution of the Exceptional Blocking High over Eurasia and Its Impact on Weather and Climate in 2010 Summer

WANG Xiaoling[1,2,3] DING Yihui[3]

1 Institute of Atmospheric Physics, Chinese Academy of Sciences, Beijing 100029
2 University of Chinese Academy of Sciences, Beijing 100049
3 Laboratory of Climate Studies of CMA, National Climate Centre, Beijing 100081

Abstract: During June－August 2010, significant circumglobal teleconnections existed in the Northern Hemisphere which originated from the negative disturbance around the exit of upper-level jet stream over the Atlantic. The disturbance propagated downstream along the teleconnection wave train, causing Russian heat wave, heavy rains and floods in Pakistan and northwestern and northeastern China. The teleconnection analysis shows that the negative disturbance firstly caused positive perturbation and the development of blocking high in western Russia, resulting in persisting high temperature and drought. Secondly, the negative disturbance propagated to northern West Asia, causing cold air to move southward and meet the northward and westward Indian summer monsoons in northern Pakistan and produced torrential rains. In early August, the disturbance continued to propagate downstream along the upper-level jet stream over

* 国家重点基础研究发展计划(973)项目(2010CB950404)资助
2012 年 9 月 14 日收稿； 2013 年 2 月 26 日收修定稿
第一作者：王小玲，主要从事环流异常及气候变化研究. Email：xlwang@cma.gov.cn

Asia, causing floods in northwestern and northeastern China and the Korea Peninsula. The sudden rainstorm and landslide in Zhouqu, Gansu Province and the extremely heavy rain in Songhuajiang River region occurred just in this stage. The meridional circulation over the Eurasia developed exceptionally during 2010 summer and the meridional cell of the upper-level jet stream was great, causing cold air from high latitudes and warm air from low latitudes to interact continuously. This induced the establishing, strengthening, and maintaining of high-latitude blocking high in western Russian, and low-latitude severe floods in Pakistan and rainstorm in mid-latitudes of China. Monsoons acted as a key factor for the heavy rains and floods with the display of interaction of two warm and humid air flows from the Arabian Sea and Bay of Bengal and the southward cold air flow along the blocking high over northern Pakistan, as well as the interaction of warm and humid air flows from the Indian Ocean and the Pacific and the moisture from westerlies over northeastern China and the Korea Peninsula.

Key words: 2010 summer, Eurasia circulation, blocking high, teleconnection, heat wave, flood

引 言

自 2010 年 6 月中旬起,俄罗斯西部上空持续维持阻塞高压近 2 个月(Dole et al,2011;Grumm,2011)。作为中高纬地区典型的持续性环流异常,阻塞高压通过上下游效应影响大范围地区的天气气候(叶笃正等,1962;Dole,1986;赵振国,1999;丁一汇等,2008)。先是俄罗斯出现持续高温天气,强烈的高温引发多处森林大火;接下来巴基斯坦经历了严重洪涝(Houze et al.,2011);在我国,甘肃舟曲发生严重暴雨泥石流,东北地区则出现暴雨洪涝(国家气候中心,2011);而日本则经历了 1898 年以来的最热夏季(WMO,2011)。这一系列的极端天气和气候事件与局部海域海温异常升高引起大气环流异常,从而改变了季风有直接关系(Trenberth et al,2012)。2010 年夏季俄罗斯西部阻塞高压(以下简称阻高)维持时间之久,引起的高温和洪涝之最,以及社会经济影响,使得这次事件备受关注。我国的重大洪涝与阻高的维持有重要联系(赵振国,1999),这次阻高对我国有什么影响,其发展过程如何,弄清这些问题对我国的气候监测和预测有重要意义。本文重点分析了 2010 年夏季俄罗斯西部阻高的发展演变过程,以及下游环流形势和天气气候特点,讨论阻塞高压的启动机制,以及上游扰动在欧亚地区的传播特征,以期对我国的短期气候预测提供理论依据。

1 资料和方法

本文所用资料为 1948—2010 年 NCEP 逐日再分析资料,要素包括位势高度,经、纬向风速,绝对湿度,地表面气压和垂直速度。根据 Green(1977)的算法,计算了 300 hPa 准地转位涡,以及平均流和瞬变流分别对位涡的输送(分别为 $\overline{\boldsymbol{V}}\cdot\nabla\overline{q}$ 和 $\overline{\boldsymbol{V}'\cdot\nabla q'}$)。垂直积分的水汽输送自地面积分至 300 hPa。欧亚地区(45°～65°N、0°～150°E)西风指数采用赵振国(1999)的算法。利用吴国雄等(1994)的方法,计算了时间平均动能向扰动动能的转化[公式(1)],以及扰动拟能向时间平均拟能的转化,在计算之前,首先通过滤波提取 2～6 天的天气扰动;根据 Ding 等(2005)确定北半球夏季遥相关波列的方法,计算了 200 hPa 高度场的一点相关系数。气候平均值采用 1971—2000 年平均。

$$C(\overline{K}\rightarrow K_e)=\frac{\overline{u'v'}}{a}\left[\cos\varphi\frac{\partial}{\partial\varphi}\left(\frac{\overline{u}}{\cos\varphi}\right)+\frac{1}{\cos\varphi}\frac{\partial\overline{v}}{\partial\lambda}\right]-\frac{1}{a}\left[\overline{(v')^2}-\overline{(u')^2}\right]\left[\frac{1}{\cos\varphi}\frac{\partial\overline{u}}{\partial\lambda}-\tan\varphi\cdot\overline{v}\right] \quad (1)$$

2 阻塞高压的发展演变过程及重要天气特征

从逐候的 500 hPa 高度演变,可以清晰地看到俄罗斯西部阻塞高压的发展演变过程。根据逐候的环流演变以及对下游天气气候的影响,可将阻塞的发展过程分为 4 个阶段(图 1):I 启动阶段(6 月 2—5 候);II 阻塞发展期(6 月 6 候至 7 月 4 候);III 阻塞鼎盛期(7 月 5 候至 8 月 1 候);IV 阻塞衰退期(8 月 2—4 候)。

I 启动阶段:自 6 月 2 候起,随着北大西洋东岸低槽加深并沿地中海向东移动,其槽前的偏南气流

向北输送了大量水汽，在西欧造成了明显降水；以后空气变干，并继续向东北输送，致使俄罗斯西部高度场逐渐升高，至 6 月 5 候，阻塞形势基本建立。这期间，欧亚大陆高纬地区为低槽控制，而中纬度呈多短波槽脊活动的纬向环流（图 1a）。这时上游高空急流开始出现分支。值得注意的是，6 月 5 候，北大西洋东部又有低槽出现。

II 阻塞发展期：6 月 6 候起，北大西洋东部的低槽迅速加深，欧亚地区的环流经向度随之加大（西风指数迅速减弱，图略），高压脊不断加强并向北扩展至斯堪的纳维亚半岛，高压脊与地中海低槽共同形成偶极子型的阻塞形势（图 1b）。贝加尔湖以北地区为宽广槽区，下游东北亚和我国东北、朝鲜半岛亦为偶极型的阻塞形势。结果在欧亚地区上下游形成一个稳定的阻高，这使欧亚环流能够在长时期稳定下来，这是造成这时期南北冷暖空气交汇的大尺度环流背景。在阻塞维持期间，高空急流中心有明显的东传过程，并沿阻高南北两侧出现分支（图 2）。这一时期欧亚大陆上空急流核位于欧洲东南部和西亚北部上空（图 2a），此时期偶极子型阻高系统的低压槽位于急流的入口区右侧，欧洲东南部出现了异常降水；另一个急流核位于我国西北部上空。俄罗斯西部为大范围的水汽辐散区，这使得旱情持续发展（图略）。

III 阻塞鼎盛期（巴基斯坦大水）：东欧至俄罗斯西部的 Ω 型的阻塞形势发展至鼎盛时期，并出现闭合中心，正距平中心超过 12 dagpm（图 1c）。分别位于高压上游和下游的西欧低槽和巴尔克什湖低槽向东南和西南方向伸展，巴尔克什湖低槽南伸到了 30°N 附近。同时，西太平洋副热带高压（以下简称西太副高）深入我国内陆并北抬。高空急流核向东北方向伸展，强度有所加强，北美—北大西洋急流也有所加强（图 2b）。位于阻高东部的巴尔克什湖低槽异常向西南方向伸展至30°N附近，巴基斯坦北

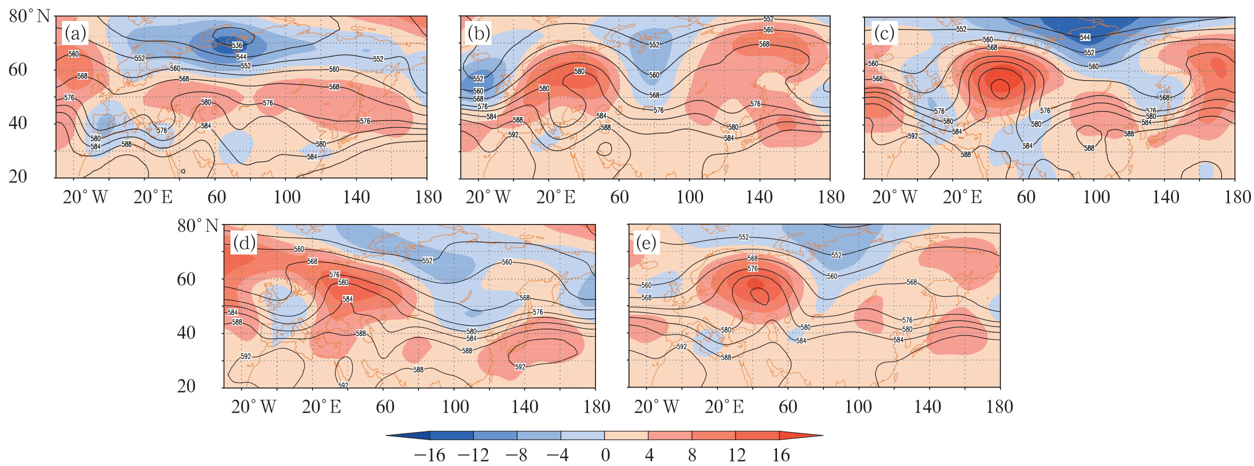

图 1　2010 年夏季欧亚地区 500 hPa 高度及距平（单位：dagpm）
(a) 6 月 2—5 候，(b) 6 月 6 候至 7 月 4 候，(c) 7 月 5 候至 8 月 1 候，(d) 8 月 2—4 候，(e) 6 月 5 候至 8 月 3 候

Fig. 1　Geopotential height and anamolies at 500 hPa over Eurasia during 2010 summer (unit: dagpm)
(a) June 6 to 25, (b) June 26 to July 20, (c) July 21 to August 5, (d) August 6 to 20, (e) June 21 to Augtst 15

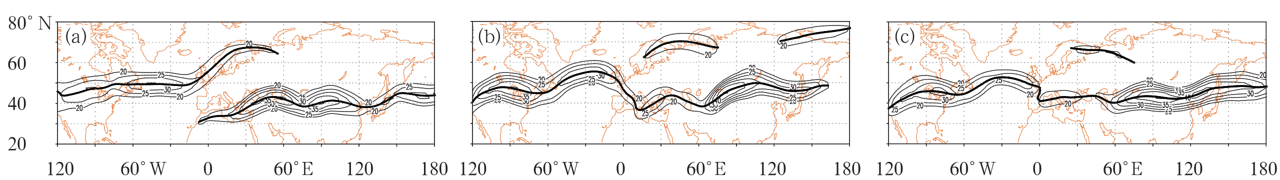

图 2　2010 年夏季高空急流（200 hPa 等风速线）的平均位置（单位：m·s^{-1}）
(a) 6 月 6 候至 7 月 4 候，(b) 7 月 5 候至 8 月 1 候，(c)8 月 2—4 候

Fig. 2　The jet stream at 200 hPa in the upper troposphere with the magnitude greater than 20 m·s^{-1} during 2010 summer (unit: m·s^{-1})
(a) June 26 to July 20, (b) July 21 to August 5, (c) August 6 to 20

部出现大暴雨，这一区域处于深厚的上升运动区（图3），且正好位于高空急流中心入口区右侧，索马里越赤道低空急流北部（图 4a）。从整层水汽输送可以看出，巴基斯坦大水的水汽来源有两个通道，一支来自阿拉伯海，在印度西北部上空转向西北输送；另一支来自孟加拉湾，在喜马拉雅山南麓转向西北方向，这正是 Houze 等（2011）指出的异常向西移动的孟加拉湾低压。暖湿气团（$\theta_{se}\geqslant$340 K）异常向北伸展至 40°N。来自低纬的两支暖湿气流与沿着阻高东侧南下的冷空气在巴基斯坦北部上空交汇，高低纬冷暖空气的相互作用对大暴雨的形成起到了至关重要的作用（Hong et al，2011）。

Ⅳ 阻塞衰退期（我国东北松花江、鸭绿江大水）：西伯利亚低槽向东南扩展，贝加尔湖至我国东北部为低槽控制。西太副高进一步向西扩展，592 dagpm 闭合中心位于日本上空（图 1d）。受下游高压系统的阻挡，降雨系统（低涡、切变线）在东北亚持续发展，造成该地区暴雨洪涝。8 月 19 日，随着一场冷空气到来，上游阻高迅速崩溃（WMO，2011），以后下游地区也迅速转变为平直环流型。在这一阶段，高空急流中心继续向东传播，急流核位于我国北方至朝鲜半岛上空（图 2c）。亚洲季风区的水汽输送由前期集中在印度季风区转向东亚季风区，同时，中纬度西风带也出现较强的水汽输送（图 4b）。分别来自西风带、印度季风区和西北太平洋的 3 支水汽交汇在我国西北、华北、东北地区以及朝鲜半岛上空。

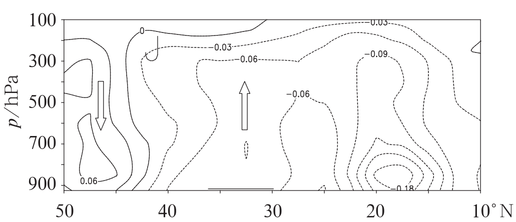

图 3　2010 年 7 月 5 候至 8 月 1 候平均的沿 72.5°E 垂直速度剖面
（单位：Pa·s^{-1}，J 表示高空急流的位置，横坐标上粗线表示巴基斯坦大水的位置，箭头分别表示上升/下沉运动）

Fig. 3　Section of vertical velocity along 72.5°E from July 21 to August 5, 2010
(unit: Pa·s^{-1}, J illustrates the position of the jet stream at 200 hPa, solid line along the zonal axis illustrates the heavy rain in northern Pakistan, vector illustrates vertical upward/downward motion)

根据 Dole 等（2011）定义的俄罗斯高温关键区（50°～60°N、35°～55°E），我们计算了区域平均的 850 hPa 温度指数和 500 hPa 高度指数，两个指数均在 6 月 5 候至 8 月 3 候持续超过 1 个标准差，在阻高鼎盛时期甚至超过 3 个标准差，这期间的高度场分布（图 1e）与阻高鼎盛时期的分布类似。不仅俄罗斯西部出现了持续高温，在下游日本地区，整个时段也主要处于高压脊的控制之下，也出现了高温天气。

3　上游大西洋低槽的东移对阻塞发展的影响

在阻塞启动阶段，可以清楚地看到北大西洋东岸低槽的东移。自 6 月 5 候阻塞形势建立起，北大西洋东部洋面上空始终维持低槽，一直持续到 8 月 3 候（图 5）。在阻塞发展时期，北大西洋东部低槽逐

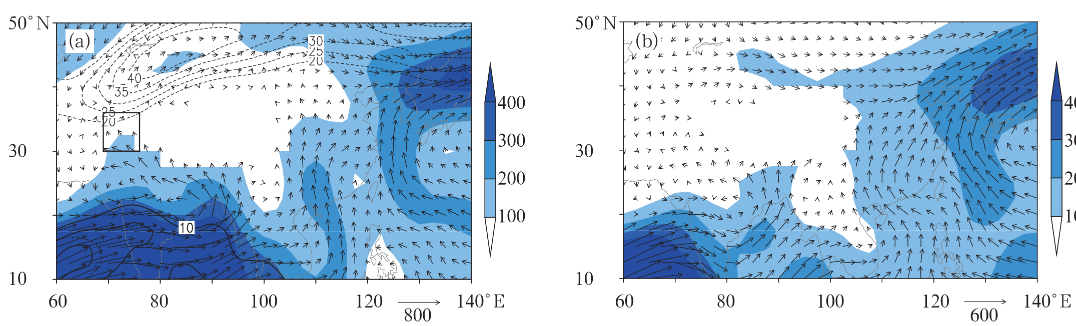

图 4　垂直积分的整层水汽输送（单位：kg·m^{-1}·s^{-1}）
(a)2010 年 7 月 5 候至 8 月 1 候平均［黑色虚线表示 200 hPa 高空急流，实线表示 850 hPa 低空急流（单位：m·s^{-1}），方框表示巴基斯坦北部］，(b)2010 年 8 月 2—4 候平均

Fig. 4　Vertically integrated atmospheric moisture transport (unit: kg·m^{-1}·s^{-1})
(a) July 21 to August 5, 2010, (b) August 6 to 20, 2010

渐加深并略向东移动，槽区相对较为宽广；7 月 5 候起，槽区突然变窄，形成一东南—西北向的低槽，并且十分稳定，而欧洲阻塞的发展改变了欧亚环流场和急流区分布，同时说明环流的经向度加大了，阻高也进入鼎盛时期。从空间分布上看，北大西洋东部的低槽正好位于北美—北大西洋高空急流的出口区（图 6），急流出口区对低槽的发展和维持十分有利（Ding et al，2005），而低槽对阻塞的维持和发展起到了至关重要的作用。正是高空急流引起扰动，从而引起下游环流的一系列变化。同时，下游的变化对上游也有一定的影响。李双林等（2001）的研究表明，上游低槽和下游阻高的发展有相互促进的作用，上游瞬变波的活动有利于下游的正高度异常，而下游的正高度异常越强，越有利于上游瞬变活动的增强。

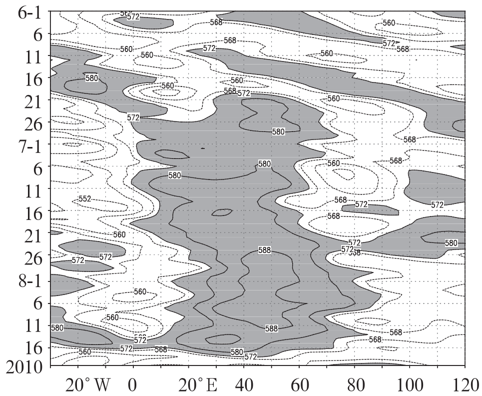

图 5　2010 年 6 月 1 日至 8 月 20 日沿 55°N 的 500 hPa 位势高度时间-经度剖面（单位：dagpm）

Fig. 5　Time-longitude section of daily geopotential height at 500 hPa along 55°N during June 1 to August 20, 2010 (unit: dagpm)

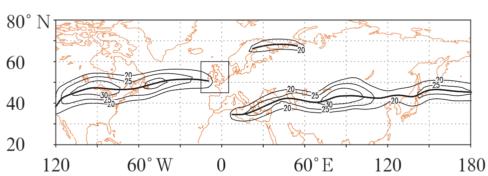

图 6　2010 年 6 月 21 日至 8 月 15 日平均的 200 hPa 等风速线（单位：m・s^{-1}；方框表示北大西洋急流出口区）

Fig. 6　The mean jet stream at 200 hPa in the upper troposphere with the magnitude greater than 20 m・s^{-1} from June 21 to August 15, 2010 (unit: m・s^{-1}, The box illustrates the exit of the jet stream over the northern Atlantic)

对 300 hPa 准地转位涡的分布可以看出，阻塞上游和下游均为高位涡区，下游的高位涡区自东北向西南方向伸展并切入到阻塞南部；脊区则为低位涡分布（图 7）。对于阻塞的维持机制，瞬变波向高压中心输送低位涡有重要作用（Green，1977；Shutts，1983；毕慕莹等，1992；刘辉等，1995）。而对这次阻塞过程，从平均流对位涡的输送可以看出（图 8a），高压脊西北部有一正值中心，表明有低位涡输入高压脊区，平均流位涡平流使阻高西北部位涡减小，有利于阻高的向北伸展。瞬变位涡输送在阻高后部有低位涡输入高压脊区（图8b），其中心强

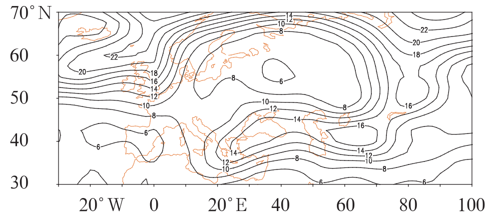

图 7　2010 年 6 月 21 日至 8 月 15 日平均 300 hPa 准地转位涡（单位：10^{-5} s^{-1}）

Fig. 7　The distribution of 300 hPa quasi-geostrophic potential vorticity averaged from June 21 to August 15, 2010 (unit: 10^{-5} s^{-1})

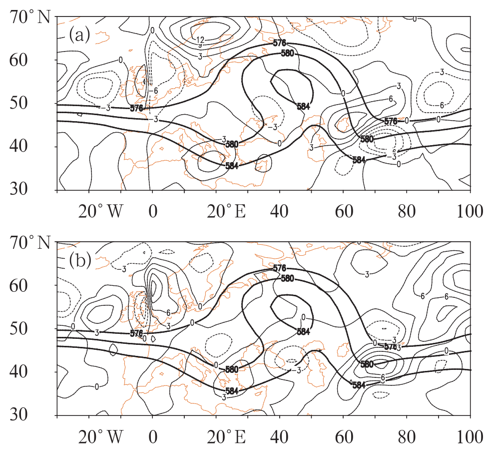

图 8　2010 年 6 月 21 日至 8 月 15 日平均季 300 hPa 平均流（a）和瞬变波（b）对准地转位涡的输送（单位：10^{-10} m・s^{-2}，粗实线表示阻塞高压，单位：dagpm）

Fig. 8　Transport of 300 hPa quasi-geostrophic potential vorticity by (a) mean flow and (b) transient eddy averaged from June 21 to August 15, 2010 (unit: 10^{-10} m・s^{-2}, Solid lines illustrate the blocking high, unit: dagpm)

度($12\times10^{-10}\ m\cdot s^{-2}$)约为这一区域平均流高位涡向阻高的输送(即对阻高的破坏作用)的2倍,从而抵消了平均流位涡平流的作用,使这个阻塞系统得以维持。为了进一步证实阻高的维持能量来源于北大西洋急流出口区的天气扰动,我们进一步计算了天气扰动拟能向时间平均拟能的转化,以及天气扰动动能向时间平均动能的转化,由于拟能比动能的量级小得多,这里仅给出动能转化的空间分布图(图9)。可以看出,在大西洋高空急流出口区,有较强的天气扰动动能向时间平均动能的转化,扰动动能主要沿急流分支的南支传播,输送给时间平均流。

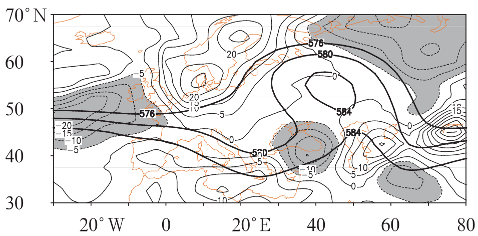

图9 2010年6月21日至8月15日
平均气流动能向天气尺度扰动
(2～6天滤波)动能的转化空间分布
(单位:$10^{-4}\ m^2\cdot s^{-3}$,负值表示扰动动能向平均流动能转化,阴影表示低于$-5\times10^{-4}\ m^2\cdot s^{-3}$)

Fig.9 Transfer of kinetic energy from mean flow to transient eddy (2－6 d) averaged from June 21 to August 15, 2010
(unit: $10^{-4}\ m^2\cdot s^{-3}$, Minus illustrates the transfer from transient eddy to mean flow, shaded indicates less than $-5\times10^{-4}\ m^2\cdot s^{-3}$, solid lines illustrate the blocking high, unit: dagpm)

4 遥相关

Ding等(2005)发现,北半球夏季中纬度地区存在绕球的遥相关(CGT),起始于北大西洋急流出口区的扰动异常通过波列的传播,可以影响印度季风,从而影响下游地区。我们计算了阻高期间的200 hPa高度一点相关系数,其空间分布如图10所示。可以清晰地看到源自北大西洋急流出口区的遥相关波列,波列沿阻高出现南北两个分支,这两个分支又在日本东部洋面汇合。波列沿高空急流向下游传播的传播如下:急流出口区的负相关,欧洲的正相关,接下来是西亚的负相关,中亚的正相关,这一正相关一直向东延伸到日本东部,北太平洋东部的负相关,北美大陆的正相关,美国东部洋面的负相关相对较弱。由此看来,2010年夏季北半球存在典型的CGT遥相关,位于北大西洋急流出口区的扰动负异常首先引起俄罗斯西部的正异常,阻高发展,接下来为西亚的负异常,导致冷空气异常向南伸展,印度季风区(巴基斯坦北部)出现暴雨、洪涝,接着在我国华北、东北至朝鲜半岛出现负异常,而日本以东地区为正异常,造成了日本的高温热浪。

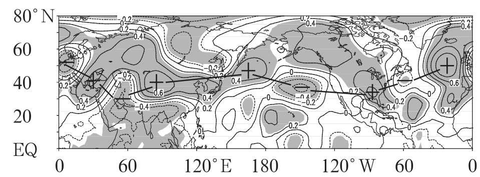

图10 2010年6月21日至8月15日
200 hPa高度一点相关(50°N、20°W)
(阴影区表示相关通过0.05显著性水平检验)

Fig.10 One-point correlation map of 200-hPa geopotential height from June 21 to August 15, 2010
(Shaded illustrates the correlation coefficients have passed the 0.05 significance test)

5 小 结

(1) 2010年夏季欧亚大陆中高纬呈现上、下游阻塞长期维持的现象,尤其是俄罗斯西部出现近2个月的阻塞高压。源于北大西洋东部高空急流出口区的低槽维持了俄罗斯西部阻高的发展,涡度收支表明瞬变扰动对低位涡的输送主要维持了阻高的低位涡,天气尺度扰动动能向平均流动能的转化是阻高维持的重要能量来源。

(2) 200 hPa高空急流中心有明显的东传过程,伴随着环流形势的调整,出现大振幅的经向环流型,地面的天气特征也有阶段性变化。在这种情况下,高、低纬冷暖空气相互作用造成持续季风降水,来自低纬阿拉伯海和孟加拉湾的两支暖湿气流与沿着阻高东侧南下的冷空气在巴基斯坦北部上空交汇,形成大暴雨;来自印度洋、太平洋的暖湿气流和中纬度西风带的水汽交汇在我国华北、东北以及朝鲜半岛上空。

(3) 2010年夏季北半球存在典型的CGT遥相关,首先在北大西洋高空急流出口区出现负扰动,扰动以波列形式沿高空急流向下游传播,在下游负异

常区造成局地的暴雨洪涝。一点相关分析表明,急流出口区的负扰动首先引起俄罗斯西部的正扰动,阻塞高压发展,造成持续高温干旱;接下来引起西亚北部的负扰动,造成印度季风区巴基斯坦北部洪涝;扰动沿高空急流继续向下游传播,在我国华北、东北以及朝鲜半岛造成洪涝。在日本造成正扰动,有利于该地区持续性阻塞的发展,造成了高温热浪天气。

对于此次事件出现的气候背景,Trenberth 等(2012)的研究表明,2010 年夏季北印度洋、印尼附近海域以及热带大西洋海温异常偏高,同时又有 La Niña 事件出现。李双林等(2001)提出了一种在热带正异常热源驱动下,瞬变波与准定常行星波双向相互作用维持阻高的物理概念。2010 年夏季的欧亚大气环流异常正是热带热源强迫和大气内部动力过程(瞬变强迫)的共同作用,本文重点探讨了大气内部动力过程,至于外强迫和内部过程的贡献各有多少,还需要进一步研究。

致谢:吴国雄院士和刘屹岷研究员对本研究提出建议并给予帮助,在此表示感谢。

参考文献

毕慕莹,丁一汇. 1992. 1980 年夏季华北干旱时期东亚阻塞形势的位涡分析. 应用气象学报,3(2):145-156.

丁一汇,王遵娅,宋亚芳,等. 2008. 中国南方 2008 年 1 月罕见低温雨雪冰冻灾害发生的原因及其与气候变暖的关系. 气象学报,66(5):808-825.

国家气候中心. 2011. 全国气候影响评价:2010. 北京:气象出版社,27-32.

李双林,纪立人,倪允琪. 2001. 夏季乌拉尔地区大气环流持续异常. 科学通报,46(9):753-758.

刘辉,吴国雄,曾庆存. 1995. 北半球阻寒高压的维持. I:准地转和 Ertel 位涡分析. 大气科学,19:177-185.

吴国雄,刘辉,陈飞,等. 1994. 时变涡动输送和阻塞高压的形成:1980 年夏季我国的南涝北旱. 气象学报,52:308-320.

叶笃正,陶诗言. 1962. 北半球冬季阻塞形成的研究. 北京:科学出版社,1-1324.

赵振国. 1999. 中国夏季旱涝及环境场. 北京:气象出版社,75-78.

Ding Q, Wang B. 2005. Circumglobal teleconnection in the Northern Hemisphere summer. J Climate, 18(9):3483-3505.

Dole R. 1986. The life cycles of persistent anomalies and blocking over the North Pacific. Adv Geophy, 29:31-69.

Dole R, Hoerling M, Perlwitz J, et al. 2011. Was there a basis for anticipating the 2010 Russian heat wave? Geophys Res Lett, 38, L06702, doi: 10.1029/2010GL046582.

Green J S A. 1977. The weather during July 1976: Some dynamical consideration of the drought. Weather, 32:120-128.

Grumm, R H. 2011. The central European and Russian heat event of July-August 2010. Bull Amer Meteorol Soc,1285-1296,doi: 10.1175/2011BAMS3174.1.

Hong C C, Hsu H H, Lin N H, et al. 2011. Roles of European blocking and tropical-extratropical interaction in the 2010 Pakistan flooding. Geophys Res Lett, 38, L13806, doi: 10.1029/2011GL047583.

Houze Jr R A, Rasmussen K L, Medina S, et al. 2011. Anomalous atmospheric events leading to the summer 2010 floods in Pakistan. Bull Amer Meteor Sci, 291-298, doi: 10.1175/2010BAMS3173.1

Shutts G J. 1983. The propagation of eddies in diffluent jet streams: eddy vorticity forcing of 'blocking' flow fields. Quart J Roy Meteor Soc, 109(462):737-761.

Trenberth K E, Fasullo F. 2012. Climate extremes and climate change: The Russian heat wave and other climate extremes of 2010. J Geophys Res, 117, D17103, doi: 10.1029/2012JD018020.

WMO. 2011. WMO statement on the status of the global climate in 2010.

物 理 学 报 Acta Phys. Sin. Vol. 62, No. 22 (2013) 229201

中国冬季区域性极端低温事件分类及其与气候指数极端性的联系*

王晓娟[1)2)] 沈柏竹[1)] 龚志强[3)†] 封国林[4)]

1) (兰州大学大气科学学院, 兰州 730000)

2) (常熟理工学院物理与电子工程学院, 常熟 215500)

3) (国家气候中心监测诊断室, 北京 100081)

4) (中国气象局国家气候中心开放实验室, 北京 100081)

(2013年4月10日收到; 2013年7月1日收到修改稿)

基于区域性极端低温事件客观识别技术, 对 1951—2010 年中国冬季的区域性极端低温事件进行客观识别. 根据事件的空间分布特征, 将综合指数前 60 位的事件划分为全国型、东部型、东北 - 华北型、华北 - 华南型、北方型和西北 - 华南型六类; 通过分析不同区域类型低温事件形成的环流背景场验证了分类的有效性. 在此基础上, 以 1971 年 1 月 21 日开始的典型事件为例, 分析了事件对应的海温场、高度场和风场的异常, 确定与区域性极端低温事件联系较密切的可能气候因子, 进而分析不同类型事件与各气候指数异常的对应关系. 总体而言, 赤道中东太平洋海温指数异常偏小、北太平洋涛动指数异常偏小、北极涛动指数异常偏小和冬季风异常偏强时, 发生区域性极端低温事件的概率较高; 且这四种指数的历年冬季平均值达到 15%(或 85%) 极端阈值的年份中, 发生区域性极端低温事件的百分率分别达到 80.0%, 77.8%, 60.0%和 62.5%, 从而为区域性极端低温事件的诊断和预测研究等提供了一定的参考.

关键词: 区域性极端低温事件, 空间分类, 气候指数, 极端

PACS: 92.60.Wc **DOI:** 10.7498/aps.62.229201

1 引 言

近半个世纪以来, 在全球变暖的整体格局下, 亚洲及中国大部分区域的温度呈持续增长的趋势 [1,2]. 中国的年平均气温在过去的 50 年里上升了约 1.1 °C[3]. 与此同时, 在全球变暖的背景下, 地球气候系统也存在着各种类型的短时期、区域性的异常变化. 例如, 近几年北半球范围内区域性极端低温事件 (regional low temperature extreme events, RELTE) 频繁发生, 且影响范围大、持续时间长. 就我国而言, 近年来频繁发生的 RELTE 主要有: 2008 年 1 月中国南方地区经历了历史上罕见的大范围低温、雨雪和冰冻灾害 [4−6]; 2009/2010 年冬季, 包括中国在内的北半球多个国家和地区遭受大范围低温冰雪的袭击; 2011 年 1 月, 我国发生了近年来极为罕见的一次全国性极端低温事件, 其影响范围之广、持续时间之长是 1977 年以来最重大的一次事件 [7].

全球增暖背景下, 区域性极端低温事件的频繁发生往往会造成巨大的灾难. 这也对 RELTE 的检测、诊断分析及其预测等提出了新的挑战 [8−14]. 目前, 国内已经开展了一些相关研究, 例如: 张宗婕和钱维宏 [15] 发展了针对区域持续性低温事件的识别技术, 建立了区域持续性低温事件库, 初步分析了低温事件的时空特征; 任福民等 [16] 在客观

* 国家自然科学基金 (批准号: 41305075)、国家重点基础研究计划 (批准号: 2012CB955203, 2012CB955902) 和公益性行业专项 (批准号: GYHY201106016) 资助的课题.

† 通讯作者. E-mail: gzq0929@126.com

天气图分析法的基础上, 提出了一种持续性区域极端事件客观识别方法, 能够有效识别事件的空间范围和时间持续的过程特征; 龚志强等 [17] 对该方法进行完善, 发展了区域性极端低温事件客观识别技术 (objective identification technique for regional low temperature extreme events, OITRELTE), 并建立了检测得到的 RELTE 库; 王晓娟等 [18] 利用 OITRELTE 对我国近 50 年的区域性低温事件进行了检测, 并从空间分布和时间变化趋势等角度研究了 RELTE 的时空变化特征. 此外, 张宗婕和钱维宏 [19] 通过大气变量物理分解的方法, 提取出对极端事件有指示意义的天气尺度扰动信号, 追踪区域性极端事件发生之前天气扰动的来源、传播路径及提前时间 (日数). 龚志强等 [20] 分析了欧亚 500 hPa 高度场关键区异常配置与中国冬季 RELTE 的联系. 但值得指出的是, 由于气候系统是一个复杂的多种因子相互作用的系统, 气候诊断和预测离不开各种环流和海洋指数等 [21−25]. 因此, 本文在前人研究基本确定一些可能影响要素的前提下, 借鉴已有的 RELTE 研究成果 [17,18], 分析不同类型事件与各种环流和海温指数等的联系, 尤其探讨各种指数出现极端异常情况下与 RELTE 的对应关系, 这将有助于深入理解 RELTE 形成的机制及其与气候系统背景因子的联系, 进而对 RELTE 有全面的认识.

2 资料与方法

OITRELTE 检测所用的逐日最低温度资料为: 国家气象信息中心发布的经过质量控制的 731 站点的逐日最低温度资料, 研究时段为 1951—2010 年当年 11 月份至次年 3 月份. 环流背景分析采用 NCEP/NCAR 逐日高度场和风场资料 [26], 水平分辨率为 $2.5^\circ \times 2.5^\circ$, 垂直分辨率为 17 层. 海表温度资料采用 1961—2010 年 NOAA ERSST 的逐月海面温度资料 [27], 分辨率为 $2^\circ \times 2^\circ$.

北太平洋涛动 (NPO) 指数采用刘宗秀等 [28] 计算的 500 hPa 高度场的区域均值差的标准化值; 西风漂流区海表温度指数采用廉毅等 [29] 计算的规定区域的海表温度的平均值的标准化值; 西太平洋副高西伸脊点、西太平洋副高脊线、亚洲极涡强度、亚洲极涡面积、东亚槽强度、东亚槽位置指数采用国家气候中心的 74 项环流指数; 北极涛动 (AO) 指数和赤道中东太平洋海温 (NINO3.4) 指数采用 NCEP 网站的逐月资料. 冬季风指数采用施能等 [30] 定义的海陆 500 hpa 高度场的差值重新计算得到. 考虑到各种指数多数为逐月资料, 在分析与区域性低温事件联系时, 根据事件发生的月份和持续时间进而考虑当月的指数值或两个月指数的平均值的异常情况.

RELTE 的识别采用 Ren 等 [16]、龚志强等 [17] 发展的 OITRELTE. 该方法主要包括: 1) 极端低温阈值的确定; 2) 极端低温事件空间区域的识别; 3) 空间区域的连续性过程提取; 4) 指标体系. 首先, 对单日极端低温事件进行空间区域识别, 进而识别临时事件和低温带的重合信息, 对每日临时事件和低温带的信息进行整合, 可客观识别出连续过程的极端低温事件. 采用该技术对 1951—2010 年的我国冬季区域性低温事件进行客观识别以建立 RELTE 库.

区域性极端低温事件, 既包含空间特征, 又包含时间演变特征, 因此采用两个级别的指标 [17,13]: 一级指标为过程量, 二级指标为逐日变化量. 二级指标主要描述一次极端低温事件的逐日演变, 主要包括逐日极端值 (Q_d)、逐日累计强度 (L_d)、逐日影响面积 (A_d) 和综合考虑上述三种特征的综合指数 (Z_d) 和事件逐日影响范围几何中心 (Loc_d):

$$Q_d = \min(T_j) \quad j = 1, 2, \cdots, m, \tag{1}$$

$$L_d = \sum_j (T_j - T_0^j) \quad j = 1, 2, \cdots, m, \tag{2}$$

$$A_d = \sum_j (a_j) \quad j = 1, 2, \cdots, m_p, \tag{3}$$

$$Z_d = e_1 Q_d + e_2 L_d + e_3 A_d, \tag{4}$$

其中, j 表示逐日发生达到极端事件阈值的站点, T_0^j 表示各台站极端事件阈值, m 为区域性极端事件过程中的逐日台站数. (3) 式中计算逐日影响面积时, 先采用 $0.5^\circ \times 0.5^\circ$ 分辨率对站点网格化再计算面积, a_j 为每个网格点代表的面积, m_p 为事件过程中逐日最大影响范围内的网格数. (4) 式中 e_1, e_2, e_3 为加权系数. 一级指标主要描述极端低温事件过程的综合特征, 包括过程极端值 (Q)、过程累计强度 (L)、累计影响面积 (A)、最大覆盖面积 ($A_{\max}$)、持续天数 (N)、综合指数 (Z) 和事件最大影响范围的几何中心:

$$Q = \min(Q_d) \quad d = 1, 2, \cdots, N, \tag{5}$$

$$L=\sum_{i=1}^{N} L_d, \tag{6}$$

$$A_{\max}=\min(A_d) \quad d=1,2,\cdots,N, \tag{7}$$

$$A=\sum_{i=1}^{N} A_d, \tag{8}$$

$$Z=e_1Q+e_2L+e_3N+e_4A, \tag{9}$$

其中, d 为事件过程中的某天, N 为事件持续天数, (9) 式中 e_1, e_2, e_3, e_4 为加权系数, 计算过程综合指数时, 先对逐日事件进行标准化, 再加权求和 [18]. 事件几何中心的计算方法如 (10) 式所示,

$$Lat=\sum_{i=1}^{m} lat_i/m,$$

$$Lon=\sum_{i=1}^{m} lon_i/m, \tag{10}$$

其中 lat_i 为单个站点的纬度, lon_i 为单个站点的经度.

OITRLTE 的优点在于: 1) 给定一组参数以后, OITRLTE 能够客观识别区域性极端低温事件, 这类事件有别于传统的单个站点的极值, 而是空间上集中于某一区域, 时间上有一定持续性的事件; 传统的研究中是无法给出此类事件空间范围的界定、起始时间和结束时间的判断等; 2) OITRLTE 同时包含了一套内容相对丰富的指标体系, 能够从事件的极端程度、影响范围、持续时间和综合影响等角度对事件进行多方面的描述.

3 结果与分析

3.1 区域性极端低温事件的分类

利用 OITRELTE 对我国 1951—2010 年当年 11 月份至次年 3 月份的逐日最低温度进行检测, 在一定的检测标准下, 共检测得到区域性极端低温事件 559 次. 图 1 是 559 次区域性极端低温事件几何中心的空间分布情况. 从图中可以看出, 559 次区域性极端低温事件的几何中心存在两个显著的事件带: 东北 - 华北 - 黄淮的事件带, 新疆北部 - 西北中部 - 西北东部的事件带. 此外, 青藏高原东部和西南南部低温事件中心出现的次数也相对密集.

从等概率的角度考虑, 近 60 年中十年一遇的极端异常事件发生的次数约为 6 次, 如果以 10%作为极端异常事件的划分标准, 则这类综合影响较大的异常事件约为 60 次. 这 60 次事件的共同特点是: 影响范围大、持续时间长、强度大, 对社会和经济造成的影响大. 因此, 对综合指数值最大的 60 次事件根据其地理位置的不同进行分类. 根据这 60 次区域性极端低温事件最大的影响范围, 我们大致可以将其分成 6 类 (如图 2 所示): 分别是全国型、东部型、东北 - 华北型、华北 - 华南型、北方型、西北 - 华南型. 其中, 全国型共 20 次, 东部型共 15 次, 东北 - 华北型共 5 次, 华北 - 华南型共 7 次, 北方型共 3 次, 西北 - 华南型共 10 次.

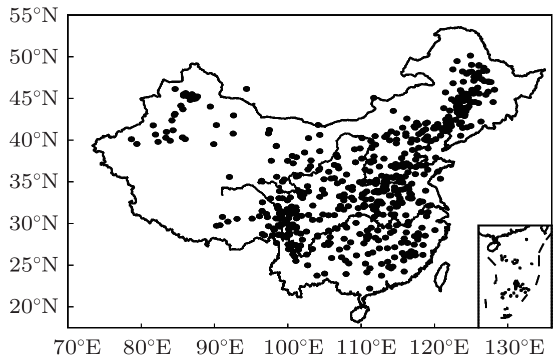

图 1 559 次区域性极端低温事件几何中心的空间分布

为了进一步分析不同区域类型的低温事件对应的环流特征, 将不同类型区域性极端低温事件的 500 hPa 高度场及 850 hPa 距平风场进行了合成分析 (北方型和东北 - 华北型的高度场和距平风场的合成分析特征较为类似, 故下文分析归为一类). 从图 3 可以看出, 全国型区域性极端低温事件的 850 hPa 距平风场在中国的东部地区存在显著的异常偏北风, 西部地区则存在显著异常东北风, 而 500 hPa 高度场中东亚槽异常的深厚和稳定, 从而容易形成覆盖我国大部分区域的全国型极端低温事件; 东部型事件的 850 hPa 距平风场在中国的东部地区存在异常的偏北风, 异常风场主要沿着东部路径南下, 且东亚槽显著偏东, 冷空气沿着槽南下, 主要影响中国东北地区, 容易在东部形成大范围持续低温; 东北型和北方型事件则 850 hPa 距平风场在中国的北方地区存在异常偏东北风, 北方冷空气对中国南方地区的影响较小, 东亚槽位置偏东, 相对全国型浅薄一些, 且呈西南 - 东北方向, 不利于冷空气南下影响南方地区; 华北 - 华南型事件对应东亚槽显著偏东, 850 hPa 距平风场在华北以北地区存在显著的异常偏东风, 在华北至华南则存在显著的异常偏

北风, 有利于冷空气影响到南方地区, 西北 - 华南型事件对应东亚槽偏深, 且呈西北 - 东南方向, 有利于冷空气持续南下, 且 850 hPa 距平风场存在显著的西北至东南沿海的异常西北气流, 容易造成西北至南方地区的低温.

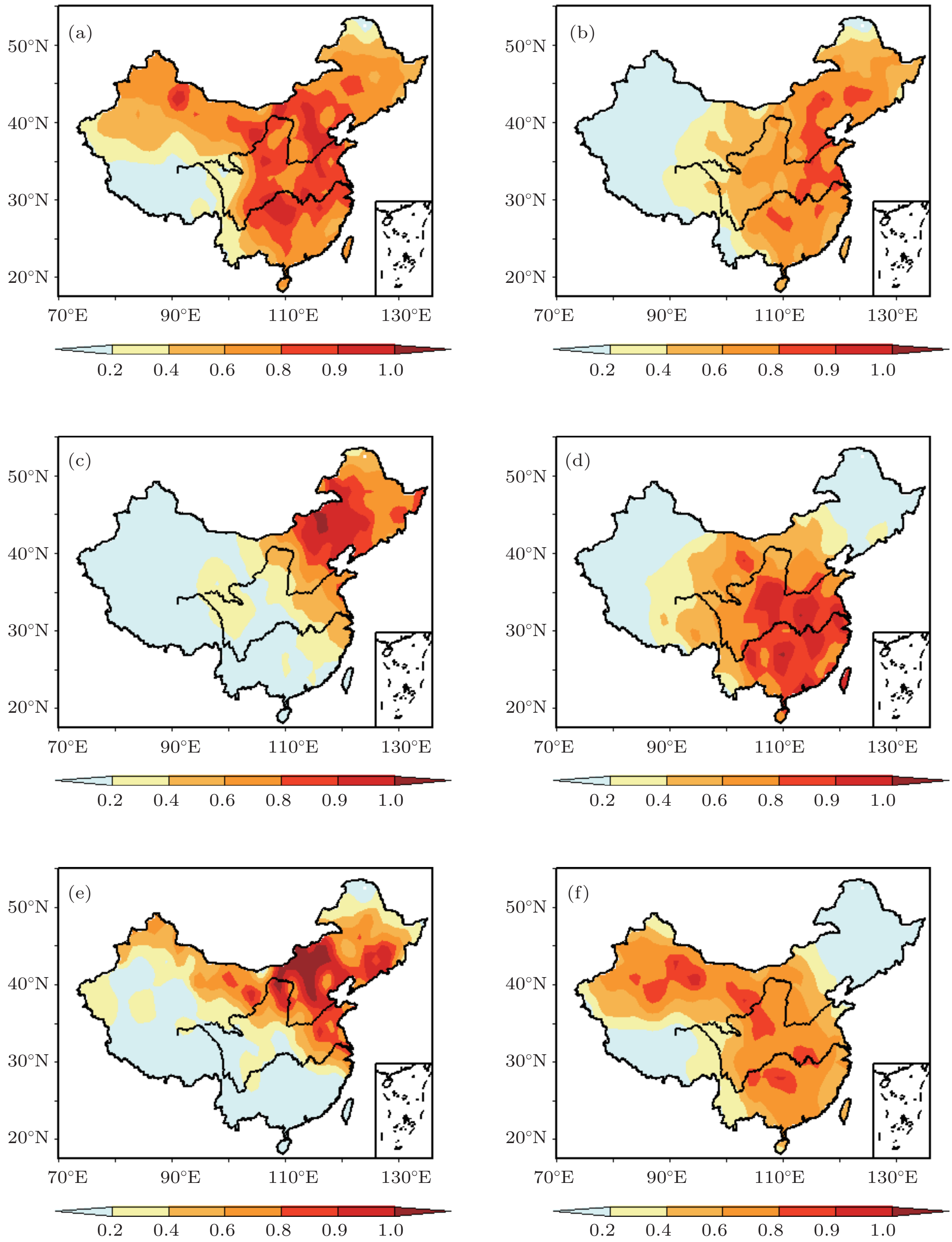

图 2 综合指数值最大的 60 次区域性极端低温事件的分类 (a) 全国型; (b) 东部型; (c) 东北 - 华北型; (d) 华北 - 华南型; (e) 北方型; (f) 西北 - 华南型 (填色图表示的是站点发生区域性极端低温事件的相对频次)

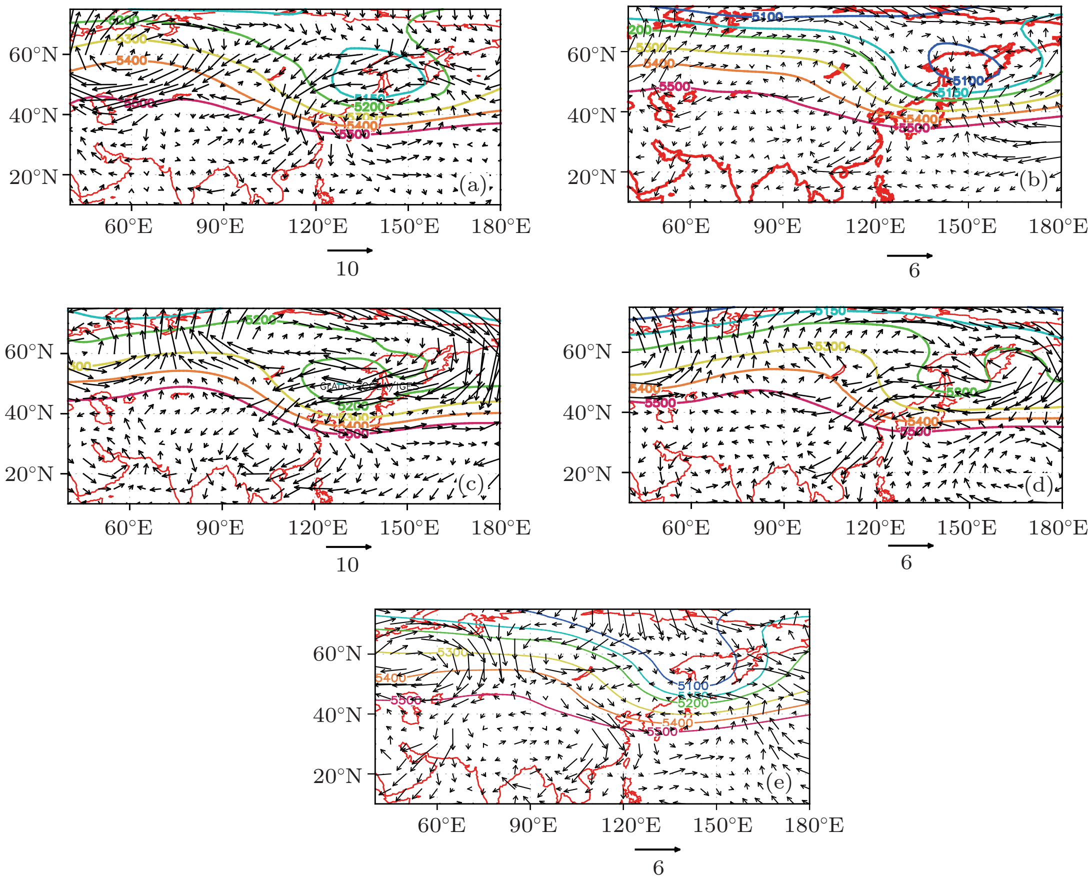

图 3 5 种主要区域性低温事件类型的合成 500 hPa 高度场及 850 hPa 距平风场 (a) 全国型; (b) 东部型; (c) 北方型/东北 - 华北型; (d) 华北 - 华南型; (e) 西北 - 华南型

3.2 区域性极端低温事件个例分析

对区域性极端低温事件分类的基础上, 首先结合个例讨论对区域性极端低温事件需要重点考虑哪些可能的影响因子. 1971 年 1 月 21 日 —2 月 9 日发生了一次典型区域性极端低温事件, 结合该次事件分析与区域性低温事件所对应的大气和海温等可能的影响因素. 该事件持续时间为 20 天, 过程极端低温值为 −40.4 °C, 综合指数值为 2.043. 事件主要发生的区域包括内蒙古中部、华北大部、西北东部、西南大部、江南、华南等大范围区域, 属于第四类华北 - 华南型事件 (图 4), 且本次事件主要以冷干型为主.

图 5 是 1970/1971 年冬季的海表温度距平图. 从图中可以看出: 这次事件期间赤道中东太平洋海温异常偏低, 属于中等强度的 La Nina 事件范畴. 已有研究表明 [31–36]: 强 La Nina 事件发生的当年冬季, 亚洲中纬度大气环流的经向发展会异常强烈. 由暖空气构成的高压脊可向北延伸到极区, 引导那里的冷空气频繁南下, 侵入中国, 造成中国北方和东部大部分地区气温偏低. 同时, 在副热带和热带地区副高位置偏北偏西, 南支槽偏弱, 有利于长江以北地区降水偏多, 南方降水偏少.

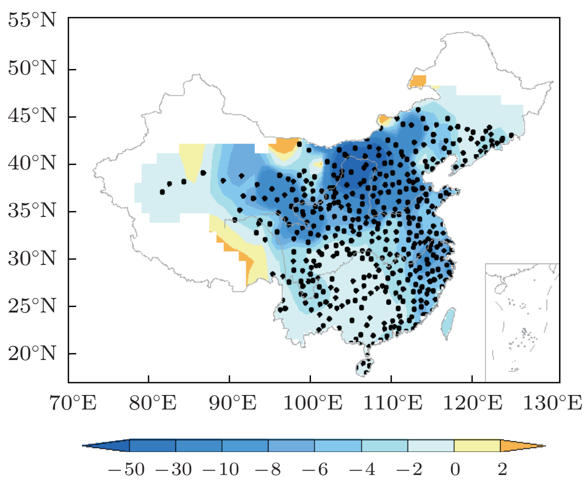

图 4 1971 年 1 月 21 日开始的区域性极端低温事件最大影响范围的站点分布 (黑点表示该次事件发生期间达到极端低温阈值的站点; 填色图表示过程累计强度值, 即事件过程中最低温度与极端低温阈值差值的累计值)

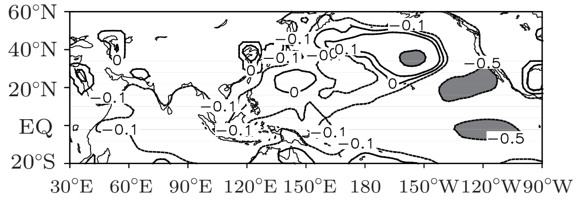

图 5 1970/1971 年冬季的海表温度距平

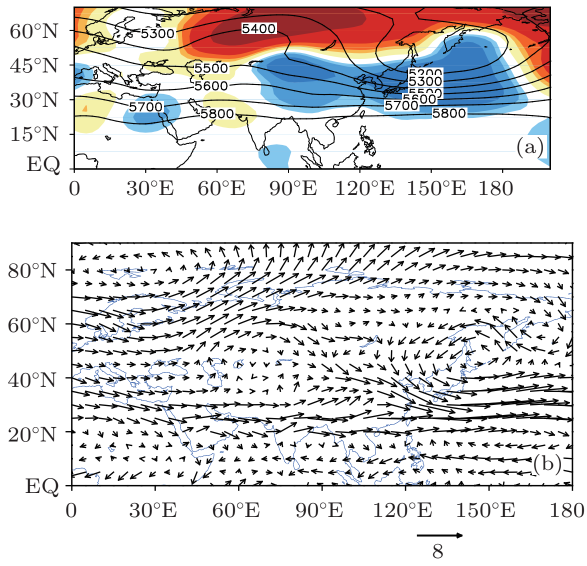

图 6 1971 年 1 月 21 日 —2 月 9 日 500 hPa 距平场 (阴影) 和原始场 (等值线)(a), 700 hPa 平均风场 (b)

图 6(a) 中, 500 hPa 原场中东亚大槽位置偏东, 偏强; 对应同期的距平场在中高纬度地区异常偏强, 低纬度地区异常偏弱, 在乌拉尔山附近存在一个异常正距平中心, 有利于乌山阻高偏强, 在白令海附近也存在一个异常的正距平中心, 中国东北区域主要受正距平控制; 在中国东部及日本南部附近存在一个异常的负距平中心. 从这种北高南低形势的维持有利于冷空气持续活跃, 并南下影响我国. 图 6(b) 中 700 hPa 距平风场可以看出, 来自青藏高原北部的西北风距平偏强, 并且我国华北及以南地区为异常的东北风控制, 两支异常气流在江南等地交汇, 为华北 - 华南地区出现区域性极端低温事件提供了冷空气条件. 此外, 图 6(b) 中孟加拉湾及南海区域的异常的南风距平较弱, 这样不利于副热带高压西侧的偏南风把南方暖湿空气向北输送, 不容易造成冷暖空气在中国长江中下游及其以北地区交汇而形成持续性的低温雨雪天气.

通过上述分析可以看出, 区域性极端低温事件的诊断研究必然离不开对下列因子的异常情况进行分析研究: 与 500 hPa 高度场相联系的东亚槽、NPO、西太平洋副高、与海平面气压相联系的 AO、与海温相联系的 NIINO 3.4 海温指数等.

3.3 各类区域性极端低温事件与指数异常的对应关系

通过统计各类区域性极端低温事件与主要同期气候指数异常的对应关系, 从而进一步探究各类事件发生的可能内在机制. 表 1 给出了 1951—2010 年持续天数 10 天以上, 综合指数排序最靠前的 33 次区域性极端低温事件. 其中主要时间发生在 12 月份的事件有 7 次, 发生在 1 月份的有 19 次, 发生在 2 月份的有 7 次, 因此 1 月份是区域性低温事件的高发期. 这 33 次低温事件中, 1980 年之后有 11 次, 1980 年之前则有 22 次, 这可能和全球增暖有一定的联系. 结合概率统计方法, 分析区域性极端低温事件与海温和大气环流指数之间的可能联系, 重点揭示各类指标异常情况与发生区域性极端低温事件的对应关系, 尤其是揭示指数极端性与区域性极端低温事件的联系.

在表 1 中, 33 次区域性极端低温事件对应的各指数的不同情况分别用符号 “1”, “0”, “−1” 三种状态来表示. 其中符号 “1” 表示指数有利于低温的出现, 并已达到异常 (超过均值的 0.5 倍标准偏差); 符号 “0” 表示指数是符号一致的正常态 (处于均值与 0.5 倍标准偏差之间), 即有利于低温的出现但并未达到异常; 符号 “−1” 表示指数是符号相反的负异常态, 即不利于低温的出现. 从表 1 可以看出, NPO 指数异常偏小, NINO3.4 异常偏低, 亚洲区极涡强度和面积、AO 指数异常偏小和冬季风指数偏强的异常情况与区域性极端低温事件有较好的对应关系. 如果考虑符号一致的正常态, 概率百分比均超过了 60.0%; 其中 NPO 指数异常偏小、亚洲区极涡面积和冬季风强度达到正异常的概率均达到了 50.0%以上. 此外, 东亚槽位置异常偏深和西风漂流区海温指数异常偏强与区域性极端低温事件有一定的对应关系, 联系符号一致的正常态则对应的百分比都大于 50.0%. 但副高西伸脊点、副高脊线位置异常偏北、东亚槽强度的异常情况与区域性低温事件的对应关系则相对差一些. 同时, 根据不同类型低温事件对应各种指数的 “1” 出现的概率是否超过 50%, 作为该类型的低温事件与相

应指数是否具有较好对应关系的判断标准 (超过则有, 不超过则无), 进而确定与不同类型事件对应关系较好的指数 (表 2). 总体而言, I 型事件与 AO 指数、极涡强度、极涡面积、东亚槽位置和冬季风的对应关系较好; II 型事件与 NINO3.4、NPO、极涡面积、东亚槽位置和西风漂流区海温的对应关系较好; III 型事件与 NPO、副高脊线、极涡强度、极涡面积、AO 指数的对应关系相对较好; IV 型事件则与 NPO、副高脊线、极涡强度、东亚槽强度和西风漂流区海温的对应关系较好; VI 型事件则与 NINO3.4、极涡面积和冬季风的对应关系较好.

表 1 1951—2010 年冬季的区域性极端低温事件主要指标及其与海温、环流指数异常值的联系

类型	开始日期	持续天数	NPO	NINO3.4	西伸脊点	副高脊线	极涡强度	极涡面积	东亚槽强度	东亚槽位置	AO	西风漂流	冬季风
I	1959-1-10	11	−1	−1	1	−1	0	−1	−1	1	1	0	0
I	1960-1-14	16	0	0	1	0	0	−1	−1	0	1	−1	0
I	1961-1-9	12	−1	0	1	1	−1	−1	−1	0	1	−1	1
I	1963-1-3	34	1	1	−1	−1	0	−1	1	1	−1	0	1
I	1966-12-29	22	−1	0	−1	1	−1	−1	−1	−1	0	0	1
I	1968-1-29	14	1	1	−1	−1	1	1	1	−1	1	1	1
I	1968-12-29	11	−1	−1	−1	−1	−1	1	−1	0	1	1	−1
I	1969-1-27	13	−1	−1	−1	−1	−1	1	−1	1	1	1	−1
I	1972-2-2	10	1	0	−1	−1	−1	1	1	1	0	1	−1
I	1976-12-24	16	1	−1	−1	0	1	1	−1	0	1	−1	1
I	1977-1-26	11	−1	−1	−1	1	1	1	−1	−1	1	−1	1
I	1980-1-29	13	−1	−1	1	−1	1	1	−1	−1	0	−1	1
I	1984-1-19	10	1	1	−1	1	1	0	1	1	−1	−1	1
I	1984-1-29	11	1	0	0	1	0	1	−1	1	0	1	1
II	1956-1-18	10	1	1	−1	−1	−1	1	−1	1	1	1	1
II	1957-1-12	13	−1	0	−1	−1	−1	1	1	−1	−1	1	0
II	1966-12-21	10	1	0	−1	0	1	1	−1	0	1	−1	1
II	1967-12-21	15	1	0	−1	−1	1	1	0	1	0	1	0
II	1973-12-22	17	1	1	−1	−1	0	1	0	0	−1	1	0
II	2000-1-24	11	1	1	−1	−1	1	−1	1	1	−1	1	−1
III	1964-1-27	10	0	−1	−1	1	0	0	0	−1	0	−1	0
III	1967-12-4	13	0	0	−1	−1	1	1	0	1	0	1	0
III	2001-1-9	10	1	1	0	1	−1	1	−1	−1	0	−1	−1
III	2009-12-28	12	1	−1	1	0	1	−1	0	1	1	−1	−1
IV	1964-2-16	12	1	−1	−1	1	1	0	−1	−1	0	−1	1
IV	1971-1-21	20	1	1	−1	−1	0	1	1	1	0	1	−1
IV	1993-1-14	13	0	1	0	0	−1	0	1	−1	−1	0	−1
IV	1999-12-20	11	1	1	−1	1	1	−1	1	−1	−1	1	1
V	1954-12-8	10	1	1	1	−1	1	0	1	1	−1	−1	1
V	1975-12-9	26	0	1	0	−1	1	0	0	−1	−1	1	1
V	1984-12-15	17	−1	1	−1	−1	−1	1	−1	−1	−1	−1	0
V	1991-12-26	11	−1	−1	1	0	−1	−1	−1	−1	−1	−1	−1
V	2008-1-22	19	−1	1	−1	1	0	1	−1	−1	−1	−1	1
(正异常态 + 正常态)/ 正异常态			22/17	23/14	11/7	16/10	22/14	24/18	16/10	19/13	21/12	18/14	24/16

注: 其中 1 表示正异常态, 对区域性低温事件正贡献, 0 表示与 1 符号一致的正常态, −1 表示负异常态, 对区域性低温事件负贡献

通过上述分析, NPO 指数为负值, 赤道中东太平洋处于海温异常偏低的 La Nina 状态、AO 指数为负指数, 有利于极涡偏强, 北半球中高纬度高度场在东亚区域以北正南负的形势为主, 相应的乌拉尔山阻高偏强, 东亚槽偏强、中低纬度区域受负距平控制, 这些都利于区域性极端低温事件的发生. 同时, AO 为异常负位相时则容易发生全国范围的 I 类事件. 因此, 区域性低温事件的发生必然是多种因素共同作用的结果, 而 NPO, AO, 赤道中东太平洋海温指数为区域性极端事件的发生提供形势背景. 此外, 就冬季风而言, 冬季风异常偏强, 大多对应发生 I 类和 V 类的区域性低温事件.

表 2 不同类型区域性极端低温事件的主要影响指数

事件类型	NPO	NINO3.4	副高脊线	极涡强度	极涡面积	东亚槽强度	东亚槽位置	AO 指数	西风漂流	冬季风
I				√	√		√	√		√
II	√	√			√		√		√	
III	√		√	√	√			√		
IV	√		√	√		√			√	
V		√			√					√

下面分析 NPO 指数、NINO3.4 指数、AO 指数和冬季风指数这些与极端低温事件对应关系较好的指数达到极端事件标准时, 是否对应有区域性极端低温事件, 进而从海温和环流极端性的角度理解区域性极端事件. 表 3 给出了四种指数的冬季平均值达到 15%(或 85%) 极端阈值情况下与持续时间长、影响范围广的区域性极端低温事件 (表 1 中的事件) 的对应关系. NPO 指数达阈值的 10 年中, 8 年对应发生区域性极端低温事件, NINO3.4 则 9 年对应 7 年发生, AO 则 10 年对应有 6 年发生, 冬季风则 8 年对应有 5 年发生, 达极端阈值年发生区域性极端低温事件的百分率分别为 80.0%, 77.8%, 60.0%和 62.5%, 基本都超出了 60.0%. 由此可知, 区域性低温事件本身可能是多种因素共同作用的结果, 其中包括: 1) 单因子极端异常, 并起主导作用而形成区域性低温极端事件; 2) 单一因子未出现极端异常, 但多种因子异常, 多因子的共同作用也会导致极端事件发生. 此外, 由于 NPO, NINO3.4, AO 和冬季风达到极端阈值的年份, 发生重大区域性极端低温事件的概率在 60.0%以上, 即有可能从主要影响因子极端性的角度对常规要素的极端事件进行描述.

表 3 冬季 NPO 指数、NINO3.4、AO 指数和冬季风指数达到 15%的极端阈值与区域性极端低温事件的对应关系

NPO			NINO3.4			AO			冬季风		
达阈值年份	指数值	对应事件	达阈值年份	指数值	对应事件	达阈值年份	指数值	对应事件	达阈值年份	指数值	对应事件
1955	−1.00	√	1955	25.52	√	1959	−1.58	√	1952	2.03	
1956	−1.09	√	1970	24.97	√	1962	−1.91	√	1954	1.61	√
1961	−1.12		1973	24.79	√	1965	−1.50		1956	1.02	√
1962	−1.26	√	1975	25.03	√	1968	−2.29	√	1962	1.40	√
1967	−0.88	√	1984	25.37	√	1969	−1.86		1976	1.23	√
1970	−0.89	√	1988	24.73		1976	−2.62	√	1980	1.34	
1973	−0.80	√	1998	25.03		1978	−1.30		1983	1.29	√
1980	−1.10		1999	24.91	√	1985	−1.81		1995	1.36	
1983	−0.68	√	2007	24.84	√	2000	−1.31	√	—		
1999	−0.83	√	—			2009	−3.42	√	—		

注: 画勾则表示这一年出现了区域性极端低温事件

4 讨论与结论

本文利用 OITRELTE 对我国 1951—2010 年当年 11 月份至次年 3 月份的逐日最低温度资料进行了检测, 在一定的标准下, 共检测得到了 559 次区域性极端低温事件. 首先研究了这些 RELTE 几何中心的空间分布情况, 继而选取此类综合影响较大的异常事件 60 次, 按照事件发生所覆盖的地理位置的不同进行类型的划分. 结合个例, 具体分析了典型 RELTE 发生期间的海温场、风场和高度场的异常特征, 得到一些可能对 RELTE 有影响的气候因子. 在此基础上, 通过统计不同类型 RELTE 与各气候指数异常的对应关系, 进一步研究各类 RELTE 与主要影响因子异常的可能联系, 并分析了四种对应关系较强的指数达到极端异常标准的年份中, RELTE 的发生概率情况. 主要的研究结论如下.

1) 559 次区域性极端低温事件几何中心的空间分布特征显示: 事件几何中心存在两个显著的事件带, 分别是东北 - 华北 - 黄淮的事件带、新疆北部 - 西北中部 - 西北东部的事件带. 此外, 青藏高原东部和西南南部低温事件中心出现的次数也相对密集. 对 599 次事件中综合指数最大的 60 次事件的影响范围进行分析归类, 按其地理位置的不同大致分为了 6 类: 分别是全国型、东部型、东北 - 华北型、华北 - 华南型、北方型、西北 - 华南型. 通过不同类型事件的 500 hPa 高度场及 850 hPa 距平风场的合成, 简要分析了不同区域类型的低温事件形成的主要环流异常特征.

2) 以 1971 年 1 月 21 日开始的华北 - 华南型区域性低温极端事件为例, 给出了对应的海温场、风场和高度场等方面的异常特征. 事件发生期间, 赤道中东太平洋海温异常偏低, 是中等偏强的 La Nina 特征. 中高纬度地区高度场异常偏强, 低纬度地区异常偏弱, 呈现北高南低的偶极子形势, 有利于冷空活跃, 并南下影响我国. 同时, 来自青藏高原北部偏强的西北风距平和我国华北及以南地区强大的东北风距平在西南大部、江南、华南等大范围区域的交汇, 直接为华北 - 华南地区出现区域性极端低温事件提供了冷空气条件.

3) 统计了持续时间 10 天以上、综合指数最靠前的 33 次不同区域类型的事件与海温和大气环流等各类指数异常之间的对应关系. 总结了各种类型事件的主要影响指数. 总体而言: NPO 指数异常偏小, NINO3.4 指数异常偏低, 亚洲区极涡强度和面积、AO 指数异常偏小和冬季风指数偏强的异常情况与 RELTE 有较好的对应关系. 如果考虑符号一致的正常态, 对应概率百分比均超过了 60.0%.

4) NPO 指数, NINO3.4 指数, AO 指数和冬季风四种指数的冬季平均值达到 15% (或 85%) 极端阈值的年份中, 发生重大区域性极端低温事件的百分率均超过 60.0%. 因此可以进一步确认这些指数是 RELTE 的主要影响因子, 尤其可以从这些因子极端异常的角度, 为 RELTE 的预测研究等提供一定的参考.

[1] Zhao Z C, Wang S W, Xu Y, Ren G Y, Luo Y, Gao X J 2005 *Climat. Environ. Res.* **10** 808 (in Chinese) [赵宗慈, 王绍武, 徐影, 任国玉, 罗勇, 高学杰 2005 气候与环境研究 **10** 808]

[2] Tang G L, Ding Y H, Wang S W, Ren G Y, Liu H B, Zhang L 2009 *Adv. Climate Change Res.* **5** 1673 (in Chinese) [唐国利, 丁一汇, 王绍武, 任国玉, 刘洪滨, 张莉 2009 气候变化研究进展 **5** 1673]

[3] Ren G Y, Guo J, Xu M Z, Chu Z Y, Zhang L, Zou X K, Li Q X, Liu X N 2005 *Acta Meteorol. Sin.* **63** 942 (in Chinese) [任国玉, 郭军, 徐铭志, 初子莹, 张莉, 邹旭凯, 李庆祥, 刘小宁 2005 气象学报 **63** 942]

[4] Ding Y H, Wang Z Y, Song Y F, Zhang J 2008 *Acta Meteorol. Sin.* **66** 808 (in Chinese) [丁一汇, 王遵娅, 宋亚芳, 张锦 2008 气象学报 **66** 808]

[5] Wang D H, Liu C J, Liu Y, Wei F Y, Zhao N, Jiang Z N, Li Y, Chen J Y, Wang Y F, Shi X H, Xu X D 2008 *Acta Meteorol. Sin.* **66** 405 (in Chinese) [王东海, 柳崇健, 刘英, 魏凤英, 赵南, 姜智娜, 李英, 陈菊英, 王亚非, 施晓晖, 徐祥德 2008 气象学报 **66** 405]

[6] Shen B Z, Liu S, Lian Y, Feng G L, Li S F, Gong Z Q 2011*Acta Meteorol. Sin.* **69** 320 (in Chinese) [沈柏竹, 刘实, 廉毅, 封国林, 李尚锋, 龚志强 2011 气象学报 **69** 320]

[7] Wang X J, Shen B Z, Gong Z Q, Feng G 2013 *Acta Meteorol. Sin.* (in Chinese) [王晓娟, 沈柏竹, 龚志强, 封国林 2013 气象学报] (in press)

[8] Feng G L, Hou W, Zhi R, Gong Z Q 2011 *Research on Detecting, Diagnosing and Predictability of Extreme Climate Events* (Beijing: Science Press) p5 (in Chinese) [封国林, 侯威, 支蓉, 龚志强 2011 极端气候事件的检测、诊断和可预测性研究 (北京: 科学出版社) 第 5 页]

[9] Gong Z Q, Wang X J, Feng G L 2009 *Acta Phys. Sin.* **58** 4342 (in Chinese) [龚志强, 王晓娟, 封国林 2009 物理学报 **58** 4342]

[10] Feng G L, Gong Z Q, Zhi R 2008 *Acta Meteorol. Sin.* **66** 892 (in Chinese) [封国林, 龚志强, 支蓉 2008 气象学报 **66** 892]

[11] Gong Z Q, Zou M W, Gao X Q, Dong W J 2005 *Acta Phys. Sin.* **54** 3947 (in Chinese) [龚志强, 邹明玮, 高新全, 董文杰 2005 物理学报 **54** 3947]

[12] Gong Z Q, Zhi R, Feng G L, Zhang Q 2011 *Acta Meteorol. Sin.* **25** 142

[13] Hou W, Zhang D Q, Qian Z H, Feng G L 2011 *Acta Phys. Sin.* **60** 109203 (in Chinese) [侯威, 章大全, 钱忠华, 封国林 2011 物理学报

60 109203]

[14] Peng J B, Bueh C 2011 *Atmosph. Ocean. Sci. Lett.* **4** 281

[15] Zhang Z J, Qian W H 2011 *Adv. Atmosph. Sci.* **28** 338

[16] Ren F M, Cui D L, Gong Z Q 2012 *J. Climate* **25** 7015

[17] Gong Z Q, Wang X J, Cui D L, Wang Y J, Ren F M, Feng G L, Zhang Q, Zou X K, Wang X L 2012 *J. Appl. Meteorol.* **23** 195 (in Chinese) [龚志强, 王晓娟, 崔冬林, 王艳姣, 任福民, 封国林, 张强, 邹旭凯, 王小玲 2012 应用气象学报 **23** 195]

[18] Wang X J, Gong Z Q, Ren F M, Feng G L 2012 *Adv. Climate Change Res.* **8** 8 (in Chinese) [王晓娟, 龚志强, 任福民, 封国林 2012 气候变化研究进展 **8** 8]

[19] Zhang Z J, Qian W H 2012 *Chin. J. Atmosph. Sci.* **36** 1269 (in Chinese) [张宗婕, 钱维宏 2012 大气科学 **36** 1269]

[20] Gong Z Q, Wang X J, Feng G L, Ren F M 2013 *Chin. J. Atmosph. Sci.* **37** (in Chinese) [龚志强, 王晓娟, 封国林, 任福民 2013 大气科学 **37**] (in press)

[21] Dai X G, Fu Z B, Wang P 2005 *Chin. Phys.* **14** 850

[22] Shi N 2005 *Chin. Phys.* **14** 844

[23] Peng J B, Bueh C 2011 *Atmosph. Ocean. Sci. Lett.* **4** 281

[24] Wang Q G, Zhi R, Gong Z Q, Feng G L 2009 *Acta Phys. Sin.* **58** 2853 (in Chinese) [王启光, 支蓉, 龚志强, 封国林 2009 物理学报 **58** 2853]

[25] Gong Z Q, Wang X J, Zhi R, Feng G L 2009 *Acta Phys. Sin.* **58** 4342 (in Chinese) [龚志强, 王晓娟, 支蓉, 封国林 2009 物理学报 **58** 4342]

[26] Kistler R, Kalnay E, Kanamitsu M 2001 *Bull. Amer. Meteor. Soc.* **82** 247

[27] Smith T M, Reynolds R W 2003 *J. Climate* **16** 1495

[28] Liu Z X, Lian Y, Shen B Z, Gao Z T, Tang X L 2003 *J. Appl. Meteorol.* **14** 553 (in Chinese) [刘宗秀, 廉毅, 沈柏竹, 高枞亭, 唐晓玲 2003 应用气象学报 **14** 553]

[29] Lian Y, Shen B Z, Gao Z T 2004 *Acta Meteorol. Sin.* **2** 781 (in Chinese) [廉毅, 沈柏竹, 高枞亭 2004 气象学报 **2** 781]

[30] Shi N, Zhu Q G 1996 *J. Tropic. Meteorol.* **12** 26 (in Chinese) [施能, 朱乾根 1996 热带气象学报 **12** 26]

[31] Mu M Q, Li C Y 1999 *Chin. J. Atmosph. Sci.* **23** 276 (in Chinese) [穆明权, 李崇银 1999 大气科学 **23** 276]

[32] He X C, Li Q P, Ding Y H, He J H 2007 *Acta Meteorol. Sin.* **65** 18 (in Chinese) [何溪澄, 李巧萍, 丁一汇, 何金海 2007 气象学报 **65** 18]

[33] Chen W 2002 *Chin. J. Atmosph. Sci.* **26** 595 (in Chinese) [陈文 2002 大气科学 **26** 595]

[34] Wang X J, Feng A X, Zhi R, Feng G L 2012 *Chin. Phys.* B **21** 029201

[35] Shen B Z, Lin Z D, Lu R Y 2011 *Sci. China*: *Earth Sci.* **54** 1095

[36] He W P, Feng G L, Dong W J, Li J P 2005 *Chin. Phys.* **14** 21

The classification of winter regional extreme low temperature events in China and their corresponding relationship to climatic indices extreme anomaly*

Wang Xiao-Juan[1)2)] Shen Bai-Zhu[1)] Gong Zhi-Qiang[3)†] Feng Guo-Lin[4)]

1) (*Department of Atmospheric and Sciences, Lanzhou University, Lanzhou* 730000*, China*)

2) (*College of Physics and Electronic Project, Changshu Institute of Technology, Changshu* 215500*, China*)

3) (*Laboratory for Climate Monitoring and Diagnose, National Climate Center, China Meteorological Administration, Beijing* 100081*, China*)

4) (*Laboratory for Climate Studies, National Climate Center, China Meteorological Administration, Beijing* 100081*, China*)

(Received 10 April 2013; revised manuscript received 1 July 2013)

Abstract

We identify China regional low temperature extreme events (RELTEs) in winter during the periods from 1951 to 2010 using objective identification technique for regional low temperature extreme events (OITRELTEs). The 559 RELTEs are identified and classified into 6 types, i.e. , nationwide style, east style, northeast-north China style, north-south China style, south style, and northwest-south China style, according to the spatial distribution of these events. The circulation backgrounds of different styles of low temperature events are also analyzed. In addition, taking the classical event that began from January 21st in 1971 for example, anomaly characteristics of sea surface temperature, geopotential height and winds vectors are investigated specifically. Based on these analyses, the corresponding relationships between different types of events and anomalies of climatic indices are further studied, and the relations between mainly influencing index and event are obtained for different types of events. On the whole, when the NINO3.4, the Pacific decadal oscillation, and the Arctic oscillation are small and the winter wind index is strong, the probability with which the RELTE happens is high; in the years in which the winter average values of the four indices reach 15% of extreme threshold, the percentages of occurrence of RELTE reach up to 80.0%, 77.8%, 60.0% and 62.5%, respectively. Therefore, certain signals can be offered for diagnosing and predicting the RELTE from the index anomalies.

Keywords: regional low temperature extreme events, spatial distribution, climatic index, extreme

PACS: 92.60.Wc **DOI:** 10.7498/aps.62.229201

* Project supported by the National Natural Science Foundation of China (Grant No. 41305075), the National Basic Research Program of China (Grant Nos. 2012CB955203, 2012CB955902), and the Special Scientific Research Projects for Public Interest, China (Grant No. GYHY201106016).

† Corresponding author. E-mail: gzq0929@126.com

Atmospheric Research 120–121 (2013) 112–126

Contents lists available at SciVerse ScienceDirect

Atmospheric Research

journal homepage: www.elsevier.com/locate/atmos

Effect of non-spherical dust aerosol on its direct radiative forcing

Zhili Wang [a], Hua Zhang [b,*], Xianwen Jing [a,b], Xiaodong Wei [c]

[a] *Chinese Academy of Meteorological Sciences, Beijing 100081, China*
[b] *Laboratory for Climate Studies, National Climate Center, China Meteorological Administration, Beijing 100081, China*
[c] *Meteorological Center, East China Bureau of Air Control, Shanghai 201702, China*

ARTICLE INFO

Article history:
Received 27 April 2012
Received in revised form 13 August 2012
Accepted 17 August 2012

Keywords:
Dust
Spherical/non-spherical particles
IRF
AF

ABSTRACT

The optical properties of spherical and non-spherical dust aerosols are calculated using the Lorenz–Mie theory and the combination of T-matrix method and an improved geometric optics method. The resulting optical properties are then applied in an interactive system that coupled a general circulation model with an aerosol model to quantitatively analyze the effect of non-spherical dust aerosol on its direct radiative forcing (DRF). Our results show that the maximum difference in dust instantaneous radiative forcing (IRF) between spherical and non-spherical particles is 0.27 W m^{-2} at the top of the atmosphere (TOA) and appears over the Sahara Desert due to enhanced absorption of solar radiation by non-spherical dust. The global annual means of shortwave (longwave) IRFs due to spherical and non-spherical dust aerosols at the TOA for all sky are −0.62 (0.074) W m^{-2} and −0.61 (0.073) W m^{-2}, respectively, and the corresponding values for clear sky are −1.16 (0.092) W m^{-2} and −1.14 (0.093) W m^{-2}, which indicates that the non-spherical effect of dust has almost no effect on their global annual mean IRFs.
However, non-spherical dust displays more evident influences than above on its atmospheric- and land-temperature adjusted radiative forcing (AF) at the TOA over the Saharan Desert, West Asia, and northern China, with an approximate maximum increase of 3.0 and decrease of 0.5 W m^{-2}. The global annual means of shortwave (longwave) AFs due to spherical and non-spherical dust aerosols are −0.55 (0.052) W m^{-2} and −0.48 (0.049) W m^{-2} at the TOA for all sky, respectively, and the corresponding values for clear sky are −1.07 (0.066) W m^{-2} and −0.95 (0.062) W m^{-2}. All AFs of dust become much weaker than their corresponding IRFs. The absolute values of annual mean AF for non-spherical dust are approximately 13% (11.2%) and 6% (6%) less than those of spherical dust for the shortwave and longwave for all sky (clear sky), respectively. The results indicate that the non-spherical effect of dust can reduce their AFs more obviously than do their IRFs.

1. Introduction

Dust aerosols are a major contributor to aerosol loading on a global scale and play a crucial role in the radiative processes of the earth-atmosphere system. An estimated 1–3 billion tons of dust particles are emitted into the atmosphere globally each year, accounting for more than half of the total atmospheric particles (IPCC, 2001, 2007). Dust aerosols originate largely from deserts and semi-desert areas (e.g., the Sahara in Africa and deserts of Central and West Asia). There are also a large number of dust aerosols emitted in the western USA and northwestern China. Anthropogenic dust sources have been increasing since industrialization, largely because of desertification in some areas (Zhang et al., 2008).

Dust aerosols can scatter and absorb solar radiation, as well as absorb and emit longwave radiation, thereby directly disturbing the energy balance of the earth-atmosphere system (Haywood et al., 2003; Wang, 2010; Zhang et al., 2010; El-Metwally et al., 2011). Moreover, dust can change the

* Corresponding author. Tel./fax: +86 10 68400070.
E-mail address: huazhang@cma.gov.cn (H. Zhang).

0169-8095/$ – see front matter © 2012 Elsevier B.V. All rights reserved.
http://dx.doi.org/10.1016/j.atmosres.2012.08.006

optical properties of clouds by acting as cloud or ice condensation nuclei, thus indirectly affecting climate (Carrió et al., 2007; Hendricks et al., 2011; Rosenfeld et al., 2011). Therefore, dust is regarded as an important climate-forcing factor. IPCC (2007) reported that the global annual mean direct radiative forcing (DRF) of dust aerosols due to anthropogenic contributions is -0.3–$+0.1$ W m^{-2}. However, there are still many uncertainties, primarily in terms of emission sources and the optical properties of dust. For example, multiple observation results have shown that the single scattering albedo of dust particles in the Sahara Desert ranged from 0.95 to 0.99 at 550 nm wavelength (Haywood et al., 2003; McFarlane et al., 2009). However, corresponding values for a desert in northwestern China ranged between 0.73 and 0.85, the value much smaller than that for the African Sahara region and with stronger absorptivity (Ge et al., 2010). The single scattering albedo depends on the refractive index, particle shape, particle size distribution, thus varying from region to region (Sokolik and Toon, 1996; Claquin et al., 1999; Yi et al., 2011).

Most studies have assumed spherical dust particles and used the Lorenz-Mie theory to obtain the optical properties of dust particles when calculating the radiative forcing of dust aerosols in either a general circulation model (GCM) or a radiative transfer model. However, investigations using both scanning electron microscopes and field observations have shown that most dust particles have non-spherical shapes (Nakajima, 1989; Gao and Anderson, 2001; Okada et al., 2001). Several studies have also reported that the optical properties of dust vary significantly depending on whether the particles are considered spherical or non-spherical (Yang et al., 2000; Zhao et al., 2003; Barnaba et al., 2004; Kalashnikova and sokolik, 2004). Yang et al. (2007) compared the optical properties of spherical and spheroidal dust particles using the Lorenz-Mie theory and a combination of the T-matrix method and improved geometric optics method (IGOM) and found that the effects of non-spherical shape were large at short wavelengths but essentially negligible at infrared wavelengths. Fu et al. (2009) calculated the single-scattering properties of dust aerosols with both spheroidal and spherical shapes at the 550 nm wavelength and found that the relative errors of the spheres used to approximate the spheroids were <1% for the extinction efficiency and single-scattering albedo, and less than <2% for the asymmetry factor. Wei and Zhang (2011) found that the difference of phase function between non-spherical and spherical dust was significant, especially in the visible region, and the extinction to backscattering ratio in the so-called lidar equation was affected by the shape of dust greatly in shortwave region. Yi et al. (2011) investigated the non-spherical effect of dust particles on DRF through prescribing the solar zenith and azimuthal angles to be 45° and 0°, respectively, and the dust AOD and surface albedo to be 0.5 and 0.1, respectively, and assuming the shape of dust to be tri-axial ellipsoidal, using a 32-stream DISORT-based radiative transfer model. They found that the non-spherical effect was an important source of dust DRF uncertainties, which were particularly large over water surfaces and capable of causing a 30% difference in dust forcing calculated at the TOA. Satellite observations have also shown that the scattering properties of aerosols assumed to be spheres differ greatly from those of actual dust particles. Thus, it is important to consider the non-spherical effect when estimating the optical depth and micro-physical properties of dust aerosols (Wang et al., 2003; Herman et al., 2005; Dubovik et al., 2006).

Several recent studies have examined the different optical properties of dust particles arising from their spherical and non-spherical shapes (e.g., Yang et al., 2007; Fu et al., 2009; Wei and Zhang, 2011; Yi et al., 2011). However, none of these studies quantified the effect of non-spherical dust on global DRF. In this study, we calculated the optical properties of spherical and non-spherical dust particles using the Lorenz-Mie theory and a combination of the T-matrix method and IGOM. The resulting optical properties were then applied in an interactive system coupling GCM and an aerosol model to analyze the effects of non-sphericity on dust instantaneous radiative forcing (IRF) and adjusted radiative forcing (AF). The IRF is defined as the change in net irradiance at the TOA with surface and atmospheric temperatures and state held fixed at the unperturbed values. The AF is defined as the change in net irradiance at the TOA after allowing for atmospheric and land temperatures, water vapor, clouds and land albedo to adjust, but with sea surface temperatures (SSTs) and sea ice cover unchanged (Hansen et al., 2005). In the following section, we introduce basic model information, the methods for calculating the optical properties of spherical and non-spherical dust particles, and our experimental design. We then present results from our comparisons of the various optical properties of dust particles calculated by the two methods and analyze the differences between simulated optical properties, IRF, and AF for spherical and non-spherical dust aerosols.

2. Model description and methods

2.1. Basic model information

An interactive system for coupling a GCM (BCC_AGCM2.0.1) with the Canadian Aerosol Module (CAM) is developed by Zhang et al. (2012a) and used here to study the non-spherical effect of dust. The BCC_AGCM2.0.1 is developed by the National Climate Center of the China Meteorological Administration (NCC/CMA) based on the Community Atmosphere Model Version 3 (CAM3) developed by the US National Center for Atmospheric Research. The model uses horizontal triangular truncation at wavenumber 42 (T42, approximating 2.8°×2.8°) and vertical hybrid σ-pressure coordinates to include 26 vertical layers with the top layer having a pressure of 2.9 hPa. Some improvements in dynamics, convection scheme, dry adiabatic adjustment, turbulent fluxes over the ocean, and snow cover fraction parameterization have been implemented in BCC_AGCM2.0.1 in comparison to CAM3, allowing for better performance in climate simulations (Wu et al., 2010). The CAM, a size-segregated multi-component aerosol algorithm, is developed by Gong et al. (2002, 2003a). The algorithm includes processes for the emission, transport, chemical transformation, cloud interaction, and deposition of atmospheric aerosols. Five aerosol species were included: sulfate, black carbon (BC), organic carbon (OC), soil dust, and sea salt. The emissions of sulfate, BC and OC are derived from AeroCom data (Dentener et al., 2006). The emissions of soil dust and sea salt are calculated online using the scheme developed by Marticorena and Bergametti (1995) and Gong et al. (2002), respectively. In this model, the aerosol size is divided into 12 bins with radii between 0.005–0.01, 0.01–0.02, 0.02–0.04, 0.04–0.08, 0.08–

0.16, 0.16–0.32, 0.32–0.64, 0.64–1.28, 1.28–2.56, 2.56–5.12, 5.12–10.24, and 10.24–20.48 μm. Three lognormal population distributions for dust in China are used, and the mass median diameters and standard deviations of these three populations are determined by considering the soil features in China and source region dust size-distribution measurements (Gong et al., 2003b; Zhang et al., 2003b). Out of China, the two-mode size distribution for dust from the observation by Chatenet et al. (1996) is used (Marticorena and Bergametti, 1995). Finally, the dust emissions are distributed into each size bin by using the above-mentioned size distributions. The refractive indices of aerosols are adopted from D'Almeida et al. (1991). BCC_AGCM2.0.1 and CAM have achieved complete online coupling and can simulate the mass concentration, optical properties, and DRF of typical aerosols with a high level of accuracy (Zhang et al., 2012a). Detailed information on the simulation performance of this interactive system has been provided by Zhang et al. (2012a).

In this study, the cloud overlap processing developed by Collins (2001) for the above-mentioned version is replaced with a new method developed by Jing and Zhang (2012) that simulates cloud overlap using a Monte Carlo independent column approximation (McICA). We also replace the primary radiative parameterization from Briegleb (1992) with the correlated k-distribution radiation scheme developed by Zhang et al. (2003a, 2006a, 2006b). These two modifications allow for improved representations of gas absorption and of the structure and radiative transfer of subgrid-scale clouds. Under the new radiation scheme, wavelengths are classified into 17 bands (eight for longwave radiation and nine for shortwave radiation) which are 10–250, 250–550, 550–780, 780–990, 990–1200, 1200–1430, 1430–2110, 2110–2680, 2680–5200, 5200–12,000, 12,000–22,000, 22,000–31,000, 31,000–33,000, 33,000–35,000, 35,000–37,000, 37,000–43,000, and 43,000–49,000 cm^{-1}, respectively, and the absorption of five main greenhouse gases: H_2O, CO_2, O_3, N_2O, CH_4, and CFC (CFC11, CFC12, CCL4 and CFC22), and O_2 continuum absorption are included. The new scheme also allow for the simulation of the scattering and absorbing processes of clouds and aerosols. The optical properties of aerosols are calculated by Wei and Zhang (2011) and Zhang et al. (2012b). The optical properties of water clouds are taken from Nakajima et al. (2000). The optical properties of ice clouds are obtained by incorporating data on ice cloud particle shapes and spectral distribution by Fu (1996), phase function data by Yang et al. (2005), and the hybrid method of different shapes of ice cloud particles by Baum et al. (2005).

2.2. Methods and experimental design

The optical properties of non-spherical dust aerosols including the extinction coefficient, single scattering albedo, and asymmetry factor are calculated by combining the T-matrix method and an IGOM, where the shape of non-spherical dust particles is approximated using a rotational symmetric spheroid (Wei and Zhang, 2011). The T-matrix code developed by Mishchenko and Travis (1994) is used to compute the single scattering properties of spheroidal particles with size parameters (specified in terms of the radius of volume-equivalent sphere) less than 50. For randomly oriented particles, the optical properties are determined by the size, shape and composition of particles in the T-matrix method without considering the orientation of particles. For particles much larger than the wavelength of light, the IGOM is adopted to calculate the single scattering properties of particles, which is developed by Yang and Liou (1996) based on the principles of geometric optics, and the ray-tracing technique has been used in the method (Please see Yang et al. (2007) for detail calculation). It is shown that the optical properties of dust calculated by the spheroidal approximations are similar to those of actual dust (Mishchenko and Travis, 1994; Gobbi et al., 2002). Moreover, the size distributions of dust particles are provided by the online BCC_AGCM2.0.1_CAM. The optical properties of corresponding spherical dust particles are calculated using Wiscombe's (1980) algorithm based on Lorenz-Mie theory.

Two groups of experiments are designed for this work, each of which includes two experiments. In the first group of experiments (EXPIRF), the two simulations calculate the IRFs of dust aerosols using the optical properties of spherical (EXPIRF_sphere) and non-spherical (EXPIRF_nonsphere) dust particles, respectively. This method calls on the radiation scheme twice at each radiative time step in each simulation. The effect of dust on radiation is taken into account only in the first call, in which the simulated radiative fields are used to diagnose the dust radiative forcing rather than feedback into the GCM climate. Thus, the difference between the two simulated forcings only results from the difference between two kinds of optical properties of dust particles. In the second group of experiments (EXPAF), the two simulations calculate the AF of spherical (EXPAF_sphere) and non-spherical (EXPAF_nonsphere) dust aerosols, respectively. The method also calls on the radiation scheme twice, but the radiative effect of dust is only considered in the second call. The radiative fields are fed back into the atmospheric fields, and the model evolution is modified by the radiative effect of dust, whereas SST is fixed (Hansen et al., 2005). Therefore, the difference between the two simulated forcings results from not only the two kinds of dust optical properties, but also changed temperature profiles after responding to the radiative feedback of spherical and non-spherical dust. The AF has been shown to provide a better estimate than IRF of the eventual temperature change (Hansen et al., 2005).

3. Results

3.1. Comparison between the optical properties of spherical and non-spherical dust particles

Fig. 1 shows the relative differences of the extinction efficiency factor, single scattering albedo, and asymmetry factor between non-spherical and spherical dust particles calculated by the Lorenz-Mie theory and the combination of T-matrix method with IGOM. The effect of non-spherical dust particles on extinction efficiency exists across nearly the entire wavelength spectrum. There are obvious differences in extinction of nuclei mode dust from the two shapes. The fluctuations of extinction efficiency factor with the increase of size parameter ($2\pi r/\lambda$) for small spherical and non-spherical dust particles are larger than those for larger particles, so the non-spherical effect on the extinction efficiency factor of small particles is more obvious than that of larger particles. However,

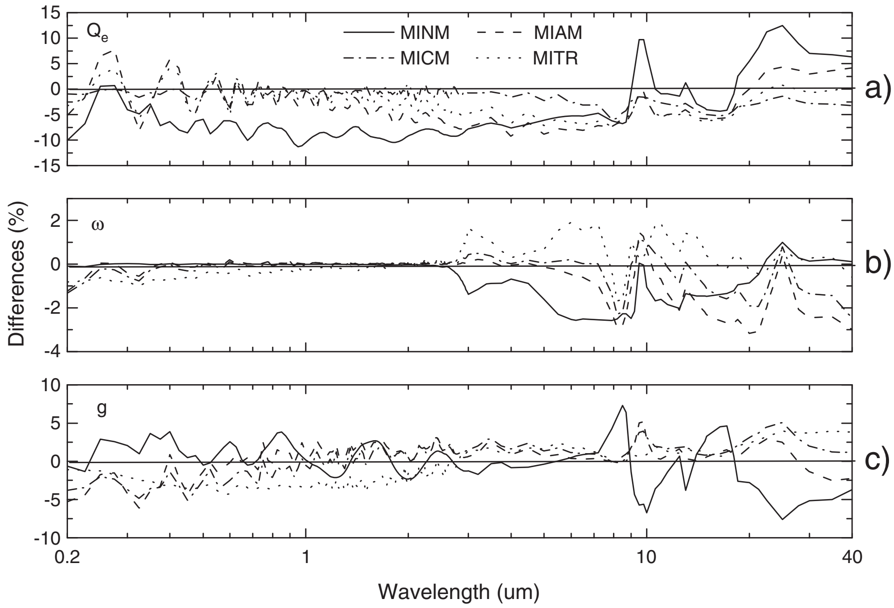

Fig. 1. The relative differences of (a) extinction efficiency factor, (b) single scattering albedo and (c) asymmetry factor between non-spherical and spherical dust particles. MINM, MIAM, MICM and MITR represent the nuclei mode, accumulation mode, coarse mode and transported mode, respectively. The mode radii and standard deviations for the four modes are (0.07 μm, 1.95), (0.39 μm, 2.0), (1.90 μm, 2.15) and (0.50 μm, 2.2), respectively.

the mass concentration of nuclei mode dust is small, so the effect on radiation flux caused by different particle shapes is also small. For accumulation mode and transported mode dust, the relative deviation of extinction efficiency factors is within $\pm 10\%$ between the non-spherical and spherical dust. The difference between non-spherical and spherical dust extinctions for the coarse mode is smaller, with a relative deviation of less than $\pm 5\%$ (Fig. 1a). The relative deviations of single scattering albedo due to non-spherical and spherical dust are within $\pm 4\%$ for the four modes across all wavebands, with a primarily focus on wavebands larger than 3 μm. The relative difference between the two particle shapes is within $\pm 2\%$ in the shortwave band where scattering plays a major role (Fig. 1b). The relative deviation of asymmetry factors between non-spherical and spherical dust particles is within $\pm 8\%$, concentrating in the wavebands smaller than 2 μm and between approximately 10 and 40 μm (Fig. 1c).

In Fig. 2, the band-mean relative differences in optical properties between non-spherical and spherical dust particles are shown for the 17-band radiation scheme used in BCC_AGCM2.0.1. Generally, differences in the extinction coefficient, single scattering albedo, and asymmetry factor are less than 15%. As can be seen from Fig. 2, the non-spherical effect of dust primarily affects the dust extinction and asymmetry factor, and only has small impact on the single scattering albedo except the medium sized dust particles in the 13–17 wavebands (Fig. 2b and c). The differences of dust extinction mainly concentrate in the 1–5 and 11–17 wavebands, with the highest value exceeding 10%. The differences of dust asymmetry factor are located in the 3–9 and 13–15 wavebands, but the asymmetry factor of large dust particles is affected less due to dust non-spherical effect (Fig. 2d).

3.2. Difference in IRF between non-spherical and spherical dust aerosols

The IRFs of dust aerosols are calculated in EXPIRF, and the difference between the two simulated dust radiative forcings is due only to the differing optical properties of spherical and non-spherical dust. Fig. 3 shows the global distribution of annual mean column burden for dust aerosol simulated in EXPIRF. The dust column burdens are found to be located mainly in the North African Sahara region and in West Asia, with maximum values exceeding 1000 mg m^{-2}, due to year-round dry air and little vegetation that increase dust emissions in these areas. The second highest values of more than 100 mg m^{-2} are located in Inner Mongolia and the Xinjiang region of China. There is also an extended distribution of dust aerosol in central and western areas of North America. The simulated global annual mean dust column burden is 57.8 mg m^{-2}. Table 1 compares the global load, lifetime, and optical depth of dust simulated in this study with a number of reference models. We note that the dust load and optical depth in our model is comparative with those in most of other models, but the simulated dust lifetime is shorter than others. This is because that the range of dust size in our model is larger (from 0.005 to 20.48 μm) than those in other models and the larger particles tend to have shorter lifetimes.

Fig. 4 shows the global annual mean distributions of simulated dust optical depth from EXPIRF_sphere and the difference between dust optical depths from EXPIRF_nonsphere versus EXPIRF_sphere at 550 nm. The simulated optical depth of non-spherical dust aerosols is greater than that of spherical dust aerosols at 550 nm, due to an increase in the extinction coefficient of dust in both the coarse and transported modes,

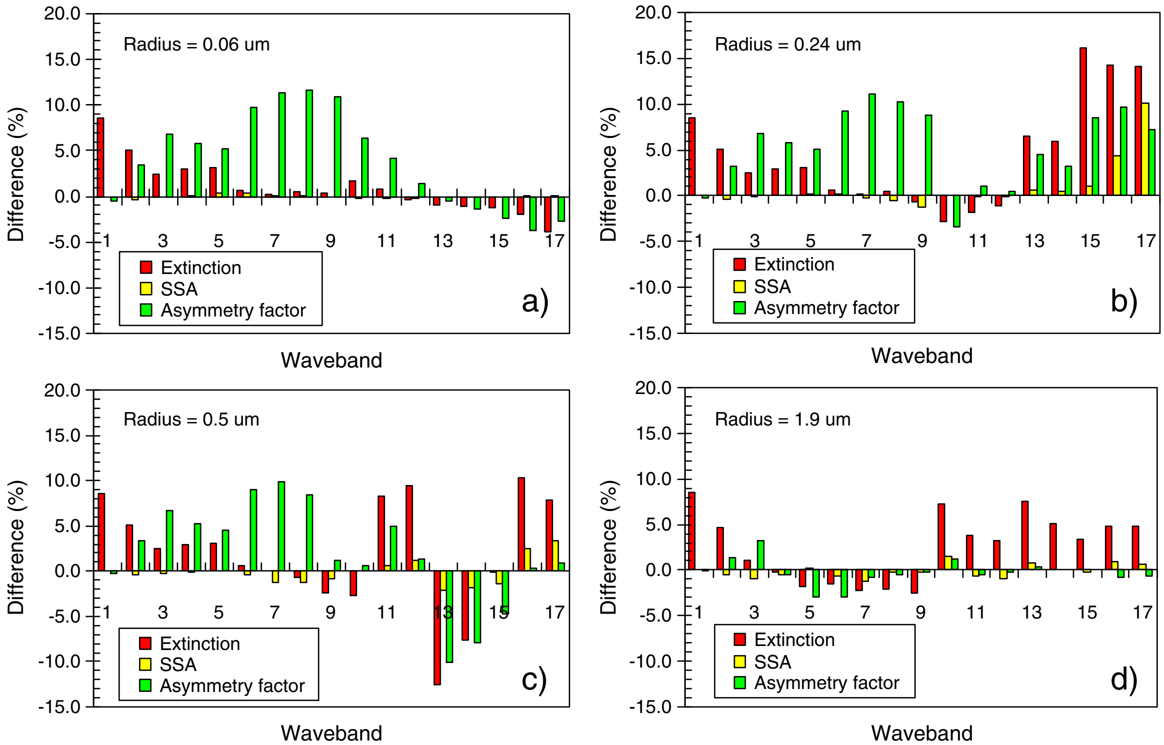

Fig. 2. The band-mean relative differences of extinction coefficient, single scattering albedo (SSA) and asymmetry factor between non-spherical and spherical dust for 17-band radiation scheme when particle radius equals to 0.06, 0.24, 0.5 and 1.9 μm.

the principal modes for dust modeling. The dust optical depths are increased by over 2% in most regions. The greatest increase, nearly 4%, appears over the Sahara Desert near 15°N as a result of a high loading of coarse dust in the atmosphere. The dust optical depth also increases by about 3% over northern China. The relative differences in the simulated aerosol single scattering albedo and asymmetry factor between EXPIRF_sphere and EXPIRF_nonsphere at 550 nm are not obvious, approximately less than 1% (Figures not shown).

Dust aerosols not only absorb and scatter solar radiation but also absorb and emit infrared radiation, leading to both positive and negative radiative forcings simultaneously at the TOA under different atmospheric conditions. As can be seen from the simulated global distribution of annual mean shortwave

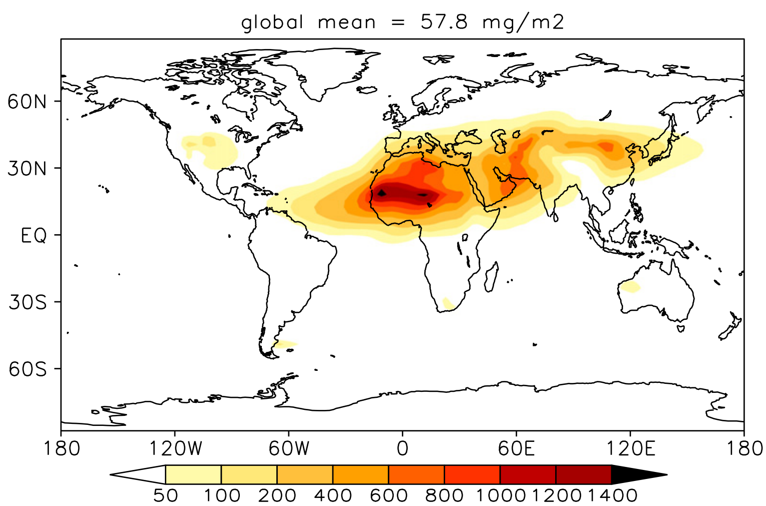

Fig. 3. The global annual mean distribution of simulated dust column burden in EXPIRF (unit: mg m^{-2}).

Table 1
Summary of the global load, lifetime and optical depth at 550 nm (OD550) of dust.

Model	Load (Tg)	Lifetime (days)	OD550 dust	References
CAM	25.7	4.6	0.035	Huneeus et al. (2011)
ECMWF	54.7	3.3	0.027	
GISS	29.0	7.1	0.034	
SPRINTARS	17.2	1.6	0.024	
MOZGN	21.1	3.3	0.022	
ECHAM5-HAM	8.2	4.4	0.01	
MIRAGE	22.0	3.9	0.053	
This study				
EXPIRF_sphere	29.5	1.5	0.038	
EXPIRF_nonsphere	–	–	0.039	
EXPAF_sphere	25.8	1.5	0.033	
EXPAF_nonsphere	23.4	2.8	0.031	

IRF at the TOA for all sky from EXPIRF_sphere (Fig. 5a), the largest forcing occurs over West Asia, north China, and especially over northern and western Africa. In these regions, maximum forcing exceeds -12 W m^{-2} due to the multiple scattering of solar radiation caused by the considerable dust loading above the abundant large-scale stratus clouds (Schumacher and Houze, 2006). Dust aerosols produce an apparent positive forcing over the Tibetan Plateau with the maximum exceeding $+5$ W m^{-2} owing to a high surface albedo there.

Surface albedo is a key factor to control dust radiative forcing. Fig. 6 shows the comparisons of simulated annual mean surface albedo with the MODIS data. As can be seen from the Fig. 6, the distribution of simulated surface albedo is basically consistent with the observation in most of regions. However, the simulated values are slightly lower in northern Africa and larger in the snow cover regions of boreal high latitudes than those observed. Especially, the simulated surface albedo is obviously larger than the observed in the Tibetan Plateau due to the simulated more snow cover and depth and the differences of snow properties in model (grain size especially), which possibly results in the larger positive forcing over these areas.

The forcing becomes weaker when non-spherical particles are used, because they are effectively more absorbing (Figs. 1b and 5c). Compared to the spherical dust IRF, the IRF by non-spherical dust is weakened by 1–4%. Regions of larger weakening appear in areas with larger dust radiative forcing. For example, the forcing is weakened by up to 0.27 W m^{-2} over the Sahara Desert and by 0.12~0.18 W m^{-2} over West Asia and the Tibetan Plateau. The effect of non-spherical dust on longwave IRF also represents an increase in longwave radiation absorption; however, this increase is small, having a relative difference of about 1% (Fig. 5b and d). The global annual means of simulated dust shortwave (longwave) IRFs at the TOA for all sky in EXPIRF_sphere and EXPIRF_nonsphere are -0.62 (0.073) W m^{-2} and -0.61 (0.074) W m^{-2}, respectively. Non-spherical dust shape has little influence on IRF (Table 2) because the differences between non-spherical and spherical dust optical properties are relatively small, especially in the solar wavebands, in the coarse (primary dust) mode. Furthermore non-spherical effects can cancel each other for some bands and particle sizes (Fig. 2). It can be noted that the dust has a weak longwave radiative forcing in our results. We find that the mass median diameter of dust particles used in our model given by Marticorena and Bergametti (1995) is smaller than those in other models, which may be the primary reason that leads to the weak longwave effects.

In order to get rid of cloud effect in above comparison of spherical and non-spherical dust, Fig. 7 shows the global distributions of simulated dust shortwave and longwave IRF at the TOA for clear sky in EXPIRF_sphere and the differences of forcing in EXPIRF_nonsphere versus EXPIRF_sphere. The strength and range of dust absolute shortwave IRF and longwave IRF for clear sky are larger than those for all sky because of reduction effects of clouds to dust IRF (Zhang et al., 2010), and the absolute changes of IRF due to non-spherical

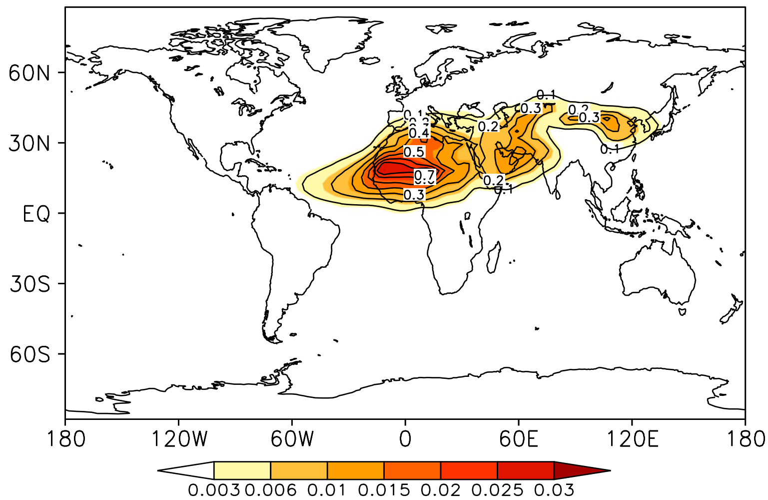

Fig. 4. The global annual mean distributions of simulated dust optical depth in EXPIRF_sphere (contour line) and the difference in dust optical depths in EXPIRF_nonsphere versus EXPIRF_sphere (shaded) at 550 nm.

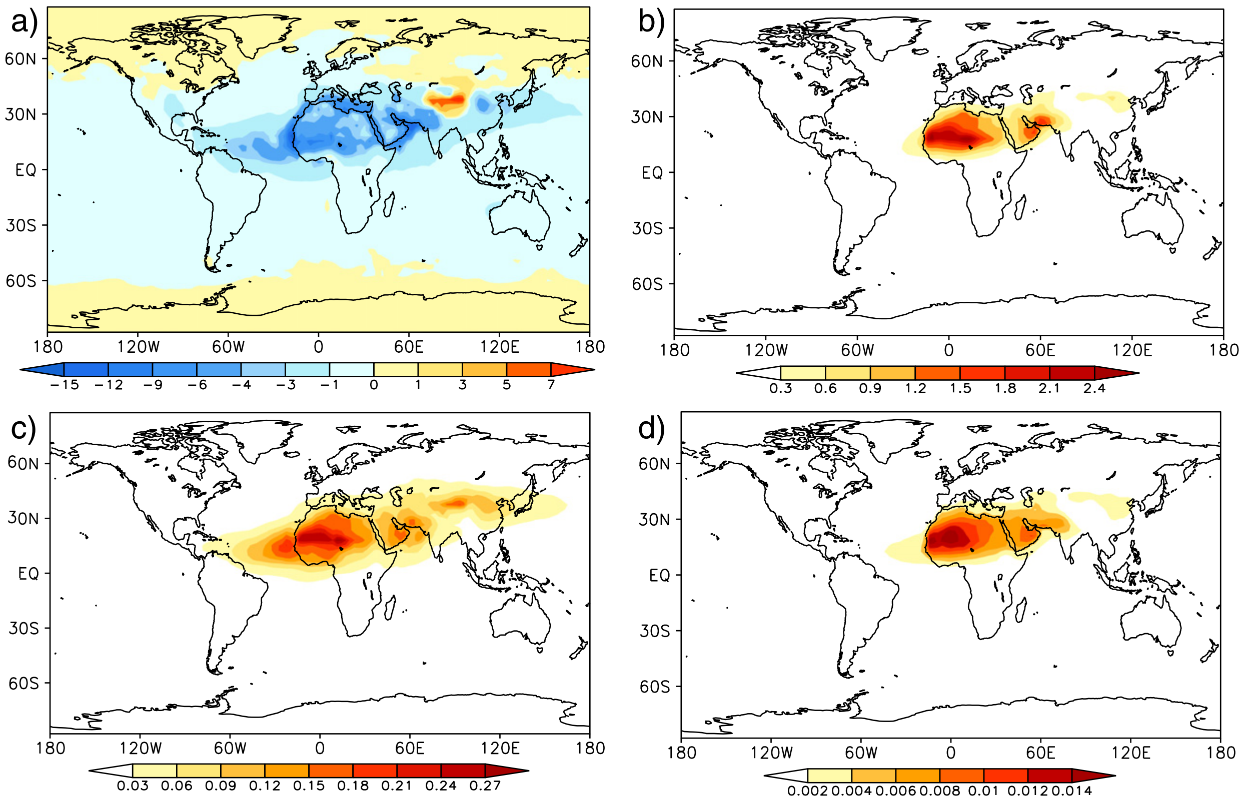

Fig. 5. The global annual mean distributions of simulated dust (a) shortwave and (b) longwave IRF at the TOA in EXPIRF_sphere and the differences in dust (c) shortwave and (d) longwave IRF in EXPIRF_nonsphere versus EXPIRF_sphere for all sky (units: W m^{-2}).

effect of dust for clear sky are more extensive and stronger than those for all sky. The global annual means of simulated dust shortwave (longwave) IRFs at the TOA for clear sky in EXPIRF_sphere and EXPIRF_nonsphere also become larger with values of −1.16 (0.092) W m^{-2} and −1.14 (0.093) W m^{-2}, respectively (Table 2), each of which is stronger than the corresponding value for all sky, while non-spherical effect of dust on their IRFs is also very small with relative difference of 1.7% and 1.1% reduction for shortwave and longwave, respectively, almost similarly to those of all sky case.

3.3. Difference in AF between non-spherical and spherical dust aerosols

The AFs of spherical and non-spherical dust aerosols are simulated in EXPAF. The simulated dust burdens change due to the adjustment of atmospheric and land temperatures to reflect the different radiative effects of non-spherical and spherical dust. Fig. 8 gives the global distributions of the annual mean column burden of simulated dust aerosols in EXPAF_sphere and EXPAF_nonsphere, respectively. The simulated distributions of dust aerosol column burden in EXPAF_sphere and EXPAF_nonsphere are very similar, but the magnitudes of the annual mean column burden of dust in the two simulations are different: 50.6 mg m^{-2} and 45.8 mg m^{-2} for EXPAF_sphere and EXPAF_nonsphere, respectively. The simulated column burdens of dust aerosols decrease in West Asia, south of African Sahara Desert and near its western ocean, with maximum value over 200 mg m^{-2}, but the column burdens increase in north of African Sahara Desert, middle North America and northern China, with maximum value exceeding 150 mg m^{-2}, in EXPAF_nonsphere compared with EXPAF_sphere (Fig. 8c). This is mainly due to the difference in optical and radiative properties between the two shapes of dust aerosols. The adjustment of atmospheric and land temperatures effectively results in differences in the atmospheric heating rate, thereby altering the dust aerosol emission, deposition, and load. It can be seen from the simulated global annual averaged budget of dust that the dust emission is reduced obviously in EXPAF_nonsphere which contributes most to be the change in burden. Fig. 9 indicates that the changes of solar and longwave heating rate due to the non-spherical effect of dust may cause the atmosphere to be more and less stable in the south and north of 25°N, respectively, which suppress and facilitate the dust transport and deposition in corresponding regions, thereby resulting in the changes of dust burden (Fig. 8).

A change in simulated dust column burden caused by the optical properties of spherical and non-spherical dust particles will inevitably alter the dust optical depth, which is consistent with changes seen in dust column burden (Figs. 10 and 8c). The simulated optical depth of non-spherical dust aerosols at 550 nm over the north of the Sahara Desert and northern China is 5–20% higher than that of spherical dust aerosols. The dust optical depth in the south Sahara Desert and West Asia also decreases distinctly more for spherical aerosols than for

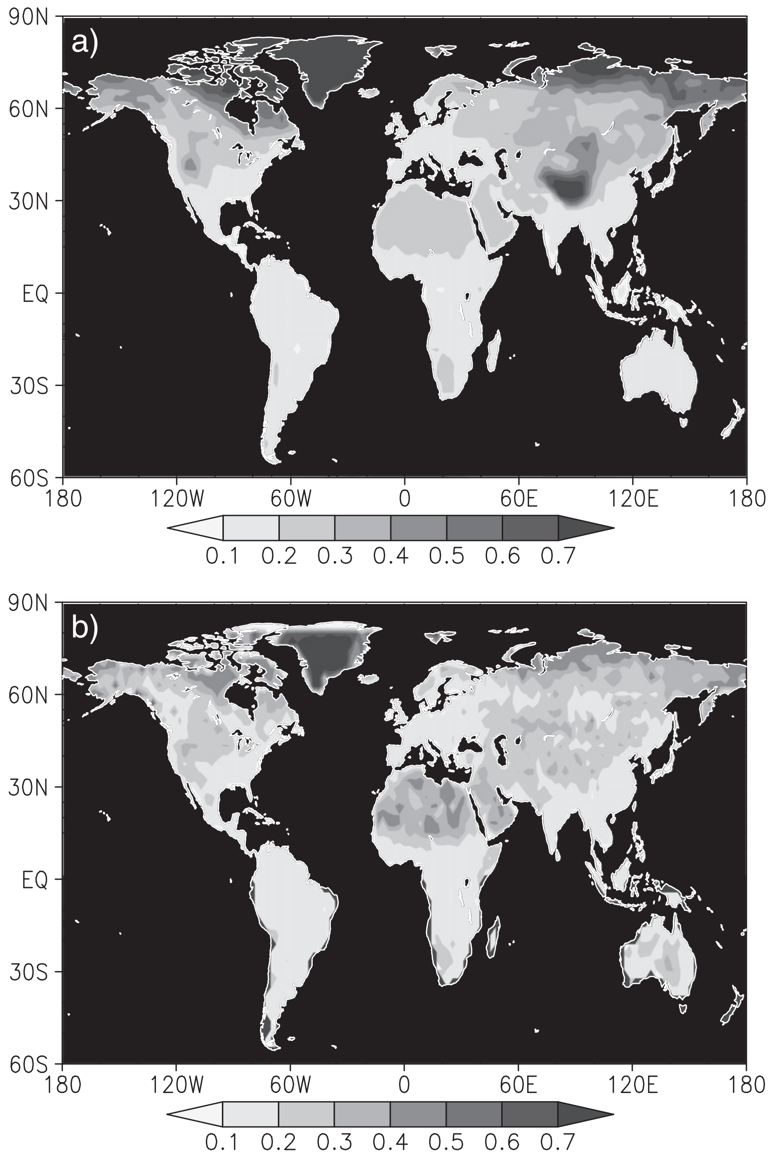

Fig. 6. The global annual mean distributions of (a) simulated and (b) MODIS retrieval surface albedo.

non-spherical aerosols by up to 30%. The differences between the two simulations in the single scattering albedo, and asymmetry factor at 550 nm are also small, varying by less than 1% (figures not shown). Table 3 gives the comparisons of simulated annual mean total AODs in EXPAF with those measured at 550 nm at some sites that are located in the dust

Table 2
Global annual means and differences of simulated dust optical properties and DRF between different experiments.

	AOD_D	SSA	g	RF_S	RF_L	$RFCS_s$	$RFCS_L$
	(λ = 550 nm)			(units: W m^{-2})			
EXPIRF_sphere	0.038	0.98	0.74	−0.62	0.073	−1.16	0.092
EXPIRF_nonsphere	0.039	0.98	0.74	−0.61	0.074	−1.14	0.093
DIFIRF	+2.6%	–	–	+2.0%	+1.4%	+1.7%	+1.1%
EXPAF_sphere	0.033	0.98	0.74	−0.55	0.052	−1.07	0.066
EXPAF_nonsphere	0.031	0.98	0.74	−0.48	0.049	−0.95	0.062
DIFAF	−6.1%	–	–	+13%	−6%	+11%	−6%

AOD_D represents the dust optical depth; SSA and g represent the single scattering albedo and asymmetry factor of aerosol, respectively; RF_S, RF_L, $RFCS_s$ and $RFCS_L$ represent the dust shortwave and longwave IRF in EXPIRF and AF in EXPAF at the TOA for all sky and clear sky, respectively; DIFi represents the differences of each variable due to dust spherical and non-spherical in EXPIRF and EXPAF ((EXPi_nonsphere − EXPi_sphere)/EXPi_ sphere, i = IRF, AF).

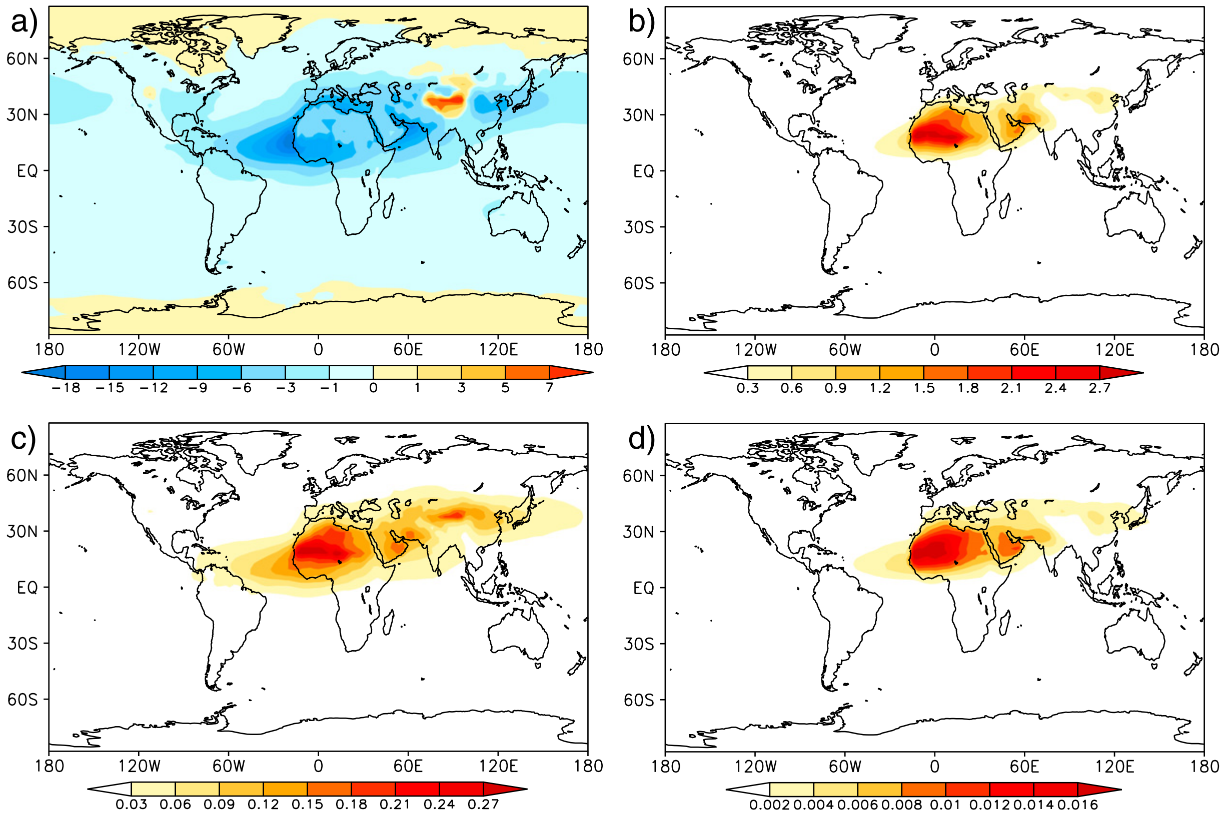

Fig. 7. Same as in Fig. 5, but for clear sky.

source regions. The measurements are from the AERONET Level 2.0 products except the Dunhuang and Ejinaqi sites that are from the CARSNET (China Meteorological Administration Aerosol Remote Sensing NETwork) (Che et al., 2009). Daily-averaged aerosol optical depths are acquired at the AERONET and CARSNET sites, from which monthly-mean values and standard deviations are computed weighted by the daily number of observations. Then, the corresponding yearly-mean values equal to the averages of 12 months. The four-point interpolation scheme is used to match the locations of model grids with the measured sites. It can be seen that the simulated AODs are more consistent with the observations at most of sites except the Saada, Dhadnah, Kuwait sites when dust particles are assumed to be non-spherical. However, the improvements due to non-spherical particles on the comparison are difficult to assess, since standard deviations on observations are large.

Fig. 11 shows global distributions of annual mean shortwave and longwave AF for simulated dust aerosols at the TOA for all sky in EXPAF_sphere, as well as the differences in dust shortwave and longwave AF in EXPAF_nonsphere versus EXPAF_sphere. The simulated distributions of annual mean shortwave and longwave AF of dust aerosols in EXPAF_sphere are consistent with those in EXPIRF_sphere. Shortwave and longwave AFs of non-spherical dust are weaker than those of spherical dust at the TOA over West Asia, south of the Sahara Desert, and along Africa's west coast. The largest decrease in shortwave forcing exceeds 3 W m^{-2}, accounting for over 20% of the non-spherical dust shortwave AF, resulting from a distinct decrease in dust column burden and optical depth in these areas, when dust particles are assumed to be non-spherical. The dust column burden and optical depth in northern China increased, but the shortwave AF in these areas decreased, when dust particles are considered non-spherical. This suggests that the absorption of radiation by dust in these regions has obviously increased and the negative AF of dust has been offset by non-spherical aerosol influences. Non-spherical dust intensifies AF in north of the Sahara Desert by 0.1–0.5 W m^{-2}. The global annual means of simulated dust shortwave (longwave) AFs at the TOA are −0.55 (0.052) W m^{-2}, and −0.48 (0.049) W m^{-2} in EXPAF_sphere and EXPAF_nonsphere, respectively. The absolute values of annual mean AF for non-spherical dust are approximately 13% and 6% less than those of spherical dust for shortwave and longwave radiation, respectively (Table 2). We also find that the absolute values of dust AF are smaller than those of IRF primarily due to the decrease in dust column burden after temperature adjustment, which is consistent with the results of Hansen et al. (2005).

In order to get rid of cloud effects on dust AFs, Fig. 12 shows the global distributions of simulated dust shortwave and longwave AF at the TOA for clear sky in EXPAF_sphere and the differences of forcing in EXPAF_nonsphere versus EXPAF_sphere. Similar to the IRF, the strength and range of dust negative shortwave AF and positive longwave AF for clear sky are larger than those for all sky, and the absolute changes of AF due to non-spherical effect of dust for clear sky are more

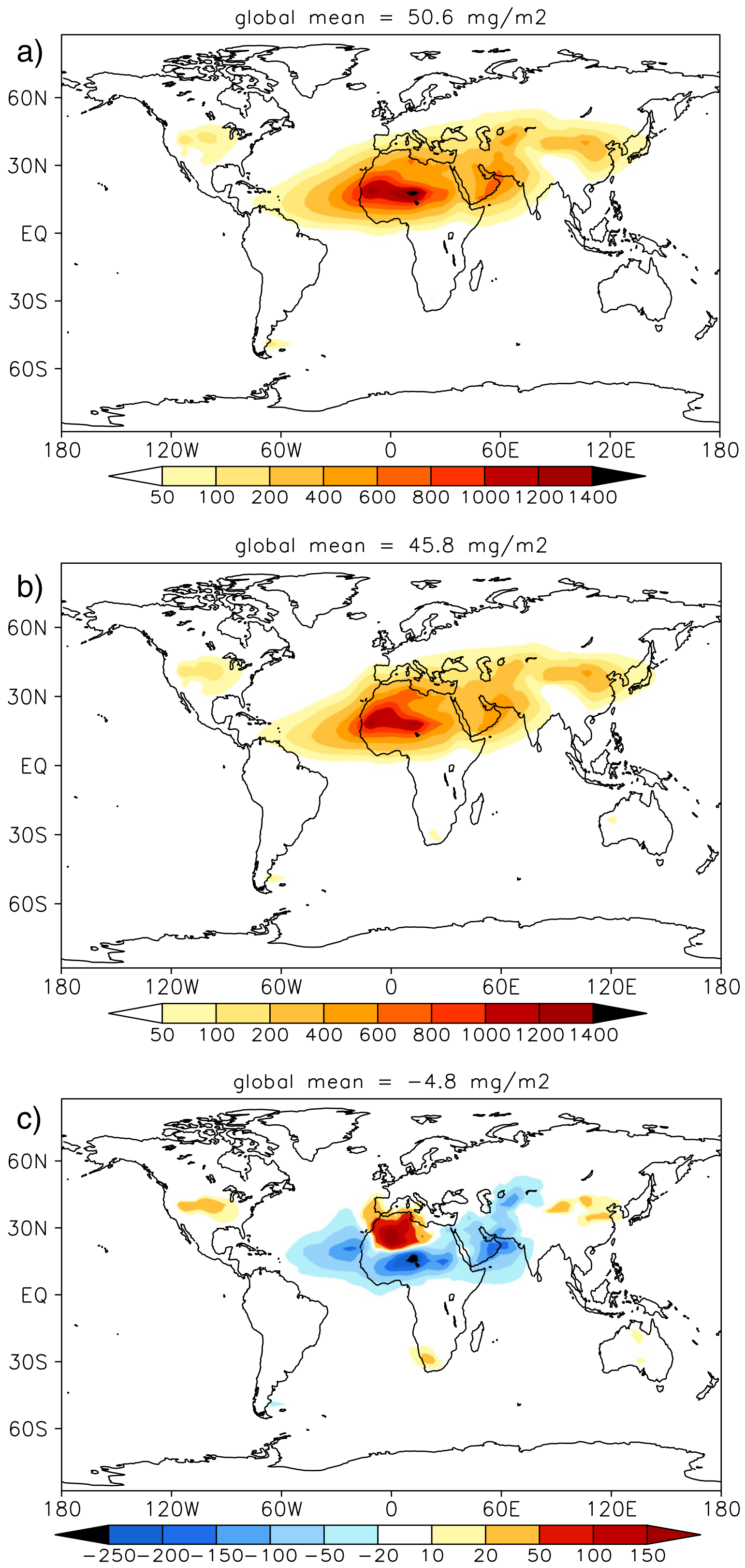

Fig. 8. The global annual mean distributions of simulated dust column burdens in (a) EXPAF_sphere and (b) EXPAF_nonsphere and (c) the difference in dust column burdens in EXPAF_nonsphere versus EXPAF_sphere (units: mg m^{-2}).

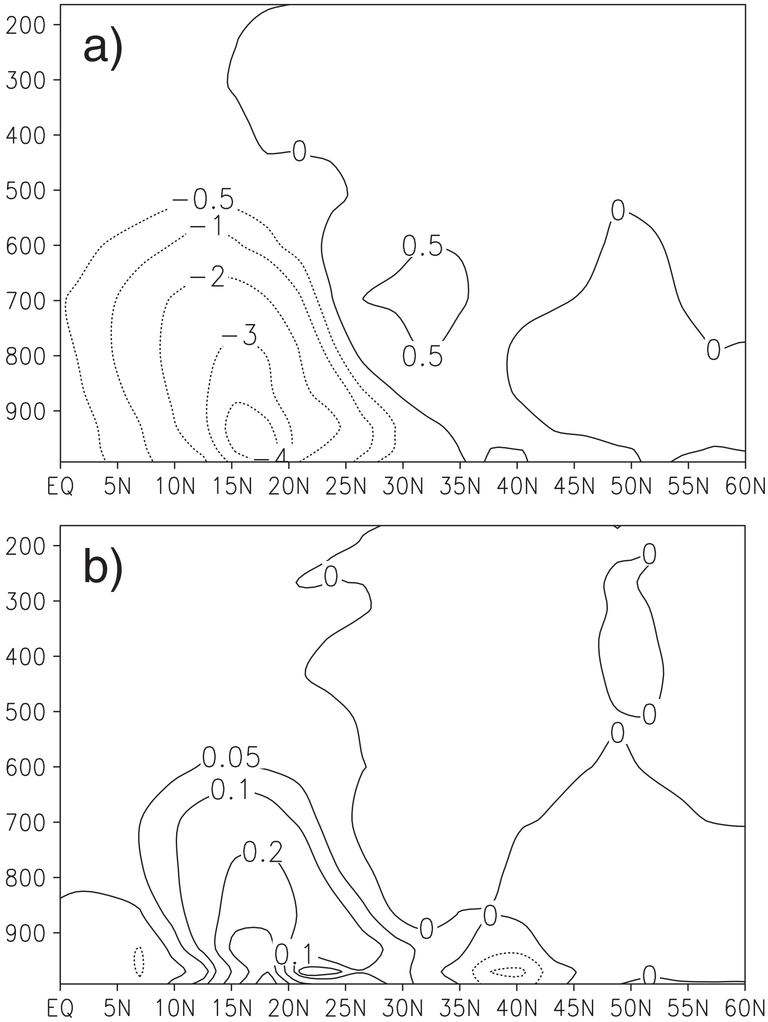

Fig. 9. The changes of zonally averaged (a) solar and (b) longwave heating rate due to the non-spherical effect of dust (units: 10^{-7} K s^{-1}).

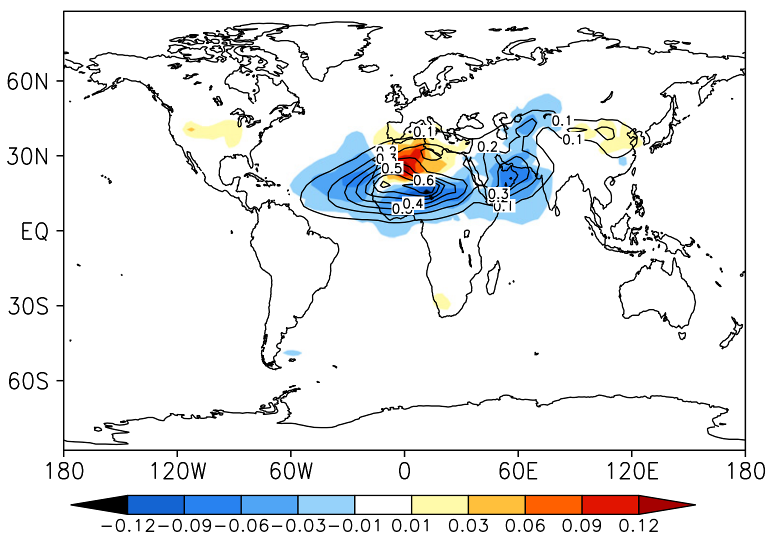

Fig. 10. Same as in Fig. 4, but for the experiment EXPAF.

Table 3
Comparisons of simulated annual mean total AODs in EXPAF with those measured at 550 nm at some sites that are located in the dust source regions. The measurements are from the AERONET except the Dunhuang and Ejinaqi sites that are from the CARSNET (China Meteorological Administration Aerosol Remote Sensing NETwork) (Che et al., 2009).

Site	Location	Sphere	Nonsphere	Obs.	Obs. years
Blida	2.9E, 36.5 N	0.12	0.14	0.21 ± 0.13	2003–2009
Malaga	4.5 W, 36.7 N	0.11	0.13	0.14 ± 0.08	2009–2011
Saada	8.2 W, 31.6 N	0.21	0.26	0.22 ± 0.14	2004–2009
La_Laguna	16.3 W, 28.5 N	0.25	0.23	0.14 ± 0.13	2006–2009
Dahkla	16.0 W, 23.7 N	0.42	0.37	0.29 ± 0.21	2002–2003
IER_Cinzana	5.9 W, 13.3 N	0.54	0.49	0.47 ± 0.30	2004–2009
Agoufou	1.5 W, 15.3 N	0.64	0.58	0.51 ± 0.35	2003–2009
Kuwait	48.0E, 29.3 N	0.27	0.25	0.54 ± 0.32	2007–2010
Hamin	54.3E, 23.0 N	0.388	0.307	0.345 ± 0.15	2004–2007
SEDE_BOKER	34.8E, 30.9 N	0.184	0.181	0.18 ± 0.11	1996–2010
Issyk-Kul	77.0E, 42.6 N	0.14	0.12	0.12 ± 0.08	2007–2010
Dunhuang	94.7E, 40.2 N	0.25	0.28	0.35 ± 0.31	2003–2008
Ejinaqi	101.1E, 42.0 N	0.17	0.18	0.22 ± 0.19	2002–2008

extensive and stronger than those for all sky, especially in northern Africa and Arabia. Clouds can greatly reduce AFs of dust too. The global annual means of simulated dust shortwave (longwave) AFs at the TOA for clear sky in EXPAF_sphere and EXPAF_nonsphere are −1.07 (0.066) W m^{-2} and −0.95 (0.062) W m^{-2}, respectively (see Table 2), while non-spherical effect of dust on their AFs become larger with relative difference of 11.2% and 6.0% reduction for shortwave and longwave, respectively, almost the same as the results of all sky case too.

In our experiments, the non-spherical dust effects on radiative forcing are larger in EXPAF than in EXPIRF. This is because the temperature profiles are the same for both shapes of dust particles in EXPIRF, and the differences in dust forcing result from the differences in optical properties between the two simulations. However, there are two factors affecting dust radiative forcing in the two simulations of EXPAF: one is the optical properties of the dust, and the other is the atmospheric profiles that are altered in fast response to radiative feedback from spherical and non-spherical dust (Fig. 9). The net

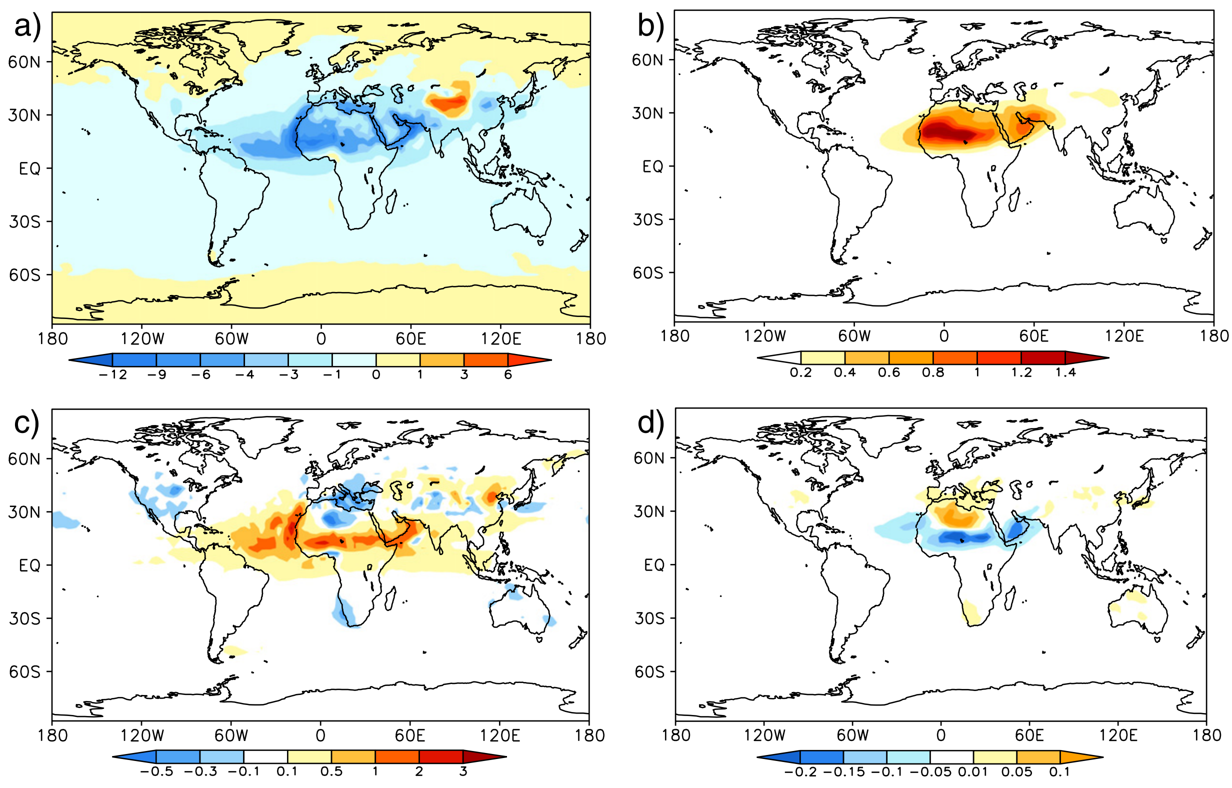

Fig. 11. Same as in Fig. 5, but for the AF in experiment EXPAF.

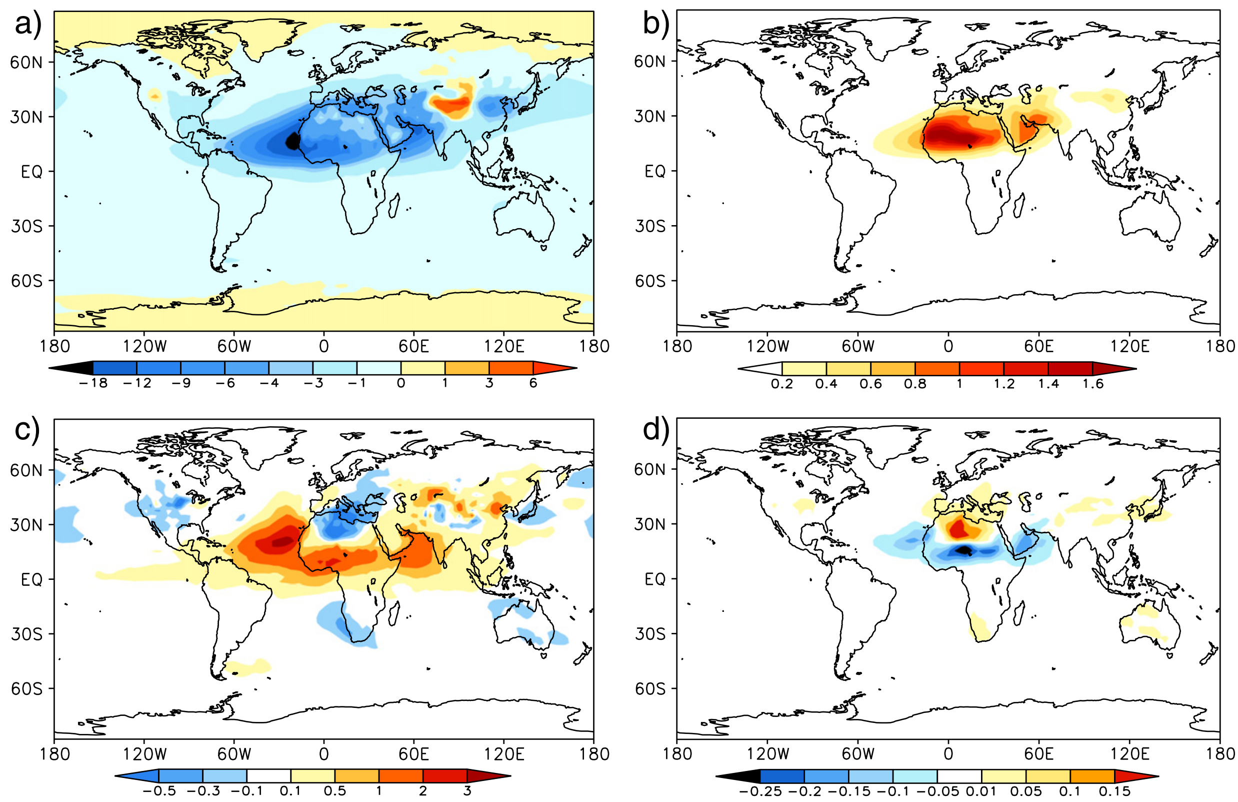

Fig. 12. Same as in Fig. 11, but for clear sky.

radiation flux at the TOA is more affected by non-spherical dust in EXPAF than it is in EXPIRF (0.14 W m^{-2} versus 0.02 W m^{-2} for the global annual mean, respectively), which indicates that these fast responses act collectively to increase the effect of non-spherical dust on AF.

4. Conclusions

We calculate the optical properties of spherical and non-spherical dust aerosols using the Lorenz-Mie theory and a combination of the T-matrix method with an IGOM. We use the resulting optical properties in an interactive system coupling GCM and an aerosol model (BCC_AGCM2.0.1_CAM) to calculate the IRF and AF of spherical and non-spherical dust aerosols and to discuss the effect of non-spherical dust on radiative forcing.

The simulated optical depths at 550 nm for non-spherical are greater than those for spherical dust particles, usually greater than 2%. The increase in dust optical depth due to non-spherical particles is the most distinct (about 4%) over the Sahara Desert, and is about 3% over northern China. The effects of non-spherical dust on aerosol single scattering albedo and asymmetry factor at 550 nm are more limited, and the relative deviations are less than 1%. These effects intensified the absorption of shortwave and longwave radiation by dust by 1~4% and less than 1%, respectively. Non-spherical dust causes the largest change in dust IRF at the TOA for all sky over the Sahara Desert, with a maximum increase of 0.27 W m^{-2}, due to enhanced absorption of solar radiation. The global annual means of shortwave (longwave) IRF for spherical and non-spherical dust at the TOA for all sky are −0.62 (0.074) W m^{-2} and −0.61 (0.073) W m^{-2}, respectively. The non-spherical effect of dust has little influence on their IRFs. The global annual means of shortwave (longwave) IRF for spherical and non-spherical dust at the TOA for clear sky are −1.16 (0.092) W m^{-2} and −1.14 (0.093) W m^{-2}, respectively, each of which is stronger than those for all sky. However, the non-spherical effect of dust on their IRFs for clear sky is similar to those for all sky.

When atmosphere and land temperatures are adjusted to reflect the radiative effect of spherical and non-spherical dust, the simulated global annual mean column burdens of both dusts respond differently and become 50.6 mg m^{-2} and 45.8 mg m^{-2} for spherical and non-spherical dust, respectively. Compared to spherical dust aerosols, the simulated column burdens of non-spherical dust aerosols in West Asia, south of the Sahara Desert, and the west coast of Africa are decreased; whereas column burdens are increased in north of the Sahara Desert, over the middle of North America, and over northern China. Non-spherical dust leads to a 5~20% increase in simulated dust optical depth at 550 nm over areas north of the Sahara Desert and northern China, but up to 30% decrease in south of the Sahara Desert and over West Asia, changing the corresponding shortwave and longwave AFs of dust at the TOA. The greatest change in dust AF at the TOA for all sky also occurs over the Sahara Desert, where shortwave forcing increases as much as 3 W m^{-2}. The global annual means of shortwave (longwave) AF of spherical and non-spherical dust at the TOA for all sky are −0.55 (0.052) W m^{-2} and −0.48 (0.049) W m^{-2}, respectively. The absolute values of non-spherical dust AF are about 13% and 6% less than spherical dust AF for shortwave and longwave radiation, respectively. Similar to the IRF, the absolute changes of AF due to non-spherical effect of dust for clear sky are more extensive and stronger than those for all sky, especially in northern Africa and Arabia. The global annual means of shortwave (longwave) AF of spherical and non-spherical dust at the TOA for clear sky are −1.07 (0.066) W m^{-2} and −0.95 (0.062) W m^{-2}, respectively. It is found in this work that non-spherical effect of dust on their AFs become larger with relative difference of 11.2% and 6.0% reduction for shortwave and longwave, respectively, almost the same as the results of all sky case.

The effects of non-spherical dust on both IRF and AF that we find here are far less than the uncertainties that exist in dust emission source data. It should be noted that the two-stream approximation scheme is applied in current modeling. Most of studies indicate that non-spherical effect of dust has a significant impact on the phase function, but the two-stream approximation only requires the asymmetry factor which is the first moment of the Legendre expansion of the phase function. This may impact on the non-spherical effect of dust to some extent. Therefore, the non-spherical effect of dust may be considered in the higher stream radiative transfer scheme in future climate models.

Acknowledgements

This work was financially supported by National Basic Research Program of China (2012CB955303 and 2011CB403405), CAMS Basis Research Project (2012Y003) and the Public Meteorology Special Foundation of MOST (Grant No. GYHY200906020).

References

Barnaba, F., De Tomasi, F., Gobbi, G.P., Perrone, M.R., Tafuro, A., 2004. Extinction versus backscatter relationships for lidar applications at 351 nm: maritime and desert aerosol simulations and comparison with observations. Atmos. Res. 70, 229–259.

Baum, B.A., Heymsfield, A.J., Yang, P., Bedka, S.T., 2005. Bulk scattering properties for the remote sensing of ice clouds. Part I: microphysical data and models. J. Appl. Meteorol. 44, 1885–1895.

Briegleb, B.P., 1992. Delta-Eddington approximation for solar radiation in the NCAR Community Climate Model. J. Geophys. Res. 97, 7603–7612.

Carrió, G.G., van den Heever, S.C., Cotton, W.R., 2007. Impacts of nucleating aerosol on anvil-cirrus clouds: a modeling study. Atmos. Res. 84, 111–131.

Chatenet, B., Marticorena, B., Gomes, L., Bergametti, G., 1996. Assessing the size distribution of desert soils erodible by wind. Sedimentology 43, 901–911.

Che, H., et al., 2009. Instrument calibration and aerosol optical depth validation of the China Aerosol Remote Sensing Network. J. Geophys. Res. 114, D03206. http://dx.doi.org/10.1029/2008JD011030.

Claquin, T., Schultz, M., Balkanski, Y., 1999. Modeling the mineralogy of atmospheric dust sources. J. Geophys. Res. 104, 22243–22256.

Collins, W.D., 2001. Parameterization of generalized cloud overlap for radiative calculations in general circulation models. J. Atmos. Sci. 58, 3224–3242.

D'Almeida, G.A., Koepke, P., Shettle, E.P., 1991. Atmospheric aerosols: global climatology and radiative characteristics. A. Deepak Publishing, Virginia, p. 561.

Dentener, F., Kinne, S., Bond, T., Boucher, O., Cofala, J., Generoso, S., Ginoux, P., Gong, S., Hoelzemann, J.J., Ito, A., Marelli, L., Penner, J.E., Putaud, J.P., Textor, C., Schulz, M., van der Werf, G.R., Wilson, J., 2006. Emissions of primary aerosol and precursor gases in the years 2000 and 1750 prescribed data-sets for AeroCom. Atmos. Chem. Phys. 6, 4321–4344.

Dubovik, O., Sinyuk, A., Lapyonok, T., Holben, B.N., Mishchenko, M., et al., 2006. Application of spheroid models to account for aerosol particle nonsphericity in remote sensing of desert dust. J. Geophys. Res. 111 (D11208). http://dx.doi.org/10.1029/2005JD006619.

El-Metwally, M., Alfaro, S.C., Wahab, M.M.A., Favez, O., Mohamed, Z., Chatenet, B., 2011. Aerosol properties and associated radiative effects over Cairo (Egypt). Atmos. Res. 99, 263–276.

Fu, Q., 1996. An accurate parameterization of the solar radiative properties of cirrus clouds for climate models. J. Climate 9, 2058–2082.

Fu, Q., Thorsen, T.J., Su, J., Ge, J.M., Huang, J.P., 2009. Test of Mie-based single-scattering properties of non-spherical dust aerosols in radiative flux calculations. J. Quant. Spectrosc. Radiat. Transfer 110, 1640–1653.

Gao, Y., Anderson, J.R., 2001. Characteristics of Chinese aerosols determined by individual-particle analysis. J. Geophys. Res. 106 (D16), 18037–18045.

Ge, J.M., Su, J., Ackerman, T.P., Fu, Q., Huang, J.P., Shi, J.S., 2010. Dust aerosol optical properties retrieval and radiative forcing over northwestern China during the 2008 China-U.S. joint field experiment. J. Geophys. Res. 115. http://dx.doi.org/10.1029/2009JD013263.

Gobbi, G.P., Barnaba, F., Blumthaler, M., Labow, G., Herman, J.R., 2002. Observed effects of particles nonsphericity on the retrieval of marine and desert dust aerosol optical depth by lidar. Atmos. Res. 61, 1–14.

Gong, S.L., Barrie, L.A., Lazare, M., 2002. Canadian Aerosol Module (CAM), a size-segregated simulation of atmospheric aerosol processes for climate and air quality models 2. Global sea-salt aerosol and its budgets. J. Geophys. Res. 107 (D24), 4779. http://dx.doi.org/10.1029/2001JD002004.

Gong, S.L., Barrie, L.A., Blanchet, J.P., von Salzen, K., Lohmann, U., Lesins, G., Spacek, L., Zhang, L.M., Girard, E., Lin, H., Leaitch, R., Leighton, H., Chylek, P., Huang, P., 2003a. Canadian aerosol module: a size-segregated simulation of atmospheric aerosol processes for climate and air quality models 1. Module development. J. Geophys. Res. 108. http://dx.doi.org/10.1029/2001JD002002.

Gong, S.L., Zhang, X.Y., Zhao, T.L., McKendry, I.G., Jaffe, D.A., Lu, N.M., 2003b. Characterization of soil dust aerosol in China and its transport and distribution during 2001 ACE-Asia: 2. Model simulation and validation. J. Geophys. Res. 108 (D9), 4262. http://dx.doi.org/10.1029/2002JD002633.

Hansen, J., Sato, M., Ruedy, R., et al., 2005. Efficacy of climate forcings. J. Geophys. Res. 110 (D18104). http://dx.doi.org/10.1029/2005JD005776.

Haywood, J., Francis, P., Osborne, S., Glew, M., Loeb, N., Highwood, E., Tanre, D., Myhre, E., Formenti, P., Hirst, E., 2003. Radiative properties and direct radiative effect of Saharan dust measured by the C-130 aircraft during SHADE: 1. Solar spectrum. J. Geophys. Res. 108. http://dx.doi.org/10.1029/2002JD002687.

Hendricks, J., Kärcher, B., Lohmann, U., 2011. Effects of ice nuclei on cirrus clouds in a global climate model. J. Geophys. Res. 116. http://dx.doi.org/10.1029/2010JD015302.

Herman, M., Deuze, J.L., Marchand, A., Roger, B., Lallart, P., 2005. Aerosol remote sensing from POLDER/ADEOS over the ocean: improved retrieval using a nonspherical particle model. J. Geophys. Res. 110. http://dx.doi.org/10.1029/2004JD004798.

Huneeus, N., Schulz, M., Balkanski, Y., et al., 2011. Global dust model intercomparison in AeroCom phase I. Atmos. Chem. Phys. 11, 7781–7816.

IPCC, 2001. Climate Change 2001: the scientific basis. In: Houghton, J.T., et al. (Ed.), Contribution of Working Group I to the Third Assessment Report of the Intergovernmental Panel on Climate Change. Cambridge Univ. Press, Cambridge and New York, pp. 291–348.

IPCC, 2007. Climate change 2007: the physical science basis. In: Solomon, S., et al. (Ed.), Contribution of Working Group I to the Fourth Assessment Report of the Intergovernmental Panel on Climate Change. Cambridge Univ. Press, Cambridge and New York, p. 996.

Jing, X.W., Zhang, H., 2012. Application and evaluation of McICA cloud-radiation framework in the GCM of the National Climate Center. Chinese J. Atmos. Sci. 36 (5). http://dx.doi.org/10.3878/j.issn.1006-9895.2012.11155.

Kalashnikova, O.V., Sokolik, I.N., 2004. Modeling the radiative properties of nonspherical soil-derived mineral aerosols. J. Quant. Spectrosc. Radiat. Transfer 87, 137–166.

Marticorena, B., Bergametti, G., 1995. Modeling the atmospheric dust cycle. 1: design of a soil-derived dust emission scheme. J. Geophys. Res. 100, 16415–16430.

McFarlane, S.A., Kassianov, E.I., Barnard, J., Flynn, C., Ackerman, T.P., 2009. Surface shortwave aerosol radiative forcing during the Atmospheric Radiation Measurement Mobile Facility deployment in Niamey, Niger. J. Geophys. Res. 114. http://dx.doi.org/10.1029/2008JD010491.

Mishchenko, M.I., Travis, L.D., 1994. Light scattering by polydispersions of randomly oriented spheroids with sizes comparable to wavelengths of observations. Appl. Opt. 33, 7206–7225.

Nakajima, T., 1989. Aerosol optical characteristics in the yellow sand events observed in May, 1982 at Nagasaki–Part II Models. J. Meteorol. Soc. Jpn. 67, 279–291.

Nakajima, T., Tsukamoto, M., Tsushima, Y., Numaguti, A., Kimura, T., 2000. Modeling of the radiative process in an atmospheric general circulation model. Appl. Opt. 39 (27), 4869–4878.

Okada, K., Heintzenberg, J., Kai, K., Qin, Y., 2001. Shape of atmospheric mineral particles collected in three Chinese arid-egions. Geophys. Res. Lett. 28 (16), 3123–3126.
Rosenfeld, D., Clavner, M., Nirel, R., 2011. Pollution and dust aerosols modulating tropical cyclones intensities. Atmos. Res. 102, 66–76.
Schumacher, C., Houze, R.A., 2006. Stratiform precipitation production over sub-Saharan Africa and the tropical East Atlantic as observed by TRMM. Q. J. R. Meteorolog. Soc. 132, 2235–2255.
Sokolik, I.N., Toon, O.B., 1996. Direct radiative forcing by anthropogenic airborne mineral aerosols. Nature 381, 681–683.
Wang, K.Y., 2010. Profiles of the atmospheric temperature response to the Saharan dust outbreaks derived from FORMOSAT-3/COSMIC and OMI AI. Atmos. Res. 96, 110–121.
Wang, J., Liu, X., Christopher, S.A., Reid, J.S., Reid, E., Mering, H., 2003. The effects of non-sphericity on geostationary satellite retrievals of dust aerosols. Geophys. Res. Lett. 30. http://dx.doi.org/10.1029/2003GL018697.
Wei, X.D., Zhang, H., 2011. Analysis of optical properties of nonspherical dust aerosols. Acta Optica Sinica 31 (5).
Wiscombe, W.J., 1980. Improved Mie scattering algorithms. Appl. Opt. 19 (9), 1505–1509.
Wu, T., Yu, R.C., Zhang, F., Wang, Z.Z., Dong, M., Wang, L., Jin, X., Chen, D., Li, L., 2010. The Beijing Climate Center atmospheric general circulation model: description and its performance for the present-day. Clim. Dyn. 34, 123–147.
Yang, P., Liou, K.N., 1996. Geometric-optics-integral-equation method for light scattering by nonspherical ice crystals. Appl. Opt. 35 (33), 6568–6584.
Yang, P., Liou, K.N., Mishchenko, M.I., Gao, B.C., 2000. Efficient finite-diference time-domain scheme for light scattering by dielectric particles: application to aerosols. Appl. Opt. 39, 3727–3737.
Yang, P., Wei, H., Huang, H.L., Baum, B.A., Hu, Y.X., Kattawar, G.W., Mishchenko, M.I., Fu, Q., 2005. Scattering and absorption property database for nonspherical ice particles in the near-through far-infrared spectral region. Appl. Opt. 44 (26), 5512–5523.
Yang, P., Feng, Q., Hong, G., Kattawar, G.W., Wiscombe, W.J., Mishchenko, M.I., Dubovik, O., Laszlo, I., Sokolik, I.N., 2007. Modeling of the scattering and radiative properties of nonspherical dust-like aerosols. J. Aerosol Sci. 38 (10), 995–1014.
Yi, B.Q., Hsu, C.N., Yang, P., Tsay, S.C., 2011. Radiative transfer simulation of dust-like aerosols: uncertainties from particle shape and refractive index. J. Aerosol Sci. 42, 631–644.
Zhang, H., Nakajima, T., Shi, G.Y., Suzuki, T., Imasu, T., 2003a. An optimal approach to overlapping bands with correlated k-distribution method and its application to radiative calculations. J. Geophys. Res. 108. http://dx.doi.org/10.1029/2002JD003358.
Zhang, X.Y., Gong, S.L., Shen, Z.X., Mei, F.M., Xi, X.X., Liu, L.C., Zhou, Z.J., Wang, D., Wang, Y.Q., Cheng, Y., 2003b. Characterization of soil dust aerosol in China and its transport and distribution during 2001 ACE-Asia: 1. Network observations. J. Geophys. Res. 108 (D9), 4261. http://dx.doi.org/10.1029/2002JD002632.
Zhang, H., Shi, G.Y., Nakajima, T., Tsuneaki, S., 2006a. The effect of the choice of the k-interval number on radiative calculation. J. Quant. Spectrosc. Radiat. Transfer 98, 31–43.
Zhang, H., Suzuki, T., Nakajima, T., Shi, G.Y., Zhang, X.Y., Liu, Y., 2006b. Effects of band division on radiative calculations. Opt. Eng. 45 (1). http://dx.doi.org/10.1117/1.2160521.
Zhang, X., Wang, X., Yan, P., 2008. Re-evaluating the impacts of human activity and environmental change on desertification in the Minqin Oasis, China. Environ. Geol. 55, 705–715.
Zhang, H., Ma, J.H., Zheng, Y.F., 2010. Modeling study of the global distribution of radiative forcing by dust aerosol. Acta Meteorol. Sin. 24, 558–570.
Zhang, H., Wang, Z.L., Wang, Z.Z., Liu, Q., Gong, S., Zhang, X., Shen, Z., Lu, P., Wei, X., Che, H., Li, L., 2012a. Simulation of direct radiative forcing of aerosols and their effects on East Asian climate using an interactive AGCM-aerosol coupled system. Clim. Dyn. 38, 1675–1693.
Zhang, H., Shen, Z., Wei, X., Zhang, M., Li, Z., 2012b. Comparison of optical properties of nitrate and sulfate aerosol and the direct radiative forcing due to nitrate in China. Atmos. Res. 113, 113–125.
Zhao, T.X.-P., Laszlo, I., Dubovik, O., Holben, B.N., Sapper, J., Tanre, D., Pietras, C., 2003. A study of the effect of nonspherical dust particles on the AVHRR aerosol optical thickness retrievals. Geophys. Res. Lett. 30 (6), 1317. http://dx.doi.org/10.1029/2002GL016379.

Dr. Zhili Wang is an assistant researcher at Chinese Academy of Meteorological Sciences. His main research interests are aerosol direct and indirect radiative forcings and their effect on climate; and development of physical process in aerosol-cloud interaction in GCM.

Education
Ph. D., 2011, Chinese Academy of Meteorological Sciences, China
M. Sc., 2008, College of Atmospheric Science, Nanjing University of Information Science and Technology, China
B. Sc., 2005, College of Atmospheric Science, Nanjing University of Information Science and Technology, China

Dr. Hua Zhang is a professor at Laboratory for Climate Studies, National Climate Center, China Meteorological Administration. Her research interests are development and improvement of radiation scheme in GCM; cloud overlapping treatment in GCM; and GHGs and aerosol radiative forcings and their effects on climate.

Education
Ph. D., 1999, Institute of Atmospheric Physics, Chinese Academy of Sciences, China
M. Sc., 1989, Department of Atmospheric physics, Nanjing Institute of Meteorology, China
B. Sc., 1986, Department of Atmospheric physics, Nanjing Institute of Meteorology, China

Xianwen Jing is an engineer at National Climate Center, China Meteorological Administration. His research topic is cloud and radiation processes in GCM.

Education
Ph. D., 2012, Chinese Academy of Meteorological Science, China
M. Sc., 2009, College of Atmospheric Science, Nanjing University of information Science and Technology, China
B. Sc., 2006, College of Applied Meteorology, Nanjing University of Information Science and Technology, China

Xiaodong Wei took the master degree from Chinese Academy of Meteorological Sciences in 2011. His M. Sc. study is aerosol optical properties.

Education
M. Sc., 2011, Chinese Academy of Meteorological Sciences, China
B. Sc., 2008, College of Atmospheric Physics, Nanjing University of Information Science and Technology, China

JOURNAL OF GEOPHYSICAL RESEARCH: ATMOSPHERES, VOL. 118, 3662–3675, doi:10.1002/jgrd.50312, 2013

Radiative forcing and climate response due to the presence of black carbon in cloud droplets

Zhili Wang,[1] Hua Zhang,[2] Jiangnan Li,[3] Xianwen Jing,[2] and Peng Lu[4]

Received 27 August 2012; revised 1 March 2013; accepted 4 March 2013; published 8 May 2013.

[1] Optical properties of clouds containing black carbon (BC) particles in their water droplets are calculated by using the Maxwell Garnett mixing rule and Mie theory. The obtained cloud optical properties were then applied to an interactive system by coupling an aerosol model with a General Circulation Model. This system is used to investigate the radiative forcing and the equilibrium climate response due to BC in cloud droplets. The simulated global annual mean radiative forcing at the top of the atmosphere due to the BC in cloud droplets is found to be 0.086 W m^{-2}. Positive radiative forcing can be seen in Africa, South America, East and South Asia, and West Europe, with a maximum value of 1.5 W m^{-2} being observed in these regions. The enhanced cloud absorption is shown to increase the global annual mean values of solar heating rate, water vapor, and temperature, but to decrease the global annual mean cloud fraction. Finally, the global annual mean surface temperature is shown to increase by +0.08 K. The local maximum changes are found to be as low as −1.5 K and as high as +0.6 K. We show there has been a significant difference in surface temperature change in the Southern and Northern Hemisphere (+0.19 K and −0.04 K, respectively). Our results show that this interhemispheric asymmetry in surface temperature change could cause a corresponding change in atmospheric dynamics and precipitation. It is also found that the northern trade winds are enhanced in the Intertropical Convergence Zone (ITCZ). This results in northerly surface wind anomalies which cross the equator to converge with the enhanced southern trade winds in the tropics of Southern Hemisphere. This is shown to lead to an increase (a decrease) of vertical ascending motion and precipitation on the south (north) side of the equator, which could induce a southward shift in the tropical rainfall maximum related to the ITCZ.

Citation: Wang, Z., H. Zhang, J. Li, X. Jing, and P. Lu (2013), Radiative forcing and climate response due to the presence of black carbon in cloud droplets, *J. Geophys. Res. Atmos.*, *118*, 3662–3675, doi:10.1002/jgrd.50312.

1. Introduction

[2] Clouds, which cover about 60% of the Earth's surface, play a significant role in the radiation budget of the earth-atmosphere system. Clouds reflect solar radiation back into space and reduce the radiative flux to the surface. They also absorb the infrared radiation emitted from surface of the Earth and reduce the loss of energy in the earth-atmosphere system [*Forster et al.*, 2007]. Therefore, any change of cloud optical properties can disturb the energy balance of the earth-atmosphere system.

[3] Black carbon (BC) is an important anthropogenic aerosol produced from the incomplete combustion of hydrocarbon-containing materials. Since pre-industrial time, the BC loading in the atmosphere has grown considerably. This reflects the increasing usage of fossil fuels and biofuels, coupled with the increasing world population [*Bond et al.*, 2007; *Lu et al.*, 2010]. BC aerosol comprises a small portion of atmospheric aerosols (typically less than 15% of the total aerosol mass). However, the impact of BC aerosol on the climate is substantial. BC is a strong absorber of solar radiation. This can enhance the absorption of solar energy in the earth-atmosphere system and increase the atmospheric temperature directly. This effect has been considered as a potential source of global warming [*Jacobson*, 2002; *Menon et al.*, 2002; *Chung and Seinfeld*, 2005; *Ramanathan and Carmichael*, 2008; *Shindell et al.*, 2012]. When BC is mixed with sulfate and other water-soluble aerosols, it can act as the condensation nuclei for a water cloud. BC can even act as ice nuclei. Thus, BC can change cloud albedo and lifetime and so indirectly affect the climate system [*Hansen et al.*, 2005; *Lohmann and Feichter*, 2005; *Zhang and Wang*, 2011]. BC aerosol affects clouds in two major ways. First, the embedding of BC in cloud droplets can affect the cloud optical properties. In particular, BC can reduce the cloud droplet single scattering albedo (SSA) due to its strong absorbing ability. This can increase the absorption of solar

[1]Chinese Academy of Meteorological Sciences, Beijing, China.
[2]Laboratory for Climate Studies, National Climate Center, China Meteorological Administration, Beijing, China.
[3]Canadian Centre for Climate Modeling and Analysis, Victoria, Canada.
[4]Jiangsu Climate Center, Nanjing, China.

Corresponding author: H. Zhang, Laboratory for Climate Studies, National Climate Center, China Meteorological Administration, Beijing 100081, China. (huazhang@cma.gov.cn)

2169-897X/13/10.1002/jgrd.50312

radiation, and this extra heating in clouds can exacerbate cloud evaporation. Thus, the atmospheric heating rate profile is affected [*Chuang et al*., 2002; *Jacobson*, 2006; *Zhuang et al*., 2010; *Ghan et al*., 2012; *Li et al*., 2013]. Second, BC particles interstitially existing between cloud droplets can also enhance the absorption compared to BC existing in clear sky. This is due to the fact that relative humidity is higher inside a cloud [*Jacobson*, 2012]. Both effects increase the cloud absorption and so have impact on cloud burn-off and climate.

[4] BC aerosols are mostly hydrophobic when emitted, but they gradually become hygroscopic over time due to chemical and physical processes in the atmosphere. The hydrophilic BC particles can act as effective cloud condensation nuclei [*Cooke et al*., 2002; *Roberts and Jones*, 2004], which results in the mixing of BC in cloud droplets. As far back as 1984, *Chýlek et al*. [1984] investigated the effect of BC on the absorption of solar radiation by clouds by assuming the water droplet containing the arbitrarily distributed spherical BC particles. BC aerosol has drawn more attention in recent years, but there has been little research on the climate impact of BC in cloud droplets. *Chuang et al*. [2002] developed a scheme to calculate the cloud droplet SSA of BC in cloud droplets. They were the first to take into account the impact of the extra BC absorption in the climate model of CCM1/NCAR. Their results showed that the effect of BC in cloud droplets could reduce the reflection of solar radiation and causes an increase of radiative forcing at the top of the atmosphere (TOA). *Zhuang et al*. [2010] investigated the impact on regional cloud radiative forcing and climate by BC in cloud droplets, using a regional climate model based on the method of *Chuang et al*. [2002]. Their results also indicated that BC in cloud droplets could cause a positive radiative forcing at TOA. They also found that the extra heating from BC in cloud droplets could affect atmospheric circulation and hydrologic cycle. The above two works, however, used only an empirical formula to calculate the cloud droplet SSA for BC in cloud droplets.

[5] *Li et al*. [2011] pointed out that the method to calculate SSA by *Chuang et al*. [2002] was deficient in several aspects. Specifically, it was suggested the cloud effective radius should be used instead of cloud droplet size since the cloud effective radius is used in cloud optical property parameterizations to represent cloud drop size distribution. Second, the cloud optical properties should be calculated exactly by Mie theory instead of an empirical formula. Third, all cloud optical properties rather than just the SSA should be taken into account to avoid the inconsistency with the cloud optical property variables used in climate models.

[6] Thus, further investigation is needed, based on using an accurate method for calculation of cloud optical properties, to evaluate the impact on radiative forcing and climate response, due to BC in cloud droplets. This paper mainly addresses these issues.

[7] In this study, we first calculate the cloud droplet refractive index by the Maxwell-Garnett (MG) mixing rule [*Chýlek et al*., 1988, 1996]. Then the cloud optical properties are obtained based on the Mie theory and cloud droplet size distribution. The refractive index obtained by the MG mixing rule is derived from an effective-medium approximation that gives an average complex refractive index based on the volume fractions and complex refractive indices of both the medium and the absorbing substance within it.

[8] The refractive index of cloud droplets can be calculated in a more sophisticated way by using the dynamic effective medium approximation (DEMA) [*Stroud and Pan*, 1978; *Chýlek et al*., 1988; *Jacobson*, 2006]. This method takes into account the polydispersion of spherical absorbing inclusions within the medium. DEMA gives different efficiencies for the same volume fraction but different size distributions of absorbing material. For a fixed water droplet size, *Jacobson* [2006] showed that the absorption efficiency could be slightly higher by DEMA compared to that of MG. However, the relationship between aerosol size distribution and cloud droplet size distribution is difficult to determine, as both are assumed to have long tails in their size distributions. A question arises as to how to treat the aerosol size distribution inside a very small cloud droplet. Is the aerosol size distribution in different sizes of cloud droplets the same? The method of DEMA could be more accurate when we have better observational evidence to understand the size distributions of aerosols inside cloud droplets.

[9] This model, like most of other GCMs, does not explicitly calculate the activation of cloud condensation nuclei (acted by aerosols including BC) to cloud droplets. Instead the concentration of BC in cloud droplets is determined by the mass concentrations of hydrophilic BC and cloud liquid water. This could be a source of uncertainty. Recently, the physical evolution of cloud droplets from aerosol particles (including the hygroscopic BC) has been applied to some climate models [*Jacobson*, 2006; *Gustafson et al*., 2007; *Ghan et al*., 2012].

[10] After obtaining the cloud optical properties, we apply them to an interactive system by coupling a climate model with an aerosol model. The purpose is to investigate the radiative forcing and the equilibrium climate response due to BC in cloud droplets. In section 2, the climate and aerosol models used in the study are introduced and the method for calculating the optical properties of mixing droplets is discussed. Also, the experimental design is presented. In section 3, the corresponding results in radiative forcing and climate response are analyzed. Finally, we conclude with a brief summary.

2. Model and Scheme

2.1. Aerosol-Climate Online Coupled Model

[11] A General Circulation Model (GCM) of BCC_AGCM2.0.1 (Beijing Climate Center atmospheric general circulation model) coupled with a Canadian Aerosol Module (CAM) [*Zhang et al*., 2012] is used in this study. BCC_AGCM2.0.1 was developed by the National Climate Center of the China Meteorological Administration based on the Community Atmosphere Model Version 3 (CAM3) developed by the National Center for Atmospheric Research in the United States. This model employs a spectral resolution of T42 (approximately 2.8° latitude × 2.8° longitude grid) and a terrain-following hybrid vertical coordinate with 26 levels with a rigid lid at 2.9 hPa. The main features of BCC_AGCM2.0.1 are described by *Wu et al*. [2010]. However, the primary radiative parameterization and the cloud overlap scheme in BCC_AGCM2.0.1 are replaced with a correlated k-distribution radiation scheme and a

Monte Carlo independent column approximation developed by *Zhang et al.* [2003, 2006a, 2006b] and *Jing and Zhang* [2012]. These two modifications have improved the accuracy in gaseous absorption and radiative transfer process through subgrid-scale clouds. The new radiation scheme contains 17 bands (eight for longwave radiation and nine for shortwave radiation), and the spectral ranges of each band are listed in *Zhang et al.* [2003]. The model includes the main greenhouse gasses of H_2O, CO_2, O_3, N_2O, CH_4, and CFC (CFC_{11}, CFC_{12}, CCL_4, and CFC_{22}). In this study, BCC_AGCM2.0.1 is coupled with a slab ocean model, which is from *Hansen et al.* [1984].

[12] The CAM, a size-segregated multi-component aerosol model, was developed by *Gong et al.* [2002, 2003]. The following five aerosol types were included: sulfate, BC, organic carbon (OC), soil dust, and sea salt. Each aerosol type is divided into 12 bins as a geometric series for radius between 0.005–20.48 μm. The total number of advected aerosol quantities is 60 in the model. The model includes the processes of emission, transport, chemical transformation, cloud interaction, and deposition for atmospheric aerosols. BC particles are mostly hydrophobic when emitted. However, BC aerosols become hydrophilic as they age in the atmosphere. The detailed aerosol aging process is shown in *Gong et al.* [2003]. The wet removal of aerosols follows two processes: below-cloud scavenging and in-cloud rainout [*Gong et al.*, 2003]. The removal rate of aerosols due to below-cloud scavenging by precipitation is calculated according to *Slinn* [1984], and the rainout removal tendency inside the clouds is expressed according to *Giorgi and Chameides* [1986]. The emissions of sulfate, BC, and OC are derived from AeroCom data [*Dentener et al.*, 2006]. The emission of soil dust and emission of sea salt are calculated online using the schemes developed by *Marticorena and Bergametti* [1995] and *Gong et al.* [2002], respectively. BCC_AGCM2.0.1 and CAM have been coupled online and can simulate the mass concentration, optical properties, and direct radiative forcing of typical aerosols with a high level of accuracy [*Zhang et al.*, 2012].

2.2. Parameterization of Optical Properties of Cloud Droplets Including BC

[13] BC particles can be assumed to be randomly embedded in cloud droplets since the mean radius of BC is much smaller than that of cloud droplets. The refractive index of cloud droplets containing various particles can be calculated by the MG mixing rule [*Chýlek et al.*, 1988, 1996]:

$$m^2 = m_w^2 \frac{m_{BC}^2 + 2m_w^2 + 2\eta\left(m_{BC}^2 - m_w^2\right)}{m_{BC}^2 + 2m_w^2 - \eta\left(m_{BC}^2 - m_w^2\right)}, \tag{1}$$

where $m = n + i \cdot k$ is the refractive index for the mixture droplet with n and k being the real and imaginary parts, m_w and m_{BC} are the refractive indices of water and BC, respectively, and η is the volume fraction of BC in clouds. The volume fraction of BC in clouds, η, in climate models is defined as [*Li et al.*, 2011]

$$\eta = f \cdot \frac{M_{BC}/\rho_{BC}}{M_w/\rho_w}, \tag{2}$$

where f is the cloud fraction in a model grid cell, M_{BC} and M_w are the mass concentrations of hydrophilic BC and cloud liquid water, respectively, and ρ_{BC} and ρ_w are the densities of hydrophilic BC and cloud liquid water, respectively. According to *Hansen et al.* [2005], the soluble proportion of BC particles should be set as 0.6 for industrial (fossil fuel) BC and 0.8 for biomass burning BC. All the hydrophilic BC is assumed to be embedded in the cloud droplets due to the lack of physical parameterization of cloud microphysics in this model. In reality, some hydrophilic BC particles could exist interstitially between cloud droplets. The proportions of soluble BC to total BC and the amount of hydrophilic BC entering into cloud droplets are depend strongly on many local physical and chemical conditions. Also the results should be expected to vary greatly by regions. In this work, the assumption that all hydrophilic BC is embedded in cloud droplets could generate uncertainties in results.

[14] The cloud droplet size distribution, $n(r)$, in the atmosphere is represented by gamma functions [*Pruppacher and Klett*, 1997]:

$$n(r) = Ar^{\alpha}e^{-\beta r}, \tag{3}$$

where A, α, and β are constants and r is the radius of the cloud droplet. α and β can be obtained from the effective radius, r_e, and effective variance, v_e. *Li et al.* [2011] showed that cloud radiative forcing is very sensitive to r_e but not to v_e, so a constant value of $v_e = 0.172$ has been adopted in the parameterization of cloud optical properties [*Dobbie et al.*, 1999]. Based on these, we can calculate the cloud droplet optical properties using Mie theory. The refractive indices of water and BC are from *D'Almeida et al.* [1991], with a value of $1.75 + 0.44\ i$ at 550 nm for BC.

[15] The cloud droplet effective radius is divided into six bins with size of 1.5, 3.0, 5.0, 10.0, 20.0, and 40.0 μm, which matches the radiation scheme used in BCC_AGCM2.0.1. We divide the values of η into eight bins as 0, 10^{-9}, 10^{-8}, 10^{-7}, 10^{-6}, 10^{-5}, 10^{-4}, and 10^{-2}. Accordingly, the cloud droplet optical properties defined as an (6×8) array for effective radius and η are calculated and incorporated into the model. At each model time step, the cloud optical properties at any values of droplet effective radius and η can be obtained through bilinear interpolation. This table look-up method is different from the perturbation method shown in *Li et al.* [2011]. Both methods can effectively handle the cloud optical properties.

2.3. Experimental Design

[16] Two experiments were performed. In the first experiment (EXP1), clouds are assumed to consist of pure water and so their optical properties are not affected by BC. In the second experiment (EXP2), the extra absorption due to the presence of BC in cloud droplets is taken into account. The microphysical role of BC is assumed to be the same in both experiments. The instantaneous radiative forcing is calculated by calling the radiation scheme twice at each radiative time step in EXP1. In the first, the radiative effect due to BC in cloud droplets is included; in the second, BC particles in cloud droplets are not activated in radiation. The difference of net solar radiation flux at TOA or the surface between the two calls is defined as the corresponding radiative forcing. Each experiment is run for 80 years. The first 30 years is the spin-up period and the last 50-year simulation is averaged and analyzed to determine the

radiative forcing and climate response. We also performed an additional experiment to simulate the direct radiative forcing based on the assumption that all the BC particles are in the atmosphere.

[17] The model's results have been subjected to a *t*-test to estimate their statistical significance by assuming each model year to be an independent sample. We also divide the data into N-year segments (N = 2, 3, 4, 5) instead of 1-year segments to test the temporal correlation of the samples. The results show that the areal fraction of significant differences is roughly the same with increasing N, especially for the main features. It is therefore suitable to use each model year as an independent sample for evaluating statistical significance.

3. Results and Discussions

3.1. Change of Cloud Optical Properties Due to Presence of BC in Cloud Droplets

[18] The imaginary part of cloud droplet refractive index is very sensitive to the presence of BC in cloud droplets, while the real part shows very little sensitivity. The change in the imaginary part of the refractive index mainly occurs in the solar spectral range, especially for the wavelengths $\lambda \leq 1\ \mu m$ as shown in *Chýlek et al*. [1984] and *Li et al*. [2011]. The imaginary part of the cloud droplet refractive index increases substantially with the increase of η. This suggests that the presence of BC in cloud droplets can strongly increase the cloud solar energy absorption.

[19] *Reddy and Boucher* [2004] pointed out that in the atmosphere, $\eta = 10^{-7}$ is a common value of the BC volume fraction in clouds based on a GCM simulation. In Figure 1, the changes of cloud optical properties for different cloud droplet effective radius are shown for $\eta = 10^{-7}$. It is found that the change of the extinction coefficient is very small. However, the changes of the absorption coefficient, SSA, and asymmetry factor are clearly seen in Figure 1. With increases of effective radius, the changes in SSA and asymmetry factor become larger, but the change in absorption coefficient becomes smaller. This is attributed to the decrease of extinction coefficient with the increase of effective radius, since the absorption coefficient is defined as the extinction coefficient times the co-single scattering albedo. In Figure 2, the band-mean absolute differences of cloud optical properties due to BC in cloud droplets are shown for the 17 bands used in BCC_AGCM2.0.1. Generally, the differences of cloud optical properties appear in the solar wavebands of 10–17. The results are consistent with those in Figure 1.

[20] Considering the difference between the absorption cross-section of cloud droplets with and without BC, the enhancement ratio is defined as this difference divided by the absorption cross-section of an equal mass of BC residing within the air [*Flanner et al*., 2012]. Figure 3 shows the enhancement ratio versus wavelength for two BC volume fractions. For the smaller volume fraction, $\eta = 10^{-7}$, the enhancement ratios drop to close to zero for a wavelength larger than 1.8 μm; for the larger volume fraction, $\eta = 10^{-5}$, the enhancement ratio can exceed 3 even when the wavelength is close to 4 μm. Additionally, the enhancement ratio is

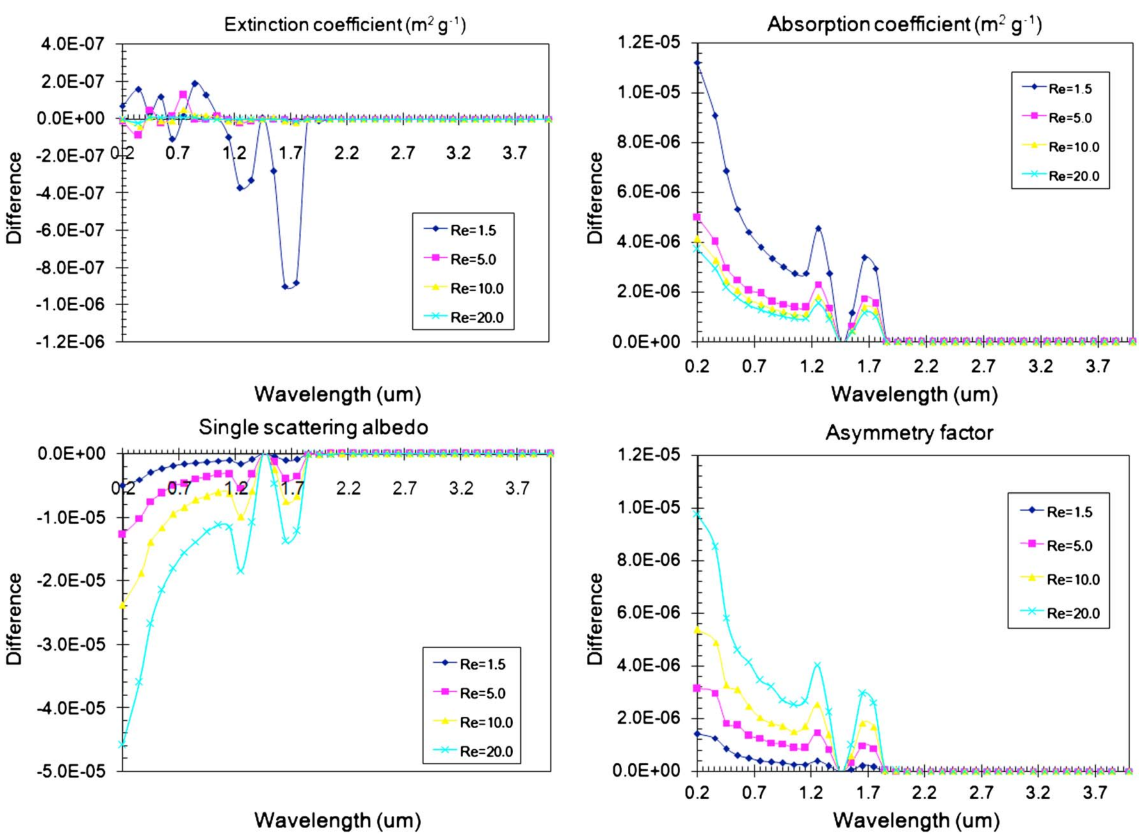

Figure 1. The absolute differences of cloud optical properties for $\eta = 10^{-7}$. Re is cloud droplet effective radius (unit: μm).

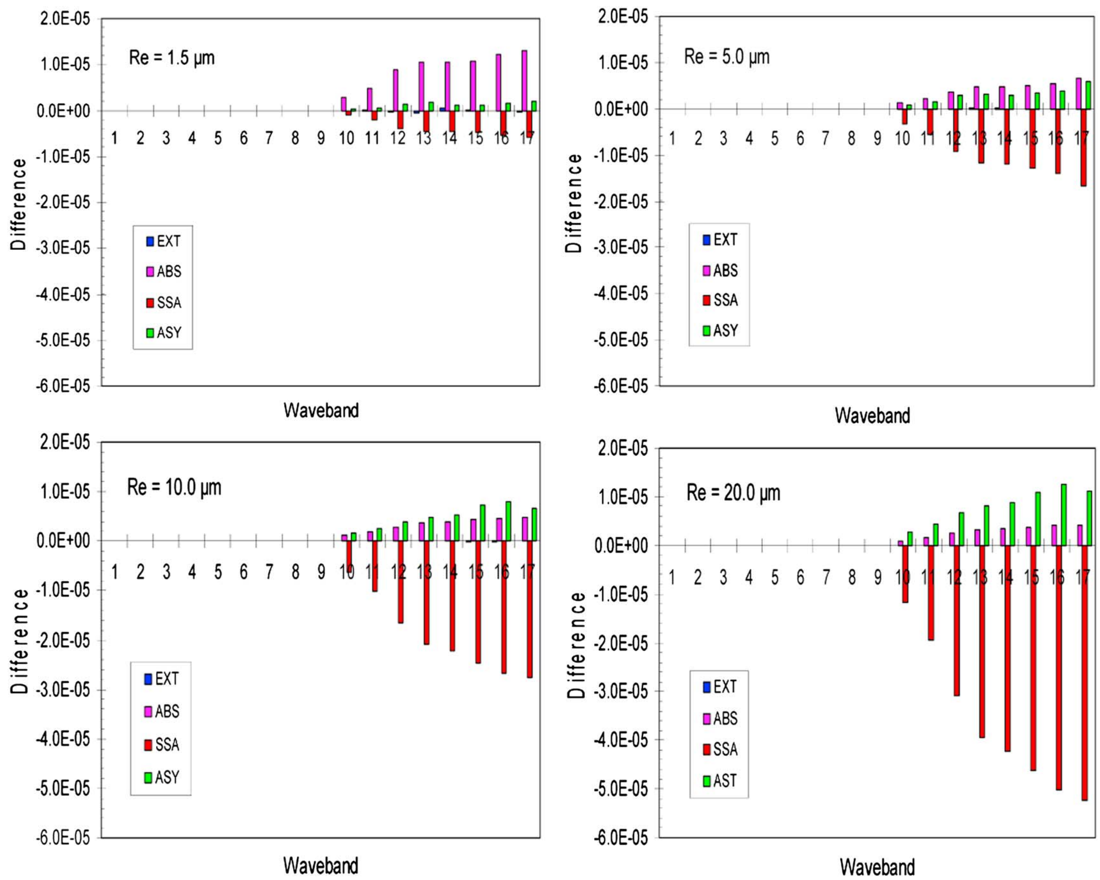

Figure 2. Same as in Figure 1, but is the band-mean differences for the 17 bands used in BCC_AGCM2.0.1. The horizontal axis represents 17 wavebands including 1000.0–40.0, 40.0–18.182, 18.182–12.821, 12.821–10.101, 10.101–8.333, 8.333–6.993, 6.993–4.739, 4.739–3.731, 3.731–1.923, 1.923–0.833, 0.833–0.455, 0.455–0.323, 0.323–0.303, 0.303–0.286, 0.286–0.270, 0.270–0.233, and 0.233–0.204 μm, respectively.

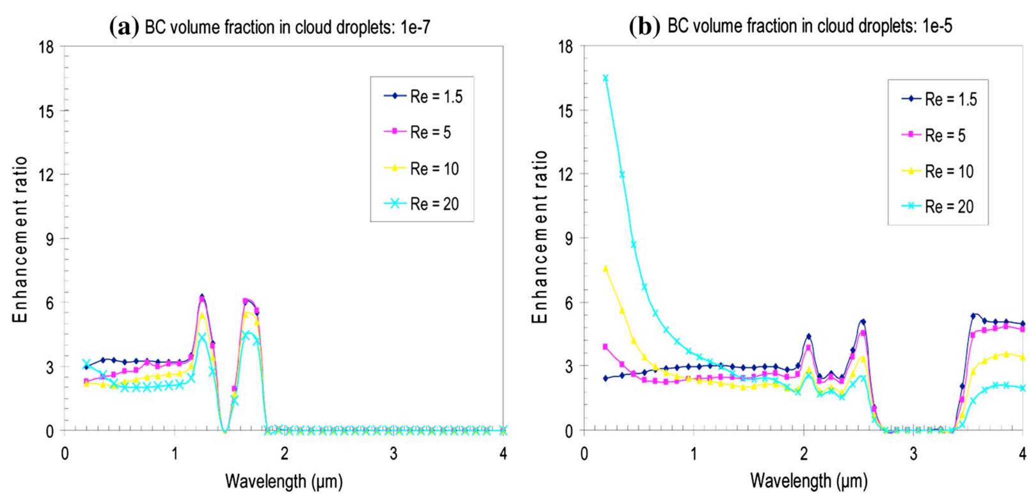

Figure 3. The changes of enhancement ratio with the wavelength for different values of BC volume fraction in cloud droplets. Re is cloud droplet effective radius (unit: μm). The size distribution of BC in air is assumed to be the same as that in cloud droplets. When Re equals to 1.5, 5, 10 and 20 μm, the absorption cross-sections for interstitial BC at 550 nm are 0.000013, 0.00023, 0.0018, and 0.015 μm^2 for $\eta = 10^{-7}$ and 0.0016, 0.027, 0.13, and 0.47 μm^2 for $\eta = 10^{-5}$, respectively.

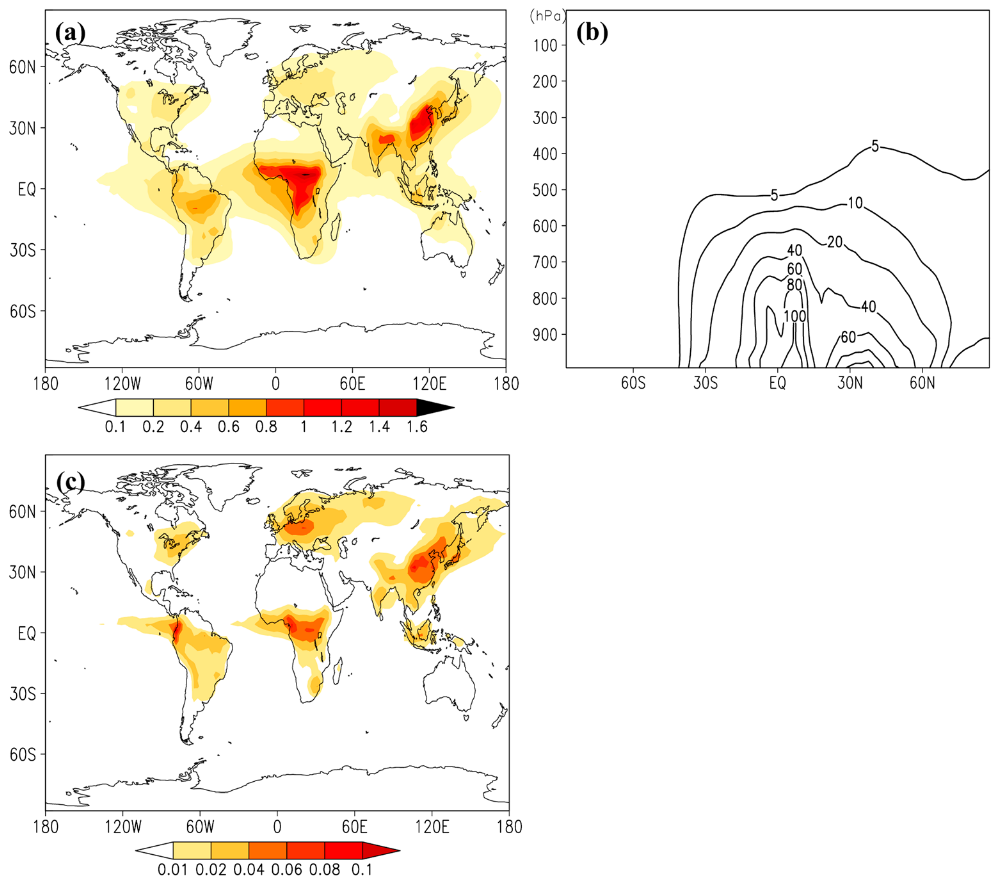

Figure 4. Annual mean distributions of simulated (a) column burden (unit: $mg\,m^{-2}$), (b) zonally averaged concentration (unit: $ng\,m^{-3}$) of total BC, and (c) column burden of BC within cloud droplets (unit: $mg\,m^{-2}$).

sensitive to the cloud droplet size, in particular for $\eta = 10^{-5}$. The enhancement ratios are in the range of 2–4 at 0.55 μm except for the case of large cloud droplets (e.g., Re = 20.0 μm) at $\eta = 10^{-5}$. *Chýlek et al.* [1996] found that the absorption of BC in a cloud droplet was increased by a factor of 2–2.5 at 550 nm. Also, the enhancement in absorption for a soot-water drop mixture was a factor of 2.5–4.5 at 635 nm measured by *Mikhailov et al.* [2006]. These are consistent with the results of Figure 3.

3.2. Distributions of the Simulated BC Concentration and η

[21] Figure 4(a) shows the annual mean distribution of the simulated BC burden. The maximum BC burdens appear over central Africa, South America, and East Asia. In particular, in eastern and northern China and India-Bengal, the maximum value is about 1.6 $mg\,m^{-2}$. There are also relatively large BC concentrations in eastern North America, West Europe, and Australia. The simulated global annual mean burden of BC is found to be 0.14 $mg\,m^{-2}$. The distribution and magnitude of the simulated BC concentration in this study are consistent with the results of other models in AeroCom (http://aerocom.met.no/cgi-bin/aerocom/surfobs_annualrs.pl). The BC aerosol is mainly located in the mid and low troposphere, and the highest concentrations appear over the surface layer close to the BC sources in tropical and subtropical regions of the Northern Hemisphere (NH). BC concentrations drop rapidly with height (Figure 4b). A similar vertical distribution of BC concentrations was provided by *Reddy and Boucher* [2004]. Figure 4(c) shows the annual mean distribution of the simulated column burden of BC within cloud droplets. Generally, the large in-cloud BC column burdens occur over the strong source regions. The global annual mean burden of BC within cloud droplets is about 0.006 $mg\,m^{-2}$, which is larger than the corresponding value of 0.0041 $mg\,m^{-2}$ estimated by *Jacobson* [2012].

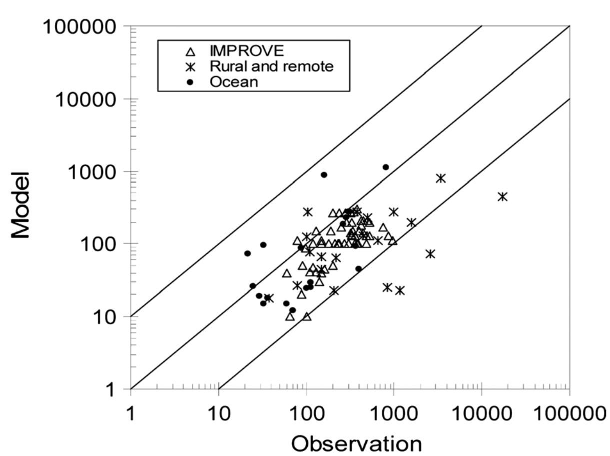

Figure 5. Comparisons of simulated BC concentrations with those measured (unit: $ng\,m^{-3}$). The symbols of triangle, asterisk, and dot represent the IMPROVE sites, rural and remote sites and marine sites [*Chung and Seinfeld*, 2002], respectively.

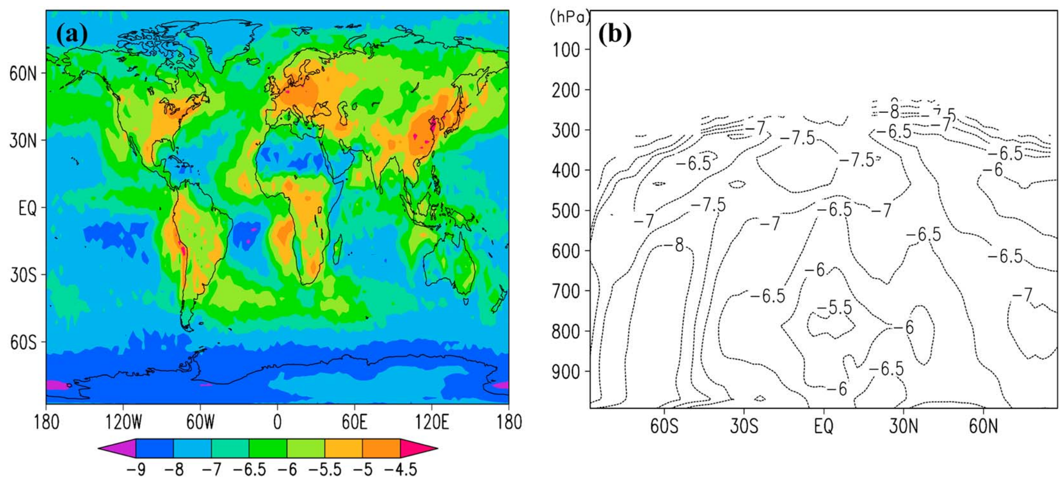

Figure 6. Annual mean distributions of simulated (a) $\log_{10}\eta$ at lowest model layer and (b) zonally averaged $\log_{10}\eta$.

[22] In Figure 5, the comparison of the simulated BC mass concentrations with the measured results is shown. The IMPROVE (Interagency Monitoring of Protected Visual Environments) monitoring network consists of aerosol, light scattering, light extinction, and scene samplers in a number of National Parks and Wilderness areas in the United States. The measured data in rural, remote, and marine sites are obtained from *Chung and Seinfeld* [2002]. All of them are surface measurements. It is seen that the magnitudes of the simulated BC concentration by our model agree reasonably with those of the measurements at most of these sites. However, the simulated values are less than the measured results at some rural and remote sites. This could be caused by various factors including the uncertainty in source emissions, the error of the observational instruments, the limitations in model resolution, and the implementation of

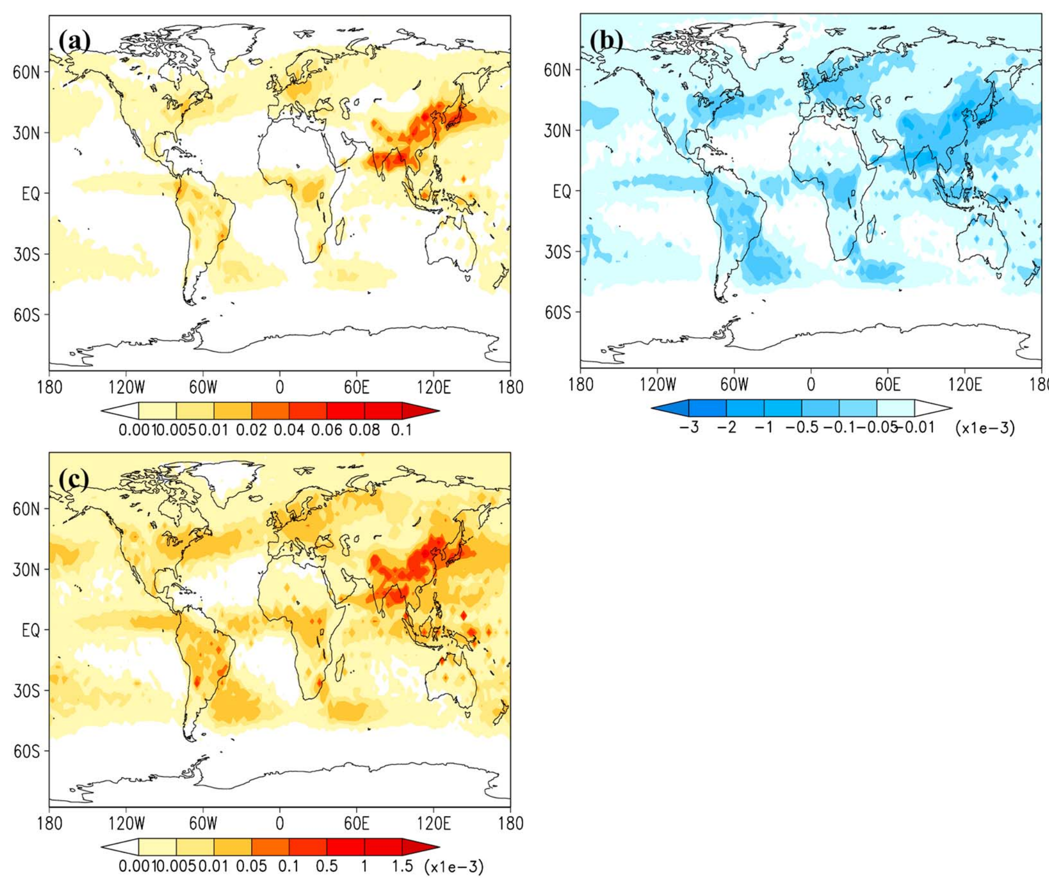

Figure 7. Annual mean changes of simulated cloud (a) column absorption optical depth, vertical averaged (b) SSA, and (c) asymmetry factor at 550 nm due to the internal mixture of BC in cloud droplets.

physical processes in the model. The underestimation of BC concentrations could cause an underestimation of the related radiative effect.

[23] Equation (2) indicates that the magnitude of η is determined by the BC mass concentrations, cloud water content, and cloud fraction. Figure 6a presents the annual mean global distribution of the simulated η at the lowest model layer in logarithmic scale. η is found in magnitude of 10^{-7} in most regions, especially over ocean. This is consistent with the results given by *Reddy and Boucher* [2004]. η reaches a magnitude of 10^{-5} in East Asia, West Europe, and the west coast of Africa with the maximum value approximating 4×10^{-5}. This is due to the high BC loading and large cloud fraction. It is seen from the vertical distribution of η in Figure 6b that the large values of η appear in the mid and low troposphere and the values drop rapidly with height. This is similar to the vertical distribution of BC concentrations.

3.3. Changes of the Simulated Cloud Optical Properties

[24] Figure 7 shows the annual mean changes of the simulated cloud optical properties at 550 nm, due to the presence of BC in cloud droplets. It is found in Figure 7a that the cloud absorption optical depth increases substantially in areas such as East Asia and South Asia, where the BC emission is large. The largest change of cloud column absorption optical depth can exceed 0.06 (Figure 7a). The decrease of cloud SSA primarily occurs in East Asia, South Asia, West Europe, eastern USA, central Africa, and South America, with the maximum change of -3.0×10^{-3} in North China (Figure 7b). The cloud asymmetry factor generally increases in the above areas with the maximum change up to 1.5×10^{-3}. The increase of asymmetry factor is caused by the weaker back scattering due to the enhancement of absorption by including BC (Figure 7c). It can be seen from Figure 7 that relatively small changes in cloud optical properties also occur over large ocean areas. We conclude that this is because of the long-distance transport of BC.

3.4. Radiative Forcing Due to Mixing of BC in Cloud Droplets

[25] The presence of BC in cloud droplets leads to an increase of solar absorption, thereby causing a positive radiative forcing at TOA. The simulated global annual mean radiative forcing at TOA is 0.086 W m^{-2}, which is larger than the results of 0.07 W m^{-2} obtained by *Chuang et al.* [2002] and 0.069 W m^{-2} obtained by *Zhuang et al.* [2010]. Though the global mean forcing is very small, the regional forcings can be much larger. They can even be comparable to the global annual mean direct radiative forcing (DRF) of BC at TOA, as shown by this model (Figure 8c). DRF is defined as the instantaneous change of net radiative flux at TOA for all sky from two calculations at each model time step. The first calculation accounts for BC radiative effect. In the second calculation, the concentration of BC is set to zero in model radiation algorithm. A positive forcing

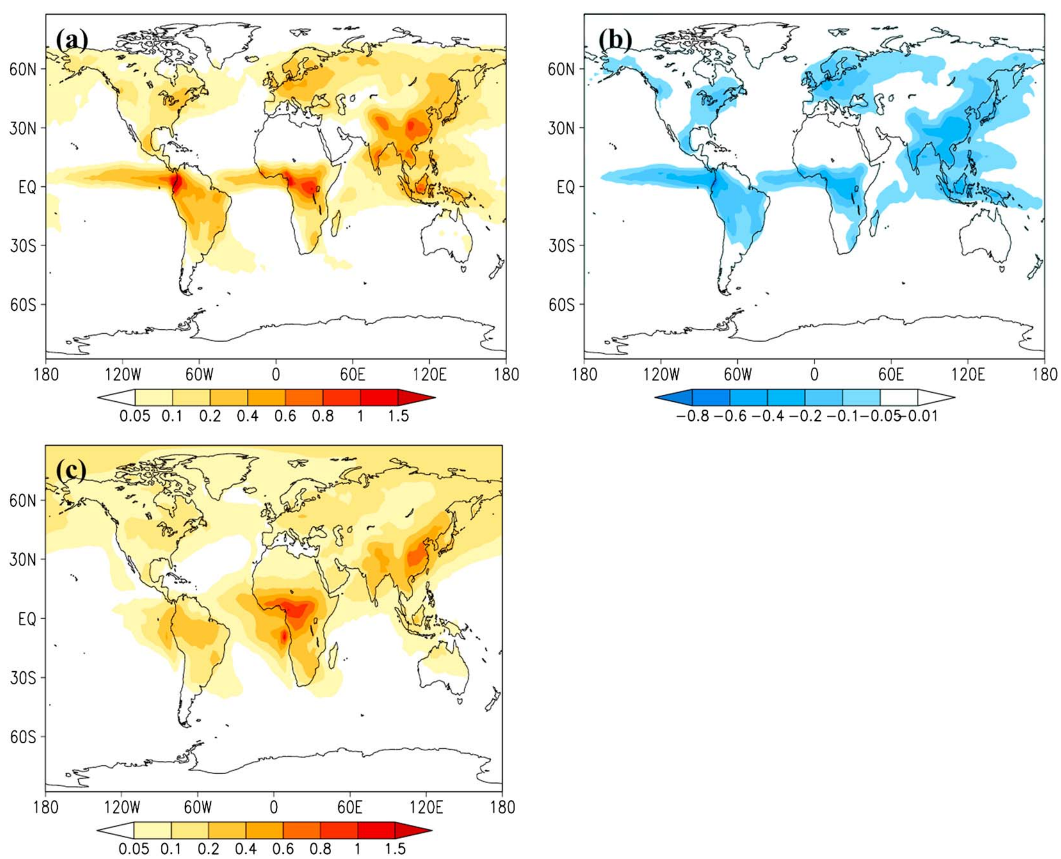

Figure 8. Annual mean distributions of simulated radiative forcing (a) at TOA and (b) surface due to the internal mixture of BC in cloud droplets and (c) direct radiative forcing of BC at TOA for all sky assuming all BC is interstitial (units: W m^{-2}).

exceeding 0.2 W m^{-2} occurs in most regions of East Asia, South Asia, West Europe, and eastern North America. This is particularly true in South America and Africa with a maximum forcing up to 1.5 W m^{-2}, as shown in Figure 8a. It is seen from Figure 8c that large BC DRF at TOA appears in East Asia, central Africa, Western Europe, eastern U.S., and South America, where the maximum value reaches approximately 1.0 W m^{-2}. The simulated global annual mean DRF of BC at TOA is 0.09 W m^{-2}. The downward solar radiation flux at the surface is decreased due to the increase in cloud absorption, thereby leading to a negative forcing at the surface (Figure 8b). The simulated global annual mean radiative forcing at the surface is -0.04 W m^{-2}. The negative forcing at the surface mainly appears in East Asia, South Asia, West Europe, eastern North America, and equatorial South America and Africa.

3.5. Climate Response

[26] Figure 9 shows the differences between EXP2 and EXP1 in global annual mean vertical profiles of several

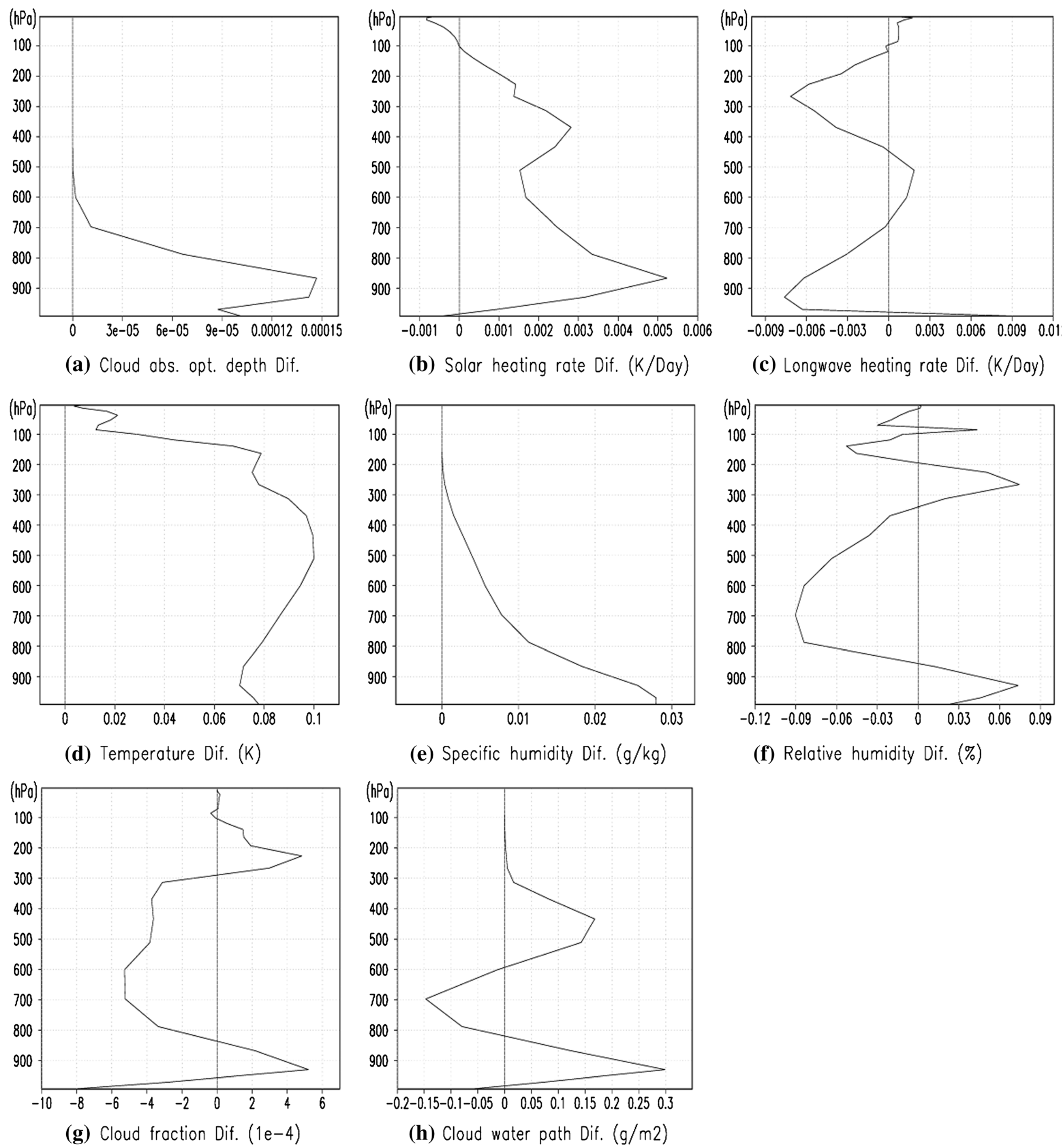

Figure 9. Simulated differences in global annual mean vertical profiles for several physical quantities between EXP2 and EXP1.

Table 1. Global Annual Mean Difference for Several Physical Quantities Between EXP2 and EXP1

Parameter	EXP1	Difference (EXP2-EXP1)
Surface temperature (K)	287.7	0.08*
550 nm column cloud optical depth	42.6	0.045
550 nm column cloud absorption optical depth	0.0003	0.0017*
Total cloud fraction	3.4	−0.004
Column cloud water path ($g\,m^{-2}$)	137.5	0.18*
Total water vapor ($g\,kg^{-1}$)	61.7	0.18*
Surface latent heat flux ($W\,m^{-2}$)	77.5	0.1
Precipitation ($mm\,day^{-1}$)	2.7	0.003
Net solar radiation flux at TOA ($W\,m^{-2}$)	230.3	0.21*

*Represents significance at ≥95% confidence level from the *t*-test. The column cloud optical depth and absorption optical depth, column cloud water path, total cloud fraction, and total water vapor are defined as the sum of the global mean results from each individual model layer, respectively.

physical quantities. The presence of BC in cloud droplets evidently decreases the cloud SSA in the low and mid troposphere, where BC is mainly located. This results in an increase in cloud absorption optical depth, with a maximum value exceeding 0.00014 at 550 nm (Figure 9a). The enhanced solar absorption by cloud droplets causes an obvious increase in solar heating rate and temperature in the troposphere (Figures 9b and 9d). The largest increase in global annual mean atmospheric temperature appears in the mid troposphere, with a maximum value close to 0.1 K. Also, the change in global annual mean temperature near the surface is 0.08 K. The increase in temperature causes more surface evaporation and enhances the water-holding capacity of the air. This leads to an increase in atmospheric water vapor amount (Figure 9e and Table 1). In turn, the water vapor in the atmosphere, which acts as greenhouse gas and solar energy absorber, can further warm the surface. This produces a positive feedback mechanism [*Jacobson*, 2006].

[27] The increase in absorption of solar radiation by cloud can change the atmospheric thermodynamics, which leads to changes in relative humidity and cloud fraction. These changes of temperature and water vapor lead to an increase in relative humidity and cloud fraction in the lower troposphere (Figures 9f and 9g). In the mid and higher troposphere, the increase in temperature causes a decrease in relative humidity and cloud fraction. From Figures 9f and 9g, it is seen that the cloud fraction is decreased corresponding to the reduction of relative humidity in the mid troposphere, though the cloud water path is increased in some altitudes. The changes of cloud fraction and cloud water path result in changes of longwave heating rate as well (Figures 9c and 9h).

[28] Table 1 shows the differences between EXP2 and EXP1 for several global annual mean physical quantities. BC in cloud droplets causes an increase in the cloud optical

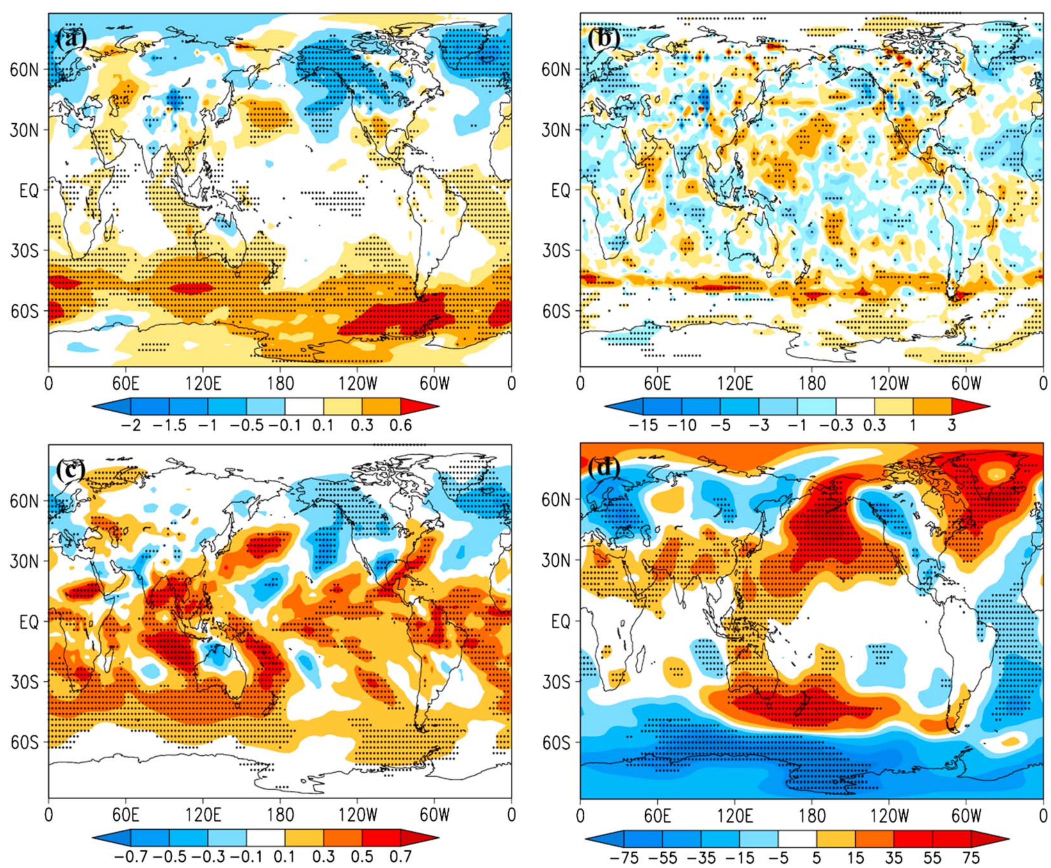

Figure 10. Annual mean distributions of simulated differences in (a) surface temperature (unit: K), (b) surface net radiation flux (unit: $W\,m^{-2}$), (c) column water vapor (unit: $g\,kg^{-1}$), and (d) surface pressure (unit: Pa) between EXP2 and EXP1. The dots represent significance at ≥95% confidence level from the *t*-test.

depth and absorption optical depth at 550 nm by 0.045 and 0.0017, respectively. Additionally, BC in cloud droplets causes a 0.4% decrease of cloud fraction, and an increase of 0.08 K in surface temperature. The local maximum changes in the annual mean surface temperature exceed −1.5 K and +0.6 K in NH and Southern Hemispheres (SH), respectively (Figure 10a). The changes in surface temperature mainly occur in the mid and high latitudes of both the NH and SH. It is seen from Figure 10b that the net radiative flux at the surface is lower in most of the mid and high latitudes of NH, especially in the northern Pacific and Atlantic, central Eurasia, Western Europe and western North America. This can lead to the decrease of surface temperature. The surface cooling in the NH causes less surface water evaporation and weakens the water-holding capacity of the air (Figure 10c). This kind of positive feedback effect further cools the atmosphere. Over most ocean areas in the mid latitudes of SH, the increase of surface net radiative flux is also consistent with the increase of surface temperature. This enhances the surface evaporation and the water-holding capacity of air in these areas (Figure 10c).

[29] The changes in surface temperature can also be interpreted from the vertical changes in cloud fraction shown in Figure 11a. In the NH, the effect of BC in cloud droplets results in an increase in low cloud fraction and a decrease in mid and high cloud fractions. The increase of low cloud fraction can cause more solar reflection, and the decrease of mid and high cloud fractions can cause more outgoing longwave radiation. Both effects can cool the surface temperature. In the SH, the change of cloud fraction is generally opposite to that of the NH, especially for the mid and high clouds. This could cause an increase in surface temperature. *Jacobson* [2006] also indicated that the increases of surface temperature in the SH are possibly due to the long-distance transport of BC and local feedback of clouds to large-scale meteorology. A response to changed atmospheric circulation may be the primary cause that leads to these changes in mid-to-high latitudes of SH.

[30] Figure 11 also shows the simulated annual mean differences in zonally averaged temperature and relative humidity between EXP2 and EXP1. In the NH, the decrease of the net radiation flux at the surface (Figure 11a) results in the decrease of surface temperature, which leads to less water vapor in the atmosphere due to weaker surface evaporation. This causes a decrease of tropospheric temperature since water vapor has strong greenhouse effect. It is shown in Figure 11b that the local zonally averaged near-surface temperature is reduced by 0.2 K near 60°N. However, the temperature is increased in other latitudes of the troposphere. The changes of tropospheric relative humidity are not always consistent with changes of temperature, but they are largely consistent with changes of cloud fraction (Figures 11a and 11c). The relative humidity is mainly decreased in the middle troposphere between 0°–60°N. This is probably due to a significant decrease of water vapor. It is increased in the most other regions.

[31] The local temperature changes cannot necessarily be explained by the local processes, but can be strongly influenced by the changes in heat transport. In Figure 10d,

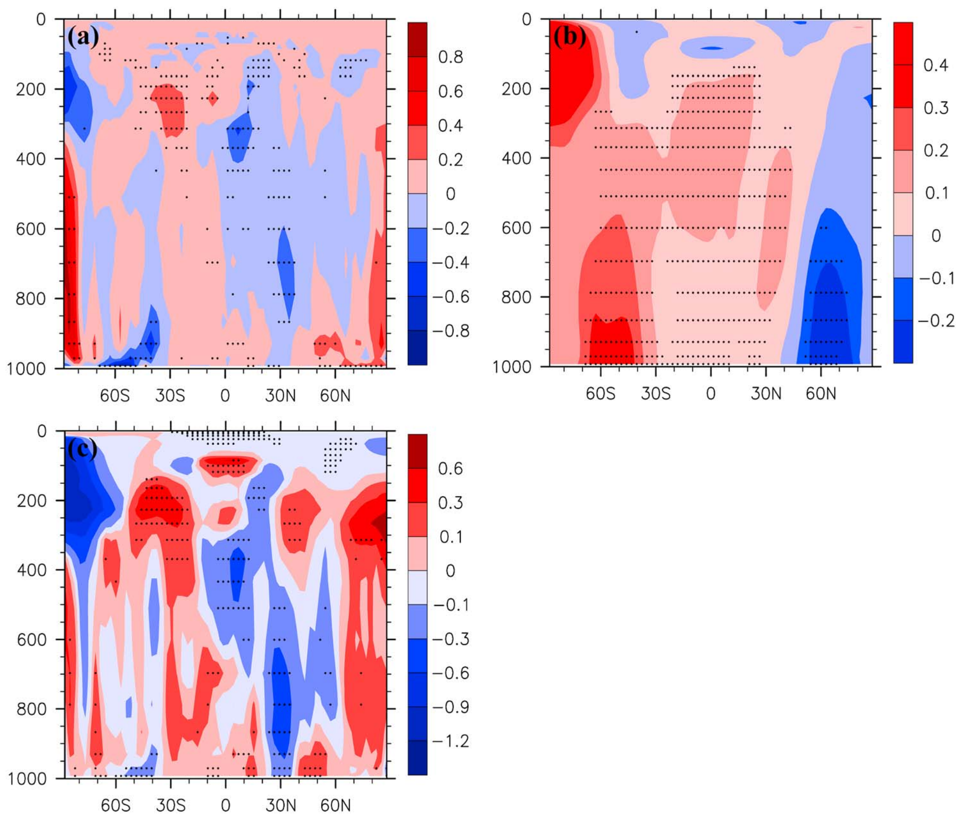

Figure 11. Simulated annual mean differences in zonally averaged (a) cloud fraction (%), (b) temperature (unit: K), and (c) relative humidity (unit: %) between EXP2 and EXP1. The vertical coordinate is pressure (unit: hPa). The dots represent significance at ≥95% confidence level from the *t*-test.

it is shown that BC in cloud droplets causes a decrease in surface pressure in northern USA, Western Europe and eastern Russia, but an increase in the North Pacific, Northwest Atlantic, and western Russia. This leads to the cold advections in northwestern USA, North Atlantic, and central Russia (Figure 12b), and pronounced cold anomalies in surface temperature in those regions (Figure 10a). There are also regions of positive temperature anomalies caused by warm advection due to changes in surface pressure at the high latitudes of NH (Figures 10a and 12b). Likewise, the change in the pressure gradient suggests a southward shift of the southern storm track in the SH. The warm anomalies at the high latitudes of SH (~60°S) are more likely the result of heat transport by baroclinic eddies penetrating further south. The changes of meridional circulation also show the southward moving of cold or warm air (Figure 12). The clockwise circulations appearing in the mid and high latitudes of NH can cause the ascending motion developed between 40°N and 60°N and the descending motion in Arctic, which leads to an increase of southward transport of cold air in the lower troposphere. A similar circulation occurs in the mid and high latitudes of SH, which leads to an increase of southward transport of warm anomalies. Figure 13 shows the zonally averaged change in total atmospheric heat transport due to BC inclusions in cloud droplets. It is seen that BC in cloud droplets induces an increase of total heat transport significantly from the tropics to the high latitudes of SH and a decrease of total heat transport to the extratropics of NH. The changes of heat transport result in a warming effect in the SH and a cooling effect in the NH. Furthermore, the warming/cooling effect can have feedback on surface temperature.

[32] In summary, the presence of BC in cloud droplets leads to more absorption of solar radiation by cloud, which directly affects the vertical distributions of cloud and water vapor. Thus, the net radiation flux arriving at surface is influenced, as the net radiation at surface is decreased significantly in the northern Pacific and Atlantic, central Eurasia, and western North America. This leads to a change in surface temperature in those regions. The changes in thermodynamics can have an influence on atmospheric circulation and heat transport. The result of heat transport helps to understand the warming/cooling effect in the SH/NH.

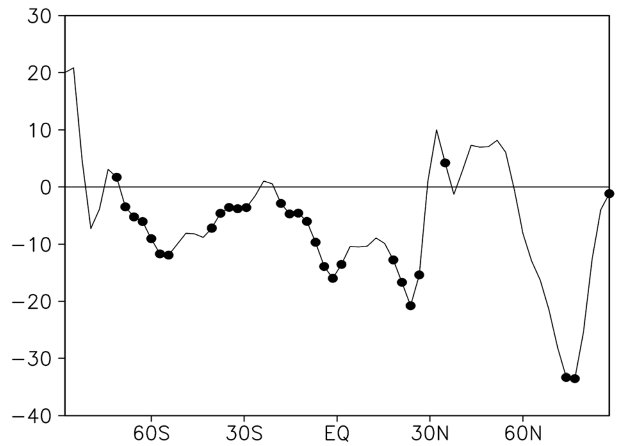

Figure 13. Simulated annual mean difference in zonally averaged total atmospheric heat transport between EXP2 and EXP1 (unit: $\mathrm{K\,m\,s^{-1}}$). The dots represent significance at ≥95% confidence level from the *t*-test.

[33] Figure 14 shows the simulated annual mean differences of precipitation between EXP2 and EXP1. The precipitation decreases in most tropical regions of NH, while it mainly increases in the tropical areas of SH. The largest change of precipitation appears in the tropical Pacific and Indian Oceans, with a maximum increase (decrease) up to $\pm 0.4\,\mathrm{mm\,day^{-1}}$ (Figure 14a). It is noted that the change of the annual mean surface temperature is +0.19 K in the SH and −0.04 K in the NH. This interhemispheric asymmetry in surface temperature change can significantly affect the atmospheric dynamics. Thus, the northern trade winds are enhanced in the Intertropical Convergence Zone (ITCZ), and the northerly surface wind anomalies cross the equator to converge with the enhanced southern trade winds in the tropics of SH (Figure 12b). Therefore, the enhancing (weakening) of the vertical ascending motion and precipitation appears on the south (north) side of

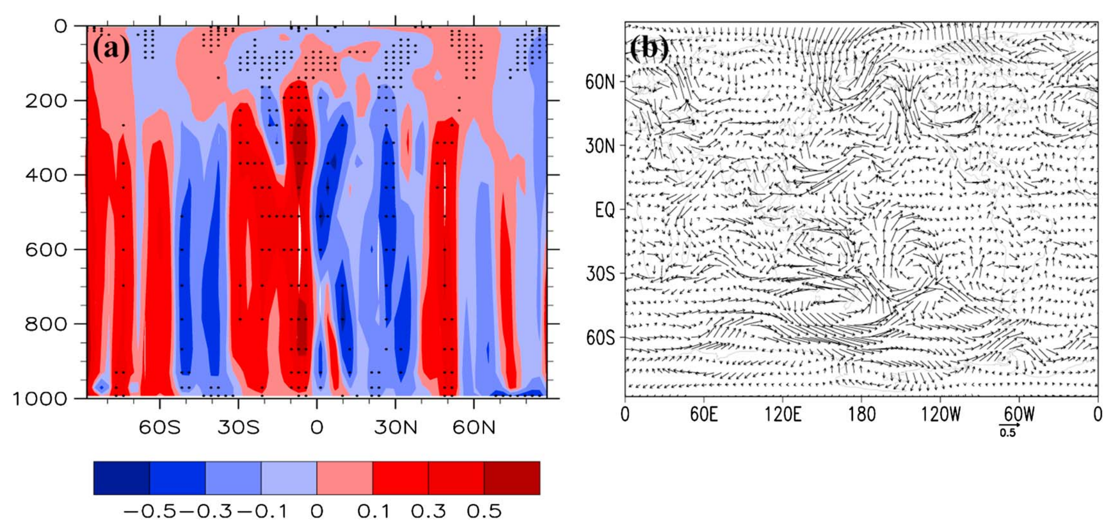

Figure 12. Simulated annual mean differences in (a) zonally averaged vertical velocity (unit: $-10^{-3}\mathrm{Pa\,s^{-1}}$) and (b) global wind field at 850 hPa (unit: $\mathrm{m\,s^{-1}}$) between EXP2 and EXP1. The vertical coordinate in left panel is pressure (unit: hPa). The dots represent significance at ≥95% confidence level from the *t*-test.

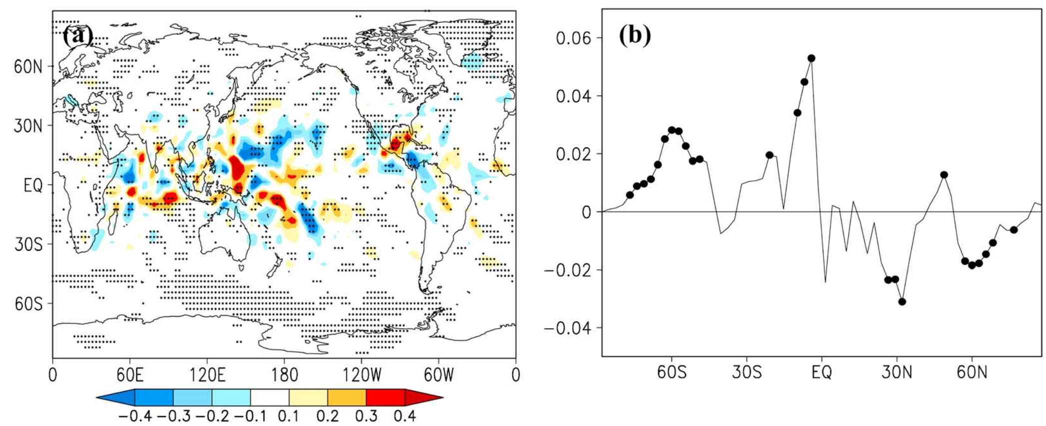

Figure 14. Simulated annual mean differences of (a) global and (b) zonally averaged precipitation (unit: mm dayP^{-1P}) between EXP2 and EXP1. The dots represent significance at ≥95% confidence level from the *t*-test.

equator (Figure 12a). This possibly induces a southward shift in the tropical rainfall maximum related to the ITCZ. This is consistent with the hypothesis that the ITCZ should move toward the relatively warmer hemisphere in response to surface temperature changes [*Broccoli et al*., 2006]. It is worth noting that the enhanced SH warming and southward shift of the ITCZ in these simulations are opposite of what has actually occurred during recent decades.

4. Conclusions

[34] The purpose of this work is to study the radiative forcing and climate impact due to the changes of cloud optical properties by BC in cloud droplets. In contrast to previous works on this topic, our study is based on the accurate calculation of cloud optical properties from the MG mixing rule and Mie theory. The obtained cloud optical properties are then applied to an interactive system coupling, a GCM with an aerosol model. We are then able to investigate the radiative forcing and the equilibrium climate response due to BC in cloud droplets.

[35] The presence of BC in cloud droplets leads to a positive radiative forcing at TOA. The simulated global annual mean forcing at TOA is 0.086 W m^{-2}. The local radiative forcing can be much larger. The forcing exceeds 0.2 W m^{-2} in most regions of East Asia, South Asia, West Europe, and eastern North America, especially in South America and Africa where the maximum forcing reaches 1.5 W m^{-2}. The downward solar radiation flux at the surface inevitably decreases due to the increase of cloud absorption, thereby leading to the negative forcing at the surface.

[36] The increase in solar absorption when BC is present in cloud droplets causes an increase in solar heating rate and temperature in troposphere. The largest increase in global annual mean atmospheric temperature of approximate 0.1 K appears in the mid troposphere. The global mean surface temperature is increased by 0.08 K. The increase in temperature causes a higher surface evaporation, a larger water-holding capacity of the air, and a lower cloud fraction. All of these cause the further warming of the atmosphere. This process produces a positive feedback mechanism.

[37] The changes in annual mean surface temperature, due to BC in cloud droplets, mainly occur in the mid and high latitudes of both Hemispheres. In the NH, this effect results in an increase of low cloud fraction and a decrease of mid and high cloud fractions. The increase in low cloud causes more solar reflection, and the decrease in mid and high cloud fractions causes more outgoing longwave radiation. Both can cool the surface temperature. The surface cooling in the NH causes less surface water evaporation and weakens the water-holding capacity of the air in these areas. This kind of positive feedback further cools the atmosphere. In the SH, the change of cloud fraction is generally opposite to that of the NH, especially for the mid and high clouds, which could cause the increase of surface temperature.

[38] From the perspective of heat transport, it is found that BC in cloud droplets induces an increase of heat transport from the tropics to the high latitudes of SH and a decrease from the equator to the extratropics of NH. This leads a warming effect in the SH and a cooling effect in the NH.

[39] There are significant changes of surface temperature in the SH and NH (+0.19 K and −0.04 K, respectively). The interhemispheric asymmetry in surface temperature changes causes significant changes in atmospheric dynamics and precipitation. In the ITCZ, the northern trade winds are strengthened, and the northerly surface wind anomalies cross the equator and converge with the enhanced southern trade winds in the tropics of SH. This results in an increase (a decrease) of vertical ascending motion and precipitation on the south (north) side of equator. This can possibly induce a southward shift in the tropical rainfall maximum related to the ITCZ.

[40] **Acknowledgments.** The authors would like to thank three anonymous reviewers and Editor Dr. Steven Ghan for their constructive comments. This work was financially supported by National Basic Research Program of China (2011CB403405), National Natural Science Foundation of China (41205116), and CAMS Basis Research Project (2012Y003).

References

Bond, T. C., E. Bhardwaj, R. Dong, R. Jogani, S. K. Jung, C. Roden, D. G. Streets, and N. M. Trautmann (2007), Historical emissions of black and organic carbon aerosol from energy-related combustion, 1850–2000, *Global Biogeochem. Cycles*, *21*, GB2018, doi:10.1029/2006GB002840.

Broccoli, A. J., K. A. Dahl, and R. J. Stouffer (2006), Response of the ITCZ to Northern Hemisphere cooling, *Geophys. Res. Lett.*, *33*, L01702, doi:10.1029/2005GL024546.

Chuang, C. C., J. E. Penner, J. M. Prospero, K. E. Grant, G. H. Rau, and K. Kawamoto (2002), Cloud susceptibility and the first aerosol indirect forcing: Sensitivity to black carbon and aerosol concentrations, *J. Geophys. Res.*, *107*(D21), 4564, doi:10.1029/2000JD000215.

Chung, S. H., and J. H. Seinfeld (2002), Global distribution and climate forcing of carbonaceous aerosols, *J. Geophys. Res.*, *107*, 4407, doi:10.1029/2001JD001397.

Chung, S. H., and J. H. Seinfeld (2005), Climate response of direct radiative forcing of anthropogenic black carbon, *J. Geophys. Res.*, *110*(D11102), doi:10.1029/2004JD005441.

Chýlek, P., V. Ramaswamy, and R. J. Cheng (1984), Effect of graphitic carbon on the albedo of clouds, *J. Atmos. Sci.*, *41*, 3076–3084.

Chýlek, P., V. Srivastava, R. G. Pinnick, and R. T. Wang (1988), Scattering of electromagnetic waves by composite spherical particles: Experiment and effective medium approximations, *Appl. Opt.*, *27*, 2396–2404, doi:10.1364/AO.27.002396.

Chýlek, P., G. B. Lesins, G. Videen, J. G. D. Wong, R. G. Pinnick, D. Ngo, and J. D. Klett (1996), Black carbon and absorption of solar radiation by clouds, *J. Geophys. Res.*, *101*, 23365–23371, doi:10.1029/96JD01901.

Cooke, W. F., V. Ramaswamy, and P. Kasibhatla (2002), A general circulation model study of the global carbonaceous aerosol distribution, *J. Geophys. Res.*, *107*, 4279, doi:10.1029/2001JD001274.

D'Almeida, G. A., P. Koepke, and E. P. Shettle (1991), Atmospheric Aerosols: global climatology and radiative characteristics, A. Deepak Publishing, 561 pp, Virginia, U.S.A.

Dentener, F., et al. (2006), Emissions of primary aerosol and precursor gases in the years 2000 and 1750 prescribed data-sets for AeroCom, *Atmos. Chem. Phys.*, *6*, 4321–4344, doi:10.5194/acp-6-4321-2006.

Dobbie, J. S., J. Li, and P. Chýlek (1999), Two- and four-stream optical properties for water clouds and solar wavelengths, *J. Geophys. Res.*, *104*(D2), 2067–2079, doi:10.1029/1998JD200039.

Flanner, M. G., X. Liu, C. Zhou, J. E. Penner, and C. Jiao (2012), Enhanced solar energy absorption by internally-mixed black carbon in snow grains, *Atmos. Chem. Phys.*, *12*, 4699–4721, doi:10.5194/acp-12-4699-2012.

Forster, P., et al. (2007), Changes in atmospheric constituents and in radiative forcing, in Climate Change 2007: The Physical Science Basis. Contribution of Working Group I to the Fourth Assessment Report of the Intergovernmental Panel on Climate Change, edited by S. Solomon et al., pp. 131–234, Cambridge Univ. Press, Cambridge, U. K.

Ghan, S. J., X. Liu, R. C. Easter, R. Zaveri, P. J. Rasch, J.-H. Yoon, and B. Eaton (2012), Toward a minimal representation of aerosols in climate models: Comparative decomposition of aerosol direct, semidirect, and indirect radiative forcing, *J. Climate*, *25*, 6461–6476, doi:http://dx.doi.org/10.1175/JCLI-D-11-00650.1.

Giorgi, F., and W. L. Chameides (1986), Rainout lifetimes of highly soluble aerosols and gases as inferred from simulations with a general circulation model, *J. Geophys. Res.*, *91*, 14367–14376, doi:10.1029/JD091iD13p14367.

Gong, S. L., L. A. Barrie, and M. Lazare (2002), Canadian Aerosol Module (CAM): A size-segregated simulation of atmospheric aerosol processes for climate and air quality models 2. Global sea-salt aerosol and its budgets, *J. Geophys. Res.*, *107*(D24), 4779, doi:10.1029/2001JD002004.

Gong, S. L., et al. (2003), Canadian Aerosol Module: A size-segregated simulation of atmospheric aerosol processes for climate and air quality models 1. Module development, *J. Geophys. Res.*, *108*, 4007, doi:10.1029/2001JD002002.

Gustafson Jr., W. I., E. G. Chapman, S. J. Ghan, R. C. Easter, and J. D. Fast (2007), Impact on modeled cloud characteristics due to simplified treatment of uniform cloud condensation nuclei during NEAQS 2004, *Geophys. Res. Lett.*, *34*, L19809, doi:10.1029/2007GL030021.

Hansen, J., A. Lacis, D. Rind, G. Russell, P. Stone, I. Fung, R. Ruedy, and J. Lerner (1984), Climate sensitivity: Analysis of feedback mechanisms, in Climate Processes and Climate Sensitivity, edited by J. E. Hansen, and T. Takahashi, 130–163, Amer. Geophys. Union, Washington, D.C.

Hansen, J., et al. (2005), Efficacy of climate forcings, *J. Geophys. Res.*, *110*, D18104, doi:10.1029/2005JD005776.

Jacobson, M. Z. (2002), Control of fossil-fuel particulate black carbon plus organic matter, possibly the most effective method of slowing global warming, *J. Geophys. Res.*, *107*(D19), 4410, doi:10.1029/2001JD001376.

Jacobson, M. Z. (2006), Effects of externally-through-internally-mixed soot inclusions within clouds and precipitation on global climate, *J. Phys. Chem.*, *110*(21), 6860–6873, doi:10.1021/jp056391r.

Jacobson, M. Z. (2012), Investigating cloud absorption effects: Global absorption properties of black carbon, tar balls, and soil dust in clouds and aerosols, *J. Geophys Res.*, *117*, D06205, doi:10.1029/2011JD017218.

Jing, X. W., and H. Zhang (2012), Application and evaluation of McICA cloud-radiation framework in the GCM of the National Climate Center, *Chin. J. Atmos. Sci.*, *35*(5), doi:10.3878/j.issn.1006-9895.2012.11155.

Li, J., E. Mlawer, and P. Chýlek (2011), Parameterization of cloud optical properties for semidirect radiative forcing, *J. Geophys. Res.*, *116*, D23212, doi:10.1029/2011JD016611.

Li, J., K. von Salzen, Y. Peng, H. Zhang, and X. Liang (2013), Evaluation of black carbon semi-direct radiative effect in a climate model, *J. Geophys. Res.*, doi:10.1002/jgrd.50327.

Lohmann, U., and J. Feichter (2005), Global indirect aerosol effects: A review, *Atmos. Chem. Phys.*, *5*, 715–737, doi:10.5194/acp-5-715-2005.

Lu, Z., D. G. Streets, Q. Zhang, S. Wang, G. R. Carmichael, Y. F. Cheng, C. Wei, M. Chin, T. Diehl, and Q. Tan (2010), Sulfur dioxide emissions in China and sulfur trends in East Asia since 2000, *Atmos. Chem. Phys.*, *10*, 6311–6331, doi:10.5194/acpd-10-8657-2010.

Marticorena, B., and G. Bergametti (1995), Modeling the atmospheric dust cycle. 1: Design of a soil-derived dust emission scheme, *J. Geophys. Res.*, *100*, 16415–16430, doi:10.1029/95JD00690.

Menon, S., J. Hansen, L. Nazarenko, and Y. F. Luo (2002), Climate effects of black carbon aerosols in China and India, *Science*, *297*, 2250–2253.

Mikhailov, E. F., S. S. Vlasenko, I. A. Podgorny, V. Ramanathan, and C. E. Corrigan (2006), Optical properties of soot-water drop agglomerates: An experimental study, *J. Geophys. Res.*, *111*, D07209, doi:10.1029/2005JD006389.

Pruppacher, H. R., and J. D. Klett (1997), Microphysics of Clouds and Precipitation, Kluwer Academic Publishers, 954 pp, Norwell, Mass.

Ramanathan, V., and G. Carmichael (2008), Global and regional climate changes due to black carbon, *Nat. Geosci.*, *1*(4), 221–227.

Reddy, M. S., and O. Boucher (2004), A study of the global cycle of carbonaceous aerosols in the LMDZT general circulation model, *J. Geophys. Res.*, *109*, D14202, doi:10.1029/2003JD004048.

Roberts, D. L., and A. Jones (2004), Climate sensitivity to black carbon aerosol from fossil fuel combustion, *J. Geophys. Res.*, *109*, D16202, doi:10.1029/2004JD004676.

Shindell, D., et al. (2012), Simultaneously mitigating near-term climate change and improving human health and food security, *Sciences*, *335* (13), 183–188.

Slinn, W. G. N. (1984), Precipitation scavenging, in Atmospheric Science and Power Production, edited by D. Randerson, Doc. DOE/TIC-27601, pp. 466–532, Tech. Inf. Cent., Off. of Sci. and Tech. Inf., U.S. Dep. Of Energy, Washington, D. C.

Stroud, D., and F. P. Pan (1978), Self-consistent approach to electromagnetic wave propagation in composite media: Application to model granular metals, *Phys. Rev.*, *B17*, 1602–1610.

Wu, T., R. C. Yu, F. Zhang, Z. Z. Wang, M. Dong, L. Wang, X. Jin, D. Chen, and L. Li (2010), The Beijing Climate Center atmospheric general circulation model: Description and its performance for the present-day, *Clim. Dyn.*, *34*, 123–147, doi:10.1007/s00382-009-0594-8.

Zhang, H., and Z. Wang (2011), Advances in the study of black carbon effects on climate, *Adv. Clim. Change Res.*, *2*(1), doi:10.3724/SP. J.1248.2011.00023.

Zhang, H., T. Nakajima, G.-Y. Shi, T. Suzuki, and T. Imasu (2003), An optimal approach to overlapping bands with correlated k-distribution method and its application to radiative calculations, *J. Geophy. Res.*, *108*, doi:10.1029/2002JD003358.

Zhang, H., G.-Y. Shi, T. Nakajima, and S. Tsuneaki (2006a), The effect of the choice of the k-interval number on radiative calculation, *J. Quant. Spectro. Rad. Trans.*, *98*, 31–43, doi:10.1016/j.jqsrt.2005.05.090.

Zhang, H., T. Suzuki, T. Nakajima, G.-Y. Shi, X.-Y. Zhang, and Y. Liu (2006b), Effects of band division on radiative calculations, *Opt. Eng.*, *45*(1), 016002, doi:10.1117/1.2160521.

Zhang, H., et al. (2012), Simulation of direct radiative forcing of typical aerosols and their effects on global climate using an online AGCM-aerosol coupled model system, *Clim. Dyn.*, *38*, 1675–1693, doi:10.1007/s00382-011-1131-0.

Zhuang, B. L., L. Liu, F. H. Shen, T. J. Wang, and Y. Han (2010), Semidirect radiative forcing of internal mixed black carbon cloud droplet and its regional climatic effect over China, *J. Geophys. Res.*, *115*, D00K19, doi:10.1029/2009JD013165.

第 24 卷 第 5 期
2013 年 10 月

应 用 气 象 学 报
JOURNAL OF APPLIED METEOROLOGICAL SCIENCE

Vol. 24, No. 5
October 2013

吴焕萍,张永强,孙家民,等. 气候信息交互显示与分析平台(CIPAS)设计与实现. 应用气象学报,2013,24(5):631-640.

气候信息交互显示与分析平台(CIPAS)设计与实现

吴焕萍* 张永强 孙家民 邵鹏程

(国家气候中心 中国气象局气候研究开放实验室,北京 100081)

摘 要

气候信息交互显示与分析平台(CIPAS)设计为面向气候监测、诊断、预测等基础业务支撑系统。CIPAS 设计了面向气候业务应用的集约化基础数据环境,内容涵盖全时间序列的地面常规观测、指数资料、再分析资料以及数值预报产品等,并提供基于要素、层次、时间、范围、种类等查询参数的统一、简单的访问接口(API);CIPAS 设计采用多层次分布式架构并形成轻量级客户端,而客户端则采用组件化和插件化设计方法,涵盖数据、图形、分析处理、版面制图、配置管理等核心组件,形成可扩展和组装的基础业务功能模块及二次开发接口,并以工具箱的形式提供各种气候业务分析能力,如 EOF,SVD 等诊断分析工具。该文重点对 CIPAS 的建设原则、总体框架、主要功能、运行流程等设计进行详细介绍,并对平台实现所涉及的若干关键技术问题进行深入分析。CIPAS 初步具备了气候资料综合检索、多维显示、统计诊断分析产品生成等综合业务功能,其建设成果在国家级和试点省份的试用显示其较好的业务应用能力与发展前景。

关键词: 气候监测预测;人机交互;数据管理

引 言

国家气候中心作为国家级业务单位,承担着国家级气候、气候变化业务和对省级气候业务部门工作指导责任,经过多年发展已逐步建成了集气候系统监测、气候诊断、气候预测、气候影响评估和气候变化研究为一体的业务科研支撑体系。但随着现代气候业务的不断发展,这种以现代气象资料综合应用和气候综合信息分析处理为技术支撑的发展思路,表现出了基础信息平台支撑能力严重不足。

从国家级业务系统建设与应用来看,尽管不同规模和数量、种类的业务系统也在不断发展,但由于缺乏良好的顶层设计、配套的信息化标准与规范以及持续性发展,多年来一直未能形成面向气候监测预测等全国性基础业务的应用支撑平台。从国内外天气领域业务系统发展模式来看,美国 AWIPS、德国 NinJo、欧洲中心 MetView/Magics++、法国 Synergie、挪威 Diana 以及中国 MICAPS 等[1-3],均坚持了基础性平台不断持续发展版本升级的长期发展思路,并朝着集约化、自动化、专业化、规范化、流程化、标准化、开放性等方向不断改进。气候业务虽然属于典型的科研型业务,但天气领域的业务系统发展思路仍值得借鉴。同时也关注到国外的一些较为成熟的气候业务和科研系统,如美国大气海洋局 NOAA 地球系统实验室(ESRL)开发的在线气候分析系统(PSD Interactive Plotting and Analysis Pages)[4],美国国际气候研究院 IRI 的 CPT(Climate Predictability Tool)[5],美国能源部科学办公室资助下的气候模式诊断和分析小组的 CDAT (Climate Data Analysis Tools)[6],以及日本东京气候中心 TCC 的 ITACS(Interactive Tool for Analysis of Climate System)[7],无论是系统框架、功能还是技术发展方向这些系统均值得借鉴。

国家气候中心于 2010 年底启动了面向气候监测、诊断、预测等基本业务的气候信息交互显示与分析平台(Climate Interactive Plotting and Analysis System,CIPAS)的建设[8],并立足于全国现代气候业

2012-10-19 收到, 2013-05-06 收到再改稿。
资助项目:国家科技支撑计划项目(2009BAC51B05)
* email: whp@pku.org.cn

务基础业务需求[9-12]，着力实现软件设计通用化、数据共享集约标准化、系统结构网络化、交互工具人性化等基础目标。本文对CIPAS的建设原则、总体框架、主要功能、运行流程进行详细介绍，同时对平台实现所涉及的若干关键技术问题进行深入分析，最后也给出应用案例和未来发展方向。

1　总体框架及主要功能

1.1　设计思路

CIPAS是集气候监测、诊断、预测等功能于一体的基础业务平台，属于功能较为齐全、应用较为复杂、用户范围较为广泛的综合应用系统，并将通过不断的滚动发展逐步满足全国气候业务部门的气候资料综合检索、多维显示、统计诊断分析、产品生成、信息标准化，并兼顾系统运行维护、平台定制和二次开发等多类用户的多层次需求。CIPAS的建设与规划将遵循总体设计、分步实施，统一环境、规范业务，技术先进、安全可靠的基本设计思路。

总体设计，分步实施。CIPAS进行全面统筹规划，做好顶层设计，进而分步骤实施。优先考虑系统架构的合理设计，在此基础上逐步进行各功能组件及系统接口的深化设计，使组件之间实现高内聚、低耦合，力求形成为一个布局合理、功能完备、能力均衡、分工明确的平台。

统一环境，规范业务。CIPAS应用的核心思想是“统一”，包括统一业务标准、数据环境、软件架构、技术实现、软硬件环境等，进一步规范气候业务操作与流程，实现国家级、省级两级灵活部署和分布式应用的气候综合业务平台。

技术先进，安全可靠。CIPAS建设充分借鉴信息技术发展前沿，综合运了数据库、三维可视化、地理信息系统（GIS）、分布式计算等多项信息技术[13-16]，并遵循稳定性（7×24 h运行稳定）、可扩展性（功能、数据、可视化、用户界面等）、可配置性、跨平台性（跨操作系统和硬件环境等能力）、标准性和规范性等设计原则。

1.2　总体框架

面向气候监测、诊断、预测等基本业务需求，采用自顶向下、分层设计、逐步求精的设计思路，将CIPAS功能设计划分为面向数据库及应用服务器、业务应用服务器、窗口程序三大实体组件，如图1所示，它是一种典型的多层体系结构。

表现层是平台面向用户的人机交互部分，其主要表现形式为客户端窗口界面程序（GUI），覆盖了面向用户的所有功能，业务用户可以通过客户端窗

图1　CIPAS总体框架图

Fig.1　Framework of CIPAS

口程序与平台进行交互式操作，实现监测预测业务功能。

应用层是平台的中间层，由气候业务相关组件组成，包括监测、预测、诊断分析算法、数据访问、可视化、输出等基础组件，以及数据访问、自动执行引擎、流程定制、任务调度等面向产品自动生成的扩展组件。应用层除了完成需要后台自动分析处理的应用并负责与数据层接口访问外，还接受来自于表现层窗口程序的调用，如一些在线气候诊断分析功能的具体实现。

数据层是平台的数据库、文件系统及相应管理系统，有利于数据的安全访问和屏蔽数据源不同对业务逻辑层的影响。数据层主要存储多类基础数据，如观测资料、指数资料、模式资料、预报预测资料等，同时包括了这些数据的采集、处理、入库、分发等等基本功能。

标准规范主要包括了形成 CIPAS 信息化要求的统一的气候数据、存储、交换、应用、产品和管理等各方面的标准和规范；技术体系包括了系统建设实施中所需要遵循和应用的一系列软、硬件支持环境。

1.3　主要功能

结合 CIPAS 提出的总体框架，并满足气候资料综合检索、多维显示、统计诊断分析、产品生成等业务需求，其系统的主要功能设计如图 2 所示，客户端主界面见图 3。

数据支持：CIPAS 设计支持多种数据格式。支持 NetCDF，HDF，GRIB1/2，CTL 二进制(GRADS)等多维数据模型存储的气候数据，如 NCEP 再分析资料通常采用 NetCDF 格式，而国内的 T639 等模式资料采用 GRIB 格式；CIPAS 兼容 MICAPS 多类文件格式，如地面、高空填图、观测站、格点、预报员交互等数据，以最大化接入 MICAPS 数据服务器中大量的资料；此外，CIPAS 对地理信息如 Shape file 矢量、GeoTiff 影像等格式得到了较好支持，以实现精细化的地理信息接入。

地图管理：地图管理支持地图缩小、地图放大、地图漫游、地图全屏、投影变换、空间显示范围设置、地图背景设置等操作，图层管理支持图层新建、移动、删除、叠加、空间显示范围设置等操作，上述功能实现了各种气候信息与基础地理信息等无缝高效集成精细化显示与管理。此外，CIPAS 设计还支持了多窗口及联动显示，以方便预报员进行多种资料的对比显示与分析。

综合显示：CIPAS 设计充分考虑了气候业务产品显示要求，还充分兼容了 MICAPS 显示方式。主要显示类型包括地面填图、高空填图、站点图、等值线图、色斑图、格点图、风场图、流场图、剖面图、曲线图等。其中，曲线实现支持 CIPAS 数据库文件以及本地文件的显示并提供历年值、多年滑动、平均值、

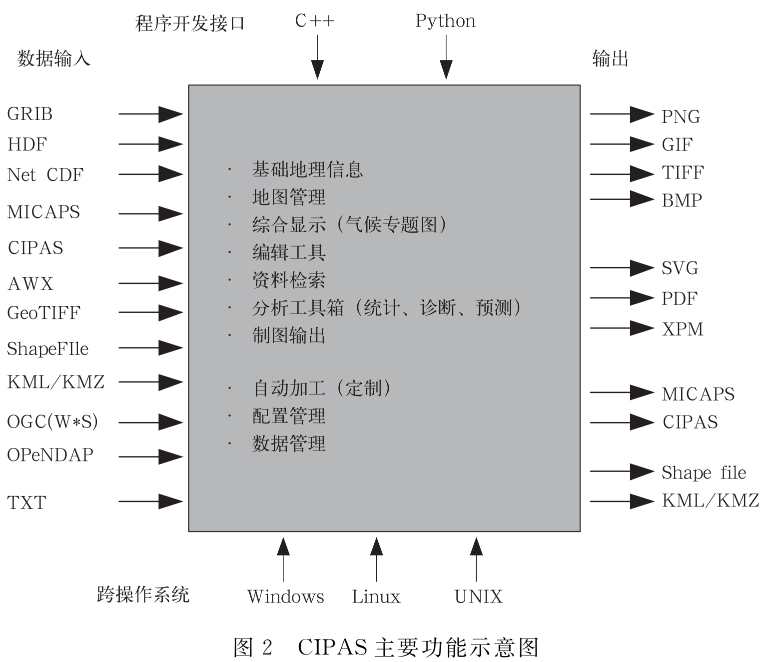

图 2　CIPAS 主要功能示意图

Fig. 2　Main features of CIPAS

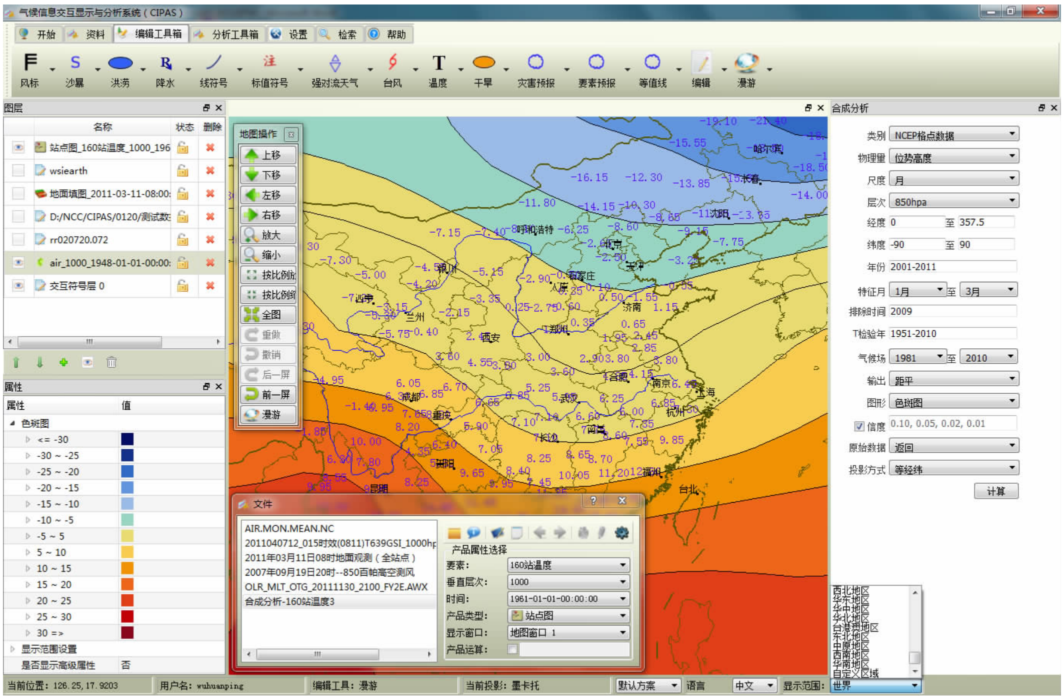

图 3 CIPAS 客户端主界面示意图

Fig. 3 Main user interface of CIPAS client

距平值等多种信息显示。此外，CIPAS 还支持类 GIS 方式的专题图显示，如按唯一、分类等显示、文字标注等操作，以最大化地提高气候业务产品的可视化水平。

资料检索：客户端支持用户通过快速定制 CIPAS 数据环境和 MICAPS 服务器中的数据文件来实现各类资料的快速浏览，定制资料可以通过综合显示功能提供给用户可视化查看分析。

编辑与订正工具：支持通用的等值线、线条、文字、落区(封闭多边形)绘制，支持常用天气气候现象符号绘制，支持气候常用灾害现象绘制，同时支持修改、移动、删除、后退撤消、前进重做等操作，为主观气候要素预报产品交互式制作、订正提供了良好的用户界面。

分析工具箱：设计面向气候监测、诊断、预测等业务需求人基本数学计算、统计诊断分析、预测分析功能，并形成可分类管理的工具箱，属于 CIPAS 分析应用的核心功能。目前设计的主要工具有合成分析、EOF 分析、SVD 分析、回归分析、相关分析、剖面分析、曲线分析、t 检验、U 检验、累加计算、距平计算、平均值计算、滑动平均计算、极值计算等。针对一些重要的分析工具直接支持了用户选择数据源(如站点资料、再分析资料、数值预报产品、指数资料等)、空间区域、时间尺度等，并在服务器端运算后再返回分析结果至 CIPAS 客户端并进行合理的可视化。此外，工具箱中还提供了面向气温、降水要素预报落区反演至站点等专用分析工具。工具箱设计具有添加、删除、分类管理等功能并支持用户自己定义开发工具的扩展。用户通过一系列已有的工具以及扩展能力，可以快速形成面向特定的业务功能甚至业务流程，以满足气候诊断与预测业务的动态需求。

产品加工与输出：通过制图窗口实现交互式气候图形产品的制作与输出能力，支持页面设置、图例设置、标题设置、图片导入、模板管理(保存、导入)、比例尺设置、几何图形添加、图形布局(排列、顺序)；支持多种图片输出格式(PDF，PNG，JPG，BMP，TIFF 等)，支持所见即所得的直接打印输出。

产品自动生成定制：CIPAS 设计实现面向监测、诊断、预测日常产品的定制作业流程与自动生成。包括气候业务算法和通用算法管理、产品自动加工流程作业装载和实现等功能，同时还提供图形模板管理功能。后台加工可以根据业务人员定制的产品加工作业计划，以批处理方式自动执行作业任务。

气候数据管理：实现 CIPAS 气候应用数据库、文件库的综合管理。数据管理主要包括从数据接口

实时采集获取原始数据，进行相应处理后再进入气候应用数据库，同时相应处理流程上的监控与日志等信息。此外，还提供数据库备份和恢复、分发等辅助功能。

应用扩展与配置：CIPAS 设计提供应用扩展、界面定制和二次开发功能。界面定制提供可视化的界面，为用户提供用户菜单、工具栏、启动界面、应用程序名称、LOGO 等定制工具和系统功能级别的定制功能，配置参数的保存以及支持不同用户的配置功能项；CIPAS 窗口程序提供 C＋＋和 Python 等程序语言二次开发接口和扩展(数据组件、显示组件、制图组件、分析组件等核心接口)等高级应用，以实现省级业务单位的本地化应用需求。

1.4　部署与运行流程

CIPAS 国家级与省级的部署和运行流程如图 4 所示。CIPAS 采用分布式构架部署，其客户端部署在用户业务高性能 PC 机上或者图形工作站上，而产品自动生成及应用处理等服务器端应用等部署在刀片服务器上(或者 PC 服务器)，数据环境部署在相应的数据服务器上，而国家级和省级部署方案一致。

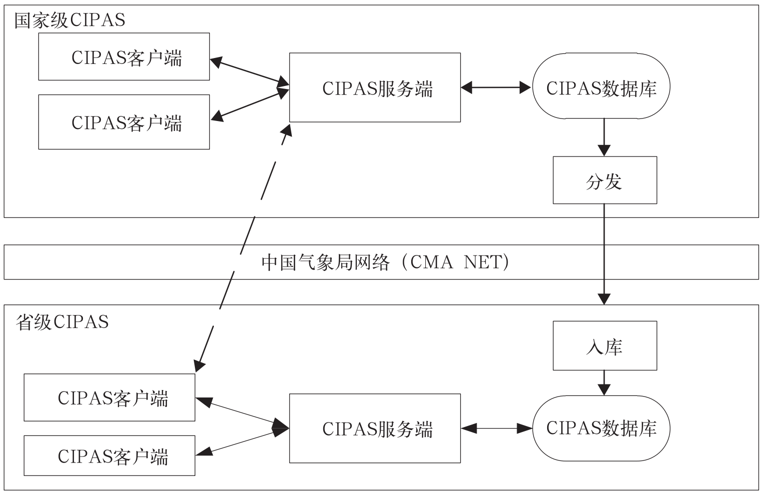

图 4　CIPAS 部署与运行流程示意图

Fig. 4　CIPAS deployment and workflow

为了省级数据环境接入的简单快捷性、数据的统一性，CIPAS 将国家级数据环境中处理后的资料(最小时次为日)利用中国气象宽带网(CMA NET)通路实时分发至 CIPAS 省级数据环境中，以实现数据同步更新。若 CMA NET 允许，省级 CIPAS 客户端也可以连接国家级的 CIPAS 服务器，直接调用国家级 CIPAS 应用服务器及数据资源，如实现在线气候诊断分析并获取分析后的相应数据(如图 4 虚线部分所示)。

2　关键技术

2.1　数据管理与存储

CIPAS 较好地设计支持了文件系统，即通过打开本地文件读入多种天气气候数据格式，实现气候信息有效接入。此外，针对气候业务长时间序列资料等应用需求，CIPAS 还设计了面向其基础应用的专题数据库。

数据库中主要包括全时间序列的地面常规观测资料、指数资料、再分析资料以及数值预报产品，主要分为站点和格点类型。关系型数据库能够对站点等类型的数据进行存储与管理，还可以通过数据库分区、索引、视图等方面进行优化，直接面向应用。但对于格点类型的数据，目前由于数据库不能支持这种非结构化数据，通常是采用关系型数据库存储其主要元数据信息，而真正的数据文件则通过文件系统进行存储。由于格点资料来源的格式差异性(如 NetCDF，GRIB 等)，为了进一步增强访问效率，CIPAS 引入了格点库的概念，即将不同格式、不同时效、不同层次、不同要素、不同种类的数据源进行统一转换为中间二进制格式。为了简化客户端应用的复杂度，CIPAS 对站点、格点等数据的访问封装成统一的 API 接口，接口主要包括了要素、层次、时间、范围、种类等参数。

为了进一步规范CIPAS数据和产品的对外共享与交换，制定了CIPAS交换格式标准，包括了站点格式、格点格式、指数格式以及人机交互格式，并在平台中实现。交换格式包括了元数据信息和数据项两部分内容，其元数据信息部分设计包括时间、空间、投影、数据单位、数据质量等方面，而数据项设计遵循了数据表达的简洁性、可读性、交换性、传输性等原则，并充分考虑数据的时间、空间特性及表达形式等，以实现数据高效存储与交换目的。

2.2 图形引擎及核心算法

CIPAS图形显示的设计考虑到了未来二维、三维一体化发展趋势，因此直接采用了三维可视化显示引擎技术，主要采用了OpenGL(Open Graphics Library)图形库。OpenGL较好地支持了二维、三维图形图像并具有较高的显示与加速性能。系统二维显示的基础上可以快速扩展至三维显示，从而达到气候信息二维、三维一体化显示。

CIPAS在OpenGL的基础上进行了有效封装，如封装了显示地理信息通用数据结构(点、线、多边形线、栅格等)的显示图元，封装了显示气候信息的专用数据结构，如等值线、色斑图、流场图、风羽图、高空地面填图等，封装了显示图元颜色、样式、透明度、纹理贴图等辅助功能。这些图元采用树形结构的管理方式增强效率，并通过图形引擎提供一组相对稳定的接口供外部调用。

CIPAS技术实现上的图形引擎部分涉及的多种核心图形图像算法均需要高效实现，如图形裁减、线条光滑、区域填充、投影变换、空间插值方法等，限于篇幅本文不再赘述。

2.3 产品自动生成方法

CIPAS客户端可以较好地满足业务人员人机交互式显示与分析的业务需求，但面向一些常规的气候监测产品，用户总是希望能自动、定时生成并快速调阅。因此，CIPAS设计时充分考虑了此项需求，引入工作流、可视化建模、任务调度等信息技术来实现产品的定制批处理生成流程，并期望不断发展，突破传统的采用脚本的方式(如NCL[17]和GRADS[18])来定义产品生成。

可视化建模的实现，首先将CIPAS的核心功能组件化，然后采用GUI方式提供若干工具(Tool)，供用户将这些工具组合形成加工流程的连接工具，允许用户指定输入、输出参数以及必要产品显示模板等，这样用户就可以将这些工具组合起来实现某一类产品的加工作业(Task)流程，如典型的产品生成流程读取数据、插值分析、显示、图片生成。任务调度的实现，需要完成作业流程的定时启动，合理调度并充分利用多服务器资源，支持多任务并发执行等策略，加快产品生成处理速度。此外，作业流程中的工具运行时需要识别和保存当前的运行状态等信息，并采用日志方式输出供监控功能调用，避免后台作业等待人为干预而停止。

2.4 分布式通讯与异步机制

CIPAS设计要求实现采用分布式部署，即可以将算法复杂、消耗系统资源较大的分析组件部署在服务器端，CIPAS客户端可以通过数据通信发送分析任务请求到服务器端，由服务器端根据请求从数据基础环境获取数据、调用算法进行统计分析处理，将分析结果通过数据通信返回给发送请求的客户端(如分析工具箱中的在线诊断分析)。

CIPAS采用远程过程调用协议(RPC)来实现服务器端和客户端的通讯，主要利用了数据通信ICE(Internet Communications Engine)开源中间件来实现。ICE可以为构建面向对象的客户-服务器应用提供工具、API和库支持，并具有在异种环境中使用的特性。在实现CIPAS客户端提供的在线诊断分析等时，对ICE两端定义了具体的传输内容(如数据、显示参数等)和格式来确保高效通讯。

CIPAS平台具有典型的人机交互行为，为了进一步提高界面的响应速度，给用户更好的交互体验，使用了多线程技术。界面为交互线程，用来处理用户的交互请求，而逻辑处理线程用来处理用户的处理逻辑。当后台处理较慢时则不影响界面响应速度，从而实现异步机制。

2.5 跨平台实现方法

CIPAS是典型的以图形图像可视化为核心的应用程序，要求较高的效率和响应速度，并要求跨操作系统运行，因此在软件开发语言、开发工具以及所使用的开源中间件上都做了较高的要求。

CIPAS窗口程序采用了C/C++开发语言及编译后运行，C/C++语言支持OOP特性，可以提高软件的重用性、灵活性和扩展性及跨平台开发与运行；而CIPAS应用服务器端则主要采用了JAVA语言，天生具有跨平台特性；CIPAS客户端采用Qt开发平台，它是诺基亚跨平台的C++图形用户界面应用程序框架，提供了高质量的图形用户界面功能。Qt的完全面向对象、扩展性允许真正地组件式

编程;图形引擎采用了 OpenGL,它定义了一个跨平台的图形图像编程接口,实现了与硬件无关的特性;分布通讯采用 ICE,它作为一种面向对象的开源中间件,也适合于异种环境中使用,其源码均可移植。

因此,CIPAS 通过将部分代码进行再次编译,就可以做到不同版本在不同的操作系统环境中运行,如 Windows, Unix, Linux, MacOS, OS/2,甚至嵌入式操作系统,具有很好的移植性。

2.6　开发接口、工具箱插件机制

CIPAS 在保证基础平台特性的同时,还应具有扩展专业性应用版本的能力,这就要求提供二次开发接口和工具箱的插件机制。工具箱是 CIPAS 的核心功能之一,它为气候监测、诊断以及预测提供了基础的分析工具,这些分析工具并具有不断完善与发展的业务需求,因此工具箱的动态添加、更新、分类等管理以及插件机制的实现显得尤为重要。为了满足上述需求,CIPAS 本质上全部采用了面向对象的组件化设计思路,组件除了内部调用外,并将其封装好接口提供给外部开发和扩展用户调用。

CIPAS 组件设计充分运用设计模式技术,其组件粒度设计合理划分,实现组件高内聚、轻耦合,其涵盖了数据、图形、分析处理、版面制图、配置管理等核心组件,并将一步开放更小粒度的组件,对支持更加复杂的二次开发应用、客户端功能、分析工具箱扩展。CIPAS 直接提供核心 C++组件供外部用户直接做组件二次开发扩展,如采用 Qt 插件宏来实现插件的开发,以省去插件开发中的定义插件接口、加载插件、导出插件函数等。此外,CIPAS 设计还可以提供用户通过 PyQt (PyQt 是一个创建 GUI 应用程序的工具包,为 Python 语言和 Qt 库的融合)环境下采用 Python 脚本语言作为快速开发工具,使用户插件编写简单化。

3　CIPAS 初步应用

2011 年 CIPAS 已完成核心框架、主要功能和相应数据环境建设,并初具规模。CIPAS 遵循了边研发边应用的模式,2011 年底以来建设成果已经在国家级业务单位和 5 个试点省份投入了试用,2012 年开展了全国试用,在业务应用中发挥了重要作用。

3.1　气候诊断分析应用

气候诊断分析方面,CIPAS 首次集约化的提供了基于多种数据源、多时间尺度的合成分析、EOF、相关分析、SVD、剖面与曲线分析等通用工具箱,初步形成了面向基础气候业务的监测诊断能力。

如预报员利用首先利用系统提供的曲线分析工具对各种资料进行时间系列分析后形成指数并保存为磁盘文件,然后在相关分析工具中通过自定义上传指数功能将其上传至服务器,最后采用该指数与其他与在线资料进行相关分析,图 5 给出了中国区域气温与环流场位势高度的相关分析结果。

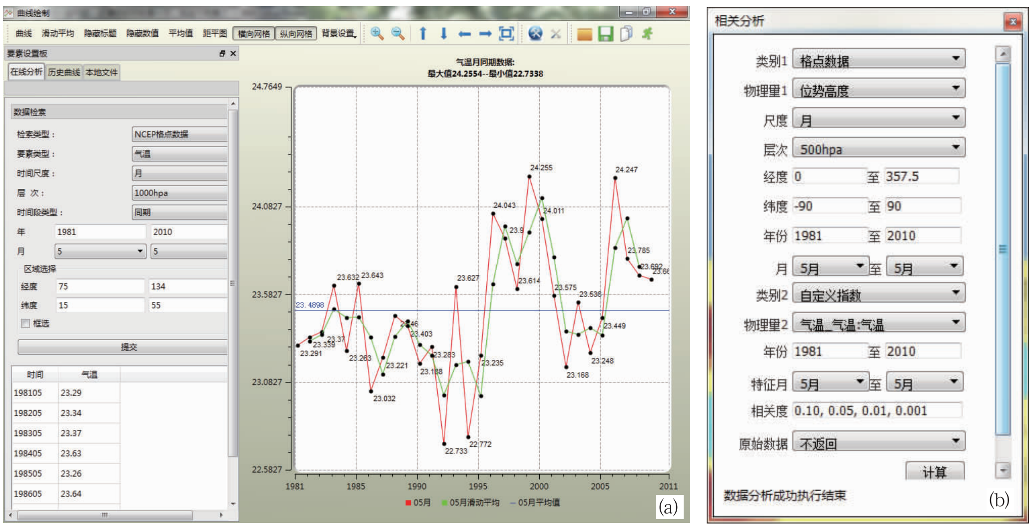

图 5　气候诊断分析应用示意

(a)曲线分析,(b)相关分析,(c)相关分析结果

Fig. 5　Climate diagnosis applicatioon

(a)curve analysis, (b)correlation analysis, (c)correlation analysis result

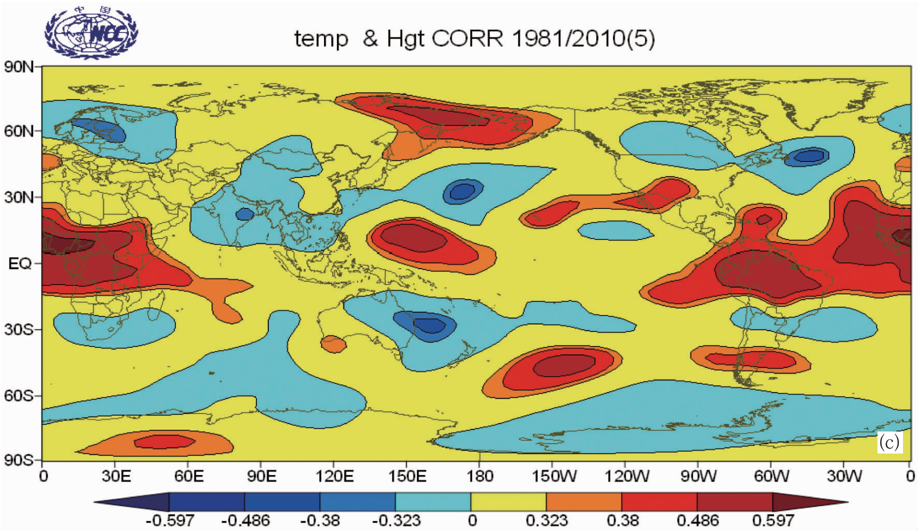

续图 5

3.2 要素预报应用

结合工具箱中的多类工具，在气温、降水等要素预报方面，业务人员可以通过 CIPAS 提供的集约化的人机交互落区绘制、站点反演、产品制作、出图等一系列工具，完成气候资料调阅、降水、气温等月、季甚至滚动时间尺度的距平预报，然后反演到基于站点的预报，并对反演结果作进一步交互式订正（如站点标值、显示预报值、空间定位查询后交互式订正），最后结合模板快速形成较高质量的要素预报图形和数据产品（CIPAS 格式），如图 6 所示，整个业务流程清晰并较好地提高了工作效率。

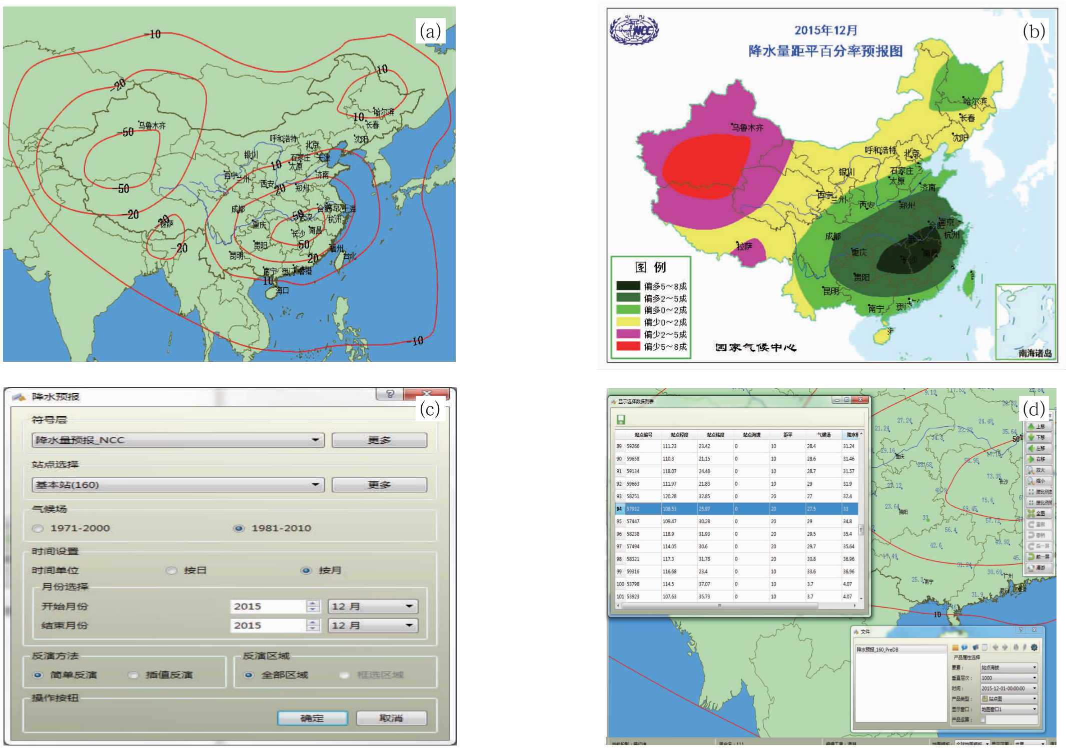

图 6 月降水量预报交互生成应用

(a)预报员绘制的降水距平百分率，(b)运用预报模板后的预报图形产品

(c)从落区预报反演到站点工具，(d)反演结果及交互订正界面

Fig. 6 Interactive monthly precipitation prediction (a)precipitation anomaly percentage, (b)final service product with proper cartography template,(c)interface of rainfall converting from falling area to station,(d)interface of human-computer interaction on rainfall forecast correction

4 小结与讨论

CIPAS是中国气象局正在着力发展的面向现代气候业务的基础平台,综合运用了数据库、三维可视化、地理信息系统(GIS)、计算机分布式等多项信息技术,从技术实现的选型上坚持了自主创新原则,由于不依赖于商业中间件而拥有完全自主知识产权和核心技术,有利于项目的全国推广应用和可持续性发展。CIPAS使用了具有三维特性的显示引擎,从而奠定了二维、三维一体化气候信息综合可视化基础。CIPAS采用了分布式软件架构,保证了服务器与客户端资源的分布高效利用,实现了较好的负载均衡。CIPAS设计了二次开发接口,为其在数据、显示、分析功能等方面提供了省级本地化应用扩展能力。CIPAS具备跨操作系统(平台)运行能力,为全国气候部门复杂的软、硬件环境提供快速部署能力。

CIPAS的未来发展,将进一步完善网络化核心框架和图形化用户界面,优化系统框架及插件机制,规范化二次开发与本地化应用接口,提高系统的内核性能、扩展性、稳定性以及系统显示效率,进一步实现CIPAS向软件设计组件化、数据共享集约标准化、系统结构网络化、交互工具人性化、图形显示二维、三维一体化、文本生成自动化、二次开发简单化、分析工具箱丰富化、流程化方向发展,以进一步增强气候监测诊断预测业务应用能力。

参考文献

[1] Steve S S, Henry R K, Hopkins T. AWIPS II Technology Infusion-Extended Projects Overview and Status. 28th Conference on Interactive Information Processing Systems (IIPS). New Orleans, USA, 2012.
[2] 于连庆,胡争光. MICPAS中天气图交互制作子系统. 应用气象学报,2011,22(3):375-384.
[3] 吴焕萍. 赴荷兰参加欧洲气象预报业务系统工作组会议(EGOWS)第20届会议总结. 气象科技合作动态,2009(6):1-4.
[4] Interactive Plotting and Analysis Pages. [2012-02-15]. http://www.esrl.noaa.gov/psd/cgi-bin/data/getpage.pl.
[5] Simon J. Mason Seasonal Forecasting Using the Climate Predictability Tool (CPT). 36th Annual Climate Diagnostics and Prediction Workshop Fort Worth, TX, 2011.
[6] CDAT (Climate Data Analysis Tools). [2012-02-15]. http://www-pcmdi.llnl.gov/software-portal/cdat/.
[7] ITACS Ver 4.0 Tutorial. [2012-02-15]. http://extreme.kishou.go.jp/tool/itacs-tcc2011/.
[8] 宋连春. 现代气候业务与服务. 第27届中国气象学会年会,北京,2010.
[9] 魏凤英. 我国短期气候预测的物理基础及其预测思路. 应用气象学报,2011,22(1):1-11.
[10] 魏凤英. 气候统计诊断与预测方法研究进展. 应用气象学报,2006:17(6):736-742.
[11] 肖子牛. 我国短期气候监测预测业务进展. 气象,2010,36(7):21-25.
[12] Wu Huanping, Yan Jinghui, Sun Chaoyang, et al. Introduction of the Ongoing Project of NCC Climate Operational and Services System. 28th Conference on Interactive Information Processing Systems (IIPS). New Orleans, USA, 2012.
[13] 刘旭林,赵文芳,刘国宏. 基于WebGIS的气象信息显示和查询系统. 应用气象学报,2008,19(1):116-120.
[14] 吴焕萍,罗兵,王维国,等. GIS技术在决策气象服务系统建设中的应用. 应用气象学报,2008,19(3):380-383.
[15] 吴焕萍. GIS技术在气象领域中的应用. 气象,2010,36(3):90-100.
[16] 赵立成. 气象信息系统. 北京:气象出版社,2011.
[17] Overview of NCL. [2012-03-15]. http://www.ncl.ucar.edu/overview.shtml.
[18] 朱禾. GrADS绘图实用手册. 北京:气象出版社,2011.

Designing and Implementation of Climate Interactive Plotting and Analysis System

Wu Huanping Zhang Yongqiang Sun Jiamin Shao Pengcheng

(*Laboratory for Climate Studies*, *National Climate Center*, *CMA*, *Beijing* 100081)

Abstract

Climate Interactive Plotting and Analysis System (CIPAS) is an ongoing application project for the modern climate monitoring, diagnosis and prediction operation launched by China Meteorological Administration since 2011, which has enhanced the capability of climate data retrieval, multi-visualization, diagnosis, statistics, and products generation. CIPAS provides an integrated data environment that contains meteorological surface observations, index data, reanalysis data and numerical forecast products with long time series. The data environment also implements the simple and unified application program interface (API) with parameters in data property of element, level, time, spatial region, and data type and so on. A distributed architecture with multi-ties and a light client are designed for CIPAS, which allows procedures with massive computing and backend production generation to run on the server. The component and plugin design patterns are used to implement the core components of CIPAS client. The CIPAS core components mainly consist of data accessing, graphic rendering, climate diagnosis and analysis, page layout, setting, and these components can be constructed into the basic operational features and the tool box of climate analysis as well, for instance, EOF, SVD and so on. Also, it can be used to encapsulate APIs for extension application. The construction principle, general system framework, main features, deployment and workflow of CIPAS are discussed in detail. Meanwhile, some key issues involving the implementation of the CIPAS are further discussed, such as data management, graphic rendering engine and related algorithms, production automatic generation, distributed and asynchronous communication mechanism, crossing platform, development API, and plug-in for toolbox. The data type, the accessing API and data exchange format are introduced in data management section. The graphic renderer engine involves OpenGL implementation. Production generation uses workflow engine for automation and customization. Distributed communication is implemented using ICE open source component to avoid different client and server deployment environment. C++ and JAVA language is adopted to ensure crossing platform compatibility. Plug-in implementation covers the component and interface technique. In terms of operation application, two typical operation scenarios are introduced in detail. One case focuses on how to get the given climate diagnosis result using multi-tool in toolbox, and the other case explains how to get the monthly station forecast production both with graphic and text format by using several interactive tools. The pilot using of the current system for the national and provincial operation offices present that CIPAS meets the basic operational requirement and shows the operation and development prospect of CIPAS features. Some advancing directions are also proposed for the further development of CIPAS.

Key words: climate monitoring & prediction; human-computer interaction (HCI); data management

吴佳,高学杰.一套格点化的中国区域逐日观测资料及与其它资料的对比.地球物理学报,2013,56(4):1102-1111,doi:10.6038/cjg20130406.

Wu J, Gao X J. A gridded daily observation dataset over China region and comparison with the other datasets. *Chinese J. Geophys.* (in Chinese), 2013, 56(4):1102-1111,doi:10.6038/cjg20130406.

一套格点化的中国区域逐日观测资料及与其它资料的对比

吴 佳,高学杰

中国气象局气候研究开放实验室,北京 100081

摘 要 为高分辨率气候模式检验等的需要,基于2400余个中国地面气象台站的观测资料,通过插值建立了一套0.25°×0.25°经纬度分辨率的格点化数据集(CN05.1).CN05.1包括日平均和最高、最低气温,以及降水4个变量.插值通过常用的“距平逼近”方法实现,首先将计算得到的气候平均场使用薄板样条方法进行插值,随后使用“角距权重法”对距平场进行插值,然后将两者叠加,得到最终的数据集.将CN05.1与CN05、EA05和APHRO三种日气温和降水资料(四种资料的分析时段统一为1961—2005年)进行对比,分析了它们对气候平均态和极端事件描述上的不同,结果表明几者总体来说在中国东部观测台站密集的地方差别较小,而在台站稀疏的西部差别较大,相差最大的是青藏高原北部至昆仑山西段等地形起伏较大而很少或没有观测台站的地方,反映了格点化数据在这些地区的不确定性,在使用中应予以注意.

关键词 观测资料插值,日数据,气温,降水,中国

doi:10.6038/cjg20130406 **中图分类号** P467 **收稿日期** 2011-11-18,2013-01-15收修定稿

A gridded daily observation dataset over China region and comparison with the other datasets

WU Jia, GAO Xue-Jie

Laboratory for Climate Studies, China Meteorological Administration, Beijing 100081, *China*

Abstract A new gridded daily dataset with the resolution of 0.25° latitude by 0.25° longitude, CN05.1, is constructed for the purpose of high resolution climate model validation over China region. The dataset is based on the interpolation from over 2400 observing stations in China, includes 4 variables: daily mean, minimum and maximum temperature, daily precipitation. The “anomaly approach” is applied in this interpolation. The climatology is first interpolated by thin-plate smoothing splines and then a gridded daily anomaly derived from angular distance weighting method is added to climatology to obtain the final dataset. Intercomparison of the dataset with other three daily datasets, CN05 for temperature, and EA05 and APHRO for precipitation is conducted. The analysis period is from 1961 to 2005. For multi-annual mean temperature variables, results show small differences over eastern China with dense observation stations, but

基金项目 国家重点基础研究发展规划项目(2010CB428401),科技部国际合作重点项目“粮食安全预警的关键空间信息技术合作研究”(2010DFB10030-3),中-英-瑞中国适应气候变化项目(ACCC)共同资助.

作者简介 吴佳,女,1984年生,博士,从事区域气候模拟及气候变化研究.E-mail:wujia@cma.gov.cn

* **通讯作者** 高学杰,男,1966年生,研究员,从事区域气候模拟及气候变化研究.E-mail:gaoxj@cma.gov.cn

larger differences (warmer) over western China with less stations between CN05.1 and CN05. The temperature extremes are measured by TX3D (mean of the 3 greatest maximum temperatures in a year) and TN3D (mean of the 3 lowest minimum temperatures). CN05.1 in general shows a warmer TX3D over China, while a lower TN3D in the east and greater TN3D in the west are found compared to CN05. A greater value of annual mean precipitation compared to EA05 and APHRO, especially to the latter, is found in CN05.1. For precipitation extreme of R3D (mean of the 3 largest precipitations in a year), CN05.1 presents lower value of it in western China compared to EA05.

Keywords Interpolation, Daily data, Temperature, Precipitation, China

1 引　言

随着计算机技术的发展，气候模式的分辨率在逐渐提高，以更好地模拟和再现当代气候及预估未来气候的变化[1]，其中如区域气候模式在中国地区气候变化模拟中所使用的分辨率，已达到 20～25 km[2-4]．此外在气候变化问题上，大家对极端事件也越来越关注，使得发展高分辨率的格点化观测数据的必要性逐渐增加．

目前包括有中国地区的日时间尺度观测数据，有 Xie 等[5]发展的 0.5°×0.5°(经纬度，下同)的降水资料 EA05，Xu 等[6]发展的 0.5°×0.5°气温观测资料 CN05，Yatagai 等[7]所发展的 0.25°×0.25°降水资料 APHRO，以及沈艳等[8]、Chen 等[9]所发展的降水数据等．这些资料在高分辨模式的模拟检验中，得到了广泛的应用[3-4,6,10-14]．但它们普遍存在一些问题．一方面，大部分资料的分辨率为 0.5°×0.5°，较难检验更高分辨率模式模拟所得到的空间分布细节；另一方面，在中国范围内，数据基本都是使用中国气象局所属的 700 余个台站(国家基准气候站和基本气象站)观测资料进行的，观测站点相对较少(其中 EA05 额外使用了黄河流域约 1000 个水文站点的资料)．

针对上述问题，本文基于中国气象局所属的 2400 余个台站的观测资料(包括上述基准站、基本站和国家一般气象站)，使用和 CN05 同样的方法，制作了一套分辨率为 0.25°×0.25°的格点化观测数据集 CN05.1，以满足现阶段高分辨率气候模式检验的需要．数据集目前共包括日平均和最高、最低气温以及降水 4 个变量，时段为 1961—2007 年．本文中我们同时将此数据集与其它格点资料进行了气候平均态和极端事件方面的对比．

2 方法和数据介绍

气候要素由在空间上分布不规则的站点观测向规则的格点插值，可以使用多种方法，除对各个时次的要素场分别进行插值外，使用更多的是所谓的“距平逼近”方法(anomaly approach)[15]，即首先进行气候场的插值，随后进行距平场的插值，最后将两者叠加，得到所需结果．之所以首先进行气候场的插值，是因为一般气候要素，特别是降水等在空间分布上具有较大的不连续性，而气候场则相对连续性较好，对气候场首先进行插值，有利于在一定程度上减少由于这种不连续性带来的分析误差，从而提高插值的准确率．上文所述的 CN05、EA05 和 APHRO 均使用这种方法得到，但所使用的插值方法则有所不同．

具体 CN05 气温资料[6]是参照 CRU 资料[15-16]的插值方法制作的，对于气候场的插值，使用了薄板样条方法，通过 ANUSPLIN 软件实现[17-18]．ANUSPLIN 是澳大利亚国立大学基于平滑样条原理开发的一套 FORTRAN 插值程序包，通过拟合数据序列计算并优化薄盘平滑样条函数，最终利用样条函数进行空间插值，它可以引入协变量子模型，如考虑气温随海拔高度的变化，其结果可以反映气温垂直递减率的变化、降水和海岸线之间的关系、以及水汽压随海拔高度的变化可以反映其垂直递减率的变化等．ANUSPLIN 软件在地理和生态学研究等中经常被用于产生非常高分辨率的气候要素场(如 1 km 等)，以满足其特定需求[19-21]．因此本文采用ANUSPLIN软件，以经度和纬度作为薄盘样条函数自变量，以海拔高度作为协变量对气候场(站点数据 1971—2000 年 365 天的日平均)进行插值．对于距平场(站点数据 1961—2005 年相对 1971—2000 年的日距平)，则采用的是“角距权重法”(ADW, Angular Distance Weighting)[15,22]，格点上的数值以站点数值在考虑

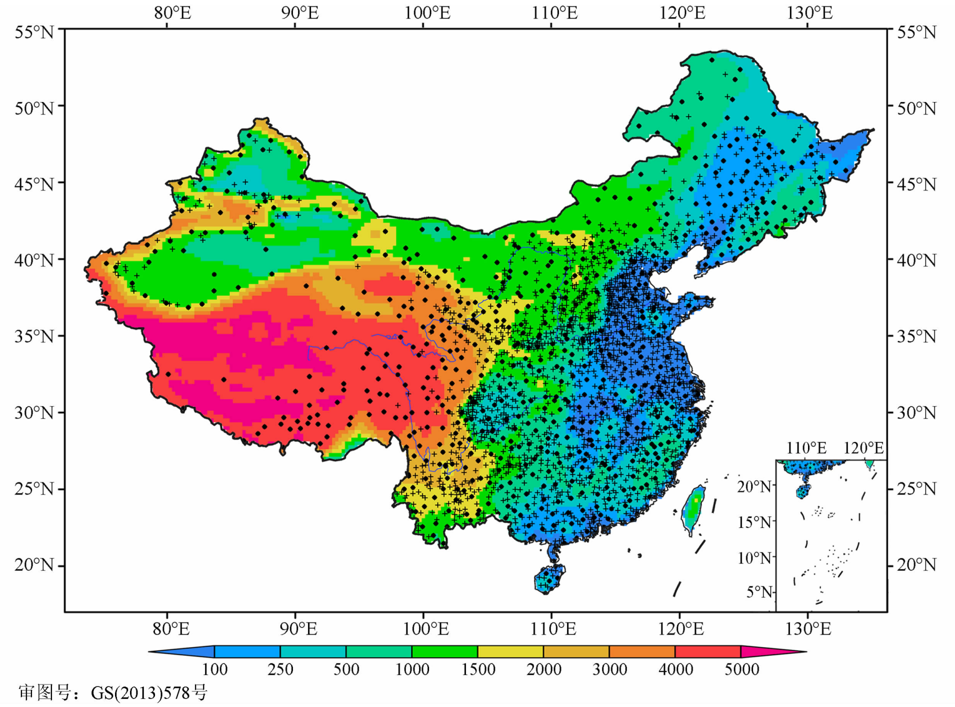

图 1　插值所用的 2416 站点分布和地形高度(单位:m)

图中的圆点标记为国家基准气候站和基本气象站,十字为国家一般站.

Fig.1　Position of the 2416 stations and topography (units: m) used in the interpolation

The dot indicates the national reference climatological stations and basic meteorological observing stations, while the cross indicates the ordinary meteorological observing stations.

其距格点的角度和距离的权重后得到.New 等[23]曾对比了各种插值方法的结果,表明这两种插值方法得到的最终格点场效果较好.CN05 和 CRU 产生气候场的时段有所不同,前者为 1971—2000 年,后者为 1961—1990 年.

EA05 的制作中[5],降水的气候场(时段为 1978—1997 年)及其百分率距平场,均采用的是基于 Gandin[24] 的最优插值方法(OI, the optimal interpolation).在气候场的计算中,首先对各站点多年观测序列进行傅里叶展开,并选取其前 6 个截断的平均作为气候场,以减少高频噪音.在气候场的插值中应用了 PRISM 模型(Parameter-Elevation Regressions on Independent Slopes Model)[25-26]进行地形订正,同时为更好地进行地形订正,气候场和距平场都是首先插值到 0.05°×0.05°的格点上,然后使用面积平均的方法,得到最终所需的 0.5°×0.5°资料.基于 EA05 的方法,沈艳等[8]建立了“中国逐日格点降水量实时分析系统 v1.0”并在国家气象信息中心进行业务试运行.

APHRO 数据[7]的制作方法和 EA05 基本类似,但没有使用黄河流域的水文站点观测资料,同时没有进行 PRISM 的地形订正,最终产生的资料分辨率为 0.25°×0.25°.韩振宇和周天军[27]曾对这一数据在中国的适用性进行了分析.

在 CN05.1 的制作中,我们沿用 CN05 的做法[6],但引入了更多的观测台站资料,此外除日平均及最高最低气温外,增加了降水这一变量,得到的最终格点数据的分辨率为 0.25°×0.25°.观测台站分布情况参见图 1,其中的填色部分为插值中所使用的地形高度分布,圆点为 CN05 所使用的 751 站观测资料(国家基准气候站和基本气象站),十字标记为新增加的站点(国家一般气象站),两者合计共为 2416 个.这套数据已经过基础的质量控制,包括删除与气候态或周边站点值差别过大的数据等.由图 1 可以看到,总体来说我国的气象观测站点偏于东部经济发达地区及平原地带,密度最大可以达几至十几公里一个站,而在西部相对则较少,其中在青藏高原北部至昆仑山北麓,及新疆的塔克拉玛干沙漠腹地等,则基本没有观测站点的分布,这也决定了这些地区插值所得数据具有相对较大的不确定性.

在下文中,为比较方便,将 CN05 和 EA05 分别使用双线性方法(使用被插值点周围 4 个邻近点值,通过两个方向上的线性加权平均计算),由原 0.5°×0.5°插值到和 CN05.1 相同的 0.25°×0.25°格点上,

另外 APHRO 0.25°×0.25°数据的格点位置和 CN05.1 不同，同样对其进行了插值处理．选择几个数据集的共有的时段 1961—2005 年进行比较．

文中的极端事件，气温以多年平均的每年最高的 3 个日气温值的平均 TX3D 和最低的 3 个日气温值的平均 TN3D 表示，降水以多年平均的每年最大的 3 个日降水量的平均 R3D 表示．

3　气温数据的对比

图 2a 中首先给出基于 CN05.1 绘制的 1961—2005年中国区域冬季(12—2 月)平均气温分布．其特点基本为东部地区明显受纬度影响，呈现北冷南暖的形势，华南和海南地区气温最高，在 12 ℃以上，

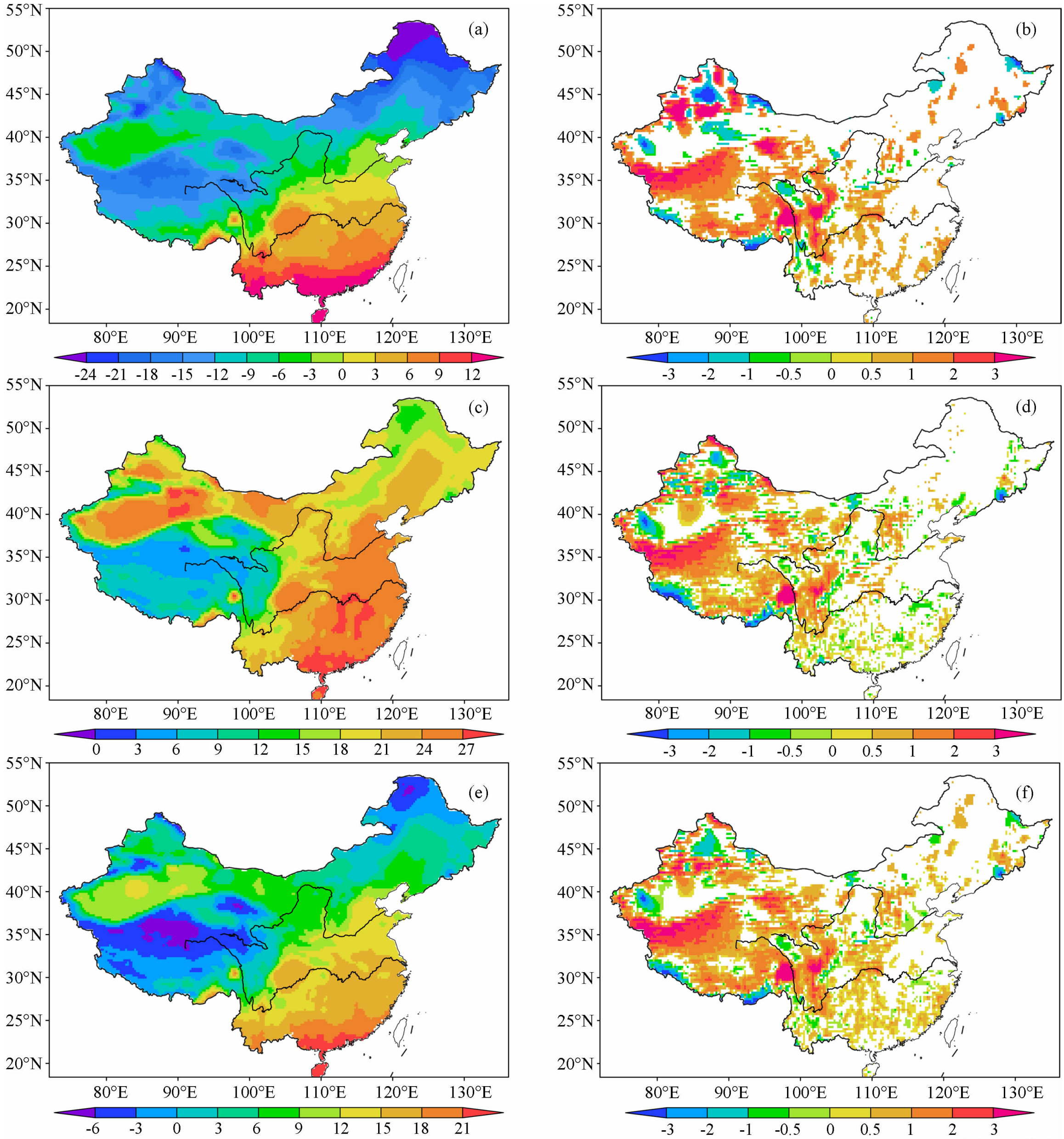

图 2　研究区 1961—2005 年 CN05.1 平均气温分布(左侧)及其与 CN05 的差(右侧)：(a,b)冬季；(c,d)夏季；(e,f)年平均(单位：℃)(b,d,f 的差值中仅给出达到 99%统计显著检验的地方，余图同)

Fig. 2　Distribution of mean temperature during 1961—2005 from CN05.1 (left column) and the difference between it and CN05 in the study area: (a,b) December-January-February; (c, d) June-July-August; and (e, f) annual mean (units: ℃) (In b, d, f, only the differences significant at 99% statistical confidence level are shown. The same for the figures below)

东北的北部地区则达到−24 ℃以下,为全国最冷.中国西部受地形影响显著,地形较低的塔克拉玛干盆地的气温在−6～−3 ℃,而天山和阿尔泰山的部分地方则低于−21 ℃.为比较 CN05.1 与 CN05 的差别,图 2b 给出两个平均场的差值中,达到 99%统计显著性检验部分的分布(下文中的其它差值图同).可以看到,在东部地形变化平缓的地区,两者的差别较小,数值基本在±0.5 ℃之间,差异显著的格点数也较少.两者在地形梯度大的西部地区有显著性差别,比如准噶尔盆地,CN05.1 比 CN05 低 3 ℃以上,而在天山、昆仑山以及青藏高原东麓这些复杂地形过渡地区,CN05.1 比 CN05 偏高 3 ℃以上.这两个数据集区域平均的冬季气温差为 0.48 ℃.注意到上述差别较大的地方,一般都对应着观测站点稀少或没有的地区(图 1),所得格点化数据在这些地区存在较大的不确定性,在应用中应予以注意.

图 2c、2d 中分别给出夏季(6—8 月)CN05.1 的分布及其与 CN05 的差.夏季气温在东部地区的纬向分布特征较冬季要弱,中国东部自南方至华北,基本在 24～27 ℃之间,而在西北如新疆等地随地形的变化更明显,夏季最低气温出现在青藏高原北部,但一般都在 0 ℃以上.CN05.1 与 CN05 的差值分布基本上与冬季类似,同样在东部较小,西部较大并在大部分地区的差异显著,但总体数值较冬季要小,两套数据中国区域平均的差值为 0.30 ℃.

图 2e、2f 为年平均的情况,其基本特征同样以在东部呈纬向分布、西部受地形影响明显为主,年平均气温在中国南方沿海地区最高,低温中心位于青藏高原和东北北部等地.CN05.1 与 CN05 的差值分布及差异显著性情况总体上和冬、夏季保持一致,区域平均差值为 0.44 ℃.

由以上可以看出,整体上 CN05.1 较 CN05 偏暖,偏暖程度在西部较东部更大,此外冬季差别较夏季更大,年平均介于两者之间.偏差最大的地区位于青藏高原北部至昆仑山西段以南.但总体而言,CN05.1 冬、夏季及年平均气温与 CN05 的分布类似,两者间的空间相关系数值均达到 0.99 以上.

图 3a 给出由 CN05.1 数据计算得到的 1961—2005 年平均 TX3D 分布,可以看到 TX3D 极大值中心主要出现在新疆的几个盆地中,数值大于39 ℃,除沿海地区外的华北至江南及四川盆地的 TX3D 也较高,一般在 36～39 ℃之间.TX3D 低值中心位于青藏高原部分地区,不到 15 ℃.总的来说 TX3D 的空间分布与夏季平均气温(图 2c)较为一致.CN05.1 与 CN05 的差异(图 3b)在青藏高原与四川盆地、昆仑山与塔里木盆地之间的过渡地带最为明显,差值超过 3 ℃.CN05.1 的 TX3D 除在个别地区较 CN05 偏低外,在整个区域基本上表现为偏高,区域平均偏高值为 0.62 ℃.对比图 2d 和图 3b 可以看到,尽管 CN05.1 和 CN05 的夏季平均气温在东部差别较小,但由 TX3D 反映的极端暖事件两者则有所不同,CN05.1 中的暖事件偏强.

TN3D 的分布(图 3c)与冬季平均气温类似(图 2a),数值在华南和西南的南部及四川盆地最大,在 0～3 ℃之间或以上,东北大部分和西北部分地区的 TN3D 最小,在−33 ℃以下.CN05.1 与 CN05 的差异(图 3d)在西部与 TX3D(图 3b)较为一致,以偏暖为主,但数值更大一些;在 105°E 以东,与冬季平均气温以偏暖为主不同(图 2b),CN05.1 中的极端冷事件的数值较 CN05 更低.同样对比图 2b 和图 3d 可以看到,CN05.1 和 CN05 的冬季平均气温在东部差别较小,但在 CN05.1 中极端冷事件强度更大一些.CN05.1 和 CN05 中的 TX3D 和 TN3D 的相关系数均在 0.99 以上.

为更好地了解不同月份两个资料的差别,图 4 给出各月平均和最高、最低气温的区域平均数值.从图中可以明显看到,两组资料集的平均、最高和最低气温间的差异在各月接近.相比 CN05,CN05.1 的气温在 2—6 月均偏低,以 3 月份最大(−0.9 ℃);7—1 月偏高,其中以 9—11 月最明显,最大偏高值出现在 11 月,达到 1.8 ℃.总体来说,CN05.1 在春季偏低,其它季节偏高,并以秋季的偏高值最大,年平均表现为偏高.从空间分布上看,这种平均差值主要来自于东部地区(图略).

4 降水数据的对比

图 5a 中给出 CN05.1 数据中多年平均降水的分布.其分布特点基本为由东南沿海向西北内陆地区逐渐减少,东南沿海地区降水中心值在 1500 mm 以上,西北的塔里木盆地等的降水不足 50 mm.

图 5c、5e 分别给出 CN05.1 的年平均降水与 EA05 和 APHRO 的差值.在东部地区,CN05.1 的降水量较 EA05 和 APHRO 的差别均较小,尤其是相对于前者,差别基本在±10%内,差异达到显著水平的格点数很少,相对于APHRO则偏大一些,部分地区偏大值可达 10%～25%,差异显著.

在青藏高原的西北部至昆仑山西段地区,

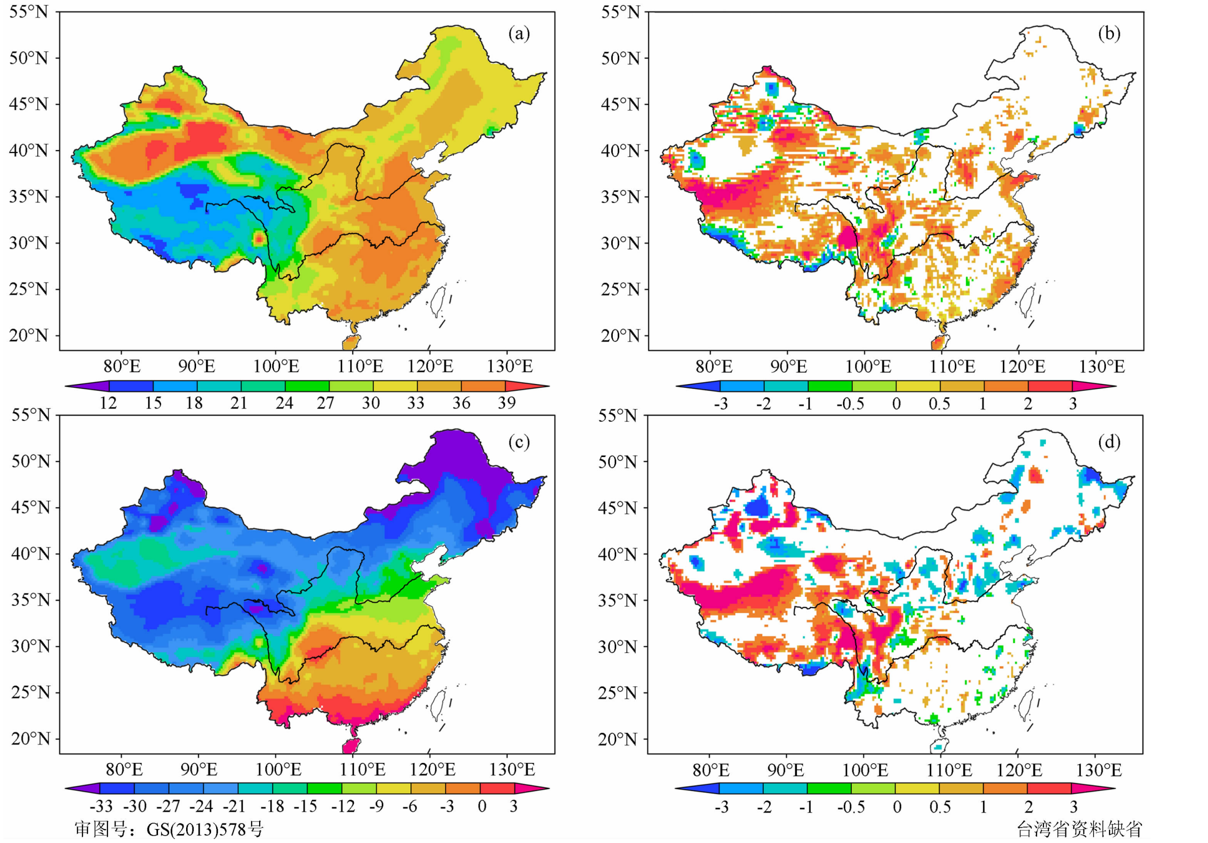

图 3　研究区 CN05.1 的气温极端事件(左侧)及与 CN05 的差(右侧)：(a，b)TX3D；(c，d)TN3D(单位：℃)

Fig. 3　Extreme temperature indices from CN05.1 (left column) and the difference between it and CN05 in the study area: (a, b) TX3D; (c, d) TN3D (units: ℃)

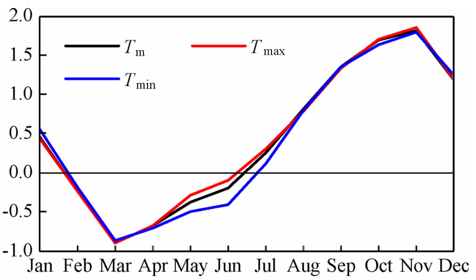

图 4　中国区域平均的 CN05.1 与 CN05 的平均(黑色)、最高(红色)、最低(蓝色)气温在各月的差(单位：℃)

Fig. 4　Differences of the Regional averaged daily mean (T_m, black), maximum (T_{max}, red), and minimum (T_{min}, blue) temperature between CN05.1 and CN05 over China for each months of the year (units: ℃)

CN05.1 中的降水量较 EA05 和 APHRO 偏大，特别是后者，这可能和实际气候更符合. 这些地区存在的较大降水使得冰川能够在这里稳定存在，其融化并成为塔里木盆地南侧各河流水量的来源[28]. 但在塔里木盆地中的降水则较其它两个资料略微偏大，一般在 25%～50%间. 实际上有研究表明这里的降水量一般小于 25 mm，可以达到 10 mm 以下[29-30]，而这些地区没有观测台站(图 1)，这里的降水量是由盆地周边降水量较大的台站的结果插值过来的，会导致 CN05.1 在这里的降水量和 EA05、APHRO 一样有所高估. 此外一些区域气候模式的结果，也报告了降水在昆仑山地区较多，而在盆地中较少的现象[4]. 但总体来说，所得格点化数据在这些地区的应用中，需要注意其不确定性.

区域平均 CN05.1 的年平均降水与 EA05 和 APHRO 的差值分别为 6.5% 和 21.2%. APHRO 降水较 EA05 偏少的原因可能与其未像 EA05 一样经过 PRISM 的地形订正处理有关(参见前文). 计算得到的 CN05.1 与 EA05 和 APHRO 多年平均降水间的空间分布相关系数分别为 0.92 和 0.87.

CN05.1 给出的 R3D 的分布型(图 5b)与年平均降水(图 5a)类似，均为由东南向西北递减. R3D 的最大值出现在南方沿海，数值在 75 mm 以上，自华北南部至长江中下游和江南地区、四川盆地等的 R3D均在50 mm以上，而西北地区则除天山等地外，普遍低于 10 mm.

图5d、5f分别给出CN05.1的R3D与EA05和

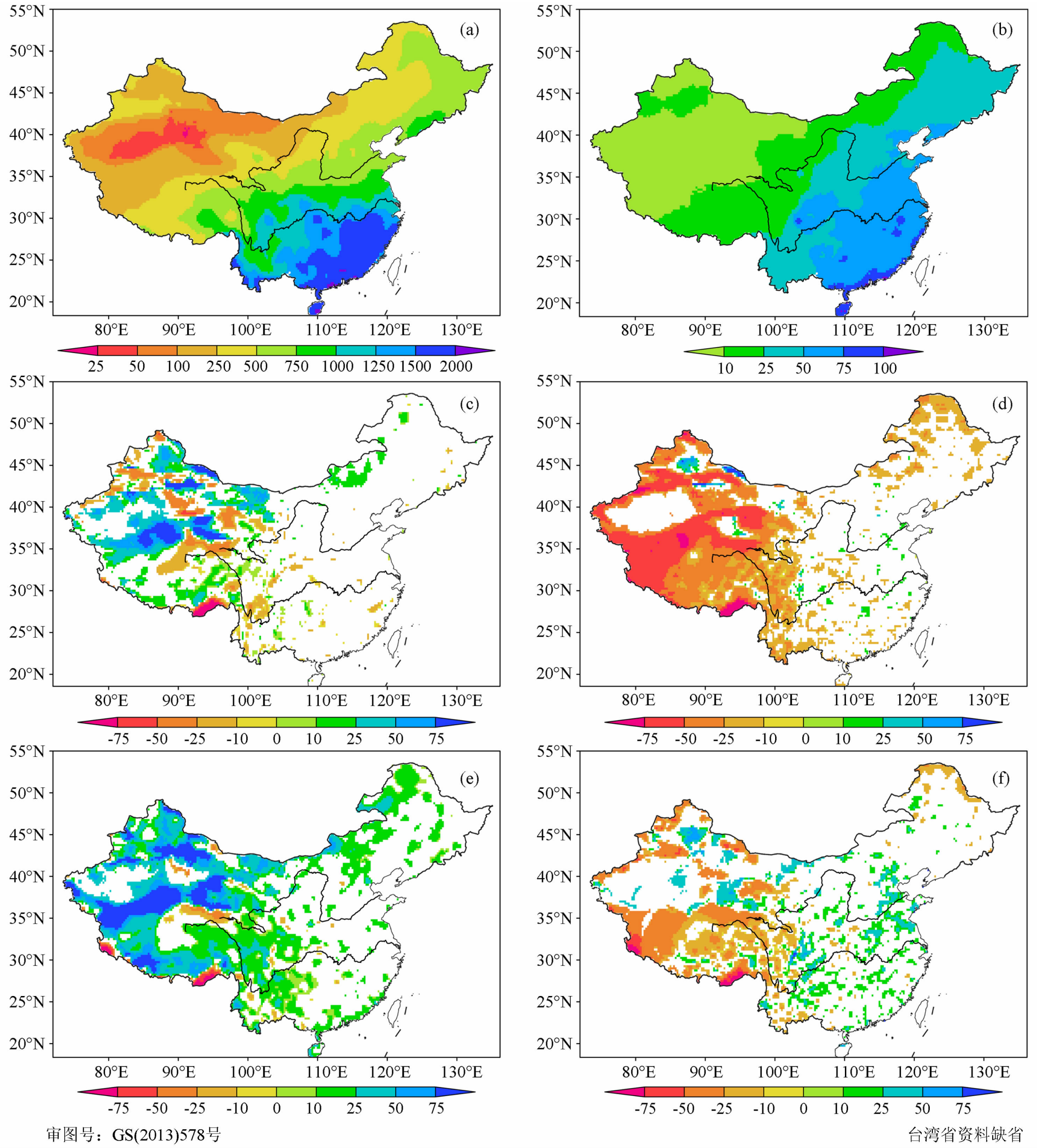

图 5 研究区 CN05.1 的年平均降水(左侧)和极端降水指数 R3D(右侧)(单位:mm)及其与 EA05 和 APHRO 数据的差值(单位:%):(a,b)年平均降水及 R3D;(c,d)与 EA05 的差;(e,f)与 APHRO 的差

Fig. 5 Annual mean precipitation (left column) and R3D (right column) (unit: mm) and their difference with EA05 and APHRO data (unit: %) in the study area: (a, b) annual mean precipitation and R3D; (c, d) differences with EA05; and (e,f) differences with APHRO

APHRO 的差.两者均在东部差别较小,西部较大.CN05.1 的 R3D 与 EA05 的相比,在东部除东北部分地区偏少较多并显著外,一般不超过±10%,在西部山区的差别则显著,数值可以达到 25% 以上.CN05.1 与 APHRO 的差别在东部地区也较小,仅在华北及黄淮等地略偏大,在西部 CN05.1 与 APHRO 的差别分布在盆地类似,均为有所高估,在高山地区同样为偏少,但程度远小于与 EA05 的差别.注意到在中国西部,CN05.1 和 EA05 相比,前者的平均降水偏多,而后者的极端降水强度更大;同时 APHRO 的平均降水偏少更多,但极端降水的强度则相对有所偏大.区域平均 CN05.1 的 R3D 与 EA05 和 APHRO 的差值分别为−16.9%和−0.6%.CN05.1 与 EA05 和 APHRO 的 R3D 间的相关系数分别为 0.71 和 0.90.

图 6 给出 CN05.1 中国区域逐月降水与 EA05 和 APHRO 的差.由图中可以看出,CN05.1 的降水量在上半年的各月较 EA05 少,下半年各月较 EA05

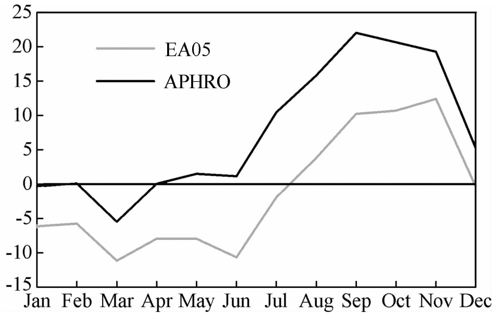

图 6　中国区域平均的 CN05.1 降水与 EA05(浅灰色)和 APHRO(黑色)在各月的差(单位：%)

Fig. 6　Differences between the regional averaged precipitation of CN05.1 with EA05 (light grey), and APHRO (black) over China for each month of the year (units：%)

多，幅度一般在±10%间，年平均的差别因正负相抵，相对较小；而 CN05.1 与 APHRO 的降水量在上半年接近，下半年则明显多很多，最大出现在 9 月，达 22.0%，年平均差异较大. 在空间分布上，这种逐月偏差主要发生在东部(图略)，这是因为东部地区降水量更大的原因造成的. 此外总体来说，EA05 与 APHRO 相比，各月均小 5%左右，其形成原因有待进一步的深入分析.

5　结论与讨论

本文使用中国 2416 个气象台站的气温和降水观测资料，建立了一套分辨率为 0.25°×0.25°的格点化数据集 CN05.1，并与其它资料进行了比较. 结果表明，年平均的 CN05.1 中的平均、最高、最低气温与 CN05 相比，在东部地区差别较小，西部地区较大(以偏暖为主). 区域平均的差别在各个季节中除春季偏低外均为偏高，以秋季最大. 此外 CN05.1 的 TX3D 也比 CN05 要整体偏大，TN3D 则在东部地区有所偏小，但整体上仍表现为偏大.

CN05.1 的年平均降水量相对于 EA05 和 APHRO 均偏大，尤其是后者，偏大以在西部更明显. 逐月平均结果则表明，这三种降水数据在冬春季偏差较小，秋季较大. 对于 R3D 而言，CN05.1 较 EA05 在西部偏小明显，与 APHRO 整体上的差异相对较小.

本文工作的首要目的在于满足高分辨率气候模式检验的急需，除此之外，该数据集在气候变化的检测、监测，农业，水文，生态等领域的研究中也具有潜在应用价值. 但需要指出的是，台站观测资料的格点化是一个非常复杂的工作，以本文为例，尚有不少有待改进的地方，其中包括如：

(1)更多观测资料的搜集. 除本文使用的中国气象局所属台站外，中国地区还有为数众多的水文、林业、民航及农垦等部门和系统管理的观测站点，尽量多地搜集这些站点的观测数据，将会在很大程度上提高最终格点化资料的准确性. 此外，由本文中看到的不同数据集之间差别较大的地区，一般都是缺少台站观测的地方，是未来调整台站布局中需要注意到的问题[31].

(2)原始资料的整理. 包括资料的均一化处理[32]，热岛效应的扣除等[33]. 同时研究表明固态降水观测经常因为风导致的偏小误差(可以达到 10%～20%[34])，也需要在针对中国不同地区特点的基础上予以订正[35].

(3)一般的观测台站，都位于平原或山区的河谷地带，使得周边高山格点上的插值，需要进行地形方面的订正. 在本研究中，是通过 ANUSPLIN 软件实现的，所得到的订正系数在整个应用区域内是一个统一的值，这个值在所使用站点数目不同的情况下，会有一定差别，如 CN05.1 中实际使用的温度垂直递减率，较 CN05 低大约 0.1 ℃/100 m(详细分析及图略). 未来可以考虑按照气候特征进行适当的分区后，在不同地区分别进行插值. 此外可以尝试使用再分析资料驱动高分辨率区域气候模式，在模拟结果中分析得到随空间和时间变化的地形订正参数，用于观测资料的插值.

参考文献(References)

[1] Christensen J H, Hewitson B, Busuioc A, et al. Regional climate projections. // Solomon S, Qin D, Manning M eds. Climate Change 2007: The Physical Science Basis. Contribution of Working Group I to the Fourth Assessment Report of the Intergovernmental Panel on Climate Change. Cambridge, New York: Cambridge University Press. 2007.

[2] 石英，高学杰. 温室效应对我国东部地区气候影响的高分辨率数值试验. 大气科学，2008，32(5)：1006-1018.
Shi Y, Gao X J. Influence of greenhouse effect on eastern China climate simulated by a high resolution regional climate model. *Chinese J. Atmos. Sci.* (in Chinese), 2008, 32(5): 1006-1018.

[3] Gao X J, Shi Y, Song R Y, et al. Reduction of future monsoon precipitation over China: Comparison between a high resolution RCM simulation and the driving GCM. *Meteor. Atmos. Phys.*, 2008, 100(1-4): 73-86.

[4] Gao X J, Shi Y, Zhang D F, et al. Uncertainties in monsoon precipitation projections over China: results from two high-resolution RCM simulations. *Climate Res.*, 2012, 52: 213-

226, doi: 10.3354/cr01084.

[5] Xie P P, Chen M Y, Song Y, et al. A gauge-based analysis of daily precipitation over East Asia. *J. Hydrometeor.*, 2007, 8(3): 607-626.

[6] Xu Y, Gao X J, Shen Y, et al. A daily temperature dataset over China and its application in validating a RCM simulation. *Adv. Atmos. Sci.*, 2009, 26(4): 763-772.

[7] Yatagai A, Arakawa O, Kamiguchi K, et al. A 44-year daily gridded precipitation dataset for Asia based on a dense network of rain gauges. *SOLA*, 2009, 5: 137-140.

[8] 沈艳, 冯明农, 张洪政等. 我国逐日降水量格点化方法. 应用气象学报, 2010, 21(3): 279-286.
Shen Y, Feng M N, Zhang H Z, et al. Interpolation methods of China daily precipitation data. *J. Appl. Meteor. Sci.* (in Chinese), 2010, 21(3): 279-286.

[9] Chen D L, Ou T H, Gong L B, et al. Spatial interpolation of daily precipitation in China: 1951-2005. *Adv. Atmos. Sci.*, 2010, 27(6): 1221-1232.

[10] 高学杰, 石英, Giorgi F. 中国区域气候变化的一个高分辨率数值模拟. 中国科学 (D辑: 地球科学), 2010, 40(7): 911-922.
Gao X J, Shi Y, Giorgi F. A high resolution simulation of climate change over China. *Science China Earth Sciences*, 2011, 54(3): 462-472.

[11] Yu E T, Wang H J, Sun J Q. A quick report on a dynamical downscaling simulation over china using the nested model. *Atmos. Oceanic Sci. Lett.*, 2011, 3(6): 325-329.

[12] Ju L X, Lang X M. Hindcast experiment of extraseasonal short-term summer climate prediction over China with RegCM3_IAP9L-AGCM. *Acta Meteor. Sin.*, 2011, 25(3): 376-385.

[13] Wang A H, Zeng X B. Sensitivities of terrestrial water cycle simulations to the variations of precipitation and air temperature in China. *J. Geophys. Res.*, 2011, 116(D2): D02107.

[14] Feng L, Zhou T J, Wu B, et al. Projection of future precipitation change over China with a high-resolution global atmospheric model. *Adv. Atmos. Sci.*, 2011, 28(2): 464-476.

[15] New M, Hulme M, Jones P. Representing twentieth-century space-time climate variability. Part II: Development of 1901-96 monthly grids of terrestrial surface climate. *J. Climate*, 2000, 13(13): 2217-2238.

[16] New M, Hulme M, Jones P. Representing twentieth-century space-time climate variability. Part 1: Development of a 1961-90 mean monthly terrestrial climatology. *J. Climate*, 1999, 12(3): 829-856.

[17] Hutchinson M F. Interpolating mean rainfall using thin plate smoothing splines. *Int. J. Geogr. Inf. Sys.*, 1995, 9(4): 385-403.

[18] Hutchinson M F. ANUSPLIN Version 4.0 user guide. Centre for Resources and Environmental Studies. Canberra: Australian National University, 1999.

[19] 王军邦, 刘纪远, 邵全琴等. 基于遥感-过程耦合模型的1988—2004年青海三江源区净初级生产力模拟. 植物生态学报, 2009, 33(2): 254-269.
Wang J B, Liu J Y, Shao Q Q, et al. Spatial-temporal patterns of net primary productivity for 1988—2004 based on GLOPEM-CEVSA Model in the "Three-River Headwaters" region of Qinghai province, China. *Chinese Journal of Plant Ecology* (in Chinese), 2009, 33(2): 254-269.

[20] 於琍, 李克让, 陶波等. 植被地理分布对气候变化的适应性研究. 地理科学进展, 2010, 29(11): 1326-1332.
Yu L, Li K R, Tao B, et al. Simulating and assessing the adaptability of geographic distribution of vegetation to climate change in China. *Progress in Geography* (in Chinese), 2010, 29(11): 1326-1332.

[21] 赵志平, 刘纪远, 邵全琴. 近30年来中国气候湿润程度变化的空间差异及其对生态系统脆弱性的影响. 自然资源学报, 2010, 25(12): 2091-2100.
Zhao Z P, Liu J Y, Shao Q Q. Spatial diversity of humidification and its impact on ecosystem venerability in China during the last 30 years. *Journal of Natural Resources* (in Chinese), 2010, 25(12): 2091-2100.

[22] Shepard D S. Computer mapping: The SYMAP interpolation algorithm. //Gaile G L, Willmott C J eds. Spatial Statistics and Models. Dordrecht: D. Reidel Publishing, 1984: 133-145.

[23] New M, Lister D, Hulme M, et al. A high-resolution data set of surface climate over global land areas. *Climate Res.*, 2002, 21(1): 1-25.

[24] Gandin L S. Objective Analysis of Meteorological Fields. Israel Program for Scientific Translations, 1965.

[25] Daly C, Gibson W P, Taylor G H, et al. A knowledge-based approach to the statistical mapping of climate. *Climate Res.*, 2002, 22(2): 99-113.

[26] Daly C, Neilson R P, Phillips D L. A statistical-topographic model for mapping climatological precipitation over mountainous terrain. *J. Appl. Meteor.*, 1994, 33(2): 140-158.

[27] 韩振宇, 周天军. APHRODITE高分辨率逐日降水资料在中国大陆地区的适用性. 大气科学, 2012, 36(2): 361-373.
Han Z Y, Zhou T J. Assessing the quality of APHRODITE high-resolution daily precipitation dataset over contiguous China. *Chinese J. Atmos. Sci.* (in Chinese), 2012, 36(2): 361-373.

[28] 沈永平, 梁红. 高山冰川区大降水带的成因探讨. 冰川冻土, 2004, 26(6): 806-809.
Shen Y P, Liang H. High precipitation in Glacial Region of high mountains in High Asia: possible cause. *Journal of Glaciology and Geocryology* (in Chinese), 2004, 26(6): 806-809.

[29] 《中华人民共和国气候图集》编委会. 中华人民共和国气候图集. 北京: 气象出版社, 2002.
Editorial Board of Climatological Atlas of the People's Republic of China. Climatological Atlas of the People's Republic of China (in Chinese). Beijing: Meteorological Press, 2002.

[30] 李生宇，雷加强，徐新文等. 塔克拉玛干沙漠腹地沙尘暴特征——以塔中地区为例. 自然灾害学报，2006，15(2)：14-19.
Li S Y，Lei J Q，Xu X W，et al. Features of sandstorms in hinterland of Taklimakan Desert：a case of Tazhong area. *Journal of Natural Disasters* (in Chinese)，2006，15(2)：14-19.

[31] 胡婷，周江兴，代刊. USCRN 气候基准站网布局理论在我国的应用. 应用气象学报，2012，23(1)：40-46.
Hu T，Zhou J X，Dai K. Application of USCRN station density strategy to China climate reference network. *J. Appl. Meteor. Sci.* (in Chinese)，2012，23(1)：40-46.

[32] Li Z，Yan Z W. Application of multiple analysis of series for homogenization to Beijing daily temperature series (1960—2006). *Adv. Atmos. Sci.*，2010，27(4)：777-787.

[33] 龚道溢，王绍武. 全球气候变暖研究中的不确定性. 地学前缘，2002，9(2)：371-376.
Gong D Y，Wang S W. Uncertainties in the global warming studies. *Earth Science Frontiers* (in Chinese)，2002，9(2)：371-376.

[34] Adam J C，Lettenmaier D P. Adjustment of global gridded precipitation for systematic bias. *J. Geophys. Res.*，2003，108(D9)：4257，doi：10.1029/2002JD002499.

[35] 叶柏生，成鹏，杨大庆等. 降水观测误差修正对降水变化趋势的影响. 冰川冻土，2008，30(5)：717-725.
Ye B S，Cheng P，Yang D Q，et al. Effects of the bias-correction on changing tendency of precipitation over China. *Journal of Glaciology and Geocryology* (in Chinese)，2008，30(5)：717-725.

（本文编辑　何　燕）

LETTERS
PUBLISHED ONLINE: 1 SEPTEMBER 2013 | DOI: 10.1038/NGEO1931

nature geoscience

Similar spatial patterns of climate responses to aerosol and greenhouse gas changes

Shang-Ping Xie[1,2,3]*, Bo Lu[3,4,5] and Baoqiang Xiang[3]

Spatial variations in ocean warming have been linked to regional changes in tropical cyclones[1], precipitation[2,3] and monsoons[4]. But development of reliable regional climate projections for climate change mitigation and adaptation remains challenging[5]. The presence of anthropogenic aerosols, which are highly variable in space and time, is thought to induce spatial patterns of climate response that are distinct from those of well-mixed greenhouse gases[4,6–9]. Using CMIP5 climate simulations that consider aerosols and greenhouse gases separately, we show that regional responses to changes in greenhouse gases and aerosols are similar over the ocean, as reflected in similar spatial patterns of ocean temperature and precipitation. This similarity suggests that the climate response to radiative changes is relatively insensitive to the spatial distribution of these changes. Although anthropogenic aerosols are largely confined to the Northern Hemisphere, simulations that include aerosol forcing predict decreases in temperature and westerly wind speed that reach the pristine Southern Hemisphere oceans. Over land, the climate response to aerosol forcing is more localized, but larger scale spatial patterns are also evident. We suggest that the climate responses induced by greenhouse gases and aerosols share key ocean–atmosphere feedbacks, leading to a qualitative resemblance in spatial distribution.

Anthropogenic aerosols are an important radiative forcing that cools the global climate[10]. Highly variable in space and time, anthropogenic aerosols induce changes in atmospheric circulation and regional climate, including rainfall change in Asian monsoons[6–8] and the African Sahel[4,9]. Important for life, precipitation change is to first order spatially variable with large disagreement among models. Climate response to aerosol forcing consists of fast and slow components, defined as adjustments without and owing to ocean change, respectively[11]. The fast response to aerosol forcing has received much attention, affecting precipitation by perturbing radiation and cloud physics[12]. The regional distribution of precipitation change is due mostly to the slow response involving ocean–atmosphere interaction (Supplementary Fig. S1). Regional patterns of the slow response are poorly constrained and the physical mechanisms poorly understood. Here we probe the coupled ocean–atmospheric dynamics by contrasting climate response to greenhouse gas (GHG) and aerosol forcing. Despite distinct three-dimensional structure in forcing, the spatial characteristics of the response are remarkably similar, strongly hinting at a common global mode of radiative-induced climate change (RICC).

The surface air temperature (SAT) response to GHG and aerosol forcing shows some resemblance to each other[13], due mostly to two patterns: larger response over land than ocean; and the polar amplification. It is unclear whether the sea surface temperature (SST) pattern is also similar between two types of forced response. The SST response pattern is dynamically more fundamental than SAT because of its importance in determining changes in atmospheric convection[3] and tropical cyclone[1]. Upper tropospheric temperature response is flattened in space by fast equatorial waves and set by the tropical mean SST (refs 14,15). As a result, the SST pattern controls local convective stability over the ocean. This warmer-get-wetter view calls for increased rainfall where local SST change exceeds the tropical mean and vice versa. We study the SST pattern in relation to precipitation change.

We use a set of single-forcing (aerosol and GHG separately) simulations for the twentieth century from three models. Radiative forcing due to CO_2 change at the top of the atmosphere (Methods) is relatively smooth in space whereas the aerosol-induced radiative forcing shows large spatial variations (Supplementary Fig. S2).

Figure 1 compares the twentieth-century radiative forcing and climate response in zonal mean between aerosol and GHG runs. Aerosol forcing peaks in the Northern Hemisphere mid-latitudes and decays to vanishing levels in the Antarctic. The SST response shows a similar meridional profile with a decreasing trend from the Northern Hemisphere mid-latitudes towards the Southern Ocean. Rainfall decreases on and north of the Equator[9,16,17], a change that is often characterized as a southward shift of the intertropical convergence zone, with the Sahel drought as a regional manifestation[9]. We stress that the tropical rainfall response is mediated by the SST change, negligible in atmospheric runs with fixed SST (Supplementary Fig. S1). Specifically in the tropics, the interhemispheric SST gradient induces precipitation change in a manner consistent with the warmer-get-wetter view.

By contrast, GHG radiative forcing does not vary much in the meridional direction except near the poles. The SST response correlates poorly with the radiative forcing, peaking on the Equator despite a local minimum in forcing. The equatorial enhancement in SST results from an evaporative damping that peaks in the subtropics with a minimum on the Equator[3,18]. The SST warming is weaker in the Southern Hemisphere than in the Northern Hemisphere because the deeper winter mixed layer mutes the response in the Southern Ocean[19]. This cross-equatorial SST gradient induces tropical rainfall change that is remarkably similar to that in aerosol runs with sign reversed (Fig. 1). The SST response is weaker in magnitude in the aerosol than the GHG run but comparable in interhemi-

[1]Scripps Institution of Oceanography, University of California at San Diego, La Jolla, California 92093-0206, USA, [2]Physical Oceanography Laboratory, Ocean University of China, Qingdao 266100, China, [3]International Pacific Research Center, University of Hawaii at Manoa, Honolulu, Hawaii 96822, USA, [4]Laboratory for Climate Studies, National Climate Center, China Meteorological Administration, Beijing 100081, China, [5]Department of Atmospheric and Oceanic Sciences, Peking University, Beijing 10081, China. *e-mail: sxie@ucsd.edu

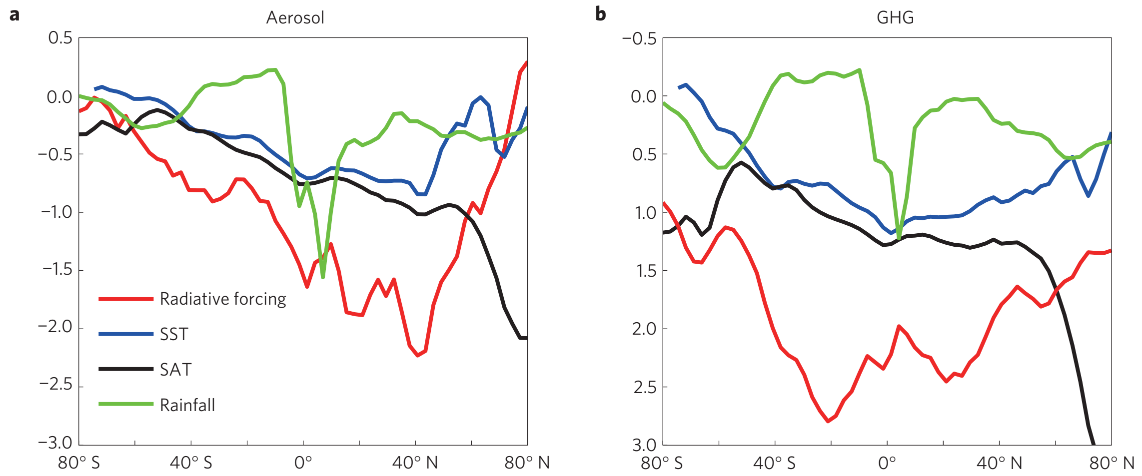

Figure 1 | Radiative forcing and climate response. a,**b**, SST (in K), SAT (in K) and precipitation (in mm per day) changes for the twentieth century in aerosol (**a**) and GHG (**b**) single-forcing runs. Rainfall trends are multiplied by a factor of four, and the radiative forcing (in W m^{-2}) from model runs with quadruple CO_2 levels is scaled by a factor of 0.3 to fit the twentieth-century change in global GHG forcing as reported in ref. 27. The vertical axis is reversed in **b** for easy comparison.

spheric gradient, indicating a sensitivity to forcing type. Consistent with the SST gradient change, the tropical rainfall response is comparable in both shape and magnitude between the two runs[17].

We apply the empirical orthogonal function (EOF) analysis to SST anomalies separately for aerosol and GHG runs (Fig. 2a,b). The leading principal component tracks the composition change very well and shows a pronounced trend for both aerosol and GHG runs (Fig. 2e,f). The principal component for aerosol-induced response is rather flat for the 1920s–1940s, trends downward rapidly with the post-war economic growth and shows a tendency of levelling off in the 1990s owing to worldwide air pollution control. The GHG principal component, by contrast, features a robust rising trend that accelerates around 1970.

Despite these differences in temporal evolution, the SST response is remarkably similar in spatial distribution between aerosol and GHG runs (the tropical mean has been removed in Fig. 2a,b). The pattern correlation amounts to 0.87 for the multimodel ensemble mean response as compared with −0.02 for clear sky radiative forcing. The mid-latitude North Pacific is notably sensitive to forcing type, with an enhanced (reduced) SST response in the aerosol (GHG) run, a difference tied to the distinct response of the atmospheric Aleutian low[20].

The SST pattern affects atmospheric convection over tropical oceans[3]. We repeat the EOF analysis for precipitation over the ocean. The leading principal components look almost identical to their SST counterparts (Fig. 2e,f). The precipitation EOFs (Fig. 2c,d) are correlated in space at 0.67 between aerosol and GHG runs, suggestive of a common RICC mode. The common precipitation response is mediated by SST. The cross-correlation in space between SST and precipitation in the tropics (30° S–30° N) is 0.57 and 0.51 for aerosol and GHG runs, respectively. Following the warmer-get-wetter pattern, rainfall increases where the SST change exceeds the tropical mean temperature. In particular, the equatorial warming (cooling) peak anchors zonal bands of rainfall increase (reduction) across the Pacific in GHG (aerosol) runs.

Why is the climate response to GHG and aerosol experiments similar? One important reason is that a common set of ocean–atmospheric feedback is involved in spatial pattern formation. Net surface heat flux with sign reversed represents the ocean heat transport effect on SST (*Do*)[3]. The *Do* distribution indicates that in both aerosol and GHG runs, the SST response is subdued in the extratropical North Atlantic and Southern Ocean owing to heat absorption by the deep winter mixed layer and reorganization of ocean currents (Fig. 3a,c). Bjerknes feedback is important over the tropical Indian Ocean: for the GHG response, the zonal gradient in SST change induces easterly wind anomalies on the Equator, lifting the thermocline and cooling SST in the east (Supplementary Fig. S3).

Other major patterns over the tropical Pacific include the enhanced SST response on the Equator owing to the local minimum in evaporative damping[18]. In the tropical southeast Pacific, the reduced warming (cooling) in the GHG (aerosol) run is associated with the intensified (weakened) southeast trade winds (Fig. 3b,d), as quantified in Supplementary Table S1. Indeed, the spatial anomalies of SST and scalar wind are correlated in the global tropics at −0.46 (−0.55) for the aerosol (GHG) run, suggestive of wind–evaporation–SST (WES) feedback. Two recent studies corroborate this feedback: in double CO_2 experiments where the WES mechanism is disabled, spatial patterns of SST and precipitation response weaken substantially[21]; and an antisymmetric WES mode dominates intermodel spread in Coupled Model Intercomparison Project phase 3 (CMIP3) global warming projections[22]. As for what suppresses the SST response in southern tropical oceans, the muted SST response in the Southern Ocean—owing to the deep ocean heat absorption and, in the case of aerosols, weak local radiative forcing—can trigger the tropic response[23] of north–south asymmetry as required by the balance of cross-equatorial energy transport between the ocean and atmosphere[24–26]. The muted response in the Southern Ocean and hence the interhemispheric asymmetry in SST response to GHG forcing are likely to weaken as the deep ocean approaches equilibrium[27].

The tropospheric temperature change shows a remarkable equatorial symmetry in both GHG and aerosol runs (Supplementary Fig. S4). Flattened in the tropics by fast equatorial waves[14], tropospheric temperature change is insensitive to forcing location. A coupled model experiment we conducted shows that a featureless tropospheric warming creates SST, precipitation and wind patterns that are remarkably similar to the double CO_2 run of the same model (Supplementary Fig. S6) and to CMIP5 runs analysed here. Coupled ocean–atmospheric feedback mechanisms including WES are at work in the SST pattern formation. The horizontal homogenization of tropospheric temperature perturbations in the tropics is thus instrumental in forming a common global RICC mode insensitive to forcing distribution. Corroborating this mechanism, the tropical SST pattern remains largely unchanged when Asian aerosols are excluded (Supplementary Fig. S7).

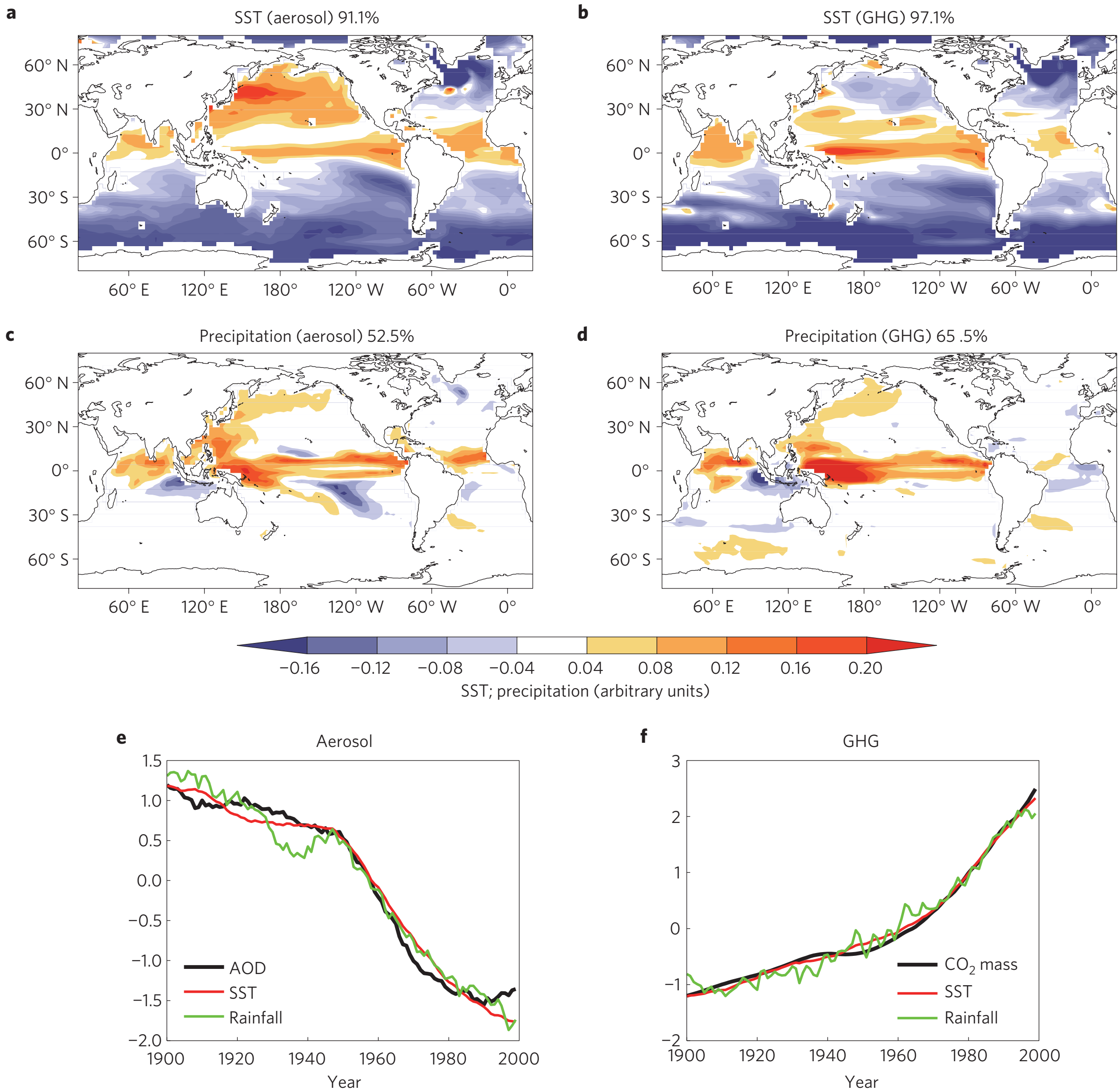

Figure 2 | Climate response pattern. a–d, Leading EOF patterns with explained variance noted at the upper right: SST in aerosol (**a**) and GHG (**b**) runs; rainfall in aerosol (**c**) and GHG (**d**) runs. The tropical mean (30° S–30° N) has been removed from the SST modes. **e**,**f**, Normalized time series of climate parameters. Changes in global AOD (sign reversed) for aerosol runs (**e**) and CO_2 concentration for GHG runs (**f**) are plotted, along with SST and precipitation principal components.

Over land, the fast response to aerosols and their interaction with the slow response create localized patterns but the effect of the global RICC mode is still apparent. The spatial correlation for land precipitation change between GHG and aerosol runs remains high for CanESM2 and CM3 models (0.59 and 0.53). The correlation is lower in MK3.6 (Supplementary Table S2), suggesting some sensitivity to forcing type[28]. The spatial correlations for SAT between GHG and aerosol runs range from 0.58 to 0.85 (Supplementary Table S3). These correlations emerge despite considerable natural variability in mid–high latitudes[29].

Figure 4 examines the relative importance of the global RICC mode and local aerosol effect for SAT in regions of large aerosol emission. As an index of the RICC mode, global aerosol optical depth (AOD) tracks the regional SAT response better than local AOD does in the eastern USA and Europe, where SAT fails to follow the rapid decrease in local AOD after 1970 (an effect of the Clean Air Act). In East Asia where local AOD closely tracks global AOD, SAT shows a gentle bottom out despite a continuing sharp increase in local AOD in the 1990s.

In the South Pacific, the local aerosol forcing is miniscule but the SAT change (Fig. 4d) closely tracks that in the Northern Hemisphere emission regions, highlighting the influence of the global RICC mode. Other robust responses in the pristine Southern Hemisphere to aerosol forcing include an eastward-shifted South Pacific convergence zone (Fig. 2c, with sign reversed) and decelerated westerly winds in the Southern Ocean (Fig. 3b). Thus localized aerosol forcing can excite a global response, enabled by ocean–atmospheric feedback that imprints characteristic patterns.

Radiative considerations predict distinct precipitation response between GHG and aerosol forcing, as in the fast response of the global mean[11]. We show that regional precipitation change induced by aerosols is dominated by the slow response in coupled models, mediated by the SST pattern that is remarkably similar to that in the GHG run despite a vast difference in forcing distribution. Although

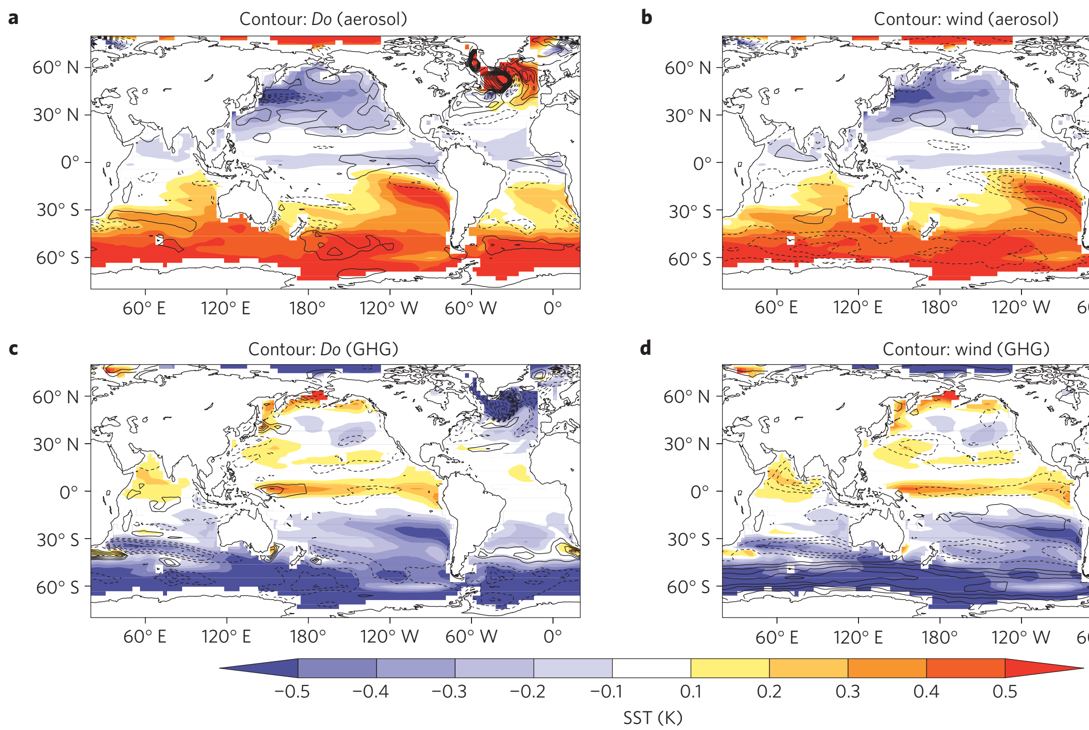

Figure 3 | Mechanisms for ocean temperature pattern. a–d, Twentieth-century changes in aerosol (**a**,**b**) and GHG (**c**,**d**) runs. Ocean heat transport effect *Do* (**a**,**c**; contour interval, 3 W m^{-2}) and surface scalar wind speed (**b**,**d**; contour interval, 0.08 m s^{-1}) superimposed on SST (colour shading; K). The tropical mean (30° S–30° N) has been removed from the SST trend pattern and zero contours omitted for clarity.

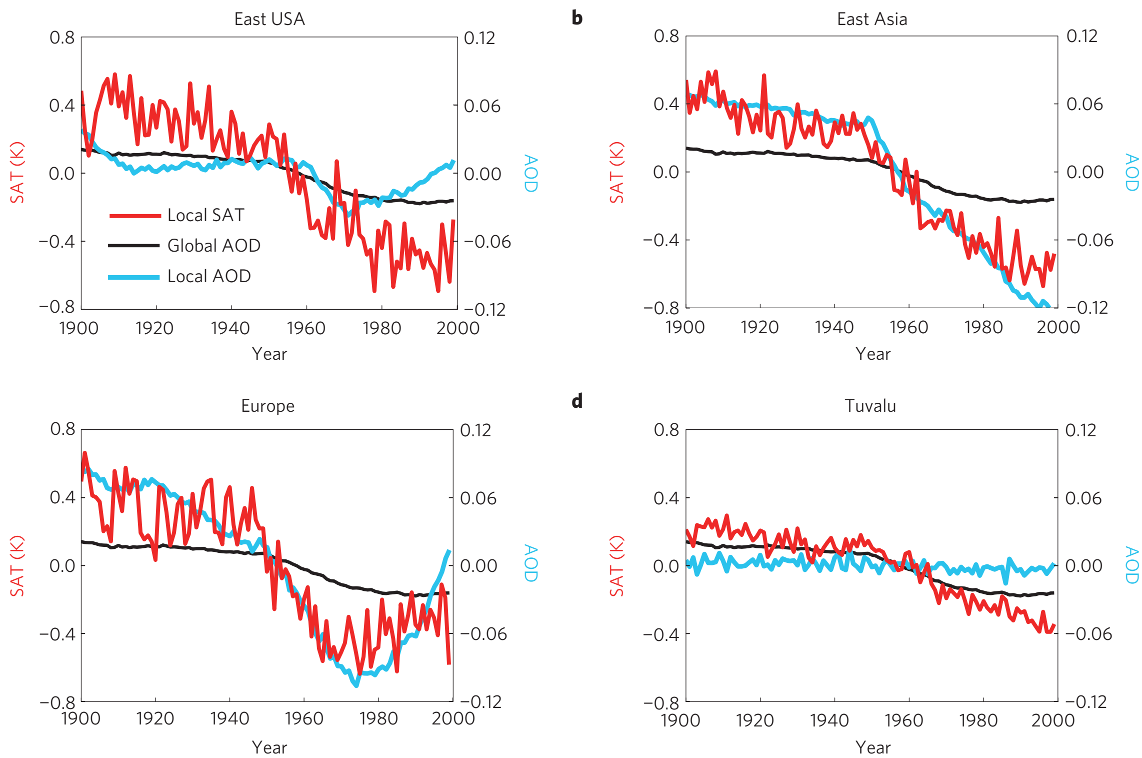

Figure 4 | Aerosol forcing and temperature response. a–d, Time series of SAT (in K), global and local AOD (sign reversed) in the eastern USA (**a**, 30° N–60° N, 60° W–100° W); East Asia (**b**, 20° N–40° N, 100° E–160° E); Europe (**c**, 37° N–60° N, 10° W–60° E); and the South Pacific around Tuvalu (**d**, 15° S–5° S, 170° E–180°).

much of the aerosol research has focused on microphysical processes, here we suggest that there are robust macroscale structures in climate response over the ocean that are qualitatively insensitive to the details of microphysics as judged from cross-model consistency. The GHG- and aerosol-induced climate change shares a common set of ocean–atmospheric feedback, explaining the spatial resemblance between the two types of response. Innovative model experimentations are needed to probe ocean–atmosphere interaction mechanisms for pattern formation. Such predictive pattern dynamics is crucial to guide developing observational constraints towards reliable regional climate projections.

Methods

Historical runs. A set of historical simulations in the CMIP5 is used here, including historical single-forcing (aerosol and GHG) and full radiative-forcing simulations. Three state-of-art models (Geophysical Fluid Dynamics Laboratory CM3, Australian CSIRO MK3.6 and Canadian Centre CanESM2) are chosen for analysis because multiple runs with different initial conditions are available for each single-forcing simulation. For a given type simulation, we obtain the multimember average for each model first to reduce the effect of internal variability and then construct the multimodel ensemble mean. For historical single-forcing runs, either aerosols or GHGs are the only time-varying forcing agents with other forcing fixed at the pre-industrial level. The climate response to GHG and aerosol forcing is not exactly additive and the sources of the nonlinearity are an area of active research[17]. Nevertheless, it is important to study the response to single forcing both for the sake of physical understanding and in light of the trend that the GHG forcing will continue to intensify whereas the aerosol forcing is likely to abate in the near future.

The climatology is defined as the 1900–1999 average and annual mean anomalies are calculated for analysis. The 11-year running mean is applied before the EOF analysis to suppress interannual variability. Sen's Method[30] is employed to derive a median-type trend and eliminate the effect of extreme points. The twentieth-century change refers to the trend for 1900–1999.

Fixed SST runs. Radiative forcing is defined here at the top of the atmosphere with atmospheric and land temperatures adjusted to composition change, derived from atmospheric model runs with SST fixed at the monthly climatology[27]. Results are available for MK3.6 and CanESM2, forced separately by year 2000 minus pre-industrial aerosol change and quadruple CO_2 (all other forcing agents are fixed at the pre-industrial level). The atmospheric runs are 30 and 50 years long for MK3.6 and CanESM2, respectively. Results from the past 25 years for each model are used for analysis.

Received 26 May 2013; accepted 29 July 2013; published online 1 September 2013

References

1. Vecchi, G. A. & Soden, B. J. Effect of remote sea surface temperature change on tropical cyclone potential intensity. *Nature* **450,** 1066–1070 (2007).
2. Giannini, A., Saravanan, R. & Chang, P. Oceanic forcing of Sahel Rainfall on interannual to interdecadal timescales. *Science* **302,** 1027–1030 (2003).
3. Xie, S-P. *et al*. Global warming pattern formation: Sea surface temperature and rainfall. *J. Clim.* **23,** 966–986 (2010).
4. Chung, C. E. & Ramanathan, V. Weakening of North India sea surface temperature gradient and the monsoon rainfall in India and the Sahel. *J. Clim.* **19,** 2036–2045 (2006).
5. Kerr, R. A. Time to adapt to a warming world, but where's the science? *Science* **334,** 1052–1053 (2011).
6. Menon, S., Hansen, J., Nazarenko, L. & Luo, Y. Climate effect of black carbon aerosols in China and India. *Science* **297,** 2250–2253 (2002).
7. Lau, K. M., Kim, M. K. & Kim, K. M. Asian summer monsoon anomalies induced by aerosol direct forcing: The role of the Tibetan Plateau. *Clim. Dyn.* **26,** 855–864 (2006).
8. Bollasina, M. A., Ming, Y. & Ramaswamy, V. Anthropogenic aerosols and the weakening of the South Asian summer monsoon. *Science* **334,** 502–505 (2011).
9. Rotstayn, L. D. & Lohmann, U. Tropical rainfall trends and the indirect aerosol effect. *J. Clim.* **15,** 2103–2116 (2002).
10. Forster, P. *et al.* in *IPCC Climate Change 2007: The Physical Science Basis* (eds Solomon, S. *et al.*) (Cambridge Univ. Press, 2007).
11. Andrews, T., Forster, P. M. & Gregory, J. M. A surface energy perspective on climate change. *J. Clim.* **22,** 2557–2570 (2009).
12. Rosenfeld, D. *et al*. Flood or drought: How do aerosols affect precipitation? *Science* **321,** 1309–1313 (2008).
13. Boer, G. J. & Yu, B. Climate sensitivity and response. *Clim. Dyn.* **20,** 415–429 (2003).
14. Sobel, A. H., Held, I. M. & Bretherton, C. S. The ENSO signal in tropical tropospheric temperature. *J. Clim.* **15,** 2702–2706 (2002).
15. Johnson, N. C. & Xie, S-P. Changes in the sea surface temperature threshold for tropical convection. *Nature Geosci.* **3,** 842–845 (2010).
16. Yoshimori, M. & Broccoli, A. J. Equilibrium response of an atmosphere-mixed layer ocean model to different radiative forcing agents: Global and zonal mean response. *J. Clim.* **21,** 4399–4423 (2008).
17. Ming, Y. & Ramaswamy, V. A model investigation of aerosol-induced changes in tropical circulation. *J. Clim.* **24,** 5125–5133 (2011).
18. Liu, Z., Vavrus, S., He, F., Wen, N. & Zhong, Y. Rethinking tropical ocean response to global warming: The enhanced equatorial warming. *J. Clim.* **18,** 4684–4700 (2005).
19. Manabe, S. & Stouffer, R. J. Role of ocean in global warming. *J. Meteorol. Soc. Jpn* **85,** 385–403 (2007).
20. Ming, Y., Ramaswamy, V. & Chen, G. A model investigation of aerosol-induced changes in boreal winter extratropical circulation. *J. Clim.* **24,** 6077–6091 (2011).
21. Lu, J. & Zhao, B. The role of oceanic feedback in the climate response to doubling CO_2. *J. Clim.* **25,** 7544–7563 (2012).
22. Ma, J. & Xie, S-P. Regional patterns of sea surface temperature change: A source of uncertainty in future projections of precipitation and atmospheric circulation. *J. Clim.* **26,** 2482–2501 (2013).
23. Alexander, M. A., Vimont, D. J., Chang, P. & Scott, J. D. The impact of extratropical atmospheric variability on ENSO: Testing the seasonal footprinting mechanism using coupled model experiments. *J. Clim.* **23,** 2885–2901 (2010).
24. Chiang, J. C. H. & Friedman, A. R. Extratropical cooling, interhemispheric thermal gradients, and tropical climate change. *Annu. Rev. Earth Planet. Sci.* **40,** 383–412 (2012).
25. Kang, S. M., Held, I. M., Frierson, D. M. W. & Zhao, M. The response of the ITCZ to extratropical thermal forcing: idealized slab-ocean experiments with a GCM. *J. Clim.* **21,** 3521–3532 (2008).
26. Frierson, D. M. W. & Hwang, Y-T. Extratropical influence on ITCZ shifts in slab ocean simulations of global warming. *J. Clim.* **25,** 720–733 (2012).
27. Hansen, J. *et al.* Efficacy of climate forcings. *J. Geophys. Res* **110,** D18104 (2005).
28. Shindell, D. T., Voulgarakis, A., Faluvegi, G. & Milly, G. Precipitation response to regional radiative forcing. *Atmos. Chem. Phys.* **12,** 6969–6982 (2012).
29. Deser, C., Knutti, R., Solomon, S. & Phillips, A. S. Communication of the role of natural variability in future North American climate. *Nature Clim. Change* **2,** 775–779 (2012).
30. Sen, P. K. Estimates of the regression coefficient based on Kendall's tau. *J. Am. Stat. Assoc.* **63,** 1379–1389 (1968).

Acknowledgements

This work was supported by the NSF (ATM-0854365), the National Basic Research Program of China (2012CB955600), the NOAA Climate Program Office (NA10OAR4310250), the China Scholarship Council and JAMSTEC.

Author contributions

S-P.X. and B.L. designed the study, conducted analysis and wrote the paper. They contributed equally. B.X. carried out the tropospheric temperature perturbation experiments.

Additional information

Supplementary information is available in the online version of the paper. Reprints and permissions information is available online at www.nature.com/reprints. Correspondence and requests for materials should be addressed to S-P.X.

Competing financial interests

The authors declare no competing financial interests.

杨明珠,陈丽娟,宋文玲.2013.黑潮区海温对中国北方初霜冻日期的影响研究.气象,39(9):1125-1132.

黑潮区海温对中国北方初霜冻日期的影响研究*

杨明珠　陈丽娟　宋文玲

国家气候中心,中国气象局气候研究开放实验室,北京 100081

提　要:利用站点观测和再分析资料研究了黑潮海温(SST)与中国北方初霜冻日期的关系。结果表明,前期夏季各月及初秋黑潮区SST异常变化和中国北方秋季初霜冻日期的关系十分显著。当黑潮区SST偏高(低)时,华北大部、黄淮北部、河套北部、内蒙古中部和东北部、环渤海区域初霜冻日期偏晚(早)。进一步分析显示,夏末和初秋黑潮区SST异常主要通过影响其上空初秋及秋季局地大气环流系统,对华北、黄淮北部等地区初霜冻造成影响。当黑潮区SST偏高(低)时,我国华北至日本以东区域上空500 hPa高度场偏高(低),低层风场则出现东南(西北)风,从而导致东亚大槽偏弱(强),来自北方的冷空气活动势力被削弱(增强),从而导致上述区域初霜冻发生较常年偏晚(早)。

关键词:黑潮区SST指数,初霜冻日期,环流系统

中图分类号:P461　　**文献标志码**:A　　**doi**:10.7519/j.issn.1000-0526.2013.09.006

Impact of Kuroshio SST on First Frost Dates in Northern China

YANG Mingzhu　CHEN Lijuan　SONG Wenling

Laboratory for Climate Studies of CMA, National Climate Centre, Beijing 100081

Abstract: The relationship between Kuroshio sea surface temperature index (KuSSTI) and the first frost dates (FFDs) in northern China are analyzed on the basis of observation data and reanalysis data. The results show that the monthly KuSSTIs of respective months of summer and early autumn have significant impacts on FFDs in northern China. The warmer (cooler) the Kuroshio SSTs are, the later (earlier) FFDs in North China, Huang-Huai Region, northern Hetao Region, middle and northeastern Inner Mongolia and the region around the Bohai Sea are. Further analysis indicates that the warm (cold) Kuroshio SST anomalies significantly influence the general circulation from northern China, Japan Sea to north Pacific, increasing (decreasing) the 500 hPa geopotential height and weakening (strengthening) the East Asia trough. The lower level wind anomaly shows southeast (northwest) direction over North China and Huang-Huai Region, weakening (strengthening) the cold wave from the north, so that the FFDs in North China and Huang-Huai Region come later (earlier) than normal.

Key words: Kuroshio SST index, the first frost date, general circulation

引　言

霜冻是一种严重的农业气象灾害,发生地区几乎遍及全国,严重影响粮食产量。尤其是在中国北方地区,当初霜出现偏早时,常常会影响农作物籽粒成熟度,导致农业减产,因此提供准确及时的初霜冻预测信息,有利于帮助用户尤其是农业生产部门采

* 国家科技支撑项目(2009BAC51B05)、国家重点基础研究发展规划(973)项目(2012CB955902)、公益性行业(气象)科研专项(GYHY201306018和GYHY201306070)、国家自然科学基金面上项目(41275073)及中国气象局短期气候预测创新团队共同资助

2012年12月17日收稿;　2013年5月3日收修定稿

第一作者:杨明珠,主要从事气候异常诊断和预测方法研究.Email:yangmz@cma.gov.cn

通信作者:陈丽娟,主要从事气候异常诊断和预测方法研究.Email:chenlj@cma.gov.cn

取适当的措施减轻灾害损失。

已经有大量的研究分析了初霜、霜期和霜冻的气候特征(杨克明等,1999;李想等,2005;林纾等,2007;叶殿秀等,2008;王国复等,2009;韩荣青等,2010;李辑等,2010;温晶等,2010;钱锦霞等,2010;王业宏等,2011),时间尺度包括年际变化、年代际变化和气候变化趋势,空间尺度包括全国或者区域/省级,还有部分研究从天气角度分析了温度对结霜的影响(温显罡等,2012),然而从气候学角度探讨造成初霜冻日期早晚变化的气候趋势预测工作较少,尤其是预测用的前期信号十分匮乏,也缺少有效的预测方法。即使是尝试在业务中应用的一些可能影响初霜冻出现时间的预测因子,也需要审视在气候变化背景下预测对象和预测因子的关系是否依然稳定或显著。

对于月-季节尺度的短期气候预测而言,海表温度(SST)异常是一个重要的外强迫信号,尤其是热带太平洋海温异常导致的海气相互作用可能对东亚季风和我国天气气候造成不同程度的影响。近期一些研究表明,我国近海的海温异常也对我国区域天气气候异常有影响。例如东海及附近海域 SST 的变化与东亚冬季风年代际减弱具有明显的关系(蔡榕硕等,2011),也有研究认为中国近海的 SST 更多是被动地随气温改变(康丽华等,2009),但海温与中国秋、冬季气温确实具有密切的关系。那么在气候变暖的背景下,中国近海海温对秋季气候,包括秋季初霜冻时间的早晚究竟起到什么作用值得进一步研究。

本文首先对比了气候值改变对中国北方地区初霜冻日期气候特征的影响,简要分析了其整体趋势,比较了气候平均值改变后,ENSO 循环对初霜冻日期早晚影响的变化。通过分析发现黑潮区 SST 对北方部分地区初霜冻出现早晚有显著的关系,从而进一步分析了黑潮区 SST 异常影响北方初霜冻时间早晚的可能途径。

1 资 料

本文采用的初霜日期为国家气候中心常规业务秋冬季初霜冻日期标准(韩荣青等,2010):以地面 0 cm 最低温度≤0℃的第一天定义为初霜日,初霜日期资料为中国北方 30°N 以北的台站资料,其中 1961—2011 年有 188 个站无缺测,本文选取该 188 个站(图 1)进行分析。

所使用的环流和海温资料为:(1) NCEP/NCAR 从 1948 年 1 月至 2011 年 12 月的再分析格点资料(Kalney 等,1996),水平分辨率为 2.5°×2.5°;(2)黑潮区海温指数为国家气候中心整编的业务用特征量指数,取(25°～35°N、125°～160°E)范围内海温空间平均值。

主要采用的方法有:Pearson 相关分析方法、合成方法以及经验正交函数分解方法(EOF)。

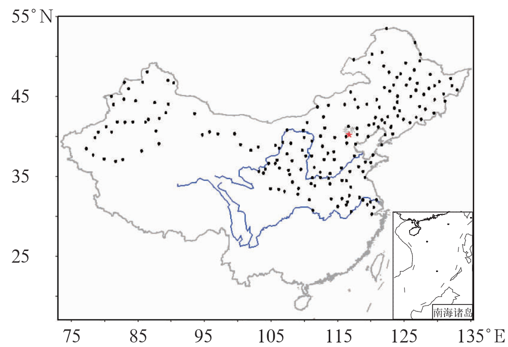

图 1 中国北方地区初霜冻日期分析代表站分布

Fig. 1 Distribution of representative observation stations for the analysis of the first frost dates in northern China

2 中国北方初霜冻日期的气候特征

1981—2010 年气候平均初霜冻日期(图 2a)显示,中国北方初霜冻出现日期由北往南顺次出现,东北大部、内蒙古中部和东部、新疆北部局部、西北西部于 9 月中旬或之前出现初霜冻,其中黑龙江西北部局部、内蒙古东北部、新疆北部的东北部和西北部局部地区在 9 月上旬或之前出现初霜冻;东北中部大部、内蒙古西部局部、新疆中部、西北东部、华北北部在 9 月下旬出现初霜冻;东北南部、华北大部、西北东南部、黄淮北部等地区在 10 月中旬至下旬出现初霜冻,黄淮南部在 11 月上旬出现初霜冻,黄淮以南的地区在 11 中旬之后发生初霜冻。即北方大部出现霜冻的气候值处于 9—11 月期间,当然每年的年际变化也比较大。

将 1981—2010 年初霜冻日期气候值与 1971—2000 年气候值比较(图 2b),中国北方初霜冻除新疆东北部局部和黑龙江北部局部区域外,发生日期整体偏晚,新疆北部、西北中部和东南部、内蒙古西部、

华北大部平均推后 3～5 d,其中内蒙古西部、甘肃中部、新疆东北部推后 5～10 d。

对 1961—2010 年初霜冻日期进行经验正交函数分解(EOF),EOF 第一模态的方差贡献为 58.6%,其特征值一致为负值的空间分布,时间系数(图 3)在 20 世纪 90 年代之前为正值,之后为负值,表明中国北方初霜冻日期在 90 年代之后具有整体趋于偏晚的特征。由于处于偏晚的气候背景下,采用 1981—2010 年平均作为气候值是否会影响对初霜日期影响系统的诊断结果? 由于海洋异常(如 ENSO 事件)对大气环流及我国年际气候异常具有重要的影响(贾小龙等,2011),下面首先分析短期气候预测重要的外强迫因子,即 ENSO 循环对初霜日期早晚的可能影响。

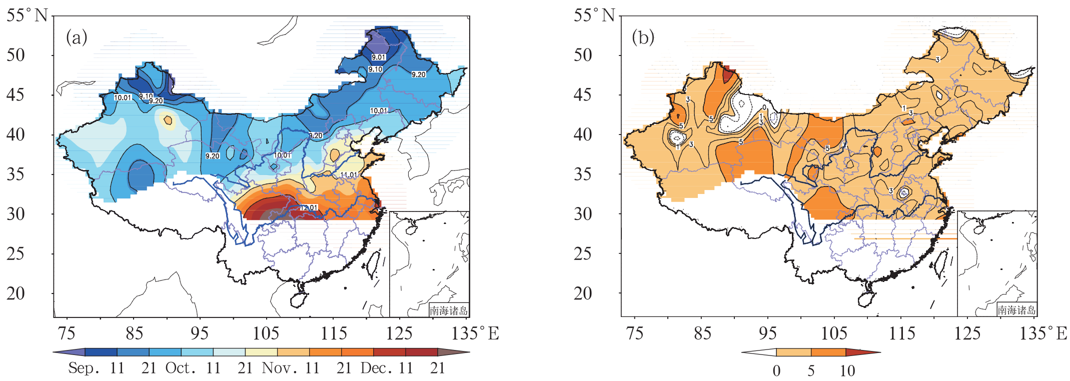

图 2　我国北方初霜冻日(a)1981—2010 年平均气候值,(b)1981—2010 年平均值与 1971—2000 年平均值之差(单位:d)

Fig. 2　The first frost dates averaged from 1981 to 2010 (a), and the differences of average values from 1981 to 2010 and from 1971 to 2000 (unit: d)

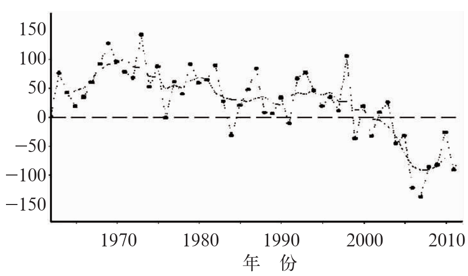

图 3　中国北方初霜冻日期 EOF 分析第一模态时间系数

Fig. 3　The time coefficients of EOF one for the first frost dates of northern China

3　ENSO 对初霜冻日期的可能影响

从前期各季和各月 Nino3.4 指数与中国北方初霜冻日期的相关分析来看,中东太平洋 SST 与中国北方初霜冻的日期关系并不显著。根据国家气候中心对 ENSO 的定义(李晓燕等,2000),采用 1981—2010 年平均值,1961—2011 年厄尔尼诺、拉尼娜事件分别有 13 个,拉尼娜事件到秋季结束或仍然持续的年份有 18 年:1962、1963、1964、1967、1970、1973、1974、1975、1984、1985、1988、1989、1995、1998、1999、2000、2007 和 2010 年;秋季处于厄尔尼诺暖事件的年份有 11 年:1963、1965、1969、1972、1982、1987、1991、1997、2002、2006 和 2009 年。拉尼娜年初霜冻日期正距平频次合成分析表明(图略),中国北方大部初霜冻日期偏早,其中东北大部、华北大部、西北大部初霜冻日期偏早年份居多,而偏晚年份偏多的区域主要在黑龙江西北部局部、内蒙古东北部和中部局部、新疆东部等地。厄尔尼诺年初霜冻日期正距平频次合成分析显示(图略),除东北西部北部、内蒙古东北部和中部局部以及新疆东北部偏晚外,中国北方其余大部偏早的年份居多。分析 20 世纪 80 年代前后拉尼娜/厄尔尼诺年的初霜冻日期,结果显示,20 世纪 80 年代之前,无论是拉尼娜年还是厄尔尼诺年,我国北方大部初霜冻日期均偏早(图略);而 80 年代之后的拉尼娜年(图 4a),除了东北中部、内蒙古中西部、华北东部、新疆西部和西北东部局部等地偏早外,中国北方大部地区初霜冻偏晚的可能性较大,而厄尔尼诺年(图 4b)中国北方大部初霜冻偏早的可能性较大,偏

晚的区域仅在东北南部和东部局部、新疆中南部等地。因此，采用 1981—2010 年平均值之后，ENSO 循环对于初霜冻的影响在 1980 年之前没有参考意义，而 20 世纪 80 年代之后发生的 ENSO 事件对初霜冻日期出现早晚的区域在华北大部、东北中部和南部、内蒙古中东部区域的影响差异不明显。

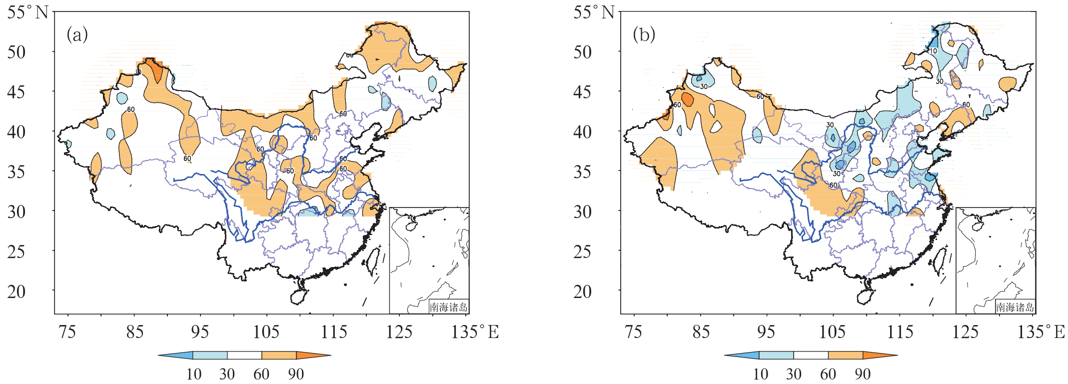

图 4　1980 年代之后拉尼娜年(a)和厄尔尼诺年(b)中国北方初霜冻日期正距平频次合成分布(采用 1981—2010 年气候值)

Fig. 4　The positive anomalies frequency composite distributions of La Nina years (a) and El Nino years (b) for first frost dates in northern China (climate: 1981－2010)

4　黑潮区 SST 异常与中国北方初霜冻日期的可能联系

上面的相关和合成分析表明，即使是 20 世纪 80 年代之后 ENSO 循环对初霜冻影响显著的阶段，其对中国北方初霜冻的指示意义也是十分有限，尤其对于华北、内蒙古中部、东北、黄淮北部等中国北方的东部区域，在拉尼娜年和厄尔尼诺年对初霜日期的早晚影响差别不明显。有研究表明，中国近海的 SST 变化与东亚冬季风的关系密切(蔡榕硕等，2011)，东亚季风的强弱明显受到纬向海陆热力差异的影响(郭其蕴，1983；赵汉光等，1996；祝从文等，2000；孙秀荣等，2002)，作为东亚季风系统的直接下垫面，西北太平洋及我国近海 SST 对东亚局地环流的影响可能更加直接。监测表明，2012 年夏季中东太平洋 SST 为近中性状态，作为大气的外强迫信号相对较弱，而黑潮区 SST 在春、夏季持续为显著的负异常，同时亲潮区 SST 为显著正异常分布，这些区域 SST 异常是否会影响局地环流并对我国秋季气候产生影响，值得进一步分析。初步计算显示黑潮区 SST 与中国北方初霜冻日期具有很好的相关，本文将探讨黑潮区 SST 对中国初霜冻的影响途径。以下分析采用 1981－2010 年平均作为气候值。

4.1　黑潮区 SST 指数与中国北方初霜冻日期的关系

黑潮区 SST 指数于 20 世纪 90 年代后期进入偏暖阶段(图 5)，对应着中国北方初霜冻日期也进入偏晚的阶段(图 3)。图 6 为 8 和 9 月黑潮区 SST 与中国北方初霜冻日期的相关，在华北大部、黄淮北部、河套北部、内蒙古中部和东北部、环渤海区域均稳定超过显著性检验水平，实际上在前期 6 和 7 月也有类似的相关分布(图略)。因此，相关分析显示前期及同期黑潮区 SST 与初霜冻日期具有很好的相关，并且相关区域稳定通过显著性检验水平。

黑潮区 SST 在 5—12 月的自相关系数(表 1)均

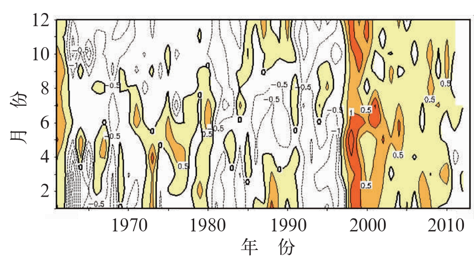

图 5　1961 年 1 月至 2011 年 7 月黑潮区 SST 指数时间演变图
(阴影区为 KuSSTI>0 的区域)

Fig. 5　Variation of Kuroshio SST index (KuSSTI) during January 1961 to July 2011
(KuSSTI>0 are shaded)

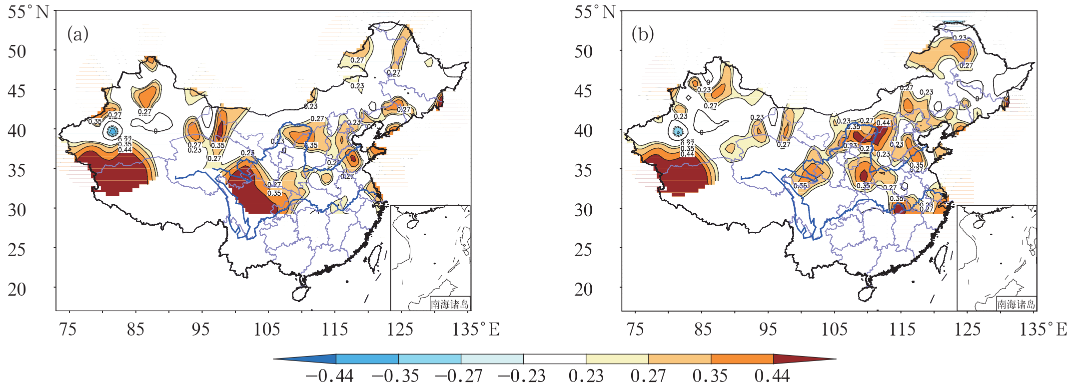

图 6　1961—2011 年 8 月(a)及 9 月(b)黑潮区 SST 指数与中国北方初霜冻日期的相关分布

(阴影区由浅至深依次为相关性通过 0.10、0.05、0.01、0.001 显著性检验的区域)

Fig. 6　Correlations of Kuroshio SST index (KuSSTI) in August (a) and September (b) with first frost dates in northern China

(The shaded areas from light to dark denote significant level exceeding 0.1, 0.05, 0.01 and 0.001 respectively)

表 1　1961—2011 年 5—12 月黑潮区 SST 自相关系数

Table 1　Self correlations of monthly KuSSTI from May to December during 1961－2011

月份	5	6	7	8	9	10	11	12
5	**1**	**0.632**	**0.450**	**0.449**	**0.470**	**0.458**	**0.437**	**0.443**
6		**1**	**0.758**	**0.545**	**0.419**	**0.459**	**0.471**	**0.523**
7			**1**	**0.677**	**0.499**	**0.432**	0.327	**0.370**
8				**1**	**0.642**	**0.476**	**0.376**	0.293
9					**1**	**0.712**	**0.548**	**0.376**

注:加粗字体为相关通过 0.001 显著性水平检验的值

Bold numbers denote correlations exceeding 0.001 significanl level test

达到或超过 0.05 显著性水平检验,表明黑潮区 SST 异常在月际变化上具有很好的持续性。因此黑潮区 SST 异常可以作为一个先兆信号来尝试预测中国北方初霜冻日期,这其中的可能机制值得进一步分析。

4.2　黑潮区 SST 指数对 500 hPa 环流的影响

8 和 9 月黑潮区 SST 指数与 9 月及秋季 500 hPa 高度场的相关显示(图 7),无论是 8 月还是 9 月,高相关区从华北、黄淮向东伸展到北太平洋呈带状分布,达到 0.05 的显著性检验水平,表明当黑潮区 SST 偏暖(冷)时,有利于从中国华北区域至北太平洋位势高度场偏高(低)。其中在我国华北至日本群岛附近的相关区更加显著,9 月黑潮区 SST 指数与同期 500 hPa 高度场相关在上述区域达到 0.001 的显著性检验水平,而该区域是东亚大槽活动的区域,即黑潮区 SST 暖(冷)时,东亚大槽偏弱(强),从而有利于造成北方南下的冷空气活动偏弱(强),进而造成华北、黄淮、内蒙古中部、环渤海区域初霜冻日期偏晚(早)。

黑潮区上空(30°～45°N、120°～160°E)范围内 500 hPa 高度场与黑潮区 SST 具有很好的相关。对该区域的空间平均值进行逐月自相关分析(表 2),结果显示,6 月和秋季各月、8 月和 9、10 月,9 月与 10 月的高度场具有较好相关,但其他月相关性不显著,因此可见黑潮区上空大气环流的月季变化持续性较差。从黑潮区 SST 的自相关分析来看,黑潮区上空大气环流的变化更多受到 SST 异常的影响。

4.3　黑潮区 SST 对低层风场的影响

初霜发生早晚的区域与冷空气活动范围、风场变化密切相关。图 8a 为 9 月 850 hPa 风场与前期 8 月黑潮 SST 指数的相关分布,中国江南、江淮、黄淮、华北至内蒙古中部区域为显著相关分布,矢量风为东南方向;中国东部和北方大部为正的经向风相关分布。9 月黑潮区 SST 指数与秋季 850 风场的相

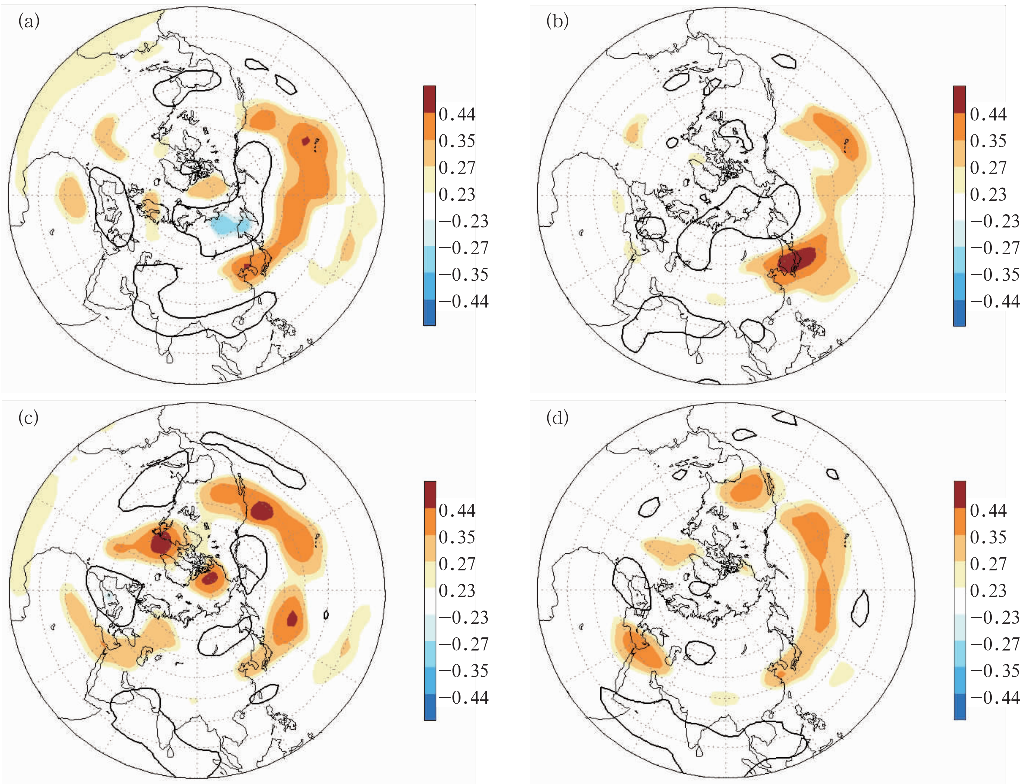

图 7　黑潮区 SST 指数与 500 hPa 位势高度场相关分布

(a) 8 月黑潮区 SST 与 9 月 500 hPa 位势高度场，(b) 9 月黑潮区 SST 与 9 月 500 hPa 位势高度场，(c) 8 月黑潮区 SST 与秋季 500 hPa 位势高度场，(d) 9 月黑潮区 SST 与秋季 500 hPa 位势高度场

(阴影区由浅到深依次为相关性通过 0.10、0.05、0.01、0.001 显著性检验的区域)

Fig. 7　Correlation of KuSSTI and H_{500} during 1961－2011

(a) KuSSTI in August and H_{500} in September, (b) KuSSTI and H_{500} in September, (c) KuSSTI in August and H_{500} in SON, (d) KuSSTI in September and H_{500} in SON

(The shaded areas from light to dark denote significant level exceeding 0.10, 0.05, 0.01 and 0.001 respectively)

表 2　1961—2011 年 5—12 月 H_{500} (30°～45°N、120°～160°E) 自相关系数

Table 2　Self correlations of monthly H_{500} (30°－45°N, 120°－160°E) from May to December during 1961－2011

月份	5	6	7	8	9	10	11	12
5	**1**	0.186	－0.004	0.012	0.094	**0.301**	－0.003	0.077
6		**1**	**0.380**	0.143	**0.400**	**0.411**	**0.304**	0.239
7			**1**	0.240	0.222	0.207	－0.076	－0.035
8				**1**	**0.410**	**0.357**	－0.051	－0.212
9					**1**	**0641**	0.213	0.012

加粗字体为相关通过 0.05 显著性检验的值

Same as Table 1, but for 0.05

关分布(图 8b)与对 9 月的分布相似，同样对我国东部和北方区域具有显著的影响。实际上，前期 6、7 月的相关场与此类似(图略)。相关分析表明，邻近及同期黑潮区 SST 偏暖(冷)时，初秋和秋季我国东部和北部区域易受东南(西北)异常环流的影响，这种作用使得北方冷空气势力得以削弱(增强)，从而有利于华北及黄淮地区的初霜冻发生较常年偏晚(早)。

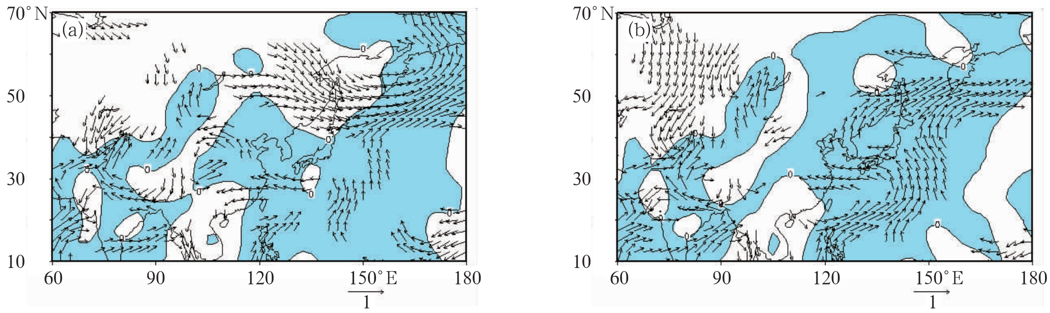

图 8　8 月黑潮区 SST 指数与 9 月(a)及秋季(b)850 hPa 风场的矢量相关图,
仅显示出通过 0.05 显著性检验的相关矢量分布
(阴影区为经向相关>0 的区域)

Fig. 8　Correlation vectors between KuSSTI in August and winds at 850 hPa
in September (a) and SON (b)
(Shaded area denotes longitudinal correlations pointing to north)

5　小　结

本文对中国 30°N 以北的 188 站初霜冻日期采用 1981—2010 年平均值的气候分布状况进行了分析,并与 1971—2000 年平均值进行了对比,进一步分析了初霜冻日期在采用 1981—2010 年气候值后与 ENSO 事件关系的变化,最后从外强迫异常影响的角度,发现黑潮海温异常对我国北方初霜冻日期有一定的影响,探讨了其中的可能机制。主要结论如下:

(1) 1981—2010 年初霜冻日期气候值显示,我国北方初霜冻日期由北往南次第出现,东北中北部、内蒙古、西北新疆中北部在 9 月发生初霜冻,东北南部、华北大部、西北东南部、黄淮北部在 10 月发生,而黄淮以南区域在 11 月之后发生初霜冻,主要分布在秋季时节。与 1971—2000 年的气候平均值相比,中国北方初霜冻日期除新疆东北部局部和黑龙江北部局部外整体偏晚,该趋势在 20 世纪 90 年代之后显著。

(2) 采用 1981—2010 年平均值之后,ENSO 循环对于初霜冻日期的影响在 1980 年之前没有参考意义;而 20 世纪 80 年代之后发生的 ENSO 事件,对初霜冻日期出现早晚的区域在华北大部、东北中部和南部、内蒙古中东部区域的影响差异不显著,缺少较好的指示意义。

(3) 夏季各月及初秋黑潮区 SST 指数与华北大部、黄淮北部、河套北部、内蒙古中部和东北部以及环渤海区等区域具有稳定的显著正相关关系。进一步的分析表明,夏末和初秋黑潮区 SST 主要通过影响其上空初秋及秋季局地大气环流系统,对中国北方东部初霜冻造成影响,当黑潮区 SST 偏高(低),我国东部及北方区域至日本以东区域上空 500 hPa 高度场偏高(低),低层风场易出现东南(西北)风,从而导致东亚大槽偏弱(强),来自北方的冷空气活动势力得以削弱(增强),从而导致上述区域初霜冻发生较常年偏晚(早)。

(4) 黑潮区 SST 异常在月际变化上具有很好的持续性,而黑潮区上空大气环流的月际变化显示持续性较低,因此黑潮区 SST 异常可以作为一个先兆信号来尝试预测中国北方初霜冻日期。

上述分析是在未去趋势情况下得到的结果。那么这种关系是否由于气候变暖背景下初霜冻日期、海温及环流的线性趋势变化造成的虚假信息?我们对初霜冻日期、黑潮区海温指数和环流等均去趋势后,再进行相关分析,结果表明:黑潮区海温与我国北方东部初霜冻日期的显著相关区范围稍有缩小,但中心位置与未去趋势前一致;环流场上,黑潮区与华北、黄淮向东伸展到北太平洋的相关仍然通过显著性检验(图略)。分析表明,尽管在气候变暖背景下,我国北方初霜冻日期具有推后趋势、黑潮区海温有升温趋势、环流场有增高趋势,但黑潮区海温异常与环流的相关关系并不是各自线性趋势变化造成的虚假关系。

本文是探寻影响我国北方初霜冻日期先兆信号的初步工作，在机理和预测模型建立方面有待做深入研究。

参考文献

蔡榕硕，陈际龙，谭红建. 2011. 全球变暖背景下中国近海表层海温变异及其与东亚季风的关系. 气候与环境研究，16(1)：94-104.

郭其蕴. 1983. 东亚夏季风强度指数及其变化的分析. 地理学报，38(3)：207-217.

韩荣青，李维京，艾婉秀，等. 2010. 中国北方初霜冻日期变化及其对农业的影响. 地理学报，65(5)，525-532.

贾小龙，陈丽娟，龚振淞，等. 2011. 2010年海洋和大气环流异常对中国气候的影响. 气象，37(4)：446-453.

康丽华，陈文，王林，等. 2009. 我国冬季气温的年际变化及其与大气环流和海温异常的关系. 气候与环境研究，14(1)：45-53.

李辑，严晓瑜，王颖. 2010. 辽宁省近50年霜的气候变化特征. 气象，36(11)：38-45.

李想，陈丽娟，张培群. 2005. 1954—2005年长江以北地区初霜期变化趋势. 气候变化研究进展，4(1)：21-25.

李晓燕，翟盘茂. 2000. ENSO事件指数与指标研究. 气象学报，58(1)：102-109.

林纾，陈丽娟，王润元，等. 2007. 西北地区初终霜冻的气候特征分析. 地球科学进展，22(特刊)：133-139.

钱锦霞，张霞，张建新，等. 2010. 近40年山西省初终霜日的变化特征. 地理学报，65(7)：801-808.

孙秀荣，陈隆勋，何金海. 2002. 东亚海陆热力差指数及其与环流和降水的年际变化关系. 气象学报，60(2)，164-172.

温晶，胡丽甜，李霞，等. 2010. 近55年广州霜冻的年际和年代际变化特征. 广东气象，32(2)：1-3.

温显罡，马舒庆，杜波，等. 2012. 草温与露点温度对结露和结霜指示性分析. 气象，38(6)：745-750.

王国复，许艳，朱燕君，等. 2009. 近50年我国霜期的时空分布及变化趋势分析. 气象，35(7)：61-67.

王业宏，高惠君，张璇. 2011. 山东省霜冻的气候变化特征分析. 安徽农业科学，39(15)：9062-9076.

杨克明，陈秀凤，王东升，等. 1999. 东北地区初霜冻的天气气候特征. 气象，25(6)：13-18.

叶殿秀，张勇. 2008. 1961—2007年我国霜冻变化特征. 应用气象学报，19(6)：661-665.

赵汉光，张先恭. 1996. 东亚季风和我国夏季雨带的关系. 气象，22(4)：8-12.

祝从文，何金海，吴国雄. 2000. 东亚季风指数及其与大尺度热力环流年际变化关系. 气象学报，58(4)：391-402.

Kalney E，Kanamitsu M，Kistler R，et al. 1996. The NCEP/NCAR 40-year reanalysis project. Bull Amer Meteor Soc，77(3)：437-471.

Spatial and Temporal Characteristics of Beijing Urban Heat Island Intensity

PING YANG

China Meteorological Administration Training Center, Beijing, China

GUOYU REN

Laboratory for Climate Studies, National Climate Center, China Meteorological Administration, Beijing, China

WEIDONG LIU

Institute of Urban Meteorology, China Meteorological Administration, Beijing, China

(Manuscript received 15 May 2012, in final form 12 March 2013)

ABSTRACT

An hourly dataset of automatic weather stations over Beijing Municipality in China is developed and is employed to analyze the spatial and temporal characteristics of urban heat island intensity (UHII) over the built-up areas. A total of 56 stations that are located in the built-up areas [inside the 6th Ring Road (RR)] are considered to be urban sites, and 8 stations in the suburban belts surrounding the built-up areas are taken as reference sites. The reference stations are selected by using a remote sensing method. The urban sites are further divided into three areas on the basis of the city RRs. It is found that the largest UHII generally takes place inside the 4th RR and that the smallest ones occur in the outer belts of the built-up areas, between the 5th RR and the 6th RR, with the areas near the northern and southern 6th RR experiencing the weakest UHI phenomena. On a seasonal basis, the strongest UHII generally occurs in winter and weak UHII is dominantly observed in summer and spring. The UHII diurnal variations for each of the urban areas are characterized by a steadily strong UHII stage from 2100 local solar time (LST) to 0600 LST and a steadily weak UHII stage from 1100 to 1600 LST, with the periods 0600–1100 LST and 1600–2100 LST experiencing a swift decline and rise, respectively. UHII diurnal variation is seen throughout the year, but the steadily strong UHII stage at night is longer (shorter) and the steadily weak UHII stage during the day is shorter (longer) during winter and autumn (summer and spring).

1. Introduction

Human activities have modified the composition, structure, and energy balance of the earth's surface and the lower atmosphere in highly industrialized regions such as Europe, North America, and eastern Asia. These artificial factors determine a distinct local climate in big cities, expressed as urban climate. With the urban modification to the natural land cover, surface air temperature (SAT) in the urban areas increases significantly relative to the SAT in surrounding suburbs. This phenomenon is known as the urban heat island (UHI) effect. Two different heat islands composed of a canopy layer and a boundary layer have been identified. The first layer is of a microscale nature, being dominated by the immediate surroundings, and the second layer is of a local or mesoscale nature, being affected by the presence of an urban area at its lower boundary (Oke 1976). The most important features of urbanization are the urban structure, the urban cover, the urban fabric, and the urban metabolism (Oke 2006).

The features of the UHI have been extensively studied during the past several decades (Landsberg 1981; Oke 1988; Arnfield 2003). Large UHI effects have been measured and reported for most regions of the world (Morris et al. 2001; Grimmond 2006; Grimmond et al. 2010). A UHI intensity (UHII) of up to 10°C has been observed for some large cities on clear and calm winter nights (Jáuregui 1973; Sakakibara and Owa 2005; Rosenzweig et al. 2005).

In parallel, of particular interest for investigators are the causes of UHI formation. It has been demonstrated

Corresponding author address: P. Yang, Training Development Dept., China Meteorological Administration Training Center, 46 Zhongguancun Nandajie, Haidian, Beijing 100081, China.
E-mail: zz96998@163.com

DOI: 10.1175/JAMC-D-12-0125.1

that the UHI effect is closely related to urban/rural energy-balance differences. It is also found that the impact of urbanization is to favor partitioning of energy into sensible heat rather than latent heat and to increase the importance of heat storage by the system. The mechanisms for the canopy-layer anomaly are not the same as those in the boundary layer, with the former consisting of a wide range of energy-balance systems and being largely the result of the immediate site character and the latter probably representing both an advective accumulation and internal radiative effects (Oke 1982, 1987). Also, city size and synoptic weather conditions are both essential causes, especially for long time periods (Oke 1988; Karl et al. 1988). For shorter periods, however, the local-scale factors such as site exposure, land cover, surface moisture, human activity, and so on are more important (Davey and Pielke 2005; Peterson 2003; Kim and Baik 2005; Stewart and Oke 2012).

In China, analysis of the UHI has been conducted for big cities, and interesting conclusions have been drawn thereby. The previous works were mostly based on SAT data from meteorological stations (Wang et al. 1990; Zhou et al. 2004; Chu and Ren 2005; Feng et al. 2010; A. Y. Zhang et al. 2010), and vehicle temperature traverses and remote sensing technology were also used to investigate the spatial structure of the UHI (Weng 2001; Zhang et al. 2005; Xu et al. 2006; Xie and Yang 2008; Fang et al. 2011; Ren and Ren 2011). The investigation of UHI features in Shanghai, China, has shown that the UHII is stronger at night and in autumn/winter than during the day and in summer (Deng et al. 2001). Other research by different authors for Beijing, China, has also found an apparent UHI in the urban area (Zhang et al. 2002; Xu et al. 2006; Yang et al. 2013). In addition, for different sizes of cites, the increases of UHII near most meteorological stations have significantly enhanced the SAT trends in mainland China over the past 50 years (Zhou et al. 2004; Chu and Ren 2005; Hu et al. 2006; Ren et al. 2007, 2008, 2010; A. Zhang et al. 2010). There are also some analyses of the UHI effects for big cities of China using the data of land surface temperature retrieved from satellite products such as the Landsat Thematic Mapper (TM) and the Earth Observing System Moderate Resolution Imaging Spectroradiometer (MODIS; e.g., Zhang et al. 2005; Fang et al. 2011). The results are relevant, but they are not directly comparable to those obtained by using surface air temperature data (Roth et al. 1989).

A major problem in the previous studies on the climatological features of UHII in China is that if the detailed diurnal variation is considered then the spatial distribution is often ignored (Hu et al. 2009). Likewise, the diurnal characteristics of the UHII have often been neglected when in-depth study is given to the spatial structure of the UHII (J. Zhang et al. 2010). For example, Li et al. (2007) revealed the characteristics of the Beijing UHI in July on the basis of both manual stations and automatic weather stations (AWS), demonstrating the spatial distribution and the diurnal variation of the UHII. Because only the data from two AWSs in 2003 were used, the detailed features of the spatial and temporal variation still need to be examined. Other studies were also restricted to an outline description of the UHI or to a single season by using data from only urban–rural station pairs. The main reason for this contradiction is the insufficiency of observations, especially the limited routine meteorological observations.

AWSs were not deployed over mainland China until the end of the 1990s, and the countrywide installations and applications of AWSs at national meteorological stations were completed only by ~2004. Since then, a huge number of AWSs have been installed and applied in urban and rural areas in the country as based on the operational standard issued by the China Meteorological Administration (China Meteorological Administration 2003, 104–125). By 2010, for example, a dense AWS network with more than 200 stations had been established in Beijing Municipality. This network can provide hourly SAT data, helping in investigations into the UHII features in big cities like Beijing.

By applying the hourly SAT data from AWSs in Beijing, the climatological features of UHII are investigated in detail in this paper. In the following sections, the basic conditions, including the stations' information and climatological characteristics, are introduced at first, and then the spatial distribution, seasonal variation, and diurnal cycle of UHII in urban areas are examined. Furthermore, the urban region of Beijing is divided into three belts for analyzing the spatial differences of UHII in detail. The causation of the UHII variation is briefly discussed before the conclusions are drawn.

2. Study area, data, and methods

Beijing Municipality, with an area of 1.6 million km^2, is located in the north of the North China Plain and to the south of the Yanshan Mountains. The southeast plain occupies 38.8% of the total area of Beijing. Most parts of the plain are below 100 m above sea level. Beijing is characterized climatologically by a typical temperate continental climate, with a hot summer and a cold winter, and a seasonally highly concentrated summer precipitation regime.

Since the 1980s, Beijing has experienced rapid urbanization. Through 2007, the urbanized regions have extended and covered a much larger area than that of the 1980s. The present extent of the built-up areas is

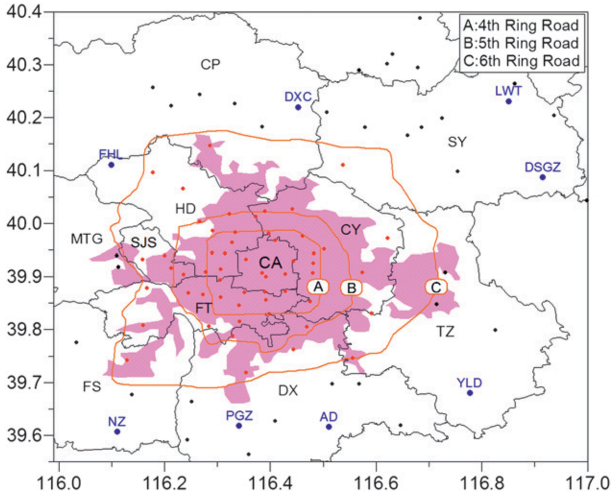

FIG. 1. Study region and locations of the 4th–6th Ring Roads and the 98 temperature gauge stations used in this study, including 8 reference stations marked in blue and 56 urban stations marked in red. Abbreviations of the station names are FHL for Feng Huang Ling, YLD for Yong Le Dian, PGZ for Pang Ge Zhuang, AD for An Ding, NZ for Nan Zhao, DXC for Dong Xin Cheng, DSGZ for Da Sun Ge Zhuang, and LWT for Long Wan Tun. Abbreviations marked in black are for the 10 districts of Beijing Municipality: CP is Chang Ping, SY is Shun Yi, TZ is Tong Zhou, DX is Da Xing, FS is Fang Shan, MTG is Men Tou Gou, SJS is Shi Jing Shan, HD is Hai Dian, FT is Feng Tai, CY is Chao Yang, and CA is Central Area.

marked in pink in Fig. 1 (Mu et al. 2012), and the current population of the Beijing Municipality is 20 million, which is 2 times the census result in 1986. Over 50% of the population lives in the downtown areas and the nearby suburban areas, which together make up the study area of this paper as outlined in Fig. 1.

As a result of the bewildering urban sprawl, an express transportation system became a necessity in Beijing City, and a multiple-ring-road (RR) system of transportation (Fig. 1) was developed (Wang et al. 2010). The 4th RR was opened in 2001 and is 65.3 km in length, and the area inside the 4th RR reaches about 300 km^2. The 5th RR (98.6 km long) was opened in 2003 and is ~10 km away from the city center. Six years later, the 6th RR (187.6 km long) was built to relieve the traffic pressure in Beijing City (red loops in Fig. 1). The areas inside the different RRs actually represent the radial extensions of the urban areas with varied densities of population and buildings as well. In this paper, the sites located inside the 6th RR in Beijing are considered to be urban stations, and those inside the 4th RR are considered to be central urban stations (Fig. 1).

Hourly temperature data from 185 stations across Beijing Municipality for the time period 2007–10 were obtained from the Meteorological Information Center of the Beijing Meteorological Bureau (MIC/BMB). The height of the AWS temperature sensors from the ground surface is 2 m, which is consistent with those of the manual stations. By considering the urban structure, the urban cover, the urban fabric, and the urban metabolism (Oke 1981, 2006), the BMB installed the AWSs in accord with the operational standard issued by the China Meteorological Administration (China Meteorological Administration 2003, 104–125), which is based on World Meteorological Organization guidance.

To increase the robustness of our analyses, all hourly temperature data from MIC/BMB have been checked and quality controlled. The missing values, which account for 0.37% of the total records, were replaced by the instantaneous valid values of the nearest five stations by using spatial interpolation with the inverse-distance-weighting technique (Lin et al. 2002). The possible erroneous data have been detected, proved, and adjusted, and those stations with too many erroneous records have been ruled out. The details of the quality control have been provided by Yang et al. (2011).

Thus, 98 observation stations evenly distributing in the entire study area were chosen (Fig. 1) for describing the climatological features. In the following analysis of the UHII characteristics, however, only the 56 urban stations inside the 6th RR and 8 reference stations are used. Indeed, it is noteworthy that the selection of the reference stations surrounding the built-up areas is a key to determining the UHII of a city. We choose the eight reference stations according to a strictly defined standard using a remote sensing method (Ren and Ren 2011). By specifying the locations of the suburban stations in the fields of land surface temperature distribution, those that are unaffected by the UHI or are located in the background climatic conditions are identified. Relative to the other approaches used for classifying climatic stations, the remote sensing method does not rely so much on social and economic data, and data updating can be easily done (Ren and Ren 2011).

In addition, the reference sites, far enough from the built-up areas and in different directions from the urban center, are all located within a distance of 53.7 km [Long Wan Tun (LWT)] from Tiananmen Square, the center of the city. All of the reference stations lie on open ground with a countryside setting, completely away from the impacts of high buildings. The average elevation of the reference stations is 39.6 m, which is only 8.8 m lower than that of the 56 urban stations (48.4 m), ensuring more accurate estimation of the UHII because of similarities in the topography.

To differentiate the UHII among the distinct sites of the built-up areas, we examined three groups of urban stations in the analysis, including those inside the 4th RR (composed of 25 stations), those in the zones of the 4th

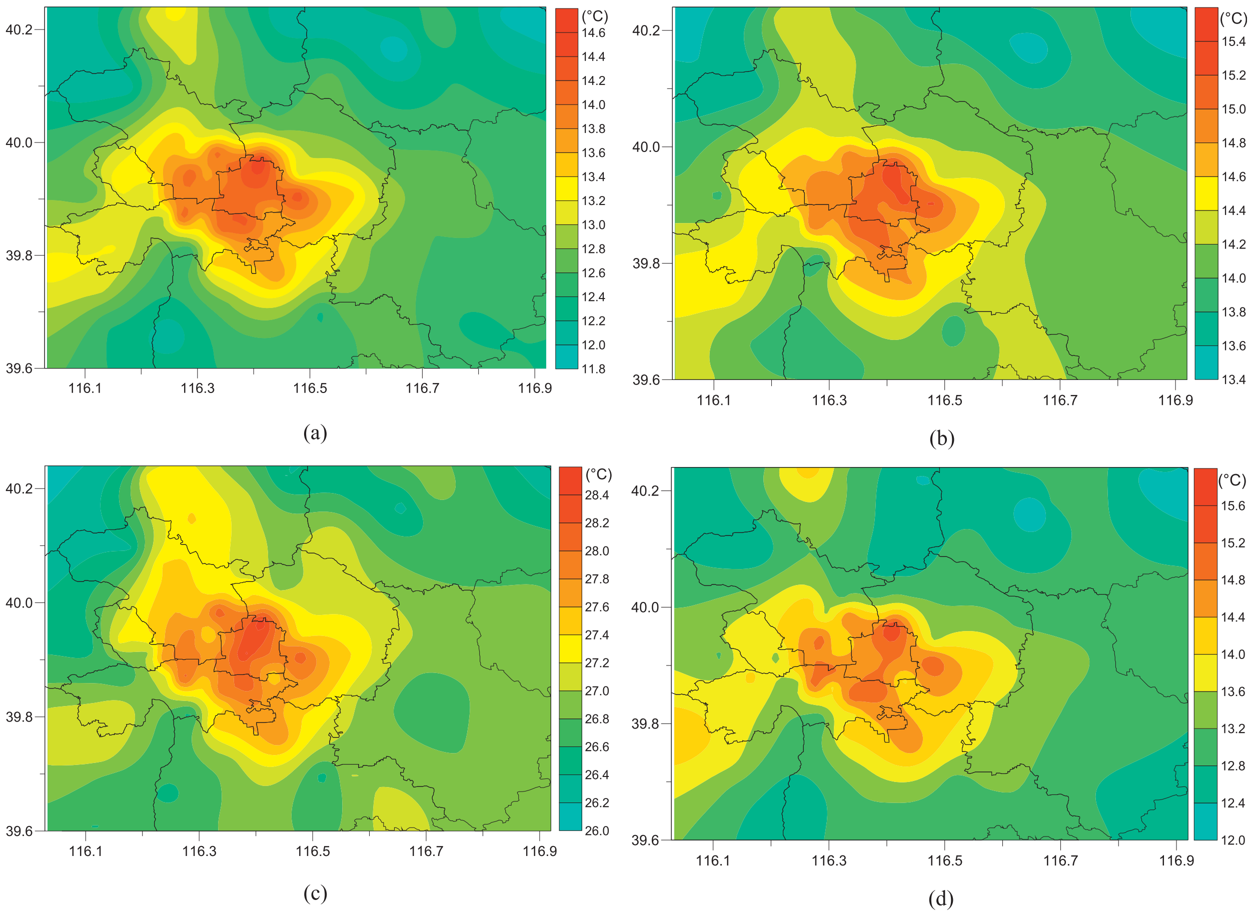

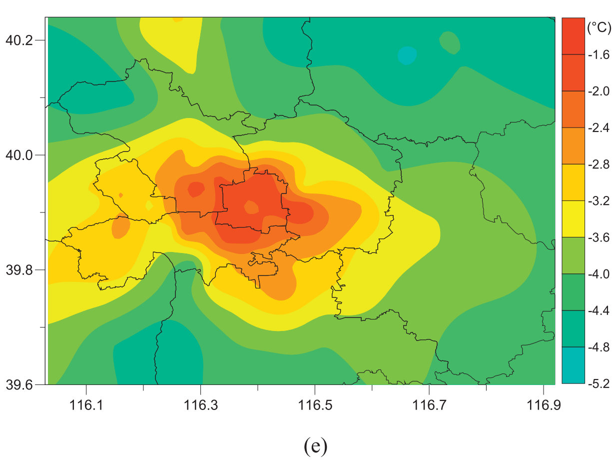

FIG. 2. Spatial distributions of the mean temperature (°C) during (a) the whole year, (b) spring, (c) summer, (d) autumn, and (e) winter in Beijing during 2007–10.

and 5th RRs (composed of 14 stations), and those in the zones of the 5th and 6th RRs (composed of 17 stations). The reason for applying the classification is that the city RR loops were constructed surrounding the city center and they well differentiated the urban features in terms of densities of population, buildings, and, to some extent, the functional areas (He et al. 2002; Miao et al. 2011). He et al. (2002) indicated that the urbanization rate by 1997 had reached 94.6% within the 4th RR while it had reached only 68.4% within the 4th–5th RR and was lower outside the 5th RR. The RR loops represented well the urban–rural boundaries for different time periods in Beijing during 1984–2007 (Mu et al. 2012), with the densest and tallest buildings and almost all of the central commercial areas appearing within the 4th RR. It is therefore reasonable to make such a first-order

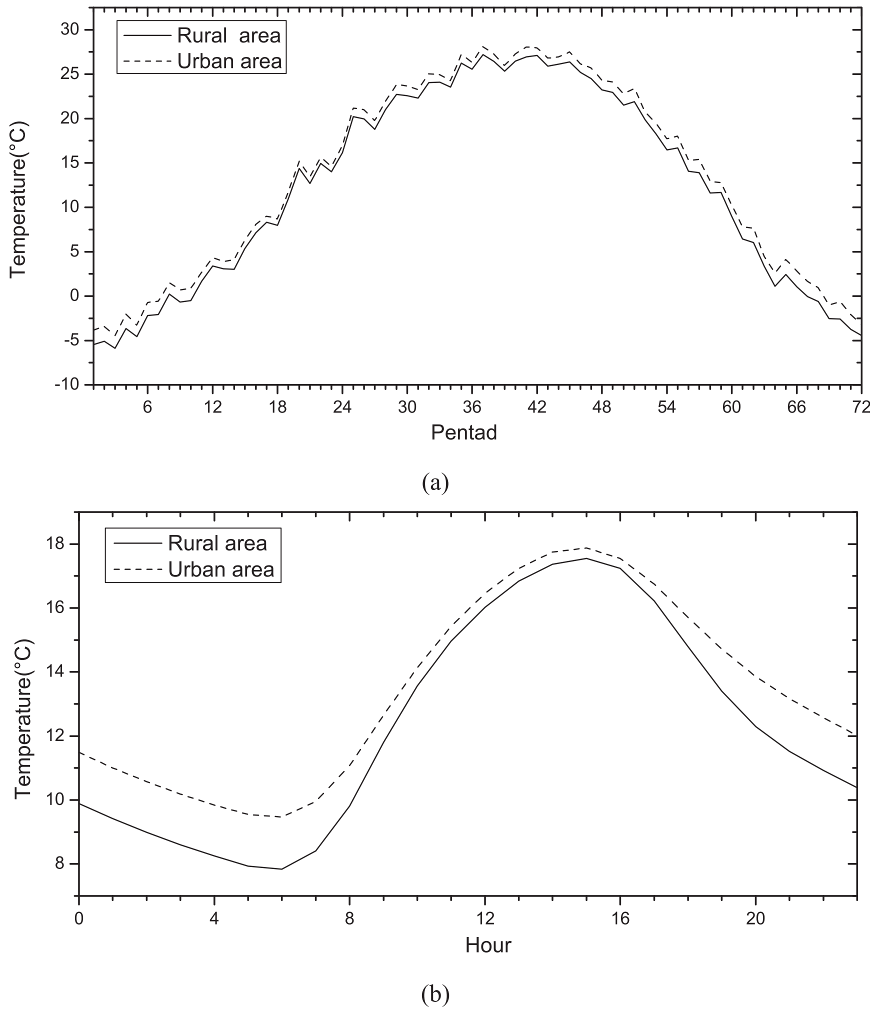

FIG. 3. (a) Pentad averaged and (b) annual-averaged diurnal cycle of mean temperature in urban and rural areas in the study region.

classification of the urban stations for showing the macro- and integrated features of UHI effects.

In the study, UHII is estimated by calculating the SAT difference between urban and rural stations (areas). The rural SAT T_{rural} is the average SAT of the eight reference stations, and the urban SAT T_{urban} is the SAT of any urban station or the average SAT values of the urban stations inside any specific urban area. Therefore, UHII, or ΔT_{u-r}, can be defined as

$$\mathrm{UHII} = \Delta T_{u-r} = T_{\mathrm{urban}} - T_{\mathrm{rural}}. \quad (1)$$

3. Characteristics of temperature

The annual and seasonal mean SATs over the study region are shown in Fig. 2. During the 4-yr period, the annual mean SAT over the study region is 13.04°C, with the highest value (14.71°C) appearing in He Ping Xi Qiao (HPXQ) near the joint belt of the Central Area (CA) and Chao Yang (CY) districts. The lowest record (11.82°C) is seen in Shun Yi Sai Ma Chang (SYSMC) in the southwestern Shun Yi (SY) district. Centers of relatively high temperature can be identified inside the 4th RR or in CA, the adjacent zones to the 4th RR such as CY, Feng Tai (FT) district, and Hai Dian (HD) district. The secondary high centers mainly occur in the southwestern part in FT, Men Tou Gou (MTG), and HD districts and in the northern part of the CY district. In the northwest and northeast, the annual mean SAT is generally less than 12°C.

In a similar way, high-temperature centers for each season mostly concentrate on the 4th RR (Figs. 2b–e), and low-temperature centers often appear over the northwestern and northeastern parts of the study

TABLE 1. Annual and seasonal mean temperatures (°C) for the whole urban area, the urban station groups (inside the 4th RR, 4th–5th RRs, and 5th–6th RRs), and the rural areas.

	Inside 4th RR	4th–5th RRs	5th–6th RRs	Urban areas	Rural areas
Year	13.90	13.24	12.96	13.36	12.21
Spring	14.79	14.30	14.08	14.39	13.51
Summer	26.57	26.08	25.80	26.15	25.36
Autumn	14.09	13.30	13.00	13.46	12.13
Winter	−0.01	−0.88	−1.19	−0.69	−2.20

region. The spatial variability varies by season, however. The spatial variability of SAT is small in spring. The mean SAT differences among the sites are consistently larger in summer than those in spring, and they are even larger in autumn and winter. Although the scope of the centers of high seasonal mean SAT in autumn is smaller than that in winter, and only a few sporadic high centers are observed inside the 4th RR, the site-to-site SAT contrast reaches 3.79°C, which is slightly larger than that in winter. It is obvious that the large spatial contrasts of annual mean and seasonal mean SAT result from the UHI effects, which lead to a significant increase in temperature over the built-up areas relative to the surrounding countryside (Xu et al. 2006; Lin and Yu 2005; Liu et al. 2009).

Figure 3 displays the seasonal and diurnal cycles of SATs over the urban area represented by the 56 urban stations and the rural areas represented by the 8 reference stations. Similar variations appear in urban and rural areas, but there is a systematic positive SAT difference between the urban and rural areas throughout the year. The difference clearly indicates the UHI effect over the urban areas. Table 1 shows that the hourly mean SAT in the urban areas is 13.36°C but varies from 13.90°C in CA to 12.96°C between the 5th and 6th RRs. Mean urban SATs in various seasons all appear to be the highest in CA, followed by the 4th and 5th RRs, with the lowest record registered in the 5th and 6th RRs. The SAT differences between adjacent urban areas generally decrease from CA to the outskirts for all seasons, with the largest difference occurring between CA and the 4th and 5th RRs in wintertime and the smallest one between the 4th and 5th RRs and the 5th and 6th RRs in springtime.

The hourly SAT difference between urban and rural stations is also evident, and the urban SAT is higher at all times during a day. The diurnal cycle is smaller in urban areas than in rural areas. This is consistent with previous research reporting that the pace of SAT decline in urban areas is slower than that in the rural areas after sunset (e.g., Oke 1982; Li et al. 2008).

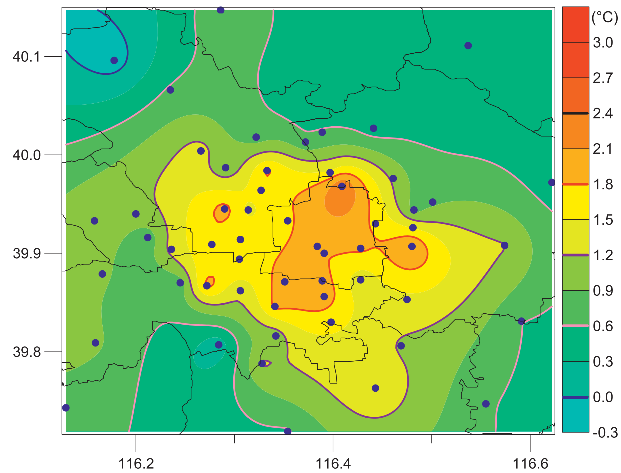

FIG. 4. Spatial distribution of the annual mean UHII in the urban areas during 2007–10. Blue, pink, purple, red, and black lines mark the UHII isotherms of, 0°, 0.6°, 1.2°, 1.8°, and 2.4°C, respectively. Blue points represent the stations in the urban areas.

4. Characteristics of UHII in urban areas

a. Spatial distribution of UHII

The spatial distribution of annual mean UHII over the urban areas (corresponding to the built-up areas inside the 6th RR) is shown in Fig. 4. The maximum UHII center (2.45°C) appears at HPXQ (39.97°N, 116.41°E), in the northeastern part of CA. This station is surrounded by dense buildings and several expressways (Fig. 5a). The only station with negative UHII (−0.16°C) is Dao Xiang Hu (DXH; 40.10°N, 116.18°E) in the northwest part of the built-up areas. The sparser buildings and a nearby small lake might be reasons for the negative UHII recorded at this station (Fig. 5b).

Figure 6 shows the spatial distribution of the seasonal mean UHII over the urban areas of Beijing. The high UHII centers, such as those around CA, CY, and HD, are all economically developed and densely populated parts of the city. It is obvious that the UHII is stronger in winter and autumn than in spring and summer. The feature of a seasonal cycle is supported by previous studies, including Xie et al. (2006), Lin and Yu (2005), and Chu and Ren (2005) for Beijing City and Liu et al. (2005) and Han et al. (2007) for Shijiazhuang and Tianjin, the nearby big cities in the North China Plain. The lowest seasonal mean UHII is identified in spring, with most areas outside the central urban area being less than 1.2°C. Areas with spring mean UHII of less than 0.6°C are found in the northeastern and northwestern parts of the domain. In autumn, the seasonal mean UHII experiences a considerable increase, with the 1.2°C isotherm covering most areas inside the 5th RR and the maximum UHII in the northern CA

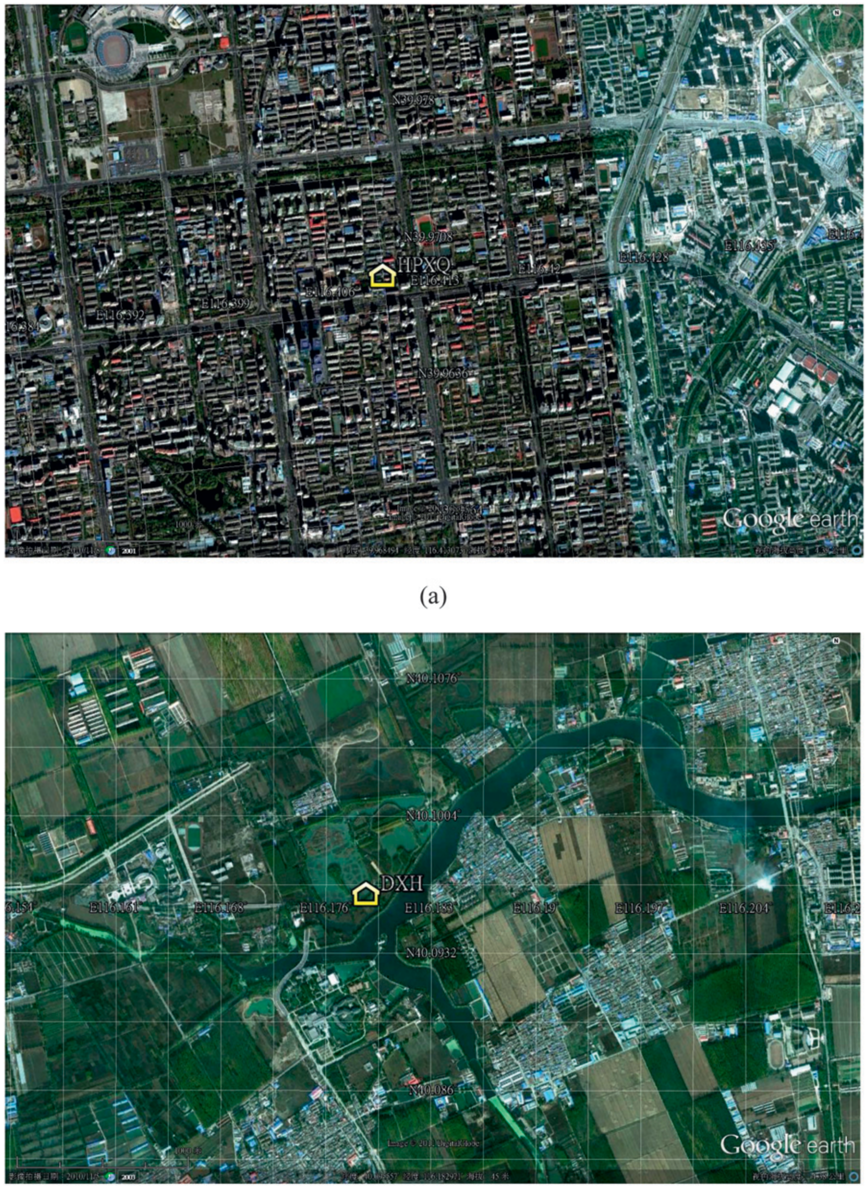

(a)

(b)

FIG. 5. Stations and the surrounding landscapes: (a) HPXQ and (b) DXH. [Photographs are from Google Earth; ©2011 Google; image ©2011 DigitalGlobe.]

reaching 3.15°C. The winter has the largest seasonal mean UHII, and almost the entire central urban area is surrounded by the 2.4°C isotherm, with the maximum value reaching 2.90°C, whereas the minimum UHII of −0.07°C occurs at DXH in the northwestern most part of the domain.

Table 2 illustrates the considerable differences among the seasons. The largest seasonal mean UHII of the whole urban areas is 1.65°C in winter, followed by 1.38°C in autumn, 0.92°C in summer, and 0.80°C in spring. The largest seasonal difference between winter and spring reaches 0.85°C.

The fact that UHII is largest in winter can be explained by rural areas cooling more rapidly under strong inversions and radiation-type weather at night during this season in the North China Plain. Heat release by building heating in winter might be another reason (Chen and Shi, 2012). The maximum wind speeds in the urban areas occur in spring, reaching 1.84 m s^{-1} on average while the average UHII is 1.05°C, and strong wind is therefore

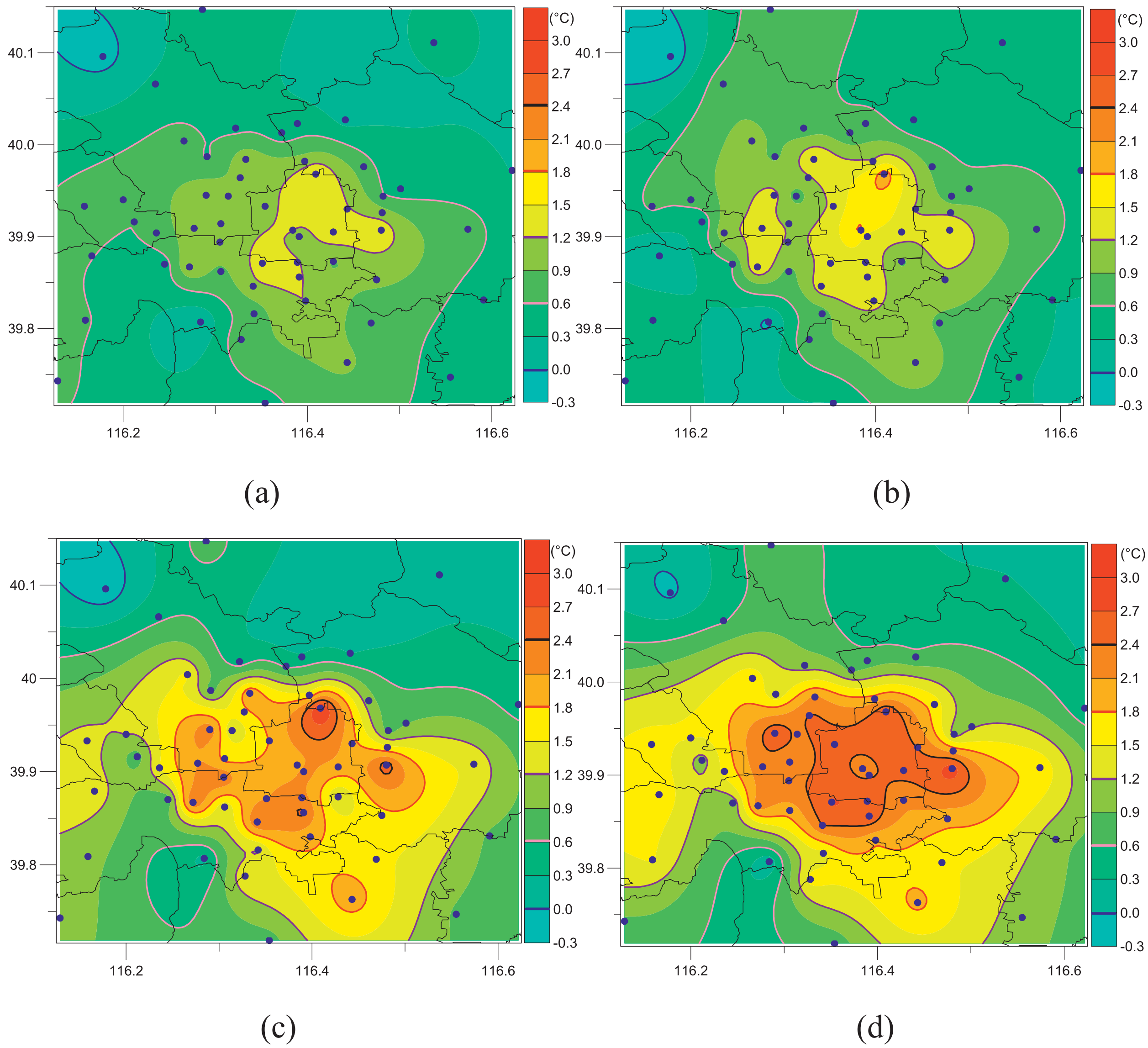

FIG. 6. As in Fig. 4, but for (a) spring, (b) summer, (c) autumn, and (d) winter.

very important for weaker UHII during spring. The autumn mean UHII is larger, and this is usually associated with calm weather and a stable lower atmosphere. Of the four seasons, autumn is the one in which urban areas have the lowest average wind speed ($1.19\,\mathrm{m\,s^{-1}}$). Previous research indicated that frequent rainfalls and the unstable lower atmosphere in the monsoon might have been the most important reason for the smaller UHI during summer (Zhang et al. 2005). To examine this, we compared the average UHIIs of total urban areas in summer for rainy days and no-rain days and preliminarily found a good association of the UHI with the weather phenomena, with the UHII on rainy days much lower than on sunny days.

b. Diurnal variation of UHII

Figure 7 shows the annual mean diurnal UHII in the three urban areas divided by the 4th, 5th, and 6th RRs.

TABLE 2. Annual and seasonal means, maximum, minimum, and range values of UHII over the urban areas of Beijing (°C).

	Mean	Max	Min	Range (max − min)
Year	1.23	2.45	−0.16	2.61
Spring	0.80	1.53	−0.12	1.65
Summer	0.92	1.98	−0.24	2.23
Autumn	1.38	3.15	−0.22	3.37
Winter	1.65	2.90	−0.07	2.97

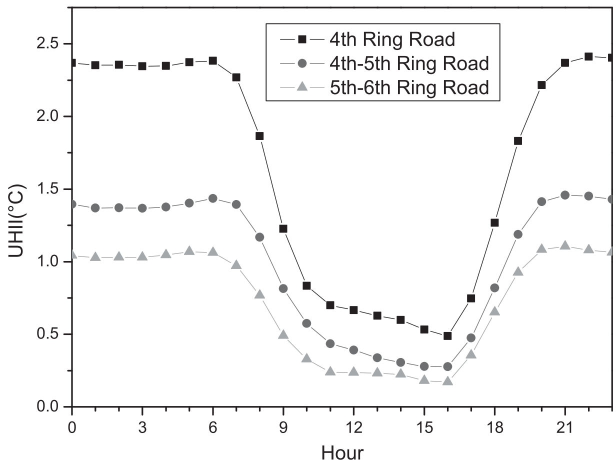

FIG. 7. Diurnal variations of UHII in the urban areas inside the 4th RR and between the 4th and 5th and 5th and 6th RRs.

Among the three belts, a common diurnal variation pattern has been found to contain two relatively stable stages separated by two swiftly changing stages. One stable stage is characterized by strong UHII lasting from 2100 LST until early the next morning (about 0600 LST), and another is characterized by weak UHII lasting from 1100 to 1600 LST. The two swiftly changing stages are from 0600 to 1100 LST and from 1600 to 2100 LST, characterized by a fast decline and an abrupt rise, respectively.

Table 3 shows the average UHII for the 24-h and the steadily strong and weak UHI stages. We can see that inside the 4th RR the largest annual mean UHII occurs during the steadily strong UHI stage in CA, reaching 2.37°C, and the smallest annual mean UHII of 0.21°C appears during the weak UHI stage in the area between the 5th and 6th RRs. The 24-h average UHII difference between CA and the 4th–5th RR area is 0.65°C, and that between the areas of the 4th–5th RRs and 5th–6th RRs is only 0.27°C. This spatial contrast is more remarkable during the steadily strong UHI stage, with the difference between CA and the 4th–5th RR area reaching 0.97°C, which is almost 3 times the difference between the areas of the 4th–5th RRs and 5th–6th RRs (0.34°C). On the contrary, the spatial contrasts for the neighboring areas are small for the steadily weak UHI stage.

The average UHII isotherms in the two stable stages are shown in Fig. 8. During the strong UHI stage, the central urban area is almost surrounded by the 2.4°C UHII isotherm, and UHII values of 1.2°C or greater are recorded at 39 out of the total 56 urban stations (Fig. 8a). Only three stations near the 6th RR exhibit notably weak UHII (lower than 0.6°C). Nevertheless, noticeable discrepancies are observed in the UHII isotherm distribution during the steadily weak UHI stage (Fig. 8b).

TABLE 3. Average UHII for 24 h and for the steadily strong and weak UHI stages (°C).

	24-h avg	Strong UHI stage (2100–0600 LST)	Weak UHI stage (1100–1600 LST)
Inside 4th RR	1.65	2.37	0.60
4th–5th RRs	1.00	1.40	0.38
5th–6th RRs	0.73	1.06	0.21

Although the central area is surrounded by the 0.6°C isotherm, nowhere inside the 4th RR does the UHII surpass 1.2°C, and the area between the 5th and 6th RRs has a very low UHII of only 0°–0.3°C.

c. *Seasonal variation of UHII*

The pentad-mean UHII for the three urban areas for the time period 2007–10 is shown in Fig. 9. The seasonal

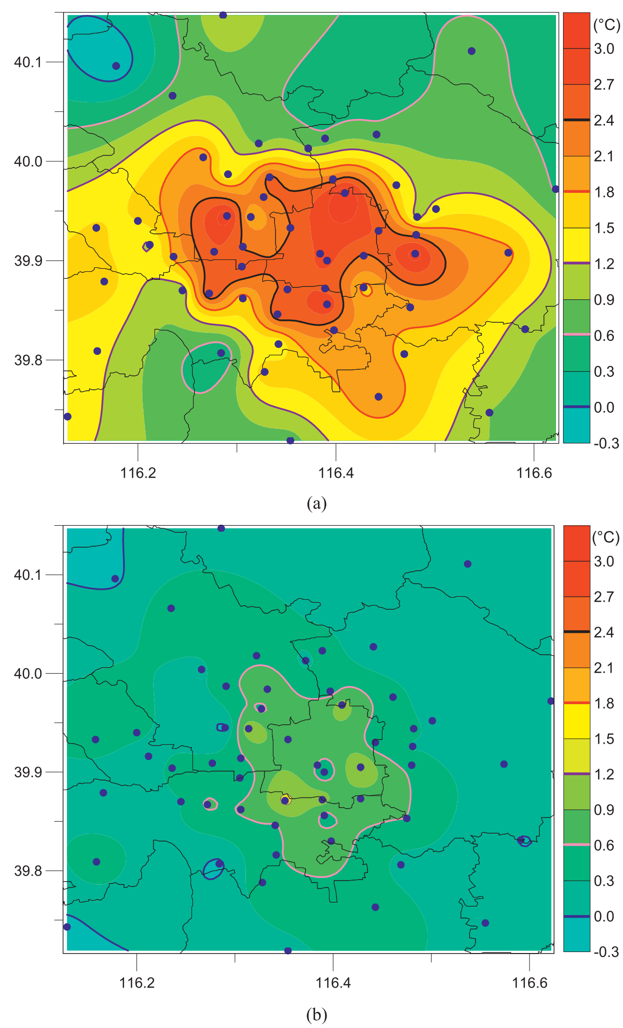

FIG. 8. As in Fig. 4, but for the spatial distribution of the UHII for (a) a strong UHII stage (2100–0600 LST) and (b) a weak UHII stage (1100–1600 LST).

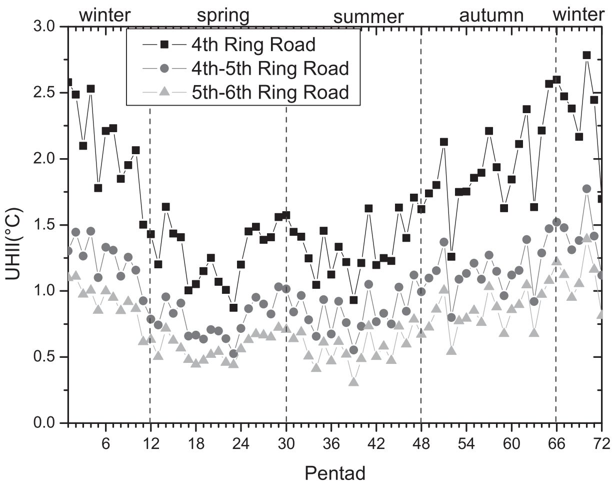

FIG. 9. Variations in pentad-mean UHII for the three urban areas: squares indicate the CA, circles are for the area between the 4th and 5th RRs, and triangles are for the area between the 5th and 6th RRs. Dashed vertical lines mark the boundaries of the four seasons.

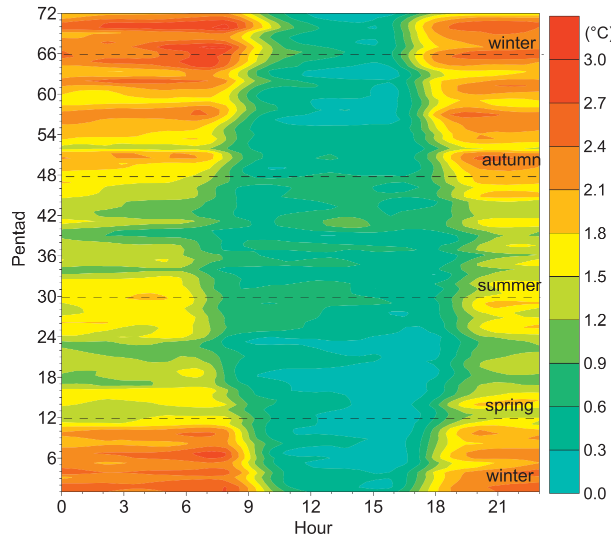

FIG. 10. Hour–pentad plots of the UHII averaged for the whole urban area for the time period 2007–10. Dashed horizontal lines mark the boundaries of the four seasons.

variations in the UHII in the different areas are consistent. The largest pentad-mean UHII of 2.75°C occurs in the urban center in the 70th pentad, and the smallest pentad-mean value of 0.27°C appears in the 5th–6th RRs in the 38th pentad. The winter mean UHIIs are 2.15°, 1.27°, and 0.96°C for CA, the area between the 4th and 5th RRs, and the area between the 5th and 6th RRs respectively. The weakest UHII take place in spring, with the seasonal mean values being 1.29°, 0.79°, and 0.58°C for the three areas, respectively. Figure 10 shows the hour-pentad plots of the UHII averaged for all of the urban areas for the time period 2007–10. Figure 10 clearly shows that the UHII in summer experiences a smaller diurnal variation in comparison with the other seasons. It also indicates that the night-to-day shift is large in winter and small in autumn, which might be to some extent due to the heat release by building heating during the cold and long winter nights. It is interesting to note that, although the UHII at nights in summer is weaker than those in winter and autumn, the UHII during the daytime in summer is obviously the strongest among the seasons. A similar conclusion has been reported by Zhang et al. (2005) using remote sensing data. In addition, there are obvious multipentadal fluctuations in nighttime UHII, especially in winter and autumn. The frequency of the fluctuations is lower in autumn and early winter but becomes higher in the first 10 pentads, or later in the winter. Whether this phenomenon is related to the local weather disturbances needs to be investigated in the future.

Figure 11 presents hour-pentad plots of UHII averaged for the different urban areas for the time period 2007–10. Considerable differences exist among the urban areas. In the central urban area, the hourly mean UHII can reach as high as 3.0°C during the nighttime strong UHII stage in winter—a value is approximately 1.2°C higher than that in summer. Once again, the hourly mean UHII during the daytime shows obviously higher values in summer than in the other seasons in the central urban area. Nevertheless, higher summer daytime UHII is not captured within the areas of the 4th–5th and 5th–6th RRs. For example, the maximum UHII in the 4th–5th RRs reaches 2.7°C around 0800 LST in the 70th pentad (early winter), and the relatively stronger UHII phenomenon during the summer daytime is not notable. Between the 5th and 6th RRs, extremely low UHII values prevail in daytime in every season, especially on spring afternoons, and even a few negative values are registered in the early afternoon around the 18th pentad (Fig. 11c).

5. Discussion

The analysis performed here shows that the number of observational sites, the length of the dataset, and the selection of the reference or rural stations are all important for analyzing the UHI. Many studies of urban climate have been conducted for Beijing City, and they have reported some basic features of the UHI (Xie et al. 2006; Xu et al. 2006; Zhang et al. 2002; Chu and Ren 2005; Liu et al. 2009; Wang and Lu 2005; Wang et al. 2011). The previous studies could barely describe the fine-resolution structure of the UHII in Beijing urban areas, however, because of the lack of observational

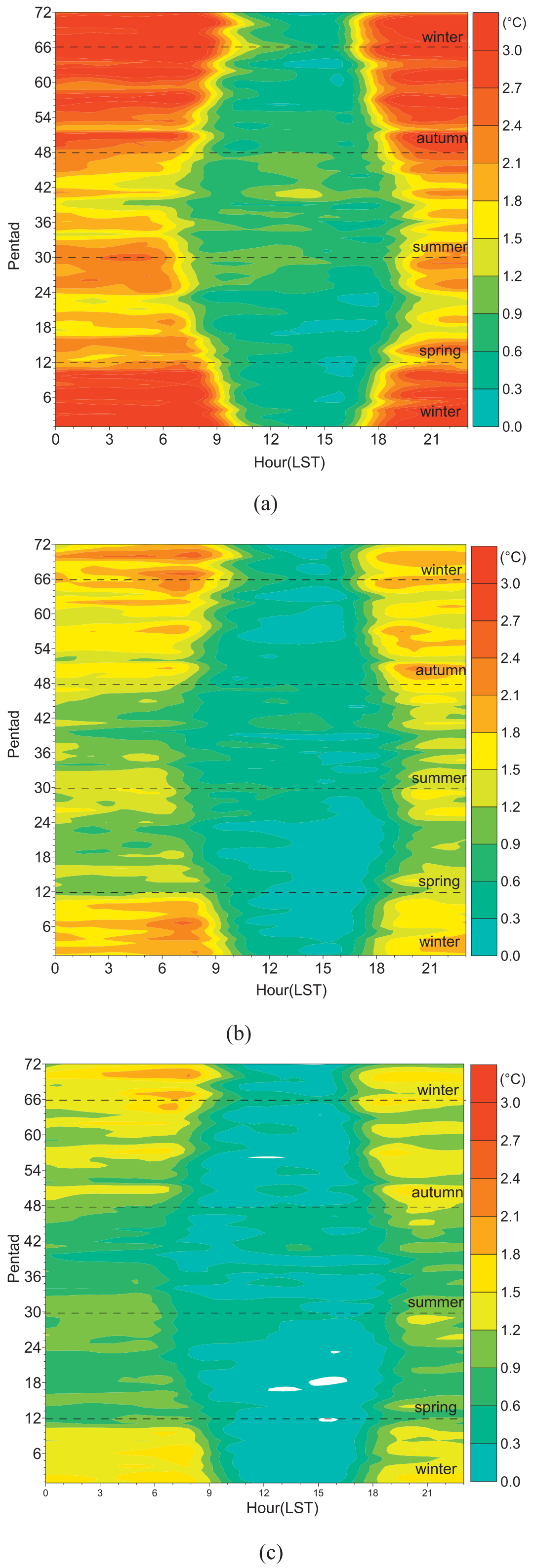

FIG. 11. Hour–pentad plots of the UHII averaged for (a) the central urban area, (b) the 4th–5th RRs, and (c) the 5th–6th RRs for the time period 2007–10. Dashed horizontal lines mark the boundaries of the four seasons.

data, and most of the studies could not give precise estimates of the UHII for any urban sites because of the incomplete method for selecting reference stations. In choosing rural stations, for example, previous studies often took terrain and elevation into consideration (e.g., Wang et al. 2011) or simply relied on administrative boundaries to classify stations (e.g., A. Zhang et al. 2010) but did not at the same time take into account the specific positions of the observational stations in the urban thermal fields.

Applying densely distributed AWS observations for 2007–10, we extend our analysis to reveal the detailed features of the fine-resolution diurnal and seasonal variations and spatial distribution of the UHII in the Beijing urban areas. The objective criteria used for selecting reference stations can guarantee the accuracy of the estimates of the UHII. Moreover, unlike in previous studies, we perform the regionalization of the urban areas by referring to the positions of the three ring roads. This procedure better reveals the spatial differentiation of the Beijing urban climate, because the urban area has sprawled outward from the center and the ring roads are consistent with the boundaries of past urban areas at different urbanization stages (He et al. 2002; Li et al. 2009). To separate the urban areas into residential and business districts is a common practice (e.g., Liu and Yang 2009), but there is often a mosaic distribution in Beijing, and, although the procedure would be better to be applied in a functional classification, it might be not be proper for use in urban regionalization in the city. The ring-road-based regionalization applied in this paper represents well the spatial differentiation of the urban climate.

The results of our study are generally consistent with previous works using daily or hourly records from a smaller number of meteorological stations (e.g., Wang and Hu 2006; J. Zhang et al. 2010; Dong et al. 2011). These other studies also found that winter is the season that is most influenced by the UHI effect, despite the fact that J. Zhang et al. (2010) showed the weakest UHII in summer rather than in spring as we found. The differences are likely related to the different densities of station networks and the criteria for defining urban and rural stations. The weakest UHII in spring could be well explained by the more frequent windy conditions and the largest seasonal mean wind speed from March to May in northern China (Zhang and Ren 2003; Liu et al. 2004). A steadily strong UHII stage was found at night, whereas a steadily weak UHII phase is evident during the daytime. We also calculated the urban area-averaged hourly mean UHII and show that the steadily strong and weak UHI stages have the same timing and duration in the three urban areas, but with varied magnitudes.

The daytime UHII in summer is higher than those in other seasons. This phenomenon was also found by J. Zhang et al. (2010). Our results indicate, however, that it is most evident in the central urban area. Relative to the urban area, the rural area has a stronger evapotranspiration and latent heat flux exchange during the daytime in summer, and this fact might contribute to the UHII difference. It is also possible that the larger anthropogenic heat release in the central urban area during summer afternoons results in a stronger UHII in comparison with the rural area.

Zhang et al. (2005) investigated the seasonal features of the UHII in Beijing in 2001. They used land surface temperature products from EOS MODIS, and showed that the UHII in Beijing urban areas is strongest in summer and weakest in winter. By using data of seasonal land surface temperature from the Landsat TM in 2005 and 2006, Fang et al. (2011) also drew the conclusion that the urban areas of Beijing have a more evident UHI effect in summer. These results from remote sensing products are different from our analyses, which show that the largest seasonal mean UHII for total urban areas occurs in wintertime (1.65°C) and that the seasonal mean UHII in the Beijing urban areas in summer is only 0.92°C, marginally higher than the smallest seasonal mean UHII in spring (0.80°C). Our result is consistent with the general sense of a strong temperature inversion and stable lower atmospheric layer in winter nights and the extra heat release by heating in buildings (Chen and Shi 2012). The reasons for the large differences between our analysis and previous works are not clear at present, but they indicate that the land surface temperature retrieved from satellite products might have been representing a different physical quantity from that measured by thermometers at the meteorological stations. An alternative explanation is the difference in the definitions and calculation methods of the UHII that were used in the previous studies versus those of this study.

6. Conclusions

A study was conducted to analyze the UHI phenomenon in Beijing urban areas through an application of a quality-controlled hourly dataset of AWSs. The following four meaningful findings are drawn from the study:

1) The strongest annual mean UHII occurs in the central urban area inside the 4th RR, whereas weaker UHIIs generally occur between the 4th and 5th RRs and the 5th and 6th RRs, including the urban areas in HD, FT, southwestern CY, and northern DX. In addition, the weakest UHII appears in the area between the 5th and 6th RRs, with sites near the northern and southern 6th RR having the smallest UHI phenomena.
2) The annual mean UHII for the whole urban area is 1.23°C, and the seasonal mean UHIIs for the urban area are 1.65°C for winter, 1.38°C for autumn, 0.92°C for summer, and 0.80°C for spring. Most of the urban stations experience their strongest UHII in winter, but a few record their strongest UHII in autumn.
3) The diurnal variations of hourly mean UHII are characterized by a stage with steadily high values from 2100 to 0600 LST and a stage with steadily low values from 1100 to 1600 LST, with the 0600–1100 LST period containing the swiftly declining stage and the 1600–2100 LST period representing the rapidly rising stage. The annual and seasonal mean UHI differences among the three divided regions result mostly from the different contributions in the nighttime UHII.
4) There are always a steadily UHI strong stage and a stable weak UHI stage during the diurnal variation all through the year. Moreover, the steadily strong UHI stage during nighttime is longer and the steadily weak UHII stage in daytime is shorter in winter and autumn.

Acknowledgments. This study is supported by the National Natural Science Foundation of China (Grant 41005043), National Basic Research Program of China (Grant 2012CB955901), and Special Fund Projects for Public Welfare (Grant GYHY201206012). We are grateful to Dr. Y. Y. Ren for her help in drawing the isotherms of remote sensing–based land surface temperature in the study region.

REFERENCES

Arnfield, A. J., 2003: Two decades of urban climate research: A review of turbulence, exchanges of energy and water, and the urban heat island. *Int. J. Climatol.,* **23,** 1–26.

Chen, B., and G.-Y. Shi, 2012: Estimation of the distribution of global anthropogenic heat flux. *Atmos. Oceanic Sci. Lett.,* **5,** 108–112.

China Meteorological Administration, 2003: *Specification of Ground Meteorological Observation* (in Chinese). China Meteorological Press, 151 pp.

Chu, Z. Y., and G. Y. Ren, 2005: Effect of enhanced urban heat island magnitude on average surface air temperature series in Beijing region (in Chinese). *Acta Meteor. Sin.,* **63,** 534–540.

Davey, C. A., and R. A. Pielke Sr., 2005: Microclimate exposures of surface-based weather stations: Implications for the assessment of long-term temperature trends. *Bull. Amer. Meteor. Soc.,* **86,** 497–505.

Deng, L. T., J. Shu, and C. Y. Li, 2001: Character analysis of Shanghai urban heat island (in Chinese). *J. Trop. Meteor.,* **17,** 273–280.

Dong, Y., X. Li, and Y. Yang, 2011: Distributive characters of urban heat island effect in Xi'an City (in Chinese). *J. Arid Land Resour. Environ.,* **25** (8), 107–112.

Fang, Y. X., S. H. Shen, Y. Han, S. B. Yang, and M. Y. Yin, 2011: A study of seasonal urban heat environment in Beijing based on TM image (in Chinese). *Climatic Environ. Res.,* **16,** 487–493.

Feng, G. L., Z. Q. Gong, and R. Zhi, 2010: Latest advances of climate change detecting technologies (in Chinese). *Acta Meteor. Sin.,* **4,** 1–16.

Grimmond, C. S. B., 2006: Progress in measuring and observing the urban atmosphere. *Theor. Appl. Climatol.,* **84,** 1–22.

——, and Coauthors, 2010: Climate and more sustainable cities: Climate information for improved planning and management of cities (producers/capabilities perspective). *Procedia Environ. Sci.,* **1,** 247–274.

Han, S., J. Guo, S. Huang, and H. Bian, 2007: Study on the evolution of urban heat island in Tianjin city (in Chinese). *Ecol. Environ.,* **16,** 280–284.

He, C. Y., P. J. Shi, J. Chen, and X. L. Xu, 2002: Process and mechanism of urbanization of Beijing area (in Chinese). *Acta Geogr. Sin.,* **27,** 363–371.

Hu, F., Z. X. Hong, J. Y. Chen, and X. M. Liu, 2006: The field experiment of atmospheric boundary layer over heterogeneous surface in Baiyangdian area—Introduction and preliminary data analysis (in Chinese). *Chin. J. Atmos. Sci.,* **30,** 883–893.

Hu, W. Z., Y. G. Liang, H. W. Lei, and Z. X. Li, 2009: A study on the difference between urban and rural climate in Hong Kong (in Chinese). *Meteor. Monogr.,* **35** (2), 71–79.

Jáuregui, E., 1973: The urban climate of Mexico City. *Erdkunde,* **27,** 398–307.

Karl, T. R., H. F. Diaz, and G. Kukla, 1988: Urbanization: Its detection and effect in the United States climate record. *J. Climate,* **1,** 1099–1123.

Kim, Y. H., and J. J. Baik, 2005: Spatial and temporal structure of the urban heat island in Seoul. *J. Appl. Meteor.,* **44,** 591–605.

Landsberg, H. E., 1981: *The Urban Climate*. Academic Press, 275 pp.

Li, X. R., F. Hu, and W. J. Shu, 2007: Analysis and numerical simulation of summer strong urban heat island in Beijing (in Chinese). *Meteor. Monogr.,* **33** (6), 25–31.

——, ——, ——, and B. L. Liang, 2008: Characteristics of urban heat island effect and its meteorological influencing factors over Beijing in autumn (in Chinese). *Climatic Environ. Res.,* **13,** 291–299.

——, X. L. Wang, and Z. K. Feng, 2009: Research on urban expansion based on land use degree (in Chinese). *Prog. Geogr.,* **28,** 398–402.

Lin, X. C., and S. Q. Yu, 2005: Inter decadal changes of temperature in the Beijing region and its heat island effect (in Chinese). *Chin. J. Geophys.,* **48,** 39–45.

Lin, Z. H., X. G. Mo, H. X. Li, and H. B. Li, 2002: Comparison of three spatial interpolation methods for climate variables in China (in Chinese). *Acta Geogr. Sin.,* **57,** 47–56.

Liu, J. M., and Z. F. Yang, 2009: Dynamics of temperature and humidity in under laying surface of different landscape type in winter in Beijing City China (in Chinese). *Acta Ecol. Sin.,* **29,** 3241–3252.

Liu, W. D., H. L. You, and J. X. Dou, 2009: Urban–rural humidity and temperature differences in the Beijing area (in Chinese). *Theor. Appl. Climatol.,* **96,** 201–207.

Liu, X. D., Z. Y. Yin, X. Y. Zhang, and X. C. Yang, 2004: Analyses of the spring dust storm frequency of northern China in relation to antecedent and concurrent wind, precipitation, vegetation, and soil moisture conditions. *J. Geophys. Res.,* **109,** D16210, doi:10.1029/2004JD004615.

Liu, X. F., X. Ruan, and Y. L. Gu, 2005: Study of temperature change and heat island effect in Shijiazhuang area (in Chinese). *Res. Environ. Sci.,* **18** (5), 12–13.

Miao, L. J., X. F. Cui, Y. B. Luan, and B. He, 2011: Similarities and differences of Beijing and Shanghai's land use changes induced by urbanization (in Chinese). *J. Meteor. Sci.,* **31,** 398–404.

Morris, C. J. G., I. Simmonds, and N. Plummer, 2001: Quantification of the influences of wind and cloud on the nocturnal urban heat island of a large city. *J. Appl. Meteor.,* **40,** 169–182.

Mu, X. D., H. P. Liu, and X. J. Xue, 2012: Urban growth in Beijing from 1984–2007 as gauged by remote sensing. *J. Beijing Norm. Univ.,* **48,** 81–85.

Oke, T. R., 1976: The distinction between canopy and boundary-layer urban heat islands. *Atmosphere,* **14,** 269–277.

——, 1981: Canyon geometry and the nocturnal urban heat island: Comparison of scale model and field observations. *J. Climatol.,* **1,** 237–254.

——, 1982: The energetic basis of the urban heat island. *Quart. J. Roy. Meteor. Soc.,* **108,** 1–24.

——, 1987: *Boundary Layer Climates*. 2nd ed. Methuen, 435 pp.

——, 1988: The urban energy balance. *Prog. Phys. Geogr.,* **12,** 471–508.

——, 2006: Initial guidance to obtain representative meteorological observations at urban sites. World Meteorological Organization Instruments and Observing Methods Rep. 81 and Tech. Doc. WMO/TD-No. 1250, 47 pp. [Available online at http://www.wmo.int/pages/prog/www/IMOP/publications/IOM-81/IOM-81-UrbanMetObs.pdf.]

Peterson, T. C., 2003: Assessment of urban versus rural in situ surface temperatures in the contiguous United States: No difference found. *J. Climate,* **16,** 2941–2959.

Ren, G. Y., Z. Y. Chu, Z. H. Chen, and Y. Y. Ren, 2007: Implications of temporal change in urban heat island intensity observed at Beijing and Wuhan stations. *Geophys. Res. Lett.,* **34,** doi:10.1029/2006GL027927.

——, Y. Q. Zhou, Z. Y. Chu, J. X. Zhou, A. Y. Zhan, J. Guo, and X. F. Liu, 2008: Urbanization effects on observed surface air temperature trends in north China. *J. Climate,* **21,** 1333–1348.

——, A. Y. Zhang, Z. Y. Chu, and Y. Y. Ren, 2010: Principles and procedure for selecting reference surface air temperature stations in China (in Chinese). *Mater. Sci. Technol.,* **38,** 85–98.

Ren, Y. Y., and G. Y. Ren, 2011: A remote-sensing method of selecting reference stations for evaluating urbanization effect on surface air temperature trends. *J. Climate,* **24,** 3179–3189.

Rosenzweig, C., W. D. Solecki, L. Parshalla, M. Chopping, G. Pope, and R. Goldberg, 2005: Characterizing the urban heat island in current and future climates in New Jersey. *Environ. Hazards,* **6,** 51–62.

Roth, M., T. R. Oke, and W. J. Emery, 1989: Satellite-derived urban heat islands from three coastal cities and the utilization of such data in urban climatology. *Int. J. Remote Sens.,* **10,** 1699–1720.

Sakakibara, Y., and K. Owa, 2005: Urban–rural temperature differences in coastal cities: Influence of rural sites. *Int. J. Climatol.,* **25,** 811–820.

Stewart, I. D., and T. R. Oke, 2012: Local climate zones for urban temperature studies. *Bull. Amer. Meteor. Soc.,* **93,** 1879–1900.

Wang, J. P., J. S. Sun, and S. G. Wang, 2011: Impact of basin terrain urban heat island effect on precipitation in surrounding region of Xi' an (in Chinese). *J. Arid Meteor.,* **29,** 168–173.

Wang, M. Y., and D. R. Lu, 2005: Diurnal and seasonal variation of clear-sky land surface temperature of several representative land surface types in China retrieved by GMS 5 (in Chinese). *Acta. Meteor. Sin.,* **63,** 957–967.

Wang, W. C., Z. Zeng, and T. R. Karl, 1990: Urban heat islands in China. *Geophys. Res. Lett.,* **17,** 2377–2380.

Wang, X. L., X. R. Li, and Z. K. Feng, 2010: Research on urban extension based on Shannon entropy (in Chinese). *China Popul. Resour. Environ.,* **20** (3), 88–92.

Wang, Y., and F. Hu, 2006: Variations of the urban heat island in summer of the recent 10 years over Beijing and its environment effect (in Chinese). *Chin. J. Geophys.,* **49,** 61–68.

Weng, Q., 2001: A remote sensing–GIS evaluation of urban expansion and its impact on surface temperature in the Zhujiang Delta, China. *Int. J. Remote Sens.,* **22,** 1999–2014.

Xie, H., and T. B. Yang, 2008: An analysis of urban thermal characteristics using Landsat satellite data—A case study in Lanzhou (in Chinese). *Remote Sens. Technol. Appl.,* **23** (6), 677–681.

Xie, Z., J. L. Cui, D. G. Chen, and B. K. Hu, 2006: The annual, seasonal and monthly characteristics of diurnal variation of urban heat island intensity in Beijing (in Chinese). *Climatic Environ. Res.,* **11,** 69–75.

Xu, X. D., G. A. Ding, and L. G. Bian, 2006: Beijing city air pollution observation experiment (in Chinese). *J. Appl. Meteor. Sci.,* **17,** 815–828.

Yang, P., W. D. Liu, J. Q. Zhong, and J. Yang, 2011: Evaluating the quality of temperature measured at Automatic Weather Stations in Beijing (in Chinese). *J. Appl. Meteor. Sci.,* **22,** 706–715.

——, Z. N. Xiao, and W. D. Liu, 2013: Comparison of diurnal temperature variation in urban and rural areas in Beijing and its seasonal change (in Chinese). *Chin. J. Atmos. Sci.,* **37,** 101–112.

Zhang, A. Y., G. Y. Ren, J. X. Zhou, Z. Y. Chu, Y. Y. Ren, and G. L. Tang, 2010: Urbanization effect on surface air temperature trends over mainland China (in Chinese). *Acta. Meteor. Sin.,* **68,** 957–966.

Zhang, G. Z., X. D. Xu, J. Z. Wang, and Y. Q. Yang, 2002: A study of characteristics and evolution of urban heat island over Beijing and its surrounding area (in Chinese). *J. Appl. Meteor. Sci.,* **13,** 43–50.

Zhang, J., X. P. Zhang, and X. Y. Wang, 2010: Time scale analysis of temperature and its urban heat island effect in Beijing (in Chinese). *Arid Land Geogr.,* **33,** 52–58.

Zhang, J. H., Y. Y. Hou, G. C. Li, H. Yan, and L. M. Yang, 2005: The research of the satellite sensing and the influence factor over Beijing and its surrounding zones (in Chinese). *Sci. China,* **35D,** 187–194.

Zhang, L., and G. Y. Ren, 2003: Change in dust storm frequency and the climatic controls in northern China (in Chinese). *Acta Meteor. Sin.,* **61,** 744–750.

Zhou, L. M., R. E. Dickinson, Y. H. Tian, J. Y. Fang, Q. X. Li, and R. K. Kaufmann, 2004: Evidence for a significant urbanization effect on climate in China. *Proc. Natl. Acad. Sci.,* **101,** 9540–9544.

Global and Planetary Change 111 (2013) 268–279

Contents lists available at ScienceDirect

Global and Planetary Change

journal homepage: www.elsevier.com/locate/gloplacha

Can temperature extremes in China be calculated from reanalysis?

Qinglong You [a,b,*], Klaus Fraedrich [b], Jinzhong Min [a], Shichang Kang [c,d], Xiuhua Zhu [b], Guoyu Ren [e], Xianhong Meng [f]

[a] Key Laboratory of Meteorological Disaster, Ministry of Education, Nanjing University of Information Science and Technology, Nanjing 210044, China
[b] Max Plank Institute for Meteorology, KlimaCampus, Hamburg 20144, Germany
[c] State Key Laboratory of Cryospheric Science, Chinese Academy of Sciences (CAS), Lanzhou 730000, China
[d] Laboratory of Tibetan Environment Changes and Land Surface Processes, Institute of Tibetan Plateau Research, CAS, Beijing 100085, China
[e] Laboratory for Climate Studies, National Climate Center, China Meteorological Administration (CMA), Beijing 100081, China
[f] Key Laboratory of Land Surface Process and Climate Change in Cold and Arid Regions, CAS, Lanzhou 730000, China

ARTICLE INFO

Article history:
Received 7 February 2013
Revised 23 September 2013
Accepted 8 October 2013
Available online 17 October 2013

Keywords:
temperature extremes
reanalysis
NCEP/NCAR and ERA-40
China

ABSTRACT

Based on daily maximum, minimum and mean surface air temperature from National Centers for Environmental Prediction/National Center for Atmospheric Research Reanalysis (NCEP/NCAR) and European Centre for Medium-Range Weather Forecasts (ECMWF) reanalyses, the distributions of twenty temperature indices are examined in China during 1958–2011. ECMWF includes ERA-40 for the period 1958–2001 and ERA-Interim during 2002–2011. The consistency and discrepancy of extreme indices between reanalyses and observations (303 stations) are assessed. In most cases, temperature indices between NCEP/NCAR and ECMWF have good agreements. For both reanalysis, cold days/nights have decreased, while warm days/nights have increased since 1980. Temperatures of the coldest days/nights and warmest days/nights significantly increase over the entire China, and the diurnal temperature range demonstrates slight variations; the amounts of growing season length, and summer/tropical days have increased, consistent with the decrease in numbers of frost/ice days. Furthermore, the persistence of heat wave duration and warm spell days has increased and consecutive frost days have reduced. Meanwhile, consecutive frost days, cold wave duration and cold spell days from NCEP/NCAR have decreased and consecutive frost days have increased, while these indices from ECMWF turn to the opposite directions. Compared with observations, temperature extremes from two reanalyses have small relative bias and the root mean squared errors, while correlation coefficients are positively high. These suggest that both reanalyses can reproduce the variability of temperature extremes obtained from observations, and can be applied to investigate climate extremes to some extent, although the biases exist due to the assimilation differences.

1. Introduction

Due to the contradiction between the lack of observations and the increasing demand from the scientific community, it becomes urgent to acquire dataset with high resolution and long record in support of climate research and modeling, especially in the data scarce region such as the Tibetan Plateau (Kang et al., 2010). Reanalysis data refer to the results of state-of-the-art model output, data assimilation of numerical models, and the integration of non-regular observations, rawinsonde, aircraft, satellite and other data sources (Kalnay et al., 1996; Kistler et al., 2001). Reanalysis data extend for several decades, cover the entire globe from the Earth's surface to the above of the stratosphere, and play an extremely important role in the field of atmospheric science and climate research. Meanwhile, reanalysis data can be applied to understand the laws of atmospheric motion, investigate global and regional climate change and variability, identify the causes of climate variations and prepare for the input datasets for climate modeling. Reanalysis data are widely used in atmospheric science, diagnostic analysis, as well as the initial field for driving the regional and global climate models (Kalnay et al., 1996; Kistler et al., 2001; Uppala et al., 2005; Dee and Uppala, 2009).

However, it is noticed that that reanalysis data should not be equated with “observations” and “reality”. The changing mix of observations and biases between observations and models can produce spurious variability and trend in the reanalysis. Zhao and Fu (2006) divided the reanalysis errors into the two classifications: (1) observing system changes such as lack of observations and errors in observations may lead to discrepancies and errors in reanalysis products, which can be regarded as the systematic errors; (2) numerical prediction models and assimilation programs such as shortcoming in the assimilating model/methodology can produce inaccurate/false data for reanalysis data. In summary, the uncertainties in the reanalysis data are difficult to understand and qualify, and more recent researches are to facilitate comparisons between reanalysis and observational datasets (Bengtsson et al., 2004; Simmons et al., 2004).

The widespread used reanalysis included the National Centers for Environmental Prediction/National Center for Atmospheric Research

* Corresponding author at: Key Laboratory of Meteorological Disaster, Ministry of Education, Nanjing University of Information Science and Technology, Nanjing, 210044, China.
E-mail address: yqingl@126.com (Q. You).

0921-8181/$ – see front matter © 2013 Elsevier B.V. All rights reserved.
http://dx.doi.org/10.1016/j.gloplacha.2013.10.003

Reanalysis (NCEP/NCAR hereafter) (1948–present) (Kalnay et al., 1996) and European Centre for Medium-Range Weather Forecasts (ECMWF) 40 year reanalysis (ERA-40 hereafter) (1957–2002) (Uppala et al., 2005). ERA-Interim is the latest global atmospheric reanalysis produced by ECMWF covering the data since 1979 (Dee et al., 2011), and it is regarded as the new, more ambitious and next generation reanalysis to succeed ERA-40 (Dee and Uppala, 2009). On the global and regional scales, several studies have been retrieved different parameters and variables from reanalysis to compare the credibility with observations (Kalnay et al., 1996; Su et al., 1999; Zhang and Qian, 1999; Xu et al., 2001; Wei and Li, 2003; Simmons et al., 2004; Frauenfeld et al., 2005; Zhao and Fu, 2006; Xie et al., 2007; Zhao et al., 2007, 2008; You et al., 2009). However, the results are sensitive to the time period, regions, and selected observations.

In China, the observed surface air temperatures have been applied to evaluate the applicability of NCEP/NCAR reanalysis. The preliminary analysis shows that the monthly mean temperature from reanalysis is lower than the observed value. On a seasonal basis, surface air temperature in summer has a good credibility for reanalysis, while the winter has a poor credibility (Xu et al., 2001; Zhao and Fu, 2006; Ma et al., 2008; Zhao et al., 2008). Compared with NCEP/NCAR, ERA-40 reanalysis represents the temperature of the lower troposphere over East Asia very well, and can be used to study the inter-decadal climate change in that region (Huang, 2006). There are studies focusing on the applicability of reanalysis in the Tibetan Plateau. It is found that the surface air temperature from NCEP/NCAR does not identify significant warming and there are large geographical differences, while it shows more pronounced warming in the North China Plain region (Su et al., 1999; Xu et al., 2001; Ma et al., 2008). Over the Tibetan Plateau and its vicinity, Su et al. (1999) analyzed and tested the credibility of NCEP/NCAR reanalysis, and pointed out that the reanalysis is more reasonable because the mean distribution patterns from reanalysis are similar to observations. Wei and Li (2003) carried out the applicability of NCEP/NCAR reanalysis along the Qinghai-Tibet Railway, and found systematic temperature values obtained from reanalysis are less than the actual observed values. Frauenfeld et al. (2005) compared ERA-40 reanalysis with observations, and revealed that ERA-40 reanalysis is less susceptible to the influence of the local assimilation system after the spectral models with the real terrain are used. Xie et al. (2007) investigated two automatic weather stations' data in the southern Nyainqentanglha Mountains and Everest Northern Slope, and compared them with NCEP/NCAR reanalysis. They indicated that NCEP/NCAR reanalysis can reflect changes in the temperature at the synoptic scale, but temperature value from reanalysis is lower than the corresponding observed values. You et al. (2009) analyzed the applicability of NCEP/NCAR reanalysis in the glacier nearby Namco Lake district, and illustrated that reanalysis of the temperature is relatively good, and application of reanalysis in the critical region should take the impact of altitude into account. These results are identified for the surface air temperature in the entire Tibetan Plateau by the comparisons between observations and reanalyses including NCEP/NCAR and ERA-40 reanalysis (You et al., in press).

Overall, the applicability of reanalysis has been assessed and compared with the climate mean anomalies (such as the monthly and annual mean temperature). Fewer studies have been focused on the extreme climate and weather events such as extreme heat waves, extreme low temperatures, cold wave duration, which are more sensitive to climate change than their mean values (IPCC, 2007). Reanalysis data can be a potentially useful source of data for monitoring long-term changes in extremes in data sparse regions, but they have not been used in the field of temperature extremes (Zhang et al., 2011). The purpose of the present study is to evaluate the climate extremes calculated from reanalysis in China, the applicability of the inter-annual climate is evaluated with observations, which are needed to better understand the pattern, cause, frequency and intensity of climate extreme in China.

2. Data and methods

2.1. Reanalysis data

In this study, the daily maximum, minimum and mean temperatures from NCEP/NCAR, ERA-40 and ERA-Interim reanalysis are selected, which are in accordance with 190 grid points covering the entire China (Fig. 1). NCEP/NCAR reanalysis is provided by the National Oceanic and Atmospheric Administration (NOAA)/Earth System Research Laboratory (ESRL)/Physical Sciences Division (PSD), Boulder, Colorado, USA, from their website at http://www.cdc.noaa.gov/. The datasets cover January 1948 to the present with a spatial resolution of 2.5° × 2.5° (Kalnay et al., 1996), and are initialized with a wide variety of weather observations, including ships, planes, satellite observations. The daily maximum, minimum and mean temperatures of ERA-40 and ERA-Interim reanalysis data are obtained from the ECMWF website (http://www.ecmwf.int/). For ERA-40 reanalysis, it is available from September 1957 to August 2002 with a spatial resolution of 2.5° × 2.5° (Uppala et al., 2005). Compared with NCEP/NCAR, ERA-40 is produced by use of a wide range of observing systems, such as the satellite data and vertical temperature profile radiometer radiances starting in 1972 (Ma et al., 2009). Due to ERA-40 stop by 2002, ERA-Interim (1979–present) is used to extend ERA-40 to the present. It is shown that the difference of temperature between ERA-40 and ERA-Interim is slight during the overlapping period (1979–2001) (Fig. 1). Thus ERA-40 is used before 2001 ERA-Interim is applied after 2001 for this study. ERA-Interim use input observations prepared for ERA-40 until 2002 and has a spatial resolution of 1.5° × 1.5° (Dee et al., 2011). Both NCEP/NCAR and ERA-40 were assimilated using a 6-hourly 3D variational analysis (3DVAR), but ERA-Interim is based on a 12-hour four-dimensional variational analysis (4DVAR). Furthermore, the surface sea temperature and sea-ice concentrations described as boundary conditions differ in each reanalysis, and the forecast models and physical parameterizations are also different (Zhang et al., 2012). To qualify the comparison, all reanalyses are interpolated into 2.5° × 2.5° horizontal resolution using the linear interpolation methods.

2.2. Observations

To validate the reanalysis data, the daily maximum, minimum and mean temperatures for 303 stations are used in China (Fig. 1), provided by the National Meteorological Information Center, China Meteorological Administration (NMIC/CMA). The quality of observational data in China, meeting the World Meteorological Organization's (WMO) standards, and the climate extreme and its connection with atmospheric patterns have been discussed (You et al., 2011). For the calculation of observations, the internationally agreed indices are adopted, which are generated by the WMO Commission for Climatology (CCl), the World Climate Research Program (WCRP) project on Climate Variability and Predictability (CLIVAR) and Joint WMO-Intergovernmental Oceanographic Commission (IOC) Technical Commission for Oceanography and Marine Meteorology (JCOMM) Expert Team (ET) on Climate Change Detection and Indices (ETCCDI) (http://cccma.seos.uvic.ca/ETCCDI) (Peterson and Manton, 2008). Releasing climate indices and sharing the ETCCDI's indices are of great use to scientific community working on adaptation and climate model validation. In this study, the ETCCDI's indices from observations derived from You et al. (2011) will be applied to compare and validate the reanalyzed temperature extremes indices.

2.3. Extreme indices and calculation

Twenty temperature indices are selected in this study (Table 1). As it can be seen, some indices are commonly used to assess the intensity, frequency and duration of climate extreme events, and widely analyzed on the regional and global scales (e.g. Alexander et al., 2006; Peterson

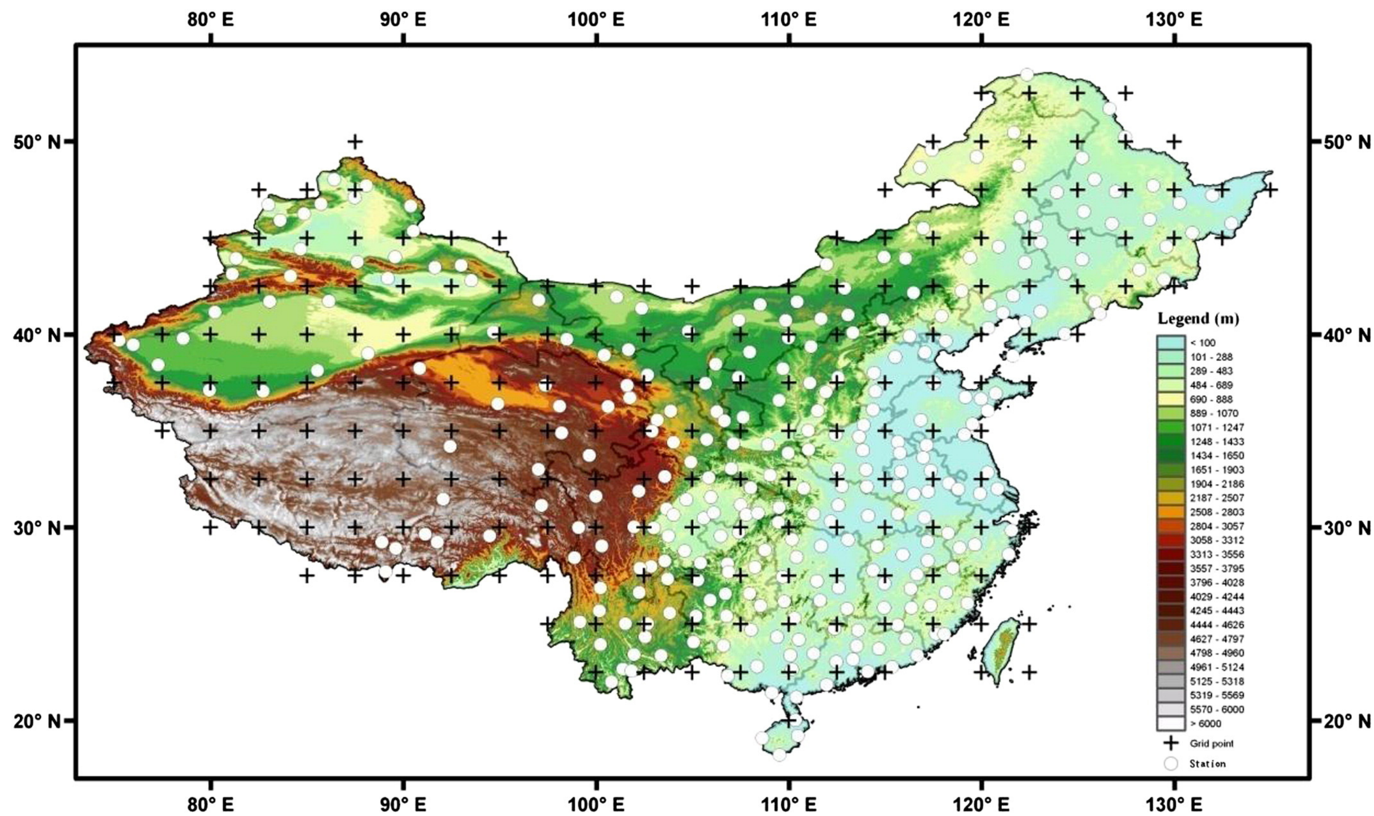

Fig. 1. Topography of China and the distribution of 190 grid points used in this study. The white dots are the 303 observational stations used as reference stations.

and Manton, 2008). Detailed descriptions are provided in Table 1, and more knowledge is available from http://cccma.seos.uvic.ca/ETCCDI.

The Mann–Kendall test for a trend and Sen's slope estimates are used to estimate trends in annual and seasonal temperature extreme series (Sen, 1968). The method has been widely used to compute trends in hydrological and meteorological series. In this paper, a trend is considered to be statistically significant if it is significant at the 5% level (Table 2). When repeating multiple statistical tests at different stations and if the indices are correlated between the different stations, it requires field significance testing. Different procedures have been developed to take into account cross-correlations in trend analysis, including the block-bootstrap (Douglas et al., 2000) or the False Dis-covery Rate (Ventura et al., 2004; Wilks, 2006) methods.

In the present study the block-bootstrap (Douglas et al., 2000) method has been applied to evaluate the field significance of the correlation between reanalyses and observations. Both reanalyses and observations are resampled to create 1000 different datasets, and the correlation between them is computed for each dataset.

3. Results

Figs. 3 and 4 show the time series of twenty temperature extremes during 1958–2011 based on NCEP/NCAR and ECMWF reanalysis averaged 190 grid points in China. It is notable that the ECMWF includes ERA-40 for the period of 1958–2001 and ERA-Interim during 2002–2011. The trends of temperature extremes for the period of 1958–1979, 1980–2011 and 1958–2011 are summarized in Table 1. As shown in Table 1, the trends for the period of 1958–1979 and 1980–2011 are different, indicating the inter-decadal variations for temperature extremes are significant. In this study, only the spatial trends of temperature extreme for NCEP/NCAR and ECMWF during 1958–2011 are demonstrated and discussed in Figs. 5 and 6.

3.1. Percentile-based indices (TX10, TN10, TX90, and TN90)

Percentile-based indices include occurrences of cold days (TX10), cold nights (TN10), warm days (TX90) and warm nights (TN90), which selected the coldest and warmest deciles for both maximum and minimum temperature (Alexander et al., 2006). For TX10 and TN10, the spatial trends derived from NCEP/NCAR and ECMWF are negative in most northern China, but they have discrepancies in the Tibetan Plateau, where trends of NCEP/NCAR show negative but those of ECMWF display positive. For the time series anomalies, TX10 and TN10 calculated from NCEP/NCAR decrease for the period 1958–1979 and 1980–2011, and the regional trends of both indices during 1958–2011 are −0.71 days/decade and −0.42 ($P < 0.05$) days/decade, respectively, and the absolute trend magnitude of TX10 is higher than TN10 (Fig. 2). Meanwhile, TX10 from ECMWF slightly increases but TN10 decreases, and the regional trends for both indices during 1958–2011 are 0.15 days/decade and −0.30 days/decade, respectively, and only the latter has passed the significance level. Thus, TX10 and TN10 from NCEP/NCAR and ECMWF have inconsistencies, although the correlation coefficients between two reanalyses are positively high ($R = 0.43$ for TX10 and $R = 0.78$ for TN10). For the global and regional studies, both TX10 and TN10 from observations have negative trends and TN10 decreases rapidly than TX10 (Peterson et al., 2002; Aguilar et al., 2005; Alexander et al., 2006; Peterson et al., 2008; Aguilar et al., 2009). For example, the global means of TX10 and TN10 during 1951–2003 have decreased with rates of −0.62 days/decade and −1.26 days/decade, respectively (Alexander et al., 2006), and the regional trends of both indices in central and northern South America during 1961–2003 are −2.4 days/decade and −2.2 days/decade, respectively (Aguilar et al., 2005).

For TX90 and TN90, both indices calculated from NCEP/NCAR and ECMWF have positive trends in the entire China, and there have significant positive correlations between two reanalyses ($R = 0.91$ for TX90 and $R = 0.78$ for TN90). TX90 and TN90 from NCEP/NCAR depict

Table 1
Definitions of temperature extreme indices used in this study.

Index	Descriptive name	Definition	Units
TX10	Cold day frequency	Percentage of days when TX < 10th percentile of 1961–1990	%
TN10	Cold night frequency	Percentage of days when TN < 10th percentile of 1961–1990	%
TX90	Warm day frequency	Percentage of days when TX > 90th percentile of 1961–1990	%
TN90	Warm night frequency	Percentage of days when TN > 90th percentile of 1961–1990	%
DTR	Diurnal temperature range	Annual mean difference between TX and TN	°C
TXn	Coldest day	Annual lowest TX	°C
TNn	Coldest night	Annual lowest TN	°C
TXx	Warmest day	Annual highest TX	°C
TNx	Warmest night	Annual highest TN	°C
GSL	Growing season length	Annual count between the first span of at least 6 days with TG > 5 °C after winter and first span after the summer of 6 days with TG < 5 °C	days
FD	Frost days	Annual count when TN < 0 °C	days
ID	Ice days	Annual count when TX < 0 °C	days
SU	Summer days	Annual count when TX > 25 °C	days
TR	Tropical nights	Annual count when TN > 20 °C	days
CSU	Consecutive summer days	Annual largest number of consecutive days when TX > 25 °C	days
CFD	Consecutive frost days	Annual largest number of consecutive days when TN < 0 °C	days
CWDI	Cold wave duration index	Annual account number of days when, intervals of at least 6 consecutive days, TN < TNnorm-5 °C	days
CWFI	Cold spell days index	Annual account number of days when, intervals of at least 6 consecutive days, TG < 10th percentile of 1961–1990	days
HWDI	Heat wave duration index	Annual account number of days when, intervals of at least 6 consecutive days, TX > TXnorm + 5 °C	days
HWFI	Warm spell days index	Annual account number of days when, intervals of at least 6 consecutive days, TG > 90th percentile of 1961–1990	days

Note: TX is the daily maximum temperature; TN is the daily minimum temperature; TG is daily mean temperature; TNnorm is the mean of daily minimum temperatures for the period of 1961–1990; TXnorm is the mean of daily maximum temperatures for the period of 1961–1990.

consistent negative trends before 1980 and positive trends afterwards, which result to positive trends during 1958–2011 with rates of 1.39 days/decade and 2.24 days/decade ($P < 0.05$), respectively. The patterns for TX90 and TN90 from ECMWF are in good agreements with those from NCEP/NCAR during 1958–2011 (1.72 days/decade and 0.30 days/decade ($P<0.05$)). It is distinct that TX90 from two reanalyses has larger trend magnitudes than TN90. The asymmetrical changes for TX90 and TN90 are inconsistent with observations in China (Zhai et al., 1999; You et al., 2011), the eastern and central Tibetan Plateau (You et al., 2008), Southern Africa (Aguilar et al., 2009), North America (Peterson et al., 2008), but are consistent with the characteristic in central South America (Aguilar et al., 2005).

3.2. Absolute indices (TXn, TXx, TNx, TNn, and DTR)

Absolute indices represent maximum or minimum values within a selected period, and the annual basis is selected (Table 1), which includes temperatures of coldest days and nights (TXn and TNn) and warmest days and nights (TXx and TNx) in each year. The diurnal temperature range (DTR) is the difference between the daily maximum and minimum temperature, which is regarded as the absolute index in this study.

During 1958–2011, TXn and TNn from NCEP/NCAR and ECMWF show positive trends before 1980, and negative trends afterwards, while they demonstrate positive trends in the whole period. TXn and TNn for NCEP/NCAR have positive rates of 0.25 °C/decade and 0.18 °C/decade, respectively, and the significant increases for both indices occur in the northeastern China, consistent with the rapid increases of surface air temperature (You et al., 2011). Variability of TXn and TNn from ECMWF is very similar to NCEP/NCAR throughout the period 1958–2011, reflected by the high positive correlations with NCEP/NCAR ($R = 0.90$ and $R = 0.84$). The regional trends for TXn and TNn from ECMWF are 0.12 °C/decade and 0.21 °C/decade, respectively. For TXx and TNx, variabilities in NCEP/NCAR and ECMWF are very similar, and the correlations between two reanalyses are substantially higher

Table 2
Trends per decade for the regional indices of temperature extremes in China based on NCEP/NCAR and ECMWF reanalysis for the period of 1958–1979, 1980–2011 and 1958–2011. ECMWF includes ERA-40 during 1958–2001 as well as ERA-Interim during 2002–2011. The trends are calculated by the Mann–Kendall slope estimator. Values for trends significant at the 10% level are marked in bold. The values with asterisk indicate trends significant at the 5% level.

Indices	Unit	1958–1979		1980–2011		1958–2011	
		NCEP/NCAR	ECMWF	NCEP/NCAR	ECMWF	NCEP/NCAR	ECMWF
TX10	days/decade	−0.09	0.93	**−0.48** *	0.30	**−0.71***	0.15
TN10	days/decade	0.98	1.05	**−0.42**	−0.39	**−0.42***	**−0.30**
TX90	days/decade	−0.81	−1.28	**4.27***	**3.92***	**1.78***	**1.72***
TN90	days/decade	**−2.41***	**−1.22** *	**3.71***	**4.71***	**1.39***	**2.24**
DTR	°C/decade	**0.22***	−0.04	**0.08***	**−0.05***	**0.08***	**−0.05***
TXn	°C/decade	0.15	−0.14	0.05	−0.09	**0.25***	0.12
TNn	°C/decade	−0.02	−0.12	0.04	0.06	**0.18***	**0.21***
TXx	°C/decade	0.09	−0.08	**0.38***	**0.34***	**0.23***	**0.14***
TNx	°C/decade	0.01	−0.12	**0.29***	**0.42***	**0.16***	**0.16***
GSL	days/decade	0.71	−0.14	**3.98***	**2.14**	0.72	**1.15**
FD	days/decade	**3.52***	0.80	**−2.50** *	**−2.79***	**−0.54**	**−1.16***
ID	days/decade	−0.53	1.65	**−1.75***	**−1.44**	**−1.28***	**−0.68***
SU	days/decade	2.05	**−1.64**	**4.67***	**4.88***	**3.13***	**1.89***
TR	days/decade	**−1.38**	**−1.65**	**2.61***	**4.25***	**1.40***	**1.77***
CSU	days/decade	0.34	**−1.54**	**1.86***	**1.20***	**1.11***	−0.03
CDF	days/decade	0.86	0.80	−1.07	**−2.05***	−0.42	**−0.94***
CWDI	days/decade	0.41	0.75	0.24	**0.71***	−0.19	0.14
CWFI	days/decade	0.29	0.72	0.57	**2.51***	−0.18	**0.70***
HWDI	days/decade	−0.54	−1.12	**3.45***	**3.75***	**1.35***	**1.57***
HWFI	days/decade	**−4.37**	**−2.51**	**6.83***	**8.25***	**2.25***	**3.40***

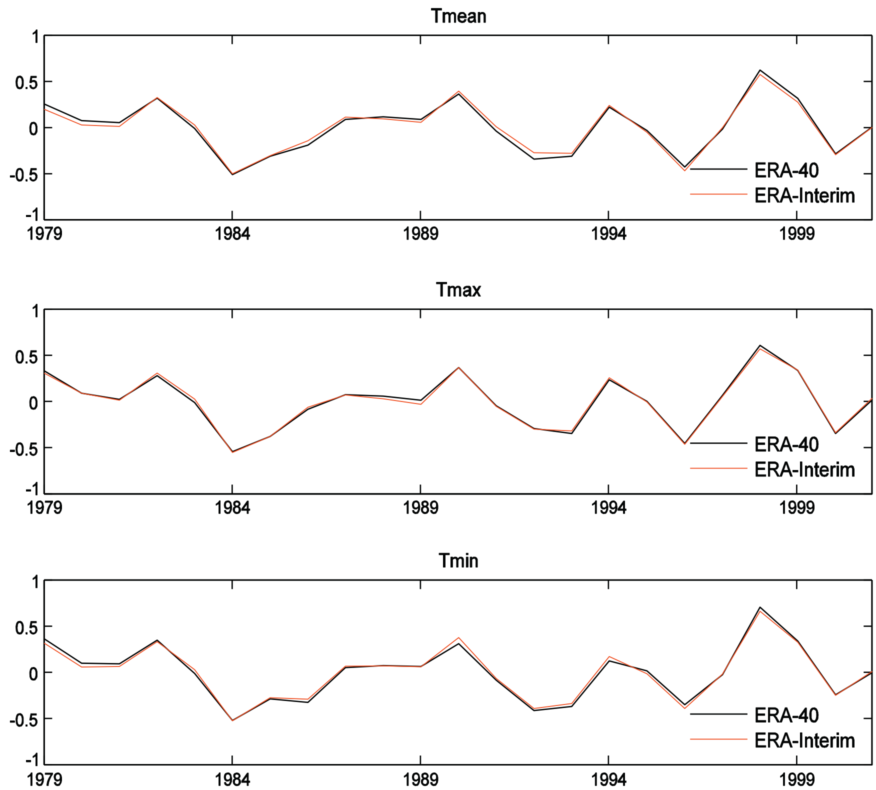

Fig. 2. Anomalies of daily maximum, minimum and mean temperatures in China during 1979–2001. The black curve shows the ERA-40 and red one represents ERA-Interim.

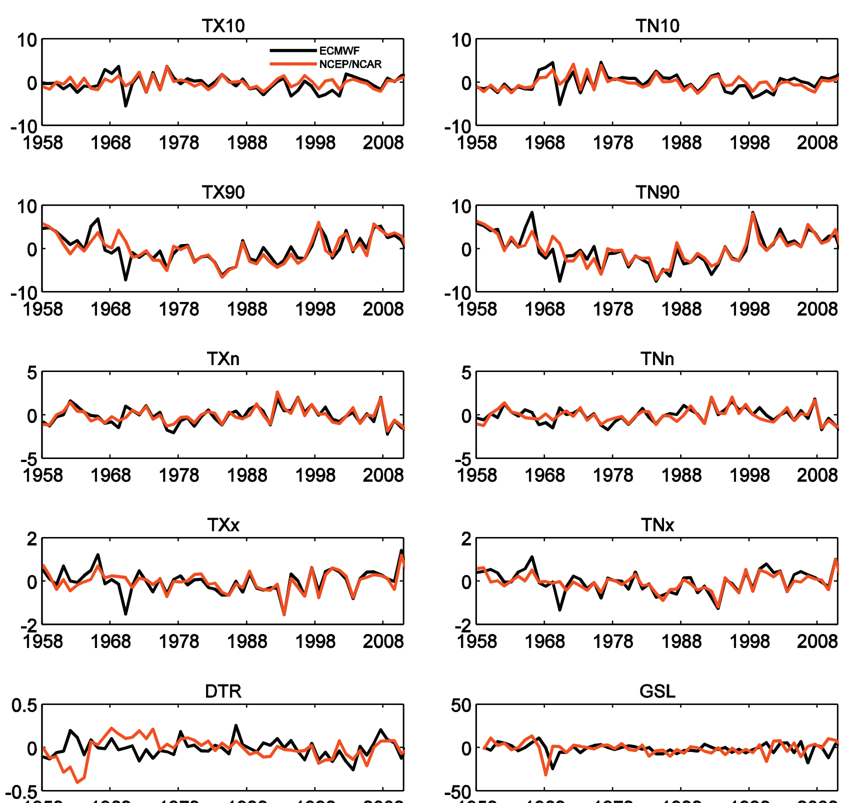

Fig. 3. Anomalies of TX10, TN10, TX90, TN90, TXn, TNn, TXx, TNx, DTR and GSL in China during 1958–2011. The black curve shows the NCEP/NCAR reanalysis and red one represents ECMWF. ECMWF includes ERA-40 during 1958–2001 as well as ERA-Interim during 2002–2011. (For interpretation of the references to color in this figure legend, the reader is referred to the web version of this article.)

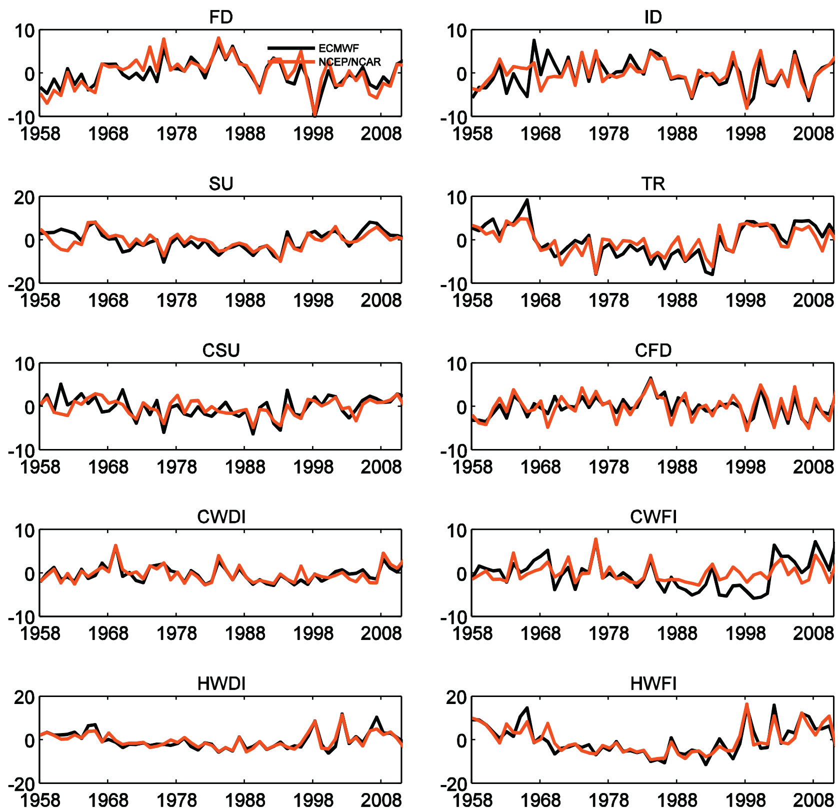

Fig. 4. Anomalies of temperature extremes indices (FD, ID, SU, TR, CSU, CFD, CWDI, CWFI, HWDI and HWFI) in China during 1958–2011. The black curve shows the NCEP/NCAR reanalysis and red one represents ECMWF. (For interpretation of the references to color in this figure legend, the reader is referred to the web version of this article.)

(R = 0.82 for TXx and R = 0.86 for TNx). During 1958–2011, TXx and TNx from NCEP/NCAR show increases in most regions in China, with the regional rates of 0.23 °C/decade and 0.16 °C/decade, respectively, which are distinctly higher than ECMWF (0.14 °C/decade and 0.16 °C/decade). Beside differences of the trend magnitudes between NCEP/NCAR and ECMWF, differential changes of indices from maximum and minimum temperatures for two reanalysis are also found. Indices of maximum temperature from NCEP/NCAR (such as TXn and TXx) are more sensitive to warming than those of the minimum temperature (such as TNn and TNx), in contradiction with ECMWF. For the observational studies in Africa, indices of minimum temperature have larger trend magnitudes than those of maximum temperature (New et al., 2006; Aguilar et al., 2009), which are opposite to that in central South America (Aguilar et al., 2005).

Previous studies show that changes in DTR can be an evidence of climate change (Easterling et al., 1997; Alexander et al., 2006). Although DTR from NCEP/NCAR and ECMWF has a negative correlation (R = −0.37), slight variations are seen in both reanalyses during the period 1958–2011, and these are particularly the case for the spatial patterns of trend in the entire China. Both two reanalyses cannot capture the variability of DTR observed from stations in China (You et al., 2011), which shows that the trend in DTR during 1961–2003 is −0.18 °C/decade with a significant at the 0.05 level. On the global scale, decreased DTR from observations is identified due to the minimum temperatures that have increased at a faster rate than the maximum temperatures (Easterling et al., 1997; Alexander et al., 2006), which were probably affected by local effects such as urban growth, irrigation, desertification, and land use change.

3.3. Threshold indices (FD, ID, SU, and TR)

Threshold indices are defined as the number of days on which the temperature values fall above or below a fixed threshold, including occurrence of frost days (FD), ice days (ID), summer days (SU) and tropical nights (TR) (Alexander et al., 2006). The numbers of FD and ID from NCEP/NCAR and ECMWF have increased before 1980, and decreased afterwards. The positive correlations of FD and ID between two reanalyses are higher than 0.8, indicating both reanalyses have highly correlated. During 1958–2011, FD and ID from two reanalyses represent negative trends in most regions in China. FD and ID from NCEP/NCAR have negative trends, with rates of −0.54 days/decade and −1.28 days/decade, respectively, while the trends of two indices from ECMWF are −1.16 days/decade and −0.68 days/decade, respectively. The change of FD from two reanalyses is similar to that in the Middle East, which shows the regional trend of FD is −0.6 days/decade during 1950–2003 (Zhang et al., 2005). In the Tibetan Plateau, FD is also negative with a rate of −4.32 days/decade during 1961–2005 (You et al., 2008).

The numbers of SU and TR from NCEP/NCAR and ECMWF are in good agreements during 1958–2011, with a correlation coefficient of about 0.7. Both SU and TR decrease before the 1990s and significantly increase afterwards, and the positive trends can be seen in most regions in China. The rates of both indices for NCEP/NCAR during 1958–2011 are 3.13 days/decade and 1.4 days/decade, and 1.89 days/decade and 1.77 days/decade for ECMWF. The reanalyzed rates for SU and TR are less than the regional trends in southern Africa during 1961–2000 (New et al., 2006), which shows the trends are 5.05 days/decade and 2.93 days/decade, respectively. In the Middle East during 1950–2003, the trends for SU and TR also significantly decrease with rates of 1 days/decade and 3.7 days/decade (Zhang et al., 2005).

3.4. Duration indices (GSL, CSU, CDF, CWDI, CWFI, HWDI, and HWFI)

Duration indices define the periods of excessive warmth, cold, wetness or dryness or in the case of growing season length, periods of mildness (Alexander et al., 2006). In this study, duration indices include

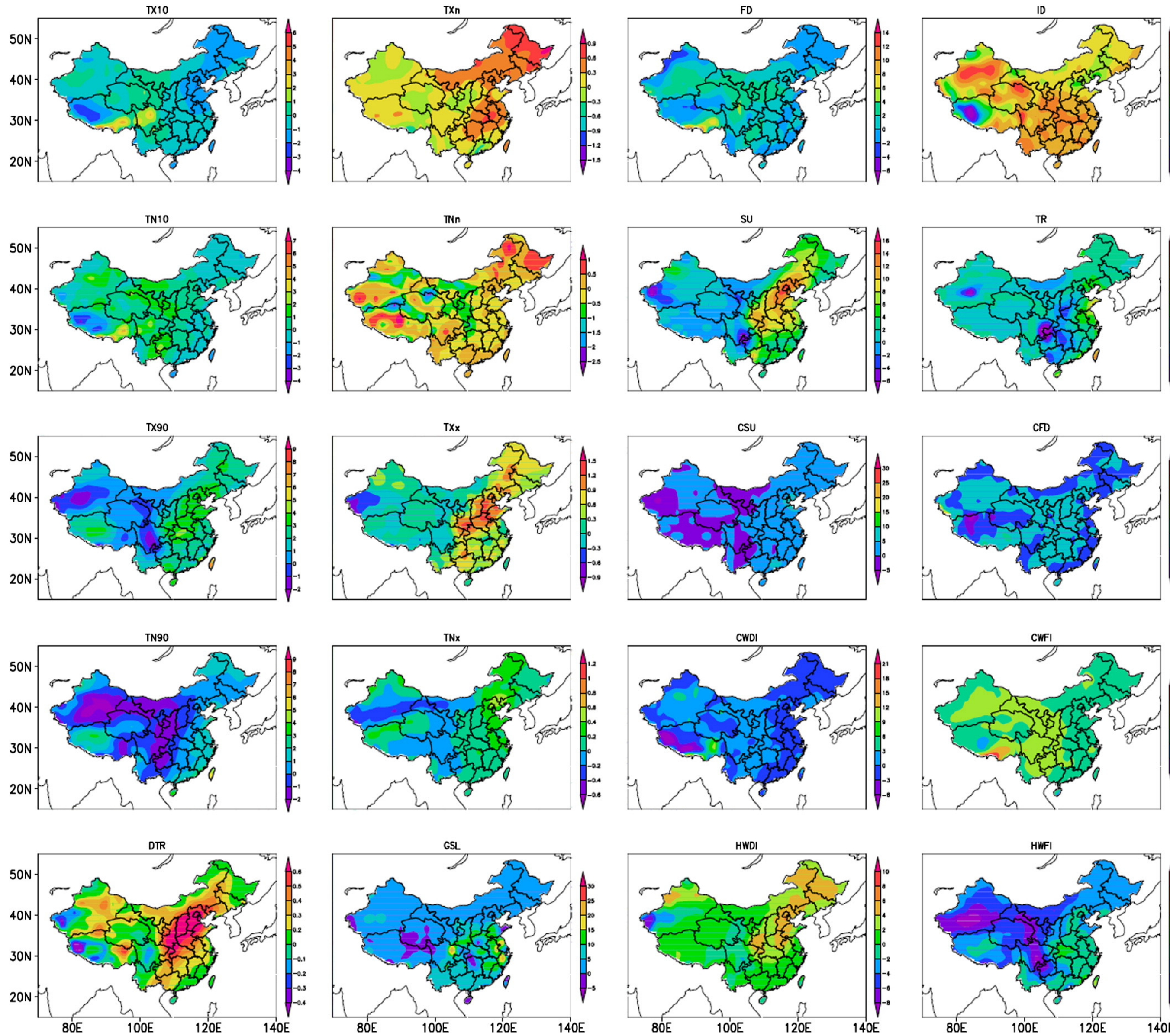

Fig. 5. Spatial trend patterns of temperature extreme indices from NCEP/NCAR reanalysis in China during 1958–2011. The unit of each index is the same as in Table 1.

growing season length (GSL), consecutive summer days (CSU) and consecutive frost days (CFD), cold wave duration index (CWDI) and cold spell days index (CWFI), heat wave duration index (HWDI) and warm spell days index (HWFI).

Although GSL from NCEP/NCAR and ECMWF has a slight negative correlation ($R = -0.02$), it rapidly increases since the 1980s, especially for NCEP/NCAR, which leads to the positive trends for both reanalyses during 1958–2011 (0.72 days/decade and 1.15 days/decade). The observed GSL in the Tibetan Plateau increases with a rate of 4.25 days/decade during 1961–2005 (You et al., 2008). The trends of reanalyzed GSL is also lower than the observations in China (You et al., 2011).

The number of CSU from NCEP/NCAR is positively correlated with that from ECMWF ($R = 0.6$), and CSU from both reanalyses decreases before the mid-1980s and increases afterwards, leading to the rates of 1.11 days/decade and −0.03 days/decade during 1958–2011. Same as other temperature extreme indices, the number of CDF from NCEP/NCAR is positively correlated with that from ECMWF ($R = 0.84$), and CDF from both reanalyses increases/decreases before/after the mid-1980s, and the rates are −0.42 days/decade and −0.94 days/decade during 1958–2011.

Although CWDI from NCEP/NCAR is positively correlated with that from ECMWF ($R = 0.86$), the trend from NCEP/NCAR is negative (−0.42 days/decade), but that for ECMWF is positive (0.14 days/decade). The entire China has the same trend patterns. For CWFI from NCEP/NCAR, it decreases before the 1980s and increases afterwards, resulting to the trend of −0.18 days/decade. CWFI from ECMWF is positively correlated with that from NCEP/NCAR, especially before the 1980s, while the trend for the whole period is 0.70 days/decade.

For HWDI and HWFI, both indices from NCEP/NCAR slightly decrease before the 1980s, and increases during the 1990s. The regional trends for both reanalyses are 1.35 days/decade and 2.25 days/decade, respectively, which the positive trends are apparent in the northern China. HWDI and HWFI from ECMWF positively correlate with those from NCEP/NCAR ($R = 0.86$ for HWDI and $R = 0.92$ for HWFI), the positive trends for two indices during 1958–2011 are 1.57 days/decade and 3.4 days/decade.

4. Discussion and conclusions

In this study, the spatial and temporal distributions of trends in temperature extremes from NCEP/NCAR and ECMWF reanalyses have

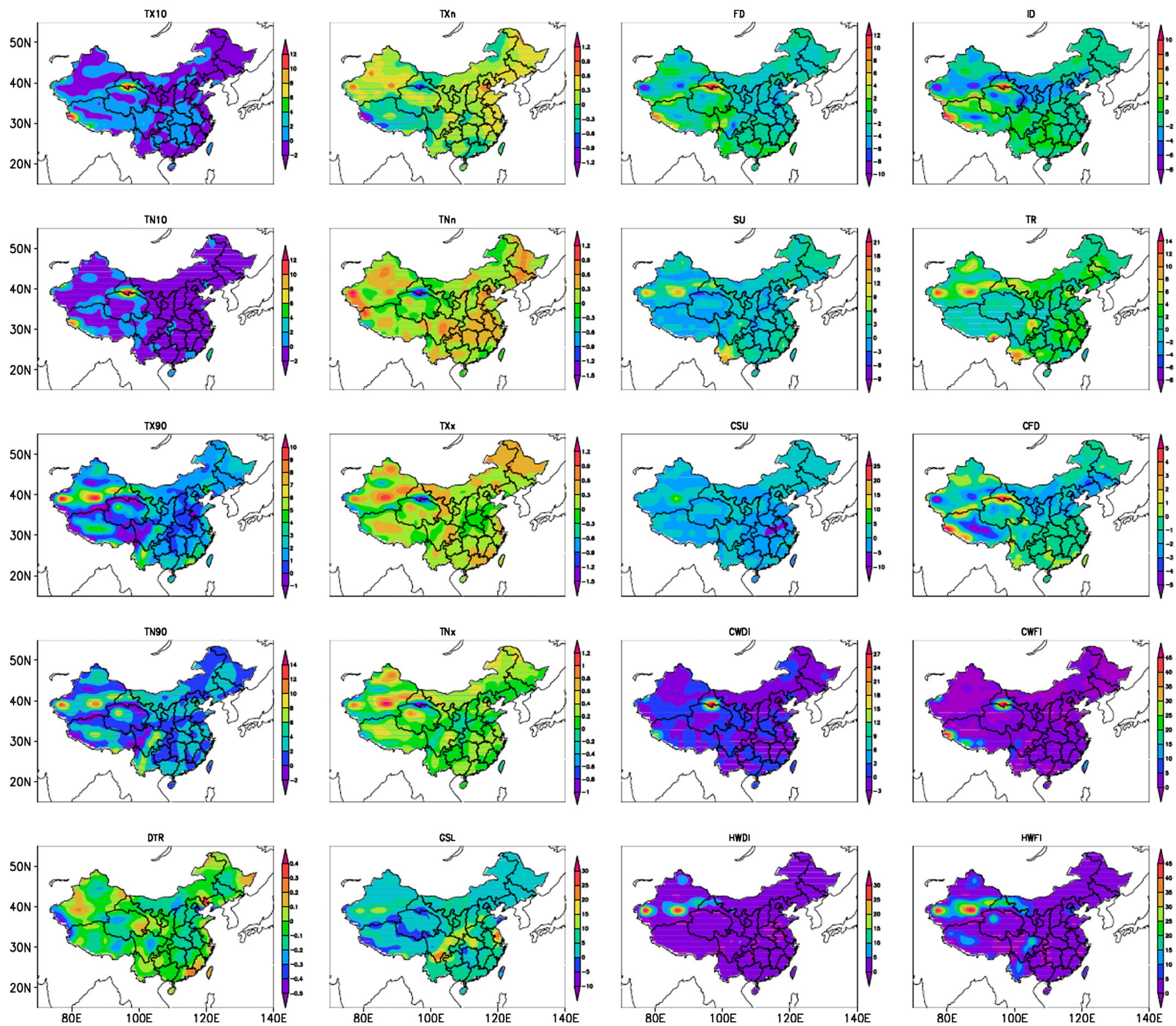

Fig. 6. Spatial trend patterns of temperature extreme indices from ECMWF reanalysis in China during 1958–2011. The unit of each index is the same as in Table 1.

been examined during 1958–2011. Twenty temperature indices developed by the joint CC1/CLIVAR/JCOMM Expert Team on Climate Change Detection and Indices have been selected. For the percentile-based indices, significant increases in warm nights/days and significant decreases in cold nights/days are obtained from two reanalyses during 1958–2011, especially for the period 1980–2011. The absolute indices show patterns consistent with a general warming trend, which are consistent with previous studies in the world (e.g. Alexander et al., 2006; You et al., 2011). Based on the two reanalyses, trends in minimum temperature extremes are same as those in maximum temperature extremes (Fig. 7), which lead to the slight variation in DTR, inconsistent with the observational studies such as You et al. (2011) and Easterling et al. (1997). For the threshold indices, the warming climate has caused the numbers of frost/ice days to decrease while the numbers of summer/tropical days have increased. The duration indices have also changed during the past decades, while the discrepancies exist between two reanalyses.

It seems that the temperature extremes have connections with the global warming. In recent decades, China has experienced significant climate changes and the atmospheric circulation is characterized by an inter-decadal transition in the late 1970s (Wang et al., 2012). Overall, the annual and seasonal mean, maximum and minimum temperatures in China have increased since the 1950s (Table 3). The annual mean surface air temperature has increased with a rate of 0.22 °C/decade during 1956–2002, and the daily maximum and minimum air temperatures have increased at rates of 0.13 and 0.32 °C/decade from 1955 to 2000, respectively (Wang and Gong, 2000). It is clear that the daily minimum temperatures significantly increased at a higher rate than the daily maximum and mean temperatures, and warming is more pronounced in the northeast China and less in the southwest China (Wang and Gong, 2000; Liu et al., 2004). Seasonally, the changes in daily minimum, maximum and mean temperatures are more significant in winter, which mostly contribute to the increase on the annual basis (Zhai et al., 1999). Meanwhile, the observed temperature extremes in China are significant. Zhai et al. (1999) revealed that upward trends in whole China have been detected for the frequencies of warm days/nights, with the largest increases since the mid-1980s. At the same time, the downward trends are also significant for the frequencies of cold days/nights. The frost day has a significant downward trend, indicating that the frost-free season in China

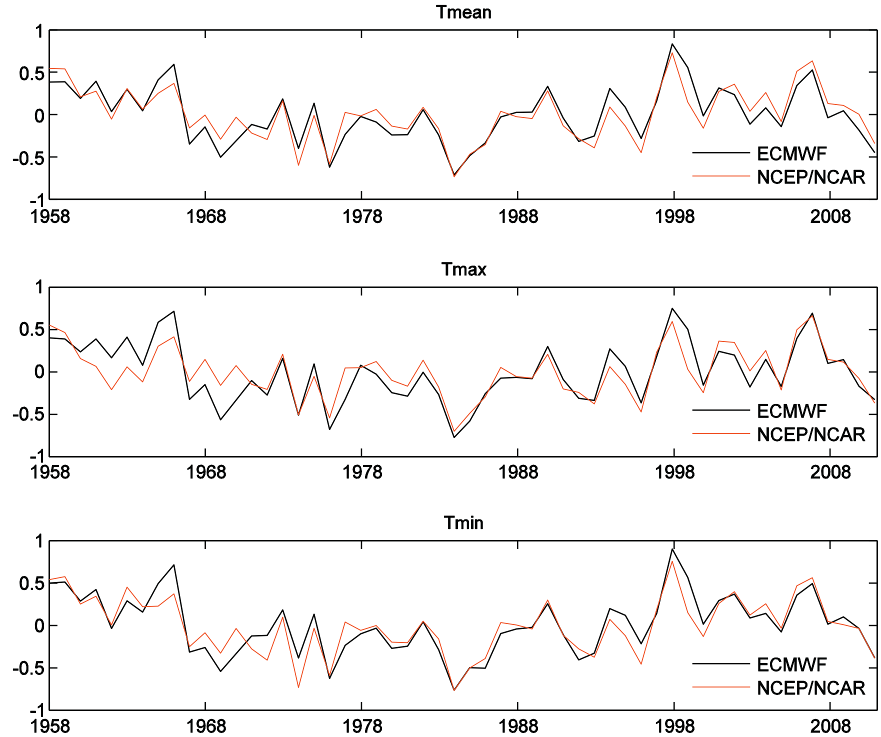

Fig. 7. Anomalies of annual maximum, minimum and mean temperature from ECMWF and NCEP/NCAR in China during 1958–2011.

has been prolonged. Furthermore, the warming climate is always accompanied by changes in the mean and extreme climate, which have great impacts on the society and economy (Wang et al., 2012).

Whether the temperature extremes derived from reanalyses represent the real extreme change, it is unclear in previous studies. To assess the reanalysis, ten temperature indices derived from NCEP/NCAR and ECMWF reanalyses are compared with those from the observational stations during 1961–2003 (Table 4). The indices at each grid point are interpolated with the inverse distance weighting method for the 303 stations (Fig. 1), and the temperature extremes from stations are obtained from You et al. (2011). In comparison with the observational data, temperature extremes from NCEP/NCAR reanalysis have a small relative bias (<2%), and are positively correlated with the observations ($R > 0.4$) with the exception of DTR. In most temperature indices, the values of the root mean squared error are very low. For the temperature extremes from ECMWF reanalysis, the patterns are similar to those from NCEP/NCAR. In most temperature indices, the relative bias and the root mean squared error are relatively small while the correlation coefficients between observations and ECMWF reanalysis are positively high. Figs. 8 and 9 show the histogram of bootstrapped

Table 3
Trends of temperature during various studied periods based on the observational data in China.

Regions	Period	Variable	Trend	Reference
Eastern and central Tibetan Plateau	1961–2003	Monthly TX	0.18	Liu et al. (2006)
Eastern and central Tibetan Plateau	1961–2003	Monthly TN	0.41	Liu et al. (2006)
China	1951–1995	TX in spring	0.027	Zhai et al. (1999)
China	1951–1995	TX in summer	−0.006	Zhai et al. (1999)
China	1951–1995	TX in autumn	0	Zhai et al. (1999)
China	1951–1995	TX in winter	0.144	Zhai et al. (1999)
China	1951–1995	Annual mean TX	0.03	Zhai et al. (1999)
China	1951–1995	TN in spring	0.179	Zhai et al. (1999)
China	1951–1995	TN in summer	0.001	Zhai et al. (1999)
China	1951–1995	TN in autumn	0.153	Zhai et al. (1999)
China	1951–1995	TN in winter	0.417	Zhai et al. (1999)
China	1951–1995	Annual mean TN	0.175	Zhai et al. (1999)
Northeastern China	1951–1994	TG in winter	0.35	Wang and Gaffen (2001)
Northwestern China	1951–1994	TG in winter	0.31	Wang and Gaffen (2001)
China	1951–1994	TG in winter	0.23	Wang and Gaffen (2001)
China	1955–2000	TX in winter	0.265	Liu et al. (2004)
China	1955–2000	TX in spring	0.094	Liu et al. (2004)
China	1955–2000	TX in summer	0.054	Liu et al. (2004)
China	1955–2000	TX in autumn	0.095	Liu et al. (2004)
China	1955–2000	TN in winter	0.557	Liu et al. (2004)
China	1955–2000	TN in spring	0.296	Liu et al. (2004)
China	1955–2000	TN in summer	0.19	Liu et al. (2004)
China	1955–2000	TN in autumn	0.275	Liu et al. (2004)

Note: TX is the daily maximum temperature; TN is the daily minimum temperature; TG is daily mean temperature; The unit of trend is °C/decade.

Table 4
Comparison of temperature extreme based on observations and reanalysis in China during 1961–2003. The observational temperature indices derived from You et al. (2011). The unit of trend in each index is same as Table 1.

Index	Relative bias(%)	Correlation coefficients	Root mean squared error
NCEP/NCAR			
DTR	−0.52	−0.47	0.85
TN10	−0.04	0.77	0.31
TN90	0.23	0.97	0.43
TX10	−0.08	0.70	0.25
TX90	0.26	0.89	0.47
TNn	0.26	0.75	0.57
TNx	−0.11	0.89	0.40
TXn	1.55	0.86	1.23
TXx	−0.23	0.75	1.23
FD	0.33	0.66	5.22
ECMWF			
DTR	−0.34	0.70	0.55
TN10	−0.06	0.69	0.34
TN90	0.29	0.91	0.54
TX10	−0.05	0.67	0.25
TX90	0.26	0.89	0.47
TNn	0.16	0.84	0.36
TNx	−0.10	0.80	0.36
TXn	0.98	0.88	0.77
TXx	−0.17	0.84	0.91
FD	0.27	0.84	4.18

correlation coefficients between reanalyses and observations for the temperature indices. The histogram shows the variation of the correlation coefficient across all the bootstrap samples, indicating that the relationship between reanalyses and observations is not accidental. These comparisons with the observations suggest that the temperature indices from reanalysis can capture the variability of the observations, although there have differences of absolute values with observations and the discrepancies between two reanalysis are apparent in some indices such as duration indices. This is also suggested the discrepancies in temperature extremes between reanalysis and observations exist, although the annual maximum, minimum and mean temperature between NCEP/NCAR and ECMWF are consistent (Fig. 7).

The differences between the actual and model topography and scale issues between point measurements and grid cell average values should be one of the reasons accounting for the origin of these discrepancies between two reanalyses (Betts et al., 2003). On a global scale, linear trends computed during 1958–2011 are generally lower in ERA-40 and NCEP/NCAR compared with the climate research unit (CRU) data, but there are agreements to within about 10% for ERA-40 in the rate of warming of the terrestrial Northern Hemisphere since the late 1970s (Simmons et al., 2004). Due to improvements in technique of data assimilation schemes and physical parameterizations, surface temperature from ERA-40 has a better agreement with CRU than NCEP/NCAR (Simmons et al., 2004). The cold bias in reanalysis has been found in China, where the annual mean surface temperature from ERA-40 and NCEP/NCAR are lower than the observations by −0.93 °C and −2.78 °C, respectively, primarily contributed by the negative differences in the western China (Ma et al., 2008). In general, surface air temperature from ERA-40 better represents observed air temperatures in China than NCEP/NCAR does (Ma et al., 2008). For a varied study period, underestimation of ERA-40 temperature is generally less than 1 °C in the eastern China and greater than 12 °C in the western China (Su et al., 1999; Zhao and Fu, 2006; Zhao et al., 2008). In the Tibetan Plateau, topographical differences between grid points and observations, and other reanalysis model differences such as surface land schemes, cause differences in trend identification and patterns for both NCEP/NCAR and ERA-40 reanalysis (You et al., 2010). After calibrating of altitude effects in reanalysis, Zhao et al. (2008) found that the accuracy of surface temperature from reanalysis depends much on the attitudes of the original data and the increase of local elevation and topographical complexity can improve bias of temperature for reanalysis. Thus, the discrepancies in temperature extremes between two reanalysis and observations come from the discrepancies in the assimilation systems in two reanalyses, which

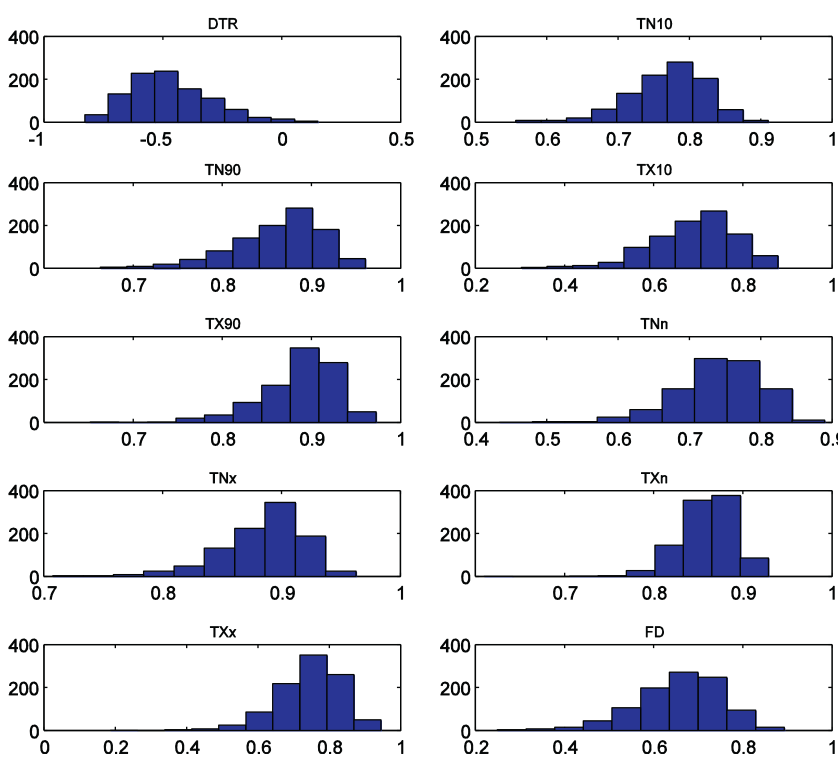

Fig. 8. Histogram of bootstrapping a correlation coefficient between NCEP/NCAR and observations for the temperature indices. Both NCEP/NCAR and observations are resampled to create 1000 different datasets, and the correlation between them is computed for each dataset.

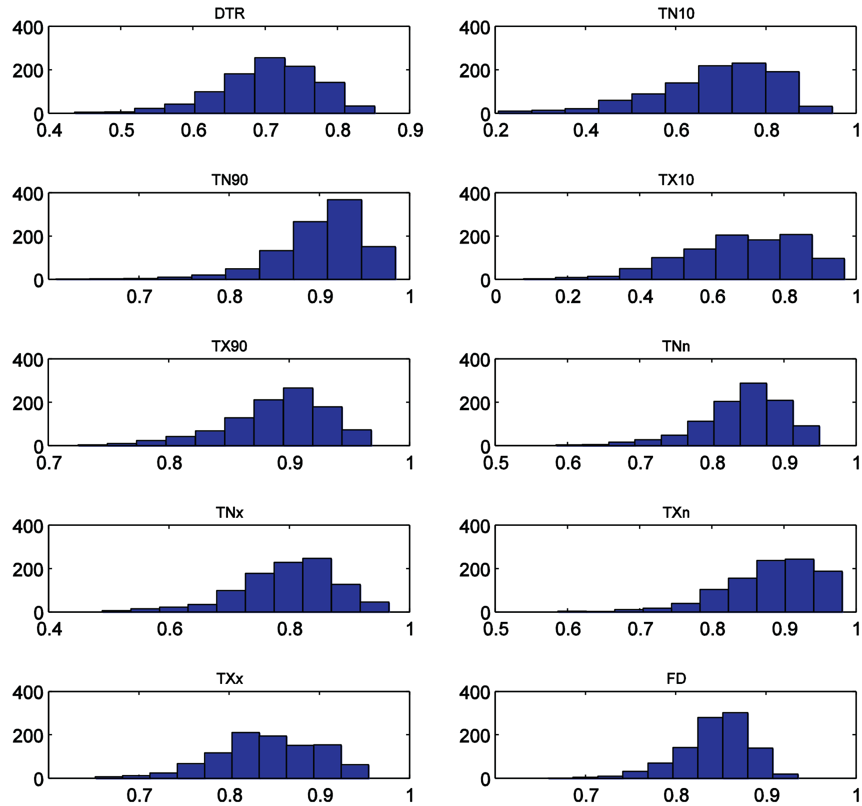

Fig. 9. Same as Fig. 8, but for ECMWF.

should be acknowledged as the reanalyses are considered to calculate the climate extremes.

Acknowledgments

This study is supported by the National Natural Science Foundation of China (41201072 and 41375015). This study is also funded by the Ministry of Science and Technology of China (Grand No. GYHY201206012) and "the Priority Academic Program Development of Jiangsu Higher Education Institutions" (PAPD). QY and KF acknowledge support of the Max Planck Fellowship. We are very grateful to the reviewers for their constructive comments and thoughtful suggestions.

References

Aguilar, E., et al., 2005. Changes in precipitation and temperature extremes in Central America and northern South America, 1961–2003. J. Geophys. Res.-Atmos. 110, D23107.
Aguilar, E., et al., 2009. Changes in temperature and precipitation extremes in western central Africa, Guinea Conakry, and Zimbabwe, 1955–2006. J. Geophys. Res.-Atmos. 114, D02115.
Alexander, L.V., et al., 2006. Global observed changes in daily climate extremes of temperature and precipitation. J. Geophys. Res.-Atmos. 111, D05109.
Bengtsson, L., Hagemann, S., Hodges, K.I., 2004. Can climate trends be calculated from reanalysis data? J. Geophys. Res.-Atmos. 109 (D11), D11111.
Betts, A.K., Ball, J.H., Viterbo, P., 2003. Evaluation of the ERA-40 surface water budget and surface temperature for the Mackenzie River basin. J. Hydrometeorol. 4 (6), 1194–1211.
Dee, D.P., Uppala, S., 2009. Variational bias correction of satellite radiance data in the ERA-Interim reanalysis. Q. J. R. Meteorol. Soc. 135 (644), 1830–1841.
Dee, D.P., et al., 2011. The ERA-Interim reanalysis: configuration and performance of the data assimilation system. Q. J. R. Meteorol. Soc. 137 (656), 553–597.
Douglas, E.M., Vogel, R.M., Kroll, C.N., 2000. Trends in floods and low flows in the United States: impact of spatial correlation. J. Hydrol. 240, 90–105.
Easterling, D.R., et al., 1997. Maximum and minimum temperature trends for the globe. Science 277 (5324), 364–367.
Frauenfeld, O.W., Zhang, T.J., Serreze, M.C., 2005. Climate change and variability using European Centre for Medium-Range Weather Forecasts reanalysis (ERA-40) temperatures on the Tibetan Plateau. J. Geophys. Res.-Atmos. 110, D02101.
Huang, G., 2006. The assessment and difference of the interdecadal variations of climate change in northern part of China with the NCEP/NCAR and ERA-40 reanalysis data. Clim. Environ. Res. 11 (3), 310–320 (in Chinese with English abstract).
IPCC, 2007. Summary for policymakers of climate change 2007: the physical science basis. Contribution of Working Group I to the Fourth Assessment Report of the Intergovernmental Panel on Climate Change. Cambridge University Press, Cambridge, UK.
Kalnay, E., et al., 1996. The NCEP/NCAR 40-year reanalysis project. Bull. Am. Meteorol. Soc. 77 (3), 437–471.
Kang, S.C., Xu, Y.W., You, Q.L., Flugel, W.A., Pepin, N., Yao, T.D., 2010. Review of climate and cryospheric change in the Tibetan Plateau. Environ. Res. Lett. 5 (1), 015101.
Kistler, R., et al., 2001. The NCEP-NCAR 50-year reanalysis: monthly means CD-ROM and documentation. Bull. Am. Meteorol. Soc. 82 (2), 247–267.
Liu, B.H., Xu, M., Henderson, M., Qi, Y., Li, Y.Q., 2004. Taking China's temperature: daily range, warming trends, and regional variations, 1955–2000. J. Clim. 17 (22), 4453–4462.
Liu, X.D., Yin, Z.Y., Shao, X.M., Qin, N.S., 2006. Temporal trends and variability of daily maximum and minimum, extreme temperature events, and growing season length over the eastern and central Tibetan Plateau during 1961–2003. J. Geophys. Res.-Atmos. 111 (D19), D19109.
Ma, L.J., Zhang, T.J., Li, Q.X., Frauenfeld, O.W., Qin, D.H., 2008. Evaluation of ERA-40, NCEP-1, and NCEP-2 reanalysis air temperatures with ground-based measurements in China. J. Geophys. Res.-Atmos. 113, D15115.
Ma, L.J., Zhang, T., Frauenfeld, O.W., Ye, B.S., Yang, D.Q., Qin, D.H., 2009. Evaluation of precipitation from the ERA-40, NCEP-1, and NCEP-2 reanalyses and CMAP-1, CMAP-2, and GPCP-2 with ground-based measurements in China. J. Geophys. Res.-Atmos. 114, D09105.
New, M., et al., 2006. Evidence of trends in daily climate extremes over southern and west Africa. J. Geophys. Res.-Atmos. 111, D14102.
Peterson, T.C., Manton, M.J., 2008. Monitoring changes in climate extremes — a tale of international collaboration. Bull. Am. Meteorol. Soc. 89 (9), 1266–1271.
Peterson, T.C., et al., 2002. Recent changes in climate extremes in the Caribbean region. J. Geophys. Res.-Atmos. 107, D07113.
Peterson, T.C., Zhang, X.B., Brunet-India, M., Vazquez-Aguirre, J.L., 2008. Changes in North American extremes derived from daily weather data. J. Geophys. Res.-Atmos. 113 (D7), D07113.
Sen, P.K., 1968. Estimates of regression coefficient based on Kendall's tau. J. Am. Stat. Assoc. 63, 1379–1389.
Simmons, A.J., Jones, P.D., Bechtold, V.D., Beljaars, A.C.M., Kallberg, P.W., Saarinen, S., Uppala, S.M., Viterbo, P., Wedi, N., 2004. Comparison of trends and low-frequency variability in CRU, ERA-40, and NCEP/NCAR analyses of surface air temperature. J. Geophys. Res.-Atmos. 109, D24115.
Su, Z.X., Lu, S.H., Luo, S.W., 1999. The examinations and analysis of NCEP/NCAR 40 years global reanalysis data in China. Plateau Meteorol. 18 (2), 209–218 (in Chinese with English abstract).

Uppala, S.M., et al., 2005. The ERA-40 re-analysis. Q. J. R. Meteorol. Soc. 131 (612), 2961–3012.
Ventura, V., Paciorek, C.J., Risbey, J.S., 2004. Controlling the proportion of falsely rejected hypotheses when conducting multiple tests with climatological data. J. Clim. 17 (22), 4343–4356.
Wang, J.X.L., Gaffen, D.J., 2001. Late-twentieth-century climatology and trends of surface humidity and temperature in China. J. Clim. 14 (13), 2833–2845.
Wang, S.W., Gong, D.Y., 2000. Enhancement of the warming trend in China. Geophys. Res. Lett. 27 (16), 2581–2584.
Wang, H.J., Sun, J.Q., Chen, H.P., Zhu, Y.L., Zhang, Y., Jiang, D.B., Lang, X.M., Fan, K., Yu, E.T., Yang, S., 2012. Extreme climate in China: facts, simulation and projection. Meteorol. Z. 21 (3), 279–304.
Wei, L., Li, D.L., 2003. Reliability of NCEP/NCAR reanalysis data in climatic change along Tibet railway. Plateau Meteorol. 22 (5), 488–494 (in Chinese with English abstract).
Wilks, D., 2006. On “field significance” and the false discovery rate. J. Appl. Meteorol. Climatol. 45 (9), 1181–1189.
Xie, A.H., Qin, D.H., Ren, J.R., Qing, X., Kang, S.C., Jiang, Y.Y., 2007. Reliability of NCEP/NCAR reanalysis data on Mount Qomolangma and Western Nyainqentanglha range. Acta Geograph. Sin. 62 (3), 268–278 (in Chinese with English abstract).
Xu, Y., Ding, Y.H., Zhao, Z.C., 2001. Confidence analysis of NCEP/NCAR 50-year global reanalyzed data in climate change research in China. Q. J. Appl. Meteorol. 12 (3), 337–347 (in Chinese with English abstract).
You, Q.L., Kang, S.C., Aguilar, E., Yan, Y.P., 2008. Changes in daily climate extremes in the eastern and central Tibetan Plateau during 1961–2005. J. Geophys. Res.-Atmos. 113, D07101.
You, Q.L., Kang, S.C., Li, C.L., Zhang, Q.G., Li, M.S., Liu, J.S., 2009. Reliability of NCEP/NCAR reanalysis data in the lake and glacier area in the Nam Co Basin. Meteorol. Mon. 35 (5), 66–73 (in Chinese with English abstract).
You, Q.L., Kang, S.C., Pepin, N., Flugel, W.A., Yan, Y.P., Behrawan, H., Huang, J., 2010. Relationship between temperature trend magnitude, elevation and mean temperature in the Tibetan Plateau from homogenized surface stations and reanalysis data. Glob. Planet. Chang. 71 (1–2), 124–133.
You, Q.L., Kang, S.C., Aguilar, E., Pepin, N., Flugel, W.A., Yan, Y.P., 2011. Changes in daily climate extremes in China and their connection to the large scale atmospheric circulation during 1961–2003. Clim. Dyn. 36, 2399–2417.
You, Q.L., Fraedrich, K., Ren, G.Y., Nicholls, N., Kang, S.C., 2013. Variability of temperature in the Tibetan Plateau based on homogenized surface stations and reanalysis data. Int. J. Climatol 33 (6), 1337–1347. http://dx.doi.org/10.1002/joc.3512.
Zhai, P.M., Sun, A.J., Ren, F.M., Liu, X.N., Gao, B., Zhang, Q., 1999. Chances of climate extremes in China. Clim. Chang. 42 (1), 203–218.
Zhang, Q., Qian, Y.F., 1999. Monthly mean surface albedo estimated from NCEP/NCAR reanalysis radiation data. Acta Geograph. Sin. 54 (4), 309–317 (in Chinese with English abstract).
Zhang, X.B., et al., 2005. Trends in Middle East climate extreme indices from 1950 to 2003. J. Geophys. Res.-Atmos. 110, D22104.
Zhang, X.B., Alexander, L., Hegerl, G.C., Jones, P., Tank, A.K., Peterson, T., Trewin, B., Zwiers, F., 2011. Indices for monitoring changes in extremes based on daily temperature and precipitation data. Wiley Interdiscip. Rev. Clim. Chang. 2, 851–870.
Zhang, Q., Kornich, H., Holmgren, K., 2012. How well do reanalyses represent the southern African precipitation? Clim. Dyn. http://dx.doi.org/10.1007/s00382-012-1423-z.
Zhao, T., Fu, C., 2006. Comparison of products from ERA-40, NCEP-2, and CRU with station data for summer precipitation over China. Adv. Atmos. Sci. 23 (4), 593–604.
Zhao, P., Zhou, Z.J., Liu, J.P., 2007. Variability of Tibetan spring snow and its associations with the hemispheric extratropical circulation and East Asian summer monsoon rainfall: an observational investigation. J. Clim. 20 (15), 3942–3955.
Zhao, T., Guo, W., Fu, C., 2008. Calibrating and evaluating reanalysis surface temperature error by topographic correction. J. Clim. 21 (6), 1440–1446.

INTERNATIONAL JOURNAL OF CLIMATOLOGY
Int. J. Climatol. (2013)
Published online in Wiley Online Library
(wileyonlinelibrary.com) DOI: 10.1002/joc.3852

Comparison of NCEP/NCAR and ERA-40 total cloud cover with surface observations over the Tibetan Plateau

Qinglong You,[a*] Yang Jiao,[a] Houbo Lin,[a] Jinzhong Min,[a] Shichang Kang,[b,c] Guoyu Ren[d] and Xianhong Meng[e]

[a] *Key Laboratory of Meteorological Disaster, Ministry of Education, Nanjing University of Information Science and Technology, Nanjing, China*
[b] *State Key Laboratory of Cryospheric Science, Chinese Academy of Sciences (CAS), Lanzhou, China*
[c] *Laboratory of Tibetan Environment Changes and Land Surface Processes, Institute of Tibetan Plateau Research, CAS, Beijing, China*
[d] *Laboratory for Climate Studies, National Climate Center, China Meteorological Administration (CMA), Beijing, China*
[e] *Key laboratory of land surface process and climate change in cold and arid regions, CAS, Lanzhou, China*

ABSTRACT: The annual and seasonal total cloud cover (TCC) variations in the eastern and central Tibetan Plateau (TP) during 1961–2005 are analysed using 71 surface observational stations. The mean TCC decreases from the southeastern to the northwestern TP, consistent with the patterns of atmospheric moisture in the region. The annual mean TCC shows a significant decreasing trend of -0.09 percent decade^{-1}, mainly contributed by winter. About 65% of the stations show significant downward trends on the annual basis with large trend magnitudes occurring in the central TP. The seasonal patterns confirm the annual patterns in most cases. Compared with the surface observations, both National Center for Environmental Prediction/National Center for Atmospheric Research reanalysis (NCEP/NCAR) (1961–2005) and ERA-40 (1961–2001) can reproduce the decreasing TCC trends. The shift of TCC before and after the mid-1980s is obvious in observations and both reanalyses, reflecting the changes of large-scale atmospheric circulation. However, NCEP/NCAR underestimates and ERA-40 overestimates observations on the annual and seasonal basis, presumably caused by the different cloud parameterization schemes. A Taylor diagram diagnose summarizes the discrepancies between observations and reanalyses.

KEY WORDS total cloud cover; NCEP/NCAR and ERA-40; Tibetan Plateau

Received 23 August 2013; Revised 23 September 2013; Accepted 27 September 2013

1. Introduction

Clouds cover about 60% of the Earth's surface, and have great effects on climate change by producing precipitation, reflecting shortwave solar radiation coming from the sun and returning outgoing longwave radiation from the surface (IPCC, 2007). Clouds also act as a blanket similar to that of the greenhouse gases such as water vapour and carbon dioxide, and tend to warm the Earth's surface (IPCC, 2007). Clouds exert great effects on the Earth's radiation budget, and make an important contribution to the greenhouse effect (Wild *et al.*, 2004). There are still large uncertainties about the effects of clouds on climate, which not only depend on cloud height, thickness, horizontal extent and variety, water content, phase (liquid or ice), and the sizes of droplets and crystals, but also rely on the geographical location of the clouds, the albedo and temperature of the underlying surface, and the season of the year and time of day (Warren *et al.*, 2007; Sanchez-Lorenzo *et al.*, 2012).

It is appropriate to investigate the inter-annual variations and trends of clouds, and several studies have analysed clouds at the regional and global scales. Total cloud cover (TCC) shows an increasing trend in the United States during 1976–2004 (Dai *et al.*, 2006), Australia during 1957–2007 (non-significant) (Jovanovic *et al.*, 2011), the former Soviet Union during 1936–1990 (Sun and Groisman, 2000) and Russia during 1991–2010 (Chernokulsky *et al.*, 2011). In other regions and countries, the TCC has decreased including China during 1951–1994 (Kaiser, 1998, 2000), India during 1961–2007 (Jaswal, 2010), most of South Africa during 1960–2005 (Kruger, 2007), and Italy during 1951–1996 (Maugeri *et al.*, 2001). On the other hand, TCC varies from regions, and some parts have increasing trends whereas other regions have decreasing trends, such as Canada during 1953–2003 (Milewska, 2008), Poland during 1971–2000 (Filipiak and Mietus, 2009) as well as the Iberian Peninsula during 1982–2004 (Calbo and Sanchez-Lorenzo, 2009).

The Tibetan Plateau (TP) is the highest and most extensive highland in the world. It is called the 'third Pole', and the cryosphere and climate in the TP are undergoing significant changes caused by global climate

* Correspondence to: Q. You, Key Laboratory of Meteorological Disaster, Ministry of Education, Nanjing University of Information Science and Technology, Nanjing 210044, China. E-mail: yqingl@126.com

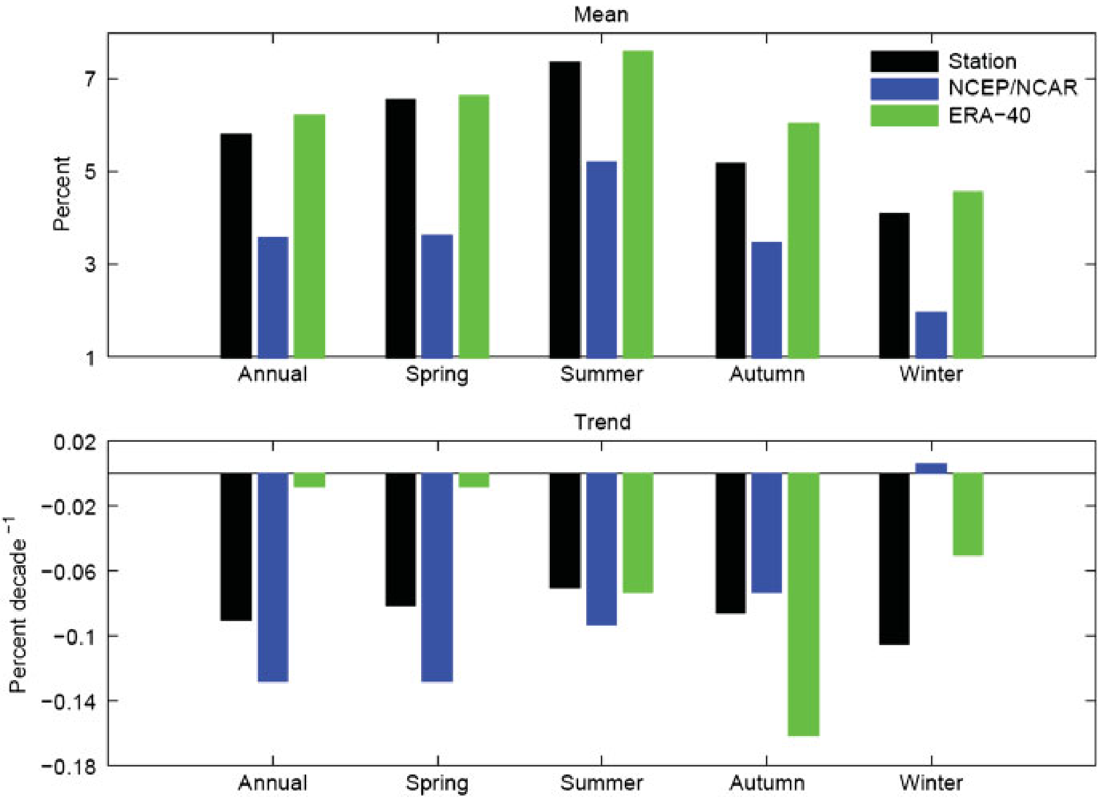

Figure 1. Annual and seasonal means and trends of total cloud cover in the Tibetan Plateau during the period of 1961–2005. The study period for ERA-40 is during 1961–2001.

change (Kang *et al.*, 2010). In the recent years, some meteorological elements in the TP have been investigated by the scientific community, such as extreme temperature changes (You *et al.*, 2008a, 2008b), precipitation (Xu *et al.*, 2008), wind speed (You *et al.*, 2010), surface energy budget in the permafrost (Yao *et al.*, 2011), and cloud (Duan and Wu, 2006). Duan and Wu (2006) found that the low level cloud amount exhibits an increasing trend during the night times, whereas the total and low level cloud amounts display decreasing trends during daytime in the TP during 1961–2003. However, the knowledge of the clouds is limited and largely based on the measurements. The remote sensing products such as ISSCP D2 and MODIS/TERRA have been applied to examine seasonal climatology of high, middle and low clouds in the TP and other regions (Kotarba, 2009; Li *et al.*, 2006; Naud and Chen, 2010). But the evaluations of TCC between observations and reanalyses have not been analysed in detail. In this study, the annual and seasonal (winter: DJF; spring: MAM; summer: JJA; autumn: SON) characteristics of TCC in the eastern and central TP during 1961–2005 are investigated based on the surface observational and reanalyses datasets. Two reanalyses are selected: the National Center for Environmental Prediction/National Center for Atmospheric Research reanalysis (NCEP/NCAR) (Kalnay *et al.*, 1996; Kistler *et al.*, 2001) and the European Centre for Medium-Range Weather Forecasts (ECMWF) reanalysis (ERA-40) (Uppala *et al.*, 2005).

2. Data and methods

Monthly surface TCC data for 71 stations in the TP are provided by the National Meteorological Information Center, China Meteorological Administration (NMIC/CMA). The daily TCC (0–10 tenths of sky cover) is the average of every six hourly observation at the standard synoptic times: 00:00 (midnight), 06:00 (dawn), 12:00 (noon) and 18:00 (dark) at Lhasa Time. The monthly TCC is calculated as daily means averaged four time values. Seventy-one stations were selected according to procedures described in our recent papers (You *et al.*, 2008a, 2008b). Most stations are situated in the eastern and central TP and were installed in 1950s. The elevations of these stations are 2000 m above sea level (a.s.l.) ranging from 2109.5 to 4700 m a.s.l. In order to obtain comparable time series with reanalysis, we selected the data only during 1961–2005 for analysis.

Monthly mean surface TCC from NCEP/NCAR reanalysis is provided by the NOAA/OAR/ESRL PSD, Boulder, CO, USA, from their website at http://www.cdc.noaa.gov/. It covers January 1948 to the present and contains T62 Gaussian grid (192 × 94 points), covering 88.542°N–88.542°S and 0°E–358.125°E (Kalnay *et al.*, 1996; Kistler *et al.*, 2001). It was derived from an empirical relative humidity–cloud cover relationship based on short-range predictions with the operational version of the model (Kalnay *et al.*, 1996; Kistler *et al.*, 2001). The monthly mean surface TCC from ERA-40 reanalysis is obtained from the ECMWF website

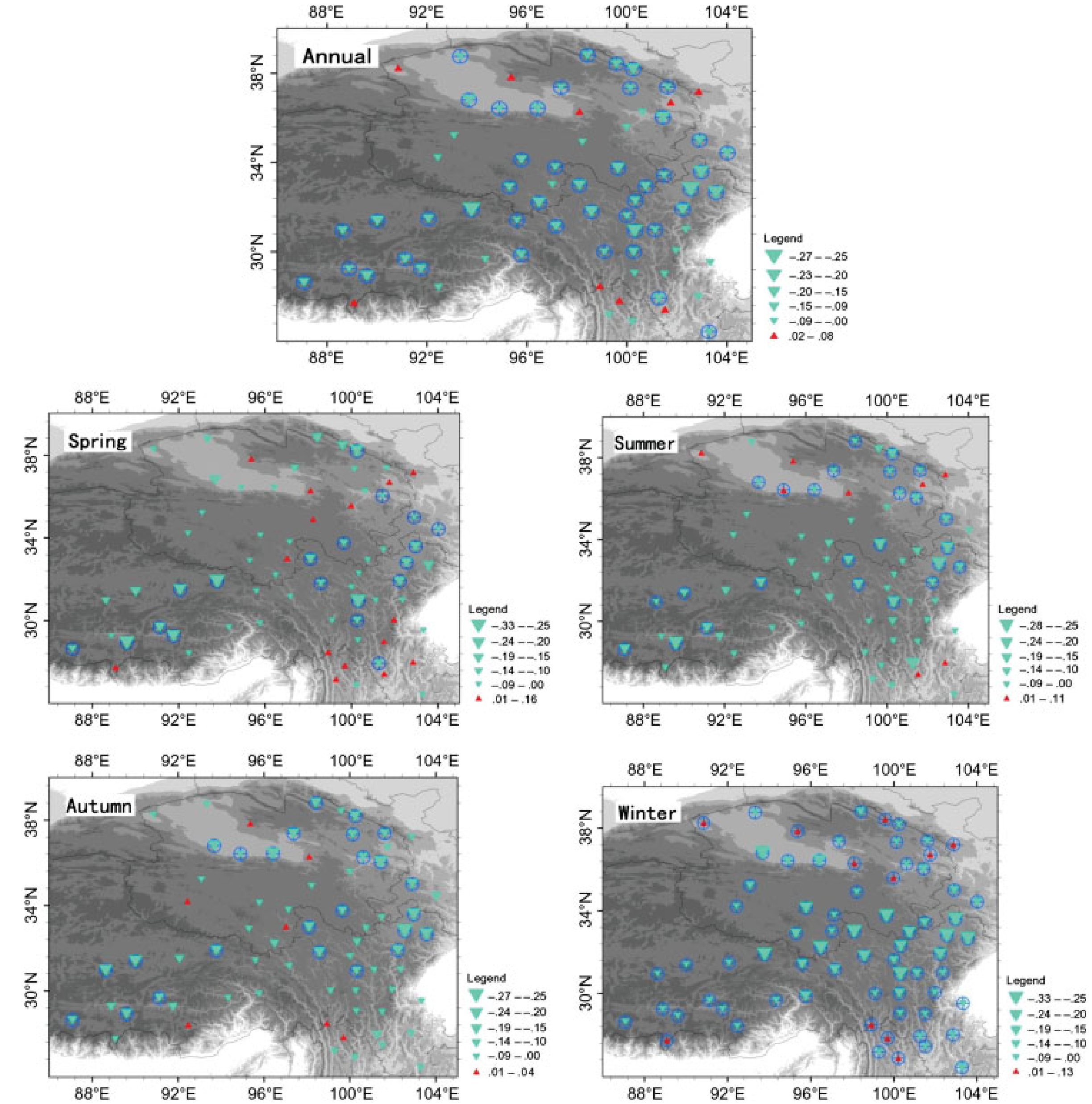

Figure 2. Spatial patterns of trends of annual and seasonal total cloud cover from 71 surface stations in the Tibetan Plateau during 1961–2005. Positive trends are shown as upward triangle, negative trends as downward triangle. The size of the triangle is proportional to the magnitude of the trends. The trends are calculated by the Mann–Kendal methods and trends with the significant level are marked. The unit is percent per decade.

(http://www.ecmwf.int/). ERA-40 reanalysis is available from September 1957 to August 2002 with a spatial resolution of $2.5^{\circ} \times 2.5^{\circ}$ (144×73) (Uppala *et al.*, 2005). Previous studies show that the assimilation of satellite humidity data may affect the cloud data in the ERA-40, and this is clear in the tropics and oceans (Betts *et al.*, 2006b; Calbo and Sanchez-Lorenzo, 2009).

The grid datasets (NCEP/NCAR and ERA-40) have different spatial resolutions, and are interpolated to 2.5° horizontal resolution with linear interpolation for easy comparison. After that, grid points of TCC in each reanalysis are interpolated to the 71 observational stations. Periods of 1961–2005 (NCEP/NCAR) and 1961–2001 (ERA-40) are selected. The Mann–Kendall test for trends and Sen's slope estimates are used to detect and estimate trends in annual and seasonal TCC (Sen, 1968), with a significance level defined as $P < 0.05$.

3. Results and comparisons

3.1. TCC from surface station

The regional mean and trend of TCC in the TP on the annual and seasonal basis are shown in Figure 1. Figure 2 shows the spatial patterns of trends of annual and seasonal TCC of the 71 surface stations in the TP during 1961–2005. Positive trends are shown as upward triangle, negative trends as downward triangle. The trends

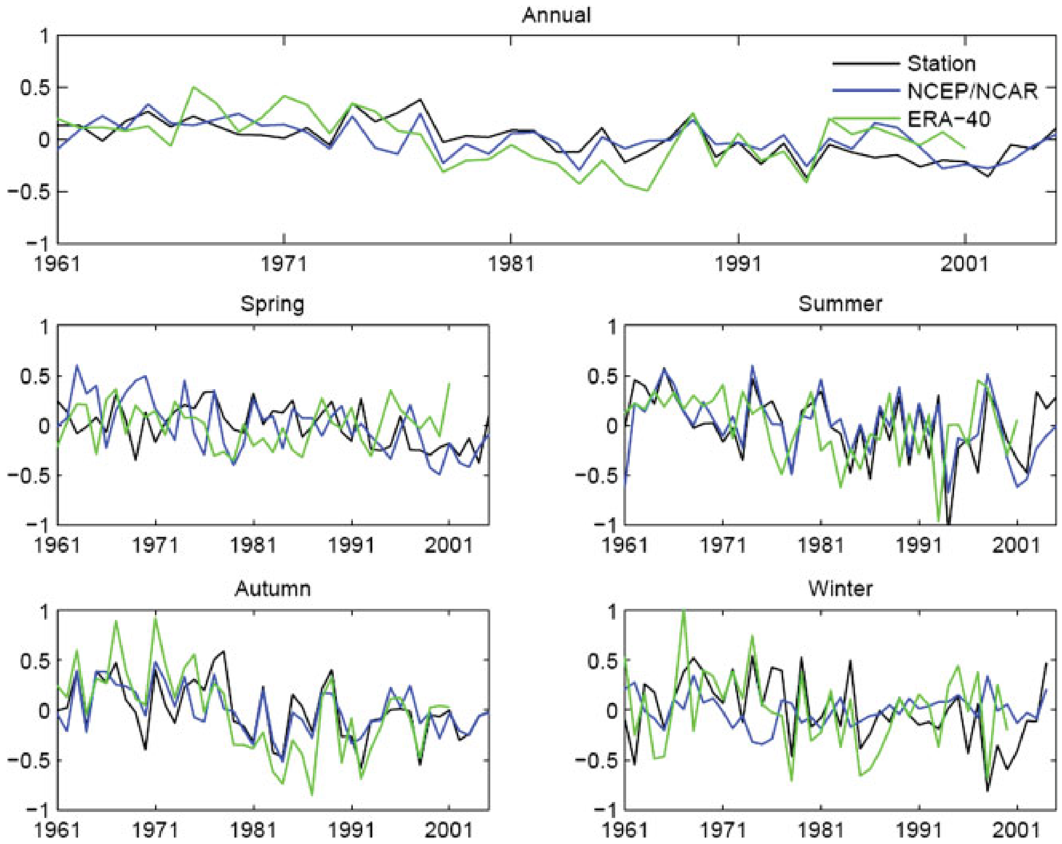

Figure 3. Total cloud cover anomalies from surface stations, NCEP/NCAR and ERA-40 on the annual and seasonal basis in the Tibetan Plateau during 1961–2005.

are calculated by the Mann–Kendal method and those significant ones are marked by circles. The regional anomalies of annual and seasonal mean TCC averaged from 71 surface stations in the TP during 1961–2005 are shown in Figure 3.

Averaging the 71 series available in the TP, the annual mean TCC is 5.81%, with a mean maximum value in summer (7.36%) and a mean minimum value in winter (4.11%). TCC gradually decreases from the southeastern to the northwestern TP with the largest value occurring in the southeastern TP (not shown). This is consistent with the previous studies based on observations during 1971–2004 (Zhang *et al.*, 2008) and International Satellite Cloud Climatology Project C2 dataset (ISCCP-C2) (Wang *et al.*, 2001).

On the annual basis, the mean TCC series in the TP shows a fluctuation before the 1970s and a decreasing trend after that until the 2000s, followed by a statistically significant increasing trend afterwards. Thus, the mean TCC exhibits a significant decreasing trend during 1961–2005 with a rate of −0.090 percent decade^{-1} ($P < 0.05$) (Figure 1). Sixty-two stations have negative trends for TCC, with 46 stations being significant. Stations in the central TP have larger trend magnitudes, while there are still nine stations that have increasing trends in the northern TP. On a seasonal basis, the largest negative trend of TCC is found in winter (−0.104 percent decade^{-1}). The trends for spring, summer, and autumn are −0.081, −0.07, and −0.086 percent decade^{-1}, respectively, and all seasons are statistically significant. Similar to the annual basis, the majority of the stations show a significant decrease, and the patterns of trends are similar to the annual values (Figure 2). Discrepancies on the variation of seasonal TCC trends occur in the central TP with a significant decrease in winter, whereas less pronounced in spring (Zhang *et al.*, 2008).

3.2. TCC from reanalysis data

To compare the TCC variation in the TP with observations, both NCEP/NCAR and ERA-40 reanalysis are derived and interpolated to the 71 stations. Both mean values and trend magnitudes of TCC from NCEP/NCAR and ERA-40 are presented in Figure 1 on the annual and seasonal basis, and the regional anomalies are shown in Figure 3. The spatial patterns of means and trends based on two reanalyses are shown in Figures 4 and 5.

For NCEP/NCAR, the annual mean TCC of 3.57% varies between 2 and 5%, and decreases from the southeastern to the northwestern TP (Figure 4). The pattern of annual mean TCC is similar to observations, but the absolute values are lower in most regions. The annual TCC has a decreasing trend before the 1980s and tends to fluctuate afterwards, with the annual trend of −0.067 percent decade^{-1} during 1961–2005. The decreasing/increasing trend occurs in the southern/northern TP. On the seasonal basis, the largest/smallest mean TCC occurs in

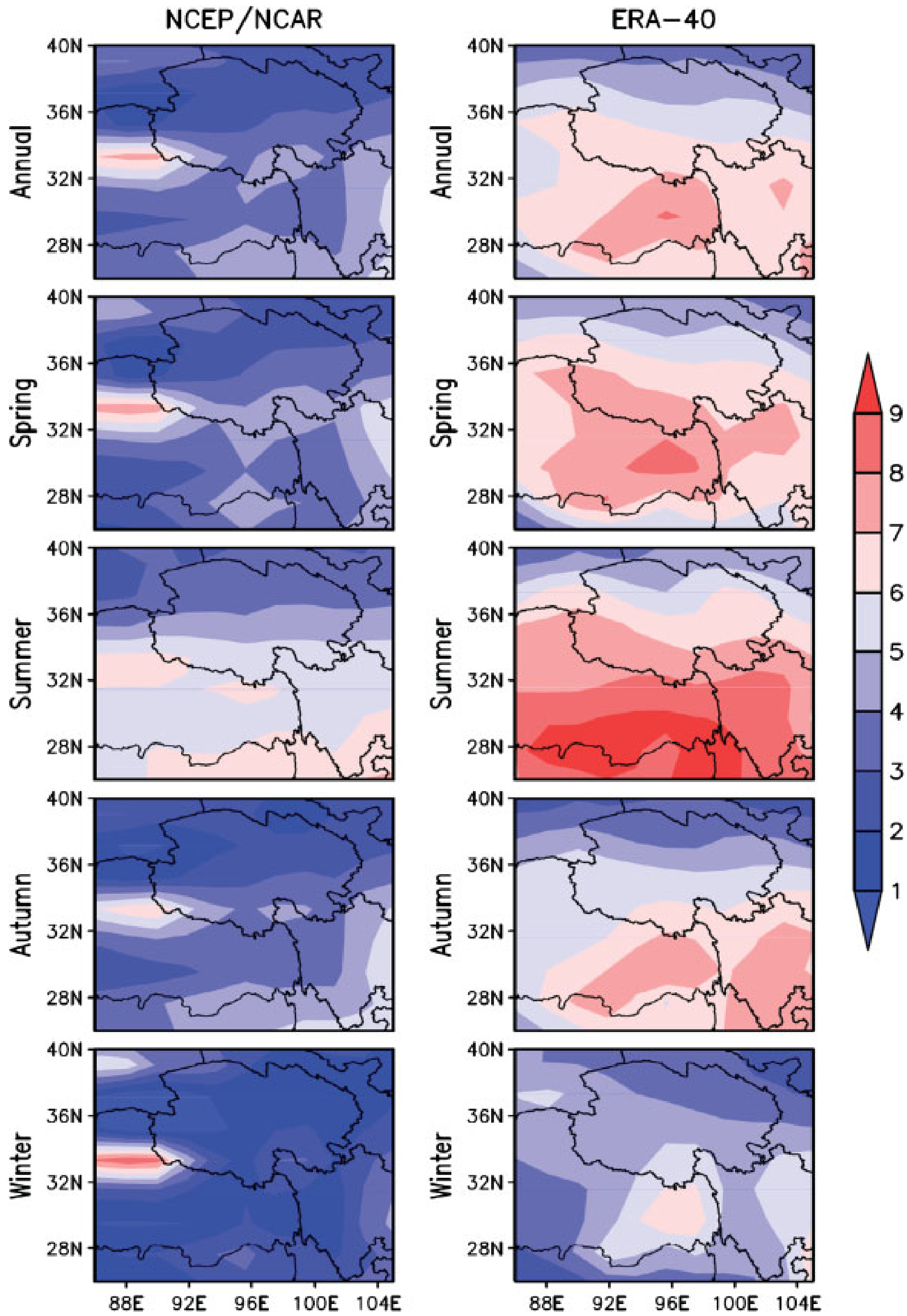

Figure 4. Spatial patterns of mean total cloud cover from NCEP/NCAR during 1961–2005 and ERA-40 reanalysis during 1961–2001 in the Tibetan Plateau on the annual and seasonal basis. The unit is percent.

summer/winter, with the mean values of 5.21 and 1.96%, respectively, consistent with observations. Mean TCC in both spring and autumn is about 3.5%. All seasons with the exception of winter have negative trends, with the largest trend magnitude in spring (−0.128 percent decade^{-1}). The TCC in winter has increased during 1961–2005, profoundly in the northern region, with a mean value of 0.006 percent decade^{-1} (Figure 5).

For ERA-40, the annual mean TCC (6.21%) is larger than the observed mean. The annual mean TCC ranges from 3 to 8%, and larger/smaller mean values occur in the southern/northern TP (Figure 4). Similar to NCEP/NCAR, the annual mean TCC from ERA-40 decreases before the mid-1980s and fluctuates afterwards, leading to a negative trend of −0.085 percent decade^{-1} during 1961–2001. The decreasing trend in the south-eastern TP such as the Sichuan basin is very clear, whereas the western TP has increasing trends. On the seasonal basis, the largest/smallest mean TCC occurs in summer/winter, with the mean values of 7.59 and 4.57%, respectively, which is in accordance with observations and NCEP/NCAR. Mean TCC in spring (6.65%) is

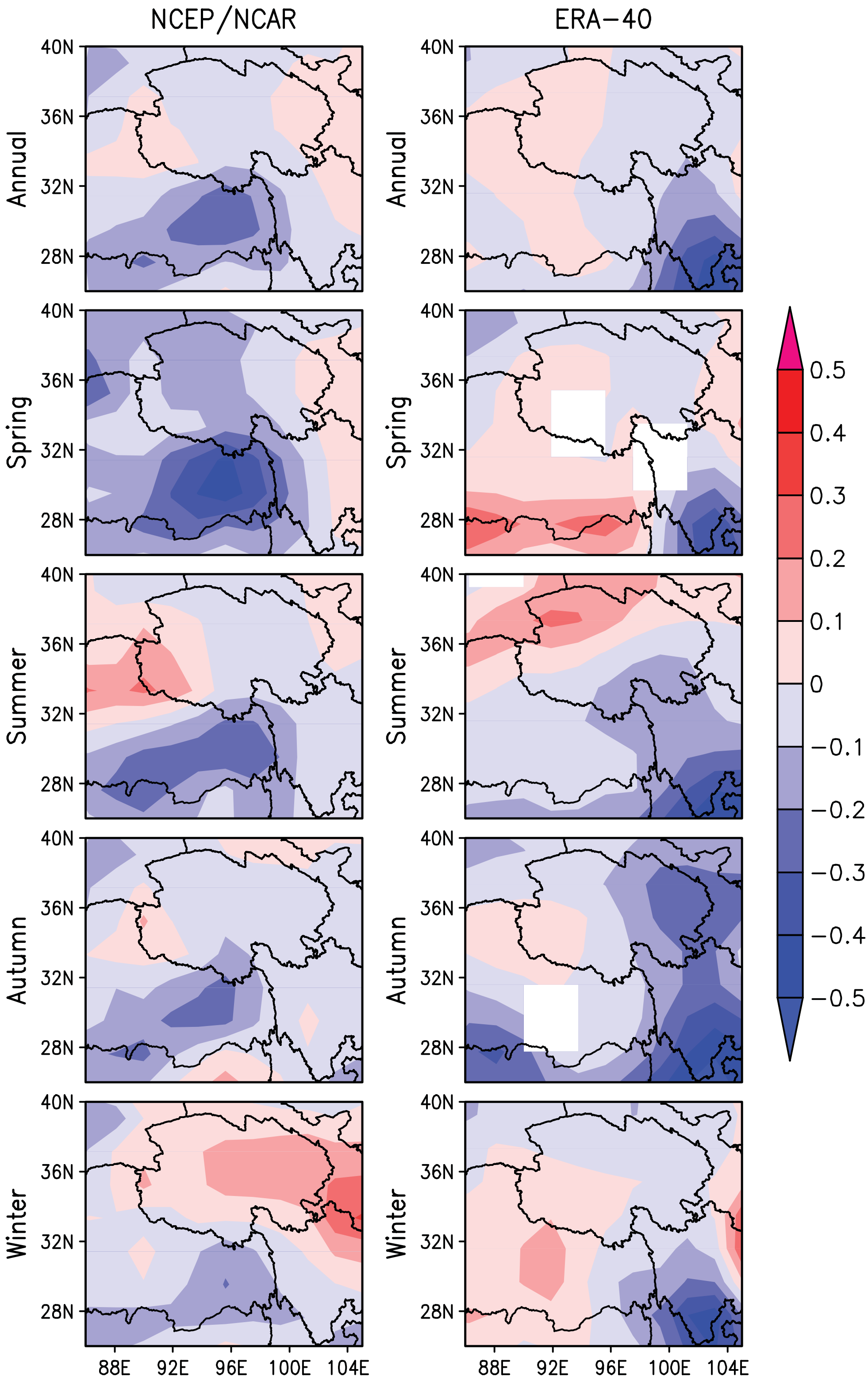

Figure 5. Spatial patterns of trends of annual and seasonal total cloud cover from NCEP/NCAR during 1961–2005 and ERA-40 reanalysis during 1961–2001 in the Tibetan Plateau. The blank area in the ERA-40 means the missing data. The unit is percent per century.

slightly larger than that in autumn (6.03%). TCC of four seasons has decreasing trends, with the largest magnitude in autumn (-0.161 percent decade^{-1}). The trends of TCC in spring, summer, and winter are -0.008, -0.093, and -0.05 percent decade^{-1}, respectively.

3.3. Comparison TCC between observations and reanalyses

To evaluate the TCC from observations, NCEP/NCAR and ERA-40 reanalyses are interpolated to the stations. A Taylor diagram is considered for observations and

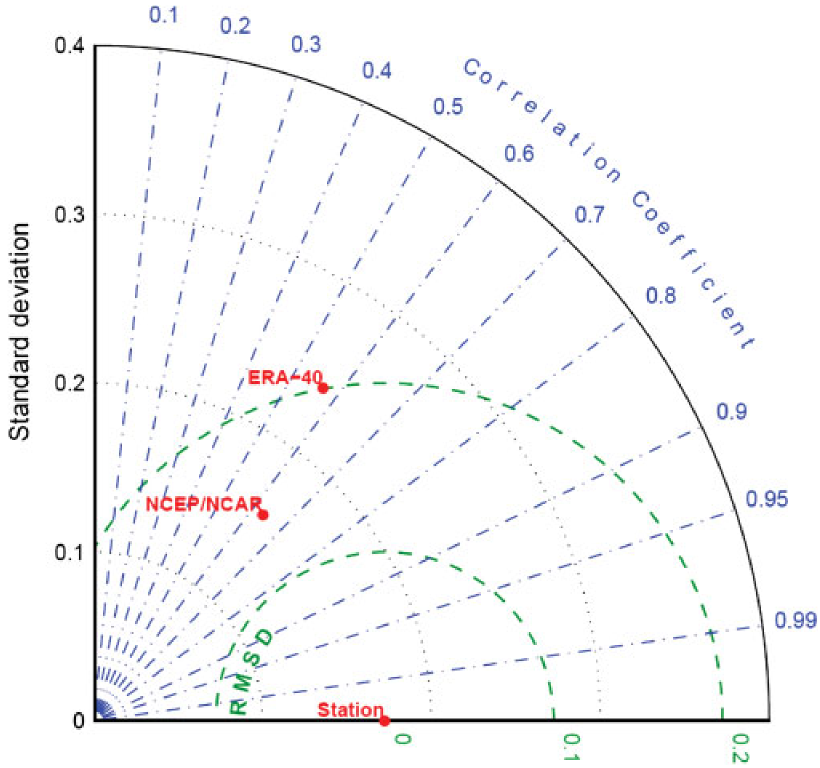

Figure 6. Taylor diagrams showing correlation coefficients, standard deviation, and RMSD of total cloud cover between the surface stations, NCEP/NCAR, and ERA-40 on the annual basis. The radial coordinate is the magnitude of standard deviation, and the concentric semi-circles are the RMSD values. Meanwhile, the angular coordinate shows the correlation coefficient.

reanalyses, which provides a concise statistical summary of how well patterns match each other in terms of their correlation, root mean square difference (RMSD), and the ratio of their variances (Taylor, 2001). Figure 6 shows the correlation coefficients, standard deviation, and the RMSD of TCC between observations, NCEP/NCAR and ERA-40 on the annual basis. The radial coordinate represents the magnitude of standard deviation, the concentric semi-circles are the RMSD values, and the angular coordinate shows the correlation coefficient.

On the annual basis, the mean TCC from observations has positive correlations with NCEP/NCAR and ERA-40 reanalyses, with the correlation coefficients of 0.64 and 0.56, respectively. Taylor diagram analysis reveals that NCEP/NCAR has the lowest standard deviation and smallest root mean square error (RMSE), and captures observations better than ERA-40. For the biases between observations and reanalyses, Taylor diagram has not been used as the visual comparison as reflected in Figure 1. Overall, ERA-40 slightly overestimates observations and NCEP/NCAR underestimates observations on the annual and seasonal basis, while TCC from both reanalyses is in good agreement with the inter-annual variations of observations in the TP.

4. Discussion and conclusions

In this study, the spatial and temporal variations of TCC are analysed based on 71 stations in the eastern and central TP during 1961–2005. In most stations, TCC in the TP has significantly decreasing trends on the annual and seasonal basis (winter: DJF; spring: MAM; summer: JJA; autumn: SON), and a pronounced decrease occurs in winter and autumn. The decreasing TCC was closely connected with recent warming in the TP (Kang *et al.*, 2010). During 1961–2003, TCC and low cloud cover at daytime has decreasing trends in the TP, resulting in more solar radiation and more surface warming. Meanwhile, decreasing TCC and increasing low cloud cover at nighttime also contribute to the nocturnal surface warming (Duan and Wu, 2006).

The mean TCC decreasing from the southeastern to the northwestern TP is controlled by the essential conditions for the formation of clouds, such as water vapour and its condensation (Zhang *et al.*, 2008). Under the influence of the monsoon more water vapour, transported from the ocean and forced to rise, is intercepted by complex topography, which supports conditions to condense from moisture to droplets and cause more clouds in the southern TP. With the weakening of the monsoon and the blocking by topography, less water vapour reaches the northern part, causing fewer clouds in the hinterland TP (not shown).

The decreasing TCC in the TP is in accordance with other studies, such as eastern China (Kaiser, 1998, 2000), India (Jaswal, 2010), South Africa (Kruger, 2007), and Italy (Maugeri *et al.*, 2001). During 1951–1994, most stations in central, eastern and northeastern China show statistically significant decreases of 1–3% sky cover per decade (Kaiser, 1998, 2000). In the previous studies, Zhang *et al.* (2008) concluded that there are two factors accounting for the decreasing TCC in the TP. Firstly, the direct effect of aerosols can be a factor causing for the decreasing TCC. As aerosols can cool the Earth's surface by reflecting sunlight and warm the aerosol layer by absorbing downward longwave radiation, the lapse rate will decrease and atmospheric stability will increase, suppressing cloud formation and reducing the cloudiness (Dai *et al.*, 1997; IPCC, 2007). The TP is regarded as a region with clear atmospheric conditions, and the aerosol amount is sparse (Li *et al.*, 2007; Kang *et al.*, 2010), and can present a clean continental background for the atmospheric composition investigation, such as Nam Co region (Cong *et al.*, 2009). Thus, how the aerosols influence the TCC requires more attention. Secondly, ozone depletion should be another reason for the decreasing TCC in the TP. Previous studies have shown that the ozone depletion in the stratosphere in the TP is confirmed (Zou, 1996; Zhou and Zhang, 2005), which will change the variation of temperature in the middle and upper stratosphere, thus affecting the change of both middle and high level cloud amount. Besides that, cyclonic activity can alter the variations of clouds (Calbo and Sanchez-Lorenzo, 2009). In summary, the mechanism contributing to the decreasing in the TP is unknown and uncertain at present (Zhang *et al.*, 2008).

Both TCC from NCEP/NCAR and ERA-40 are derived to compare with observations and analyse the variability. In the model parameterizations of NCEP/NCAR, a diagnostic cloud scheme has been assimilated, and some tunings of the cloudiness and cloud optical properties have been performed to correct systematic cloudiness errors (Kalnay *et al.*, 1996; Kistler *et al.*, 2001). Meanwhile, a neural-network algorithm (Krasnopolsky *et al.*, 1995) was applied to assimilate SSM/I data after 1987 to improve the clouds (Kalnay *et al.*, 1996; Kistler *et al.*, 2001). Although diagnostic cloud parameterization is made, TCC from NCEP/NCAR underestimates observations on the annual and seasonal basis. ERA-40 assimilation model employs a two-time level semi-Lagrangian advection scheme and a finite element scheme for its vertical discretization, which include improvements of the parameterizations of clouds (Uppala *et al.*, 2005). TCC from ERA-40 overestimates observations on the annual and seasonal basis. This is consistent with the studies in the Iberian Peninsula, especially in its eastern regions where ERA-40 underestimates the clouds due to its underestimation of cyclogenesis in the Mediterranean (Calbo and Sanchez-Lorenzo, 2009). However, the reasons for underestimation of TCC from ERA-40 in the TP need further investigation. Both ERA-40 and NCEP/NCAR reanalyses use their own codes, meteorological profiles, and model fields to compute clouds (Betts *et al.*, 2006a), and there exist discrepancies and uncertainties with observations (Ernst *et al.*, 2007).

Acknowledgements

This study is supported by the National Natural Science Foundation of China (41201072 and 41375015). This study is also funded by the Ministry of Science and Technology of China (Grand No. GYHY201206012) and 'the Priority Academic Program Development of Jiangsu Higher Education Institutions' (PAPD). We are very grateful to the reviewers for their constructive comments and thoughtful suggestions.

References

Betts AK, Zhao M, Dirmeyer PA, Beljaars ACM. 2006a. Comparison of ERA40 and NCEP/DOE near-surface data sets with other ISLSCP-II data sets. *J. Geophys. Res.-Atmos.* **111**: D22S04.

Betts AK, Zhao M, Dirmeyer PA, Beljaars ACM. 2006b. Comparison of ERA40 and NCEP/DOE near-surface data sets with other ISLSCP-II data sets. *J. Geophys. Res.-Atmos.* **111**(D22): D22S04.

Calbo J, Sanchez-Lorenzo A. 2009. Cloudiness climatology in the Iberian Peninsula from three global gridded datasets (ISCCP, CRU TS 2.1, ERA-40). *Theor. Appl. Climatol.* **96**: 105–115.

Chernokulsky AV, Bulygina ON, Mokhov II. 2011. Recent variations of cloudiness over Russia from surface daytime observations. *Environ. Res. Lett.* **6**(3): 035202.

Cong Z, Kang S, Smirnov A, Holben B. 2009. Aerosol optical properties at Nam Co: a remote site in central Tibetan Plateau. *Atmos. Res.* **92**(1): 42–48.

Dai A, DelGenio AD, Fung IY. 1997. Clouds, precipitation and temperature range. *Nature* **386**(6626): 665–666.

Dai A, Karl TR, Sun B, Trenberth KE. 2006. Recent trends in cloudiness over the United States – a tale of monitoring inadequacies. *Bull. Am. Meteorol. Soc.* **87**(5): 597–606.

Duan AM, Wu GX. 2006. Change of cloud amount and the climate warming on the Tibetan Plateau. *Geophys. Res. Lett.* **33**(22): L22704.

Ernst B, Sergey KG, Macke A. 2007. Intercomparison of global cloud cover fields over oceans from the VOS observations and NCEP/NCAR reanalysis. *Int. J. Climatol.* **27**(13): 1707–1719.

Filipiak J, Mietus M. 2009. Spatial and temporal variability of cloudiness in Poland, 1971–2000. *Int. J. Climatol.* **29**(9): 1294–1311.

IPCC. 2007. Summary for Policymakers of Climate change 2007: the physical science basis. In *Contribution of Working Group I to the Fourth Assessment Report of the Intergovernmental Panel on Climate Change*. Cambridge University Press: Cambridge, UK.

Jaswal AK. 2010. Changes in total cloud cover over India based upon 1961–2007 surface observations. *Mausam* **61**(4): 455–468.

Jovanovic B, Collins D, Braganza K, Jakob D, Jones DA. 2011. A high-quality monthly total cloud amount dataset for Australia. *Clim. Change* **108**(3): 485–517.

Kaiser DP. 1998. Analysis of total cloud amount over China, 1951–1994. *Geophys. Res. Lett.* **25**(19): 3599–3602.

Kaiser DP. 2000. Decreasing cloudiness over China: an updated analysis examining additional variables. *Geophys. Res. Lett.* **27**(15): 2193–2196.

Kalnay E, Kanamitsu M, Kistler R, Collins W, Deaven D, Gandin L, Iredell M. 1996. The NCEP/NCAR 40-year reanalysis project. *Bull. Am. Meteorol. Soc.* **77**(3): 437–471.

Kang SC, Xu YW, You QL, Flugel WA, Pepin N, Yao TD. 2010. Review of climate and cryospheric change in the Tibetan Plateau. *Environ. Res. Lett.* **5**(1): 015101.

Kistler R, Collins W, Saha S, White G, Woollen J, Kalnay E. 2001. The NCEP-NCAR 50-year reanalysis: monthly means CD-ROM and documentation. *Bull. Am. Meteorol. Soc.* **82**(2): 247–267.

Kotarba AZ. 2009. A comparison of MODIS-derived cloud amount with visual surface observations. *Atmos. Res.* **92**(4): 522–530.

Krasnopolsky VM, Breaker LC, Gemmill WH. 1995. A neural network as a nonlinear transfer function model for retrieving surface wind speeds from the special sensor microwave imager. *J. Geophys. Res.-Oceans* **100**(C6): 11033–11045.

Kruger AC. 2007. Trends in cloud cover from 1960 to 2005 over South Africa. *Water SA* **33**(5): 603–608.

Li Y, Liu X, Chen B. 2006. Cloud type climatology over the Tibetan Plateau: a comparison of ISCCP and MODIS/TERRA measurements with surface observations. *Geophys. Res. Lett.* **33**: L17716.

Li C, Kang S, Zhang Q, Kaspari S. 2007. Major ionic composition of precipitation in the Nam Co region, Central Tibetan Plateau. *Atmos. Res.* **85**(3–4): 351–360.

Maugeri M, Bagnati Z, Brunetti M, Nanni T. 2001. Trends in Italian total cloud amount, 1951–1996. *Geophys. Res. Lett.* **28**(24): 4551–4554.

Milewska EJ. 2008. Cloud type observations and trends in Canada, 1953–2003. *Atmosphere–Ocean* **46**(3): 297–316.

Naud CM, Chen Y-H. 2010. Assessment of ISCCP cloudiness over the Tibetan Plateau using CloudSat-CALIPSO. *J. Geophys. Res.-Atmos.* **115**: D10203.

Sanchez-Lorenzo A, Calbo J, Wild M. 2012. Increasing cloud cover in the 20th century: review and new findings in Spain. *Climate Past* **8**(4): 1199–1212.

Sen PK. 1968. Estimates of regression coefficient based on Kendall's tau. *J. Am. Stat. Assoc.* **63**: 1379–1389.

Sun BM, Groisman PY. 2000. Cloudiness variations over the former Soviet Union. *Int. J. Climatol.* **20**(10): 1097–1111.

Taylor KE. 2001. Summarizing multiple aspects of model performance in a single diagram. *J. Geophys. Res. Atmos.* **106**(D7): 7183–7192.

Uppala SM, Kållberg PW, Simmon AJ, Andrae U, Bechtold V, Fiorino M. 2005. The ERA-40 re-analysis. *Q. J. Roy. Meteorol. Soc.* **131**(612): 2961–3012.

Wang KL, Hao J, Chen SQ. 2001. Cloud cover over Qinghai-Xizang Plateau: comparison among meteorological station observations, ISCCP-C2, and NCEP reanalysis data. *Plateau Meteor.* **20**(3): 252–257 (in Chinese with English abstract).

Warren SG, Eastman RM, Hahn CJ. 2007. A survey of changes in cloud cover and cloud types over land from surface observations, 1971–96. *J. Climate* **20**(4): 717–738.

Wild M, Ohmura A, Gilgen H, Rosenfeld D. 2004. On the consistency of trends in radiation and temperature records and implications for the global hydrological cycle. *Geophys. Res. Lett.* **31**(11): L11201.

Xu ZX, Gong TL, Li JY. 2008. Decadal trend of climate in the Tibetan Plateau – regional temperature and precipitation. *Hydrol. Processes* **22**(16): 3056–3065.

Yao J, Zhao L, Gu L, Qiao Y, Jiao K. 2011. The surface energy budget in the permafrost region of the Tibetan Plateau. *Atmos. Res.* **102**(4): 394–407.

You QL, Kang SC, Pepin N, Yan YP. 2008a. Relationship between trends in temperature extremes and elevation in the eastern and central Tibetan Plateau, 1961–2005. *Geophys. Res. Lett.* **35**(4): L04704.

You QL, Kang SC, Aguilar E, Yan YP. 2008b. Changes in daily climate extremes in the eastern and central Tibetan Plateau during 1961–2005. *J. Geophys. Res.-Atmos.* **113**(D7): D07101.

You QL, Kang SC, Flugel WA, Pepin N, Yan YP, Huang J. 2010. Decreasing wind speed and weakening latitudinal surface pressure gradients in the Tibetan Plateau. *Climate Res.* **42**(1): 57–64.

Zhang XQ, Peng LL, Zheng D, Tao J. 2008. Cloudiness variations over the Qinghai-Tibet Plateau during 1971–2004. *J. Geogr. Sci.* **18**: 142–154.

Zhou SW, Zhang RH. 2005. Decadal variations of temperature and geopotential height over the Tibetan Plateau and their relations with Tibet ozone depletion. *Geophys. Res. Lett.* **32**(18): L18705.

Zou H. 1996. Seasonal variation and trends of TOMS ozone over Tibet. *Geophys. Res. Lett.* **23**(9): 1029–1032.

Clim Dyn (2013) 40:2073–2086
DOI 10.1007/s00382-012-1383-3

Decadal variation of surface solar radiation in the Tibetan Plateau from observations, reanalysis and model simulations

Qinglong You · Arturo Sanchez-Lorenzo · Martin Wild · Doris Folini · Klaus Fraedrich · Guoyu Ren · Shichang Kang

Received: 4 February 2012 / Accepted: 23 April 2012 / Published online: 9 May 2012

Abstract In this study, the annual and seasonal variations of all-sky and clear-sky surface solar radiation (SSR) in the eastern and central Tibetan Plateau (TP) during the period 1960–2009 are investigated, based on surface observational data, reanalyses and ensemble simulations with the global climate model ECHAM5-HAM. The mean annual all-sky SSR series shows a decreasing trend with a rate of -1.00 Wm^{-2} decade^{-1}, which is mainly seen in autumn and secondly in summer and winter. A stronger decrease of -2.80 Wm^{-2} decade^{-1} is found in the mean annual clear-sky SSR series, especially during winter and autumn. Overall, these results confirm a tendency towards a decrease of SSR in the TP during the last five decades. The comparisons with reanalysis show that both NCEP/NCAR and ERA-40 reanalyses do not capture the decadal variations of the all-sky and clear-sky SSR. This is probably due to a missing consideration of aerosols in the reanalysis assimilation model. The SSR simulated with the ECHAM5-HAM global climate model under both all-sky and clear-sky conditions reproduce the decrease seen in the surface observations, especially after 1980. The steadily increasing aerosol optical depth (AOD) at 550 nm over the TP in the ECHAM5-HAM results suggests transient aerosol emissions as a plausible cause.

Keywords Surface solar radiation · NCEP/NCAR · ERA-40 · ECHAM5-HAM · Tibetan Plateau

Q. You (✉) · S. Kang
Laboratory of Tibetan Environment Changes and Land Surface Processes, Institute of Tibetan Plateau Research, Chinese Academy of Sciences (CAS), Beijing 100085, China
e-mail: yqingl@126.com

Q. You · K. Fraedrich
Meteorological Institute, University of Hamburg, KlimaCampus, 21044 Hamburg, Germany

Q. You · G. Ren
Laboratory for Climate Studies, National Climate Center, China Meteorological Administration (CMA), Beijing 100081, China

A. Sanchez-Lorenzo · M. Wild · D. Folini
Institute for Atmospheric and Climate Science, ETH Zurich, Zurich, Switzerland
e-mail: arturo.sanchez@env.ethz.ch

M. Wild
e-mail: martin.wild@env.ethz.ch

D. Folini
e-mail: doris.folini@env.ethz.ch

S. Kang
State Key Laboratory of Cryospheric Science, Chinese Academy of Sciences (CAS), Lanzhou 730000, China

1 Introduction

Variations in solar radiation at the Earth's surface (or surface solar radiation, SSR), profoundly affect the human and terrestrial environment, which for example has significant implications for the intensity of the hydrological cycle, the carbon cycle, the cryosphere, and consequently for climate change scenarios. In recent decades, a decrease in SSR (also known as "global dimming") of about 7 Wm^{-2} was observed worldwide from the 1960s to 1980s at land stations and this topic has been widely studied (e.g. Gilgen et al. 1998; Liepert 2002; Stanhill and Cohen 2001; Qian et al. 2006, 2007; Kaiser and Qian 2002). More recent studies showed that the declining SSR faded during the 1980s, with an increase until the end of the twentieth century (also known as "brightening") (Wild et al. 2005). The SSR records suggest a continuation of the brightening after 2,000 at numerous stations in Europe and the United States, although with a renewed decrease in some developing countries such as China or India (Wild et al. 2009). For a complete review of the subject see Wild (2009). In China, several studies have focused in the analysis of the SSR series, including their spatial and temporal patterns (e.g. Cha 1996; Li et al. 1998; Qian et al. 2006), data quality assessment (e.g. Shi et al. 2008; Tang et al. 2010), and causes of the observed changes (e.g. Xia et al. 2006; Qian et al. 2007).

The Tibetan Plateau (TP) with an average elevation of over 4,000 m a.s.l. and an area of approximately 2.5×10^6 km^2, is the highest and most extensive highland in the world. It has the largest area of snow and ice in the mid-latitudes and serves as "the world water tower" (Xu et al. 2008). The TP acts as water storage tower for South and East Asia, releasing melt water to the Indus, Ganges, Brahmaputra, and other river systems (Barnett et al. 2005; Immerzeel et al. 2010). However, the climate and cryosphere in the TP are undergoing rapid change (Kang et al. 2010), as seen in a significant warming or a weakening of wind speed (e.g. You et al. 2008a, b, 2010a, c). In a previous paper, the temporal variability of sunshine duration series in the TP has been analyzed (You et al. 2010b), and a significant decrease is shown since the 1980s. However, a systematic assessment of the long-term trends of all-sky and clear-sky SSR using surface observations, reanalyses and climate simulations over the TP is still lacking.

In this study, the annual and seasonal variations of SSR in the TP during the period 1960–2009 are investigated based on the available surface observational data as well as two reanalysis products. To better understand the variations in SSR and its causes in the TP, results of simulations performed with the global climate model ECHAM5-HAM are also analyzed.

2 Data and methods

2.1 Surface dataset

Daily SSR data from stations in the TP are provided by the National Meteorological Information Center, China Meteorological Administration (NMIC/CMA). The Chinese SSR dataset contains 20 stations within the domain of 26°–40°N and 73°–105°E, a window that covers the main area of the TP in China. Five stations (Kashi, Mianyang, Lijiang, Pazhihua, Emeishan) are excluded because their locations are away from the actual boundary of TP. At the same time, five stations with measurements starting in the 1990s are also not considered. The remaining 10 stations are selected for the homogenisation step. Table 1 shows the details of the SSR stations used in this study, with their World Meteorological Organization (WMO) number, name, longitude, latitude, elevation and missing data during the 1960–2009 period. The SSR measurement network in China began in 1957 in the framework of the 1957–1958 International Geophysical Year (Shi et al. 2008), and most of the stations initiated systematic SSR measurements after 1960. Consequently, this study covers the period from 1960 to 2009.

Shi et al. (2008) pioneered the systematic assessment of data quality of 122 SSR observations in China during 1957–2000. Tang et al. (2010) categorized the errors related to SSR measurements in China into two classes: one is caused by equipment errors and uncertainty, the other is due to operation-related problems and errors. The CMA performed some quality checks on the SSR data, which are affected by several factors such as accuracy and modification of instruments, artificial factors and location change. Shi et al. (2008) explained the calibration procedure in China: (1) calibration at least once per month at the stations against the reference instruments; (2) calibration of the reference radiometers against the regional reference instruments; (3) calibration of the regional reference instruments every 2 year against the Chinese reference instruments.

The homogenization of a dataset is a necessary step before trends can be calculated because erroneous data can seriously impact the trends. The homogeneity assessment and adjustment can be a complex process which often requires close neighbour stations and detailed station history, because inhomogeneities can be caused, for example, by changes in instrumentation, station relocations or changes in the local environment such as urbanization (Vincent et al. 2005). For the SSR dataset in the TP, a possible inhomogeneity due to changes in the instrumentation occurred in the early 1990s, when pyranometers were systematically replaced in the Chinese network. As summarized by Shi et al. (2008), before the early 1990s the instruments used to measure SSR were identical to the ones used in the former Soviet Union, named Yanishevsky thermoelectric pyranometer. Afterwards, the DFY-4 pyranometers manufactured in China were used to measure SSR. Unfortunately, no information about the exact year of change at each station is available to our knowledge. In fact, Shi et al. (2008) suggest a change in the pyranometers in the early 1990s, whereas Tang et al. (2011) assume this change in 1994 for all stations in China. Nevertheless, the former study (Shi et al. 2008) does not assume a systematic bias in the series as a consequence of the change (although a possible effect is not completely rejected). On the other hand, the latter study (Tang et al. 2011) suggests that a strong inhomogeneity occurred in all SSR series in 1994, assuming that the measurements before these years were non-reliable in China. Although their conclusion cannot be ruled out entirely, it seems implausible that this instrument change occurred at all Chinese stations at the same time. Equally, a change in the pyranometers cannot be considered as a cause of inhomogeneity per se, especially because

Table 1 Details of the 10 selected stations in the Tibetan Plateau, including the World Meteorological Organization (WMO) code, station name, latitude, longitude, elevation, and starting year of the SSR series, and data missing during the period 1960–2009

Code	Station	Lat. (N)	Lon. (E)	Alt. (m)	Starting year
51777	**Ruoqiang**	39.02	88.10	888	1957
51828	**Hetian**	37.08	79.56	1374	1957
52681	Minqin	38.38	103.05	1367	1961
52818	**Germu**	36.25	94.54	2807	1957
52866	Xining	36.43	101.45	2295	1959
55228	Geer	32.3	80.05	4278	1971
55299	Naqu	31.29	92.04	4507	1961
55591	Lhasa	29.4	91.08	3649	1961
56029	Yushu	33.01	97.01	3681	1960
56137	**Changdu**	31.09	97.1	3306	1961

The names of the 4 homogeneous SSR series are highlighted in bold

the estimated errors in SSR measurements for both types of instruments are similar (Shi et al. 2008). Further evidence for a non-common break due to the instrumental change in the Chinese SSR series during the early 1990s is shown by Wang et al. (2011, Fig. 3), where the mean seasonal SSR series in different regions of China suggest that a strong increase in the early 1990s can only be seen clearly in the mean series of the TP and South China (Wang et al. 2011), but not in the mean series of the other regions in China. Consequently, a widespread inhomogeneity of the SSR measurements in China during the period before 1992 cannot be assumed as a plausible phenomenon.

In the present study, the homogeneity of each of the 10 SSR series was checked by means of the Standard Normal Homogeneity Test (SNHT) (Alexandersson and Moberg 1997). Our procedure rejects the priori existence of homogenous reference series and consists of testing each of the 10 series against the other series. Note that in the homogenization produce some stations in the surroundings of the TP have been used (e.g. the Emeishan series that has been excluded from the SSR dataset as previously detailed), as they are highly correlated with some of the 10 selected series. When a break is identified in one series (test series), the series used to estimate the adjustments, which were calculated on a monthly basis, is chosen among the highest correlated series that prove to be homogeneous. The results confirm that 5 (Xining, Geer, Naqu, Lhasa and Yushu) of the 10 series (i.e. 50 % of the series) show evidence of inhomogeneities in the early 1990s, most of them clearly as a result of low values during the preceding 5–10 years, as has been previously pointed out by Shi et al. (2008). Another statistical inhomogeneity was detected in Minqin during the mid-1970s. The remaining 4 series (Ruoqiang, Hetian, Germu, Changdu) proved to be homogeneous (see Table 1). These 4 series have been used as reference series in order to estimate the corrections of the breaks identified in the inhomogeneous series. After the homogenization, all gaps were filled with monthly mean values for each station.

In order to study the trends under clear-sky SSR conditions, only the 4 stations considered as homogenous for all-sky SSR series are used (Sanchez-Lorenzo et al. 2009). Firstly, the daily mean total cloud cover records are obtained from the NMIC/CMA for these 4 series. Secondly, a day was defined as clear-sky if the daily mean total cloud cover is equal or less than 12.5 %. Finally, the clear-sky SSR monthly values for each station were obtained by averaging the SSR values of all clear-days available in each month.

2.2 NCEP/NCAR and ERA-40 reanalysis

In addition to the observed data, SSR fluxes as estimated by two reanalysis products are used in this study, i.e. the reanalysis from the National Centers for Environmental Prediction/National Center for Atmospheric Research (NCEP/NCAR) (Kalnay et al. 1996) and the reanalysis from the European Centre for Medium-Range Weather Forecasts (ECMWF) (ERA-40) (Uppala et al. 2005).

The NCEP/NCAR dataset covers the period from 1948 to present with a spatial resolution of 2.5° × 2.5° (Kalnay et al. 1996). Only data from 1960 to 2009 are analyzed in this study. The ERA-40 reanalysis is available from 1957 to mid-2002 with a spatial resolution of 2.5° × 2.5° (Uppala et al. 2005). Only data covering the 1960–2001 period are used in this study. As downward clear-sky SSR data is not directly available in ERA-40, we use net clear-sky SSR instead.

2.3 The ECHAM5-HAM model

The fourth data set we analyse are transient simulation data computed with the global climate model ECHAM5, developed at the Max Planck Institute of Meteorology (MPI), (Roeckner et al. 2003, 2006), coupled to the

Hamburg Aerosol Module (HAM) (Stier et al. 2006a) and equipped with detailed cloud microphysics (Lohmann et al. 2007). The ECHAM5-HAM is particularly well suited for the present study, as aerosol-cloud interactions are considered as a main factor in the explanation of the observed decadal variations in SSR (e.g. Ohmura 2009; Wild 2009).

In the present simulations, aerosol emissions are taken from the Japanese National Institute for Environmental Studies (NIES) (Roeckner et al. 2006; Stier et al. 2006b). Fossil fuel emissions of SO2, BC and OC are prescribed annually, while emissions from wild fires, agricultural burning and domestic fuel-wood consumption are prescribed monthly. Optical depths of volcanic aerosols in the stratosphere are prescribed on a monthly basis on six latitudinal bands. Total solar irradiance varies on an annual basis (Solanki and Krivova 2003). Monthly mean sea surface temperatures (SSTs) and sea ice concentrations (SICs) are taken from the Hadley Centre (Rayner et al. 2003). An ensemble of 13 experiments is performed at spectral resolution T42 (about 2.8 $\times$ 2.8 degrees), with 19 vertical levels from ground to 10 hPa, and covering the time period from 1870 to 2005. In recent studies, these simulation data have already been analysed on the global scale (Bichet et al. 2011) and for Europe (Folini and Wild 2011). Here, we look at the TP and focusing on the period 1960–2005.

3 Methods

Annual and seasonal series are computed from the monthly data previously described. In this study the seasons are defined as spring (MAM), summer (JJA), autumn (SON), and winter (DJF). The winter season was defined as the mean of the December of the year indicated and the January and February of the subsequent year.

Annual and seasonal anomalies, obtained as deviations from the 1971–2000 period, were calculated for each one of the 10 (4) series of observed all-sky (clear-sky) SSR. Mean series for the TP were computed as an arithmetic mean of these 10 (4) series for all-sky (clear-sky) SSR. The same approach has been applied for the reanalysis and ECHAM5-HAM simulations, but using the time series of the nearest grid point to the 10 (4) stations (see Fig. 1). Overall, the use of anomalies avoids the introduction of a bias in case of missing data and different absolute values, and the mean series enhances the signal-to-noise ratio, which permits a better identification of decadal trends than individual series.

The linear trends of all series in this paper were calculated by means of least squares linear fitting and their significance estimated by the Mann–Kendall nonparametric test (Sen 1968) at the 0.05 level of significance. In order to improve the visualization of the decadal variability, the mean time series are plotted together with their 17-year Gaussian low-pass filter (hereafter referred as 17GLPF), which only consider the values on one side at the start and end of the series in order to filter the full period of 1961–2009.

Finally, correlation analyses are used to compare the observed and simulated SSR series. All correlations are based on the mean time series smoothed with the 17GLPF in order to evaluate the agreement in the decadal variability rather than the interannual variations which are not deterministic in global climate models.

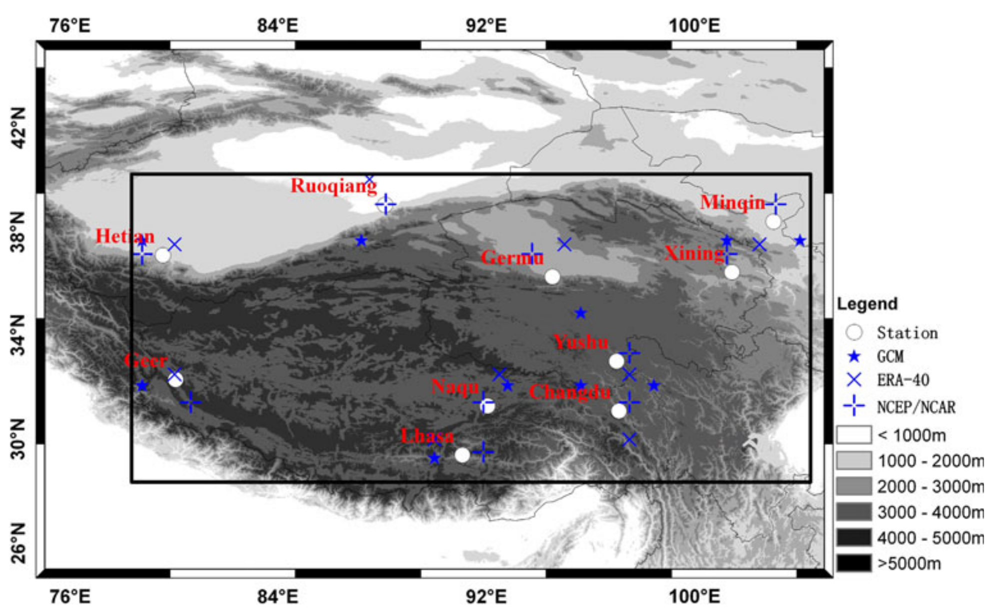

Fig. 1 Distribution of the 10 stations with SSR measurements and the corresponding nearest reanalysis and ECHAM-HAM grid points in the Tibetan Plateau

4 Results

4.1 Changes of all-sky and clear-sky SSR from observational data

The climatological means for all-sky SSR on annual and seasonal basis are summarized in Table 2. The annual mean all-sky SSR value, obtained by averaging the 10 series available in the TP, is 210.1 Wm^{-2}, with a clear maximum in summer (263.1 Wm^{-2}) and minimum in winter (143.4 Wm^{-2}).

Figure 2 shows the mean annual and seasonal all-sky SSR series in the TP during the period 1960–2009. The linear trends for the all-sky SSR series, calculated over the whole available period (1960–2009) and different subperiods, are summarized in Table 3. On the annual basis, the mean all-sky SSR series in the TP shows an increasing tendency before the 1970s, followed by a decrease during the 1970–1990 period. Subsequently, the series shows a new increase in the 1990s, followed by a strong decrease during the first decade of the new century. Totally, the all-sky SSR exhibits a significant decreasing trend for the whole study period with a rate of −1.00 Wm^{-2} decade^{-1}. Equally, both the 1960–1992 and 1993–2009 subperiods show a significant decrease of −1.68 and −5.48 Wm^{-2} decade^{-1}, respectively. The trends of these subperiods confirm a tendency towards a decrease before and after 1992, the year with the possible inhomogeneity remaining in the series due to the instrumentation change. On a seasonal basis, the results highlight a general decrease in all-sky SSR, with the highest rate of significant decrease found in autumn (−2.16 Wm^{-2} decade^{-1}), followed by summer (−1.26 Wm^{-2} decade^{-1}) and winter (−1.09 Wm^{-2} decade^{-1}), and a non-significant increase in spring (Table 3).

Figure 3 shows the mean annual and seasonal clear-sky SSR series in the TP during the studied period, based on the 4 homogeneous stations. Trends in clear-sky SSR for different subperiods are shown in Table 3. In contrast to all-sky SSR, the annual clear-sky SSR series starts with two decades without relevant variations, followed by a sharp decrease during 1982–1984. Afterwards, there is a slight recovery between mid-1980s and the beginning of 2000, only interrupted by another strong decrease during the 1991–1992, ending with a clear decrease during the final years. Regarding long-term trends over the 1961–2009 period, the clear-sky SSR annual series shows a significant decrease of −2.80 Wm^{-2} decade^{-1}, caused mainly by a decrease in winter (−4.45 Wm^{-2} decade^{-1}) and autumn (−3.78 Wm^{-2} decade^{-1}). The largest decreasing trend occurs in the subperiod of 1993–2009 (−11.40 Wm^{-2} decade^{-1}). In most cases, it becomes evident that the SSR trends under all-sky conditions are slightly smaller than under clear-sky conditions, both on annual and seasonal basis (Table 3).

Table 3 also contains the trends of the mean all-sky SSR series if only the 4 series used for the clear-sky analysis are considered. The results show a tendency toward larger linear trends with the subset of the 4 series, although the main features remain fundamentally unchanged. The strong spatial autocorrelation in the SSR series, as illustrated with the correlation of 0.87 between these smoothed annual all-sky SSR series, suggests a similar decadal variability when the 4 series rather than the 10 series are considered.

4.2 Changes of all-sky and clear-sky SSR from reanalysis data

For the NCEP/NCAR reanalysis, the climatological mean of all-sky SSR (Table 2) tends to be higher than the observational stations, with an annual value of 275.9 Wm^{-2} (bias of +31.3 % with respect to the observations), which is in line with the differences found by in the middle reaches of the Yangtze River (Xia et al. 2006). A similar overestimation is found throughout the seasons, with the largest bias in spring (+36.9 %). For the ERA-40, the climatological mean all-sky SSR (Table 2) is smaller than the NCEP/NCAR, and closer to the surface observations, with a slight positive bias (+0.6 %) on the annual basis, whereas an overestimation (underestimation) around 5–10 % is found in spring and winter (summer and autumn).

Table 2 Annual and seasonal mean of all-sky SSR in the TP as observed, determined in reanalyses (NCEP/NCAR and ERA40) and simulated by the ECHAM5-HAM

	Annual	Spring	Summer	Autumn	Winter
Observations all-sky SSR	210.1	243.0	263.1	191.1	143.4
NCEP/NCAR all-sky SSR	275.9 (+31.3)	332.7 (+36.9)	339.3 (+29.0)	239.8 (+25.5)	192.2 (+34.0)
ERA-40 all-sky SSR	211.5 (+0.7)	268.0 (+10.3)	247.0 (−6.1)	180.1 (−5.8)	151.4 (+5.6)
ECHAM5-HAM all-sky	203.7 (−3.0)	239.8 (−1.3)	246.7 (−6.2)	184.3 (−3.6)	144.0 (+0.4)

Units are Wm^{-2}, and the reference period used is 1971–2000. For the mean calculations only the 10 stations (nearest grid point to the station) are used for the observations (reanalyses and ECHAM5-HAM simulations). Relative differences (%) with respect to the observations are given in parentheses

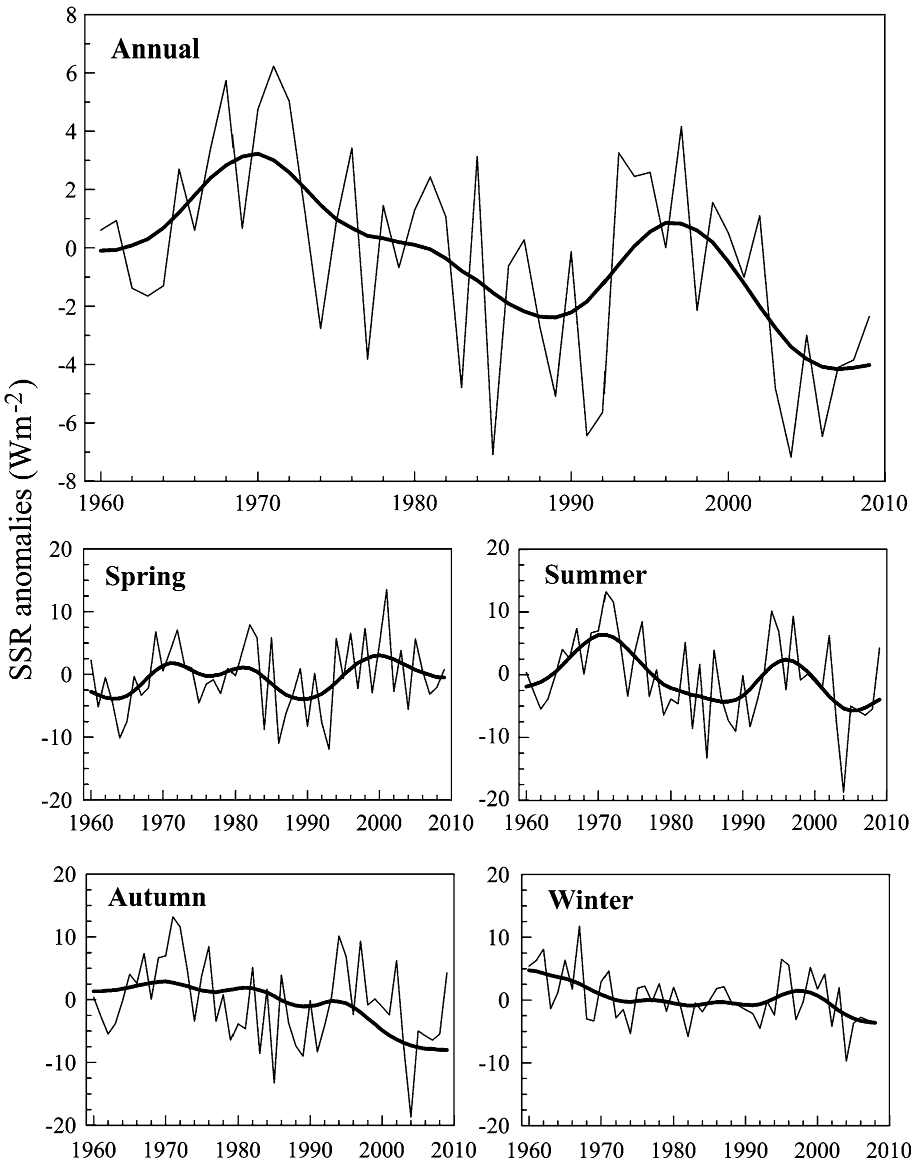

Fig. 2 Mean annual and seasonal all-sky SSR series (*thin line*) in the Tibetan Plateau during the period 1960–2009, plotted together with a GLPF17 (*thick line*). The series are expressed as differences (anomalies in Wm^{-2}) relative to the 1971–2000 reference period

Table 3 Linear trends in the mean Tibetan Plateau (TP) all-sky and clear-sky SSR observational series, given as Wm^{-2} $decade^{-1}$

	Annual	Spring	Summer	Autumn	Winter
Obs. all-sky, 1960–2009	−1.00* (−2.09)	0.52 (−1.02)	−1.26* (−2.25*)	−2.16* (−2.40)	−1.09* (−2.56*)
Obs. all-sky, 1960–1992	−1.68* (−3.14*)	−0.31 (−3.48*)	−2.61* (−3.75*)	−1.37 (−2.21*)	−2.01* (−2.97*)
Obs. all-sky, 1993–2009	−5.48* (−5.50)	0.02 (−1.50)	−7.24* (−8.02)	−8.27* (−8.34*)	−4.5 (−5.77)
Obs. all-sky, 1993–2005	−6.83* (−6.01)	3.73 (4.76)	−12.81* (−15.76*)	−11.26* (−11.42*)	−4.86 (−5.53)
Obs. clear-sky, 1960–2009	−2.80*	−1.81	−1.22	−3.78*	−4.45*
Obs. clear-sky, 1960–1992	−4.76*	−5.48*	−2.91	−5.65*	−4.84*
Obs. clear-sky, 1993–2009	−11.40*	−14.85*	−14.68*	−8.56	−7.46*
Obs. clear-sky, 1993–2005	−11.73	−11.09	−22.18*	−9.72	−4.00

The trends are shown for the 1960–2009, 1960–1992, 1993–2009 and 1993–2005 periods. Trends values of the mean TP all-sky SSR only considering the 4 homogeneous series are given in parentheses

* Significant at the 0.05 level

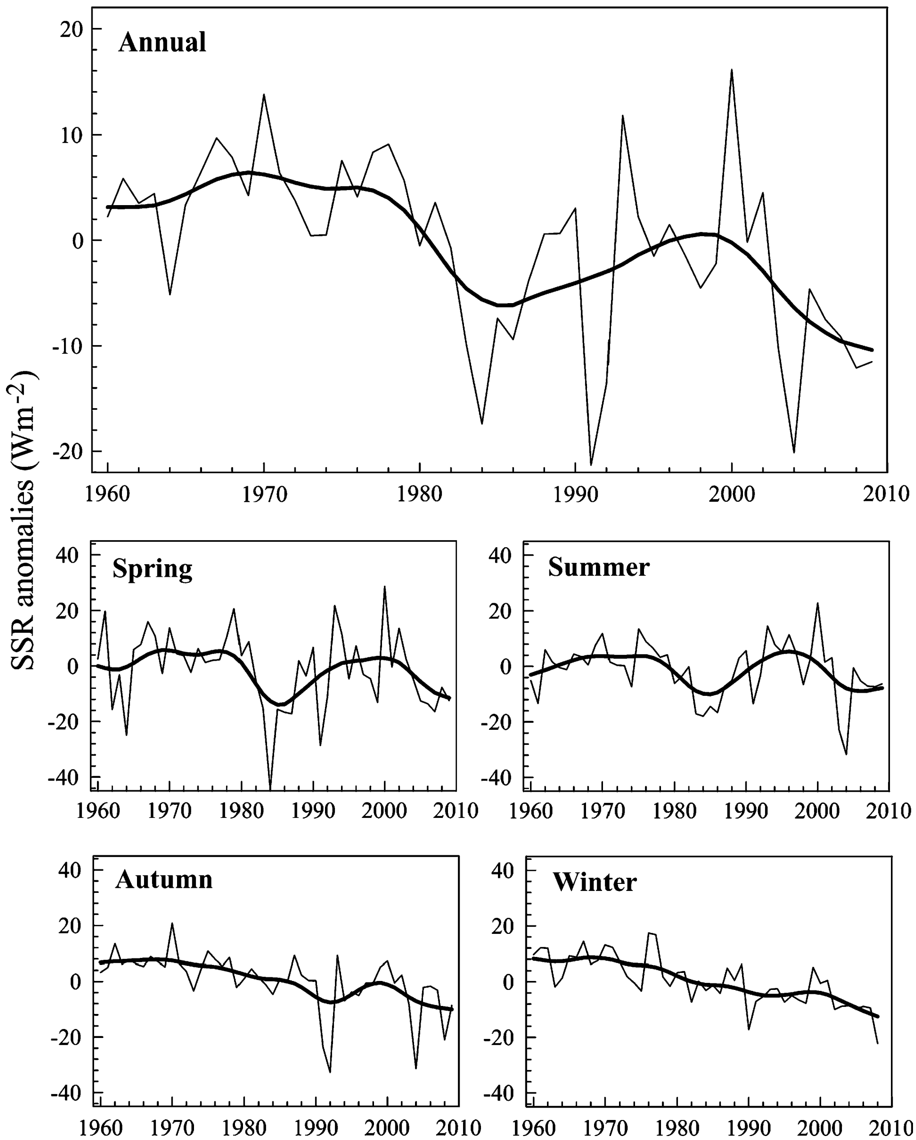

Fig. 3 As Fig. 2, but for clear-sky SSR observational series in the Tibetan Plateau. The mean series are constructed only considering the SSR and TCC daily records of the 4 homogeneous series. A day is defined as clear if the TCC daily mean is less than 1 okta

Figure 4 (top) shows the annual mean all-sky SSR series from NCEP/NCAR and ERA-40 in the TP composed from the grid points closes to the 10 stations. The annual all-sky SSR mean series from NCEP/NCAR shows a tendency towards a decrease before 1970 and during the 1980s, and an increasing trend during the 1970s and the 1990s and turns to decrease after that. The annual all-sky SSR has an increasing trend with a rate of 1.06 Wm^{-2} $decade^{-1}$ during the period 1960–2009. On the other hand, the mean annual all-sky SSR series from the ERA-40 shows a decrease before 1970 and after 1980 and increases during the 1970s and 1980s. The linear trend, estimated over the 1960–2004 period, is slightly positive, but not significant. The time variability and trends of all-sky SSR on a seasonal basis show similar features to the annual series for both reanalysis (not shown).

Figure 4 (bottom) shows the mean annual clear-sky (net clear-sky) SSR series from NCEP/NCAR (ERA-40) in the TP. Clear-sky SSR series from NCEP/NCAR show a slight but significant increase (0.17 Wm^{-2} $decade^{-1}$) during the whole period. The seasonal anomalies series show similar features and the largest trend magnitude is found in spring (not shown). For the ERA-40, the mean annual clear-sky net SSR series has a sharp decrease before the 1970s followed by a period without relevant variations up to the present, with a significant decrease (-0.91 Wm^{-2} $decade^{-1}$) during the whole period 1960–2001, and with the largest seasonal trend in spring (not shown).

Overall, the all-sky and clear-sky SSR trends derived from both NCEP/NCAR and ERA-40 cannot capture the decadal variations seen in surface observations in the TP.

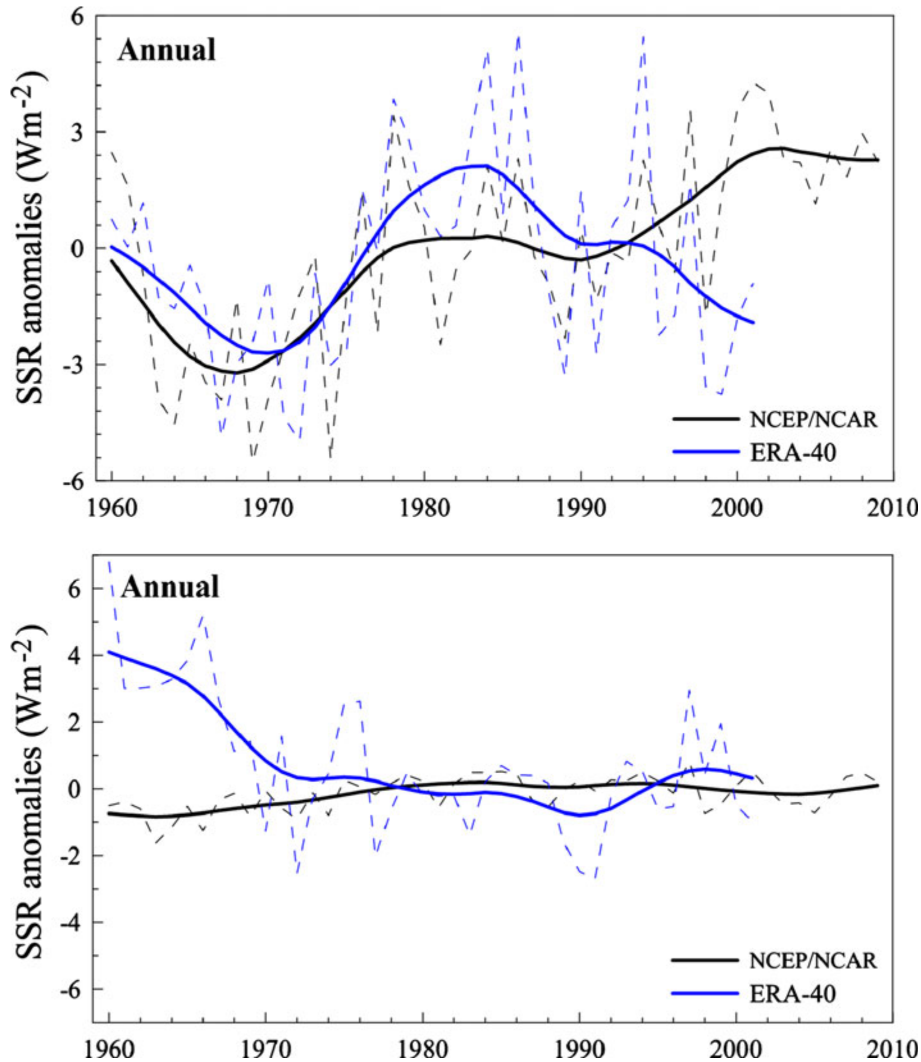

Fig. 4 Mean annual (*top*) all-sky and (*bottom*) clear-sky SSR series (*thin dashed lines*) in the Tibetan Plateau for the NCEP/NCAR (in *black*) and ERA-40 (in *blue*) reanalyses, together with a GLPD17 (*thick solid lines*), during the 1960–2009 and 1960–2001 period, respectively. The series are expressed as differences (anomalies in Wm^{-2}) relative to the 1971–2000 reference period, and are calculated using the nearest grid points to the 10 (4) surface stations with all-sky (clear-sky) SSR series

4.3 Changes of simulated all-sky and clear-sky ensemble SSR by ECHAM5-HAM

Figures 5 and 6 show the annual and seasonal all-sky and clear-sky ensemble mean SSR series from ECHAM5-HAM simulations for the TP from 1960 to 2005. The means and trends of these values are summarized in Tables 2 and 4. For comparison, Table 3 also shows trends covering the 1993–2005 subperiod in the observational series.

The climatological mean of the annual mean ensemble SSR from the ECHAM5-HAM at all-sky condition is 203.7 Wm^{-2}, which is slightly lower than both the surface observations (−3.0 %) and reanalysis. On the seasonal basis, all seasons except winter underestimate the observations and summer shows both the largest mean value (246.7 Wm^{-2}) and underestimation (−6.2 %) (Table 2).

Figure 5 shows that the annual ensemble mean all sky SSR series from ECHAM5-HAM decreases before 1980, increases during the 1980s, and then decreases during the 1990s and 2000s, with a significant negative trend of −0.54 Wm^{-2} $decade^{-1}$ during the 1960–2009 period. All seasonal series show decreasing trends and the variability is similar to the annual series. The largest trends occur in spring (−1.39 Wm^{-2} $decade^{-1}$) (Table 4).

Any potential direct aerosol effect on SSR should be most easily detectable and interpretable under clear-sky condition (Folini and Wild 2011). Figure 6 shows that the annual ensemble mean clear-sky SSR from ECHAM5-HAM decreases before the mid-1970s and after the mid-1980s, and has a significantly decreasing trend of −0.67 Wm^{-2} $decade^{-1}$, which is larger than under all-sky conditions. All seasons have decreasing trends, and the largest trend also occurs in summer (−0.88 Wm^{-2} $decade^{-1}$) (Table 4). Overall, the ensemble mean SSR shows larger trends under clear sky conditions than under all sky conditions, except spring (Table 4).

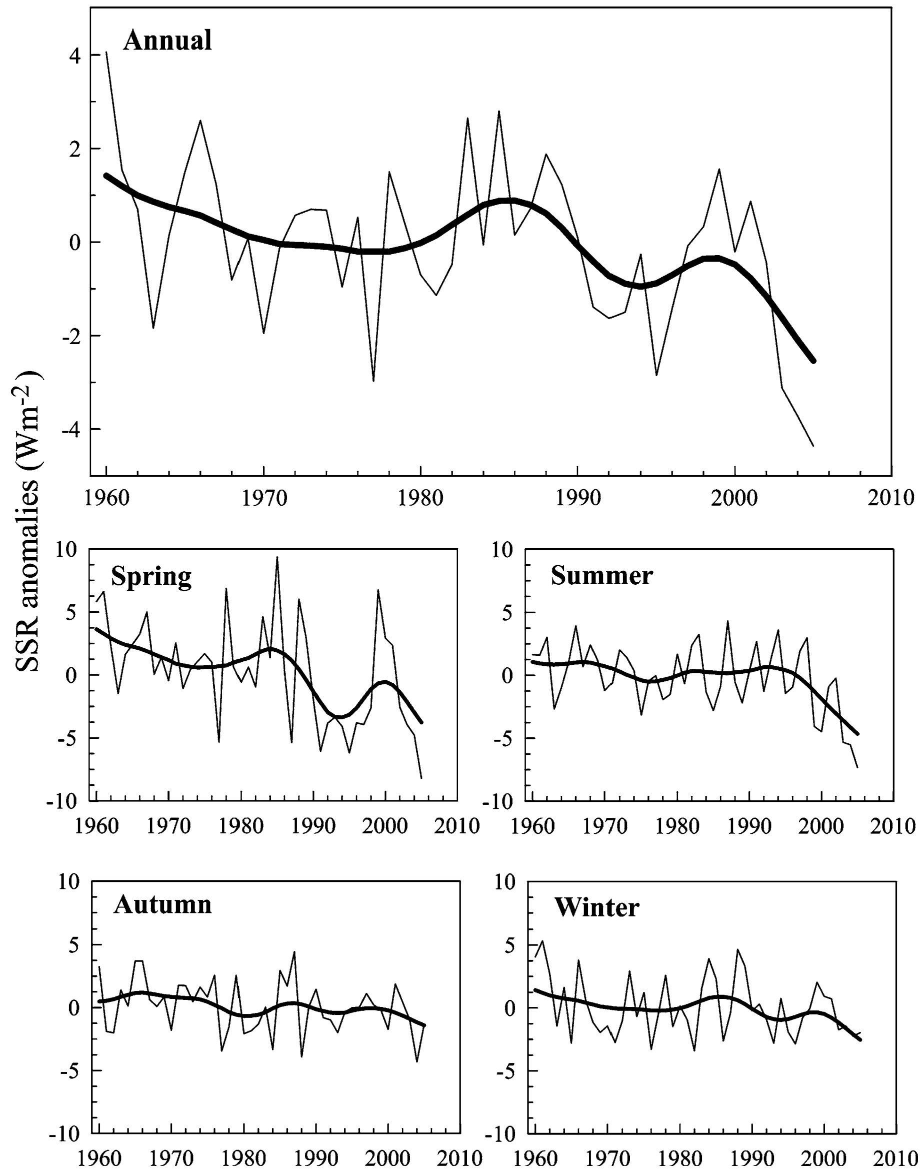

Fig. 5 ECHAM5-HAM simulated mean annual and seasonal all-sky ensemble SSR series (*thin lines*) in the Tibetan Plateau during the period 1960–2005. The series are expressed as differences (anomalies in Wm^{-2}) relative to the 1971–2000 reference period, and are plotted together with a GLPD17 (*thick lines*)

5 Discussion and conclusions

This study analyzed the temporal variability of all-sky and clear-sky surface solar radiation (SSR) data in the eastern and central Tibetan Plateau (TP) during the 1960–2009 period. The results provide observational evidence for an overall decrease of SSR in the TP from 1960 to 2009. The observed decrease is, however, far from linear. Periods of both increasing and decreasing SSR are identified, both under clear sky and all sky conditions. Our results are in line with the all-sky SSR overall decrease observed in China (including a partial recovery in the 1990s) (Che et al. 2005; Liang and Xia 2005; Norris and Wild 2009; Shi et al. 2008; Wild et al. 2009) and India (Kumari et al. 2007; Kumari and Goswami 2010) during the last decades, although the TP shows much smaller amplitudes in the trends. In China, Shi et al. (2008) have shown that the change of direct irradiance is similar to that of global irradiance, with a decreasing trend during 1957–2000, and the most noticeable decrease occurred in the Sichuan and Guizhou area and in the middle and lower reaches of the Yangtze River. In the TP, direct irradiance at most stations shows decreasing trends, varying from −1 to −6 % per decade during the past 40 years. The patterns and magnitudes of trends are consistent with previous studies (Che et al. 2005; Liang and Xia 2005).

Similar conclusions can be reached for clear-sky SSR trends, as a downward trend from the 1960s to the 1990s and a partial recovery thereafter has been observed for the whole China (Liu et al. 2004; Qian et al. 2007; Xia 2010), which is consistent with the clear-sky SSR trends shown in this study before the 2000s. It is noticeable that distinctly

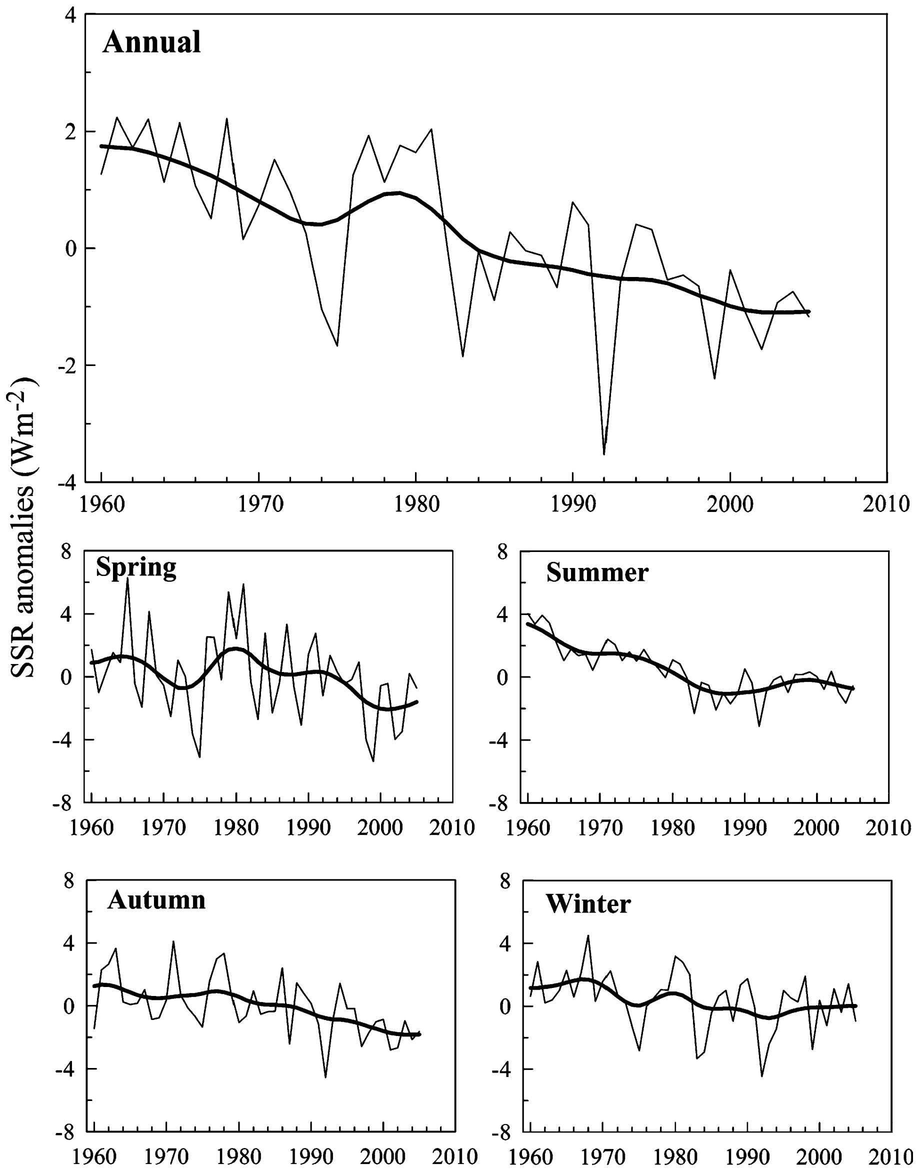

Fig. 6 As Fig. 5, but for clear-sky ensemble SSR series. In order to facilitate the comparison with the clear-sky ensemble SSR observations, only the nearest grid points to the 4 homogeneous stations are considered

Table 4 Linear trends in the mean Tibetan Plateau all-sky and clear-sky ensemble SSR as determined by the ECHAM5-HAM transient simulation, given as Wm^{-2} $decade^{-1}$, considering the 1960–2005 period and two subperiods (before and after 1993)

	Annual	Spring	Summer	Autumn	Winter
ECHAM5-HAM all-sky, 1960–2005	−0.54*	−1.39*	−0.79*	−0.42	−0.42
ECHAM5-HAM all-sky, 1960–1992	−0.27	−1.14*	−0.35	−0.42	−0.21
ECHAM5-HAM all-sky, 1993–2005	−1.71	−0.08	−6.81*	−1.04	−0.04
ECHAM5-HAM clear-sky, 1960–2005	−0.67*	−0.58	−0.88*	−0.70*	−0.44*
ECHAM5-HAM clear-sky, 1960–1992	−0.78*	−0.13	−1.54*	−0.61	−0.71*
ECHAM5-HAM clear-sky, 1993–2005	−1.03*	−1.97	−0.41	−1.77*	+0.80

* Significant at the 0.05 level

low clear-sky SSR anomalies appear around 1963, 1983–1984 and 1992, which occur immediately following to the Agung (1963, Indonesia), El Chichon (1982, Mexico) and Pinatubo (1991, Philippines) volcanic eruptions. These strong decreases detected in the clear-sky SSR series can be the consequence of the direct effect of the aerosols released by these volcanic eruptions. A strong decrease is also observed in 2004, which cannot be explained by volcanic eruptions but agrees with a sudden increase of aerosols observed in the TP (Luedeling et al. 2011), which is consistent with Xia et al. (2008) based on the satellite AOD retrievals using MISR measurements which indicated that AOD in 2004 is generally larger than the 9-year average. Thus, lower SSR in 2004 is probably associated with larger AOD, possibly as a result of the extraordinary dust storm that occurred in the Gobi desert in 2004 (Qu et al. 2006). Whether the sources of dust come from local emission or long-range transportation are unclear in 2004.

In order to learn more about the causes of the TP dimming, we first note that neither NCEP/NCAR nor ERA-40 reanalysis data are able to capture the observed SSR decrease. Although both reanalyses assimilate a comprehensive amount of weather data which constrains the simulated atmospheric states, they cannot reproduce the decadal variations in the all-sky and clear-sky SSR. Inaccurate representation of clouds and the neglect of time varying aerosols in the reanalysis assimilation model are considered as the most likely cause of this disagreement with surface observations (Wild and Schmucki 2011; Xia et al. 2006, 2008). Note that there are differences between the observations, NCEP/NCAR, ERA-40 and ECHAM-HAM with respect to the mean SSR patterns, although ECHAM-HAM can simulate the dimming of SSR shown by observations. This can be caused by the insufficient absorption of solar irradiance in the parameterization in the reanalysis and numerical modes. This is consistent with the previous finding by Wild (2001). Wild (2001) showed that the atmosphere in both NCEP/NCAR and in many GCMs is significantly too transparent for SSR, leading to excessive insolation at the surface. The same should be applied under cloud-free conditions (Wild et al. 2006).

In contrast, transient simulations with ECHAM5-HAM show an overall dimming of annual mean SSR from 1960 to 2005 at a statistically significant level under both all-sky and clear-sky conditions, in line with observational evidence. Correlations between observed and modelled (ensemble mean) annual and seasonal mean all-sky and clear-sky SSR time series smoothed with the 17GLPF range from 0.3 to 0.8 (see Table 5). Differences between observed and modelled SSR exist, however, for some seasons and with regard to the absolute magnitudes of the trends. Despite these shortcomings, the ECHAM5-HAM simulations further support the hypothesis that the dimming observed in the TP is caused by increased aerosol emissions in the TP or in the surrounding regions. The model simulations calculate an almost linear increase in 550 nm AOD over the TP from 1960 to 2005 (Fig. 7), in line with the linear decrease in clear-sky SSR. The correlations between SSR and AOD series (Table 5) provide values of −0.72 and −0.81 for the smoothed annual series of all-sky and clear-sky SSR series, respectively. High correlations are also found on a seasonal basis, especially during autumn. Whether the source of these aerosols lies in the TP or in surrounding regions remains a subject for future studies, as for example with the help of dedicated sensitivity experiments.

Compared with other regions, the TP should be regarded as a region with clear atmospheric condition. Taking Nam Co in the central TP as an example, the baseline AOD of Nam Co is 0.029, which is about half of that over the Pacific Ocean and the Atlantic Ocean (Xia et al. 2011). At the same time, aerosol radiative effects are exponentially correlated with AOD. This suggests that the TP is sensitive to aerosol direct and indirect radiative effects and an equivalent increase of AOD here can produce much larger aerosol direct and indirect effects as compared with regions with larger background AOD. This hypothesis has been supported by the evidence that the atmospheric brown clouds (mostly as a result of biomass burning and fossil fuel consumption) can amplify the warming in the TP and may account for the observed retreat of Himalayan glaciers (Ramanathan et al. 2007). On the other hand, black soot aerosols deposited on glaciers in the TP significantly contribute to the rapid glacier retreat (Xu et al. 2009).

However, one may speculate that the sources of these aerosols have a large-scale rather than a local origin, which has been a hot topic in recent years (e.g. Xu et al. 2009; Xia

Table 5 Correlation coefficients between the mean all-sky and clear-sky GLPF17 series from observed SSR and ECHAM5-HAM transient simulations in the Tibetan Plateau on the annual and seasonal basis

	Annual	Spring	Summer	Autumn	Winter
Observed all-sky SSR					
ECHAM5-HAM all-sky SSR	0.31	−0.28	0.43	0.68	0.59
ECHAM5-HAM clear-sky SRR	0.59	−0.59	0.52	0.89	0.64
ECHAM5-HAM AOD	−0.72	0.33	−0.60	−0.84	−0.54
Observed clear-sky SSR					
ECHAM5-HAM all-sky SSR	0.30	−0.06	0.31	0.79	0.36
ECHAM5-HAM clear-sky SSR	0.71	−0.12	0.39	0.85	0.84
ECHAM5-HAM AOD	−0.81	−0.40	−0.38	−0.90	−0.93

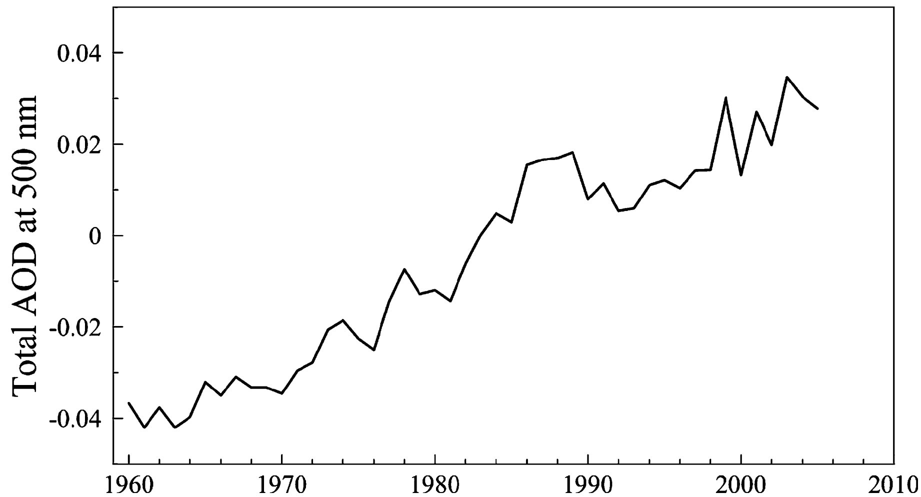

Fig. 7 ECHAM5-HAM simulated mean annual aerosol optical depth (AOD) at 550 nm in the Tibetan Plateau during the period 1960–2005. The series are expressed as differences (anomalies) relative to the 1971–2000 reference period, and are calculated using the nearest grid points to the 10 surface stations with all-sky SSR series

et al. 2008; Kopacz et al. 2011). Based on the back-trajectory analysis, Lu et al. (2012) found that the black carbon in the TP has increased by 41 % during 1961–2010, and South Asia and East Asia are the two main source regions, accounting for 67 and 17 % of black carbon transported to the TP on an annual basis. This is slightly different from Kopacz et al. (2011), suggesting that the TP receives most black carbon from western and central China, as well as from India, Nepal, the Middle East, Pakistan and other countries. The south westerly winds associated with the Indian summer monsoon may lead to some exports of Indian aerosol to the TP. However, the contributions of different source regions transported to the TP vary with season and location (Xia et al. 2011; Lu et al. 2012). The rather steady decrease of observed and modelled SSR in the TP in summer may be partly attributable to increasing Indian aerosol emissions, although the amounts of anthropogenic aerosol such as black carbon reaching the TP in summer are lower than that in winter (Lu et al. 2012). Other sources of aerosols transported to the TP in summer cannot be ruled out. For example, dust transportation from Taklimakan Desert to the TP mainly occurs in summer (Xia et al. 2008). In the winter half year, prevailing winds are rather from the north, i.e. from the desert regions north of the TP, and consequently a predominant influence of the desert dust is a possible cause of the decreasing SSR in the TP in winter.

Furthermore, it cannot be excluded that the observed SSR trends in the TP are affected by the increasing local aerosol emissions (Qian et al. 2006, 2007; Kaiser and Qian 2002), e.g. connected with heating, despite the scarcity of population in the region. In fact, the industrial waste gas and soot emissions and number of civilian vehicles in the Tibet have been increasing in the last decades, especially after the 1980s (e.g. see statistics in You et al. (2010b)). This increase of anthropogenic activities would imply a rapid increase in the emissions of aerosol in the TP, although at a lower rate than in East China and India.

In conclusion, as in many other parts around the globe, an overall decrease in SSR has been documented in the TP since the 1960s, based on both observational and modelling approaches. This decrease is found under both all sky and clear sky conditions and seems to be related to increasing aerosols emissions during the last decades, as has been shown by the simulations performed with the ECHAM5-HAM global climate model. However, further research is needed in order to better assess the origin of the aerosols over the TP.

Acknowledgments This study has been supported by the Global Change Research Program of China (2010CB951401), the Chinese Academy of Sciences (KZCX2-YW-145), and the National Natural Science Foundation of China (40870743). It became possible through a Sino-Swiss Science and Technology Cooperation (SSSTC) research grant (EG76-032010 and EG23-092011). The China postdoctoral science foundation (the 49th) is also appreciated. The authors thank the National Meteorological Information Center, China Meteorological Administration (NMIC/CMA), for providing the data for this study. Qinglong You is supported by the Alexander von Humboldt Foundation. Arturo Sanchez-Lorenzo is supported by a postdoctoral fellowship from the "Comissionat per a Universitats i Recerca del Departament d'Innovació, Universitats i Empresa de la Generalitat de Catalunya" (2009 BP-A 00035). ECHAM5-HAM simulations were carried out at the Swiss National Supercomputing Center (CSCS). We are very grateful to the reviewers for their constructive comments and thoughtful suggestions.

References

Roeckner E et al (2003) The atmospheric general circulation model ECHAM5. Part I: model description. Hamburg: Max-Planck-Institute for Meteorology MPI Report No. 349

Sanchez-Lorenzo A et al (2009) Dimming/brightening over the Iberian Peninsula: Trends in sunshine duration and cloud cover and their relations with atmospheric circulation. J Geophys Res 114: D00D09

Wild M et al (2009) Global dimming and brightening: an update beyond 2000. J Geophys Res 114:D00D13
Alexandersson H, Moberg A (1997) Homogenization of Swedish temperature data 1. Homogeneity test for linear trends. Int J Climatol 17(1):25–34
Barnett TP et al (2005) Potential impacts of a warming climate on water availability in snow-dominated regions. Nature 438:303–309
Bichet A et al (2011) Global precipitation response to changing external forcings since 1870. Atmos Chem Phys 11:9961–9970
Cha LS (1996) A study on spatial and temporal variation of solar radiation in China (in Chinese). Sci Geograph Sin 16:232–237
Che HZ et al (2005) Analysis of 40 years of solar radiation data from China, 1961–2000. Geophys Res Lett 32:L06803
Folini D, Wild W (2011) Aerosol emissions and dimming/brightening in Europe: sensitivity studies with ECHAM5-HAM. J Geophys Res 116:D2114
Gilgen H et al (1998) Means and trends of shortwave irradiance at the surface estimated from GEBA. J Clim 11:2042–2061
Immerzeel WW et al (2010) Climate change will affect the Asian Water Towers. Science 328(5984):1382–1385
Kaiser DP, Qian Y (2002) Decreasing trends in sunshine duration over China for 1954–1998: indication of increased haze pollution? Geophys Res Lett 29:2042
Kalnay E et al (1996) The NCEP/NCAR 40-year reanalysis project. Quart J Roy Meteor Soc 77(3):437–471
Kang SC et al (2010) Review of climate and cryospheric change in the Tibetan Plateau. Environ Res Lett 5(1):015101
Kopacz M et al (2011) Origin and radiative forcing of black carbon transported to the Himalayas and Tibetan Plateau. Atmos Chem Phys 11:2837–2852
Kumari BP, Goswami BN (2010) Seminal role of clouds on solar dimming over the Indian monsoon region. Geophys Res Lett 37:L06703
Kumari BP et al (2007) Observational evidence of solar dimming: offsetting surface warming over India. Geophys Res Lett 34:L21810
Li XW et al (1998) Analysis of the solar radiation variation of the China in recent 30 years (in Chinese). Quart J Appl Meteor 9:24–31
Liang F, Xia XA (2005) Long-term trends in solar radiation and the associated climatic factors over China for 1961–2000. Ann Geophys 23(7):2425–2432
Liepert BG (2002) Observed reductions of surface solar radiation at sites in the United States and worldwide from 1961 to 1990. Geophys Res Lett 29(10):1421
Liu B et al (2004) Taking China's temperature: daily range, warming trends, and regional variations, 1955–2000. J Clim 17:4453–4462
Lohmann U et al (2007) Cloud microphysics and aerosol indirect effects in the global climate model ECHAM5-HAM. Atmos Chem Phys 7:3425–3446
Lu Z et al (2012) A novel back-trajectory analysis of the origin of black carbon transported to the Himalayas and Tibetan Plateau during 1996–2010. Geophys Res Lett 39:L01809
Luedeling E et al (2011) Replies to Shen, Chen et al. and Yi and Zhou: linear regression analysis misses effects of winter temperature on Tibetan vegetation. Proc Natl Acad Sci USA 108(19):E95
Norris JR, Wild M (2009) Trends in aerosol radiative effects over China and Japan inferred from observed cloud cover, solar "dimming,'' and solar "brightening''. J Geophys Res 114: D00D15
Ohmura A (2009) Observed decadal variations in surface solar radiation and their causes. J Geophys Res 114:D00D05
Qian Y et al (2006) More frequent cloud-free sky and less surface solar radiation in China from 1955 to 2000. Geophys Res Lett 33:L01812
Qian Y et al (2007) Variability of solar radiation under cloud-free skies in China: the role of aerosols. Geophys Res Lett 34:L12804
Qu JJ et al (2006) Asian dust storm monitoring combining terra and aqua MODIS SRB measurements. IEEE Geosci Remote Sens 3(4):484–486
Ramanathan V et al (2007) Warming trends in Asia amplified by brown cloud solar absorption. Nature 448:575–578
Rayner NA et al (2003) Global analyses of sea surface temperature, sea ice, and night marine air temperature since the late nineteenth century. J Geophys Res 108:4407
Roeckner E et al (2006) Sensitivity of simulated climate to horizontal and vertical resolution in the ECHAM5 atmosphere model. J Clim 19(16):3771–3791
Sen PK (1968) Estimates of regression coefficient based on Kendall's tau. J Am Stat Assoc 63:1379–1389
Shi GY et al (2008) Data quality assessment and the long-term trend of ground solar radiation in China. J Appl Meteorol Climatol 47(4):1006–1016
Solanki SK, Krivova NA (2003) Can solar variability explain global warming since 1970? J Geophys Res 108:1200
Stanhill G, Cohen S (2001) Global dimming: a review of the evidence for a widespread and significant reduction in global radiation with discussion of its probable causes and possible agricultural consequences. Agric For Meteorol 107(4):255–278
Stier P et al (2006a) Emission-induced nonlinearities in the global aerosol system: results from the ECHAM5-HAM aerosol-climate model. J Clim 19(16):3845–3862
Stier P et al (2006b) The evolution of the global aerosol system in a transient climate simulation from 1860 to 2100. Atmos Chem Phys 6:3059–3076
Tang WJ et al (2010) Quality control and estimation of global solar radiation in China. Sol Energy 84:466–475
Tang WJ et al (2011) Solar radiation trend across China in recent decades: a revisit with quality-controlled data. Atmos Chem Phys 11:393–406
Uppala SM et al (2005) The ERA-40 re-analysis. Q J R Meteorol Soc 131(612):2961–3012
Vincent LA et al (2005) Observed trends in indices of daily temperature extremes in South America 1960–2000. J Clim 18(23):5011–5023
Wang CH et al (2011) Factors affecting the surface radiation trends over China between 1960 and 2000. Atmos Environ 45:2379–2385
Wild M (2001) Surface and atmospheric radiation budgets as determined in reanalyses. Irs 2000: current problems in atmospheric radiation, pp 602–605
Wild M (2009) Global dimming and brightening: a review. J Geophys Res 114: D00D16
Wild M, Schmucki E (2011) Assessment of global dimming and brightening in IPCC-AR4/CMIP3 models and ERA40. Clim Dyn 37:1671–1688
Wild M et al (2005) From dimming to brightening: decadal changes in solar radiation at earth's surface. Science 308(5723):847–850
Wild M et al (2006) Evaluation of clear-sky solar fluxes in GCMs participating in AMIP and IPCC-AR4 from a surface perspective. J Geophys Res 111:D01104
Xia XA (2010) A closer looking at dimming and brightening in China during 1961–2005. Ann Geophys 28(5):1121–1132
Xia XA et al (2006) Analysis of down welling surface solar radiation in China from National Centers for Environmental Prediction reanalysis, satellite estimates, and surface observations. J Geophys Res 111:D09103

Xia XA et al (2008) Aerosol optical depth over the Tibetan Plateau and its relation to aerosols over the Taklimakan Desert. Geophys Res Lett 35:L16804

Xia XA et al (2011) Baseline continental aerosol over the central Tibetan plateau and a case study of aerosol transport from South Asia. Atmos Environ 45:7370–7378

Xu XD et al (2008) World water tower: an atmospheric perspective. Geophys Res Lett 35:L20815

Xu BQ et al (2009) Black soot and the survival of Tibetan glaciers. Proc Natl Acad Sci USA 106:22114–22118

You QL et al (2008a) Changes in daily climate extremes in the eastern and central Tibetan Plateau during 1961–2005. J Geophys Res 113:D07101

You QL et al (2008b) Relationship between trends in temperature extremes and elevation in the eastern and central Tibetan Plateau, 1961–2005. Geophys Res Lett 35:L04704

You QL et al (2010a) Decreasing wind speed and weakening latitudinal surface pressure gradients in the Tibetan Plateau. Clim Res 42(1):57–64

You QL et al (2010b) From brightening to dimming in sunshine duration over the eastern and central Tibetan Plateau (1961–2005). Theor Appl Climatol 101(3–4):445–457

You QL et al (2010c) Climate warming and associated changes in atmospheric circulation in the eastern and central Tibetan Plateau from a homogenized dataset. Glob Planet Change 72(1–2):11–24

INTERNATIONAL JOURNAL OF CLIMATOLOGY
Int. J. Climatol. **33**: 1337–1347 (2013)
Published online 17 May 2012 in Wiley Online Library
(wileyonlinelibrary.com) DOI: 10.1002/joc.3512

Royal Meteorological Society

Variability of temperature in the Tibetan Plateau based on homogenized surface stations and reanalysis data

Qinglong You,[a,b,c]* Klaus Fraedrich,[b] Guoyu Ren,[c] Nick Pepin,[d] and Shichang Kang[c,e]
[a] *Laboratory of Tibetan Environment Changes and Land Surface Processes, Institute of Tibetan Plateau Research, Chinese Academy of Sciences (CAS), Beijing, China*
[b] *Meteorological Institute, Klima Campus, University of Hamburg, Hamburg, Germany*
[c] *Laboratory for Climate Studies, National Climate Center, China Meteorological Administration (CMA), Beijing, China*
[d] *Department of Geography, University of Portsmouth, UK*
[e] *State Key Laboratory of Cryospheric Science, CAS, Lanzhou, China*

ABSTRACT: The Tibetan Plateau (TP) with an average elevation of over 4000 m a.s.l. is the world's highest and most extensive highland. The scarcity of climatic observations limits our understanding of surface air temperature change in the region. Thus, we compare temperatures and their trends from 71 homogenized surface stations (with elevations above 2000 m a.s.l.) with National Centers for Environmental Prediction/National Center for Atmospheric Research (NCEP/NCAR) Reanalysis (NCEP/NCAR hereafter) and European Centre for Medium-Range Weather Forecasts (ECMWF) reanalysis (ERA-40 hereafter) in the eastern and central TP during 1961–2004. For current climatology, ERA-40 is more similar to the surface stations than NCEP/NCAR. Compared with surface stations, both NCEP/NCAR and ERA-40 reanalyses have cold biases, which are mainly a result of differences in topographical height, and station aspect and slope. Warming trends at the surface stations are on average stronger than in both reanalyses, but ERA-40 captures the surface warming more clearly than NCEP/NCAR on an annual and seasonal basis. Since ERA-40 more closely represents the surface temperatures and their trends in the central and eastern TP, ERA-40 predictions are selected to examine change in the western TP where there are few surface stations. NCEP/NCAR, on the other hand, is more representative of free air temperature conditions. The 'observation minus reanalysis' (OMR) method can be used to estimate the impact of surface changes on climate by computing the difference between surface observations and NCEP/NCAR (which only contains the forcing influencing the assimilated atmospheric trends). The OMR trend is significantly increasing but the extent to which the changes in local environment are responsible needs further study.

KEY WORDS warming trend; elevation dependency; Tibetan Plateau; reanalysis

Received 8 November 2011; Revised 28 February 2012; Accepted 15 April 2012

1. Introduction

The Tibetan Plateau (TP) with an average elevation of over 4000 m a.s.l. and an area of approximately 2.5×10^6 km^2 is the highest and most extensive highland in the world. The TP exerts profound influences not only on the local climate and environment but also on the global atmospheric circulation through its thermal and mechanical forcing (Yeh and Gao, 1979; Duan and Wu, 2005). The TP has the largest area of snow and ice in the mid-latitude regions and has therefore been called the 'Asian water tower' (Yeh and Gao, 1979), while it gets less attention than the Arctic or Antarctic. In the context of global warming, the air temperature in the TP is increasing (Liu and Chen, 2000), with an accelerating melt of glaciers (such as Tian *et al*., 2006; Kang *et al*., 2007) corroborating that this. In the past half-century, 82% of the plateau's glaciers have retreated and 10% of its permafrost has degraded (Qiu, 2008). These changes are expected to continue, changing the water supply for billions of people and probably altering the atmospheric circulation (Qiu, 2008). Being a crucial water resource for most of the Asian continent (Barnett *et al*., 2005; Zhang, 2007), the variability of water on the plateau is of critical importance. Zhu *et al*. (2011) found that dryness/wetness in the TP is associated with the dominance of a Scandinavian or Mediterranean/East Asia wave train, respectively.

Owing to both terrain complexity and extreme environmental conditions, most surface observational stations are situated in the lower parts of the eastern and central TP, often in valley locations. Temperature in the TP has been widely studied (Liu and Chen, 2000; Wang *et al*., 2008; Xu *et al*., 2008; Bothe *et al*., 2010). Warming in the TP is significant and can influence the atmospheric circulation at a large scale (Wang *et al*., 2008). Previous studies concerning temperature variability based on raw observations, such as Liu and Chen (2000) and You *et al*.

* Correspondence to: Q. You, Laboratory of Tibetan Environment Changes and Land Surface Processes, Institute of Tibetan Plateau Research, Chinese Academy of Sciences (CAS), Beijing 100085, China. E-mail: yqingl@126.com

(2008a, 2008b), are spatially biased with little coverage of the western TP and higher elevations (>4000 m). A reanalysis in theory overcomes this problem, but to be used to assess widespread climate change it requires validation against real observations where both exist. Hence temperatures retrieved from two reanalysis products are investigated and compared with surface observations in this study. Reanalyses include the National Center for Environmental Prediction/National Center for Atmospheric Research (NCEP/NCAR) Reanalysis (NCEP/NCAR hereafter) (Kalnay *et al.*, 1996) and the European Centre for Medium-Range Weather Forecasts (ECMWF) reanalysis (ERA-40 hereafter) (Uppala *et al.*, 2005). Frauenfeld *et al.* (2005) have compared ERA-40 with the raw observational data in the TP and Ma *et al.* (2008) have investigated homogenized surface observations with reanalyses over the whole China. Despite these studies, detailed comparisons between reanalyses data and homogenized observations are limited in the TP where topography is complex. Previous work (You *et al.*, 2010a; 2010b) has analysed warming trends from both reanalyses and surface data, examining the relationships between trend magnitudes, elevation and atmospheric circulation changes. This study uses similar datasets but includes more detailed examination of local-scale and short-term differences between them. In particular, a comparison of instantaneous climatology, the modeling of bias between observations and reanalyses, and gaining an understanding of what controls the contrasts between station and reanalysis-based trends can extend understanding of climate variability in this important region.

After data sources and methods are outlined (Section 2), the current temperature climatology of the TP from surface observations and both reanalyses is compared in Section 3.1 and the differences in trends are described in Section 3.2. Based on this, ERA-40 is used to examine trend patterns in the western TP where surface data are virtually non-existent (Section 4.1), and NCEP/NCAR is selected to contrast surface and free-air warming patterns in the rest of the region (Section 4.2 and 4.3). The predictability of the differences between the datasets and the wider implications of our work are discussed in Section 5.

2. Datasets and methods

A brief description of the near surface air temperature dataset is presented. Those data provide the basis for the analysis of TP temperature variability and its relation to surface elevation.

2.1. Surface air temperature homogenized dataset

The surface air temperature homogenized dataset is the China Homogenized Historical Temperature Dataset (1951–2004 period) (version 1.0), which was released in 2006 by the National Meteorological Information Center, China Meteorological Administration (NMIC/CMA). The data have been homogenized to minimize the effect of station relocations. Discontinuities have been adjusted (Li *et al.*, 2004a; 2004b). Detailed descriptions of data quality control and homogenization procedure are available in the above papers.

The TP in China ranges from approximately 26° to 40 °N and from 73° to 105 °E (Zhang *et al.*, 2002), and there are 156 stations in the original dataset within this area. As coverage in the western TP is extremely patchy, the 71 stations above 2000 m a.s.l. are selected in the eastern and central TP with complete data for 1961–2004 for comparison with the reanalysis products (Figure 1). More details regarding station selection are described in our previous papers (You *et al.*, 2008a, 2008b).

2.2. Reanalysis datasets

Monthly mean 2 m surface air temperatures for NCEP/NCAR were downloaded from the National Oceanic and Atmospheric Administration – Cooperative Institute for Research in Environmental Sciences (NOAA-CIRES) Climate Diagnostics Centre (http://www.cdc.noaa.gov/). The NCEP/NCAR reanalysis is a continually-updated gridded dataset representing the state of the Earth's atmosphere, incorporating observations (such as ship, rawinsonde, pibal, aircraft, satellite, and other data) with numerical weather prediction model output, quality controlling and assimilating these data with a data assimilation system. This dataset covers January 1948 to the present with a spatial resolution of 2.5° × 2.5° (Kalnay *et al.*, 1996) and sub-daily temporal resolution. The NCEP/NCAR 2 m air temperature is a standard modelled field, which represents a linear interpolation between the surface skin temperature and free-air temperature at the lowest model sigma level (Kalnay *et al.*, 1996).

Monthly mean 2 m surface air temperature ERA-40 reanalysis data were obtained from the European Centre for Medium-Range Weather Forecasts website (http://www.ecmwf.int/). ERA-40 temperatures are available from September 1957 to August 2002 with a spatial resolution of 2.5° × 2.5° (Uppala *et al.*, 2005). The data include satellite-borne instruments, observations from aircraft, ocean-buoys, radiosonde and other surface platforms, but with a declining number of radiosonde ascents since the late 1980s. ERA-40 2 m air temperature is a post-processing product and is obtained by interpolation between the lowest model level and the surface (Uppala *et al.*, 2005). ERA-40 is the most recent comprehensive reanalysis and the first to provide an alternative to the earlier NCEP/NCAR reanalysis for the years before 1979 (Bengtsson *et al.*, 2004). Periods of 1961–2004 and 1961–2001 were selected from NCEP/NCAR and ERA-40 data, respectively.

2.3. Spatial comparision of datasets

To compare with surface stations, two slightly different approaches were investigated to identify the appropriate reanalysis value for comparison with the observed values. One is to compare the surface stations with reanalyses grid points with at least one surface station in the

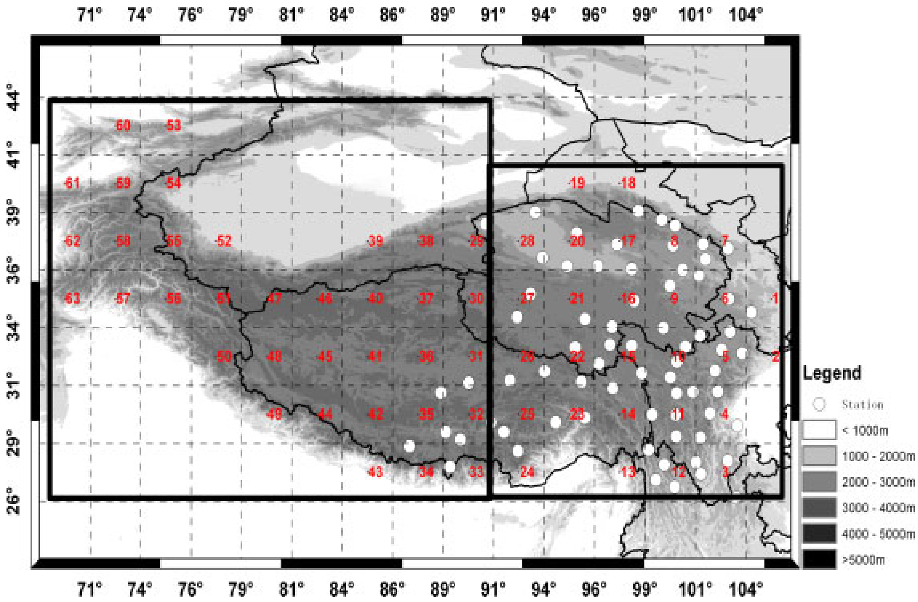

Figure 1. Topography of Tibetan Plateau (labelled 1–63). The white dots represent the 71 stations and the red numbers show the reanalysis grid points in the whole TP. The whole TP was subdivided into two parts by the rectangle: the eastern TP (labelled 1–28) and western TP (labelled 29–63).

immediate vicinity. This includes 29 grid points (labelled 1–35 in Figure 1 with the exception of 2, 13, 14, 18, 19 and 30). Surface stations are assigned to their nearest grid point (based on distance) and data from all the relevant stations are averaged for a given grid point. This average is not weighted by distance or corrected according to elevation, which means that the differences in elevation and/or location distribution between the stations and the grid point may be important (see Section 4). The other is to compare surface stations with reanalysis point obtained from the weighted average of the reanalysis values of the four grid boxes whose centers lie closest to the station. The average of the four grid boxes is obtained using the inverse distance weighted average (Mooney *et al.*, 2011). Both methods shows the grid points from reanalysis have higher correlation coefficients with the observations, and the bias between two methods are very lower, suggesting both methods have no significant influence on the results (not shown). Thus, the first and simple comparison method is adopted for subsequent study.

2.4. Surface elevation data and trend calculations

Surface elevations come from four datasets: (1) elevation of each surface station provided by the NMI/CMA, (2) NCEP/NCAR reanalysis model topography (available from website http://www.cdc.noaa.gov/), (3) ERA-40 reanalysis model topography (available from http://www.ecmwf.int/), and (4) GTOPO30 digital elevation data (available from http://eros.usgs.gov).

The Mann-Kendall test for a trend and Sen's slope estimates were used to detect and estimate trends in annual and seasonal (winter: DJF; spring: MAM; summer: JJA; autumn: SON) mean temperature series (Sen, 1968). A trend is considered to be statistically significant if it is significant at the 5% level ($P < 0.5$). The formula is as follows:

The Mann–Kendall statistic S is calculated as:

$$S = \sum_{k=1}^{n-1} \sum_{j=k+1}^{n} sgn(x_j - x_k) \cdots sgn(x_j - x_k)$$

$$= \left\{ \begin{matrix} +1 & \text{if} & x_j - x_k > 0 \\ 0 & \text{if} & x_j - x_k = 0 \\ 1 & \text{if} & x_j - x_k < 0 \end{matrix} \right\}$$

The variance for the statistic S is defined by:

$$\mathrm{Var}(S) = \frac{n(n-1)(2n+5) - \sum_{p=1}^{q} t_p(t_p - 1)(2t_p + 5)}{18}$$

The test statistic Z is estimated as:

$$Z = \begin{cases} \dfrac{S-1}{\sqrt{\mathrm{VAR}(S)}} & \text{if} \quad S > 0 \\ 0 & \text{if} \quad S = 0 \\ \dfrac{S+1}{\sqrt{\mathrm{VAR}(S)}} & \text{if} \quad S < 0 \end{cases}$$

In which Z follows a standard normal distribution, If $|Z| > Z_{1-\alpha/2}$, where α denotes the significant level, then the trend is significant. Sen's method is used to estimate the Kendall slope, and it is defined as the median over all combinations of record pairs for the whole dataset. It is given as follows:

$$Q = \mathrm{Median}\left(\frac{x_j - x_k}{j - k}\right); i = 1, \ldots, N.$$

The Mann-Kendall test is a nonparametric method without considering distribution of the observational data, and has been widely used to perform trends in climate variables, such as temperature (Xu *et al*., 2008), precipitation (Liu *et al*., 2011a, 2011b) and extreme climate series (You *et al*., 2008a, 2008b). Meanwhile, the scientific communities of hydrology and water resources prefer the Mann-Kendall test. For example, the method was applied to analyse the river discharge during 1956–2000 (Cao *et al*., 2006), pan evaporation and vapour pressure in the TP (Liu *et al*., 2011a, 2011b).

3. Comparing TP near surface air temperature datasets: means and trends

Climatological means and half-century trends of the temperature datasets are analysed and compared with related studies before discussing the results.

3.1. Current climatology: surface stations and reanalysis data

Figure 2 shows the relationship between mean seasonal (MAM, JJA, SON, DJF) temperatures at each individual surface station and those from the nearest NCEP/NCAR and ERA-40 reanalysis grid point during 1961–2004. Subpanels give the seasonal breakdown. Each grid point is included only once. Descriptive statistics summarizing relationships between surface temperature and reanalysis temperatures are listed in Table I.

NCEP/NCAR shows a fairly good spatial correlation with the surface stations (a correlation of 0.58 on an annual basis) (You *et al*., 2010a). The strongest correlation occurs in winter ($R = 0.69$) (Table I). In most cases and seasons, the values of NCEP/NCAR are located to the right of the diagonal line of equality in Figure 2, meaning that NCEP/NCAR has a cold bias (Figure 1). ERA-40, on the other hand, shows a less systematic bias, revealing that the difference between stations and ERA-40 is smaller (Figure 1). Correlations are also usually slightly higher than with NCEP/NCAR. Like NCEP/NCAR, the weakest correlation occurs in summer with a value of 0.47 and the strongest in winter (0.77) (Table I). This is probably related to the enhanced latitudinal and elevational gradients in temperature across the domain in winter, making spatial patterns easier to model.

Compared with NCEP/NCAR, ERA-40 has higher correlation coefficients and lower standard deviations (Table I), indicating that it is more consistently closer to surface observations. This finding is consistent with other studies (Frauenfeld *et al*., 2005; Zhao and Fu, 2006; Ma *et al*., 2008; Zhao *et al*., 2008). This capability to produce a more realistic analysis of surface temperatures stems from improvements in observing systems, techniques of data assimilation, and the realism of the assimilating model (Simmons *et al*., 2004). ERA-40 has benefited from many of these more than NCEP/NCAR has. In

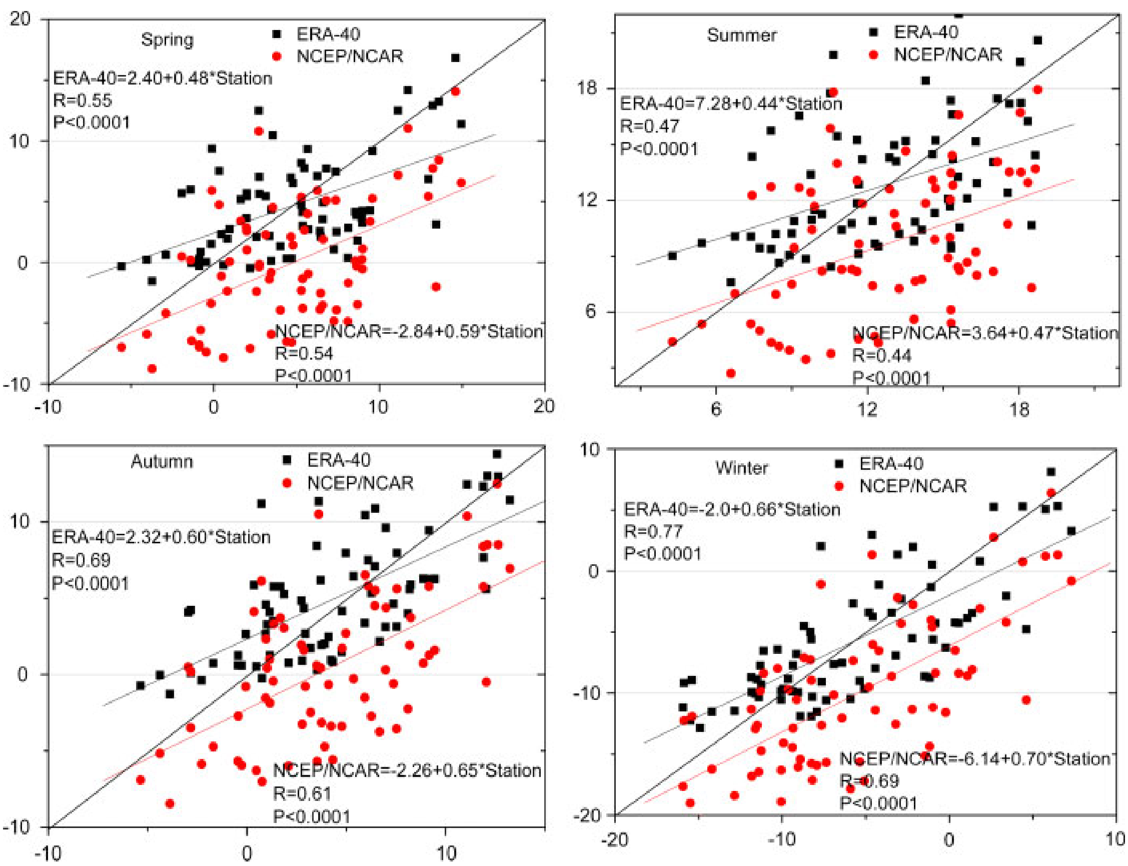

Figure 2. Comparison of temperature of surface stations during 1961–2004 with temperature from NCEP/NCAR and ERA-40 reanalysis data on a seasonal basis. The straight lines are linear fits, and R stands for correlation coefficients and P for statistical significance.

Table I. Descriptive statistics of relationships between surface temperature of stations and that from reanalysis on an annual and seasonal basis. The study period periods for stations, NCEP/NCAR and ERA-40 are during 1961–2004, 1961–2004 and 1961–2001. The linear fits formula (Reanalysis $= a + b^*$ Stations) is used. R stands for correlation coefficients and P for statistical significance.

		a	b	Standard deviation	R	P value
NCEP/NCAR	Annual	−2.50	0.61	3.98	0.58	<0.0001
	Spring	−2.84	0.59	4.29	0.54	<0.0001
	Summer	3.65	0.47	3.50	0.44	<0.0001
	Autumn	−2.26	0.65	3.81	0.61	<0.0001
	Winter	−6.14	0.70	4.39	0.60	<0.0001
ERA-40	Annual	3.12	0.54	2.83	0.66	<0.0001
	Spring	2.40	0.48	3.42	0.55	<0.0001
	Summer	7.28	0.44	2.97	0.47	<0.0001
	Autumn	2.32	0.60	2.83	0.69	<0.0001
	Winter	−2.0	0.66	3.31	0.77	<0.0001

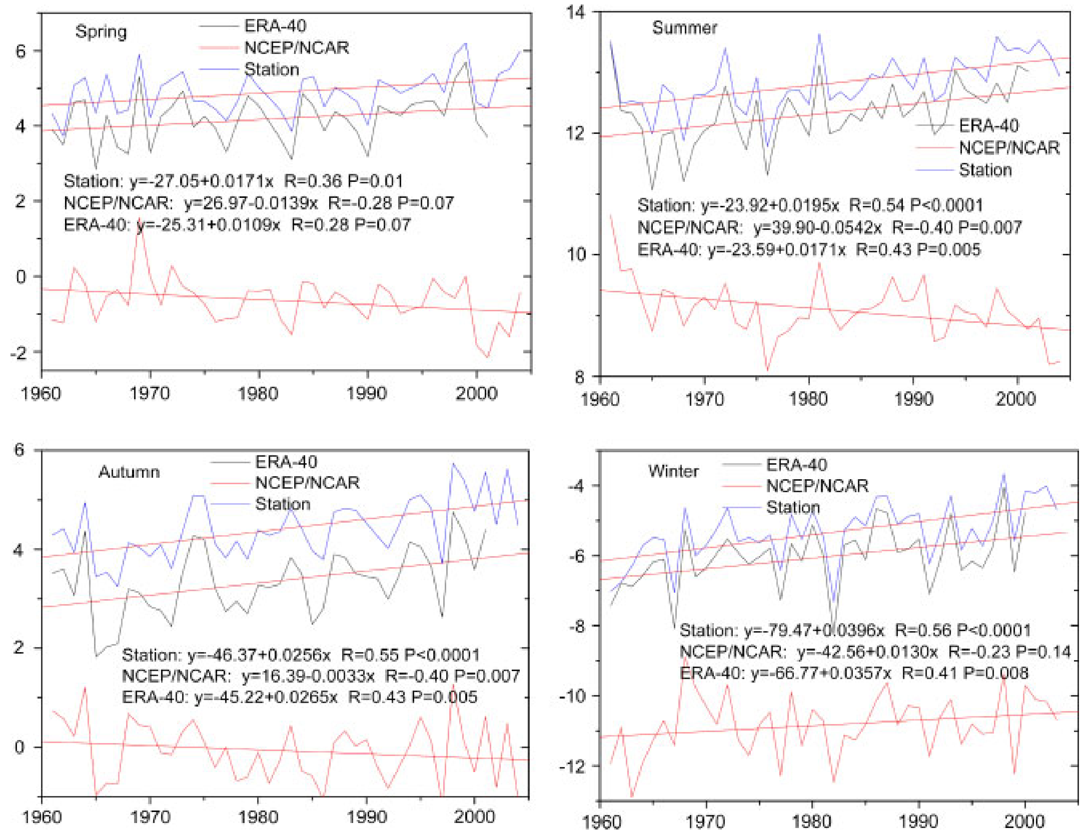

Figure 3. Average regional trends for surface stations, NCEP/NCAR and ERA-40 during 1961–2004 on a seasonal basis. Other is same as Figure 2.

particular, ERA-40 uses surface synoptic observations but NCEP/NCAR does not and is more dependent on free-air forcing (Simmons *et al.*, 2004).

3.2. Temperature trends from surface stations and reanalysis data

Figure 3 shows regional temperature trends (based on calculating the unweighted mean temperature of all stations or grid points for each year solely for the geographical area of overlap between surface stations and reanalysis) for surface stations, NCEP/NCAR and ERA-40 during 1961–2001 on a seasonal basis. The surface stations show a mean regional temperature trend of 0.25 °C/decade (as in You *et al.*, 2010a). Stations in the northwestern, southwestern and southeastern TP have the largest trends, in agreement with previous analysis of temperature extremes (You *et al.*, 2008a). Although the regional trend is dominated by warmer winter (0.40 °C/decade) and autumn (0.26 °C/decade), consistent with the previous study by Liu and Chen (2000) and Ren *et al.* (2005) warming occurs in all seasons. Rising

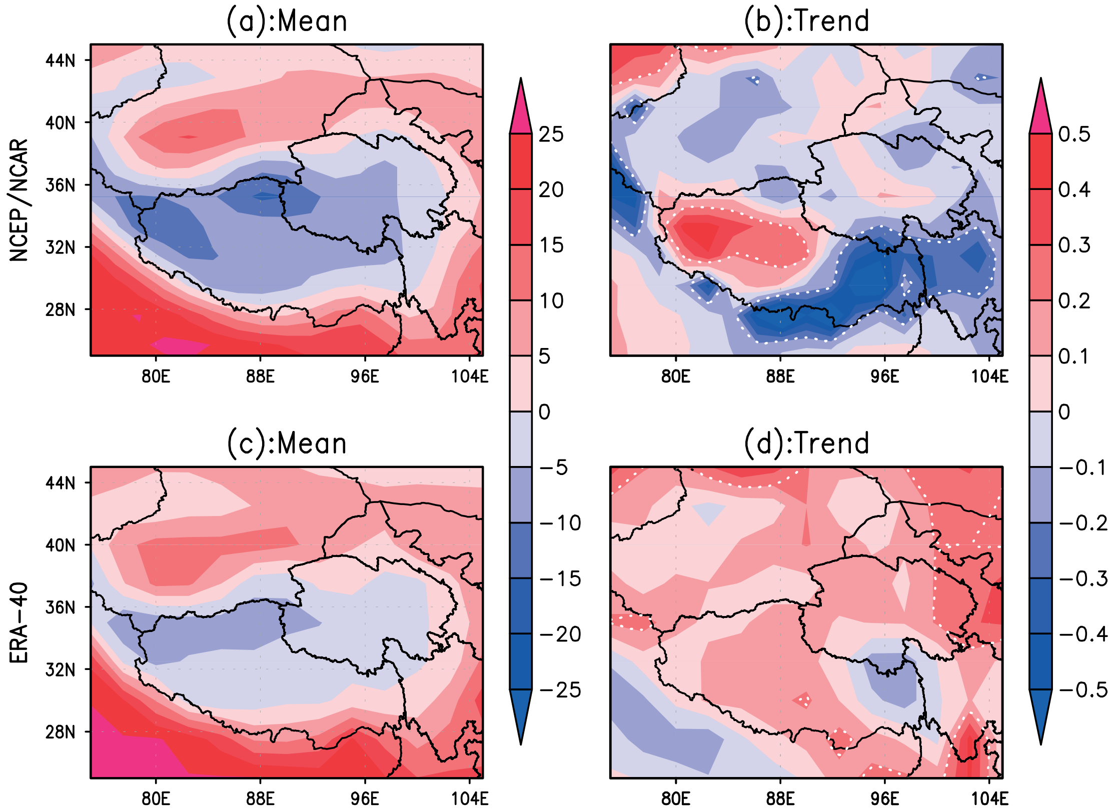

Figure 4. Spatial distribution of annual mean temperature (left plot, unit:° C/decade) and temperature trend magnitudes (right plot, unit:° C/decade) based on NCEP/NCAR and ERA-40 during 1961–2004 and 1961–2001, respectively.

temperatures are accompanied by abundant evidence of dramatic glacier shrinkage in the TP (Zhang, 2007).

For NCEP/NCAR, the regional annual temperature trend (unweighted mean of all grid points) shows a slight decrease (−0.02 °C/decade) and many grid points in the southeastern TP have decreasing trends (Figure 4). A large cooling trend also occurred in the southwestern region of the grid, mainly in northern India (Figure 4). On a seasonal basis, the regional temperature trend is positive only in winter (0.13 °C/decade) and cooling occurs in spring, summer and autumn. The cooling trend from NCEP/NCAR in the TP is quite different from other regions in the world (Simmons *et al*., 2004; Ma *et al*., 2008).

For ERA-40, the regional annual temperature trend is 0.22 °C/decade, and it is strongest in winter (0.36 °C/decade) and autumn (0.27 °C/decade). Most grid points in the southwestern TP have large increasing trends, but there is a cooling trend outside the plateau region in northern India, centering on 73 °E and 28°N (Figure 4). It is therefore possible that both NCEP/NCAR and ERA40 are inaccurately describing the climate change in that region. If the cooling is real, it may be related to the anthropogenic emission of air pollutants with an increase in population and industrialization in the region. Air pollutants from this region lead to a brownish haze, reducing the surface solar insolation and cooling the surface (Krishnanl and Ramanathan, 2002). This aspect definitely needs further study.

4. Discussions

4.1. Can reanalysis be applied to the TP?

Temperatures in the eastern TP are higher than that in the western TP because of the lower elevations (Frauenfeld *et al*., 2005). Owing to the relatively higher terrain and inaccessibility, long-term observational data in the western TP are lacking. Thus, other methods have been used to examine climate change in this region. Rangwala *et al*. (2010) used simulated output from two model experiments (SRES A1B and control) and showed that the western TP had relatively greater warming than the eastern TP during the late 20th and the 21st centuries, although the comparisons between warming rates varied significantly with the observation period (Rangwala *et al*., 2009).

There is scarce surface observational data in the western TP. Since ERA-40 is a good representation of surface trends in the eastern TP, assuming this is the case in the western TP we can extend our examination of ERA-40 temperature trends to 63 grid points to capture the larger area (Figure 1). Figure 5 shows the regional temperature trend for the whole TP (63 grid points), eastern TP (29) and western TP (34) based on ERA-40 during 1961–2001. Mean temperature trend magnitudes and average air temperatures during the same period are listed in Table II. The mean temperatures in the western TP are lower than in the east because of higher elevations.

Table II. Temperature trend magnitudes and average air temperature for the whole TP, eastern TP and western TP based on ERA-40 during 1961–2001 on an annual and seasonal basis. Bold values indicate trends with significance level higher than 95%. Units are degree per decade.

		Annual	Spring	Summer	Autumn	Winter
Trend magnitudes	Whole TP	3.44	4.06	13.28	3.52	−7.11
	Eastern TP	4.33	5.17	13.77	4.13	−5.77
	Western TP	2.73	3.17	12.90	3.03	−8.18
Average air temperature	Whole TP	**0.14**	0.04	0.04	**0.19**	**0.29**
	Eastern TP	**0.21**	0.12	**0.19**	**0.27**	**0.31**
	Western TP	0.09	0.01	−0.08	**0.14**	**0.30**

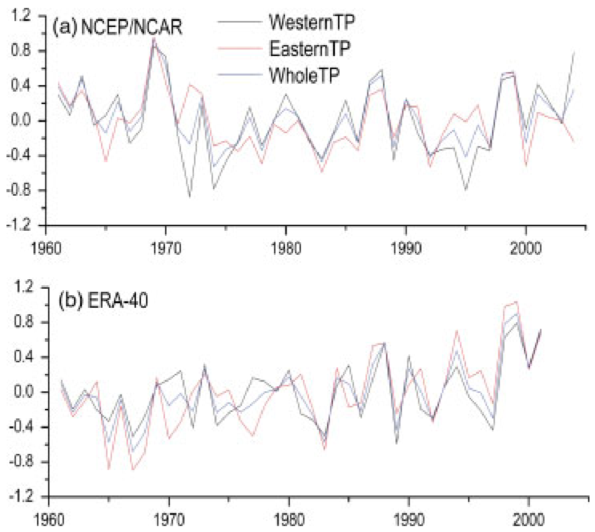

Figure 5. Average annual regional trends for the whole TP, eastern TP and western TP based on NCEP/NCAR (a) and ERA-40 (b) during 1961–2004 and 1961–2001, respectively.

Correlations between regional mean annual temperature for the whole TP, the eastern and western TP are 0.49 and 0.51, respectively. Figure 5 indicates that the variability of temperature based on ERA-40 is quite different in different regions. The regional air temperature for the whole TP is increasing, with a rate of 0.14 °C/decade, and trends are more prominent in winter and autumn (Table II). Although both the eastern and western TP show warming trends, especially in winter, the trends in the east appear to be larger (0.21 °C/decade) than in the west (0.09 °C/decade). This is inconsistent with model output results by Rangwala *et al.* (2010). It is notable that temperature trend assessment using reanalysis data is sometimes dangerous because of the changes in the amount and quality of assimilation data. For example, changes of data source can result in climatic jumps and produce spurious trends before and after the late 1970s because of different assimilation datasets (Frauenfeld *et al.*, 2005).

There are two issues should be paid attention in the TP. One is the interpolating methods. The interpolating temperature from a coarse resolution into a finer resolution, can improve the results in the region with complex topography, but the interpolation method can also produce obvious bias between reanalysis and observation. The other is that the western TP has low density of stations, which need more multi-datasets such as remote sensing and field observation, to improve the scientific understanding. To summarize, the primary problem associated with climate analysis in the western TP is the lack of good horizontal resolution of historic climate records (Xu *et al.*, 2008).

4.2. Can the 'observation minus analysis' method be used in the TP?

NCEP/NCAR clearly does not represent surface conditions well and is more representative of regional scale free atmosphere conditions. The 'observation minus reanalysis' (OMR) method calculated by the difference between observation and reanalysis, has been used with NCEP/NCAR to estimate the impact of surface properties (including urbanization and agricultural practices such as irrigation) on climate trends. Several studies therefore compute the trend in the difference between surface observations (which reflect all the sources of climate forcing, including surface effects) and NCEP/NCAR reanalysis (which only contains forcing influencing assimilated free-atmospheric trends) (Kalnay and Cai, 2003; Lim *et al.*, 2005, 2008; Nunez *et al.*, 2008). Pepin and Seidel (2005) take a similar approach to examine 'real' trends in surface/free-air temperature differences at mountain sites. Figure 6 shows the standardized anomaly of regional OMR for both NCEP/NCAR and ERA-40 on an annual and seasonal basis during 1961–2004. In general, seasonal trends of OMR for both reanalyses are similar to their annual trends. The OMR for ERA-40 shows a limited trend because ERA-40 uses surface air temperatures in the initialization of soil temperature and moisture, indicating that ERA-40 includes not only assimilated free atmospheric trends but also surface effects. In order to know whether NCEP/NCAR and ERA-40 are converging in describing the climatology and changes in the free atmosphere, the annual mean temperature differences between 1981–2001 and 1961–1980 at 850, 600, 400 and 200hPa are analysed (Figure 7), and the right and left plots are for NCEP/NCAR and ERA-40 reanalysis data respectively. It is clear that both the differences between NCEP/NCAR and ERA-40 are apparently larger at lower troposphere, and both reanalyses become more similar at upper tropospheric levels (400 and 200 hPa).

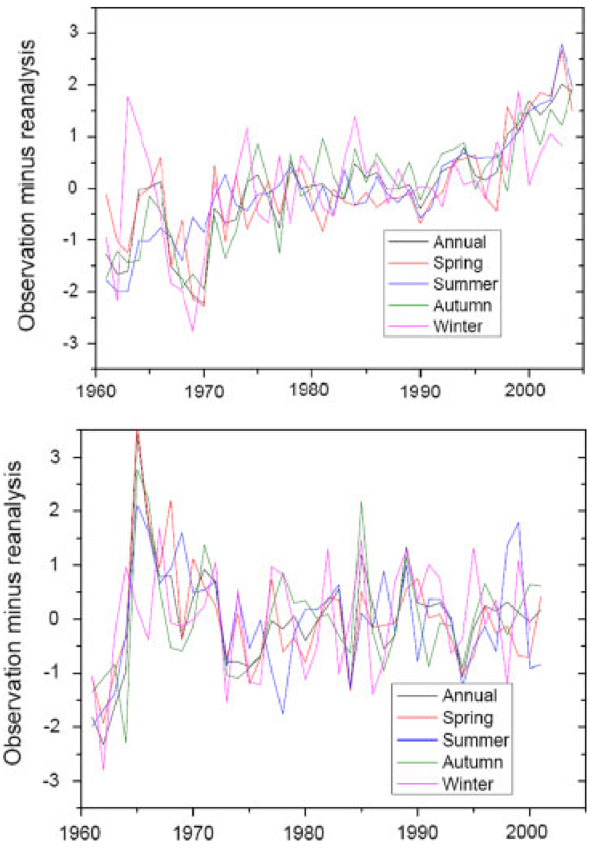

Figure 6. The anomaly of standard deviation for observation minus reanalysis (OMR) for NCEP/NCAR (top plot) and ERA-40 (bottom plot) during 1961–2004 and 1961–2001, respectively.

Since 1990, the OMR for NCEP/NCAR has increased dramatically, coinciding with rapid urbanization and dramatic economic growth in southeastern China (Zhou *et al.*, 2004). The regional diurnal temperature range (DTR) for the surface component also exhibits a statistically decreasing trend at a rate of −0.20 °C/decade during the same period (You *et al.*, 2008a). The positive OMR trend is likely therefore partly to be the result of extensive local and regional land use changes (Kalnay and Cai, 2003; Nunez *et al.*, 2008), which have been reported in eastern China (Zhou *et al.*, 2004). A recent analysis (Zhang *et al.*, 2010) shows that urbanization-induced increase of annual mean surface air temperature in the lower parts of the TP during 1961–2004 reaches 0.06 °C/decade, accounting for about 23% of the overall warming recorded by the commonly used national observation stations. Thus, the regional surface mean temperature trend in the TP (0.25 °C/decade) probably includes the combined effects of urbanization and large-scale surface forcing. According to the China Compendium of Statistics (Department of Comprehensive Statistics of the National Bureau of Statistics, 2006), the total population during the 1990s doubled from that of the 1960s, and the total sown area increased by 50% between 1961 and 2004 for the Tibet Autonomous region as a whole (Figure 8). A general atmospheric circulation model (ECHAM5) also indicates that human-induced land use changes in the TP have had a significant impact on local and regional climate (Cui *et al.*, 2006). Increasing OMR in all seasons from our analysis also strengthens the case for additional surface forcing on climate change in the TP.

4.3. Can the temperature differences between stations and reanalysis be modeled in the TP?

In summary, both the instantaneous climatology and pattern of temperature trends appear to be more similar to the surface stations when using ERA-40 rather than NCEP/NCAR. Further analysis has examined how the differences in temperatures can be explained by model topography. The complex elevated topography of the TP means that the differences in elevation between surface stations and the ERA-40 and NCEP/NCAR reanalyses model elevations are not trivial (Zhao and Fu, 2006; Ma *et al.*, 2008). The model elevation is often higher than the surface stations elevation because stations are located preferentially in flat or valley bottom locations. Classifying each of the 71 stations into one of three topographic types (summit, flat or valley) using a definition based on the relative heights of surrounding grid cells derived from GTOPO30 digital elevation data (You *et al.*, 2008b) demonstrates this point (You *et al.*, 2010a).

In previous paper (You *et al.*, 2010a), we have analysed the relationships between annual air temperature differences (station minus reanalysis, dT) and elevation differences (mean surface station minus reanalysis model elevation, dH) for NCEP/NCAR and ERA-40 during 1961–2004. There is a negative correlation between dT and dH in both reanalyses, but the relationship is much stronger in ERA-40, annually and seasonally. Most of the temperature bias in ERA-40 is therefore due to the elevation difference, highlighting the possibility of 'topographic correction' and removal of 'elevation-induced bias' when evaluating reanalysis data (Zhao *et al.*, 2008). In most cases, the model elevation in ERA-40 is lower than that in NCEP/NCAR (Figure 6 in You *et al.*, 2010a), resulting in higher surface temperature in ERA-40. This is consistent with the conclusions in Ireland that the discrepancies between reanalysis and observations result from the difference in the treatment of land and sea surfaces in the reanalysis datasets (Mooney *et al.*, 2011).

Although elevation accounts for a lot of the bias, aspect and slope could also be influential. Aspect and slope at each grid point are extracted from GTOPO30 digital elevation data. Temperature trend magnitudes were compared with aspect and slope for stations, NCEP/NCAR and ERA-40 data on an annual basis (not shown). In most cases, there is a slight negative relationship between temperature trend magnitudes and aspect as well as slope for stations, NCEP/NCAR and ERA-40. This suggests that change in topographic slope or station orientation should influence the trend magnitudes to a certain degree.

Topography also influences temperature trend magnitudes, which is consistent with other studies. Dobrowski *et al.* (2009) show that both regional synoptic-scale and landscape-scale physiographic factors control patterns of

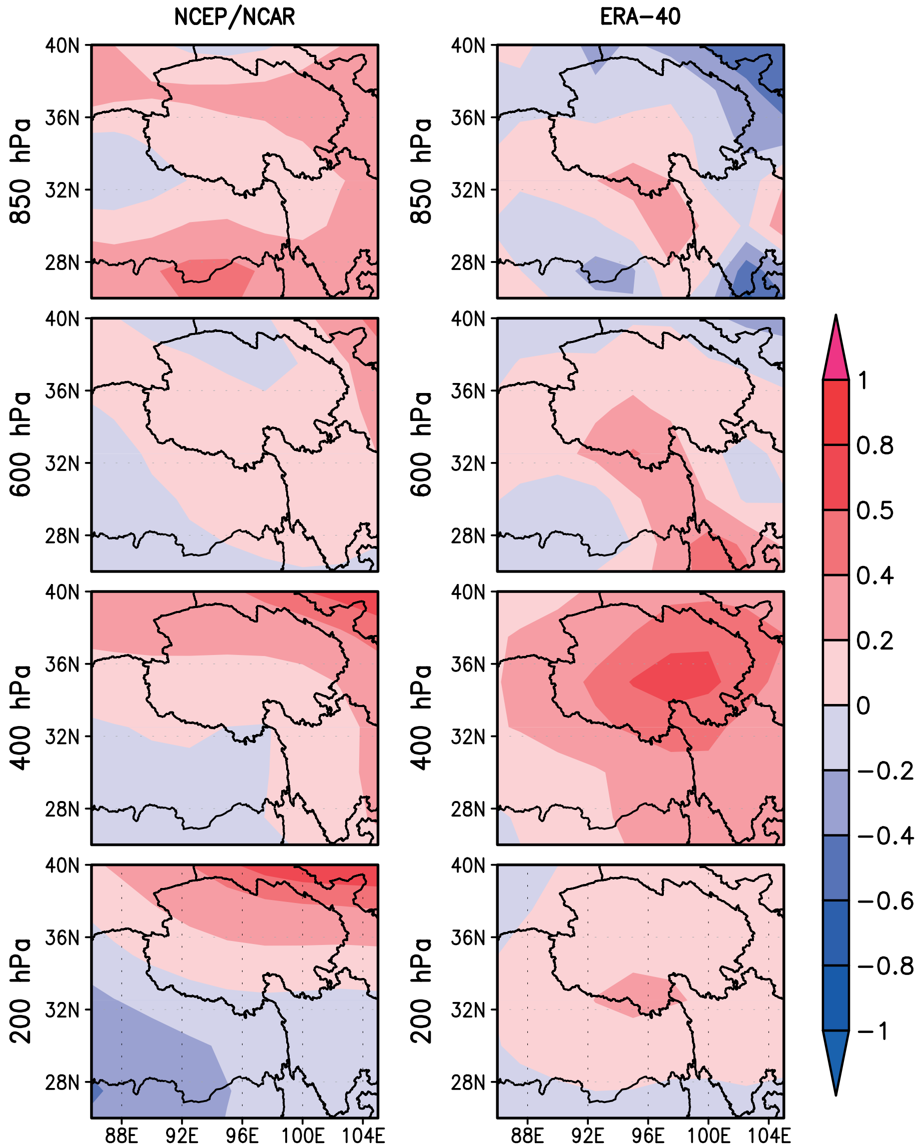

Figure 7. Annual mean temperature differences between 1981–2001 and 1961–1980 at 850, 600, 400 and 200hPa, and the right and left plots are for NCEP/NCAR and ERA-40 reanalysis data respectively.

temperature in mountain environments, and Thomas and Herzfeld (2004) try to generate new climatic data for East Asia based on localized relief information and geostatistical methods. Furthermore, on a daily basis the difference between the surface and free-air datasets is also correlated with meteorological factors such as snow cover, cloud cover and wind vectors, illustrating the importance of local surface radiative exchange at mountain locations (Pepin and Seidel, 2005). More attention to such issues should be given when examining trends in the TP from different sources, since topographical differences between grid point and station locations are clearly related to mean bias and differences in trend magnitudes and patterns (You *et al*., 2010a).

5. Conclusions

We have compared observed surface temperatures and their trends based on 71 homogenized surface stations with elevations above 2000 m a.s.l. in the eastern and central TP with equivalent temperatures at the nearest NCEP/NCAR and ERA-40 reanalysis grid points. The regional annual mean trend of 0.25 °C/decade is substantiated by many environment consequences, such as glacier shrinkage and land degradation. The warming in the surface stations is on average stronger than in both reanalyses. Although ERA-40 shows pronounced warming on an annual and seasonal basis, the regional annual mean trend is slightly less steep than surface stations, and most temperature trend magnitudes at grid points are lower than at individual surface stations. NCEP/NCAR fails to capture any warming trends with the exception of winter and the regional annual mean temperature trend is negative. As was the case for current climatology, ERA-40 is much more similar to the surface stations and captures the surface warming trends better than NCEP/NCAR on an annual and seasonal basis. NCEP/NCAR and ERA-40 are similar in representing

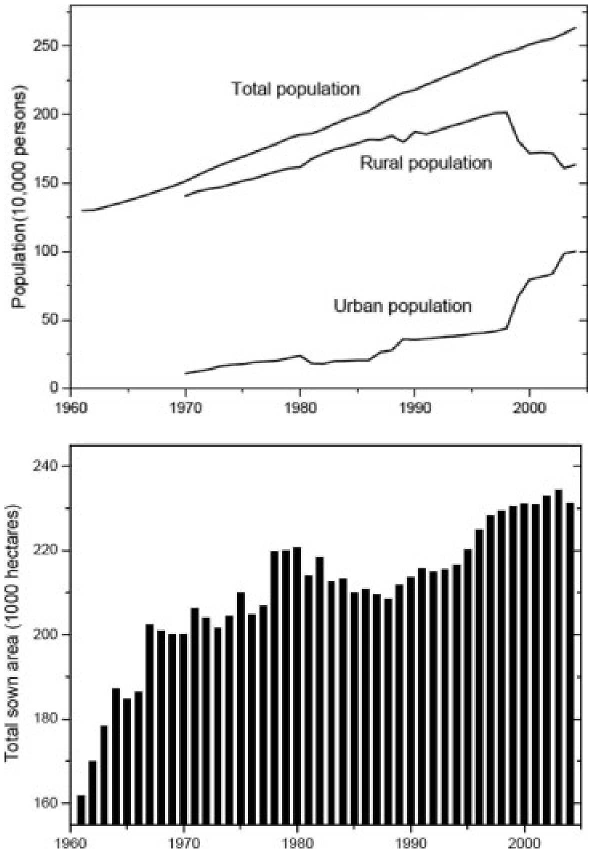

Figure 8. The total population grouped by residence (top plot) and total sown area (bottom plot) of Tibet Autonomous region during 1961–2004.

the free atmospheric conditions over the TP; however, NCEP/NCAR is not as good at representing surface temperatures or their trends in the TP.

Using ERA-40, we assess temperature trend magnitudes and mean temperature for the whole, eastern and western sections of the TP. Both the eastern and western TP show warming trends, especially in winter, but the trend in the eastern TP is larger (0.21 °C/decade) than in the west (0.09 °C/decade). Since NCEP/NCAR largely represents the free atmosphere, the OMR method has been used to estimate the impact of changes in land use (including urbanization and agricultural practices such as irrigation) by computing the trend in the difference between surface and NCEP/NCAR temperatures. The regional OMR trend is significantly increasing, which corresponds with a rapidly increasing urban population and an increase in total sown area. Our results further strengthen the case for using surface station in the TP to represent surface climate should be acknowledged the land use changes.

Correlations between air temperature differences ($\mathrm{d}T$) and elevation differences ($\mathrm{d}H$) shows that there are significant negative correlations for NCEP/NCAR and ERA-40. In most cases, the elevation differences (model elevation minus surface stations elevation) are positive because surface stations are situated in flat areas and valley bottoms which are lower than the reanalysis model topography. In ERA-40, the elevation difference is the main reason for the cold biases but the pattern is less systematic for NCEP/NCAR. The relationships between temperature trend magnitudes and aspect as well as slope for stations, NCEP/NCAR and ERA-40 data show that changes in topographic slope or station orientation should influence the trend magnitudes in the TP to a certain degree. Because much of the variation between ERA-40 and the surface stations is explained by topography, we suggest topographic correction is made to remove most of the elevation induced bias when making future comparisons.

Acknowledgements

This study is supported by the Global Change Research Program of China (2010CB951401), the Chinese Academy of Sciences (KZCX2-YW-145) and the National Natural Science Foundation of China (40870743). The China postdoctoral science foundation (the 49th) is also appreciated. This study became possible through a Sino-Swiss Science and Technology Cooperation (SSSTC) research grant (EG76-032010 and EG23-092011). The authors thank the National Meteorological Information Center, China Meteorological Administration (NMIC/CMA), for providing the data for this study. Qinglong You is supported by the Alexander von Humboldt Foundation. We are very grateful to the reviewers for their constructive comments and thoughtful suggestions.

References

Barnett TP, Pierce DW, AchutaRao KM, Gleckler PJ, Santer BD, Gregory JM, Washington WM. 2005. Potential impacts of a warming climate on water availability in snow-dominated regions. *Nature* **438**: 303–309.

Bengtsson L, Hagemann S, Hodges KL. 2004. Can climate trends be calculated from reanalysis data?. *Journal of Geophysical Research-Atmospheres* **109**: D11111.

Bothe O, Fraedrich K, Zhu XH. 2010. The large-scale circulations and summer drought and wetness on the Tibetan plateau. *International Journal of Climatology* **30**: 844–855.

Cao JT, Qin DH, Kang ES, Li YY. 2006. River discharge changes in the Qinghai-Tibet Plateau. *Chinese Science Bulletin* **51**(5): 594–600.

Cui XF, Graf HF, Langmann B, Chen W, Huang RH. 2006. Climate impacts of anthropogenic land use changes on the Tibetan Plateau. *Global and Planetary Change* **54**: 33–56.

Department of Comprehensive Statistics of National Bureau of Statistics. 2006. *China Compendium of Statistics 1949–2004*. China Statistics Press: Beijing.

Dobrowski SZ, Abatzoglou JT, Greenberg JA, Schladow SG. 2009. How much influence does landscape-scale physiography have on air temperature in a mountain environment? *Agricultural and Forest Meteorology* **149**(10): 1751–1758.

Duan AM, Wu GX. 2005. Role of the Tibetan Plateau thermal forcing in the summer climate patterns over subtropical Asia. *Climate Dynamics* **24**: 793–807.

Frauenfeld OW, Zhang TJ, Serreze MC. 2005. Climate change and variability using European Centre for Medium-Range Weather Forecasts reanalysis (ERA-40) temperatures on the Tibetan Plateau. *Journal of Geophysical Research-Atmospheres* **110**: D02101.

Kalnay E, Cai M. 2003. Impact of urbanization and land-use change on climate. *Nature* **423**: 528–531.

Kalnay E, Kanamitsu M, Kistler R, Collins W, Deaven D, Gandin L, Iredell M. 1996. The NCEP/NCAR 40-year reanalysis project. *Bulletin of the American Meteorological Society* **77**: 437–471.

Kang S, Zhang YJ, Qin DH, Ren JW, Zhang QG, Grigholm B, Mayewski PA. 2007. Recent temperature increase recorded in an ice core in the source region of Yangtze River. *Chinese Science Bulletin* **52**: 825–831.

Krishnanl R, Ramanathan V. 2002. Evidence of surface cooling from absorbing aerosols. *Geophysical Research Letters* **29**: 1340.

Li, QX, Liu XN, Zhang HZ, Peterson TC, Easterling DR. 2004a. Detecting and adjusting temporal inhomogeneity in Chinese mean surface air temperature data. *Advances in Atmospheric Sciences* **21**: 260–268.

Li QX, Zhang H, Liu X, Huang J. 2004b. Urban heat island effect on Annual Mean Temperature during Recent 50 Years in China. *Theoretical and Applied Climatology* **79**(4): 165–174.

Lim YK, Cai M, Kalnay E, Zhou LM. 2008. Impact of vegetation types on surface temperature change. *Journal of Applied Meteorology and Climatology* **47**: 411–424.

Lim YK, Cai M, Kalnay E, Zhou LM. 2005. Observational evidence of sensitivity of surface climate changes to land types and urbanization. *Geophysical Research Letters* **32**: L22712.

Liu XC, Xu ZX, Yu YH. 2011a. Trend of climate variability in China during the past decades. *Climatic Change* **109**: 503–516.

Liu XM, Zheng HX, Zhang MH, Liu CM. 2011b. Identification of dominant climate factor for pan evaporation trend in the Tibetan Plateau. *Journal of Geographical Science* **21**(4): 594–608.

Liu XD, Chen BD. 2000. Climatic warming in the Tibetan Plateau during recent decades. *International Journal of Climatology* **20**: 1729–1742.

Ma LJ, Zhang TJ, Li QX, Frauenfeld OW, Qin DH. 2008. Evaluation of ERA-40, NCEP/NCAR-1, and NCEP/NCAR-2 reanalysis air temperatures with ground-based measurements in China. *Journal of Geophysical Research-Atmospheres* **113**: D15115.

Mooney PA, Mulligan FJ, Fealy R. 2011. Comparison of ERA-40, ERA-Interim and NCEP/NCAR reanalysis data with observed surface air temperatures over Ireland. *International Journal of Climatology* **31**(4): 545–557.

Nunez MN, Ciapessoni HH, Rolla A, Kalnay E, Cai M. 2008. Impact of land use and precipitation changes on surface temperature trends in Argentina. *Journal of Geophysical Research-Atmospheres* **113**: D06111.

Pepin NC, Seidel DJ. 2005. A global comparison of surface and free-air temperatures at high elevations. *Journal of Geophysical Research-Atmospheres* **110**: D03104.

Qiu J. 2008. The third pole. *Nature* **454**(7203): 393–396.

Rangwala I, Miller JR, Xu M. 2009. Warming in the Tibetan Plateau: possible influences of the changes in surface water vapor. *Geophysical Research Letters* **36**: L06703.

Rangwala I, Miller J, Russell G, Xu M. 2010. Using a global climate model to evaluate the influences of water vapor, snow cover and atmospheric aerosol on warming in the Tibetan Plateau during the twenty-first century. *Climate Dynamics* **34**(6): 859–872.

Ren GY, Xu MZ, Chu ZY. 2005. Change in surface air temperature over China during 1951–2004. *Climatic and Environmental Research* **10**(4): 717–727 (in Chinese).

Sen PK 1968. Estimates of regression coefficient based on Kendall's tau. *Journal of the American Statistical Association* **63**: 1379–1389.

Simmons AJ, Jones PD, Bechtold VD, Beljaars ACM, Kallberg PW, Saarinen S, Uppala SM, Viterbo P, Wedi N. 2004. Comparison of trends and low-frequency variability in CRU, ERA-40, and NCEP/NCAR analyses of surface air temperature. *Journal of Geophysical Research-Atmospheres* **109**: D24115.

Thomas A, Herzfeld UC. 2004. Regeotop: new climatic data fields for East Asia based on localized relief information and geostatistical. *International Journal of Climatology* **24**(10): 1283–1306.

Tian LD, Yao TD, Li Z, MacClune K, Wu GJ, Xu BQ, Li YF, Lu AX, Shen YP. 2006. Recent rapid warming trend revealed from the isotopic record in Muztagata ice core, eastern Pamirs. *Journal of Geophysical Research-Atmospheres* **111**: D13103.

Uppala SM, Kallberg PW, Simmons AJ, Andrae U, Bechtold VD, Fiogino M, Gibson JK, Haseler J. 2005. The ERA-40 re-analysis. *Quarterly Journal of Royal Meteorological Society* **131**: 2961–3012.

Wang B, Bao Q, Hoskins B, Wu GX, Liu YM. 2008. Tibetan plateau warming and precipitation changes in East Asia. *Geophysical Research Letters* **35**: L14702.

Xu ZX, Gong TL, Li JY. 2008. Decadal trend of climate in the Tibetan Plateau – regional temperature and precipitation. *Hydrological Processes* **22**(16): 3056–3065.

Yeh TC, Gao YX. 1979. *Meteorology of the Qinghai-Xizang (Tibet) Plateau (in Chinese)*. Science Press: Beijing.

You QL, Kang SC, Aguilar E, Yan YP. 2008a. Changes in daily climate extremes in the eastern and central Tibetan Plateau during 1961–2005. *Journal of Geophysical Research-Atmospheres* **113**: D07101.

You QL, Kang SC, Pepin N, Yan YP. 2008b. Relationship between trends in temperature extremes and elevation in the eastern and central Tibetan Plateau, 1961–2005 *Geophysical Research Letters* **35**: L04704.

You QL, Kang SC, Pepin N, Fluegel WA, Yan YP, Behrawan H, Huang J. 2010a. Relationship between temperature trend magnitude, elevation and mean temperature in the Tibetan Plateau from homogenized surface stations and reanalysis data. *Global and Planetary Change* **71**(1–2): 124–133.

You QL, Kang SC, Pepin N, Fluegel WA, Sanchez-Lorenzo A, Yan YP, Zhang YJ. 2010b. Climate warming and associated changes in atmospheric circulation in the eastern and central Tibetan Plateau from a homogenized dataset. *Global and Planetary Change* **72**: 11–24.

Zhang YL, Li BY, Zheng D. 2002. A discussion on the boundary and area of the Tibetan Plateau in China. *Geographical Research* **21**: 1–8 (in Chinese).

Zhang T. 2007. Perspectives on environmental study of response to climatic and land Cover/Land use change over the Qinghai-Tibetan Plateau: an introduction. *Arctic Antarctic and Alpine Research* **39**: 631–634.

Zhang AY, Ren GY, Zhou JX. 2010. Urbanization effect on surface air temperature trends over China *Acta Meteorologica Sinica* **68**(6): 957–966 (in Chinese).

Zhao T, Fu C. 2006. Preliminary comparison and analysis between ERA-40, NCEP/NCAR-2 reanalysis and observations over China. *Climate Environmental Research* **11**: 14–32.

Zhao T, Guo W, Fu C. 2008. Calibrating and evaluating reanalysis surface temperature error by topographic correction. *Journal of Climate*: **21**: 1440–1446.

Zhou LM, Dickinson RE, Tian YH, Fang JY, Li QX, Kaufmann RK, Tucker CJ, Myneni RB. 2004. Evidence for a significant urbanization effect on climate in China. *Proceedings of the National Academy of Sciences of the United States of America* **101**: 9540–9544.

Zhu X, Bothe O, Fraedrich K. 2011. Summer atmospheric bridging between Europe and Central Asia: influence on drought and wetness on the Tibetan Plateau. *Quaternary International* **236**: 151–157.

INTERNATIONAL JOURNAL OF CLIMATOLOGY
Int. J. Climatol. **33**: 1444–1455 (2013)
Published online 7 June 2012 in Wiley Online Library
(wileyonlinelibrary.com) DOI: 10.1002/joc.3525

Winter temperature extremes in China and their possible causes

Qinglong You,[a,b,c]* Guoyu Ren,[b] Klaus Fraedrich,[c] Shichang Kang[a,d], Yuyu Ren[b] and Pengling Wang[b]

[a] *Laboratory of Tibetan Environment Changes and Land Surface Processes, Institute of Tibetan Plateau Research, Chinese Academy of Sciences (CAS), Beijing, China*
[b] *Laboratory for Climate Studies, National Climate Center, China Meteorological Administration (CMA), Beijing, China*
[c] *Meteorological Institute, KlimaCampus, University of Hamburg, Hamburg, Germany*
[d] *State Key Laboratory of Cryospheric Science, CAS, Lanzhou, China*

ABSTRACT: Cold and warm temperature extremes predominantly occurring in winter gained much more attention than mean temperatures. On the basis of daily maximum and minimum surface air temperature records at 303 meteorological stations in China, the spatial and temporal distributions of five indices for winter (DJF: December, subsequent January and February) temperature extremes are analysed during 1961–2003. For the majority of stations, the frequency of cold days/nights decreases by −1.33/−2.98 and warm days/nights increases by 0.92/2.35 d/decade, respectively. Cold days/nights are significantly negatively correlated with the Arctic Oscillation (AO) index, while warm days/nights are positively correlated with the AO. The diurnal temperature range (DTR) has a declining trend with rate of −0.25 °C/decade and positive correlation with the AO index. Compared with other regions in China, stations in the northern China have larger trend magnitudes and stronger correlations with the AO index, and the AO can explain more than 50% of winter temperature extreme change in China. Compared with the annual basis, the winter temperature extremes have larger trend magnitudes, which reflect the rapid warming. During strongly positive AO index years, enhanced contrast tropospheric temperature (defined as the average of air temperature vertically integrated between 200 hPa and 1000 hPa based on the National Centers for Environmental Prediction/National Center for Atmospheric Research reanalysis) between the north of China and the southern China weakens the East Asian winter monsoon which in turn reduces cold outbreaks in the northern and eastern China. The composites of large-scale atmospheric circulation are consistent with the asymmetrical changes of the geopotential height, zonal and meridional winds at high and mid latitudes at troposphere. Meanwhile, the linkage between the AO and solar activity also modulates the winter temperature extremes, while the mechanism needs to be investigated.

KEY WORDS temperature extremes; Arctic Oscillation; atmospheric circulation; China

Received 1 October 2011; Revised 16 April 2012; Accepted 1 May 2012

1. Introduction

Extreme climate events can cause property damage, injury and loss of life and understanding their occurrence is very important to natural and human systems (Katz and Brown, 1992; Easterling *et al*., 2000; Aguilar *et al*., 2009). As a consequence, the Fourth Assessment Report of the Intergovernmental Panel on Climate Change (IPCC) paid more attention to climate extremes change (IPCC, 2007). Recent studies on global, regional and national scales have significantly improved the understanding of temperature and precipitation extremes (Peterson *et al*., 2002; Aguilar *et al*., 2005, 2009; Alexander *et al*., 2006; Klein Tank *et al*., 2006; New *et al*., 2006; Brown *et al*., 2008; Peterson and Manton, 2008; Peterson *et al*., 2008; You *et al*., 2008a,b; Choi *et al*., 2009; Caesar *et al*., 2011; You *et al*., 2011a). Most of these studies have been fostered by the World Meteorological Organization (WMO) Joint Expert Team on Climate Change Detection and Indices (ETCCDI) (Peterson and Manton, 2008). They have revealed that cold extremes are generally changing more rapidly than warm extremes, but the exact reasons have not been explored in detail.

The Arctic Oscillation (AO), currently known as Northern Annular Mode, is one of the dominant patterns of Northern Hemisphere climate variability, and it is most prevalent in winter and in the mid and high latitudes. It strongly influences surface air temperatures over the Eurasian continent, especially Europe (Hurrell, 1995; Thompson and Wallace, 1998; 2001; Hurrell *et al*., 2001; Hurrell and Deser, 2010). AO is a major controlling factor in basic meteorological variables such as surface wind, temperature and precipitation (Bojariu and Gimeno, 2003). AO is defined as a hemispheric mode

*Correspondence to: Q. You, Laboratory of Tibetan Environment Changes and Land Surface Processes, Institute of Tibetan Plateau Research, Chinese Academy of Sciences (CAS), Beijing 100085, China. E-mail: yqingl@126.com

whose dipole has suffered a displacement to the West during the last decades (Ramos *et al*., 2010). The AO index has been used to describe the variability of AO in this study.

Recent studies have shown that the winter AO index has a strong positive correlation with temperatures in northern China (Gong and Wang, 2003) and is also correlated with the strength of the East Asian winter monsoon and Siberian Higher pressure system (Gong *et al*., 2001; Wu and Wang, 2002). Since the 1980s, China has experienced significant temperature increases (Wang and Gong, 2000; Ding *et al*., 2007), and warming is projected to continue. Although trends in temperature extremes on the annual basis have been studied (Zhai *et al*., 1999; Zhai and Pan, 2003; Ren *et al*., 2011; You *et al*., 2011a), there have been little investigations of how the AO influences winter temperature extremes. Thus we quantify changes in winter temperature extremes during 1961–2003 throughout China, based on indices designed by the Commission for Climatology/Climate Variability and Predictability/Joint WMO Intergovernmental Oceanographic Commission Technical Commission for Oceanography and Marine Meteorology ETCCDI. The relationships between the AO index and winter temperature extremes are also examined.

2. Data and methods

Daily maximum and minimum temperatures for 303 stations in China are provided by the National Meteorological Information Center, China Meteorological Administration. Both the spatial density of stations and the quality of observational data in China meet the World Meteorological Organization's standards. Stations were selected according to procedures described in our recent papers (You *et al*., 2011a). The selected stations should have the long-term data records and good data quality. The calculation of indices is facilitated using the information provided by ETCCDI (see http://cccma.seos.uvic.ca/ETCCDI for available calculated station-level indices) (Peterson and Manton, 2008). We concentrate on the winter (DJF) variation of five temperature indices (Table I), which have been shown to be most sensitive to climate change in previous studies (You *et al*., 2008a, 2011a). The winter temperature extremes have the same definition as in previous studies (Aguilar *et al*., 2005, 2009; Alexander *et al*., 2006; Klein Tank *et al*., 2006; New *et al*., 2006; You *et al*., 2008a,b; Caesar *et al*., 2011; You *et al*., 2011a). RClimDex software was used to perform data quality control and calculate the indices, and RHtest was used to assess homogeneity. Details about data quality control and homogeneity tests are described in our previous papers (You *et al*., 2008a, 2011a).

The AO index is defined as the difference in the normalized monthly zonal-mean sea level pressure (SLP) between 35 and 65°N (Li and Wang, 2003), derived from http://web.lasg.ac.cn/staff/ljp/data-NAM-SAM-NAO/NAM-AO.htm. Monthly mean geopotential height, air temperature, zonal and meridional wind were obtained from the National Centers for Environmental Prediction/National Center for Atmospheric Research (NCEP/NCAR) reanalysis (available from their website at http://www.cdc.noaa.gov/) (Kalnay *et al*., 1996). The relationships between solar activity and winter temperature extremes are studied in the study and the solar activity is derived from the studies in Kodera (2002) and Ogi *et al*(2003).

The Mann–Kendall test for trends and Sen's slope estimates are used to detect and quantify trends in winter temperature extremes (Sen, 1968), with magnitudes of trends and slopes assessed at the 0.05 significance level ($p < 0.05$).

3. Results

3.1. Winter temperature extremes (TX10, TN10, TX90, TN90 and DTR)

Figure 1 shows the spatial patterns of trend for five winter temperature indices (for 303 meteorological stations) along with the time series of the entire country. Aggregated regional trends of winter temperature extremes are listed in Table II (third column), calculated as the arithmetic mean of all station. The number of stations with negative, no trend and positive trends, as well as the number of stations passing the significant level for each index is also shown in Table II.

For cold days (TX10) and cold nights (TN10), about 97 and 98% of stations have decreasing trends, whereas 31 and 84% of stations are statistically decreasing trends. For TX10, stations in the northern China (such as Gansu province) show larger trend magnitudes, and significant

Table I. Definitions of five winter temperature indices used in this study. All indices are calculated by RClimDeX software.

Index	Descriptive name	Definition	Units
Temperature			
TX10	Cold day frequency	Percentage of days when TX < 10th percentile of 1961–1990	%
TN10	Cold night frequency	Percentage of days when TN < 10th percentile of 1961–1990	%
TX90	Warm day frequency	Percentage of days when TX > 90th percentile of 1961–1990	%
TN90	Warm night frequency	Percentage of days when TN > 90th percentile of 1961–1990	%
DTR	Diurnal temperature range	Annual mean difference between TX and TN	°C

TX is the daily maximum temperature; TN is the daily minimum temperature.

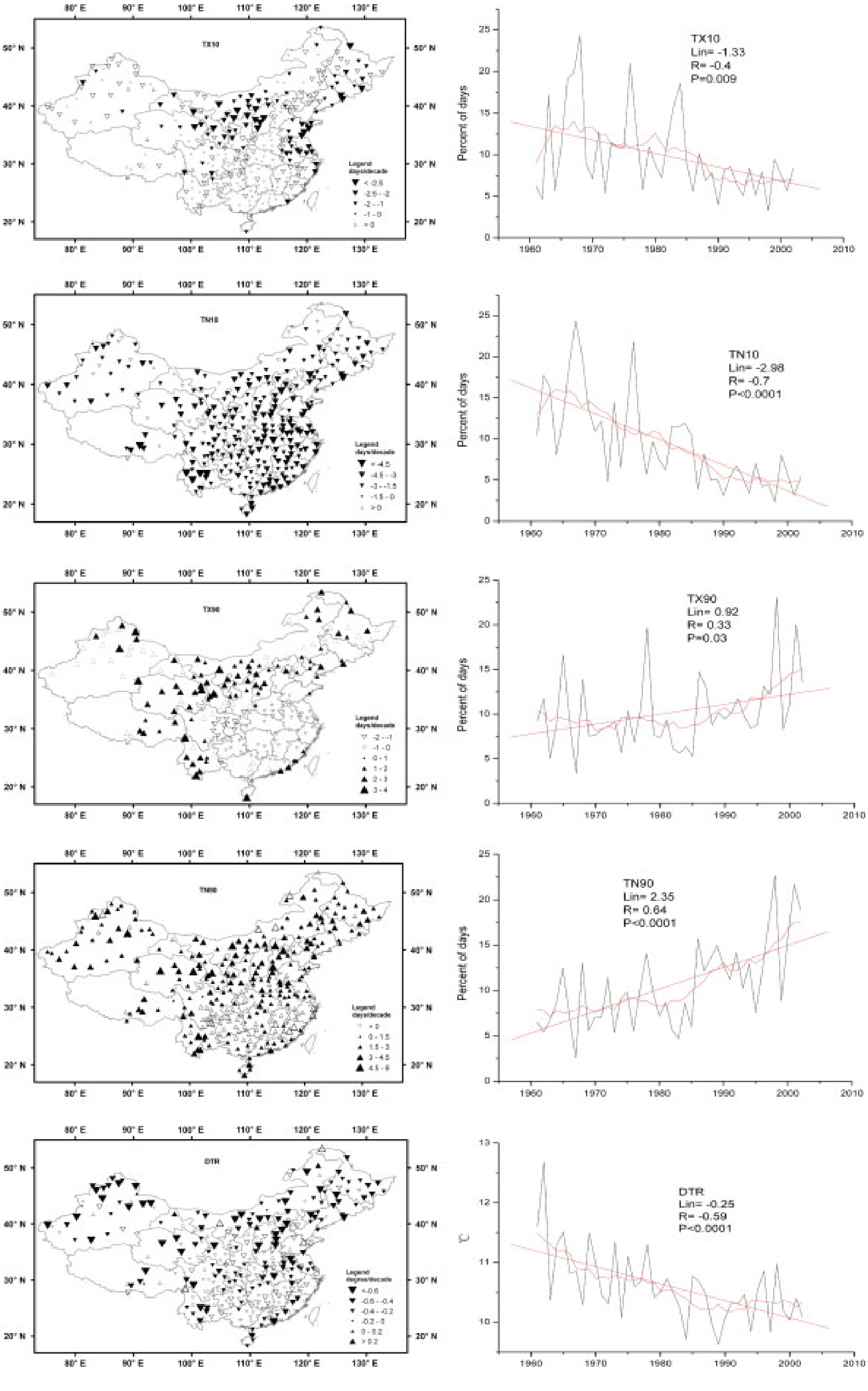

Figure 1. Spatial patterns of trends per decade and series of winter temperature indices (TX10, TN10, TX90, TN90 and DTR) during 1961–2003 in China. Positive/negative trends are shown as up/down triangles, and the filled symbols represent statistically significant trends (significant at the 0.05 level). The size of the triangles is proportional to the magnitude of the trends. The smoother line is the 9 year smoothing average.

decreasing trends are shown over most regions in China for TN10 (Figure 1). TX10 has shown some slight increasing changes since 1990, but the decrease in TN10 has been much more consistent before the 1990s, with only a slight levelling off after that. The countrywide trend (in % of days) for these two indices are −1.33 and −2.98 d/decade, respectively ($p < 0.05$).

For the percentage of days exceeding the 90th percentiles (TX90 and TN90), about 79 and 98% of stations have increasing trends, and about 30 and 70% of stations show statistically significant and increasing trends. Stations in the northern China show larger trend magnitudes for both TX90 and TN90 (Figure 1). Some stations in the southern China have decreasing

Table II. Trends per decade (with 95% confidence intervals in parentheses), and the number of stations with positive (significant at the 0.05 level), non-trend, and negative (significant at the 0.05 level) trends for winter temperature indices in the entire country.

Index	Units	Trends	Positive	Non-trend	Negative
TX10	d/decade	−1.33 (−2.70 to −0.25)	4 (1)	5	294 (93)
TN10	d/decade	**−2.98** (−3.96 to −1.90)	4 (1)	1	298 (254)
TX90	d/decade	0.92 (0.05 to 1.85)	238 (90)	2	63 (4)
TN90	d/decade	**2.35** (1.30 to 3.27)	298 (213)	0	5 (1)
DTR	°C/decade	**−0.25** (−0.39 to −0.14)	40 (4)	0	263 (141)

Values for trends significant at the 5% level (t-test) are set in bold.

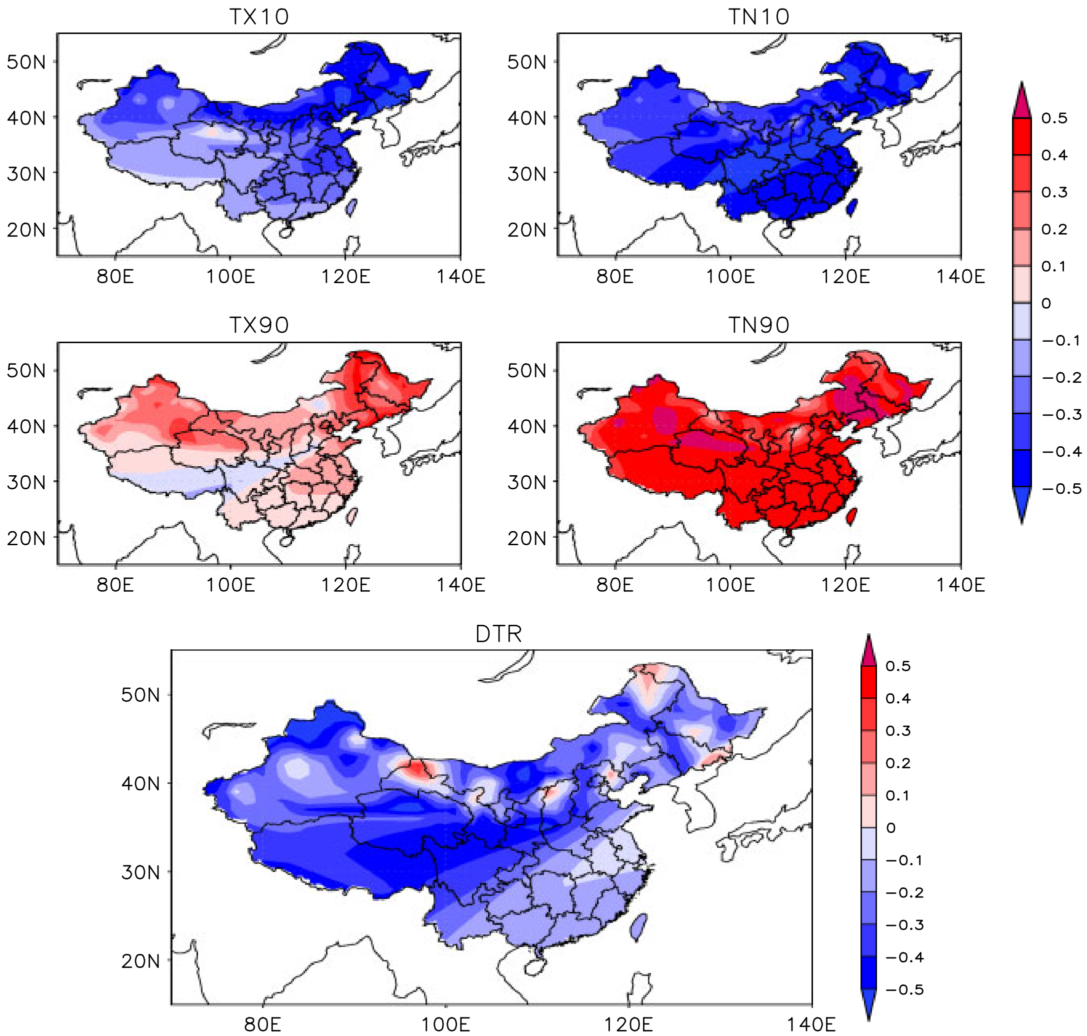

Figure 2. Spatial correlation coefficients between winter temperature indices (TX10, TN10, TX90, TN90 and DTR) and winter AO index during 1961–2003 in China.

trends for TX90 and non-significant increasing trends for TN90. Before the mid-1980s, both TX90 and TN90 have fluctuant (decreasing and increasing) changes, and show statistically increasing trends after that. The trends in the entire country for these two indices are 0.92 and 2.35 d/decade, respectively ($p < 0.05$).

For diurnal temperature range (DTR), about 87% of stations show decreasing trends, while 47% of stations decrease significantly. Similarly, stations in the northern China between 40° and 50°N show larger trend magnitudes, where have more pronounced warming. This illustrates that more warming leads to larger decreases for DTR (You *et al.*, 2008a, 2011a). DTR has shown a significant decreasing trend before the 1990s, with only a slight levelling off after that 1990. The overall trend in the entire country for DTR is −0.25 °C/decade ($p <$ 0.05), which is larger than the annual DTR trend in the Tibetan Plateau (−0.20 °C/decade) during 1961–2005 (You *et al.*, 2008a) and entire China (−0.18 °C/decade) during 1961–2003 (You *et al.*, 2011a).

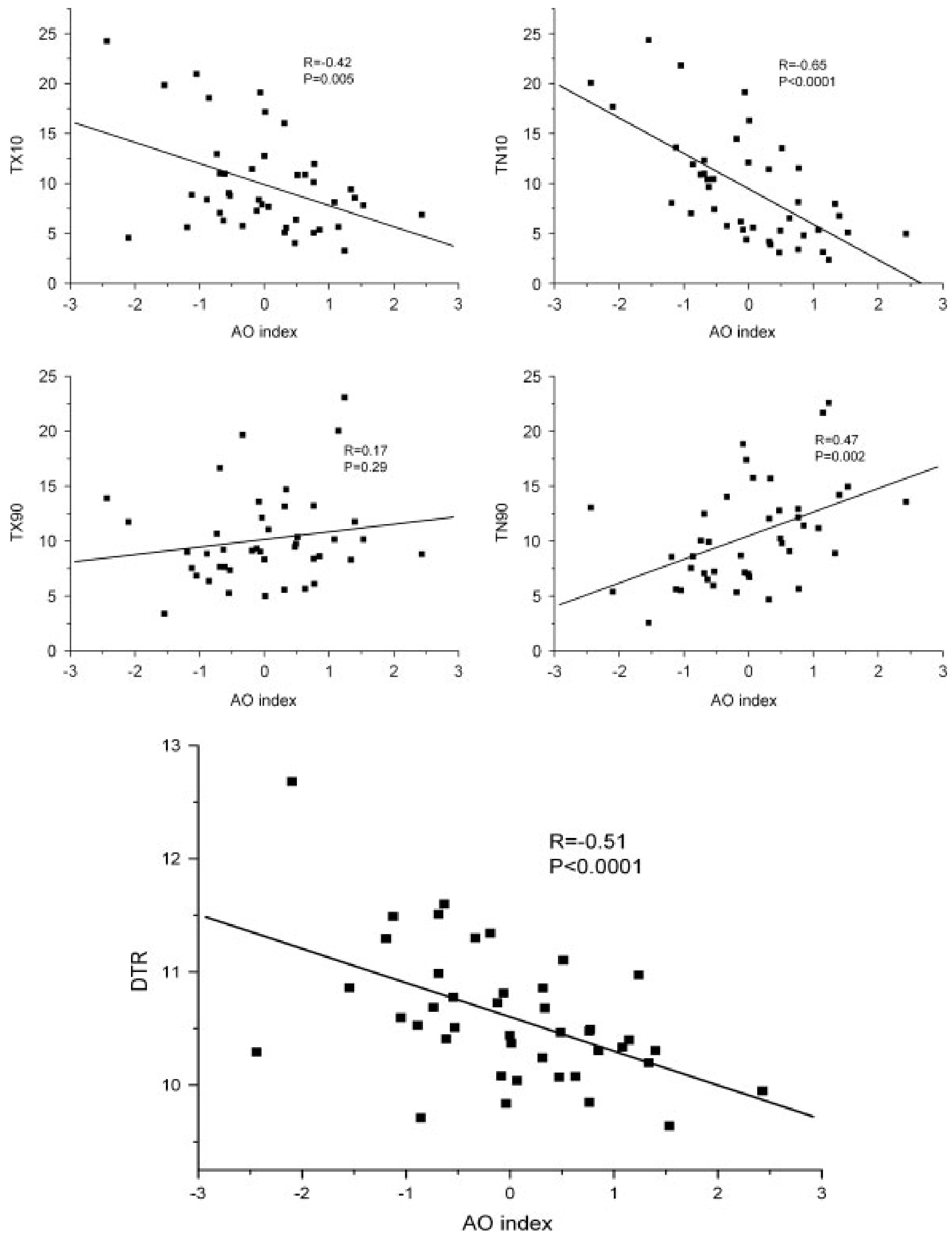

Figure 3. Correlations between winter temperature indices (TX10, TN10, TX90, TN90 and DTR) and the AO index during 1961–2003 in China. All dots in each panel are the mean values for the entire China. The straight lines, R and P are linear fits, correlation coefficients and statistical significance, respectively.

3.2. Comparison with the annual temperature extremes

In the previous study, the spatial and temporal distributions of temperature extremes on the annual basis have been analysed using the same datasets (You *et al.*, 2011a). Countrywide, the annual trends for TX10, TN10, TX90, TN90 and DTR are −0.47 d/decade, −2.06 d/decade, 0.62 d/decade, 1.75 d/decade, −0.18 °C/decade, respectively. For TX10, TN10 and DTR, about 77, 97, 80% of stations have decreasing trends, and about 83 and 94% of stations have increasing trends for TX90 and TN90, respectively. Compared with the results at the annual scale, the absolute trend magnitudes of winter temperature extremes are higher, and the proportions of stations with positive/negative trends are larger with the exception of TX90. Thus, the spatial and temporal patterns of winter temperature extremes are broadly similar to those on the annual basis, but the trends of temperature extremes in winter are generally higher, indicating pronounced climate warming in winter.

3.3. Correlation with the AO

The correlation between winter temperature indices and the AO in China during 1961–2003 are shown in Figure 2. National linear correlations and coefficients are listed in Figure 3. Strongest correlations occur in the northern China for TX10 and TN10 (some values lower than −0.5), and the correlations are slight in the southeastern part of the Tibetan Plateau for TX10 and TN10 (Figure 2). Taking China as a whole, the AO

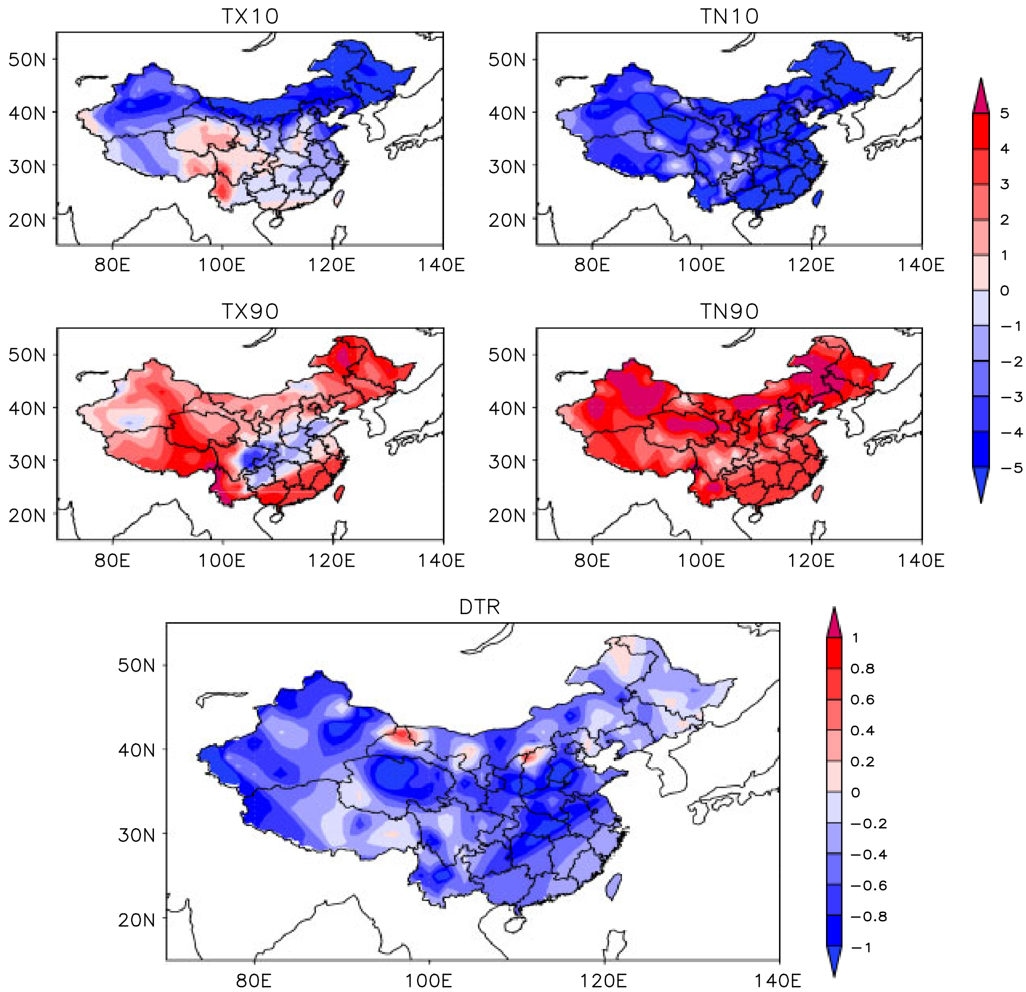

Figure 4. Differences of mean winter temperature extremes in positive and negative winter AO years during 1961–2003 are presented. The 23 positive (1963, 1966, 1971–1972, 1974–1975, 1982–1983, 1986–1994 and 1996–2001) and 19 negative (1961–1962, 1964–1965, 1967–1970, 1973, 1976–1981, 1984–1985, 1995 and 2002) winter AO years are selected whether the AO index is above or below the mean value. The unit is same as Table I.

index is significantly correlated with the winter cold temperature extremes (TX10 and TN10). It is negatively correlated with TX10 ($R = -0.42$, $p < 0.01$) and TN10 ($R = -0.65$, $p < 0.01$) during the studied period. For the winter warm temperature extremes, the AO index is positively correlated with TX90 and TN90, but only the correlations with TN90 ($R = 0.47$, $p < 0.01$) pass the significant level. In most cases, it is clear that the northern and northwestern China have larger correlation coefficients, and the southeastern China have lower values for the winter warm temperature extremes (TX90 and TN90, especially for TN90). Meanwhile, the AO index also has significantly negative correlation with DTR with the value of −0.51 (Figure 3), and correlation coefficients in most regions are more than −0.3. Thus winter temperature extremes are strongly connected with the AO index, especially in the northern China.

3.4. Atmospheric circulation composite analysis

In order to examine the influence of AO on climate extremes, the differences of mean winter temperature extremes in positive and negative winter AO years during 1961–2003 are presented (Figure 4). The 23 positive and 19 negative winter AO years are based on whether the AO index is above or below the mean value. The differences (positive minus negative AO years) show that the majority of stations have negative values for TX10, TN10 and DTR, and positive values for TX90 and TN90, while there has spatial variability (Figure 4). Thus winter temperature extremes are significantly different during winters with positive *versus* negative AO phases, which is consistent with that there are significant relationships between AO and temperature extremes (Figures 2 and 3).

To show the influence of atmosphere circulation on winter temperature extremes, Figure 5 shows the differences (positive minus negative AO years) of mean geopotential height and wind field (m s^{-1}) at 850 hPa during 1961–2003. The selected region covers the domain 10° – 70°N and 40° – 160°E. The largest negative differences in geopotential height are approximately 30 geopotential meter (gpm), with enhanced cyclonic circulation over the region (focused near 60°N and 60°E) (You *et al.*, 2011b). This generates an anomalous southwesterly flow in the Siberian region and northern China

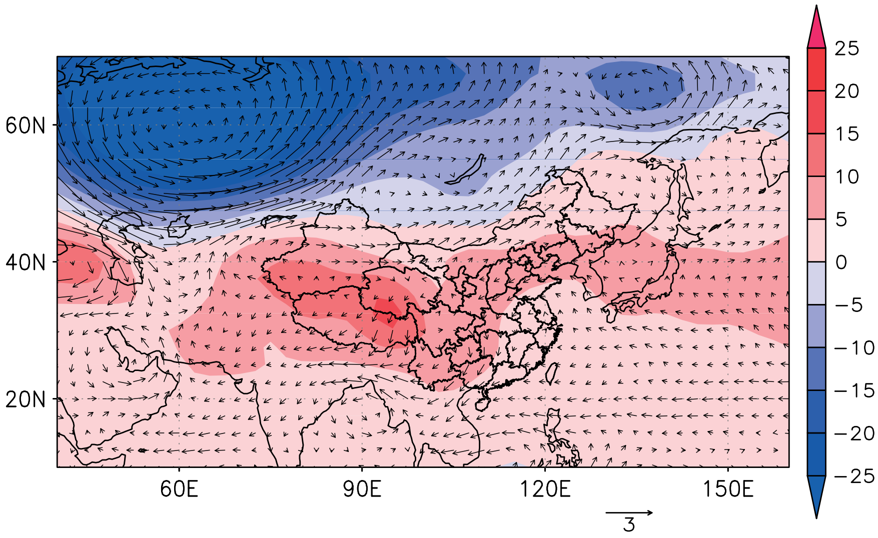

Figure 5. Differences (positive minus negative winter AO years) of mean geopotential height and wind field (m s^{-1}) at 850 hPa during 1961–2003.

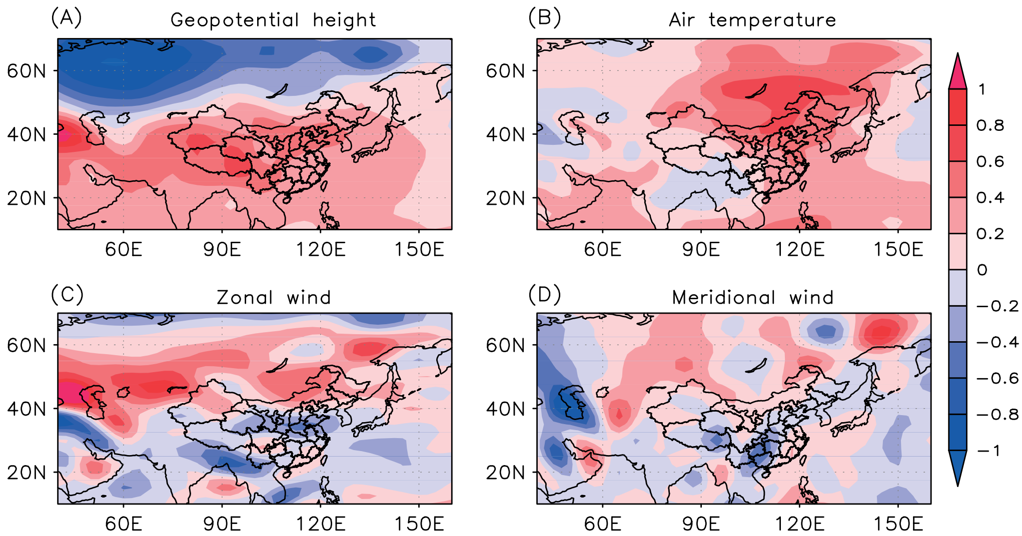

Figure 6. Spatial trends of geopotential height (A), air temperature (B), zonal wind (m s^{-1}) (C) and meridional wind (m s^{-1}) (D) at 850 hPa in winter during 1961–2003. The datasets come from NCEP/NCAR reanalysis. The units for geopotential height, air temperature, zonal wind and meridional wind are gpm/decade, 10× °C/decade, 10×m s^{-1}/decade and 10×m s^{-1}/decade, respectively.

which carries relative warm air into inland, reducing the intensity of Asian winter monsoon. These results suggest that decreasing trends for winter cold temperature extremes and increasing trends for winter warm temperature extremes are highly related to the circulation change (You *et al.*, 2011b).

To examine the atmosphere circulation, the spatial trends of geopotential height (A), air temperature (B), zonal wind (m s^{-1}) (C) and meridional wind (m s^{-1}) (D) at 850 hPa in winter during 1961–2003 are presented in Figure 6. The geopotential height at 850 hPa has decreasing trends at high latitude between 40° and 60°N and increasing trends at low latitude between 10° and 40°N (Figure 6(A)), suggesting that the asymmetrical changes between high latitude and mid latitude will begin to reduce the winter monsoon system, which is consistent with the asymmetrical global warming (IPCC, 2007). Although, the air temperature has increasing trends and more pronounced warming in the northeastern China (Figure 6(B)), the zonal and meridional wind increases significantly between 40° and 60°N (Figure 6(C) and (D)), revealing that the western and southern wind are increasing. The atmosphere conditions support the hypothesis that the increasing contrast between high and mid latitude will reduce the winter monsoon and influence the outbreak of winter temperature extremes.

The tropospheric temperature contrast between high and mid latitude is also of great importance to form the winter monsoon, supporting the atmospheric circulation for the change of temperature extremes. The tropospheric temperature (unit is °C) is defined as the average of air temperature vertically integrated between 200 and 1000 hPa based on the NCEP/NCAR reanalysis. The differences of composite tropospheric temperature

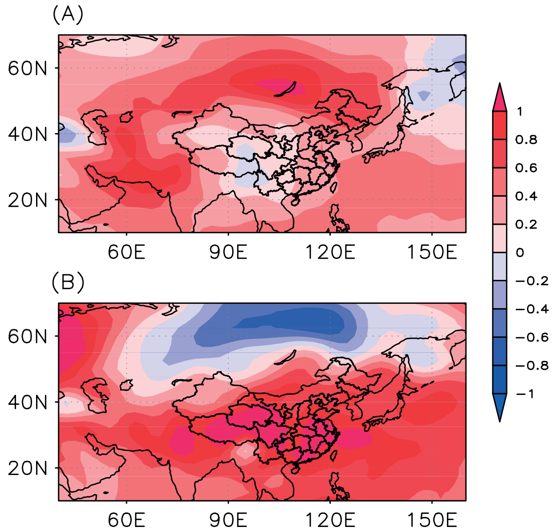

Figure 7. Differences of composite tropospheric temperature during the period of 1961–1982 and 1983–2003 [latter minus former, top plot (A)] and in strongly positive and strongly negative winter AO years during 1961–2003 [bottom plot (B)] are shown. Strongly positive (1982, 1988, 1989, 1991, 1994) and strongly negative (1962, 1964, 1968, 1976, 1978) winter AO years are those with index anomalies exceeding $\pm 1\sigma$. The study area is 40°W–160°E and 10° – 70°N. Tropospheric temperature (unit is °C) is defined the average of air temperature vertically integrated between 200 hPa and 1000 hPa based on the NCEP/NCAR reanalysis.

during the period of 1961–1982 and 1983–2003 (latter minus former) are show in Figure 7 (top plot). The tropospheric temperature has larger values at the higher latitude, especially near the 55°N and 100°E (1.2 °C). These atmospheric patterns will reduce the transport of energy through baroclinic waves, diminish the strength of troughs and ridges, and increase the occurrence of calm atmospheric conditions (Niu *et al.*, 2010). Thus, the transport of cold air originating from high latitude around 70°N will become less powerful and influence the frequency of warm temperature extremes (Gong *et al.*, 2001; Niu *et al.*, 2010).

The AO may influence the warm temperature extremes in China through the contrast of atmosphere conditions. Differences of composite tropospheric temperature in strongly positive and strongly negative winter AO years during 1961–2003 are shown in Figure 7 (bottom plot). Strongly positive (1982, 1988, 1989, 1991 and 1994) and strongly negative (1962, 1964, 1968, 1976 and 1978) winter AO years are those with index anomalies exceeding $\pm 1\sigma$. During the positive AO years, the tropospheric temperature is positive in most southern China (near 1 °C), and there has negative anomaly in the north of China (almost 0.8 °C). Thus, the enlarging contrast of tropospheric temperature between high (around 60°N) and mid latitude (around 30°N) are helpful to bring more warm air flow from the ocean and prevent the cold air flow from the north, which will weaken the Asian winter monsoon and reduce the cold outbreaks. The patterns are similar to the correlation map of vertical-latitude from the 1000 to 10 hPa (Figure 8), which the AO has significant negative/positive correlations with atmospheric variables (geopotential height, temperature and wind) at high/mid latitude at both troposphere and stratosphere.

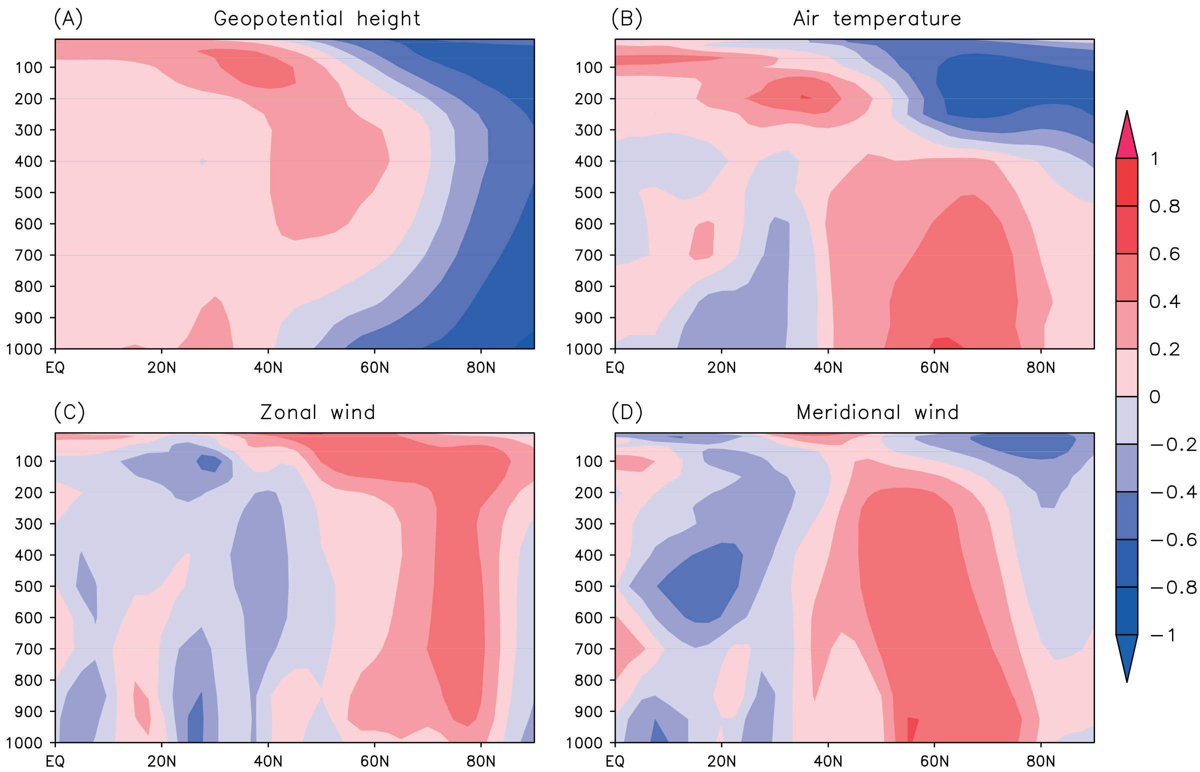

Figure 8. Vertical-latitude correlation coefficients between winter AO index and geopotential height (A), air temperature (B), zonal wind (m s^{-1}) (C) and meridional wind (m s^{-1}) (D) during 1961–2003.

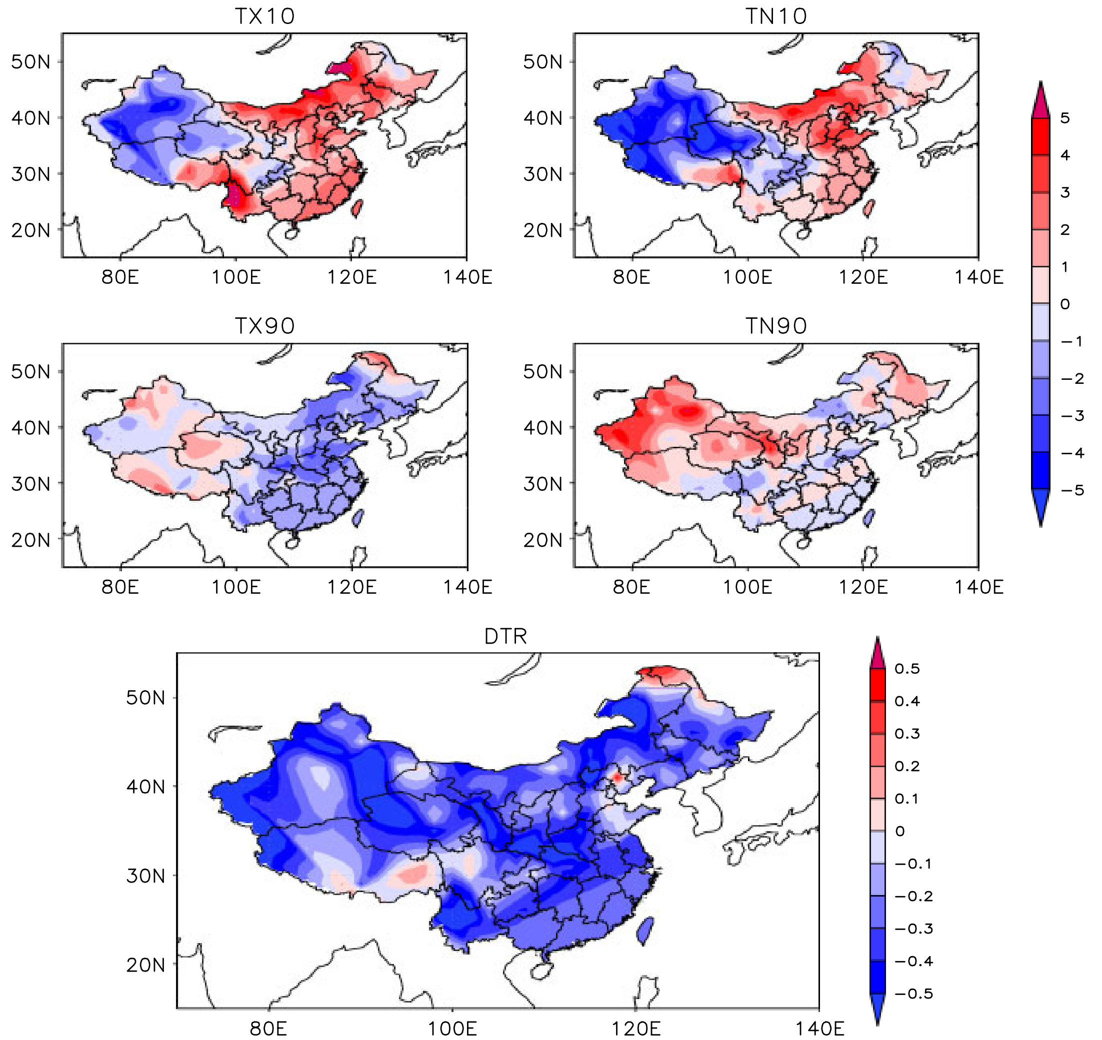

Figure 9. Differences of mean winter temperature extremes in solar maximum and minimum years are shown. The solar maximum years (1967–1971, 1979–1983, 1989–1992, and 1999–2002) and minimum years (1961–1966, 1972–1978, 1984–1988, and 1993–1998) are based on whether the solar fluxes are above or below the mean value. The unit is same as Table I.

3.5. Influenced by the solar activity

Previous studies have shown that the extension of the AO differs significantly for different phases of solar activity (Kodera, 2002; Gimeno *et al*., 2003; Ogi *et al*., 2003). In order to investigate the effect of solar activity on winter temperature, the studied period has been separated into two phases for maximum and minimum solar activity, depending on whether the solar fluxes are above or below the mean value (Kodera, 2002; Gimeno *et al*., 2003; Ogi *et al*., 2003). The 18 years (1967–1971, 1979–1983, 1989–1992 and 1999–2002) are classified as the solar maximum years, and the 24 years (1961–1966, 1972–1978, 1984–1988 and 1993–1998) as the solar minimum years. The classification is the same as the studies in Kodera (2002) and Ogi *et al*(2003).

During solar maximum years, about 70, 49, 17 and 47% of stations for TX10, TN10, TX90 and TN90, respectively, have larger values than that during solar minimum years. It is clear that the larger negative differences between solar maximum and minimum years for both TX10 and TN10 are shown in the western and northwestern China, while stations in the western and northwestern China show larger positive values for both TX90 and TN90 (Figure 9). In most regions, DTR is sensitive to the change of solar activity, and about 93% of stations have larger values during solar minimum years than that during solar maximum years, resulting the negative differences between them (Figure 9). This is probably because more solar activity will heat the surface and increase the winter surface temperature, thus influencing the winter temperature extremes. Moreover, solar activity can also influence the atmospheric circulations which are memorized in the snow-cover, ice and permafrost regions (Ogi *et al*., 2003). The western China especially in the Tibetan Plateau is more sensitive to climate change due to the larger cryospheric area, and shows stronger signal. This probably suggests that solar activity can influence the winter temperature extremes to some extents and vary with the surface conditions, while the detailed mechanism needs to be investigated in future studies.

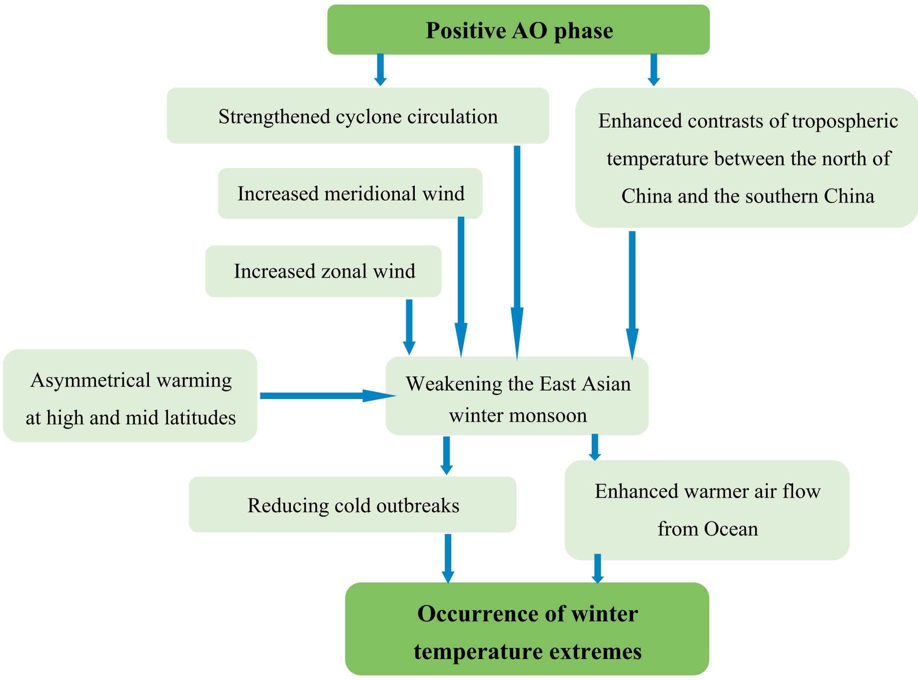

Figure 10. Possible causes of winter temperature extremes in China.

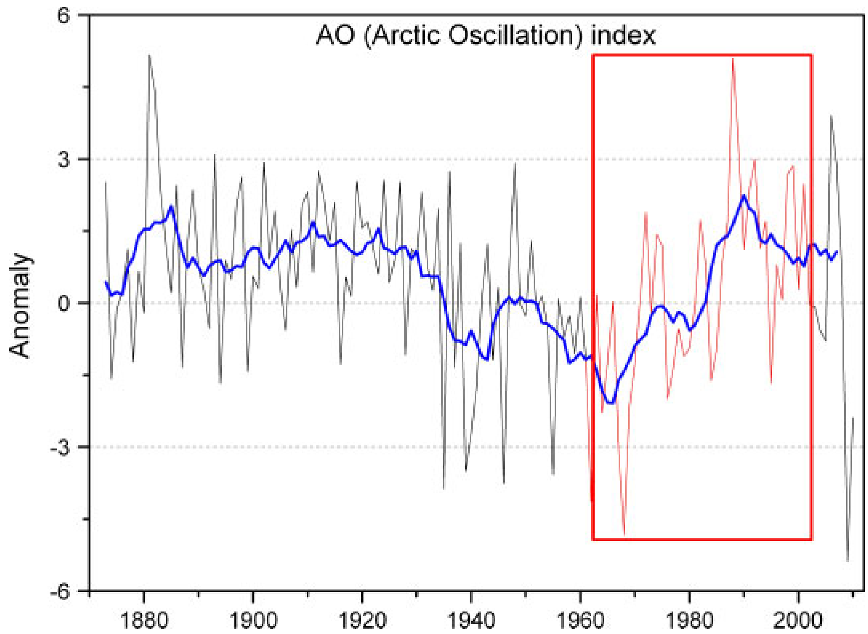

Figure 11. Time series of winter AO index during 1873–2010. The studied period of 1961–2003 is showed in the red rectangle. The smoother line is the 9 year smoothing average. The AO index is updated from Li and Wang (2003).

4. Discussion and conclusions

Winter temperature extremes have been shown to be warming faster than annual mean warm extremes (Aguilar *et al.*, 2009) and are therefore particularly sensitive to future change. We have examined the spatial and temporal distributions of trends for four winter temperature extreme indices, using 303 stations in China over the period 1961–2003. For the majority of stations, significant decreases in cold days/nights (TX10/TN10) are observed with mean rates of −1.33 and −2.98 d/decade, respectively, while significant increases in warm d/nights (TX90/TN90) are also observed with mean rates of 0.92 and 2.35 d/decade, respectively. Such changes are consistent with previous studies in other parts of the world (Peterson *et al.*, 2002, 2008; Aguilar *et al.*, 2005, 2009; Alexander *et al.*, 2006), and show that changes in winter temperature extremes reflect the consistent winter warming in China (You *et al.*, 2008a,b, 2011a). The asymmetric changes in minimum and maximum temperature result in the declining DTR with rate of −0.25 °C/decade. In most cases, stations in the north of China have the largest trend magnitudes, again consistent with rapid warming in the region (Wang and Gong, 2000; Ding *et al*., 2007).

Changes in winter temperature extremes are consistent with the report of You *et al*. (2011a) at the annual scale, but the trend magnitudes are higher than those, suggesting the winter is more sensitive to the extremes. The causes about the temperature extremes change have been studied, but require further study. Besides gas greenhouse gas emissions, You *et al*. (2011a) considered that temperature extremes change is probably associated with rapid urbanization, increased industrial aerosols and non-climate factors such as population, economic activity and local energy usage. The influences become particularly significant in China because of its rapid urbanization and economic activity (Qian and Lin, 2004).

The AO influences surface air temperature not only over the bulk of the Eurasian continent (Hurrell, 1995; Thompson and Wallace, 1998) but also in northern China (Gong and Wang, 2003). The winter AO index is significantly negatively correlated with TX10/TN10 and DTR, and positively correlated with TX10/TN10, indicating that the AO influences winter cold/warm extreme temperature. During the strongly positive AO index years, enhanced cyclonic circulation over the Urals (focused near 50°N and 60 °E) brings more warm airflow into northern China, decreasing the strength of the East Asian winter monsoon and limiting its southward extension (Figure 10). This is consistent with previous research that shows that atmospheric circulation changes have contributed to the changes in climate extremes in China (You *et al*., 2011a). Other work has also suggested that an increase in strong positive AO phases could lead to a decreasing East Asian winter monsoon (Gong *et al*., 2001; Wu and Wang, 2002). Composites of atmospheric circulation shown in this study also support the relationship between AO variability and the strength of winter cold outbreaks in the northern China.

It is notable that the winter AO index has shifted several phases during 1873–2010 (Figure 11), derived from Li and Wang (2003). Winter AO index increases since the 1960s and has the downward trend since 1990 (Hurrell and Deser, 2010), confirmed by the weakening East Asian winter monsoon (Niu *et al*., 2010). The asymmetrical change in geopotential height, zonal and meridional wind may reflect a weakening of the East Asian winter monsoon. At the same time, more warming at high latitudes also reduce the thermal contrast, contributing to the weakening the East Asian winter monsoon (Figure 10). This will reduce the invasion of dry and cold air from the northern regions, creating a favourable background for temperature extremes. The limitation of this study is that the study period stops at the end of 2003, and the recent winters have strongly negative AO values in 2009 and 2010, especially in 2010 (Figure 11). In 2010, China has experienced the coldest winter since 1987, with the annual mean temperature of −4.7 °C (Ren *et al*., 2011). This supports the hypothesis that the AO can modulate the winter temperature extremes by the atmosphere conditions. Meanwhile, the AO can be modulated by the 11 year solar cycles (Kodera, 2002). In this study, winter temperature extremes have stronger values during solar maximum years in most cases. But the mechanical linkage between solar activities, the AO and temperature extremes need to be investigated in future studies. Our results indicate also that further investigation of the linkage between the AO and climate extremes in China is worthwhile.

Acknowledgements

This study is supported by the Global Change Research Program of China (2010CB951401), the Chinese Academy of Sciences (KZCX2-YW-145), and the National Natural Science Foundation of China (40870743). The China postdoctoral science foundation (the 49th) is also appreciated. This study became possible through a Sino-Swiss Science and Technology Cooperation (SSSTC) research grant (EG76-032010 and EG23-092011). The authors thank the National Meteorological Information Center, China Meteorological Administration (NMIC/CMA), for providing the data for this study. Qinglong You is supported by the Alexander von Humboldt Foundation.

References

Aguilar E, Peterson TC, Obando PR, Frutos R, Solera M, Soley J, Garcia IG, Araujo RM, Santos AR, Valle VE, Brunet M, Aguilar L. 2005. Changes in precipitation and temperature extremes in Central America and northern South America, 1961–2003. *Journal of Geophysical Research-Atmospheres* **110**: D23107, DOI: 10.1029/2005jd006119.

Aguilar E, Barry AA, Brunet M, Ekang L, Fernandes A, Massoukina M, Mbah J, Mhanda A, do Nascimento DJ, Peterson TC, Umba OT, Tomou M, Zhang X. 2009. Changes in temperature and precipitation extremes in western central Africa, Guinea Conakry, and Zimbabwe, 1955–2006. *Journal of Geophysical Research-Atmospheres* **114**: D02115, DOI: 10.1029/2008jd011010.

Alexander LV, Zhang X, Peterson TC, Caesa J, Gleason B, Klein Tank AMG, Haylock M, Collins D, Trewin B, Rahimzadeh F, Tagipour A, Rupa Kumar K, Revadekar J, Griffiths G, Vincent L. 2006. Global observed changes in daily climate extremes of temperature and precipitation. *Journal of Geophysical Research-Atmospheres* **111**: D05109, DOI: 10.1029/2005jd006290.

Bojariu R, Gimeno L. 2003. Predictability and numerical modelling of the North Atlantic Oscillation. *Earth-Science Reviews* **63**(1–2): 145–168.

Brown SJ, Caesar J, Ferro CAT. 2008. Global changes in extreme daily temperature since 1950. *Journal of Geophysical Research-Atmospheres* **113**: D05115, DOI: 10.1029/2006jd008091.

Caesar J, Alexander LV, Trewin B, Tse-ring K, Sorany L, Vuniyayawa V, Keosavang N, Shimana A, Htay MM, Karmacharya J. 2011. Changes in temperature and precipitation extremes over the Indo-Pacific region from 1971 to 2005. *International Journal of Climatology* **31**: 791–801, DOI: 10.1002/joc.2118.

Choi G, Collins D, Ren GY, Trewin B, Baldi M, Fukuda Y, Afzaal M, Pianmana T, Gomboluudev P, Huong PTT, Lias N, Kwon WT, Boo KO, Cha YM, Zhou YQ. 2009. Changes in means and extreme events of temperature and precipitation in the Asia-Pacific Network region, 1955–2007. *International Journal of Climatology* **29**(13): 1906–1925, DOI: 10.1002/joc.1979.

Ding YH, Ren GY, Zhao ZC, Xu Y, Luo Y, Li QP, Zhang J. 2007. Detection, causes and projection of climate change over China: an overview of recent progress. *Advances in Atmospheric Sciences* **24**(6): 954–971, DOI: 10.1007/s00376-007-0954-4.

Easterling DR, Meehl GA, Parmesan C, Changnon SA, Karl TR, Mearns LO. 2000. Climate extremes: observations, modeling, and impacts. *Science* **289**(5487): 2068–2074.

Gimeno L, de la Torre L, Nieto R, Garcia R, Hernandez E, Ribera P. 2003. Changes in the relationship NAO-northern hemisphere temperature due to solar activity. *Earth and Planetary Science Letters* **206**(1–2): 15–20.

Gong DY, Wang SW, Zhu JH. 2001. East Asian winter monsoon and Arctic Oscillation. *Geophysical Research Letters* **28**(10): 2073–2076.

Gong DY, Wang SW. 2003. Influence of Arctic Oscillation on winter climate over China. *Journal of Geographical Sciences* **13**(2): 208–216.

Hurrell JW. 1995. Decadal trends in the North-Atlantic Oscillation – regional temperatures and precipitation. *Science* **269**(5224): 676–679.

Hurrell JW, Kushnir Y, Visbeck M. 2001. Climate – the north Atlantic Oscillation. *Science* **291**(5504): 603–605.

Hurrell JW, Deser C. 2010. North Atlantic climate variability: the role of the North Atlantic Oscillation. *Journal of Marine Systems* **79**(3–4): 230–230.

IPCC. 2007. *Summary for Policymakers of Climate change 2007: The Physical Science Basis. Contribution of Working Group I to the Fourth Assessment Report of the Intergovernmental Panel on Climate Change*. Cambridge University Press: Cambridge, UK.

Kalnay E, Kanamitsu M, Kistler R, Collins W, Deaven D, Gandin L, Iredell M. 1996. The NCEP/NCAR 40 year reanalysis project. *Bulletin of the American Meteorological Society* **77**(3): 437–471.

Katz RW, Brown BG. 1992. Extreme events in a changing climate – variability is more important than averages. *Climatic Change* **21**(3): 289–302.

Klein Tank AMG, Peterson TC, Quadir DA, Dorji S, Zou X, Tang H, Santhosh K, Joshi UR, Jaswal AK, Kolli RK, Sikder AB, Deshpande NR, Revadekar JV. 2006. Changes in daily temperature and precipitation extremes in central and south Asia. *Journal of Geophysical Research-Atmospheres* **111**: D16105, DOI: 10.1029/2005jd006316.

Kodera K. 2002. Solar cycle modulation of the North Atlantic Oscillation: implication in the spatial structure of the NAO. *Geophysical Research Letters* **29**(8): 1218.

Li JP, Wang J. 2003. A modified zonal index and its physical sense. *Geophysical Research Letters* **30**(12): 163, DOI: 10.1029/2003gl017441.

New M, Hewitson B, Stephenson DB, Tsiga A, Kruger A, Manhique A, Gomez B, Coelho CAS, Masisi DN, Kululanga E. 2006. Evidence of trends in daily climate extremes over southern and west Africa. *Journal of Geophysical Research-Atmospheres* **111**: D14102, DOI: 10.1029/2005jd006289.

Niu F, Li ZQ, Li C, Lee KH, Wang MY. 2010. Increase of wintertime fog in China: potential impacts of weakening of the Eastern Asian monsoon circulation and increasing aerosol loading. *Journal of Geophysical Research-Atmospheres* **115**: D00K20, DOI: 10.1029/2009jd013484.

Ogi M, Yamazaki K, Tachibana Y. 2003. Solar cycle modulation of the seasonal linkage of the North Atlantic Oscillation (NAO). *Geophysical Research Letters* **30**(22): 2170, DOI: 10.1029/2003gl018545.

Peterson TC, Taylor MA, Demeritte R, Duncombe DL, Burton S, Thompson F, Porter A, Mercedes M, Villegas E. 2002. Recent changes in climate extremes in the Caribbean region. *Journal of Geophysical Research-Atmospheres* **107**: D07113, DOI: 10.1029/2002jd002251.

Peterson TC, Manton MJ. 2008. Monitoring changes in climate extremes – a tale of international collaboration. *Bulletin of the American Meteorological Society* **89**(9): 1266–1271, DOI: 10.1175/2008bams2501.1.

Peterson TC, Zhang XB, Brenet-India M, Vazquez-Aguirre JL. 2008. Changes in North American extremes derived from daily weather data. *Journal of Geophysical Research-Atmospheres*. **113**: D07113, DOI: 10.1029/2007jd009453.

Qian WH, Lin X. 2004. Regional trends in recent temperature indices in China. *Climate Research* **27**(2): 119–134.

Ramos AM, Lorenzo MN, Gimeno L. 2010. Compatibility between modes of low-frequency variability and circulation types: a case study of the northwest Iberian Peninsula. *Journal of Geophysical Research-Atmospheres* **115**: D02113, DOI: 10.1029/2009jd012194.

Ren GY, Chen Y, Zou XK, Zhou YQ, Ren YY, Jiang Y, Ren FM, Zhang Q, Wang XL, Zhang L. 2011. Changes in climatic extremes over mainland China. *Climate Research* **50**: 105–111, DOI: 10.3354/cr01023.

Sen PK. 1968. Estimates of regression coefficient based on Kendall's tau. *Journal of the American Statistical Association* **63**: 1379–1389.

Thompson DWJ, Wallace JM. 1998. The Arctic Oscillation signature in the wintertime geopotential height and temperature fields. *Geophysical Research Letters* **25**(9): 1297–1300.

Thompson DWJ, Wallace JM. 2001. Regional climate impacts of the Northern Hemisphere annular mode. *Science* **293**(5527): 85–89.

Wang SW, Gong DY. 2000. Enhancement of the warming trend in China. *Geophysical Research Letters* **27**(16): 2581–2584.

Wu B, Wang J. 2002. Winter Arctic Oscillation, Siberian high and East Asian winter monsoon. *Geophysical Research Letters* **29**(19): 1897.

You QL, Kang SC, Aguilar E, Yan YP. 2008a. Changes in daily climate extremes in the eastern and central Tibetan Plateau during 1961–2005. *Journal of Geophysical Research-Atmospheres* **113**: D07101, DOI: 10.1029/2007jd009389.

You QL, Kang SC, Pepin N, Yan YP. 2008b. Relationship between trends in temperature extremes and elevation in the eastern and central Tibetan Plateau, 1961–2005. *Geophysical Research Letters* **35**: L04704, DOI: 10.1029/2007gl032669.

You QL, Kang SC, Aguilar E, Pepin N, Fluegel WA, Yan YP. 2011a. Changes in daily climate extremes in China and their connection to the large scale atmospheric circulation during 1961–2003. *Climate Dynamics* **36**: 2399–2417, DOI: 10.1007/s00382-009-0735-0.

You QL, Kang SC, Ren GY, Fraedrich K, Pepin N, Yan YP, Ma LJ. 2011b. Observed changes in snow depth and number of snow days in the eastern and central Tibetan Plateau. *Climate Research* **46**: 171–183, DOI: 10.3354/cr00985.

Zhai PM, Pan XH. 2003. Trends in temperature extremes during 1951–1999 in China. *Geophysical Research Letters* **30**(17): 1913.

Zhai PM, Sun AJ, Ren FM, Liu XN, Gao B, Zhang Q. 1999. Chances of climate extremes in China. *Climatic Change* **42**(1): 203–218.

Clim Dyn
DOI 10.1007/s00382-013-1960-0

Present and projected degree days in China from observation, reanalysis and simulations

Qinglong You · Klaus Fraedrich · Frank Sielmann · Jinzhong Min · Shichang Kang · Zhenming Ji · Xiuhua Zhu · Guoyu Ren

Received: 23 August 2013 / Accepted: 30 September 2013

Abstract Degree days are usually defined as the accumulated daily mean temperature varying with the base temperature, and are one of the most important indicators of climate changes. In this study, the present-day and projected changes of four degree days indices from daily mean surface air temperature output simulated by Max Planck Institute, Earth Systems Model of low resolution (MPI-ESM-LR) model are evaluated with the high resolution gridded-observation dataset and two modern reanalyses in China. During 1979–2005, the heating degree days (HDD) and the numbers of HDD (NHDD) have decreased for observation, reanalyses (ERA-Interim and NCEP/NCAR) and model simulations (historical and decadal experiments), consistent with the increasing cooling degree days (CDD) and the numbers of CDD (NCDD). These changes reflect the general warming in China during the past decades. In most cases, ERA-Interim is closer to observation than NCEP/NCAR and model simulations. There are discrepancies between observation, reanalyses and model simulations in the spatial patterns and regional means. The decadal hindcast/forecast simulation performance of MPI-ESM-LR produce warmer than the observed mean temperature in China during the entire period, and the hindcasts forecast a trend lower than the observed. Under different representative concentration pathway (RCP) emissions scenarios, HDD and NHDD show significant decreases, and CDD and NCDD consistently increase during 2006–2100 under RCP8.5, RCP4.5 and RCP2.6, especially before the mid-21 century. More pronounced changes occur under RCP8.5, which is associated with a high rate of radiative forcing. The 20th century runs reflect the sensitivity to the initial conditions, and the uncertainties in terms of the inter-ensemble are small, whereas the long-term trend is well represented with no differences among ensembles.

Keywords Degree days · MPI-ESM-LR · NCEP/NCAR and ERA-Interim · China

Q. You (✉) · J. Min
Key Laboratory of Meteorological Disaster, Ministry of Education, Nanjing University of Information Science and Technology, Nanjing 210044, China
e-mail: yqingl@126.com

Q. You · K. Fraedrich · F. Sielmann · X. Zhu
Max Plank Institute for Meteorology, KlimaCampus, 20144 Hamburg, Germany

S. Kang
State Key Laboratory of Cryospheric Science, Chinese Academy of Sciences (CAS), Lanzhou 730000, China

S. Kang · Z. Ji
Laboratory of Tibetan Environment Changes and Land Surface Processes, Institute of Tibetan Plateau Research, Chinese Academy of Sciences (CAS), Beijing 100085, China

G. Ren
Laboratory for Climate Studies, National Climate Center, China Meteorological Administration (CMA), Beijing 100081, China

1 Introduction

According to the Intergovernmental Panel on Climate Change (IPCC) Fourth Assessment Report (AR 4), the global average surface air temperature has risen by 0.74 ± 0.18 °C during 1906–2005, and most of the observed increase in globally averaged temperature since the mid-20th century is very likely due to the observed increase in anthropogenic greenhouse gas concentrations (IPCC 2007). However, trends of temperature always

Published online: 08 October 2013

exhibit temporal variations. In China, the warming is very evident, supporting by the proxy indices such as the ice core and tree ring (Wang and Gong 2000). Based on 740 observational stations, the surface air temperature in China's mainland as a whole rose by about 1.1 °C for the last 50 years, with a warming rate of about 0.22 °C/decade, which is more rapid than the average values of the world and Northern Hemisphere. Moreover, the most evident warming has occurred in winter and spring, and the Northeast China, North China and Northwest China experienced more significant warming in terms of annual mean temperature (Ding et al. 2007; Ren et al. 2005, 2011a, b). Thus, the trends in annual mean temperatures show a large spatial heterogeneity and regional differences across China, which may be explained by the feedbacks of cold waves and snow cover change (Wang et al. 2010). Except for the warming of surface temperature, both the low-level atmospheric temperature and the middle-upper troposphere air temperatures have changed responding to the global warming (Wang et al. 2012).

The impact of climate change in China has been observed in many records and is discussed in the previous studies (Wang et al. 2010, 2012). For example, the glacier areas in China have shrunk about 2–10 % over the past four decades, and the total glacier area has receded by about 5.5 % (Li et al. 2008; Yao et al. 2012). The permafrost in China is significantly degenerating, indicated by shrinking areas of permafrost, increasing depths of the active layer, rising of lower limit of permafrost and thinning areas of the seasonal frost depth (Li et al. 2008; Zhang 2007). In addition, the spatial pattern and variability of snow cover in China has changed, mainly explained by the linear variations of snowfall and snow season temperature (Qin et al. 2006). Meanwhile, the climate extreme is also accompanied by climate change in China, and the previous studies have addressed the observed and projected trends in frequency and intensity of climate extremes (Ren et al. 2011b; You et al. 2011; Zhai and Pan 2003). Twelve indices of extreme temperature have been analyzed during 1961–2003, which reflect the consistent warming (You et al. 2011). This is in good agreement with the previous results that the frequency of warm nights significantly has increased, and the cool nights decreased over most China (Zhai and Pan 2003). A new climate extreme index with evident climatological and socio-economic significance is developed, which has been composed with the country-averaged frequencies of high temperature, low temperature, intense precipitation, dust storm and strong wind events, meteorological drought area percentage, and number of land-falling tropical cyclones (Ren et al. 2011b).

To summarize, the previous temperature studies focus on the seasonal and annual temperature, and the consequences of climate change in China. However, there are no results about degree days in China under the representative concentration pathway (RCP) scenarios (Moss et al. 2010). Degree days can be defined as a measure of heating or cooling, and are usually considered as one of the important indicators of global climate change. As degree days indices are a measure to indicate the demand for energy to heat or cool building. The monthly and/or annual cooling and heating requirements of specific buildings in different locations can be estimated by means of the degree days concept. The methods assure that the energy needs of a building are proportional to the difference between the mean daily temperature and a base temperature. The base temperature is the outdoor temperature below or above which heating or cooling is needed (Büyükalaca et al. 2001).

Traditionally, heating degree days (HDD) are calculated at a base temperature of 18 °C and cooling degree days (CDD) are determined at a base temperature of 22 °C. However, the base temperature varied widely from one building to another due to different building characteristics, it has been questioned by a number of authors and must be employed with caution (Büyükalaca et al. 2001; Jiang et al. 2009; OrtizBeviá et al. 2012; Rehman et al. 2011). In Turkey, the base temperature for HDD are selected in the range of 18–28 °C, which is from 18 to 28 °C for cooling degree day (Büyükalaca et al. 2001). In Saudi Arabia, a heating base temperature in the range of 14–22 °C is suitable, and the recommended cooling base temperature is between 23 and 25.5 °C for buildings without insulation and between 25.5 and 27.8 °C for well-insulated buildings (Rehman et al. 2011). In China, 18 °C is usually accepted as the base temperature for HDD and 24 °C for CDD (Jiang et al. 2009). In this study, the base temperature of 18 and 24 °C is used for heating and CDD, respectively. The present and projected degree days in China are studied by the outputs of a global climate model (GCM), which contribute to the IPCC AR5 under the different emissions scenario. The comparison between reanalysis and model outputs has also been evaluated. The objective of this study is to provide a reliable basis for decision making and formulation of environmental policy in China.

2 Data and methods

For the coming IPCC AR 5, the simulations from the new generation of state-of-the-art GCMs are available for analysis within the Coupled Model Intercomparison Project Phase 5 (CMIP5) (Taylor et al. 2012). Compared with the previous models, CMIP5 includes more comprehensive global climate modes such as earth system models with generally higher spatial resolution, and have been used to evaluate the extreme climate and weather events on the global scales (Sillmann et al. 2013a, b). The model used in this study is the latest version of Max Planck Institute for Meteorology (MPI-M), Earth Systems Model (MPI-ESM), Hamburg, Germany, performed with the version of MPI-ESM coupled model of low resolution (MPI-ESM-LR). The model outputs by MPI-ESM-LR have been organized by the Program for Climate Model Diagnosis and Intercomparison (PCMDI) for the IPCC AR 5. The historical, decadal and long-term experiments simulations are selected in this study. The historical experiments are aimed at reproducing the climate evolution of the twentieth century as accurately as possible, by considering all major natural and anthropogenic forcing, such as changes in atmospheric greenhouse gases, aerosol loadings, solar output and land use (Wild et al. 2013). Most historical experiments start around 1860 and end around 2005. The decadal experiments will be possible to assess the skill of the forecast system in predicting climate statistics for times when the initial climate state may exert some detectable influences, which is a set of 10-year hindcasts initialized from observed climate states near the years 1960, 1965, and every 5 years to 2005 (Taylor et al. 2012). The long-term experiments are forced by observed atmospheric composition changes (reflecting both anthropogenic and natural sources) and include time-evolving land cover. The long-term experiments have three future projection simulations forced with specified concentrations, consistent with a high emissions scenario (RCP8.5), a midrange mitigation emissions scenario (RCP4.5), and a low emissions scenario (RCP2.6) (Taylor et al. 2012). The CMIP5 projections of climate change are driven by concentration or emission scenarios consistent with the RCPs (Moss et al. 2010). In contrast to the scenarios described in the IPCC "Special Report on Emissions Scenarios" (SRES) used for CMIP3, which did not include policy intervention, the RCPs are mitigation scenarios that assume policy actions will be taken to achieve certain emission targets (Taylor et al. 2012). For example, RCP8.5 emission scenarios mean that radiative forcing increases throughout the 21st century before reaching a level of about 8.5 W m^{-2} at the end of the century.

In addition to the CMIP5 models, daily mean surface temperatures estimated from NCEP/NCAR and ERA-Interim reanalysis are selected. NCEP/NCAR reanalysis is provided by the National Oceanic and Atmospheric Administration (NOAA)/Earth System Research Laboratory (ESRL)/Physical Sciences Division (PSD), Boulder, Colorado, USA, from their website at http://www.cdc.noaa.gov/. The datasets cover January 1948 to the present with a spatial resolution of 2.5° × 2.5° (Kalnay et al. 1996), and are initialized with a wide variety of weather observations, including ships, planes and satellite. The ERA-Interim reanalysis data are obtained from the European Centre for Medium-Range Weather Forecasts (ECMWF) website (http://www.ecmwf.int/), available from January 1979 to the present with a spatial resolution of 1.5° × 1.5° (Dee et al. 2011). It includes a large variety of 3-h surface parameters, describing weather as well as ocean-wave and land-surface conditions, and 6-h upper-air parameters covering the troposphere and stratosphere (Dee et al. 2011). Compared with ERA-40 (Uppala et al. 2005), ERA-Interim has been improved on the representation of the hydrological cycles, the quality of the stratospheric, and the consistency in time of reanalyzed geophysical fields.

Table 1 Definitions of four degree days indices used in this study

Index	Descriptive name	Definition	Units
HDD	Heating degree day	Sum of absolute TG where TG < 18 °C	°C
CDD	Cooling degree day	Sum of TG where TG > 18 °C	°C
NHDD	Number of heating degree day	Account number of days where TG < 24 °C	day
NCDD	Number of cooling degree day	Account number of days where TG > 24 °C	day

TG is daily mean temperature

For the purpose of reanalyses (NCEP/NCAR and ERA-Interim) and MPI-ESM-LR climate model validation (history and decadal experiments), we use the 0.5° × 0.5° daily temperature datasets in China for the period of 1979–2005 (Xu et al. 2009). The dataset is primarily developed for the validation of climate models, and has potential applications in the studies such as climate, hydrology and ecology.

Four indices of degree days are used and detailed descriptions are provided in Table 1. The HDD, the numbers of HDD (NHDD), the CDD and the numbers of CDD (NCDD) are based on the daily mean temperatures from multi-datasets. In order to validate the indices from model simulations and reanalyses, they are compared with observations during 1979–2005. After that, indices from the long-term experiments under RCP8.5, RCP4.5 and RCP2.6 are analyzed from 2006 to 2100. Due to different resolutions between CMIP5 output, reanalyses and observations, all the indices are interpolated into a common 144 × 73 grid (2.5° × 2.5°) using the bilinear interpolation procedure implemented in the Climate Data Operators (http://code.zmaw.de/projects/cdo). To produce the values for the whole China, there are 190 grid points covering the entire region (Fig. 1).

The Mann–Kendall test for a trend and Sen's slope estimates are used to detect trends in degree days indices series (Sen 1968). A trend is considered to be statistically significant if it is significant at the 5 % level. Three statistical metrics are used to quantify the accuracy of the reanalysis and simulations: Relative bias (RB), root-mean-square error (RMSE) and correlation coefficient (R).

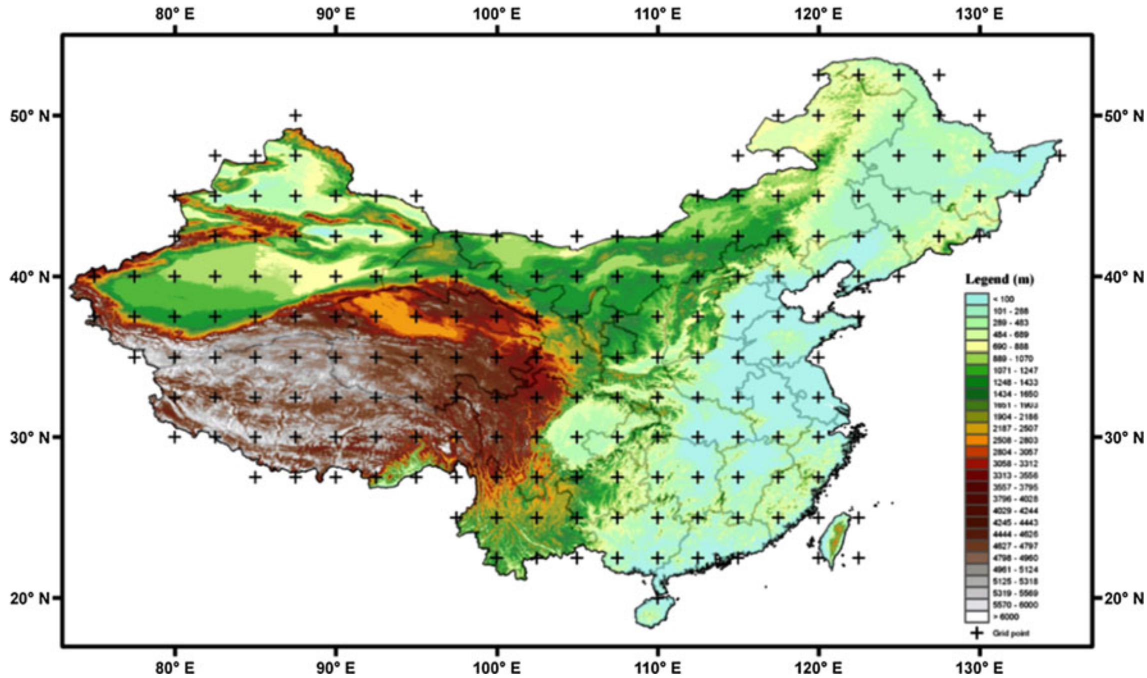

Fig. 1 Topography of China and the distribution of 190 grid points used in this study

Fig. 2 Anomalies of HDD, CDD, NHDD and NCDD from observation, ERA-Interim, NCEP/NCAR reanalysis data, the historical and decadal experiments simulation outputs in China during 1979–2005

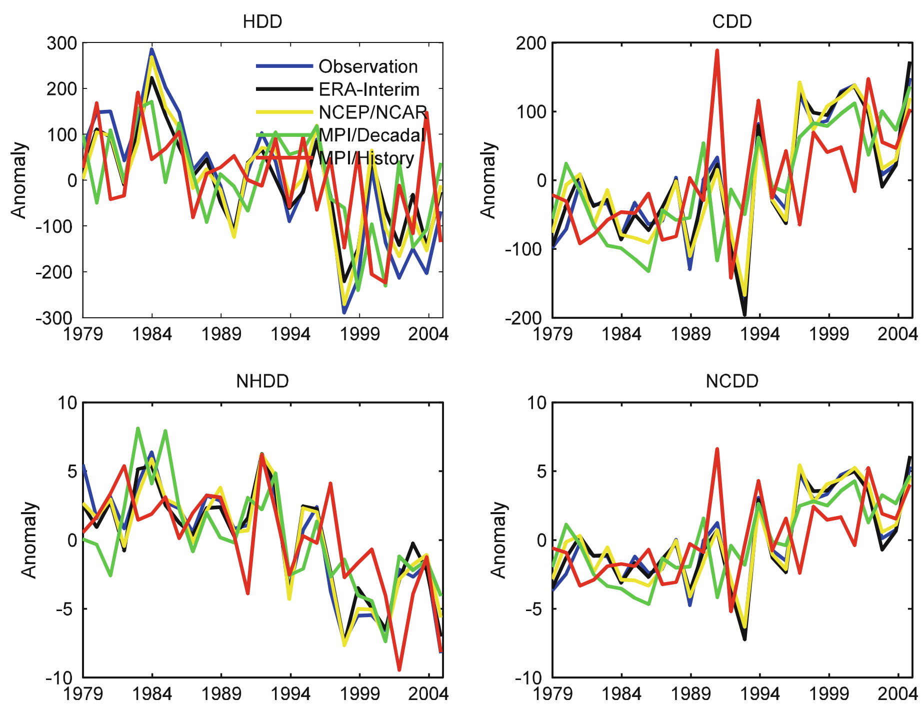

3 Results: past and future changes of degree days

Figure 2 shows the regional changes of HDD, CDD, NHDD and NCDD from observation, two reanalyses and two experiments simulations in China on the annual basis during 1979–2005. The spatial patterns of trends for HDD, CDD, NHDD and NCDD from multi-datasets in China during 1979–2005 are shown in Figs. 3, 4 and 5, respectively. The seasonal and annual trends of each series of indices calculated by Mann–Kendall slope estimator (Sen 1968) are summarized in Table 2. The correlation coefficients between multi-datasets are listed in Table 3.

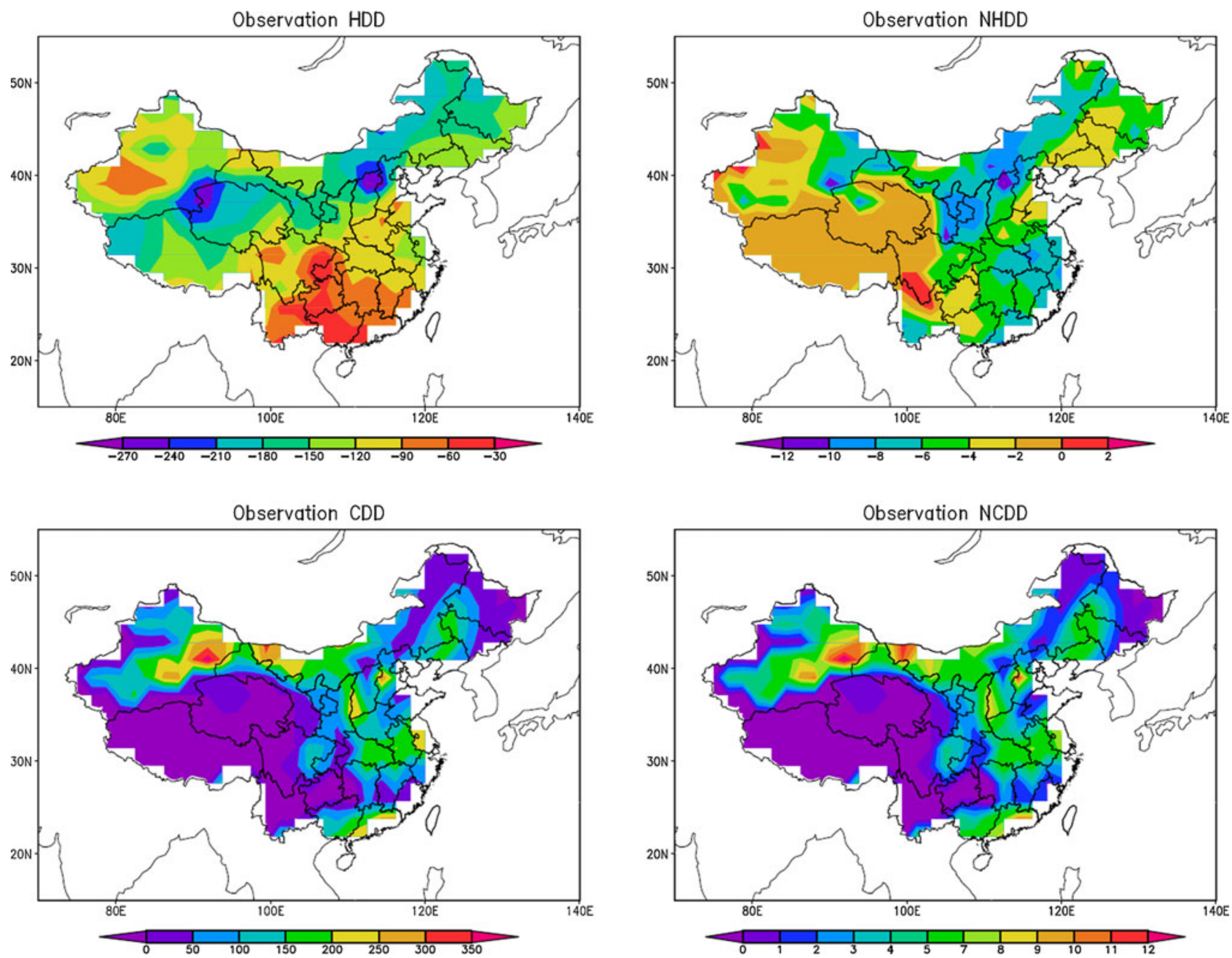

Fig. 3 Spatial trends of HDD, NHDD, CDD and NCDD from observation in China during 1979–2005. The unit is °C/decade for HDD and CDD, and is day/decade for NHDD and NCDD, respectively

3.1 Heating degree days (HDD)

It can be seen from Fig. 2 that the HDD from multi-datasets has decreased during the studied period. The decreasing rates are −130.97, −82.48, −80.52, −65.45 and −69.48 °C/decade for observation, ERA-Interim, NCEP/NCAR, the decadal experiments and historical experiments, respectively. The HDD from both ERA-Interim and NCEP/NCAR reanalyses is closer to observation than the decadal experiment than the historical experiments, indicated by the high correlation coefficients ($R > 0.9$). There are some differences of the season with the largest trend magnitudes. The largest decreasing trends for observation, ERA-Interim and NCEP/NCAR occur in the transition season of spring and autumn, respectively, while both the decadal experiments and historical experiments reveal largest decreasing trends in winter. Overall, the multi-datasets show large decreasing trend magnitudes in the high terrain (such as the Tibetan Plateau) and in high latitude regions (such as the northeastern China), with the exception of the historical experiments. Due to the lower altitudes and latitudes, southeastern China has smallest decreasing trends for all the used datasets. It should be noted that the historical experiments show greatest increases in the northern China, which is not consistent with the observed global warming in the region (Liu et al. 2004).

3.2 Cooling degree days (CDD)

In contrast to HDD, the decreasing trends of CDD are significant for all datasets during 1979–2005, and the observed trend magnitude is 76.91 °C/decade on the annual basis. The correlation coefficients between observation, reanalyses and simulations are higher ($R > 0.45$), and reanalyses are very well captured than the simulations. In most cases, the pronounced increases occur in spring and autumn. For the spatial patterns, the southeastern China have larger increasing trends and the Tibetan Plateau have

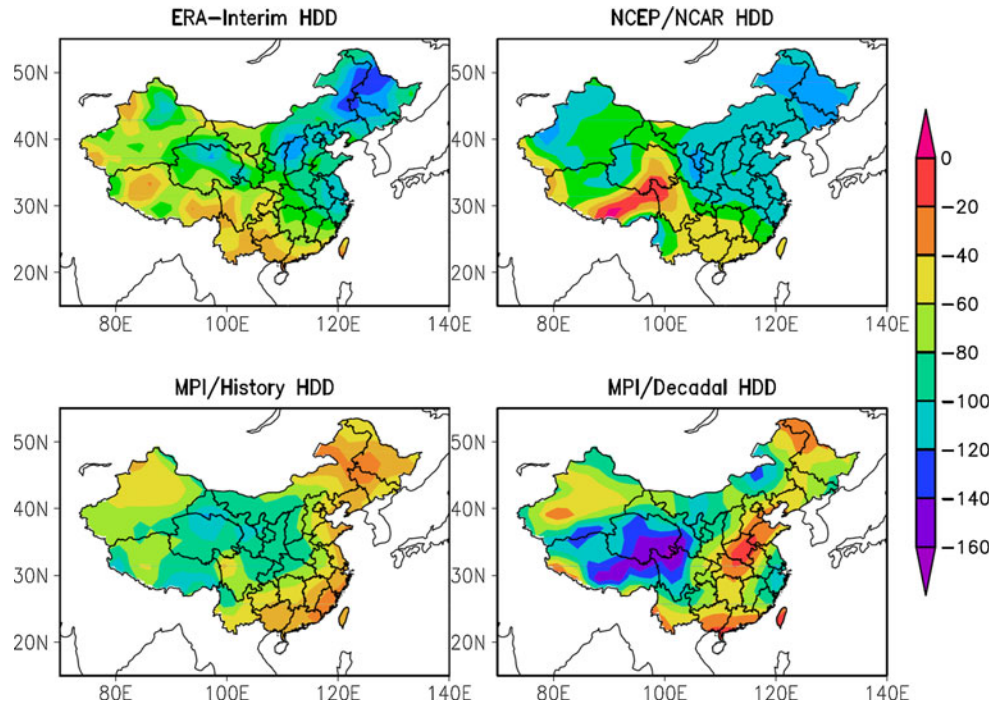

Fig. 4 Spatial trends of HDD from ERA-Interim, NCEP/NCAR reanalysis data and the historical and decadal experiments simulation outputs in China during 1979–2005. The unit is °C/decade

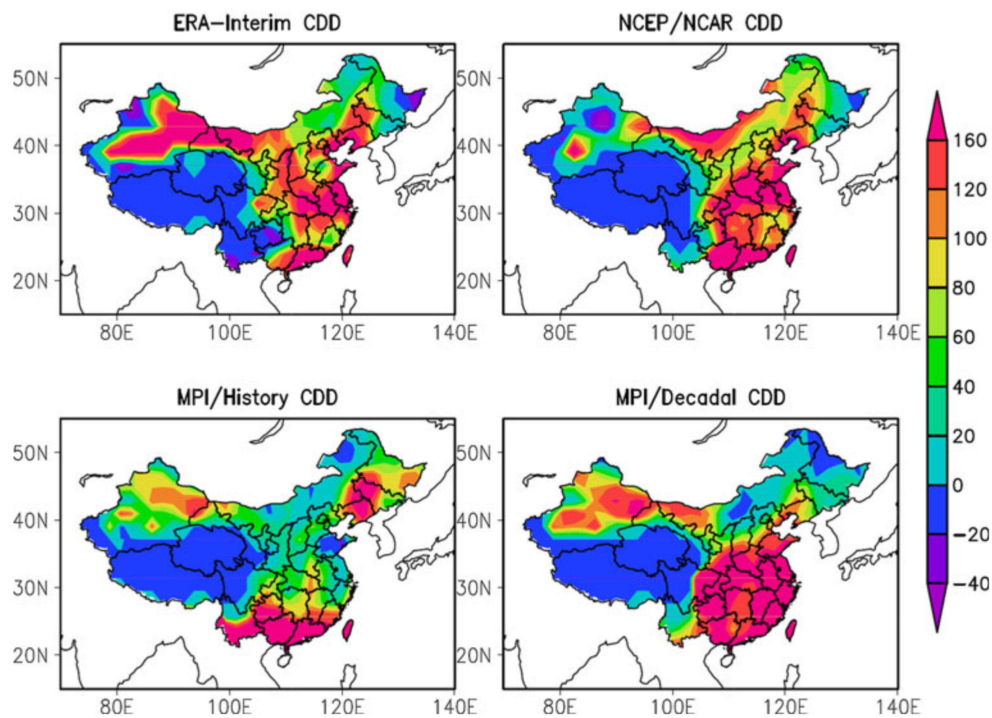

Fig. 5 Same as Fig. 4, but for CDD

the smaller increases, and the differences between reanalyses and model simulations exist in the northeastern TP.

3.3 Number of degree days (NHDD and NCDD)

For NHDD and NCDD, the decreased NHDD and increased NCDD are clear during 1979–2005 for observation, reanalyses and model simulations. Compared with observation, ERA-Interim data reproduce the variabilities of NHDD and NCDD better than NCEP/NCAR, as reflected by the mean anomalies and correlation coefficients. NCEP/NCAR overestimate NHDD and underestimate NCDD, due to the data assimilation in the model system (Ma et al. 2008). On the annual basis, the

Table 2 Regional trend of HDD, CDD, NHDD and NCDD from observation, ERA-Interim, NCEP/NCAR reanalysis data and the simulation outputs under different run experiments in China during 1979–2005 on the annual and seasonal basis

Index	Unit	Annual	Spring	Summer	Autumn	Winter
Observation						
HDD	°C/decade	**−130.97**	**−43.61**	−2.17	**−37.71**	−40.32
CDD	°C/decade	**76.91**	6.18	**53.26**	**12.27**	0
NHDD	Day/decade	**−3.84**	**−1.30**	**−1.45**	**−1.09**	−0.13
NCDD	Day/decade	**2.83**	0.23	**1.86**	**0.47**	0
ERA-Interim						
HDD	°C/decade	**−82.48**	**−33.52**	−0.93	−19.25	−21.81
CDD	°C/decade	**74.95**	6.68	**44.14**	**14.97**	**0.59**
NHDD	Day/decade	**−2.99**	**−0.94**	**−0.90**	**−0.93**	−0.26
NCDD	Day/decade	**2.67**	0.26	**1.68**	**0.56**	0.02
NCEP/NCAR						
HDD	°C/decade	**−80.52**	**−19.06**	**11.80**	**−30.29**	−31.67
CDD	°C/decade	**64.64**	**5.75**	**43.54**	**12.86**	0.13
NHDD	Day/decade	**−3.22**	**−0.68**	**−1.10**	**−1.18**	−0.30
NCDD	Day/decade	**2.47**	**0.22**	**1.55**	**0.49**	0.01
MPI/decadal						
HDD	°C/decade	**−65.45**	**−25.81**	**−12.98**	−3.77	−35.15
CDD	°C/decade	**76.93**	0.52	**56.73**	**22.66**	**1.84**
NHDD	Day/decade	**−2.66**	**−0.79**	−0.93	−0.92	−0.29
NCDD	Day/decade	**2.73**	0.02	**2.01**	**0.87**	**0.08**
MPI/history						
HDD	°C/decade	**−69.48**	−1.37	**−20.04**	**−20.19**	−21.75
CDD	°C/decade	**55.49**	**21.04**	**27.86**	4.41	0.01
NHDD	Day/decade	**−2.80**	**−0.72**	−0.93	**−1.05**	−0.07
NCDD	Day/decade	**2.01**	**0.74**	**0.95**	0.17	0

The linear trends of all series are calculated by Mann–Kendall slope estimator. Trends at the 5 % level are marked in bold

decreasing trends of NHDD for observation, ERA-Interim, NCEP/NCAR, the historical and decadal experiments are −3.84, −2.99, −3.22, −2.66 and −2.80 day/decade, respectively, which are mostly contributed by winter. Meanwhile, the increased annual trends of NHDD for observation, ERA-Interim, NCEP/NCAR, the historical and decadal experiments are 2.83, 2.76, 2.47, 2.73 and 2.01 day/decade, respectively, which are slightly larger than NHDD with the exception of the historical experiments. For the spatial patterns of NHDD, the multi-datasets reveal the negative trends in the western China, and positive trends in the southern China. The differences between ERA-Interim and NCEP/NCAR are found in the Tibetan Plateau, where the pronounced upward trends occur in NCEP/NCAR and slight downward trends for ERA-Interim. In most regions, both the historical and decadal experiments show similar spatial patterns of trends, while they differ for ERA-Interim and NCEP/NCAR in the northeastern China. For the spatial trends of NCDD, the multi-datasets show slight increases in the southern China, and larger increases in the northeastern China. The differences between ERA-Interim and NCEP/NCAR occur in the Tibetan Plateau, similar to NHDD, and both reanalyses depict pronounced positive trends in the northeastern China. Both the historical and decadal experiments of NCDD show consistencies, which differ from renalyses in the northeastern China.

3.4 Future changes

Figure 6 shows the regional changes of HDD, CDD, NHDD and NCDD from the long-term simulations in China during 2006–2100 under RCP8.5, RCP4.5 and RCP2.6. The spatial patterns of trends for HDD, CDD, NHDD and NCDD under RCP8.5 and RCP2.6 are displayed in Figs. 7 and 8, respectively. The seasonal and annual trends of HDD, CDD, NHDD and NCDD are summarized in Table 4.

During the period 2006–2100, HDD and NHDD in China display significant decreases under RCP8.5, with the rates of −142.17 °C/decade and −5.11 day/decade, respectively, mostly contributed by winter. Both HDD and NHDD show

Table 3 Correlation coefficients between observation, ERA-Interim, NCEP/NCAR reanalysis data and the simulation outputs under different run experiments in China in China during 1979–2005 on the annual basis

	Observation	ERA-Interim	NCEP/NCAR	MPI/decadal	MPI/history
HDD					
Observation	1.00				
ERA-Interim	0.97	1.00			
NCEP/NCAR	0.96	0.97	1.00		
MPI/decadal	0.61	0.52	0.59	1.00	
MPI/history	0.33	0.24	0.27	0.34	1.00
CDD					
Observation	1.00				
ERA-Interim	0.99	1.00			
NCEP/NCAR	0.96	0.97	1.00		
MPI/decadal	0.70	0.72	0.75	1.00	
MPI/history	0.49	0.47	0.45	0.34	1.00
NHDD					
Observation	1.00				
ERA-Interim	0.96	1.00			
NCEP/NCAR	0.97	0.98	1.00		
MPI/decadal	0.73	0.74	0.73	1.00	
MPI/history	0.64	0.63	0.64	0.45	1.00
NCDD					
Observation	1.00				
ERA-Interim	0.99	1.00			
NCEP/NCAR	0.96	0.97	1.00		
MPI/decadal	0.70	0.72	0.75	1.00	
MPI/history	0.49	0.46	0.45	0.34	1.00

larger decreasing trends in the northeastern China and the Tibetan Plateau, and slight changes in the southeastern China. Contrarily, CDD and NCDD in China represent the positive trends, with the rates of 154.66 °C/decade and 5.12 day/decade, respectively. The variabilities of HDD, NHDD, CDD and NCDD under RCP4.5 are similar to those under RCP8.5 before the mid-21 century, turning to mild changes afterwards, which lead to rates of −51.75 °C/decade, −1.91 day/decade, 46.31 °C/decade and 1.61 day/decade, respectively. Meanwhile, the spatial patterns of trends are also closer to those under RCP8.5. Under RCP2.6, the variability of HDD, NHDD, CDD and NCDD is closer to both RCP 4.5 and RCP 8.5 before 2050, which turns into opposite directions afterwards. Thus, the annual rates of the four indices during 2006–2011 are not significant, and most regions in China have no change for these indices.

4 Discussions and conclusion

In this study, the HDD, numbers of HDD (NHDD), CDD and the numbers of CDD (NCDD) have been analyzed in China from Max Planck Institute, Earth Systems Model of low resolution (MPI-ESM-LR) model in the CMIP5. To evaluate how the realistic the models are in simulating the recent past, the historical and decadal experiments simulations are compared to observation, ERA-Interim and NCEP/NCAR reanalyses. Four degree days indices are calculated as the accumulated of daily mean temperature and the numbers of days during the period in which daily mean temperature is above/below base temperatures. In this study, the base temperature of 18 and 24 °C is used for heating and CDD, respectively. The degree days indices provide a good supplement for the 27 temperature and precipitation indices for climate extremes defined by the Expert Team on Climate Change Detection and Indices (ETCCDI) (IPCC 2007); they are relevant parameters to study the climate change, especially for the cryospheric region (Kang et al. 2010; Li et al. 2008).

During 1979–2005, both HDD and NHDD have decreased for observation, reanalyses (ERA-Interim and NCEP/NCAR) and model simulations (historical and decadal experiments), consistent with the increased CDD and NCDD. These changes of the four degree days reflect the general warming in China during the past decades, identified by observations and model simulations (Wang et al. 2012). The variability of four degree days is also in accordance with the temperature extremes from observation in China. During 1961–2003, for the majority of stations, significant increases in warm nights/days and significant decreases in cold nights/days are observed in China, consistent with a long-term decrease in diurnal temperature range (You et al. 2011). On the global scale, the widespread significant changes in temperature extremes are associated with warming, especially for those indices derived from daily minimum temperature (Alexander et al. 2006). In the previous studies, the over 10 °C accumulated temperature is regarded as an indicator to study various crop development stages and the threshold for cold invasion, which also has increased in the northeastern China in recent decades (Yan et al. 2011). Thus, degree days keep consistency with other temperature indices and

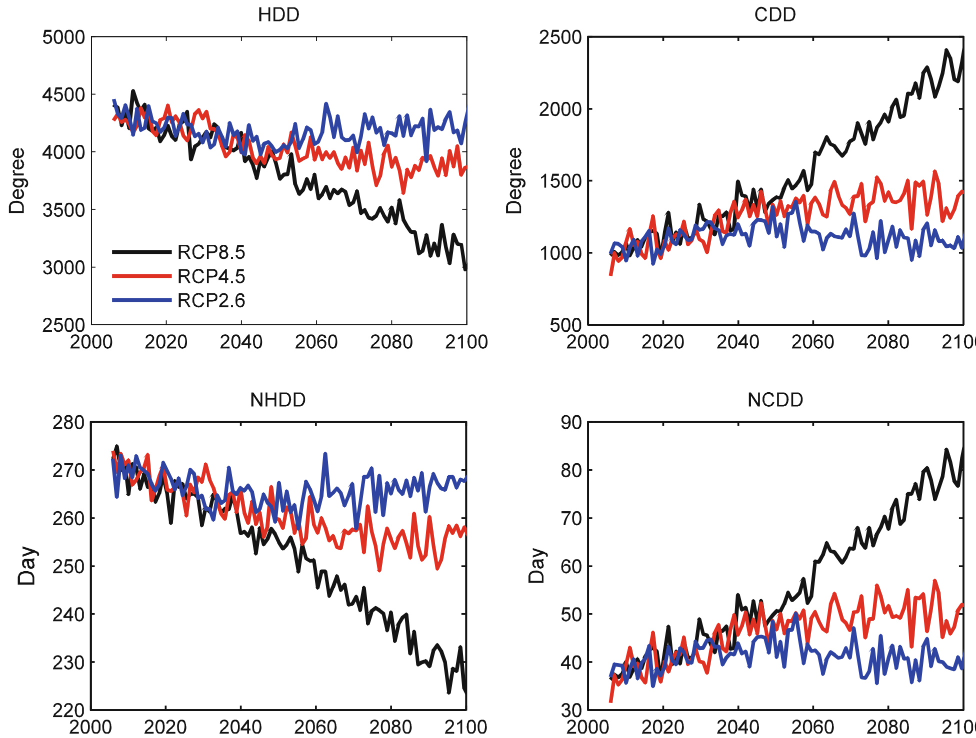

Fig. 6 Regional change of HDD, CDD, NHDD and NCDD from the simulation outputs in China 2006–2100 under RCP8.5, RCP4.5 and RCP2.6

accumulated temperature, and can be used as an indicator to detect climate changes in China.

In most cases, both the decadal experiments and historical experiments can represent the decadal variability of HDD, NHDD, CDD and NCDD shown by observation, ERA-Interim and NCEP/NCAR, and correlation coefficients among them are very high. For the decadal experiments and historical experiments, the spatial patterns of trends for NHDD and NCDD are similar. For spatial patterns of HDD and CDD, the discrepancy between the decadal experiments and historical experiments occurs in the northeastern China, probably due to the CMIP5 strategy of two experiments about aspects of climate model forcing, response, and processes (Taylor et al. 2012). Meanwhile, the historical experiments initialize from the end of freely evolving simulations of the historical period, which in some cases may be coupled to a carbon cycle model, while the decadal experiments will be initialized with observed ocean state and sea-ice (Taylor et al. 2012).

The actual prediction skill of natural climate variability on decadal timescales has received great attention. The CMIP5 has devised an innovative experimental design to assess the predictability and prediction skill at decadal time scales of state-of-the-art climate models. The MPI-ESM-LR decadal hindcasts and forecasts have been conducted. The data consist of simulations over a 10 year period that are initialized every five years during the period 1960/1961 to 2005/2006 (Taylor et al. 2012). The model prediction skill is examined by comparing the annual mean surface temperature from observation, ERA-Interim, NCEP/NCAR reanalysis data, the historical and the ensemble-mean of the MPI-ESM-LR 10 year hindcast/forecast during 1979–2005 (initialized every 5 years) (Fig. 9). During the entire period, MPI-ESM-LR model simulate higher mean surface temperature in China than the observation and NCEP/NCAR, and lower mean surface temperature than ERA-Interim. At the same time, MPI-ESM-LR model simulate close mean surface temperature as the historical simulations. Thus, the decadal hindcast/forecast simulation performance of MPI-ESM-LR produce warmer than the observed mean temperature in China during the entire period. This is consistent with other seven state-of-the-art-ocean–atmosphere coupled models (Kim et al. 2012). The skill in decadal forecasting is associated with boundary conditions (mainly greenhouse gas concentrations but also tropospheric and stratospheric aerosol distributions) and initial conditions (mainly the ocean state) (Kim et al. 2012; Smith et al. 2012; van Oldenborgh et al. 2012).

Besides the differences of degree days from two experiments simulations, there are discrepancies between ERA-Interim and NCEP/NCAR on the spatial patterns and the regional means, which have been confirmed in the study of hydrological process of temperature, precipitation and evaporation, surface radiation and cloud fields (Betts et al. 2009). Compared with two experiments simulations and ERA-Interim, NCEP/NCAR underestimates CDD and NCDD, and overestimates NHDD, suggesting that the cold biases exist for the temperature for NCEP/NCAR. This is

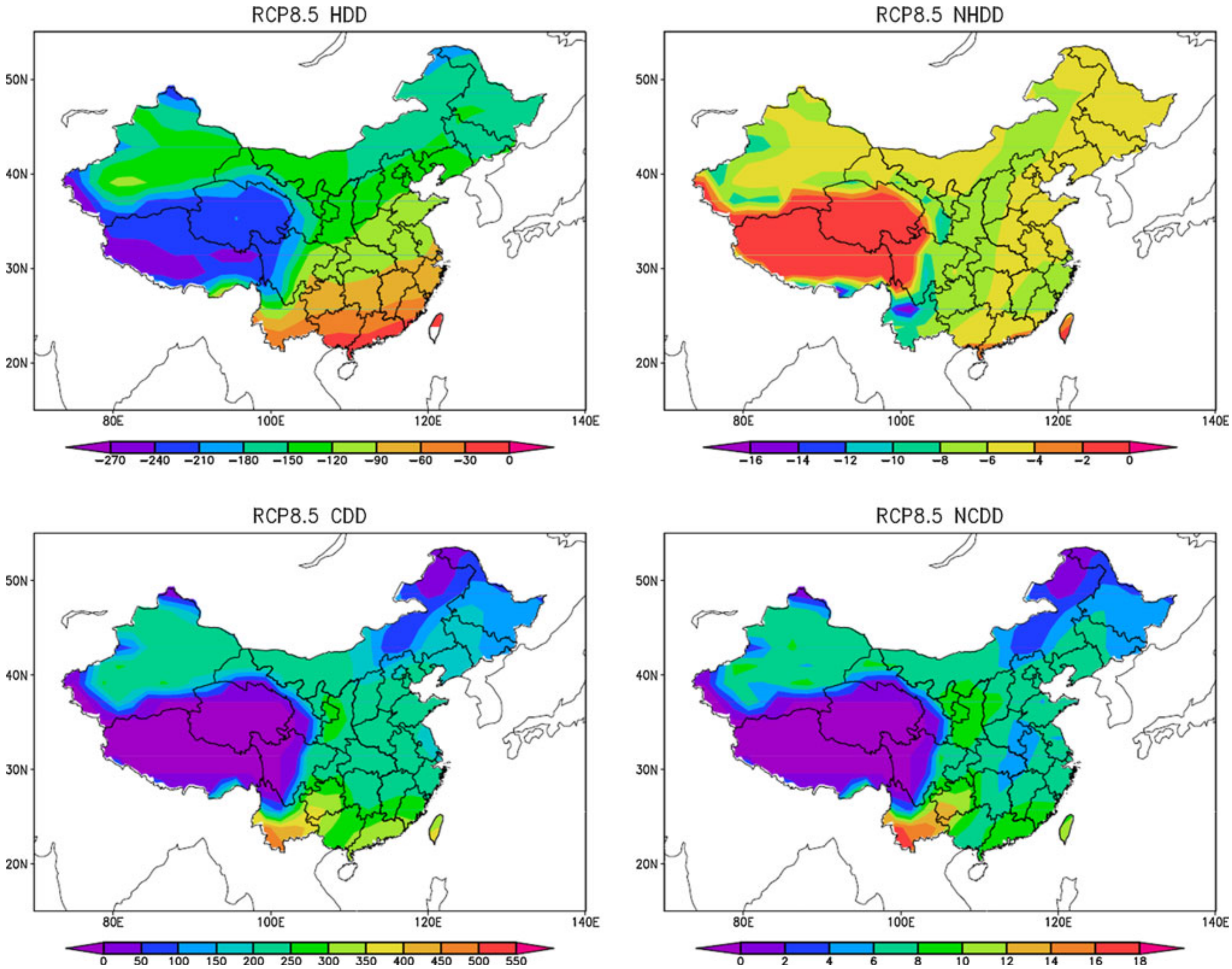

Fig. 7 Spatial trends of HDD, CDD, NHDD and NCDD from the simulation outputs in China during during 2006–2100 under RCP8.5 scenario

in accordance with the previous studies that ERA-40 temperatures correspond closely to the observations than NCEP/NCAR, and the biases are due mainly to the elevation differences in the model assimilation (Ma et al. 2008; You et al. 2010). Moreover, ERA-Interim uses mostly the sets of observations acquired for ERA-40, supplemented by data for later years from the European Centre for Medium-Range Weather Forecasts (ECMWF) operational archive (Dee et al. 2011), and could capture the observations better than ERA-40 and NCEP/NCAR.

Under different RCP emissions scenarios in the CMIP5, HDD and NHDD show significant decreases, and both CDD and NCDD consistently increase during 2006–2100 under RCP8.5, RCP4.5 and RCP2.6, especially before the mid-21 century. More pronounced changes of degree days indices occur in most regions in China under RCP8.5. The variability of HDD, NHDD, CDD and NCDD has good agreements with the radiative forcing trajectories in RCP, which can reflect various possible combinations of economic, technological, demographic, and policy developments (Moss et al. 2010). For example, the RCP2.6 scenario is designed to meet the 2 °C global average warming target compared to pre-industrial conditions, and it has a peak in the radiative forcing at approximately 3 W/m^2 (440 ppm CO_2) before 2050 and then declines to 2.6 W/m^2 by the end of 2100 (330 ppm CO_2). Radiative forcing in RCP4.5 peaks at about 4.5 W/m^2 (540 ppm CO_2) in 2100, which is comparable to the "Special Report on Emissions Scenarios" (SRES) scenarios B1 with similar CO_2 concentrations and median temperature increases by 2100. RCP8.5 assumes a high rate of radiative forcing increasing, peaking at 8.5 W/m^2 (940 ppm CO_2) in 2100 (Rogelj et al. 2012). The degree days indices are results of daily mean temperature influenced by the radiative forcing.

Models lose their memory of the initial conditions and create their own climates and trends. As shown by Bordi et al. (2010) for ECMWF model forecasts, a trend mismatch between observations and model occurs at midlatitudes,

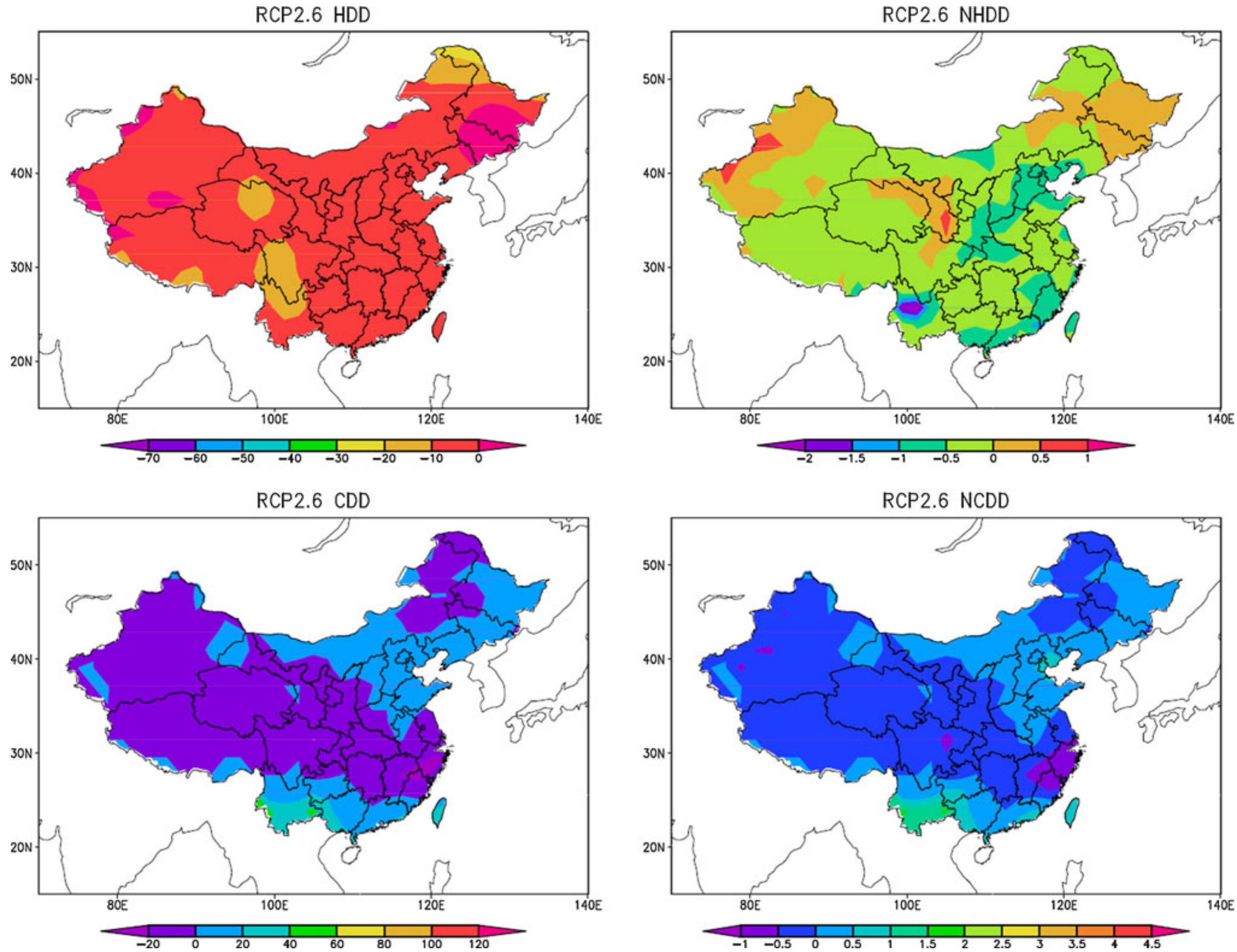

Fig. 8 Spatial trends of HDD, CDD, NHDD and NCDD from the simulation outputs in China during 2006–2100 under RCP2.6 scenario

which might be connected with the model dynamic response rather than with the variations in the imposed external forcing (Bordi et al. 2010). That is, climate extrapolation by simply using climate models may be affected by different trends that observations and models have even at short lead time. Thus, both reanalyses and short-term forecasts by GCMs are required, if the climate has to be predicted. That is, appears to be more important to comprehend the statistics of the short-term tendencies rather than the forecast accuracy of long-term averages. A first step in this direction is the detailed use of the lead-time dependent climate predictions based on the five year updated forecasts. Such analysis needs to be supported by dynamical underpinning as, for example, the dynamics of stationary waves and the stratosphere–troposphere interaction.

There is considerable interest in exploring the degree days to which future climate states depend on the initial climate state, focusing in particular on whether we can more accurately predict the actual trajectory of future climate (including both forced and unforced change) if we initialize the models with at least the observed ocean state (and perhaps also sea ice and land surface) (Taylor et al. 2012). Hence, the differences of decadal runs and the 20th century runs simply reflect the sensitivity to the initial conditions, as stated above. Addressing these uncertainties, that are an intrinsic feature of all climate models, being the main motivation for decadal predictions. To estimate the uncertainty of decadal experiment, the three ensembles are taken showing the time series of annual mean surface temperature in China for the mean of MPI decadal hindcasts and forecasts during 1979–2005 (Fig. 10). For three ensembles, the decadal hindcasts and forecasts are consistent and similar, indicating there is no strong positive/negative deviations from the ensemble mean temperature. The uncertainties in terms of the inter-ensemble root mean square difference are in a range of some tenth of a degree, whereas the long-term trend is well represented and showing no difference among ensembles.

Table 4 Regional trend of HDD, CDD, NHDD and NCDD from the simulation outputs under RCP8.5, RCP4.5 and RCP2.6 in China during 2006–2100 on the annual and seasonal basis

Index	Unit	Annual	Spring	Summer	Autumn	Winter
RCP8.5						
HDD	°C/decade	**−142.17**	**−30.38**	**−9.10**	**−38.62**	**−54.00**
CDD	°C/decade	**154.66**	**25.65**	**93.97**	**29.26**	**4.34**
NHDD	Day/decade	**−5.11**	**−1.40**	**−1.71**	**−1.63**	**−0.33**
NCDD	Day/decade	**5.12**	**0.89**	**2.97**	**1.03**	**0.17**
RCP4.5						
HDD	°C/decade	**−51.75**	**−12.18**	**−3.73**	**−12.42**	**−20.74**
CDD	°C/decade	**46.31**	**9.09**	**27.43**	**8.00**	**1.22**
NHDD	Day/decade	**−1.91**	**−0.51**	**−0.72**	**−0.53**	**−0.12**
NCDD	Day/decade	**1.61**	**0.33**	**0.93**	**0.28**	**0.05**
RCP2.6						
HDD	°C/decade	−3.51	−1.63	0.32	−0.08	−1.57
CDD	°C/decade	1.12	1.80	−0.28	−0.56	0.25
NHDD	Day/decade	−0.14	**−0.11**	0.01	−0.04	−0.05
NCDD	Day/decade	0.04	0.06	−0.01	−0.02	0.01

The linear trends of all series are calculated by Mann–Kendall slope estimator. Trends at the 5 % level are marked in bold

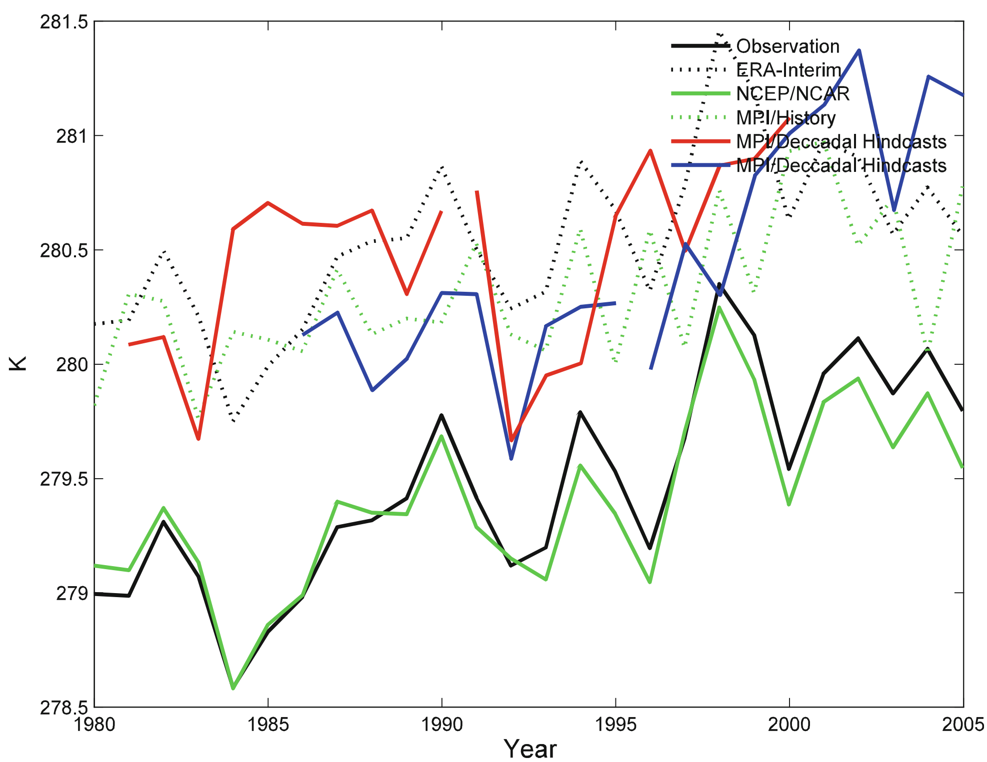

Fig. 9 Time series of averaged annual mean surface temperature (K) in China for observation, ERA-Interim, NCEP/NCAR reanalysis data, the historical and the ensemble-mean of MPI decadal hindcasts and forecasts (*Red* and *blue line*) during 1979–2005. It is 5-year decadal forecasts with 0-year lead for every 5 years during 1979–2005

In this study, the differences of degree days between CMIP3 and CMIP5 are not evaluated, while the main results should be the same from both CMIP3 and CMIP5. The previous studies have addressed that for the temperature indices, the performance of the CMIP3 and CMIP5 multi-model ensembles is similar in regard to their ensemble mean and median, but that the spread amongst CMIP3 models tends to be larger than amongst CMIP5 models, probably due to higher spatial resolution and more comprehensive GCMs of CMIP5 (Sillmann et al. 2013a, b).

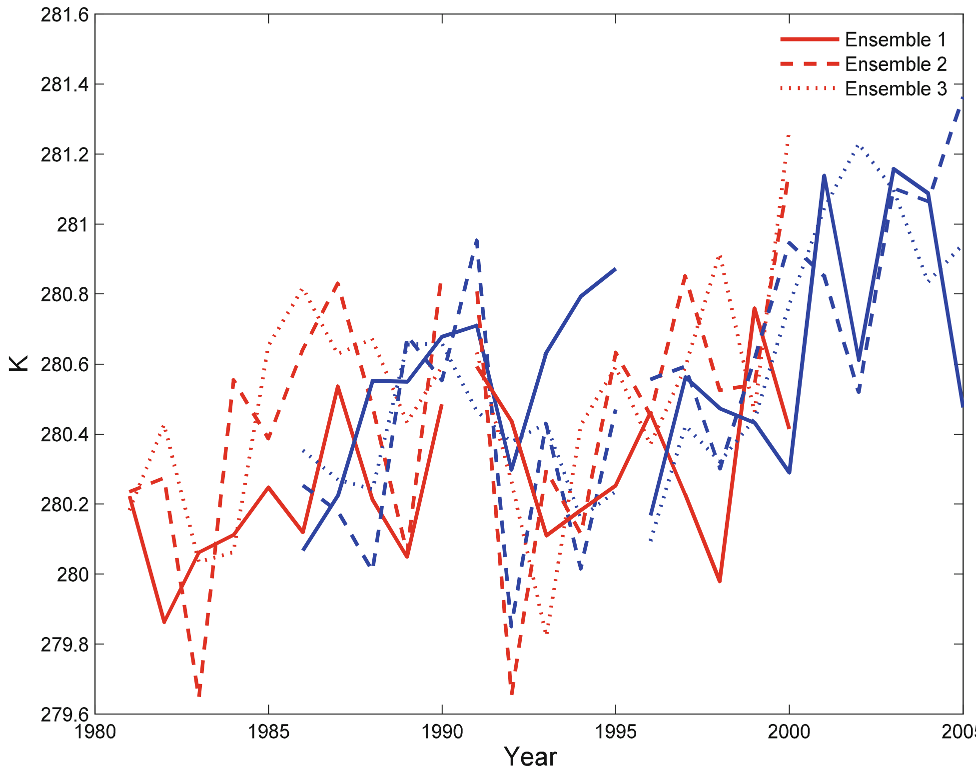

Fig. 10 Time series of averaged annual mean surface temperature (K) in China for three ensembles for the mean of MPI decadal hindcasts and forecasts (*Red* and *blue line*) during 1979–2005. It is 5-year decadal forecasts with 0-year lead for every 5 years during 1979–2005

More attention should be paid to the relationship between degree days and the cryosphere, to improve the understanding and predictability of cryosphere in China in the context of future climate change.

Acknowledgments This study is supported by the National Natural Science Foundation of China (41201072). The authors thank the National Climate Center, China Meteorological Administration, for providing the meteorological data for this study. QY and KF acknowledge support of the Max Planck Fellowship. This study is also funded by the Ministry of Science and Technology of China (Grand No. GYHY201206012) and "the Priority Academic Program Development of Jiangsu Higher Education Institutions" (PAPD). We are very grateful to the reviewers for their constructive comments and thoughtful suggestions.

References

Alexander LV et al (2006) Global observed changes in daily climate extremes of temperature and precipitation. J Geophys Res-Atmos 111:D05109

Betts AK, Kohler M, Zhang YC (2009) Comparison of river basin hydrometeorology in ERA-Interim and ERA-40 reanalyses with observations. J Geophys Res-Atmos 114:D02101

Bordi I, Fraedrich K, Sutera A (2010) Northern Hemisphere climate trends in reanalysis and forecast model predictions: the 500 hPa annual means. Geophys Res Lett 37:L11809

Büyükalaca O, Bulut H, Yılmaz T (2001) Analysis of variable-base heating and cooling degree-days for Turkey. Appl Energy 69(4):269–283

Dee DP et al (2011) The ERA-Interim reanalysis: configuration and performance of the data assimilation system. Q J R Meteorol Soc 137(656):553–597

Ding YH, Ren GY, Zhao ZC, Xu Y, Luo Y, Li QP, Zhang J (2007) Detection, causes and projection of climate change over China: an overview of recent progress. Adv Atmos Sci 24(6):954–971

IPCC (2007) Summary for policymakers of climate change 2007: the physical science basis. Contribution of working group I to the fourth assessment report of the Intergovernmental Panel on Climate Change. Cambridge University Press, Cambridge

Jiang F, Li X, Wei B, Hu R, Li Z (2009) Observed trends of heating and cooling degree-days in Xinjiang Province, China. Theor Appl Climatol 97(3–4):349–360

Kalnay E et al (1996) The NCEP/NCAR 40-year reanalysis project. Bull Am Meteorol Soc 77(3):437–471

Kang SC, Xu YW, You QL, Flugel WA, Pepin N, Yao TD (2010) Review of climate and cryospheric change in the Tibetan Plateau. Environ Res Lett 5(1):015101

Kim HM, Webster PJ, Curry JA (2012) Evaluation of short-term climate change prediction in multi-model CMIP5 decadal hindcasts. Geophys Res Lett 39:L10701

Li X, Cheng GD, Jin HJ, Kang E, Che T, Jin R, Wu LZ, Nan ZT, Wang J, Shen YP (2008) Cryospheric change in China. Glob Planet Change 62(3–4):210–218

Liu BH, Xu M, Henderson M, Qi Y, Li YQ (2004) Taking China's temperature: daily range, warming trends, and regional variations, 1955–2000. J Clim 17(22):4453–4462

Ma LJ, Zhang TJ, Li QX, Frauenfeld OW, Qin DH (2008) Evaluation of ERA-40, NCEP-1, and NCEP-2 reanalysis air temperatures with ground-based measurements in China. J Geophys Res-Atmos 113:D15115

Moss RH et al (2010) The next generation of scenarios for climate change research and assessment. Nature 463(7282):747–756

OrtizBeviá M, Sánchez-López G, Alvarez-Garcìa F, RuizdeElvira A (2012) Evolution of heating and cooling degree-days in Spain: trends and interannual variability. Glob Planet Change 92:236–247
Qin DH, Liu SY, Li PJ (2006) Snow cover distribution, variability, and response to climate change in western China. J Clim 19(9):1820–1833
Rehman S, Al-Hadhrami LM, Khan S (2011) Annual and seasonal trends of cooling, heating, and industrial degree-days in coastal regions of Saudi Arabia. Theor Appl Climatol 104(3–4):479–488
Ren GY, Gu J, Xu MZ, Li QX, Liu XN (2005) Climate changes of China's mainland over the past half century. Acta Meteorol Sinica 63:942–956 (in Chinese with English abstract)
Ren GY, Guan ZY, Shao XM, Gong DY (2011a) Changes in climatic extremes over mainland China. Clim Res 50:105–111
Ren GY, Chen Y, Zou X, Zhou KYQ, Ren YY, Jiang Y, Ren FM, Zhang Q, Wang XL, Zhang L (2011b) Change in climatic extremes over mainland China based on an integrated extreme climate index. Clim Res 50:113–124
Rogelj J, Meinshausen M, Knutti R (2012) Global warming under old an new scenarios using IPCC climate sensitivity range estimates. Nat Clim Change 2(4):248–253
Sen PK (1968) Estimates of Regression Coefficient Based on Kendalls Tau. J Am Stat Assoc 63(324):1379–1389
Sillmann J, Kharin V, Zhang X, Zwiers F, Bronaugh D (2013a) Climate extremes indices in the CMIP5 multimodel ensemble: part 1. Model evaluation in the present climate. J Geophys Res-Atmos 118:1716–1733
Sillmann J, Kharin V, Zwiers F, Zhang X, Bronaugh D (2013b) Climate extremes indices in the CMIP5 multimodel ensemble: part 2. Future climate projections. J Geophys Res-Atmos 118:2473–2493
Smith DM, Scaife AA, Boer GJ, Caian M, Doblas-Reyes FJ, Guemas V, Hawkins E, Hazeleger W, Hermanson L, Ho CK (2012) Real-time multi-model decadal climate predictions. Clim Dyn. doi:10.1007/s00382-012-1600-0
Taylor KE, Stouffer RJ, Meehl GA (2012) An overview of CMIP5 and the experiment design. Bull Am Meteorol Soc 93(4): 485–498
Uppala SM et al (2005) The ERA-40 re-analysis. Q J R Meteorol Soc 131(612):2961–3012
van Oldenborgh GJ, Doblas-Reyes FJ, Wouters B, Hazeleger W (2012) Decadal prediction skill in a multi-model ensemble. Clim Dyn 38(7–8):1263–1280
Wang SW, Gong DY (2000) Enhancement of the warming trend in China. Geophys Res Lett 27(16):2581–2584
Wang SP, Wang ZH, Piao SL, Fang JY (2010) Regional differences in the timing of recent air warming during the past four decades in China. Chin Sci Bull 55(19):1968–1973
Wang HJ, Sun JQ, Chen HP, Zhu YL, Zhang Y, Jiang DB, Lang XM, Fan K, Yu ET, Yang S (2012) Extreme climate in China: facts, simulation and projection. Meteorol Zeitschrift 21(3):279–304
Wild M, Folini D, Schaer C, Loeb N, Dutton EG, Koenigh-Langlo G (2013) The global energy balance from a surface perspective. Clim Dyn 40:3107–3134
Xu Y, Gao XJ, Yan SY, Xu CH, Shi Y, Giorgi F (2009) A daily temperature dataset over China and its application in validating a RCM simulation. Adv Atmos Sci 26(4):763–772
Yan M, Liu X, Zhang W, Li X, Liu S (2011) Spatio-temporal changes of >= 10° accumulated temperature in northeastern China since 1961. Chin Geogr Sci 21(1):17–26
Yao T et al (2012) Different glacier status with atmospheric circulations in Tibetan Plateau and surroundings. Nat Clim Change 2(9):663–667
You QL, Kang SC, Pepin N, Flugel WA, Yan YP, Behrawan H, Huang J (2010) Relationship between temperature trend magnitude, elevation and mean temperature in the Tibetan Plateau from homogenized surface stations and reanalysis data. Glob Planet Change 71(1–2):124–133
You QL, Kang SC, Aguilar E, Pepin N, Flugel WA, Yan YP (2011) Changes in daily climate extremes in China and their connection to the large scale atmospheric circulation during 1961–2003. Clim Dyn 36:2399–2417
Zhai PM, Pan XH (2003) Trends in temperature extremes during 1951–1999 in China. Geophys Res Lett 30(17):1913
Zhang TJ (2007) Perspectives on environmental study of response to climatic and land cover/land use change over the Qinghai-Tibetan plateau: an introduction. Arct Antarct Alp Res 39:631–634

第28卷 第10期
2013年10月

自 然 资 源 学 报
JOURNAL OF NATURAL RESOURCE

Vol.28 No.10
Oct., 2013

黑龙江省大气边界层不同高度风速变化

于宏敏[1]，任国玉[2]，刘玉莲[1*]

(1. 黑龙江省气候中心，哈尔滨 150030；2. 中国气象局 气候研究开放实验室 国家气候中心，北京 100081)

摘要：利用黑龙江省1961—2010年哈尔滨、嫩江、齐齐哈尔、伊春4个气象站探空和地面风速资料，分析了边界层内不同高度风速的气候学特征和时间变化趋势，获得以下结论：①黑龙江省边界层内不同高度年平均风速随高度增加而增大，10 m到300 m风速垂直递增率最大；风速在年内具有明显的季节性特征，各高度都是春季最大，近地面层冬季风速最小，其余高度夏季风速最小。②1961—2010年，近地面10 m高度平均风速1970年代最大，其后各年代风速逐渐减小，2000年代风速最小；300、600、900 m高度，平均风速1980年代最大，从1980年代到2000年代逐渐减小，300 m高度平均风速最小出现在1960年代，600 m和900 m最小出现在1970年代。③1961—2010年，近地面10 m高度平均风速呈明显减弱趋势，递减率为 0.162 m/(s·10 a)，递减趋势主要发生在1970年代以后，但300、600和900 m高度平均风速变化均不显著。④黑龙江省近地面风速变化趋势可能主要与观测环境改变和城市化等非自然因素影响有关，上层的风速变化则主要受大尺度大气环流变化的影响。

关 键 词：气候变化；风能资源；风速；边界层；黑龙江省

中图分类号：P425　　**文献标志码**：A　　**文章编号**：1000-3037(2013)10-1718-13

DOI：10.11849/zrzyxb.2013.10.007

大气边界层，是指接近地球表面、受地面摩擦阻力影响的大气层。大气流过地面时，地面上各种粗糙元，如土丘、庄稼、树木、房屋等，会使大气流动受阻，这种摩擦阻力由于大气中的湍流而向上传递，并随高度的增加而逐渐减弱，达到某一高度后便可忽略。此高度即称为大气边界层厚度，它随气象条件、地形、地面粗糙度而变化，一般为300～1 000 m。

近地面和大气边界层的风速及其变化对于气候变化监测和风能资源评价具有重要意义，得到越来越多的关注[1-5]。研究发现，最近几十年我国大范围地区近地面风速已经明显减弱，北方地区风速下降更为明显，部分地区变化速率可达0.2 m/(s·10 a)[1, 6-9]。刘传顺等[10]根据地面气象观测资料对黑龙江省地面风速变化进行了分析，指出近50 a黑龙江省地面10 m高风速也呈明显的减小趋势，减小速率为0.3 m/(s·10 a)，进入1970年代以后减小趋势更加显著。

对于我国近地面风速明显减弱的原因，刘学锋等[11-12]和张爱英等[8]认为主要和城市化

收稿日期：2012-07-19；**修订日期**：2013-02-05。

基金项目：中国气象局气候变化专项（CCSF2011-18）；公益性行业(气象)科研专项（GYHY201106013, GYHY201206012）；国家科技支撑计划课题（2007BAC29B02）；水利部公益性行业专项（200801001）。

第一作者简介：于宏敏（1966-），女，黑龙江哈尔滨人，硕士，高级工程师，主要从事区域气候变化研究。E-mail: yuhongmin66@163.com

***通信作者简介**：刘玉莲（1974-），女，高级工程师，主要研究方向为区域气候变化。E-mail：liuyl74@qq.com

及观测场周围人工建筑物增加有关，但大尺度大气环流的变化也具有一定作用。刘学锋等[12]发现，河北省边界层内300 m以上各高度层平均风速一般也呈降低趋势，但远没有近地面明显，说明背景大气环流变化是近地面风速下降的一个原因，同时城市化和台站周围观测环境改变对风速减弱具有更重要影响。卞林根等[13]在对北京大气边界层风廓线观测研究中发现，近地面郊区风速大于城区，城、郊风速的垂直分布特征也有较大差异，说明随着城市化发展，被人工建筑包围起来的气象观测站近地面风速将呈现下降趋势。但是，对于观测到的近地面风速减弱的原因，目前还没有完全达成共识[2,9]，需要开展进一步研究。分析探讨不同地区各类台站大气边界层内风速变化以及各高度风速与近地面风速之间的关系，为了解观测场周围环境变化对风速变化产生的影响提供了一种新的思路。

就风能资源评价来说，目前主流风机高度多在50 m和70 m，而我国气象观测站网的风速观测中没有这两个高度的信息，评估时需要采用地面观测风速对拟建风电场测风数据进行订正。背景大气环流的变化对边界层内风速变化的影响、城市化和观测场周边环境改变对气象站测风资料的影响，直接关系到测风数据订正的准确性，对风电场的设计方案及经济性分析产生影响。分析了解大气边界层中风速气候特征及其变化规律，认识不同层次风速变化的原因，包括理解近地面风速观测的代表性和测量偏差，对于客观评价风能资源潜力及其随时间变化规律，推动未来风能资源开发和规划，也具有实际价值。

本文应用黑龙江省近地面边界层内风速观测资料，比较分析不同高度风速变化情况，以期进一步理解区域地面风速变化的机理，为当地风能资源评价工作提供科学信息。

1　资料及方法

1.1 资料来源和处理

资料来自黑龙江省内4个气象探空观测站（哈尔滨、嫩江、齐齐哈尔、伊春）1961—2010年逐日探空和地面风速观测记录。4个站按国家一级高空站设置标准，间距300 km，分别位于不同气候区域，对于黑龙江全省城镇气象台站具有一定代表性（图1）。

哈尔滨站位于黑龙江省南部，松嫩平原东部，东临张广才岭支脉丘陵，北部为小兴安岭山区，中部有松花江流过，平原辽阔（表1）。原址在哈尔滨市东郊，1969年6月迁至西郊，1981年1月又迁回东郊，两址距离14 km。随城市化发展，现址周围有不同高度建筑物环绕。嫩江站位于黑龙江省西北部，北依大兴安岭伊勒呼里山，东接小兴安岭，南连松嫩平原。1971年6月由原址迁到南郊，距离1 km。齐

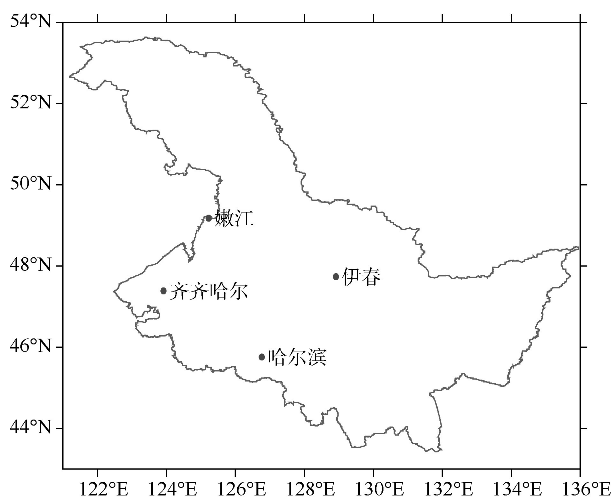

图1　黑龙江省4个探空台站地点

Fig.1 Distribution of the four sounding stations in Heilongjiang Province

齐哈尔站位于黑龙江省西部的松嫩平原腹地，地势北高南低，北部和东部是小兴安岭南麓，中部和南部为冲积平原。1964年1月由原址北迁6 km，2002年1月又北迁1 km。伊春站位于黑龙江省东北部，小兴安岭纵贯全境。1989年1月由原址北迁41 km。气象站迁址可以对某些气候变量的地面观测历史记录产生非均一性，即在时间序列上出现不连续点或断点，影响气候变化时间特征特别是趋势变化特征的分析。但是，采用统计方法检验4个站近地面和高空年平均风速数据，没有发现明显的非均一性，因此未作资料均一化处理。

表1 黑龙江省4个探空站位置及其变动情况

Table 1 The locations and relocations of the four sounding stations in Heilongjiang Province

站号	站名	东经 / (°E)	北纬 / (°N)	海拔/m	迁站次数	迁站年份
50953	哈尔滨	126.77	45.75	142.3	2	1969, 1981
50557	嫩江	125.23	49.17	242.2	1	1971
50745	齐齐哈尔	123.92	47.38	145.9	2	1964, 2002
50774	伊春	128.92	47.73	240.9	1	1989

首先将各探空站每日07:00、19:00两个时次不同高度测风资料进行信息化处理；然后用2个时次平均作为不同高度的日平均风速，依次统计边界层内300、600、900 m高度的月、季、年单站平均风速和4个站平均风速；同时计算4个站近地面10 m高EL型电接风07:00、19:00测风记录的平均值作为地面日平均风速，并统计了与各高度层相对应的月、季、年平均地面风速。4个站均为国家基本站，资料的完整性较好，为了利于比较，均选用1961—2010年完整的50 a观测资料。

1.2 计算方法

气候变化趋势或速率的估计采用最小二乘法，计算样本与时间序号（自然数列1，2……）的线性回归系数。趋势系数为风速序列与时间序号（自然数列1，2……）的相关系数。趋势系数为正（负），则表示平均风速在所统计的时间内有线性增多（减少）的趋势；反之亦然。采用t检验法对风速变化趋势进行显著性检验，并选择$\alpha=0.05$为显著性水平，分别对各站和4站平均风速的变化趋势进行显著性检验。

采用气象季节划分方法，以3—5月为春季，6—8月为夏季，9—10月为秋季，11月至翌年2月为冬季，季平均风速是季内各月平均风速平均值，年平均风速是年内12个月平均风速的平均值，气候平均取1971—2000年30 a平均，全省平均为4站风速的算术平均。

2 结果及分析

2.1 风速年内变化特征

从图2可见，全省平均不同高度平均风速具有明显的季节变化特征，春季风速较大，风速较小的季节除近地面10 m高度为冬季外，其余高度都在夏季。近地面10 m高度的风速最大值出现在5月，其次是4月和6月，最小值在1月；300 m高度风速最大值出现在4月，其次是10月和5月，最小值在7月；600 m高度风速最大值出现在4月，其次是10月和11月，最小值在7月；900 m高度风速最大值出现在4月和11月，其次是10月，最小值在7月。多年平均风速随高度增加而递增，10、300、600、900 m高度年平均

风速分别为2.9、7.4、8.3、8.6 m/s（表2），从10 m到300 m风速递增最明显，增幅达4.5 m/s，300 m以上层次平均风速垂直递增速率明显减小，说明随高度增加风速受地面粗糙度的影响在逐渐弱化。

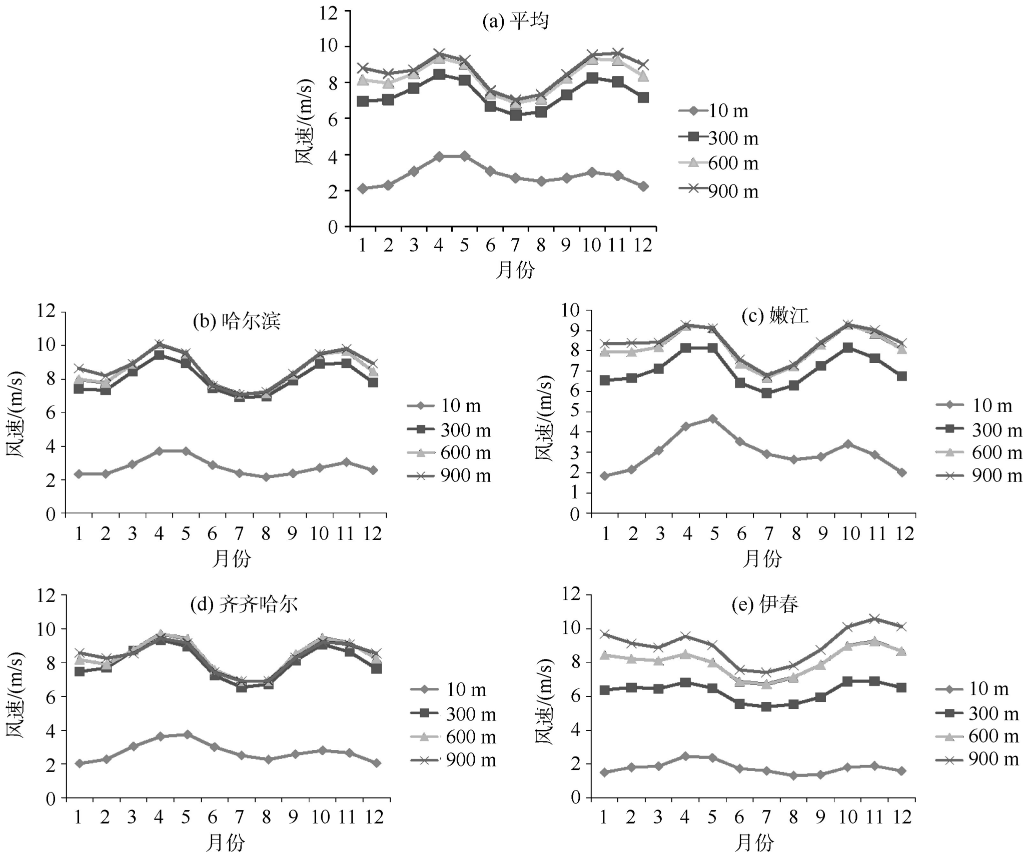

图2 黑龙江省边界层内不同高度月平均风速比较

Fig. 2 The monthly mean wind speed at different heights in boundary layer in Heilongjiang Province

表2 不同高度年平均风速（1971—2000年）

Table 2 Annual mean wind speed at different heights in Heilongjiang Province (1971 – 2000) (m/s)

	10 m	300 m	600 m	900 m
哈尔滨	3.375	8.035	8.513	8.663
嫩江	3.183	7.087	8.184	8.363
齐齐哈尔	3.038	8.003	8.382	8.354
伊春	1.812	6.282	8.061	9.047
4站平均	2.852	7.352	8.285	8.607

各站不同高度风速季节变化和月变化特点有相似，也有差异。从季节变化看，地面10 m高度4个站季节平均风速都是春季最大，冬季最小；其它高度，除伊春600 m和900 m的季节平均风速最大值在冬季外，其余台站都出现在春季，夏季风速最小。从月变化看，10 m高度月平均风速最大值哈尔滨和伊春出现在4月，嫩江和齐齐哈尔在5月，最小值都在1月；其它高度，月平均风速最大值哈尔滨和齐齐哈尔在4月，嫩江在

10月，伊春在11月，最小值都在7月。

比较各高度4个站年平均风速（表2、图3），10 m高度风速最大是哈尔滨，其次为嫩江、齐齐哈尔，最小是伊春；300 m和600 m高度均是哈尔滨年平均风速最大，其次为齐齐哈尔、嫩江，伊春风速最小；900 m高度是伊春风速最大，其次为哈尔滨、嫩江，齐齐哈尔风速最小。从4个站年平均风速垂直递增率看（表3），各地各高度层之间存在明显差异。10 m到300 m垂直递增率最大的是齐齐哈尔，最小的是嫩江；300 m到600 m垂直递增率最大的是伊春，最小的是齐齐哈尔；600 m到900 m垂直递增率最大的是伊春，齐齐哈尔略有减小。伊春站由300 m到600 m再到900 m垂直递增率明显高于其他站，主要与小兴安岭的山地地形有关。从地面到900 m高度，垂直递增率从大到小依次为伊春、齐齐哈尔、哈尔滨、嫩江，平均为0.647 m/(s·100 m)。

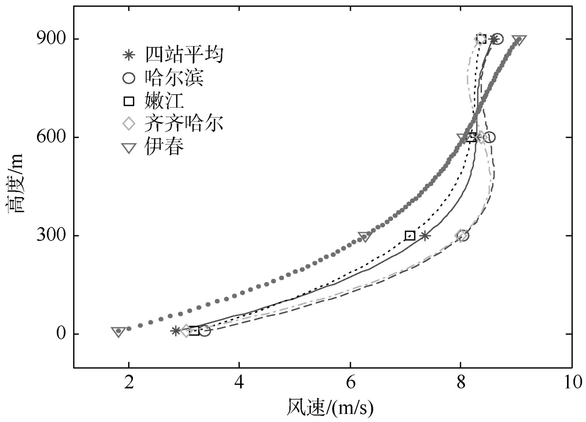

图3 边界层内不同高度各站及其平均年平均风速垂直分布（1971—2000年）

Fig.3 Vertical distribution of annual mean wind speed at different heights in Heilongjiang Province (1971－2000)

表3 不同高度4站及其平均年平均风速垂直递增率（1971—2000年）

Table 3 The vertical rate of annual mean wind speed between different heights in Heilongjiang Province (1971－2000) (m/(s·100 m))

	10～300 m	300～600 m	600～900 m	10～900 m
哈尔滨	1.607	0.159	0.050	0.594
嫩江	1.346	0.366	0.060	0.582
齐齐哈尔	1.712	0.126	−0.009	0.597
伊春	1.541	0.593	0.329	0.813
4站平均	1.552	0.311	0.107	0.647

图4是各站低层各月平均风速与900 m高度月平均风速差值序列，选取的时段为各站都无迁站与仪器变更的稳定期。边界层内越往上，大气流动受地面摩擦影响越小，本文以900 m高度风速为基准，计算下面各层风速与其差值，分析各层风速受地面摩擦影响程度。可见，600 m高度风速，平原（哈尔滨、齐齐哈尔）和半山（嫩江）测站各月受地面影响程度相对较山地（伊春）测站小，冬季受地面影响风速减小程度大于其它各季。300 m高度风速，平原测站（哈尔滨、齐齐哈尔）受地面影响风速减小程度略大于600 m，夏季受地面影响风速减小程度较弱，冬季较强；半山（嫩江）测站受地面影响

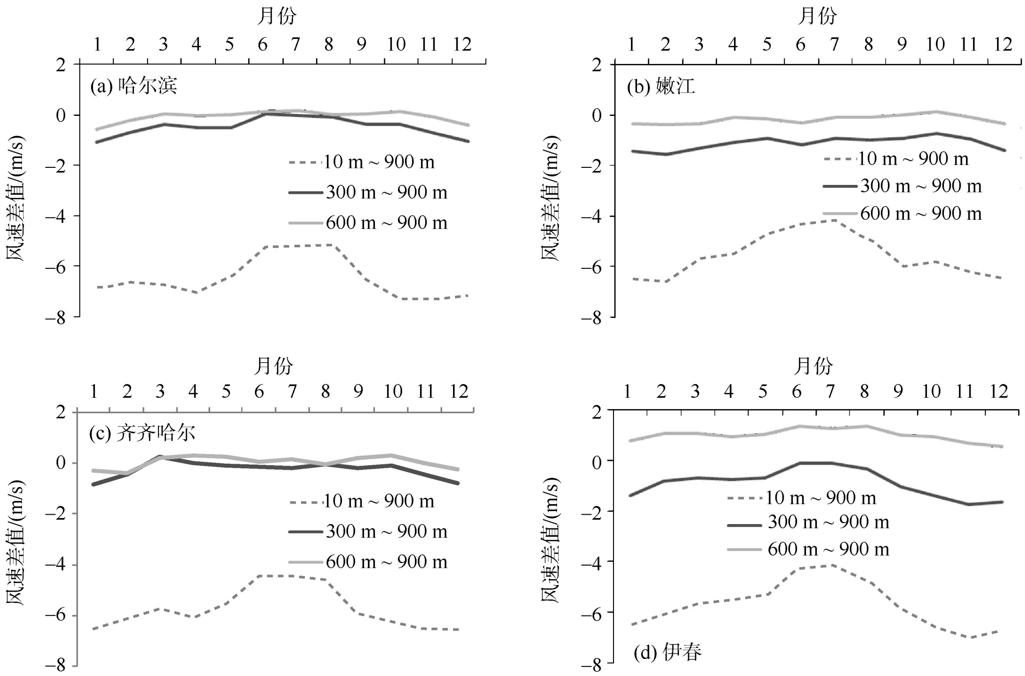

图4 各站10、300、600 m月平均风速与900 m月平均风速差值（1989—2001年）

Fig.4 The monthly mean wind speed difference based on the 10 m, 300 m, 600 m and 900 m in Heilongjiang Province (1989－2001)

表4 不同地面条件台站10、300、600 m平均风速与900 m平均风速差值（1971—2000年）

Table 4 The mean wind speed difference of 10 m, 300 m and 600 m from 900 m at different stations in Heilongjiang Province(1971－2000) (m/s)

季节		年度	春季	夏季	秋季	冬季
平原	10～900 m	−5.63	−5.51	−4.52	−6.08	−6.34
	300～900 m	−0.95	−0.87	−0.61	−0.84	−1.34
	600～900 m	−0.16	−0.06	−0.06	−0.05	−0.38
半山地	10～900 m	−5.64	−5.57	−4.48	−6.06	−6.37
	300～900 m	−0.35	−0.05	−0.25	−0.15	−0.76
	600～900 m	0.03	0.24	0.05	0.23	−0.25
山地	10～900 m	−7.27	−6.92	−6.04	−7.82	−8.18
	300～900 m	−2.76	−2.56	−2.10	−3.00	−3.27
	600～900 m	−0.99	−0.95	−0.69	−1.00	−1.21

风速减小程度较600 m更强，冬季受影响程度大于其它各季；山地（伊春）测站受地面影响，风速减小程度最强。近地面10 m高度风速（表4），平原和半山地测站减小5.63 m/s和5.64 m/s，山地测站减小7.27 m/s，多于平原与半山测站1.64 m/s和1.63 m/s；不同下垫面测站冬季受地面摩擦影响，风速减弱程度均较大，夏季风速受地面摩擦减弱程度均 较小。

2.2 风速年代和趋势变化特征

表5为各年代各站不同高度平均风速距平，图5表示边界层内不同高度各年代平均风

表5 边界层内不同高度各年代年平均风速距平值

Table 5 Wind speed anomaly at different heights in each decade in Heilongjiang Province (m/s)

层次	站名	1960年代	1970年代	1980年代	1990年代	2000年代
10 m	哈尔滨	0.143	0.877	−0.191	−0.686	−1.202
	嫩江	−1.002	0.285	0.062	−0.346	−0.413
	齐齐哈尔	0.463	0.040	0.258	−0.298	0.011
	伊春	0.394	0.119	−0.042	−0.078	−0.281
300 m	哈尔滨	−0.269	−0.212	0.097	0.115	0.002
	嫩江	0.021	−0.139	0.072	0.065	0.293
	齐齐哈尔	0.194	−0.269	0.136	0.132	−0.774
	伊春	−0.697	−0.004	0.210	−0.205	−0.080
600 m	哈尔滨	−0.075	−0.161	0.054	0.106	0.043
	嫩江	−0.014	0.084	−0.002	−0.082	0.100
	齐齐哈尔	0.211	−0.304	0.191	0.113	−0.391
	伊春	−0.359	0.015	0.027	−0.042	0.073
900 m	哈尔滨	0.139	−0.104	0.056	0.049	−0.015
	嫩江	0.215	0.076	−0.032	−0.043	0.051
	齐齐哈尔	0.089	−0.364	0.200	0.164	−0.061
	伊春	−0.459	−0.077	0.064	0.014	−0.008

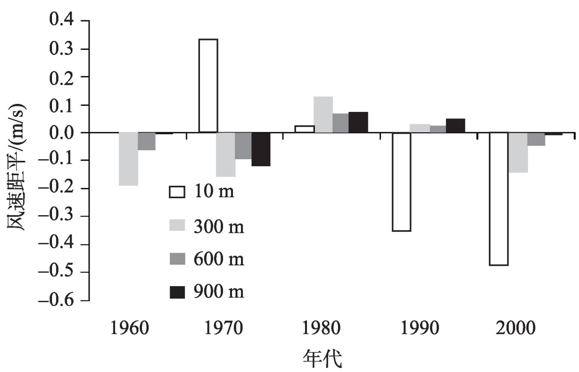

图5 边界层内不同高度4站平均各年代平均风速距平

Fig.5 The 4-station averaged annual mean wind speed anomaly at different heights in each decade in Heilongjiang Province

速距平变化。对近地面10 m高度，各站平均风速1960年代较小，1970年代最大（3.182 m/s），从1970年代到2000年代逐渐减小，2000年代达到最小值（2.381 m/s）；哈尔滨和嫩江从1970年代到2000年代都是减小趋势，伊春从1960年代到2000年代风速持续减小，而齐齐哈尔从1960年代到2000年代的变化规律是：大—小—大—小—大；平均风速最大的年代哈尔滨（4.252 m/s）、嫩江（3.468 m/s）都出现在1970年代，齐齐哈尔（3.501 m/s）、伊春（2.206 m/s）出现在1960年代，平均风速最小的年代哈尔滨、伊春均出现在2000年代，嫩江和齐齐哈尔分别出现在1960年代和1990年代。因此，哈尔滨、嫩江、伊春3站的近地面年代平均风速均表现出长期减小趋势，但齐齐哈尔没有明显趋势变化，地面平均风速年代和趋势变化明显不同于其它站。该站于2002年有一次迁站，其后台站周围建筑物减少，观测环境改善，致使地面平均风速增大，可能是导致其2000年代风速增加的主要原因之一。

对300、600、900 m高度风速，各站平均1980年代到2000年代都呈减小趋势，平均风速最大年代在1980年代，除300 m平均风速最小在1960年代外，600 m和900 m风速最小都出现在1970年代。

随高度和季节变化，各站平均年平均风速变化具有明显差异（表6、图6）。1961—2010年，近地面10 m高度风速变化具有明显的递减趋势，递减率为0.162 m/(s·10a)，通过了0.05的显著性检验；1971—2010年和1981—2010年，近地面10 m高度风速下降速率更大（均通过0.05的显著性检验）。而300 m高度年平均风速变化在1961—2010年和1971—2010年呈增加趋势，1981—2010年呈下降趋势，但均未通过显著性检验；600 m和900 m高度风速变化也不明显，1961—2010年和1971—2010年间呈不显著的上升趋势，1981—2010年间则为不显著的下降趋势。

1961—2010年，各站平均近地面10 m高度各季节平均风速变化均呈减小趋势，并通过了0.01显著性检验。高空300 m及以上高度，春季和冬季平均风速均为增加趋势，其中300 m高度冬季增加通过0.05显著性检验，其余均未通过显著性检验；夏季全部表现为不明显的减小，但均未通过显著性检验；秋季900 m高度是不明显的减小趋势，600 m高度是不明显的增加趋势，300 m高度的增加趋势通过了0.05显著性检验(表6)。

表6 4站平均不同高度年和季节平均风速变化速率（1961—2010年）

Table 6 Changing rate of 4-station averaged annual and seasonal mean wind speed for different heights in Heilongjiang Province (1961－2010) (m/(s·10a))

层次	春季	夏季	秋季	冬季	年
10 m	−0.218**	−0.113**	−0.156**	−0.161**	−0.162*
300 m	0.000	−0.006	0.023*	0.068*	0.028
600 m	0.010	−0.034	0.006	0.053	0.016
900 m	0.028	−0.032	−0.001	0.039	0.015

注：**α=0.01水平下通过显著性检验；*α=0.05水平下通过显著性检验。下同。

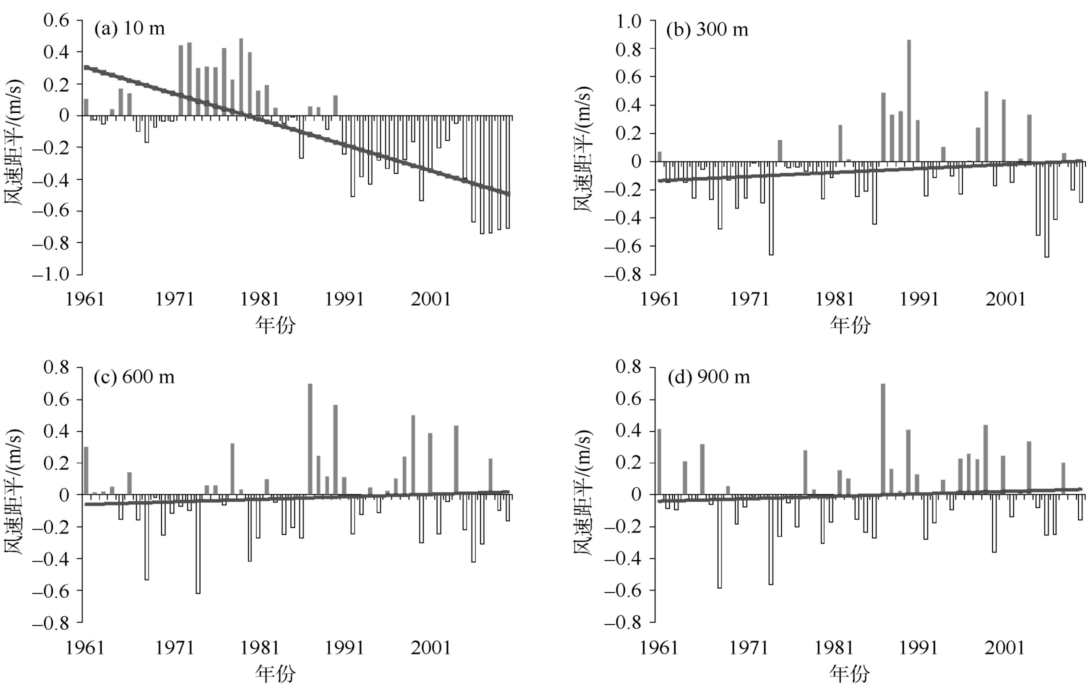

图6 边界层内不同高度年平均风速距平变化

Fig.6 The change of wind speed anomaly at different heights in Heilongjiang Province

表7给出各站不同高度年和季节平均风速变化趋势，图7表示各站各高度年平均风速变化速率的垂直分布情况。哈尔滨站近地面10 m高度平均风速变化年和四季都呈显著的减小趋势，300 m和600 m高度风速变化冬季均表现为显著增加，900 m高度年和四季风速变化趋势不显著；嫩江站近地面10 m高度风速变化年和四季不明显，300 m高度风速变化年和秋、冬季明显增加，600 m高度风速变化年和四季都无明显趋势，900 m高度仅夏季表现为显著减小；齐齐哈尔站近地面10 m高度风速变化年和四季都表现为明显的减小趋势，300 m高度风速变化年和四季为减小趋势，除冬季外其它季节的减小都通过0.05显著性检验，600 m和900 m高度风速年和四季变化趋势不显著；伊春站近地面10 m高度风速变化年和四季都表现为减小趋势，300、600 m高度风速变化年和春季、冬季表现为递增趋势，900 m高度年和春季增加趋势明显。

表7 4站不同高度年和季节平均风速变化趋势

Table 7 Changing trend of annual and seasonal mean wind speed at different heights of four stations in Heilongjiang Province (m/(s·10a))

层次	站名	春季	夏季	秋季	冬季	年
10 m	哈尔滨	−0.529**	−0.322**	−0.433**	−0.393**	−0.413**
	嫩江	0.033	0.075	0.086	0.064	0.065
	齐齐哈尔	−0.202**	−0.082*	−0.118**	−0.154**	−0.144**
	伊春	−0.173**	−0.124**	−0.159**	−0.160**	−0.156**
300 m	哈尔滨	−0.006	0.030	0.109	0.145*	0.074
	嫩江	0.042	0.004	0.140*	0.105*	0.084*
	齐齐哈尔	−0.167*	−0.150*	−0.156*	−0.114	−0.145*
	伊春	0.131*	0.091	0.000	0.137**	0.100*
600 m	哈尔滨	−0.033	−0.003	0.061	0.150*	0.051
	嫩江	−0.023	−0.069	0.037	0.017	0.005
	齐齐哈尔	−0.049	−0.101	−0.070	−0.057	−0.070
	伊春	0.145*	0.035	−0.004	0.102*	0.077*
900 m	哈尔滨	−0.088	−0.072	−0.016	0.098	−0.012
	嫩江	−0.048	−0.120*	−0.045	−0.044	−0.047
	齐齐哈尔	0.068	−0.010	0.035	0.020	0.026
	伊春	0.178*	0.074	0.020	0.082	0.094*

哈尔滨和伊春站年平均风速变化趋势的垂直剖面比较相似，均表现为近地面显著下降，300 m及以上高度呈不明显上升趋势；但嫩江和齐齐哈尔站比较特殊，前者近地面没有显著下降，900 m高度却出现了比较明显的减小，而后者近地面风速呈明显减小趋势，但与哈尔滨和伊春站比较减小程度略小，而且300 m和600 m高度年平均风速变化与其他站截然不同，呈现出比较明显的下降趋势，300 m高度下降趋势尤其明显（图7）。

3 讨论

对于黑龙江省4个探空站的高空风速观测数据，在资料处理当中曾使用SHNT方法[14]对其进行了非均一性检验，没有发现明显断点，因此未作均一化处理。但是，在1961—2010年间，有两次全国范围的测风仪器变更，1967—1970年期间，地面测风仪由维尔德

型转换为EL电接风风速计，2004—2007年期间，又由EL电接风风速计转换为DYYZⅡ风向风速计自动站仪器测风，可能在一定程度上导致近地面风速观测记录出现不连续性。本文获得的近地面10 m平均风速在1970年代初期确比1960年代中后期系统偏高，可能在一定程度上与更换仪器引起的非均一性有关。但是，由于近地面10 m风速下降主要发生在1970年代中期以后（图6），即使考虑变更仪器产生的非均一性，使用订正后资料计算获得整个时期地面平均风速序列，其长期下降趋势也将很明显。因此，更换仪器引起的非均一性不至于对本文主要分析结果产生显著影响。地面环境改变对测风影响无疑具有显著影响[11]，其对黑龙江省地面平均风速的影响已有另文分析讨论[15]。

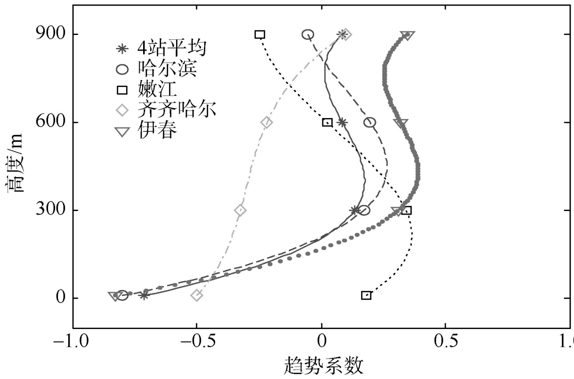

图7 边界层内不同高度年平均风速变化趋势系数分布（1961—2010年）

Fig.7 Tendency coefficient of annual mean wind speed for four stations at different heights in Heilongjiang Province (1961－2010)

本文分析发现，黑龙江省各探空站各个季节平均近地面风速冬季最小，边界层内其它高度却是夏季较小。任国玉等[16]对全国风速气候学特征的分析结果表明，全国平均来看，850 hPa（海拔约1 500 m）以下平均风速均为夏季最小；刘学锋等[12]在分析河北省边界层内平均风速变化时也指出夏季平均风速最小。在北半球中高纬度地带，南北温度差异造成的热成风影响占据主导地位，这种南北温度差异在冬季、春季和秋季较大，因而这些季节的平均风速也较强，夏季风速一般较弱；另外，中国大部地区处于盛行西风带，上层以偏西风为主，夏季来自海洋的偏南暖湿气流活跃，偏南风较多，低层气流和高空气流运动不完全一致，东部沿海地带近地面和高层气流运动方向甚至相反，促使低层的偏东风因受高层偏西风的影响而削弱，而冬季近地面则盛行西北风，与高空气流方向基本一致，低层西北风得到加强，这也是我国大部分地区近地面风速在夏季很弱的一个原因。但是，黑龙江省探空站所测得夏季近地面风速却不是最小，最小风速发生在冬季，与其他地区存在明显差异。造成这一差异的主要因素可能在于探空站处于较高的纬度和特殊的地形区域，同时也与探空站所在地城市化发展有关。黑龙江省是我国纬度最高的省份，冬季受西伯利亚高压影响明显，盛行沉降运动，地面空气静稳，风速微弱；另外，除哈尔滨站外，其余3个站或者位于大兴安岭东坡背风坡，或者处于小兴安岭山地内部，地形作用突出，冬季地面风速进一步降低。本文分析还发现，与全国平均或北方其他地区比较，黑龙江省春季最大风速出现在5月，而不是通常的4月。这与纬度偏高，中春时节相对推迟有关。

本文所选4个探空站不同高度年平均风速的差异，应该与台站所处的地理位置、地形条件和大气环流综合影响有关。哈尔滨、齐齐哈尔和嫩江站位于松嫩平原，地势开阔，年内特别是春季多大风，近地面风速较大，10 m到300 m高度年平均风速的垂直递增率也较大；伊春位于小兴安岭山地，地形起伏较大，域内生长大面积的原始森林，600 m高度以下年平均风速均较小，300 m到600 m垂直递增率明显高于其他站，900 m

高度平均风速也比其他站大。

随着高度增加，各站年平均风速多表现为增大，但齐齐哈尔900 m风速却不比600 m风速大，反而略有减小。这可能与城市建筑物或城市“冠层”的影响有关。这种影响导致“冠层”顶部高度以下风速明显减弱，“冠层”以上的300 m和600 m附近由于气流爬升或“狭管”效应致使风速增大，并与900 m附近自由大气风速接近甚至超过。齐齐哈尔站长期位于市区西部，2002年迁至市区西北部，探空气球经由城市“冠层”的频次比较高，距离较长，因而平均风速垂直廓线明显不同于其他台站。

黑龙江省4个探空站近地面平均风速呈现明显的随时间减弱的趋势，但上层各层平均风速变化呈现出不明显的增强趋势。近地面风速的明显减弱现象与针对全国和河北省的研究一致，但上层风速具有弱增强趋势却与先前分析结果不完全一致，先前研究表明对流层下层或边界层上层风速变化呈不明显的下降趋势[8, 12]。朱锦红等[17]发现，20世纪80年代中期以后对流层中高纬度西风有明显加强趋势。Lucarini等[18]研究表明，1960—2000年间北半球高层年平均位势高度在中纬度地带上升，高纬度地带降低，夏季从华北到阿留申群岛一带为位势高度上升区，西伯利亚北部为下降中心，这说明高空西风的增强主要发生在中高纬度。中国大陆大部处于中纬度地区，而黑龙江省处于中国最北部，纬度偏高，其边界层上层平均风速的不明显增强可能主要是大尺度大气环流变化的结果。

对于多数站近地面风速的显著减弱，最主要的原因应该是局地人为活动影响，包括观测场周围环境改变和城市化的影响。模拟分析[7]和观测分析表明[10]，城市以外地区平均地面风速的减少没有气象台站观测到的明显；刘学锋等[12]分析发现，河北省乡村站或观测环境变化不大的台站地面风速也有减少，但减少幅度显著偏低。黑龙江省4个探空站观测的平均风速减弱，主要发生在近地面附近，说明城市化和观测环境改变造成的影响比其他地区还要显著。这一结论对于正确评价风电场区域近地面风速和风能密度的真实变化具有实际意义。

4 结论

利用1961—2010年哈尔滨、嫩江、齐齐哈尔、伊春4个气象站探空和地面风速资料，分析了黑龙江省边界层内不同高度风速的时空变化特征，得到以下结论：

（1）黑龙江省边界层内不同高度年平均风速随着距地面高度的增加而增大，10 m到300 m风速垂直递增率最大；风速在年内时间分布上具有明显的季节性特征，各高度都是春季风速最大，近地面层冬季风速最小，其余高度夏季风速最小。

（2）在1961—2010年间，近地面10 m平均风速1970年代最大，从1970年代到2000年代逐渐减小，2000年代风速最小；在300、600、900 m高度，平均风速1980年代最大，从1980年代到2000年代逐渐减小，300 m高度平均风速最小年代在1960年代，600 m和900 m高度风速最小年代均在1970年代。

（3）1961—2010年期间，近地面10 m高度平均风速明显减弱，递减率为0.162 m/(s·10 a)，这个变化主要发生在1970年代以后；而300、600和900 m各高度平均风速的趋势变化都不够显著。

（4）黑龙江省近地面风速变化趋势可能主要与观测环境改变和城市化等非自然因素影响有关，但上层的风速变化则主要受大尺度大气环流变化的影响。

参考文献(References)：

[1] 任国玉, 郭军, 徐铭志, 等. 近50年中国地面气候变化基本特征[J]. 气象学报, 2005, 63(6): 948-952. [REN Guo-yu, GUO Jun, XU Ming-zhi, *et al*. Climate changes of China's mainland over the past half century. *Acta Meteorologica Sinica*, 2005, 63(6): 948-952.]

[2] Fu G, Yu J, Zhang Y, *et al*. Temporal variation of wind speed in China for 1961–2007 [J]. *Theoretical and Applied Climatology*, 2011,104:313-324. doi:10.1007/s00704-010-0348-x.

[3] 金巍, 任国玉, 曲岩, 等. 1971—2010年东北三省平均地面风速变化[J]. 干旱区研究, 2012, 29(4): 648-653. [JIN Wei, REN Guo-yu, QU Yan, *et al*. Change in surface mean wind speed of northest China during the period of 1971 – 2010. *Arid Zone Research*, 2012, 29(4): 648-653.]

[4] 张文佳, 张永战. 中国风电的时空分布特征和发展趋势[J]. 自然资源学报, 2007, 22(4): 585-596. [ZHANG Wen-jia, ZHANG Yong-zhan. Studies on characteristics of the spatial-temporal distribution and development trend for wind farms in China. *Journal of Natural Resource*, 2007, 22(4): 585-596.]

[5] 吴丰林, 方创琳. 中国风能资源价值评估与开发阶段划分研究[J]. 自然资源学报, 2009, 24(8): 1412-1421. [WU Feng-lin, FANG Chuang-lin. Wind power resource appraisal and development stage regional division of China. *Journal of Natural Resource*, 2009, 24(8): 1412-1421.]

[6] 王遵娅, 丁一汇, 何金海, 等. 近50年来中国气候变化特征的再分析[J]. 气象学报, 2004, 62(2): 228-236. [WANG Zun-ya, DING Yi-hui, HE Jin-hai, *et al*. An updating analysis of the climate change in china in recent 50 years. *Acta Meteorologica Sinica*, 2004, 62(2): 228-236.]

[7] Zuo Hongchao, Li Dongliang, Hu Yinqiao, *et al*. Characteristics of climate trends and correlation between pan-evaporation and environmental factors in the last 40 years over China [J]. *Chinese Science Bulletin,* 2005, 50 (12): 1235-1241.

[8] 张爱英, 任国玉, 郭军, 等. 近30年我国高空风速变化趋势分析[J]. 高原气象, 2009, 28(3): 680-687. [ZHANG Ai-ying, REN Guo-yu, GUO Jun, *et al*. Change trend analyses on upper-air wind speed over China in past 30 years. *Plateau Meteorology,* 2009, 28(3): 680-687.]

[9] Jiang Y, Luo Y, Zhao Z C, *et al*. Changes in wind speed over China during 1956–2004 [J]. *Theoretical and Applied Climatology,* 2010, 99: 421-430.

[10] 刘传顺, 刘玉莲. 近50a黑龙江省地面平均风速变化[J]. 黑龙江气象, 2010, 27(2): 26-29. [LIU Chuan-shun, LIU Yu-lian. Change in surface mean wind speed of Heilongjiang Province in past 50 years. *Heilongjiang Meteorology,* 2010, 27(2): 26-29.]

[11] 刘学锋, 江滢, 任国玉, 等. 河北城市化和观测环境改变对地面风速观测资料序列的影响[J]. 高原气象, 2009, 28 (2): 433-439. [LIU Xue-feng, JIANG Ying, REN Guo-yu, *et al*. Effect of urbanization and observation environment change on wind speed trend in Hebei Province, China. *Plateau Meteorology*, 2009, 28(2): 433-439.]

[12] 刘学锋, 任国玉, 梁秀慧, 等. 河北地区边界层内不同高度风速变化特征[J]. 气象, 2009, 35(7): 46-53. [LIU Xue-feng, REN Guo-yu, LIANG Xiu-hui, *et al*. The characteristics of wind speed variation at different altutudes of boundary layer in Hebei Province. *Meteotological Monthly,* 2009, 35(7): 46-53.]

[13] 卞林根, 程彦杰, 王欣, 等. 北京大气边界层中风和温度廓线的观测研究[J]. 应用气象学报, 2002, 13(特刊): 13-25. [BIAN Lin-gen, CHENG Yan-jie, WANG Xin, *et al*. Observational study of wind and temperature profiles of urban boundary layer in Beijing winter. *Quarterly Journal of Applied Meteorology*, 2002, 13(S1): 13-25.]

[14] 刘小宁. 我国40年年平均风速的均一性检验[J]. 应用气象学报, 2000, 11(1): 27-34. [LIU Xiao-ning. The homogenity testonmean annual wind speed over China. *Quarterly Journal of Applied Meteorology,* 2000, 11(1):27-34.]

[15] 于宏敏, 徐永清, 张洪玲, 等. 城市化对近地面风速变化的影响: 以黑龙江省为例[J]. 太阳能学报, 待刊. [YU Hong-min, XU Yong-qing, ZHANG Hong-ling, *et al*. The impact on wind speed trend of urbanization at Heilongjiang Province. *Acta Energiae Solaris Sinica,* in press.]

[16] 任国玉, 张爱英, 王颖, 等. 我国高空风速的气候学特征[J]. 地理研究, 2009, 28(6): 1583-1592. [REN Guo-yu, ZHANG Ai-ying, WANG Ying, *et al*. Climatology of upper wind speed over China. *Geographical Research*,2009,28 (6):1583-1592.]

[17] 朱锦红, 王绍武, 张向东, 等. 全球气候变暖背景下的大气环流基本模态[J]. 自然科学进展, 2003, 13(4):417-421. [ZHU Jin-hong, WANG Shao-wu, ZHANG Xiang-dong, *et al*. Under the background of global warming of the atmospheric circulation basic mode. *Progress in Natural Sciences,* 2003, 13(4): 417-421.]

[18] Lucarini V, Russell G L. Comparison of mean climate trends in the Northern Hemiphere between National centers for Environmental Prediction and two atmosphere-ocean model forced runs [J]. *Journal of Geophysical Research*, 2002, 107, 4269, doi: 10. 1029/ 2001JD001247.

The Characteristics of Wind Speed Variation at Different Altitudes of Boundary Layer in Heilongjiang Province

YU Hong-min[1], REN Guo-yu[2], LIU Yu-lian[1]

(1. Heilongjiang Climate Center, Harbin 150030, China; 2. Laboratory for Climate Studies, National Climate Center, CMA, Beijing 100081, China)

Abstract: Using the data of upper air and surface wind speed observed from Harbin, Nenjiang, Qiqihar and Yichun of Heilongjiang Province, from 1961 to 2010, the characteristics of variation of wind speed in boundary layers are analyzed. The following conclusions are drawn: 1) The annual mean wind speed increases with height from the ground to 900 m, and the distribution of wind speed at different time of the year has obvious characteristics of seasonal variation, with the maximum in springtime and the minimum in wintertime at near-surface layer, and the minimum in summertime at the remaining height layers; the maximum wind speed vertical increasing rate appears between 10 m and 300 m. 2) In 1961－2010, the largest mean wind speed at 10 m height is in the 1970s, and gradually decreases from the 1970s to the 2000s, with the smallest value occurring in the 2000s; at 300 m, 600 m, 900 m heights, the largest mean wind speed is in the 1980s, and wind speed gradually reduces from the 1980s to the 2000s, with the smallest value being in the 1960s at 300 m and in the 1970s at 600 m and 900 m. 3) During 1961－2010, the mean wind speed at 10 m is weakening and the diminishing rate is 0.162 m/(s·10a), and the trend occurs mainly after the 1970s. At 300 m, 600 m and 900 m, the mean wind speed trends are not significant. 4) It seems that the significant slowdown trends of the surface wind speed in Heilongjiang Province is mostly caused by the fast urbanization and the change of observational environment.

Key words: climate change; wind energy resources; wind speed; boundary layers; Heilongjiang Province

战云健, 任国玉, 任玉玉, 等. 2013. 1951～2009 年东亚地区日降水趋势特征分析 [J]. 气候与环境研究, 18 (6): 767–780, doi:10.3878/j.issn.1006-9585.2013.12152. Zhan Yunjian, Ren Guoyu, Ren Yuyu, et al. 2013. Changes in daily precipitation over East Asia during 1951–2009 [J]. Climatic and Environmental Research (in Chinese), 18 (6): 767–780.

1951～2009 年东亚地区日降水趋势特征分析

战云健[1,2]　任国玉[2]　任玉玉[2]　李娇[3]

1 中国气象科学研究院，北京 100081

2 国家气候中心中国气象局气候研究开放实验室，北京 100081

3 铁岭市气象局，铁岭 112000

摘　要　研究大陆或次大陆尺度日降水长期趋势变化规律，对于检测、理解区域气候和陆地水循环对全球气候变暖的响应特征十分重要。利用美国国家气候资料中心（NCDC）和中国基准气候站、基本气象站网降水观测资料，在对该站点资料进行基本质量控制基础上，选取东亚地区 619 个站 1951～2009 年日降水数据，按照百分位阈值对降水进行分级，共分为弱、中、强、极强 4 个级别，用经纬度网格面积加权平均方法构建区域平均的时间序列，分析了各类降水事件长期变化趋势的时空特征。结果表明：东亚地区近 59 年平均总降水量表现出不显著下降趋势，降水日数没有出现趋势性变化，平均日降水强度略有减小；区域平均的年降水量、降水日数和日降水强度在中国北方大部、蒙古东部、俄罗斯远东地区南部和日本列岛多呈减少趋势，而在俄罗斯中西伯利亚南部、朝鲜半岛南部和中国长江中下游流域一般表现为增加。从季节上看，近 59 年东亚区域平均的冬、春季降水量、降水日数和日降水强度均呈增加趋势，而夏、秋季一般呈减少趋势，仅夏季日降水强度略有增加。降水的年内分配出现均匀化趋势。从不同级别降水事件看，近 59 年来东亚区域平均的各级别降水量均为下降趋势，中降水、强降水和极强降水日数也呈现下降趋势，弱降水日数表现出较明显增加；仅有全区秋季强降水量、日数减少趋势和冬季中降水量、日数增加趋势通过了显著性水平检验。分析还发现，近 30 年（1980～2009 年）东亚地区日降水趋势变化出现了新的特征，主要表现为大部分地区降水日数呈现增加，日降水强度减少，45°N 以南多数台站降水量也增加，全区降水有向非极端化方向发展趋势。

关键词　东亚地区　日降水　降水量　降水日数　降水强度　弱降水　强降水　气候变化

文章编号　1006–9585（2013）06–0767–14　　**中图分类号**　P467　　**文献标识码**　A

doi:10.3878/j.issn.1006-9585.2013.12152

Changes in Daily Precipitation over East Asia during 1951–2009

ZHAN Yunjian[1,2], REN Guoyu[2], REN Yuyu[2], and LI Jiao[3]

1 *Chinese Academy of Meteorological Sciences*, *China Meteorological Administration*, *Beijing* 100081

2 *Laboratory for Climate Studies*, *National Climate Center*, *China Meteorological Administration*, *Beijing* 100081

3 *Tieling Meteorological Bureau*, *Tieling* 112000

Abstract　Atmospheric precipitation is a critical component of the terrestrial water cycle. For detecting and understanding the response of the water cycle to global warming at the regional scale, it is important to analyze the temporal and spatial variations in daily precipitation at the continental or subcontinental scale. In this study, daily precipitation data from the US National Climate Data Center (NCDC) and the China National Reference Climate and Basic Meteorological Stations for the period of 1951–2009 were used to analyze the long-term variations in precipitation

收稿日期　2012–08–27 收到，2013–04–27 收到修定稿

资助项目　国家公益性行业专项 GYHY201206012

作者简介　战云健，男，1987 年出生，硕士研究生，主要从事气候变化研究。E-mail: zhanyunjian@foxmail.com

通讯作者　任国玉，E-mail: guoyoo@cma.gov.cn

over East Asia (25°N–55°N, 105°E–145°E). After basic quality control, 619 stations were chosen. Based on the percentile thresholds, the daily rainfall was classified into light, moderate, intense, and very intense. The regional average time series were obtained by the method of the area-weighted average for the grids. The spatial and temporal patterns of the long-term changes in all kinds of precipitation events were also analyzed.

The results showed that the average regional precipitation and precipitation intensity decreased during the last 59 years (1951–2009), whereas the rainy days exhibited no prominent trend. In most of northern China, eastern Mongolia, southern Russian-Far East, and most of Japan, the amount, frequency, and intensity of annual precipitation generally decreased. However, the southern part of Middle Siberia, the Korean Peninsula, and the Yangtze River basin witnessed increasing trends of the precipitation index series. The amount, frequency, and intensity of seasonal precipitation increased in winter and spring, and decreased in the summer and autumn except for the summer precipitation intensity. The annual seasonal precipitation variability in the last decade was gentler than the previous.

The regional average precipitation decreased in all categories in 1951–2009. The moderate precipitation decreased faster than the precipitation frequency, whereas the intense and very intense precipitation decreased slightly slower than the precipitation frequency. The moderate, intense, and very intense precipitation frequencies decreased during the last 59 years, and only the light precipitation frequency increased. Note that for the last 30 years (1980–2009), the overall precipitation intensity decreased, whereas the overall precipitation frequency increased for most areas in the study region. Most of the stations south of the 45°N latitude recorded increased annual precipitation; however, the daily precipitation intensity was less extreme.

Keywords East Asia, Daily precipitation data, Precipitation, Precipitation frequency, Precipitation intensity, Light precipitation, Intense precipitation, Climate change

1 引言

东亚地区由中国东部、日本列岛、朝鲜半岛、蒙古东部及俄罗斯西伯利亚的远东区域组成，区内人口、城市稠密，经济发达。东亚地区位于中纬度欧亚大陆东侧，为全球著名的温带和亚热带季风气候区。在季风环流的影响下，东亚气候四季分明、冬季干寒、夏季湿热、雨热同季、年际变异性很强（Ren，1991；黄荣辉和杜振彩，2010），在为农业生产和其他人类活动提供得天独厚的水热资源条件的同时，也带来了无可避免的频繁水旱灾害。研究这个地区的降水事件长期变化规律，对于理解在全球气候变化背景下区域气候和陆地水循环演化特征及原因，具有重要科学意义；对于认识区域气象灾害发生和演化的成因、评价气候变化的影响，具有实际价值。

当前，利用地面观测资料对东亚地区作为一个整体的降水趋势变化研究还很少。对全球陆地降水变化的研究发现，近 100 年来东亚中高纬的西伯利亚、蒙古等地区年总降水量和极端强降水事件频率一般增加，而处于中纬度的中国华北和东北、日本列岛大部年降水量和极端强降水事件频率一般减少（IPCC，2007；翟盘茂等，2007）。东亚地区中国以外的国家和地区，20 世纪中期以来降水变化趋势大致与中国东部相似，如日本降水日数减少，各极端降水指数趋于增加（Manton et al.，2001）；韩国夏季降水量增加显著，暴雨强度增加（Choi et al.，2008，2009）；近 30 年，俄罗斯远东地区和朝鲜北部夏季各级别降水和总降水显著减少（Yao et al.，2008）

对 20 世纪 50 年代以来中国东部降水变化特征的分析工作很多。这些研究一般发现：在年降水量变化方面，东部呈现出“北旱南涝”特征，华北地区和东北中南部降水量明显减少（任国玉等，2000，2005；丁一汇等，2007；翟盘茂等，2007；Tu et al.，2010）；冬季总降水量和极端降水量大多增加而秋季大多减少（Wang and Yan，2009）；东部多数地区小雨降水频率和降水量均显著减少，中雨变化趋势弱，强降水和极强降水事件频率变化趋势不明显，但强度有所增大，极端强降水量占总降水量的比例有所增加（翟盘茂和潘晓华，2003；王颖等，2006；翟盘茂等，2007；闵屾和钱永甫，2008；王小玲和翟盘茂，2008；任国玉等，2010），总体平均降水强度也有增加（王颖等，2006；翟盘茂等，2007）；全国大范围降水日数减少，其减少趋势大大超过了总降水量的下降（王颖等，2006），说明降水日数的趋势变化机理不完全等同于降水量，可能主要与造成小雨频数显著减少的控制因子有关（闵屾和钱永甫，2008；任国玉等，2010）。对降

水年代尺度变异分析表明，20 世纪 50 年代以来，中国东部的降水量经历了 20 世纪 50 年代的相对丰沛期，20 世纪 60 年代初至 80 年代中的偏少期，以及 20 世纪 80 年代中至 90 年代末的丰水期（Zhai et al.，2005）；Qian and Zhu（2001）发现，近百年来中国东部降水存在长期振荡和 20 年左右的年代际振荡；Ren et al.（2011）指出，中国东部年和夏季降水量没有明显长期趋势变化，但长江中下游与华北地区降水存在较明显的反相趋势和波动。

因此，目前对东亚地区蒙古国和俄罗斯西伯利亚、远东等区域的研究很少，尤其缺乏对东亚地区作为一个整体的长期降水趋势变化研究。

本文采用 1951～2009 年的日降水资料，对东亚地区的总降水及各级别降水事件趋势变化特征进行分析。本文的分析发现东亚其他国家和地区降水趋势变化既存在与中国东部区域相似的特征，也具有一定的独特性。

2 数据处理与分析方法

2.1 数据处理和选站

东亚地区范围定义为（25°N～55°N，105°E～145°E），主要包括中国东部、朝鲜、韩国、日本、蒙古大部和俄罗斯中西伯利亚南部与远东地区南部。所用数据为美国国家气候资料中心（NCDC）和中国基准气候站、基本气象站网日降水观测资料，资料时段为 1951～2009 年。由于各测站的数据质量参差不齐，缺测情况不同，对原始降水资料进行了质量控制，包括极值检查、错误数据排除、连续无变化检查和缺测值处理。

极值检查：对大于 500 mm 的全部台站逐日降水记录进行了检查，发现两类错误：（1）999.99，在蒙古国和西伯利亚出现多次，为缺测值（9999.9）小数点错位所致；（2）2000.0，共出现 3 次，均在中国，其超过全球日降水量极值 1828.8 mm，为记录错误。将以上两种日降水量记录改为缺测值。除去这两类记录错误，东亚地区日降水量极大值为 806 mm，出现在 1968 年 9 月日本东南沿海的一个观测站。经过比较附近观测站资料，确认其为当日真实降水记录。

错误数据排除：蒙古和朝鲜两国的资料质量略差，有几个特殊值（蒙古 41.9、42.9、43.9、74.9、91.9 mm；朝鲜 1973 年以前的 74.9 mm 和 150.1 mm）多次重复出现。这些数据出现年份没有其他降水记录，可认为数据有误，将全年数据改为缺测。其中蒙古所有站点 1961 年之前的记录全部为缺测。此外，蒙古国有些站点还多次出现明显偏高的 100 mm 以上的日降水记录，经检验对比 NCEP 再分析可降水量和实际降水量资料，确认其中 200 mm 以上的均为错误记录。由于这些站点的异常偏高的 100 mm 以上数据出现多次且无规律，难以定性为缺测值、错误或正确降水记录，故将这些存在异常的 100 mm 以上日降水量记录的站点剔除。

连续无变化检查：根据降水多寡，设定标准如下：俄罗斯西伯利亚地区和蒙古国[（40°N，105°E）、（55°N，130°E）两点连线以西北]连续二日降水量超过 50 mm，其他地区连续二日降水量超过 100 mm，则认为后一日降水记录有误，可能由于雨量计倾倒不及时等原因造成，将后一日降水改为缺测值。检查发现，在日本本州岛最西端的下关市 1990 年 9 月出现一次连续二日 130.0 mm，对比 NCEP 再分析可降水量和实际降水量资料，确认第二日降水量错误。其余检查结果均为上一步被剔除站点的明显数据错误。

缺测值处理：规定在降水日数较少的俄罗斯西伯利亚地区和蒙古国地区[（40°N，105°E）、（55°N，130°E）两点连线以西北]，如果某站某月缺测天数达到 50%以上，则该年年降水量记为缺测；其他地区月缺测 8 d 以上算作全年缺测。月缺测不到以上标准时，由于降水量的插补不准确，缺测值不参与计算。

在上述质量控制处理后，设立选站标准如下：研究时段（1951～2009 年）内至少有 33 年记录且标准气候参考期（1971～2000 年）内至少有 20 年记录。根据此标准，全区最终选用 619 个站，各国家选用测站数：中国 343 个、日本 145 个、韩国 20 个、朝鲜 6 个、蒙古 2 个、俄罗斯 103 个，具体分布情况如图 1a。全区长序列观测站点分布比较均匀，密度也较高，其中日本站点密度最高，蒙古国最低。后者由于数据质量较差，最终只有 2 个站入选。

在最终入选的测站中，各台站记录长短和缺测情况还有差异。统计每年有观测的台站数（图 1b）表明，1951 年有观测记录的台站数不到 300，此后逐渐增加，到 1961 年有观测记录的台站数增加到 500 以上，此后直到 2000 年台站数均维持在 500 以

上。但是，2000 年和 2001 年台站大幅减少，2001 年台站数不足最多年份的一半，俄罗斯的西伯利亚和库页岛地区减少的台站最多（图 1a 灰色测站所示）。这导致俄罗斯东部沿海（包括库页岛）缺少记录完整的整个时期观测资料。2002 年以后全区有观测台站数回升到 400 个左右。

2.2 分析方法

本文主要分析东亚地区降水量、降水日数和降水强度长期趋势变化特征。由于国外未对 1 mm 以下的降水做记录，降水日数定义为日降水量大于等于 1 mm 的天数，单位为 d。年降水量为每年全部降水日降水量的总和，单位为 mm。年降水强度为年降水量与年降水日数之比，单位为 mm/d。

由于研究区域广，各地降水气候特征差异较大，为增强不同地区各级别降水事件之间的可比性，采用相对阈值法对降水进行分级。参考 Karl and Knight（1998）以及闵屾和钱永甫（2008）的方法，按照百分位阈值对降水进行分级。将标准气候参考期（1971～2000 年）30 年所有 1 mm 以上降水从小到大排序，取第 95 百分位的降水记录所对应的降水量定义为极强降水阈值，大于此阈值的降水为极强降水；同样，定义介于第 80～95（含）百分位阈值之间的降水为强降水，第 50～80（含）百分位阈值之间的降水为中降水，第 50 及以下百分位阈值的降水为弱降水。以此方法划分的弱、中、强和极强降水，大体对应中国江淮流域以绝对阈值定义的小雨、中雨、大雨、暴雨。

按夏季为 6～8 月、冬季为 1～2 月和上年 12 月、春季为 3～5 月、秋季为 9～11 月的标准划分四季，分别分析了各季节各类降水指标的趋势变化特征。由于某些站点的标准参考期内干季（尤其是冬季）有降水记录较少，对每个季节确定百分位阈值误差较大，对降水量分级时没有区分季节，全年采用了同样的阈值。因此，降水量较小的冬、春两个季节缺乏部分较强级别的降水记录。其中春季缺乏全部年份的极强降水记录，冬季缺乏全部年份的强和极强降水记录以及 1953～1999 年共 47 年的中降水记录。因此，春季的强降水和冬季的中降水实际上已成为该季节的最强级别降水。

本文对各降水指标计算线性变化趋势时，采用各台站分别计算和划分经纬度网格建立区域平均序列计算两种方法。在台站基础上，为减小记录缺测的影响，在计算 1951～2009 年线性趋势时，选取至少具有 55 年记录的台站，对于这些台站的少量缺测，用 1951～2009 年的平均值替补；在计算 1980～2009 年近 30 年线性趋势时，选取至少具有 27 年记录的台站，并用 1980～2009 年的平均值替补缺测年份记录。以此方法计算降水线性趋势时所选用的站点分布情况见下文结果分析部分，俄罗斯东部沿海及库页岛的多数站点因为资料缺测而未能入选。

区域平均序列构建采用 Jones et al.（1999）提出的经纬度网格面积加权平均方法。首先将研究区域按经纬度划分网格。为保证每个网格内每年有至少 1 个测站的记录，将研究区域划分为 5°（纬度）×5°（经度）的 48 个网格。然后计算每年所有台站各指标值相对标准参考期（1971～2000 年）的距平百分率，并对每个网格求算术平均，得到网格内的算术平均距平百分率时间序列。其中网格平均降水强度值是由该网格内所有有观测站点的总降水量除以总降水日数得到。如果某网格某年没有观测记录，则该年该网格视为空网格。1951～2009 年拥有完整 59 年序列长度的网格如图 1c 黑色实心圆所示，其中 H5、G6、H6 等 3 个位于海上的网格没有任何站点。由于资料缺测，还有一些网格不具有完整的时间序列，但多数只有少数年份没观测值，对其做了插补处理：如果缺测少于 5 年（即至少有 55 年观测长度），则将该网格所有缺测年补以有观测值年份的平均值。插补后增加了 C1、F1、B3、G3、E4 等网格（图 1c 灰色实心圆所示）。

得到网格算术平均的距平百分率时间序列后，进行区域面积平均的计算：用各网格的距平百分率的算术平均值，乘以各自网格的中心纬度的余弦后相加，再除以参与计算的各网格中心纬度的余弦之和，便得到区域平均的距平百分率值时间序列。计算区域平均时间序列线性变化趋势，并采用 F 检验和相关系数（r）检验方法进行显著性检验。

3 结果分析

3.1 年降水变化

图 2 表示 1951～2009 年东亚区域平均年降水量、降水日数和降水强度距平百分率的时间序列；表 1 列出了同期年降水量、降水日数和降水强度的线性趋势及其显著性检验结果。全区年降水量由 20 世纪 50 年代到 60 年代中期的正距平为主，转变为

70 年代的负距平为主，其中 70 年代初到 80 年代初连续 9 年降水量为负距平，为东亚地区近 59 年最干时期。20 世纪 80 年代年降水量回升到多年平均值附近，90 年代多数年份为正距平，其中 1998 年降水量达到整个时期最高水平。此后年降水量总体变化趋势不明显，尤其自 2000 年以来降水量的年际波动还非常小（图 2）。总体来看，59 年间东亚地区年降水量变化为弱的负趋势，变化速率为 $-0.479\%\ (10\ \mathrm{a})^{-1}$，没有通过 0.05 显著性水平检验（表 1）。

2000 年之前，东亚区域平均年降水日数的变化趋势与年降水量较为接近；但此后降水日数呈现显著增加，近 10 年有 9 年为正距平，仅 1 年为很弱的负距平。59 年间全区平均年降水日数变化趋势很弱，只有 $0.033\%\ (10\ \mathrm{a})^{-1}$，没有通过 0.05 显著性水平检验（表 1）。

东亚地区年平均降水强度在 20 世纪 50 至 60 年代总体变化不大，70 年代以负距平为主，80 至 90 年代呈现增加趋势，90 年代降水强度多呈正距平，而 2000 年以来则突然下降，全部年份均为负距平。整个分析时期东亚地区年降水强度表现为下降趋势，下降速率为 $-0.421\%\ (10\ \mathrm{a})^{-1}$，未通过 0.05 显著性水平检验（表 1）。

值得注意的是，2000 年以来东亚地区降水发生了令人瞩目的变化，主要表现在降水量年际波动很小，降水日数多变为明显的正距平，致使降水强度呈现较大幅度下降（图 2）。近 10 多年东亚地区降水较之从前特别是 20 世纪 90 年代具有向非极端化方向演化特点。

图 3 表示东亚地区近 59 年降水量、降水日数和降水强度距平百分率的线性趋势空间分布情况。在 1951～2009 年期间，俄罗斯中西伯利亚大部份地区年降水量、降水日数和降水强度一般呈不显著增加趋势；中国东北东部降水量变化不明显，降水日数大多增加，而降水强度大多减少，各降水指标长期趋势变化总体上均不显著；中国东北西部和南部以及华北地区，年降水量、降水日数和降水强度一般呈减少趋势，部分站点显著减少；内蒙古西部年降水量、降水日数和降水强度均以增加为主；长江和淮河流域年降水量、降水日数和降水强度多呈增加趋势，部分站点的降水量和降水日数显著增加；朝鲜半岛西部的 2 个站年降水量增加，降水日数减少或显著减少，降水强度增加或显著增加；日本北海道岛降水量和降水强度减少，其中西部显著减少，降水日数则无明显变化趋势；日本本州岛东部沿海降水强度增加或显著增加，降水日数则多呈减少趋势，而本州岛西南部地区年降水量、降水日数和降水强度一般均显著减少，九州岛和四国岛年降水量、降水日数和降水强度也呈减少趋势，但变化不显著。

图 4 给出东亚地区近 30 年（1980～2009 年）的降水量、降水日数和降水强度线性趋势空间分布情况。1980～2009 年期间，45°N 以北大部分地区年降水量和降水强度明显减少。与近 59 年比较，年降水量减少区域向北迁移，主要出现在中国东北北部、俄罗斯和蒙古国。除了中国东北北部和东部，这些区域年降水日数一般也呈减少趋势。蒙古国东部和中西伯利亚地区年降水量减少速率超过 $-10\%\ (10\ \mathrm{a})^{-1}$，降水日数减少速率超过 $-5\%\ (10\ \mathrm{a})^{-1}$。45°N 以南大部分地区年降水量和降水日数增加，中国北方黄淮流域降水日数增加明显，山东省增加趋势更明显，超过 $10\%\ (10\ \mathrm{a})^{-1}$，但东南沿海地区和韩国、日本西部降水日数一般减少（图 4a、5b）。

东亚地区近 30 年大部分站点年平均降水强度呈减少趋势，中国东北北部和日本列岛西部减少明

表 1　1951～2009 年东亚地区各季节不同级别降水变化趋势

Table 1　Linear trends of different categories of precipitation in the four seasons and the whole year in East Asia during 1951–2009

$(10\ \mathrm{a})^{-1}$

	降水量变化趋势					降水日数变化趋势					总降水强度
	弱降水	中降水	强降水	极强降水	总降水	弱降水	中降水	强降水	极强降水	总降水	变化趋势
春季	0.086%	0.251%	0.037%		0.505%	0.66%	0.301%	0.159%		0.557%	0.243%
夏季	−0.421%	−0.59%	−0.074%	−0.456%	−0.35%	0.128%	−0.563%	−0.062%	−0.617%	−0.173%	0.162%
秋季	−0.499%	−0.84%	−2.190%*	−2.405%	−1.149%	0.053%	−0.859%	−2.150%*	−2.244%	−0.538%	−0.367%
冬季	1.135%	5.579%*			1.59%	1.776%	5.054%*			1.803%	0.656%
全年	−0.271%	−0.407%	−0.772%	−0.418%	−0.479%	0.557%	−0.348%	−0.942%	−0.622%	0.033%	-0.421%

*代表通过 0.05 显著性水平检验，表中所有趋势均未通过 0.01 显著性水平检验。

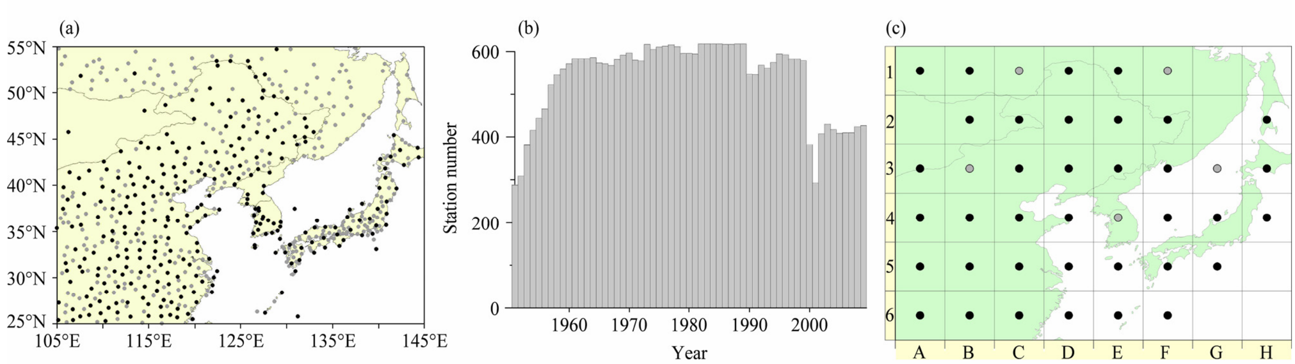

图 1 东亚地区（a）降水观测站地理分布（灰色代表 2001 年缺测的观测站）、（b）降水观测站数随时间变化、（c）插补前 1951～2009 年拥有完整序列长度的网格点（黑色）和插补后增加的 1951～2009 年拥有完整序列长度的网格点（灰色）

Fig. 1 (a) Spatial distribution of precipitation stations in East Asia (grey dots are stations without data in 2001); (b) precipitation station numbers in East Asia; (c) grids (black filled circles) with complete time series before interpolation during 1951–2009 and additional grids (grey filled circles) with complete time series after interpolation during 1951–2009

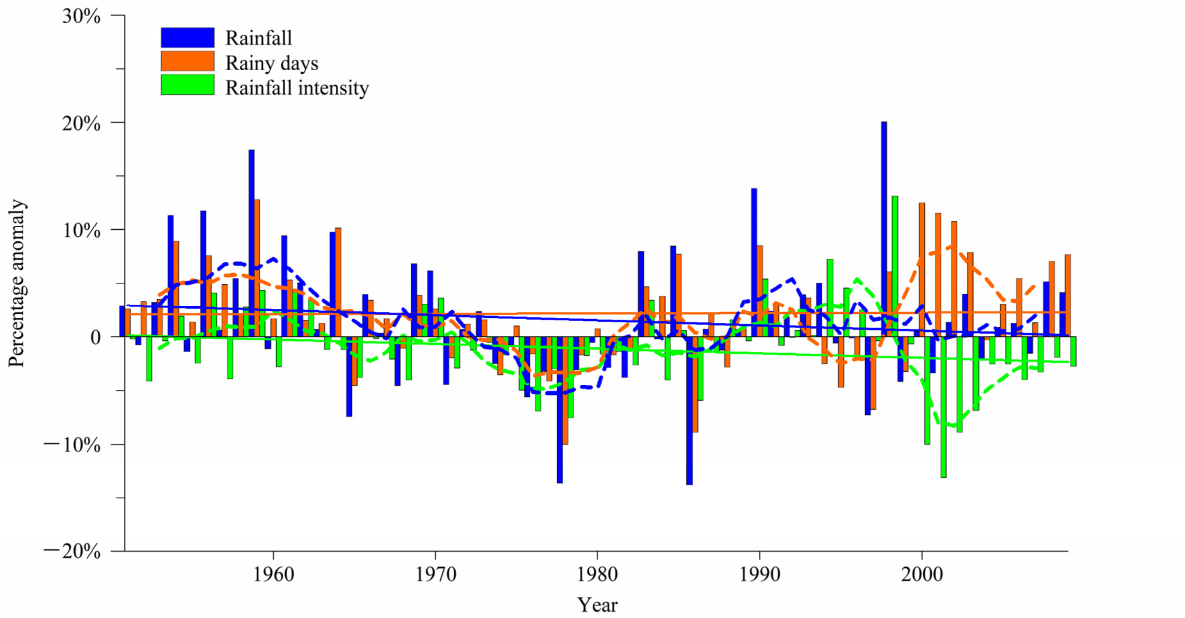

图 2 1951～2009 年东亚区域平均年降水量（蓝色）、降水日数（橙色）和降水强度（绿色）距平百分率（虚曲线为 5 年滑动平均，实直线为线性趋势）

Fig. 2 The average anomaly percentage of rainfall (blue), rainy days (orange), and rainfall intensity (green) in East Asia during 1951–2009. Dashed line is five-year moving average, and solid line is linear trend

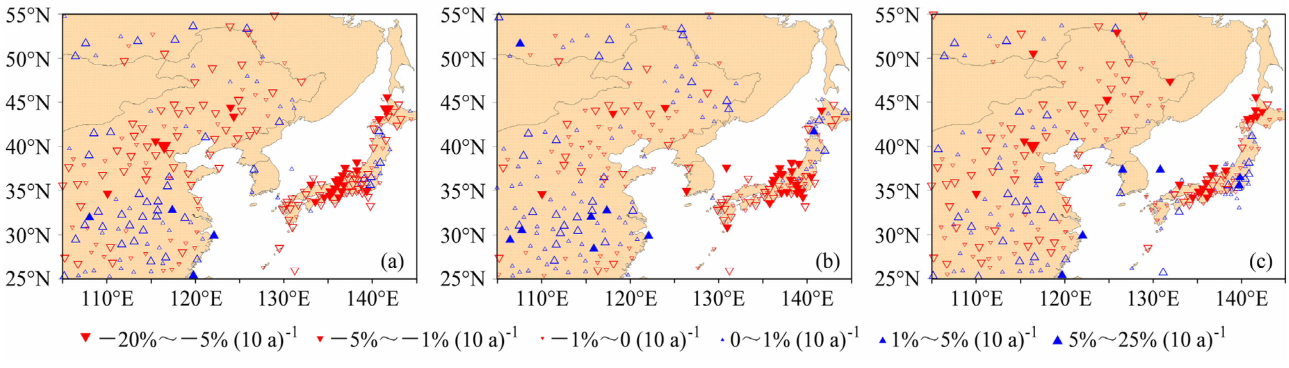

图 3 1951～2009 年东亚地区各站点（a）降水量、（b）降水日数和（c）降水强度变化趋势（其中的实心三角表示通过显著性水平为 0.05 的检验）

Fig. 3 The variation trends of (a) rainfall, (b) rainy days, and (c) rainfall intensity in East Asia during 1951–2009. Filled symbols represent statistically significant trends at 0.05 significance level

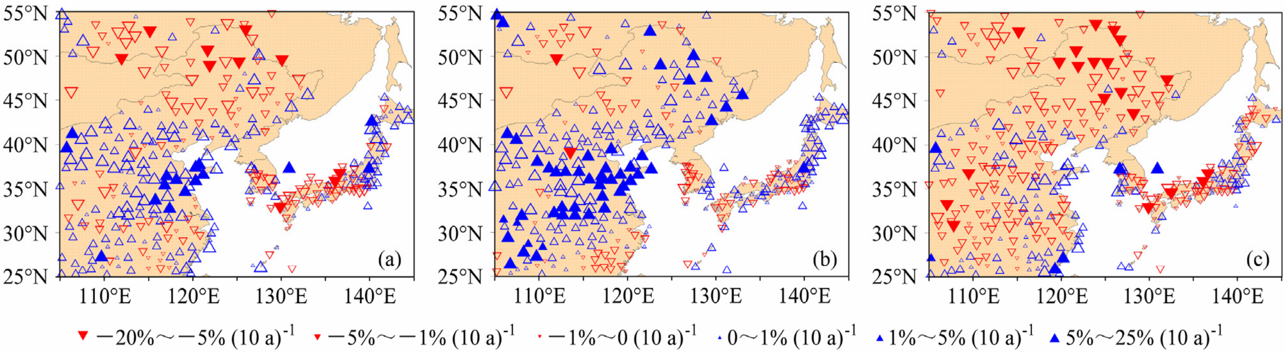

图 4　1980～2009 年东亚地区各站点（a）降水量、（b）降水日数和（c）降水强度变化趋势（其中的实心三角表示通过显著性水平为 0.05 的检验）

Fig. 4　The variation trends of (a) rainfall, (b) rain day, and (c) rainfall intensity in East Asia during 1980–2009. Filled symbols represent statistically significant trends at 0.05 significance level

显（图 4c）。东北北部降水强度的减少主要源于降水量下降和降水日数增加的共同影响，而日本西部的减少主要与降水量的明显下降有关。内蒙古西部、华北地区年降水强度有增有减，多数站点趋势未通过显著性检验。长江流域降水强度以减少为主，主要是由于降水日数增加引起；但东南沿海地区降水强度出现较明显增加，主要是降水量上升和降水日数减少共同作用的结果。日本北部降水强度变化不明显。因此，从最近 30 年来看，东亚大部分地区年平均降水强度减弱，降水具有非极端化倾向。

3.2　季节降水变化

图 5 表示 1951～2009 年间东亚区域平均的季节降水量、降水日数和降水强度距平百分率年际和年代际变化，表 1 中还列出了同时期各季节不同级别降水量、降水日数的线性趋势及其显著性检验结果，表 2、表 3 和表 4 则分别给出 1951～2009 年东亚地区各个季节和年降水量、降水日数和降水强度之间的相关矩阵。

表 2　1951～2009 年东亚地区区域平均季节和年降水量之间的相关矩阵

Table 2　Correlation coefficients between the average rainfall in the four seasons and the whole year in East Asia during 1951–2009

	相关系数				
	年平均降水量	春季平均降水量	夏季平均降水量	秋季平均降水量	冬季平均降水量
年平均降水量	1.000				
春季平均降水量	0.534**	1.000			
夏季平均降水量	0.758**	0.196	1.000		
秋季平均降水量	0.575**	0.101	0.152	1.000	
冬季平均降水量	0.290*	0.062	0.100	0.094	1.000

*表示通过 0.05 显著性水平检验，**表示通过 0.01 显著性水平检验。

表 3　1951～2009 年东亚地区区域平均季节和年降水日数之间的相关矩阵

Table 3　Correlation coefficients between the average rainy days in the four seasons and the whole year in East Asia during 1951–2009

	相关系数				
	年平均降水日数	春季平均降水日数	夏季平均降水日数	秋季平均降水日数	冬季平均降水日数
年平均降水日数	1.000				
春季平均降水日数	0.570**	1.000			
夏季平均降水日数	0.685**	0.222	1.000		
秋季平均降水日数	0.540**	0.022	0.177	1.000	
冬季平均降水日数	0.587**	0.205	0.220	0.107	1.000

*表示通过 0.05 显著性水平检验，** 表示通过 0.01 显著性水平检验。

表 4　1951～2009 年东亚地区区域平均季节和年降水强度之间的相关矩阵

Table 4　Correlation coefficients between the average rainfall intensity in the four seasons and the whole year in East Asia during 1951–2009

	相关系数				
	年平均降水强度	春季平均降水强度	夏季平均降水强度	秋季平均降水强度	冬季平均降水强度
年平均降水强度	1.000				
春季平均降水强度	0.634**	1.000			
夏季平均降水强度	0.745**	0.349**	1.000		
秋季平均降水强度	0.513**	0.283*	0.355*	1.000	
冬季平均降水强度	0.063	0.040	0.098	0.058	1.000

* 表示通过 0.05 显著性水平检验，** 表示通过 0.01 显著性水平检验。

东亚地区冬、春两季的降水量、降水日数和降水强度均呈增加趋势，其中冬季的增加趋势大于春季；秋季的降水量、降水日数和降水强度均呈减少趋势；夏季的降水量和降水日数也趋于减少，但减

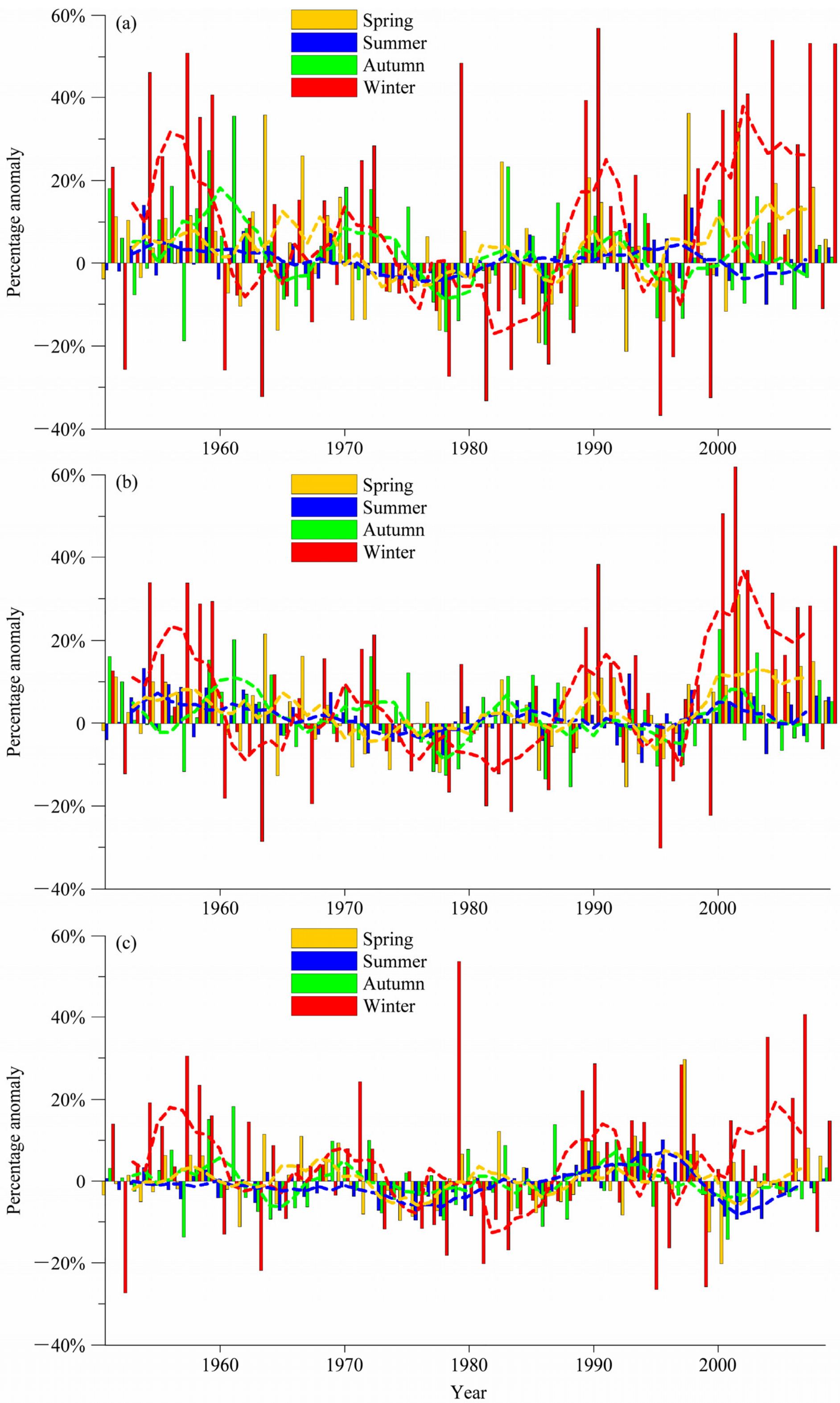

图 5 1951～2009 年东亚区域平均的各季节（a）降水量距平百分率、（b）降水日数距平百分率和（c）降水强度距平百分率（虚曲线为 5 年滑动平均）

Fig. 5 The average anomaly percentage of (a) rainfall, (b) rainy days, and (c) rainfall intensity in the four seasons in East Asia during1951–2009. Dashed line is the five-year moving average

少趋势弱于秋季，降水强度表现为增加。所有上述降水指标趋势均未通过 0.05 显著性水平检验（表 1）。秋季的强、极强降水量和降水日数下降趋势最明显，冬季的中、弱降水量则呈较明显上升趋势，其中秋季的强降水量、降水日数和冬季的中降水量、降水日数变化趋势均通过了显著性检验（表 1）。从 1951～2009 年各季节降水量和日数对全年的贡献率来看，冬、春两季的降水量和降水日数的贡献率均增加，而夏、秋两季均减少，但趋势均不显著（表 5）。因此，由于降水偏少的冬春季节的降水量和日数趋于增多，而多雨的夏秋季节降水量和日数趋于减少，东亚地区降水年内分布趋向于均匀，降水季节性对比减弱。

表 5　1951～2009 年东亚地区各季节降水量和降水日数贡献率变化趋势

Table 5　The variation trends of contribution rate of seasonal precipitation amount and frequency to the whole year in East Asia during 1951–2009

	降水量贡献率变化趋势/(10 a)$^{-1}$	降水日数贡献率变化趋势/(10 a)$^{-1}$
春季	0.091%	0.093%
夏季	－0.090%	－0.222%
秋季	－0.189%	－0.162%
冬季	0.177%	0.279%

冬季各降水指标的年际和年代际波动明显大于其他季节，距平百分率在－40%～60%之间起伏，夏季波动幅度较小。在年际尺度上，东亚地区作为一个整体，各个季节的降水量、降水日数和降水强度与年值之间一般存在显著的正相关性，夏季和年之间的相关性最高，夏季降水对年降水的贡献率最大（图 5、表 2、表 3 和表 4）。但各个季节降水指标之间的相关性均很弱，说明相邻季节之间降水的持续性不明显（表 2、表 3 和表 4）。

冬季的降水量、降水日数和降水强度存在较明显的年代际波动，在 1955、1970、1990、2003 年附近有相对高值中心，在 1962、1980、1995 年附近为低值中心；夏季的各降水指标波动幅度明显小于冬季，2000 年之前降水量和降水日数在 20 世纪 50 至 60 年代偏多，70 年代偏少，90 年代偏多，但 21 世纪前 10 年夏季降水量偏少，降水日数略偏多，降水强度从 20 世纪 90 年代的正距平迅速转变为负距平。夏季降水强度总体增加趋势主要是来自于 20 世纪 70 至 90 年代期间的明显增加。

20 世纪 90 年代末以来，东亚地区冬季降水量和降水日数都强烈增加，个别年份距平百分率超过 40%。同期春季的降水日数正距平也达 10%以上，而夏、秋两季降水日数距平较小，均不超过 10%。最近 10 年全年降水日数增加主要来自于冬、春季降水日数增加。

3.3　不同级别降水变化

图 6 给出 1951～2009 年东亚区域平均的各级别降水量和降水日数距平百分率，表 1 中列出了东亚地区 1951～2009 年全年和季节不同级别降水量和降水日数的线性趋势及其显著性检验结果。

总体上看，在每个级别上降水量和降水日数的年际和趋势变化特点非常相似（图 6 和表 1）。各级别降水量以及中、强和极强降水日数变化均为下降趋势，中降水量的下降趋势比降水日数下降趋势明显，而强和极强降水日数的下降趋势略大于降水量下降趋势；强降水量下降趋势最快，其次为中降水量和极强降水量，弱降水量下降最慢（表 1）。强、极强降水日数下降趋势明显，中降水日数下降趋势较小，弱降水日数则呈上升趋势（表 1）。全区弱降水日数的增加，主要和 1999～2002 年期间的异常偏多有关（图 6）。

从年际和年代际波动看，各级别降水量和降水日数在 20 世纪 50 至 60 年代偏多，70 年代到 80 年代初偏少。20 世纪 50 至 60 年代各级别降水量和降水日数多为正距平，到 70 年代转变为负距平，并一直延续到 80 年代中期；20 世纪 90 年代初期多呈正距平，90 年代末期极强降水量和降水日数为较强的正距平，1998 年极强降水量和降水日数达到近 59 年最高值，其他级别降水则为较弱的负距平；2000 年以来，弱和中降水量、降水日数为强正距平，极强降水量和降水日数则为负距平。弱、中和强降水量和降水日数距平百分率一般变动在－10%～20%，而极强降水降水量和降水日数距平百分率年际波动在－20%～30%。

20 世纪 90 年中以来，各级别降水量和降水日数的距平百分率差异变大。弱、中降水量和降水日数在 20 世纪 90 年代末为低值期，21 世纪前 10 年为高值期；强降水在 20 世纪 90 年代初为明显高值期，90 年代末为低值期，21 世纪前 10 年变化较小；极强降水的位相恰好和弱、中降水相反，20 世纪 90 年代达到高值期，21 世纪前 10 年进入低值期。可见，主要由于极强降水量和降水日数变化背离了

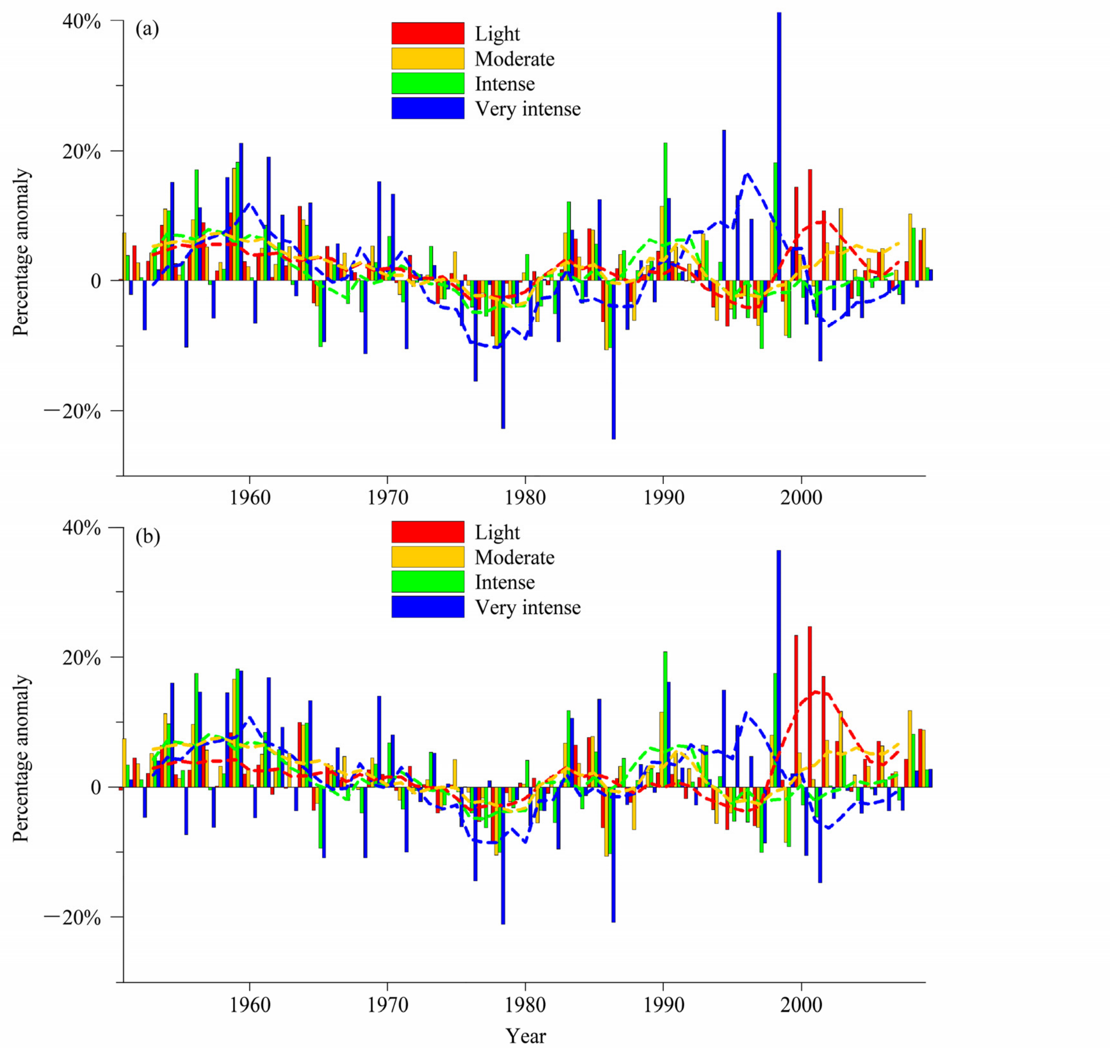

图6 1951～2009年东亚区域平均弱、中、强和极端强（a）降水量距平百分率和（b）降水日数距平百分率（虚曲线为5年滑动平均）

Fig. 6 The average anomaly percentage of light, moderate, intense, and very intense (a) rainfall and (b) rainy days in East Asia during 1951–2009. Dashed line is the five-year moving average

其他级别降水波动位相，以及弱降水日数变化幅度显著加大，造成不同级别降水年代变化之间出现明显不一致。这也反映出，2000年之后东亚地区降水具有迅速向非极端化方向演化趋势。

图7表示东亚地区近59年各级别年降水量和降水日数的线性趋势分布。中西伯利亚地区极强降水量和日数增加，其中降水量增加较明显，弱降水日数增加也较明显；中国东北和华北地区各级别降水量一般减少，其中强降水和极强降水量、降水日数减少比较显著，但东北北部和东部弱降水和中降水量、降水日数增加；长江和淮河流域大部地区各级别降水量和降水日数增加，其中弱和极强降水量、降水日数增加比较明显；朝鲜半岛西部弱降水量和日数显著减少，强降水量和日数略有减少，中降水和极强降水增加；日本列岛大部中、强降水量和降水日数呈现一致性显著减少，在全区各级别降水变化中十分独特，弱降水量亦多减少，但弱降水日数变化趋势不明显；日本本州岛极强降水事件变化出现明显的东增西减特点，降水量的对比尤其明显，增加最显著的台站出现在东京都市圈附近。

4 讨论

本文研究范围为东亚地区，中国东部占据了研究区的大部分，因此降水变化分析结果和针对中国东部或全国的研究应具有可比性和一致性。但实际上，本文对东亚降水变化的分析结果同前人有关中国东部的结论有一致性，也存在若干明显差异。

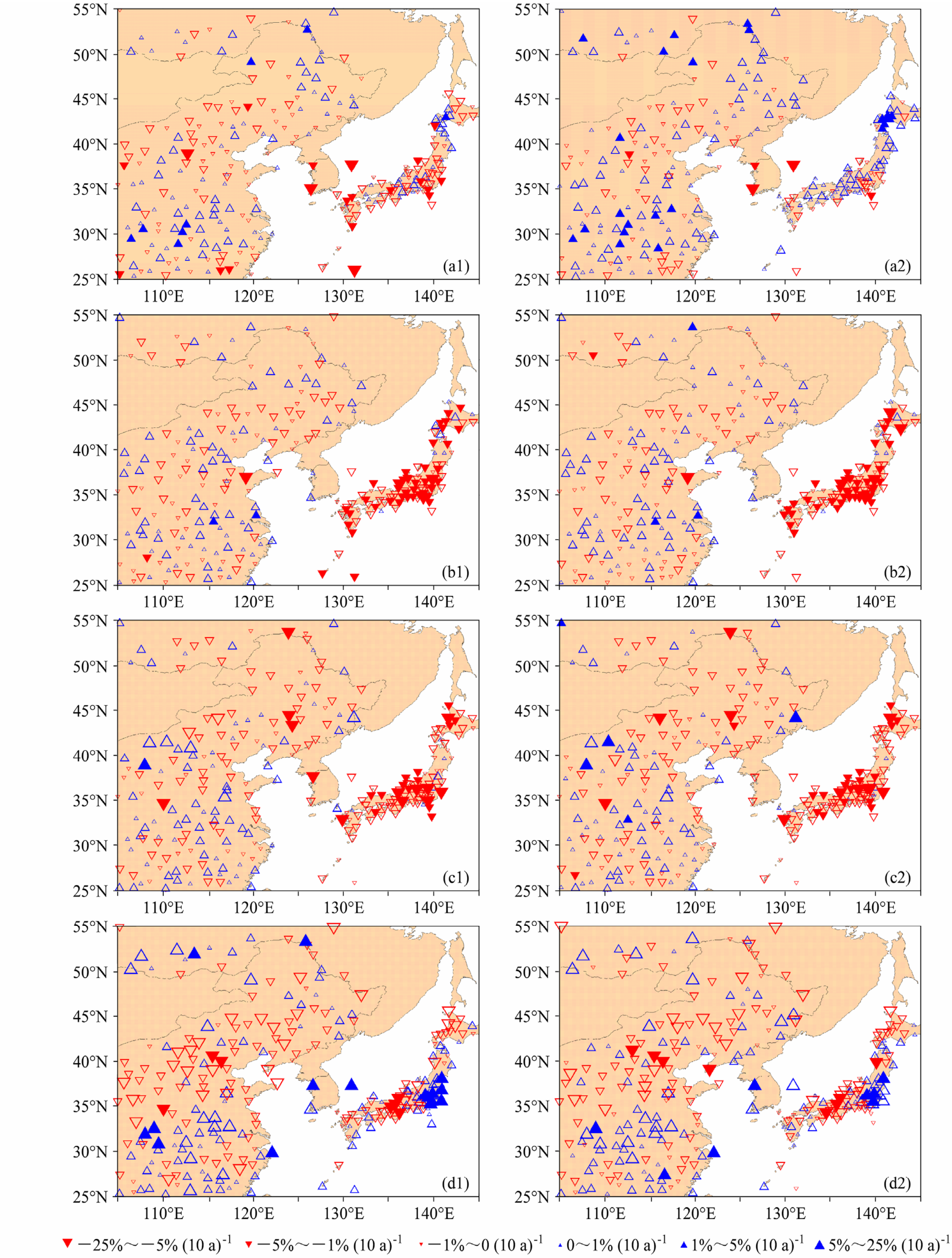

图 7 1951～2009 年东亚地区（a1、a2）弱、（b1、b2）中、（c1、c2）强和（d1、d2）极强降水量（左列）和降水日数（右列）变化趋势（其中的实心三角表示通过显著性水平为 0.05 的检验）

Fig. 7 The variation trends of rainfall amount (left column) and rainy days (right column) of (a1, a2) light, (b1, b2) moderate, (c1, c2) intense, and (d1, d2) very intense rainfall in East Asia during 1951–2009. Filled symbols represent statistically significant trends at 0.05 significance level

从总降水量和极端强降水频率长期变化看，东亚地区与我国全国或东部地区基本一致，过去几十年里均没有表现出明显的上升或下降趋势，这与不同纬度地带经历了相反的或互补的变化有关（任国玉等，2005）。因此，东亚地区降水变化与地面气温长期趋于显著增暖现象截然不同，说明前者没有表现出明显的对大气中温室气体浓度增加等外强迫因子作用的响应信号。

另一方面，多数研究指出，中国东部地区和全国降水日数明显减少，小雨日数减少更显著，中雨日数减少趋势较弱，强降水事件频率变化趋势不明显，但强度有所增大（王颖等，2006；翟盘茂等，2007）。还有研究指出，中国地区秋季极端强降水事件频率减少，冬季极端强降水事件频率增加，夏季南方和西部极端强降水事件也增加，北方极端强降水减少，极端降水量与降水总量的比值在全国多数地区有所增加，说明降水量存在向极端化方向发展的趋势（Zhai et al.，2005；翟盘茂等，2007；闵屾和钱永甫等，2008；杨金虎等，2008）。但是，本文分析表明，在近几十年中，东亚地区多数站点降水日数没有表现出显著减少，弱降水日数减少也不明显，年平均降水强度总体呈现轻微下降趋势，多数站点没有表现出明显增高，降水的季节性差异一般趋于减小。最近几十年东亚地区降水总体上具有向非极端化方向演化特征。

造成这些分析结论差异的原因是多方面的。除了研究时段和范围不一致外，一个重要原因在于对降水日定义的差异。国内业务上和研究中把日降水量大于等于 0.1 mm 作为一个降水日，还有研究者采用大于等于 0.0 mm 的降水日定义，而本文采用日降水量大于等于 1.0 mm 的标准。最近研究发现，中国东部或全国降水日数的减少，主要是由于小雨和微量降水事件频率显著下降造成的（Qian et al.，2007；任国玉等，2010；Liu et al.，2011）。小雨和微量降水事件频率显著下降则可能与中国东部地区大气气溶胶浓度增加有关（Qian et al.，2009；Bennartz et al.，2011）。因此，如果也采用国际上的降水日标准，中国东部或全国平均年降水日数长期减少趋势将不会显著，基于日降水资料计算的平均降水强度长期变化也将不会出现明显增加趋势。本文分析表明，不论是近 59 年还是近 30 年，中国东部地区多数台站年降水强度趋势变化实际上是下降的（图 3、图 4）。

分析时段更新对造成上述差异也有一定影响。20 世纪 90 年代末以后，降水日数特别是弱降水日数突然增加，并维持在相对高的水平上，在一定程度上造成平均降水强度减少，这对区域平均降水日数和降水强度长期变化趋势，尤其是近 30 年的变化趋势，带来了较大影响。先前的研究部分没有包括最近 10 年的观测资料，因而区域平均的降水日数减少和降水强度增加趋势显得更为明显。

另外，20 世纪 90 年代末至 21 世纪初降水日数的突然增加现象，还与本文研究范围包括了中国以外的东亚区域有关。以位于降水日数距平百分率峰值附近的 2001 年为例，当年东亚地区降水日数增加最明显的区域出现在日本和俄罗斯西伯利亚地区，中国东北和内蒙古大部分地区降水日数则为负距平（图 8）。包括了中国东部以外区域，可能有助于减弱降水日数长期减少趋势和降水强度长期增加趋势。

本文分析结果的主要不确定性来自观测资料质量。尽管已经对降水资料进行了初步质量控

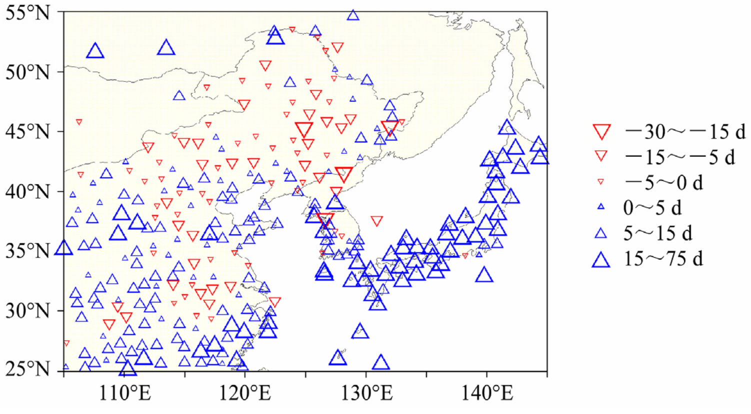

图 8　2001 年东亚地区降水日数距平分布（单位：d）

Fig. 8　The spatial distribution of annual rainy days anomalies (d) in East Asia in 2000

制，但部分地区观测站点稀少，缺测记录较多，资料质量不佳，对分析结果仍有一定影响。由于资料质量问题，蒙古国境内只有 2 个站观测数据可以利用；全区 2001 年前后观测站点缺失较严重，其中俄罗斯西伯利亚远东区 2001 年全部站点缺失（图 8），3 个网格无法参与计算。Yao et al.（2008）指出，俄罗斯远东区域近 30 年夏季降水存在显著减少趋势，遗憾的是，本文分析无法检验这一结果。同时，各网格内台站数量有差别。如图 1c 中，蒙古国东部的 B2 网格，只有 2 个观测站；日本南部海上的 F6 网格，只有一个观测站；主体位于日本海上的 G3 网格，只有 2 个观测站；俄罗斯地区 2000～2009 年期间以及 1956 年之前许多网格测站数目较少，参与计算的网格平均序列方差有差别，在全部区域平均后，站少的网格反而对总的方差贡献较大。但是，由于本文重点关注网格和区域平均序列的趋势变化，估计上述计算方法对结果的影响比较小。此外，在数据处理时缺测值不参与计算，会造成该站降水日数绝对和相对数量偏少，并可能对其他降水指标的计算分析结果产生误差。

5 结论

采用 1951～2009 年的日降水资料，对东亚地区的降水时空变化规律进行分析，得到以下主要结论：

（1）从东亚区域平均来看，年降水量由 20 世纪 50 年代至 60 年代中期以偏多为主，70 年代偏少，80 年代接近均值，90 年代多数年份偏多，此后再接近均值。59 年间年降水量变化趋势为不显著的负趋势，变化速率为－0.479% (10 a)$^{-1}$。年降水日数年代际变化与降水量相似，但 20 世纪 90 年代末以来表现出更显著的增加，59 年间总体变化趋势很弱，只有 0.033% (10 a)$^{-1}$。降水强度年代际变化在 20 世纪 90 年代末之前与降水量和降水日数相近，此后转变为明显的负距平。整个时期降水强度呈下降趋势，下降速率为－0.421% (10 a)$^{-1}$，未通过 0.05 显著性检验。

（2）近 59 年，俄罗斯中西伯利亚、内蒙古西部、江淮流域年降水量、日数和强度以增加趋势为主，中国东北西部和南部、华北地区、日本本州岛西南部、九州岛和四国岛年降水量、日数和强度多为减少；中国东北东部降水日数一般增加，降水强度多呈减少趋势；日本北海道岛降水量和降水强度减少，西部减少显著，本州岛东部降水日数减少，降水强度出现较显著增加。近 30 年期间，45°N 以北大部分地区年降水量、日数和强度一般明显减少，以南大部分地区年降水量和降水日数增加，但东南沿海和韩国、日本西部降水日数多为减少；近 30 年大部分站点年平均降水强度呈减少趋势，降水出现非极端化倾向。

（3）从不同级别降水变化看，近 59 年东亚区域平均的弱、中、强和极强降水量、降水日数总体表现出下降趋势；中降水量的下降趋势比降水日数下降趋势明显，而强和极强降水日数的下降趋势略大于降水量下降趋势；强降水量下降趋势最快，其次为中降水量和极强降水量，弱降水量下降最慢；强、极强降水日数下降趋势明显，中降水日数下降趋势较小，弱降水日数则呈上升趋势。

（4）中西伯利亚地区极强降水量和日数增加，弱降水日数也增加；中国东北、华北地区强降水和极强降水量、降水日数减少较显著；长江和淮河流域大部地区弱和极强降水量、降水日数增加较明显；朝鲜半岛西部弱降水量和日数显著减少；日本列岛中、强降水量和降水日数呈一致性显著减少趋势，弱降水量亦有减少，本州岛极强降水变化出现明显的东增西减特点；中国东部沿海极强降水量和日数多显著增加。

（5）从各个季节看，无论总降水还是各级别降水，冬、春季各降水指标均呈较显著上升趋势，其中冬季中降水量和日数增加趋势分别为 5.58% (10 a)$^{-1}$ 和 5.05% (10 a)$^{-1}$，通过了显著性检验；夏、秋季各降水指标多呈下降趋势，秋季降水量、日数和强度均呈减少趋势，其中强降水量[－2.19% (10 a)$^{-1}$]和日数[－2.15% (10 a)$^{-1}$]变化趋势通过了显著性检验。由于降水偏少季节降水量和日数趋于增多，而多雨季节降水量和日数趋于减少，东亚地区降水的季节性对比趋向减弱。

参考文献（References）

Bennartz R, Fan J, Rausch J, et al. 2011. Pollution from China increases cloud droplet number, suppresses rain over the East China Sea [J]. Geophys. Res. Lett., 38 (9): L09704.

Choi G, Kwon W T, Boo K O, et al. 2008. Recent spatial and temporal changes in means and extreme events of temperature and precipitation across the Republic of Korea [J]. Journal of the Korean Geographical

Society, 43: 681–700.

Choi G, Collins D, Ren G Y, et al. 2009. Changes in means and extreme events of temperature and precipitation in the Asia–Pacific network region, 1955–2007[J]. International Journal of Climatology, 29 (13): 1906–1925.

丁一汇, 任国玉, 赵宗慈, 等. 2007. 中国气候变化的检测及预估 [J]. 沙漠与绿洲气象, 1 (1): 1–10. Ding Yihui, Ren Guoyu, Zhao Zongci, et al. 2007. Detection, attribution and projection of climate change over China [J]. Desert and Oasis Meteorology (in Chinese), 1 (1): 1–10.

黄荣辉, 杜振彩. 2010. 全球变暖背景下中国旱涝气候灾害的演变特征及趋势 [J]. 自然杂志, 32 (4): 187–195, 201. Huang Ronghui, Du Zhencai. 2010. Evolution characteristics and trend of droughts and floods in China under the background of global warming [J]. Chinese Journal of Nature (in Chinese), 32 (4): 187–195, 201.

IPCC. 2007. Climate Change 2007: The Physical Science Basis [M]. Solomon S, Qin D, Manning M, et al., Eds. Cambridge, United Kingdom and New York, NY, USA: Cambridge University Press, 996pp.

Jones P D, Horton E B, Folland C K, et al. 1999. The use of indices to identify changes in climatic extremes [J]. Climatic Change, 42 (1): 131–149.

Karl T R, Knight R W. 1998. Secular trends of precipitation amount, frequency, and intensity in the United States [J]. Bull. Amer. Meteor. Soc., 79 (2): 231–241.

Liu B H, Xu M, Henderson M. 2011. Where have all the showers gone? Regional declines in light precipitation events in China, 1960–2000 [J]. International Journal of Climatology, 31 (8): 1177–1191.

Manton M J, Della-Marta P M, Haylock M R, et al. 2001. Trends in extreme daily rainfall and temperature in Southeast Asia and the South Pacific: 1961–1998 [J]. International Journal of Climatology, 21 (3): 269–284

闵屾, 钱永甫. 2008. 我国近 40 年各类降水事件的变化趋势 [J]. 中山大学学报 (自然科学版), 47 (3): 105–110. Min Shen, Qian Yongfu. 2008. Trends in all kinds of precipitation events in China over the past 40 years [J]. Acta Scientiarum Naturalium Universitatis Sunyatseni (in Chinese), 47 (3): 105–110.

Qian W H, Zhu Y F. 2001. Climate change in China from 1880 to 1998 and its impact on the environmental condition [J]. Climatic Change, 50 (4): 419–444.

Qian W H, Fu J L, Yan Z W. 2007. Decrease of light rain events in summer associated with a warming environment in China during 1961–2005 [J]. Geophys. Res. Lett., 34 (11): L11705.

Qian Y, Gong D Y, Fan J W, et al. 2009. Heavy pollution suppresses light rain in China: Observations and modeling [J]. J. Geophys. Res., 114 (D7): D00K02.

Ren G Y. 1991. A new discovery in the comparison of the heat resources of temperate areas between China and the United States [J]. Bull. Amer. Meteor. Soc., 72 (2): 239–241.

任国玉, 吴虹, 陈正洪. 2000. 我国降水变化趋势的空间特征 [J]. 应用气象学报, 11 (3): 322–330. Ren Guoyu, Wu Hong, Chen Zhenghong. 2000. Spatial patterns of change trend in rainfall of China [J]. Quarterly Journal of Applied Meteorology (in Chinese), 11 (3): 322–330.

任国玉, 郭军, 徐铭志, 等. 2005. 近 50 年中国地面气候变化基本特征 [J]. 气象学报, 63 (6): 942–956. Ren Guoyu, Guo Jun, Xu Mingzhi, et al. 2005. Climate changes of China’s mainland over the past half century [J]. Acta Meteorologica Sinica (in Chinese), 63 (6): 942–956.

任国玉, 封国林, 严中伟. 2010. 中国极端气候变化观测研究回顾与展望 [J]. 气候与环境研究, 15 (4): 337–353. Ren Guoyu, Feng Guolin, Yan Zhongwei. 2010. Progresses in observation studies of climate extremes and changes in main land China [J]. Climatic and Environmental Research (in Chinese), 15 (4): 337–353.

Ren G Y, Liu H B, Chu Z Y, et al. 2011. Multi-time-scale climatic variations over eastern China and implications for the south–north water diversion project [J]. Journal of Hydrometeorology, 12 (8): 600–617.

Tu K, Yan Z W, Dong W J. 2010. Climatic jumps in precipitation and extremes in drying North China during 1954–2006 [J]. J. Meteor. Soc. Japan, 88 (1): 29–42.

王小玲, 翟盘茂. 2008. 1957～2004 年中国不同强度级别降水的变化趋势特征 [J]. 热带气象学报, 24 (5): 459–466. Wang Xiaoling, Zhai Panmao. 2008. Changes in China’s precipitation in various categories during 1957–2004 [J]. Journal of Tropical Meteorology (in Chinese), 24 (5): 459–466.

Wang Y, Yan Z W. 2009. Trends in seasonal precipitation over China during 1961–2007 [J]. Atmospheric and Ocean Science Letters, 2 (3): 165–171.

王颖, 施能, 顾俊强, 等. 2006. 中国雨日的气候变化 [J]. 大气科学, 30(1): 162–170. Wang Ying, Shi Neng, Gu Junqiang, et al. 2006. Climatic variations of wet days in China [J]. Chinese Journal of Atmospheric Sciences (in Chinese), 30 (1): 162–170.

杨金虎, 江志红, 王鹏祥, 等. 2008. 中国年极端降水事件的时空分布特征 [J]. 气候与环境研究, 13 (1): 75–83. Yang Jinhu, Jiang Zhihong, Wang Pengxiang, et al. 2008. Temporal and spatial characteristic of extreme precipitation event in China [J]. Climatic and Environmental Research (in Chinese), 13 (1): 75–83.

Yao C, Yang S, Qian W H, et al. 2008. Regional summer precipitation events in Asia and their changes in the past decades [J]. J. Geophys. Res., 113 (D17): D17107.

翟盘茂, 潘晓华. 2003. 中国北方近 50 年温度和降水极端事件变化 [J]. 地理学报, 58 (增刊): 1–10. Zhai Panmao, Pan Xiaohua. 2003. Change in extreme temperature and precipitation over northern China during the second half of the 20th century [J]. Acta Geographica Sinica (in Chinese), 58 (suppl.): 1–10.

翟盘茂, 王萃萃, 李威. 2007. 极端降水事件变化的观测研究 [J]. 气候变化研究进展, 3 (3): 144–148. Zhai Panmao, Wang Cuicui, Li Wei. 2007. A review on study of change in precipitation extremes [J]. Advances in Climate Change Research (in Chinese), 3 (3): 144–148.

Zhai P M, Zhang X B, Wan H, et al. 2005. Trends in total precipitation and frequency of daily precipitation extremes over China [J]. J. Climate, 18 (7): 1096–1108.

第29卷 第5期
2013年10月

气象与环境学报
JOURNAL OF METEOROLOGY AND ENVIRONMENT

Vol. 29 No. 5
October 2013

张本志,任国玉,张子曰,等. 北京中心商务区夏季近地面气温时空分布特征[J]. 气象与环境学报,2013,29(5):26-34.
ZHANG Ben-zhi,REN Guo-yu,ZHANG Zi-yue,et al. Temporal and spatial characteristics of summer near-surface air temperature in Beijing central business district[J]. Journal of Meteorology and Environment,2013,29(5):26-34.

北京中心商务区夏季近地面气温时空分布特征

张本志[1,3] 任国玉[2] 张子曰[3] 李艳[3]

(1. 南京信息工程大学,江苏 南京 210044; 2. 中国气象局气候研究开放实验室,北京 100081;
3. 北京市朝阳区气象局,北京 100016)

摘 要:利用2012年6—8月31个自动观测站气温资料,分析了北京中心商务区(CBD)夏季近地面气温时空分布特征及影响因子,并将CBD地区夏季气温监测数据与朝阳区气象站同期地面气温进行比较。结果表明:下垫面类型和人为热排放等差异是直接影响城市CBD近地面气温空间分布的主要原因。人口密集区、高层建筑与柏油路面集中区成为夏季月平均气温高值中心,较绿地覆盖区域的低值中心偏高约1.0 ℃;夜间人类活动及车辆使用造成的人为热排放是导致夜间城市地面气温空间差异的主要原因,而白天气温空间差异相对较小。CBD地区与朝阳站平均温差存在较明显的周内和日内变化规律,且白天和夜间二者温差基本都为正值,但夜间的差值更加明显,即CBD地区平均气温一般高于朝阳站,表现出明显的附加城市热岛效应,而且这种附加城市热岛效应具有同城市热岛强度相近的日内变化规律。进一步分析表明,不同天气条件下CBD区域的附加城市热岛强度表现出显著差异,晴好微风少云天气情况下,附加城市热岛效应更明显,主要表现在夜间;阴天、高湿天气条件下,附加城市热岛效应在白天和夜间均较弱;降水天气条件下附加城市热岛效应日夜差异最小,说明日照和太阳辐射在引起附加城市热岛效应方面起着重要作用。不同天气条件下CBD地区内部的附加城市热岛效应空间分布基本一致。

关键词:CBD地区;热环境;人为热;附加城市热岛效应

中图分类号:P463.3 **文献标识码**:A doi:10.3969/j.issn.1673-503X.2013.05.005

引言

20世纪80年代以来,国内外学者针对不同区域、不同地理环境下城市发展带来的热环境变化特征、时间演化趋势、影响因子、形成原因等问题,利用多种方法从不同角度开展了很多研究,取得了大量成果。近年来,随着中国大城市规模化发展和城市人口增多,城市建成区内高楼大厦、柏油路面、钢筋水泥建筑、玻璃幕墙等日益增多,造成地表长波辐射状况显著变化,加之人口密集、空调等设备运用以及汽车行驶尾气等人为热的大量排放等,导致城市下垫面状况及城市热环境分布发生了巨大改变,城市化加剧对城市气候带来的影响日趋突显,对城市热岛研究工作中的热点问题也有许多研究和讨论[1]。白杨等[2]研究指出,随着城市规模的高速发展和城市人口的急剧膨胀,因城市下垫面的急剧变化和城市人为热排放的迅速增加所引起的城市热岛效应已逐渐成为严重影响城市居住环境和居民健康的重要因素。研究指出[3-4],北京城市化影响不仅导致北京气象站近地面平均气温上升趋势比乡村站明显偏高,而且常用极端气温指数的长期趋势变化也明显高于乡村,其城市化影响均通过了0.01显著性水平检验。

国外学者关于城市热环境的研究工作开展的较早[5-11],Myrup[5]应用能量平衡模式对城市气温及热岛强度进行了分析,认为城市中心蒸发量的减少、城市建筑物和铺设材料的热属性等是造成热岛效应的主要因素。Mitchell[6]指出,美国城市最大热岛强度与城市人口的平方根有较好的正相关。Oke[7]认为城市热岛强度与人口对数呈线性关系 Streutker[8]根据休斯敦地区1985—1987年和1999—2001年获取的数百幅夜间NOAA影像地表温度图,系统地分析了这两个时期的城市热岛特征;Roth等[9]利用AVHRR热红外数据评估了美国西海岸几个城市的热岛强度,并发现白天地表温度与土地利用类型有关,工业区地表温度高于植被覆盖地表,而夜间城市与郊区的地表温度差异较小。

收稿日期:2013-04-11;**修订日期**:2013-05-27。
基金项目:北京市朝阳区科技计划项目“朝阳区热岛效应监测和商务中心区气象节能措施研究”(KC1103)、北京市科技计划课题“北京地区气候变化对城市热环境影响评估及气象节能关键技术研究”(Z111100074211010)和北京市气象局气象科技研发专项“北京市商务中心区热环境观测及气象节能措施示范研究”(2011BMBKYZX12)共同资助。
作者简介:张本志,男,1977年生,工程师,主要从事城市热岛研究,E-mail:zhangbz@bjmb.gov.cn。
通信作者:任国玉,E-mail:guoyoo@cma.gov.cn。

在国内,针对北京、上海等大城市发展带来的热环境问题,前人进行了深入分析研究[12-23]。丁金才等[16]对上海盛夏热岛效应的研究指出,城市市区建成面积、土地利用类别、人口密度等城市化因素都影响到城市热岛的范围和强度;初子莹和任国玉[18]通过对北京地区 20 个台站 1961—2000 年月平均气温资料的对比分析发现,由于快速的城市化过程,北京站和密云站地面平均气温的上升趋势比远郊乡村站明显偏高,表现出显著的城市热岛强度随时间增强作用的影响。季崇萍等[19]研究指出,北京城市建成区范围与城市热岛效应影响范围呈同步变化趋势;程兴宏等[20]采用晴空过程北京城郊地面自动气象站气温观测值对卫星遥感云顶黑体气温高分辨率场实施变分订正,揭示了北京城市建筑群面积及中高层建筑群布局对城市热岛群总体演变趋势;杨萍等[22]利用北京地区 20 个气象观测站 1978—2007 年逐日平均气温资料,分析了近 30 a 北京地区极端气温事件的变化趋势,得出近 10 a 夏季显著的热岛效应是城区极端高温事件发生频次明显高于其他地区的重要原因;大量研究表明,不同土地利用、土地覆盖类型与地表城市热环境有着密切关系,地表城市热岛强度增加的区域与城市扩展区域一致,城市化过程是城市热岛面积不断增加的主要原因[17,21]。

随着观测手段和方法的不断完善,城市热岛效应的研究进入了一个新的时期。近年,自动观测气象站的布设密度加大,为城市气候研究积累了较多资料。国内学者已经开始利用自动观测站资料进行深入的城市热岛效应研究。但在城市功能区开展微气候观测和研究工作仍然较少,目前缺乏对更小城市区域和范围的精细观测、分析和研究,所选取的自动气象站点分布密度有限,目前的观测还未达到开展北京中心商务区(以下简称 CBD,Central Business District)如此小尺度区域热环境研究所需要的布点密集程度。本文选取以国内最具城市化发展特征的北京 CBD 核心区为研究对象,首次对国内特大城市商务功能区的城市热环境特征开展观测研究。利用在 CBD 区域布设的 31 个温湿观测站点进行加密数据监测,结合附近朝阳气象站观测资料, CBD 区域地理信息以及商务功能区的下垫面特征资料,开展小网格距夏季热环境精细化研究。

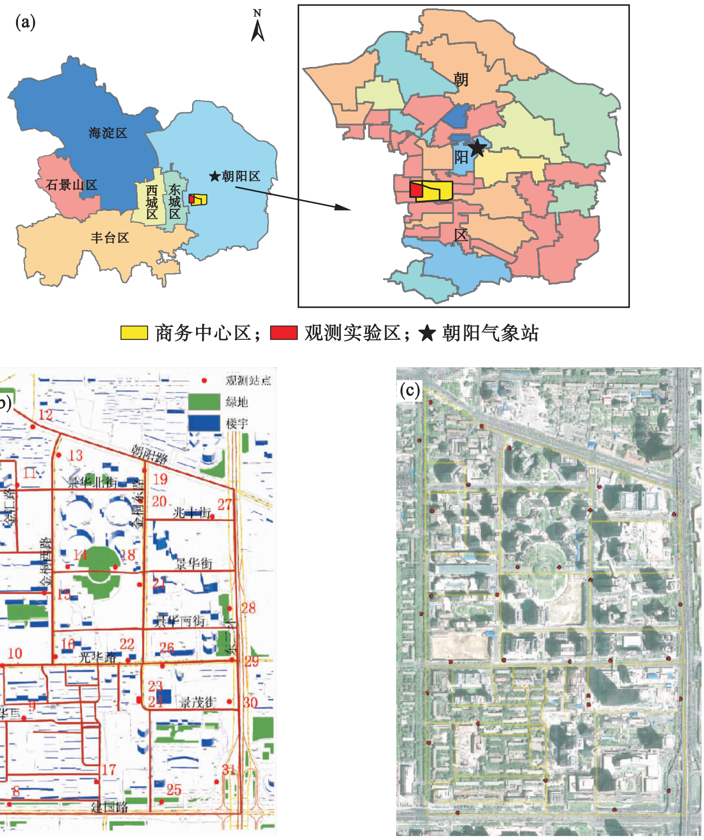

图 1b 与图 1c 红点代表仪器的位置和编号

图 1　北京 CBD 区域和观测试验区位置(a)、观测试验区下垫面特征及其测点分布(b)和观测试验区下垫面特征卫星影像图及其测点分布(c)

Fig. 1　The Beijing CBD area and the experimental area (a), the land surface types and distribution of the observational stations (b) and its image as well as corresponding distribution of stations (c)

1 CBD区域特征及仪器安装

1.1 CBD区域特征

北京CBD位于朝阳区(图1a中黄色区域),西起朝阳区东大桥路,东至东四环路,南临通惠河,北接朝阳北路,其核心区约3.99 km^2,东扩区约3.0 km^2,建筑面积达1 000万m^2[24]。目前,该区域建有330 m高的国贸三期及银泰大厦等标志性建筑群,2012年又新开建500 m高中国尊,是国内金融、保险、地产、网络等高端企业地区总部集中区。

1.2 气象仪器安装

气象观测仪器采用美国ONSET公司生产的HOBO Pro v2气温、湿度采集器,采集1组气温、相对湿度观测数据的最短时间间隔可为1 s,该传感器气温在0—50 ℃范围内测量精确度为±0.21 ℃,湿度在0—90%范围内测量精确度为±2.5%。安装之前将仪器与朝阳气象站(国家一般气象站,站号为54433,以下简称“朝阳站”)的温湿度观测数据进行了比对,对仪器存在的系统误差进行了校准。

选取CBD核心发展区域作为观测试验区,将CBD近地面气温精细化监测区域设在南北约1.5 km、东西约1.0 km的梯形区域内。观测试验区域所在位置见图1a中红色区域。根据前期流动观测分析结果及实际安装条件,制定出观测仪器安装布点方案,共安装31个HOBO温湿记录仪对区内近地面气温进行观测,测点具体分布见图1。仪器全部安装在路灯灯杆上,统一高度为3 m,与中国气象站观测场地面气温观测标准高度基本一致,测点水平间隔距离大约在200—400 m之间,大致均匀分布,主要代表了交通干线附近、写字楼附近、居民小区及公园等下垫面环境条件。

2 资料与方法

2.1 资料选取和处理

从选取的31个观测点2012年5—9月HOBO数据集中截取6—8月(代表夏季)的完整数据进行分析,观测数据采样间隔设定为5 min,检验比对所获得的数据资料未发现极端异常值。对采集的3个月数据进行处理,小时平均气温采用整点前后30 min内气温平均值,处理方法为:

$$\overline{T_i} = \frac{1}{12}\sum_{j=12i+1}^{12i+12} T_j (i = 0,1,2,3,\cdots,n) \tag{1}$$

式(1)中,$\overline{T_i}$为整点平均气温;T_j为气温5 min观测序列。采用式(1)处理可滤去正点前后随分钟脉动变化的波。本文研究内容主要以处理后获得的小时平均气温作为基础数据开展相关分析。

2.2 分析方法

人工数据分类法是根据数据本身的分布情况将数据分段,使数据在演示图中表示时,断点出现在极小值,而断点排列顺序依据极小值的大小排列,最大的极小值作为第一个断点。此方法可将演示图中气温色标进行分割,使组内气温色标差距最小,组间气温色标差距最大,从而清晰演示出气温的空间分布特征。本文通过人工数据分类法分析CBD地区小时平均气温和附加城市热岛效应分布特征。

2.3 附加城市热岛效应定义

本文将CBD观测试验区各测点和区域平均气温与同一时间朝阳气象站地面气温的差值定义为附加城市热岛效应(EUHI)。之所以选取朝阳站作为参考,是因为安装的仪器与朝阳站气温观测数据进行了比对,并对仪器存在的系统误差进行了校准;但由于朝阳站位于北京城区,观测试验区与朝阳站之间距离仅约为6 km,朝阳站本身又受到了城市热岛效应(UHI)影响,因此这里称为附加城市热岛效应。CBD区域平均的EUHI强度用式(2)计算:

$$\Delta T_k = T_k - t_k \quad (k = 1,2,3,\cdots,24) \tag{2}$$

式(2)中,ΔT_k代表k时刻的附加城市热岛效应强度;T_k代表k时刻CBD区域31个观测站小时平均气温;t_k代表k时刻朝阳气象站小时平均气温。

2.4 不同天气条件的选取

为了解不同天气条件下CBD区域EUHI强度的差异及其原因,选取晴好微风少云、中等能见度(少云微风)、多云阴天、高湿、降水天气5种不同类型的典型代表性天气条件,比较分析各类天气条件下的EUHI强度及其时间变化情况。考虑到代表性天气状况在一日内出现的时长以及强度对附加城市热岛效应的影响,因此,限定了代表性天气的选取条

件并对 6—8 月满足限定条件的不同类型的典型代表性天气进行筛选(表1),在此基础上计算并得到不同天气条件下小时 EUHI 强度。

表 1　2012 年 6—8 月北京 CBD 区域代表性天气的选取条件及典型代表性天气出现日数

Table 1　The threshold of representative weather and the number of corresponding weather from June to August of 2012 in the CBD of Beijing

天气情况	选取条件	6 月/d	7 月/d	8 月/d
晴好微风少云	能见度为 20 km 以上,总云量小于 3 成,最大风速小于 3 级	1	2	1
中等能见度(少云微风)	能见度为 5—20 km,总云量小于 3 成,最大风速小于 3 级	2	0	1
多云、阴天	总云量、低云量在 9 成以上	2	2	1
高湿天气	日最小相对湿度 >75%	4	6	0
降水天气	日内降水时间在 12 h 以上	1	2	0

3　结果分析

3.1　CBD 区域夏季热环境空间分布特征

3.1.1　夏季平均气温空间分布特征

由图 2 可见,CBD 地区夏季极端最高气温出现在 7 月(图 2c),月平均气温最高值为 28.8 ℃;夏季平均气温的高值中心较低值中心偏高1.0 ℃左右

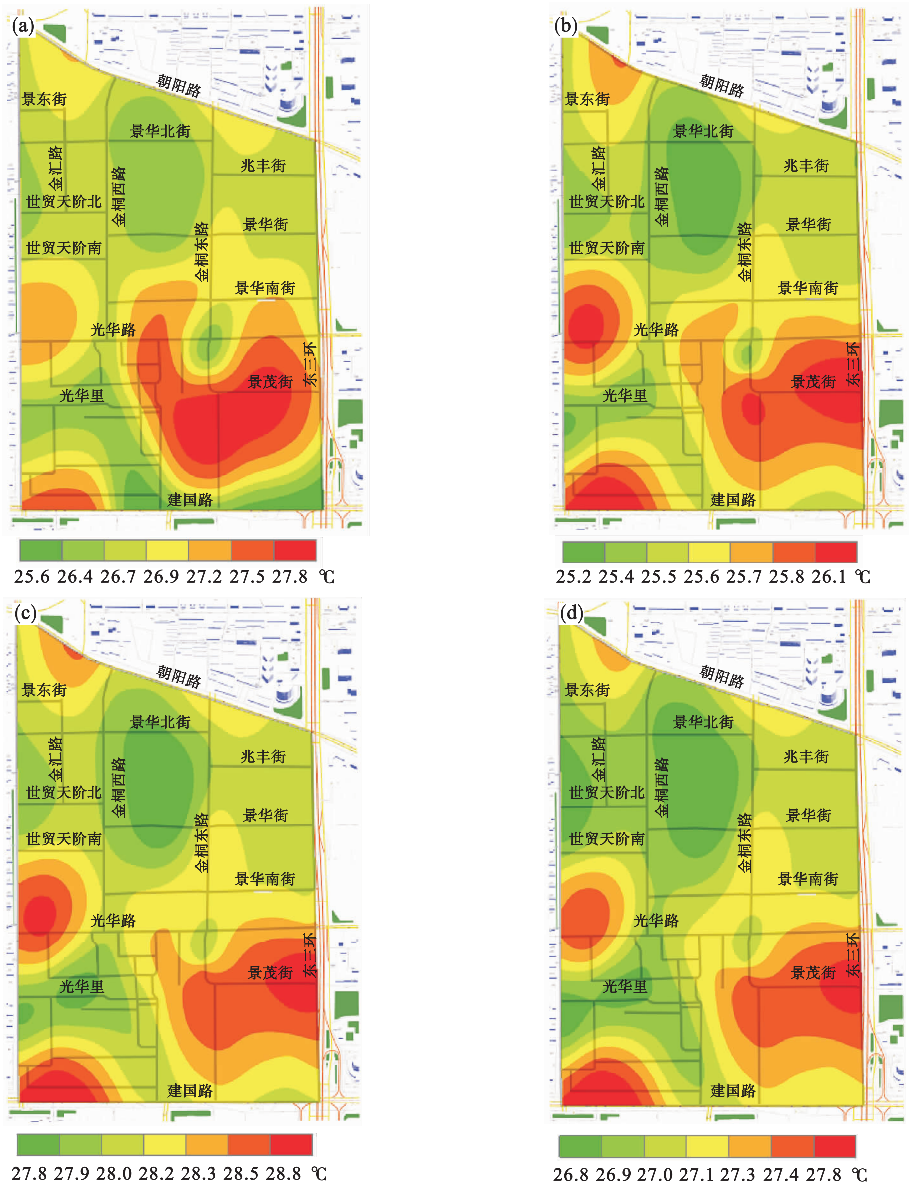

图 2　2012 年 6—8 月(a)、6 月(b)、7 月(c)和 8 月(d)北京 CBD 观测试验区平均气温空间分布

Fig. 2　The spatial distribution of mean air temperature during June to August (a), in June (b), July (c) and August (d) of 2012 at the experimental area in the CBD of Beijing

(图2a)。6—8月各月平均气温的空间分布特征较一致,高值中心、低值中心的空间位置较为稳定,说明高值中心、低值中心的出现与所在区域的下垫面环境存在密切关系。其中,景华北街和景华街之间及光华里两处低值中心的下垫面特征为景华北街和景华街之间为CBD地区的中心公园绿化带,绿地和树木较多;光华里区域内CBD早期的老旧居民小区比较集中,而且为低层建筑,绿化程度较好;而位于光华路西边东三环路南侧和建国路西侧及朝阳路西侧的两处高值中心,处于主要路段的交叉点,高值中心的出现主要与该区域柏油路面地表和周边建筑热辐射、人为热排放以及植被相对较少等因素有关。金桐东路与景茂街交叉点北侧亦为次低值中心,该中心观测站点受到国贸三期大楼对太阳辐射的遮挡,而且该站点周边植被绿化较好,因此造成气温较周围站点偏低。

3.1.2　夏季昼夜气温周变化特征

选取05时和14时两个时次分别代表夜间和白天,利用两个时次的31个观测站的夏季平均气温分别与同时次朝阳气象站的平均气温进行EUHI的周变化对比分析。从05时和14时EUHI强度的周变化曲线(图3)可以看出,CBD地区6—8月05时与14时的平均气温均明显比同时次朝阳站气温偏高,平均EUHI约为0.9 ℃。EUHI较强的时段在05时,即夜间CBD区域EUHI最强,其中最高值出现在周三与周六,达到1.8 ℃,最低值出现在周日,但也达到1.3 ℃;14时的EUHI强度明显减弱,最高值

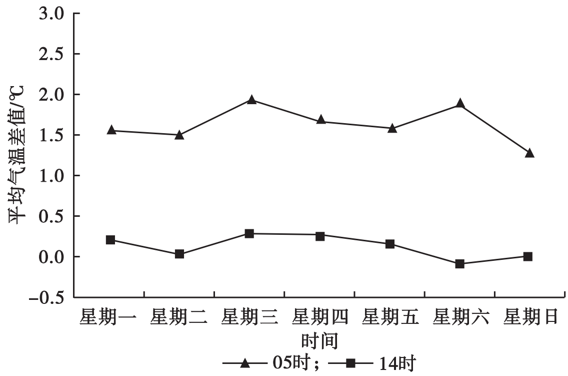

图3　2012年6—8月05时和14时北京CBD区域平均附加城市热岛效应强度周变化曲线

Fig. 3　The weekly variation of EUHI at 05:00 and 14:00 during June to August of 2012 in the CBD of Beijing

出现在周三,为0.3 ℃,最低值出现在周六,为−0.1 ℃。

由于CBD地区城市建筑物密集并以沥青和水泥地面为主,而且CBD地区作为商务区车流量大、人们活动频繁,造成的人为热排放远比朝阳站附近高;而朝阳站观测场为标准的建设绿地,附近高层建筑较少,对太阳短波辐射吸收和地面长波辐射外逸以及感热和潜热交换均与CBD区域具有明显差异,造成CBD地区白天和夜间的EUHI值多数情况下为正值,即平均气温明显高于朝阳站。由于白天太阳辐射增温使得低层湍流加强,热量的垂直和水平交换比夜间强,CBD区域EUHI强度较弱;而夜间各种人工建筑特别是高层建筑物将把白天吸收和存贮的热量释放出来,加上空气静稳,浓度更高的颗粒污染物和温室气体更多地吸收地面长波辐射,致使近地面大气中的热量不易很快散失,EUHI强度一般要比白天明显增大。

3.1.3　气温日内变化

由图4可见,2012年夏季北京CBD观测试验区逐

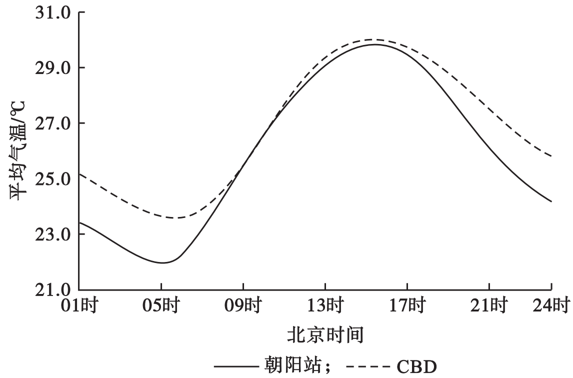

图4　2012年夏季北京CBD观测试验区和朝阳站平均小时气温日变化曲线

Fig. 4　The hourly air temperature in summer of 2012 at the experimental area in the CBD of Beijing and at Chaoyang weather station

小时的平均气温均高于朝阳站,且夜间差别较大,午间气温差别较小。平均气温最高值均出现在15时,CBD观测试验区最高平均气温达30 ℃;平均气温最低值出现在早晨05时,朝阳站最低气温为22 ℃。

为进一步量化CBD观测试验区平均气温与朝阳站的差别,图5给出了2012年夏季北京CBD观测实

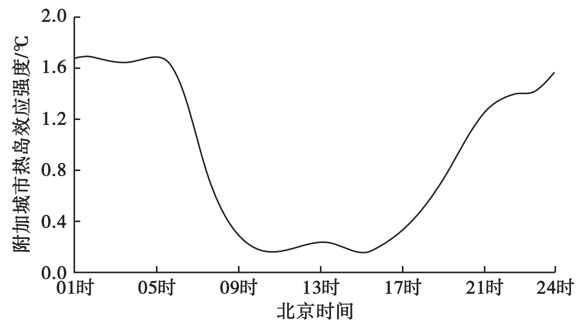

图5　2012年夏季北京CBD观测实验区附加城市热岛效应强度日变化曲线

Fig. 5　The diurnal variation of EUHI intensity in summer of 2012 at the experimental area in the CBD of Beijing

验区平均 EUHI 强度的日变化曲线。从图 5 可以看出,夏季平均 EUHI 强度在夜间变化不大,而在白天变化较为明显。EUHI 强度夜间维持较大值,最大值出现在 01 时到 05 时之间,达到 1. 6 ℃以上;05 时到 09 时之间是 EUHI 急剧下降阶段,午间降至最低值,其中 09 时左右 EUHI 强度首先达到最低,并维持低值状态至 16 时左右,最低值出现在 14 时附近,约为 0. 18℃;16 时以后 EUHI 开始增大,至 24 时左右强度达到峰值。EUHI 强度日变化幅度最大出现在 05—09 时之间,变化幅度达到 1. 5 ℃。

2012 年夏季北京 CBD 观测实验区 EUHI 强度日变化特征与已有研究中城市热岛强度夜间维持最大值而午间降至最低值的结论基本一致。与北京市四环以内区域平均 UHI 强度日变化特征[24]比较,CBD 区域平均 EUHI 强度在清晨和上午的急剧降低趋势要更明显,到 09 时即达到最低值,而前者在 10 时左右接近最低值;午后到傍晚的急剧上升则更和缓,到 21 时仍然没有停止上升,而前者的上升过程则十分剧烈,至 20 时即已接近夜间高峰区域。20 时至 24 时 CBD 观测实验区 EUHI 强度仍然逐渐增强,这可能在一定程度上与 CBD 区域高层建筑更为密集、夏季夜晚人类活动丰富多样、人为热量释放更大等因素有关,也可能和朝阳站本身具有较明显的 UHI 效应有关。

3. 2　不同天气条件下 CBD 观测试验区附加城市热岛效应特征

3. 2. 1　附加城市热岛效应的日变化特征

图 6 给出了不同天气条件下 2012 年夏季 CBD 观测试验区平均每日逐小时 EUHI 强度变化情况。

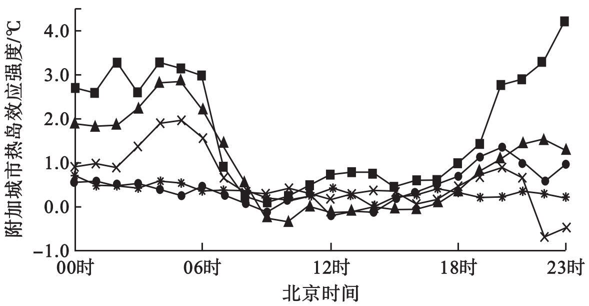

图 6　不同天气条件下北京 CBD 观测试验区附加城市热岛效应强度日变化

Fig. 6　The diurnal variation of EUHI intensity at the experimental area in the CBD of Beijing under different weather conditions

在晴好微风少云天气情况下,EUHI 效应更加明显,特别是在夜间,最高可达到 4. 3 ℃,白天较弱,其中 09 时最小,仅有 0. 1 ℃;在阴天、高湿天气条件下,EUHI 效应在白天和夜间均较弱,09 时和 12—14 时甚至出现负值,即研究区域平均气温比朝阳站附近还略低;降水天气条件下 EUHI 效应日夜差异最小,说明日照和太阳辐射在引起 EUHI 效应方面起着重要作用。

CBD 地区由于下垫面多人为建筑,加上风对气温差异的混合作用不明显,不同类型天气条件下夜间平均 EUHI 强度最大差值达 4. 3 ℃,白天 EUHI 强度差异不大;在能见度转差的时候,EUHI 效应也被减弱。阴天由于太阳辐射少,人为热释放的影响相对更明显,EUHI 强度一般在 1. 0 ℃左右。在高湿和有降水的时候,EUHI 效应表现最弱,与太阳辐射弱和潜热交换强等因素有关。从不同天气条件下 CBD 观测试验区 EUHI 效应差异分析看,下垫面条件、日照和太阳辐射、风力、能见度、空气湿度、人类热释放等对 EUHI 效应均有影响,但不同天气条件下,各个因子的影响程度具有明显差异。

3. 2. 2　附加城市热岛效应空间分布特征

采用人工数据分类法进行附加城市热岛效应分析。图 7 分别代表晴好微风少云、少云微风(中等能见度)、多云阴天、高湿、降水 5 种天气条件下EUHI 效应空间分布。通过对比发现,5 种天气条件下 EUHI 效应空间分布基本一致,高值中心主要出现在光华路北与世贸天阶南之间、景茂街与东三环路交界、建国路西侧,最高值出现在晴好微风少云天气条件下,达 2. 4 ℃(图 7a);而低值中心主要位于景华北街和景华街之间及光华里,最低值出现在降水天气条件下,仅有 0. 1 ℃(图 7e)。

EUHI 强度高值中心均处于主要路段的交叉点,多为硬化路面,车流量大,而且周边写字楼等高层建筑较多,绿化较少,人为活动频繁;而景华北街和景华街之间的 EUHI 强度低值中心为 CBD 地区的公园绿化带,绿地和树木较多;光华里区域的 EUHI 强度低值中心位于老旧居民小区,低层建筑较多,树木繁茂,与朝阳站周边环境类似。因此,下垫面类型差异是影响 CBD 区域 EUHI 强度空间分布的主要原因之一。

4　结论与讨论

(1)CBD 观测试验区 2012 年夏季各月平均气温分布特征比较稳定,绿地覆盖的小区、公园夏季平均气温较低,而主要交通路段交叉点和高层建筑密集区为气温高值中心。夏季平均气温的高值中心较低值中心偏高 1. 0 ℃左右。下垫面类型和人为热排

放等差异是影响北京 CBD 观测试验区近地面气温空间分布的主要原因。

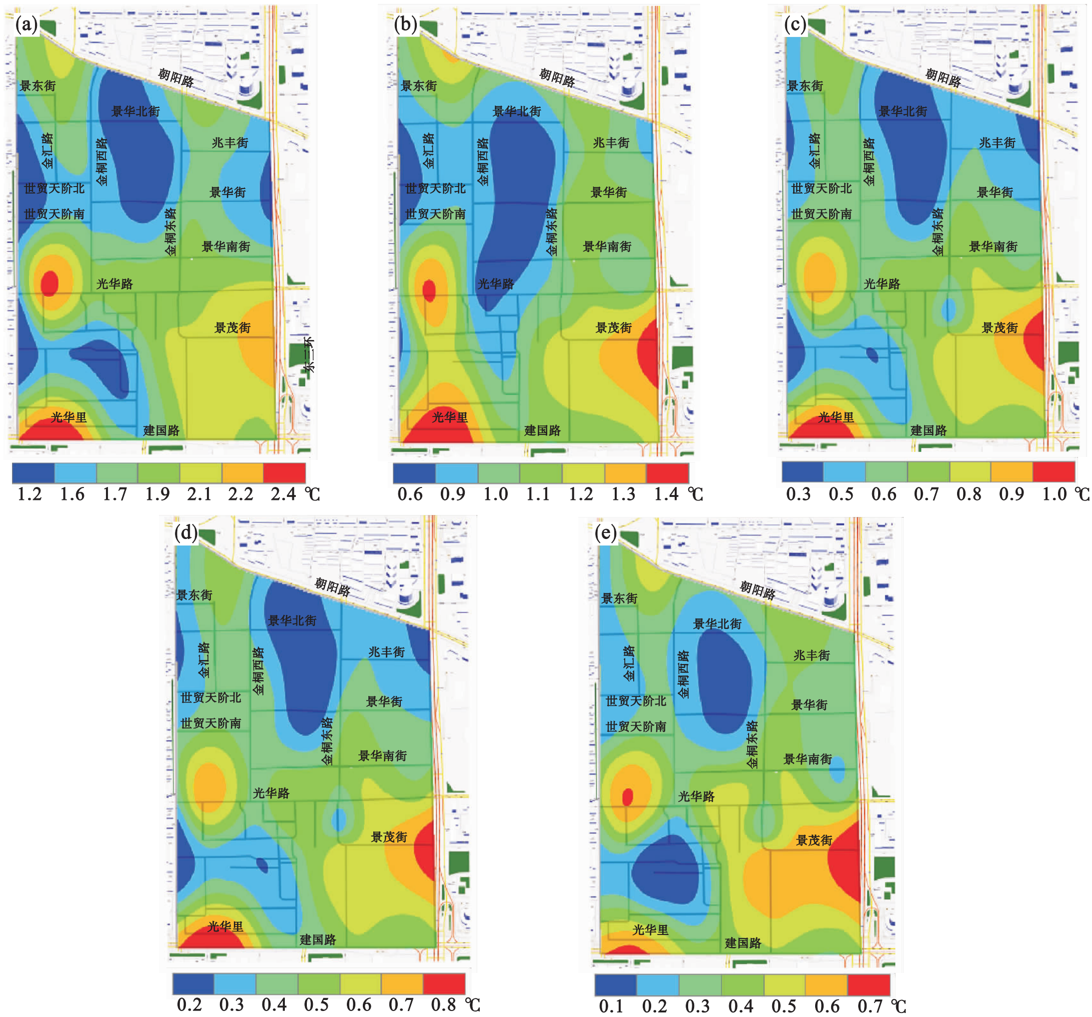

图7　晴好微风少云天气(a)、少云微风天气(b)、多云阴天天气(c)、高湿天气(d)和降水天气(e)条件下 CBD 区域附加城市热岛效应空间分布

Fig. 7　The spatial distribution of EUHI in a sunny day with breeze and partly cloud (a), a partly cloud and breeze day (b), a cloud day (c), a high humidity day (d) and a rainy day (e) at the experimental area in the CBD of Beijing

(2)CBD 观测试验区与朝阳站之间的地面气温差值即附加城市热岛效应周内变化具有明显的时间特征,清晨05时 CBD 观测试验区附加城市热岛效应较明显,周三和周六更为明显,可达1.8 ℃,周日较弱,但也达到1.3 ℃;午后14时附加城市热岛效应明显减弱,周三最明显,但仅有0.3 ℃,周六表现为负值(-0.1 ℃)。

(3)CBD 观测试验区2012年夏季平均附加城市热岛效应在24 h 内存在明显的时间变化特征。CBD 观测试验区夏季逐小时的平均气温均高于朝阳站,且夜间差别较大,午间差别较小。附加城市热岛强度在夜间维持较大值,最大值出现在01—05时之间,达到1.60 ℃以上;05—09时之间强度急剧下降,09时左右首先达到最低,并维持低值状态至16时左右,最低值出现在14时附近,约为0.18 ℃;16时以后附加城市热岛强度开始增大,至24时左右达到峰值。

(4)不同天气条件下 CBD 核心地区附加城市热岛效应表现明显不同。晴好微风少云天气情况下夜间附加城市热岛效应最为明显,最大强度可达4.3 ℃;阴天、高湿和降水天气条件下附加城市热岛效应较弱;降水天气条件下附加城市热岛效应的日夜差异最小。日照和太阳辐射在引起附加城市热岛强度差异中起着重要作用。不同天气条件下附加城市热岛效应空间分布基本一致。

(5)由于北京 CBD 地区的常年观测资料有限,本文利用2012年夏季加密观测资料的分析结论还有待今后深入研究验证。但本文分析结果与前人针对北京和其他大城市的研究结论具有较好可比性,其中附加城市热岛效应的时间变化规律与前人研究基本一致。但是,北京 CBD 观测试验区平均附加城市热岛强度在清晨和上午的急剧降低趋势比北京四

环内平均城市热岛强度降低更明显,达到最低值的时间也提前 1 h 多,午后到傍晚的急剧上升趋势则更和缓,到 21 时仍未停止上升,比四环内平均城市热岛强度上升过程延长,达到最高值时间延后数小时。造成这一差异的原因可能与 CBD 区域高层建筑更为密集、夏季夜晚人类活动强烈、人为热量释放较大等因素有关,也可能与参考站附近具有较明显的城市热岛效应有关。

(6)此外,CBD 观测试验区内下垫面包含了绿地、硬化路面、高大植被等,这些不同下垫面特性具有不同的附加城市热岛效应特征,人为热源(空调使用、中心区的污染和汽车尾气排放等)在附加城市热岛效应强度变化中可能也起到了重要作用。北京 CBD 地区下垫面条件、日照和太阳辐射、风力、能见度、空气湿度和人类活动等因素均对城市热环境和附加城市热岛效应时空分布具有影响,但各种因素作用所占比例仍需结合更完善观测资料和数值模拟研究进一步探讨。

参考文献

[1] 黄良美,邓超冰,黎宁. 城市热岛效应热点问题研究进展[J]. 气象与环境学报,2011,27(4):54 – 58.

[2] 白杨,王晓云,姜海梅,等. 城市热岛效应研究进展[J]. 气象与环境学报,2013,29(2):101 – 106.

[3] 张雷,任国玉,刘江,等. 城市化对北京气象站极端气温指数趋势变化的影响[J]. 地球物理学报,2011,54(5):1150 – 1159.

[4] 李书严,陈洪滨,李伟. 城市化对北京地区气候的影响[J]. 高原气象,2008,27(5):1102 – 1110.

[5] Myrup L O. A numerical model of the urban heat island[J]. Journal of Appliled Meteorology,1969(8):908 – 918.

[6] Mitchell J M J. The thermal climate of cities[R]. Symposium on Air Over Cities,SEC Technical Report A62-5,U. S. Robert A. Taft Sanitary Engineering Center, Cincinnati,1962.

[7] Oke T R. City size and the urban heat island[J]. Atmospheric Environment,1973,7(8):769 – 779.

[8] Streutker D R. A remotesensing study of the urban heat island of Houston, Texas[J]. International Journal of Remote Sensing,2002,23(13):2595 – 2608.

[9] Roth M,Oke T R,Emery W J. A satellite-derived urban heat island from three coastal cities and the utilization of such data in urban climatology[J]. International Journal of Remote Sensing,1989,10(11):1699 – 1720.

[10] Taha H. Urban climates and heat islands:albedo,evapotranspiration,and anthropogenic heat[J]. Energy and Buildings,1997,25(2):99 – 103.

[11] Brown M J,Leach M,Reisner J,et al. Numerical modeling from mesoscale urban cale to building scale[R]. The 3rd Symposium on the Urban Environment,2000.

[12] Zhou S Z. Five island effects of Shanghai urban climate[J]. Science in China (series B),1990,33 (1):67 – 78.

[13] 张光智,徐祥德,王继志,等. 北京及周边地区城市尺度热岛特征及其演变[J]. 应用气象学报, 2002,1(13):43 – 50.

[14] Zhou L M,Dickinson R E,Tian Y H,et al. Evidence for a significant urbanization effect on climate in China[J]. Proceedings of the National Academy of Sciences of the United States of America,2004,101(26):9540 – 9544.

[15] 林学椿. 北京城市热岛强度的变化[J]. 气候变化通讯, 2004,3(2) :12 – 13.

[16] 丁金才,张志凯,奚红,等. 上海地区盛夏高温分布和热岛效应的初步研究[J]. 大气科学,2002,26(3):412 – 420.

[17] 佟华,刘辉志,李延明,等. 北京夏季城市热岛现状及楔形绿地规划对缓解城市热岛的作用[J]. 应用气象学报, 2005, 16(3):358 – 366.

[18] 初子莹,任国玉. 北京地区城市热岛强度变化对区域气温序列的影响[J]. 气象学报,2005,63(4):534 – 540.

[19] 季崇平,刘伟东,轩春怡. 北京城市化进程对城市热岛的影响研究[J]. 地球物理学报,2006,49(1):69 – 77.

[20] 程兴宏,徐祥德,张胜军,等. 北京地区热岛非均匀分布特征的卫星遥感 – 地面观测综合变分分析[J]. 气候与环境研究,2007, 12(5):683 – 692.

[21] 彭静,刘伟东,龙步菊,等. 北京城市热岛的时空变化分析[J]. 地球物理学进展,2007,22(6):1942 – 1997.

[22] 杨萍,刘伟东,侯威. 北京地区极端气温事件的变化趋势和年代际演变特征[J]. 灾害学,2011,26(1):61 – 64.

[23] 王清川,郭立平,张绍恢. 不同天气条件下廊坊城市热岛效应变化特征[J]. 气象与环境学报,2009,25(6):44 – 48.

[24] Yang P,Ren G Y,Hou W,et al. Spatial and diurnal characteristics of summer rainfall over Beijing muncipality based on a high-density AWS dataset[J]. International Journal of Climatology,2012,DOI:10. 1002/joc,3622.

Temporal and spatial characteristics of summer near-surface air temperature in Beijing central business district

ZHANG Ben-zhi[1,3] REN Guo-yu[2] ZHANG Zi-yue[3] LI Yan[3]

(1. Nanjing University of Information Science & Technology, Nanjing, 210044, China; 2. Climate Research laboratory of China Meteorological Administration, Beijing 100081, China; 3. Meteorological Service in Chaoyang District of Beijing, Beijing 100016, China)

Abstract: Based on the air temperature data from 31 automatic weather stations (AWS) during June to August of 2012, the temporal and spatial characteristics of summer near-surface air temperature and the possibly controlling factors in the Beijing central business district (CBD) were analyzed. Air temperature from the AWS of CBD and from the national meteorological station at Chaoyang district of Beijing was compared. The results show that the spatial distribution of the near-surface air temperature in the CBD is directly affected by the difference of underlying surface types and anthropogenic heating. The mean monthly air temperature in summer of 2012 in the densely populated, high-rising buildings and asphalt surface areas is about 1.0 ℃ higher than that in the green coverage area in the CBD. Anthropogenic heat emission due to human activity and use of vehicles at night is the main reasons for large spatial differences of the urban heating environment, while its difference in the daytime is relatively small. The daily and weekly variations of air temperature are significant in the CBD and in Chaoyang weather station. The air temperature difference between them is a positive value regardless in the daytime or at night. Surface air temperature is higher in the CBD than in Chaoyang weather station in the daytime and at night, which suggests an extra urban heat island (EUHI) effect in the Beijing CBD. The daily variations of urban heat island and EUHI are similar. Under different weather conditions, intensity of EUHI effect is different. The EUHI effect is strong in a sunny day with breeze and partly cloud, especially at night, while is weak in a cloudy day with high humidity; it is the weakest in a rainy day. Sunshine and solar radiation is important to the EUHI. The spatial distribution of EUHI in the CBD is similar under the different weather conditions.

Key words: Central business district (CBD); Thermal environment; Anthropogenic heat; Extra urban heat island (EUHI) effect

Geosci. Model Dev. Discuss., 6, 4933–4982, 2013
www.geosci-model-dev-discuss.net/6/4933/2013/
doi:10.5194/gmdd-6-4933-2013

Geoscientific Model Development
Discussions
Open Access

Application and evaluation of McICA scheme with new radiation code in BCC_AGCM2.0.1

H. Zhang[1,2], X. Jing[1], and J. Li[3]

[1]Laboratory for Climate Studies, National Climate Center, China Meteorological Administration, Beijing, China
[2]Nanjing University of Information Science and Technology, Nanjing, China
[3]Canadian Center for Climate Modeling and Analysis, University of Victoria, Victoria, British Columbia, Canada

Received: 26 July 2013 – Accepted: 2 September 2013 – Published: 16 September 2013

Correspondence to: H. Zhang (huazhang@cma.gov.cn)

Published by Copernicus Publications on behalf of the European Geosciences Union.

Abstract

This research incorporates the Monte Carlo Independent Column Approximation (McICA) scheme with the correlated k-distribution BCC-RAD radiation model into the climate model BCC_AGCM2.0.1 and examines the impacts on modeled climate through several simulations with variations in cloud structures. Results from experiments with consistent sub-grid cloud structures show that both clear-sky radiation fluxes and cloud radiative forcings (CRFs) calculated by the new scheme are mostly improved relative to those calculated from the original one. The modeled atmospheric temperature and specific humidity are also improved due to changes in the radiative heating rates.

The vertical overlap of fractional clouds and horizontal distribution of cloud condensation are important for computing CRFs. The maximum changes in seasonal CRF using the general overlap assumption (GenO) with different decorrelation depths (L_{cf}) are larger than 10 and 20 Wm^2 for longwave (LW) CRF and shortwave (SW) CRF, respectively, mostly located in the Tropics and mid-latitude storm tracks. Larger (smaller) L_{cf} in the Tropics (mid-latitude storm tracks) yield better cloud fraction and CRF compared with observations. The inclusion of an observation-based horizontal inhomogeneity of cloud condensation has a distinct impact on LW CRF and SW CRF, with global means of $\sim 1.2\,\mathrm{Wm}^{-2}$ and $\sim 3.7\,\mathrm{Wm}^{-2}$ at the top of atmosphere, respectively, making these much closer to observations.

These results prove the reliability of the new model configuration to be used in BCC_AGCM2.0.1 for climate simulations, and also indicate that more detailed real-world information on cloud structures should be obtained to constrain cloud settings in McICA in the future.

1 Introduction

Clouds are critically important in modulating the radiation budget of the earth–atmosphere system. The representation of clouds and cloud-radiation feedback contributes the greatest uncertainty to simulations of general circulation models (GCMs) (IPCC, 2007). This arises mostly from the relatively coarse spatial resolution of GCMs (dozens to hundreds of kilometers), which leaves cloud-relevant processes and the inherent sub-grid variations of clouds unresolved (Barker and Räisänen, 2005; Zhang et al., 2013a).

Typically, cloud condensation (water and ice) is treated as horizontally homogeneous (the plane parallel homogeneous, or PPH, assumption) within a GCM grid cell. Additionally, certain predetermined assumptions about the vertical overlap of fractional clouds are required. However, both the PPH and overlap treatments are inefficient for producing accurate radiation flux and heating rates and thus bring enormous biases to climate responses. The PPH assumption can easily overestimate the radiative fluxes at the top of the atmosphere (TOA) and the surface by dozens or even $> 100\ \mathrm{W/m^2}$ and produce heating rate errors, often more than 30 % (Cahalan et al., 1994; Oreopoulos and Davies, 1998). The widely used max-random or random overlap assumption yields even more radiative flux errors than does PPH (Barker et al., 1999). Stephens et al. (2004) showed that other climate variables, such as surface temperature and water vapor, suffer severely from biases in sub-grid cloud structures. All of these studies have emphasized the importance of faithfully addressing sub-grid cloud variability in GCMs.

One of the solutions to this problem is to develop high-resolution cloud-resolving models. However, this is currently too computationally expensive for operational use considering the computer speeds available today. Therefore, more attempts are being made toward statistically precise parameterizations for the representation of clouds in GCMs. Abundant approaches for handling parameterization of sub-grid clouds in GCMs have been developed. These include the “tripleclouds” scheme (Shonk and Hogan, 2008), the mosaic treatment (Liang and Wu, 2005), and the multi-column

(Stubenrauch et al., 1999) and quasi-column approaches (Li et al., 2005). However, most of these approaches are highly embedded in their radiation transfer codes. The twisting of cloud structure description and radiative transfer causes them to lack the flexibility required to adjust to updated observational results or other transplanted radiation codes.

To make representation of sub-grid cloud properties flexible and modularized and to maintain computational efficiency, a new scheme, the Monte Carlo Independent Column Approximation (McICA) method, was developed (Pincus et al., 2003). It uses a sophisticated stochastic sub-grid cloud generator (hereafter SCG) (Räisänen et al., 2004) to explicitly obtain cloud subcolumn structures according to certain rules that constrain cloud overlap and horizontal distribution. Moreover, McICA also uses the spectral integration method to reduce computing time by reducing the full ICA (independent column approximation) approach through a Monte Carlo selection of subcolumns (Pincus et al., 2003). The advantages of McICA greatly facilitate adjustment or alteration of both cloud structure and radiative transfer and thus accelerate future development of GCMs.

Because of the advantages of the McICA scheme for treating the sub-grid cloud-radiation process, we here incorporate the McICA scheme into the Beijing Climate Center's general circulation model BCC_AGCM2.0.1 with the BCC-RAD radiation algorithm, which is based on the advanced correlated *k*-distribution (CKD) (Zhang et al., 2003, 2006a, b). CKD code is included to fulfill the requirement of spectral integration of McICA, to which the original band model is not applicable. Previous work has shown that the BCC_AGCM2.0.1 model, similar to other GCMs, is generally insensitive to McICA noise and that the performance of the model depends only on its own physics and dynamics (Jing and Zhang, 2013). Hence, the McICA scheme may possibly be applied for future development of BCC_AGCM2.0.1.

For this purpose, the current research evaluates climate simulation with the application of McICA and our radiation scheme BCC-RAD in BCC_AGCM2.0.1, specifically for investigating radiation and cloud-related fields. First, we analyze the differences in radiation budgets, surface climatology, and atmospheric states between the new and old model configurations. Second, the impacts of the changes in the radiation scheme, cloud overlap assumption, and cloud-water inhomogeneity on the radiation budget and simulated climate are discussed. This preliminary work preceding the availability of observation-based sophisticated cloud information also aims to archive the impact of the modifications in the cloud-radiation process on simulated climate and the model response to these changes and thereby provide suggestions for future development.

Section 2 of this paper briefly describes the McICA scheme, the BCC_AGCM2.0.1 model, and the BCC-RAD radiation scheme. The design of the experiments is given in Sect. 3. Results of simulations with various model configurations are described in Sect. 4, and a discussion and conclusions are presented in Sect. 5.

2 Model description

2.1 Description of the McICA scheme

The McICA scheme is based on the ICA algorithm for computation of domain mean radiation fields. It greatly and effectively reduces computation time while maintaining the accuracy of ICA from a statistical perspective. The basic principles of McICA were first explained in detail by Pincus et al. (2003); Räisänen and Barker (2004) then provided additional ways to diminish induced noise. For clarity and completeness, we provide a brief summary here.

Conceive a domain R (a GCM grid). The sub-grid clouds could be represented by a certain number of subcolumns, which contain individual cells in each layer that are either clear or overcast. Moreover, the domain mean of these subcolumns should hold the cloud profiles provided by the GCM. Given these subcolumns, radiative computation can be liberated from the description of partial clouds and their vertical overlap. The required subcolumns could be derived through SCG with consideration of certain overlap and horizontal distribution rules for clouds. For a thorough methodology of SCG, one can refer to Räisänen et al. (2004).

Within the domain R composed of subcolumns, the domain-averaged radiative fluxes can be accurately given by ICA as:

$$\left\langle F^{\mathrm{ICA}} \right\rangle = \int S(\lambda) \left\{ \int \int_R F(x,y,\lambda)\,\mathrm{d}x\mathrm{d}y \right\} d\lambda \tag{1}$$

where x and y are subcolumn counters along the zonal and meridional axis, respectively, $S(\lambda)$ is the spectral weight at wavelength λ, and $F(x,y,\lambda)$ denotes the radiative flux at location (x,y) and wavelength λ.

If R is partially cloudy, $\left\langle F^{\mathrm{ICA}} \right\rangle$ can be split into clear $\left\langle F^{\mathrm{clr}} \right\rangle$ and cloudy $\left\langle F^{\mathrm{cld}} \right\rangle$ parts weighted by the cloud fraction Ac:

$$\left\langle F^{\mathrm{ICA}} \right\rangle = (1 - Ac) \left\langle F^{\mathrm{clr}} \right\rangle + Ac \left\langle F^{\mathrm{cld}} \right\rangle \tag{2}$$

The most time-consuming part of Eq. (2) is $\left\langle F^{\mathrm{cld}} \right\rangle$ due to the full spectral integration in all cloudy subcolumns. To diminish the computational burden, Pincus et al. (2003) reduced the two-dimensional integration to a single dimension by introducing a Monte Carlo (random sampling) process:

$$\left\langle F^{\mathrm{cld}} \right\rangle \approx \int S(\lambda) F^{\mathrm{cld}}(s_{\mathrm{rnd}}, \lambda)\, d\lambda \tag{3}$$

where s_{rnd} is a randomly selected cloudy subcolumn number for radiative calculation at λ. Equation (2) tremendously reduces computation time compared with Eq. (2) and represents the kernel of McICA.

It should be noted that the random selection of s_{rnd} in Eq. (2) inevitably introduces random noise. Although this may yield deviated results for a single calculation, averaging over a number of calculations generates almost unbiased results with respect to ICA (Barker et al., 2008). One method for reducing the noise is to increase the number of s_{rnd} for optically critical spectral intervals (Räisänen and Barker, 2004). To date, the McICA scheme has already been operationally utilized in several climate models and numerical weather prediction models (Morcorrete et al., 2008; Räisänen and Jarvinen, 2010; Neale et al., 2010).

2.2 Description of BCC_AGCM2.0.1

BCC_AGCM2.0.1 was developed by the Beijing Climate Center (BCC) at the China Meteorological Administration (CMA) based on the Community Atmosphere Model Version 3 (CAM3) of the National Center for Atmospheric Research (NCAR) (Wu et al., 2010). The model runs at T42 spectral resolution (approximately $2.8^{\circ} \times 2.8^{\circ}$) horizontally, and it uses vertical hybrid δ-pressure coordinates including 26 layers with the top located at about 2.9 hPa. An additional layer is added above the topmost layer in the radiative calculation to prevent excessive heating. The default timestep is 20 min, and the radiation code is invoked every three timesteps.

Relative to CAM3, several revisions have been made to improve the physics of the model. These include new reference atmosphere and surface pressures; a revised convection scheme (Zhang and Mu, 2005) that significantly improves the tropical rainfall simulation; a different function for calculating the snow-cover fraction that influences the resulting surface albedo, especially in polar and plateau regions (Wu and Wu, 2004); a new adiabatic adjustment originated by Yan (1987); and new methods for calculating turbulent fluxes over ocean surface that remove the systematic biases in the wind stress and sensible and latent heat fluxes in CAM3. A more detailed description of BCC_AGCM2.0.1 can be found in Wu et al. (2010). In the present research, the interactive Canadian Aerosol Module (CAM) (Gong et al., 2003) with updated aerosol emission sources (Zhou et al., 2012) is used to predict atmospheric aerosol burdens (Zhang et al., 2012).

2.3 Description of radiation schemes

To satisfy the requirement of the spectral integration of the McICA scheme, our radiation model, BCC-RAD, is adopted. This model is substantially different from the previous radiation scheme used in BCC_AGCM2.0.1. To explain the importance of this radiation scheme in modulating the climate simulation, it is necessary to describe this revision in advance. A detailed comparison between the old and new schemes is provided in Table 1.

The previous radiation scheme in BCC_AGCM2.0.1 is basically a band model. Although some band models simulated well the broadband fluxes and heating rates, this may have been partly fortuitous because of band overlap effects (Ellington et al., 1991). Another defect of band models is the use of a scaling procedure to account for inhomogeneous atmospheric paths, although these can be made arbitrarily accurate for a homogeneous atmosphere (Kratz, 1995). Therefore, there has been a trend over the past decades to replace band models with CKD methods in GCMs (Fu and Liou, 1992; Sun and Rikus, 1999; Nakajima et al., 2000; reference therein). As discussed in the introduction, the spectral information is needed in application of McICA.

In this work, we incorporate the CKD model by Zhang et al. (2003, 2006a, b), i.e., the Beijing Climate Center RADiation transfer model (BCC-RAD), into BCC_AGCM2.0.1 within the framework of McICA. The 10–49000 cm^{-1} (0.204–1000 µm) spectral range in BCC-RAD is divided into 17 bands (8 LW and 9 SW). Five major greenhouse gases (GHGs), H_2O, CO_2, O_3, N_2O, and CH_4, as well as chlorofluorocarbons (CFCs) are considered. The major absorbers in the solar bands are H_2O (including continuum absorption), CO_2, N_2O, O_3, and O_2. The HITRAN2000 database (Rothman et al., 2003) was used to provide line parameters and cross sections. Lu et al. (2012) compared the line parameters in different HITRAN versions and found that the difference in the simulated radiative fluxes between the updated HITRAN2008 and HITRAN2000 is very small, so the use of HITRAN2000 should not affect the final modeled climates in this research. In BCC-RAD, the effective absorption coefficients of CKD are calculated based on the line-by-line radiative transfer model (LBLRTM; Clough and Iacono, 1995) with a spectral interval of 1/4 the mean half-width and a 25 cm^{-1} cutoff for line wings over each band (Clough and Iacono, 1995). The thermal radiation transfer calculation is solved with a two-stream algorithm developed by Nakajima et al. (2000), and the solar radiation transfer is solved with the δ-Eddington method (Coakley et al., 1983). SW radiation model comparisons, including BCC-RAD, are given in Randles et al. (2013).

Cloud and aerosol optical properties in BCC-RAD are also different from those in the original scheme. The optical properties of cloud droplets are from Nakajima (2000), and those of ice crystals are calculated based on several datasets: observational size distribution data from Fu (1996), optical properties of single particles of different shapes from Yang et al. (2005), and the fractional mixing of particles of various shapes suggested by Baum et al. (2005). Aerosol optical properties are from Wei and Zhang (2011) and Zhang et al. (2012).

3 Experimental design

We now have considered two model configurations, the new one with McICA and BCC-RAD to handle the cloud-radiative procedure and the old one with the traditional overlap treatment by Collins (2001) and radiation scheme described in Briegleb (1992). The details of these are listed in Table 1. Experiments were designed to reveal (a) the differences in simulated climate between the two configurations and (b) the impact of changing sub-grid cloud structures on simulated climate within the new configuration. All of the experiments are integrated with observed monthly distributions of SST from September 1979 to December 1990, and the results of the last 10 yr are used for analysis.

3.1 Experiments comparing the new and old model configurations

First, an experiment with the old scheme, denoted OLD, was performed as a control run. Second, two McICA experiments, a diagnostic offline (OL) run denoted NEW_MRO_OL and an interactive run denoted NEW_MRO, were conducted for comparison. Both the offline and interactive run utilized PPH and the max-random overlap (MRO) assumption (Tian and Curry, 1989) to be consistent with the OLD run. The NEW_MRO_OL and OLD simulations used identical atmospheric and cloud profiles for the cloud-radiation process; hence, the comparison between NEW_MRO_OL and OLD demonstrates the initial distinctions between the new and old configurations, whereas the comparison between NEW_MRO and OLD illustrates differences in the climate response.

3.2 Experiments exploring the impacts of sub-grid cloud structures

As the McICA scheme is flexible in depicting sub-grid cloud structures, four more experiments were implemented to test the model's sensitivity to cloud-structure variations.

First, the impact of changing cloud overlap was tested by including a so-called general overlap (hereafter GenO) (Mace and Benson-Troth, 2002). In GenO, the vertically projected cloud fraction of the two cloud layers k and l ($C_{k,l}$) is defined as the linear combination of maximum ($C_{k,l}^{\text{max}}$) and random overlap ($C_{k,l}^{\text{ran}}$):

$$C_{k,l} = \alpha_{k,l} C_{k,l}^{\text{max}} + \left(1 - \alpha_{k,l}\right) C_{k,l}^{\text{ran}} \tag{4}$$

where

$$C_{k,l}^{\text{max}} = \max\left(C_k, C_l\right) \tag{5}$$

$$C_{k,l}^{\text{ran}} = C_k + C_l - C_k C_l \tag{6}$$

and the overlap parameter $\alpha_{k,l}$ is prescribed via an exponential decay function of altitude separation between cloud layers:

$$\alpha_{k,l} = \exp\left[-\int_{Z_k}^{Z_l} \frac{\mathrm{d}z}{L_{\mathrm{cf}}(z)}\right] \tag{7}$$

The lapse rate of the decay is controlled by a "decorrelation depth" (L_{cf} in Eq. 7), which has a global mean value of about 2 km (Barker, 2008) but it is highly related to cloud type and atmospheric dynamics (Naud et al., 2008). Zhang et al. (2013b) found that L_{cf} ranges, in terms of seasonal mean, within 0–3 km in different regions of East Asia. Thus, in this paper, three simulations with global constants L_{cf} of 1, 2, and 3 km, termed NEW_GO1, NEW_GO2, and NEW_GO3, respectively, were performed. Comparisons among NEW_GO1, NEW_GO2, NEW_GO3, and NEW_MRO will demonstrate the impact of changes in cloud overlap within the McICA scheme.

Additionally, the impact of breaking the default PPH assumption is addressed by perturbing the horizontal distribution of cloud condensation (water and ice) with an ideal distribution function. The gamma function of cloud condensation applied by Shonk et al. (2010) is used here. In such distribution, the magnitude of inhomogeneity is constrained by the fractional standard deviation (f), which is defined as:

$$f = \frac{\sigma_{\mathrm{c}}}{\bar{c}} \tag{8}$$

where $\bar{c}$ is the layer mean cloud condensation ignoring the cloud phase, and σ_{c} is the standard deviation of the condensation. In this work, f was set to 0.75 for both the liquid and ice phases, as was obtained by Shonk et al. (2010) from an extensive collection of observations. This inhomogeneity setting was tested in conjunction with GenO, with an L_{cf} of 2 km globally, denoted as NEW_GO2_IH. Because cloud vertical overlap assumptions are consistent between NEW_GO2 and NEW_GO2_IH, any discrepancies illustrate the impact of including horizontally inhomogeneous clouds.

The simulated radiation fields, cloud fractions, and other climate variables were validated against corresponding observations or reanalysis data.

4 Results

This section reports the results of various simulations in three groups: (i) first, results from OLD, NEW_MRO_OL, and NEW_MRO are provided to clarify the differences between the new and old model configurations; (ii) second, results from NEW_MRO, NEW_GO1, NEW_GO2, and NEW_GO3 are presented to show the impact of cloud overlap variations within the scheme on radiation and other fields; and finally (iii) a comparison between NEW_GO2 and NEW_GO2_IH is given to show the influence of changing the horizontal distribution of cloud condensation on simulated climate.

4.1 Comparison between the new and old model configurations

4.1.1 Radiation budget

We first investigate the instantaneous difference between the old and new schemes under identical atmospheric and cloud conditions. Figure 1 shows the global annual mean radiation fields for various simulations at the top of the atmosphere (TOA) and at the surface (SFC) with a comparison against the satellite-derived 11 yr (2000–2010) mean CERES_EBAF datasets (http://ceres.larc.nasa.gov/order_data.php). We focus on the results of OLD, NEW_MRO_OL, and NEW_MRO in this section.

The central panels of Fig. 1 show that the new scheme (NEW_MRO_OL and NEW_MRO cases) obtains much improved net all-sky LW and SW TOA radiative fluxes. This is due to both improvement in the revised cloud optics and net clear-sky fluxes calculated by the new radiation scheme in this work.

Compared with CERES_EBAF data, the OLD run shows notable discrepancies in TOA LW and SW CRF (right panels of Fig. 1), which are overestimated by $\sim 3\,\mathrm{W\,m^{-2}}$ and $\sim 7\,\mathrm{W\,m^{-2}}$, respectively. The offline NEW_MRO_OL run shows large reductions in these biases (except for LW CRF at the surface), with TOA LW and SW CRF errors reduced to ~0.5 and ~1.5 $\mathrm{W\,m^{-2}}$, respectively. The interactive NEW_MRO run mostly retains the features of NEW_MRO_OL. As the same cloud overlap assumptions are used, the improved CRF in NEW_MRO and NEW_MRO_OL runs should come mainly from the revised cloud optics (see Table 1). Moreover, the differences in CRF between NEW_MRO and NEW_MRO_OL are also distinct, indicating that clouds have changed noticeably compared to OLD as a result of introducing the new configuration, which will be discussed below.

As for the clear-sky net flux at TOA (F^{clr}, the left panels in Fig. 1), the OLD run overestimates LW and SW F^{clr} by ~5 and ~1.5 $\mathrm{W\,m^{-2}}$, respectively. The biases at the surface are also large, up to ~4 $\mathrm{W\,m^{-2}}$ for SW F^{clr}. Again, NEW_MRO_OL and NEW_MRO produce clear-sky fluxes much closer to the observations (except for LW F^{clr} at surface). The differences between the simulated TOA LW F^{clr} and SW F^{clr} and those from CERES_EBAF observation are reduced to ~2 and ~0.5 $\mathrm{W\,m^{-2}}$, respectively, for both NEW_MRO_OL and NEW_MRO.

The improvements in both F^{clr} and CRF suggest that the implementation of the McICA with our new radiation scheme fares much better at modeling the inner balance between the radiation components from clear and cloudy regimes. Thus, the new configuration behaves in a more physically coherent manner than the original one in our BCC_AGCM2.0.1, and it predictably yields more reasonable all-sky net fluxes (F^{net}, central panels of Fig. 1).

The other results shown in Fig. 1 will be explained in Sects. 4.2.1 and 4.3.1.

Figure 2 displays zonal annual mean F^{clr}, F^{net}, and CRF at the TOA from the OLD, NEW_MRO_OL, and NEW_MRO runs, as well as the CERES_EBAF dataset. The simulated zonal distributions of these variables are all in reasonable agreement with observations. However, the NEW_MRO and NEW_MRO_OL runs give LW and SW F^{net} much closer to observations, especially at mid–low latitudes (Fig. 2c, d). This occurs mainly because the vast overestimation of LW and SW CRF by the OLD scheme is reduced overall by the new scheme (Fig. 2e, f). Moreover, NEW_MRO and

NEW_MRO_OL also show notable improvement in LW F^{clr} in the subtropics and mid-latitudes (Fig. 2a). The SW F^{clr} is calculated well at most latitudes in all experiments, except at the Polar Regions where there are noticeable underestimations. This may be linked to the enhanced solar albedo over snow surfaces compared with observations in the Community Land Model version 3 (CLM3) used in the BCC_AGCM2.0.1 model (Oleson et al., 2003), which results in overestimated solar energy loss to space.

We will provide detailed discussions of the simulated TOA CRF here and in the following two paragraphs. Figures 3 and 4 show the global distribution of errors in annual mean LW and SW CRF relative to CERES_EBAF, as well as the differences between NEW_MRO_OL and OLD. In the OLD run, LW CRF is overestimated over most tropical and subtropical oceans with very few exceptions, but it is underestimated over intensively convective tropical regions such as central Africa, the west Pacific warm pool, and the Amazon forests of South America (Fig. 3a). The NEW_MRO and NEW_MRO_OL produced similar distributions of these biases; however, the positive biases in tropical and subtropical oceans are reduced, whereas the negative biases are enhanced somewhat (Fig. 3b, c). Figure 3d shows that the initial differences in LW CRF between the new and old configurations are located mainly in the intertropical convective zone (ITCZ) and in high altitude areas such as the Tibetan Plateau and Andes Mountains, with maximum values of more than $6\,\mathrm{W\,m^{-2}}$. As these areas are all sufficient in high-level ice clouds, the differences may be ascribed to the different ice-cloud optical properties used in the two configurations.

The OLD run exhibits negative biases in SW CRF at most low and mid-latitudes (see Fig. 4a). Again, the NEW_MRO_OL and NEW_MRO runs significantly reduce these errors (see Fig. 4b, c), but enhanced positive biases appear over subtropical oceans near the west coasts of continents and over East Asia. Interestingly, the initial differences in SW CRF between the new and old configurations (see Fig. 4d) show a quite similar geographic distribution to those of LW CRF (see Fig. 3d), with a maximum value of more than $14\,\mathrm{W\,m^{-2}}$ in the tropical East Pacific. There are only minor differences in areas with large SW CRF along 60° S, where a large amount of low-level cloud (mostly liquid) exists (see Fig. 2f), because the liquid cloud optics in the two configurations are almost equivalent for CRF calculation. Consequently, the changes in ice cloud optical properties are the main cause of the changed SW and LW CRF in the McICA runs.

The cooling effect by SW CRF and heating effect by LW CRF at the TOA in tropical deep convective regions have been shown to be nearly linearly correlated and to generally compensate for each other (Kiehl and Ramanathan, 1990), which means that the (SW CRF)/(LW CRF) slope is about −1. This slope is often used as a criterion for showing the performance of modeled CRF. The (SW CRF)/ (LW CRF) slopes in the Indonesian region (10° S–20° N, 110–160° E) for various simulations and CERES_EBAF observations are given in Table 2. The table shows that the OLD run overestimates the (SW CRF)/(LW CRF) slopes for the annual mean and for different seasons. NEW_MRO shows a generally noticeable decrease in SW CRF, especially for the annual mean and summer (JJA). This results in decreased (SW CRF)/(LW CRF) slopes (Table 2). As shown in Table 2, NEW_MRO_OL gives very similar results to OLD. Thus, it can be inferred that the two model configurations are comparable for diagnosing the SW and LW CRF ratio, whereas the climate feedback evidently changes the simulated cloud fractions. This will be addressed later.

Radiative heating/cooling within the atmosphere is a critical driving factor in climate simulation. Figures 5 and 6 compare the clear-sky and all-sky LW heating rate of NEW_MRO_OL and OLD, respectively. For the clear-sky condition, NEW_MRO_OL shows a remarkable (more than 10 %) cooling trend in the lower troposphere within 60° S–60° N and a heating trend in most of the middle troposphere. These may be related to the different treatments of greenhouse gases, especially O_3 and water vapor. The difference in the all-sky LW heating rate (see Fig. 6c) is similar to the pattern shown in Fig. 5c, indicating that differences in the heating rates of clouds are less important for determining the final state in this case. This pattern tends to increase the stability of the atmosphere below 600 hPa but enhance vertical mixing above 600 hPa. The differences in SW heating rate are much smaller than are those for LW (figure not shown).

As shown above, the application of the McICA scheme with BCC-RAD remarkably influences the radiation budget at both boundaries and within the atmosphere. These changes will extensively affect the final simulated climate.

4.1.2 Surface climatology

In this subsection, the simulated surface temperature and precipitation in two seasons (DJF and JJA) are evaluated.

Zonal comparisons of surface temperature are shown in Fig. 7. Although both NEW_MRO and OLD yield similar zonal mean distributions compared with the ERA-40 reanalysis data, there are substantial differences between both simulations and the ERA-40 (Uppala et al., 2005). For instance, in DJF, surface temperatures are underestimated by about 1.5 K in the mid-latitudes and by 6–7 K around the North Pole (see Fig. 7a); in JJA, the zonal mean negative biases reach a maximum of 3–4 K at 60–70° S/N (see Fig. 7b). The global distribution of surface temperature biases from the NEW_MRO and OLD runs are quite similar (figures not shown), with local maximum differences between the NEW_MRO and OLD runs reaching ±2–4 K. The differences between the simulations and observation are much larger than the differences between the NEW_MRO and OLD simulations.

Similar to Fig. 7, Fig. 8 shows comparisons of the precipitation rate. Both the NEW_MRO and OLD simulations capture the main features of the meridional distribution of precipitation, such as the maximum in the Tropics and secondary maxima at the mid-latitude storm tracks. However, errors are also clear relative to observations, especially in the Tropics (gray lines in Fig. 8a, b). The two simulations are comparable in their simulation of the zonal mean distribution of precipitation, but there are noticeable local differences in the tropical and subtropical regions (figures not shown). These differences probably result from the altered atmospheric thermodynamics and dynamics caused by changes in the radiation budget. The increases and decreases in precipitation often coincide with the decreases and increases in surface temperature (figures not shown), respectively; thus, the changes in precipitation obviously influence the surface energy balance.

It should be noted that, in this work, we altered only the sub-grid cloud structures used in the radiation calculation, whereas those in precipitation parameterization were not changed. Physically, cloud overlaps in the radiation and precipitation processes should be consistent with each other, but the latter may have a larger effect on the simulated precipitation (Morcrette and Jakob, 2000). However, this is beyond the scope of this study.

4.1.3 Atmospheric states

Simulated atmospheric temperature, specific humidity, and cloud condensation (water and ice) are analyzed in this subsection.

Figure 9 shows comparisons of the latitude–height distribution of atmospheric temperature. Notable cold biases relative to ERA-40, about 1–2 degrees in the low–mid troposphere, exist throughout almost the entire troposphere in the OLD case (see Fig. 9a). The NEW_MRO simulation inherits most of these biases, but the relative warming (up to 0.4–0.8 K) within the central troposphere (800 ~ 500 hPa) is a desirable change compared with OLD (see Fig. 9c). This is definitely related to the reduced LW cooling rate in the central troposphere, as shown in Figs. 5 and 6.

Likewise, Fig. 10 shows comparisons of atmospheric specific humidity. In addition to the improvements in tropospheric temperature, there are favorable changes in specific humidity. Compared with ERA-40, the OLD run is subject to considerable dry biases in the tropical lower troposphere (see Fig. 10a). This is likely caused by LW heating rate biases related to the LW parameterization of water vapor (Collins et al., 2002). Due to changes in heating rate, as shown in Figs. 5 and 6, the NEW_MRO run notably increases the specific humidity in the Tropics, typically reducing the original biases by about 30 %.

The changes in atmospheric temperature and specific humidity exert influences on the formation and maintenance of cloud water and ice (figures not shown), affecting the modeled local radiation budget, such as by altering the SW and LW CRF ratios, as mentioned above.

Overall, the incorporation of the new scheme influences radiative fluxes and heating rates remarkably. Due to these changes, the simulated surface and atmospheric climate are comparable or improved relative to the old model configuration. Therefore, the new scheme used here has been demonstrated to be a viable option for long-term climate simulation.

It should also be mentioned that the differences in simulated climate between the two model configurations are relatively smaller than are those between the simulations and observations. Nevertheless, the much more flexible cloud structure and internal consistency of the new configuration will benefit further development of model physics. In regard to the convenience of the McICA scheme for modifying sub-grid clouds, the impact of the cloud structure variations is assessed as follows.

4.2 The impact of altering the cloud overlap assumption

Tests NEW_GO1, NEW_GO2, and NEW_GO3 implemented GenO with L_{cf} set at 1, 2, and 3 km, respectively. In GenO, the overlap of two vertical cloud layers depends on L_{cf}. For two fixed cloud layers, the larger L_{cf} is, the more they tend toward maximum overlap; conversely, smaller L_{cf} results in a tendency toward random overlap (Eqs. 4–7). The sensitivity of the simulations to changes in cloud overlap assumptions is demonstrated by the differences among the NEW_GO1, NEW_GO2, NEW_GO3, and NEW_MRO tests.

4.2.1 Radiation and cloud fraction

The 2nd to 6th columns in each panel of Fig. 1 show the global annual mean radiation budget from McICA runs with different cloud vertical overlap assumptions. As expected, both LW and SW CRF decrease from NEW_GO1 to NEW_GO3 because clouds tend increasingly to maximum overlap, and cloud fractions decrease. As also seen in Fig. 1, NEW_MRO shows the smallest CRF among the McICA runs with the PPH assumption. This occurs because BCC_AGCM2.0.1 tends to generate frequent occurrences of vertically continuous cloudy layers. Thus NEW_MRO, which depends on the separation of cloudy layers to arrange the cloud vertical distribution, tends to underestimate the vertically projected cloud fraction and diminish CRF. This has also been proven in previous studies using the CAM3 model (Barker and Räisänen, 2005). Quantitatively, the extent of variations in global mean CRF caused by changes in cloud overlap is here about $1\,\mathrm{Wm}^{-2}$ for LW and $2\,\mathrm{Wm}^{-2}$ for SW (at both the TOA and surface). However, CRF is more accurately represented in all the McICA simulations than in the OLD run.

As all the McICA tests considered in this section adopt the PPH assumption and the same cloud optical properties, the differences in the modeled radiation fields stem predominantly from differences in the vertically projected cloud fraction. Figure 11 compares the annual mean total cloud fraction (C_{TOT}) from all the simulations with ISCCP observations. Although the NEW_MRO run roughly captures the meridional variation in C_{TOT} (see Fig. 11a, b), Fig. 11c shows that it generally overestimates (underestimates) total cloud fraction in the Tropics and at high latitudes (in the mid-latitudes), typically by 20–30 %. When using GenO with $L_{\mathrm{cf}} = 1$ km, the positive (negative) biases in the Tropics and high latitudes (mid-latitudes) are enlarged (shrunken) (see Fig. 11d). When L_{cf} is increased to 3 km (Fig. 11f), the positive biases decrease in the Tropics and at higher latitudes, whereas the negative biases in the mid-latitudes increase compared with NEW_GO1. This indicates that a larger L_{cf} should be used in tropical regions and at high latitudes and a smaller L_{cf} should be used in mid-latitude areas to make the modeled total cloud fraction more realistic.

Note that even 3 km of L_{cf} is not yet enough in the Tropics. A considerable portion of clouds, especially the deep convective type, possesses a larger L_{cf} of even more than 10 km in some cases (Barker, 2008), so there is still space left in which to constrain the presentation of cloud overlap. Additionally, the cloud overlap procedure is done on cloud profiles provided by the diagnostic cloud fraction scheme based on only relative humidity (Rasch and Kristjansson, 1998), and cloud fraction also can be more accurately calculated by its improvement.

The zonal mean biases in modeled C_{TOT} are shown in Fig. 12a. As stated above, all simulations generate larger (smaller) C_{TOT} than observation in the Tropics and at high latitudes (mid-latitudes); the positive biases in the Tropics and at high latitudes decrease as the L_{cf} used in GenO increases (and vice versa for the mid-latitudes). Also shown in Fig. 12b–d are the differences in modeled low (> 700 hPa), middle (700–400 hPa), and high (< 400 hPa) cloud fractions between other McICA runs and NEW_MRO. The maximum differences between NEW_GO1 and NEW_MRO are up to 5–7 % in the Tropics for all cloud levels, and those between NEW_GO3 and NEW_MRO reach 2–3 %. Although the differences generally decrease poleward for low and middle clouds, the modeled high clouds differ as much at high latitudes as in the Tropics. This occurs because at high latitudes, modeled lower-level clouds are more frequently overcast or near overcast, whereas higher-level clouds are much less likely to occupy a grid cell (figure not shown). These remarkable differences in cloud fractions at different levels exert large influences on modeled CRFs.

Figures 13 and 14 show the differences in LW and SW CRF, respectively, during DJF and JJA. NEW_GO1 primarily blocks more LW flux emitted upward (see Fig. 13a, d) and reflects more SW flux (see Fig. 14a, d) than NEW_MRO does due to the increased cloud fraction. The greatest differences tend to appear in the tropical region and around the 60° S/N storm tracks, especially over the ITCZ and SPCZ regions, with local maximums of more than 10 W m^{-2} for LW CRF and more than 20 W m^{-2} for SW CRF. This pattern occurs because clouds in these regions are often vertically extensive and thus the overlap assumption plays a more critical role in judging the vertically integrated cloud fraction. Figure 14 shows that from NEW_GO1 to NEW_GO3, SW CRF increases remarkably in the Tropics and storm track regions. Considering the basically negative biases of SW CRF in these regions (see Fig. 4), this implies that SW CRF may be better represented in these regions by increasing L_{cf}.

4.2.2 Simulated climate

Figures 15 and 16 show the zonal annual mean biases in surface temperature and precipitation of various McICA runs with different vertical cloud structures. All simulations yield almost identical surface temperatures at low latitudes (see Fig. 15a, b). However, there are clear discrepancies at the mid–high latitudes, especially during DJF in the Northern Hemisphere, where the largest difference reaches almost 1 K (NEW_GO1NEW_MRO). This may be attributed to the enhanced LW warming effect below cloud base in NEW_GO1 due to the increased cloud fraction. Although a SW cooling effect is also seen in NEW_GO1 because of increased reflection at cloud top, the LW warming effect seems dominant during DJF in the Northern Hemisphere. It is worth addressing the fact that the ranges of temperature variation in the mid–high latitudes caused by changing the overlap assumption may surpass the differences between the two model configurations in this work (see Fig. 7).

Surface precipitation (see Fig. 16a, b), atmospheric temperature, and humidity were also examined in NEW_GO1–NEW_GO3 (figure not shown), and we obtained similar results to those for NEW_MRO. So, the changes in the cloud overlap assumption are not likely to cause a direct, notable shift in simulated atmospheric states, etc., although the impacts of overlap assumptions on heating rates have been emphasized in offline diagnostics (see Barker et al., 1999; Li et al., 2005). It should be noted that sea–atmosphere interaction is not considered here and that it might strengthen the signal imposed on the climate system by changing the cloud overlap assumption.

4.3 The impact of breaking the PPH assumption

In this subsection, we briefly consider the impacts of breaking the traditional PPH assumption on simulated radiation and climate by comparing the NEW_GO2_IH and NEW_GO2 tests.

4.3.1 Radiation

From a global mean perspective, the changes in CRF and net fluxes caused by including horizontally inhomogeneous cloud condensation (Eq. 8) are as large as or even larger than the changes from altering the cloud overlap assumptions (see NEW_GO2_IH in Fig. 1), which has also been shown by calculations from cloud-resolving models (Barker and Räisänen 2005). The global mean reductions in LW CRF and SW CRF at the TOA are about 1.2 and 3.7 $\mathrm{W\,m^{-2}}$, respectively. The consideration of horizontally inhomogeneous clouds brings the global mean CRF and F^{net} much closer to observations.

Figure 17 shows the differences in LW CRF and SW CRF between NEW_GO2_IH and NEW_GO2 for DJF and JJA. It can be seen that NEW_GO2_IH mainly decreases LW and SW CRF all over the globe, with local maximum reductions of more than 10 and 20 $\mathrm{W\,m^{-2}}$, respectively, in the Tropics (especially the warm pool) and secondary reductions in the mid-latitudes. This is qualitatively consistent with the well-accepted conclusion that the PPH assumption of cloud condensation generally overestimates solar reflectance (Carlin et al., 2002) and LW emissivity (Pomroy and Illingworth, 2000) due to the nonlinear dependence of radiative effects on cloud water content. These changes can somewhat offset the positive (negative) differences in LW (SW) CRF in the PPH runs (see Figs. 3 and 4). Thus, it is of great importance to address the cloud water/ice horizontal distribution together with the overlap of fractional clouds in GCMs.

4.3.2 Simulated climate

The consideration of cloud horizontal distribution has a noticeable influence on surface temperature (see NEW_GO2_IH in Fig. 15). In the mid–high latitudes of the Northern Hemisphere, there is a remarkable decrease in surface temperature during DJF and an increase during JJA. These changes arise mainly from competition between LW cooling and SW heating. When inhomogeneous clouds succeed homogeneous ones, more LW flux is emitted outward, and more SW flux penetrates to the surface (see

Fig. 1). The surface energy budget is then a result of the competition between the two fluxes.

For other climate elements, such as precipitation, air temperature, specific humidity, surface pressure, zonal winds, and so forth (figures not shown), the differences between NEW_GO2_IH and NEW_GO2 are minor, like those between different overlap assumptions.

Generally speaking, modifications of cloud sub-grid configurations have distinct impacts on the simulated radiation budget and surface temperature. Considering the improved LW and SW budget for clear-sky and all-sky conditions, the new model configuration can be used in BCC_AGCM2.0.1 to improve physical processes and perform climate simulations.

5 Discussion and conclusions

The McICA scheme with the BCC-RAD radiation code was incorporated into the BCC_AGCM2.0.1 model in this work as a replacement for the original CAM3 cloud-radiation scheme. This new configuration is flexible for treating arbitrarily complex sub-grid cloud structures, including the vertical overlap of fractional clouds and horizontal distribution of cloud condensation. The advantages of the new configuration suggest that it is a better option for future development of BCC_AGCM2.0.1. This work aimed to investigate the impact of this modification on climate simulated by BCC_AGCM2.0.1. Several configurations of sub-grid cloud structures, including variations in vertical overlap and horizontal distribution, were tested, and the model's sensitivity to changes in cloud structures and the newly adopted radiation scheme were exhibited and clarified.

The results show that the new scheme markedly improves the representation of the SW and LW radiation budget for both clear-sky and all-sky conditions, whether in the global mean or in geographic distribution. The simulated relationship between SW and LW CRFs in deep convective regions is improved by the new scheme compared with the old scheme. These results all indicate that using the McICA scheme with our BCC-RAD code makes the cloud-radiation process more intrinsically coherent and reasonable. The modeled temperature and specific humidity benefited from changes in the LW heating rate, resulting in a reduction in temperature biases by 0.4–0.8 °C at the middle troposphere and a reduction in moisture biases by 1/3 in the tropical lower troposphere relative to the ERA-40 reanalysis. This shows the superior of a CKD radiation algorithm to the band model based CAM3 radiation scheme.

The impacts of altering cloud overlap within the McICA scheme were assessed by including a so-called "general overlap." Results demonstrated that changes in cloud overlap assumptions have remarkable effects on the boundary radiation budgets. The global annual mean SW (LW) CRF differs by at most $\sim 2\,\mathrm{Wm}^{-2}$ ($\sim 1\,\mathrm{Wm}^{-2}$) at both the TOA and surface, with the test NEW_GO1 (L_{cf} = 1 km) always showing the largest CRF and the test NEW_MRO always showing the smallest due to differences in cloud cover generation. CRF in the Tropics and storm track regions, especially over the ITCZ and the SPCZ, is most notably influenced by the choice of overlap assumptions due to frequently occurring extensive clouds, with local differences of $> 10\,\mathrm{Wm}^{-2}$ for LW CRF and $> 20\,\mathrm{Wm}^{-2}$ for SW CRF. It is found in this work that the results of cloud fraction and CRF are very sensitive to the chosen of L_{cf}, especially in the Tropics and mid-latitude storm track regions. Therefore a constant value of L_{cf} can always lead large bias in climate simulations.

The effect of horizontal inhomogeneity of cloud condensation was then considered by including an observation-based gamma function in an additional test. The changes compared with its PPH counterpart test were strikingly significant, with decreases in global mean TOA longwave and shortwave CRF of $\sim 1.2\,\mathrm{Wm}^{-2}$ and $\sim 3.7\,\mathrm{Wm}^{-2}$, respectively, making the simulation results much closer to the observations. This emphasizes the importance of addressing cloud horizontal distribution in GCMs along with the cloud overlap issue. However, the cloud horizontal inhomogeneity has not been paid enough attention in climate simulations so far.

For simulated climate, the changes in cloud structures showed a notable effect on surface temperatures in mid–high latitudes, with the largest zonal mean differences being about 1 K, exceeding the differences between the new and old configurations. The impacts on precipitation and atmospheric temperature were minor. However, it should be noted that we did not here include sea–atmosphere interaction, which could enlarge the effect of the signal imposed by the changing cloud structures.

The results of this study are encouraging for future improvement of the McICA. By analyzing the CloudSat dataset, Zhang et al. (2013b) have found that the decorrelation depth is usually changeable from 0–3 km or more depending on area and season, except for individual areas with values larger than 9 km. However, the current McICA scheme usually adopts the decorrelation depth of a constant 2 km over the globe. Because of the substantial flexibility of the McICA scheme, a more realistic cloud overlap assumption or cloud horizontal distribution, achieved from satellite observations or any other objective sources, could be used to constrain the model simulation. Therefore, to make full use of the new scheme, we will consider, as our next work, ways to obtain changeable and reasonable information on global decorrelation depths and implement these into GCMs.

Acknowledgements. This work was financially supported by National Basic Research Program of China (2011CB403405 and 2012CB955303). The authors would like to give thanks to McICA authors for the code.

The English in this document has been checked by at least two professional editors, both native speakers of English. For a certificate, please see: http://www.textcheck.com/certificate/LpJMwJ.

References

Baum, B. A., Heymsfield, A. J., Yang, P., and Bedka, S. T.: Bulk Scattering Properties for the Remote Sensing of Ice Clouds, Part I: Microphysical Data and Models, J. Appl. Meteorol., 44, 1885–1895, 2005.

Barker, H. W.: Overlap of fractional cloud for radiation calculations in GCMs: A global analysis using CloudSat and CALIPSO data, J. Geophys. Res., 113, D00A01, doi:10.1029/2007JD009677, 2008.

Barker, H. W. and Räisänen, P.: Radiative sensitivities for cloud structural properties that are unresolved by conventional GCMs, Q. J. Royal Meteorol. Soc., 131, 3103–3122, 2005.

Barker, H. W., Stephens, G. L., and Fu, Q.: The sensitivity of domain-averaged solar fluxes to assumptions about cloud geometry, Q .J. Royal Meteorol. Soc., 125, 2127–2152, 1999.

Barker, H. W., Cole, J. N. S., Morcrette, J. J., Pincus, R., Räisänen, P., von Salzen, K., and Vaillancourt, P. A.: The Monte Carlo independent column approximation: an assessment using several global atmospheric models, Q. J. Royal Meteorol. Soc., 134, 1463–1478, 2008.

Briegleb, B. P.: Delta-Eddington approximation for solar radiation in the NCAR Community Climate Model, J. Geophys. Res., 97, 7603–7612, 1992.

Cahalan, R. F., Ridgway, W., Wiscombe, W. J., Gollmer, S., and Harshvardhan, Independent Pixel and Monte Carlo Estimates of Stratocumulus Albedo, J. Atmos. Sci., 51, 3776–3790, 1994.

Carlin, B., Fu, Q., Lohmann, U., Mace, G. G., Sassen, K., and Comstock, J. M.: High-Cloud Horizontal Inhomogeneity and Solar Albedo Bias, J. Clim., 15, 2321–2339, 2002.

Clough, S. A. and Iacono, M. J.: Line-by-line calculation of atmospheric fluxes and cooling rates 2: Application to carbon dioxide, ozone, methane, nitrous oxide and the halocarbons, J. Geophys. Res., 100, 16519–16535, 1995.

Coakley, J. A., Cess, R. D., and Yurevich, F. B.: The Effect of Tropospheric Aerosols on the Earth'sRadiation Budget: A Parameterization for Climate Models, J. Atmos. Sci., 40, 116–138, 1983.

Collins, W. D.: Parameterization of Generalized Cloud Overlap for Radiative Calculations in General Circulation Models, J. Atmos. Sci., 58, 3224–3242, 2001.

Collins, W. D., Hackney, J. K., and Edwards, D. P.: An updated parameterization for infrared emission and absorption by water vapor in the National Center for Atmospheric Research Community Atmosphere Model, J. Geophys. Res., 107, doi:10.1029/2001JD001365, 2002.

Ebert, E. E. and Curry, J. A.: A Parameterization of Ice Cloud Optical Properties for Climate Models, J. Geophys. Res, 97, 3831–3836, 1992.

Ellingson, R. G., Ellis, J., and Fels, S.: The Intercomparison of Radiation Codes Used in Climate Models: Long Wave Results, J. Geophys. Res., 96, 8929–8953, 1991.

Fu, Q.: An Accurate Parameterization of the solar radiative properties of cirrus clouds for climate models, J. Clim., 9, 2058–2082, 1996.

Fu, Q. and Liou, K. N.: On the Correlated k-Distribution Method for Radiative Transfer in Nonhomogenecous Atmospheres, J. Atmos. Sci., 49, 2139–2156, 1992.

Gong, S. L., Barrie, L. A., Blanchet, J. P., von Salzen, K., Lohmann, U., Lesins, G., Spacek, L., Zhang, L. M., Girard, E., Lin, H., Leaitch, R., Leighton, H., Chylek, P., and Huang, P.: Canadian Aerosol Module: A size-segregated simulation of atmospheric aerosol processes for climate and air quality models 1. Module development, J. Geophys. Res., 108, 864007, doi:10.1029/2001JD002002, 2003.

Hong, G., Yang, P., Baum, B. A., Heymsfield, A. J., and Xu, K. M.: Parameterization of Shortwave and Longwave Radiative Properties of Ice Clouds for Use in Climate Models, J. Clim., 22, 6287–6312, 2009.

IPCC: Climate Change 2007: Impacts, Adaptation and Vulnerability. Contribution of Working Group II to the Fourth Assessment Report of the Intergovernmental Panel on Climate Change, Cambridge University Press, Cambridge, 2007.

Jing, X. W. and Zhang, H.: Application and evaluation of McICA scheme in BCC_AGCM2.0.1, AIP Conf. Proc., 1531, 756–759, doi:10.1063/1.4804880, 2013.

Kiehl, J. T. and Briegleb, B. P.: A new parameterization of the absorptance due to the 15 µm band system of carbon dioxide, J. Geophys. Res., 96, 9013–9019, 1991

Kiehl, J. T. and Ramanathan, V.: Comparison of Cloud Forcing Derived From the Earth Radiation Budget Experiment with That Simulated by the NCAR Community Climate Model, J. Geophys. Res., 95, 11679–11698, 1990.

Kiehl, J. T., Hack, J. J., and Briegleb, B. P.: The simulated Earth radiation budget of the National Center for Atmospheric Research Community Climate Model CCM2 and comparisons with the Earth Radiation Budget Experiment (ERBE), J. Geophys. Res., 99, 20815–20827, 1994.

Kratz, D. P.: The correlated k-distribution technique as applied to the AVHRR channels, J. Quantitative Spectrosc. Radiat. Transf., 53, 501–517, 1995.

Kristjansson, J. E., Edwards, J. M., and MitChell, D. L.: Impact of a new scheme for optical properties of ice crystals on climates of two GCMs, J. Geophys. Res., 105, 10063–10079, 2000.

Li, J., Dobbie, S., Räisänen, P., and Min, Q.: Accounting for unresolved clouds in a 1-D solar radiative-transfer model, Q. J. Royal Meteorol. Soc., 131, 1607–1629, 2005.

Liang, X. Z. and Wu, X.: Evaluation of a GCM subgrid cloud-radiation interaction parameterization using cloud-resolving model simulations, Geophys. Res. Lett., 32, L06801, doi:10.1029/2001JD002002, 2005.

Lu, P., Zhang, H. and Jing, X. W.: The effects of different HITRAN versions on calculated longwave radiation and uncertainty evaluation, Acta Meteor. Sinica, 26, 389–398, 2012.

Mace, G. G. and Benson-Troth, S.: Cloud-Layer Overlap Characteristics Derived from Long-Term Cloud Radar Data, J. Clim., 15, 2505–2515, 2002.

Morcrette, J. J. and Jakob, C.: The Response of the ECMWF Model to Changes in the Cloud Overlap Assumption, Mon. Weather Rev., 128, 1707–1732, 2000.

Morcrette, J. J., Barker, H. W., Cole, J. S., Iacono, M. J., and Pincus, R.: Impact of a new radiation package, McRad, in the ECMWF Integrated Forecasting System, Mon. Weather Rev., 136, 4773–4798, doi:10.1175/2008MWR2363.1, 2008.

Nakajima, T., Tsukamoto, M., Tsushima, Y., Numaguti, A., and Kimura, T.: Modeling of the Radiative Process in an Atmospheric General Circulation Model, Appl. Opt., 39, 4869–4878, 2000.

Naud, C. M., Del Genio, A., Mace, Gerald G., Benson, S., Clothiaux, E. E., and Kollias, P.: Impact of Dynamics and Atmospheric State on Cloud Vertical Overlap, J. Clim., 21, 1758–1770, 2008.

Neale, R. B., Chen, C. C., Andrew, G., Lauritzen, P. H., Park, S., Williamson, D. L., Conley, A. J., Garcia, R., Kinnison, D., Lamarque, J. F., Marsh, D., Mills, M., Smith, A. K., Tilmes, S., Vitt, F., Morrrison, H., Cameron-Smith, P., Collins, W. D., Iacono, M. J., Easter, R. C., Ghan, S. J., Liu, X., Rasch, P. J., and Taylor, M. A.: Description of the NCAR Community Atmosphere Model (CAM 5.0). NCAR Tech. Note TN-486, available at: http://www.cesm.ucar.edu/models/cesm1.2/cam/docs/description/cam5_desc.pdf, 2010.

Oleson, K. W., Bonan, G. B., Schaaf, C., Gao, F., Jin, Y., and Strahler, A.: Assessment of global climate model land surface albedo using MODIS data, Geophys. Res. Lett., 30, 1443, doi:10.10292002GL016749, 2003.

Oreopoulos, L. and Davies, R.: Plane Parallel Albedo Biases from Satellite Observations. Part I: Dependence on Resolution and Other Factors, J. Clim., 11, 919–932, 1998.

Pincus, R., Barker, H. W., and Morcrette, J. J.: A fast, flexible, approximate technique for computing radiative transfer in inhomogeneous cloud fields, J. Geophys. Res., 108, 4376, doi:10.1029/2002JD003322, 2003.

Pomroy, H. R. and Illingworth, A. J.: Ice cloud inhomogeneity: Quantifying bias in emissivity from radar observations, Geophys. Res. Lett., 27, 2101–2104, 2000.

Räisänen, P. and Barker, H. W.: Evaluation and optimization of sampling errors for the Monte Carlo Independent Column Approximation, Q. J. Royal Meteorol. Soc., 130, 2069–2085, 2004.

Räisänen, P. and Järvinen, H.: Impact of cloud and radiation scheme modifications on climate simulated by the ECHAM5 atmospheric GCM, Q. J. Royal. Meteorol. Soc., 136, 1733–1752, 2010.

Räisänen, P., Barker, H. W., Khairoutdinov, M. F., Li, J., and Randall, D. A.: Stochastic generation of subgrid-scale cloudy columns for large-scale models, Q. J. Royal Meteorol. Soc., 130, 2047–2067, 2004.

Ramanathan, V. and Downey, P.: A nonisothermal emissivity and absorptivity formulation for water vapor, J. Geophys. Res., 91, 8649–8666, 1986.

Randles, C. A., Kinne, Myhre, S., Schulz, M., Stier, P., Fischer, J., Doppler, L., Highwood, E., Ryder, C., Harris, B., Huttunen, J., Ma, Y., Pinker, R. T., Mayer, B., Neubauer, D., Hitzenberger, R., Oreopoulos, L., Lee, D., Pitari, G., Di Genova, G., Quaas, J., Rose, F. G., Kato, S., Rumbold, S. T., Vardavas, I., Hatzianastassiou, N., Matsoukas, C., Yu, H., Zhang, F., Zhang, H., and Lu, P.: Intercomparison of shortwave radiative transfer schemes in global aerosol modeling: results from the AeroCom Radiative Transfer Experiment, Atmos. Chem. Phys., 13, 2347–2379. doi:10.5194/acp-13-2347-2013, 2013.

Rasch, P. J. and Kristjansson, J. E.: A comparison of the CCM3 model climate using diagnosed and predicted condensate parameterizations, J. Clim., 11, 1587–1614, 1998.

Rothman, L. S., Barbe, A. , Chris Benner, D., Brown, L. R., Camy-Peyret, C., Carleer, M. R., Chance, K., Clerbaux, C., Dana, V., Devi, V. M., Fayt, A., Flaud, J. M., Gamache, R. R., Goldman, A., Jacquemart, D., Jucks, K. W., Lafferty, W. J., Mandin, J. Y., Massie, S. T., Nemtchinov, V., Newnham, D. A., Perrin, A., Rinsland, C. P., Schroeder, J., Smith, K. M., Smith, M. A. H., Tang, K., Toth, R. A., Vander Auwera, J., Varanasi, P., and Yoshino, K.: The HITRAN molecular spectroscopic database: edition of 2000 including updates through 2001, J. Quantitative Spectrosc. Radiat. Transf., 82, 5–44, 2003.

Shonk, J. K. P. and Hogan, R. J.: Tripleclouds: An Efficient Method for Representing Horizontal Cloud Inhomogeneity in 1-D Radiation Schemes by Using Three Regions at Each Height, J. Clim., 21, 2352–2370, 2008.

Shonk, J. K. P., Hogan, R. J., Edwards, J. M., and Mace, G. G.: Effect of improving representation of horizontal and vertical cloud structure on the Earth's global radiation budget. Part I: Review and parametrization, Q. J. Royal Meteorol. Soc., 136, 1191–1204, 2010.

Slingo, A.: A GCM Parameterization for the Shortwave Radiative Properties of Water Clouds, J. Atmos. Sci., 46, 1419–1427, 1989.

Stephens, G. L., Wood, N. B., and Gabriel, P. M.: An Assessment of the Parameterization of Subgrid-Scale Cloud Effects on Radiative Transfer. Part I: Vertical Overlap, J. Atmos. Sci., 61, 715–732, 2004.

Stubenrauch, C. J., Rossow, W. B., Chéruy, F., Chédin, A., and Scott, N. A.: Clouds as Seen by Satellite Sounders (3I) and Imagers (ISCCP), Part I: Evaluation of Cloud Parameters, J. Clim., 12, 2189–2213, 1999.

Sun, Z. and Rikus, L.: Improved application of ESFT to inhomogeneous atmosphere, J. Geophy. Res., 104, 6291–6303, 1999.

Tian, L. and Curry, J. A.: Cloud Overlap Statistics, J. Geophys. Res., 94, 9925–9935, 1989.

Uppala, S. M., KÅllberg, P. W., Simmons, A. J., Andrae, U., Bechtold, V. Da Costa, Fiorino, M., Gibson, J. K., Haseler, J., Hernandez, A., Kelly, G. A., Li, X., Onogi, K., Saarinen, S., Sokka, N., Allan, R. P., Andersson, E., Arpe, K., Balmaseda, M. A., Beljaars, A. C. M., Berg, L. Van De, Bidlot, J., Bormann, N., Caires, S., Chevallier, F., Dethof, A., Dragosavac, M., Fisher, M., Fuentes, M., Hagemann, S., Hólm, E., Hoskins, B. J., Isaksen, L., Janssen, P. A. E. M., Jenne, R., McNally, A. P., Mahfouf, J. F., Morcrette, J. J., Rayner, N. A., Saunders, R. W., Simon, P., Sterl, A., Trenberth, K. E., Untch, A., Vasiljevic, D., Viterbo, P., and Woollen, J.: The ERA-40 re-analysis, Q. J. Royal Meteorol. Soc., 131, 2961–3012, 2005.

Wei, X. D. and Zhang, H.: Analysis of optical properties ofnonspherical dust aerosols, Acta Optica. Sinica, 31, 0501002-1, 2011.

Wu, T. W. and Wu, G. X.: An empirical formula to compute snow cover fraction in GCMs, Adv. Atmos. Sci., 21, 529–535, 2004.

Wu, T., Yu, R., Zhang, F., Wang, Z., Dong, M., Wang, L., Jin, X., Chen, D., and Li, L.: The Beijing Climate Center atmospheric general circulation model: description and its performance for the present-day climate, Clim. Dyn., 34, 123–147, doi:10.1007/s00382-008-0487-2, 2010.

Wyser, K.: The Effective Radius in Ice Clouds, J. Clim., 11, 1793–1802, 1998.

Xie, P. and Arkin, P. A.: Global Precipitation: A 17-Year Monthly Analysis Based on Gauge Observations, Satellite Estimates, and Numerical Model Outputs, Bull. Am. Meteorol. Soc., 78, 2539–2558, 1997.

Yan, H.: The design of a nested fine-mesh model over complex topography part 2: parameterization of sub grid physical processes, Plateau Meteorol, 6, 64–139, 1987(in Chinese).

Yang, P., Wei, H., Huang, H. L., Baum, B. A., Hu, Y. X., Kattawar, G. W., Mishchenko, M. I., and Fu, Q.: Scattering and absorption property database for nonspherical ice particles in the near- through far-infrared spectral region,. Appl. Opt., 44, 5512–5523, 2005.

Zhang, G. and Mu, M.: Effects of modification to the Zhang-Mcfarlane convection parameterization on the simulation of the tropical precipitation in the National Center for Atmosphere Research Community Climate Model, Version 3, J. Geophys. Res., 110, D09109, doi:10.1029/2004JD00517, 2005.

Zhang, F., Liang, X. Z., Li, J., and Zeng, Q.: Dominant roles of subgrid-scale cloud structures in model diversity of cloud radiative effect, J. Geophys. Res., 118, 7733–7749, doi:10.1002/jgrd.50604, 2013a.

Zhang, H., Nakajima, T., Shi, G., Suzuki, T., and Imasu, R.: An optimal approach to overlapping bands with correlated k-distribution method and its application to radiative calculations, J. Geophys. Res., 108, 4641, doi:10.1029/2002JD003358, 2003.

Zhang, H., Peng, J., Jing, X. W., and Li, J.: The features of clouds overlapping in Eastern Asia and their effect on cloud radiative forcing, Sci. China Earth Sci. ,56, 737–747, 2013b.

Zhang, H., Shi, G., Nakajima, T., and Suzuki, T.: The effect of the choice of the k-interval number on radiative calculation, J. Quant. Spectro. Rad. Trans., 98, 31–43, 2006a.

Zhang, H., Suzuki, T., Nakajima, T., Shi, G., Zhang. X., and Liu, Y.: Effects of band division on radiative calculations, Opt. Eng., 45, 016002, doi:doi:10.1117/1.2160521, 2006b.

Zhang, H., Wang, Z., Wang, Z., Liu, Q., Gong, S., Zhang, X., Shen, Z., Lu, P., Wei, X., Che, H., and Li, L.: Simulation of direct radiative forcing of aerosols and their effects on East Asian climate using an interactive AGCM-aerosol coupled system, Clim. Dyn., 38, 1675–1693, 2012.

Zhou, C. H., Gong, S. L., Zhang, X. Y., Liu, H. L., Xue, M., Cao, G. L., An, X. Q., Che, H. Z., Zhang, Y. M., and Niu, T.: Towards the improvements of simulating the chemical and optical properties of Chinese aerosols using an online coupled model CUACE/Aero, Tellus B, 64, 18965, doi:10.3402/tellusb.v64i0.18965, 2012.

Table 1. Comparison of the new and old schemes.

	Old	New
Absorbing gases in LW	H_2O, CO_2, and O_3 CH_4, N_2O, CFC11, CFC12	The same as in Old
Absorbing gases in SW	H_2O, CO_2, O_3, and O_2	H_2O, CO_2, O_3, N_2O, and O_2
Range of LW	0–2000 cm^{-1}	0–2680 cm^{-1}
Range of SW	2000–50000 cm^{-1}	2110–49000 cm^{-1*}
Band transmittance scheme	Band model (LW: Kiehl and Briegleb, 1991) (SW: Briegleb, 1992)	CKD scheme Zhang (2003, 2006a, 2006b)
RT solver in LW	Absorptivity/emissivity formulations Ramanathan and Downey (1986)	Two-stream approximation Nakajima et al. (2000)
RT solver in SW	$\delta-$Eddington method Briegleb (1992)	$\delta-$Eddington method Coakley et al. (1983)
Cloud fraction parameterization	Diagnostic scheme Rasch and Kristjansson (1998)	The same as in OLD
Cloud optics	LW: emissivity formulations Ebert and Curry (1992) SW: formulas of Slingo (1989) for liquid and of Ebert and Curry (1992) for ice	Ice cloud: computed using data from Fu (1996), Yang et al. (2005), and Hong et al. (2009) liquid cloud: Nakajima et al. (2000)
Cloud effective radius	Ice cloud: Kristjansson et al. (2000) Liquid cloud: Kiehl et al. (1994)	Ice cloud: Wyser (1998) Liquid cloud: the same as in Old
Cloud overlap	Maximum random overlap (MRO) Collins (2001)	McICA Räisänen and Barker (2004), Barker et al. (2008)
Aerosol-radiation coupling scheme	BCC_AGCM2.0.1_CAM Zhang et al. (2012)	BCC_AGCM2.0.1_CAM Zhang et al. (2012)

* In the new scheme, contributions from the solar spectrum and terrestrial emission are mixed within 2110–2680 cm^{-1}.

Table 2. The modeled and observed (SW CRF)/(LW CRF). slopes in the tropical warm pool region (10° S–20° N, 110° E–160° E).

	OLD	NEW_MRO_OL	NEW_MRO	NEW_GO1	NEW_GO2	NEW_GO3	NEW_GO2_IH	OBS
ANN	−1.17	−1.11	−0.94	−0.94	−1.01	−0.98	−0.98	−1.13
DJF	−1.55	−1.51	−1.34	−1.49	−1.43	−1.41	−1.45	−1.14
JJA	−1.83	−1.65	−1.51	−1.60	−1.57	−1.60	−1.58	−1.09

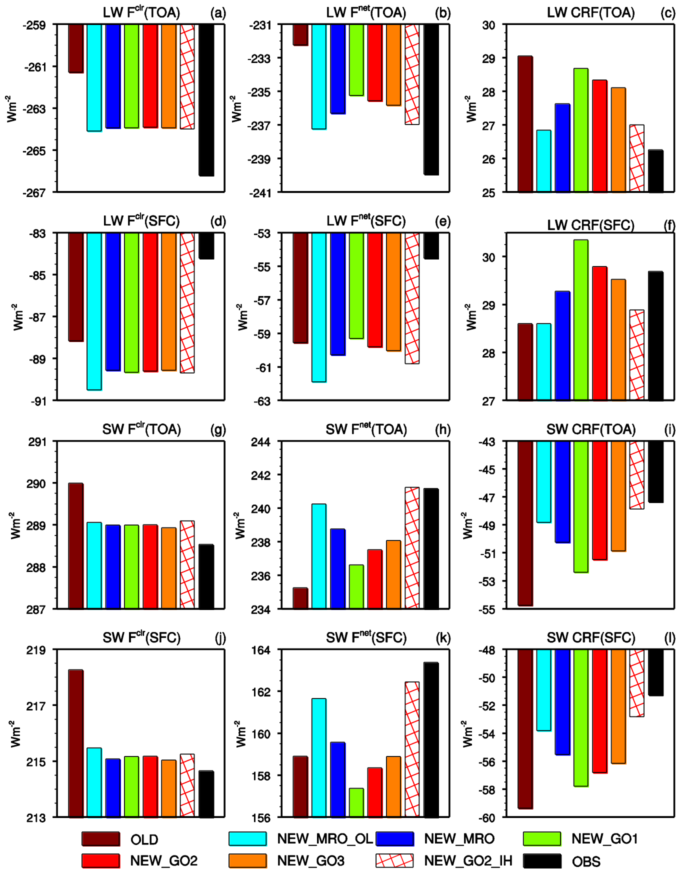

Fig. 1. Global annual mean clear-sky net flux (F^{clr}, left panels), all-sky net flux (F^{net}, central panels), and CRF (right panels) for TOA LW (upmost row), surface LW (second row), TOA SW (third row), and surface SW (bottom row) from the various simulations and CERES_EBAF observations.

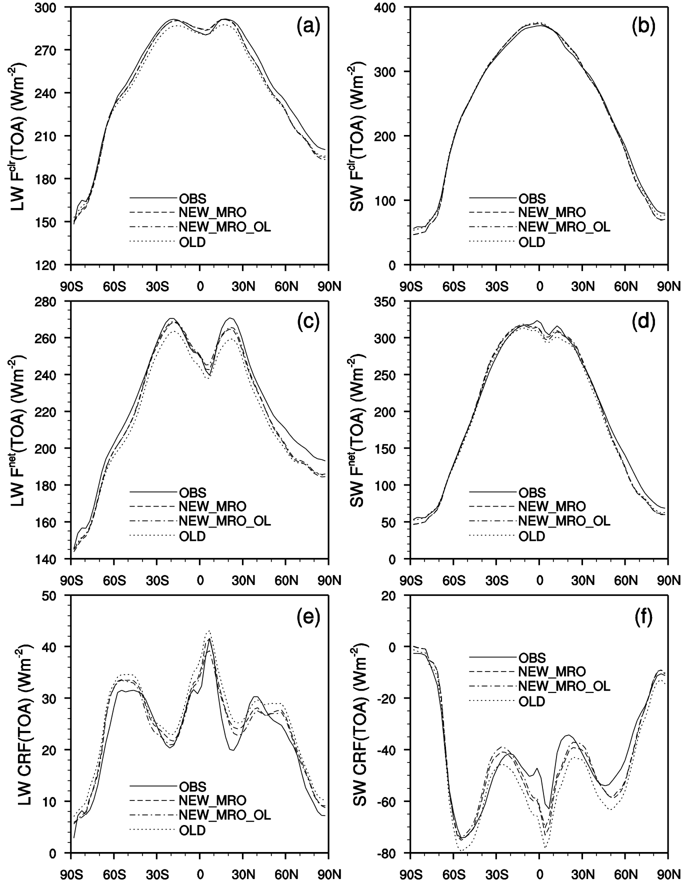

Fig. 2. F^{clr} (top), F^{net} (central), and CRF (bottom) at the TOA for LW (left) and SW (right) from OLD, NEW_MRO, NEW_MRO_OL, and CERES_EBAF observation.

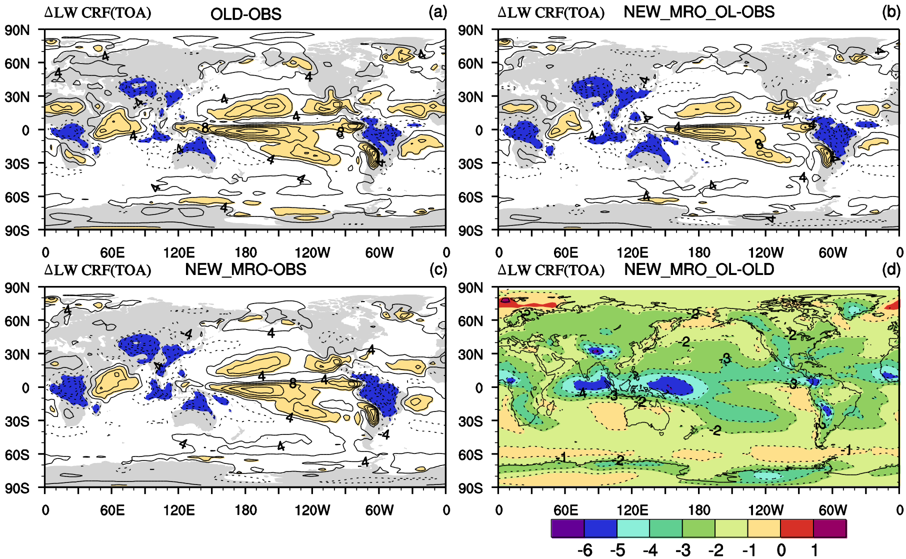

Fig. 3. The annual mean differences in LW CRF among the **(a)** OLD, **(b)** NEW_MRO_OL, and **(c)** NEW_MRO simulations and CERES_EBAF observations with differences larger (smaller) than 8 (−8) Wm^{-2} shaded in yellow (blue). Annual mean differences between NEW_MRO_OL and OLD are shown in **(d)**.

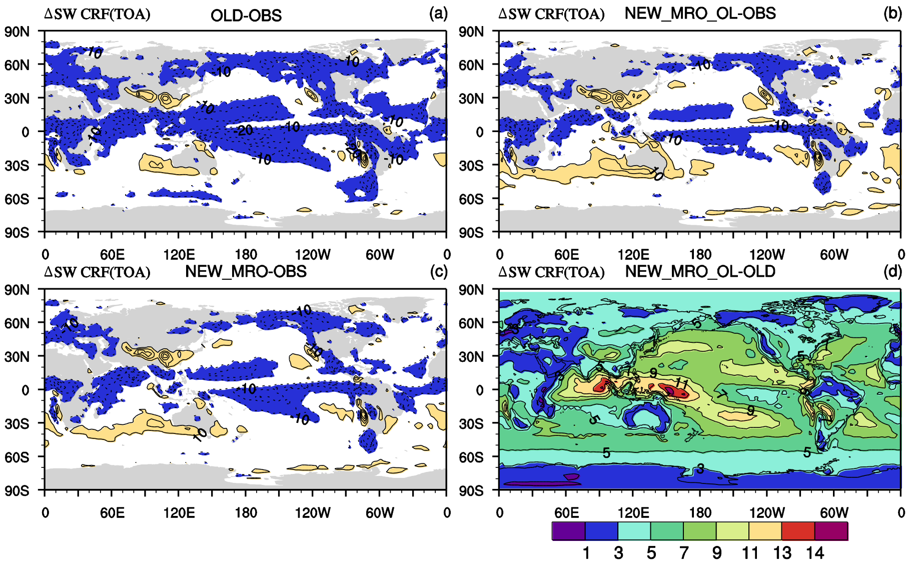

Fig. 4. The same as Fig. 3 but for SW CRF. Differences larger (smaller) than 10 (−10) $\mathrm{Wm^{-2}}$ are shaded in yellow (blue) in **(a–c)**.

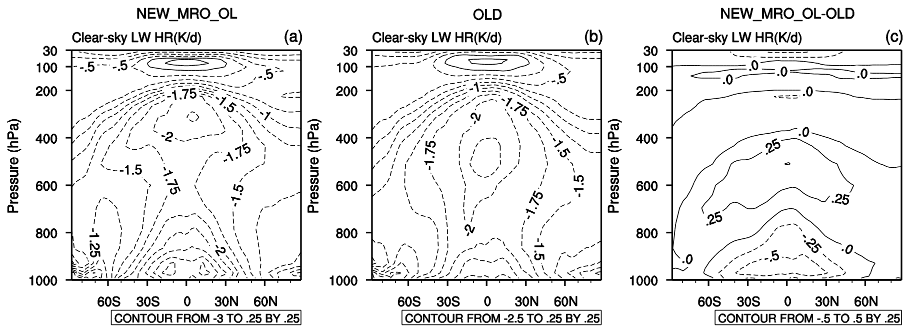

Fig. 5. Zonal annual mean clear-sky LW heating rate for **(a)** NEW_MRO_OL and **(b)** OLD and **(c)** the difference between them.

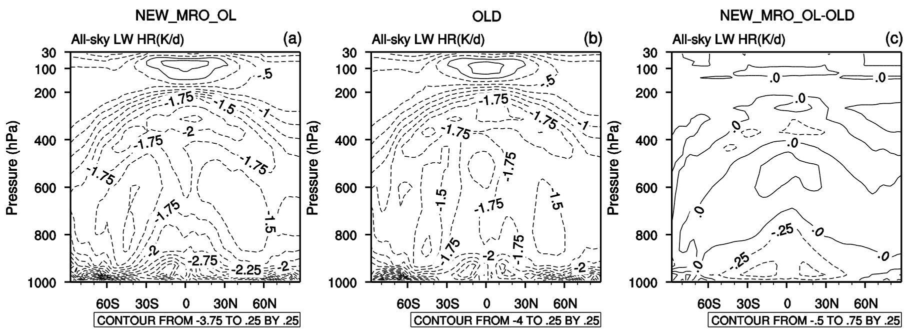

Fig. 6. The same as Fig. 5, but for the all-sky LW heating rate.

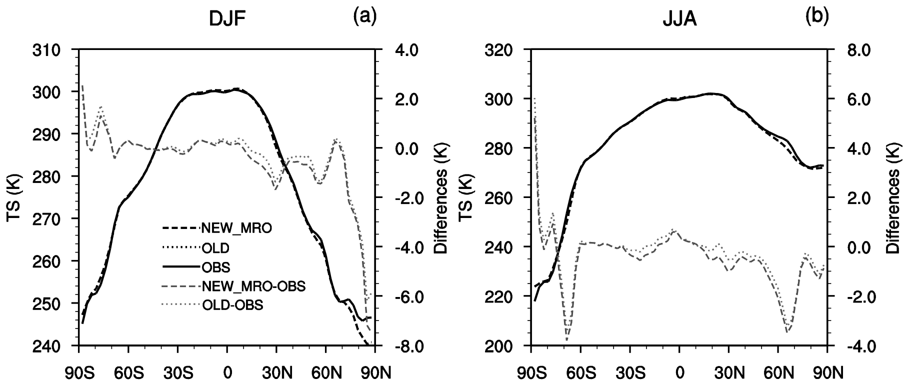

Fig. 7. Zonal mean surface temperature in DJF (left) and JJA (right) from NEW_MRO (black dashed), OLD (black dotted), and ERA-40 reanalysis data (black solid), as well as the differences between NEW_MRO and ERA-40 (gray dashed) and between OLD and ERA-40 (gray dotted).

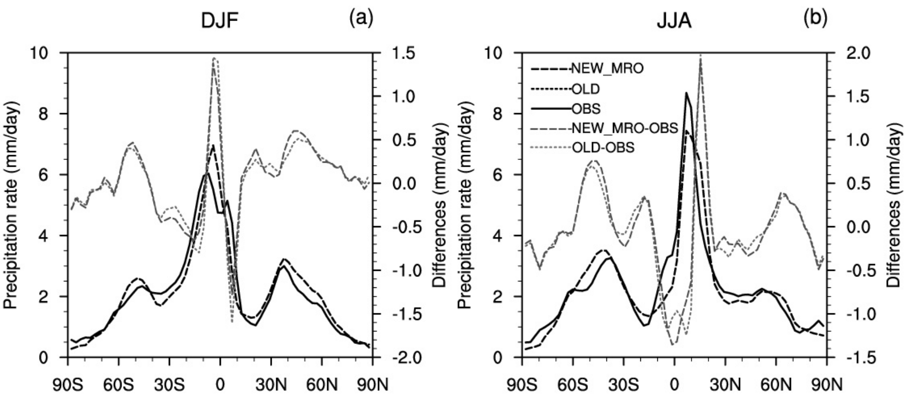

Fig. 8. The same as Fig. 7 but for precipitation rate. The observational dataset is from Xie and Arkin (1997).

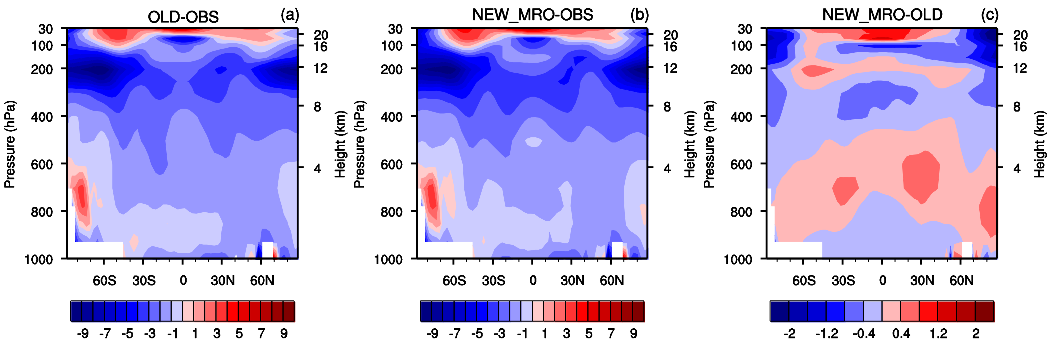

Fig. 9. Biases in zonal annual mean atmospheric temperature compared with ERA-40 reanalysis for **(a)** OLD and **(b)** NEW_MRO simulations and **(c)** the differences between NEW_MRO and OLD.

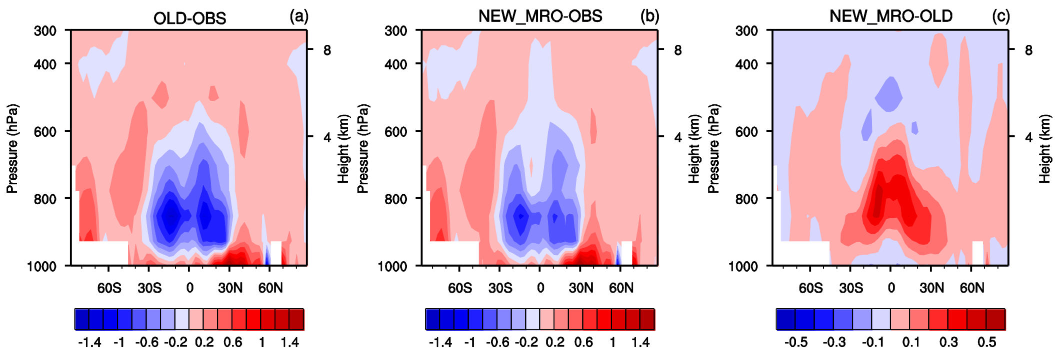

Fig. 10. The same as Fig. 9 but for specific humidity.

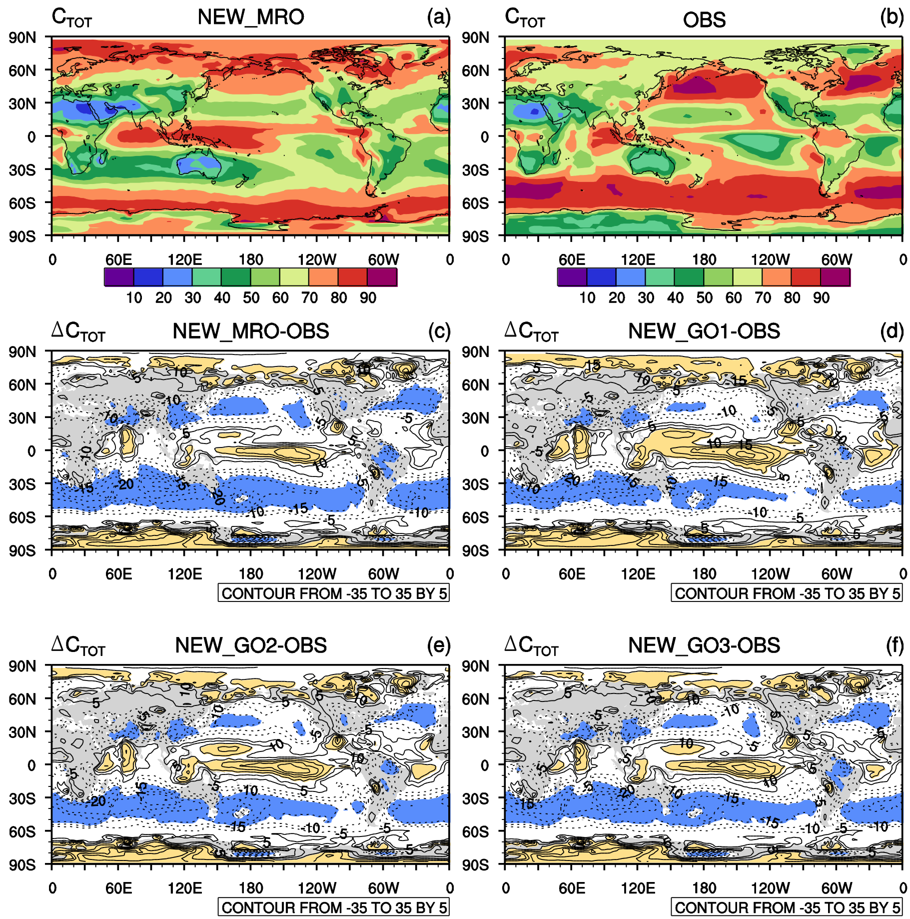

Fig. 11. The annual mean total cloud fraction (C_{TOT}) from **(a)** the NEW_MRO and **(b)** ISCCP observations and the differences between ISCCP observations and **(c)** NEW_MRO, **(d)** NEW_GO1, **(e)** NEW_GO2, and **(f)** NEW_GO3.

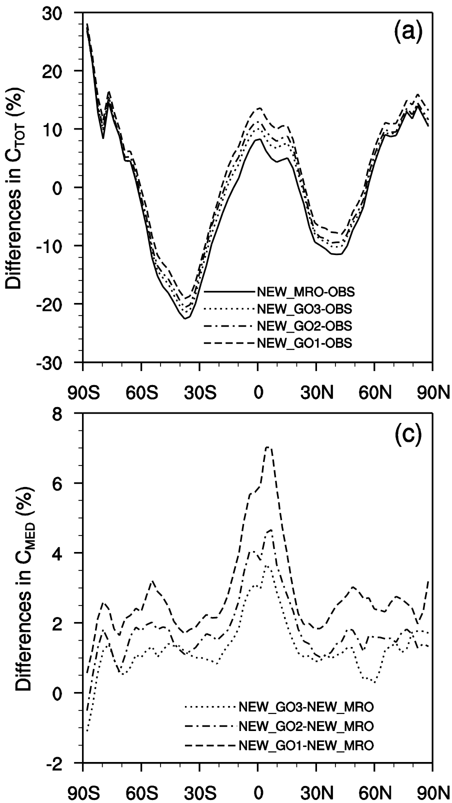

Fig. 12. Differences in **(a)** total cloud fraction between simulations and ISCCP observations and **(b)** low (C_{LOW}), **(c)** middle (C_{MED}), and **(d)** high (C_{HGH}) cloud fractions between NEW_GO1, NEW_GO2, NEW_GO3, and NEW_MRO.

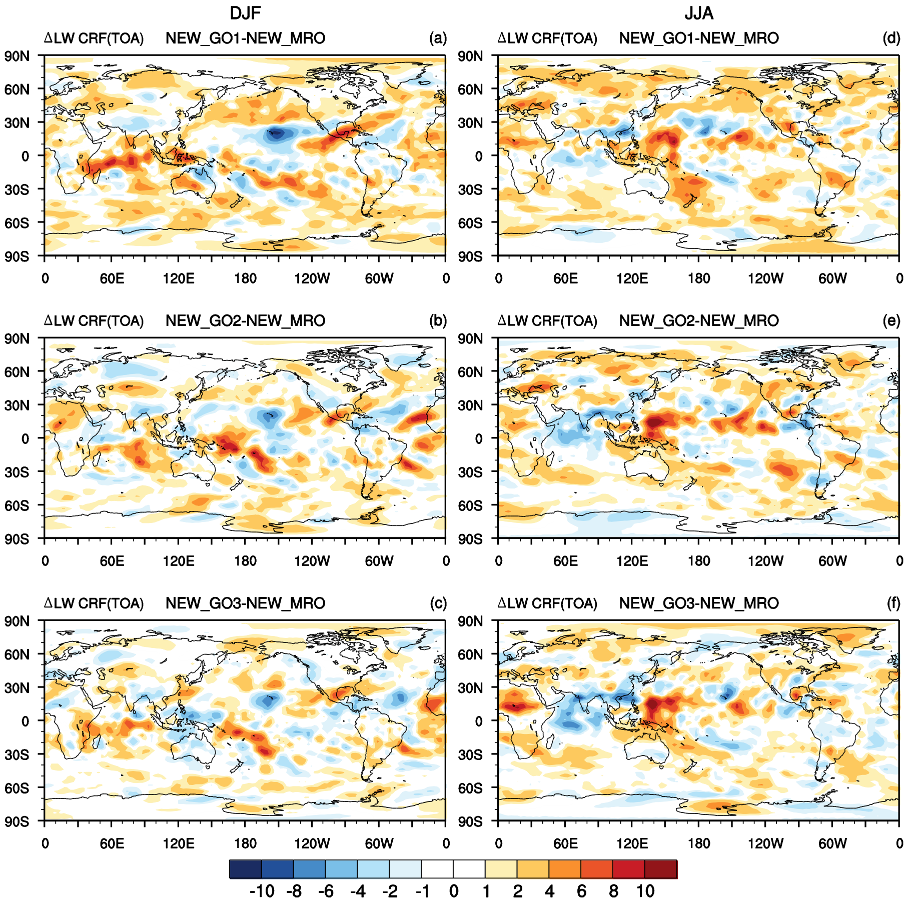

Fig. 13. Differences in LW CRF between NEW_GO1, NEW_GO2, and NEW_GO3 and NEW_MRO in DJF (left) and JJA (right).

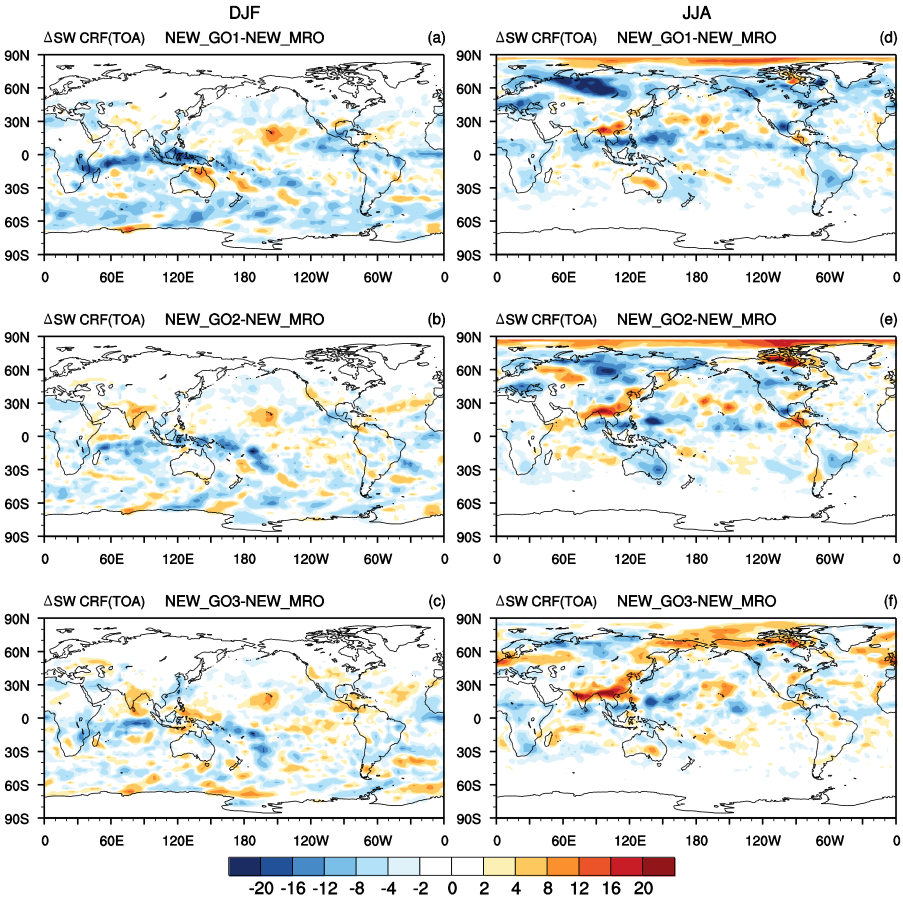

Fig. 14. The same as Fig. 13, but for SW CRF.

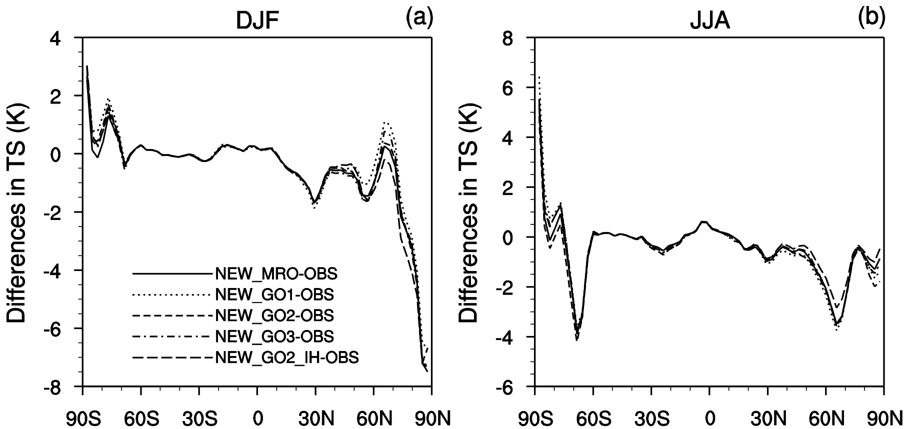

Fig. 15. Zonal mean biases in surface temperature of McICA simulations with different cloud configurations during **(a)** DJF and **(b)** JJA compared with ERA-40 reanalysis.

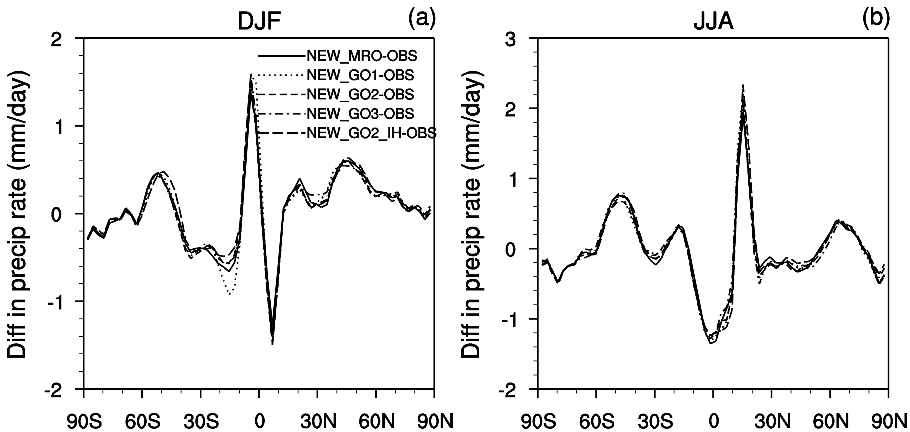

Fig. 16. The same as Fig. 15, but for precipitation rate.

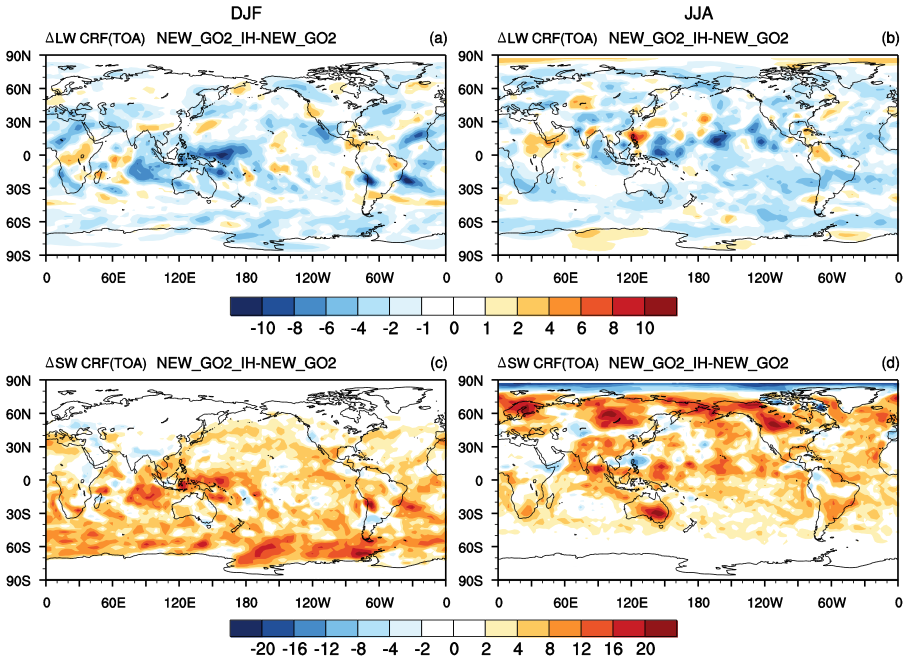

Fig. 17. Differences in **(a–b)** LW CRF and **(c–d)** SW CRF between NEW_GO2_IH and NEW_GO2.

SCIENCE CHINA
Earth Sciences

Progress of Projects Supported by NSFC
• RESEARCH PAPER •

May 2013 Vol.56 No.5: 737–747
doi: 10.1007/s11430-012-4489-x

The features of cloud overlapping in Eastern Asia and their effect on cloud radiative forcing

ZHANG Hua[1*], PENG Jie[1,3], JING XianWen[1,2] & LI JiangNan[4]

[1] *Laboratory for Climate Studies of CMA, National Climate Center, Beijing 100081, China;*
[2] *Chinese Academy of Meteorological Sciences, Beijing 100081, China;*
[3] *Nanjing University of Information Science and Technology, Nanjing 210044, China;*
[4] *Canadian Center for Climate Modeling and Analysis, University of Victoria, Victoria, BC V8W 3V6, Canada*

Received October 10, 2011; accepted June 14, 2012; published online October 28, 2012

Characteristics of cloud overlap over Eastern Asia are analyzed using a three-year dataset (2007–2009) from the cloud observing satellite CloudSat. Decorrelation depth L_{cf}^* is retrieved, which represents cloud overlap characteristics in the simulation of cloud-radiation processes in global climate models. Results show that values of L_{cf}^* in six study regions are generally within the range 0–3 km. By categorizing L_{cf}^* according to cloud amount in subregions, peak L_{cf}^* appears near subregions with cloud amount between 0.6 and 0.8. Average L_{cf}^* is 2.5 km. L_{cf}^* at higher altitudes is generally larger than at lower latitudes. Seasonal variations of L_{cf}^* are also clearly demonstrated. The sensitivity of cloud radiative forcing (CRF) to L_{cf}^* in Community Atmosphere Model 3.0 of the National Center for Atmospheric Research (CAM3/NCAR) is analyzed. The result shows that L_{cf}^* can have a big impact on simulation of CRF, especially in major monsoon regions and the Mid-Eastern Pacific, where the difference in CRF can reach 40–50 W m^{-2}. Therefore, accurate parameterization of cloud vertical overlap structure is important to CRF simulation and its feedback to climate.

cloud overlap hypothesis, decorrelation depth, CloudSat, stochastic cloud generator (SCG), cloud radiation

Citation: Zhang H, Peng J, Jing X W, et al. The features of cloud overlapping in Eastern Asia and their effect on cloud radiative forcing. Science China: Earth Sciences, 2013, 56: 737–747, doi: 10.1007/s11430-012-4489-x

The formation and distribution of cloud is a combined result of thermodynamic, dynamic, and earth surface processes [1–4]. Clouds play a key role in the earth atmosphere system [5] and are important in the radiation budget and global hydrologic cycle. They also impact climate change. However, simulation of clouds is always a difficult problem in climate modeling [6, 7], which makes them one of the biggest uncertainties in the study of climate change. Therefore, accurate description of clouds and cloud radiative processes is necessary to reduce uncertainty of cloud radiative feedback in climate models.

In model simulation of cloud radiative processes, major uncertainty comes from treatment of cloud vertical overlap. Ground-based observation indicates [2] that clouds often vertically overlap. How to treat multi-layer cloud overlap can greatly influence the cloud radiative heating rate, which can in turn affect cloud development and radiation balance in the atmosphere and at the surface [8, 9]. In current general circulation models (GCMs), clouds with scale smaller

*Corresponding author (email: huazhang@cma.gov.cn)

than grid resolution are not distinguishable and can only be described by sub-grid parameterization. There is no universal theory to describe the distributions of cloud at different heights in sub-grid scale. In most GCMs, the commonly used hypothesis is maximum cloud overlap, random overlap, or a combination of the two [10–13]. It has been found that a combination of maximum and random overlap largely agrees with statistical characteristics of observed cloud distributions [14]. However, given limited observational data, such a hypothesis is not yet fully supported [15].

Barker et al. [16] used the cloud resolving model (CRM) to conduct high-accuracy Monte Carlo simulation of convective cloud. They found that overlap of simulated cloud differed from the commonly assumed maximum and random overlap, leading to shortwave flux differences as high as 100 W m^{-2}. Li [17] found that among representative research, radiation flux error caused by the overlap scheme widely used in GCMs could be 155 W m^{-2}, and heating rate error could reach 16 K d^{-1}. Liang and Wang [18] proposed a MOASAIC approach to handle the multiple layer cloud overlap issue, which treats the vertical relevance of cloud in GCM radiative parameterization explicitly. Their result shows that a GCM is very sensitive to the treatment of cloud vertical distribution. In comparison with the result of random cloud overlap, a GCM with explicit treatment of cloud relevance produces a very different distribution of atmospheric radiative heating rate—the middle and upper regions of the tropical and subtropical troposphere warm by over 3°C annually, and the stratosphere in the Northern Hemisphere polar region warms as much as 15°C in the nighttime.

In general, the above three overlap schemes are characterized by a fixed cloud description and are unable to represent true cloud overlap, which is strongly dependent on cloud type and spatial and temporal variation. For instance, extensive altostratus tends to coexist with cumulus, whereas cumulonimbus and cirrus often appear in tropical areas simultaneously. Adjacent clouds may have the greatest relevance, whereas clouds separated by clear sky are relatively independent [18]. By considering such adjustable overlap factors, Hogan and Illingworth [19] proposed a cloud overlap scheme that assumes the actual total cloud amount is between maximum and random overlap. This scheme, called the general overlap hypothesis, makes the description of cloud overlap more flexible. In such a hypothesis, a parameter of decorrelation depth L_{cf}^{*} is proposed, which can effectively eliminate the dependence of cloud vertical structure on model vertical resolution. The L_{cf}^{*} currently reflects the relevance of cloud vertical overlap. Observational study of L_{cf}^{*} is in an initial stage. Based on satellite and ground-based radar observations, a global mean value of L_{cf}^{*} was obtained [20], and the commonly used value in GCMs is 2 km. However, spatial and temporal variation of L_{cf}^{*} is not known [20]. How to address uncertainty in climate models owing to a fixed value of L_{cf}^{*} is an interesting problem. Here, we conduct a related study over the China region using available satellite datasets, which permits precise evaluation of L_{cf}^{*}. The result is used in a GCM to indicate climate impact.

On 28 April 2006, NASA launched the sun-synchronous, polar orbiting satellite CloudSat, which carries a 94 GHz millimeter wave radar with very high vertical resolution. Data from CloudSat makes it possible to conduct quantitative research on characteristics of cloud vertical overlap.

Recently, a new 3D sub-grid cloud scheme called the Stochastic Cloud Generator (SCG) has demonstrated unique advantages [16, 21–26]. It can describe cloud structure independent of radiative transfer module. Therefore, it is easy to adjust cloud structure without changing radiative transfer code. As a result, artificial uncertain factors in handling radiative transfer via complicated cloud structures can be avoided. The method of SCG, which facilitates adjustment of both cloud and radiation, provides good prospects for modeling cloud and cloud radiation interaction within climate models.

We used datasets of the polar orbiting satellite CloudSat in combination with SCG, to analyze spatial and temporal variation of L_{cf}^{*} over Eastern Asia. Sensitivity of global cloud radiative forcing to L_{cf}^{*} will also be examined.

1 Description and processing of CloudSat data

Observed data was from the 94 GHz millimeter cloud profiling radar (CPR) aboard CloudSat from 2007 to 2009. CloudSat is a cloud observing satellite. As indicated in Figure 1, each orbit of CloudSat is about 2 h, with 37081 scans. The satellite sub-point of each scan covers 1.1 km (along orbit direction) × 1.4 km (perpendicular to orbit direction). It scans 30 km in the vertical direction, yielding 125 layers, each of thickness 0.24 km. Data was stored in pixels of 1.1 km × 1.4 km × 0.24 km. Recently, several level 2 products have also been retrieved.

We used level 2 products of 2B-GEOPROF and 2B-GROPROF-Lidar (see http://cloudsat.cria.colostate.edu/data-specs.php). The former obtained data from the CPR, and the latter collocated the CPR information and lidar data from the CALIPO instrument aboard CALIPSO (Cloud-Aerosol Lidar and Infrared Pathfinder Satellite Observations). The CALIPSO has the same orbit as CloudSat, with only a 15 s time difference. This combination takes advantage of both millimeter-wave radar and lidar. We calculated data of CPR_Cloud_mask and Radar_Reflectivity in 2B-GEOPROF, and data of CloudFraction in 2B-GEO-PROF-Lidar. The instruction of CPR_Cloud_mask is shown in Table 1.

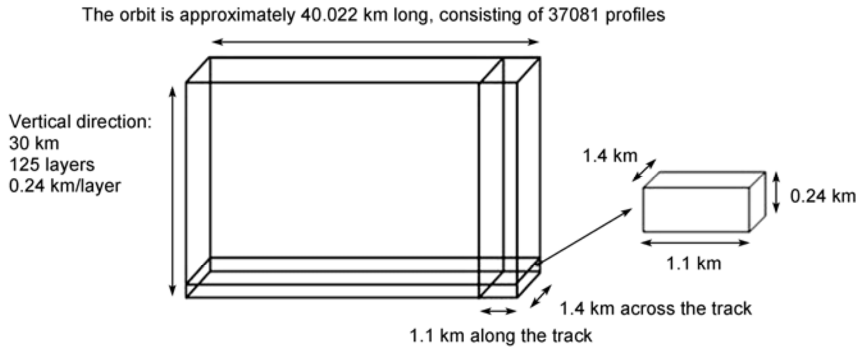

Figure 1 The orbit of CloudSat.

Table 1 Explanation of CPR_Cloud_mask

Value	Explanation
0	No cloud detected
1	Likely bad data
5	Likely ground clutter
5–10	Weak detection found
20–40	Cloud detected; the larger value, the smaller the chance of a false detection

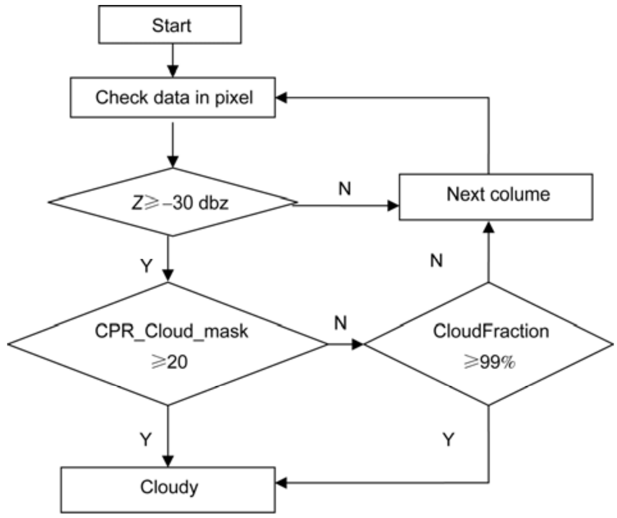

Figure 2 The schematic of cloud determination.

Data of Radar_Reflectivity are logarithmic values of radar reflectivity factor with unit dBZ. The minimum detectable signal of the CPR is about −30 dBZ. Data of CloudFraction are the fraction of cloud within a CPR pixel detected by the CALIPO lidar. Therefore, when the data of each pixel satisfy Radar_Reflectivity ⩾–30 dBZ and CPR_Cloud_mask ⩾20, or Radar_Reflectivity ⩾–30 dBZ, CPR_Cloud_mask ⩽20 and CloudFraction ⩾99%, we assume cloud in the pixel. This procedure is shown Figure 2.

Figure 3 shows the five study regions in Eastern Asia, divided according to local climatic characteristics; Eastern Asia is the sixth region. These are northern regions (North), southern regions (South), northwest regions (NW), Western regions (West), eastern oceans (EO), and all of Eastern Asia (Total). We defined an area consisting of 50 scanning profiles as a subregion. Each subregion has an area of 50 (number of profiles) × 1.1 km (along track) × 1.4 km (cross track) × 125 (vertical layer numbers) × 0.24 km (layer thickness). After the calculation of decorrelation depth in each subregion, the statistic characteristics of the six study regions were analyzed.

2 Method

2.1 Scheme description

In most climate models, the commonly used cloud overlap scheme is maximum overlap, random overlap, or their combination. Maximum overlap considers the overlapping area of a cloud block as the maximum. Random overlap considers locations of cloud blocks as completely random. In their combination, with adjacent cloud layers, such clouds are assumed the same cloud and have maximum overlap; when two cloud blocks are separated by at least one clear-sky layer, they are assumed to have random distribution. Hogan and Illingworth [19] proposed a new cloud overlap hypothesis-general overlap. It assumes the actual total cloud amount is between maximum and random overlap, which makes the expression of cloud overlap closer to reality. This scheme determines the cloud overlap relationship according to vertical correlation between cloud layers.

If C_k and C_l stand for the cloud amount of two cloud layers, and $C_{k,l}$ is their total cloud amount, the general overlap hypothesis can be expressed as

$$C_{k,l} = \alpha_{k,l} C_{k,l}^{\max} + (1-\alpha_{k,l}) C_{k.l}^{ran}, \tag{1}$$

where $C_{k,l}^{\max} = \max(C_k, C_l)$ and $C_{k,l}^{ran} = C_k + C_l - C_k C_l$. $\alpha_{k,l}$ is called the overlapping parameter, which indicates the degree of overlap of two layers. The larger the $\alpha_{k,l}$, the larger overlapping area between the two layers k and l. The overlapping parameter can be expressed as [19]:

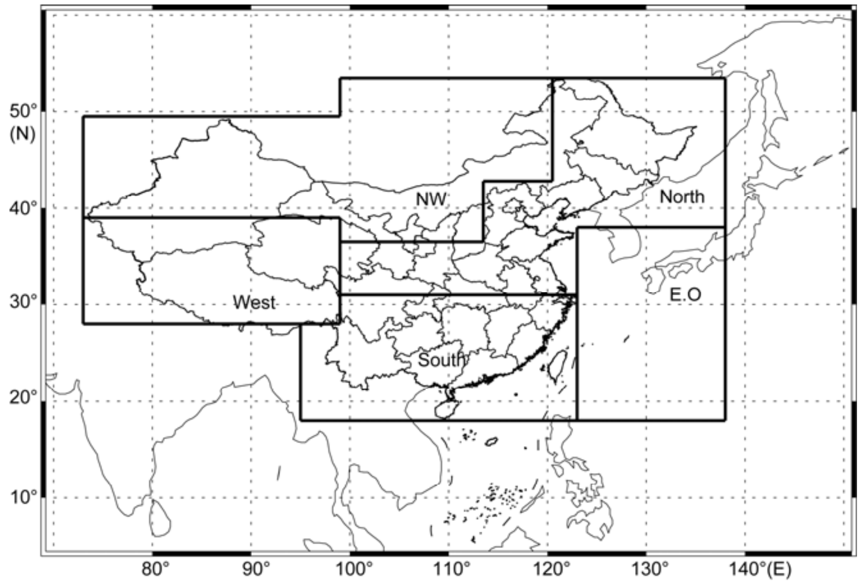

Figure 3 The schematic of regional divisions in this work.

$$\alpha_{k,l} = \exp\left(-\int_{Z_k}^{Z_l} \frac{\mathrm{d}Z}{L_{cf}(Z)}\right), \tag{2}$$

where Z is height of the cloud layer and $L_{cf}(Z)$ is the so-called decorrelation depth L_{cf}. In the following, L_{cf}^* stands for the retrieved value of decorrelation depth. L_{cf} indicates the distance at which $\alpha_{k,l}$ decays to e^{-1}, where e is the natural exponential. $\alpha_{k,l}$ must be greater than 0. Since $\alpha_{k,l} = \frac{C_{k,j} - C_{k,l}^{ran}}{C_{k,l}^{\max} - C_{k,l}^{ran}}$, if the total cloud amount of the two cloud layers is less than 100% and they do not completely overlap each other, then $C_{k,l} > C_{k,l}^{ran}$. This makes $\alpha_{k,l}$ smaller than 0, since $C_{k,l}^{\max} < C_{k,l}^{ran}$. This situation is not proper for definition of the overlapping parameter. It is also not proper if $\alpha_{k,l}$ equals 0, since the cloud amount of any layer is equal to 1. However, such situations rarely occur.

When given a cloud vertical profile in a GCM grid, we coupled SCG into CAM3.0 of the NCAR global atmospheric GCM to simulate sub-grid cloud structure, by which the cloud amount of such a grid was obtained. Using SCG, three initial conditions must be set—the cloud overlap hypothesis, cloud vertical profile, and value of L_{cf}. SCG can simulate high resolution, 3D sub-grid cloud structure, based on the cloud vertical profile (cloud cover, water/ice content of each model layer) in a model grid. The average of all the sub-grids must be consistent with the previous set grid mean, though the locations of sub-grid clouds can be different. Based on the general overlap hypothesis and by inputting the cloud vertical profile obtained from CloudSat data, SCG generates the cloud sub-grid structure with a defined total cloud amount, for a given value of L_{cf}. Therefore, we obtained a functional relationship between cloud amount and L_{cf}, denoted as $\hat{C}(L_{cf})$. By changing the value of L_{cf}, $\hat{C}(L_{cf}^*)$ changes accordingly; when $\hat{C}(L_{cf}^*)$ is equal to the total cloud amount from CloudSat data, L_{cf}^* is then considered the scaled parameter that properly represents cloud overlap in the grid. The basic physics of this method is such that realistic sub-grid cloud structures can be simulated by SCG, as long as the general overlap hypothesis is nearly true.

By checking CloudSat data from 2007 to 2009, we found the global mean sea level altitude in the 105th among 125 radar scanning layers. Therefore, only information from the top layer to 104th layer was used. However, the number of sub-grids in three spatial directions must be set in SCG to simulate the 3D sub-grid cloud structures; a larger sub-grid number generally results in better cloud sub-grid structure simulation [21–23]. Along with setting the sub-grid number in the vertical direction to 104 (corresponding to the layer number of data), we set the sub-grid number in the portrait direction to 1. Consequently, the sub-grid number in the landscape direction is the only parameter that influences 3D cloud simulation in SCG. We have checked the impact on the result by considering different sub-grid numbers in the landscape direction. It was found that when the sub-grid number is progressively increased from 1000, 2000, 5000 to 10000, biases of L_{cf}^* decrease from 0.01 to 0.001. However, when the sub-grid number is continuously increased to 20000, biases are maintained at 0.001. Therefore, we chose

10000 as the sub-grid number in the landscape direction. In the following, we define the area consisting of 50 CPR profiles as a subregion. Therefore, a subregion contains 50 (number of profiles) × 1.1 km (along track) × 1.4 km (cross track) × 104 (number of vertical layers) × 0.24 km (vertical layer thickness). Each subregion was divided into 3D sub-grids of (104 × 1 × 1000), in that cloud sub-grid structures and total cloud amount were generated by SCG.

2.2 Approach to obtain L_{cf}^*

The subregion range from 33.48°N, 98.73°E to 34.44°N, 98.46°E was chosen within orbit 03609 of January 2007. Total cloud amount in this subregion was 0.85, according to CloudSat data. The observed vertical profile of cloud amount is shown in Figure 4(a) as the dotted line. In SCG calculations, by gradually changing L_{cf} input from 0.1 to 10 km at an interval of 0.1 km, we obtain the function of $\hat{C}(L_{cf}^*)$, shown in Figure 4(b). In Figure 4(b), the simulated cloud amount is 0.848 when L_{cf}^* =0.6 km, which is closest to the observed value of 0.85. Therefore, we take $L_{cf}^* = 0.6$ km as the decorrelation depth in this subregion, and the corresponding simulated cloud vertical profile from SCG is also shown in Figure 4(a). The error bar represents the difference between the simulated cloud vertical profile and observed cloud results (dotted line). The differences are within a very small range of 0.01 to 0.07, which shows that the cloud profile simulated by SCG agrees well with observations.

3 Result and discussion

3.1 Decorrelation depth

After checking the feasibility of the research method in a single subregion, we calculated the L_{cf}^* of all the subregions (Figure 5). L_{cf}^* is generally within the range 0–3 km for most subregions (over 90%); in only a few cases, it was as large as 9 km. This result agrees with previous studies [20]. To obtain all characteristics for each region, mean values of L_{cf}^* in the six study regions were calculated. Table 2 lists the sampling numbers and mean values of L_{cf}^* in these regions, in four seasons from 2007 to 2009. In addition, L_{cf}^* are categorized into 20 groups based on cloud amount in the subregions from $\hat{C} \in [0, 0.05)$ to $\hat{C} \in [0.95, 1.0)$, with step 0.05. The result of $\hat{C} = 1$ was removed, because it does not satisfy eq. (2). The frequency of occurrence of $\hat{C} = 1$ in different study regions is within 10%−15%. However, sample numbers of the remaining subregions still meet the requirement of this study. Figure 5 shows mean values of L_{cf}^* as a function of cloud amount in the study regions, over the four seasons.

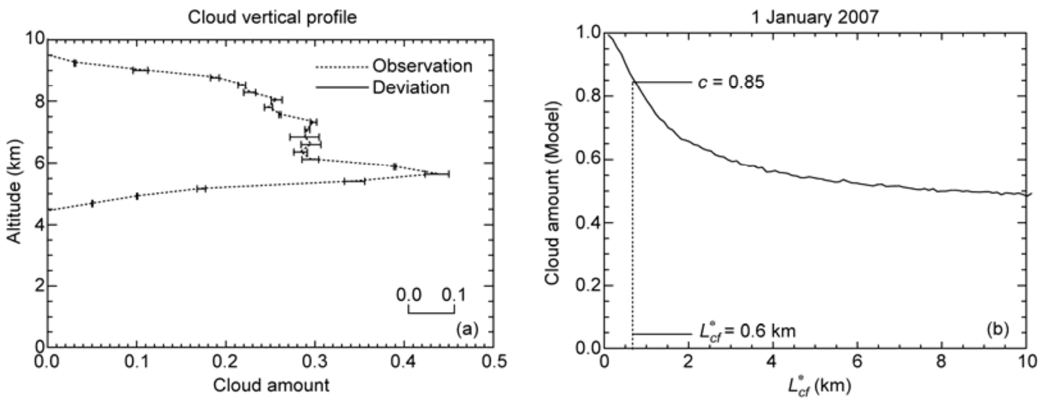

Figure 4 (a) Differences of observed and generated cloud amount at different altitudes; (b) cloud function as L_{cf} $(\hat{C}(L_{cf}))$ at subregions from 33.48°N, 98.73°E to 34.44°N, 98.46°E.

Table 2 The mean value of L_{cf}^* and number of subregions for six regions in four seasons

	Total	NW	North	South	West	E.O
Spring	0.97 km/48608	1.00 km/11572	0.98 km/8443	0.83 km/7801	1.00 km/8285	1.04 km/12507
Summer	1.11 km/53815	1.35 km/12846	1.00 km/9166	0.95 km/8448	1.14 km/9259	1.11 km/14096
Autumn	1.03 km/40474	1.12 km/9240	0.98 km/7331	0.82 km/6595	1.03 km /6671	1.22 km/10637
Winter	0.95 km/44002	0.99 km/9785	1.10 km/7917	0.69 km/7196	0.91 km/7451	1.13 km/11653

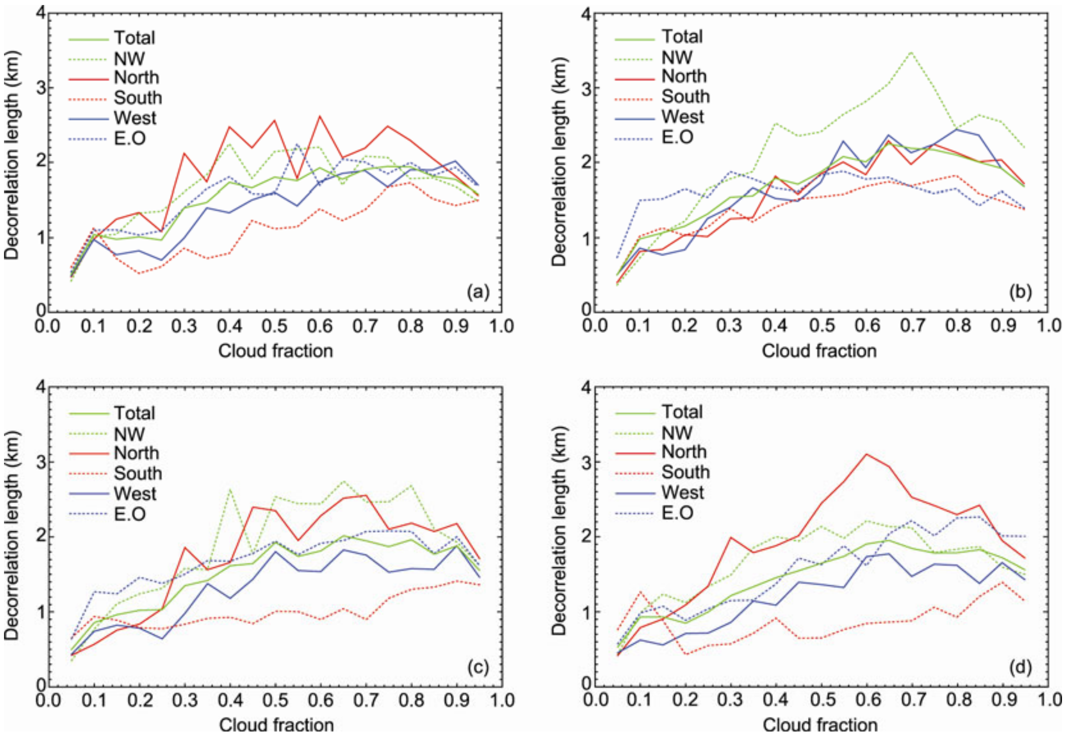

Figure 5 The mean value of L_{cf}^{*} as functions of cloud amount for six regions in spring (a), summer (b), autumn (c), and winter (d).

With increasing cloud amount, generally L_{cf}^{*} first increases, then decreases. The peak L_{cf}^{*} was in subregions with cloud amount between 0.6 and 0.8. Average peak values of L_{cf}^{*} in the six regions were 2.12, 2.33, 2.04 and 2.15 km for spring, summer, autumn and winter, respectively. When subregion cloud amounts were between 0.2 and 0.9, L_{cf}^{*} was generally larger at higher latitudes (such as North and NW) than at lower latitudes (such as South, EO). When subregion cloud amounts were 0.4–0.9, L_{cf}^{*} in the North and NW were still greater than in the EO, with differences of 0 to 3 km. With subregion cloud amounts less than 0.2, L_{cf}^{*} in the North and NW was equal to or slightly smaller than in the South and EO, with differences less than 0.5 km. Generally, L_{cf}^{*} in West was slightly larger than in the South and EO in summer, but between the values of those two regions in the remaining seasons.

For seasonal variation, L_{cf}^{*} in the NW, West and South, which are in the western part of Eastern Asia, were maximum in summer, smaller in spring and autumn, and minimum in winter. In summer, peak values of L_{cf}^{*} in the NW, Tibetan Plateau and South were 3.42, 2.41 and 1.85 km, which appeared near subregions with cloud amounts 0.72, 0.83, 0.81, respectively. In winter, peak values decreased to 2.22, 1.75 and 1.38 km, respectively, which all appeared near subregions with cloud amount 0.6. The L_{cf}^{*} in the EO and North, which are in the eastern part of Eastern Asia, were maximum in winter, smaller in spring and autumn, and minimum in summer. In summer, the peak values of L_{cf}^{*} in the EO and North were 1.82 and 2.28 km, respectively, appearing near subregions with cloud amounts 0.62 and 0.86; in winter, peak values increased to 2.28 and 3.15 km, and appeared near subregions with cloud amounts 0.62 and 0.86, respectively. The L_{cf}^{*} in West varied dramatically between summer and winter. The peak was 1.78 km and appeared near subregions with cloud amount 0.66 in winter, whereas in summer the peak significantly increased to 2.45 km, and appeared near subregions with cloud amount 0.78.

Compared to the South and EO (regions partly or completely composed of oceans), the North and NW (inland regions) are less moist, and the property of controlling air mass is relatively simple. Therefore, in the North and NW, clouds at different heights tend to be closer, but not greatly spread out. These clouds thus have greater vertical overlap, resulting in a larger L_{cf}^{*}. The seasonal variations of L_{cf}^{*} across study regions show that clouds in the NW and South have greater vertical overlap in summer, and clouds in the North greater overlap in winter. As stated earlier, there is significant L_{cf}^{*} change between winter and summer in West. This could be related to the character of the Tibetan Plateau. In winter, dynamic and thermal effects of this plateau produce higher humidity and more cloud compared to other regions that are under control of the East Asian winter monsoon. This causes complex cloud formation and variation, and lower relevance between vertical cloud blocks. However in summer, because of a strong heat source from solar radiation, the plateau has more convective clouds that have greater vertical relevance to each other, and this leads to a larger L_{cf}^* in that season. This phenomenon becomes more obvious when the cloud amount of this subregion is within 0.6–0.8.

Next, L_{cf}^* and the grid mean cloud vertical profiles obtained from CloudSat for all six subregions were input into SCG. We wished to discover whether the simulated cloud profiles were close to observations. The vertical distributions of mean cloud amount for each layer in the six regions from CloudSat are shown in Figure 6, for the four seasons. The error bar shows the difference between simulated and observed results, with a maximum value less than 0.02. Therefore, similar to the single subregion result, the simulated total cloud amount is close to the observed. The simulated mean cloud amounts at different layers also approximate the observations. The results shown in Figure 6 also indicate that the selection of grid number 10000 in the landscape direction is suitable for simulating cloud amount.

In most GCMs, L_{cf}^* is generally set to 2 km, with no seasonal variation or geographic distribution. To evaluate the impact of this simple setting on cloud amount in climate models, we analyzed the difference between observed cloud amount C_{obs} and simulated cloud amount C_{mod}. Figure 7 shows results of $D = C_{\text{mod}} - C_{\text{obs}}$ for the six regions, in different seasons. The gray lines show results of individual subregions, and colored lines the regional averages. The values of D are generally large for any individual subregion. Among all subregions, 82% of D values are less than 0.1, 12% are from 0.1–0.2, and 6% are larger than 0.2. The peak value of D exceeds 0.4. However, the regional average of D is small, generally between 0.05 and 0.15 across different regions. For the study regions, Table 3 lists maxima of regional average D in the four seasons, and related cloud amounts. Figure 7 and Table 3 demonstrate that simply setting $L_{cf}^* = 2$ km can cause errors in simulated cloud amount. Therefore, accurate parameterization of L_{cf}^* by considering geographical and seasonal variation is necessary.

3.2 Sensitivity of cloud radiative forcing to L_{cf}^*

Based on the analysis of geographical distribution and seasonal variation of L_{cf}^*, we now address the impact of L_{cf}^* on the simulation of cloud radiative effect in the GCM, especially for cloud radiative forcing (CRF). CRF is defined as the difference in net radiative flux between cloudy and cloud-free conditions. This definition is applicable at the top of the atmosphere and at the surface [27]. SCG is coupled with CAM3/NCAR to conduct sensitivity tests, by setting $L_{cf}^* = 1$, 2, and 3 km. These values are within the range of observed results shown in Figure 4. The model was run for

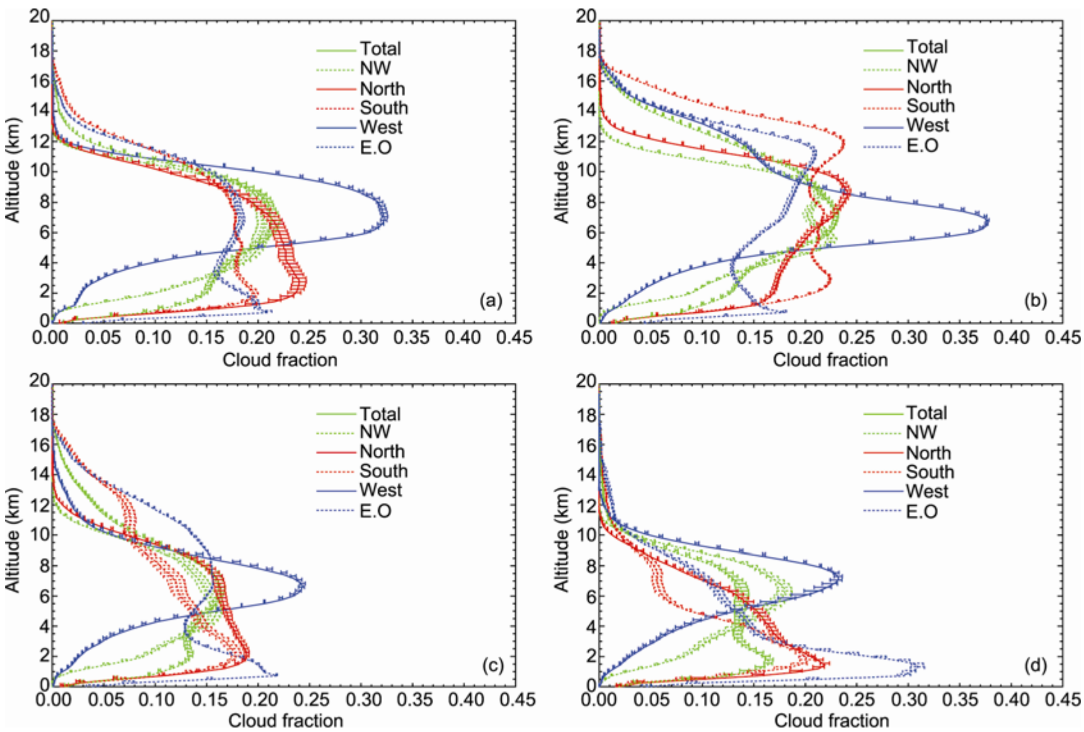

Figure 6 The observational cloud amount as function of altitude for six regions during spring (a), summer (b), autumn (c), and winter (d). Here, error bars are the differences between the simulations and observations.

Table 3 The peak value of average differences of cloud amounts between simulations and observations, and observed cloud amounts of subregions where the peak value occurs for six regions in four seasons

	Total		NW		North		South		West		E.O	
	D	Cloud amount	*D*	Cloud amount	*D*	Cloud amount	*D*	Cloud amount	*D*	Cloud amount	*D*	Cloud amount
Spring	–0.11	0.68	–0.12	0.85	–0.06	0.85	–0.12	0.72	–0.16	0.56	–0.08	0.54
Summer	–0.12	0.85	–0.11	0.86	–0.12	0.65	–0.11	0.85	–0.13	0.84	–0.13	0.87
Autumn	–0.10	0.83	–0.08	0.44	–0.09	0.46	–0.11	0.44	–0.13	0.86	–0.13	0.86
Winter	–0.12	0.76	–0.08	0.76	–0.08	0.82	–0.13	0.76	–0.17	0.76	–0.08	0.74

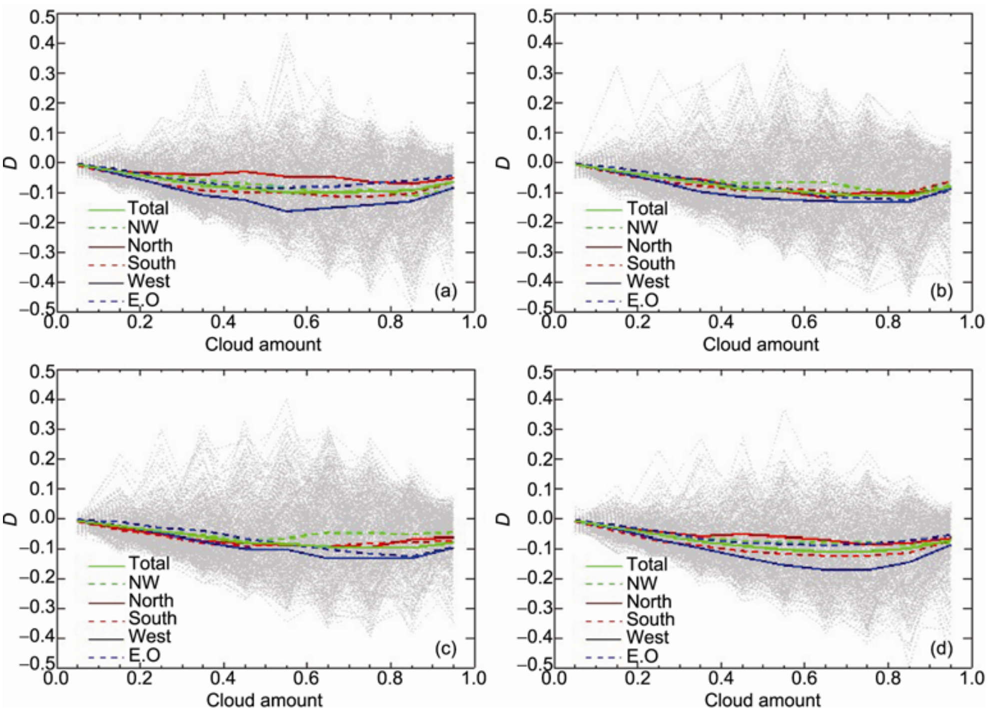

Figure 7 The differences of cloud amount between simulations and observations changes with cloud amounts when L_{cf}^{*} = 2 km in six regions for spring (a), summer (b), autumn (c) and winter (d).

September 1999 to December 2000. Taking the run of the first four months as the model adjustment time, the analysis is based on the remaining period. The CRF results based on $L_{cf}^{*}=2$ km were taken as the reference, and CRF differences between different L_{cf}^{*} were investigated. Figure 8 shows the longwave CRF in winter (January) of 2000. Figure 8(a) is the result of $L_{cf}^{*}=2$ km, Figure 8(b) and (c) shows differences between $L_{cf}^{*}=1$ km and $L_{cf}^{*}=2$ km, and between $L_{cf}^{*}=3$ km and $L_{cf}^{*}=2$ km, respectively. It is seen that CRF is sensitive to L_{cf}^{*} across different regions, especially in several major monsoon zones. Figure 8(b) shows that the difference of long-wave CRF between $L_{cf}^{*}=1$ km and $L_{cf}^{*}=2$ km exceeded –40 W m^{-2} over large oceanic areas, located in the east of middle Africa and east of South America. While Figure 8(a) shows that the long-wave CRF of $L_{cf}^{*}=2$ km in these two areas were between 50 and 90 W m^{-2}. The long-wave CRF in Southeast Asia monsoon regions was 80–100 W m^{-2} for $L_{cf}^{*}=2$ km, and the difference between $L_{cf}^{*}=1$ km and $L_{cf}^{*}=2$ km was generally positive, with the maximum exceeding 40 W m^{-2}. The difference between $L_{cf}^{*}=1$ km and $L_{cf}^{*}=2$ km in the mid-East Pacific is generally negative, with the maximum exceeding 50 W m^{-2}. Figure 8(c) shows that the difference in long-wave CRF over the mid-East Pacific has a negative contour, with absolute value over 50 W m^{-2}. This difference in central and western Africa, South Asia including the Tibetan Plateau, and the western Pacific is entirely negative, with absolute value over 20 W m^{-2}. There was a strong positive difference in Southeast Asia, with maximum over 50 W m^{-2}.

Figure 9 shows corresponding results for summer (July). Again, the longwave CRF in principal monsoon regions was very sensitive to L_{cf}^{*}. Compared to January, the sensitivity

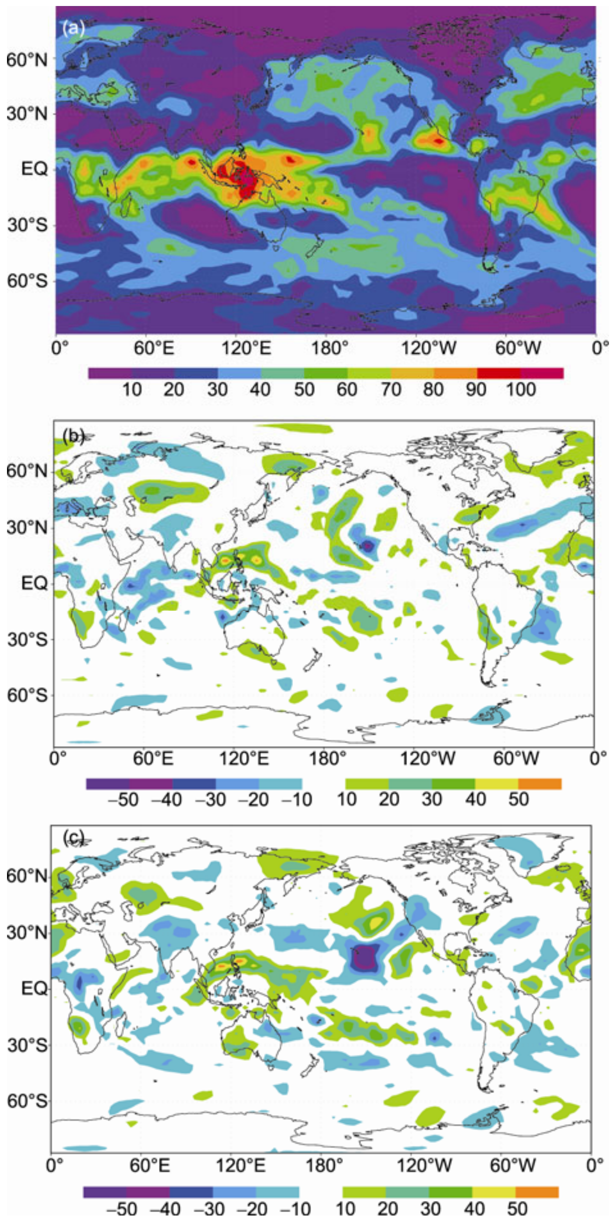

Figure 8 (a) Long wave CRFs in January 2000 (unit: W m^{-2}) when L_{cf}^{*} =2 km; (b) the difference of CRFs between L_{cf}^{*} =1 km and L_{cf}^{*} =2 km; and (c) the difference of CRFs between L_{cf}^{*} =1 km and L_{cf}^{*} =3 km.

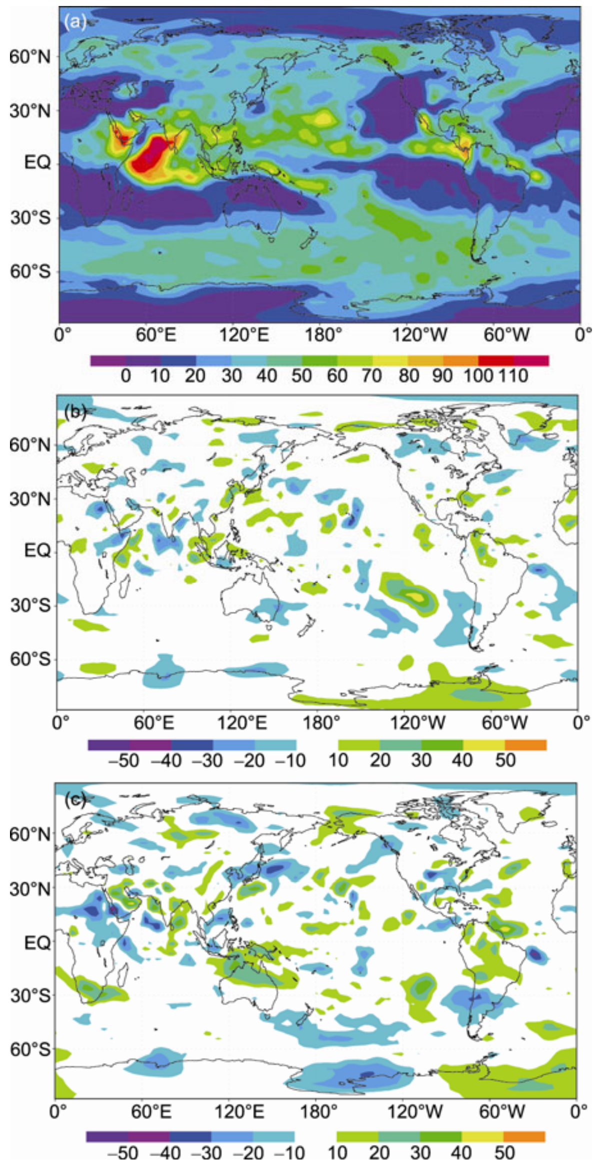

Figure 9 Same as in Figure 8, but for July 2000.

at high-latitude regions, such as Siberia, Canada and part of Antarctica, increased significantly. In summary, variation of L_{cf}^{*} could cause substantial differences in longwave CRF within climate models.

Figure 10 reveals shortwave CRF results for January 2000. Figure 10(a) shows shortwave CRF for $L_{cf}^{*}=2$ km, and Figure 10(b) and (c) shows differences between $L_{cf}^{*}=1$ km and $L_{cf}^{*}=2$ km, and between $L_{cf}^{*}=3$ km and $L_{cf}^{*}=2$ km. Figure 11 shows the corresponding result for July. Compared to the long-wave results, short-wave CRF is more sensitive to L_{cf}^{*}. Figure 10 shows that CRF in the major monsoon regions and mid-East Pacific were highly dependent on L_{cf}^{*}. The greatest difference in shortwave CRF was in the Southeast Asia monsoon region, with over 50 W/m^2. The largest positive difference was in the mid-East Pacific, with over 50 W m^{-2}. Comparison of Figure 10(b) and (c) shows that the difference in short-wave CRF was generally larger between $L_{cf}^{*}=3$ km and $L_{cf}^{*}=2$ km than between $L_{cf}^{*}=1$ km and $L_{cf}^{*}=2$ km. In July, there were obvious differences in the Southeast Asia monsoon region and mid-East Pacific. The difference in shortwave CRF between $L_{cf}^{*}=1$ km and $L_{cf}^{*}=2$ km was mainly in the East

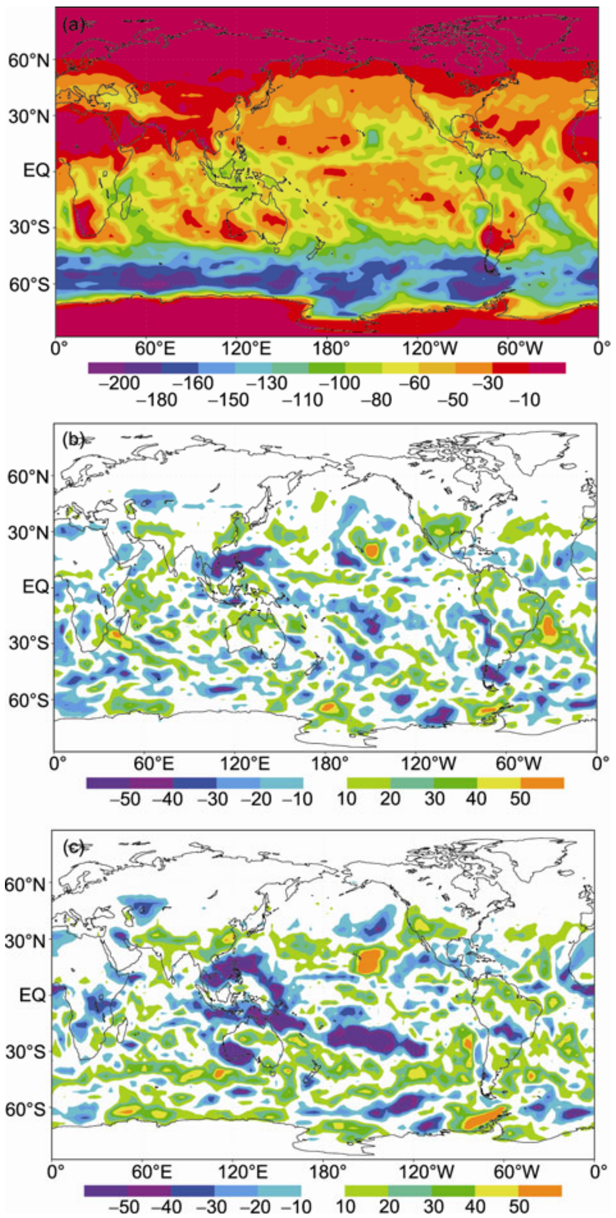

Figure 10 Same as in Figure 8, but for shortwave.

Asian monsoon regions, Central Australia and northern part of North America, whereas the corresponding difference between $L_{cf}^*=3$ km and $L_{cf}^*=2$ km was mainly in Northeast Africa, West-central Russia and Central Asia, with maximum difference in absolute value over 50 W m^{-2}.

The above sensitivity tests show that both the intensity and distribution of model-simulated CRF can be strongly affected by varying L_{cf}^*, especially in the major monsoon regions and mid-East Pacific. This demonstrates the importance in searching the correct L_{cf}^* in climate models. L_{cf}^* was fixed in the above sensitivity test, without geographical or seasonal variation, since the object was to

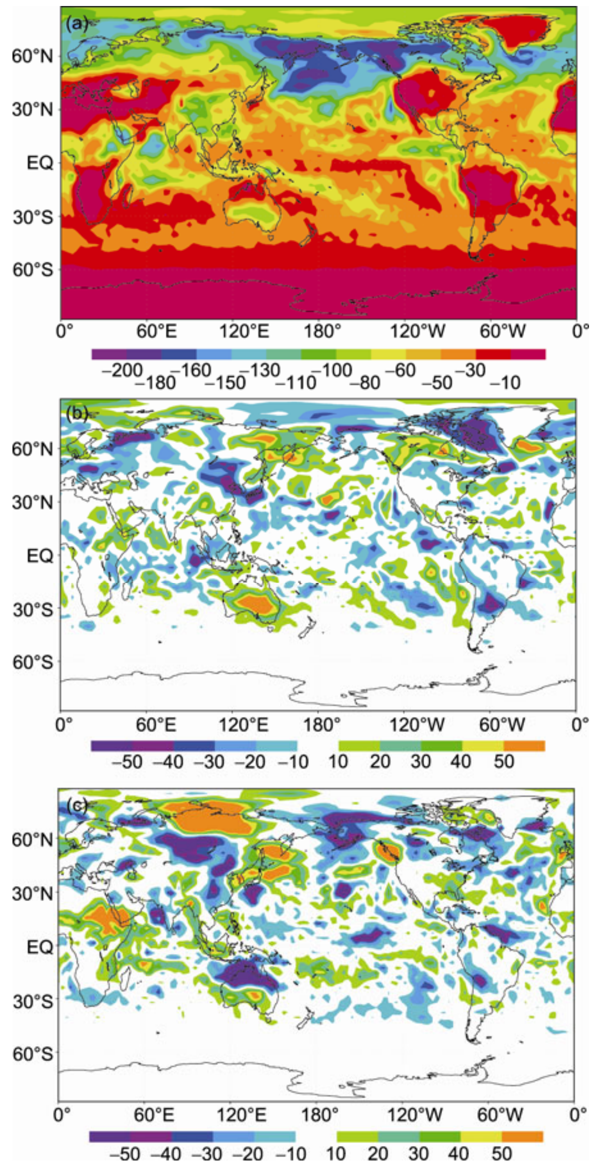

Figure 11 Same as in Figure 9, but for shortwave.

demonstrate the influence of L_{cf}^* on CRF. We believe that more interesting results will emerge with use of a true geographically and seasonally dependent L_{cf}^*.

4 Conclusions

Using a three-year CloudSat dataset and combining SCG with a climate model, we calculated the spatial distribution and seasonal variation of decorrelation depth L_{cf}^* for the first time in Eastern Asia. L_{cf}^* is the key parameter for vertical cloud overlap structure. The effect of L_{cf}^* on simulated CRF was discussed. The following are the main conclusions:

(1) L_{cf}^* in six study regions was generally from 0–3 km. By categorizing L_{cf}^* by cloud amount in subregions, its peak value appeared near subregions with cloud amount between 0.6 and 0.8. The average peak value was 2.5 km.

(2) Regarding spatial variation, L_{cf}^* at higher altitudes (North and NW regions) was generally greater than at lower latitudes (West and South regions), and results for the EO and Total regions were intermediate. As cloud amount in subregions changed from 0 to 1.0, the difference of L_{cf}^* between its maximum and minimum in the six regions was 0–1.6 km, 0–2 km, 0–1.7 km, and 0–2.4 km in spring, summer, autumn and winter, respectively.

(3) For seasonal variation, L_{cf}^* in the NW and West, which are in the western part of East Asia, was maximum in summer, smaller in spring and autumn, and minimum in winter. L_{cf}^* in the EO and North, which are in the eastern part of East Asia, was maximum in winter, smaller in spring and autumn, and minimum in summer.

(4) Using a constant $L_{cf}^* = 2$ km to simulate sub-grid cloud structure can result in error over 15% in cloud amount estimation, which can substantially influence CRFs.

(5) L_{cf}^* significantly affected long-wave and short-wave CRFs, especially in several principal monsoon regions and the western part of East Asia, where the CRF difference reached 40–50 W m^{-2}. This indicates the importance of accurate parameterization of L_{cf}^*, with realistic geographical and seasonal variation. This should be a direction for future study.

We are thankful to the NASA CloudSat project and CloudSat data processing center for providing us the CloudSat data used in this study, we also would like to thank Dr. Howard Barker of Environment Canada for providing the SCG code. This work was supported by National Basic Research Program of China (Grant No. 2011CB403405), National Natural Science Foundation of China (Grant No. 41075056), and Public Meteorology Special Foundation of MOST (Grant No. GYHY201106022).

1 Ramanathan V, Cess R D, Harrison E F, et al. Cloud-radiative forcing and climate: Results from the earth radiation budget experiment. Science, 1989, 243: 57–63
2 Wang H Q, Zhao G X. Cloud and radiation. Sci Atmos Sin, 1994, 18(Suppl): 910–932
3 Ding S G, Zhao C S, Shi G Y, et al. Analysis of global total cloud amount variation over the past 20 years. J Appl Meteorol, 2005, 16: 670–676
4 Sun B, Groisman P Y. Cloudiness variations over the former Soviet Union. Int J Climatol, 2000, 20: 1097–1111
5 Houghton J T, Ding Y, Griggs D J, et al. Climate Change: The Scientific Basis. New York: Cambridge University Press, 2001. 1–421
6 Wetherald R T, Manabe S. Cloud feedback processes in a general circulation model. J Atmos Sci, 1988, 45: 1397–1415
7 Houghton J T, Ding Y, Griggs D J, et al. Climate Change: The Scientific Basis. Cambridge: Cambridge University Press, 2001. 148–149
8 Zhang H, Jing X W. Effect of cloud overlap assumptions in climate models on modeled earth-atmosphere radiative fields (in Chinese). Chin J Atmos Sci, 2010, 34: 520–532
9 Jing X W, Zhang H, Guo P W. A study of the effect of sub-grid cloud structure on global radiation in climate models (in Chinese). Acta Meteorol Sin, 2010, 67: 1058–1068
10 Manabe S, Strickler R F. Thermal equilibrium of the atmosphere with a convective adjustment. J Atmos Sci, 1964, 21: 361–385
11 Geleyn J F, Hollingsworth A. An economical analytical method for the computation of the interaction between scattering and line absorption of radiation. Cont Atmos Phys, 1979, 52: 1–16
12 Morcrette J J, Fouquart Y. The overlapping of cloud layers in shortwave radiation parameterizations. J Atmos Sci, 1986, 43: 321–328
13 Barker H W, Stephens G L, Partain P T, et al. Assessing 1D atmospheric solar radiative transfer models: Interpretation and handling of unresolved clouds. J Clim, 2003, 16: 2676–2699
14 Morcrette J J, Jakob C. The response of the ECMWF model to changes in cloud overlap assumption. Mon Weather Rev, 2000, 128: 1707–1732
15 Tian L, Curry J A. Cloud overlap statistics. J Geophys Res, 1989, 94: 9925–9935
16 Barker H W, Stephens G L, Fu Q. The sensitivity of domain-averaged solar fluxes to assumptions about cloud geometry. Q J R Meteorol Soc, 1999, 125: 2127–2152
17 Li J. Accounting for unresolved clouds in a 1D infrared radiative transfer model. Part I: Solution for radiative transfer, cloud scattering, and overlap. J Atmos Sci, 2002, 59: 3302–3320
18 Liang X Z, Wang W C. Cloud overlap effects on general circulation model climate simulations. J Geophys Res, 1997, 102: 11039–11047
19 Hogan R J, Illingworth A J. Deriving cloud overlap statistics from radar. Quart J Roy Meteor Soc, 2000, 128: 2903—2909
20 Barker H W. Overlap of fractional cloud for radiation calculations in GCMs: A global analysis using CloudSat and CALIPSO data. J Geophys Res, 2008, 113: D00A01
21 Räisänen P, Barker H W, Khairoutdinov M, et al. Stochastic generation of subgrid-scale cloudy columns for large-scale models. Q J R Meteorol Soc, 2004, 130: 2047–2068
22 Barker H W, Räisänen P. Radiative sensitivities for cloud structural properties that are unresolved by conventional GCMs. Q J R Meteorol Soc, 2005, 131: 3103–3122
23 Räisänen P, Barker H W, Cole J N S. The Monte Carlo Independent Column Approximation's conditional random noise: Impact on simulated climate. J Clim, 2005, 18: 4715–4730
24 Pincus R H, Klein S A. Using stochastically generated subcolumns to represent cloud structure in a large scale model. Mon Weather Rev, 2006, 134: 3644–3656
25 Räisänen P, Järvenoja S, Järvinen H, et al. Tests of Monte Carlo independent column approximation in the ECHAM5 atmospheric GCM. J Clim, 2007, 20: 4995–5011
26 Morcrette J J, Barker H W, Cole J N S, et al. Impact of a new radiation package, McRad, in the ECMWF Integrated Forecasting System. Mon Weather Rev, 2008, 136: 4773–4798
27 Shi G Y. Atmospheric Radiation (in Chinese). Beijing: Science Press, 2007. 302–318

中国科学: 地球科学　2013 年　第 43 卷　第 4 期: 523 ~ 535
www.scichina.com　earth.scichina.com
《中国科学》杂志社
SCIENCE CHINA PRESS

自然科学基金项目进展专栏

论 文

东亚地区云的垂直重叠特性及其对云辐射强迫的影响

张华[①③*], 彭杰[①②③], 荆现文[①③], JiangNan LI[④]

① 中国气象科学研究院, 北京 100081;
② 南京信息工程大学, 南京 210044;
③ 中国气象局气候研究开放实验室, 国家气候中心, 北京 100081;
④ Canadian Center for Climate Modeling and Analysis, University of Victoria, Victoria, BC, Canada
* E-mail: huazhang@cma.gov.cn

收稿日期: 2011-10-10; 接受日期: 2012-06-14
国家自然科学基金(批准号: 41075056)、国家重点基础研究计划课题(编号: 2011CB403405)和科技部公益性行业(气象)科研专项课题(编号: GYHY201106022)资助

摘要　本文通过对云观测卫星-CloudSat 的 2007~2009 年 3 年的观测资料的分析, 研究了东亚地区的云的垂直结构. 首次计算了在气候模式的云辐射过程中表征云的垂直结构特征的一个重要参数: 抗相关厚度 L_{cf}^{*}. 本文结果表明: 6 个研究域的抗相关厚度基本处于 0~3 km 的范围之中, 根据研究子域的云量不同来划分, 抗相关厚度极值出现在云量为 0.6~0.8 的子域附近, 平均约为 2.5 km. 6 个研究域的 L_{cf}^{*} 纬向差异明显, 处于较高纬度的北方地区和西北地区的 L_{cf}^{*} 整体大于较低纬的青藏高原地区和南方地区, 而东部海域和东亚地区介于两者之间. 不同季节之间的差异表明东亚地区研究域和位于东亚地区西部的西北地区, 青藏高原地区和南方地区三个研究域的 L_{cf}^{*} 具有夏季最大, 春、秋次之, 冬季最小的特点; 位于东亚地区较东部的东部海域和北方地区研究域的 L_{cf}^{*} 则呈现出冬季最大, 春秋次之, 夏季最小的特点. 其次, 利用全球气候模式研究了不同的 L_{cf}^{*} 值对模拟的云辐射强迫的影响, 研究结果表明, 不同 L_{cf}^{*} 取值对模拟的云辐射强迫有很大影响, 特别是对全球几个主要的季风区和中东太平洋地区的影响非常大, 最高达 40~50 W m^{-2} 左右. 因此, 在气候模式中精确描述云的垂直重叠结构对提高云辐射强迫模拟精度及其反馈有重要的意义.

关键词
云重叠方案
抗相关厚度
CloudSat 云观测卫星
随机云生成器
云辐射

云的形成与分布是大气各种热力、动力过程和地表过程共同作用的结果[1~4], 在地气系统中起着重要的作用[5], 是调节地球辐射平衡和全球水汽与水分循环的重要因子, 对气候变化有着重要影响. 但是对于

中文引用格式:　张华, 彭杰, 荆现文, 等. 东亚地区云的垂直重叠特性及其对云辐射强迫的影响. 中国科学: 地球科学, 2013, 43: 523–535
英文引用格式:　Zhang H, Peng J, Jing X W, et al. The features of cloud overlapping in Eastern Asia and their effect on cloud radiative forcing. Science China: Earth Sciences, 2013, 56: 737–747, doi: 10.1007/s11430-012-4489-x

云的描述与模拟一直是气候模式中的薄弱环节[6,7], 使得云成为气候模拟和气候变化研究中最大的不确定因子之一. 因此, 气候模式作为气候变化研究的重要工具, 精确的描述云及云辐射过程是提高其对气候模拟能力的重要方面, 可以最大程度地减少云辐射反馈的不确定性.

在气候模式对云辐射过程的模拟中, 云量垂直分布的不确定性是研究云对气候影响的最大障碍之一. 地表观测表明[2], 云层常常是重叠的, 多层云的重叠问题对大气和地表的辐射加热(或冷却)率有很大影响, 而云的加热率不仅影响云的发展, 也对大气和地表的辐射收支平衡产生重要影响[8,9]. 目前, 在大气环流模式(GCM)中, 小于 GCM 网格分辨率的云是不能被分辨的, 必须用一定的次网格参数化来描述. 到目前为止还没有普遍适用的理论来描述次网格尺度上不同高度的云应该怎样重叠, 所以, 必须事先规定云在垂直方向上的相关性. GCM 发展至今, 最常用的云重叠假定分别为: 最大重叠, 随机重叠以及最大/随机重叠方案的组合[10~13]. 三种假设之中, 最大/随机重叠的组合方案与观测的云分布的统计特征最接近[14]. 但是, 由于观测资料的限制, 还不能完全支持这种假定[15].

Barker 等[16]用云分辨模式(CRM)对对流云实施了高精度的蒙特卡罗(Monte Carlo)模拟, 发现模式云的重叠不同于通常假定的最大/随机重叠, 导致短波通量差别高达 100 W m^{-2}; Li[17]发现, 在一些代表性的研究中, 由 GCM 中通常使用的重叠方案带来的辐射通量误差可以达到 155 W m^{-2}, 加热率的误差高达 16 K d^{-1}; Liang 和 Wang[18]提出了一个处理多层云重叠的“马赛克”(MOASAIC)方法, 在 GCM 辐射参数化中显式地考虑云的垂直相关, 结果表明, GCM 对云的垂直分布的处理非常敏感, 与假定随机云重叠的结果相比, 显式处理云相关的 GCM 结果具有非常不同的大气辐射加热率分布, 所导致的气候影响非常大: 热带和副热带对流层的中高层大气在全年变暖超过 3℃, 北半球极区平流层变得更暖, 最大超过 15℃.

总体而言, 以上三种重叠方案表达形式固定、不够灵活, 而实际上云的重叠关系是随时间、地点和云的类型等变化的. 例如, 大范围的高层云趋向于与积云同时存在, 而积雨云和卷云常常同时出现在热带地区; 相邻的云层可能具有最大的相关性, 而被晴空层分离的云层之间则是相互独立的[18]. Hogan 和 Illingworth[19]通过加入一个可调节的重叠系数, 将整体云层的真实云量假设为垂直各层云的最大重叠云量和随机重叠云量中的某一个值, 被称之为一般重叠假设方案, 它使云的重叠关系表达灵活可变. 研究发现, 重叠系数呈指数分布, 并因此获得了一种可以有效去除云垂直结构对于模式垂直分辨率的依赖的系数-抗相关厚度(L_{cf}^{*}). L_{cf}^{*} 表示一般重叠假设方案内的重叠系数减小为 e^{-1} 时云层之间的距离, 其反应的是云层在垂直方向上的重叠关系. 有关抗相关厚度的观测研究在国际上处于起始阶段, 目前由卫星和地面雷达等观测尚不能明确给出其随时空的变化, 仅能得到取值为 2 km 的全球平均. 因此常见的气候模式或将其简单参数化为一定值, 或线性拟合为随纬度变化的函数, 均无法描述出理论上的复杂性, 从而成为气候模式不确定性的重要来源之一[20], 因此有必要利用可以获得的卫星资料来进行中国地区的相关研究.

在 2006 年 4 月美国航天航空局成功发射了太阳极轨云观测卫星 CloudSat, 其上搭载的 94 GHz 毫米波雷达具有非常高的垂直分辨率, 使得定量化研究云垂直重叠的特性成为可能.

近年来一种新的、被称为随机云产生器(Stochastic Cloud Generator, SCG)的次网格云参数化方案显示出独特的优越性[16,21~26], 它可以将云的结构和辐射传输计算分离开来, 在辐射传输模块外描述云的结构, 因此可以很容易进行云的结构调整而不用涉及辐射传输代码的改变, 避免了人为不确定性因素的引入. 这种同时易于对云和辐射方案调整的方法为模式的发展提供了广阔的空间.

1 卫星观测数据描述与处理

本文采用了 CloudSat 所搭载的 94 GHz 毫米波云廓线雷达(CPR)提供的观测资料, 分析了 2007~2009 年 3 整年的资料, CloudSat 卫星是 2006 年 4 月 28 日(UTC)由美国航天航空管理局(NASA)成功发射入太空的太阳极轨云观测卫星, 几周后开始获得相关数据. 如图 1 所示, CloudSat 每根轨道运行时间约为 2 h 进行约 37081 次扫描, 扫描星下点为 1.1 km (沿轨道运行方向)×1.4 km(垂直轨道运行方向)的区域, 垂直方向扫描 30 km, 并分为厚度为 0.24 km 的 125 层, 探测的

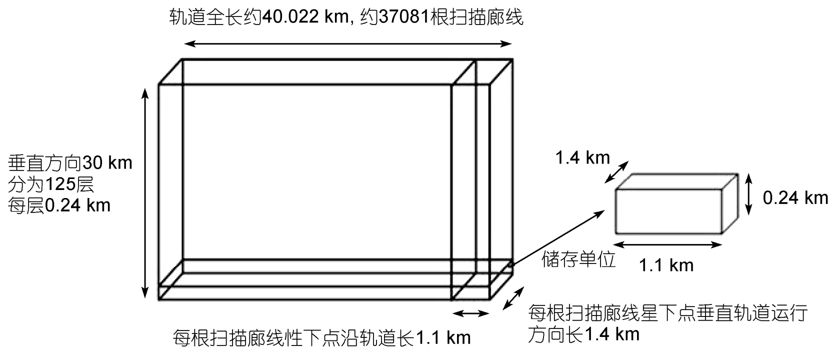

图 1 CloudSat 轨道示意图

信息以 1.1 km×1.4 km×0.24 km 的扫描格点为单位储存, 目前已经反演出多种二级产品.

本文工作主要使用了二级产品中 2B-GEOPROF 和 2B-GROPROF-Lidar(参见网站 http://cloudsat.cria.colostate.edu/dataspecs.php), 前者信息来自于 CloudSat 卫星上搭载的 94 GHz 毫米波雷达(CPR), 后者信息同时整合了 CloudSat 搭载的 CPR 的信息和与 CloudSat 同轨道, 运行时差只有 15 s 的 CALIPSO 卫星搭载的CALIPO激光雷达的信息, 结合两者可同时发挥毫米波雷达和激光雷达的优点. 我们用到了 2B-GEOPROF 产品中的 CPR_Cloud_mask 和 Radar_Reflectivity 数据以及 2B-GEOPROF-Lidar 中的 CloudFraction 数据. 其中, CPR_Cloud_mask 的数据说明见表 1.

Radar_Reflectivity 中所含的信息是雷达的反射率因子的对数表现值, 单位是 dbz, CPR 的最小可探测信号约是 30 dbz; CloudFraction 所包含的数据是经过 CALIPO 激光雷达探测到的扫描格点中云的百分比. 因此, 当每个扫描格点的数据满足 Radar_Reflectivity≥−30 dbz 和 CPR_Cloud_mask≥20; 或者 Radar_Reflectivity≥−30 dbz 和 CPR_Cloud_mask≤20 和 CloudFraction≥99%时, 我们认为该扫描格点有云存在. 我们按照图 2 流程判定每个扫描格点是否有云.

表 1 CPR_Cloud_mask 数据值说明

值	含义
0	没有探测到云
1	损坏的数据
5	地面噪音
5~10	弱探测信号
20~40	探测到有云存在, 值越大, 探测越准

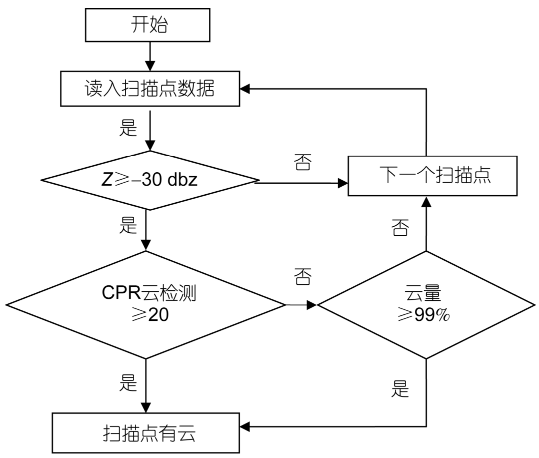

图 2 判定扫描点是否有云流程

图 3 给出本文选取的东亚地区及根据气候特征划分的 5 个地区示意图. 共 6 个研究域, 包括整个东亚地区, 北方地区, 南方地区, 西北地区, 青藏高原地区和东部海域. 本文选取 50 个扫描廓线组成的部分, 即 50(廓线个数)×1.1 km(星下点沿轨道运行方向长度)×1.4 km(星下点垂直轨道运行方向长度)×125(垂直层数)×0.24 km(垂直每层厚度)作为一个整体, 称之为子域, 计算出每个子域的抗相关厚度后, 根据子域所处的研究域归类, 最后计算抗相关厚度在 6 个研究域的统计特性.

2 研究方法

2.1 研究方案

在气候模式中, 对于云层的垂直关系采用过不同的假设方案, 依次有随机重叠, 即考虑不同云层之间的重叠是完全随机的; 最大重叠, 即不同云层之间

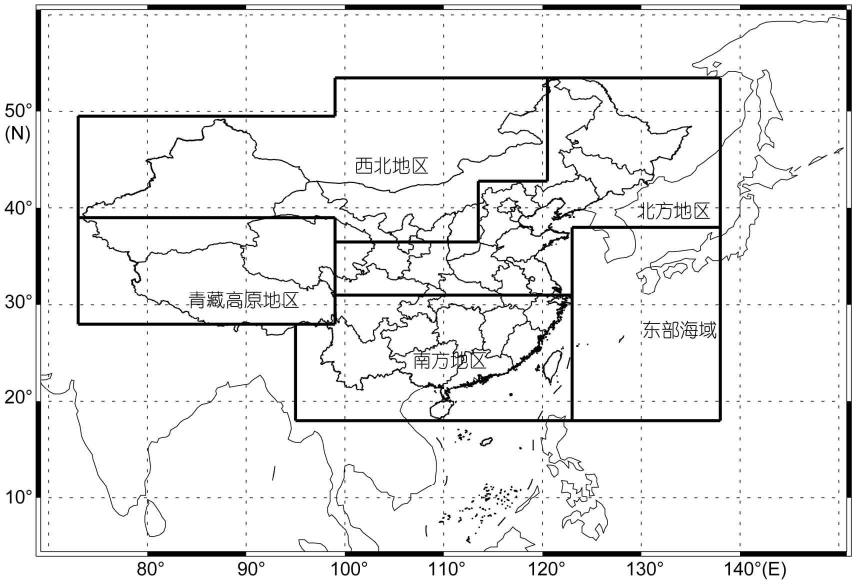

图 3　研究区域示意图

的重叠面积最大; 最大/随机重叠的组合, 在考虑重叠的时候将云层按照其间是否存在无云区而划分为两种情况, 存在无云区的时候认为两者是随机重叠, 而不存在无云区的时候认为是最大重叠. Hogan 和 Illingworth[19]提出一种新的云重叠假设方法——一般重叠, 即将任意两层云的真实云量假定在最大重叠和随机重叠之中的一个值, 使云的重叠特征更加灵活而趋于真实情况. 它根据两层云或者多层云之间的垂直相关性判断其重叠关系, 使云的重叠结构具有多样性.

如果 C_k 和 C_l 分别代表两层云的云量, $C_{k,l}$ 代表两层作为一个整体的真实云量, 那么一般重叠假设可以表示为

$$C_{k,l} = \alpha_{k,l} C_{k,l}^{\max} + (1-\alpha_{k,l}) C_{k,l}^{\mathrm{ran}}, \tag{1}$$

其中, $C_{k,l}^{\max} = \max(C_k, C_l)$, $C_{k,l}^{\mathrm{ran}} = C_k + C_l - C_k C_l$. $\alpha_{k,l}$ 是两层云的重叠系数, 反映两层云之间的重叠程度, $\alpha_{k,l}$ 越大, 则重叠程度越高. 研究表明[19], $\alpha_{k,l}$ 可以由以下公式计算:

$$\alpha_{k,l} = \exp\left(-\int_{Z_k}^{Z_l} \frac{\mathrm{d}Z}{L_{cf}(Z)}\right), \tag{2}$$

其中, Z 是垂直高度, $L_{cf}(Z)$称为云的抗相关厚度(以下简称为 L_{cf}, 而 L_{cf}^* 表示本文反演后的值), 是两层云的重叠系数减少到 e^{-1} 时的距离. 而该公式中的 $\alpha_{k,l}$ 是大于 0 的, 因此对于两层云完全不重叠, 并且云量总和小于 100%时所导致的 $\alpha_{k,l}$ 小于 0 以及任意层云量 $\hat{C}=1$ 时导致的 $\alpha_{k,l}$ 等于 0 是不适用的, 虽然这些情况在极少数情况下可以出现.

在 GCM 中, 当有了网格点中的各层云量, 即云量廓线, 可以有许多种方法生成次网格的云分布, 以便获得网格点的云量, 如前文所述, 我们将 SCG 放入 NCAR(The National Center for Atmospheric Research) 的全球大气模式 CAM3.0 中来完成这一过程. SCG 的原理是通过建立高分辨率的三维次网格结构对任意给定的模式格点云廓线的信息进行模拟, 在所有次网格信息的平均依旧遵循于原格点廓线信息的同时, 研究模式格点无法分辨的次网格水平上的云信息. 鉴于次网格随机产生的云仅需满足平均信息遵循原廓线这一条件, 而在次网格尺度的上几何位置并无限制, 所以可以十分灵活的基于任意给定的云重叠方案进行模拟, 并且 SCG 已整合有随机重叠方案, 最大/随机重叠方案与一般重叠方案[21], 因此非常适用于通过对由卫星观测得到的云量廓线信息进行模拟, 进而研究云的垂直重叠问题. 使用 SCG 时需要给定 3 个初始条件: 假设的云重叠方案、云量垂直廓线和抗相关厚度 $-L_{cf}^*$, 即可通过模拟的次网格云结构获得网格点的总云量. 在这里, 云的垂直廓线由 CloudSat 数据计算得到, 重叠方案我们选取了新的一

般重叠方案[19], 同时需要给定云的垂直重叠关系(即设定抗相关厚度–L_{cf} 的值)来完成模拟. 本文通过从小到大设定 L_{cf} 的值来获得对网格点总云量 $\hat{C}$ 的不同模拟值, 由此得到 $\hat{C}(L_{cf})$ 这样一个函数关系. 我们通过选取 L_{cf}^* 使得 $\hat{C}(L_{cf}^*)$ 与我们从 CloudSat 数据计算得到的网格点总云量相同, 此时获得的 L_{cf}^* 就是与观测相一致的描述云重叠特性的尺度参数. 上述方法的思路是在采用一般重叠假设方案的情况下, 给定云量廓线(即各个高度上的云量), 通过调整云在垂直方向的重叠关系(即调整 L_{cf} 的取值), 使 SCG 模拟出的总云量与观测一致, 此时的重叠关系(即 L_{cf}^*)就是正确表述云重叠特性的参数. 我们检测了 2007~2009 年的卫星数据, 发现在 125 层雷达垂直扫描层中, 全球平均海平面高度位于第 105 层, 因此我们只提取从扫描顶层到第 104 层的探测信息. SCG 生成的是三维次网格云的结构, 因此, 需要给定 3 个空间方向的格点数目. 我们设定垂直方向为 104 层与 CloudSat 的垂直分层相对应; 纵向选取 1 层. 对横向的层的数目, 我们测试了选取不同层数对计算结果的影响, 发现: 在逐步增加层数为 1000, 2000, 5000 和 10000 模拟时, L_{cf}^* 的随机误差有明显的降低, 从 0.01 的量级减少到 0.001 的量级, 而如果继续增加横向模拟层数到 20000 层时, 随机误差仍然位于 0.001 量级. 因此我们对横向选取了 10000 层来进行计算. 同时我们选取: 50(廓线个数)×1.1 km(星下点沿轨道运行方向长度)×1.4 km(星下点垂直轨道运行方向长度)×104(垂直层数)×0.24 km(每个垂直层的厚度)的卫星扫描区域作为研究的子域, 每一个子域被我们分成 104×1×10000 的立体网格, 通过 SCG 在这些小网格中生成云来模拟总云量和云量的垂直廓线.

2.2 获取 L_{cf}^* 的方法

我们首先选取了 2007 年 1 月份的第 03609 轨道中经纬度范围(98.732°~98.461°E, 33.482°~34.441°N)作为研究的子域. 首先, 从 CloudSat 数据计算出该子域的总云量为 0.85, 然后计算出云量的垂直廓线(图 4(a))并输入给 SCG; 以 0.1 km 为间隔, 设定 L_{cf} 从 0.1 km 递增到 10 km, 通过 SCG 生成不同的云量廓线, 得到 $\hat{C}(L_{cf})$ 的函数关系(图 4(b)). 从图 4(b)中可以看出, 当选取 L_{cf}^* =0.6 km 时, 生成的云量为 0.848, 与该子域 CloudSat 数据得出的云量 0.85 最为接近, 因此, 我们认为在该子域选取 L_{cf}^* =0.6 km 作为其抗相关厚度是最合适的. 图 4(a)给出的是该子域从地面到 20 km 高度的各层云量, 其中点线是由 CloudSat 观测获得, 而不同高度的误差棒则代表了选取 L_{cf}^* =0.6 km 作为参数由 SCG 模拟得到的云量的垂直廓线与相应的观测廓线在不同高度上的差值, 可以看出误差在 0.01~0.07 的范围之内, 非常小, 说明选取 L_{cf}^* =0.6 km 时 SCG 对云量垂直廓线的模拟与观测结果符合较好. 需要特别指出的是, 在获取所有研究子域的 L_{cf}^* 时, SCG 云生成器生成的气柱云量与由观测资料得到的气柱云量之间的差值均在 0.001~0.01 量级范围, 精度非常高.

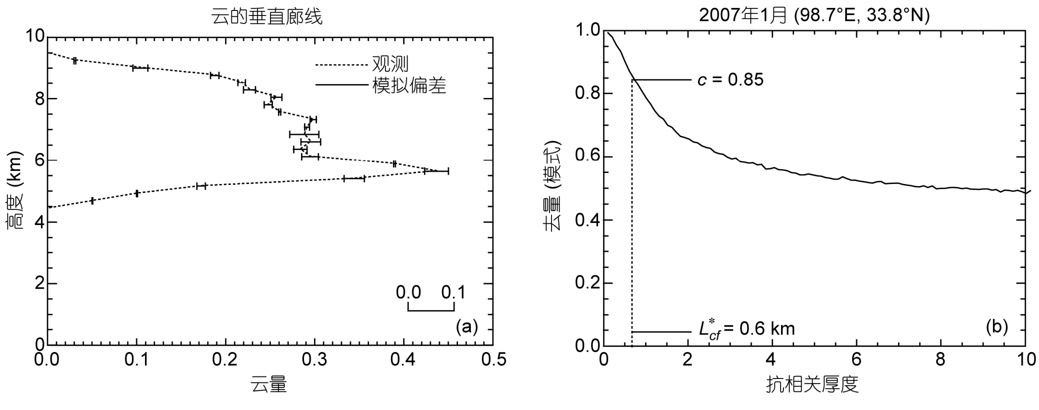

图 4 (a) SCG 模拟生成的各高度层云量与观测得到的各高度层云量之间的误差; (b) 2007 年 1 月份在子域(98.732°E, 33.482°N)~(98.461°E, 34.441°N)上 $\hat{C}(L_{cf})$ 函数图

3 结果与讨论

3.1 抗相关厚度

在通过上述单个子域验证了方法的可行性之后, 我们计算了所有子域的抗相关厚度. 结果表明, 90%以上的子域的 L_{cf}^{*} 在0~3 km之间, 只有极个别子域的 L_{cf}^{*} 超过了 9 km, 此计算结果与以往的研究结果相符合[20]. 为了表征 6 个研究域的整体情况, 我们对这些 L_{cf}^{*} 做了算数平均. 表 2 给出 6 个研究域 2007~2009 年春夏秋冬 4 个季节的取样个数和按照取样个数平均的 L_{cf}^{*}. 与此同时, 我们将每个子域的 L_{cf}^{*} 按照其云量的不同归类至 20 个档, 每档云量的变化为 0.05, 从 $\hat{C}\in[0, 0.05)$ 递增到 $\hat{C}\in[0.95, 1.00)$, 同时也就除去了 $\hat{C}=1$ 不满足式(2)的情况. 统计发现在不同的研究域域这种情况发生的比例为 10%~15%, 剔除 $\hat{C}=1$ 之后的样本个数仍能满足本研究的需要. 图 5 给出了 L_{cf}^{*} 分档后在 4 个季节和 6 个研究域的平均值随子域的云量的变化.

结果表明, 4 个季节中 6 个研究域的 L_{cf}^{*} 基本都处于 0~3 km 的范围, 随着子域的云量的递增, L_{cf}^{*} 呈现出波动增大而后回落的趋势, 极值出现在云量位于 0.6 至 0.8 之间的子域, 6 个研究域 L_{cf}^{*} 极值的平均值在春夏秋冬四个季节分别为 2.12, 2.33, 2.04 和 2.15 km. 不同研究域之间的差异体现出, 对 4 个季节, 当云量在 0.2~0.9 时, 处于较高纬度的北方地区和西北地区的 L_{cf}^{*} 都高于处于较低纬度的南方地区的相应值, 当云量为 0.4~0.9 时, 也高于以低纬地区为主的东部海域研究域的相应值, 差值位于 0~3 km; 而当云量小于 0.2 时, 北方地区和西北地区的 L_{cf}^{*} 等于或略小于南方地区和东部海域的相应值, 差值小于 0.5 km. 包含有青藏高原特殊地形的青藏高原地区研究域的 L_{cf}^{*} 在夏季略大于东部海域和南方地区, 在其他 3 个季节位于东部海域和南方地区之间.

从 L_{cf}^{*} 的季节性变化来看, 位于东亚地区西部的西北地区, 青藏高原地区和南方地区三个研究域的 L_{cf}^{*} 对于大部分云量范围都呈现出夏季最大, 春、秋次之, 冬季最小的特点. 夏季 L_{cf}^{*} 的峰值在西北地区, 青藏高原地区和南方地区分别出现在云量为 0.72 的子域附近, 值为 3.42 km、云量为 0.83 的子域附近, 值为 2.41 km 和云量为 0.81 的子域附近, 值为 1.85 km; 而在冬季这一峰值均出现在云量为 0.6 的子域附近, 值分别减小为 2.22, 1.75 和 1.38 km. 位于东亚地区较东部地区的东部海域和北方地区研究域的 L_{cf}^{*} 则呈现出冬季最大, 春秋次之, 夏季最小的特点. 夏季 L_{cf}^{*} 的峰值在东部海域和北方地区分别出现在云量为 0.55 的子域附近, 值为 1.82 km 和云量为 0.66 的子域附近, 值为 2.28 km; 而在冬季这一峰值分别出现在云量为 0.62 和 0.86 的子域附近, 值增加到 2.28 和 3.15 km. 青藏高原地区研究域的 L_{cf}^{*} 在夏冬季的变化较为明显, 冬季峰值出现在云量为 0.66 的子域附近, 值为 1.78 km, 而夏季的峰值出现在云量为 0.78 的子域附近, 值显著增加到 2.45 km.

以上特点表明因北方地区和西北地区主要由内陆组成, 相较于包含有海洋的南方地区和以海样下垫面为主的东部海域, 水汽条件弱, 控制气团性质更为单一, 因此北方地区和西北地区研究域中云层之间相关比南方地区和东部海域更高. 各个研究域 L_{cf}^{*} 的季节变化则呈现出西北地区和南方地区在夏季、北方地区在冬季云层的相关性分别比相应地区的其他季节高, 而青藏高原地区冬夏两季 L_{cf}^{*} 的明显变化可能与青藏高原这一大地型有着密切的关系, 冬季青藏高原的动力和热力作用导致在整个亚洲冬季风背景下高原局部地区具有相对多云且湿度偏大的特点,

表 2　L_{cf}^{*} 在 6 个研究域 4 个季节的平均值及子域个数

	东亚地区	西北地区	北方地区	南方地区	青藏高原地区	东部海域
春	0.97 km/48608	1.00 km/11572	0.98 km/8443	0.83 km/7801	1.00 km/8285	1.04 km/12507
夏	1.11 km/53815	1.35 km/12846	1.00 km/9166	0.95 km/8448	1.14 km/9259	1.11 km/14096
秋	1.03 km/40474	1.12 km/9240	0.98 km/7331	0.82 km/6595	1.03 km/6671	1.22 km/10637
冬	0.95 km/44002	0.99 km/9785	1.10 km/7917	0.69 km/7196	0.91 km/7451	1.13 km/11653

这使得成云条件更为复杂, 因此云层的变化较复杂, 云的相关性较低; 而到了夏季, 高原作为大的热源, 该地区多为对流性云, 彼此相关性比较高, 因此夏季的 L_σ^* 值明显增大, 这一趋势在云量位于 0.6~0.8 之间的子域表现更为明显.

随后, 本文分别将计算得到的 6 个研究域的所有子域的 L_σ^* 和其云量的垂直廓线输入到 SCG 中, 检测 SCG 在生成的子域的模拟总云量与观测总云量最接近时, 垂直方向上各层的云量模拟是否足够精确. 图 6 分别给出了四个季节从观测数据计算得到的 6 个研究域各层云量平均值的垂直分布; 误差棒给出的是模拟值与观测值的差, 其峰值在 4 个季节均小于 0.02. 这表明与单一子域的模拟结果类似, 在保证了子域模拟总云量和观测总云量最接近的前提下, 垂直方向各层平均云量的模拟值与相应的观测值也非常一致; 同时也说明在本研究中横向选取 10000 层作为次网格参数来模拟云量是合适的, 因此计算得到的表征云的垂直结构的特征量 L_σ^* 能够保证模拟的子域云量垂直廓线和总云量都与相应的观测值保持一致.

在目前全球已经耦合了 SCG 的气候模式中, 为了节约计算时间, 通常将 L_σ^* 简单设定为 2 km, 即在全球均匀分布, 没有地理和季节变化. 为了评估这样的设定所导致的模式对格点云量模拟的误差, 本文将选取 L_σ^* =2 km 时, SCG 模拟的气柱总云量(C_{mod})与相应的观测值(C_{obs})之间的差别定义为 D:

$$D=C_{\text{mod}}-C_{\text{obs}}, \tag{3}$$

并加以分析.

图 7 给出 D 值在不同季节和研究域的平均值, 其中灰色线给出未平均之前的 D 值作为参考. 结果显示选取 L_σ^* =2 km 模拟得到的各子域云量与观测值的差异很大, D 值有 82%小于 0.1, 12%的位于 0.1~0.2, 6%大于 0.2, 峰值超过了 0.4; 而区域平均后的模拟与观测之间的差异比较小, 对于不同的研究域的模拟存在着 0.05~0.15 的差异, 表 3 给出 6 个研究域在 4 个季节模拟与观测差异平均值的峰值及峰值所处子域的观测云量, 可以看出这一峰值存在着时间和空间差异. 说明简单设定 L_σ^* 为 2 km, 对于云量的模拟在某些地区和不同季节仍然会存在一定的误差, 因此在

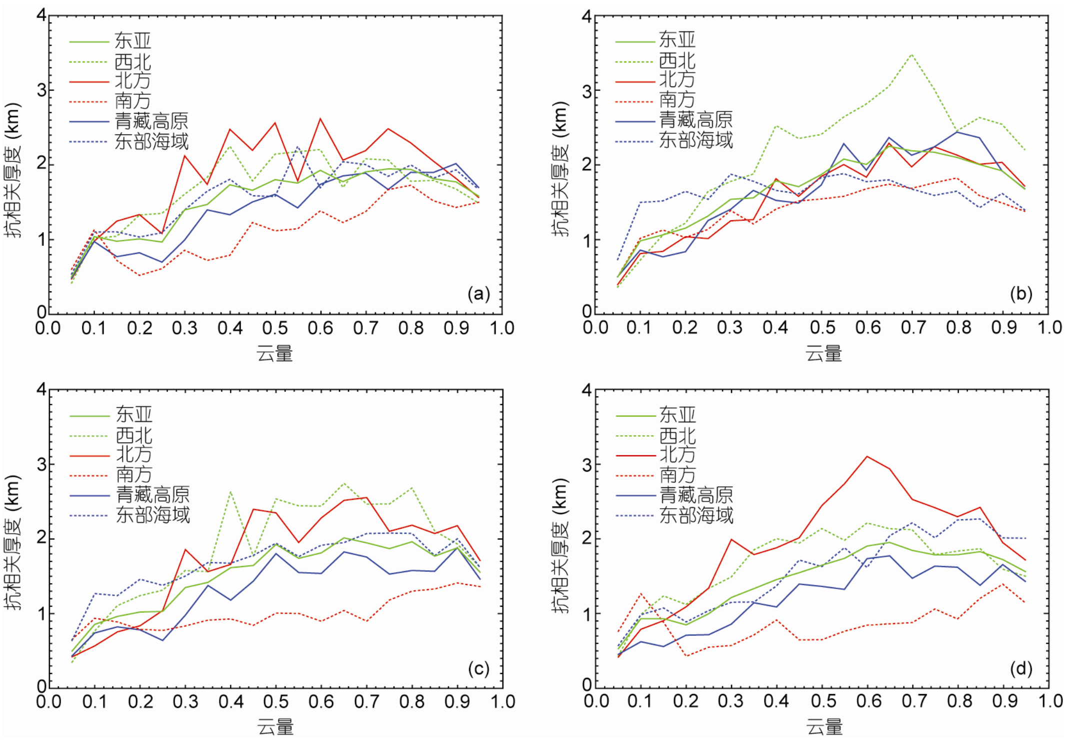

图 5　6 个研究域 L_σ^* 平均值随云量的变化

(a) 春季; (b) 夏季; (c) 秋季; (d) 冬季

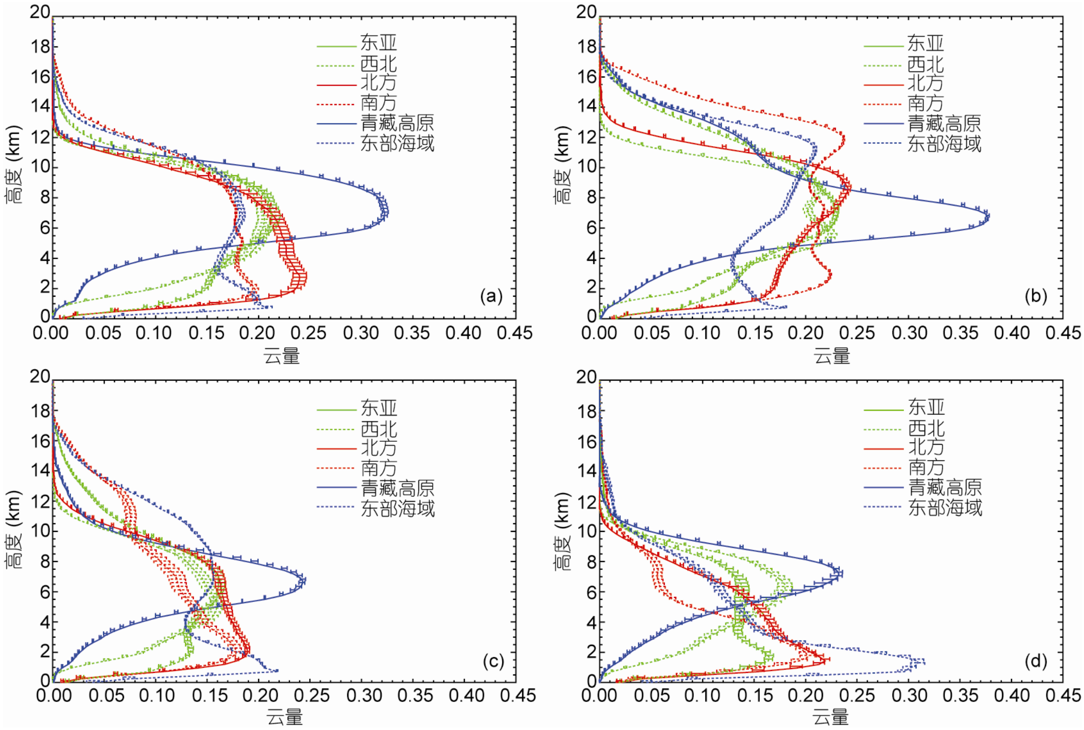

图 6　6 个研究域各层观测平均云量

(a) 春季; (b) 夏季; (c) 秋季; (d) 冬季. 其中, 误差棒为模拟值与观测值的差

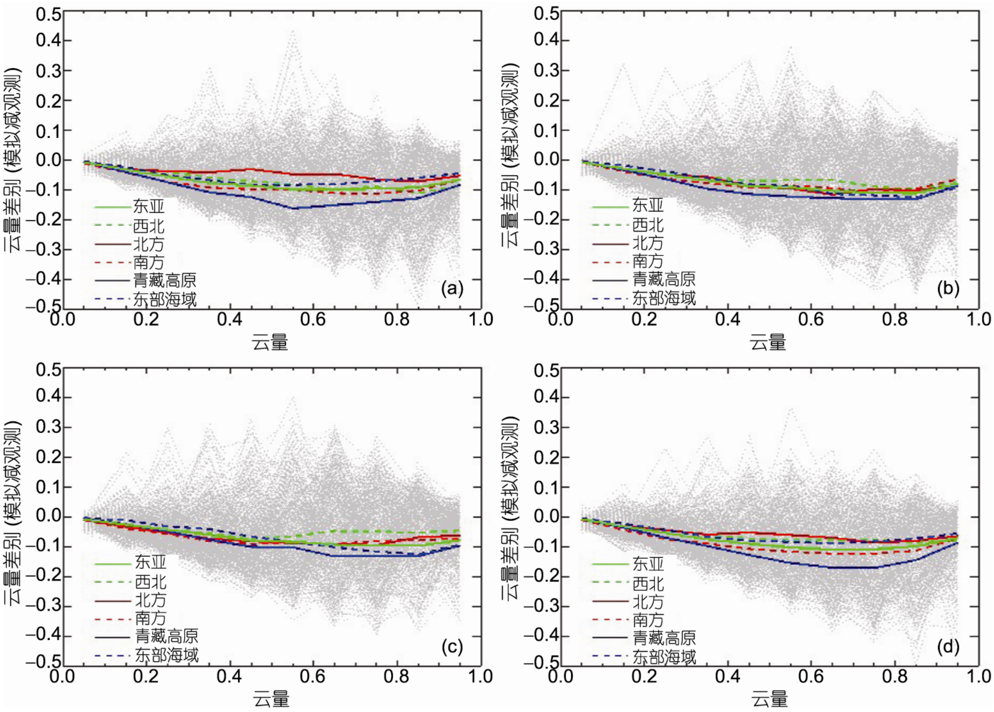

图 7　选取 L_{cf}^{*} =2 km 时所有子域模拟的云量与观测值之间的差别随云量的变化

(a) 春季; (b) 夏季; (c) 秋季; (d) 冬季

表 3　模拟云量与相应观测值差别的平均值在 6 个区域 4 个季节的峰值及峰值所处位置的子域的观测云量

	东亚地区		西北地区		北方地区		南方地区		青藏高原地区		东部海域	
	差	云量	差	云量	差	云量	差	云量	差	云量	差	云量
春	–0.11	0.68	–0.12	0.85	–0.06	0.85	–0.12	0.72	–0.16	0.56	–0.08	0.54
夏	–0.12	0.85	–0.11	0.86	–0.12	0.65	–0.11	0.85	–0.13	0.84	–0.13	0.87
秋	–0.10	0.83	–0.08	0.44	–0.09	0.46	–0.10	0.44	–0.13	0.86	–-0.13	0.86
冬	–0.12	0.76	–0.08	0.76	–0.08	0.82	–0.13	0.76	–-0.17	0.76	–0.08	0.74

不同地区、不同季节精确参数化 L_{cf}^* 是很有必要的.

3.2　云辐射强迫对 L_{cf}^* 取值的敏感性试验

在计算和分析了 L_{cf}^* 的地理分布和季节变化后, 下面我们将讨论不同的 L_{cf}^* 分布对气候模式中云辐射计算的影响, 特别是对云的辐射强迫的影响.

云的辐射强迫(Cloud Radiative Forcing, CRF)定义为某一给定大气的净辐射通量与假定云不存在时同一大气的净辐射通量(向下通量减去向上通量, 且假定向下为正)的差值, 这一定义适用于大气顶和地面[27]. 这里分别将其应用于短波和长波辐射.

本文首先将 SCG 与全球气候模式 CAM3/NCAR 耦合起来, 利用该耦合模式来做敏感性试验. 在模式中分别设置 L_{cf}^* =1, 2 和 3 km, 从 1999 年 9 月积分至 2000 年 12 月. 利用上述模式, 首先设定 L_{cf}^* =2 km, 把在该条件下计算得到的云的辐射强迫作为参考值, 计算并分析在其他两种情况下云的辐射强迫与该参考值的差别. 经分析, 本文将模式积分的前 4 个月作为模式调整时间, 取 4 个月后的结果进行分析不会带来大的误差, 故本文取后 11 个月的结果进行讨论. 图 8 给出模式 2000 年冬季(1 月)的长波云辐射强迫. 图 8(a)是 L_{cf}^* =2 km 的结果, 而图 8(b)和(c)分别表示设定 L_{cf}^* =1 和 3 km 时的长波 CRF 结果与 L_{cf}^* =2 km 的长波 CRF 结果差别. 由图 8(b)和(c)发现, 全球不同地区的长波云辐射强迫对抗相关厚度存在不同的敏感性, 特别是几个主要的季风区海域. 图 8(b)给出当 L_{cf}^* =1 km 时非洲中部东面海域和南美东面海域的长波 CRF 与 L_{cf}^* =2 km 时的长波 CRF 存在负的偏差, 最大达到了–40 W m^{-2}; 而图 8(a)给出 L_{cf}^* =2 km 时这两个地区的长波 CRF 值在 50~90 W m^{-2} 之间; 相应的,长波 CRF 在东南亚季风区有正的偏差, 最大超过了 40 W m^{-2}, 而图 8(a)中 L_{cf}^* =2 km 时该区域长波 CRF 在

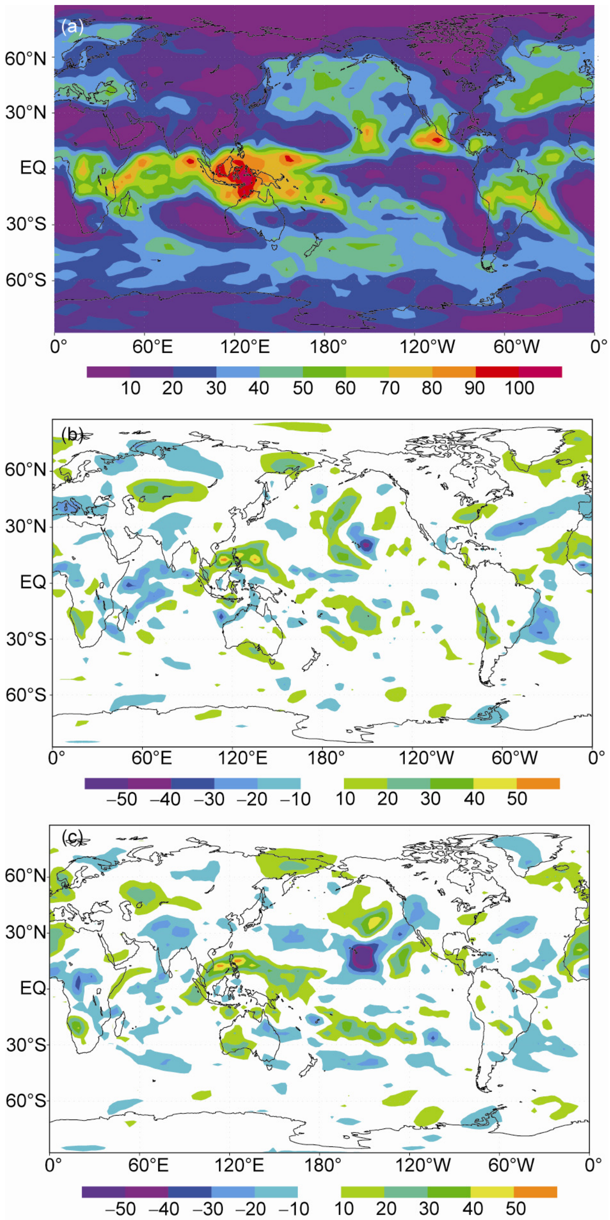

图 8　2000 年 1 月份模式模拟的长波云辐射强迫

(a) L_{cf}^* =2 km; (b) L_{cf}^* =1 km 与 L_{cf}^* =2 km 的差值; (c) L_{cf}^* =3 km 与 L_{cf}^* =2 km 的差值. 单位: W m^{-2}

80~100 W m^{-2} 的范围; 另一个敏感性比较大的地方位于中东太平洋地区, 负差值中心的绝对值超过了 50 W m^{-2}. 图 8(c)给出当 L_{cf}^* =3 km 时长波 CRF 与 L_{cf}^* =2 km 时的长波 CRF 存在的偏差, 中东太平洋地区同样是负差值中心, 差值的绝对值也超过了 50 W m^{-2}, 非洲中西部和包括青藏高原在内的南亚地区以及太平洋偏西部海域为较强的负差值区域, 差值的绝对值都超过 20 W m^{-2}, 东南亚海域有较强的正偏差区域, 差值最大的绝对值同样超过了 50 W m^{-2}.

下面再来看图 9 表示的夏季(7 月份)的情况. 同样可以得出, 全球几个主要季风区的长波 CRF 仍然是对抗相关厚度敏感性比较大的区域, 与 1 月份相比, 处在高纬地区的西伯利亚, 加拿大以及南极洲部分地区的敏感性明显增加. 因此改变抗相关厚度 L_{cf}^* 会给气候模式计算的长波 CRF 带来很大的差别.

图 10 给出的是模式模拟的 2000 年 1 月份短波云辐射强迫. 图 10(a)是 L_{cf}^* =2 km 的情况, 而图 10(b)和(c)分别是设定 L_{cf}^* =1 km 和 L_{cf}^* =3 km 时模式模拟的短波 CRF 结果与 L_{cf}^* =2 km 时模式计算的短波 CRF 结果的差别. 图 11 给出的是夏季 7 月份的相应结果. 与长波 CRF 结果相比, 抗相关厚度 L_{cf}^* 的改变导致云垂直结构的改变对短波云辐射强迫的影响明显增大. 由图 10 得到: 全球几个主要季风区和中东太平洋地区对抗相关厚度的改变的敏感性最大. 其中由图 10(b)看出, 东南亚季风区负差值最大超过了 50 W m^{-2}, 中东太平洋地区正差值也超过了 50 W m^{-2}. 通过比较图 10(b)和(c)发现, 在 L_{cf}^* =3 km 时的相应差值比 L_{cf}^* =1 km 时的差值还大. 与 L_{cf}^* =2 km 时的参考值相比, 这些差别分别达到了 50%~70%不等. 夏季 7 月份的情况在这些地区同样显示出明显的差别, L_{cf}^* =1 km 与 L_{cf}^* =2 km 时模式计算得到的短波 CRF 差值中心主要位于东亚季风区、澳大利亚中部和北美洲北部, 而 L_{cf}^* =3 km 与 L_{cf}^* =2 km 的相应差值中心还增加了非洲东北部, 俄罗斯中西部和中亚地区等地区, 正偏差和负偏差的绝对值的最大值都超过了 50 W m^{-2}.

通过以上对比, 可以看出, 选取不同的 L_{cf}^* 值, 对气候模式中模拟的云辐射强迫的强度和分布都有很大的影响, 特别是对全球几个主要的季风区和中东太平洋等地区的影响程度非常大, 这说明在气候模式中给出正确的抗相关厚度是非常必要的. 这里需要说明的是, 由于在上述敏感性数值试验中, 三种情况 L_{cf}^* 值都假定不存在地理和季节变化, 即在全球是均匀分布的, 这与上节从卫星资料分析的结果是不符合的. 这里数值试验的主要目的是说明 L_{cf}^* 取值对云辐射强迫的计算会产生重要的影响.

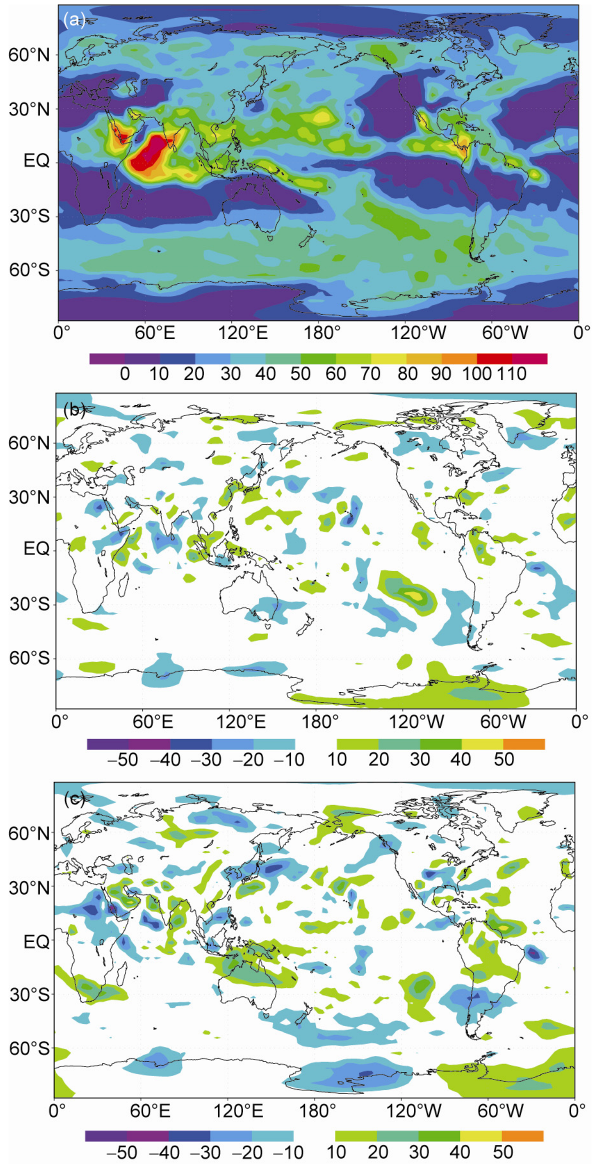

图 9　2000 年 7 月份模式模拟的长波云辐射强迫

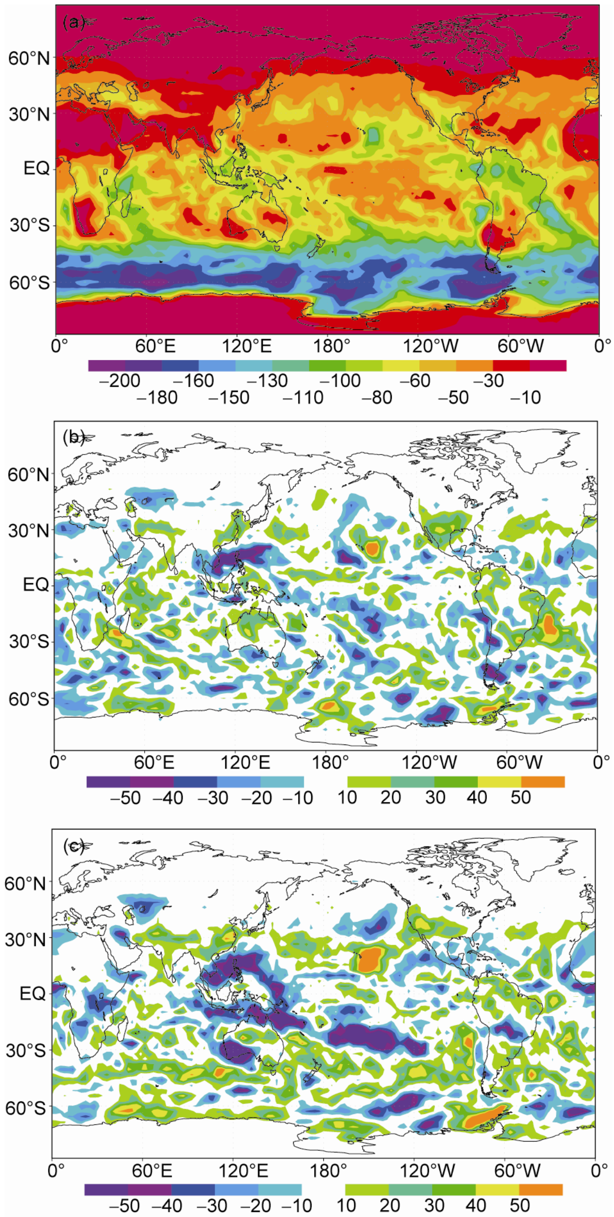

图 10 2000 年 1 月份模式模拟的短波云辐射强迫

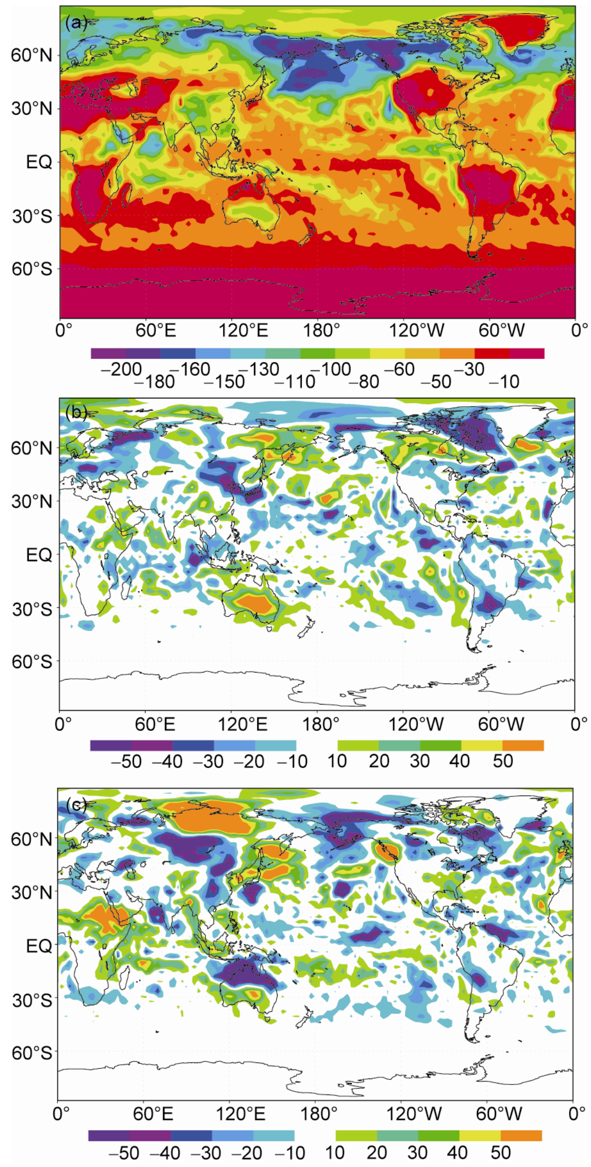

图 11 2000 年 7 月份模式模拟的短波云辐射强迫

4 结论

本文利用 2006 年 4 月发射成功的云观测卫星 CloudSat 获取的 2007~2009 年三整年的观测资料, 结合气候模式中产生次网格云结构的云产生器 SCG, 首次计算了东亚地区表征云的垂直结构的特征量−抗相关厚度 (L_{cf}^{*}) 的季节变化和空间分布; 并讨论了该参数的选取对云辐射强迫计算的影响. 得到如下结论:

(1) 6 个研究域的抗相关厚度基本处于 0~3 km 的范围之中, 根据研究子域的云量不同来划分, 抗相关厚度极值出现在云量为 0.6~0.8 的子域附近, 平均约为 2.5 km.

(2) 在所划分的 6 个研究域中 L_{cf}^{*} 值的地理分布差异: 较高纬度的北方地区和西北地区的 L_{cf}^{*} 整体大于较低纬的青藏高原地区和南方地区, 而东部海域和东亚地区介于两者之间. 根据所处子域云量的不

同, 6 个区域中 L_{cf}^{*} 最大值与 L_{cf}^{*} 最小值在四个季节的差值分别位于 0~1.6 km, 0~2 km, 0~1.7 km 和 0~2.4 km 的范围.

(3) L_{cf}^{*} 值的季节差异: 6 个研究域中, 东亚地区研究域和位于东亚地区西部的西北地区、青藏高原地区以及南方地区三个研究域的 L_{cf}^{*} 对于大部分云量范围都呈现出夏季最大, 春、秋次之, 冬季最小的特点; 位于东亚地区较东部区域的东部海域和北方地区研究域的 L_{cf}^{*} 则呈现出冬季最大, 春秋次之, 夏季最小的特点.

(4) 简单的设定 L_{cf}^{*} 值为 2 km 对次网格气柱总云量进行模拟时, 会产生平均约为 15%左右的误差, 这些误差会对气候模式中云辐射计算和辐射收支平衡产生很大影响.

(5) 选取不同的 L_{cf}^{*} 值, 对气候模式计算的长、短波辐射强迫均有较为显著的影响, 特别是对全球几个主要的季风区和中东太平洋地区的影响非常大. 说明在气候模式中给出精确的抗相关厚度的地理和季节分布是非常必要的. 这将是我们下一步工作的主要内容, 并将在另文给予研究.

致谢 本文所使用的云产生器 SCG 代码来自加拿大 Barker 教授, 在此对 Barker 教授表示感谢.

参考文献

1 Ramanathan V, Cess R D, Harrison E F, et al. Cloud-radiative forcing and climate: Results from the earth radiation budget experiment. Science, 1989, 243: 57–63
2 Wang H Q, Zhao G X. Cloud and radiation. Sci Atmos Sin, 1994, 18(Suppl): 910–932
3 Ding S G, Zhao C S, Shi G Y, et al. Analysis of global total cloud amount variation over the past 20 years. J Appl Meteorol, 2005, 16: 670–676
4 Sun B, Groisman P Y. Cloudiness variations over the former Soviet Union. Int J Climatol, 2000, 20: 1097–1111
5 Houghton J T, Ding Y, Griggs D J, et al. Climate Change: The Scientific Basis. New York: Cambridge University Press, 2001. 1–421
6 Wetherald R T, Manabe S. Cloud feedback processes in a general circulation model. J Atmos Sci, 1988, 45: 1397–1416
7 Houghton J T, Ding Y, Griggs D J, et al. Climate Change: The Scientific Basis. New York: Cambridge University Press, 2001. 148–149
8 张华, 荆现文. 气候模式中云的垂直重叠假定对模拟的地-气辐射的影响研究. 大气科学, 2010, 3: 520–532
9 荆现文, 张华, 郭品文. 气候模式中云的次网格结构对全球辐射影响的研究. 气象学报, 2010, 67: 1058–1068
10 Manabe S, Strickler R F. Thermal equilibrium of the atmosphere with a convective adjustment, J Atmos Sci, 1964, 21: 361–385
11 Geleyn J F, Hollingsworth. An economical analytical method for the computation of the interaction between scattering and line absorption of radiation. Cont Atmos Phys, 1979, 52: 1–16
12 Morcrette J J, Fouquart Y. The overlapping of cloud layers in shortwave radiation parameterizations, J Atmos Sci. 1986, 43: 321–328
13 Barker H W, Stephens G L, Partain P T, et al. Assessing 1D atmospheric solar radiative transfer models: Interpretation and handling of unresolved clouds. J Clim, 2003, 16: 2676–2699
14 Morcrette J J, Jakob C. The response of the ECMWF model to changes in cloud overlap assumption. Mon Weather Rev, 2000, 128: 1707–1732
15 Tian L, Curry J A. Cloud overlap statistics. J Geophys Res, 1989, 94: 9925–9935
16 Barker H W, Stephens G L, Fu Q. The sensitivity of domain-averaged solar fluxes to assumptions about cloud geometry. Q J R Meteorol Soc, 1999, 125: 2127–2152
17 Li J. Accounting for unresolved clouds in a 1D infrared radiative transfer model. Part I: Solution for radiative transfer, including cloud scattering and overlap. J Atmos Sci, 2002, 59: 3302–3320
18 Liang X Z, Wang W C. Cloud overlap effects on general circulation model climate simulations. J Geophys Res, 1997, 102: 11039–11047
19 Hogan R J, Illingworth A J. Deriving cloud overlap statistics from radar. Quart J Roy Meteor Soc, 2000, 126: 2903–2909
20 Barker H.W. Overlap of fractional cloud for radiation calculations in GCMs: A global analysis using CloudSat and CALIPSO data. J Geophys Res, 2008, 113: D00A01, doi: 10.1029/2007JD009677
21 Räisänen P, Barker H W, Khairoutdinov M, et al. Stochastic generation of subgrid-scale cloudy columns for large-scale models. Q J R Meteorol Soc, 2004, 130: 2047–2067

22 Barker H W, Räisänen P. Radiative sensitivities for cloud structural properties that are unresolved by conventional GCMs. Q J R Meteorol Soc, 2005, 131: 3103–3122
23 Räisänen P, Barker H W, Cole J N S. The Monte Carlo Independent Column Approximation's conditional random noise: Impact on simulated climate. J Clim, 2005, 18: 4715–4730
24 Pincus R H, Klein S A. Using stochastically generated subcolumns to represent cloud structure in a large scale model. Mon Weather Rev, 2006, 134: 3644–3656
25 Räisänen P, Järvenoja S, Järvinen H, et al. Tests of Monte Carlo Independent Column Approximation in the ECHAM5 Atmospheric GCM. J Clim, 2007, 20: 4995–5011
26 Morcrette J J, Barker H W, Cole J N S, et al. Impact of a new radiation package, McRad, in the ECMWF integrated forecasting system. Mon Weather Rev, 2008, 136: 4773–4798
27 石广玉. 大气辐射学. 北京: 科学出版社, 2007. 302–318

Influence of Changes in Solar Radiation on Changes of Surface Temperature in China

ZHANG Hua[1*] (张 华), YIN Qing[1,2,3] (尹 青), Teruyuki NAKAJIMA[4], Nakata Mukai MAKIKO[5], LU Peng[1,3] (卢 鹏), and HE Jinhai[3] (何金海)

1 *Laboratory for Climate Studies, National Climate Center, China Meteorological Administration, Beijing* 100081, *China*

2 *Meteorological Center of Air Force in Beijing Military Area, Beijing* 100061, *China*

3 *Nanjing University of Information Science & Technology, Nanjing* 210044, *China*

4 *Center for Earth Surface System Dynamics, Atmosphere and Ocean Research Institute, University of Tokyo, Chiba* 277-8564, *Japan*

5 *Kinki University, Osaka* 577-8502, *Japan*

(Received October 28, 2011; in final form June 8, 2012)

ABSTRACT

The long-term trends of total surface solar radiation (SSR), surface diffuse radiation, and surface air temperature were analyzed in this study based on updated 48-yr data from 55 observational stations in China, and then the correlation between SSR and the diurnal temperature range (DTR) was studied. The effect of total solar radiation on surface air temperature in China was investigated on the basis of the above analyses. A strong correlation between SSR and DTR was found for the period 1961–2008 in China. The highest correlation and steepest regression line slope occurred in winter, indicating that the solar radiation effect on DTR was the largest in this season. Clouds and water vapor have strong influences on both SSR and DTR, and hence on their relationship. The largest correlations between SSR and DTR occurred in wintertime in northern China, regardless of all-day (including clear days and cloudy days) or clear-day cases.

Our results also showed that radiation arriving at the surface in China decreased significantly during 1961–1989 (dimming period), but began to increase during 1990–2008 (brightening period), in agreement with previous global studies. The reduction of total SSR offset partially the greenhouse warming during 1961–1989. However, with the increase of SSR after 1990, this offsetting effect vanished; on the contrary, it even made a contribution to the accelerated warming. Nonetheless, the greenhouse warming still played a controlling role because of the increasing of minimum and mean surface temperatures in the whole study period of 1961–2008. We estimated that the greenhouse gases alone may have caused surface temperatures to rise by 0.31–0.46℃ (10 yr)$^{-1}$ during 1961–2008, which is higher than previously estimated. Analysis of the corresponding changes in total solar radiation, diffuse radiation, and total cloud cover indicated that the dimming and brightening phenomena in China were likely attributable to increases in absorptive and scattering aerosols in the atmosphere, respectively.

Key words: global dimming/brightening, global warming, surface solar radiation, surface air temperature

Citation: Zhang Hua, Yin Qing, Teruyuki Nakajima, et al., 2013: Influence of changes in solar radiation on changes of surface temperature in China. *Acta Meteor. Sinica*, **27**(1), 87–97, doi: 10.1007/s13351-013-0109-8.

1. Introduction

Solar radiation drives many surface processes including evaporation and snow and glacier melt (Wild, 2009) that result in near-surface air temperature changes. Since the International Geophysical Year

Supported by the National Basic Research and Development (973) Program of China (2011CB403405), National Science and Technology Support Program of China (2008BAC40B02), and China Meteorological Adminstration Special Public Welfare Research Fund (GYHY200906020).

*Corresponding author: huazhang@cma.gov.cn.

(1957–1958), extensive worldwide observations of surface solar radiation (SSR) have been conducted. Analysis of the obtained datasets reveals that SSR has shifted from a decreasing trend to an increasing trend during the past 50 years in most areas of Asia, Oceania, North America, Europe, and the South and North Poles. This shift is described as a change from "dimming" to "brightening" (Long et al., 2009; Norris and Wild, 2007; Ohmura, 2006; Liley, 2009; Wild et al., 2009). Studies of various areas of China reached similar conclusions. For example, Che et al. (2005) and Shi et al. (2008) studied the long-term change in total, direct, and diffuse radiation during 1960–2000 using radiation data from 64 and 72 stations in China, respectively. Both studies showed that the total and direct radiation at the surface began to increase from 1990. However, the exact reasons for such changes are unknown.

The Fourth Assessment Report of the Intergovernmental Panel on Climate Change (IPCC, 2007) noted that observed global averaged surface air temperature rose 0.74℃ during 1906–2005 and the warming rate in the last 50 years had almost doubled compared to the previous 50 years. Many researchers have examined long-term temperature changes in China (Ren et al., 2005a, b, c; Ding and Dai, 1994; Wang et al., 1998; Gong and Wang, 1999; Tang and Lin, 1992; Zhang et al., 2006). Surface air temperature in China also showed a clear increasing trend in the 96-yr period of 1905–2001. The increasing rate of 0.08℃ (10 yr)$^{-1}$ was slightly higher than the global mean in the same period (Ren et al., 2005b). The warming rate of the annual mean surface air temperature in China was 0.25℃ (10 yr)$^{-1}$ during 1951–2004, when the most significant warming occurred in winter and spring in northern China and over the Qinghai-Tibetan Plateau (Ren et al., 2005c). Based on the dataset during 1955–2000 from 305 observational stations in China, Liu et al. (2004) gave the trend of daily maximum temperature ($T_{\max}$), daily minimum temperature ($T_{\min}$), and diurnal temperature range (DTR), which were 1.27℃ (100 yr)$^{-1}$, 3.23℃ (100 yr)$^{-1}$, and –2.5℃ (100 yr)$^{-1}$, respectively; whereas the corresponding values from Tang et al. (2005) based on the dataset during 1951–2002 from 733 observational stations in China were 0.14℃ (10 yr)$^{-1}$, 0.33℃ (10 yr)$^{-1}$, and –0.19℃ (10 yr)$^{-1}$, respectively. While the climate system is clearly warming, difficulties remain in explaining observed temperature changes on scales smaller than continental levels. Changes in greenhouse gases (GHG) and aerosol concentrations, solar radiation, and land cover all can alter the energy balance of the climate system (IPCC, 2007). However, these major factors influencing surface temperature changes may vary by region. Some studies suggested that a reduction in surface solar radiation was one reason why significant rises in surface air temperature from the 1950s to 1980s were not found in some regions such as the Arctic (Stanhill and Callaghan, 1995), China (Liu et al., 2004), America (Liepert, 2002), and India (Menon et al., 2002). Wild et al. (2007) showed that solar dimming was effective at masking greenhouse warming until the 1980s, but with the shift from solar dimming to solar brightening, the unmasked greenhouse effect has produced a rapid temperature rise. In light of these studies, we explore the possible influences on surface air temperature of the change from solar dimming to brightening in China.

Using updated SSR, surface air temperature, and cloud cover data for China during 1961–2008, we first analyze the long-term trend of the correlation between SSR and DTR. We then discuss the effect of the change in total solar radiation on the surface air temperature change. Finally, we present an explanation for the dimming and brightening in China.

2. Data

The SSR and surface air temperature data were from the National Meteorological Information Center of the China Meteorological Administration. The temperature data included DTR, mean, maximum, and minimum temperatures. Fifty-five stations with more than 40 yr of continuous observational data were selected. Figure 1 shows the locations of these 55 stations, which are distributed widely throughout China, except on the Qinghai-Tibetan Plateau and in Inner Mongolia. For consistency with the solar radiation data, the other daily meteorological data used in this study were from the same stations. To achieve

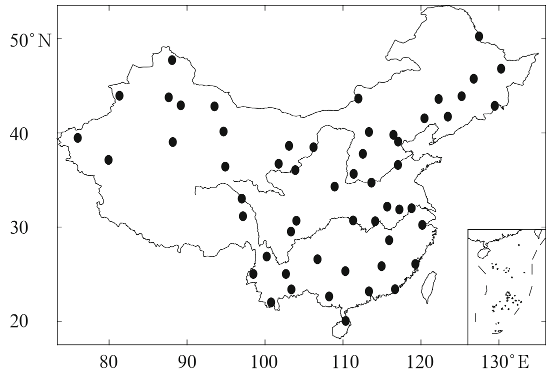

Fig. 1. Locations of the 55 stations.

better accuracy, the data quality control treatment of Shi et al. (2008) was applied to the solar radiation datasets, including physical threshold, sunshine duration, and standard deviation tests (details in Shi et al., 2008).

3. Long-term changes in SSR

3.1 Changes in total radiation

Figure 2 shows the long-term changes in annual mean total solar radiation at the 55 stations. The total solar radiation showed a decreasing trend before 1990, with the most significant decrease from the mid 1960s to late 1980s. The decreasing trend in total solar radiation reversed in the early 1990s, but the absolute magnitude never reached the level of the 1960s again. This result agrees with that of Wild et al. (2007). The total solar radiation remained approximately stable after 1995. The shift in the trend around 1990 was consistent with previous findings (Che et al., 2005; Shi et al., 2008). The minimum value (153.4 W m^{-2}) appeared in 1989. Over the whole period of 1960–2008, the total solar radiation decreased by 2.73 W m^{-2} (10 yr)$^{-1}$, with a decline rate of 7.78 W m^{-2} (10 yr)$^{-1}$ from 1961 to 1989. This was significant at the 95% confidence level. From 1990 to 2008, total solar radiation increased at a rate of 1.12 W m^{-2} (10 yr)$^{-1}$, which was not significant at the 95% confidence level.

3.2 Changes in diffuse radiation

The changes in diffuse solar radiation were obviously different from those in total solar radiation, as shown in Fig. 3. There was an increasing tendency in the 1960s, after which fluctuations in diffuse solar radiation continued until around 1980. Diffuse solar radiation then decreased continuously during the whole 1980s and approached a minimum value in 1990. From 1990 to the present, a gradual increasing trend has occurred, as shown by the almost linear trend line in Fig. 3. These features for diffuse solar radiation are similar to those found in previous studies, except that the slope of the linear trend depended on which stations were selected (Che et al., 2005). The trends were –0.1, –0.26, and 1.81 W m^{-2} (10 yr)$^{-1}$ for the periods 1961–2008, 1961–1989, and 1990–2008, respectively. Of these, only the change during 1990–2008 was significant at the 95% confidence level. Volcanic eruptions had a large effect on diffuse solar radiation, as

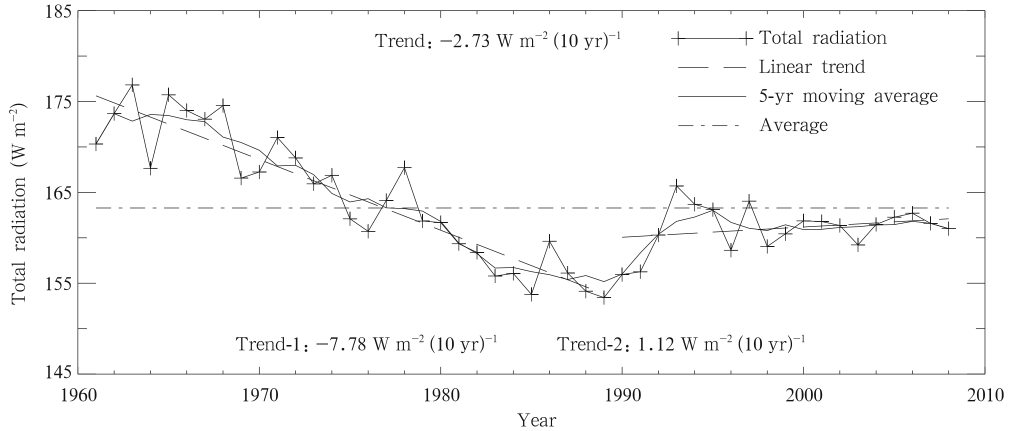

Fig. 2. Time series of annual mean total solar radiation of the 55 stations in China. Trend: from 1960 to 2008; Trend-1: from 1961 to 1989; Trend-2: from 1990 to 2008.

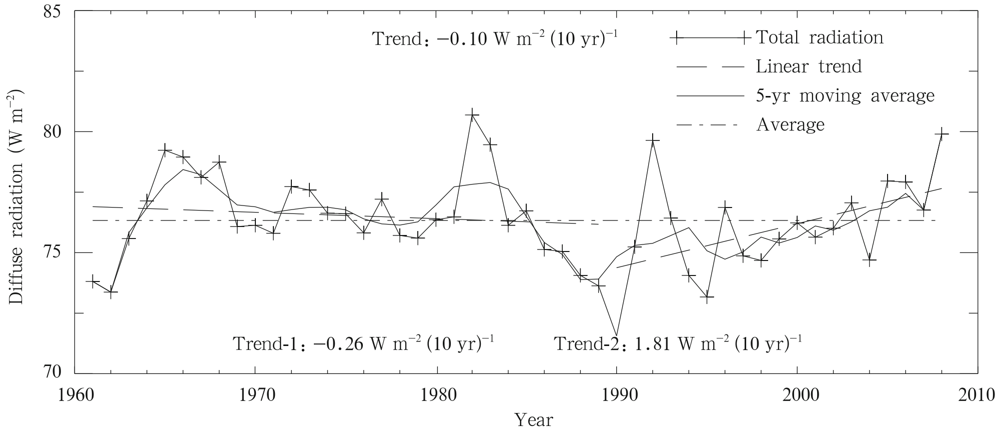

Fig. 3. Time series of annual mean diffuse solar radiation of the 55 stations in China.

shown in Fig. 3. There were three obvious peaks in the eruption years 1966, 1982, and 1991.

4. Dimming and brightening in China

On the basis of numerical simulations, Shen and Zhang (2009) suggested that the solar radiation arriving at the surface depends on atmospheric absorption by water vapor and ozone, and atmospheric scattering by clouds, aerosol, and molecules. The largest effects come from clouds, followed by atmospheric absorption and aerosols. To explain the dimming and brightening over China, we analyzed the long-term changes in annual mean total and low cloud cover during the same period (1961–2008) for the average of the same 55 stations examined earlier for SSR (Figs. 4a and 4b). In general, the trend in cloud cover over China for the whole period of 1961–2008 was consistent with previous reports (Baker et al., 1995; Kaiser, 2000).

By combining Figs. 2 and 3, we can see that the diffuse solar radiation remained almost unchanged during the 1961–1989 dimming period, and then began to increase rapidly during the 1990–2008 brightening period. This indicates that the diffuse radiation did not contribute to the dimming, but made a large contribution to the brightening occurring in the second period. Therefore, direct and diffuse radiation should play important roles in the dimming and brightening periods, respectively. The factors affecting direct solar radiation were mainly clouds, absorptive aerosols, and GHGs (mainly water vapor and ozone), whereas clouds, scattering aerosols, and atmospheric molecules were major factors affecting diffuse radiation. The Rayleigh scattering of molecules was smaller than the other two factors and was spherical, so it could be ignored here. Figure 4 shows that the total cloud cover decreased gradually in the first dimming period, but increased more rapidly in the subsequent brightening period. Thus, the direct radiation reaching the surface could be enhanced by the total cloud cover change during the dimming period, which was opposite to the change of SSR during 1961–1989. Consequently, the clouds did not contribute to the dimming process. Therefore, in the first dimming stage, the absorptive aerosol and GHGs were likely the main factors in reducing the direct solar radiation arriving at the surface.

The simultaneous decreases in surface solar radiation and cloud coverage can be attributed to a combination of the effects of GHGs and fossil fuel aerosols (FFAs). Figure 5 shows the surface solar radiation trend in China simulated by a general circulation model coupled with an aerosol transport model and an ocean mixed-layer model. The detailed description of these models was given in Mukai et al., (2008). Columns represent the simulation conditions. The right column shows the simulation results using annual mean statistics, which are divided into clear, cloudy, and all sky cases in the left, center, and right columns, respectively. Each row shows the effects of FFAs, GHGs, and the mixture of FFAs and GHGs from top to bottom. FFAs can cause a direct decrease

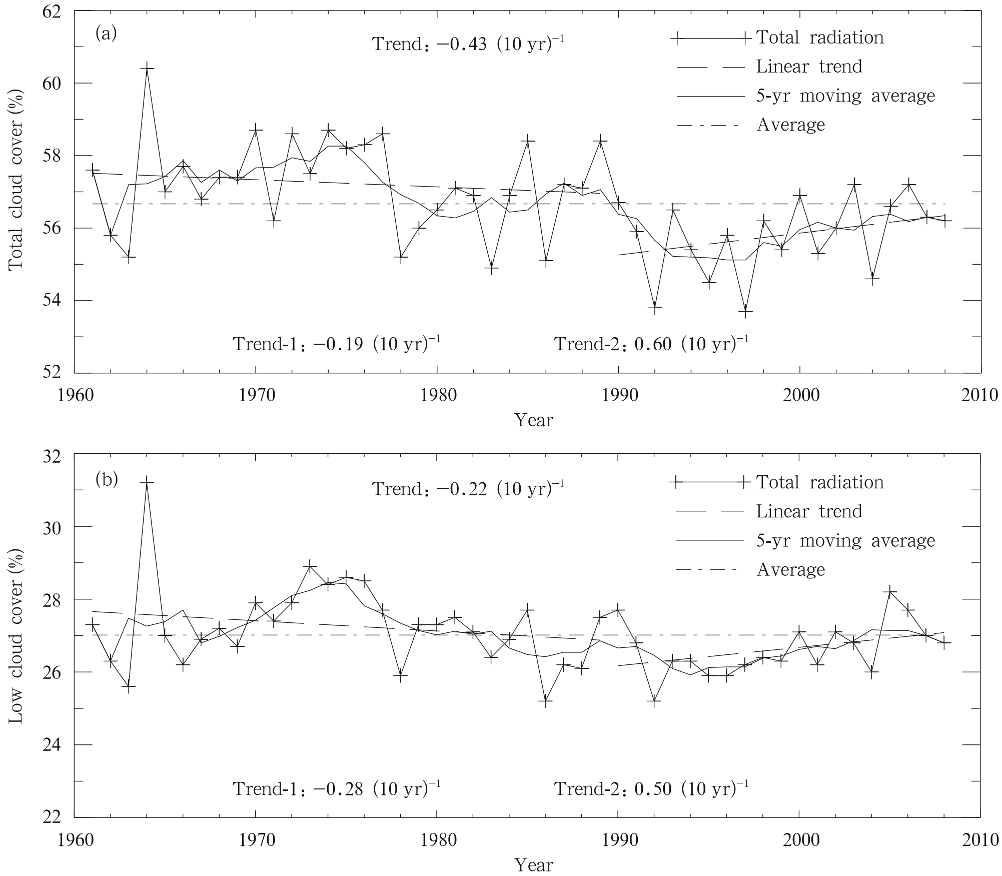

Fig. 4. Time series of annual mean total and low cloud cover of the 55 stations in China. (a) Total cloud cover and (b) low cloud cover.

in surface solar radiation in the clear sky case, whereas the radiation decrease in the cloudy sky case suggests an increase in cloud coverage through the aerosol indirect effect. GHGs can lead to an increase in solar radiation in the cloudy sky case, which suggests a decrease in cloud coverage, but they cannot explain the decrease in solar radiation in the clear sky case. Finally, the mixture of FFA and GHG effects shows a decrease in solar radiation in the all sky case and also an increase in the cloudy sky case, which suggests a decrease in cloud coverage. Comparison of the clear sky cases shown in the left columns of Fig. 5 shows that the effect of FFAs on the decrease in solar radiation was larger than that of GHGs in China. Thus, absorbing FFAs are considered to have played the most important role in reducing the direct radiation arriving at the surface during the first dimming period. This is also consistent with the modeling results of Mukai et al. (2008).

In the second period, diffuse radiation at the surface may have been reduced by increased cloud cover. This suggestion was confirmed by model results, as shown in Fig. 6 when the cloud coverage is more than half. We used a column radiative transfer model called BCC_RAD (Zhang et al., 2003, 2006a, b) to calculate the downward diffuse fluxes (DDFs) at the surface. The results (Fig. 6) show an increase in DDF with cloud cover of low, middle, and high clouds, when the cloud amount was less than half. When the cloud amount was larger than half, the situation was reversed. In the calculation, we took the solar zenith angle as 60 degrees to represent the average situation in the atmosphere. We placed low, middle, and high clouds at 1–2, 4–5, and 10–12 km, separately, with cloud water contents of 0.22, 0.28, and 0.0048 g m^{-3} and effective radii of 5.89, 6.2, and 41.5 microns, respectively. The total cloud amount over China was larger than 50% during 1960–2008 as shown in Fig. 4a,

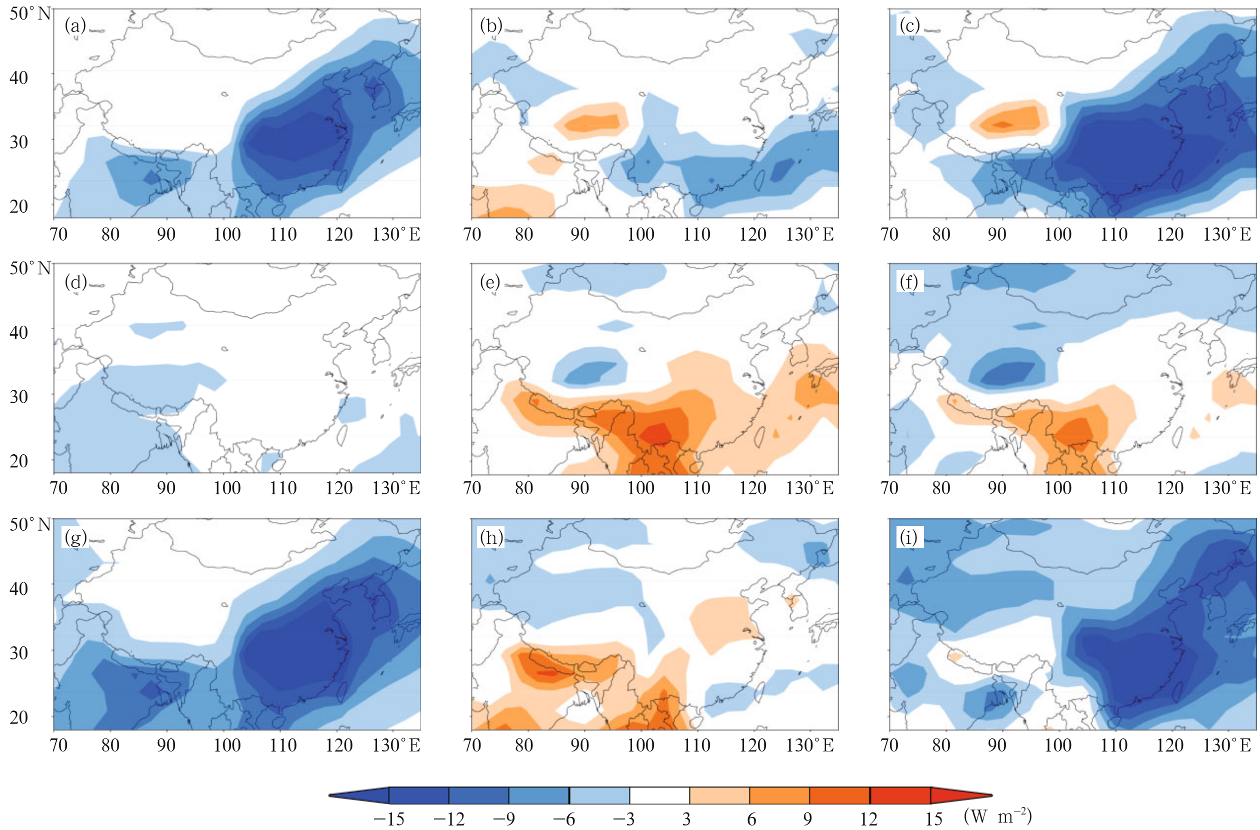

Fig. 5. Effects of FFA (a, b, c), GHGs (d, e, f), and clouds (g, h, i) on the solar radiation at the surface. (a, d, g) Clear sky, (b, e, h) cloudy sky, and (c, f, i) all sky.

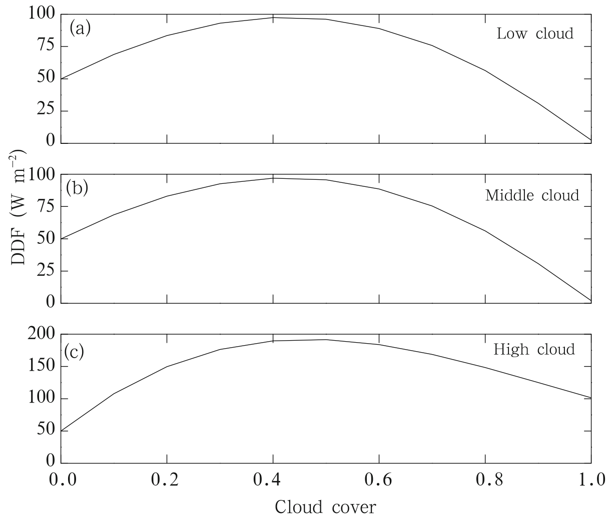

Fig. 6. Change of downward diffuse flux (DDF) at the surface with (a) low, (b) middle, and (c) high cloud cover.

thus we took the total cloud effects on DDF in China in Fig. 6 as those occurring when the cloud amount was larger than 50% in Fig. 4a. In other words, the DDF was reduced when the cloud cover increased. Therefore, clouds could not have played any role in the brightening process in the second period by combining Figs. 3, 4, and 6.

Considering the above analyses, we concluded that increasing concentrations of absorbing and scattering aerosols (including sulfate) were the major causes for the dimming and brightening in the two respective periods. This conclusion was different from that proposed by Liu et al. (2004), who considered sulfate to be a major factor in the dimming process. Sulfate aerosols from industries have greatly increased because of the rapid economic development in China since 1989 (Streets et al., 2003). However, long-term continuous observational emission data for absorptive and scattering aerosols are not available over the entire period of 1961–2008 in China, making further quantitative validation impossible.

Note that this work ignores changes in surface albedo due to land-use changes in China during this period. The effect of such changes on diffuse radiation is much less than that of aerosols, as indicated by Shen and Zhang (2009).

5. Relation between SSR and DTR

DTR, which is defined as the difference between daily maximum and minimum temperature, is useful for studying the counteracting effects of longwave and shortwave radiative forcings because the diurnal minimum temperature is closely linked to longwave radiation, whereas the diurnal maximum temperature is predominantly determined by shortwave radiation (Makowski et al., 2008). Figures 7 and 8 show scatter plots of the anomaly annual mean and seasonal mean of DTR and SSR. The seasonal and annual means were used here to reduce the influence of weather on the relationship between total SSR and DTR. The annual mean correlation coefficient between SSR and DTR was 0.84, as shown in Fig. 7, similar to the value of 0.88 reported by Liu et al. (2004). The correlation coefficients were higher in winter (0.90), smallest in summer (0.75), and intermediate in spring (0.79) and autumn (0.78). All values were significant at the 99% confidence level. The slope of the regression line can represent the effect of SSR on DTR (Makowski et al., 2009); the higher the slope, the greater the effect. The slope was biggest in winter, medium in spring and autumn, and smallest in summer, as shown in Fig. 8. Thus, we concluded that the influence of SSR on DTR was greater when the slope was larger and there was higher correlation between them. The relationship between SSR and DTR was not strictly linear, as shown by the different slopes for the four seasons in Fig. 8. The variations of water vapor and clouds in different seasons and the Stefan-Boltzmann Law showing the relationship between radiation flux at the surface and surface temperature can explain the nonlinear relationship between DTR and SSR (Wild et al., 2007).

Figures 9a and 9b show distributions of the stations with the highest correlation coefficients of DTR and SSR over the four seasons in China for all days and clear days (cloud cover less than 10%), respectively. For all-day case, there were 27 stations with the highest correlation coefficient in winter (about 50% of the total). They were mainly distributed near the southeast coast, but also in Southwest China (Sichuan and Guizhou), Northwest China (Xinjiang, Gansu, and Qinghai), and Northeast China. The stations could be classified into two types. One type was the stations near the southeast coast, Sichuan, and Guizhou, where water vapor was abundant in summer the influence of SSR on DTR was reduced in summer, and the correlation coefficient became largest in winter. The other type was stations in northern China, where there are long periods of continuous fine weather in winter due to the influence of the Siberian high, leading to the largest SSR effect on DTR. For clear-day case in wintertime, strong correlations occurred at most stations in northern China. In southern China, strong correlations occurred mostly in autumn, followed by summer and spring. This indicated that clouds and water vapor have strong influences on both SSR and DTR and hence on their relationship. The largest correlation between SSR and DTR usually occurred in northern China during wintertime, regardless of whether all-day or clear-day data were used.

6. Annual changes in surface temperature

Figure 10 shows time series of T_{mean}, T_{max}, T_{min}, and DTR for the selected 55 stations in China. Because the total SSR reversed from dimming to brightening at the beginning of 1990, the linear trends of these quantities were also divided into two periods: 1961–1989 and 1990–2008.

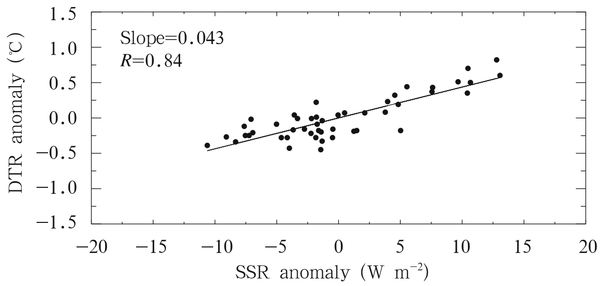

Fig. 7. Scatter plots of anomaly annual mean of DTR and SSR for all days. Solid line denotes the best fit regression line.

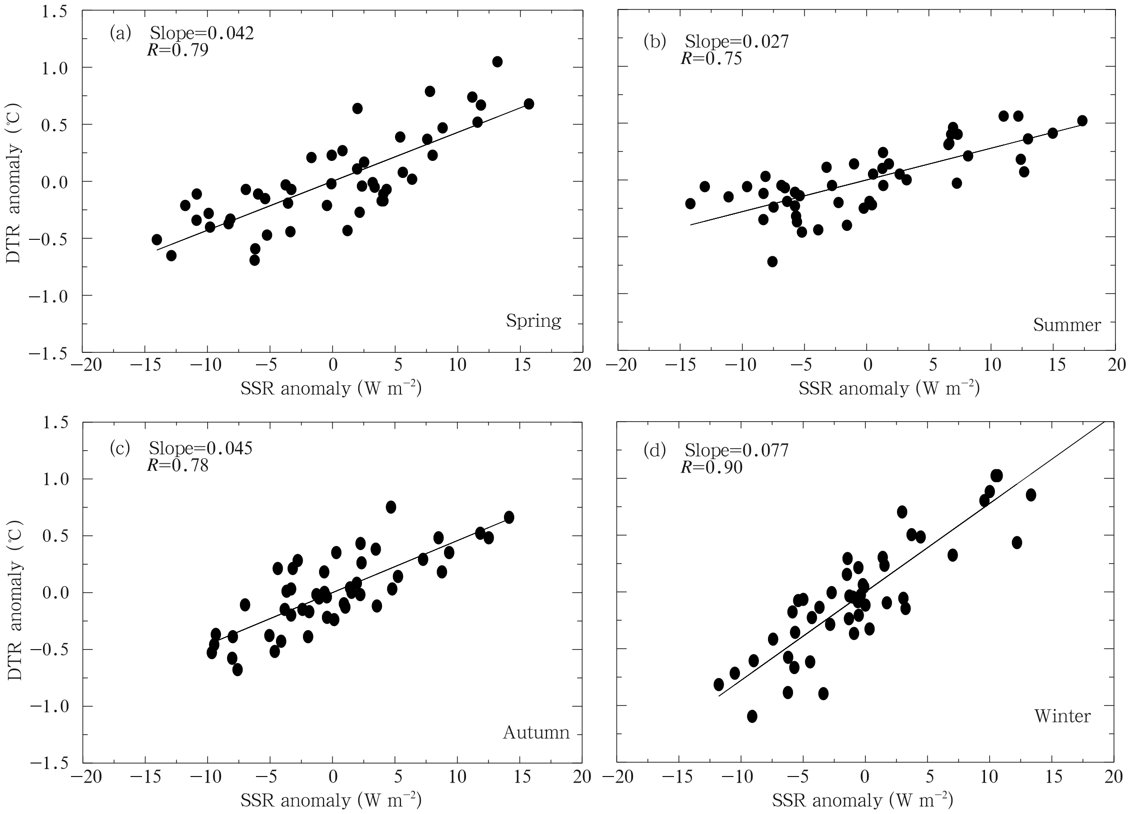

Fig. 8. Scatter plots of anomaly seasonal mean of DTR and SSR for all days. (a) Spring, (b) summer, (c) autumn, and (d) winter. Solid line denotes the best fit regression line.

Figure 10a shows that there was generally an increasing trend in T_{mean} with a rate of 0.31℃ (10 yr)$^{-1}$ for the whole period, a smaller value of 0.10℃ (10 yr)$^{-1}$ in the former period (1961–1989), and a larger value of 0.46℃ (10 yr)$^{-1}$ after 1990. Considering these results in combination with the above analysis of SSR, we concluded that T_{mean} increased slowly when SSR decreased during 1961–1989, but increased quickly when SSR switched from dimming to brightening after 1990, indicating an obvious effect of total SSR on surface air temperature. SSR and thermal radiation have different effects on temperature, as reported by Wild et al. (2007). SSR only works during daytime, and hence has more influences on maximum temperature than on minimum temperature. In contrast, the minimum temperature is mainly controlled by thermal radiation at the surface, especially surface radiative cooling at night, which depends on the ability of the atmosphere to absorb and re-emit the thermal radiation to the surface. Therefore, we can calculate how much the SSR changes the surface temperature by analyzing the changes in T_{max}, T_{min}, and DTR in China. Figure 10b shows only a slight decrease in the annual mean maximum temperature during 1961–1989, which was consistent with the decrease in SSR in this period. It almost canceled the effects of SSR reduction and GHG concentration increases on T_{max} (Liu et al., 2004). The idea that the dimming process can affect the surface air temperature (Wild et al., 2007) was hence validated in this work. In contrast, the minimum temperature, which was little influenced by the total SSR, was increasing during this period (see Fig. 10c), suggesting that the greenhouse effect was enhanced. Comparing the linear tendency rates of temperature between 1961–1989 and 1990–2008 in Figs. 10b and 10c, we see that the difference in the slope of maximum temperature (0.54℃ (10 yr)$^{-1}$) between the two periods was much higher than that of the minimum temperature (0.32℃ (10 yr)$^{-1}$). This illustrates that the increase in maximum temperature exceeded that in minimum temperature, which was consistent with the reversal of total SSR from

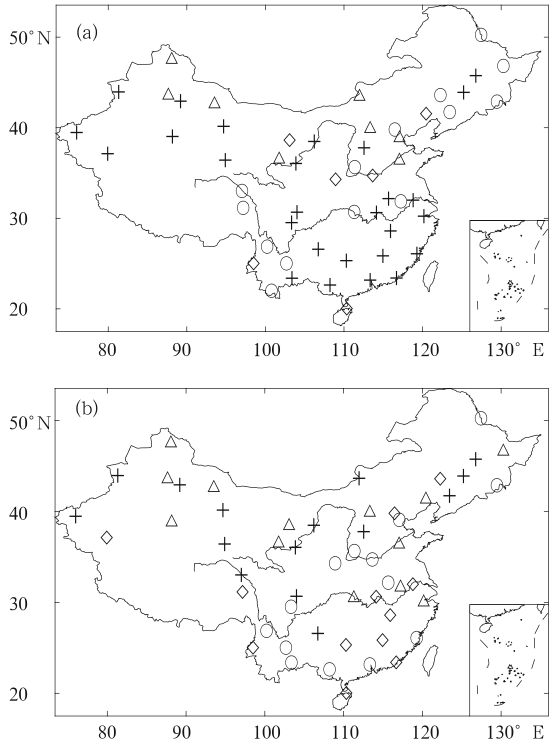

Fig. 9. Distributions of the stations with the highest correlation coefficient between DTR and SSR over four seasons in China for (a) all days and (b) clear days. △: spring; ○: summer; ◇: autumn; and +: winter.

dimming to brightening from the beginning of the 1990s. There were corresponding changes in DTR (see Fig. 10d). During 1961–1989, DTR decreased quickly at a rate of 0.30℃ (10 yr)$^{-1}$ due to the decrease in mean maximum temperature and increase in mean minimum temperature. However, after 1990, DTR decreased much more slowly, at a rate of only 0.07℃ (10 yr)$^{-1}$, due to the almost simultaneous increase in both the maximum and minimum temperatures, i.e., SSR did not prevent the maximum and minimum temperatures from a synchronized increase.

Assuming that SSR did not decrease in the first period, the slope of mean temperature would be almost the same (about 0.24℃ (10 yr)$^{-1}$) as that of minimum temperature. However, the actual value of the mean temperature slope was only 0.10℃ (10 yr)$^{-1}$, which implies that the dimming process dampened about 58% of the increase in mean temperature. This estimate was slightly less than the global value of about 60%–70% provided by Wild et al. (2007). The surface temperature response after 1990 should more realistically reflect the increase in GHG concentration because there are no solar dimming mask effects during the second period. The annual mean temperature of the 55 stations increased by 0.46℃ (10 yr)$^{-1}$ during 1990–2008. This was possibly the upper limit of the climate system response to the greenhouse effect. However, during the whole period of 1961–2008, the temperature increase of 1.48℃ (0.31℃ (10 yr)$^{-1}$) may have been the lower limit of climate system response to the changing greenhouse effect because of the dimming of total SSR (see Fig. 2). This result also indicates that the greenhouse effect was increasing in the past 48 years. Therefore, the increase in surface temperature due to GHGs in China should be between 0.31 and 0.46℃ (10 yr)$^{-1}$. These values are larger than the respective estimates of 0.20℃ (10 yr)$^{-1}$ and 0.38℃ (10 yr)$^{-1}$ given by Wild et al. (2007) over all continents.

7. Conclusions

Using radiation, temperature, and cloud cover data at 55 stations in China during 1961–2008, long-term changes in annual mean total surface solar radiation, diffuse radiation, and surface air temperature were analyzed to study the effect of SSR changes on surface temperature in China. The major conclusions are as follows.

(1) Total SSR decreased before 1990, most significantly from the mid 1960s to the end of the 1980s. The trend in total SSR switched from decreasing to increasing at the beginning of the 1990s and remained almost unchanged after 1995. The dimming and brightening over China were likely due to the increase in absorptive and scattering aerosols in the atmosphere, respectively.

(2) Generally, there was a close correlation between total SSR and DTR. The correlation coefficient was the highest in winter and the slope of the linear regression line was also the greatest in winter. This indicates that the total SSR had the largest influence on DTR in winter on average for the 55 stations. For all days, the best correlation occurred in winter at about half of the stations.

(3) For the whole period of 1961–2008, the total

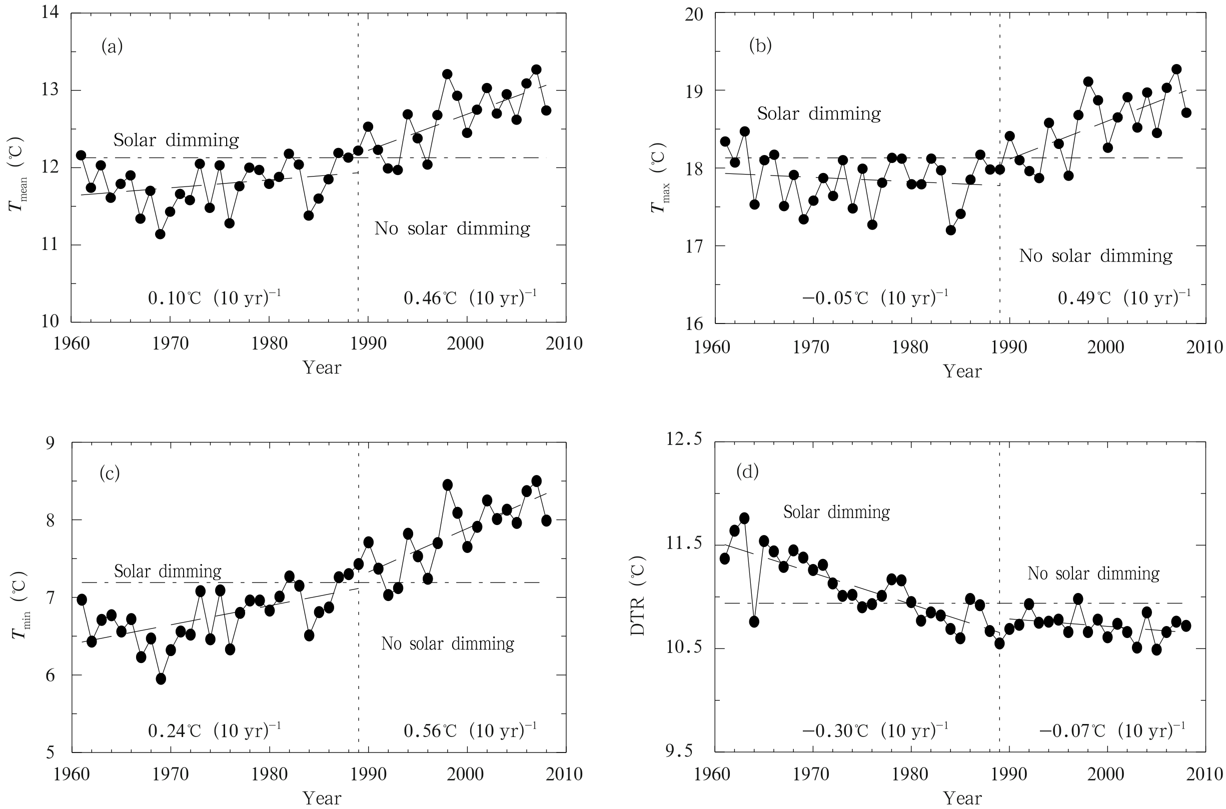

Fig. 10. Time series of annual means of daily temperature of the 55 stations in China. (a) T_{mean}, (b) $T_{\max}$, (c) $T_{\min}$, and (d) DTR. The dashed lines are the linear trend in both periods.

SSR also had influences on the surface temperature in China although the greenhouse effect was still the major driver of surface temperature rises. The surface temperature increase due to the greenhouse effect was higher than 0.31℃ (10 yr)$^{-1}$ and lower than 0.46℃ (10 yr)$^{-1}$ in the past 48 years in China. These values are larger than those given by Wild et al. (2007) over all the continents.

Acknowledgments. The authors would like to thank Mr. Jing Xianwen, Miss Zhao Shuyun, and Dr. Wang Fenjuan for their great efforts, and the anonymous reviewers for their helpful comments and suggestions.

REFERENCES

Baker, C. B., R. G. Quayle, and W. Wang, 1995: The influence of night time cloud cover on the observed minimum temperature in China. *Atmos. Res.*, **37**(1–3), 27–35.

Che, H. Z., G. Y. Shi, X. Y. Zhang, et al., 2005: Analysis of 40 years of solar radiation data from China, 1961–2000. *Geophys. Res. Lett.*, **32**, L06803, doi: 10.1029/2004GL022322.

Ding Yihui and Dai Xiaosu, 1994: Temperature variation in China during the last 100 years. *Meteor. Mon.*, **20**(12), 19–26. (in Chinese)

Gong Daoyi and Wang Shaowu, 1999: 1998: The warmest year on record of the century in China. *Meteor. Mon.*, **25**(8), 1–3. (in Chinese)

IPCC, 2007: *Climate Change 2007: The Physical Science Basis. Contribution of Working Group I to the Fourth Assessment Report of the Intergovernmental Panel on Climate Change.* S. Solomon, et al., Eds., Cambridge University Press, Cambridge, UK, 996 pp.

Kaiser, D. P., 2000: Decreasing cloudiness over China: An updated analysis examining additional variables. *Geophys. Res. Lett.*, **27**(15), 2193–2196.

Liepert, B. G., 2002: Observed reductions of surface solar radiation at sites in the United States and worldwide from 1961 to 1990. *Geophys. Res. Lett.*, **29**(10), 1421, doi: 10.1029/2002GL014910.

Liley, J. B., 2009: New Zealand dimming and brightening. *J. Geophys. Res.*, **114**, D00D10, doi: 10.1029/2008JD011401.

Liu, B. H., M. Xu, M. Henderson, et al., 2004: Taking China's temperature: Daily range, warming trends, and regional variation, 1955–2000. *J. Climate*, **17**(22), 4453–4462.

Long, C. N., E. G. Dutton, and J. A. Augustine, 2009: Significant decadal brightening of downwelling shortwave in the continental United States. *J. Geophys. Res.*, **114**, D00D06, doi: 10.1029/2008JD011263.

Makowski, K., M. Wild, and A. Ohmura, 2008: Diurnal temperature range over Europe between 1950 and 2005. *Atmos. Chem. Phys.*, **8**, 6483–6498.

——, E. B. Jaeger, M. Chiacchio, et al., 2009: On the relationship between diurnal temperature range and surface solar radiation in Europe. *J. Geophys. Res.*, **114**, D00D07, doi: 10.1029/2008JD011104.

Menon, S., J. Hansen, L. Nazarenko, et al., 2002: Climate effects of black carbon aerosols in China and India. *Science*, **297**(5590), 2250–2253.

Mukai, M., T. Nakajima, and T. Takemura, 2008: A study of anthropogenic impacts of the radiation budget and the cloud field in East Asia based on model simulations with GCM. *J. Geophys. Res.*, **113**, D12211, doi: 10.1029/2007JD009325.

Norris, J. R., and M. Wild, 2007: Trends in aerosol radiative effects over Europe inferred from observed cloud cover, solar 'dimming,' and solar 'brightening'. *J. Geophys. Res.*, **112**, D08214, doi: 10.1029/2006JD007794.

Ohmura, A., 2006: Observed long-term variations of solar irradiances at the Earth's surface. *Space Sci. Rev.*, **125**(1–4), 111–128.

Ren Guoyu, Guo Jun, Xu Mingzhi, et al., 2005a: Climate changes of China's mainland over the past century. *Acta Meteor. Sinica*, **63**(6), 942–956. (in Chinese)

——, Chu Ziying, Zhou Yaqing, et al., 2005b: Recent progress in studies of regional temperature changes in China. *Clim. Environ. Res.*, **10**(4), 701–716. (in Chinese)

——, Xu Mingzhi, Chu Ziying, et al., 2005c: Changes of surface air temperature in China during 1951–2004. *Clim. Environ. Res.*, **10**(4), 717–727. (in Chinese)

Shen Zhongping, and Zhang Hua, 2009: An analysis on the factors affecting surface solar radiation and its spectral distribution. *Acta Energiae Solaris Sinica*, **28**(2), 419–424.

Shi, G. Y., T. Hayasaka, A. Ohmura, et al., 2008: Data quality assessment and the long-term trend of ground solar radiation in China. *J. Appl. Meteor. Climatol.*, **47**(4), 1006–1016.

Stanhill, G., and T. V. Callaghan, 1995: Global irradiance, air pollution and temperature changes in the Arctic. *Phil. Trans. R. Soc.*, **352**(1699), 247–258, doi: 10.1098/rsta.1995.0068.

Streets, D. G., T. C. Bond, G. R. Carmichael, et al., 2003: An inventory of gaseous and primary aerosol emissions in Asia in the year 2000. *J. Geophys. Res.*, **108**, D21, 8809, doi: 10.1029/2002JD003093.

Tang Guoli, and Lin Xuechun, 1992: Average air temperature series and its variations in China. *Meteor. Mon.*, **18**(7), 3–6. (in Chinese)

Tang Hongyu, Zhai Panmao, and Wang Zhenyu, 2005: On change in mean maximum temperature, minimum temperature and diurnal range in China during 1951–2002. *Climatic Environ. Res.*, **10**(4), 728–735. (in Chinese)

Wang Shaowu, Ye Jinlin, Gong Daoyi, et al., 1998: Construction of mean annual temperature series for the last one hundred years in China. *J. Appl. Meteor. Sci.*, **9**(4), 392–401. (in Chinese)

Wild, M., 2009: Global dimming and brightening: A review. *J. Geophys. Res.*, **114**, D00D16, doi: 10.1029/2008JD011470.

——, A. Ohmura, and K. Makowski, 2007: Impact of global dimming and brightening on global warming. *Geophys. Res. Lett.*, **34**, L04702, doi: 10.1029/2006GL028031.

——, B. Trussel, A. Ohmura, et al., 2009: Global dimming and brightening: An update beyond 2000. *J. Geophys. Res.*, **114**, D00D13, doi: 10.1029/2008JD011382.

Zhang, H., T. Nakajima, G. Y. Shi, et al., 2003: An optimal approach to overlapping bands with correlated k-distribution method and its application to radiative calculations. *J. Geophys. Res.*, **108**, 4641–4653.

——, G. Y. Shi, T. Nakajima, et al., 2006a: The effects of the choice of k-interval number on radiative calculations. *J. Quant. Spectrosc. Radiat. Transfer*, **98**(1), 31–43.

——, T. Suzuki, T. Nakajima, et al., 2006b: The effects of band division on radiative calculations. *Opt. Eng.*, **45**(1), 016002.

Zhang Jingjing, Chen Shuang, and Zhao Xinyi, 2006: Spatial divergency of temperature change during 1951–2000 in China and its correlation with global climate change. *J. Arid Land Resources Environ.*, **20**(4), 1–6. (in Chinese)

ADVANCES IN ATMOSPHERIC SCIENCES, VOL. 30, NO. 4, 2013, 1017–1024

An Updated Estimation of Radiative Forcing due to CO_2 and Its Effect on Global Surface Temperature Change

ZHANG Hua*[1] (张 华), ZHANG Ruoyu[2,1] (张若玉), and SHI Guangyu[3] (石广玉)

[1] *Laboratory for Climate Studies, China Meteorological Administration, National Climate Center, Beijing* 100081

[2] *Atmosphere Science Academy, Nanjing University of Information Science and Technology, Nanjing* 210044

[3] *State Key Laboratory of Numerical Modeling for Atmospheric Sciences and Geophysical Fluid Dynamics, Institute of Atmospheric Physics, Beijing* 100029

(Received 20 August 2012; revised 8 October 2012; accepted 26 October 2012)

ABSTRACT

New estimations of radiative forcing due to CO_2 were calculated using updated concentration data of CO_2 and a high-resolution radiative transfer model. The stratospheric adjusted radiative forcing (ARF) due to CO_2 from the year 1750 to the updated year of 2010 was found to have increased to 1.95 W m^{-2}, which was 17% larger than that of the IPCC's 4th Assessment Report because of the rapid increase in CO_2 concentrations since 2005. A new formula is proposed to accurately describe the relationship between the ARF of CO_2 and its concentration. Furthermore, according to the relationship between the ARF and surface temperature change, possible changes in equilibrium surface temperature were estimated under the scenarios that the concentration of CO_2 increases to 1.5, 2, 2.5, 3, 3.5 and 4 times that of the concentration in the year 2008. The result was values of +2.2°C, +3.8°C, +5.1°C, +6.2°C, +7.1°C and +8.0°C respectively, based on a middle-level climate sensitivity parameter of 0.8 K (W $m^{-2})^{-1}$. Non-equilibrium surface temperature changes over the next 500 years were also calculated under two kinds of emission scenarios (pulsed and sustained emissions) as a comparison, according to the Absolute Global Temperature change Potential (AGTP) of CO_2. Results showed that CO_2 will likely continue to contribute to global warming if no emission controls are imposed, and the effect on the Earth-atmosphere system will be difficult to restore to its original level.

Key words: CO_2, radiative forcing, surface temperature change, Global Temperature change Potential

Citation: Zhang, H., R. Y. Zhang, and G. Y. Shi, 2013: An updated estimation of radiative forcing due to CO_2 and its effect on global surface temperature change. *Adv. Atmos. Sci.*, **30**(4), 1017–1024, doi: 10.1007/s00376-012-2204-7.

1. Introduction

Many human activities involve emissions of major greenhouse gases, such as CO_2, CH_4, N_2O and halocarbons, and as such concentrations of these gases in the atmosphere have increased greatly since the Industrial Revolution (IPCC, 2007), bringing about important changes in the composition of the atmosphere and contributing significantly to global warming. In order to slow down global warming, these greenhouse gases were all identified in the Kyoto Protocol, and requirements were placed on controlling their emissions. Of these, CO_2 is the most significant greenhouse gas and is the largest radiative forcing factor. Therefore, an increase of CO_2 concentration in the atmosphere will produce the greatest impact for global climate change in the future (IPCC, 2007).

The main sources responsible for the increase of CO_2 concentration include human activities such as the combustion of fossil fuels and changes in land use. Exchanges of CO_2 with the terrestrial biosphere and surface-ocean take place rapidly after its initial release into the atmosphere, and it is then redistributed over hundreds of years, meaning it persists in the atmosphere for a relatively long period of time. Furthermore, CO_2 is very good at absorbing longwave ra-

*Corresponding author: ZHANG Hua, huazhang@cma.gov.cn

diation in the spectral region 500–800 cm^{-1} (15-μm band). Over the 8000 years before the Industrial Revolution, the concentration of CO_2 only increased by 20 ppmv, basically remaining at a level below 300 ppmv (IPCC, 2007). However, the Industrial Revolution broke this balance and caused a rapid increase in the concentration of CO_2 and other greenhouse gases in the atmosphere. As of 2008, the global mean mixing ratio of CO_2 had reached 385.2 ppmv (WMO, 2009), and is still growing at a rate of 1–1.5 ppmv per year.

CO_2 is the main absorbing gas in the Earth's atmosphere, and there are strong absorption bands (e.g. 15 μm and 2.7 μm) and weak absorption bands (e.g. 10 μm) where atmospheric absorption properties are affected by its concentration, which in turn has a significant influence on levels of outgoing longwave radiation. Moreover, with a lifetime of greater than 10 years, CO_2 is known to be a "long-lived" greenhouse gas that will persist in the atmosphere for anywhere between 50 and 200 years before it is totally cleaned up by natural processes. In the meantime, it continues to accumulate, and all the while persists in its influence on the atmospheric radiation balance and its contribution to global warming (IPCC, 1996).

Radiative forcing is used to assess and compare anthropogenic and natural drivers of climate change, which is defined as the change of net irradiance at the tropopause due to changes in concentrations of greenhouse gases, and other factors. WMO (1986) indicated that changes in global mean surface temperature are related to the net radiation flux at the tropopause. Thus, radiative forcing is an important index and measure for evaluating global warming. The IPCC (1996) defined radiative forcing into two categories, according to whether the stratospheric temperature is allowed to be adjusted: (1) Instantaneous Radiative Forcing (IRF), which does not consider temperature change in the stratosphere; and (2) Adjusted Radiative Forcing (ARF), which is the change of net radiation flux at the tropopause after allowing stratospheric temperature to readjust to radiative equilibrium, but with surface and tropospheric temperatures and states held at unperturbed values. It is known from these definitions that radiative forcing could reveal the general trend of climate change; positive (negative) radiative forcing would warm up (cool down) the surface–troposphere system, causing an increase (decrease) in mean surface temperature. Therefore, we can quantitatively estimate the influence of CO_2 concentration changes on the Earth's climatic system by analyzing the radiative forcing due to CO_2, which then forms the basis for studying the climatic effects of greenhouse gases. For example, when calculating Global Warming Potentials (GWPs) and Global Temperature-change Potentials (GTPs) of greenhouse gases, the values of CO_2 radiative forcing, as a reference gas, are required to be provided. In addition, the ARF of greenhouse gases can be directly related to the change of surface temperature (Hansen et al., 1997; Stuber et al., 2001), so the ARF of CO_2 can be used for evaluating its contribution to surface temperature change.

Since the 4th Assessment Report of the IPCC (IPCC, 2007), the concentration of CO_2 has again increased rapidly. As of 2008, the global mean mixing ratio of CO_2 had reached 385.2 ppmv. It is thus necessary to update the situation regarding CO_2 radiative forcing data and the corresponding global surface temperature changes. In the work reported in the present paper, we used a high-accuracy radiative transfer model (998-band scheme) developed by Zhang et al. (2006a, b) and up-to-date CO_2 concentration data to obtain the IRF and ARF of CO_2 based on previous studies (Zhang et al., 2011a, b), taking into account the influence of its persistence (lifetime) in the atmosphere on its radiative efficiency. We also studied the updated radiative forcing data due to CO_2 changes from the Industrial Revolution until 2010, and propose a new simplified fitting formula to calculate the ARF of CO_2 according to its radiative forcing values generated from different scenario concentrations. Furthermore, we estimated the equilibrium surface temperature change with prescribed scenarios of CO_2 concentration change and non-equilibrium surface temperature change from the Industrial Revolution to 500 years in the future. Together, this work provides new information on how CO_2 acts to affect global warming.

The remainder of the paper is organised as follows. Section 2 introduces the radiation model and its input dataset. Section 3 describes the calculation scheme of radiative forcing (RF), evaluates the radiation model, and discusses the calculated RF. Section 4 applies the new formula to describe the relationship between the ARF of CO_2 and its concentration. Section 5 reports the results from the experiment to predict global mean equilibrium and non-equilibrium surface temperature changes under the chosen prescribed scenarios. And finally, section 6 presents the conclusions of the study.

2. Model and data

The longwave radiative transfer model adopted in this work was developed by Zhang et al. (2003, 2006a, b). The effective absorption coefficients in the model were calculated with the correlated k-distribution method proposed by Shi (1981), the optimal approach to overlapping bands by Zhang et al. (2003), the k-interval number-choosing method by Zhang et al. (2006a), and the band division method by

Table 1. The parameters of 15 cloud categories.

	Tropical Atmosphere			Midlatitude Atmosphere			Subarctic Atmosphere		
Category	Cloud amount (%)	Water or ice content (g m^{-3})	Effective radius (μm)	Cloud amount (%)	Water or ice content (g m^{-3})	Effective radius (μm)	Cloud amount (%)	Water or ice content (g m^{-3})	Effective radius (μm)
Cu (water)	11.43	0.03	10	9.50	0.03	10	2.43	0.03	10
Sc (water)	9.38	0.07	10	10.48	0.09	10	5.36	0.11	10
St (water)	0.75	2.47	10	2.26	2.79	10	5.17	4.11	10
Cu (ice)	0.00	0.01	30	2.03	0.03	30	3.42	0.04	30
Sc (ice)	0.00	0.20	30	1.12	0.17	30	5.76	0.22	30
St (ice)	0.00	5.90	30	0.30	4.26	30	2.85	3.76	30
Ac (water)	5.55	0.05	10	2.55	0.05	10	0.38	0.06	10
As (water)	4.43	0.09	10	3.67	0.10	10	0.82	0.13	10
Ns (water)	1.14	0.07	10	1.66	0.08	10	1.03	0.10	10
Ac (ice)	0.95	0.06	30	9.02	0.09	30	9.48	0.10	30
As (ice)	0.18	0.14	30	6.43	0.18	30	12.99	0.22	30
Ns (ice)	0.06	0.11	30	2.20	0.11	30	4.93	0.10	30
Ci (ice)	15.36	0.01	30	13.27	0.01	30	6.49	0.01	30
Cs (ice)	5.25	0.06	30	6.89	0.08	30	1.59	0.09	30
Dc (ice)	2.49	0.27	30	3.54	0.25	30	0.64	0.24	30

Zhang et al. (2006b). Zhang et al. (2006a, b) divided the whole spectral region (10–49000 cm^{-1}) into different bands; for example, 17, 21, 27, 55, 998 etc. Among them, the high-accuracy 998-band scheme divided the spectral region 10–49000 cm^{-1} (0.2–1000 μm) into 998 bands, with 498 bands in the longwave region 10–2500 cm^{-1} (4–1000 μm), and with a spectral resolution of about 5 cm^{-1}. The k-interval number was optimized for each band and the values ranged from 2 to 16. For detailed information about band division, k-interval numbers and absorbing gases in each band, see Zhang et al. (2006b) and references therein.

Five main greenhouse gases (H_2O, CO_2, O_3, CH_4, N_2O and CFCs) were included in the model, which assumes that CO_2, CH_4, N_2O and CFCs are evenly mixed in the atmosphere. The concentrations of CO_2, CH_4 and N_2O were their values as of 2008, which were 385.2, 1.797 and 0.3218 ppmv, respectively. CO_2 absorptions were from 4 to 18.9 μm in the longwave region, located in bands 105–498 in the 998-band scheme. Almost all the strong and weak bands were considered in the scheme, and thus the corresponding results were comparable to those of the precise line-by-line integration (LBL) model (Zhang and Shi, 2000; Zhang et al., 2005, 2008). Zhang et al. (2011b) also confirmed that radiative forcings calculated by the 998-band scheme are much more accurate than the 17-band scheme designed for climate models. Therefore, the high-accuracy 998-band scheme was adopted to calculate the radiative forcing due to CO_2 in this work.

The whole atmosphere was divided into 100 layers with a vertical resolution of 1 km. The surface height was set at 0 km, and the top of atmosphere (TOA) at 100 km. As for the calculation of radiation flux and heating rate, six kinds of model atmosphere (Garand et al., 2001) were used for the required profiles of temperature, pressure and gas (water vapor and O_3) concentration: tropical (TRO), mid-latitude summer (MLS), mid-latitude winter (MLW), sub-arctic summer (SAS), sub-arctic winter (SAW), and United States Standard (USS). Based on these, the instantaneous radiative efficiency (IRE) (RF per unit concentration) and the stratospheric adjusted radiative efficiency (ARE) of CO_2 were calculated, and the arithmetic mean and area-weighted zonal mean were separately used to obtain the corresponding global mean results for clear and all-sky conditions.

3. CO_2 radiative forcing

3.1 *Radiative forcing calculation scheme*

In order to calculate the ARF, an iterative method in the longwave radiative transfer model was needed, as proposed in previous work (Zhang et al., 2011a, b). If the convergence condition is satisfied, then the stratosphere reaches a new radiation equilibrium after the temperature adjustment, and the net radiative flux at the tropopause is the ARF. Whereas, the net radiative flux at the tropopause caused by a perturbing concentration change of gas without temperature adjustment in the stratosphere is the IRF. For special cases, if the perturbing concentration of gas is the unit concentration (e.g. 1 ppmv or 1 ppbv), then the cor-

Table 2. Comparison of longwave radiative forcings due to CO_2 under different scenarios and different models (units: m^{-2}).

	scenario 1: Doubling the concentration of CO_2			scenario 2: Water vapor content increases by 20% after doubling the concentration of CO_2		
Model Layer	998-band	AOGCMs	LBLs	998-band	AOGCMs	LBLs
TOA	3.03	2.45	2.8	3.26	3.57	3.78
200 hPa	5.6	5.07	5.48	4.13	4.45	4.57
Surface	1.7	1.12	1.64	11.14	11.95	11.52

responding radiative forcing per unit concentration is called the radiative efficiency of the gas.

Clouds are an important factor affecting the radiative forcing due to greenhouse gases. In the present study, the method described in Zhang et al. (2011a and b) was used to consider the effect of clouds. Accordingly, the parameters of 15 cloud categories are shown in Table 1 [see Zhang et al. (2011a, b) for further details]. Zhang et al. (2011a, b) also provide the stratospheric ARE of CO_2 for all-sky cases by the follow formula:

$$R=\sum_{i=1}^{15} C_{\mathrm{d}i}R_i+(1-C_{\mathrm{d}})R_{\mathrm{clear}}\,. \tag{1}$$

Here, $C_{\mathrm{d}i}$ (cloud category: i=1–15) is the cloud cover of each cloud category; $C_{\mathrm{d}}=\sum C_{\mathrm{d}i}$ is total cloud cover; and R_{clear} and R_i are the AREs for a clear and cloudy atmosphere, respectively. Then, the global mean ARE (R_{mean}) of CO_2 for all-sky cases was adopted (Zhang et al., 2011a, b):

$$R_{\mathrm{mean}}=\frac{1}{2}\times R_{\mathrm{tro}}+\left(\frac{\sqrt{3}}{2}-\frac{1}{2}\right)\times R_{\mathrm{mid}}+\left(1-\frac{\sqrt{3}}{2}\right)\times R_{\mathrm{sub}}\,. \tag{2}$$

Here, R_{tro}, R_{mid} and R_{sub} are the AREs of the tropical, mid-latitude and subarctic atmosphere types, respectively.

3.2 *Evaluation of the radiative transfer model*

In order to assess the radiative transfer model adopted in this study, the radiative forcings due to CO_2 under two different concentration hypotheses were calculated, and the results compared with those given by the atmosphere-ocean general circulation models (AOGCMs) in Collins et al. (2006). The two scenarios were: (1) doubling the concentration of CO_2 from 287 ppmv in 1860 to 574 ppmv (scenario 1); (2) increasing the water vapor content to 1.2 times the original after doubling the concentration of CO_2(scenario 2). The IRF results under these two scenarios included: (1) net longwave radiative flux at the TOA for clear sky; (2) longwave net radiative flux at 200 hPa for clear sky; (3) longwave net radiative flux at the surface for clear sky. In the calculation, MLS was chosen to make all the calculations under the same conditions for comparison purposes, within which the model atmosphere was divided into 40 layers, and the TOA was set at 80 km (0.01 hPa). The surface was assumed to be a black body with an emissivity of 1.0. The temperature of the surface was 294 K, and the influence of cloud and aerosol was neglected.

Table 2 shows the comparison between the results of this work and those given by the different models in Collins et al. (2006) under the above scenarios. The longwave radiative forcing values at the surface, 200 hPa, and model top under scenario 1 were 1.7, 5.6 and 3.03 W m^{-2}, respectively, and the longwave radiative forcing values under scenario 2 were 11.14, 4.13 and 3.26 W m^{-2}, respectively. The results were basically located in the range of the different AOGCMs, as well as those of the line-by-line integration models (LBLs). However, under scenario 1 the results were closer to those of the LBLs, while under scenario 2 they were closer to the results of the AOGCMs (with the exception of the results for the surface), but still only a little different from the results of the LBLs. In view of the values and magnitude, all the results can be regarded as being sufficiently similar, indicating that it is reasonable to calculate the longwave radiative forcing due to CO_2 using the 998-band model.

3.3 CO_2 *radiative efficiency and heating rate*

The IRE and ARE of CO_2 for clear sky obtained by the 998-band scheme were 1.992×10^{-5} and 1.878×10^{-5} W m^{-2} $ppbv^{-1}$, respectively, and the ARE for all-sky was 1.638×10^{-5} W m^{-2} $ppbv^{-1}$, becoming 1.567×10^{-5} W m^{-2} $ppbv^{-1}$ after lifetime-adjustment (120-yr CO_2 lifetime). In order to compare with the corresponding result (1.4×10^{-5} W m^{-2} $ppbv^{-1}$) given by the IPCC (IPCC, 2007), the radiative efficiency was used (units of W m^{-2} $ppbv^{-1}$). Among the results, those for clear sky were the arithmetic mean of the values under the six model atmosphere types, and those for all-sky were the zonal area-weighted means of the above three

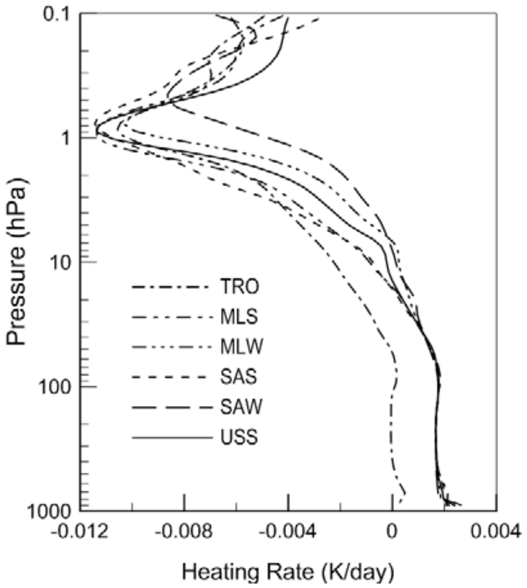

Fig. 1. The heating rates of 1 ppmv perturbation of CO_2 for the six model atmosphere types.

model atmosphere types in Eq. (2). By comparing the IRE for clear sky with the ARE, it was found that the radiative efficiency of CO_2 was reduced by 5.7% after stratospheric temperature adjustment.

Whether the effect of stratospheric temperature adjustment on radiative forcing was an increase or decrease depends on the influence of the temperature profile on the net radiative flux at the tropopause after the adjustment (Jain et al., 2000). In Fig. 1, the heating rates in the longwave region were induced by the disturbance of 1 ppmv under the six kinds of model atmosphere. It can be seen that the heating rates varied under different model atmosphere types, but the magnitudes and the vertical distributions were similar. Among the results, those of the USS model atmosphere were located basically in the middle of the results of all the model atmosphere types, thus representing an approximation of the average of heating rates for all kinds of model atmosphere. Therefore, the results from USS were taken as an example to analyze. It can be seen that the heating rates of CO_2 were all negative in the stratosphere above the tropopause, which played a cooling role in these atmosphere layers. When the stratosphere reached a new thermal balance after adjustment, the stratosphere temperature would fall, and the downward radiation flux from the lower stratosphere toward the troposphere would then be reduced, causing the decrease of net radiation flux of the tropopause, resulting in the decrease of the ARF of CO_2.

The global mean of CO_2 ARE was 1.638×10^{-5} W m^{-2} ppbv^{-1} for all-sky, which was 12.8% less than the corresponding value for clear sky, owing to the decreasing of the upward longwave radiative flux caused by clouds (Collins et al., 2006). The final lifetime-adjusted radiative efficiency in this work was a little bit larger (1.14%–12.8%) than that of the IPCC (IPCC, 2007) due to the use of a different radiative model, cloud scheme etc. Detailed analysis can be found in Zhang et al. (2011a).

The global mean concentration of CO_2 was adopted to calculate the global mean radiative forcing (efficiency) in this work. However, in the real atmosphere, the vertical distribution of CO_2 concentration also varies with altitude. Many studies (e.g. Christidis et al., 1997; Freckleton et al., 1998; Jain et al., 2000) have indicated that the vertical distribution of greenhouse gas concentrations has a significant influence on their radiative forcing, and that differences will exist between the radiative forcings caused by uniform and non-uniform concentration profiles. Therefore, an adjustment factor relevant to the atmospheric lifetime was put forward by Sihra et al. (2001) based on the work by Jain et al. (2000) for correcting the influence of a concentration decrease of greenhouse gas in the stratosphere on radiative forcing. Sihra et al. (2001) reported that the coefficient is $1-0.241\times l^{-0.358}$ if the atmospheric lifetime (l, in yr) of a gas is longer than 0.25. It should be noted that radiative forcing after lifetime-correction can also have errors. However, these errors are much less than if no lifetime-correction is applied. Using this coefficient, the radiative efficiency of CO_2 after lifetime-correction (120 years in this study) was 1.567×10^{-5} W m^{-2} ppbv^{-1}, which was reduced by 4.3% compared with the radiative efficiency without correction. Therefore, as far as CO_2 is concerned, lifetime-correction is necessary when calculating its radiative forcing.

The IPCC (2007) reported an estimated value of radiative forcing due to the increase of CO_2 by human beings from the Industrial Revolution (1750) to 2005 to be 1.66 ± 0.17 W m^{-2}. Taking the concentration of CO_2 in 1750 and 2005 as 280 ppmv and 379 ppmv, the ARF of CO_2 calculated in this work was 1.89 W m^{-2} for all-sky, which then became 1.81 W m^{-2} after lifetime-correction, which was within the estimation range of the IPCC (2007). Based on the above, we further calculated the updated ARF of CO_2 from the Industrial Revolution to the year 2010, the result of which was 2.04 W m^{-2}, and then 1.95 W m^{-2} after lifetime-correction. The updated CO_2 concentration of 391 ppmv in 2010 given by NOAA/ESRL (Earth Systems Research Laboratory) was 17% more than that of the IPCC (2007). This can be mainly attributed to the increase in CO_2 concentration since the IPCC's 4th Assessment Report (IPCC, 2007).

4. A new fitting formula for the ARF of CO_2

To calculate the radiative forcings of greenhouse gases, a variety of radiative transfer models can be employed, including LBL models, band models etc., and there are radiation-convection models and various climate models that can be applied too. Calculation of the ARF has to be completed at least with an iterative program for adjusting the stratospheric temperature profile shown in Zhang et al. (2011a, b). Therefore, the calculation of ARF is more complicated than that of the IRF; the computation burden is heavier and much more time-consuming. It has been found that the values of radiative forcing generated by changing the concentrations of greenhouse gases will change correspondingly, and there is a resultant relationship between them. Therefore, this relationship could be expressed with a simple empirical formula in order to quickly and easily calculate radiative forcing due to different future concentration changes of gases.

The concentration of CO_2 in the atmosphere has been being increased rapidly since the Industrial Revolution. Also, CO_2 absorbs infrared radiation well in the 15 μm band. It is generally agreed that the radiative forcing due to CO_2 has an approximate logarithmic relationship with its concentration. CO_2 also has several weak absorption bands, which, together with the wing parts of the central strong absorption bands, will contribute more and more to its radiative forcing with increases in its concentration. Thus, Shi (1991) and Yu and Shi (2001) added a square root of concentration variable term into their simplified formula describing the relationship between the ARF and concentration, besides a logarithmic term [see Eq. (3)], to improve its accuracy. We adopted the same form of formula as Eq. (3) (Shi, 1991; Yu and Shi, 2001), but the ARFs were calculated using the updated concentration of CO_2 and high spectral resolution 998-band scheme used in the present study.

$$\Delta F_{CO_2} = \alpha \ln \frac{C}{C_0} + \beta(\sqrt{C} - \sqrt{C_0}) \, . \tag{3}$$

Here, ΔF_{CO_2} is the ARF due to CO_2; C_n is the target concentration of CO_2; and C_0 is the reference concentration of 385.2 ppmv. Then, the fitting coefficients obtained in this work were used as α (6.2554) and β (6.2783×10^{-2}). The absolute error of this fitting formula was $\leqslant$0.1 W m^{-2}, and the relative error was $\leqslant$1%, as shown in Fig. 2.

The advantages of using Eq. (3) to calculate the ARF of CO_2 are that it is very easy and simple to apply when the concentration changes, and the use of iteration (like that in Zhang et al., 2011a, b) and other complicated models is not necessary.

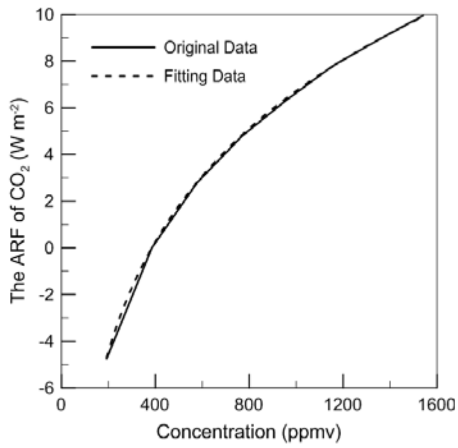

Fig. 2. The stratospheric-adjusted radiative forcing of CO_2 and its fitting curve.

5. Surface temperature change

Radiative forcing can be related by a linear relationship to the global mean equilibrium temperature change at the surface Eq. (4), providing a simple measure for both quantifying and ranking the different influences of gas concentration changes on climate change. It also offers a limited measure of climate change, as it does not attempt to represent the overall climate response. According to Eq. (3), the global mean equilibrium surface temperature change can be estimated according to radiative forcing (IPCC, 2007):

$$\Delta T_{\rm s} = \lambda \Delta F \, . \tag{4}$$

Here, $\Delta T_{\rm s}$ is the global mean equilibrium surface temperature change; ΔF is the global mean ARF; and λ is the climate sensitivity parameter, which mainly depends on whether cloud feedback is strong or weak, depending on different climate models, and ranges from 0.3 to 1.4 K (W $m^{-2})^{-1}$. We took a typical median value of 0.8 K (W $m^{-2})^{-1}$. According to the calculated results above, when the concentration of CO_2 rises from 385.2 ppmv to 1.5, 2, 2.5, 3, 3.5 and 4 times the original value, the calculated ARF values were 2.79, 4.80, 6.37, 7.79, 8.90 and 9.95 W m^{-2}, respectively. Thus, the corresponding global mean equilibrium surface temperature changes were +2.2°C, +3.8°C, +5.1°C, +6.2°C, +7.1°C and +8.0°C, respectively. It should be noted that these temperature responses were obtained with a middle value of λ. As climate sensitivity and other aspects of the climate response to external forcings remain inadequately quan-

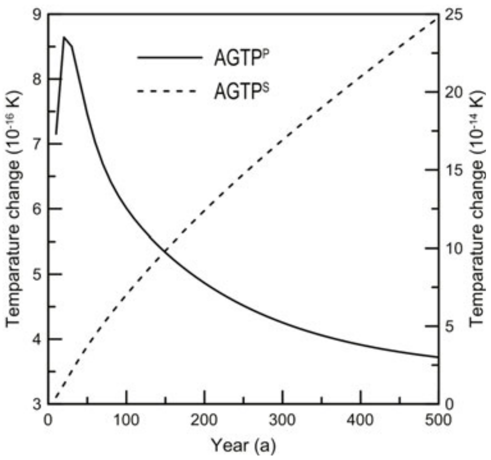

Fig. 3. Surface temperature changes caused by pulsed and sustained emissions of CO_2. The solid line represents $AGTP^P$ (left y-axis) and the dashed line $AGTP^S$ (right y-axis), both after atmospheric lifetime-adjustment.

tified, Eq. (4) has the advantage of being more readily calculable and comparable than estimates of the climate response.

We also calculated the Absolute Global Temperature change Potential (AGTP) of CO_2, $AGTP^P$ for pulsed emissions, and $AGTP^S$ for sustained emissions for 500 years into the future. The results are given in Fig. 3, which shows the global mean non-equilibrium surface temperature change caused by the two kinds of emissions for the next 500 years. $AGTP^P$ and $AGTP^S$ [units: K kg^{-1} and K (kg $yr^{-1})^{-1}$] are the global mean non-equilibrium surface temperature change at time t induced by pulsed and sustained emissions of CO_2 at the initial time. They were calculated by Eq. (5) (Shine et al., 2005), which represents the relationship between the global mean non-equilibrium surface temperature change (ΔT_s) and ARF (ΔF):

$$C_y \frac{d\Delta T_s(t)}{dt} = \Delta F(t) - \frac{\Delta T_s(t)}{\lambda} \tag{5}$$

Here, t is the developing-time of change (units: d); C_y is the thermal capacity (13.3 J K^{-1} m^{-2} kg^{-1}); λ is the climate sensitivity parameter, as above, but here it is set as 0.8 K (W $m^{-2})^{-1}$.

It can be seen from Fig. 3 that the surface temperature induced by pulsed emission of CO_2 increases quickly in the initial stage and reaches a peak after around 30 years. Then, the surface temperature begins to decrease rapidly before 200 years and continues to reduce slowly between 200 and 400 years, but does not come back to the initial state by 500 years. Figure 3 indicates that the surface temperature change caused by sustained emission involves a continuous rise during the whole 500 years. It can also be seen that the surface temperature change caused by a sustained emission of CO_2 is two orders of magnitude larger than that by pulsed emission, so sustained emission has a much greater influence on surface temperature change. It can be concluded that CO_2 will have a sustained influence on surface temperature change in the future if no controls are exerted on CO_2 emissions, and that the Earth-atmosphere system will therefore be difficult to restore to its original state.

6. Conclusions

An updated assessment of radiative forcing due to CO_2 has been recalculated according to its new concentration in the atmosphere by using a high spectral resolution radiative transfer model. The calculated radiative forcing caused by the increase of atmospheric CO_2 from 1750 to 2005 was 1.81 W m^{-2}, which was within the range of 1.66±0.17 W m^{-2} given by the IPCC (2007). Based on this, we calculated the new ARF of CO_2 from the year 1750 to 2010, and obtained a value of 1.95 W m^{-2}, which was 17% higher than the range given by the IPCC (IPCC, 2007), and which was mainly caused by the rapid increase in the concentration of CO_2 since the IPCC's 4th Assessment Report (IPCC, 2007). To simplify the calculation of the ARF of CO_2 under its changed concentrations in the future, a new fitting formula for the relationship between CO_2 ARF and its concentration has been proposed in this work.

Finally, according to the relationship between surface temperature change and the ARF, the global mean equilibrium surface temperature change caused by changes in atmospheric concentrations of CO_2 under different scenarios was estimated. If the global mean concentration of CO_2 rises to 1.5, 2, 2.5, 3, 3.5 and 4 times the value of 385.2 ppmv in the year 2008, then the corresponding global mean equilibrium surface temperature will become +2.2°C, +3.8°C, +5.1°C, +6.2°C, +7.1°C and +8.0°C higher, respectively, based on a middle level climate sensitivity parameter of 0.8 K (W $m^{-2})^{-1}$. Meanwhile, the non-equilibrium surface temperature change caused by pulsed and sustained emissions of CO_2 over the next 500 years was also calculated. This illustrated that the driving of global warming by CO_2 will remain over the next 500 years if emissions are not controlled, starting from now. Subsequently, the Earth–atmosphere system will be difficult to restore to its original state. However, attention should be paid to the fact that the results of this work were obtained under the assumption of a medium-level climate sensitivity parameter.

Acknowledgements. This work was supported by the National Basic Research Program of China (Grant

Nos. 2010CB955703 and 2011CB403405) and the Public Meteorology Special Foundation of MOST (Grant No. GYHY200906020). The authors would like to give thanks to the editors of *Advances in Atmospheric Sciences* for their contributions to the English text.

REFERENCES

Christidis, N., M. D. Hurley, S. Pinnock, K. P. Shine, and T. J. Wallington, 1997: Radiative forcing of climate change by CFC-11 and possible replacements. *J. Geophys. Res.*, **102**(D16), 19587–19609.

Collins, W., D., and Coauthors, 2006: Radiative forcing by well-mixed greenhouse gases: Estimates from climate models in the Intergovernmental Panel on Climate Change (IPCC) Fourth Assessment Report (AR4). *J. Geophys. Res.*, **111**, D14317, doi: 10.1029/2005JD006713.

Freckleton, R., S., E. J. Highwood, K. P. Shine, O. Wild, K. S. Law, and M. G. Sanderson, 1998: Greenhouse gas radiative forcing: Effects of averaging and inhomogeneities in trace gas distribution. *Quart. J. Roy. Meteor. Soc.*, **124**, 2099–2127.

Garand, L., and Coauthors, 2001: Radiance and Jacobian intercomparison of radiative transfer models applied to HIRS and AMSU channels. *J. Geophys. Res.*, **106**(D20), 24017–24031.

Hansen, J., M. Sato, and R. Ruedy, 1997: Radiative forcing and climate response. *J. Geophys. Res.*, **102**(D6), 6831–6864.

IPCC, 1996: *Climate Change 1995: The Science of Climate Change. Contribution of Working Group II to the Second Assessment Report of the Intergovernmental Panel on Climate Change.* J. T. Houghton et al., Eds., Cambridge University Press, Cambridge, U. K., 879pp.

IPCC, 2007: *Climate Change 2007: The Physical Science Basis. Contribution of Working Group I to the Fourth Assessment Report of the Intergovernmental Panel on Climate Change.* Solomon et al., Eds., Cambridge University Press, Cambridge, U. K., 996pp.

Jain, A., K., B. P. Briegleb, K. Minschwaner, and D. J. Wuebbles, 2000: Radiative forcings and global warming potentials of 39 greenhouse gases. *J. Geophys. Res.*, **105**(D16), 20773–20790.

Shi, G. Y., 1981: An accurate calculation and representation of the infrared transmission function of the atmospheric constituents. Ph. D dissertation, Tohoku University of Japan, 191pp.

Shi, G., Y., 1991: Radiative forcing and greenhouse effects due to atmospheric trace gases. *Sci. China* (B), **35**(7), 776–784. (in Chinese)

Shine, K., P., J. S. Fulestvedt, K, Hailemariam, and N. Stuber, 2005: Alternatives to the global warming potential for comparing climate impacts of emissions of greenhouse gases. *Climatic Change*, **68**(3), 281–302.

Sihra, K., M. D. Hurley, K. P. Shine, and T. J. Wallington, 2001: Updated radiative forcing estimates of 65 halocarbons and nonmethane hydrocarbons. *J. Geophys. Res.*, **106**(D17), 20493–20505.

Stuber, N., R. Sansen, and M. Ponater, 2001: Stratoshpere adjusted radiative forcing calculation in a comprehensive climate model. *Theor. Appl. Climatol.*, **68**, 125–135.

WMO, 1986: Atmospheric ozone 1985: Assessment of our understanding of the processes controlling its present distribution and change. (Global Ozone Research and Monitoring Project-Report No. 16), World Meteorological Organization, Geneva, Switzerland.

WMO, 2009: The state of greenhouse gases in the atmosphere using global observations through 2008. WMO Green House Gases Bulletin, No. 5, 4pp.

Stuber, N., R. Sansen, and M. Ponater, 2001: Stratoshpere adjusted radiative forcing calculation in a comprehensive climate model. *Theor. Appl. Climatol.*, **68**, 125–135.

Yu, X., L., and G. Y. Shi, 2001: Simplified calculation of radiative forcing with adjusted stratosphere temperature. *Plateau Meteorology*, **20**(3), 271–274. (in Chinese)

Zhang, H., and G. Y. Shi, 2000: A fast and efficient lLine-bBy-lLine calculation method for atmospheric absorption. *Chinese J. Atmos. Sci.*, **24**(1), 111–121. (in Chinese)

Zhang H, T. Nakajima, G. Y. Shi, T. Suzuki, and R. Imasu, 2003: An optimal approach to overlapping bands with correlated k distribution method and its application to radiative calculations. *J. Geophys. Res.*, **108**, 4641, doi: 10.1029/2002JD003358.

Zhang, H., G. Y. Shi, and Y. Liu, 2005: A comparison between the two line-by-line integration algorithms. *Chinese J. Atmos. Sci.*, **29**(4), 581–594. (in Chinese)

Zhang, H., G. Y. Shi, T. Nakajima, and T. Suzuki, 2006a: The effects of the choice of the k-interval number on radiative calculations. *Journal of Quantitative Spectrum and Radiative Transfer*, **98**(1), 31–43.

Zhang, H., T. Suzuki, T. Nakajima, G. Y. Shi, X. Y. Zhang, and Y. Liu, 2006b: Effects of band division on radiative calculations. *Optical Engineering*, **45**(1), 016002–016010.

Zhang, H., G. Y. Shi, and Y. Liu, 2008: The effects of line wing cutoff in LBL integration on radiation calculations. *Acta Meteorologica Sinica*, **22**(2), 248–255.

Zhang, H., J. X. Wu, and P. Lu, 2011a: A study of the radiative forcing and global warming potentials of hydrofluorocarbons. *Journal of Quantitative Spectrum and Radiative Transfer*, **112**(2), 220–229.

Zhang, H., J. X. Wu, and Z. P. Shen, 2011b: Radiative forcing and global warming potential of perfluorocarbons and sulfur hexafluoride. *Sci. China* (*D*), **54**, 764–772, doi: 10.1007/s11430-010-4155-0.

张华，张若玉，何金海，等. 2013. CH_4 和 N_2O 的辐射强迫与全球增温潜能 [J]. 大气科学, 37 (3): 745–754, doi:10.3878/j.issn.1006-9895.2012.12013.
Zhang Hua, Zhang Ruoyu, He Jinhai, et al. 2013. Radiative forcing and global warming potentials of CH_4 and N_2O [J]. Chinese Journal of Atmospheric Sciences (in Chinese), 37 (3): 745–754.

CH_4 和 N_2O 的辐射强迫与全球增温潜能

张华[1] 张若玉[1, 2] 何金海[2] 吴金秀[3]

1 中国气象局气候研究开放实验室，国家气候中心，北京 100081
2 南京信息工程大学大气科学学院，南京 210044
3 上海市气象信息传媒中心，上海 200030

摘 要 CH_4 和 N_2O 作为主要温室气体，自工业革命以来排放量急剧增加，已经被列入《京都议定书》要求控制它们的排放。本文利用高光谱分辨率的辐射传输模式，计算了 CH_4、N_2O 在晴空大气和有云大气条件下的瞬时辐射效率和平流层调整的辐射效率，以及它们的全球增温潜能（GWP）和全球温变潜能（GTP），并根据模式结果拟合了 CH_4 和 N_2O 的辐射强迫的简单计算公式。本文的研究表明：CH_4 和 N_2O 在有云大气下的平流层调整的辐射效率分别为 4.142×10^{-4} W m^{-2} ppb^{-1} 和 3.125×10^{-3} W m^{-2} ppb^{-1} (1ppb=10^{-9})，经大气寿命调整后的辐射效率分别为 3.732×10^{-4} W m^{-2} ppb^{-1} 和 2.987×10^{-3} W m^{-2} ppb^{-1}，与 IPCC（2007）的相应结果高度一致。CH_4 和 N_2O 100 年的全球增温潜能 GWP 分别为 16 和 266；100 年的脉冲排放的全球温变潜能 GTP^P 分别为 0.24 和 233；持续排放的全球温变潜能 GTP^S 分别为 18 和 268。它们在未来全球变暖和气候变化中，影响仅次于 CO_2，仍然起着非常关键的作用。
关键词 CH_4 N_2O 辐射效率 全球增温潜能（GWP） 全球温变潜能（GTP）
文章编号 1006–9895(2013)03–0745–10 **中图分类号** P422 **文献标识码** A
doi:10.3878/j.issn.1006-9895.2012.12013

Radiative Forcing and Global Warming Potentials of CH_4 and N_2O

ZHANG Hua[1], ZHANG Ruoyu[1, 2], HE Jinhai[2], and WU Jinxiu[3]

1 *Laboratory for Climate Studies*, *National Climate Center*, *China Meteorological Administration*, *Beijing* 100081
2 *Nanjing University of Information Science and Technology*, *Nanjing* 210044
3 *Shanghai Weather Information Media Center*, *Shanghai* 200030

Abstract As the main long-lived greenhouse gases, CH_4 and N_2O are included in the Kyoto Protocol, and countries are required to limit the rapid increase in their emissions since the Industrial Revolution. In this work, a radiative transfer model with a high resolution of 998 bands is used to calculate the instantaneous radiative efficiencies, stratospheric-adjusted radiative efficiencies, and lifetime-adjusted radiative efficiencies of CH_4 and N_2O for clear and cloudy skies, as well as their global warming potentials (GWPs) and global temperature potentials (GTPs). Simple fitting formulas for calculating the adjusted radiative forcing due to CH_4 and N_2O are given on the basis of the model results in this work. It is shown that the radiative efficiencies of CH_4 and N_2O for cloudy skies are 4.142×10^{-4} W m^{-2} ppb^{-1} (1ppb=10^{-9}) and 3.125×10^{-3} W m^{-2} ppb^{-1} after stratospheric adjustment, and 3.732×10^{-4} W m^{-2} ppb^{-1} and 2.987×10^{-3} W m^{-2} ppb^{-1}, respectively, after lifetime adjustment, which are highly consistent with those of the IPCC (2007). Moreover, the 100-year GWPs of CH_4 and N_2O are 16 and 266, respectively, and their corresponding 100-year GTPs are 18 and 268 for sustained emissions, and 0.24 and 233 for pulse emissions. These results indicate that CH_4 and N_2O will still play a critical role in

收稿日期 2012-02-06，2012-10-30 收修定稿
资助项目 国家重点基础研究计划 2010CB955703
作者简介 张华，女，1965 年出生，博士，研究员，主要从事大气辐射传输、温室气体辐射强迫与全球增温潜能等方面研究。
E-mail: huazhang@cma.gov.cn

future global warming, second only to CO_2.
Keywords CH_4, N_2O, Greenhouse gases, Radiative efficiency, Global warming potential (GWP), Global temperature potential (GTP)

1 引言

研究表明，自工业革命以来，大气中温室气体的含量大大增加，对大气组成、辐射强迫和全球气候变化都具有重要影响，而且对全球气候变暖有主要贡献。为了减缓全球增暖，必须限制这些温室气体的排放量。因此，二氧化碳（CO_2）、甲烷（CH_4）、氧化亚氮（N_2O）和卤化碳等长寿命温室气体，均被列入《京都议定书》中要求控制它们的排放量。

作为主要的温室气体，CH_4、N_2O 具有大气含量较高、受人类活动影响大，气体分子辐射吸收能力较强，大气寿命较长等特性。首先，CO_2、CH_4 和 N_2O 的大气含量在均匀混合的温室气体中居于前三位（非均匀混合的水汽和臭氧除外），并且造成它们浓度增加的主要因素均为人类活动的影响。大气中 CH_4 浓度与人类活动密切相关，60%的排放来自人类活动，其浓度值在工业化前约 715 ppb（IPCC，2007），到 2008 年 CH_4 的全球平均体积混合率已经达到 1797 ppb（1 ppb=10^{-9}）（WMO，2009），近年来仍有明显增加；全球大气中 N_2O 的增加也主要受到人类活动影响，浓度值已从工业化前约 270 ppb（IPCC，2007），增加到 2008 年的 321.8 ppb（WMO，2009）。其次，CH_4 和 N_2O 是地球大气的主要吸收气体，分别在 7.8 μm、3.3 μm 和 17 μm 等多个谱带有吸收，并在 7.8 μm 二者有重要的重叠吸收，因而改变了这些光谱区域大气的吸收性质，对地气系统向外空的辐射冷却产生很大的影响。再者，CH_4 和 N_2O 都具有较长的大气寿命，即：在自然过程把排放到大气中的这些温室气体清除之前，它们将在大气中存留至少十几年甚至上百年，在此期间，它们累积在大气中，对影响大气辐射平衡和全球气候产生持续的贡献。

随着全球变暖的加剧，已有愈来愈多的国内外学者关注 CH_4、N_2O，除了它们的源排放和在大气中含量的变化，定量评估它们对地球辐射平衡和气候产生的影响已经成为气候变化研究中的热点。这是因为，制定具体可行的温室气体减排政策，并为相关决策提供科学依据，要求定量地评估温室气体的气候效应，即用一定的标准来衡量不同温室气体对未来全球气候变暖的相对贡献。目前，对温室气体的气候效应采用的评估方法，主要包括辐射强迫、全球增温潜能（GWP）和全球温变潜能（GTP）等工具。Zhang et al.（2011）和张华等（2011）用高光谱分辨率的辐射传输模式分别研究了《京都议定书》限制排放的痕量温室气体 HFCs、PFCs 和 SF_6 的辐射强迫和全球增温潜能，但是没有研究《京都议定书》限制排放的 CH_4、N_2O 等主要温室气体。Shine et al.（2005）、Fuglestvedt et al.（2003）、石广玉（1991，2007）、Shi (1981)、黄兴友（2001）等学者在这方面做了很多工作，但与现在的条件相比，模式所用谱线资料不够新，辐射模式的精确性也有待提高。因此，用新的气体吸收资料、更精确的辐射计算模式和新的评估方法（GTP）来研究 CH_4、N_2O 等《京都议定书》限排气体是十分必要的。

本文在前人工作的基础上，利用 HITRAN2K 发布的分子吸收资料和高精度的辐射传输模式，首先计算了 CH_4、N_2O 的瞬时辐射效率和平流层调整的辐射效率，并考虑了大气寿命对辐射效率的影响；其次，根据不同浓度下产生的辐射强迫值，拟合了简单的气体辐射强迫计算公式，以易于评估未来气体浓度增加对全球变暖的影响；最后，计算了它们在未来 10～500 年的 GWP 和 GTP，并对两种不同的排放测量方法进行了比较。

2 资料与模式介绍

2.1 HITRAN 资料

为了准确地研究气体的温室效应，进行精确的特别是高光谱分辨率的辐射计算，需要输入大气分子吸收谱线的资料。本文采用的 HITRAN（HIgh-resolution TRANsmission，高分辨透过率）分子光谱数据库（Rothman et al.，2005），是国际科学界公认且广泛应用于大气辐射传输计算的基础资料，本文所用版本是 HITRAN2K。HITRAN2K 分子光谱数据库既收录了 H_2O、CO_2、CH_4、N_2O、O_3 等大气中主要气体的各项谱线参数，也给出了臭氧消耗物质 CFCs 和 HCFCs，及其代替品 HFCs、PFCs 和 SF_6 等诸多化合物的红外吸收截面数据，是本文研

究的基础。Lu et al.（2012）证明了 HITRAN2K 版本的 CH_4 和 N_2O 的总线强与目前释放的最新版本 HITRAN08 基本一致，没有太大变化，因此分子光谱数据的变化不会对本文的计算产生影响。

2.2 辐射传输模式

本文采用的是 Zhang et al.（2003，2006a，2006b）研制的长波辐射传输方案。该模式是基于 Zhang et al.（2003）利用 LBLRTM 计算得到的大气主要温室气体和 CFCs 的吸收系数，根据 Shi（1981）提出的相关 k-分布吸收系数重排法，Zhang et al.（2003）提出的气体吸收带重叠优化方法，Zhang et al.（2006a）提出的 k-分布间隔的选取方法，以及 Zhang et al.（2006b）的谱带划分方法建立起来的。Zhang et al.（2006a）的辐射计算方案将长波区间分为 17、21、27、55、998 等不同的谱带，同时考虑了云的作用。在长波区间云的吸收与发射算法采用了 Nakajima et al.（2000）的计算方法。Zhang et al.（2006b）给出的高精度的 998 带辐射传输方案则是将光谱区间 10～49000 cm^{-1}（0.2～1000 μm）划分为 998 个带，长波区间 10～2500 cm^{-1}（4～1000 μm）分为 498 个带，每个带的波段区间均为 5 cm^{-1}，k-间隔数量对于每个带都进行了优化，2～16 不等，具体谱带划分、k -间隔数量以及吸收气体分布见 Zhang et al.（2006b）。张华等（2011）证明了利用 998 带辐射传输方案计算温室气体的辐射强迫和全球增温潜能比利用为气候模式设计的 17 带方案要精确得多，故本文采用 998 带辐射传输方案进行研究。

该辐射模式中考虑了大气中 15 种温室气体，包括 5 种主要温室气体：H_2O、CO_2、O_3、CH_4 和 N_2O，和 CFCs、HFCs、PFCs 等 10 种痕量化合物，并假设这些痕量气体在大气中混合均匀。CH_4 主要在第 105～124 带、第 239～278 带和第 424～498 带有吸收。可见，高光谱精度的 998 带辐射方案由于谱带划分较细，k-间隔数量多，在计算可以更全面地考虑气体的强弱带吸收（Zhang et al.，2011）。

此外，模式将整层大气分为 100 层，垂直分辨率为 1 km，地面高度设为 0 km，大气顶取为 70 km。对辐射通量和加热率的计算，采用六种模式大气（Garand，2001）：热带大气（TRO），中纬度夏季大气（MLS），中纬度冬季大气（MLW），亚极夏季大气（SAS），亚极冬季大气（SAW）和美国标准大气（USS）。在此基础上，计算目标气体在六种大气下的瞬时辐射效率和平流层调整的辐射效率，并通过对六种模式大气的结果取算术等权平均和其中 3 种大气取区域加权平均，可以认为得到全球平均结果。

3 CH_4、N_2O 的辐射强迫

3.1 定义与计算方案

辐射强迫是目前应用广泛的一种评估温室气体气候效应相对大小的方法，定义为某种辐射强迫因子（如温室气体的浓度）变化时所造成的对流层顶净辐射通量的变化。IPCC（1996）按照是否允许平流层温度进行调整，将辐射强迫划分为两种：①瞬时辐射强迫（IRF，Instantaneous Radiative Forcing），不考虑平流层温度变化；②调整过的辐射强迫（ARF，Adjusted Radiative Forcing），即，在保持地表和对流层温度不变的情况下，通过调整平流层的温度结构，使平流层达到辐射平衡时，对流层顶的净辐射通量的变化。根据定义，辐射强迫可以提示气候变化的总趋势，一般而言，正的辐射强迫将增暖地面和对流层，使全球变暖，引起地表平均温度升高；负的辐射强迫使地面和对流层变冷，引起地表平均温度降低。因此，可以通过计算 CH_4 和 N_2O 的辐射强迫来估量在它们在大气中的浓度变化对气候系统产生的影响。

本文采用了 Zhang et al.（2011），张华等（2011）的迭代法来计算平流层调整的辐射强迫，如图 1 所示。图中 ε 为收敛值，Δt 为迭代的时间步长，单位为 d，本文取为 1 d。如果满足收敛条件，即可认为平流层经过温度调整达到了新的辐射平衡，此时所得到的对流层顶净辐射变化即该气体的调整辐射强迫。如果引起气候系统扰动的气体浓度为单位浓度，如 1 ppm 或 1 ppb，则对应的辐射强迫称为该气体的辐射效率（本文中单位统一为 W m^{-2} ppb^{-1}）。

云是影响气体辐射强迫的一个重要因子，本文将云参数输入辐射传输模式来考虑云的影响。根据国际卫星云气候计划（ISCCP）D2 数据计算所得到的不同云态、云顶压力和光学厚度的 15 类云的云量和云水含量等资料参见文献（Zhang et al.，2011，张华等，2011）。其中低云的高度为 1～2 km，中云的高度为 4～5 km，高云的高度为 10～12 km。低云 Cu、Sc、St 和中云 Ac、As、Ns 等 6 种云的云粒子相态有水云和冰云两种，冰云的平均有效半径为

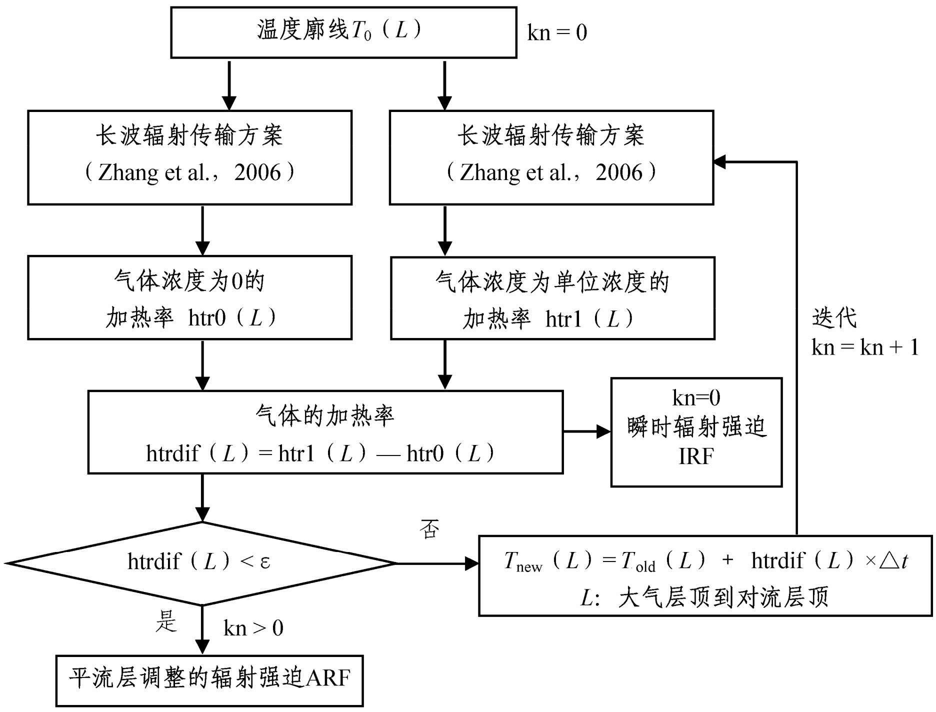

图 1 计算温室气体平流层调整的辐射强迫的迭代方法（引自 Zhang et al., 2011）

Fig. 1 Schematic of iterative method to compute the stratospheric adjusted radiative forcing of GHG (Greenhouse Gas) (from Zhang et al., 2011)

30 μm，水云为 10 μm。计算时，地表发射率设为 1.0。

通过在热带、中纬度和亚极三种大气中加入云参数，可以得到有云大气下的平流层调整的辐射效率，所采用的计算方法如下：

$$\mathrm{RE} = \sum_{i=1}^{15} C_i \mathrm{RE}_i + (1-C)\mathrm{RE}_{\mathrm{clear}}, \qquad (1)$$

其中，C_i 为每类云的云量，C=∑C_i 是总云量，$\mathrm{RE}_{\mathrm{clear}}$ 和 RE_i 分别表示晴空和有云（云类型为 i，i=1～15）大气下平流层调整的辐射效率。然后，通过公式（2）可计算全球平均的有云大气下平流层调整的辐射效率（Highwood and Shine，2000）：

$$\mathrm{RE}_{\mathrm{mean}} = \frac{1}{2}\times \mathrm{RE}_{\mathrm{tro}} + \left(\frac{\sqrt{3}}{2}-\frac{1}{2}\right)\times \mathrm{RE}_{\mathrm{mid}} + \left(1-\frac{\sqrt{3}}{2}\right)\times \mathrm{RE}_{\mathrm{sub}}, \qquad (2)$$

其中，$\mathrm{RE}_{\mathrm{mean}}$ 是全球平均平流层调整的辐射效率，$\mathrm{RE}_{\mathrm{tro}}$、$\mathrm{RE}_{\mathrm{mid}}$ 和 $\mathrm{RE}_{\mathrm{sub}}$ 分别表示热带、中纬度和亚极大气平流层调整的辐射效率。

3.2 模式检验

为了检验所用模式，本文给出了两种假设情景下计算的辐射强迫结果，与 Collins et al.（2006）给出的大气海洋环流模式（AOGCMs）的结果进行了比较。这两种情景包括：（1）CO_2 浓度由 1860 年 287 ppm 的基础上加倍至 574 ppm；（2）CO_2 浓度加倍后（574 ppm），水汽含量增加到 1860 年的 1.2 倍。其中，CO_2 浓度增加时，O_2 相应减少。这两种情景下辐射强迫的计算结果包括（1）晴空模式顶部（TOM）的长波净辐射；（2）晴空 200 hPa 处的长波净辐射；（3）晴空地表（Surface）长波净辐射。

比较时，选用统一的模式大气——中纬度夏季大气（MLS），以确保所有的计算都在相同的温度廓线下进行，模式大气分为 40 层，大气层顶为 80 km，压强为 0.01 hPa，并假设温室气体混合均匀。在本文的辐射传输模式中，参数设置如下：模式中层底云浓度为零，气溶胶含量为零。忽略云和气溶胶的影响以及平流层调整的作用。

表 1 给出了上述两种情景下本文的结果与 Collins et al.（2006）中不同模式的计算结果。本文计算的 CO_2 浓度加倍引起的地表、200 hPa 和模式顶部的长波辐射强迫分别为 1.7 W m^{-2}、5.6 W m^{-2} 和 3.03 W m^{-2}，CO_2 浓度加倍后水汽含量增加 20% 引起的长波辐射强迫分别为 11.14 W m^{-2}、4.13 W m^{-2} 和 3.26 W m^{-2}，如图 2 中的三角图标所示。由图 2 可见，本文的结果基本都位于不同大气海洋环

流模式（AOGCMs）的结果和逐线积分模式（LBL）结果范围之间。对第一种情景，本文结果更接近于 LBL 结果；对第二种情景，本文的结果位于不同大气海洋环流模式（AOGCMs）的范围内，与 LBL 的结果稍有差异，其中，对 CO_2 加倍引起的地表长波辐射强迫，本文结果更接近 LBL 结果。以上比较说明采用高光谱辐射传输模式进行本文的计算是合理的。

表 1　不同情景、不同模式下的长波辐射强迫（单位：W m^{-2}）

Table 1　Comparison among CO_2 longwave radiative forcings under different conditions (unit: W m^{-2})

模式层	CO_2 浓度加倍			CO_2 浓度加倍后，水汽含量增加 20%		
	998 带	AOGCMs	LBL	998 带	AOGCMs	LBL
TOM	3.03	2.45	2.8	3.26	3.57	3.78
200 hPa	5.6	5.07	5.48	4.13	4.45	4.57
Surface	1.7	1.12	1.64	11.14	11.95	11.52

3.3　加热率与辐射效率

表 2 列出了 CH_4 和 N_2O 晴空大气下的瞬时辐射效率和平流层调整的辐射效率，以及有云大气下的平流层调整的辐射效率。其中，晴空大气下的结果是六种模式大气的算术平均值，有云大气的结果是上面三种大气的区域加权平均值。通过对比表 2 中晴空大气下瞬时辐射效率和平流层调整后的辐射效率，可以看到，经过平流层调整，CH_4 和 N_2O 的辐射效率分别减少了 1.3%和 2.3%。平流层温度调整对辐射强迫的作用是增大或是减小，取决于平流层温度调整后，温度廓线对对流层顶净辐射通量的影响（Jain et al.，2000）。如图 3，分别给出在六种模式大气下，计算的 CH_4 和 N_2O 气体浓度变化为 1 ppb 时在长波区间引起的辐射加热率。加热率随不同模式大气而变化，但是不同模式大气的加热率量级都比较接近，并且有相似的垂直分布，可以看出，CH_4、N_2O 的加热率在对流层顶以上的平流层都为负值，在这些大气层上起冷却作用。当平流层经过调整达到新的平衡后，平流层下部会减少向对流层的向下辐射通量，引起对流层顶的辐射强迫减少。

表 2　CH_4 和 N_2O 的辐射效率（单位：W m^{-2} ppb^{-1}）

Table 2　Radiative efficiencies of CH_4 and N_2O (unit: W m^{-2} ppb^{-1})

气体	大气寿命 /a	晴空大气		有云大气		IPCC (2007)
		瞬时辐射效率	调整辐射效率	调整的辐射效率	大气寿命调整的辐射效率	
CH_4	12	5.128×10^{-4}	5.062×10^{-4}	4.142×10^{-4}	3.732×10^{-4}	3.7×10^{-4}
N_2O	114	3.874×10^{-3}	3.785×10^{-3}	3.125×10^{-3}	2.987×10^{-3}	3.03×10^{-3}

表 3 中 CH_4 和 N_2O 区域平均的有云大气下平流层调整的辐射效率分别为 4.142×10^{-4} 和 3.125×10^{-3} W m^{-2} ppb^{-1}，分别比晴空下的结果减少 18.2%和 17.4%。这是因为云引起的向上辐射通量的减少对它们的辐射强迫有较大的影响（Jain et al.，2000）。同时，表 3 还列出了 IPCC（2007）的结果作为参照。本文 CH_4 和 N_2O 在有云大气下的平流层

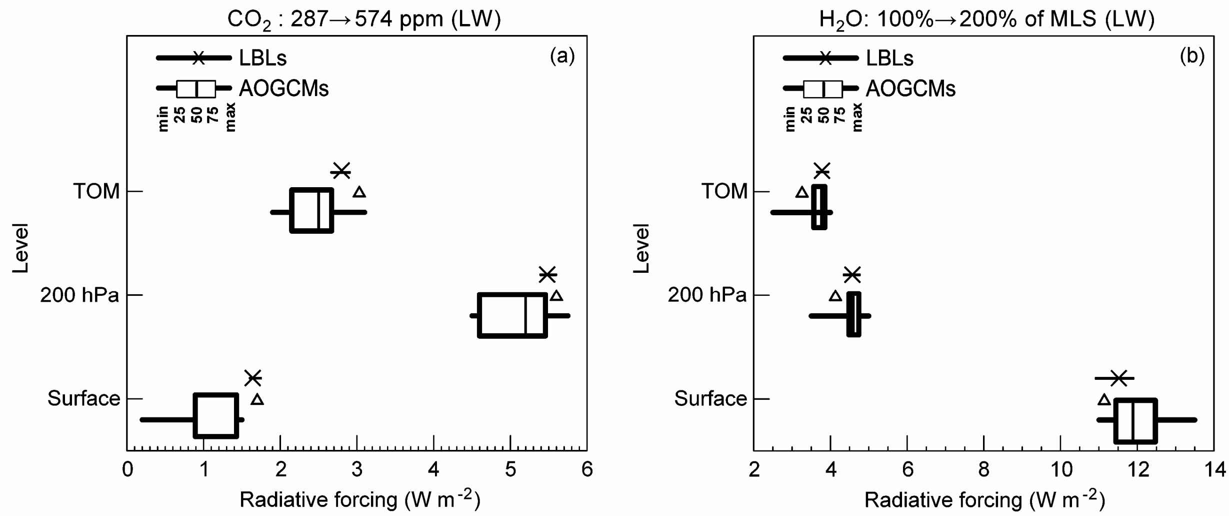

图 2　（a）CO_2 浓度从 287 ppm 增加到 574 ppm 的长波辐射强迫；（b）CO_2 浓度加倍后，水汽含量增加 20%的长波辐射强迫。三角图标表示本文计算结果

Fig. 2　(a) Longwave radiative forcing induced by increased CO_2 concentration from 287 ppm to 574 ppm; (b) longwave radiative forcing induced by moisture content increased by 20% with doubled CO_2 concentration. Triangles indicate the results calculated in this paper. Base map is from Collins et al. (2006)

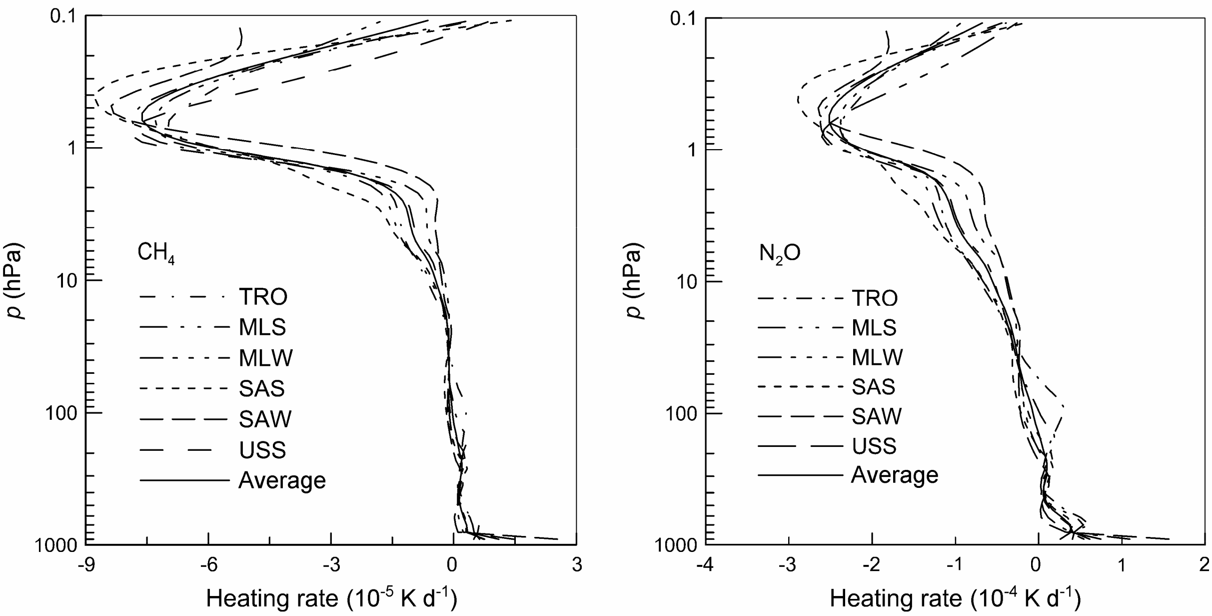

图 3 6 种模式大气下 1 ppb CH_4（a）、N_2O（b）扰动的加热率

Fig. 3 Heating rate of 1 ppb perturbation of (a) CH_4 and (b) N_2O under six kinds of model atmosphere

调整的辐射效率与 IPCC（2007）的结果相比非常一致，差别仅分别为 0.86%和 1.4%。

本文采用 CH_4、N_2O 等温室气体的全球平均浓度来计算全球平均的辐射强迫（效率），但实际上，它们的浓度都是随高度有变化的。许多研究表明，随高度不变的廓线和变化的廓线引起的辐射强迫存在差别。Sihra et al.（2001）基于 Jain et al.（2000）的工作提出了一个与大气寿命相关的调整系数来调整平流层浓度减小对辐射强迫的影响，指出对大气寿命超过 0.25 年的气体，该系数为 $1-0.241\times\tau^{-0.358}$，其中，$\tau$ 代表大气寿命，单位为 a，并且指出大气寿命调整后的辐射强迫也会有误差，但是要比完全不调整好得多（Sihra et al.，2001）。本文采用该系数计算得出，CH_4 和 N_2O 经过大气寿命调整后的辐射效率分别为 3.732×10^{-4} 和 2.987×10^{-3} W m^{-2} ppb^{-1}，比不经过大气寿命调整的辐射效率分别减少了 9.8%和 4.4%，可见大气寿命越长，调整前后的差别越小。

3.4 辐射强迫的简单计算公式

温室气体的辐射强迫，可以利用各种辐射传输模式来计算，包括逐线积分模式、带模式等，也有各种适用的气候模式。然而应用模式计算辐射强迫的运算量相对较大，会耗费大量的计算时间。而根据模式的计算结果可以得出，改变温室气体的浓度，产生的辐射强迫也相应地发生变化，且两者之间的对应关系有一定规律。因此，可以将这种对应关系表示成比较简单的经验公式，以便快速而又精确合理地计算辐射强迫。

研究表明，可定性地认为：当某种大气温室气体，或由于其吸收带的强度较弱，或由于其在大气中的浓度偏低，或是两者的综合作用，使其在大气中的吸收处于线性吸收区（即吸收率与吸收物质量成正比）时，则其辐射强迫基本上与其浓度变化成线性关系；当吸收处于平方根区（吸收率正比与吸收物质量的平方根）时，则其辐射强迫基本上与其浓度变化成平方根关系；当吸收更强时，其辐射强迫与浓度变化将变成对数关系（石广玉，1991，2007）。

计算 CH_4 浓度在一定范围内变化造成的平流层调整的辐射强迫时，必须考虑其与 CO_2、H_2O、O_3 和 N_2O 之间的重叠吸收。根据石广玉等（1991，2007）、于秀兰等（2001）的研究结果，只需考虑 N_2O 浓度的变化对吸收重叠的影响，其它可以忽略不计。本文引用了文献（石广玉等，1991，2007；于秀兰等，2001）中的简化公式形式重新对平流层调整后的辐射强迫进行了拟合，在计算 CH_4 浓度变化造成的辐射强迫时，只考虑了 N_2O 浓度变化对重叠效应的影响；同时，利用平方根项和线性项叠加，可以得到比仅用平方根项更高的拟合精度。经过计算，得出的简单公式：

$$\mathrm{ARF_{CH_4}}=\alpha(\sqrt{M}-\sqrt{M_0})+\beta(M-M_0)+\gamma\sqrt{N}(\sqrt{M}-\sqrt{M_0})+\delta\cdot N(M-M_0),$$

其中，M、N 分别为 CH_4、N_2O 的浓度，CH_4 参考浓度 M_0=1797 ppb。4 个拟合系数分别为 α=0.03195，β=1.439×10^{-4}，γ=－1.133×10^{-3}，δ=1.221×10^{-7}。

同理，计算 N_2O 浓度变化造成的辐射强迫时，只考虑 CH_4 对吸收重叠的影响，得到公式：

$$\mathrm{ARF_{N_2O}}=\alpha(\sqrt{N}-\sqrt{N_0})+\beta(N-N_0)+\gamma\sqrt{M}(\sqrt{N}-\sqrt{N_0})+\delta\cdot M(N-N_0),$$

其中，M、N 意义同上，N_2O 参考浓度 N_0 =321.8 ppb。4 个拟合系数分别为 α=0.08801，β=0.0011，γ=－3.7167×10^{-4}，δ= 2.0116×10^{-9}。

石广玉等（1991，2007）、于秀兰等（2001）的研究时间较早，所用的气体谱线和浓度资料都已陈旧。而本文用于公式拟合的样本数据则是由新的气体浓度和 998 带高光谱分辨率的辐射传输模式重新计算出的平流层调整后的辐射强迫 ARF，因此，本文拟合的公式与石广玉等（1991，2007）、于秀兰等（2001）的结果相比，不仅目标气体的背景浓度不同，计算出的气体的辐射强迫数值也更新。

使用拟合公式计算辐射强迫的优点是，当温室气体的浓度改变时，只需要一次数学公式的计算，比使用模式计算大大减少了计算量。

4 CH_4 和 N_2O 的全球增温潜能和全球温变潜能

本文根据文献（Zhang et al.，2011；张华等，2011）建立的 GWP 和 GTP 模型，计算了 CH_4 和 N_2O 未来 20、100 和 500 年的 GWP 和 GTP。

GWP 的定义是瞬时脉冲排放 1 kg 化合物 x，在一定的时间范围内引起的辐射强迫的积分相对于脉冲排放等量参考气体（本文采用 CO_2）在同一时间范围内的辐射强迫的积分。公式如下（IPCC，2007）：

$$\mathrm{GWP_x}=\frac{\int_0^{\mathrm{TH}}\mathrm{RF_x}(t)\mathrm{d}t}{\int_0^{\mathrm{TH}}\mathrm{RF_r}(t)\mathrm{d}t}=\frac{\int_0^{\mathrm{TH}}a_\mathrm{x}[x(t)]\mathrm{d}t}{\int_0^{\mathrm{TH}}a_\mathrm{r}[r(t)]\mathrm{d}t}, \quad (3)$$

$$x(t)=\mathrm{e}^{-t/\tau}, \quad (4)$$

$$r(t)=a_0+\sum_i a_i\exp\left(-\frac{t}{\alpha_i}\right), \quad (5)$$

其中，TH 是时间范围（本文分别取 20、100 和 500 年），t 表示时间，$\mathrm{RF_x}$ 和 $\mathrm{RF_r}$ 分别表示化合物 x 和参考气体 CO_2 的辐射强迫，a_x 和 a_r 分别表示相应的辐射效率，$x(t)$ 和 $r(t)$ 分别表示化合物 x 和参考气体 CO_2 的时间响应函数，公式（4）中的 τ 表示大气寿命，单位为 a，公式（5）中采用的 CO_2 时间响应函数是 IPCC（2007）给出的最新版本公式，其中 a_0、a_i 和 α_i 均为给定计算参数，详见 IPCC（2007）。

全球温变潜能（GTP）的定义为：在脉冲排放 1 kg 化合物 x 或者以 1 kg·a^{-1} 递增的持续排放化合物 x，在给定的一段时间 TH 内造成的全球平均地表温度的变化与参考气体 r（本文采用 CO_2）所造成的相应变化之比。脉冲排放和持续排放的 GTP 分别表示为 $\mathrm{GTP^P}$ 和 $\mathrm{GTP^S}$（Shine et al.，2005），公式如下：

$$\mathrm{GTP_x^{TH}}=\frac{\Delta T_\mathrm{x}^\mathrm{TH}}{\Delta T_\mathrm{r}^\mathrm{TH}}, \quad (5)$$

其中，TH 表示时间范围（这里为 20、100 和 500 年）；ΔT_x 和 ΔT_r 分别表示化合物 x 和 CO_2 引起的全球平均地表温度变化，它们可以通过求解全球平均地表温度变化 ΔT 与辐射强迫 ΔF 之间的公式（Shine et al.，2005）得到，

$$C\frac{\mathrm{d}\Delta T(t)}{\mathrm{d}t}=\Delta F(t)-\frac{\Delta T(t)}{\lambda}, \quad (7)$$

其中，t 表示时间，C 是系统的热容量，λ 是气候灵敏度参数。

脉冲排放和持续排放的绝对全球温变潜能分别记为 $\mathrm{AGTP^P}$ 和 $\mathrm{AGTP^S}$，表示在初始时刻排放的气体在时间 t 时刻引起的地表温度的变化，单位为 K $\mathrm{kg^{-1}}$ 和 K $(\mathrm{kg\ a^{-1}})^{-1}$。故脉冲排放和持续排放的 GTP 也可以分别表示为（Zhang et al.，2011；张华等，2011）

$$\mathrm{GTP^P}=\frac{\mathrm{AGTP_X^P}}{\mathrm{AGTP_C^P}}, \quad (8)$$

$$\mathrm{GTP^S}=\frac{\mathrm{AGTP_X^S}}{\mathrm{AGTP_C^S}}, \quad (9)$$

即 GTP 可表示为化合物 x 与参考气体 CO_2 的绝对温变潜能之比。计算 GWP 和 GTP 所需要的参数为气体 x 和 CO_2 的辐射效率和时间响应函数。这里采用 Zhang et al.（2012）计算的有云大气条件下平流层调整的 CO_2 辐射效率、以及本文计算的 CH_4 和 N_2O 的有云大气条件下平流层调整的辐射效率，CH_4、N_2O 和 CO_2 的时间响应函数取自 IPCC（2007），

气候灵敏度参数、热容量等参数取值与 Shine et al.（2005）相同。表 3 列出了 CH_4 和 N_2O 的 20、100 和 500 年的 GWP，脉冲排放的 GTP^P 和持续排放的 GTP^S，同时还给出 IPCC（2007）的 GWP 值作为比较，表 4 则是由大气寿命调整后的辐射效率计算得出的相应结果。计算时，CO_2 的大气寿命取 120 年，则经过大气寿命调整的 CO_2 辐射效率为 1.567×10^{-5} W m^{-2} ppb^{-1}（Zhang et al.，2013）。通过比较表 3 和表 4，可以看出不论 CH_4 或 N_2O，其大气寿命调整前后的各项指数变化不大（调整后比调整前值略有减少或不变）。此后，各项指数均取大气寿命调整后的值。

由表 3～4 中 GWP 值可以看出，对于脉冲排放等量的气体，CH_4 和 N_2O 对气候变化的贡献是 CO_2 的几十至上百倍。对 100 年的时间范围，本文计算的 CH_4 和 N_2O 结果分别比 IPCC（2007）的结果小 32%和 11%，用经过大气寿命调整的辐射效率计算出的结果则分别小 28%和 3%。通过对公式（3）的分析得出，GWP 计算主要与四个参数直接相关，即气体的辐射效率和时间响应函数以及参考气体 CO_2 的辐射效率和时间响应函数，它们共同作用造成 GWP 值的计算差别。经分析可以得出，本文 GWP 的差别主要是由 CH_4、N_2O 辐射效率的不同造成的，其中本文采用了高精度的辐射传输模式是其中差别的主要原因。

对比表 3～4 中 GTP^P 值和 GWP 值，除了大气寿命较长的 N_2O 其 20 年的 GTP^P 值略大于 GWP 值，其他 GTP^P 值都小于相应的 GWP 值，500 年 GTP^P 值更是远远小于 GWP 值；而且对于大气寿命较小的 CH_4，两者的差别大于 N_2O。Zhang et al.（2011），张华等（2011）的研究也表明，大气寿命越小的气体，GTP^P 值和 GWP 值相差越大。这是因为对大气寿命较小的气体，GWP 值大大高估了气体脉冲排放对气候变化的影响（Shine et al.，2005）。

GTP^S 考虑的是气体在持续排放情况下对地表温度的变化产生的相对影响，而在实际中，CH_4 和 N_2O 的排放量正是持续增加到大气中的。通过对比表 3～4 中 GTP^S 值和 GWP 值可以发现，两者的差别要比同一气体相同时间范围的 GTP^P 值与 GWP 值的差别小，并且随着时间范围的增大，GTP^S 值与 GWP 值差别减小。Zhang et al.（2011）和张华等（2011）分别对 HFCs、PFCs、SF_6 等温室气体的研究也显示了这一特性，并给出了解释：虽然 GTP^S 和 GWP 的概念相差很大，但在时间跨度较大的情况下 GTP^S 与 GWP 有相似的数学表达式，因而得到的结果也接近（Shine et al.，2005）。

本文还计算了 CH_4、N_2O 在未来 500 年内的绝对全球温变潜能 $AGTP^P$ 和 $AGTP^S$，表示这些气体脉冲排放或者持续排放在未来 500 年内引起的地表温度变化，见图 4。由图 4a 可见，N_2O 脉冲排放的气体引起的地表温度在排放初期迅速增加，并且在排放后 40 年左右达到一个最大值，然后地表温度开始缓慢恢复，在未来 400 年后完全得到恢复；CH_4 则是自开始的几十年内由最大值迅速减小，其后 50 年左右就得到完全恢复。可以发现，地表温度恢复的快慢与气体的大气寿命长短相关，大气寿命较短的 CH_4 恢复得较快，大气寿命较长的 N_2O 则恢复得较慢，从量级上看，N_2O 比 CH_4 对地表温度变化的影响也要大。图 4b 显示，N_2O 持续排放引起的地表温度的变化从排放时刻起一直增加，到本文计算

表 3 CH_4 和 N_2O 的 20 年、100 年、500 年 GWP、GTP^P、GTP^S 和 GWP（IPCC，2007）

Table 3 GWP, GTP^P, GTP^S, and GWP (IPCC, 2007) of CH_4 / N_2O with different TH (20 a, 50 a, and 100 a)

		GWP			GWP (IPCC, 2007)			GTP^P			GTP^S		
气体	大气寿命/a	20 年	100 年	500 年	20 年	100 年	500 年	20 年	100 年	500 年	20 年	100 年	500 年
CH_4	12	50	17	5.3	72	25	7.6	41	0.26	～0	56	19	5.4
N_2O	114	258	266	137	289	298	153	268	233	11	250	269	139

表 4 进行大气寿命调整后，CH_4 和 N_2O 的 20 年、100 年、500 年 GWP、GTP^P、GTP^S 和 GWP（IPCC，2007）

Table 4 GWP, GTP^P, GTP^S, and GWP (IPCC，2007) of CH_4 / N_2O with different TH (20 a, 50 a, and 100 a) after the atmospheric lifetime adjustment

		GWP			GWP (IPCC, 2007)			GTP^P			GTP^S		
气体	大气寿命/a	20 年	100 年	500 年	20 年	100 年	500 年	20 年	100 年	500 年	20 年	100 年	500 年
CH_4	12	47	16	5	72	25	7.6	39	0.24	～0	53	18	5
N_2O	114	257	266	136	289	298	153	268	233	11	250	269	138

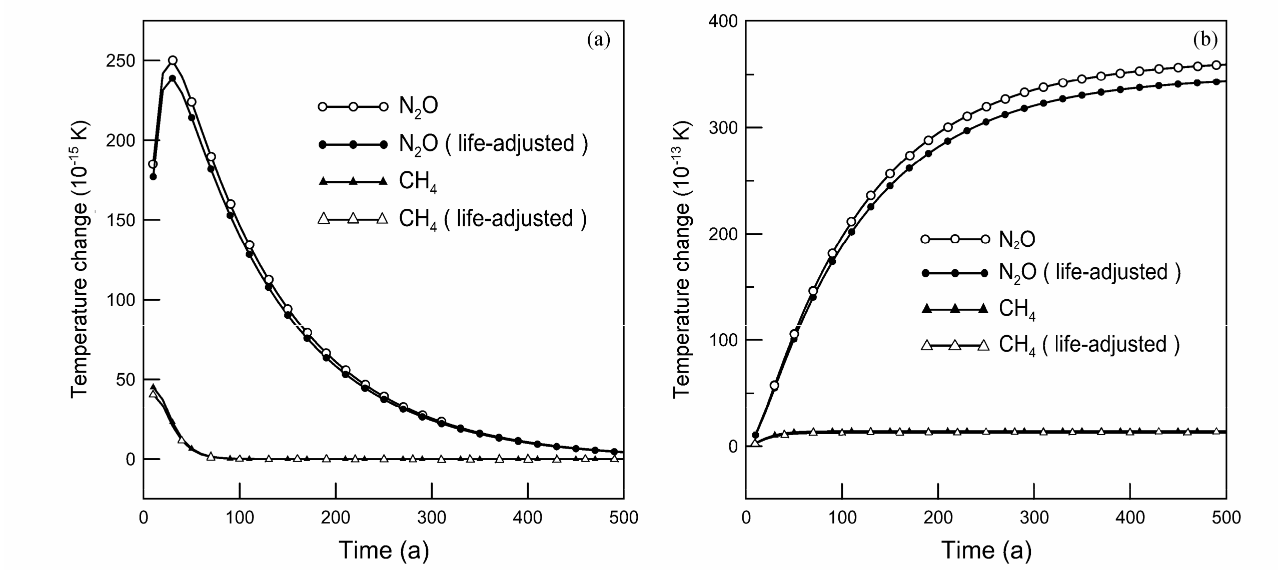

图 4 CH_4 和 N_2O 脉冲排放（a）和持续排放（b）引起的地表温度变化

Fig. 4 Surface temperature changes induced by (a) pulse emission and (b) sustained emission of CH_4/N_2O

的节点 500 年达到最大并开始变缓；而 CH_4 持续排放在整个计算时间范围内对地表温度变化的影响都比 N_2O 小得多，其变化缓慢。通过图 4 还可看出，CH_4 和 N_2O 气体持续排放引起的地表温度变化要比其脉冲排放引起的相应值大两个数量级，对地表温度变化的影响要大得多。从本文的计算得出：如果对 N_2O 的排放不加以控制，它会对未来地表温度变化的产生持续影响并且很难得到恢复，而 CH_4 对未来气候变化的影响比 N_2O 小得多，且比较容易得到恢复。

5 结论

本文计算了晴空大气和有云大气下主要温室气体 CH_4 和 N_2O 的瞬时辐射效率和平流层调整的辐射效率，得出：（1）经过平流层温度调整，CH_4 和 N_2O 的辐射效率均相对减小，这取决于平流层温度调整后，平流层温度变冷，导致其向对流层辐射通量减少所致。（2）本文计算的 CH_4 和 N_2O 经过大气寿命调整的辐射效率均与 IPCC（2007）的结果高度一致，差别仅为 0.86%和 1.4%。

以本文计算的 CH_4 和 N_2O 新的辐射效率为基础，进一步研究了 CH_4、N_2O 在未来 20、100、500 年时间尺度上的 GWP 和 GTP，并分别计算了 CH_4 和 N_2O 脉冲排放、持续排放在未来 500 年内引起的地表温度变化。结果表明：对于脉冲排放等量的气体，CH_4 和 N_2O 的 GWP 值与对应的 GTP^P 值相比显著偏高，说明 GWP 测量方法大大高估了 CH_4 和 N_2O 对气候变化的影响。

通过本文的计算和比较分析得出，持续排放 CH_4 和 N_2O 引起的地表温度变化要比其脉冲排放引起的相应值大两个数量级，对未来地表温度变化的影响要大得多。CH_4 对未来地表温度变化的影响比 N_2O 小得多，而且比较容易得到恢复。如果对 N_2O 的排放不加以控制，它会对未来地表温度变化的产生持续的影响并且很难得到恢复。因此控制 N_2O 的排放迫在眉睫。另外，本文晴空的计算结果是对六种模式大气算术平均得出的，而有云情况是对三个纬度带进行面积加权平均得到的，其中造成的不确定性也许会大于辐射模式计算精度本身造成的不确定性。

参考文献（References）

Collins W D, Ramaswamy V, Schwarzkopf M D, et al. 2006. Radiative forcing by well-mixed greenhouse gases: Estimates from climate models in the Intergovernmental Panel on Climate Change (IPCC) Fourth Assessment Report (AR4) [J]. J. Geophys. Res., 111: D14317, doi:10.1029/2005JD006713.

Fuglestvedt J S, Berntsen T K, Godal O, et al. 2003. Metrics of climate change: Assessing radiative forcing and emission indices [J]. Climatic Change, 58: 267–331.

Garand L, Turner D S, Larocque M, et al. 2001. Radiance and Jacobian intercomparison of radiative transfer models applied to HIRS and AMSU channels [J]. J. Geophys. Res., 106 (D20): 24017–24031.

Highwood E J, Shine K P. 2000. Radiative forcing and global warming potentials of 11 halogenated compounds [J]. J. Quant. Spectrosc. Radiat. Transf., 66: 169–183.

黄兴友. 2001. 温室气体全球增温潜能的研究 [D]. 中国科学院大气物理研究所博士学位论文. 107pp. Huang Xingyou. 2001. Study on global warming potential of greenhouse gas [D]. Ph. D. dissertation (in Chinese), Institute of Atmospheric Physics, Chinese Academy of Sciences, 107pp.

IPCC. 1996. Climate Change 1995: The Science of Climate Change [M] // Houghton J T, Fiho L G M, Callander B A, et al. Contribution of Working Group II to the Second Assessment Report of the Intergovernmental Panel on Climate Change. Cambridge, U K and New York: Cambridge University Press.

IPCC. 2007. Climate Change 2007: The Physical Science Basis [M] // Solomon S, Qin D, Manning M, et al. Contribution of Working Group I to the Fourth Assessment Report of the Intergovernmental Panel on Climate Change. Cambridge and New York: Cambridge University Press.

Jain A K, Briegleb B P, Minschwaner K, et al. 2000. Radiative forcings and global warming potentials of 39 greenhouse gases [J]. J. Geophys. Res., 105 (D16): 20773–20790.

Lu P, Zhang H, Jing X W. 2012. The effects of different HITRAN versions on calculated longwave radiation and uncertainty evaluation [J]. Acta Meteorologica Sinica, 26 (3): 389–398 doi:10.1007/s13351-012-0310-1.

Nakajima T, Tsukamoto M, Tsushima Y, et al. 2000. Modeling of the radiative process in an atmospheric general circulation model [J]. Appl. Opt., 39: 4869–4878.

Rothman L S, Jacquemart D, Barbe A, et al. 2005. The HITRAN 2004 molecular spectroscopic database [J]. J. Quant. Spectrosc. Radiat. Transf., 96: 139–204.

Shi G Y. 1981. An accurate calculation and representation of the infrared transmission function of the atmospheric constituents [D]. Ph. D. dissertation, Tohoku University of Japan, 191pp.

石广玉. 1991. 大气微量气体的辐射强迫与温室气候效应 [J]. 中国科学 (B 辑), 35 (7): 776–784. Shi Guangyu. 1991. Radiation forcing and greenhouse effect of atmospheric trace gases [J]. Science China Chemical Sciences (in Chinese), 35 (7): 776–784.

石广玉. 2007. 大气辐射学 [M]. 北京: 科学出版社, 402pp. Shi Guangyu. 2007. Atmospheric Radiation (in Chinese) [M]. Beijing: Science Press, 402pp.

Shine K P, Fulestvedt J S, Hailemariam K, et al. 2005. Alternatives to the global warming potential for comparing climate impacts of emissions of greenhouse gases [J]. Climatic Chang, 68 (3): 281–302.

Sihra K, Hurley M D, Shine K P, et al. 2001. Updated radiative forcing estimates of 65 halocarbons and nonmethane hydrocarbons [J]. J. Geophys. Res., 106 (D17): 20493–20505.

World Meteorological Organization (WMO). 2009. Greenhouse Gas Bulletin: The state of greenhouse gases in the atmosphere using global observations through 2008 [R]. Geneva: World Meteorological Organization.

于秀兰, 石广玉. 2001. 平流层温度调整后的辐射强迫的简化计算[J]. 高原气象, 20 (3): 271–274. Yu Xiulan, Shi Guangyu. 2001. Simplified calculation of radiative forcing with adjusted stratosphere temperature [J]. Plateau Meteorology (in Chinese), 20 (3): 271–274.

Zhang H, Nakajima T, Shi G Y, et al. 2003. An optimal approach to overlapping bands with correlated k distribution method and its application to radiative calculations [J]. J. Geophys. Res., 108 (D20): 4641, doi:10.1029/2002JD003358.

Zhang H, Shi G Y, Nakajima T, et al. 2006a. The effects of the choice of the k-interval number on radiative calculations [J]. J. Quant. Spectrosc. Radiat. Transf., 98 (1): 31–43.

Zhang H, Suzuki T, Nakajima T, et al. 2006b. Effects of band division on radiative calculations [J]. Opt Eng, 45 (1): 16002–16010.

Zhang H, Wu J X, Lu P. 2011. A study of the radiative forcing and global warming potentials of hydrofluorocarbons [J]. J. Quant. Spectrosc. Radiat. Transf., 112 (2): 220–229.

Zhang H, Zhang R Y, Shi G Y. 2013. Radiative forcing due to CO_2 and its effect on global surface temperature change [J]. Advances in Atmospheric Sciences,30 (4).

张华, 吴金秀, 沈钟平. 2011. PFCs 和 SF_6 的辐射强迫和全球增温潜能 [J]. 中国科学, 41 (2): 215–233. Zhang Hua, Wu Jingxiu, Shen Zhongping. 2011. Radiative forcing and global warming potential of perfluorocarbons and sulfur hexafluoride [J]. Science China Earth Sciences, 54 (5): 764–772, doi:10.1007/s11430-010-415-0.

Theor Appl Climatol (2014) 115:365–373
DOI 10.1007/s00704-013-0894-0

ORIGINAL PAPER

Effect of data homogenization on estimate of temperature trend: a case of Huairou station in Beijing Municipality

Lei Zhang · Guo-Yu Ren · Yu-Yu Ren · Ai-Ying Zhang · Zi-Ying Chu · Ya-Qing Zhou

Received: 16 February 2013 / Accepted: 27 March 2013 / Published online: 25 April 2013

Abstract Daily minimum temperature (Tmin) and maximum temperature (Tmax) data of Huairou station in Beijing from 1960 to 2008 are examined and adjusted for inhomogeneities by applying the data of two nearby reference stations. Urban effects on the linear trends of the original and adjusted temperature series are estimated and compared. Results show that relocations of station cause obvious discontinuities in the data series, and one of the discontinuities for Tmin are highly significant when the station was moved from downtown to suburb in 1996. The daily Tmin and Tmax data are adjusted for the inhomogeneities. The mean annual Tmin and Tmax at Huairou station drop by 1.377°C and 0.271°C respectively after homogenization. The adjustments for Tmin are larger than those for Tmax, especially in winter, and the seasonal differences of the adjustments are generally more obvious for Tmin than for Tmax. Urban effects on annual mean Tmin and Tmax trends are −0.004°C/10 year and −0.035°C/10 year respectively for the original data, but they increase to 0.388°C/10 year and 0.096°C/10 year respectively for the adjusted data. The increase is more significant for the annual mean Tmin series. Urban contributions to the overall trends of annual mean Tmin and Tmax reach 100% and 28.8% respectively for the adjusted data. Our analysis shows that data homogenization for the stations moved from downtowns to suburbs can lead to a significant overestimate of rising trends of surface air temperature, and this necessitates a careful evaluation and adjustment for urban biases before the data are applied in analyses of local and regional climate change.

L. Zhang
College of Atmospheric Science, Nanjing University of Information Science & Technology, Nanjing, China

G.-Y. Ren (✉) · Y.-Y. Ren
Laboratory for Climate Studies, National Climate Center, CMA, Beijing, China
e-mail: guoyoo@cma.gov.cn

A.-Y. Zhang · Z.-Y. Chu
Beijing Meteorological Bureau, CMA, Beijing, China

Y.-Q. Zhou
Jinzhong Meteorological Bureau of Shanxi Province, CMA, Jinzhong, China

1 Introduction

The homogeneous time series of climate variables are defined as those which contain only climatic variation and regional trend information. It is generally recognized that only by using homogenized data series can the long-term climatic trends be accurately detected. However, due to changes in observing sites, instruments, observing schedule, observing habits and micro-environment around the observational grounds, discontinuous points in the observational records can be created, especially for surface air temperature (SAT) records. The inhomogeneous data may bring certain deviation for estimating climatic trends, leading to inaccurate analyses for regional climate change detection in some circumstances (Jones et al. 1986; Easterling and Peterson 1995a; Yan et al. 2001; Ren et al. 2005; Menne et al. 2010). Therefore, researchers commonly examine and adjust the inhomogeneities before going to analyze long-term SAT trends at single sites or on regional scales, by combining varied mathematical methods and station metadata (e.g., Jones et al. 1986; Easterling and Peterson 1995a, b; Alexandersson and Moberg 1997; Aguilar et al. 2003; Menne and Williams 2005).

The inhomogeneities caused by observing schedule, instrumentation, and relocation were adjusted in SAT data of the United States USHCN (US Historical Climate Network)

(Karl and Williams 1987; Quayle et al. 1991; Easterling and Peterson 1995a, b; Menne and Williams 2009). Vincent (1998) and Vincent et al. (2002) adjusted the Canadian Tmin and Tmax series using multiple linear regression method. Researchers from other countries and regions also created their own homogeneous SAT dataset using methods such as Easterling and Peterson method, Standard Normal Homogeneity Test, Two-Phase Regression, Penalized Maximal *t* Test, and Multiple Analysis of Series for Homogenization (MASH) (Wang et al. 2007a; Aguilar et al. 2003; Reeves et al. 2007).

Chinese researchers made studies of SAT data homogenization (Song et al. 1995; Zhai and Eskridge 1996; Liu 2000; Yan et al. 2001; Yan and Jones 2008; Li et al. 2004; Li and Dong 2009; Li and Yan 2010). Using three different tests for undocumented change points, for example, Li et al. (2009) estimated the artificial discontinuities in annual mean daily Tmin and Tmax in southeastern China and found that there are more discontinuity points in annual mean Tmin series; Li and Yan (2010) apply MASH method to detect and to adjust inhomogeneities for daily SAT series of 1960–2006 at Beijing station.

Given the adjustments are accurate and applicable for monitoring and detecting regional climate change, however, there remain still a few of issues to be solved. One is what effect the homogenization will have on the estimated long-term SAT trends at a single station or in a large region. If the SAT trends are significantly different between the prior and aft adjusted data series, then what are the underlying causes? Does the adjustment for inhomogeneities significantly recover the urban bias when the breakpoints are mostly caused by the moves of stations from urban areas to rural areas, as previously suggested by Winkler et al. (1981) and Hansen et al. (2001) for the United States and recently by Ren et al. (2010) for mainland China? To answer these questions will certainly deepen our understanding of the systematic biases of the SAT data and their influences on the estimates of magnitude and rate of local and regional temperature change.

In this paper, we examine the effect of data homogenization on the estimate of Tmin and Tmax trends at Huairou station of Beijing Municipality (BM). We first make an examination of inhomogeneities of temperature data and adjust the breakpoints identified to obtain a homogenized SAT data; we then compare the linear trends of the original and adjusted SAT series and analyze the urban effects on the linear trends of the original and adjusted SAT series using the temperature data of the same reference stations.

2 Data and methods

The original daily Tmin and Tmax data of Huairou, Xiayunling, and Shangdianzi stations from 1960 to 2008 are obtained from the National Meteorological Information Center of the China Meteorological Administration. The locations of the stations are shown in Fig. 1, and the basic information of the stations is listed in Table 1. The station history records are from the Beijing Meteorological Bureau (BMB) (2009), and the population data for the residential areas near the stations are from the China Statistic Bureau (2002).

As a rapidly grown small city, Huairou is located in the northern mountainous areas of the BM, with a population of ~75 thousands in the urban area in 2000 (Fig. 1a). Huairou

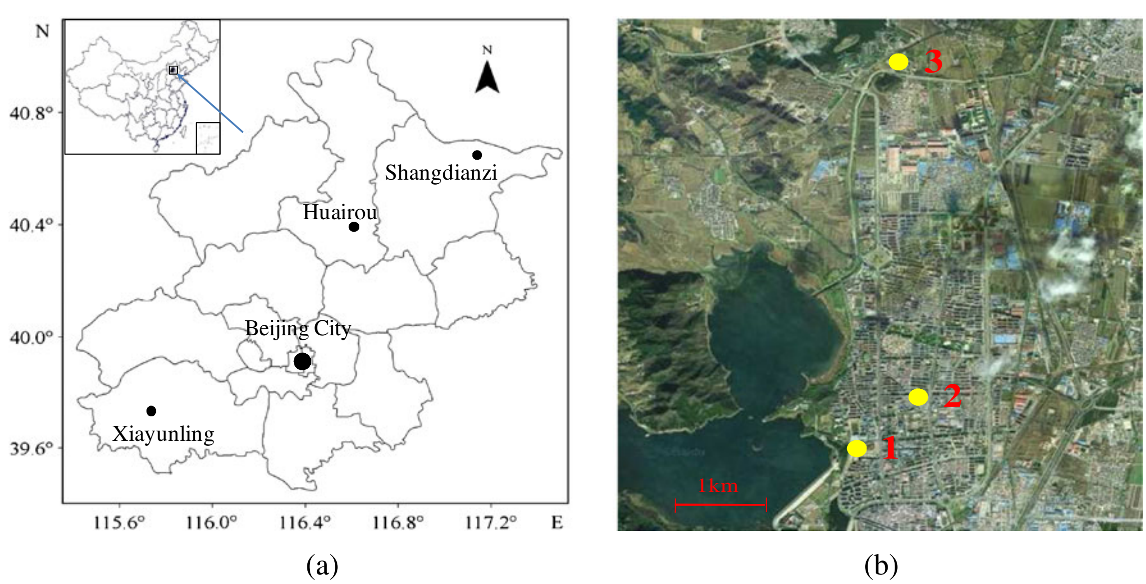

Fig. 1 Locations of the weather stations used in the study. **a** Huairou station and reference stations in present; **b** present and historical locations of Huairou station. Numbers *1*, *2*, and *3* in **b** indicate the locations before 1964, 1964–1996, and after 1996

weather station is a typical urban station (Fig. 1b), and the recent 49-year records from the station are evaluated in this paper for the data inhomogeneities and urbanization effects on the SAT trends as a target observational site. Although Xiayunling and Shangdianzi stations are also located in the mountainous areas, they are both far from larger residential areas, with the former being on a valley in the southwest and the latter on a slope near a small village having a population of no more than a thousand in the northeast (Fig. 1a). The two observational sites are chosen as the reference stations from 20 weather stations with over 30-year records in the BM. In addition to the small population of the residential areas near stations and the similar physiographic characteristics to the target station, the reference stations are also required to have the continuous observation records with as possible as less the missing observational values. The two weather stations were ever used as reference stations in previous studies of urbanization effect on the SAT trends of Beijing station (Chu and Ren 2005; Ren et al. 2007).

Inhomogeneities of SAT data can be caused by such factors as instrumentation, relocation, change in observational time, and modified statistical methods for daily averages. The introduction of the Autonomous Weather Stations (AWS) to operational observations around 2004 in mainland China may in certain extent have resulted in additional inhomogeneities in SAT records. Wang et al. (2007b) indicated, however, that the SAT of AWS has certain difference from that of manual weather stations, but overall the difference is small and not significant. No change in observational time and statistical methods of daily mean SAT occurred during the last 50 years, and these will not cause any detectable inhomogeneities of the SAT data. It has been realized that the most important factor causing the inhomogeneities of SAT data is the frequent relocations of stations in mainland China (Yan et al. 2001; Li et al. 2004; Ren et al. 2005).

Huairou station experienced relocation twice. It was moved for the first time from West Gate of the old town (Site 1 in Fig. 1b) to Beitumenzi (Site 2 in Fig. 1b) at the East Gate Road outside the old town on 1 August 1964. The second move occurred on 1 July 1996, from Beitumenzi to a suburban village called Liugezhang (Site 3 in Fig. 1b), about 5.5 km from the center of the old town (BMB 2009). For the two reference stations, on the other hand, the only move occurred for Shangdianzi station on 1 September 1989, but the horizontal distance of the movement was 750 m, and the observational grounds changed from 255 m above sea level (ASL) to 293 m ASL, increasing by 38 m in altitude.

The data are quality-controlled with the following steps: (1) if the maximum temperature (Tmax) values are lower than the minimum temperature (Tmin) values, they are registered as unreasonable readings. There is no unreasonable record in the SAT dataset of Huairou station; (2) the values beyond four times of standard deviation are marked as outliers. If outliers are detected, the reasonable records are retained, and unreasonable ones are corrected or regarded as missing values, based on the comparison to the records of the neighboring stations. There is only one outlier found in the dataset, but it is not unreasonable; (3) missing values, which account for less than 0.25% of the total records, are filled in by using the means of the same stations for the reference time period 1971–2000.

The monthly mean Tmin and Tmax series $T_{i,j}$ are calculated based on the daily records, and the monthly change-in-temperature time series dT/dt for Huairou station are then created referring to Easterling and Peterson (1995a). The i and j indicate number of year and month respectively.

$$(\mathrm{dT/dt})_{i,j} = T_{i+1,j} - T_{i,j} \quad (1)$$

The monthly reference change-in-temperature time series $(\mathrm{dT/dt})'$ are constructed by averaging the two reference station data with squares of correlation coefficients with Huairou station series as weights. We thus get the reference series T'.

$$T'_{i+1,j} = T'_{i,j} + (\mathrm{dT/dt})'_{i,j} \quad (2)$$

Discontinuous points in annual difference series of the target station and the reference stations are detected by using method of moving t test. As mentioned above, Huairou station was moved in 1964 and 1996. In order to effectively identify the discontinuities due to the relocations, the son series length is set as 3 years since the dataset started in 1960. Therefore, the series length n=49, the son series length $n1$=$n2$=3, and the significance level α=0.01. The metadata are used to validate the existence of the inhomogeneous points, and they are adjusted if proved to be real and caused by relocation. Otherwise, the original records are kept as they were.

The 5-year averages of monthly mean SAT difference between the target station and the reference series is taken as the adjustment values. If the records are less than 5 years before or after discontinuous points, then all the years of record available are used to determine the adjustment values. The adjustments for inhomogeneities are made on basis of daily SAT data. The daily adjustment values are obtained by a linear interpolation method, with the monthly mean adjustment values being assigned to the mid-month days (15th or 14th) of the neighboring months.

The sections of data after the last documented inhomogeneous points are taken as the base series, and they remain unchanged. Before the inhomogeneous points, the adjustment values are added to the original records for every day.

Urban effect (ΔT_{ur}) is defined as the SAT trends caused by the changing Urban Heat Island (UHI) intensity and/or other factors (such as aerosols) related to urbanization near the specific locations of urban weather stations (Chu and Ren 2005; Ren et al. 2008). It is estimated by formula:

$$\Delta T_{ur} = T_u - T_r \tag{3}$$

where T_u is the SAT trend of urban station and T_r is the SAT trend of reference (rural) station (series). ΔT_{ur} is larger than 0 if the urbanization raises the SAT trend at urban station, and it is smaller than 0 if the urbanization reduces the SAT trend at urban station.

ΔT_{ur} can also be estimated by calculating the annual and monthly mean SAT differences between urban station and reference series and the linear trend of the difference series over the time period analyzed. In this paper, the annual mean SAT difference series of Tmin and Tmax between Huairou station and the average reference series are constructed, and their linear trends for the time period 1960–2008 are estimated by using least-square method and are examined for statistical significance by t test.

Urban contribution (E_u) is defined as a proportion that the statistically significant urban effect accounts for the total SAT trend at urban station (Chu and Ren 2005; Ren et al. 2008). It can be expressed as:

$$E_u = \left|\frac{\Delta T_{ur}}{T_u}\right| \times 100\% = \left|\frac{T_u - T_r}{T_u}\right| \times 100\% \tag{4}$$

Generally, $\Delta T_{ur}/T_u$ is a positive value less than 100% ($0 \leq E_u \leq 100\%$); absolute value is taken because it, in certain circumstances, assumes negative value due to the effects other than increasing UHI intensity. If E_u=100%, then it shows that the SAT trend of the urban station is entirely caused by urbanization; if E_u is more than 100%, it implies that the extra trend might have been caused by other local factors not yet identified or the errors of data, but it is regarded as 100% in this study. As the definition implies, urban contribution is not calculated if the urban effect is not statistically significant.

3 The results

3.1 Detection and adjustment of data inhomogeneities

There is no discontinuous point detected in the SAT data series of the two reference stations, despite the relocation of Shangdianzi station in September 1989. This happens mainly due to the relatively small change in the altitude and the environment. No adjustment is done, therefore, and the quality-controlled data are used for producing a single and average reference series.

However, the inhomogeneities are more evident in the SAT data series of Huairou station. Figure 2 shows curves of the moving t statistics of Tmin and Tmax at Huairou station. There are three discontinuous points in the Tmin series in 1963, 1991, and 1996, respectively, and three discontinuous points in the Tmax series in 1974, 1996, and 2000, respectively. By checking the metadata, the discontinuous points in 1963 and 1996 occurred most probably due to the station moves of 1 August 1964 and 1 July 1996 (Table 1). The two discontinuous points are more significant statistically for the Tmin series than those for Tmax series, and they have to be

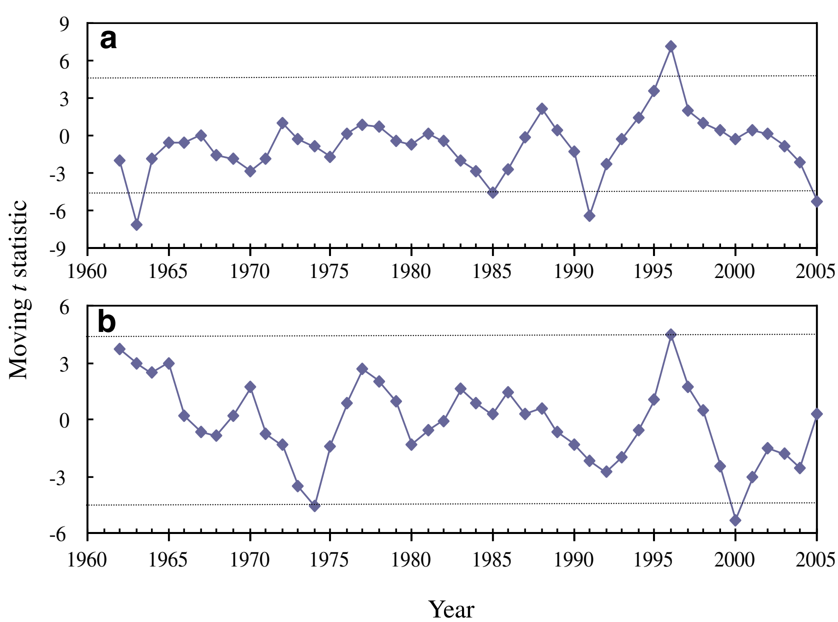

Fig. 2 The moving t statistics of Tmin (**a**), Tmax (**b**) at Huairou station (the *dotted straight lines* denote that the values are statistically significant at 0.01 confidence level)

Table 1 Information of the weather stations used in this study

Station code	Station name	Longitude (°E)	Latitude (°N)	Altitude (m)	Start time of record	Relocation (d/m/y)	Population in 2000 (10^3)
54419	Huairou	116.62	40.37	76	1959	1/8/1964 1/7/1996	74.6
54597	Xiayunling	115.72	39.72	408	1959		0
54421	Shangdianzi	117.12	40.65	293	1958	1/9/1989	Less than 1.0

adjusted for homogeneity. However, the discontinuous points statistically detected for Tmin in 1991 and for Tmax in 1974 and 2000 cannot be validated by the station historical records and have been kept as they are.

The daily mean adjustment values of Tmin and Tmax for the two discontinuous points validated are shown in Fig. 3. The monthly and daily mean adjustment values are all positive in 1964 and 1996. For the discontinuous point in 1996, however, the Tmin adjustment values are significantly larger than the Tmax adjustment values, and the Tmin adjustment values are significantly larger in winter than those in summer. It suggests that the daily Tmin and Tmax all dropped when the station was moved from within the town to outside the town, with the drop in Tmin more significant. There are also obvious seasonal differences in the Tmin adjustment values, with those in winter larger than in summer. The seasonal differences for Tmax adjustment values are smaller.

Figure 4 gives the annual mean Tmin and Tmax of the original and the homogeneity-adjusted data series at Huairou station and of the average reference data series. It is obvious that the adjusted temperature series, especially for Tmin, are more homogeneous and continuous than the original ones, and they are more consistent with the average reference series in inter-annual variability. The annual mean Tmin for the whole period analyzed decreases by 1.377°C after the adjustment, while the annual mean Tmax decreases by 0.271°C (Table 2). The average adjustment magnitudes of mean Tmin are significantly larger than those of mean Tmax.

A notable phenomenon is that the linear trends of the original annual mean Tmin and Tmax series of Huairou station are −0.006°C/10 year and 0.204°C/10 year, respectively, while the linear trends of the adjusted annual mean Tmin and Tmax series are increased to 0.385°C/10 year and 0.335°C/10 year, respectively (Table 3 and Fig. 4). The trends of annual mean Tmin and Tmax both increase obviously after the adjustment, with the former regaining 0.391°C/10 year and the latter 0.131°C/10 year, respectively. It is obvious that the increase of annual mean Tmin trend is larger and more significant, indicating that Tmin records are more sensitive to the station relocations and the data homogenizations than Tmax records. The reasons for the regains of the SAT trends will be discussed below.

The annual mean Tmin and Tmax values are all reduced after the adjustments, and the reasons for the decrease are that the adjustments are made with the section of data series at the present location of observation as baseline, and also the sections of data series adjusted before the last relocation are longer in combination than the latest section of records. Once again, the reduction of the annual mean Tmin is significantly larger than that of the annual mean Tmax.

3.2 Urban biases in adjusted and original data series

Figure 5 shows changes in annual mean SAT difference values between Huairou station and the average reference

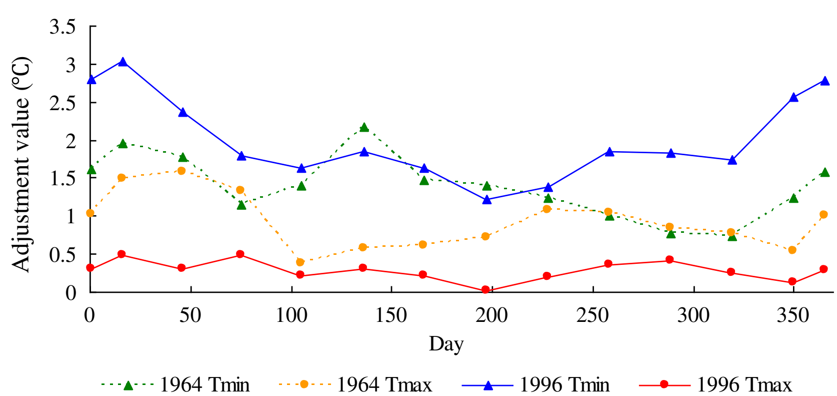

Fig. 3 The daily mean adjustment values of Tmin and Tmax at Huairou station in 1964 and 1996

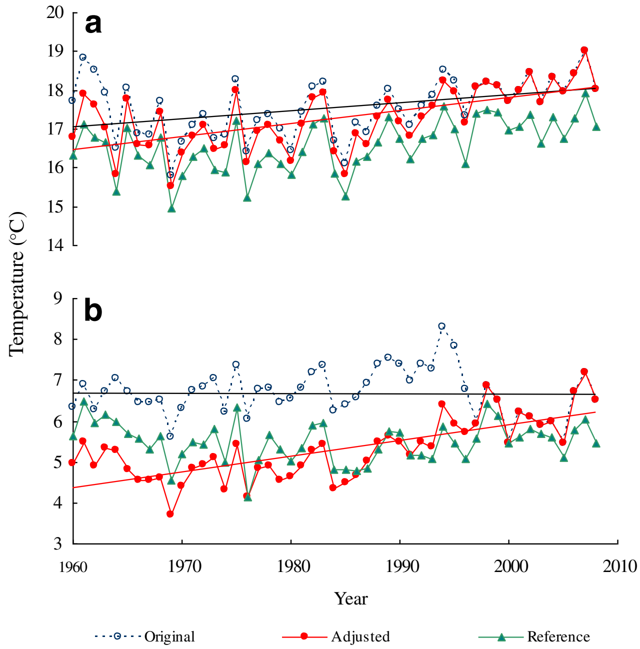

Fig. 4 The annual mean Tmax (**a**) and Tmin (**b**) of original and adjusted data series at Huairou station and of reference series during 1960–2008. The *solid straight lines* denote linear trends

series. The two SAT difference series of annual mean Tmin and Tmax for the original and homogeneity-adjusted data have highly similar inter-annual variability, but their linear trends are obviously different, with those for the adjusted data witnessing larger increasing trends, especially for Tmin series. Therefore, the relocations of Huairou station from the downtown to the suburb produced breakpoints or inhomogeneities, but they at the same time also largely reduced the urban warming trends, as seen in the original temperature series, while the data homogenization performed for welding the breakpoints now results in a recovery of the urban effect as shown in the adjusted temperature series.

Table 3 gives the urban effects and urban contributions of Huairou station for the time period 1960–2008 for the data series before and after the data adjustments. The urban effects are −0.004°C/10 year and −0.035°C/10 year, respectively, for the Tmin and Tmax before the adjustments, all non-significant statistically, but they increase to 0.388°C/10 year and 0.096°C/10 year, respectively, after the adjustments, both statistically significant at the 0.01 confidence level. The adjusted Tmin series witnesses a more significant increase in the annual mean urban warming trend.

Urban contributions to the overall temperature trends for Huairou station are not estimated for the original annual mean Tmin and Tmax series due to the non-significance of the urban effects, but they reach 100% and 28.8% for the adjusted annual mean Tmin and Tmax series, respectively. After the data adjustment for inhomogeneities, the positive trend of annual mean Tmin at Huairou station during 1960–2008 can be totally explained by the urban effect, and almost a third of the warming trend observed for annual mean Tmax at the station can be attributed to the urban effect.

4 Discussion

Relocations of weather stations from downtowns to suburbs are a common practice in mainland China during the past decades, especially for the national reference climate stations and national basic meteorological stations (Li et al. 2004; Ren et al. 2010), which have been mostly frequently applied for analyses of regional climate change. This occurs mainly due to the closeness of the weather stations to built-up areas of cities and towns and the unprecedented urbanization process over the past decades in mainland China under the rapid growth of economy (Ren et al. 2008). Our analysis and the findings of Huairou station in this paper therefore are in some extent of representativeness to the SAT datasets commonly used in studies for the country.

The frequent relocations of stations usually cause obvious inhomogeneities in SAT data, which require a homogenization before long-term trends of temperature can be analyzed. However, the adjustment may change the estimates of mean SAT trends at single stations or even in regional scale and may lead to an overestimate of the warming rates for the stations or the regions. This phenomenon were pointed out in previous studies (Hansen et al. 2001; Menne et al. 2009; Ren et al. 2010) but have not been exclusively examined. Winkler et al. (1981) found, however, that the homogeneity-adjusted SAT data depict a larger UHI intensity and UHI extent in the urban area of Minneapolis–St. Paul, Minnesota. They adjusted the data inhomogeneities induced by changes in observational time and station location. Our analysis for Huairou station in this paper shows that the increased warming rates as estimated

Table 2 The mean and variance of annual Tmin and Tmax of Huairou station before and after adjustment during 1960–2008 (degrees Centigrade)

		Before adjustment	After adjustment	Difference
Tmin	Mean	6.683	5.306	−1.377
	Variance	0.339	0.577	0.238
Tmax	Mean	17.561	17.290	−0.271
	Variance	0.542	0.629	0.087

Table 3 Urban effects on the Tmin and Tmax trends of the Huairou station (degrees Centigrade per 10 years) and the urban contribution to the overall temperature trends (percent) for the data series before and after adjustment for period 1960–2008

		Before adjustment	After adjustment	Difference
Tmin	Linear trend	−0.006	0.385[a]	0.391
	Urban effect	−0.004	0.388 [a]	0.392
	Urban contribution		100	
Tmax	Linear trend	0.204 [a]	0.335 [a]	0.131
	Urban effect	−0.035	0.096 [a]	0.131
	Urban contribution		28.8	

[a] Significant at the 0.01 confidence level

from the homogeneity-adjusted data series compared with the original data series mainly result from the recovery of the urban warming trends. The regained warming trends, especially for the annual mean Tmin, are caused by enhanced urban effect near the first location of the city station, which now has been located in the center of the built-up areas due to the urbanization. The overall trend and the urban effect in the annual mean Tmax series also increase after the homogenization, but the changes are much smaller.

Figure 6 gives a conceptual illustration of the effects of homogenization on estimates of SAT trends with those occurred at Huairou station as a case. The first move of the station from West Gate of the old town to Beitumenzi of East Gate Road in 1964 resulted in a relatively small drop of annual mean Tmin due to the short distance between the two sites, but the second move from Beitumenzi to Liugezhang in 1996 caused a tremendous drop of annual mean Tmin due to the long distance of the relocation and the radically different settings around the two sites (also see Fig. 1b). The positive linear trend of annual mean Tmin for the unadjusted data series, as shown by the black dotted line, is small and statistically insignificant as a result of the two plunges caused by the relocations. When the SAT data is adjusted for the inhomogeneities, however, the larger positive trend of annual Tmin at the station has been recovered, as shown by the red dotted line, because the annual mean Tmin values before the two breakpoints are successively lowered by subtracting the adjustment values from the original data series.

Further investigations are needed to understand to what extent the data homogenization of the national reference climate stations and national basic meteorological stations in mainland China has affected the estimates of the large scale SAT trends. It is reasonable to assume that the effect of the data homogenization on the estimates of SAT trends and urban biases for the country on a whole would be more moderate than that reported for Huairou station in this paper,

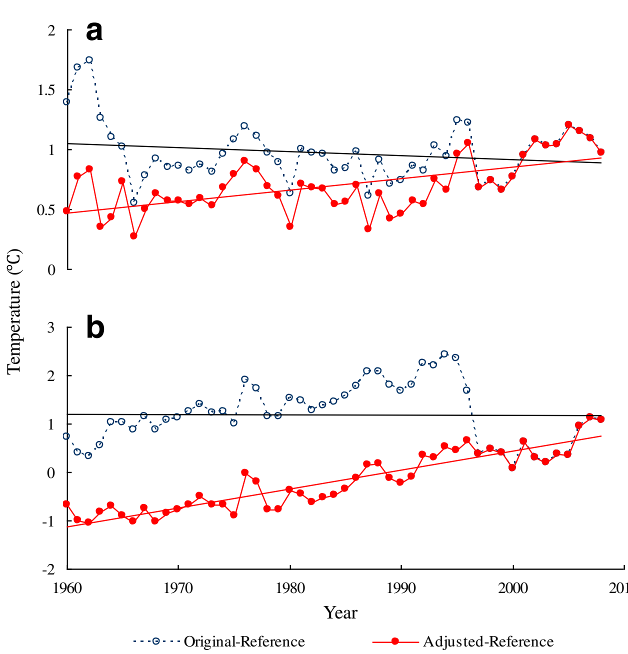

Fig. 5 The differences of annual mean Tmax (**a**) and Tmin (**b**) between Huairou station and reference data for original (dotted lines) and adjusted (solid lines) data series during 1960–2008. The *solid straight lines* denote linear trends

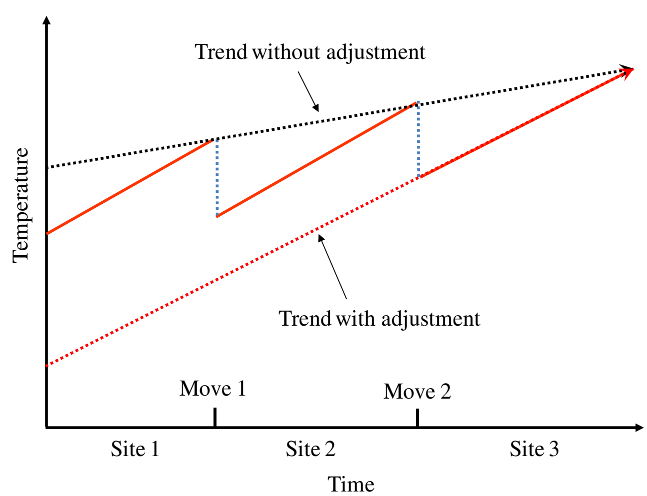

Fig. 6 A sketch of effects of Huairou station relocations on annual mean minimum temperature trends of the adjusted and unadjusted data series

but it would not be overlooked considering that a common practice is to relocate the weather stations within built-up areas to suburbs or countryside when they are regarded as being less representative for monitoring baseline climate, and this will result in obvious inhomogeneities in the SAT data series in mainland China, which has been consensually regarded as improper for applications in studies of climate change and requires a homogeneity-adjustment before they could be used in studies. If the homogenization significantly affects the SAT trends for part or even majority of the stations in the country, the urban biases in the homogenized SAT data series of the stations have to be more carefully assessed and adjusted before they are to be confidently used in analyses of climate change.

The issue is also relevant to a few of questions baffling the researchers of climate change. One is the understanding of the different trends of Tmin and Tmax in continents. The “asymmetry” in increases of Tmin and Tmax series and the resulting decline of the Diurnal Temperature Range (DTR) were reported for many regions (e.g., Karl et al. 1993; Xie and Cao 1996; Zhai and Pan 2003; Qian and Lin 2004; Choi et al. 2009; Zhou and Ren 2011). The changes were related to the increase in cloud coverage and precipitation worldwide and aerosols over some regions (Dai et al. 1999; Easterling et al. 2000). However, Zhou and Ren (2009, 2011) found a larger urban contribution to the “asymmetry” in the Tmin and Tmax increases and in the decrease of the DTR in North China. The analysis result based on the homogeneity-adjusted data in this paper also shows that the significant increase in annual mean Tmin at Huairou station might have been completely explained by urbanization, and the increase in annual mean Tmax might have been partially caused by urbanization, generally consistent with the conclusions drawn by Zhou and Ren (2009, 2011) for North China and by Zhang et al. (2011) for Beijing station.

5 Conclusions

In this paper, the daily Tmin and Tmax data at Huairou station, Beijing Municipality, from 1960 to 2008 are examined and adjusted for inhomogeneities caused by relocations of station, and the temperature trends before and after the adjustments are compared. Following conclusions are drawn:

1. The adjusted annual mean Tmin and Tmax drop by 1.377°C and 0.271°C, respectively, and the adjustment values for Tmin are significantly larger than those for Tmax. The location changes of Huairou station from downtown to the suburb, especially the second move in 1996, cause more significant drop in annual mean Tmin. The drops in monthly mean Tmin values are larger during winter than those during summer.
2. The data homogenization for the station relocations from downtown to suburb at Huairou station leads to an increase in mean SAT trends, and the increase is more significant for Tmin than for Tmax. The urban effects on annual mean Tmin and Tmax trends are statistically insignificant (−0.004°C/10 year and −0.035°C/10 year, respectively) for the original data series, but they reach 0.388°C/10 year and 0.096°C/10 year, respectively, for the homogeneity-adjusted data series. The urban contributions to the overall positive SAT trends are 100% and 28.8%, respectively, for Tmin and Tmax for the homogeneity-adjusted data.
3. The larger effects of relocations, homogenization, and urbanization on Tmin data series than on Tmax data series in a larger extent explain the "asymmetry" in daytime and nighttime SAT trends at Huairou station, and the urban effect is also a major contributor to the DTR decline as implied in the "asymmetry" changes of the annual mean Tmin and Tmax for the homogeneity-adjusted data at the station.

Acknowledgments This work is financially supported by the Ministry of Science and Technology of China (GYHY201206012). Thanks are also due to Mr. G.H. Li. at the Huairou Meteorological Bureau, Beijing Municipality, for providing the information of station history.

References

Aguilar E, Auer I, Brunet M, Peterson TC, Wieringa J (2003) Guidelines on climate metadata and homogenization. WMO-TD No.1186, WCDMP No.53. Geneva, Switzerland: World Meteorological Organization, 55

Alexandersson H, Moberg A (1997) Homogenization of Swedish temperature data. Part I: homogeneity test for linear trends. Int J Climatol 17:25–34

Beijing Meteorological Bureau (2009) The history of meteorological stations in Beijing. 147 pp., China Meteorological Press, Beijing, China (in Chinese)

China Statistic Bureau (2002) Population data of China towns and city districts. 949 pp., China Statistic Press, Beijing, China (in Chinese)

Choi G, Collins D, Ren GY, Trewin B, Baldi M, Fukuda Y, Afzaal M, Pianmana T, Gomboluudev P, Huong PTT, Lias N, Kwon WT, Boo KO, Cha YM, Zhou YQ (2009) Changes in means and extreme events of temperature and precipitation in the Asia-Pacific Network region, 1955–2007. Int J Climatol 29:1960–1925

Chu ZY, Ren GY (2005) Chang in urban heat island magnitude and its effect on mean air temperature record in Beijing region. Acta Meteor Sin 63(4):534–540 (in Chinese)

Dai A, Trenberth KE, Karl TR (1999) Effects of clouds, soil moisture, precipitation, and water vapor on diurnal temperature range. J Climate 12:2451–2473

Easterling DR, Peterson TC (1995a) A new method for detecting undocumented discontinuities in climatological time series. Int J Climatol 15:369–377

Easterling DR, Peterson TC (1995b) The effect of artificial discontinuities on recent trends in minimum and maximum temperatures. Atmos Res 37:19–26

Easterling DR, Evans JL, Groisman PY, Karl TR, Kunkel KE, Ambenje P (2000) Observed variability and trends in extreme climate events: a brief review. Bull Amer Meteor Soc 81:417–425

Hansen J, Ruedy R, Sato M, Imhoff M, Lawrence W, Easterling D, Peterson T, Karl T (2001) A closer look at United States and global surface temperature change. J Geophys Res 106(D20):23947–23963

Jones PD, Raper SCB, Bradley RS, Diaz HF, Kelly PM, Wigley TML (1986) Northern Hemisphere surface air temperature variations: 1851–1984. J Climate Appl Meteor 25(2):161–179

Karl TR, Williams CN (1987) An approach to adjusting climatological time series for discontinuous inhomogeneities. J Climate Appl Meteor 26:1744–1763

Karl TR, Jones PD, Knight RW, Kukla G, Plummer N (1993) A new perspective on recent global warming: asymmetric trends of daily maximum and minimum temperature. Bull Amer Meteor Soc 74(6):1007–1023

Li QX, Liu XN, Zhang HZ, Peterson TC, Easterling DR (2004) Detecting and adjusting on temporal inhomogeneity in Chinese mean surface air temperature data. Adv Atmos Sci 21(2):260–268

Li QX, Dong WJ (2009) Detection and adjustment of undocumented discontinuities in Chinese temperature series using a composite approach. Adv Atmos Sci 26(1):143–153

Li Z, Yan ZW (2010) Application of multiple analysis of series for homogenization to Beijing daily temperature series 1960–2006. Adv Atmos Sci 27(4):777–787

Liu XN (2000) The homogeneity test on mean annual wind speed over China. Quart J Appl Meteor 11(1):27–34 (in Chinese)

Menne MJ, Williams CN (2005) Detection of undocumented changepoints using multiple test statistics and composite reference series. J Climate 18:4271–4286

Menne MJ, Williams CN (2009) Homogenization of temperature series via pairwise comparisons. J Climate 22:1700–1717

Menne MJ, Williams CN, Palecki MA (2010) On the reliability of the U.S. surface temperature record. J Geophys Res 115, D11108

Qian WH, Lin X (2004) Regional trends in recent temperature indices in China. Clim Res 27:119–134

Quayle RG, Easterling DR, Karl TR, Hughes PY (1991) Effects of recent thermometer changes in the cooperative station network. Bull Amer Meteor Soc 72(11):1718–1723

Ren GY, Zhang AY, Chu ZY, Zhou JX, Ren YY, Zhou YQ (2010) Principles and procedures for selecting reference surface air temperature stations in China. Meteorol Sci Technol 38(1):78–85 (in Chinese)

Ren GY, Xu MZ, Chu ZY, Guo J, Li QX, Liu XN, Wang Y (2005) Changes of surface air temperature in China during 1951–2004. Clim Environ Res 10(4):717–727 (in Chinese)

Ren GY, Zhou YQ, Chu ZY, Zhou JX, Zhang AY, Guo J, Liu XF (2008) Urbanization effects on observed surface air temperature trends in north China. J Climate 21:1333–1348

Ren GY, Chu ZY, Chen ZH, Ren YY (2007) Implications of temporal change in urban heat island intensity observed at Beijing and Wuhan stations. Geophys Res Lett 34, L05711. doi:10.1029/2006GL027927

Reeves J, Chen J, Wang XL, Lund R, Lu QQ (2007) A review and comparison of changepoint detection techniques for climate data. J Appl Meteor Climatol 46:900–915

Song CH, Liu XN, Li JM (1995) A study of testing methods on inhomogeneity of temperature sequences. Quart J Appl Meteor 6(3):289–296 (in Chinese)

Vincent LA (1998) A technique for the identification of inhomogeneities Canadian temperature series. J Climate 11:1094–1104

Vincent LA, Zhang X, Bonsal BR, Hogg WD (2002) Homogenization of daily temperatures over Canada. J Climate 15:1322–1334

Wang XL, Wen QH, Wu Y (2007a) Penalized maximal *t* test for detecting undocumented mean change in climate data series. J Appl Meteor Climatol 46:916–931

Wang Y, Liu XN, Ju XH (2007b) Differences between automatic and manual observation. J Appl Meteorol Sci 18(6):849–855 (in Chinese)

Winkler JA, Skaggs RH, Baker DG (1981) Effect of temperature adjustments on the Minneapolis–St. Paul urban heat island. J Appl Meteor 20:1295–1300

Xie Z, Cao HX (1996) Asymmetric changes in maximum and minimum temperature in Beijing. Theor Appl Climatol 55:151–156

Yan ZW, Yang C, Jones P (2001) Influence of inhomogeneity on the estimation of mean and extreme temperature trends in Beijing and Shanghai. Adv Atmos Sci 18(3):309–322

Yan ZW, Jones PD (2008) Detecting inhomogeneity in daily climate series using wavelet analysis. Adv Atmos Sci 25(2):157–163

Zhai PM, Eskridge RE (1996) Analyses of inhomogeneities in radiosonde temperature and humidity time series. Int J Climatol 9:884–894

Zhai PM, Pan XH (2003) Trends in temperature extremes during 1951–1999 in China. Geophys Res Lett 30(17):1913. doi:10.1029/2003GL018004

Zhang L, Ren GY, Liu J, Zhou YQ, Ren YY (2011) Urban effect on trends of extreme temperature indices at Beijing Station. Chin J Geophys 54(5):1150–1159 (in Chinese)

Zhou YQ, Ren GY (2009) The effect of urbanization on maximum, minimum temperatures and daily temperature range in north China. Plateau meteorology 28(5):1158–1166 (in Chinese)

Zhou YQ, Ren GY (2011) Change in extreme temperature events frequency over mainland China during 1961–2008. Clim Res 50:125–139

长江中下游地区暴雨“积成效应”*

张世轩[1)] 封国林[2)†] 赵俊虎[1)]

1) (兰州大学大气科学学院, 兰州 730000)

2) (国家气候中心, 中国气象局气候研究开放实验室, 北京 100081)

(2012 年 10 月 18 日 收到; 2012 年 11 月 2 日 收到修改稿)

采用 1960—2011 年中国 740 站日降水观测数据, 以长江中下游地区为切入点, 提出暴雨“积成效应”这一概念, 旨在将暴雨这一天气尺度强降水过程拓展为类似中长期天气尺度过程来考虑, 研究它对季节尺度降水的贡献及影响. 通过统计分析从持续时间 (L_d)、控制面积 (A_r)、降水贡献率 (Q_s) 等三个角度建立暴雨“积成效应”概念及判定标准, 并进一步结合上述指标建立暴雨“积成效应”强度指数. 从这一角度出发, 探讨长江中下游地区暴雨“积成效应”与夏季降水的时空对应关系, 发现强度指数与同期夏季降水量的年际和年代际变化具有很好的一致性; 强弱指数年合成分布以及指数与中国东部夏季降水相关系数的空间分布呈现出类似于中国东部夏季雨带的分布形式; 而利用 EOF 分解对暴雨“积成效应”空间范围分类, 发现其与该地区夏季降水具有相似的 4 种空间型, 总体而言, 长江中下游地区暴雨“积成效应”造成的降水极大地影响甚至决定整个夏季降水的多寡及空间分布.

关键词: 长江中下游, 暴雨, “积成效应”, 夏季降水

PACS: 92.40.Ea, 92.60.Wc **DOI:** 10.7498/aps.62.069201

1 引 言

暴雨是指 24 h 降水量为 50 mm 或以上的强降雨过程, 多发生于夏季 6—7 月份, 由于暴雨常常带来严重的洪涝灾害, 因而是大气科学研究的热点和重要课题 [1], 也引起许多国家和地区的学者的广泛关注 [2−9]. 长江中下游是我国暴雨集中多发区域, 夏季平均暴雨日数在 3 d 以上, 降水量可占夏季总降水的 40%以上 [1], 因而对该地区夏季降水具有十分重要的影响, 降水异常年份的分析也表明, 长江中下游地区夏季雨带的形成和降水的多寡与暴雨有着密切的联系 [10−14], 如 2011 年 6 月长江中下游地区连续的 4 场暴雨过程, 使得该月降水量累积达到整个夏季降水的 60%左右 [15], 造成该地区旱涝急转 [16,17], 并决定了整个夏季主雨带的位置. 事实上, 暴雨是一个天气尺度系统, 但类似于这样的天气尺度系统频繁活动时, 其在时间和空间上会造成一定的持续性, 多次过程的累积或叠加, 会产生一种“积成效应”, 往往会形成类似于中长期天气过程的现象, 进而对夏季降水多寡和分布产生决定性作用. 然而与之相矛盾的是, 从短期气候预测的可预测性角度而言, 无法提前三个月 (中国 3 月夏季汛期预测会商制) 实现对上述降水过程的预测, 从而导致 2011 年夏季主雨带的预测失败. 因此, 如何定位暴雨这种短时强降水对整个夏季降水的贡献和影响, 以及如何对其进行预估, 是目前汛期降水预测存在的疑点和难点之一. 此外, 纵观国内外相关研究大都基于个例分析, 侧重某次暴雨过程的特征分析 [18−22], 对多次过程所造成的“积成效应”鲜为提及.

基于此, 本文提出暴雨“积成效应”这一概念, 以长江中下游地区为例, 从统计学角度分析暴雨的时 - 空分布特征, 制定相关标准划分暴雨“积成效应”, 进一步建立相关的指数对其进行描述, 探讨它与夏季降水时 - 空分布之间的对应关系, 初步确立暴雨这一类天气尺度活动对同期夏季降水具有重要贡献, 为进一步研究多次暴雨过程累积或叠加作

* 国家自然科学基金 (批准号: 40930952, 41205040, 41175067, 41275096) 和国家重点基础研究发展计划 (批准号: 2012CB955902, 2013CB430204) 资助的课题.

† 通讯作者. E-mail: fenggl@cma.gov.cn

用对夏季主雨带分布和局地气候等的影响等提供依据.

2 资料及处理

研究资料包括中国气象局气象信息中心资料室提供的中国 740 站 1960—2011 年逐日降水资料. 研究时段为夏季 6 月 1 日到 8 月 31 日共 92 d. 选取长江中下游地区 (27°N—34°N, 105°E—125°E) 进行研究, 首先对资料连续缺测 2 d 以上的站点进行剔除, 对缺测 1 d 的站点用前后两天的资料进行线性插补, 实际上由于所选研究时段为夏季, 观测资料缺测较少, 因此插补对结果影响很小. 经上述处理最终挑选出 121 个站点, 其分布如图 1 所示, 区域内所选站点分布均匀, 符合研究要求. 本文均以 1960—2011 年 52 年平均作为气候态.

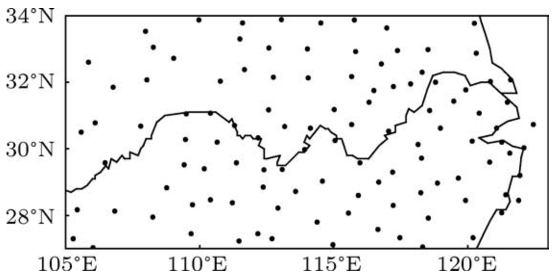

图 1 长江中下游 121 站空间分布

3 暴雨“积成效应”及其与夏季降水的关系

3.1 暴雨“积成效应”的定义

根据一般降水的级别定义, 本文分析时将日降水量在 0.1 mm 以上定为有降水发生, 而将 50 mm 及以上的降水统称为暴雨. 本文所讨论的暴雨“积成效应”由满足以下两个方面性质的暴雨所决定, 一是空间上暴雨发生的范围要达到一定的尺度, 能够对全局降水产生作用; 二是在时间上暴雨过程具有一定的持续性, 决定降水的强度.

据此, 首先从空间范围入手, 统计长江中下游区 6 月 1 日 —8 月 31 日在 1960—2011 年每年的总降水站点数 (有降水发生即可) 和暴雨站点数, 并计算多年平均逐日发生站点数. 如图 2 所示, 从演变形势可以看到长江中下游夏季平均每天发生暴雨的站点数为 3 个左右, 而平均每天发生降水的站点可达 40 个左右, 站点数分布呈现两个峰值, 较大峰值时段在第 11 d (6 月 11 日) 至第 43 d (7 月 13 日) 左右, 暴雨能达到 5 个站点左右, 对应发生降水站点为 50 个以上, 较小峰值时段为第 70 d (8 月 9 日) 至第 92 d (8 月 31 日), 暴雨能达到 3 个左右, 对应发生降水的站点数为 40 个左右. 另外, 较大峰值所对应时段与多年梅雨平均发生时段相符合, 此时每日出现暴雨的站点数平均为 5 个左右, 总降水站点能占到全区总站点的约 1/2. 进一步统计长江中下游地区 1960—2011 年夏季 6 月 1 日 —8 月 31 日共 4784 d 中, 不同暴雨发生站点数的出现频次, 并计算其频率. 图 3(a) 不同站点数发生频率分布, 可以看到统计时段内该区暴雨发生站点数最多为 25 个, 出现频率为 0.1%, 最少为 1 个, 出现频率为 24.5%, 不同暴雨发生站点数的出现频率拟合曲线呈现指数型衰减特征, 其衰减速率在 5 站之前较快, 之后则逐渐减慢. 而图 3(b) 累积百分率拟合曲线则呈指数型增长特征, 与图 3(a) 对应, 暴雨发生站点数少

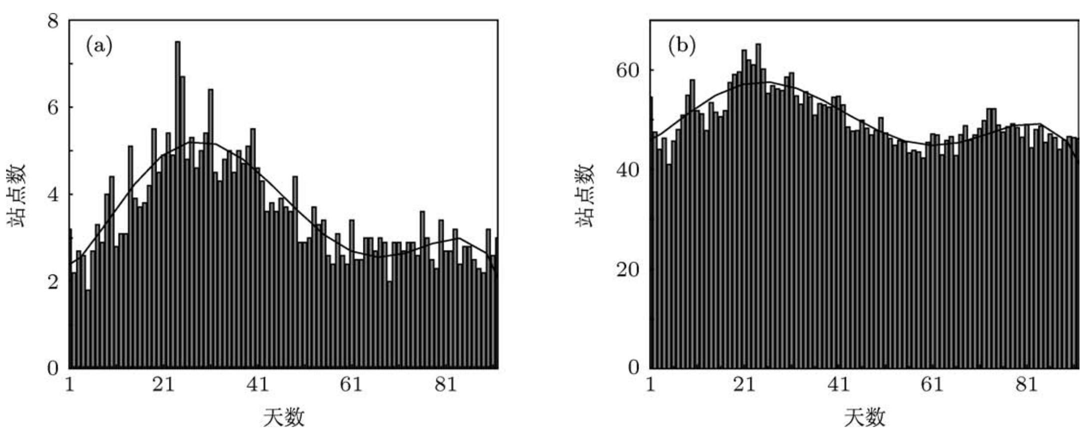

图 2 长江中下游 52 年平均逐日暴雨站点数 (a) 和总降水站点数 (b) 演变特征 (曲线为 5 次多项式拟合)

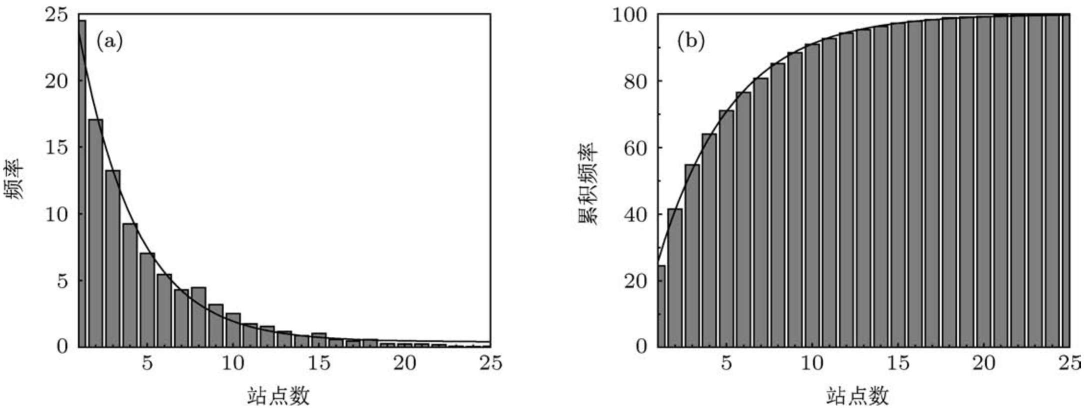

图 3 不同暴雨站点数发生频次百分率 (a) 及其累计百分率 (b) 的演变

于 5 个时, 其累积发生频率增长较快, 随后逐渐减缓, 其中发生站点数小于 5 个的出现总频率为 64.0%, 而 5 站以上 (包含 5 站) 总频率为 36%, 粗略计算所得两者的平均发生概率比为 (64/4) : (36/21)—10.7 : 1. 结合上述两方面的讨论, 我们将长江中下游地区某天满足 5 个或 5 个以上站点出现暴雨这一空间尺度特征, 作为评判暴雨 "积成效应" 发生的空间范围条件.

其次, 满足空间尺度条件的几场暴雨的时间间隔不超过一次天气过程的持续时间 (3—5 d 左右) 时, 说明几场暴雨过程具有一定的连续性, 这种性质的几次暴雨过程累积, 其时间尺度可表现出中长期天气过程的特点, 因而我们认为它在时间上也具有一定的持续性. 暴雨 "积成效应" 是由满足上述时 - 空尺度特征的几次暴雨过程的累计或叠加所产生.

对于长江中下游地区, 实际过程中可由如下的标准进行判断: 当该区某天暴雨站点数达到 5 站以上 ($\geqslant 5$) 时, 以这一天开始每 3 d 滑动求平均值, 如果连续 10 d 或 10 d 以上滑动平均值都满足上述标准, 则记录这一次暴雨降水过程, 统计整个夏季满足条件的所有过程, 这些过程的累计或者叠加对夏季降水等所产生的影响和作用, 即为长江中下游地区暴雨 "积成效应".

3.2 长江中下游地区暴雨 "积成效应" 的指标

由上述的定义可知, 要对上述事件进行刻画, 需要从持续时间 ($L_{\rm d}$)、控制面积 ($A_{\rm r}$), 以及降水贡献率 ($Q_{\rm s}$) 三个方面入手, 针对所研究的每一年, 以上指数分别定义如下:

$$L_{\rm d}=\sum_i L_i\,(i=1,2,\cdots,m), \tag{1}$$

$$A_{\rm r}=\sum_i A_i\left(i=1,2,\cdots,m_{\rm p}\right), \tag{2}$$

$$Q_{\rm s}=\left(\sum_{ij}R_{ij}\Big/R_{\rm s}\right)\times 100\% \quad \left(i=1,2,\cdots,m,\ j=1,2,\cdots,n_{\rm p}\right), \tag{3}$$

其中, 当满足以上时空选择条件时 $L_i=1$, 否则 $L_i=0$, i 为满足条件的序数日, 持续时间 $L_{\rm d}$ 为所有满足 $L_i=1$ 的总天数, m 为一次 "区域性暴雨事件" 的持续时间, $A_{\rm r}$ 为上述时间段内中心区域空间范围大小, 按照 $0.5^\circ\times0.5^\circ$ 分辨率对站点网格化, 然后计算面积, A_i 是每个网格对应的面积大小. R_{ij} 表示满足条件的第 i 天第 j 站点上的降水量, 其求和即表示暴雨 "积成效应" 所产生的总降水, $R_{\rm s}$ 表示某一年夏季降水总量, $Q_{\rm s}$ 为暴雨 "积成效应" 时段内满足条件的所有站点降水总量占当年夏季降水的比例, 其值越大, 说明暴雨 "积成效应" 时段内的降水对当年夏季降水的贡献率越大. $n_{\rm p}$ 为满足条件的站点总数.

定义的三项指标以及长江中下游区域平均降水量 $R_{\rm s}$ 随时间演变特征如图 4 所示. 图 4(a) 柱状曲线表示每年暴雨 "积成效应" 持续时间 $L_{\rm d}$, 上方的数字表示暴雨 "积成效应" 中满足条件的暴雨过程次数, 可以看到每年满足条件的暴雨过程次数并不一致, 绝大多数年份以 2 次为主, 其次为 1 次, 出现 3 次的年份有 3 年, 有 4 年没有出现满足条件的暴雨过程, 分别为 1961, 1963, 1966 和 1978 年, 与之对应的控制面积 (图 4(b)) 和降水贡献率 (图 4(c)) 在这几年也都为 0. 以上 4 年的夏季降水总量也显

著偏少, 居近 52 年中偏少年份的前 4 位 (4(d)); 说明暴雨 “积成效应” 明显偏弱时, 长江中下游地区夏季降水显著偏少. 暴雨 “积成效应” 持续时间具有明显的年际和年代际震荡变化, 其多年平均持续时间为 27.6 d 左右, 20 世纪 70 年代中期以前以及 20 世纪 80 年代中期到 90 年代初期这两个时段中, 持续时间大多在气候平均值以下, 而 20 世纪 70 年代中期到 80 年代中期和 20 世纪 90 年代初期以后这两个时段内, 持续时间大多在气候平均值附近及以上. 此外, 暴雨 “积成效应” 对应的暴雨过程发生次数与持续时间长短并不完全呈正比关系, 如 1976 年, 发生次数虽为 3 次, 但持续时间却明显比 1983 年 1 次事件短.

暴雨 “积成效应” 中心区域面积 A_r 变化曲线 (图 4(b)) 也有明显的年际和年代际变化, 总体表现为一种波动上升趋势. 年际变化表现为 20 世纪 80 年代以前, 中心区域面积年际波动幅度较大, 且基本都在平均值以下, 而 80 年代以后年际波动幅度减弱, 且基本都在平均值以上. 年代际特征变化表现为 20 世纪 70 年代中期和 80 年代中期各有一次小的波峰出现, 在 20 世纪 90 年代以后出现一次大的波峰值, 而在近 10 年呈现一种下降趋势.

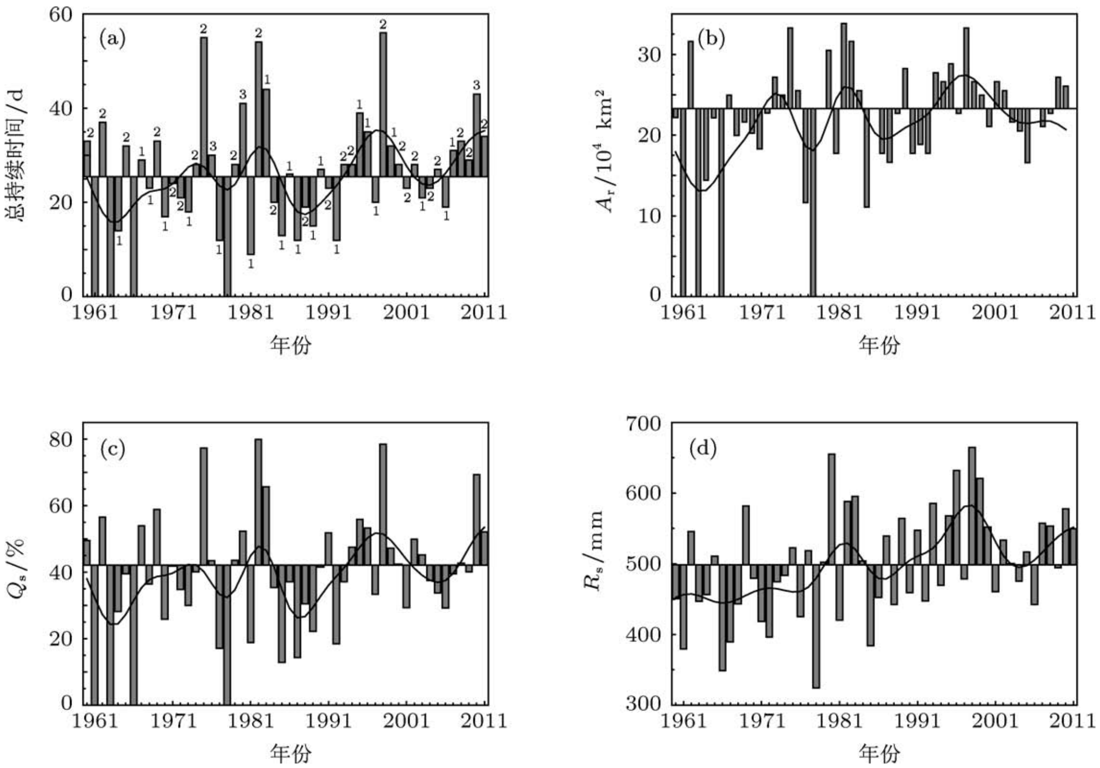

图 4 暴雨 “积成效应” 指标 (a) 持续时间; (b) 控制面积; (c) 降水贡献率及长江中下游区域平均夏季降水量; (d) 随时间演变特征 (曲线为 5 点快速傅里叶平滑曲线)

图 4(c) 为每年暴雨 “积成效应” 作用时段的降水总量占当年夏季总降水的百分比, 反应暴雨 “积成效应” 对夏季降水的贡献率大小. 事实上, 最终降水量的多少与降水过程的空间范围、持续时间以及降水强度等有直接联系, 因而这一指数实际上是几个方面的综合作用结果, 从图中也可以看到其变化特征总体与持续时间 L_d 和中心区域面积 A_r 的变化呈现较好的一致性. 不过, 从每年的对应情况来看, 也有一定的差别, 如 2005, 2007, 2009 这三年, 其持续时间 L_d 较平均值偏长, 面积 A_r 在平均值附近变化, 而降水贡献率却在气候平均值以下. 原因可能是这些年份暴雨 “积成效应” 虽然持续时间长、控制的空间范围广, 但其每次过程暴雨的降水强度并不大, 因而最终产生的降水量并不多, 对夏季降水的贡献也有限.

图 4(d) 为长江中下游地区平均夏季总降水年际变化, 该地区夏季气候平均降水为 498.7 mm, 1998 年最大为 664.3 mm, 1978 年最小为 324.8 mm; 两者相差达 339.5 mm, 可见年际变率很大. 5 点快速傅里叶平滑曲线清楚显示在 20 世纪 80 年代中后期长江中下游地区夏总降水呈现由少变多的年代际转折趋势. 对比分析图 4(d) 与图 4(a)—(c) 发

现四者年际和年代际变化具有一致性, 降水的年代际转折与各指数的年代际转折期大体相同, 而暴雨 "积成效应" 指数的强弱与降水的多寡亦有很好的对应关系. 尤其像 1998 年等一些强降水年份, 对应关系十分明显. 为进一步分析它们之间的关系, 对暴雨 "积成效应" 各指数和总降水量两两之间计算相关, 结果见表 1.

表 1 暴雨 "积成效应" 三项指数和区域平均降水量间的相关系数

	L_d	A_r	Q_s	R_s
L_d	1.0	—	—	—
A_r	0.86	1.0	—	—
Q_s	0.96	0.87	1.0	—
R_s	0.70	0.65	0.66	1.0

表 2 四项指数前 10 位年份

R_s	L_d	A_r	Q_s
1969	1962	1962	1962
1980	1975	1973	1967
1982	1980	1975	1969
1983	1982	1980	1975
1993	1983	1982	1982
1995	1995	1983	1983
1996	1996	1990	1995
1998	1998	1994	1996
1999	2010	1996	1998
2010	2011	1998	2010

由表 1 可见持续时间 L_d, 中心区域面积 A_r, 降水贡献率 Q_s, 三者之间具有很好的相关性, 相关系数都在 0.86 以上 (通过显著水平为 0.001 的显著性检验), 事实上对于一次降水过程来讲, 如果它持续时间长, 那么说明系统稳定性较好, 往往会产生大范围强降水, 因而上述三个指标紧密联系, 相辅相成. 而暴雨 "积成效应" 各指标与总降水量指数 R_s 的相关指数亦有很好的相关, 相关系数均在 0.65 以上 (通过 99.9%的置信度), 说明暴雨 "积成效应" 对整个夏季降水具较大的影响和贡献. 即对暴雨来讲, 其降水强度比一般降水明显偏大, 如果持续时间长、范围广, 那么由此产生的降水对整个夏季降水的贡献权重必然会高.

将暴雨 "积成效应" 各指数按大小排序, 选其对应的最强 10 年绘入表 2 中, 对比分析可见, 在区域平均降水 R_s 最强的 10 年中, 对应前 10 位的高 L_d 年有 7 年, 高 A_r 有 4 年, 高 Q_s 有 7 年. 总体而言具有较好的对应关系, 其中与 L_d 和 Q_s 的对应关系要好于 A_r, A_r 对应关系不好的可能是因为在实际过程中, 降水范围占整个区域的比例并不大, 但在降水范围内降水强度和降水量却很大, 最终形成的降水总量对整个区域降水的贡献仍然较大. 此外, 上述面积对应关系亦引出另外一个问题, 即以上仅从时间角度去探讨降水总量的变化, 没有考虑降水的空间分布型, 而 A_r 某种程度上是反映暴雨 "积成效应" 空间分布型的一个指标. 而在实际预报和监测过程中对降水空间分布的关注更多, 那么从整个夏季降水空间分布与暴雨 "积成效应" 空间分布的关系角度去考虑, 是否会存在更好的对应? 以下将从这一角度进行探讨.

3.3 暴雨 "积成效应" 与长江中下游夏季降水空间分布型

鉴于降水空间分布不均匀性且年际变率大, 要探讨整个夏季降水的空间分布型与暴雨 "积成效应" 控制范围间的关系, 须从宏观角度对空间分布分型进行探讨. 因此, 采用 EOF 分解寻找每年降水空间分布的共性并对其分类, 从分类的角度去探讨两者之间的关系. 对 1960—2011 年 52 年长江中下游地区夏季降水进行 EOF 分解, 其前 6 个模态的累积解释方差占总解释方差的 60.7%, 而前两个模态的累积解释方差占总解释方差的 35.5%. 因此选前两个模态所代表的空间型, 对其取正反, 得到四种空间模态分布型: 全区一致偏旱 (图 5(a))、以长江为界的 "南涝北旱" (图 5(b)) 或 "南旱北涝" (图 5(d)) 以及全区一致偏涝 (图 5(c)).

由于暴雨的局地性特征很强, 同一场暴雨相邻区域或站点的降水量可能相差很大, 而考虑空间分布时我们更注重暴雨过程控制的范围, 所以用暴雨发生频次分布更能宏观地表现其空间控制范围大小. 统计 1960—2011 年近 52 年暴雨 "积成效应" 时段内区域各站点的暴雨发生频次行, 然后对这一序列进行 EOF 分解, 其前 6 个模态的累积解释方差占总解释方差的 52.2%, 而前两个模态的累积解释方差占总解释方差的 31.6%. 与夏季总降水 EOF 分解前两个模态所占比例大致相当, 对它前两个模态按照相同处理取正反, 得到 4 种空间分布型, 如图 6 所示, 其分布与夏季总降水的 4 种分布型十分类似, 即全区一致偏弱 (图 6(a))、以长江为界的 "南强北弱" (图 6(b)) 或 "南弱北强" (图 6(d)) 以及全区一致偏强 (图 6(c)).

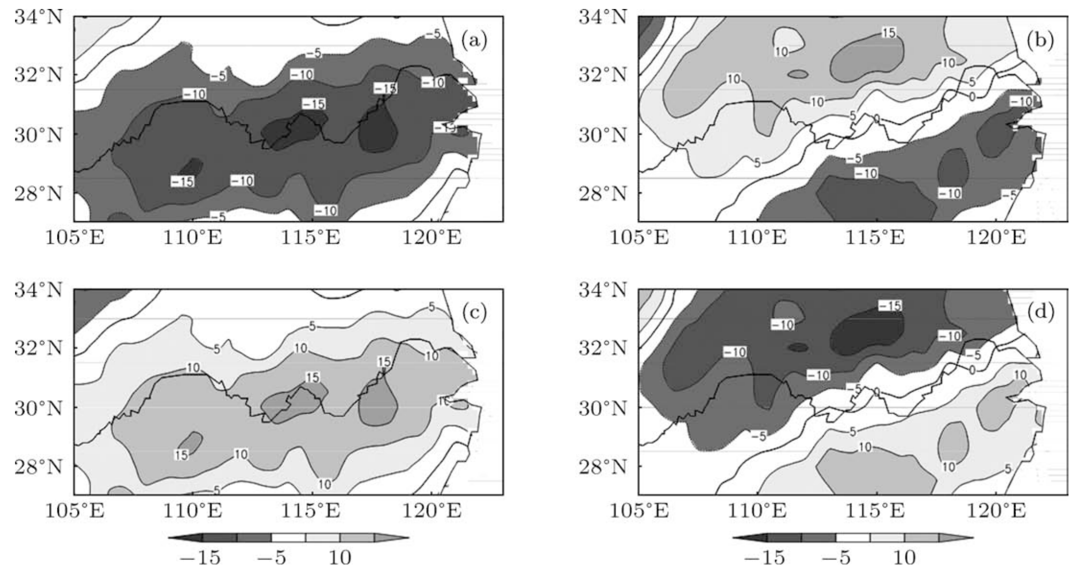

图 5 长江中下游地区夏季降水 EOF 空间分布型 (a) 全区一致偏旱; (b) “南涝北旱”; (c) 全区一致偏涝; (d) “南旱北涝”

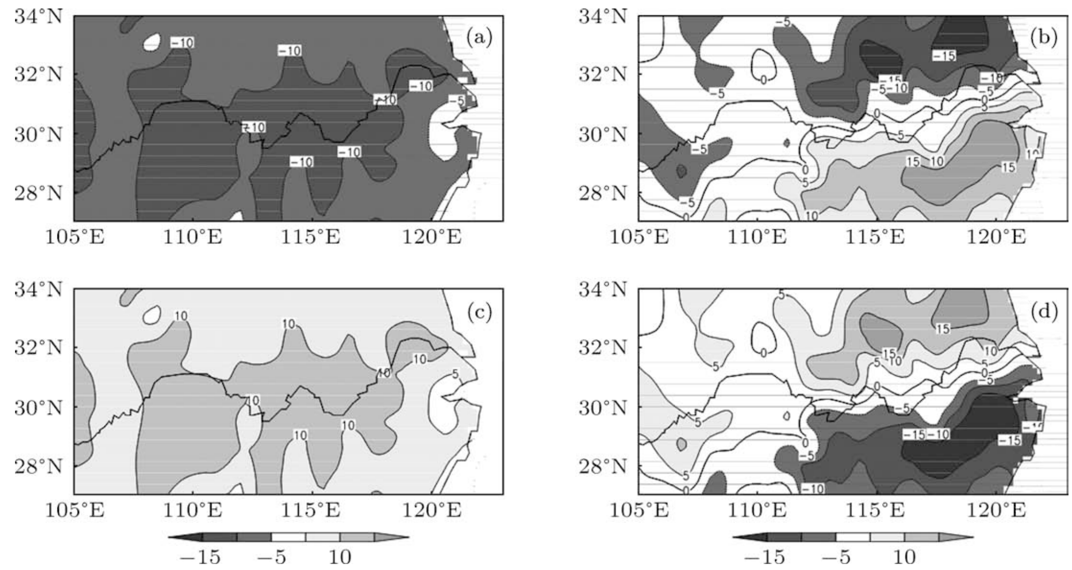

图 6 暴雨 “积成效应” 控制范围 EOF 空间分布型 (a) 全区一致偏弱; (b) “南强北弱”; (c) 全区一致偏强; (d) “南弱北强”

进一步以上述 EOF 分解结果入手, 利用每一年的实况降水和暴雨 “积成效应” 控制期暴雨发生频次空间分布与上述 4 个模态求相似, 相似系数表达式为

$$\alpha_{ij} = \arccos S_{ij}, \tag{4}$$

$$s_{ij} = \sum_{k=1}^{p} x_{ik} x_{jk} \left[\sqrt{\sum_{k=1}^{p} x_{ik}^2 \sum_{k=1}^{p} x_{jk}^2} \right]^{-1}, \tag{5}$$

式中 i 和 j 表示某一时刻两个不同空间场, S_{ij} 衡量两个空间点的相似程度, 对其取余弦得到两个场的夹角 α_{ij}, α_{ij} 越小, 表示两场间的夹角越小, 两场越相似, 反之则相反. 由此, 计算某一年实际场, 与上述 EOF 分解所得 4 个模态场的 α_{ij}, 然后以 α_{ij} 大小归类, 将长江中下游地区夏季降水和暴雨 “积成效应” 空间范围分为四种类型, 分别如表 3 与表 4 所示. 其中 A1 和 B1 型分别对应夏季降水一致偏旱和暴雨 “积成效应” 全区偏弱, A2 和 B2 型分别对应夏季降水南多北少和暴雨 “积成效应” 南强北弱, A3 和 B3 分别对应夏季降水南少北多和暴雨 “积成效应” 南弱北强, A4 和 B4 分别对应夏季降水全区偏多或暴雨 “积成效应” 全区偏强. 从表 3 和表

4 可以看出长江中下游地区夏季降水 A1 型分布为 14 年, A2 型 12 年, A3 型 14 年, A4 型 12 年, 对应暴雨 "积成效应" 空间范围 B1 型 8 年, B2 型 11 年, B3 型 22 年, B4 型 11 年.

进一步分析两者的对应关系, 对比表 3 与表 4 统计得表 5. 从表中可以看出 B1 型 8 年中有 7 年对应 A1 型, B2 型 11 年中有 9 年对应 A2 型, B3 型 22 年中有 14 年对应 A3, B4 型 11 年中有 8 年对应 A4 型, 体现了对角线占优这一特征, 即长江中下游地区夏季降水空间分布与暴雨 "积成效应" 空间分布具有很好的一一对应关系. 反之, 从整体降水型对应暴雨 "积成效应" 空间型来看, 以 A1 型为例, 即当整个夏季全区降水偏少时, 暴雨 "积成效应" 在空间上也主要表现为一致偏弱的 B1 型, 其次是 B2 型和 B4 型的 "南强北弱" 和 "南弱北强" 型, 一致偏强的 B3 型很少. 此外, A3 型全区降水偏多的 14 年全部对应了暴雨 "积成效应" 一致偏强的 B3 型. 可见暴雨 "积成效应" 空间范围的分布, 对整个夏季不同降水型的产生具有较大的影响.

表 3 长江中下游夏季降水分类

类型	年份													
A1 型	1960	1961	1966	1967	1971	1972	1976	1978	1981	1985	1988	1990	1992	2006
A2 型	1963	1965	1968	1979	1984	1986	1991	2000	2003	2004	2005	2007		
A3 型	1962	1969	1975	1980	1982	1983	1987	1989	1995	1996	1998	2008	2010	2011
A4 型	1964	1970	1973	1974	1977	1993	1994	1997	1999	2001	2002	2009		

表 4 暴雨 "积成效应" 空间分布分类

类型	年份										
B1 型	1961	1963	1966	1971	1978	1981	1985	1990				
B2 型	1965	1968	1972	1979	1984	1991	2000	2003	2004	2006	2007	
B3 型	1960	1962	1967	1969	1975	1980	1982	1983	1986	1987	1989	1993
	1995	1996	1997	1998	1999	2002	2005	2008	2010	2011		
B4 型	1964	1970	1973	1976	1977	1988	1992	1994	1997	2001	2009	

表 5 两种空间型的对应关系

	A1 型	A2 型	A3 型	A4 型
B1 型	7	1	—	—
B2 型	2	9	—	—
B3 型	2	2	14	4
B4 型	3	—	—	8

3.4 暴雨 "积成效应" 强弱与中国东部夏季降水

以上几节通过定量的刻画暴雨 "积成效应" 指标, 探讨其与长江中下游地区降水的时空分布之间的对应关系, 发现两者间具有十分紧密的联系. 因此, 有必要定义一个指数来定量化地描述暴雨 "积成效应" 强弱的变化, 以此探讨其变化特征以及与相关气象因子之间的联系. 从暴雨 "积成效应" 的本质来讲, 它是多次强降水过程的累积或叠加效应, 首先会从降水量的角度影响并决定整个夏季降水, 其次则会通过大量的降水改变土壤含水量, 从热能输送和交换等方面, 对后期降水和温度产生影响. 因此, 暴雨 "积成效应" 时段内产生降水量的多少能够较好反映出其作用的强弱. 据此定义暴雨 "积成效应" 强度指数 (BQDI):

$$\mathrm{BQDI}_i = \mathrm{Norm}\left(\frac{S_i}{S_\mathrm{m}}(i=1,2,\cdots,n)\right), \qquad (6)$$

式中 S_i 是第 i 年暴雨 "积成效应" 时段内的总降水量, S_m 是气候平均夏季降水总量, 这两者的比值越大表明暴雨 "积成效应" 越强, 其造成的降水与气候平均夏季降水越接近, 对第 i 年夏季降水的贡献也越大. $\mathrm{Norm}(\cdots)$ 表示 BQDI ($i=1,2,\cdots,52$) 为一条标准序列.

图 7(a) 为 1960—2011 年 BQDI 随时间的演变呈现出明显的年际振荡变化, 与 3.2 节中长江中下

游地区域平均夏季降水变化曲线对比, 可以看到暴雨 “积成效应” 强弱年与夏季降水多寡年 (相对于气候平均) 具有很好的对应关系, 指数值在 1 (即 1 倍标准偏差) 以上的年份基本对应降水显著偏多的年份, 而在 −1 以下的年份基本对应降水显著偏少的年, 尤其在 1961, 1963, 1966 和 1978 年这几个长江中下游大范围干旱年, 和 1969, 1980, 1982, 1998 年这几个长江中下游大范围偏涝年, 指数值都分别表现出显著偏弱和偏强的一致性响应变化特征. 将这一指数与图 4(e) 区域平均夏季降水做相关, 其相关系数为 0.79, 明显高于 3.2 节定义的三项指标与夏季降水的相关, 说明暴雨 “积成效应” 的这一新指标能更好地反映夏季降水多寡的特征. 图 7(a) 中 10 年平均曲线演变显示, 20 世纪 90 年代以前, 暴雨 “积成效应” 强度值大都在 0 以下, 说明暴雨 “积成效应” 在这一时段内强度偏弱, 而 90 年代初, 指数出现一次跳跃式变化, 从 0 值以下突然转到 0.5 以上, 随后至今都处于 0 值以上, 说明 90 年代以后至今, 暴雨 “积成效应” 处于偏强期, 这一转折变化与长江中下游降水的年代际转折变化相一致 [22], 与中国东部地区由 “南旱北涝” 向 “南涝北旱” 的年代际转折特征也有类似之处. 另外, 需要指出的是 21 世纪近 10 年, 指数相较于 20 世纪 90 年代又有所减弱, 这与近 10 年江淮雨带的向北迁移也有一定的对应.

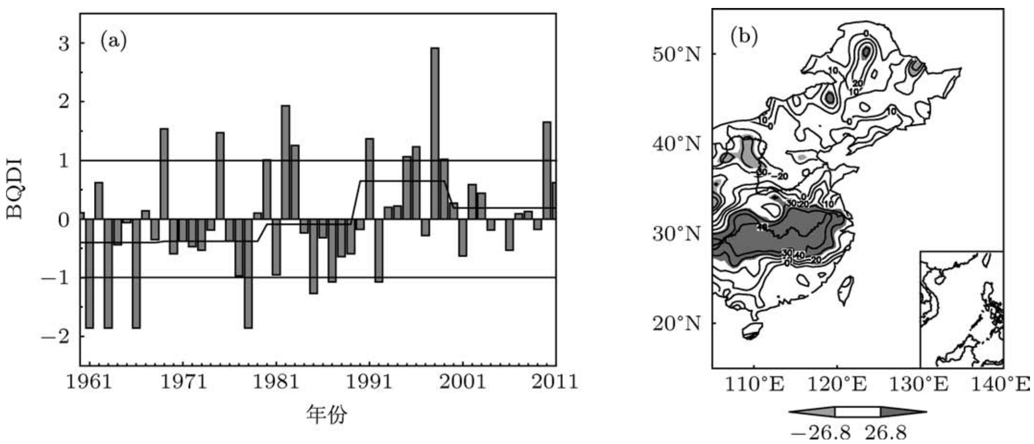

图 7　1960—2011 年 BQDI 变化 (a) 及其与中国东部地区夏季降水的相关系数分布 (b) (相关系数乘以 100, 阴影区表示通过 95%的置信度, 正负相关分别用深浅阴影)

将这一指数与所选择的中国东部 394 个站点夏季降水求相关, 可以发现相关分布的强正值区主要分布于 27°N—34°N 范围的长江中下游区, 相关性大都可通过 99%的置信度, 另一较弱的正相关区域位于 45°N 以北的东北西北部, 两个显著负相关区分别位于华南以及 35°N—45°N 范围内的部分地区 (可通过 95%的置信度), 其中华南地区中心较弱, 而河套地区以及东北东南部中心较强, 相关系数的正负带状分布与中国东部夏季降水的雨带分布也大致类似 (图 7(b)). 尽管这种同时期降水和降水的相关不具有统计学意义, 但这种相关性的好坏从某种程度上反映出两者变化的密切性和同步性, 因而可以作为评判暴雨 “积成效应” 在整个夏季降水中的重要性的依据.

此外, 选出 BQDI 最大的五年 1969, 1975, 1982, 1998 和 2010 年, 最小的五年 1961, 1963, 1966, 1978 和 1985 年, 分别合成暴雨 “积成效应” 强、弱年中国东部地区实际降水距平百分率 (图 8(a), (b)), 以及两者差值分布 (图 8(c)), 由图可见, 合成结果与上述相关分布近似一致, 即强指数年, 长江中下游地区降水明显偏多, 华南和华北大部分地区降水偏少, 东北地区除东部部分地区外降水亦呈偏多趋势 (图 8(a)); 而弱指数年则大致相反, 表现为长江中下游地区降水明显偏少, 华南部分地区、华北和东北大范围降水偏多 (图 8(b)). 强年减弱年合成差值分布更为明显, 可以看到所选长江中下游区为显著正值区 (通过 95%置信度), 而华南及华北和东北大部位显著负值区 (通过 95%置信度), 反之亦然, 说明长江中下游区 BDSI 强、弱年份, 整个东部地区的降水形式呈现出截然相反的两种分布形势.

综合而言, 长江中下游地区暴雨 “积成效应” 所产生的作用, 与同期整个夏季降水具有十分密切的联系, 其强弱随时间的变化与同期夏季降水多寡随

时间的变化具有很好的一致性, 而其控制范围与长江中下游地区夏季降水空间分布亦有很好的对应关系. 另外, 长江中下游区暴雨 “积成效应” 不仅能够反映该地区的夏季降水多寡, 还能在某种程度上反映出整个东部旱涝的分布情况. 由此可见对长江中下游地区暴雨 “积成效应” 的把握和预估, 对该区夏季降水甚至整个东部雨带分布的的评估都有一定的实际意义.

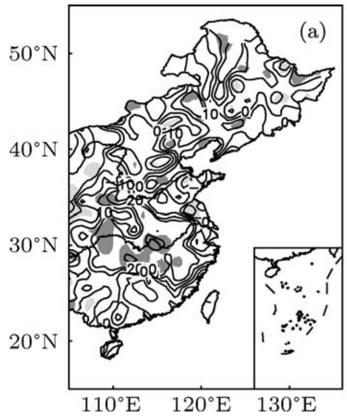

图 8 长江中下游 BQDI 强年 (a) 和弱年 (b) 中国东部降水距平百分率合成及强 - 弱年差值合成 (c) (阴影表示通过 95%置信度, 负值为浅色, 正值为深色)

4 结论和讨论

本文选长江中下游地区, 提出暴雨 “积成效应” 这一概念, 对其进行简单的刻画和分析, 探究它对同期夏季降水的贡献和联系, 得出以下结论.

1) 从持续时间 (L_d)、控制面积 (A_r), 以及降水贡献率 (Q_s) 三个角度提出暴雨 “积成效应” 的判定标准, 并对其特征进行分析, 发现 L_d, A_r 及 Q_s 三者之间具有显著的相关性, 说明三者之间具有密切的内在联系; 而长江中下游地区平均夏季降水亦有很好相关, 且表现出一致的年际和年代际变化.

2) 利用暴雨发生频次描述暴雨的空间范围, 并利用 EOF 分解, 对长江中下游地区夏季降水和暴雨 “积成效应” 空间分布进行分型, 对比发现暴雨频次分布范围和整个夏季降水型的空间模态具有较好的一一映射关系.

3) 通过定义长江中下游地区暴雨 “积成效应”BQDI, 并以此分析其与所选区域夏季降水及整个东部地区降水的关系, 发现该指数与整个夏季平均降水具有一致的年际和年代际变化特征; 而与中国东部夏季降水相关的空间分布以及合成分析显示, 长江中下游地区暴雨 “积成效应” 强弱, 与中国东部夏季降水多寡具有很好的一致性, 强指数年, 长江中下游地区降水偏多, 华南和华北偏少; 而弱指数年则大致相反.

本文通过选取暴雨这一天气尺度强降水为研究对象, 建立它与季节尺度降水的关系, 从多次暴雨累积和叠加的角度将其转化为一种中长期天气过程考虑, 提出暴雨 “积成效应”, 并以长江中下游地区为例, 对这一概念进行了定义, 并初步分析了暴雨 “积成效应” 的特征以及与同期夏季降水的关系. 相关结论表明多次暴雨形成的 “积成效应” 所造成的降水在整个夏季降水中占有十分重要的比重, 且与夏季降水年际和年代际变化的一致性以及强的相关性, 显示出两者变化的同步性以及关系的密切性. 因而暴雨 “积成效应” 概念的提出以及进一步深入的研究具有其现实意义和潜在应用价值：如对暴雨 “积成效应” 的认识, 将可能有助于我们对诸如 2011 年夏季长江中下游地区由暴雨这一天气尺度过程引发 “旱涝急转” 并导致整个夏季降水雨带异常变化的成因做进一步的深入探讨; 暴雨灾害是我国重大气象灾害之一, 每年暴雨洪涝损失所占比例仅次于干旱灾害损失, 给生态、环境、社会、经济带来诸多问题. 而暴雨 “积成效应” 造成的危害要比一般暴雨过程范围更广、影响更严重, 且极端降水频次的增加 [24], 将进一步加剧这种危害发生的频率; 因此对其进行深入研究, 分析其潜在风险特征, 对提高气象灾害监测、预警、服务能力均很有必要; 再者, 目前我国汛期预测对暴雨等这类天气过程的影响并未考虑, 而实际过程中暴雨对夏季雨带往往会产生一种决定性作用, 因而从暴雨 “积成效应” 的角度或许能够为在汛期预测的进一步提高提供一些新的思路; 此外, 暴雨 “积成效

应" 对土壤含水量的改变, 导致土壤表面的反照率和热容量以及输入大气的感热和潜热等能量的变化, 又会影响到后期的降水和温度等, 这一过程又具有某种 "气候效应", 对局地气候的变化也可能产生作用 [25−30]. 对于以上问题, 我们将在本文基础上, 结合现有理论研究成果 [31−33] 进行深入的分析和探索.

[1] Bao M, Huang R H 2006 *Chin. J. Atmosph. Sci.* **30** 1057 (in Chinese) [鲍名, 黄荣辉 2006 大气科学 **30** 1057]

[2] Tao S Y, Ding Y H, Zhou X P 1979 *Chin. J. Atmosph. Sci.* **3** 227 (in Chinese) [陶诗言, 丁一汇, 周晓平 1979 大气科学 **3** 227]

[3] Tao S Y 1980 *The Torrential Rain of China* (Beijing: Science Press) pp255 (in Chinese) [陶诗言 1980 中国之暴雨 (北京: 科学出版社) 第 255 页]

[4] Doswell III C A, Ramis C, Romero R, Alonso S 1998 *Weather Forecasting* **13** 102

[5] Ding Y H 1998 *East Asia Monsoon and Torrential Rain of China* (Beijing: China Meteorological Press) p137 (in Chinese) [丁一汇 1998 东亚季风和中国暴雨 (北京: 气象出版社) 第 137 页]

[6] Homar V, Romero R, Ramis C, Alonso S 2002 *Ann. Geophys.* **20** 2047

[7] Ducrocq V, Ricard G, Lafore J P, Orain F 2002 *Weather Forecasting* **17** 1236

[8] Gao S T, Zhao S X, Zhou X P, Sun S Q, Tao S Y 2003 *Chin. J. Atmosph. Sci.* **27** 618 (in Chinese) [高守亭, 赵思雄, 周晓平, 孙淑清, 陶诗言 2003 大气科学 **27** 618]

[9] Lebeaupin C, Ducrocq V, Giordani H 2006 *J. Geophys. Res.* **11** 1

[10] Ding Y H 1993 *Study of Durative Heavy Storm in Jiang-Huai Area in 1991* (Beijing: China Meteorological Press) p255 (in Chinese) [丁一汇 1993 1991 年江淮流域持续性特大暴雨研究 (北京: 气象出版社) 第 255 页]

[11] National Climate Center 1998 *The Heavy Flood and Climate Anomaly in 1998* (Beijing: China Meteorological Press) p139 (in Chinese) [国家气候中心 1998 1998 年大洪水和气候异常 (北京: 气象出版社) 第 139 页]

[12] Tao S Y 2001 *The Mechanism and Forecasting of Torrential Rain of China in Summer 1998* (Beijing: China Meteorological Press) p1 (in Chinese) [陶诗言 2001 1998 夏季中国暴雨的形成机理与预报研究 (北京: 气象出版社) 第 1 页]

[13] Zhang P Q, He M, Xu L 2002 *Plateau Meteorology* **21** 243 (in Chinese) [张培群, 何敏, 许力 2002 高原气象 **21** 243]

[14] Zhang Q Y, Tao S Y, Zhang S L 2003 *Chin. J. Atmosph. Sci.* **27** 1018 (in Chinese)[张庆云, 陶诗言, 张顺利 2003 大气科学 **27** 1018]

[15] Zhao J H, Yang J, Feng G L, Zhang S X 2013 *J. Appl. Meteorol. Sci.* **24** 43 (in Chinese) [赵俊虎, 杨杰, 封国林, 张世轩 2013 应用气象学报 **24** 43]

[16] Shen B Z, Zhang S X, Yang H W, Wang K, Feng G L 2012 *Acta Phys. Sin.* **61** 109202 (in Chinese) [沈柏竹, 张世轩, 杨涵洧, 王阔, 封国林 2012 物理学报 **61** 109202]

[17] Feng G L, Yang H W, Zhang S X, Wang K, Shen B Z 2012 *Chin. J. Atmosph. Sci.* **36** 1009 (in Chinese) [封国林, 杨涵洧, 张世轩, 王阔, 沈柏竹 2012 大气科学 **36** 1009]

[18] Xie Y M, Hu Y L, Sha W R, Zhu J G, Yang L 2011 *Acta Meteorol. Sin.* **1** 61

[19] Wang J J, Li Z C 2002 *Acta Meteorol. Sin.* **10** 146 (in Chinese) [王建捷, 李泽椿 2002 气象学报 **10** 146]

[20] Booth R E 2012 *Weather* **14** 171

[21] Zhang M, Zhang D L 2012 *Monthly Weather Rev.* **140** 184

[22] Cao J, Gao S T, Zhou Y S 2008 *Acta Phys. Sin.* **57** 2600 (in Chinese) [曹杰, 高守亭, 周玉淑 2008 物理学报 **57** 2600]

[23] Si D, Ding Y H, Liu Y J 2010 *Chin. Sci. Bull.* **55** 68 (in Chinese) [司东, 丁一汇, 柳艳菊 2010 科学通报 **55** 68]

[24] Zhang D Q, Hu J G, Feng G L 2008 *Chin. Phys.* B **17** 736

[25] Walker J, Rowntree P R 1977 *Quart. J. Royal Meteorol. Soc.* **103** 29

[26] Yeh T C, Wetherald R T, Manabe S 1984 *Monthly Weather Rev.* **112** 474

[27] Ma Z G, Wei H L, Fu C B 2000 *Acta Meteorol. Sin.* **58** 278 (in Chinese) [马柱国, 魏和林, 符淙斌 2000 气象学报 **58** 278]

[28] Koster R D, Dirmeyer P A, Guo Z C, Bonan G, Chan E, Cox P, Gordon C T, Kanae S, Kowalczyk E, Lawrence D, Liu P, Lu C H, Malyshey S, McAvaney B, Mitchell K, Mocko D, Oki T, Oleson K, Pitman A, Sud Y C, Taylor C M, Verseghy D, Vasic R, Xue Y K, Yamada T 2004 *Science* **305** 1138

[29] Kim J E, Hong S Y 2007 *J. Climate* **20** 5732

[30] Zhang W J, Zhou T J, Zhi H 2012 *Acta Meteorol. Sin.* **70** 78 (in Chinese) [张文君, 周天军, 智海 2012 气象学报 **70** 78]

[31] Cui X P, Li X F 2011 *Chin. Phys.* B **20** 109201

[32] Feng G L, Dong W J, Jia X J 2004 *Chin. Phys.* **13** 413

[33] Zhi R, Lian Y, Feng G L 2007 *Acta Phys. Sin.* **56** 1837 (in Chinese) [支蓉, 廉毅, 封国林 2007 物理学报 **56** 1837]

"Cumulative Effect" of torrential rain in the middle and lower reaches of the Yangtze River *

Zhang Shi-Xuan[1)] Feng Guo-Lin[2)†] Zhao Jun-Hu[1)]

1) (*College of Atmospheric Sciences, Lanzhou University, Lanzhou* 730000*, China*)

2) (*Laboratory for Climate Studies of China Meteorological Administration, National Climate Center, Beijing* 100081*, China*)

(Received 18 October 2012; revised manuscript received 2 November 2012)

Abstract

To expand the torrential rain which is a meso-and-micro scale weather process to a meso-and-long scale weather process, in this paper we choose the middle and lower reaches of the Yangtze River (MLRYZ) as a sample region, and propose the conception of "Cumulative Effect" of torrential rain (CETR) by using the daily precipitation observational data from 740 stations in China. On the statistical analysis of observations, we define CETR as the cumulation or superposition of many torrential rain processes, and three indexes, which are continuous time (L_{d}), control area (A_{r}) and precipitation contribution rate (Q_{s}), which are used for explaining the conception of CETR. Then taking these three indexes into consideration, we establish the intensity index of CETR (BQDI) and study the relationship between the BQDI and the summer precipitation in MLRYZ. Results show that the interannual and interdecadal variations of BQDI are similar to those of summer precipitation in MLRYZ. The distribution of correlation coefficient between the BQDI and the summer precipitation in Eastern China and the composite analysis of representative years in BQDI show a large positive relation area in MLRYZ (significance test at the 95% level) and two large negative relation areas in North and South China (significance test at the 95% level), which reveals that the variations of BQDI not only correspond to the variations of summer precipitation in MLRYZ but also correlate with the distribution of summer precipitation in Eastern China to some extent. Besides, an empirical orthogonal analysis is performed on the frequency of torrential rain in MLRYZ, we find that the four major spatial modes of torrential rain are also similar to those of summer precipitation in MLRYZ. In conclusion, the precipitation caused by CETR greatly influences even determines the amount and distribution of summer rainfall, which is worth further investigating.

Keywords: middle and lower reaches of the Yangtze River, torrential rain, "Cumulative Effect", summer precipitation

PACS: 92.40.Ea, 92.60.Wc **DOI:** 10.7498/aps.62.069201

---

* Project supported by the National Natural Science Foundation of China (Grant Nos. 40930952, 41205040, 41175067, 41275096), and the National Basic Research Program of China (Grant Nos. 2012CB955902, 2013CB430204).

† Corresponding author. E-mail: fenggl@cma.gov.cn

欧亚中高纬阻塞高压关键区高度场动力-统计跨季度预测实验*

赵俊虎1)2)† 杨杰1) 龚志强2) 支蓉2)

1) (兰州大学大气科学学院, 兰州 730000)

2) (国家气候中心气候研究开放实验室, 北京 100081)

(2012 年 11 月 21 日 收到; 2013 年 1 月 6 日 收到修改稿)

本文主要利用实际业务模式的预报结果和丰富的历史资料对乌拉尔山、贝加尔湖和鄂霍次克海三个阻塞高压活动关键区夏季平均的 500 hPa 高度场进行动力-统计跨季度预测实验, 其结果显示该方法能在一定程度上减小模式预报误差, 提高预报技巧, 显示出了良好的业务应用前景. 此外, 敏感性实验显示, 相似指标和相似年选取个数都对预测结果有显著影响.

关键词: 阻塞高压, 高度场, 动力-统计, 跨季度预测

PACS: 92.60.Wc, 9130.Pd **DOI:** 10.7498/aps.62.099206

1 引 言

阻塞高压是中高纬大气环流异常经向发展并最后稳定的形态, 它的生成、维持和崩溃会引起大尺度气团质量和热量的强烈经向交换, 最终导致大范围地区天气气候发生异常 [1]. 因此自 20 世纪中叶起就一直被气象学家重视, 并分别从其形成机理及指数定义 [2−8], 统计特征 [9,10]、天气气候影响 [11−13] 等方面进行了研究, 这些研究成果在后来的实际业务预报中一直发挥着重要的指导作用. 国外的研究侧重于冬季的阻塞高压, 对夏季欧亚大陆阻塞高压却涉及极少. 国内长期的业务实践和有关研究均表明, 欧亚中高纬阻塞高压是影响中国旱涝的重大灾害性环流系统, 尤其夏季, 其异常活动常常会造成中国区域性旱涝灾害 [14]. 例如, 陶诗言 [15] 通过个例分析认为乌拉尔山与鄂霍茨克海附近的阻塞高压对中国梅雨可能有重要影响; Wang[16] 对夏季的欧亚阻塞高压进行了大量的统计, 发现东亚阻塞高压的维持天数与梅雨量及梅雨天数呈正相关; 1954 年 [17]、1998 年 [18] 及 1999 年 [19] 长江流域的洪涝均与欧亚中高纬阻塞高压的异常活动有关. 因此, 研究欧亚中高纬地区的阻塞高压及其对中国天气、气候的影响有着重要的意义.

以往对具体某次阻塞高压的形成、维持和演变过程及可能物理机理的研究较多, 这些研究无疑可以加深我们对阻塞过程的认识并提供预报基础. 但这些研究时间较早, 且多停留在天气学意义上. 随着研究的深入和国家对短期气候预测的重大需求, 人们开始意识到阻塞高压对短期气候异常具有明显的作用. 在每年 3 月份的全国汛期预测会商会中, ENSO、西太副高、夏季风以及欧亚中高纬阻塞高压都是讨论的重点. 相比之下, 阻塞高压的预测更是一个薄弱环节, 这主要表现在, 阻塞高压的形成机理和变化特征极为复杂, 且统计和诊断研究多而预测性研究少. 因此, 如何客观定量化地预测阻塞高压是目前短期气候预测面临的迫切问题和难点. 而当今的相关研究表明, 动力 - 统计相结合是提高短期气候预测准确率的有效途径之一 [20,21]. 围绕两者如何有效结合的问题, 国内外开展了广泛

* 国家自然科学基金 (批准号: 40930952, 41105055) 和国家重点基础研究发展计划 (批准号: 2012CB955902, 2013CB430204) 资助的课题.

† 通讯作者. E-mail: huzi348637577@sina.com

的研究. 其中, 在气候模式预报基础上结合数理统计方法, 利用历史资料信息对模式误差进行预报是引人注目的研究方向. 早在 1958 年, 顾震潮 [22] 就提出将数值预报从初值问题改为演变问题, 并指出了数值天气预报中使用历史资料的重要性和可行性. 丑纪范 [23,24] 从理论上探讨了在长期预报中实现动力和统计相结合的做法, 在此基础上, 诸多学者 [25−29] 分别发展了适用于动力季节预测的相似误差订正方法, 并进行了预测实验, 其结果显示该方法能有效提高热带降水和环流的预报技巧, 但对中高纬的环流预报技巧依然很低; 王启光等 [30]、熊开国等 [31] 和杨杰等 [32] 利用较全面的历史资料, 发展了利用相似年的模式误差信息实现对预报年气候模式预报误差预报的汛期降水动力 - 统计客观定量化预测方法, 有效地改进了模式的预测结果.

基于此, 有必要利用近年来的新资料、数值模式的结果和动力 - 统计预报原理来改善模式对阻塞高压的预测能力. 经验表明 [33] 乌拉尔山 (40—50°N, 40—70°E)、贝加尔湖 (50—60°N, 80—110°E) 和鄂霍次克海 (50—60°N, 120—150°E) 这三个区域是阻塞高压发生频次最高的地区 (分别简称为: 乌阻区、贝阻区、鄂阻区), 这三个地区夏季有无阻塞高压建立和维持, 对中国夏季旱涝分布影响较大. 因此, 选取这三个区域 500 hPa 高度场距平作为动力 - 统计预报的对象. 本文即利用较全面的资料, 从动力-统计预报原理出发, 利用 1983—2011 年国家气候中心 (NCC) 季节/年际预测业务系统模式 (CGCM) 回报和预报资料挖掘历史相似信息, 并通过对气候因子与预报对象及其模式误差的相关性检验来确定关键影响因子, 然后利用所选因子选取历史相似对夏季阻塞高压活动关键区的 500 hPa 高度场进行动力 - 统计跨季度预测实验. 本文独立样本动力-统计预测指的是在不包含预报年及其以后年份资料信息前提下所进行的回报检验.

2 资料和方法

1) 用到的大气及海洋资料包括 NCEP/NCAR 1948—2011 年再分析 $2.5^\circ\times2.5^\circ$ 的月平均 500 hPa 位势高度场资料, 美国国家海洋和大气管理局 (NOAA)1948—2011 年全球 $2^\circ\times2^\circ$ 月平均海温重建资料; NCC/IAP T63 全球海气耦合模式 (CGCM) 生成的 1983—2011 年共 29a 回报和预报的逐月 500 hPa 高度场数据, 经纬度格点 $2.5^\circ\times2.5^\circ$, 本文选用在 2 月底起报的 48 个初始场每年 6—8 月集合平均结果, 大气模式初值采用 2 月最后 8 天 00Z 的 NCEP/NCAR 再分析资料, 海洋初值为经过扰动的 NCC 海洋同化资料;

2) 环流和气候指数: 包括 NCC 的 74 项环流特征量, 美国国家海洋和大气管理局 (NOAA) 发布的 40 项气候指数 [http://www.esrl.noaa.gov/psd/data/climateindices/list/], 南半球环状模指数 SAMI[34]、北半球环状模指数 NAMI[35]、北大西洋涛动指数 NAOI[36], 中国气象局整编的 1973—2011 年北半球、欧亚、高原、东北、新疆 5 项积雪面积指数, 亲潮区 (40—50°N, 160—180°E)、黑潮区 (22—36°N, 122—150°E)、西风漂流区 (30—40°N, 170—220°E) 海表温度距平 (SSTA) 指数, 共计 125 项因子.

3 欧亚中高纬阻塞高压关键区高度场动力-统计跨季度预测实验

随着观测资料和模式状况的不断改善, 数值天气预报和短期气候预测得以快速发展, 但目前应用水平依然不高, 仍需进一步提升预报能力 [37]. 图 1 给出了 CGCM 1983—2011 年夏季平均 500 hPa 高度场系统订正 (SEC; 预报年模式预测场与模式多年平均误差场相加) 与观测场的时间相关系数 (TCC) 分布.

由图 1 可见, 季节预测技巧主要体现在热带和海洋上, 中高纬地区环流形势的整体预测技巧不高, 这也是当前国际上普遍存在的难题 [38]. 目前, 业务上主要采用数理统计方法和基于数值模式的动力学方法做季度预报, 但二者各有优缺, 目前的共识是将二者结合起来, 发挥各自优势来改善预报, 问题的关键便成为如何将二者进行有效结合 [23,24]. 众所周知, 数值模式本身不可避免地存在误差, 相似 - 动力模式原理正是为了减小模式误差而提出的, 但对于业务预报中使用的复杂模式而言, 直接建立相似 - 动力模式在技术上存在很大困难. 目前, 主要从正面改进模式各个环节来减小模式误差, 但进一步提高预报水平的难度越来越大. 事实上, 要充分利用物理规律和现有大量实况资料, 莫过于就以现有动力模式预报结果为基础, 从反问题的角度对模式误差进行动力 - 统计订正预报. 任宏利和丑纪范 [27,28] 近期工作中发展了一种适用于动力季节预测的相似误差订正方法, 并进行了初步预测实验,

其结果显示该方法能进一步提高热带环流的预报技巧, 但对中高纬的环流预报技巧依然很低. 基于此, 本文将主要针对欧亚中高纬三个阻塞高压关键区的高度场, 有针对性的开展动力 - 统计的策略和方案研究, 并进行实际业务模式的跨季度预测实验.

3.1 动力-统计相似误差订正原理

一般来讲, 数值预报是作为偏微分方程的初值问题提出来的, 可以数学表示为

$$\frac{\partial \psi}{\partial t}+L(\psi)=0,$$
$$\psi(x,t_0)=\psi_0(x), \tag{1}$$

其中 $\psi(x,t)$ 为模式预报变量, x 和 t 分别表示空间坐标和时间, L 是 ψ 的微分算子, 对应于实际的数值模式. t_0 为初始时刻, ψ_0 为初值.

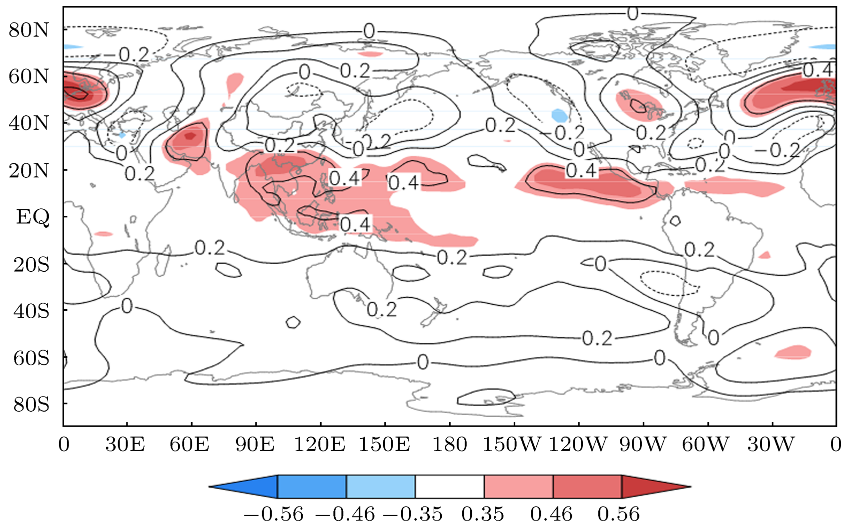

图 1 夏季平均 500 hPa 高度场系统订正与观测间的时间相关系数的空间分布 (阴影层次的相关系数为 0.35, 0.46 和 0.56, 分别对应 0.05, 0.01 和 0.001 信度的 t 检验水平; 等值线间隔为 0.2)

长期业务预报的经验表明, 在相似的初始场和边界条件下, 大气状况的演变在一定的时间尺度范围内也具有一定的相似性 [27]. 因此在相似动力模式中, 可以将当前的预报场 ψ 看成是历史相似 $\tilde{\psi}$ 加上一个小扰动 $\hat{\psi}$, 即 $\psi=\tilde{\psi}+\hat{\psi}$. 将历史参考态 $\tilde{\psi}$ 代入 (1) 式, 有

$$\frac{\partial \tilde{\psi}}{\partial t}+L(\tilde{\psi})=E(\tilde{\psi}),$$
$$\tilde{\psi}(x,0)=\tilde{\psi}_0(x), \tag{2}$$

其中, E 为模式的误差算子. (2) 式结合 (1) 式经过一系列变换 [29], 得到模式预报结果为

$$\hat{P}(\psi_0)=P(\psi_0)+\check{P}(\tilde{\psi}_j)-P(\tilde{\psi}_j), \tag{3}$$

其中 $\hat{P}(\psi_0)$ 为进行误差项相似估计的情况下所得到的预报结果, $P(\psi_0)$ 为数值预报模式对当前初值 ψ_0 的预报结果, $\check{P}(\tilde{\psi}_j)$ 为历史相似对应的实况, $P(\tilde{\psi}_j)$ 为历史相似初值的预报结果. 该方程的本质是引入历史相似对应的预报误差信息来估计当前的预报误差, 即 (3) 式右端的 $\check{P}(\tilde{\psi}_j)-P(\tilde{\psi}_j)$, 从而减小数值模式误差, 将数值模式预报问题转化为预报误差的估计问题.

3.2 相似选取方案

在动力 - 统计预报过程中, 首先由初始信息选取历史相似, 然后利用模式提取历史误差信息, 形成当前预报误差的估计, 并订正到原始预报中. 历史相似的选取是动力 - 统计预报的重要环节, 不同时间尺度和空间尺度预报问题需要采用有针对性的相似选取方案. 对于夏季欧亚中高纬三个阻塞高压关键区环流的跨季度预测而言, 我们考虑使用广义初值, 即模式初值所在的前期冬季要素场中的关键气候影响因子作为相似选取指标, 其物理依据在于大气长期天气过程中显著地存在着 3—6 个月的韵律现象. Wang[39] 对环流异常相似演变的研究显示, 在两年内如果 1 月份环流异常相似, 则 6 月或 8 月的环流异常也会有一定相似. 这种相似韵律现象, 是指在两个不同年份的月平均距平场在某个起始月相似后, 相似性会随之变差, 过了几个月后变

得又相似, 这是一种环流自身演变的韵律活动, 很多统计事实证实了长期天气异常演变过程中普遍存在半年左右的相似韵律. 事实上, 当前我国每年 3 月份的汛期预测中, 利用前冬要素场和气候因子的异常信号来预报夏季异常状况是最主要手段方法. 因此, 为了体现海气耦合系统中大气准半年相似韵律特征, 这里使用前冬平均要素场中对三个阻塞高压活动关键区 500 hPa 高度场有显著影响的气候因子来选取历史相似.

以下方案选取相似年进行误差订正: 1) 分别从 NCEP 和 CGCM 的 29a 回报数据中提取夏季平均 500 hPa 高度场观测资料和模式结果, 并求取高度场的预报误差场; 2) 提取 125 项气候因子 1982/83—2010/11 共 29 个冬季季节平均指数; 3) 分别计算 1983—2011 年 125 项前冬气候因子与乌阻区、贝阻区、鄂阻区夏季区域平均的高度场和模式误差场的相关系数, 获取关键因子后, 利用预测年因子与历史因子之间的欧式距离选取历史相似年.

其中 125 项因子包括了海温、积雪及环流等, 这些因子从不同的角度刻画了气候系统主要模态的变化特征, 对因子与阻高区高度场进行相关性检验, 可以初步得出对夏季各阻高区高度场有影响的前冬因子集; 而模式预报误差与气候系统状态的变化密切联系, 即误差是随状态而变的, 这与模式内在误差依赖于状态变量有很大关系: 当物理因子与预报误差呈正相关时, 随着因子指数的增大 (代表气候系统的某种主要模态的正位相在逐渐增强), 模式所对应的预报误差也呈增大趋势, 反之亦然; 当预报因子与预报误差呈负相关时, 随着因子指数的减小 (代表气候系统的某种主要模态的负位相在逐渐增强), 模式所对应的预报误差也会呈现增大趋势, 反之亦然. 由此可见, 气候模式对于因子指数处于较大振幅时的模拟能力逐渐变差, 这反映出模式可能对于此类气候模态的物理机理刻画不足. 因此, 通过对初步得到阻高区高度场的影响因子集与模式误差进一步进行相关性检验, 可以得到对模式误差敏感的因子, 进而作为相似选取指标.

表 1 影响阻高区夏季 500 hPa 高度场的气候因子及其与模式误差的相关系数

影响乌阻区高度场的关键因子	R_1	R_2	影响贝阻区高度场的关键因子	R_1	R_2	影响鄂阻区高度场的关键因子	R_1	R_2
热带北大西洋 sst 指数	0.48**	0.50**	全球平均陆地海洋温度	0.49**	0.45*	高原积雪面积	0.52**	0.50**
北半球极涡强度指数	−0.45*	−0.42*	印缅槽	0.44*	0.42*	西半球暖池	0.42*	0.40*
太阳黑子	−0.41*	−0.40*	大西洋几十年涛动	0.42*	0.40*	黑潮区 SST	0.39*	0.42*
大西洋副高面积指数	0.4*	0.39*	北半球副高面积指数	0.40*	0.36*	热带北大西洋 SST	0.39*	0.38*
北大西洋涛动指数	−0.4*	−0.37*	热带北大西洋 SST	0.39*	0.38*	大西洋副高强度指数	0.39*	0.36*
北半球环状模指数	−0.38*	−0.35*	西太平洋副高面积指数	0.36*	0.33	北半球极涡中心位置	−0.32	−0.31

注: R_1 为因子和阻高区夏季区域平均高度场的相关系数, R_2 为因子与夏季区域平均模式误差的相关系数; 上标 * 和 ** 分别达到 0.05 和 0.01 信度的 t 检验水平.

表 1 分别给出了影响三个阻高区夏季 500 hPa 高度场的气候因子及其与模式误差的相关系数. 由表 1 可见, 三个阻高区夏季 500 hPa 高度场的影响因子主要有海温、北半球的副高及涛动指数等, 且均包含与大西洋有关的物理因子. 在这些因子中, 选取哪个因子作为相似指标才能最好的提高预报水平? 这还需要进一步分析因子与区域误差的时间相关分布是否一致. 经普查, 乌阻区的影响因子中太阳黑子与该区域模式误差相关符号高度一致 (图 2(a)); 贝阻区的影响因子中印缅槽与该区域模式误差相关符号高度一致 (图 2(b)); 鄂阻区的影响因子中黑潮区 SST 与该区域模式误差相关高度符号一致 (图 2(c)). 因此, 这里选取太阳黑子、印缅槽和黑潮区 SST 分别作为乌阻、贝阻和鄂阻的相似选取因子.

3.3 预测实验

综上可知, 作为对阻高区夏季 500 hPa 高度场有影响的表征气候系统各模态变化的前期物理因子, 若其与模式预报误差之间存在某种显著的相关关系, 那么当因子发生变化, 所对应的气候系统状态亦发生变化, 并直接或间接影响到模式内部误差的形态和演变, 进而反映到预报误差的变化上, 这就形成了物理因子对模式预报误差分布状况的影

响过程. 用这些因子作为相似选取指标, 对相似年个数的选取需要进行敏感性实验.

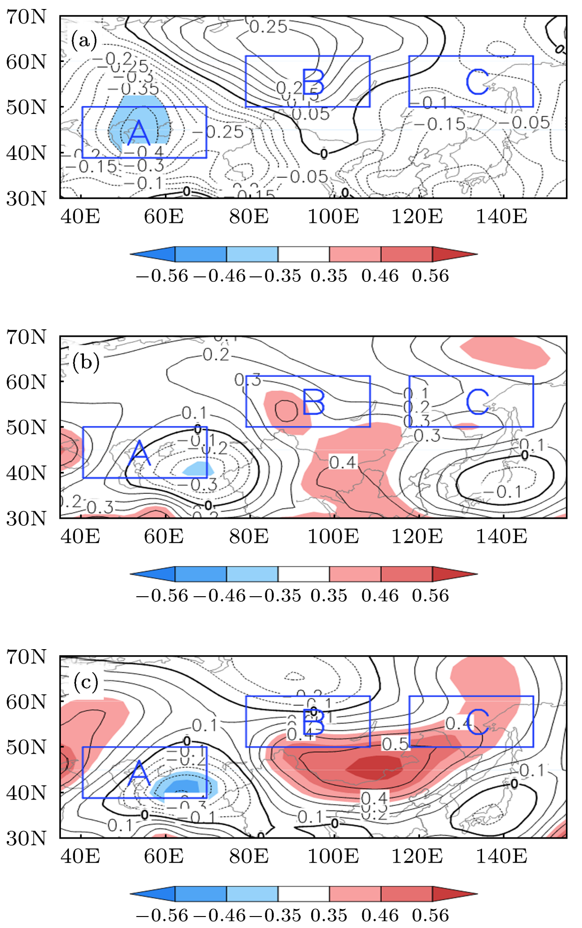

图 2　前冬气候因子与夏季 500 hPa 高度模式误差场的相关系数分布　(a) 太阳黑子; (b) 印缅槽; (c) 黑潮区 SST(等值线间隔 0.1, 其余说明同图 1)

图 3 给出了用太阳黑子、印缅槽和黑潮区 SST 分别作为乌阻、贝阻和鄂阻区域夏季平均 500 hPa 高度场的相似选取指标, 进行 2002—2011 年 10 年系统订正和动力 - 统计预测 (DSP) 时平均的距平相关系数 (ACC) 和均方根误差 (RMSE) 随相似年个数变化的情况. 由图 3 可见, 针对不同的预报对象和相似指标, 最佳相似年个数有所不同. 其中, 用太阳黑子指数预测乌阻区域 500 hPa 高度场时, 相似年个数从 1 增长到 7 时 ACC 逐渐增大, 同时 RMSE 也逐步减小; 当相似年个数为 7 时, 10 年平均 ACC 从系统订正的 −0.19 提高到 0.49, RMSE 从系统订正的 17.32 降低到 14.36; 当因子个数继续增加时, ACC 逐步下降, RMSE 也开始增大. 因此, 利用太阳黑子对乌阻区域 500 hPa 高度场进行动力 - 统计预测时, 选取 7 个相似年效果最佳. 而贝阻区选取 4 个相似年最佳, 10 年平均 ACC 从系统订正的 −0.23 提高到 0.33, RMSE 从系统订正的 17.42 降低到 16.35; 鄂阻区也是选取 4 个相似年最佳, 10 年平均 ACC 从系统订正的 −0.21 提高到 0.32, RMSE 从系统订正的 20.08 降低到 19.06.

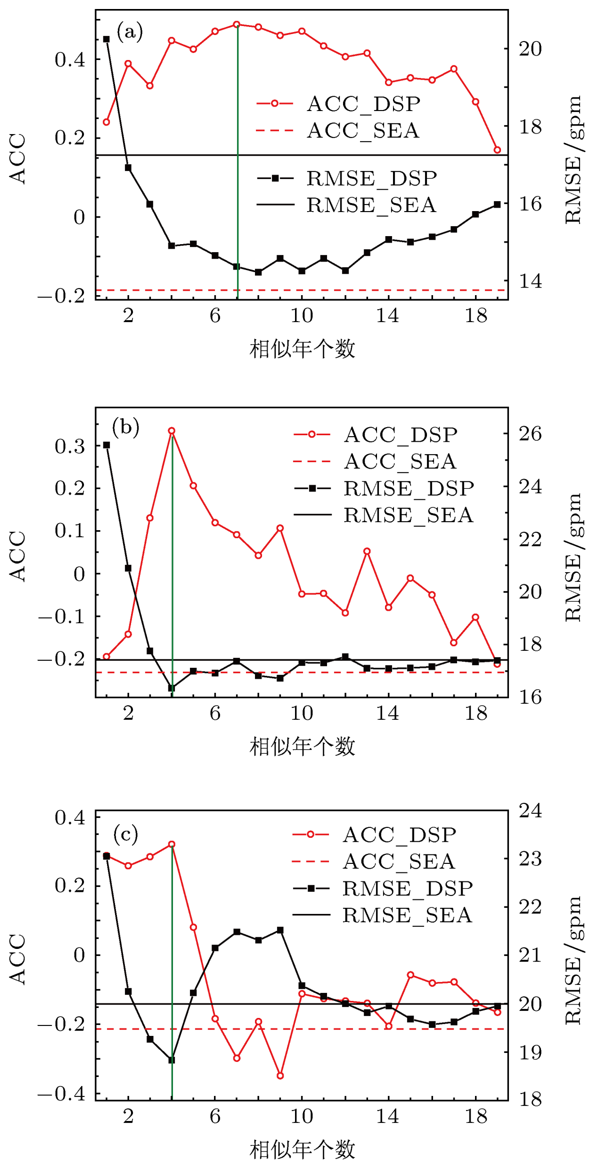

图 3　预测的 10 年平均 ACC 和 RMSE 随相似年个数的变化　(a) 太阳黑子预测乌阻区; (b) 印缅槽预测贝阻区; (c) 黑潮区 SST 预测鄂阻区

为了直观地了解动力 - 统计的预测效果, 图 4 给出了 2002—2011 年乌阻区、贝阻区和鄂阻区夏季平均 500 hPa 高度场独立样本动力 - 统计预测和系统订正的 ACC 和 RMSE 的年际变化对比. 由图 4 可见, 乌阻区 10 年动力 - 统计预测的 ACC 有 8 年比系统订正高, 2004 年和 2005 年比系统订正略低

(图 4(a)); RMSE 有 7 年降低, 2004, 2005 和 2009 年比系统订正略高 (图 4(d)). 贝阻区 10 年动力 - 统计预测的 ACC 有 9 年比系统订正高, 只有 2005 年比系统订正低 (图 4(b)); RMSE 有 8 年降低, 2005 年和 2006 年比系统订正略高 (图 4(e)). 鄂阻区 10 年动力 - 统计预测的 ACC 有 8 年比系统订正高, 2003 年和 2010 年比系统订正略低 (图 4(c)); RMSE 有 6 年降低, 2002, 2003, 2009 和 2010 年比系统订正略高 (图 4(f)). 总体来看, 动力 - 统计预测效果较系统订正有明显的提高, 预测结果也比较稳定, 仅个别年份预测改进不明显, 这一方面与模式本身的预报水平有关, 另一方面也反映了物理因子与模式误差的关系不是非常稳定、且资料长度有限只能选取条件下的最佳相似年而不能选取绝对的相似年.

2006 年是欧亚中高纬阻塞高压盛行的一年, 乌阻异常强大 (图 5(a)), 鄂阻 (图 5(b)) 和贝阻 (图 5(c)) 次之. 系统订正均没有预测出三个区域的阻塞形势 (图 5(d)—(f), 分别为乌阻区、贝阻区、鄂阻区), ACC 分别为 −0.02, −0.49, −0.92, RMSE 分别为 33.90, 9.01, 21.26; 而动力 - 统计不仅预测出了三个区域高度场距平的分布形态, 还预测出了高度场正距平中心的大体位置, 仅高度场距平量级较观测偏低 (图 5(g)—(i), 分别为乌阻区、贝阻区、鄂阻区), ACC 分别为 0.95, 0.39, 0.89, RMSE 分别为 26.86, 11.70, 13.02, 乌阻区和鄂阻区的高度场预报优于贝阻区.

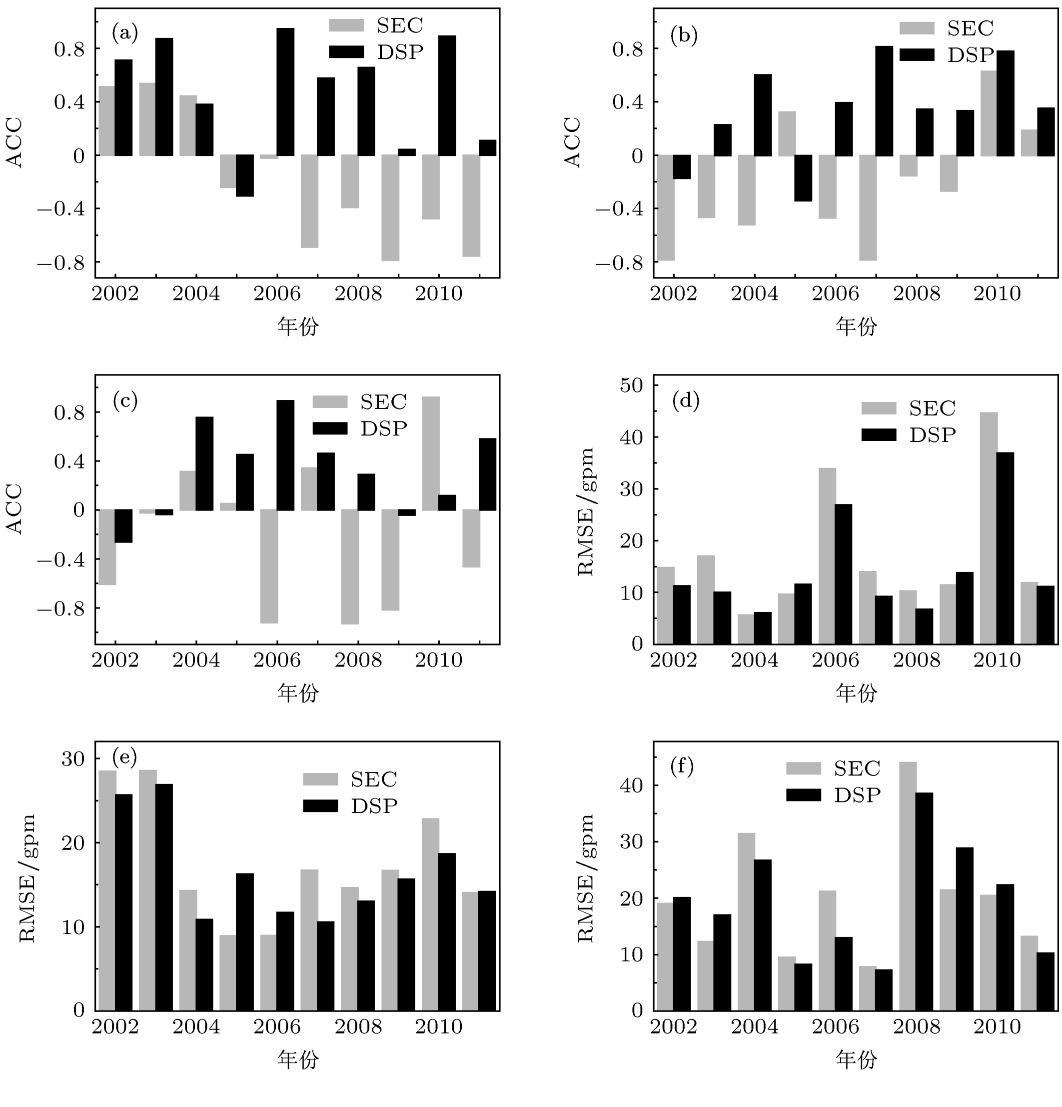

图 4 2002—2011 年系统订正和动力 - 统计预测的 ACC (a), (b), (c) 和 RMSE (d), (e), (f) (a), (b) 乌阻; (c), (d) 贝阻; (e), (f) 鄂阻

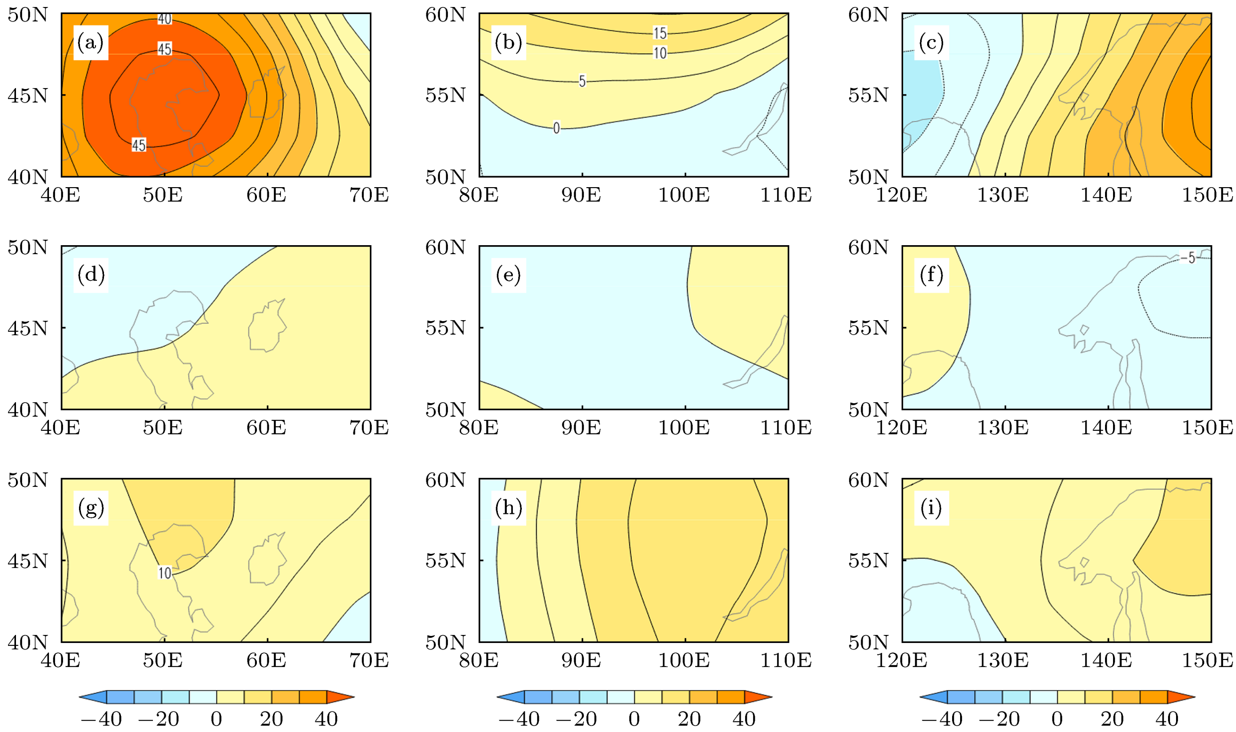

图 5 2006 年夏季乌阻区 (a), (d), (g)、贝阻区 (b), (e), (h) 和鄂阻区 (c), (f), (i) 500 hPa 高度场距平 (a), (b), (c) 观测; (d), (e), (f) 系统订正; (g), (h), (i) 动力 - 统计预测

4 结 论

本文主要利用实际业务模式的预报结果和丰富的历史资料对乌拉尔山、贝加尔湖及鄂霍次克海三个阻塞高压活动关键区夏季平均的 500 hPa 高度场进行动力 - 统计的跨季度预测实验. 具体结论简要概述如下: 三个关键区高度场 2002—2011 年 10 年独立样本预测的平均 ACC 分别从系统订正的 −0.19, −0.23 和 −0.21 提高到 0.49, 0.33 和 0.32, 平均 RMSE 分别从系统订正的 17.32, 17.42 和 20.08 降低到 14.36, 16.35 和 19.06, 可见该方法能有效减小模式预报误差、提高预报技巧, 显示出良好的业务应用前景.

由于篇幅有限, 本文仅从季节尺度给出了夏季欧亚阻塞高压的单因子预测实验方案, 而夏季逐月的阻塞形势即中高纬环流的调整及其与西太副高的配置才是决定夏季旱涝的关键因素; 另外, 影响中高纬阻塞高压的影响因子众多, 仅用单个因子进行预测难免会出现预测结果不稳定和效果不明显等问题, 因此多因子组合的预测方案和策略仍值得进一步研究. 同时, 随着历史资料的进一步丰富和数值模式的不断改进, 历史资料能更好的描述预报时段内实际大气的状态, 而数值模式提供的有效信息也越来越多, 利用历史资料的动力 - 统计预测方法也将更有用武之地.

[1] Berggren R, Bolin B, Rossby C G 1949 *Tellus.* **1** 14

[2] Rex D F 1950 *Tellus.* **2** 196

[3] Hartmann D H, Ghan S J 1980 *Mon. Wea. Rev.* **108** 1144

[4] Noar P F 1983 *Aust. Met. May.* **31** 37

[5] Kaas E, Branstator G 1993 *J. Atoms. Sci.* **50** 3061

[6] Pelly J L, Hoskins B J 2003 *J. Atmos. Sci.* **60** 743

[7] Luo Z X 1989 *Science China* B **6** 665 (in Chinese) [罗哲贤 1989 中国科学 (B 辑) **6** 665]

[8] Yang Y W 2003 *Meteorologica Mon* **29** 3 (in Chinese) [杨义文 2003 气象 **29** 3]

[9] Zhou X P 1957 *Acta Meteorologica Sinca* **28** 75 (in Chinese) [周晓平 1957 气象学报 **28** 75]

[10] Li F, Ding Y H 2004 *Acta Meteorologica Sinca* **62** 347 (in Chinese) [李峰, 丁一汇 2004 气象学报 **62** 347]

[11] Tang M C 1957 *Acta Meteorologica Sinca* **28** 282 (in Chinese) [汤懋苍 1957 气象学报 **28** 282]

[12] Zhang P Z, Yang S L 1996 *Acta Meteorologica Sinca* **54** 633 (in Chinese) [张培忠, 杨素兰 1996 气象学报 **54** 633]

[13] Zhang Q Y, Tao S Y 1998 *Acta Meteorologica Sinca* **56** 199 (in Chinese) [张庆云, 陶诗言 1998 气象学报 **56** 199]

[14] Zhang Q Y, Tao S Y, Peng J B 2008 *Chin. J. Atmos. Sci.* **32** 815 (in Chinese) [张庆云, 陶诗言, 彭京备 2008 大气科学 **32** 815]

[15] Tao S Y, Zhao Y J, Chen X M 1958 *Acta Meteorologica Sinca* **29** 119 (in Chinese) [陶诗言, 赵煜佳, 陈晓敏 1958 气象学报 **29** 119]

[16] Wang Y 1992 *J. Meteor. Soc. Japan* **70** 929

[17] Chen H Y 1957 *Acta Meteorologica Sinca* **28** 1 (in Chinese) [陈汉耀 1957 气象学报 **28** 1]

[18] Li W J 1999 *Meteorologica Mon* **25** 20 (in Chinese) [李维京 1999 气象 **25** 20]

[19] Chen J Y, Wang Y H, Wang W 2001 *Plateau Meteor* **20** 388 (in Chinese) [陈菊英, 王玉红, 王文 2001 高原气象 **20** 388]

[20] Barnett T P, Preisendorfer R W 1978 *J. Atmos. Sci.* **35** 1771

[21] Van H M 1994 *Tellus* **46A** 314

[22] Gu Z C 1958 *Acta Meteorologica Sinca* **29** 176 (in Chinese) [顾震潮 1958 气象学报 **29** 176]

[23] Chou J F 1974 *Science China.* **6** 635 (in Chinese) [丑纪范 1974 中国科学 **6** 635]

[24] Chou J F 1986 *Plateau Meteor* **5** 367 (in Chinese) [丑纪范 1986 高原气象 **5** 367]

[25] Feng G L, Dai X G, Wang A H, Chou J F 2001 *Acta Phys. Sin.* **50** 606 [封国林, 戴新刚, 王爱慧, 丑纪范 2001 物理学报 **50** 606]

[26] Feng G L, Dong W J, Jia X J, Cao H X 2002 *Acta Phys. Sin*. **51** 1181 [封国林, 董文杰, 贾晓静, 曹鸿兴 2002 物理学报 **51** 1181]

[27] Ren H L, Chou J F 2005 *Acta Meteorologica Sinca* **63** 988 (in Chinese) [任宏利, 丑纪范 2005 气象学报 **63** 988]

[28] Ren H L, Chou J F 2007 *Science China.* D **37** 1589 (in Chinese) [任宏利, 丑纪范 2005 中国科学 (D) **37** 1589]

[29] Zheng Z H, Ren H L, Huang J P 2009 *Acta Phys. Sin.* **58** 7359 (in Chinese) [郑志海, 任宏利, 黄建平 2009 物理学报 **58** 7359]

[30] Wang Q G, Feng G L, Zheng Z H, Zhi R 2011 *Chin. J. Atmos. Sci.***35** 287 (in Chinese) [王启光, 封国林, 郑志海, 支蓉 2011 大气科学 **35** 287]

[31] Xiong K G, Zhao J H, Feng G L, Huang J P, Hu J G 2012 *Acta Phys. Sin.* **69** 149204 (in Chinese) [熊开国, 赵俊虎, 封国林, 黄建平, 胡经国 2012 物理学报 **69** 149204]

[32] Yang J, Wang Q G, Zhi R, Feng G L 2011 *Acta Phys. Sin.* **60** 029204 (in Chinese) [杨杰, 王启光, 支蓉, 封国林 2011 物理学报 **60** 029204]

[33] Zhao Z G 2000 *Summer Drought and Environmental Field in China.* (Beijing: Meteorological Press) 75–78 (in Chinese) [赵振国 1999 中国夏季旱涝及环境场 (北京: 气象出版社) 第 75—78 页]

[34] Nan S L, Li J P 2003 *Geophys. Res. Lett.* **30** 2266

[35] Li J P, Wang J X L 2003 *Geophys. Res. Lett.* **30** 1632

[36] Li J P, Wang J X L 2003 *Adv. Atmos. Sci.* **20** 661

[37] Li Z C, Bi B G, Zhu T, Wang Y H, Niu R Y 2004 *Meteorologica Mon* **30** 4 (in Chinese) [李泽椿, 毕宝贵, 朱彤, 王友恒, 牛若芸 2004 气象 **30** 4]

[38] Kang I S, Lee J Y, Park C K 2004 *J. Climate* **17** 834

[39] Wang S W 1984 *Adv. Atmos. Sci.* **1** 7

The experiments of transseasonal prediction by combining together the dynamical and statistical methods of the geopotential height fields on the blocking high in the Eurasia mid-high latitudes*

Zhao Jun-Hu[1)2)†] Yang Jie[1)] Gong Zhi-Qiang[2)] Zhi Rong[2)]

1) (*College of Atmospheric Sciences, Lanzhou University, Lanzhou* 730000*, China*)

2) (*Laboratory for Climate Studies, National Climate Center, China Meteorological Administration, Beijing* 100081*, China*)

(Received 21 November 2012; revised manuscript received 6 January 2013)

Abstract

The blocking high in Eurasia mid-high latitudes (EMHBH) is one of the leading members of East Asian summer monsoon circulation system, which also has a crucial influence on the summer flood/drought in China, especially in the region of Yangtze River. However, the objective quantitative prediction of EMHBH is an urgent issue we are facing and also a complicated problem in the current short-term climate prediction. This paper, by using the dynamical and statistical prediction (DSP) methods and based on the forecast data of the numerical modal(CGCM) and the abundant historical observations, has carried out prediction experiments of the above three blocking high regions in the summer averaged 500 hPa geopotential height fields. The results show that the DSP methods can diminish the prediction errors to some extent, which is also suitable for operational application. In addition, sensitivity tests show that the selection of the number of similar targets or similar yeas has significant influences on the prediction results.

Keywords: blocking high, geopotential height fields, dynamical and statistical, transseasonal prediction experiment

PACS: 92.60.Wc, 9130.Pd **DOI:** 10.7498/aps.62.099206

* Project supported by the National Natural Science Foundations of China (Grant Nos. 40930952, 41105055), and the National Basic Research Program of China (Grant No.s 2012CB955902, 2013CB430204).

† Corresponding author. E-mail: huzi348637577@sina.com

第 33 卷 第 8 期
2013 年 8 月

光 学 学 报
ACTA OPTICA SINICA

Vol. 33, No. 8
August, 2013

黑碳与非吸收性气溶胶的不同混合方式对其光学性质的影响

周 晨[1,2] 张 华[2] 王志立[3]

[1] 南京信息工程大学大气物理学院，江苏 南京 210044
[2] 中国气象局国家气候中心气候研究开放实验室，北京 100081
[3] 中国气象科学研究院，北京 100081

摘要 为了研究不同混合方式对气溶胶粒子光学性质的影响，利用典型外混合模型和三种内混合模型，计算了黑碳与硫酸盐及有机碳组成的混合气溶胶在 550 nm 波长处的光学性质。结果表明，除 Maxwell-Garnett 模型与 Bruggeman 模型的差异普遍小于 2%外，所有混合模型对混合粒子及粒子群的光学性质都有明显影响。相比于外混合粒子群，内混合粒子群的吸收系数增强了 20%以上，散射系数则削弱了 10%～15%，并导致消光系数的最大增强达到 25%；内混合模型对于单次散射反照率的减弱效果最明显，尤其在黑碳体积比小于 30%和相对湿度高于 70%的情况下，内混合模型使粒子群的单次散射反照率降低了 20%以上。此外，除不对称因子外，混合气溶胶的其他光学性质与体积混合比以及相对湿度均呈现出明显的相关性。

关键词 散射；气溶胶；内外混合；黑碳；硫酸盐

中图分类号 P224.9 **文献标识码** A **doi**: 10.3788/AOS201333.0829001

Impact of Different Mixing Ways of Black Carbon and Non-Absorbing Aerosols on the Optical Properties

Zhou Chen[1,2] Zhang Hua[2] Wang Zhili[3]

[1] *Institute of Atmospheric Physics, Nanjing University of Information Science and Technology, Nanjing, Jiangsu 210044, China*
[2] *Laboratory for Climate Studies, National Climate Center, China Meteorological Administration, Beijing 100081, China*
[3] *Chinese Academy of Meteorological Sciences, Beijing 100081, China*

Abstract In order to study the impact of mixing ways of aerosols on their optical properties, one typical external mixing model plus three different internal mixing models of aerosols are introduced. The optical properties of mixed aerosol particles formed by black carbon, sulfate and organic carbon at 550 nm wavelength are calculated. The results show that there are great differences in optical properties of mixing particles and particle groups obtained by these models except Maxwell-Garnett model and Bruggeman model (difference less than 2%). Compared with externally mixed particle groups, the mass absorption factors of internally mixed particle groups are increased by about 20%, while the mass scattering factors of the particle groups are decreased by 10%～15% in most cases. The internal mixing models make a large enhancement of the mass extinction factors of mixed particle groups by 25% for maximum. Furthermore, the reduction of single scattering albedo is significant. In particular, the reduction of the scattering albedo of the mixed particle groups can be larger than 20% under circumstances that the volume ratio of black carbon is

收稿日期: 2013-02-25; **收到修改稿日期**: 2013-04-16

基金项目: 国家 973 计划(2011CB403405,2012CB955303)、国家自然科学基金(41205116)、中国气象科学研究院基本科研业务费(2012Y003)

作者简介: 周 晨(1988—)，男，硕士研究生，主要从事大气气溶胶光学性质及辐射强迫等方面的研究。
E-mail: zhouchen19880316@yahoo.cn

导师简介: 张 华(1965—)，女，研究员，博士生导师，主要从事温室气体、气溶胶和云的辐射强迫与气候效应等方面的研究。E-mail: huazhang@cma.gov.cn(通信联系人)

below 30% and the relative humidity is above 70%. In addition, optical properties of mixed particles, except the asymmetry parameter, are distinctly related to the change of volume ratio or relative humidity.

Key words　scattering; aerosols; internal & external mixing; black carbon; sulfate

OCIS codes　290.1090; 290.5850; 290.4020; 290.2200

1　引　　言

大气气溶胶一般是指由悬浮在大气中、粒径大小在 $10^{-2}\sim10^{2}$ μm 的固态和液态微粒共同组成的多相体系。气溶胶可以通过吸收和散射红外辐射和太阳短波辐射直接影响地球大气辐射能量收支，造成直接气候效应。气溶胶粒子也可以作为云凝结核或者冰核，通过影响云滴数浓度、云滴有效半径和云生命周期等云微物理特性而间接影响气候[1]。

黑碳(BC)气溶胶、硫酸盐气溶胶和有机碳气溶胶是大气气溶胶的重要组成部分，三者具有部分同源性。黑碳和有机碳气溶胶主要来源于化石燃料和生物质燃料的燃烧，如汽车尾气排放、农作物燃烧、森林大火和一些与燃烧石油相关的工业活动[2-3]；硫酸盐气溶胶由 SO_2 与大气中其他成分反应生成，主要来源是石油等化石燃料的燃烧；有机碳气溶胶通常伴随着黑碳气溶胶生成，但其自然来源贡献很小，主要是由污染源直接排放的一次有机气溶胶(原生气溶胶)和部分挥发性有机化合物经过大气化学反应产生的二次有机气溶胶(次生气溶胶)组成。黑碳气溶胶对于辐射的影响主要体现在其强烈的吸收作用上，它能广泛地吸收从可见光到红外波段的太阳辐射，从而增加地-气系统对太阳辐射的吸收，造成正辐射强迫，对全球大气起到增温作用[3-6]并可能对大尺度的气候过程如亚洲夏季风造成影响[7]。硫酸盐气溶胶最大的特点是对于太阳辐射具有很强的散射作用，能够有效地减少到达地表的太阳辐射，降低地-气系统的能量收入，造成负强迫辐射。有机碳气溶胶对短波和可见光波段辐射有明显的散射作用，产生负辐射强迫，对地-气系统起冷却作用[8]。

许多观测研究表明，大气中大部分气溶胶粒子是由多种成分混合形成的[9]，并且这些颗粒中有很大一部分是以内混合形式存在的。内混合可能以多种形式存在，不同的混合形式对粒子的光学性质的影响均不相同。由于内混合的形成机制尚不明确以及内混合模型自身的局限性，所以目前计算气溶胶辐射强迫通常只考虑易于实现的外混合模型或均匀混合模型。目前已经有一些专家着手开展内混合形成的大气条件和成因的研究。Riemer 等[10]研究了一天中黑碳气溶胶的老化过程，结果显示新近排放的黑碳气溶胶随着老化过程的加剧，更加倾向于和其他气溶胶成分形成内混合粒子；Ma 等[11]对比了华北地区混合粒子中碳类气溶胶的质量比的日际变化后发现碳类气溶胶的混合方式受混合层的日际变化的影响明显，其在白天偏向于外部混合，而在夜间则偏向于内部混合。

有大量的研究都指出，黑碳气溶胶在内混合气溶胶形成过程中扮演至关重要的角色，其往往作为核心部分与硫酸盐、水溶性有机碳等气溶胶形成内混合，此时包裹在黑碳周围的水溶性成分可以充当透镜[12]，从而极大地改变其本身的光学性质，增大黑碳气溶胶的正辐射强迫[13-15]。Lesins 等[16]指出在内外混合方式下气溶胶粒子光学性质的差异可能达到 25%以上，而湿状态下更可能达到 50%，而在硫酸盐-黑碳质量比为 9:1 的情况下，使用内混合模型替换外混合模型后，几乎所有原先估计的冷却效应都会消失。Jacobson[17]通过比较不同混合情况下黑碳对大气的加热效率后指出：气溶胶内混合能大幅加强黑碳的正辐射强迫，而加强的幅度又与气溶胶粒子的凝结和增长效应有很大关系，这一影响使得黑碳可能成为仅次于 CO_2 的全球变暖影响因子。

气溶胶的几何结构也是其光学性质的一个重要影响因素。许多专家学者探讨了不同几何模型对光学性质的影响：张小林等[18]使用了包含三种成分的包裹型内混合模型计算了灰尘、黑碳和水组成的气溶胶的光学性质，讨论了等效复折射率在描述此类内混合气溶胶系统时的适用性；卫晓东等[19]使用 T 矩阵和几何光学方法相结合，计算了具有一定形状和谱分布的非球形沙尘粒子的光学性质，发现非球形与球形沙尘粒子在可见光波段的相函数在短波波段存在明显差异，并指出非球形效应对雷达和卫星反演沙尘气溶胶光学厚度会造成一定影响；邵士勇等[20]利用 T 矩阵方法探讨了冰晶、沙尘和黑碳成分的单分散气溶胶的相函数随散射角的变化关系；孙贤明等[21]还将 T 矩阵法扩展到含核椭球粒子的散射性质计算中；Chung 等[22-23]利用离散偶极子近似(DDA)算法计算了 Cluster-cluster aggregation 模型的气溶胶粒子簇的光学性质，并描述了粒子簇内的基本粒子半径和个数对其光学性质的影响。

但是，迄今为止的内外混合粒子光学性质的研究中考虑的影响因素仍不全面，很难对不同混合模型的优缺点和适用条件给出详细的评估。此外，东亚地区是黑碳气溶胶的主要源区，不同混合模型对黑碳的辐射强迫影响很明显，但是目前针对该区域的内混合气溶胶光学性质的全面认识仍然比较缺乏。因此，全面地比较黑碳与非吸收性气溶胶成分在多种混合模型和外部条件下的光学性质是今后合理和精确地计算混合气溶胶辐射强迫的基础和前提，是非常重要的基础研究。

本文利用三种不同的内混合模型（Core-shell 模型、Maxwell-Garnett 模型和 Bruggeman 模型）以及典型外混合模型，结合东亚实测气溶胶数浓度谱，分别计算了黑碳-硫酸盐和黑碳-有机碳混合粒子群在不同体积混合比（即某一成分的体积相对于粒子整体的比例，以下也简称体积比）和不同相对湿度下的光学特性，全面地讨论了不同混合模型对气溶胶光学性质的影响，并解释了造成这些光学性质差异的原因，初步给出了各种模型的适用条件。

2　原理和方法

2.1　气溶胶粒子的数浓度谱

气溶胶粒子的数浓度谱表征了大气中气溶胶粒子在不同的粒径区间内的数量分布，对气溶胶粒子群的光学性质有着决定性的作用，因此合理的气溶胶数浓度谱是计算气溶胶辐射强迫的前提。目前，气溶胶粒子数浓度谱 $n(r)$ 普遍采用对数正态分布进行拟合：

$$n(r)=\frac{N}{\sqrt{2\pi}\cdot r}\exp\left[-\frac{1}{2}\left(\frac{\log r-\log r_0}{\log\delta}\right)\right],\tag{1}$$

式中 r_0 为众数半径，δ 是标准偏差，N 为单位体积大气中气溶胶粒子的个数，r 为气溶胶粒子的半径。黑碳气溶胶数浓度谱参照东亚区域实测资料[24]，众数半径取 0.13 μm，相对偏差为 1.8，能够较好地拟合中国地域的黑碳气溶胶数浓度谱。计算中假设每一个混合粒子中只有一个黑碳粒子，混合粒子群的数浓度谱积分依据其中包含的黑碳粒子所对应的数浓度谱进行。

2.2　气溶胶的复折射指数

复折射指数是计算气溶胶光学性质的重要参数，由实部、虚部两部分构成，实部的绝对值表征了气溶胶成分的散射能力，虚部的绝对值则表征了气溶胶成分的吸收能力。表 1 给出了干气溶胶颗粒在 550 nm 波长处的复折射指数和密度[25]。

表 1　三种气溶胶成分在 550 nm 波长处的复折射指数和密度

Table 1　Complex refractive index at 550 nm wavelength and density of three types of aerosol

Component	Complex refractive index	Density /(kg·m^{-3})
Sulfate	$1.43-1.0\times10^{-8}$i	1769.0
Black carbon	1.75－0.44 i	1500.0
Organic carbon	1.53－0.0059 i	1300.0

由于吸湿性气溶胶在潮解过程中与水汽混合，其介电常数会发生变化，因此其复折射指数随相对湿度也发生变化。不同相对湿度下气溶胶的复折射指数需要根据非吸收性成分体积变化分数求得，计算公式为[26]

$$m=m_{\mathrm{w}}+(m_{\mathrm{dry}}-m_{\mathrm{w}})\times\frac{[(r_{\mathrm{m}})^3-(r_{\mathrm{dry}})^3}{(r_{\mathrm{m}})^3]},\tag{2}$$

式中 m 为潮解后气溶胶的复折射指数，m_{w} 为水的复折射指数，m_{dry} 为潮解前气溶胶的复折射指数，r_{m} 为潮解后气溶胶粒子的有效半径，r_{dry} 为干气溶胶粒子的有效半径。根据 Köhler 公式，能得到不同相对湿度下硫酸盐和有机碳的增长幅度。因为黑碳的吸水性很弱，此处没有考虑黑碳的吸湿增长。

图 1 为硫酸盐和有机碳在 550 nm 波长的复折射指数的实部和虚部随相对湿度的变化。硫酸盐和有机碳的复折射指数与相对湿度密切相关，两种物质的潮解点比较接近，当相对湿度达到 35% 左右时，两者复折射指数实部和虚部都会随即出现明显的降低；此后，随着相对湿度的增加，复折射指数进一步下降，并逐渐接近于水的复折射指数。

2.3　气溶胶粒子的混合模型

外混合模型相对简单，假设不同的气溶胶粒子间并不相互发生理化作用，而是以球型粒子独立存在于大气中，粒子间发生独立散射，即电磁波经一个粒子散射后不再被另一个粒子散射，因此外混合粒子的整体光学性质为各部分性质的体积加权求和。

内混合模型中不同气溶胶成分之间存在复杂的相互关系。实际情况下内混合粒子的几何结构随机性很强，视气溶胶成分不同可能出现粘连、包裹、糅合等多种情况，由此可以形成同心球、随机核分布、均匀球、多核心、非对称和不完全包裹等多种混合状态。为了研究内混合和外混合粒子的性质差异以及内混合中不对称结构对于混合粒子光学性质的影响，选择典型气溶胶外混合和Core-shell、Maxwell-

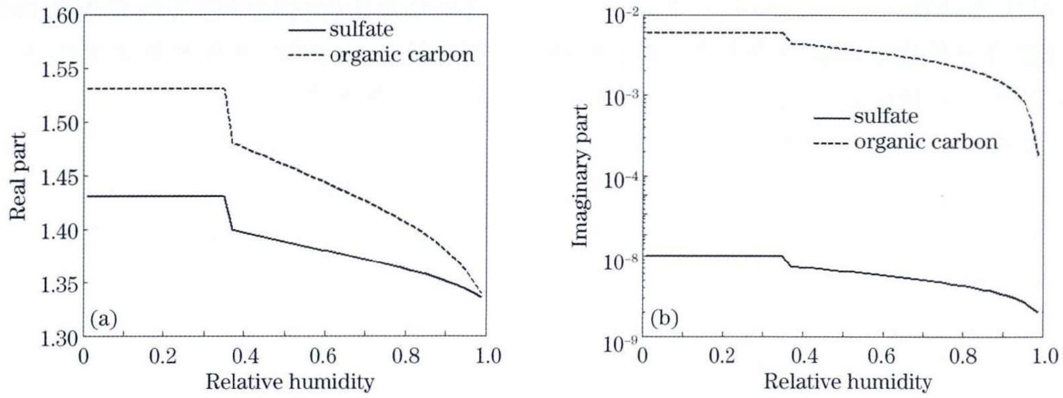

图 1　硫酸盐和有机碳复折射指数随相对湿度的变化

Fig. 1　Change of complex refractive index of sulfate and organic carbon with relative humidity

Garnett 和 Bruggeman 三种气溶胶内混合模型进行分析。

图 2 大致描绘了气溶胶粒子的几种混合方式。其中图 2(a) 表示典型外混合模型，粒子各部分以球型独立存在且不发生二次散射；图 2(b)为内混合中的 Core-shell 模型，由吸湿性成分包裹非吸湿性成分形成同心球结构；图 2(c)为 Maxwell-Garnett 模型，核心粒子的位置随机，通常由吸湿性成分包裹非吸湿性成分形成；图 2(d)为 Bruggeman 模型，当粒子各部分以相邻的拓扑关系存在时，Bruggeman 模型将其简化为相邻的球体进行处理。

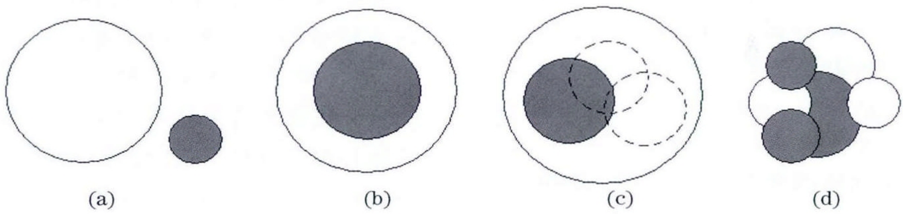

图 2　几种不同的气溶胶混合模型

Fig. 2　Several different mixing models of aerosol

2.4　内混合中吸湿性物质的透镜作用

有研究认为，内混合模型会使核心物质对于混合粒子整体光学性质的影响明显增强，这可能是由于吸湿性物质在混合粒子中充当了透镜所致。根据折射定律，由光疏介质进入光密介质的辐射能量将偏离原始的传输方向，入射角与折射角的关系为

$$\cos\theta_{\mathrm{re}}=\cos\theta_{\mathrm{in}}\rho_2/\rho_1,\tag{3}$$

式中 θ_{re} 为折射角，θ_{in} 为入射角，ρ_1 为入射前介质密度，ρ_2 为入射后介质密度。当辐射能量到达分层球粒子的外壳部分时，除去被散射和吸收的部分，剩余的辐射能量经过折射会有向中心会聚的趋势，从而增大了内核物质与辐射能量作用的机率。

2.5　光学性质的计算方法

除 Core-shell 模型外，其余模型光学性质的计算方法是基于米氏散射原理得来的。根据米氏散射理论，可通过粒子的复折射指数、粒子半径、波长等输入量求得单相系粒子的光学参数：消光系数、散射系数、吸收系数、单次散射反照率和不对称因子。由于米氏散射原理是针对单个均匀球形粒子的经典理论，并不适用于非均质的内混合模型，因此需要对这类内混合粒子进行处理使其转化为适用于米氏散射原理的等效球体。

外混合方式实际上是粒子间的独立散射，混合气溶胶性质为各气溶胶成分的体积加权之和。假设混合气溶胶粒子中含有 i 种成分，α_i 为该种气溶胶成分的某种光学性质，β 为混合气溶胶的光学性质，f_i 为该种气溶胶成分的体积分数，则计算公式为

$$\beta=\sum_i f_i\alpha_i.\tag{4}$$

对于内混合中的 Core-shell 模型，由于在粒子内部发生多次散射过程，因此简单的权重分布在这种情况下不适用，需要根据粒子的结构特性计算出该混合粒子的等效复折射指数。Core-shell 模型的计算方法来自 Bohren 等提出的分层球米氏散射方法，粒子内的多次散射过程需要依据壳物质复折射指数和核物质复折射指数，以及内核体积混合比 $f=a^3/b^3$ (a 为内核半径，b 为外壳半径）和相应的尺度参数

$2\pi a/\lambda$ 和 $2\pi b/\lambda$ 来计算。

对于内混合中的核心随机分布情况，由于核物质在混合粒子中的相对位置不确定，因此对于同一种体积混合比也可能出现很大的光学性质差异。有许多研究资料表明 Maxwell-Garnett 理论[27]对于这种情况的计算精度较高。Maxwell-Garnett 理论的简化模型是由液态成分包裹的球形固态核心构成的球形混合粒子，这些固态核心的位置是随机的。假设混合粒子的样本空间是无限的，通过统计学方法，可以将同一种混合比下的混合粒子等效复折射指数求出。通过知晓核物质的复折射指数 m_c 和外壳物质的复折射指数 m_s 以及核心的体积比 f_c 可以计算出混合粒子的等效复折射指数。计算公式为

$$m=\sqrt{m_s^2\frac{m_c^2+m_s^2+2f_c(m_c^2-m_s^2)}{m_c^2+2m_s^2-f_c(m_c^2-m_s^2)}}. \tag{5}$$

Bruggeman 理论[27]也是利用混合粒子各部分的复折射指数和体积混合比求得混合粒子的等效复折射指数后，将混合粒子作为球体导入米氏散射公式求解光学性质。计算公式为（m_1 和 m_2 分别代表两种组成物质的复折射指数）

$$f_1\frac{m_1^2-m^2}{m_1^2+2m^2}+f_2\frac{m_2^2-m^2}{m_2^2+2m^2}=0. \tag{6}$$

由于吸湿性成分的潮解作用的影响，处理吸湿增长后的粒子需要根据不同相对湿度下粒子体积混合比及复折射指数计算等效复折射指数，并将不同相对湿度下的尺度参数和粒子质量导入米氏散射方程组，求解光学性质。

3　结果分析

为了研究在不同体积混合比和相对湿度条件下内外混合模型对气溶胶粒子光学特性的影响，计算了四种混合模型（体积权重平均外混合模型、Core-shell 模型、Maxwell-Garnett 模型和 Bruggeman 模型）下的黑碳-硫酸盐和黑碳-有机碳混合气溶胶在 550 nm 波长处的光学性质。

3.1　单个混合气溶胶粒子的光学性质

粒子半径是米氏散射计算中重要的输入量，为了排除气溶胶数浓度谱对光学性质的影响，引入单个气溶胶粒子光学性质的比较。图 3 给出不同混合方式下气溶胶粒子光学性质随等效半径的变化，从左至右分别为 550 nm 波长处硫酸盐-黑碳混合气溶胶粒子的质量散射系数（Q_s）、质量吸收系数（Q_a）以及质量消光系数（Q_e）随粒子等效半径的变化曲线，混合粒子中黑碳体积比为 25%。此处等效半径的意义按照混合方式有所不同：内混合的等效半径是指球心至混合粒子表面的距离；外混合的等效半径是指与粒子中各部分体积之和相等的球体之半径。

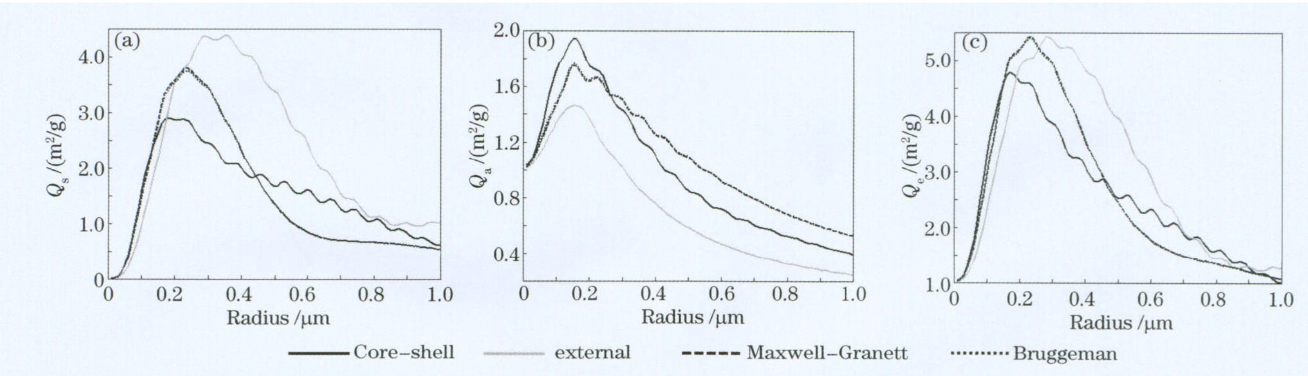

图 3　单个气溶胶粒子的光学性质（Q_s，Q_a 和 Q_e）

Fig. 3　Optical properties of single aerosol particles (Q_s, Q_a and Q_e)

一般来说米氏散射效率最大值出现在粒子直径约等于半波长时，因此过小和过大的粒子的米氏散射效率都较低，中间部分的粒子米氏散射效率最高。从图 3 可知，粒子等效半径对于粒子的散射、吸收乃至消光性质的影响趋势相似。混合气溶胶粒子的三种光学性质都随着等效半径的增长出现一个显著的上升和下降过程，除了 Maxwell-Garnett 模型和 Bruggeman 模型之间差异较小外，其他混合模型间的粒子光学性质差异明显。

质量散射系数的定义与质量吸收系数相似，表示了单位质量粒子对于辐射的散射作用。Core-shell 模型粒子的质量散射系数在半径小于 0.45 μm 的区间中小于 Maxwell-Garnett 模型和 Bruggeman 模型约 20%，而在大于 0.45 μm 的区间中则大于这两者约 30%；外混合粒子的质量散射系数在半径小于0.2 μm 的区间内与内混合粒子差异不大，但是在此后的区间

中则明显高于内混合粒子。除此之外，不同粒子质量散射系数的峰值所对应的半径也不相同，其中Core-shell模型混合粒子的峰值半径最小，约为0.18 μm；Maxwell-Garnett模型和Bruggeman模型粒子的峰值半径居中，约为0.24 μm；而外混合粒子的峰值半径最大，约为0.32 μm。造成峰值半径差异的原因主要在于不同模型中非吸收性成分的尺度差异：在Core-shell模型中，由于粒子的黑碳核心增大了硫酸盐外壳的外径，非吸收性成分的半径也因此扩大，所以导致散射系数峰值对应的半径比较小，但是由于多次散射过程中黑碳吸收了很大一部分辐射，因此Core-shell模型散射系数峰值最小；Maxwell-Garnett模型和Bruggeman模型将两种混合成分换算为另一种复折射指数介于黑碳和硫酸盐之间的等效介质，粒子的尺度仍然和Core-shell模型粒子保持一致，但散射性能有所降低，最大散射系数对应的半径有所提高，但是由于不存在透镜效应，所以散射系数的峰值明显高于Core-shell模型粒子；外混合粒子中由于黑碳和硫酸盐分别组成独立的球体，因此等效半径相同的粒子中非吸收性成分的尺度显著小于内混合粒子，从而散射系数峰值出现的位置也最靠后，但是外混合粒子各部分发生独立散射，遂使得其散射系数峰值也最高。

质量吸收系数表示的是吸收截面与粒子的质量之比，表示了单位质量该种混合粒子对于辐射的吸收作用。在质量吸收系数的图线中可以发现，在半径小于0.3 μm时Core-shell模型粒子的质量吸收系数高于Maxwell-Garnett模型和Bruggeman模型粒子，在此之后情况则恰好相反；在所有半径范围内，外混合粒子的质量吸收系数都小于内混合粒子。Core-shell模型粒子和外混合粒子的质量吸收系数峰值出现的位置是一致的，原因在于混合粒子的吸收作用绝大多数由黑碳造成，而这两种混合粒子的黑碳部分的半径相等；Maxwell-Garnett模型粒子和Bruggeman模型粒子的理论峰值半径应略大于Core-shell模型粒子，但是由于涟漪结构（由粒子衍射光和透射光相互干涉形成的光学性质曲线上有规律的起伏波动）的存在，使其实际峰值半径减小至和其他两种模型粒子大致相同。值得一提的是，随着等效半径趋近于0，粒子的质量吸收系数无限趋近于某一数值，这一数值与构成混合粒子的物质及波长均有关。

质量消光系数是质量吸收系数和质量散射系数之和，表示了单位质量的气溶胶粒子的消光能力。由图中可以看出在等效半径小于0.15 μm时，内混合模型粒子之间的质量消光系数差异很小，而在0.15～0.45 μm区间内，Maxwell-Garnett模型粒子和Bruggeman模型粒子的质量消光系数比Core-shell模型粒子高约15%，在之后的区间内，Core-shell模型粒子则比另外两者高约30%；外混合粒子的消光作用多数是由散射作用提供的，因此在等效半径大于0.3 μm的范围内，外混合粒子的消光系数明显地大于内混合粒子。

图4分别为不同混合方式下单个黑碳-硫酸盐混合粒子的单次散射反照率 ω 和不对称因子 g 随等效半径的变化规律。

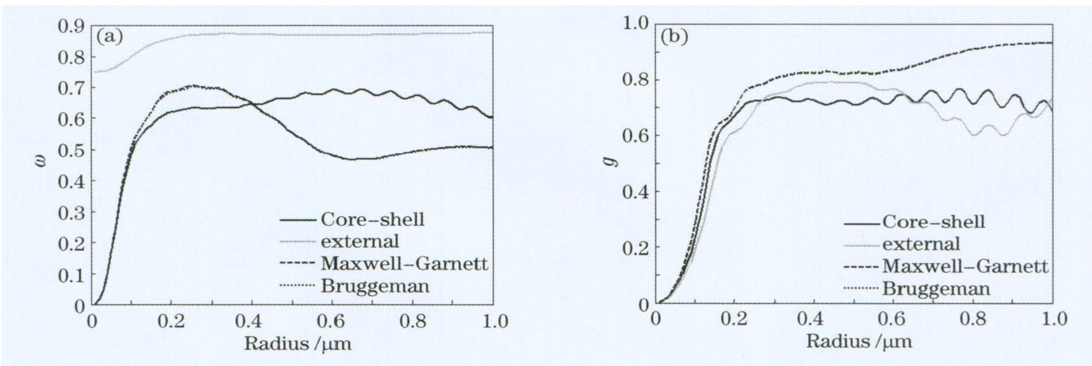

图4　单个气溶胶粒子的光学性质（ω 和 g）

Fig. 4　Optical properties of single aerosol particles (ω and g)

单次散射反照率是表征粒子散射消光占总消光中比例的一个参数，是散射截面与消光截面的一个比值。由图4可以发现外混合粒子的单次散射反照率显著地高于内混合粒子，其仅在0～0.2 μm的区间内随着等效半径的增长发生了约10%的增大，此后基本不出现波动；内混合粒子的单次散射反照率在0～0.2 μm的区间内快速上升，其中Core-shell模型粒子在0.2 μm以上的区间内单次散射反照率

大致保持不变，仅有细小的涟漪状波动，而 Maxwell-Garnett 模型粒子和 Bruggeman 模型粒子的单次散射反照率则会再经历一个显著的下降过程，最小值出现在 0.63 μm 处，相比最高值降低约 31%。

不对称因子是表征粒子前向和后向散射不对称性的参数，定义为散射角余弦的加权平均值，值域[−1,1]。不同混合模型粒子的不对称因子差异较小；等效半径 0～0.25 μm 是混合粒子不对称因子的快速上升区间；在 0.25～0.6 μm 的区间中不同模型混合粒子的不对称因子变化不大，且各自差异不超过 15%；在 0.6～1 μm 的范围内，Core-shell 模型粒子的不对称因子在 0.7 附近振荡式变化，外混合粒子经历一个振荡式下降并回升的过程，Maxwell-Garnett 模型粒子和 Bruggeman 模型粒子的不对称因子则随着等效半径增长略微升高约 13%。

总的来说，相对于 0.55 μm 波长，等效半径在 0～1 μm 范围内的变化会显著影响混合粒子光学性质：对于质量散射、吸收和消光系数的影响主要体现在 0～0.6 μm 内，均呈现出显著的先增大后减小规律；对于混合粒子的单次散射反照率与不对称因子，等效半径的影响则主要体现为 0～0.2 μm 内的快速增长过程。需要注意的是，等效半径对混合粒子光学性质的影响视物质构成和体积分数的不同会存在明显的差异。此外根据 2.1 节中计算的数浓度谱可以发现黑碳粒子主要集中于 0～0.4 μm 的半径区间，依照本节 0.25 的黑碳体积混合比换算成等效半径约为 0～0.64 μm，此后的区间内由于粒子个数稀少，等效半径对光学性质的影响并不具有显著的参考价值。

3.2　混合气溶胶光学特性随非吸收性物质体积分数的变化

图 5 表示了不同混合方式下气溶胶粒子群的质量吸收系数、质量散射系数和质量消光系数在550 nm 波长处随硫酸盐和有机碳体积分数的变化。从图 5(a)可见，由于硫酸盐和有机碳在可见光波段主要起散射作用，因此随着非吸收性物质体积分数的增长，内外混合粒子群的质量吸收系数都有明显减弱。外混合粒子群的质量吸收系数明显地小于内混合模型，尤其是在非吸收性成分体积分数超过 60%的情况下，外混合比内混合平均低了 82%，且外混合模型对于混合比的敏感性强于内混合模型。这一差异主要是因为内混合模型中透镜作用放大了黑碳对粒子光学性质的影响，因此内混合模型受非吸收性成分体积分数影响弱于外混合模型，尤其当黑碳体积分数较小时，透镜作用的影响非常明显。通过不同内混合模型结果之间的比较发现，Maxwell-Garnett 模型和 Bruggeman 模型得到的气溶胶吸收系数之间的差异在 1%以内，当外壳体积比达到 60%以上时 Core-shell 模型得到的气溶胶的吸收系数相比另外两者偏小 15%。

如图 5(b)所示，外混合粒子群的质量散射系数明显地高于其他模型，且不同模型间的变化呈现很大差异。从大趋势上看，内外混合粒子群的散射作用都随着硫酸盐和有机碳体积分数的增长呈现明显的下降趋势，造成降低的主要原因是等效复折射指数实部下降和粒子尺度增长。其中 Maxwell-Garnett 模型和 Bruggeman 模型粒子的质量散射系数下降较平稳，只是当体积分数大于 80%时下降幅度明显增大。Core-shell 模型和外混合模型粒子群质量散射系数都经历一个下降-增长-下降的过程，前者的表现更为明显，其两个极值点在 55%和 80%附近。造成这一差异的主要原因在于 Maxwell-Garnett 模型和 Bruggeman 模型是综合考虑了黑碳粒子处于不同位置得到的平均等效复折射指数。混合粒子趋向于均质化，粒子的光学性质不会出现明显的波动。Core-Shell 模型几何结构特殊，其中核心与外壳之间发生的多次散射过程会随着粒子各部分体积分数的变化发生改变并体现在粒子的散射系数上，造成明显的波动。外混合粒子群质量散射系数的第一个下降趋势是由于散射性能较弱的有机碳和硫酸盐体积分数逐渐增大造成的；随着粒子群众数直径逐渐接近半波长，米氏散射效率增大，造成了随后的质量散射系数的上升；最后的下降趋势则主要是质量和半径的增长共同影响的结果。Maxwell-Garnett 模型和 Bruggeman 模型粒子群之间质量散射系数的差异仍然很小，最大不超过 2%；Core-shell 模型在非吸收性成分体积比小于 70%时小于另外两者 9.6%，而在非吸收性成分体积比大于 70%时则比其他两者高约 7%。

由图 5(c)可见，Maxwell-Garnett 模型和 Bruggeman 模型得到的混合气溶胶粒子群的消光作用最强，但是这两者间的差异很小，可以忽略；Core-shell 模型的结果略小于前两者，差异平均为 4.9%；外混合粒子群的消光作用明显小于内混合粒子群，与 Core-shell 模型的差异最大达到 14.9%。从大趋势来看，混合粒子群质量消光系数的减弱与非吸收性成分体积分数的增长大致呈线性关系，各

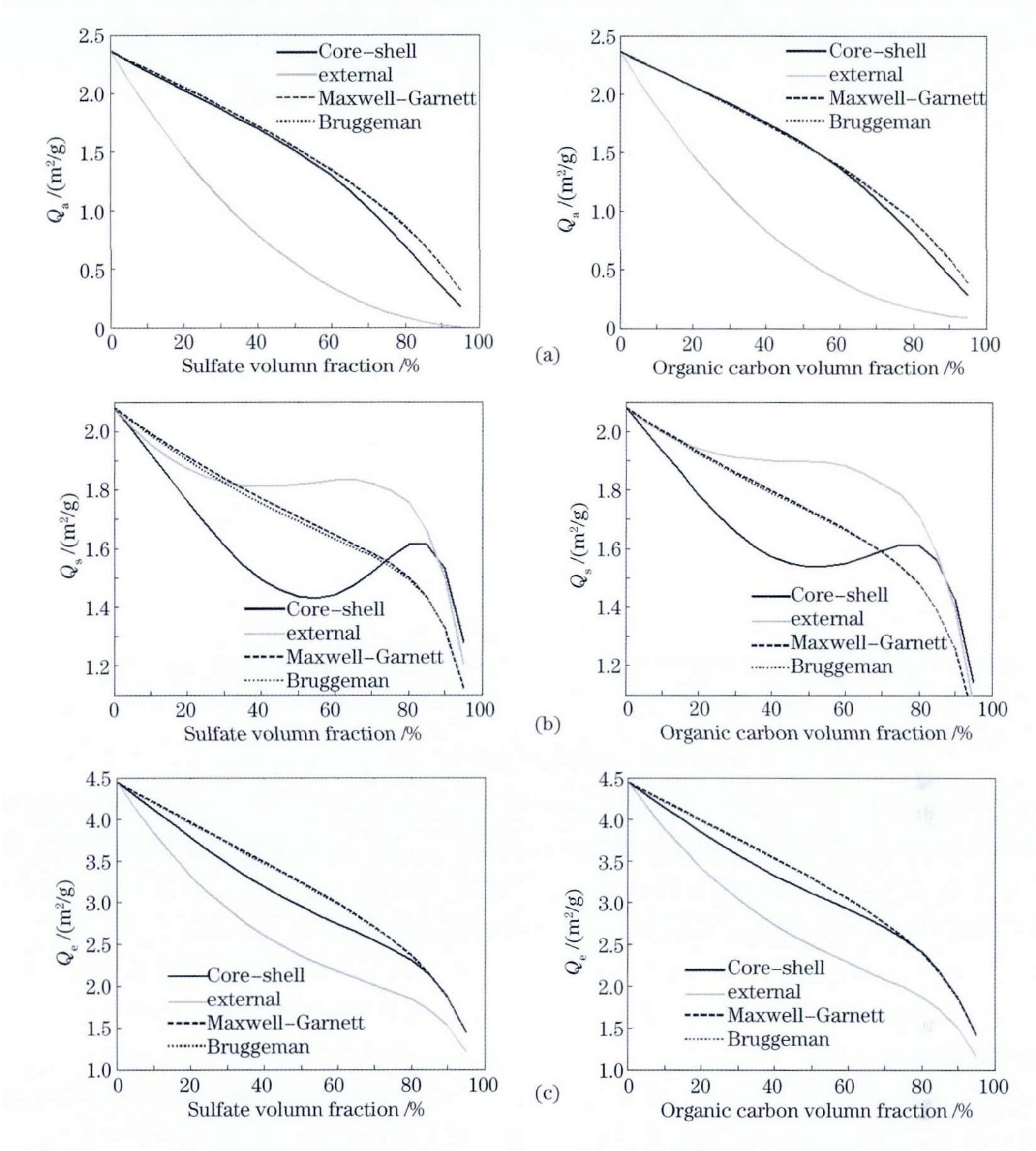

图 5　气溶胶粒子群光学性质随吸湿性物质体积分数的变化(Q_a，Q_s 和 Q_e)

Fig. 5　Change of optical properties of aerosol particle groups with the volume of the hygroscopic substance (Q_a，Q_s and Q_e)

个模型消光系数差异的最大值出现在黑碳体积分数 50%**左右。**

图 6 **表示了不同混合方式下气溶胶单次散射反照率和不对称因子随外壳体积分数的变化曲线。根据图** 6(a)**可知，外混合模型得出的粒子群单次散射反照率明显地高于内混合模型；**Maxwell-Garnett **模型和** Bruggeman **模型之间的差异依然很小，与** Core-shell **模型的平均差异为** 5.6%**。不同模型粒子群间单次散射反照率的差异主要出现在曲线右端，说明细小的黑碳核心对于混合粒子整体的单次散射反照率影响很大，而且黑碳不处于核心位置时对于粒子单次散射反照率的影响更明显。由于硫酸盐和有机碳在** 550 nm **波长的单次散射反照率接近于** 1**，因此在非吸收性成分占绝大多数时，外混合粒子群的单次散射反照率约等于** 1**。**

如图 6(b)**所示，随着非吸收性成分的体积分数的增长，外混合粒子群的不对称因子略微减小，**Maxwell-Garnett **模型和** Bruggeman **模型曲线先增大后减小，而** Core-shell **模型则呈现出正弦函数波动趋势，但是各模型的变化幅度都不大。不同模型间的差异主要体现在黑碳体积分数较小时，但差异的绝对值最大不超过** 0.12**。**

3.3　混合气溶胶的光学特性随相对湿度的变化

根据观测资料，东亚地区含有黑碳的混合气溶胶粒子半径与其中黑碳粒子的半径之比约为 1.6**。为了研究混合气溶胶粒子中非吸收性成分潮解作用**

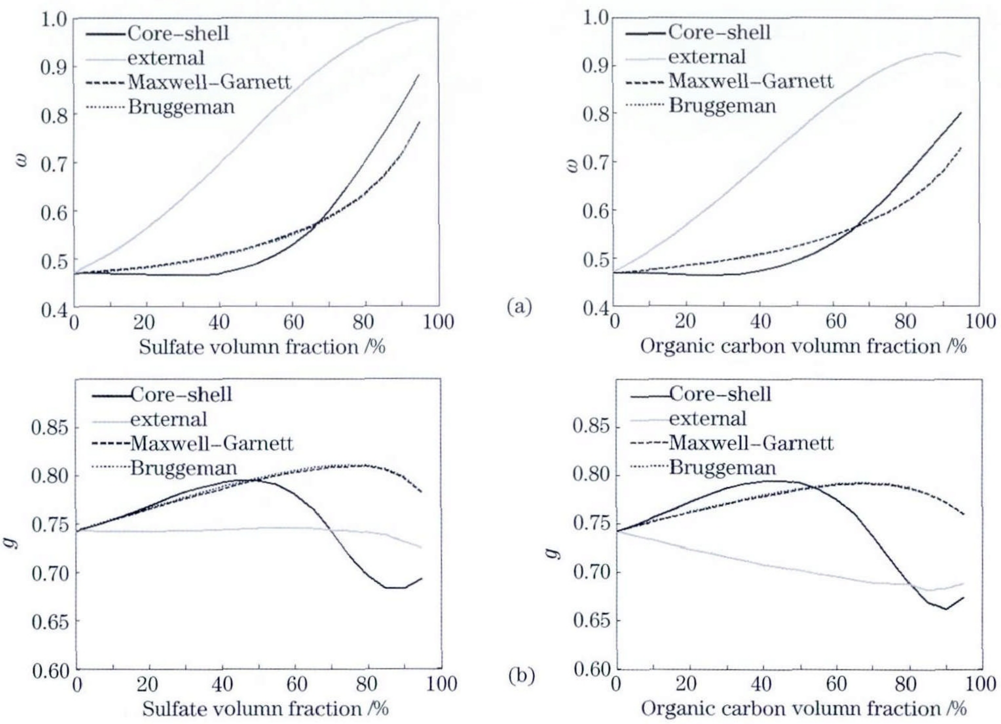

图 6　气溶胶粒子群光学性质随吸湿性物质体积分数的变化（ω 和 g）

Fig. 6　Change of optical properties of aerosol particle groups with the volume of the hygroscopic substance (ω and g)

对于混合气溶胶光学性质的影响，本组对比计算中将黑碳体积分数定为 25%（半径比约为 1.6），计算了 550 nm 波长不同相对湿度下的混合气溶胶光学性质。图 7 表示了不同混合方式下黑碳-硫酸盐和黑碳-有机碳混合气溶胶的质量吸收系数、质量散射系数和质量消光系数随相对湿度的变化。

从图 7(a)可知，除 Maxwell-Garnett 模型与 Bruggeman 模型粒子群间的质量吸收系数差异很小之外，其余模型间均存在明显的差异。外混合粒子群的质量吸收系数远小于内混合模型，因为外混合模型的整体性质是根据体积权重分配的，硫酸盐和有机碳在 550 nm 波长下的吸收系数接近于 0，而潮解过程会显著增大非吸收性成分的体积并在一定程度上减小其吸收能力；内混合模型中非吸收性成分对辐射起了会聚作用，提高了黑碳在混合粒子中的影响，因此吸收系数明显大于外混合模型。Maxwell-Garnett 模型和 Bruggeman 模型的质量吸收作用比 Core-shell 模型高约 25.8%，说明在黑碳体积比很小的情况下，随机分布的黑碳核对于混合粒子的光学性质影响明显高于处于球心位置的黑碳核。在达到吸湿性物质的潮解点之前，相对湿度对于气溶胶粒子群的光学性质没有影响，而达到潮解点之后对粒子群的质量吸收系数有越发明显的减弱趋势，主要原因是非吸收性成分与水汽混合后质量大幅上升，特别是相对湿度达到 90%以上时，粒子的质量呈指数形式上升，使单位质量的混合粒子的吸收截面显著减小。

由图 7(b)分析得，相对湿度在潮解点到 0.9 的区间内，随着非吸收性成分的体积增长各个模型粒子群质量散射系数随相对湿度呈现较为平稳的增长。外混合模型的变化幅度是四种模型中最小的，最大值出现在相对湿度 65%～70%之间。在未发生潮解前，不同内混合模型之间的质量散射系数差异很小，外混合模型则比内混合模型高 15.3%；发生潮解后，Core-shell 模型粒子群的质量散射系数增长最明显，比 Maxwell-Garnett 模型和 Bruggeman 模型高了 9.6%，在相对湿度 70%时超过外混合模型，并且在 85%～90%之间达到最大值。当相对湿度达到 90%以后，各个模型的质量散射系数都呈指数形式下降。图 7(c)的曲线比较平稳，可见大多数情况下粒子的质量消光系数和相对湿度的相关性不大。由于外混合粒子群的吸收作用大约只有内混合粒子的 20%，因此根据外混合模型求得的质量消光系数明显低于内混合模型；不同内混合模型间的差异不大，特别是有机碳-黑碳的组合，差异仅在 2%以内。当相对湿度小于 90%时，由于吸收和散射作用的变化趋势相互抵消，各个模型的质量消光系数没有明显的波动；而相对湿度达到 90%以后，混合气溶胶的

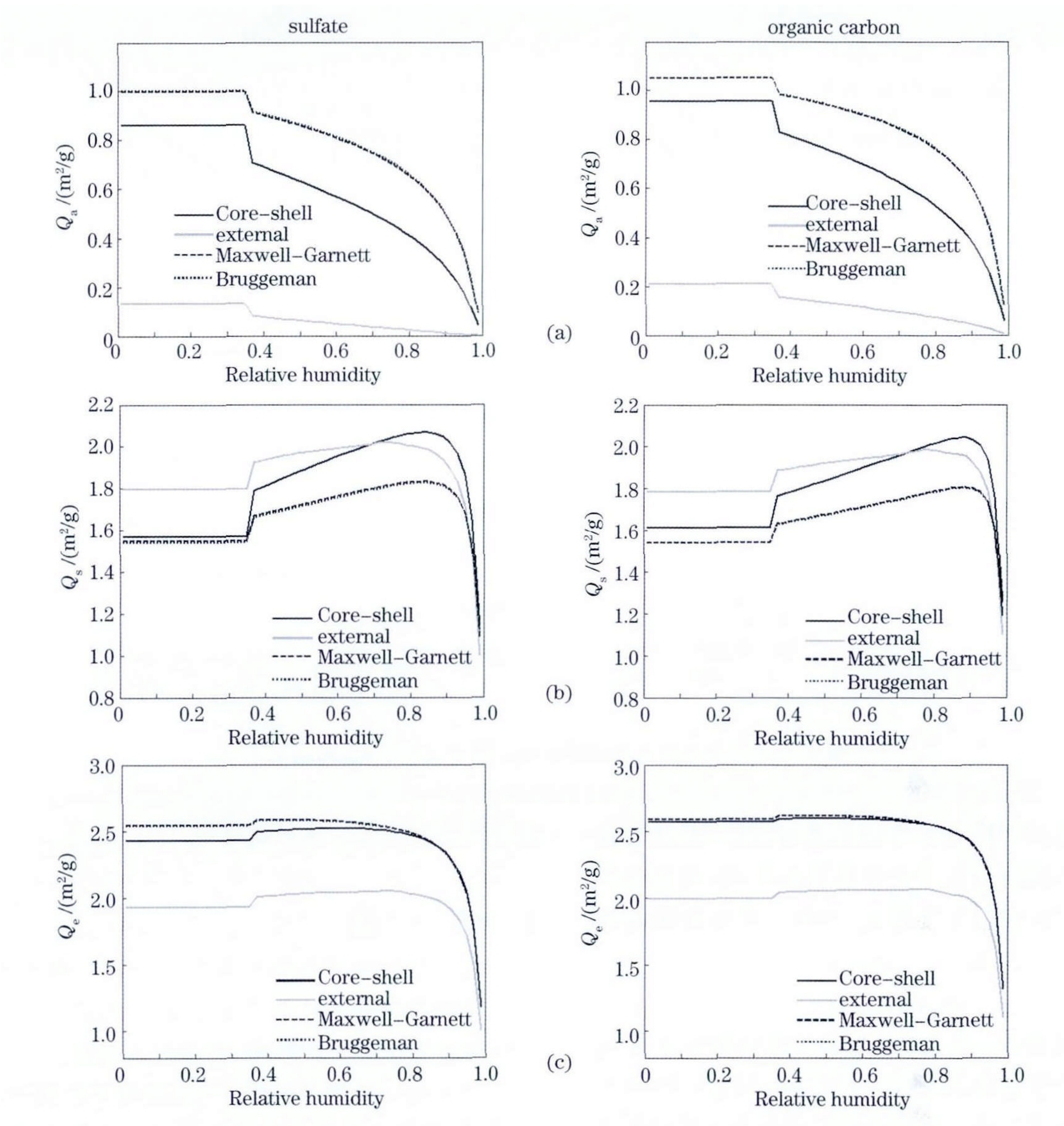

图 7　气溶胶粒子群光学性质随相对湿度的变化(Q_e，Q_a 和 Q_s)

Fig. 7　Change of optical properties of aerosol particle groups with relative humidity (Q_e, Q_a and Q_s)

质量消光系数大幅下降，最后粒子群的消光作用绝大部分都体现为散射。

图 8 给出不同混合方式下单次散射反照率和不对称因子与相对湿度的关系。由图 8(a)可知，单次散射反照率随着相对湿度的增长有明显的增大。干燥的内混合粒子群的初始值很接近；当相对湿度达到潮解点后，Core-shell 模型粒子群的单次散射反照率比 Maxwell-Garnett 模型和 Bruggeman 模型大了 11.9%。由于硫酸盐和有机碳的单次散射反照率接近于 1，因此外混合粒子群的单次散射反照率明显大于内混合粒子群且随相对湿度变化不明显，只有当黑碳占有较大的混合比时，外混合粒子的单次散射反照率才会对相对湿度表现敏感。

不对称因子对相对湿度的变化不敏感，Maxwell-Garnett 模型和 Bruggeman 模型最高，外混合模型则比 Core-shell 模型略高，且各种模型粒子群的不对称因子随相对湿度的变化十分平缓，最大差异不超过 10%。

四种混合模型各有优缺点和侧重面，受外界条件影响的程度也不尽相同。外混合模型能够处理多种气溶胶混合的情况，但是缺点也很明显：仅考虑了各部分的体积比重关系，忽略了粒子各部分间的多次散射，因此当非吸收性成分体积分数较大时，外混合模型的误差很大。内混合模型考虑了粒子内多次散射和几何特征的影响，显著地增强了混合粒子的吸收系数，但是内混合模型对于气溶胶的成分有一定要求且形成机制复杂，因此目前估计内混合在实际混合中出现的概率主要靠观测实现。Core-shell

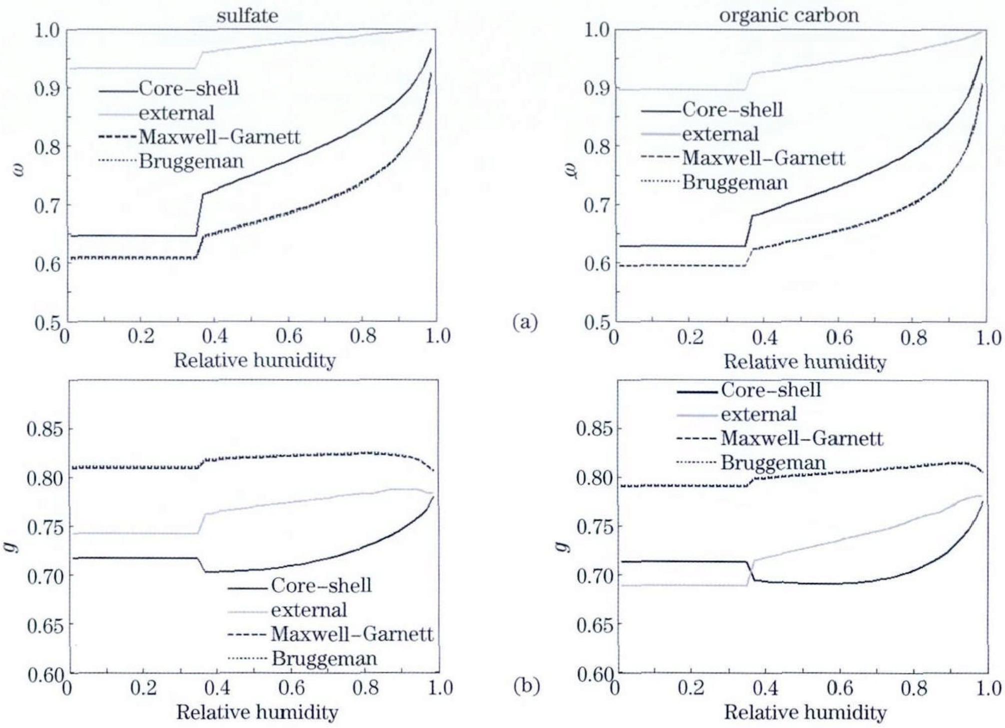

图 8　气溶胶粒子群光学性质随相对湿度的变化（ω 和 g）

Fig. 8　Change of optical properties of aerosol particle groups with relative humidity (ω and g)

模型的优势在于模拟了外壳的透镜效应，因此显著增强了核心物质对粒子光学性质的影响，但是这种模型的几何结构过于理想化，对粒子光学性质的计算结果缺乏普遍性。Maxwell-Garnett 模型和 Bruggeman 模型考虑了各部分物质在混合粒子中位置的随机分布，对于 Core-shell 模型中粒子几何结构过于理想化的问题有一定改善，但是这两种混合模型在计算过程中将混合粒子转化为等效均质球体，因此与实际情况还有一定差距。通过内混合模型的比较发现 Maxwell-Garnett 模型和 Bruggeman 模型得到的等效复折射指数差异往往非常小，粒子群的光学性质也基本一致，因此在气溶胶光学性质的计算中只需要假设两者中的一种。

讨论中涉及的内混合模型可以处理的物质种类较少，而且仅限于球形粒子，是比较基础且通用的模型，虽然不能完全真实客观地演算内混合气溶胶的光学性质，但是在现有的观测和理论设计能力下，也不失为计算混合粒子气溶胶光学性质的实用方法，比单纯假定的外混合方式更接近实际情况。希望在将来能借助更多的观测结果，在以下方面完善内混合气溶胶性质的研究：引入诸如多物质构成、多分层结构的复杂模型；使用多种等效介质原理，并引入 DDA 算法以求解混合气溶胶粒子簇的光学性质；利用 T 矩阵方法尝试将粒子外形的不对称性引入内混合气溶胶光学性质的演算中。

4　结　论

引入相对湿度和体积混合比两种影响因子，讨论了四种混合模型对黑碳-硫酸盐及黑碳-有机碳混合气溶胶光学性质的影响，得到以下结论。

对于同一种混合模型，气溶胶粒子群的质量吸收、散射和消光系数与非吸收性成分的体积比呈负相关性，单次散射反照率与其呈正相关性；相对湿度的增长对于粒子的质量吸收系数降低明显，并会大幅提高粒子的单次散射反照率。不同混合方式能显著影响气溶胶粒子群的光学性质：相对于外混合，内混合模型使粒子群的质量吸收系数增强了 20%以上，同时使质量散射系数降低了 10%～15%，并显著增强粒子群的质量消光系数；内混合模型对于单次散射反照率的减弱效果最为明显，尤其在黑碳体积小于 30%和相对湿度高于 70%的情况下，内混合模型使粒子群的单次散射反照率降低了 20%以上；三种内混合模型中，Maxwell-Garnett 模型与 Bruggeman 模型之间的差异很小，但是这两者与 Core-shell 模型在质量散射系数上存在较大的差异，当混合粒子各部分的体积分数相近时这一差异最明显。体积混合比和相对湿度的变化会对不同模型粒子群间质量散射系数的相对差异造成显著的影

响，此外相对湿度大于 90％是一个特殊的区间，在这个区间内粒子群的质量散射系数和质量消光系数会出现指数形式的降低。

参 考 文 献

1 Shi Guangyu, Wang Biao, Zhang Hua, *et al*.. The radiative and climatic effects of atmospheric aerosols [J]. Chinese J Atmospheric Sciences, 2008, 32(4): 826－840.
石广玉, 王 标, 张 华, 等. 大气气溶胶的辐射与气候效应[J]. 大气科学, 2008, 32(4): 826－840.

2 T C Bond, D G Streets, K F Yarber, *et al*.. A technology-based global inventory of black and organic carbon emissions from combustion [J]. J Geophys Res, 2004, 109(D14): D14203.

3 C Wang. A modeling study on the climate impacts of black carbon aerosols [J]. J Geophys Res, 2004, 109(D3): D03106.

4 Ma Jinghui, Zheng Youfei, Zhang Hua. The optical depth global distribution of black carbon aerosol and its possible reason analysis [J]. Scientia Meterologica Sinica, 2007, 27(5): 549－556.
马井会, 郑有飞, 张 华. 黑碳气溶胶光学厚度的全球分布与分析[J]. 气象科学, 2007, 27(5): 549－556.

5 Zhang Hua, Ma Jinghui, Zheng Youfei. The study of global radiative forcing due to black carbon aerosol [J]. Chinese J Atomospheric Sciences, 2008, 32(5): 1147－1158.
张 华, 马井会, 郑有飞. 黑碳气溶胶全球辐射强迫分布的模拟研究[J]. 大气科学, 2008, 32 (5): 1147－1158.

6 Wang Zhili, Guo Pinwen, Zhang Hua. A numberical study of direct radiative forcing due to black carbon and its effects on the summer precipitation in China [J]. Climatic and Environmental Research, 2009, 14(2): 161－171.
王志立, 郭品文, 张 华. 黑碳气溶胶直接辐射强迫及其对中国夏季降水影响的模拟研究[J]. 气候与环境研究, 2009, 14(2): 161－171.

7 Wang Zhili, Zhang Hua, Guo Pinwen. Effects of black carbon aerosol in south asia on summer monsoon [J]. Plateau Meteorology, 2009, 28(2): 419－424.
王志立, 张 华, 郭品文. 南亚地区黑碳气溶胶对亚洲夏季风的影响[J]. 高原气象, 2009, 28(2): 419－424.

8 Zhang Hua, Wang Zhili, Guo Pinwen, *et al*.. A modeling study of the effects of direct radiative forcing due to carbonaceous aerosol on the climate in East Asia [J]. Adv in Atmos Sci, 2009, 26(1): 57－66.

9 M Pósfai, J R Anderson, P R Buseck, *et al*.. Soot and sulfate aerosol particles in the remote marine troposphere [J]. J Geophys Res, 1999, 104(D17): 21621－21628.

10 Nicole Riemer, Matthew West, Rahil Zaveri, *et al*.. Estimating black carbon aging time-scales with a particle-resolved aerosol model [J]. Aerosol Science, 2010, 41(1): 143－158.

11 N Ma, C S Zhao, T Muller, *et al*.. A new method to determine the mixing state of light absorbing carbonaceous using the measured aerosol optical properties and number size distributions [J]. Atmos Chem Phys, 2012, 12(5): 2381－2397.

12 Mihály Pósfai, Renáta Simonics, Jia Li, *et al*.. Individual aerosol particles from biomass burning in southern Africa: 1. Compositions and size distributions of carbonaceous particles [J]. J Geophys Res, 2003, 108(D13): 8483.

13 S H Chung, J H Seinfeld. Global distribution and climate forcing of carbonaceous aerosols [J]. J Geophys Res, 2002, 107(D19): 4407.

14 M Sato, J Hansen, D Koch, *et al*.. Global atmospheric black carbon inferred from AERONET [J]. Proc Natl Acad Sci USA, 2003, 100(11): 6319－6324.

15 Su Xingtao, Wang Hanjie, Zhou Lin. A simulation study on temporal and spatial distribution characteristics and radiative forcing of organic carbon aerosols in China [J]. J Tropical Meteorology, 2010, 26(6): 765－772.
宿兴涛, 王汉杰, 周 林. 中国有机碳气溶胶时空分布与辐射强迫的模拟研究[J]. 热带气象学报, 2010, 26(6): 765－772.

16 Glen Lesins, Petr Chylek, Ulrike Lohmann. A study of internal and external mixing scenarios and its effect on aerosol optical properties and direct radiative forcing [J]. J Geophys Res, 2002, 107(D10): 4094.

17 Mark Z Jacobson. A physically-based treatment of elemental carbon optics: implications for global direct forcing of aerosols [J]. Geo Res Lett, 2000, 27(2): 217－220.

18 Zhang Xiaolin, Huang Yinbo, Rao Ruizhong. Equivalence of light scattering by one internal-mixed model for aerosol particles [J]. Acta Optica Sinica, 2012, 32(6): 0629001.
张小林, 黄印博, 饶瑞中. 一种内混合气溶胶粒子模型光散射的等效性 [J]. 光学学报, 2012, 32(6): 0629001.

19 Wei Xiaodong, Zhang Hua. Analysis of optical properties of nonspherical dust aerosols [J]. Acta Optica Sinica, 2011, 31(5): 0501002.
卫晓东, 张 华. 非球形沙尘气溶胶光学特性的分析 [J]. 光学学报, 2011, 31(5): 0501002.

20 Shao Shiyong, Huang Yinbo, Wei Heli, *et al*.. Phase function of prolate spheroidic mono-disperse aerosol particles [J]. Acta Optica Sinica, 2009, 29(1): 108－113.
邵士勇, 黄印博, 魏合理, 等. 单分散长椭球形气溶胶粒子的散射相函数研究 [J]. 光学学报, 2009, 29(1): 108－113.

21 Sun Xianming, Wang Haihua, Shen Jin. Study on light backscattering by spheroid with inclusion [J]. Acta Optica Sinica, 2011, 31(8): 0829001.
孙贤明, 王海华, 申 晋. 含核椭球粒子后向散射特性研究 [J]. 光学学报, 2011, 31(8): 0829001.

22 Chule E Chung, Kyunghwa Lee, Deltlef Müller. Effect of internal mixture on black carbon radiative forcing [J]. Tellus B, 2011, 63: 10925.

23 Lei Chengxin, Wu Zhensen, Feng Dongtai. Extinction characteristics of soot-silicate mixed agglomerates in random distribution [J]. Acta Optica Sinica, 2012, 32(4): 0429001.
类成新, 吴振森, 冯东太. 随机分布黑碳-硅酸盐混合凝聚粒子的消光特性研究 [J]. 光学学报, 2012, 32(4): 0429001.

24 M Shiraiwa, Y Kondo, N Motek, *et al*.. Radiative impact of mixing state of black carbon aerosol in Asian outflow [J]. J Geophys Res, 2008, 113(D24): D24210.

25 Wang Zhili. Simulation of Radiative Forcing of Typical Aerosols and Their Effects on Climate [D]. Beijing: Graduate University of the Chinese Academy of Sciences, 2011. 63－64.
王志立. 典型种类气溶胶的辐射强迫及其气候效应的模拟研究[D]. 北京: 中国科学院研究生院, 2011. 63－64.

26 Zhang Lisheng, Shi Guangyu. The impact of relative humidity on the radiative property and radiative forcing of sulface aerosol [J]. Acta Meteorologica Sinica, 2002, 60(2): 230－237.
张立盛, 石广玉. 相对湿度对气溶胶辐射特性和辐射强迫的影响[J]. 气象学报, 2003, 60(2): 230－237.

27 G A Niklasson, C G Granqvist, O Hunderi. Effective medium models for the optical properties of inhomogeneous materials [J]. Appl Opt, 1981, 20(1): 26－30.

栏目编辑: 李文喆

ATMOSPHERIC AND OCEANIC SCIENCE LETTERS, 2013, VOL. 6, NO. 3, 128–132

Evaluation and Preprocess of Chinese Fengyun-3A Sea Surface Temperature Experimental Product for Data Assimilation

ZHOU Wei[1], CHENG Yan-Jie[1], WANG Su-Juan[2], and WANG Zai-Zhi[1]

[1] *Beijing Climate Center, National Climate Center, China Meteorological Administration (CMA), Beijing 100081, China*
[2] *National Satellite Meteorological Center, CMA, Beijing 100081, China*

Received 2 November 2012; revised 4 December 2012; accepted 24 December 2012; published 16 May 2013

Abstract Validated satellite-derived sea surface temperatures (SSTs) are widely used for climate monitoring and ocean data assimilation systems. In this study, the Fengyun-3A (FY-3A) SST experimental product is evaluated using Advanced Very High Resolution Radiometer (AVHRR)-merged and in situ SSTs. A comparison of AVHRR-merged SSTs reveals a negative bias of more than 2 K in FY-3A SSTs in most of the tropical Pacific and low-latitude Indian and Atlantic Oceans. The error variance of FY-3A SSTs is estimated using three-way error analysis. FY-3A SSTs show regional error variance in global oceans with a maximum error variance of 2.2 K in the Pacific Ocean. In addition, a significant seasonal variation of error variance is present in FY-3A SSTs, which indicates that the quality of FY-3A SST could be improved by adjusting the parameters in the SST retrieval algorithm and by applying regional and seasonal algorithms, particularly in key areas such as the tropical Pacific Ocean. An objective analysis method is used to merge FY-3A SSTs with the drifter buoy data. The errors of FY-3A SSTs are decreased to –0.45K comparing with SST observations from GTSPP.

Keywords: FY-3A SST, satellite SST evaluation, AVHRR-merged SST, error analysis

Citation: Zhou, W., Y.-J. Cheng, S.-J. Wang, et al., 2013: Evaluation and preprocess of Chinese Fengyun-3A sea surface temperature experimental product for data assimilation, *Atmos. Oceanic Sci. Lett.*, **6**, 128–132.

1 Introduction

Sea surface temperature (SST) is an important indicator of climate variability. SST variation in the tropical Pacific Ocean is one of the most important indices of El Niño-Southern Oscillation (ENSO), which strongly affects the Asian monsoon and global climate change (Kawai and Kawamura, 1997). Therefore, global SST observations with high accuracy and fine resolution are necessary in climate research (Donlon et al., 2002). Satellite observations of the ocean that provide global coverage and high-accuracy measurements of SST have become the primary tool for studying SST variability.

Satellite-derived SST products are available in two types, infrared and microwave sensors, according to the sensors equipped on the satellites. Infrared sensors, which include the Advanced Very High Resolution Radiometer (AVHRR), are affected by clouds and volcanic aerosols in the atmosphere (Guan and Kawamura, 2003; Reynolds, 1993). Microwave sensors are unaffected by these factors but are influenced by others such as wind speed and rain rate (Qiu et al., 2009; Reynolds, 1993). Chinese Fengyun-3A (FY-3A), a second-generation polar-orbiting satellite launched in May 2008 (Zou et al., 2011), provides both types of satellite-derived SST products with 11 instruments including the Visible and Infrared Radiometer (VIRR) and MicroWave Temperature Sounder (MWTS).

As the amount of FY-3A SST experimental products increase, it becomes increasingly important to employ them in climate research and ocean data assimilation systems (Tang et al., 2004; Zheng et al., 2006, Zheng and Zhu, 2010). However, it is necessary to validate the accuracy of satellite-derived SSTs in the FY-3A product before assimilated into the ocean model. Currently, the number of available in situ ocean observations is increaseing, which also increases the reliability of satellite SST validation results. In this study, we evaluate the first distributed FY-3A SST experimental product with in situ observations to detect errors and provide insight to improve the quality of the final product prior to its public release. In addition, an objective analysis method is used to merge the FY-3A SSTs and in situ observations.

2 Description of SST datasets

2.1 FY-3A SST

The evaluated FY-3A SSTs include VIRR SST products. VIRR contains two infrared channels in wavelength ranges of 10.3–11.3 μm (channel 4) and 11.5–12.5 μm (channel 5). The multichannel sea surface temperature (MCSST) algorithm was used to retrieve SSTs with accuracy of 1.0–1.5 K (Dong et al., 2009). The FY-3A SST measurements are based on radiance measurements from a VIRR sensor onboard the FY-3A polar orbiting satellite. These radiances were collected by FY-3A ground stations and were post-processed to produce MCSST estimates. A detailed description of the methodology for producing MCSST observations is given by McClain et al. (1985). The FY-3A data are supplied as an averaged clear-sky radiance product with a spatial resolution of 1.1 km. The daily averaged product was stored as an Hierarchical Data Format 5 (HDF5) data type and was used to decrease the match-up time window of the five-day, 10-day, and monthly averaged products.

Corresponding author: ZHOU Wei, zhouwei@cma.gov.cn

2.2 AVHRR merged product

We used the AVHRR merged product (ftp://eclipse.ncdc.noaa.gov/pub/OI-daily/) created through optimal interpolation (OI) to investigate the spatial distribution of bias in the FY-3A product. The spatial grid resolution was 0.25°, and the temporal resolution was one-day (Reynolds et al., 2007). Two available products are based on the merging of in situ observations of different satellite products to adjust satellite biases. One employs satellite infrared data from AVHRR, and the other uses both AVHRR and satellite microwave data from the Advanced Microwave Scanning Radiometer (AMSR). In this study, we used the AVHRR-only product to compare with FY-3A SSTs, which is provided from January 1985 to the present. Further details can be found in Reynolds et al. (2007).

2.3 The Global Temperature and Salinity Profile Program (GTSPP)

GTSPP is an international operational activity designed to provide timely access to the highest quality, highest resolution temperature and salinity profile data available (http://www.nodc.noaa.gov/GTSPP/). The primary goal of the GTSPP is to conduct global measurements of ocean temperature and salinity and to offer quick and easy access to the results. The GTSPP handles all temperature and salinity profile data, which include observations by using water samplers and continuous profiling instruments such as Argo floats and other devices to measure conductivity, temperature, and depth (CTDs) (Chu, 2011). Including the Argo floats data, the yearly number of temperature and salinity profiles was approximately 1.7 million in 2009. Quality control of the GTSPP data is divided into real-time and delayed-time modes and is handled by various offices (Sun et al., 2009). We downloaded real-time GTSPP data from the Internet to obtain further quality control and more reliable in situ SSTs.

3 Validation methods and results

3.1 Comparisons of FY-3A and AVHRR SSTs

To examine simple quality control for the FY-3A SSTs data, we calculated the area-mean (MEANa) and standard deviation (STDa) of available satellite derived SSTs in each area of 0.25°×0.25°. When an absolute value of (SST-MEANa) was greater than twice the STDa, the SST observation was discarded. The selected FY-3A SSTs were then interpolated linearly onto AVHRR grids with spatial resolution of 0.25° to reduce high resolution of the FY-3A SST product.

Availability of FY-3A SSTs was defined as the ratio of the number of available FY-3A SSTs to the total number of ocean grid points in the AVHRR grids (Qiu et al., 2009). The monthly mean SST availabilities of FY-3A SSTs were in the range of 24.1%–29.3% with an annual mean value of 26.5% (not shown). The daily availability of FY-3A SSTs changed significantly during February 2012, which may have been caused by the process of cloud detection. The distributions of annual mean AVHRR-merged SSTs and FY-3A SSTs, shown in Figs. 1a and 1b respectively, indicate that the FY-3A SSTs were cooler than AVHRR-merged SSTs. The difference between these two satellite products was investigated by subtracting AVHRR-merged SSTs from FY-3A SSTs (Fig. 1c). A cool bias of more than 2 K was present in most of the tropical Pacific and low-latitude Indian and Atlantic Oceans in the FY-3A SSTs. However, a 2 K warm bias was present in the Arctic waters. The difference in these two products was relatively smaller in middle-latitude oceans. Thus, the SST retrieval algorithm could be improved by using an area-dependent algorithm in the future.

3.2 Comparisons of satellite-derived and in situ SSTs

In situ SST observations are used to assess the accuracy of FY-3A and AVHRR-merged SSTs and to confirm actual cool/warm bias in FY-3A. The in situ SST observations were obtained from GTSPP. A matchup database among FY-3A, AVHRR-merged, and in situ observed SSTs containing collocated observations was produced. We averaged the SST observations from GTSPP within each AVHRR grid (0.25°×0.25°) for daytime (7:00–19:00

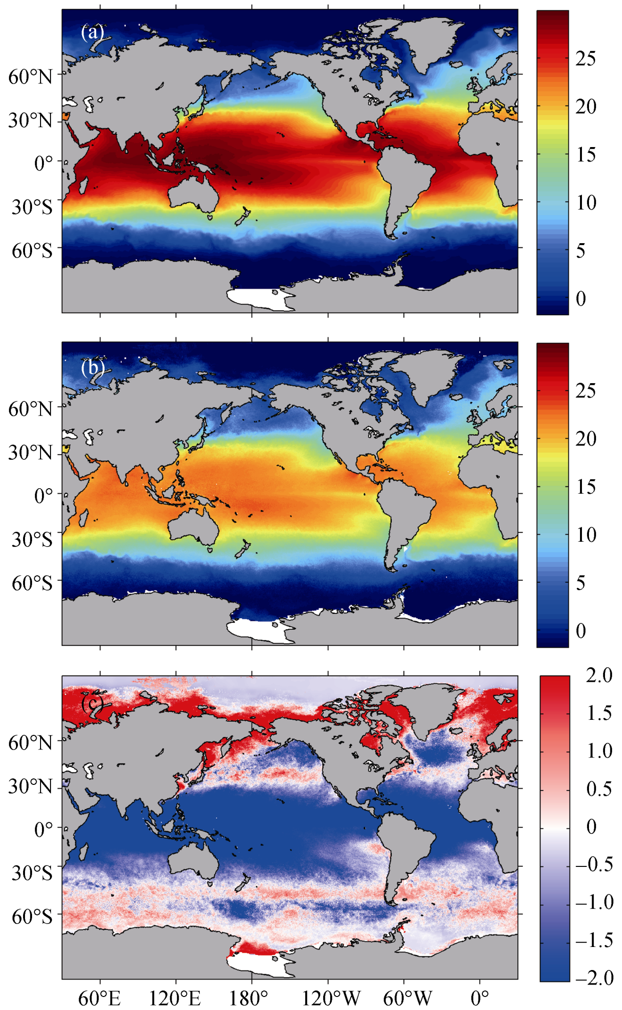

Figure 1 Annual mean (a) AVHRR-merged SSTs, (b) FY-3A SSTs, and (c) difference between AVHRR-merged and FY-3A SSTs during the period of 1 April 2011 to 1 April 2012.

LT) to correlate with FY-3A and AVHRR-merged SSTs, which is similar to the method used by Qiu et al. (2009).

The relationship between the satellite-derived and in situ SSTs is shown in Fig. 2. FY-3A SSTs had a negative bias in the range of approximately 25–31 K and both negative and positive bias in the range of approximately 15–22 K. The range of approximately 0–5 K was observed more in AVHRR-merged SSTs than that in FY-3A SSTs. Mean bias±STD of FY-3A and AVHRR-merged SST was –2.77±1.65 K and –0.01±0.47 K, respectively. The bias and STD of AVHRR-merged SST were smaller than those of FY-3A. The monthly variation of biases between the satellite-derived SSTs and in situ observations is shown in Fig. 3. The bias of FY-3A SSTs was negative at approximately –3 K and did not exhibit obvious seasonal variations. In contrast, AVHRR-merged SSTs showed a small positive bias from March to April 2012 and a smaller negative bias in other months. Although FY-3A SSTs were not merged in the in situ observations as AVHRR SSTs, the error in FY-3A SSTs is significantly large; thus, the algorithm of FY-3A SSTs should be improved in the future.

3.3 Error analysis

It is important to understand of the error characteristics of FY-3A SSTs before they are used in global ocean data assimilation. Following (O'Carroll et al., 2008), the error variance in the FY-3A, AVHRR-merged, and in situ observed SSTs can be estimated from the observation difference statistics, assuming the errors of these three observation types are unrelated. A set of simultaneous equations for estimating the error variances σ_i^2 for observation type i (where i = 1, 2, or 3) for an ensemble of collocations of observation triplets:

$$\begin{cases}\sigma_1 = [(V_{12}+V_{31}-V_{23})/2]^{1/2} \\ \sigma_2 = [(V_{23}+V_{12}-V_{31})/2]^{1/2} \\ \sigma_3 = [(V_{31}+V_{23}-V_{12})/2]^{1/2}\end{cases}, \quad (1)$$

where V_{ij} is the variance of the difference between observation types i and j. Types 1, 2, and 3 denote FY-3A, AVHRR-merged, and in situ SSTs, respectively. Detailed derivation can be found in O'Carroll et al. (2008).

To determine the regional error for these observation types and to develop the area-dependent algorithm for FY-3A SSTs, we estimated the error variance in the Pacific Ocean, Indian Ocean, North Atlantic Ocean, and South China Sea. The estimated error variances of these three observation types are summarized in Table 1. Error variance differences were significant in specific areas for FY-3A SSTs, with the maximum (minimum) error variance existing in the Pacific Ocean (North Atlantic Ocean). The difference between maximum and minimum values of error variance reached up to 0.5 K, while the regional error variance difference in AVHRR-merged SSTs was smaller. The error of in situ observation was less than 0.5 K, and the largest error existed in the South China Sea, which may be related to complex observing conditions and relatively fewer observations. In addition, the seasonal variation in error variance of FY-3A SSTs was significant, particularly in the boreal winter and autumn, which was also detected in AVHRR-merged SSTs. The regional and seasonal variations of error variance in FY-3A SSTs were obvious, which encourages the development of regional and seasonal SST retrieval algorithms, particularly in key area such as the tropical Pacific Ocean.

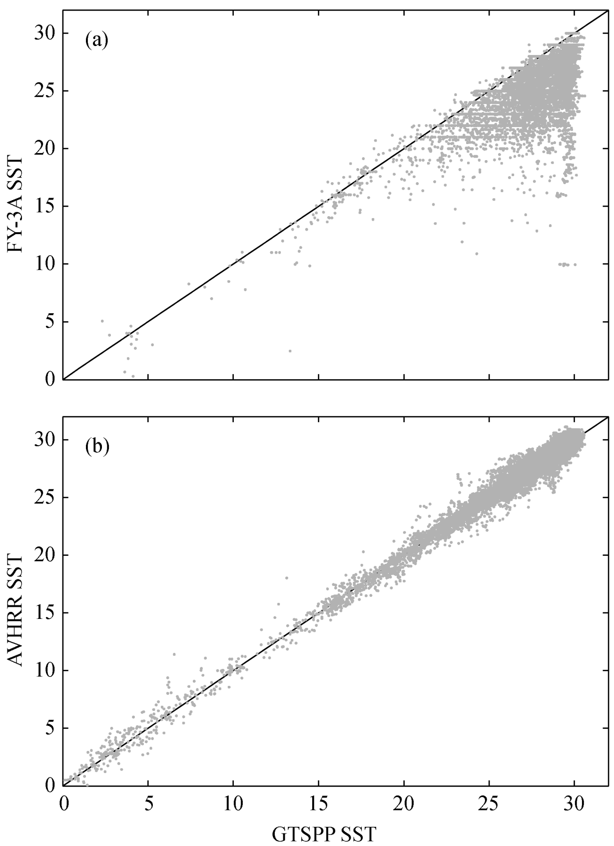

Figure 2 Scatter diagrams of (a) FY-3A and GTSPP SSTs and (b) AVHRR and GTSPP SSTs. Black lines indicate satellite SSTs equal to GTSPP SSTs (units: °C).

4 Merging FY-3A SSTs with drifter buoy data

A global operational SST product with appropriate resolution in space and time is required in the global ocean data assimilation system. The quality of FY-3A SSTs should be improved before they can be assimilated

Table 1 Seasonal and regional error variance of FY-3A, AVHRR-merged, and GTSPP.

Season/area	Number of matchups	FY-3A	AVHRR-merged	GTSPP
Winter	15960	1.75	0.57	0.15
Spring	21293	1.85	0.34	0.35
Summer	24032	2.04	0.21	0.34
Autumn	20165	2.73	0.08	0.27
Pacific Ocean	64736	2.23	0.21	0.31
Indian Ocean	10387	2.08	0.24	0.29
Atlantic Ocean	1454	1.70	0.52	0.41
South China Sea	332	1.81	0.31	0.52

in the second generation of the Global Ocean Data Assimilation System of the Beijing Climate Center (BCC_GODAS2.0). A relatively simple method used to decrease the errors of FY-3A SSTs is the merging of these temperatures with drifter buoy SSTs (http://www.meds-sdmm.dfo-mpo.gc.ca/isdm-gdsi/index-eng.html). The system errors are partly eliminated by calculating the difference between monthly averaged FY-3A and AVHRR-merged SSTs. Objective analysis is then applied to merge the FY-3A and drifter buoy SSTs to further decrease the errors, which is similar to the method introduced by Guan and Kawamura (2003):

$$X_a = X_b - \boldsymbol{Err} + \boldsymbol{W}[y - H(X_b - \boldsymbol{Err})], \quad (2)$$

where X_a is the estimated SST; X_b is FY-3A SSTs evaluated in the previous sections; $\boldsymbol{Err}$ is the system error matrix determined by computing the difference between monthly averaged FY-3A and AVHRR-merged SSTs; y is the quality-controlled SST observations from drifter buoy data; H is the observation operator which interpolates the (X_b–$\boldsymbol{Err}$) into the locations of y; and $\boldsymbol{W}$ is the weighting matrix.

Considering that various SST data are available with irregular spatial and temporal gaps from drifter buoy data, the weighting matrix $\boldsymbol{W}$ is given by:

$$\boldsymbol{W} = \exp(-r_{i,j}^{\,2}/2), \quad (3)$$

$$r_{i,j}^{\,2} = \frac{d_{i,j}^{\,2}}{L^2} + \frac{\Delta t_{i,j}^{\,2}}{T^2}, \quad (4)$$

where $d_{i,j}$ and $\Delta t_{i,j}$ are the spatial distance and temporal difference between the estimation and observation data, respectively, and L and T are spatial and temporal correlation scales, which are set to 1° and five days.

FY-3A and drifter buoy data obtained during one year from April 2011 to March 2012 were merged. However, those from high-latitude oceans in excess of 60° were exempted because they offer few observations and are influenced by sea ice. The in situ SSTs from GTSPP were used to evaluate the accuracy of the merged SST products. Figure 4 shows the comparison of merged and buoy 10-day mean SSTs. The errors of FY-3A were obviously decreased, and the biases between the FY-3A and GTSPP SSTs were decreased from –2.77 to –0.45 K.

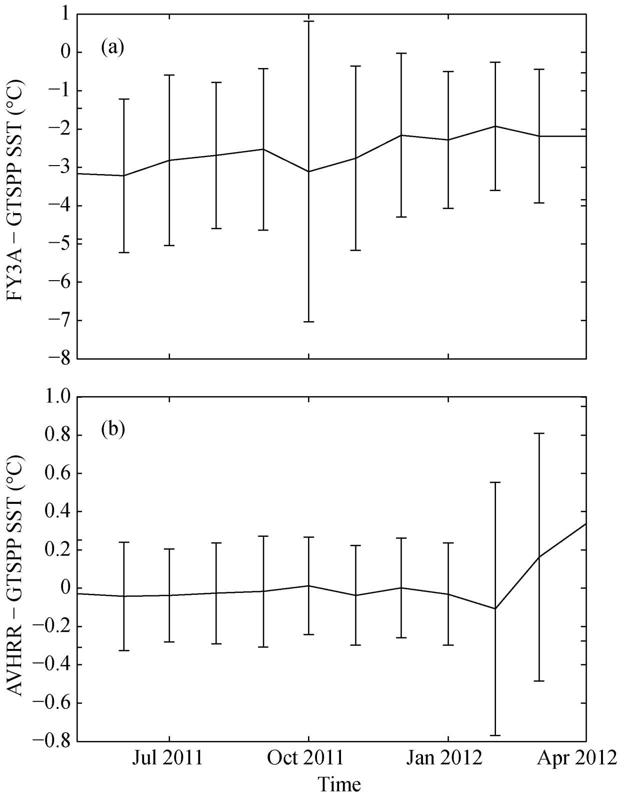

Figure 3 Monthly bias and standard deviations of (a) FY-3A and (b) AVHRR against GTSPP SSTs during the period of 1 April 2011 to 1 April 2012.

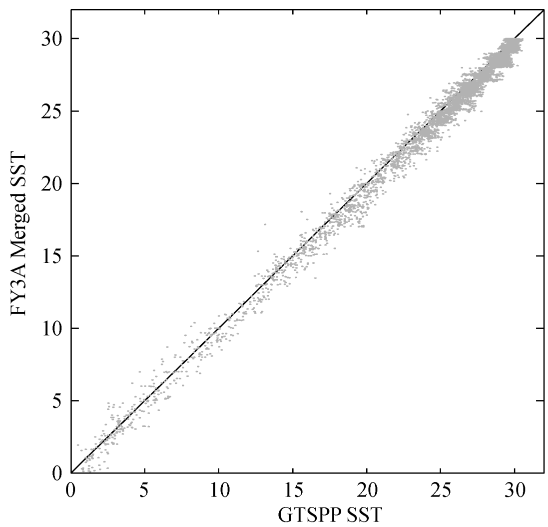

Figure 4 Comparison of FY-3A merged and GTSPP 10-day mean SSTs from April 2011 to March 2012 (units: °C).

5 Conclusions

FY-3A SST experimental product was quantitatively evaluated for one year from April 2011 to April 2012 in global oceans by using AVHRR-merged SSTs and in situ SST observations from the GTSPP. A comparison of AVHRR-merged SSTs revealed a negative bias of more than 2 K for FY-3A SSTs in the tropical Pacific and Indian Oceans and a positive bias of 2 K in the Arctic waters. Validation of the two satellite-derived SSTs by using in situ observations showed that the mean bias±STD of FY-3A and AVHRR-merged SST were –2.77±1.65 K and –0.01±0.47 K, respectively. The FY-3A SSTs exhibited regional error variance in the global oceans with a maximum error variance of 2.2 K. The regional and seasonal differences between the maximum and the minimum value of error variance were more than 0.5 K, which indicates that the quality of FY-3A SST could be improved by adjusting parameters in the SST retrieval algorithm and by applying regional and seasonal algorithms. An objective analysis method was used to merge FY-3A SSTs with the drifter buoy data. The errors of FY-3A SSTs were decreased to –0.45 K over SST observations from the GTSPP. The FY-3A SST product merged by using the objective analysis method is only a substitute for global ocean data assimilation with an improved FY-3A SST product, including a new retrieval algorithm, which will be released in the near future.

Acknowledgements. The authors wish to thank two anonymous reviewers and Dr. Qingtao SONG and Dr. Fei ZHENG for their very helpful comments, which helped us to improve the manuscript significantly. This research is supported by the National Basic Research Program of China (973 Program, Grant Nos. 2010CB951902 and 2011CB403505), the National Key Technologies R&D Program of China (Grant No. 2009BAC51B03), and the National Natural Science Foundation of China (Grant No. 41106003).

References

Chu, P., 2011: Global upper ocean heat content and climate variability, *Ocean Dyn*., **61**, 1189–1204.

Dong, C., J. Yang, Z. Yang, et al., 2009: An overview of a new Chinese weather satellite FY-3A, *Bull. Amer. Meteor. Soc.*, **90**, 1531–1544.

Donlon, C. J., P. J. Minnett, C. Gentemann, et al., 2002: Toward improved validation of satellite sea surface skin temperature measurements for climate research, *J. Climate*, **15**, 353–369.

Guan, L., and H. Kawamura, 2003: SST availabilities of satellite infrared and microwave measurements, *J. Oceanogr.*, **59**, 201–209.

Kawai, Y., and H. Kawamura, 1997: Characteristics of the satellite-derived sea surface temperature in the oceans around Japan, *J. Oceanogr.*, **53**, 161–172.

McClain, E. P., W. G. Pichel, and C. C. Walton, 1985: Comparative performance of AVHRR-based multichannel sea surface temperatures, *J. Geophys. Res*., **90**, 11587–11601.

O'Carroll, A. G., J. R. Eyre, and R. W. Saunders, 2008: Three-way error analysis between AATSR, AMSR-E, and in situ sea surface temperature observations, *J. Atmos. Oceanic Tech.*, **25**, 1197–1207.

Qiu, C., D. Wang, H. Kawamura, et al., 2009: Validation of AVHRR and TMI-derived sea surface temperature in the northern South China Sea, *Conti. Shelf Res.*, **29**, 2358–2366.

Reynolds, R. W., 1993: Impact of mount pinatubo aerosols on satellite-derived sea surface temperatures, *J. Climate*, **6**, 768–774.

Reynolds, R. W., T. M. Smith, C. Liu, et al., 2007: Daily high-resolution-blended analyses for sea surface temperature, *J. Climate*, **20**, 5473–5496.

Sun, L. C., A. Thresher, R. Keeley, et al., 2009: The data management system for the Global Temperature and Salinity Profile Program (GTSPP), in: *Proceedings of the "OceanObs'09: Sustained Ocean Observations and Information for Society" Conference (Vol. 2)*, J. Hall et al. (Eds.), ESA Publication WPP-306, Venice, 21–25 September 2009, doi:10.5270/OceanObs09.cwp.86.

Tang, Y., R. Kleeman, and A. M. Moore, 2004: SST Assimilation experiments in a tropical pacific ocean model, *J. Phys. Oceanogr.*, **34**, 623–642.

Zheng, F., and J. Zhu, 2010: Coupled assimilation for an intermediated coupled ENSO prediction model, *Ocean Dyn.*, **60**, doi: 10.1007/s10236-010-0307-1.

Zheng, F., J. Zhu, R.-H. Zhang, et al., 2006: Ensemble hindcasts of SST anomalies in the tropical Pacific using an intermediate coupled model, *Geophys. Res. Lett.*, **33**, doi:10.1029/2006GL026994.

Zou, X., X. Wang, F. Weng, et al., 2011: Assessments of Chinese Fengyun Microwave Temperature Sounder (MWTS) measurements for weather and climate applications, *J. Atmos. Oceanic Tech.*, **28**, 1206–1227.

基于三层嵌套网格的珠江口冬季盐度层化的数值模拟*

周　巍[1]　王东晓[2]　俎婷婷[2] ①　李海洋[2,3]　肖贤俊[1]

(1. 国家气候中心　中国气象局气候研究开放实验室　北京　100081; 2. 中国科学院南海海洋研究所热带海洋环境国家重点实验室　广州　510301; 3. 广州市南沙区气象局　广州　511458)

提要　运用三层嵌套网格的 ROMS 模式较好地模拟了 2009 年冬季珠江口的主要水动力过程和盐度分布。结果表明, 珠江口盐度层化具有明显的潮周期变化特征, 涨潮时表底层盐度差较小, 层化较弱; 落潮时层化较强。利用势能异常变化平衡方程分析影响层化的贡献项, 结果表明势能异常的平流项和应变项是影响珠江口势能异常变化的主要因素。

关键词　ROMS 模式; 盐度层化; 势能异常; 珠江口
中图分类号　P731

近几十年来, 由于人口增长及经济发展, 大量陆源污染物和营养盐排入珠江口, 导致水质恶化, 给珠江河口及其沿岸地区的水域带来前所未有的污染。此外由于冬季径流量小, 潮汐混合作用增强, 盐水入侵的问题很严重, 这直接影响 1500 多万人的供水安全以及工农业生产。对于盐水入侵和污染物扩散问题的治理, 需要对其物理机制进行深入地分析。层化的强度直接影响进入河口的海水体积(Dyer, 1997; Chen *et al*, 2009), 因而探讨影响珠江口水体层化的物理机制有利于掌握珠江口盐水入侵过程。

经典的河口层化理论阐述的是由经向盐度梯度产生的重力环流与潮汐混合之间的竞争关系(Hansen *et al*, 1965)。其中 Pritchard(1952)按河口的分层特点和盐度的分布状况将河口类型划分为盐水楔河口、部分混合河口和强混合河口。Hansen 等(1966)使用两个无量纲参数描述河口: 分层参数 $\delta S/S_0$ 和环流参数 U_s/U_{t0}, 其中 δS 表示表底层盐度差, S_0 表示断面平均盐度, U_s 是表层流速, U_{t0} 是垂向平均流速, 并据此提出了分层-环流河口分类图。随着观测手段的提高和数值模式的发展, 近年来学者们越来越重视潮汐剪切对盐度层化影响的研究(Jay *et al*, 1990; Lacy *et al*, 2003; Sanay *et al*, 2007)。Simpson 等(1990)观测到涨潮时水体混合良好, 而退潮时水体层化增强, 他将这种现象称作“应变导致的周期性层化”, 并首次提出潮汐应变的概念。Nepf 等(1996)在 Hudson 河口观测到潮汐应变在退潮时维持层化, 而在涨潮时促进底边界层附近的均匀混合, 靠近河床最强和最弱的层化通常发生在退潮和涨潮的末尾。Stacey 等(2001)发现潮汐混合和层化在一个潮周期内存在涨-落潮不对称, 表现在涨潮时底边界层剪切使河口环流减小, 层化减弱; 退潮时, 底边界层剪切使河口环流增强, 层化增强。Stacey 等(2005)指出潮汐应变只发生在底边界层。Geyer 等(2000)在 Hudson 河口发现涨潮时的涡动粘性系数是落潮时的两倍。Li 等(2009)探讨了层化在涨-落潮过程和大、小潮周期内的变化, 并指出盐度、速度和垂向扩散系数的垂向剖面在涨潮和落潮期间有明显的差异, 涨潮比落潮时的垂向混合更强。Cudaback 等(2000)发现退潮时底边界层的垂向剪切增强, 而涨潮时垂向剪切减弱。退潮时由于较强的剪切不稳定使得密跃层的厚度变厚, 而涨潮时变薄。

* 国家重点基础研究发展计划(973)项目, 2011CB403505 号; 国家自然科学基金青年科学基金项目, 41006012 号; 中国科学院南海海洋研究所青年人才领域前沿项目, SQ201002 号。周巍, 博士, E-mail: zhouwei@cma.gov.cn
① 通讯作者: 俎婷婷, 博士, E-mail: zutt@scsio.ac.cn
收稿日期: 2011-08-16, 收修改稿日期: 2012-01-15

目前珠江口盐度层化的研究主要集中在对观测资料的分析，如应秩甫(1983)利用 1978—1979 年现场实测资料，以混合指数、分层系数、淡水分值及分层-环流图和盐度的横向分布等来表征珠江口伶仃洋咸淡水混合特征，发现伶仃洋是一个垂直缓混合的河口，但有横向盐度的梯度，其东西航道各测点在洪季一般分层较好，枯季为缓混合型。赵焕庭(1990)也探讨了珠江河口湾的咸淡水混合特征，他指出珠江口汛期表层盐度等值线呈 NE—SW 走向，枯季盐度等值线中间略弯曲，呈“S”形。枯季，东槽属于缓混合型，西槽属于强混合型。汛期，东潮呈高度成层型，西槽呈缓混合型。包芸等(2005)根据 1999 年 7 月实测资料首次发现珠江口伶仃洋盐度高度分层的现象，并运用三维斜压模型模拟出伶仃洋盐度高度层化现象的整体分布。然而目前对珠江口盐度层化在潮周期内和大、小潮周期内的变化的报道还较少，因此本文基于 ROMS 模式建立了一个珠江口三维水动力模式，模拟珠江口冬季的盐度层化，并探讨影响盐度层化的物理机制。

1　模式介绍及设置

ROMS 模式是由 Rutgers University 与 UCLA 两校共同研发而成(Haidvogel *et al*, 2008; Shchepetkin *et al*, 2005)，它可以模拟不同尺度的运动，如全球尺度的环流模拟、中尺度涡旋和河口环流等(Barth *et al*, 2007; Gan *et al*, 2009; Han *et al*, 2009; Warner, 2005; Warner *et al*, 2005)。湍流闭合模型可选用 Mellor and Yamada 2.5 阶、the Generic Length Scale (GLS) parameterization、K-profile scheme 等(Warner *et al*, 2005)，用来计算流场中无法直接进行求解的运动过程。该模式成功地加入了多个生态模块如 NPZD、NEMURO 等，并已在多个海域的生态模拟中得到应用(Fennel *et al*, 2006; Powell *et al*, 2006)。

1.1　模式的建立及设置

为考虑珠江河口与南海北部的水体交换，尤其是南海北部遥强迫对珠江河口水动力的影响，本文在南海-珠江口海域建立一套三层嵌套网格模式，最外层包括整个南海，中间层包括南海北部，最里层是珠江河口。

1.1.1　南海区域模式的设置　　南海模式的网格范围为 95°—133.5°E、0°—30°N，包含整个南海以及西太平洋的一部分(图 1)，模式网格和设置是在本课题组之前的 POM 模式工作基础上建立起来的(Shu *et al*, 2009)。模式的西边界和北边界在岸界上，从而减少了开边界的个数，避免了由人为界定开边界而产生的误差。模式南边界选在加里曼丹海峡，这是因为该海峡深度较浅，且经过该海峡的流基本上平行于海峡，边界处的流场几乎与边界垂直，可以减少边界附近切向速度模拟的误差。东边界延伸至西太平洋，以确保东边界的流量包含较准确的北赤道流信息，并在吕宋海峡附近对网格进行加密，以更好地模拟出黑潮。模式网格为正交曲线网格，格点数为 250×150，水平网格平均的空间分辨率为 15km，垂向使用 30 层，theta-s 设为 7.0、theta-b 设为 0.1，分别对表层和底层加密。模式水深采用 National Geophysical Date Center (NGDC)提供的 Etopo5 地形数据，通过线性插值法插值到模式网格点上，并对水深进行平滑，以减小陡峭地形引起的压强梯度误差，模式最小水深设为 10m，最大为 5500m。

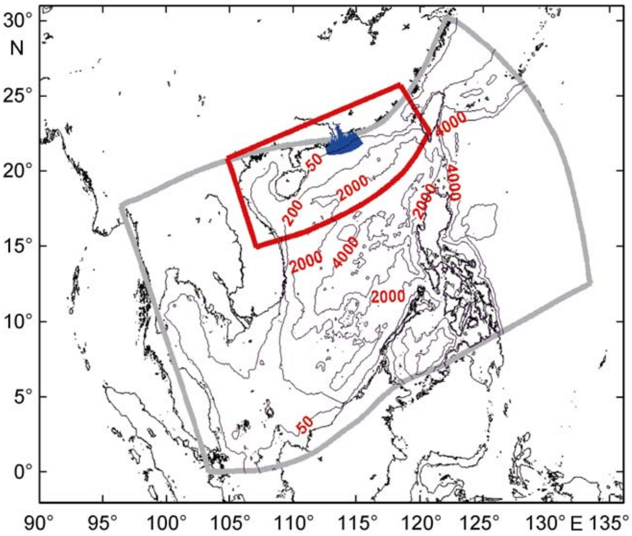

图 1　三层嵌套网格覆盖的范围
Fig.1　The domains of 3-level nested-grid models
注：最外层为南海模式网格的范围(灰色)，中层为南海北部模式网格的范围(红色)，里层为珠江口模式网格的范围(蓝色区域)

1.1.2　南海北部区域模式的设置　　此模式的区域为 116°E—121°E，15°N—25°N，模式格点数为 436×116，平均分辨率为 5km，垂向分 30 层。拉伸系数 theta_s 设为 2.5, theta_b 设为 0.4，最小水深为 5m，最大水深为 1028m。模式的初始场和开边界条件的值由南海模式提供，模式的设置方法与南海模式设置基本相同，除了加入珠江河口的淡水通量，并由多年平均的月流量赋值。

1.1.3　珠江口模式的设置　　模式区域为 112.6°E—

115.5°E、21.1°N —23.1°N。水平网格使用正交曲线网格，网格数为 356×384，在河道内的分辨率大约为 0.1km，河口外大约为 3km。垂向分 20 层，拉伸系数 theta_s 设为 5, theta_b 设为 0.4，使表底层同时得到加密。网格中珠江河道的水深由 90 年代航道水深数据插值得到，这个航道数据集包含 1532 个横向断面的水深数据。在伶仃洋和邻近海域，水深数据通过融合 ETOPO2 和数字化海图水深数据给定。模式初始场和开边界条件设置与南海北部模式设置基本相同，不同的是该模式在开边界加入了潮汐强迫，M_2、S_2、K_1、O_1、P_1、Q_1、K_2、N_2 八个分潮的调和常数来自于 OTIS (http://volkov.oce.orst.edu/tides/)。模拟时间为 2009 年 1—2 月，风场数据采用南沙气象站 2009 年每小时的观测数据(图 2)。上游河流边界的流量由石角、高要、博罗根据八大口门的分流比推算得出(图 2)，各分流比的大小参见 Zhou 等(2012)。湍流闭合方案采用 GLS 方案(Warner *et al*, 2005)。

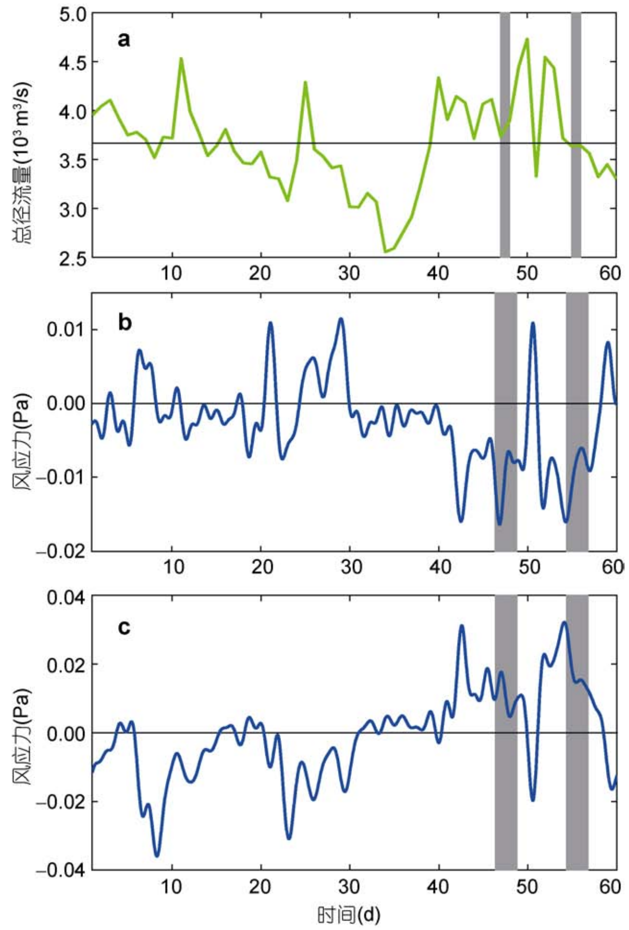

图 2　2009 年 1—2 月(a)珠江总径流量($10^3m^3/s$)、(b)东西方向的风应力(Pa)、(c)南北方向的风应力(Pa)

Fig.2　Time series of (a) daily river discharge ($10^3m^3/s$), (b) low-pass filtered east-west wind stress (Pa), (c) low-pass filtered north-south wind stress (Pa) during 2-month simulation period of 2009

1.2　模式结果验证

本文选取 2009 年 2 月多个站点(图 3)同步观测的水位、流速、盐度数据来验证珠江口模式的可靠性。为量化模拟结果与观测结果的吻合程度，本文采用 Warner(2005)定义的指标 *MS*，其中

$$MS = 1 - \frac{\sum \left| X_{\text{model}} - X_{\text{obs}} \right|^2}{\sum \left(\left| X_{\text{model}} - \overline{X_{\text{obs}}} \right| + \left| X_{\text{obs}} - \overline{X_{\text{obs}}} \right| \right)^2} \tag{1}$$

式中，X_{model} 和 X_{obs} 分别表示模拟值和观测值。该指标也被用于衡量 ROMS 在 Chesapeake 湾和 Columbia 河口模拟结果的好坏(Li *et al*, 2005; Liu *et al*, 2009)。

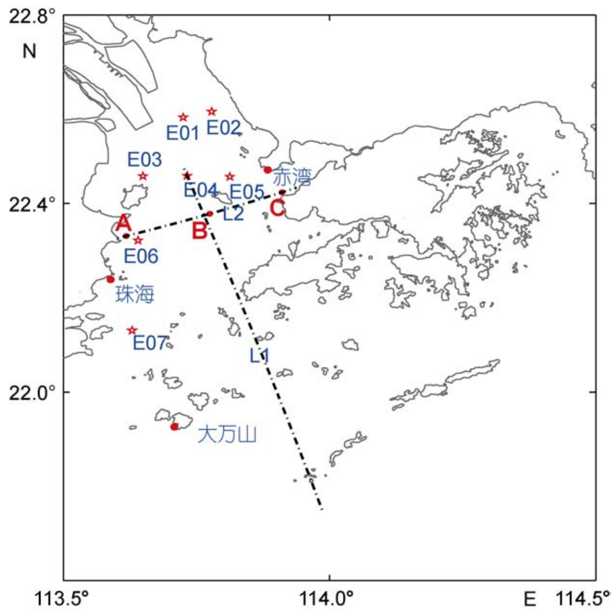

图 3　观测站位和模式分析断面的位置图

Fig.3　Locations of the observation stations and transects for model result analysis.

注：红色实心点表示验潮站，五角星表示流速和盐度观测站，黑色虚线表示模式分析断面位置。断面上 A、B、C 三点分别位于河口西滩、中槽和东滩

本文将模拟的起始时刻 2009 年 12 月 1 日 0 点作为第 0 天，标记为 Day 0，而 2009 年 2 月 28 日 0 点即第 59 日作为模拟的终止时刻，标记为 Day 59，其他时刻的标记以此类推。图 4 比较了 Day 40—48 赤湾、大万山和珠海三个站点每小时的模拟水位与观测水位。结果表明，水位的模拟结果在空间和时间变化上与观测结果能很好地吻合，且 MS 值均高于 0.95。图 5 比较了 E01—E07 七个站点模拟的经向流速与其

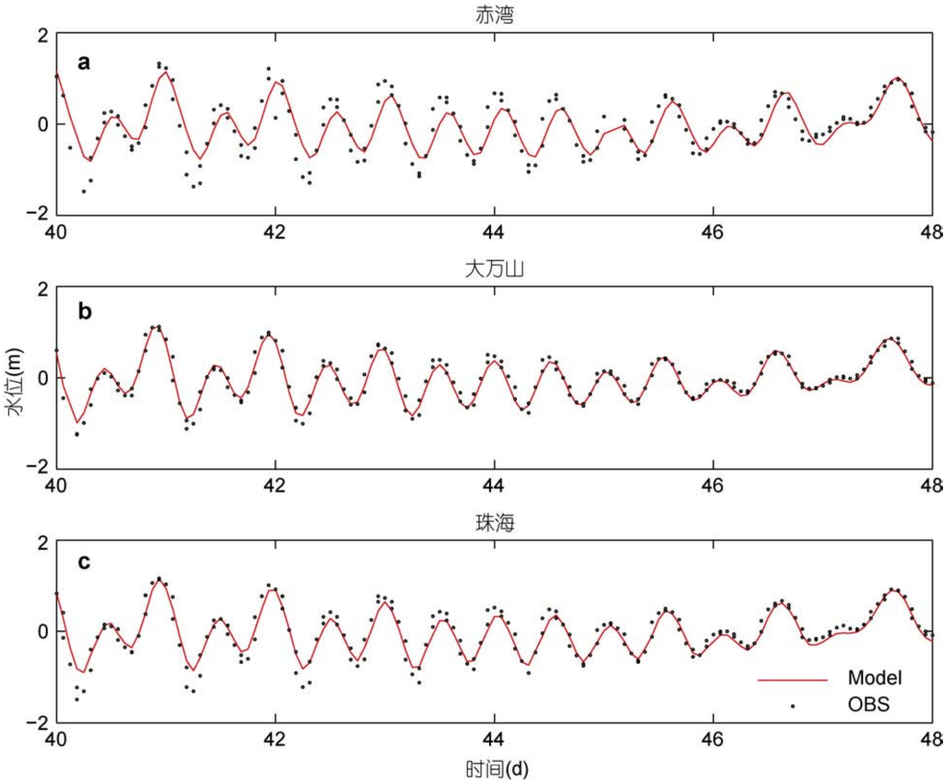

图 4 (a)赤湾、(b)大万山、(c)珠海观测(黑点)和模拟(红线)的水位(m)

Fig.4 Time series of observed (black point) and modeled (red line) tidal surface elevations (m) at (a) Chiwan, (b) Dawanshan, (c) Zhuhai

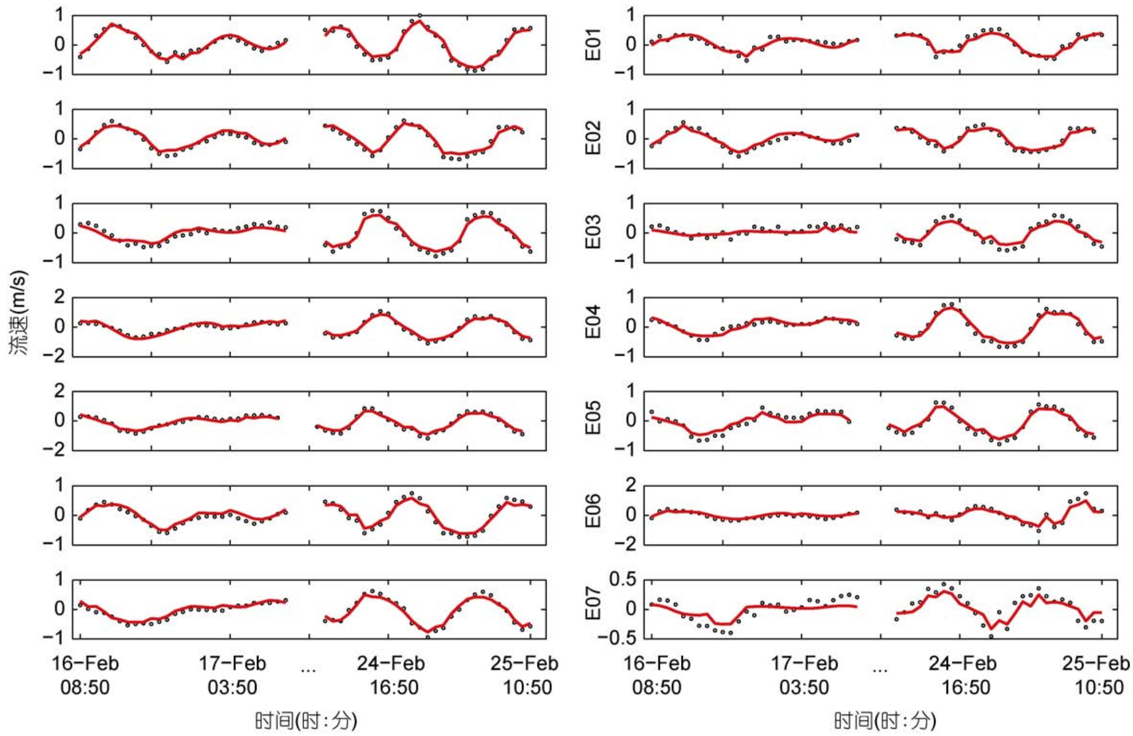

图 5 E01—E07 站观测(黑点)与模拟(红线)的表层(左边)和底层(右边)流速(m/s)

Fig.5 Time series of observed (black point) and modeled (red line) surface (left panel) and bottom (right panel) north-south velocity at seven stations (E01—E07) (m/s)

观测值, 比较时间分为两段, 分别是 2 月 16 日—18 日(小潮期间)、2 月 24 日—26 日(大潮期间)。模拟流速的 MS 值都大于 0.85, 模拟结果能较好地再现观测时的流速变化情况。盐度的观测时间和位置与流速相同, 观测频率都为 1 小时, 比较结果表明盐度的模拟精度小于水位和流速(图 6), 但除了 E01 和 E07 外, 大部分站点盐度的 MS 值都在 0.8 以上。

以上分析表明, 模型模拟的水位、流速和盐度误差均在允许范围之内, 能较好地反映珠江口的主要水动力过程和盐度分布。

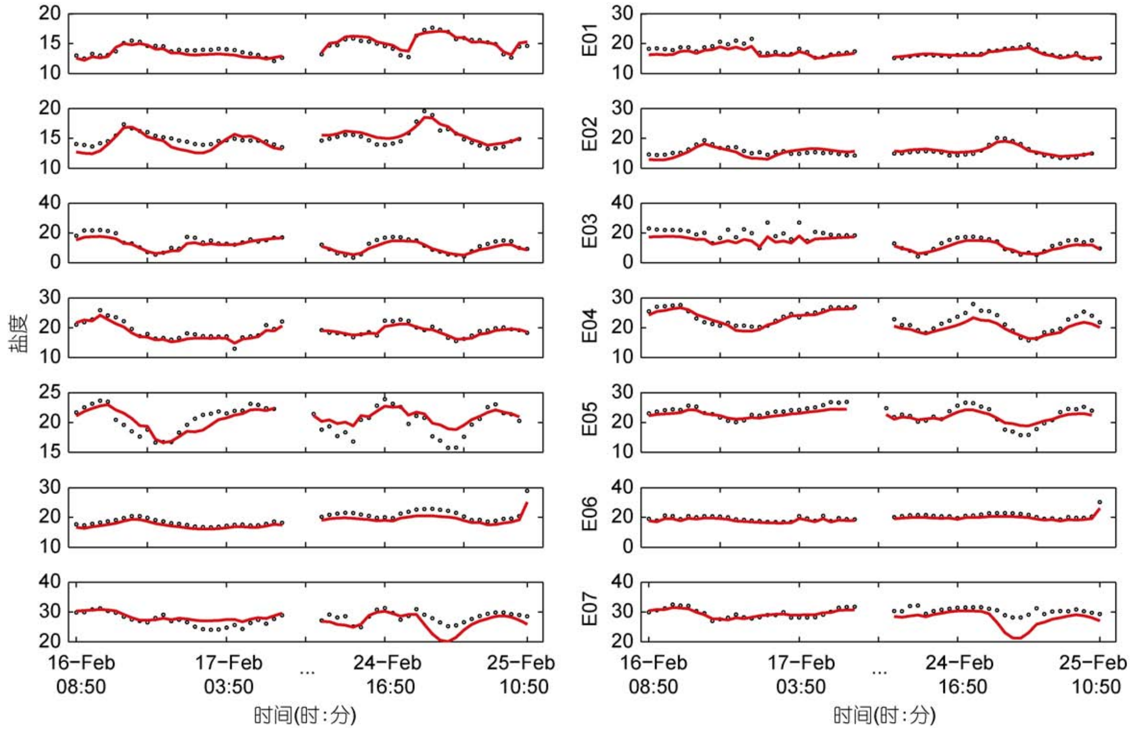

图 6　E01—E07 站观测(黑点)与模拟(红线)的表层(左边)和底层(右边)盐度

Fig.6　Time series of observed (black point) and modeled (red line) surface (left panel) and bottom (right panel) salinity at seven stations (E01—E07)

2　模式结果

为探讨潮汐混合对珠江口盐度层化影响, 本文在下面的模拟试验中将径流量设为常数 4000m^3/s,风应力设为 0, 其他设置与前面验证过的模式设置相同。

2.1　涨-落潮不对称

本文选取图 3 中横向断面 L2 上的三个点(A、B、C) , 分析涨、落潮时段的盐度、流速及垂向扩散系数的变化。这三个点分别位于西部浅滩、中部深槽和东部浅滩处, 水深分别为 4.96m、10.47m、4.62m。本文首先分析大潮期间的涨、落潮不对称。

从图 7 可以看出, A 和 B 两点涨潮的底边界层厚度比落潮时要厚, 而且落潮时底边界层的盐度略大于涨潮时, 这与 Li 等(2009)的结果比较吻合。比较 A 和 B 的盐度分布发现, 水深较大的地方, 落潮时的层化也相对较强。C 点位于东滩, 盐度明显高于位于西滩的 A 点, 尽管这两个站点的水深相差很小, 但盐度的变化却有很大的差异, C 点涨潮时底边界层厚度小于落潮时, 而盐度却高于落潮时。C 点的流速剖面显示在涨潮时出现次表层最大值。由于河口外的海表坡度与陡峭的等盐度线共同作用产生亚潮压强, 该压强在近表层指向海, 在近底层指向岸, 落潮时增加上层水体的流速以及减小下层水体的流速, 使得落潮时的流速从底部到表层呈线性增加。

本文在 ROMS 模式中采用 GLS 混合方案计算垂向湍粘性系数和扩散系数, 并且将背景粘性系数和扩散系数都设置为 5×10^{-6}。如图 7 所示, A 和 B 两点涨潮时最大的湍扩散系数约为落潮时的两倍, 这与 Geyer 等(2000)在 Hudson 河口的观测及 Li 等(2009)的模拟结果非常吻合。但东滩站点 C 的情况恰好相反, 具体原因还有待进一步分析。

图 8 显示了 L2 断面的三个固定点不同水深处的

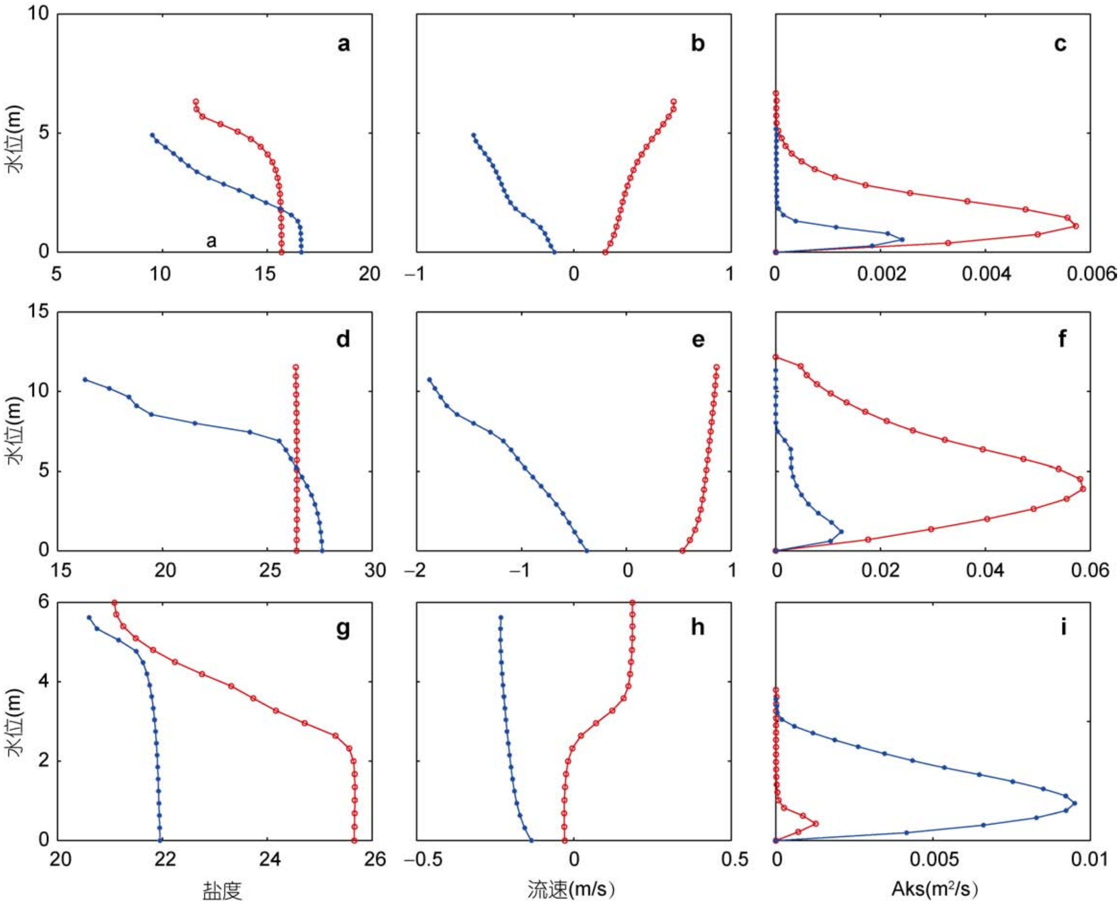

图 7　大潮期间 A、B、C 站点的盐度、流速、湍扩散系数的垂向分布图

Fig.7　The vertical profiles of salinity, current and eddy diffusivity at the peak flood (red lines) and peak ebb (blue lines) during spring tide at stations A, B and C

注: a 为大潮期间, 站点 B 正压流速(m/s)的时间变化。b、c、d 为站点 A, e、f、g 为站点 B, h、i、j 为站点 C 的盐度、流速、湍扩散系数的垂向分布。红色表示涨急, 蓝色表示落急

流速、盐度和扩散系数在 5 天观测期内变化。经向流有明显的涨、落潮变化特征, 大部分涨潮流呈现次表层最大值, 而落潮流在表层达到最大值。涨潮时, 水深较大的地方流速也相对较大; 西滩的涨、落潮流速均大于东滩。垂向盐度分布有明显的潮周期变化。落潮时, 上游低盐水使表层水偏淡; 涨潮时, 陆架高盐水的侵入, 经垂向混合作用致使底层水的盐度较高。湍扩散系数的涨、落潮不对称体现在强混合区在涨潮时比落潮时更靠近表层, 即涨潮时混合强而落潮时混合相对较弱。 涨潮时正压梯度力与底部向岸的斜压梯度力的共同作用使底边界层附近产生较强的流速剪切和底应力, 而在落潮时正压梯度力与斜压梯度力之间的竞争减弱了近底层的流速剪切和底应力。深槽的底应力大于东滩和西滩, 而西滩又略大于东滩。以上分析表明伶仃洋的盐度、流速和底应力存在涨、落潮不对称现象, 且具有明显的横向不对称。

2.2　空间变化

由于同一时刻的潮流的大小和相位在不同地点不同, 为探讨涨、落潮不对称现象在空间上的变化, 本文选取了一条横向断面和一条纵向断面分析盐度和湍扩散系数的空间变化。珠江口长度和宽度都较大, 其盐度呈现出明显的纵向和横向变化。为清楚地显示纵向断面所有点所处的相位, 本文在图 9 显示某一时刻 L1 断面所有点的正压流速, 并选取了涨急和落急两个不同时刻进行对比, 对应时刻分别为 Day 38.50 和 38.76。

如图 9a 所示, 在 Day 38.76 时, L1 断面上的点正处于退潮期, 比较图 9c 和图 9d 可以发现, 涨潮时潮汐混合大部分发生在靠近河床混合良好的底边界层, 而退潮时潮汐混合可发生在层化区, 这与 Nepf 等(1996)的观测结果相吻合。瞬时湍扩散系数与潮周期平均的湍扩散系数在底边界层相差不大, 但在近表

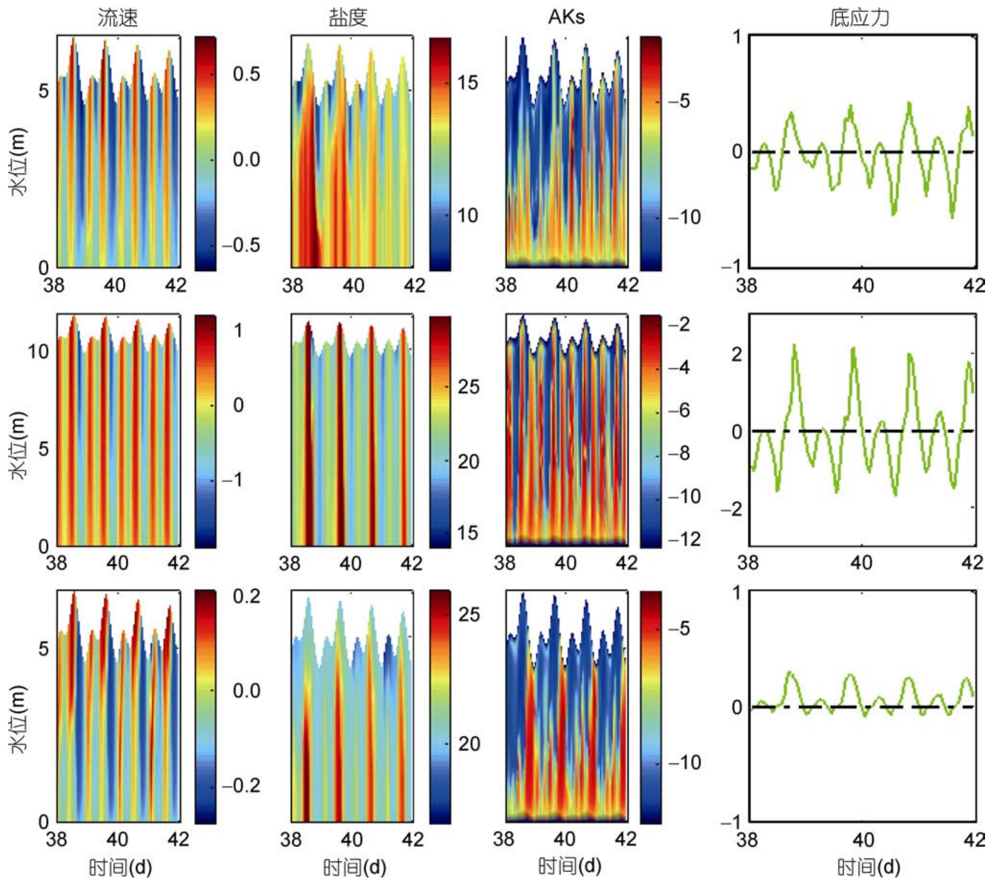

图 8　大潮期间，站点 A、B、C 的流速(m/s)、盐度、湍扩散系数的对数的时间和垂向变化以及底应力(Pa)的时间变化
Fig.8　Time-dependent vertical distributions of current (m/s), salinity and logarithm of eddy diffusivity and time series of bed stress (Pa) for station A, B and C during spring tide

层却有明显的不同，表现在退潮时刻平均的湍扩散系数在表层较强，尤其是水深较浅区域，而涨潮时近表层的垂向混合较弱(图 9)。

瞬时盐度与潮周期平均盐度之差可以反映涨、落潮周期内盐度分布的变化(图略)。涨潮时，陆架高盐水进入河口，L1 断面 22.2°N 以北的区域，盐度正异常，最大可达到 6psu；相比而言，退潮时冲淡水往下冲刷，使得河口上游的负异常达到 2。而 22°N 以南由于涨潮或退潮时潮流都较弱，盐度的变化很小。

本文在 22.38°N 选取了一条横向断面(L2)探讨盐度的侧向变化。如图 10 所示，(a)、(b)分别为退急和涨急时断面 L2 上所有点的南北向正压流，在退急时，L2 上所有点都处于退潮期，在 113.75°E 附近的深槽层化较强，强混合(梯度 Ri<0.25)都局限在底边界层；而在东、西两侧的浅滩区，强混合能延伸到近表层。在涨急时，潮流减小层化并增加底部混合层的厚度。113.75°E 附近的深槽盐度层化减弱，在东西两侧的浅滩区强混合局限在底边界层。这与之前固定站点的分析结果相吻合。此外，不管是涨急还是退急，盐度最大值都位于横向断面的中心点附近，湍扩散系数在退潮时大于涨潮时，尤其是在西部浅滩的近表层。

退潮时，西滩表层的盐度比潮周期平均的盐度要高 5 左右(图 11)，中槽表层的盐度比潮周期平均的盐度要低 5，而东滩的盐度变化相对较小。涨潮时，情况正好相反，西滩表层盐度比平均盐度要小 4，深槽表层盐度比平均盐度高 2。东滩底层盐度比平均盐度高 2。比较图 11 的平均湍扩散系数与图 10 的瞬时湍扩散系数发现，退潮时中槽表层的湍扩散系数小于平均湍扩散系数；涨潮时，西滩表层的湍扩散系数小于平均湍扩散系数。由于湍扩散系数越小，表底层盐度混合作用越弱，从而使表层盐度相对减小，这能较好地解释退潮时的中槽和涨潮时的西滩表层盐度小于平均盐度的现象。

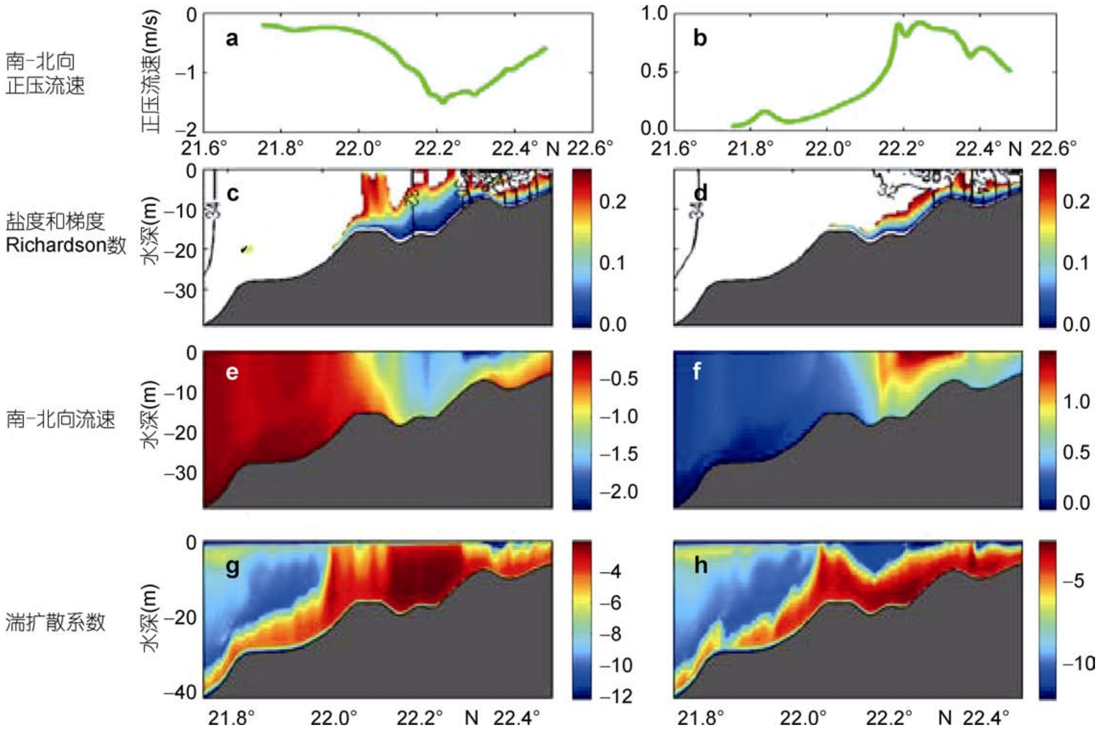

图 9　L1 断面大潮期间盐度(黑色等值线)和梯度 Richardson 数(彩色)、南北向流速、湍扩散系数对数分布图

Fig.9　Salinity (black line) and gradient Richardson Number (color contour), north-south velocity, and eddy diffusivity along transect L1 during spring tide

注：左边表示落潮，右边表示涨潮时刻

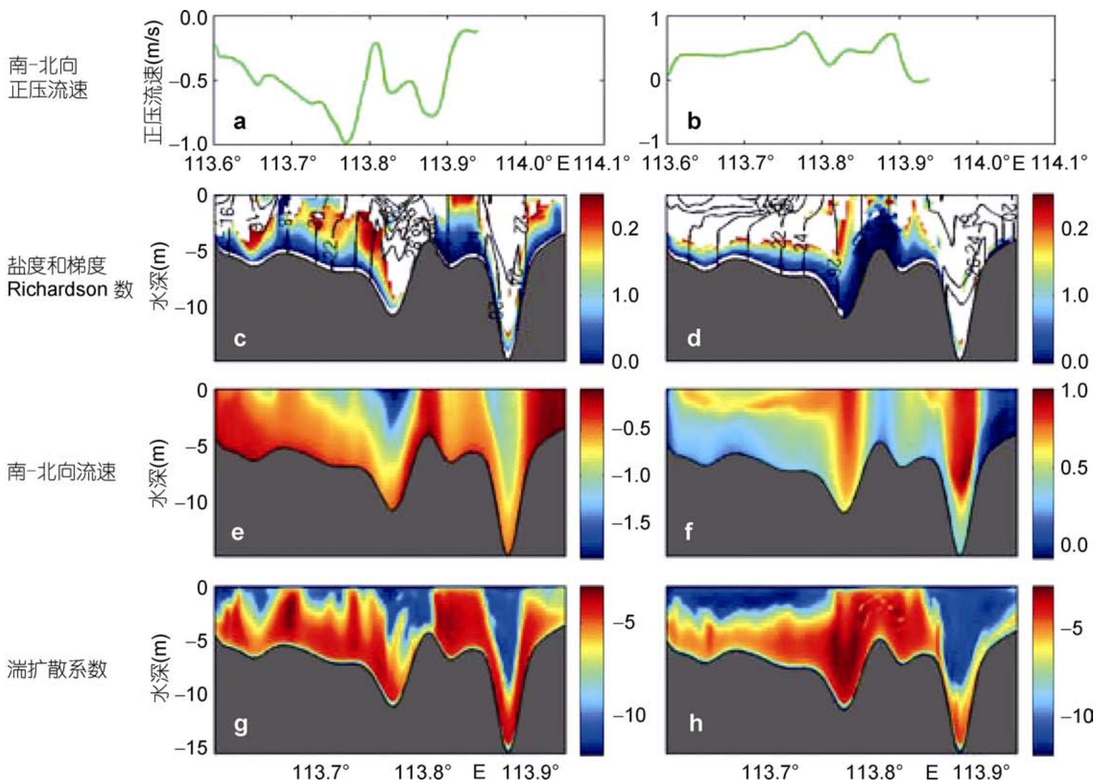

图 10　L2 断面大潮期间盐度(黑色等值线)和梯度 Richardson 数(彩色)、南北向流速、湍扩散系数对数分布图

Fig.10　Salinity (black line) and gradient Richardson Number (color contour), north-south velocity, and eddy diffusivity along transect L2 during spring tide

注：左边表示落潮，右边表示涨潮时刻

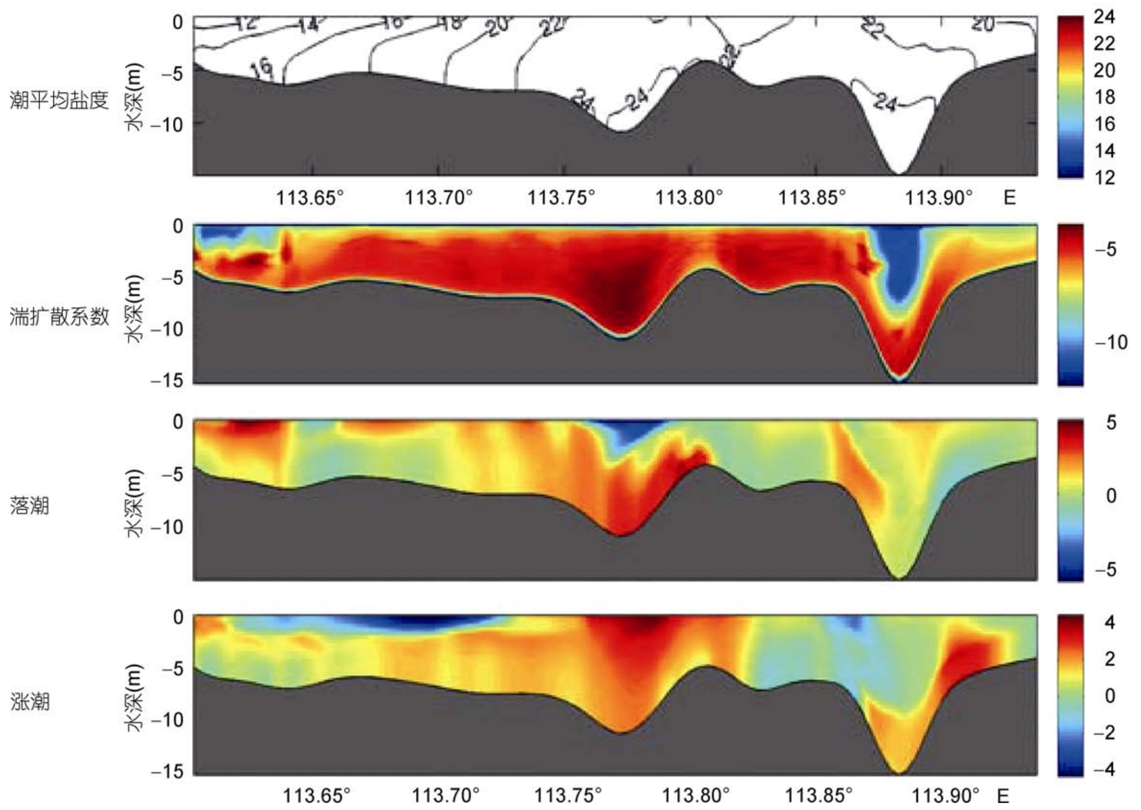

图 11　大潮期间 L2 断面的平均盐度和湍扩散系数以及落潮和涨潮时刻盐度与平均盐度之差

Fig.11　Tidally averaged salinity, logarithm of eddy diffusivity, and the salinity difference between ebb/flood and the tidal average along L2 transect at spring

3　影响层化的源汇项

本文将采用势能异常φ衡量层化的强度，Simpson 等(1990)定义势能异常的计算公式如下：

$$\varphi = \frac{1}{D}\int_{-H}^{\eta} gz(\bar{\rho}-\rho)dz \tag{2}$$

φ在物理上表示将一定密度层化的水体瞬间混合均匀所需要的能量，z 表示垂向坐标(底部为$-H$，海表面为 η)，D 表示水柱的深度($D = H + \eta$)，g 表示重力加速度，ρ 表示水体密度，$\bar{\rho}$ 表示垂向平均的密度。φ 等于 0 表示完全混合，大于 0 表示稳定层结，小于 0 表示不稳定层结。

Burchard 等(2008)推导了势能异常变化方程，其方程式为：

$$\begin{aligned}\partial_t\phi = &\underbrace{-\nabla_h(\bar{u}\phi)}_{(A)} + \underbrace{\frac{g}{D}\nabla_h\bar{\rho}\cdot\int_{-H}^{\eta} z\tilde{u}dz}_{(B)} \\ &\underbrace{-\frac{g}{D}\int_{-H}^{\eta}\left(\eta-\frac{D}{2}-z\right)\tilde{u}\cdot\nabla_h\tilde{\rho}dz}_{(C)} \\ &\underbrace{-\frac{g}{D}\int_{-H}^{\eta}\left(\eta-\frac{D}{2}-z\right)\tilde{w}\partial_z\tilde{\rho}dz}_{(D)} + \underbrace{\frac{\rho_0}{D}\int_{-H}^{\eta}P_b dz}_{(E)} \underbrace{-\frac{\rho_0}{2}\left(P_b^s+P_b^b\right)}_{(F)} \\ &\underbrace{+\frac{g}{D}\int_{-H}^{\eta}\left(\eta-\frac{D}{2}-z\right)Qdz}_{(G)} \\ &\underbrace{+\frac{g}{D}\int_{-H}^{\eta}\left(\eta-\frac{D}{2}-z\right)\nabla_h(K_h\nabla_h\rho)dz}_{(H)},\end{aligned} \tag{3}$$

$$P_b = \frac{g}{\rho_0}K_v\partial_z\rho, \tag{4}$$

其中，公式(3)中的 A、B、C、D、E、F、G、H 分别表示势能异常的平流、垂向平均应变、非垂向平均应变、垂向对流、垂向混合、海表和海底的浮力通量、内部源或汇和水平湍流输运的辐散，其它变量的含义详见(Burchard *et al*, 2008)。

河口的层化主要受潮汐应变和混合之间的竞争机制控制(Simpson *et al*, 1990)。本文将根据 Burchard 等(2008)推导的势能异常变化方程，分析影响层化的贡献项。根据势能异常的定义，φ_t 为正，表示层化

增强。

通过分析西滩和中槽两个站点的势能异常变化项与方程(10)中的源汇项之间的关系，发现在小潮期(图 12)，西滩势能异常变化具有明显的涨、落潮变化特征：在涨潮时，势能异常减小，层化减弱；落潮时，势能异常增加，层化增强。比较图 12(a)与(b)发现势能异常的增加(减小)主要由势能异常的平流项与应变项的增加(减小)引起。势能异常的平流项、应变项与水平湍流输运的辐散项是影响势能异常变化的主要因素，涨潮时，潮汐应变为负值，层化作用减弱；落潮时，潮汐应变为正值，层化作用加强。

潮汐应变的大小与势能异常的平流项具有相同的量级，相似的变化趋势。大潮时浅滩的势能异常变化幅度较小潮时增加一倍(图 13)，而势能异常的平流项、应变项与水平湍流输运变化幅度也相应地增加一倍。中槽区(站点 B)的势能异常变化幅度较浅滩区(站点 A)增加一倍(图略)，势能异常与潮汐应变对势能异常变化的贡献与浅滩基本一致，但非垂向平均应变项(C 项)比浅滩处的影响要大，在小潮时其大小甚至超过潮汐应变。值得注意的是，大潮期深槽的非垂向平均应变项的变化幅度小于小潮期。

4 结论

本文利用 ROMS 模式建立了适用于珠江口的三维水动力模型，探讨珠江口盐度的潮周期变化和空间变化特征。模型验证结果表明，模型的计算结果误差较小，能较好的反映珠江口的主要水动力过程和盐度分布。研究结果表明：

(1) 珠江口盐度层化具有明显的潮周期变化特征，涨潮时表底层盐度差较小，层化较弱；落潮时表底层盐度差较大，层化较强。垂向盐度，流速和扩散系数剖面显示出明显的涨、落潮不对称。

(2) 势能异常的平流项和应变项是影响珠江口势能异常变化的主要因素。大潮时势能异常变化幅度较小潮时增加一倍，而势能异常的平流项和应变项也相应地增加一倍。深槽区的势能异常变化幅度大于浅滩区，势能异常的平流项与潮汐应变对势能异常变化的贡献与浅滩基本一致。

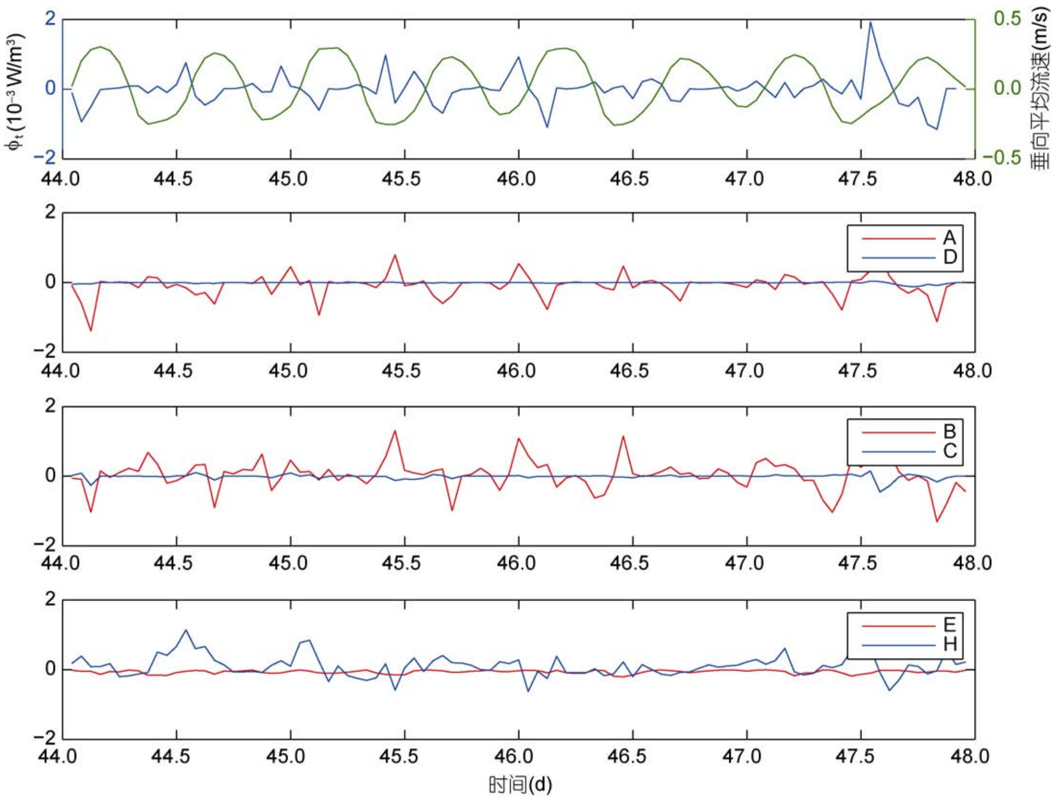

图 12 站点 A 方程 10 中的各项以及势能异常变量在小潮的时间变化

Fig.12 Time series of potential energy anomaly variation and different terms in Equation 10 at station A during neap tide

注：纵坐标单位为 10^{-3}W/m^3

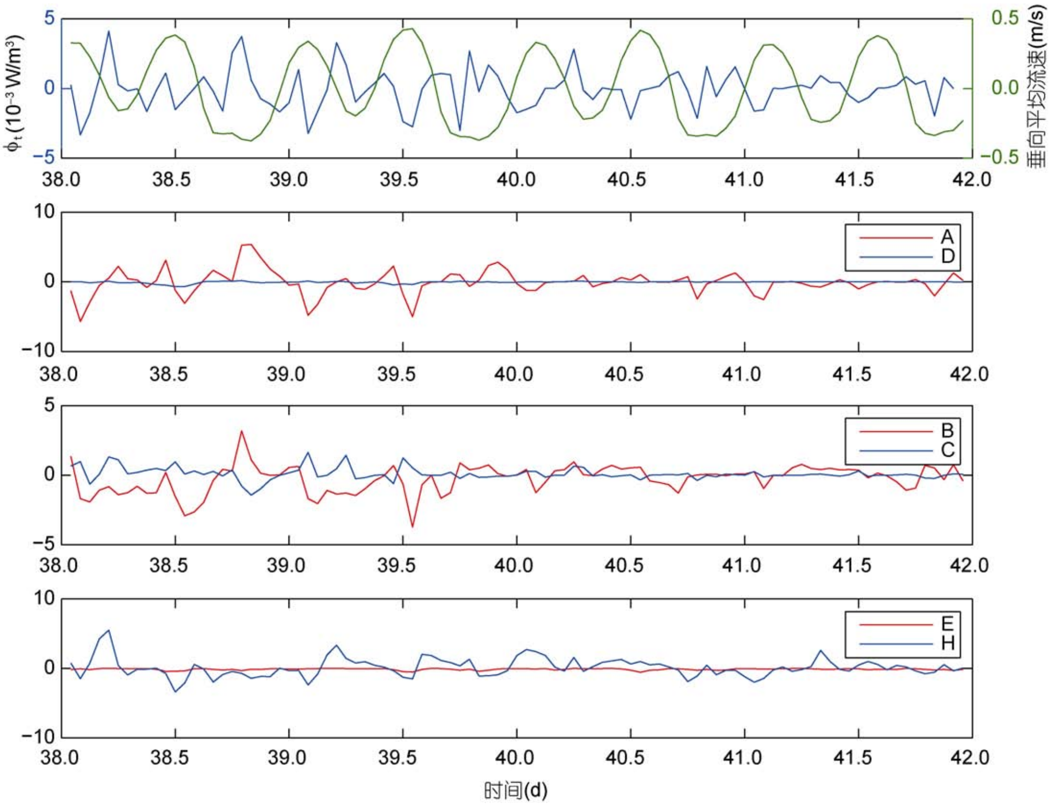

图 13　站点 A 方程 10 中的各项以及势能异常变量在大潮的时间变化

Fig.13　Time series of potential energy anomaly variation and different terms in Equation 10 at station A during spring tide

注：纵坐标单位为 10^{-3}W/m^3

参　考　文　献

包　芸，任　杰，2005．伶仃洋盐度高度层化现象及盐度锋面的研究．水动力学研究与进展 A 辑, 20(6): 689—693

应秩甫，1983．珠江口伶仃洋咸淡水混合特征．海洋学报，5: 1—10

赵焕庭, 1990．珠江河口演变．北京：海洋出版社, 127—139

Barth A, Alveraazcarate A, Weisberg R, 2007. Benefit of nesting a regional model into a large-scale ocean model instead of climatology. Application to the West Florida Shelf. Continental Shelf Research, 28: 561—573

Burchard H, Hofmeister R, 2008. A dynamic equation for the potential energy anomaly for analysing mixing and stratification in estuaries and coastal seas. Estuarine Coastal and Shelf Science, 77: 679—687

Chen S N, Sanford L P, 2009. Axial Wind Effects on Stratification and Longitudinal Salt Transport in an Idealized, Partially Mixed Estuary. Journal of Physical Oceanography, 39: 1905—1920

Cudaback C N, Jay D A, 2000. Tidal asymmetry in an estuarine pycnocline: Depth and thickness. Journal of Geophysical Research, 105: 26237—26251

Dyer K R, 1997. Estuaries: A Physical Introduction. 2nd ed. John Wiley and Sons, 1—195

Fennel K, Wilkin J, Levin J *et al*, 2006. Nitrogen cycling in the Middle Atlantic Bight: Results from a three-dimensional model and implications for the North Atlantic nitrogen budget. Global Biogeochemical Cycles, 20, GB3007, doi: 10.1029/2005GB002456

Gan J, Li L, Wang D *et al*, 2009. Interaction of a river plume with coastal upwelling in the northeastern South China Sea. Continental Shelf Research, 29: 728—740

Haidvogel D B, Arango H, Budgell W P *et al*, 2008. Ocean forecasting in terrain-following coordinates: Formulation and skill assessment of the Regional Ocean Modeling System. Journal of Computational Physics, 227: 3595—3624

Han W, Moore A M, Levin J *et al*, 2009. Seasonal surface ocean circulation and dynamics in the Philippine Archipelago region during 2004—2008. Dynamics of Atmospheres and Oceans, 47: 114—137

Hansen D V, Jr M R, 1965. Gravitational circulation in straits and estuaries. J Mar Res, 23: 104—122

Hansen D V, Jr M R, 1966. New dimensions in estuary classification. Limnology and Oceanography, 11: 319—326

Jay D A, Smith J D, 1990. Residual circulation in shallow estuaries. 1. highly stratified, narrow estuaries. Journal of Geophysical Research, 95: 711—731

Lacy J R, Stacey M T, Burau J R *et al*, 2003. Interaction of lateral baroclinic forcing and turbulence in an estuary. Journal of

Geophysical Research, 108, 3089, doi: 10.1029/2002JC001392, C3

Li M, Zhong L, Boicourt W C, 2005. Simulations of Chesapeake Bay estuary: Sensitivity to turbulence mixing parameterizations and comparison with observations. Journal of Geophysical Research, 110, C12004, doi:10.1029/2004JC002585

Li M, Zhong L, 2009. Flood-ebb and spring-neap variations of mixing, stratification and circulation in Chesapeake Bay. Continental Shelf Research 29: 4—14

Liu Y, MacCready P, Hickey B M *et al*, 2009. Evaluation of a coastal ocean circulation model for the Columbia River plume in summer 2004. Journal of Geophysical Research, 114, C00B04, doi:10.1029/2008JC004929

Nepf H M, Geyer W R, 1996. Intratidal variations in stratification and mixing in the Hudson estuary. Journal of Geophysical Research, 101: 12079—12086

Powell T M, Lewis C V W, Curchitser E N *et al*, 2006. Results from a three-dimensional, nested biological-physical model of the California Current System and comparisons with statistics from satellite imagery. Journal of Geophysical Research, 111, C07018, doi: 10.1029/2004JC002506

Pritchard D W, 1952. Salinity distribution and circulation in the Chesapeake Bay estuarine system. Journal of Marine Research, 11: 106—123

Sanay R, Voulgaris G, Warner J C, 2007. Tidal asymmetry and residual circulation over linear sandbanks and their implication on sediment transport: A process-oriented numerical study. Journal of Geophysical Research, 112, C12015, doi:10.1029/2007JC004101

Shchepetkin A F, McWilliams J C, 2005. The regional oceanic modeling system (ROMS): a split-explicit, free-surface, topography-following-coordinate oceanic model. Ocean Modelling, 9: 347—404

Shu Yeqiang, Zhu Jiang, Wang Dongxiao *et al*, 2009. Performance of four sea surface temperature assimilation schemes in the South China Sea. Continental Shelf Research, 29: 1489—1501

Simpson J H, Brown J, Matthews J *et al*, 1990. Tidal straining, density currents, and stirring in the control of estuarine stratification. Estuaries, 13: 125—132

Warner J C, 2005. Numerical modeling of an estuary: A comprehensive skill assessment. Journal of Geophysical Research, 110, C05001, doi:10.1029/2004JC002691

Warner J C, Sherwood C R, Arango H G *et al*, 2005. Performance of four turbulence closure models implemented using a generic length scale method. Ocean Modelling, 8: 81—113

Zhou Wei, Wang Dongxiao, Luo Lin, 2012. Investigation of saltwater intrusion and salinity stratification in winter of 2007/2008 in the Zhujiang River Estuary in China. Acta Oceanologica Sinica 31:31—46

NUMERICAL SIMULATION OF WINTER SALINITY STRATIFICATION IN THE PEARL RIVER ESTUARY (PRE) BASED ON A TRIPLE-NESTED MODELING SYSTEM

ZHOU Wei[1], WANG Dong-Xiao[2], ZU Ting-Ting[2], LI Hai-Yang[2, 3], XIAO Xian-Jun[1]

(1. *Laboratory for Climate Studies*, *National Climate Center*, *China Meteorological Administration*, *Beijing*, 100081;
2. *State Key Laboratory of Tropical Oceanography*, *South China Sea Institute of Oceanology*, *Chinese Academy of Sciences*, *Guangzhou*, 510301; 3. *Weather Station of Nansha District*, *Guangzhou*, 511458)

Abstract A high-resolution three-dimensional numerical model using Regional Ocean Modeling System (ROMS) was built up to reproduce the primary hydrodynamics and the characteristic of salinity distribution in the Pearl River estuary (PRE). Stratification induced by intra-tidal variation of salinity is obvious in the PRE. The salinity difference between surface and bottom is small and stratification is weak during flood, and the water tends to be stratified during ebb. A dynamic equation for the potential energy anomaly budget was used to investigate the contributing terms to the modulation of stratification. The depth-mean straining and potential energy anomaly advection appear to be the major terms that affect the potential energy anomaly in the PRE.

Key words ROMS model; salinity stratification; potential energy anomaly; Pearl River estuary

竺夏英,陈丽娟,李想.2013.2012 年冬春季高原积雪异常对亚洲夏季风的影响.气象,39(9):1111-1118.

2012 年冬春季高原积雪异常对亚洲夏季风的影响*

竺夏英 陈丽娟 李 想

国家气候中心,中国气象局气候研究开放实验室,北京 100081

提 要: 利用罗格斯大学积雪遥感资料、NCEP/NCAR 再分析格点资料和 NOAA 陆地降水分析数据 PREC/L,从 2011/2012 年冬春季青藏高原积雪偏多现象与亚洲夏季风的观测事实与以往研究结果不一致出发,诊断分析了 2011/2012 年冬春积雪与亚洲夏季风的可能联系。结果表明:2012 年春季和前期冬季,青藏高原主体上空对流层主要为气旋性环流距平且气温偏低,这与积雪偏多年的环流特征一致。尤其在 90°E 以西,自青藏高原到热带地区,前期冬春季对流层中部气温表现为北冷南暖的距平特征,有利于夏季自热带印度洋到高原温度梯度偏弱,造成南亚夏季风偏弱。但是在 90°E 以东的高原东部到东亚地区及其南侧的低纬度地区,对流层温度距平为北正南负型,温度梯度偏弱,有利于亚洲东南部大气环流冬夏季节转换偏早,南海夏季风爆发偏早,东亚夏季风偏强,这种环流特征受到高原以外的其他外强迫信息的影响。2011/2012 年冬春季积雪偏多特征可能对南亚夏季风偏弱有重要贡献,而对东亚夏季风的影响不明显。

关键词: 青藏高原,积雪,温度梯度,亚洲夏季风

中图分类号: P461 **文献标志码:** A **doi:** 10.7519/j.issn.1000-0526.2013.09.004

Impact of Tibetan Plateau Snow Cover Anomaly on Asian Summer Monsoon in 2012

ZHU Xiaying CHEN Lijuan LI Xiang

Laboratory of Climate Studies of CMA, National Climate Centre, Beijing 100081

Abstract: The East Asain summer monsoon was stronger in 2012, though the Tibetan Plateau (TP) snow cover extent was anomalously larger than the climate mean in the preceding spring and winter, which is inconsistent with the results of previous studies. This paper made an effort to investigate the possible relationship between the TP snow cover from winter 2011 to spring 2012 and the following Asian summer monsoon, using the monthly mean snow cover extent data from Rutgers University Global Snow Lab, NCEP/NCAR reanalysis monthly average data, and the monthly data set of NOAA's Precipitation Reconstruction over Land (PREC/L). The findings suggest that the TP was covered mainly by an anomalous cyclone with lower temperature in the mid-troposphere in spring 2012 and the previous winter, which agreed with the features of larger snow cover years. Particularly to the west of 90°E, the mid-tropospheric temperature anomalies from the TP to the tropical Indian Ocean were negative in the north and positive in the south from winter to spring, conducive to the weaker meridional temperature gradient there in summer and thus to the weaker South Aisan summer monsoon. However, to the east of 90°E, the mid-tropospheric temperature anomalies from East Asia to the tropics were positive in the north and negative in the south in

* 国家自然科学基金项目(41275073)、国家科技支撑计划项目(2009BAC51B05)、公益性行业(气象)科研专项(GYHY201206017)和中国气象局短期气候预测创新团队项目共同资助

2012 年 12 月 14 日收稿; 2013 年 5 月 8 日收修定稿

第一作者:竺夏英,主要从事青藏高原与亚洲季风研究. Email:zhuxy@cma.gov.cn

winter and spring, favorable for the earlier seasonal transition from winter to summer in the southeastern Asia, the earlier onset of the South China Sea summer monsoon, and also the stronger East Asian summer monsoon. They were more influenced by other forcings than the TP. Therefore, the fact of more TP snow cover from winter 2011 to spring 2012 probably made a significant contribution to the following weaker South Asian summer monsoon, and had less impact on the East Asian summer monsoon in 2012.

Key words: Tibetan Plateau, snow cover, temperature gradient, Asian summer monsoon

引　言

积雪一方面改变了下垫面的反照率,从而改变地表接受的太阳辐射;另一方面,积雪通过融雪改变地表潜热和感热的分配比例。积雪的总体效应是改变下垫面的热力状况,从而对周围大气产生影响。早在 100 多年前,Blanford(1884)和 Walker(1910)根据很少的资料发现喜马拉雅山积雪范围和厚度与印度西北部的夏季雨量呈负相关。然而在 20 世纪初以后的几十年,积雪和印度季风之间的关系变得不显著,表明青藏高原积雪与印度季风的关系具有复杂性(Bamzai et al,1999;Fasullo,2004)。我国学者在青藏高原对亚洲气候的影响方面也进行了大量研究(陈烈庭等,1979;韦志刚等,1993;刘晓东等,1994;卢咸池等,1994;陈丽娟等,1996;张顺利等,2001;朱玉祥等,2007a;2007b;韦志刚等,2008),罗勇(1995)、朱玉祥等(2007a)分别对此进行了系统的回顾,指出虽然青藏高原积雪影响东亚夏季风的研究还缺乏统一的认识,但大多数研究者认为:前期冬春季高原积雪偏多(偏少),亚洲夏季风爆发偏晚(偏早),强度偏弱(偏强)。主要的物理机制是:高原冬春积雪偏多,反射率增大,高原地表吸收太阳辐射减少;积雪融化时,吸收大量热量;积雪融化后,土壤湿度增大,与大气相互作用,以上三方面均造成高原热源偏弱,反之亦然(董敏等,1997;陈乾金等,2000;张顺利等,2001;Qian et al,2003;周悦等,2012)。另外,统计分析(孙林海等,2001)和数值实验(范广洲等,1997)均表明与欧亚大陆雪盖相比,亚洲季风对青藏高原积雪异常的响应更敏感。并且高原积雪的空间分布不同对东亚、南亚季风的影响也不一致:高原中东部多雪可能引起东亚夏季风的减弱幅度要大于印度夏季风的减弱(范广洲等,1997)。对台站观测资料的诊断分析(Wu et al,2003)也表明不同的青藏高原积雪分布型对亚洲夏季风具有不同的影响。

2012 年春季和前期冬季,青藏高原积雪范围持续偏大,印度夏季风偏弱,但南海夏季风爆发偏早,东亚副热带夏季风偏强,长江流域降水偏少(王艳姣等,2013),因此前期冬春季高原积雪异常与亚洲夏季风呈现复杂关系,不能一概而论。2012 年前期冬春季高原积雪偏多,但 ENSO 处于弱冷位相,这两个外强迫因子以及其他的外强迫信号对亚洲夏季风的作用是季节气候预测需要审视的问题。Wu 等(2012)指出近年来夏季高原西部雪盖具有偏少的趋势,在此背景下,ENSO 对东亚夏季风的作用要强于积雪。彭京备等(2005)的研究表明积雪和海温的年代际气候跃变与中国夏季降水的相关程度在某些地区高于年际变化。2012 年东亚夏季风偏强和印度夏季风偏弱与高原积雪偏多究竟具有怎样的物理联系?本文即从青藏高原积雪监测以及东亚夏季风/南亚季风的监测事实与以往研究不完全一致出发,从环流空间分布异常的角度,通过诊断分析,获得 2012 年春季和前期冬季高原积雪和亚洲夏季风特征的可能联系。

1　资　料

本文所用积雪资料为罗格斯大学全球雪实验室提供的月平均积雪范围(Robinson et al,1993),这是一种可见光遥感资料,虽然存在着分辨率低、受云的干扰大等缺点(曹梅盛,1995),但对于某些公认异常多(少)雪的年份,如 1982/1983 年和 1997/1998 年冬春多雪,1984/1985 年冬春少雪均有较好的体现,加上该资料更新及时、使用方便,故在气候监测和预测中的应用较为广泛。环流场采用 NCEP/NCAR 逐月再分析资料(Kalnay et al,1996)。另外,本文还使用了 NOAA 提供的陆地降水分析数据(PREC/L),该资料由全球超过 17000 个台站观测最优插值得到(Chen et al,2002)。文中各物理量的气候态为 1981—2010 年平均。

2　2012 年春季和前期冬季积雪及大气环流特征

国家气候中心的积雪监测业务显示 2011/2012 年冬季(2011 年 12 月至 2012 年 2 月)和 2012 年春季(3—5 月)青藏高原地区积雪指数(定义见郭艳君等,2004)为正距平,表明积雪较常年偏多。但是从积雪覆盖率距平空间分布(图 1)显示:冬季,青藏高原积雪空间分布不均,异常偏多中心区域主要有两个,一个在高原东部,另一个在高原西北部;春季,积雪偏多范围有所减小,但高原东部正距平中心依然存在,而高原西北部仍为大范围的积雪偏多区。以上特征与青藏高原台站积雪日数距平分布(图略)基本一致。这两个多雪区与气候平均状况下高原积雪鼎盛期的多雪区(李培基,1996)分布较吻合,它们的异常可能具有较强的气候效应,而高原中部积雪雪层很薄,气候效应不明显。2011/2012 年冬春季积雪分布与钱永甫等(2003)用 SVD 分析的第一模态积雪的空间分布比较一致,即高原东部地区为积雪偏多/少的典型区域。下面进一步分析高原积雪异常对环流的可能影响。

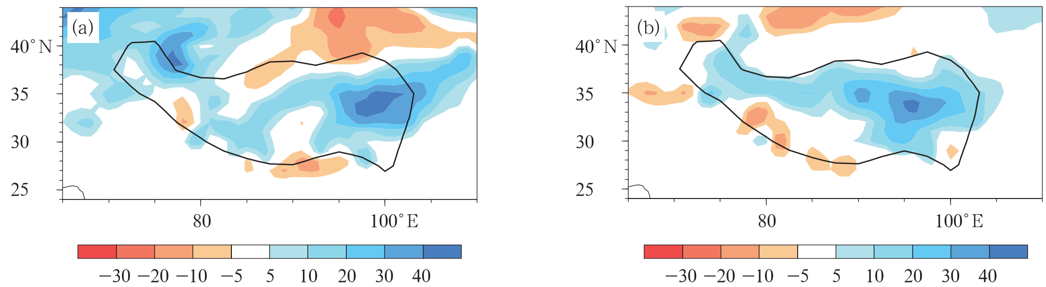

图 1　(a)2011/2012 年冬季(2011 年 12 月至 2012 年 2 月)和(b)2012 年春季(3—5 月)积雪覆盖率距平(单位:%)
(黑色粗实线为 3000 m 高度)

Fig. 1　Seasonal mean snow cover extent anomaly for (a) winter (December 2011－February 2012) and (b) spring (March－May 2012) (unit: %)
(Black solid line stands for 3000 m MSL)

张顺利等(2001)指出冬季青藏高原多雪年,在对流层中上层,亚洲副热带地区(10°～25°N)西风带偏强,东亚和西亚分别为气旋性环流距平,热带印度洋上空为反气旋性环流距平,少雪年冬季的情况几乎相反。然而 2012 年前期冬季的环流场表现为:亚洲副热带地区西风偏弱,东亚和西亚各为一个强大的反气旋式环流距平,热带印度洋上空为气旋式环流距平(图 2a),与典型多雪年的环流特征相反,只是环流异常中心位置较张顺利等(2001)给出的多雪年环流异常中心位置整体偏南约 5 个纬度。2012 年春季的环流异常基本延续了前期冬季的环流配置情况(图 2b),表现为西亚到阿拉伯半岛为反气旋式环流距平,东亚为反气旋式环流距平,中南半岛到孟加拉湾为气旋式环流距平。需要指出的是,2012年

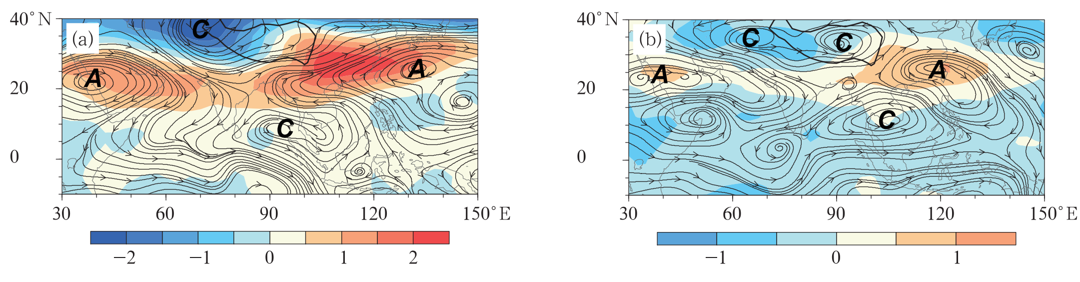

图 2　500 hPa 环流及气温(阴影,单位:K)距平
(a)2011/2012 年冬季,(b)2012 年春季

Fig. 2　500 hPa anomalies of circulation and temperature (unit: K) for (a) winter 2011/2012 and (b) spring 2012

春季在青藏高原及其以西地区为气旋式环流距平，这与典型多雪年的环流特征比较一致。以上环流信息表明2011/2012年冬季，亚洲区域的大尺度大气环流场与典型的异常多雪年环流具有较大差异，2012年春季，在青藏高原及其以西地区为典型多雪年的环流特征，但是在青藏高原以东和以南的地区为与典型多雪年相反的环流特征。

此外，在温度场上，典型多(少)雪年，高原及其附近地区为负(正)距平，高原以南地区为一致的正(负)距平(张顺利等，2001)。从2011/2012年冬春季500 hPa气温场来看(图2阴影部分)，2012年春季(图2b)，在90°E以西，自青藏高原及以西地区往南到热带印度洋，温度距平从北向南为负—正—负的空间分布，北部的气温负异常量值明显高于其南侧的正异常和负异常量值，即从大范围空间分布来看，高原及其以西的大部分地区气温和其南部的气温相比为北冷南暖的梯度分布，不利于南亚地区从冬到夏南北温度梯度的反转。在90°E以东，自青藏高原东部及其以东地区35°N往南到热带地区，气温距平呈北正南负的空间分布，即北暖南冷，有利于东亚地区从冬到夏的经向温度梯度反转；以上特征在冬季更加明显。因此，2012年春季和前期冬季对流层气温分布与典型积雪偏多年不同，在90°E以西，接近于积雪偏多年，而在90°E以东，不同于积雪偏多年。即2011/2012年冬春季，高原东部和西部的局地环流和温度场分布有差异。

综上分析，从监测看，2012年春季和前期冬季青藏高原积雪面积异常偏大，但相应的对流层中层的环流和气温异常分布与典型的积雪偏多年不同。90°E以西，尤其是南亚的环流和气温异常分布接近积雪偏多年的特征；90°E以东，高原东部及东亚地区，对流层中部气温为北正南负的距平特征，东亚为反气旋式环流距平，中南半岛及其邻近地区为气旋式环流距平，类似于积雪偏少年的特征。为什么高原积雪偏多的监测事实与东亚和南亚的环流特征不吻合呢？根据陶亦为等(2011)的工作，当前期冬春季ENSO为强暖(强冷)事件与高原积雪显著偏多(显著偏少)共同作用的配置下，我国东部夏季雨带往往偏南(偏北)。而当前期冬春季Nino3区海温略偏暖或正常偏暖(略偏冷或正常偏冷)与积雪略偏多或正常偏多(略偏少或正常偏少)的配置下，夏季雨带往往具有不确定性。而2011/2012年冬春季高原积雪偏多，但Nino3区海温为略偏暖，因此两个外强迫因子对亚洲夏季风和我国雨带的作用具有较大的不确定性。陈丽娟等(2013)对2012年夏季风偏强的成因进行了分析，认为除了东亚大气对弱La Nina事件有一定的响应外(Wang et al,2000)，冬季北极海冰异常偏少和南极涛动异常偏强也对东亚夏季风偏强有较大的贡献。下面将从诊断的角度分析2011/2012年冬春季青藏高原积雪对亚洲夏季风的贡献，着重于对南亚季风的影响。

3 2011/2012年冬春季青藏高原积雪异常对亚洲夏季风的可能影响

青藏高原抬升的地表对大气的季节性加热产生30°N以南经向温度梯度的逆转，激发了亚洲大尺度环流的变化(Flohn,1957)。青藏高原积雪的多寡会造成亚洲夏季风爆发相差20天之多(张顺利等，2001)。为考察高原积雪对季节变化的影响，我们分析了对流层温度梯度的转向和高层纬向风的逐候演变。在气候平均状况下(图3a)，亚洲东南部5月第3候左右首先由西风转为东风，然后向东、向西扩展。2012年(图3b)，5月第1候在亚洲东南部出现稳定的东风，并分别向东、西方向延伸，表明亚洲东南部冬夏环流的转换偏早，这与该地区对流层中高层前期冬春季温度距平为北正南负，即温度梯度偏弱(图2)有关，有利于春末夏初温度梯度反转偏早(图略)。南海地区(10°～20°N、110°～120°E)850 hPa平均纬向风及假相当位温逐候演变(图略)表明：2012年南海夏季风于5月4候爆发，较常年平均偏早1候(见中国气象局国家气候中心2012年第5期《东亚季风监测快报》)。因此，2012年亚洲东南部的季节转换偏早与低纬度地区大气环流特征具有密切联系，而这些环流特征与典型高原积雪偏多年不一致，即2011/2012年冬春季高原积雪偏多对东亚春夏季的环流影响很小。

Webster等(2006)研究指出在强(弱)亚洲夏季风的前期冬季和春季，亚洲副热带地区对流层上部西风偏弱(强)。冬春季对流层高层风场的这种变化很可能是亚洲夏季风强、弱变化的前兆信号之一，这种前兆信号在对流层呈正压结构，并且可能与冬春季高原积雪、南亚大陆上的土壤水分和ENSO事件有关(Yang et al,1996)。监测显示，2012年春季和前期冬季亚洲副热带地区对流层主要为东风距平，即西风偏弱，有利于亚洲夏季风偏强。而典型的青

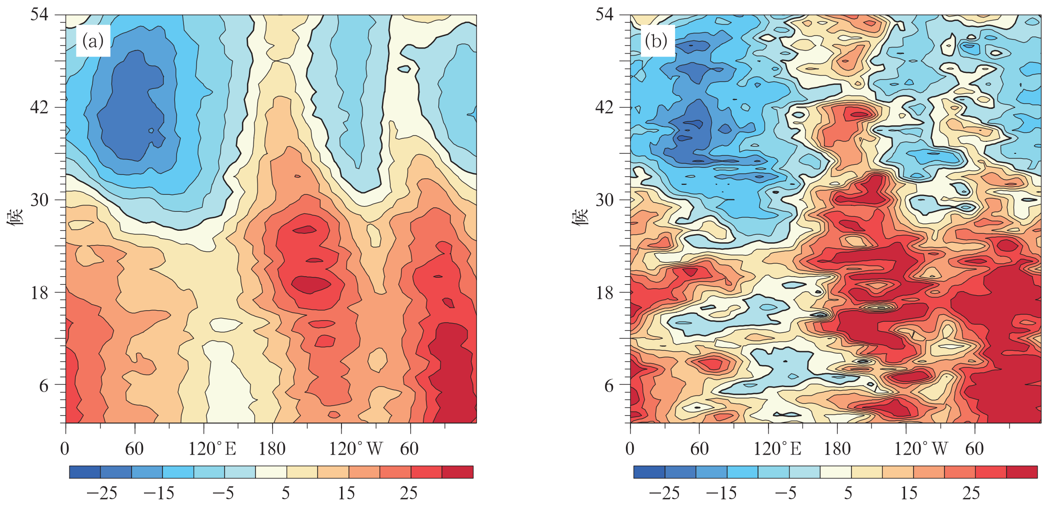

图 3　沿 15°N 200 hPa 纬向风(单位:m・s^{-1})的逐候演变

(a)1981—2010 年平均,(b)2012 年

Fig. 3　The pentad variation of 200 hPa zonal winds (unit: m・s^{-1}) along 15°N for (a) average from 1981 to 2010 and (b) 2012

藏高原积雪偏多年,高原上空气温偏低,不利于亚洲夏季风偏强。即 2012 年高原积雪偏多对亚洲夏季风的影响有限。以下做具体的诊断分析。

图 4 给出了 2012 年夏季平均 850 hPa 环流场及降水率距平。东亚地区,南海北部到西太平洋一带为气旋式环流距平,30°N 以北为反气旋式环流距平,江淮流域上空为东风距平,表明西太平洋副热带高压偏北,对应长江流域降水偏少,华北和华南降水偏多,这种形势与典型的积雪偏少年环流型相对应,该环流型主要是受弱 La Nina 事件、北极海冰偏少、南极涛动偏强的影响(Huang et al,1989;陈丽娟等,2013)造成的。南亚地区,除了印度东北部降水偏多外,印度大部分地区降水较常年偏少,相应的对流层低层为反气旋环流距平,这种环流型在对流层中部(图 5a)变得更加清晰,尤其是在印度半岛上空为闭合的反气旋式距平环流,即印度热低压偏弱;在对流层高层(图 5b),亚洲南部地区为气旋式环流距平,15°N附近为西风距平,即东风偏弱,以上这些表

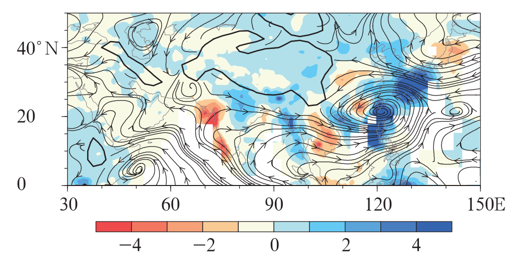

图 4　2012 年夏季(6—8 月)850 hPa 环流场距平和降水率距平(阴影,单位:mm・d^{-1})

(灰色粗实线为 1500 m 高度)

Fig. 4　850 hPa anomalies of circulation and precipitation rate (shaded, unit: mm・d^{-1}) for summer (June—August) 2012

(The areas included by the gray thick cures are 1500 m MSL)

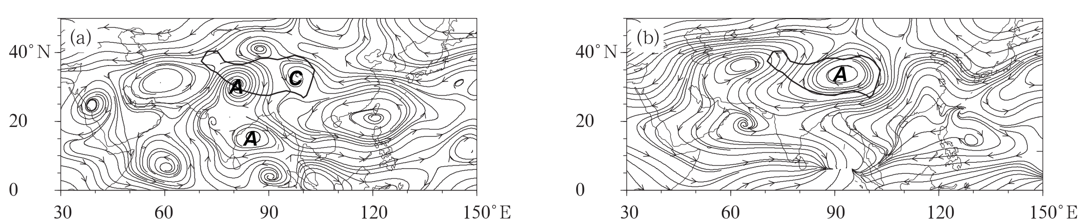

图 5　2012 年夏季流场距平

(a)500 hPa,(b)200 hPa

Fig. 5　Horizontal circulation anomaly for summer 2012

(a) 500 hPa, (b) 200 hPa

明 2012 年南亚夏季风偏弱。在青藏高原上空，500 hPa 距平流场上(图 5a)，高原东南部为气旋式环流，高原西部为反气旋式环流，对应高原东部降水偏多，西部降水偏少，这与以往积雪偏多年(张顺利等，2001；范广洲等，1997)一致；200 hPa 距平流场(图 5b)显示高原主体为反气旋式环流距平，中心在90°E 附近，表明青藏高压模态偏强，它与南亚夏季风环流偏弱成反位相变化。

为了进一步分析高原上空环流异常与南亚夏季风的关系，我们继续分析了沿 90°E 经圈环流垂直剖面图(图 6)。在气候平均状况下(图 6a)，孟加拉湾至高原南侧为强的上升区，在对流层高层气流向南运动，于 15°S 以南的南印度洋下沉，这是南亚季风环流圈。在高原北侧存在另一子经圈环流，上升支在高原上空，下沉支在新疆、甘肃地区，使得那里干旱少雨。2012 年(图 6b)，高原南侧是反向的季风经圈环流距平，20°S 为相对较弱的上升距平，孟加拉湾至高原南侧以下沉距平为主，表明南亚夏季风环流偏弱。高原北侧为一负的子经圈环流，新疆、甘肃地区的下沉运动减弱，上升运动增强，该地区降水偏多(图 4)。

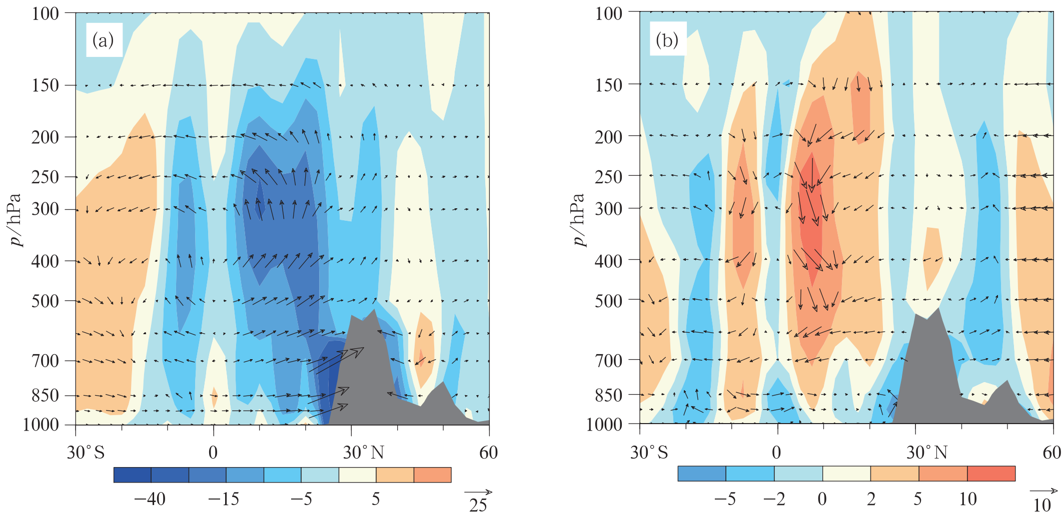

图 6　夏季平均沿 90°E 垂直环流场距平剖面图
(a)气候态，(b)2012 年
[阴影为扩大 200 倍的垂直运动(单位：Pa・s^{-1})]
Fig. 6　Height-latitude cross section of summer mean vertical circulation anomalies along 90°E for (a) climate mean and (b) 2012
[Vertical velocities (shaded, unit: Pa・s^{-1}) are enlarged 200 times]

青藏高原积雪偏多，南亚夏季风环流偏弱，这很可能是由于高原感热偏弱使得高原南侧温度对比偏弱造成的(张顺利等，2001)。我们计算了 60°～90°E 平均的 500 hPa 气温距平的逐候演变(图 7)。1—3 月，30°N 以北的高原上空气温异常偏低，而 30°N 以南的印度半岛及附近海域上空气温明显偏高，这与图 2 一致。4—8 月，20°N 至高原地区几乎持续偏冷，而 20°N 以南至热带印度洋在 5 月底才出

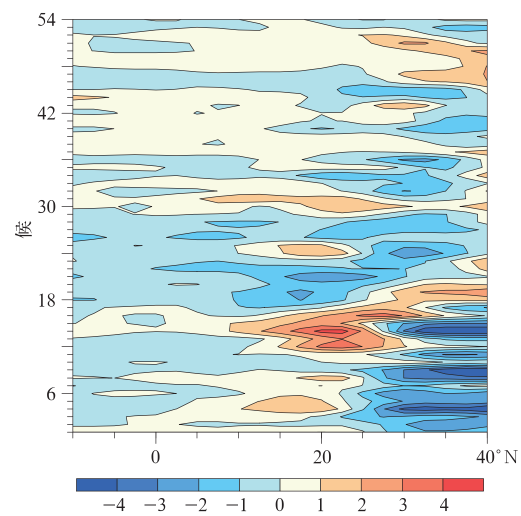

图 7　60°～90°E 平均的 500 hPa 气温距平(单位：K)逐候演变
Fig. 7　The pentad variation of 500 hPa air temperature anomalies (unit: K) average by 60°−90°E

现弱的偏暖并维持到整个夏季。这种形态在高原近地面层最明显，随着高度增加而减弱，但这足以说明高原积雪的滞后效应。因此，前期冬春季青藏高原积雪偏多，有利于夏季高原及其附近地区气温偏低，导致夏季热带印度洋到高原西部地区大尺度温度梯度偏小，利于南亚夏季风偏弱。

综上所述，2011/2012 年冬春季亚洲低纬度地区（特别是 90°E 以东）大气环流受到海温、极冰、南极涛动等因素的影响，有利于亚洲东南部的季节转换偏早；而 90°E 以西地区的环流，尤其是南亚夏季风偏弱可能受到前期冬春季高原积雪异常偏多的作用。

4　结论和讨论

2011/2012 年冬春季青藏高原积雪面积异常偏大，其上空对应的大气环流型与典型积雪偏多年具有较大差异。不能简单地以高原对亚洲夏季风的影响结果得出东亚夏季风偏弱的结论。资料分析显示 2012 年冬春季，特别是在 90°E 以东的东亚地区至其南侧的低纬度地区，对流层温度距平为北正南负型，温度梯度偏弱，有利于春末夏初温度梯度反转，即有利于亚洲东南部大气环流冬夏季节转换偏早，南海夏季风爆发偏早，但这种结果受到高原以外的其他外强迫信息的影响。另一方面，前期冬春季高原积雪偏多，有利于高原上空自冬到夏对流层中部温度持续偏低，在 90°E 以西，自青藏高原到热带地区，前期冬春季对流层中部气温距平北冷南暖，夏季自热带印度洋到高原温度梯度偏弱，南亚夏季风偏弱。

2012 年夏季，亚洲季风区的大气环流受到积雪、弱 La Nina 事件、北极海冰、南极涛动等因素的共同影响。一方面，高原积雪偏多，使得南亚夏季风偏弱；另一方面，受 La Nina、北极海冰、南极涛动等的滞后影响，南海夏季风爆发早，东亚夏季风偏强。因此，高原积雪异常和 ENSO 循环的不同位相以及其他信号的组合作用使得它们对亚洲夏季风的影响更加复杂。同时，高原积雪影响的复杂性也提示我们积雪空间分布的差异、高原上空环流分布的局地特征也能造成亚洲夏季风成员表现出不一致的影响结果，提示预报员在实际业务中应谨慎对待外强迫信号的组合效果。

参考文献

曹梅盛. 1995. 青藏高原 NOAA/NESDIS 数字化积雪监测的评价. 冰川冻土，17(4)：299-302.

陈丽娟，吕世华，罗四维. 1996. 青藏高原春季积雪异常对亚洲季风降水影响的数值试验. 高原气象，15(1)：124-130.

陈丽娟，高辉，龚振淞，等. 2013. 2012 年汛期气候预测的先兆信号和应用. 气象，39(9)：1103-1110.

陈烈庭，阎志新. 1979. 青藏高原冬春积雪对大气环流和我国南方汛期降水的影响. 中长期水文气象预报文集. 北京：水利电力出版社，185-194.

陈乾金，高波，张强. 2000. 青藏高原冬季雪盖异常与冬夏季风变异及其相互联系的物理诊断研究. 大气科学，24(4)：477-492.

董敏，余建锐. 1997. 青藏高原春季积雪对大气环流影响的模拟研究. 应用气象学报，8(增刊)：100-109.

范广洲，罗四维，吕世华. 1997. 青藏高原冬季积雪异常对东、南亚夏季风影响的初步数值模拟研究. 高原气象，16(2)：140-152.

郭艳君，李威，陈乾金. 2004. 北半球积雪监测诊断业务系统. 气象，30(11)：24-27.

李培基. 1996. 亚洲季风模拟试验中青藏高原积雪强迫问题的讨论. 高原气象，15(3)：350-355.

刘晓东，田良，韦志刚. 1994. 青藏高原地表反射率变化对东亚夏季风影响的数值试验. 高原气象，13(14)：468-472.

卢咸池，罗勇. 1994. 青藏高原冬春季雪盖对东亚夏季大气环流影响的数值试验. 应用气象学报，5(4)：385-393.

罗勇. 1995. 青藏高原冬春季雪盖对东亚夏季大气环流影响的研究. 高原气象，14(4)：505-512.

彭京备，陈烈庭，张庆云. 2005. 青藏高原异常雪盖和 ENSO 的多尺度变化及其与中国夏季降水的关系. 高原气象，24(3)：366-377.

钱永甫，张艳，郑益群. 2003. 青藏高原冬春季积雪异常对中国春夏季降水的影响. 干旱气象，21(3)：1-7.

孙林海，宋文玲. 2001. 冬季积雪对我国夏季降水预测的评估分析. 气象，27(8)：24-27.

陶亦为，孙照渤，李维京，等. 2011. ENSO 与青藏高原积雪的关系及其对我国夏季降水异常的影响. 气象，37(8)：919-928.

韦志刚，罗四维. 1993. 中国西部积雪对我国汛期降水的影响. 高原气象，12(4)：347-354.

韦志刚，陈文，黄荣辉. 2008. 青藏高原冬春积雪异常影响中国夏季降水的数值模拟. 高原山地气象研究，28(1)：1-7.

王艳姣，周兵，司东，等. 2013. 2012 年夏季我国降水异常及成因分析. 气象，39(1)：121-125.

张顺利，陶诗言. 2001. 青藏高原积雪对亚洲夏季风影响的诊断及数值研究. 大气科学，25(3)：372-390.

周悦，刘宣飞，陈海山. 2012. 青藏高原冬春积雪影响南海季风爆发的数值研究. 热带气象学报，27(6)：912-919.

朱玉祥，丁一汇. 2007a. 青藏高原积雪对气候影响的研究进展和问题. 气象科技，35(1)：1-8.

朱玉祥，丁一汇，徐怀刚. 2007b. 青藏高原大气热源和冬春积雪与中国东部降水的年代际变化关系. 气象学报，65(6)：946-958.

Bamzai A S，Shukla J. 1999. Relation between Eurasian snow cover，snow depth，and the Indian summer monsoon：An observational study. Journal of Climate,12(10):3117-3132.

Blanford H F. 1884. On the connexion of the Himalaya snowfall with dry winds and seasons of drought in India. Proceedings of the Royal Society of London,37(232-234):3-22.

Chen M,Xie P,Janowiak J E,et al. 2002. Global land precipitation: A 50-yr monthly analysis based on gauge observations. Journal of Hydrometeorology,3(3):249-266.

Fasullo J A. 2004. Stratified diagnosis of the Indian monsoon—Eurasian snow cover relationship. Journal of Climate,17(5):1110-1122.

Flohn H. 1957. Large-scale aspects of the "summer monsoon" in South and East Asia. Journal of the Meteorological Society of Japan, 75:180-186.

Huang R,Wu Y. 1989. The influence of ENSO on the summer climate change in China and its mechanism. Advances in Atmospheric Sciences,6(1):21-32.

Kalnay E,Kanamitsu M,Kistler R,et al. 1996. The NCEP/NCAR 40-year reanalysis project. Bulletin of the American Meteorological Society,77(3):437-471.

Qian Y,Zheng Y,Zhang Y,et al. 2003. Responses of China's summer monsoon climate to snow anomaly over the Tibetan Plateau. International Journal of Climatology,23(6):593-613.

Robinson D A,F Dewey K,Heim R Jr. 1993. Global snow cover monitoring: An update. Bulletin of the American Meteorological Society,74:1689-1696.

Walker G T. 1910. Correlation in seasonal variation of weather (II). Mem Indian Meteor Dept,21:22-45.

Wang B,Wu R,Fu X. 2000. Pacific-East Asian teleconnection: How does ENSO affect East Asian climate? Journal of Climate,13(9):1517-1536.

Webster P J,Yang S. 2006. Monsoon and ENSO: Selectively interactive systems. Quarterly Journal of the Royal Meteorological Society,118(507):877-926.

Wu T W,Qian Z A. 2003. The relation between the Tibetan winter snow and the Asian summer monsoon and rainfall: An observational investigation. Journal of Climate,16(12):2038-2051.

Wu Z,Li J,Jiang Z,et al. 2012. Modulation of the Tibetan Plateau snow cover on the ENSO teleconnections: From the East Asian summer monsoon perspective. Journal of Climate,25(7):2481-2489.

Yang S,Lau K M,Sankar-Rao M. 1996. Precursory signals associated with the interannual variability of the Asian summer monsoon. Journal of Climate,9(5):949-964.

ADVANCES IN CLIMATE CHANGE RESEARCH 4(4): 242-249, 2013
www.climatechange.cn
DOI: 10.3724/SP.J.1248.2013.242

CHANGES IN CLIMATE SYSTEM

Representation of the Arctic Oscillation in the CMIP5 Models

ZUO Jin-Qing[1,2], LI Wei-Jing[2], REN Hong-Li[2]

[1] *Chinese Academy of Meteorological Sciences, Beijing* 100081*, China*

[2] *Laboratory for Climate Studies, National Climate Center, China Meteorological Administration, Beijing* 100081*, China*

Abstract

The temporal variability and spatial pattern of the Arctic Oscillation (AO) simulated in the historical experiment of 26 coupled climate models participating in the Coupled Model Intercomparison Project Phase 5 (CMIP5) are evaluated. Spectral analysis of the monthly AO index indicates that 23 out of the 26 CMIP5 models exhibit no statistically significant spectral peak in the historical experiment, as seen in the observations. These models are able to reproduce the AO pattern in the sea level pressure anomaly field during boreal winter, but the intensity of the AO pattern tends to be overestimated in all the models. The zonal-mean zonal wind anomalies associated with the AO is dominated by a meridional dipole in the mid-high latitudes of the Northern Hemisphere during boreal winter, which is well reproduced by only a few models. Most models show significant biases in both strength and location of the dipole compared to the observation. In considering the temporal variability as well as spatial structures in both horizontal and vertical directions, the MPI-ESM-P model reproduces an AO pattern that resembles the observation the best.

Keywords: Arctic Oscillation; model evaluation; coupled climate model; CMIP5

Citation: Zuo, J.-Q., W.-J. Li, and H.-L. Ren, 2013: Representation of the Arctic Oscillation in the CMIP5 models. *Adv. Clim. Change Res.*, **4**(4), doi: 10.3724/SP.J.1248.2013.242.

1 Introduction

It is well known that the global mean surface temperature has been increased in recent decades [*Tang et al.*, 2012]. Detection of recent climate changes, attribution of causes, and projection of parameter changes are the main topics in climate change research [*Wang et al.*, 2012]. Coupled global climate models (CGCM) are the major objective tools available for climate change attribution and projection studies. In general, we assume that the models, which are able to reproduce past climate changes the best, might also be able to simulate future changes with high accuracy. For that reason, it is crucial to assess the ability of CGCMs in simulating the observed climate changes, especially the dominant modes of the atmospheric low-frequency variability [*Stoner et al.*, 2009].

The Arctic Oscillation (AO) is the leading mode of the extra-tropical low-frequency variability and is characterized by a seesaw of pressure anomalies between the middle and high latitudes of the Northern Hemisphere [*Thompson and Wallace*, 1998]. Due to the quasi-zonally symmetric structure of the AO, it is also referred to as the Northern Hemisphere annular mode [*Thompson and Wallace*, 2000]. Many previous studies have demonstrated that the AO has important impact on the surface climate variability and storm track activity over wide regions of the Northern Hemi-

Received: 2 July 2013
Corresponding author: ZUO Jin-Qing, zuojq@cma.gov.cn

sphere [*Thompson and Wallace*, 2000; 2001]. In particular, the surface air temperature anomalies over North America, Greenland, Eurasia, and North Africa are closely related to the AO variability during winter. Also, the AO has an obvious influence on the East Asian winter monsoon as well as the winter surface air temperature and precipitation over China [*Gong et al.*, 2001; *Wu and Wang*, 2002; *Gong and Wang*, 2003]. In the last two decades of the 20th century, the AO experienced a positive phase of extremes during winter, which intensified the warm anomalies over Eurasia, including Northeast Asia [*Thompson and Wallace*, 2001; *Jü et al.*, 2004]. Therefore, changes in the phases of the AO tend to alter the range of surface climate conditions as experienced in many locations over the Northern Hemisphere, and may have implications on future changes.

The ability of CGCMs to simulate the AO variability is an important aspect of model evaluation. Previous studies show that atmospheric general circulation models (AGCM) and atmosphere-ocean coupled models are both able to reproduce the AO pattern, but have difficulties in simulating the observed positive trend of the winter AO in the second half of the 20th century [*Yamazaki and Shinya*, 1999; *Robertson*, 2001]. The AO pattern as simulated by CGCMs has been widely evaluated using the outputs of 20th century simulations from the Coupled Model Intercomparison Project Phase 3 (CMIP3) [*Miller et al.*, 2006; *Xin et al.*, 2008; *Zhu and Wang*, 2008; *Stoner et al.*, 2009]. It has been demonstrated that almost all the CMIP3 models are able to reproduce the spatial pattern of the AO, whereas their ability to simulate the magnitude and location of the pattern as well as its temporal variability needs to be improved.

The latest CMIP project, namely CMIP5, was coordinated by the World Climate Research Programme's (WCRP's) Working Group on Coupled Modeling (WGCM). This project involved about 30 climate modeling groups around the world. The CMIP5 project is designed to advance our knowledge of climate variability and climate change, and to provide simulations for evaluation in the IPCC Fifth Assessment Report (AR5) [*Taylor et al.*, 2012]. Most CMIP5 models have been improved in physical processes and the coupled carbon cycle. For this reason, we will evaluate the ability of those state-of-the-art coupled climate models in simulating the AO variability. Here, the temporal variability and spatial pattern of the AO simulated in historical experiments of 26 CMIP5 models are focused on. A comparison of the simulated AO variability between CMIP5 and CMIP3 models was given by *Zhu et al.* [2013].

2 Model simulations and calculation methods

In this paper, the simulations from 26 coupled climate models participating in the CMIP5 project are listed. Model provenance and resolution are provided in Table 1. These models are from 18 institutions in 11 countries. Most of the atmospheric components have a horizontal resolution in the range of 2° to 3°, with the MRI-CGCM3 having the highest resolution of 1.1°. Ten models are physical climate system models that do not include the carbon cycle, while the other 16 models are Earth system models that incorporate a coupled carbon cycle.

Model outputs used in this study are obtained from the CMIP5 historical run, which is initiated from an arbitrary point of a quasi-equilibrium control run and integrating no less than 156 years (1850–2005). The CMIP5 historical run is forced by time-evolving greenhouse gases, ozone, aerosols, and a solar constant that are consistent with the observations, and, for the first time, including time-evolving land cover/land use pattern [*Taylor et al.*, 2012]. All the model outputs are interpolated to a regular grid of 2.5°×2.5°before the actual analysis.

We compare the historical simulations with observed sea level pressure (SLP) obtained from the Hadley Centre HadSLP2 dataset at a resolution of 5°×5° [*Allan and Ansell*, 2006] and quasi-observational zonal wind from the NCEP/NCAR reanalysis project at a resolution of 2.5°×2.5° [*Kalnay et al.*, 1996]. The observation and reanalysis are both referred to as observation in this study, though the reanalysis is not a real observation.

Table 1 Information of CMIP5 climate models

Model name	Country	Resolution
ACCESS1.0	Australia	1.875×1.25
BCC-CSM1.1	China	2.8×2.8
CanESM2	Canada	2.8×2.8
CCSM4	United States	1.25×0.94
CESM1-CAM5 (FV2)	United States	2.5×1.9
CNRM-CM5	France	1.4×1.4
FGOALS-g2	China	2.8×2.8
FIO-ESM	China	2.8×2.8
GFDL-CM3	United States	2.5×2.0
GFDL-ESM2M	United States	2.5×2.0
GFDL-ESM2G	United States	2.5×2.0
GISS-E2-H	United States	2.5×2.0
GISS-E2-R	United States	2.5×2.0
HadCM3	United Kingdom	3.75×2.5
HadGEM2-AO	Korea	1.875×1.25
HadGEM2-ES	United Kingdom	1.875×1.25
HadGEM2-CC	United Kingdom	1.875×1.25
INMCM4	Russia	2.0×1.5
IPSL-CM5A-LR	France	3.75×1.875
IPSL-CM5A-MR	France	2.5×1.25
MIROC5	Japan	1.4×1.4
MIROC-ESM	Japan	2.8×2.8
MPI-ESM-LR	Germany	1.9×1.9
MPI-ESM-P	Germany	1.9×1.9
MRI-CGCM3	Japan	1.1×1.1
NorESM1-M	Norway	2.5×1.875

According to *Thompson and Wallace* [2000], we define the AO as the first leading empirical orthogonal function (EOF) mode of monthly mean SLP anomalies poleward of 20°N. To ensure equal area weighting for the covariance matrix for the EOF analysis, the SLP anomalies are weighted by the square root of the cosine of latitude. The AO index is defined as the normalized time series corresponding to the first leading EOF. The spatial pattern of the AO, comparable to the EOF, is presented as the regressions of SLP anomalies onto the time series of the AO index. The regression coefficients correspond to amplitudes of one standard deviation of the index. Simulations and observations for the period of 1950–2005 are analyzed in this study. Since the AO is most prominent in the cold season, and its activity centers always move northward in winter, as compared to summer [*Barnston and Livezey*, 1987], only spatial patterns of the winter AO (December to next February) are shown in this study. All monthly data per year are used for the spectral analysis. The linear trends are removed prior to the correlation/regression analysis.

3 Comparison of AO patterns between simulations and observations

3.1 *Temporal variability*

Figure 1 shows the power spectra for the monthly AO index derived from observations and from each model simulation. Notable peaks in observations are found near 6-, 12-, and 36-month cycles (Fig. 1a), indicating semiannual and annual behavior and lower-frequency variability of the AO pattern, although all these peaks are not statistically significant at the 95% confidence level. All the spectral peaks in the model simulations are not statistically significant either, except those for three models (HadCM3, HadGEM2-CC, and HadGEM2-ES) from the Hadley Centre. Most models reproduce the semiannual behavior, as seen in the observations. However, less than half of the models capture the observed annual behavior. The GFDL-CM3, GFDL-ESM2G and MPI-ESM-LR exhibit a near 3-year cycle, similar to the observation, whereas this cycle in the GFDL-CM3 is obviously stronger than in the observation. The three models from the Hadley Centre exhibit a significant and tall peak near 1 year and two relatively smaller peaks near 4 and 6 months, indicating large seasonal and interannual variability of the AO pattern in these model simulations. In addition, some models display peaks at about 4 months, 8–9 months, 2 years and/or 4–5 years, which cannot be found in the observations.

The observational analysis shows that the negative phase of the winter AO is more frequent from the 1950s to the 1970s, but less frequent thereafter. The phase of the winter AO tends to change from positive to negative in the first decade of the 21st century, indicating a large inter-decadal variability of the AO pattern. In Figure 1a, the observed AO indices show a final peak beginning from near 6-year and increasing in power until the end of the analyzed period, which confirms the large inter-decadal variability of the AO pattern. However, only a few CMIP5 models, including BCC-CSM1.1, CNRM-CM5, HadGEM2-AO, MPI-ESM-P, and MRI-CGCM3, are able to capture the inter-decadal component in the observed AO variability. On the contrary, the power tends to decrease

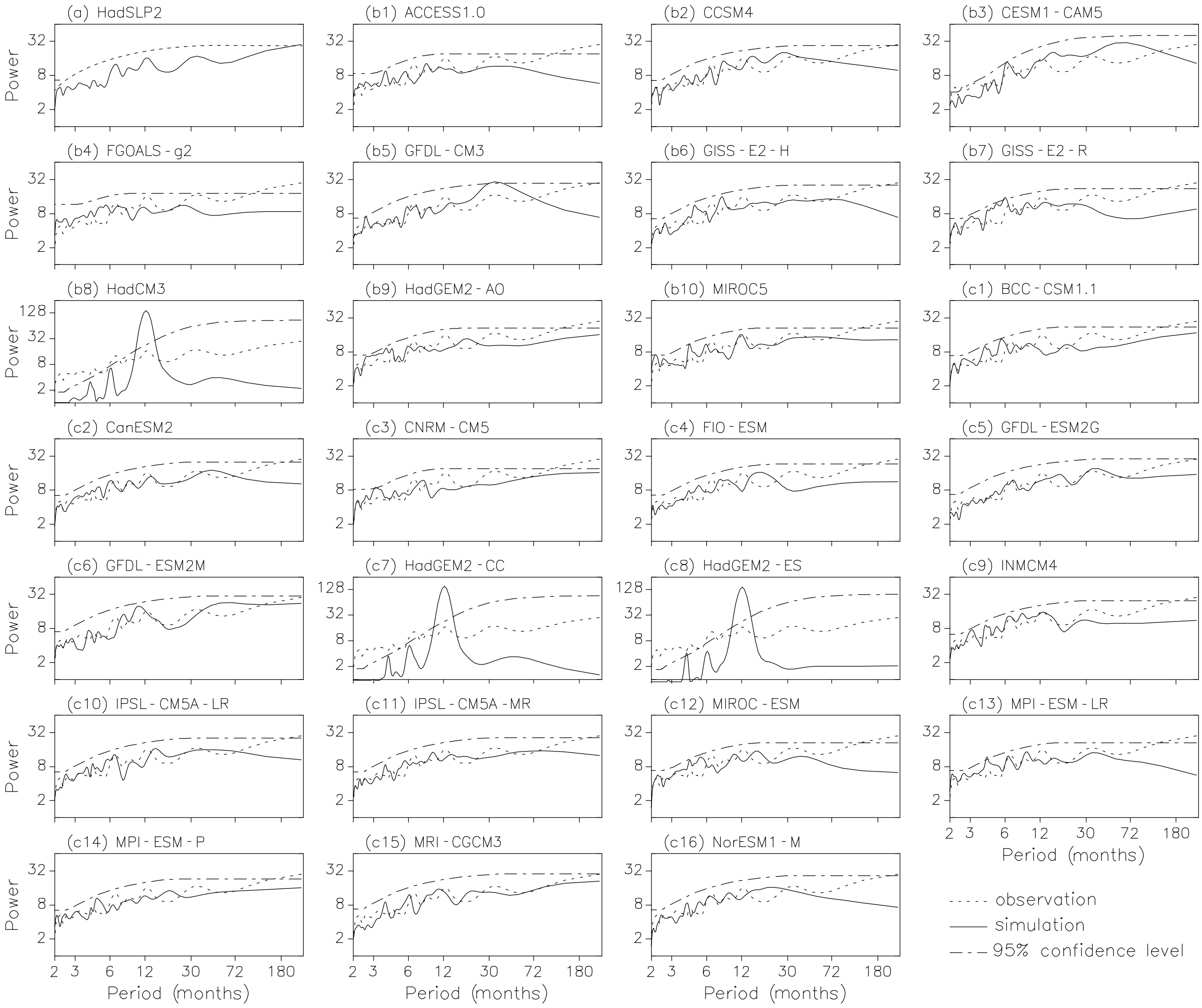

Figure 1 Smoothed power spectra for the time series of monthly AO index derived from (a) observation (HadSLP2; also dotted line), and (b, c) the CMIP5 model simulations (solid lines) (the dashed line indicates the 95% confidence limit above the red noise spectrum; b1–b10 are the physical climate system models and c1–c16 the Earth system models)

with the period in about half of the CMIP5 model simulations, indicating that the inter-decadal variability is weaker compared to the observations. In addition, the spectral analysis is applied to the winter-mean AO index (Figures not shown), where the power spectrum for the winter-mean AO index agrees well with the monthly AO index at annual to inter-decadal time scales. Overall, the majority of the CMIP5 models simulate the AO temporal variability quite poor. There is no significant difference in the ability to simulate the AO temporal variability between the physical climate system models and the Earth system models.

3.2 *Spatial patterns in the SLP field*

To assess the ability of the CMIP5 models in simulating the spatial patterns of the AO, Figure 2 shows the regression of SLP anomalies on the AO index during winter. It can be seen that all the CMIP5 models, except those from the Hadley Centre, clearly simulate a recognizable AO pattern. The first leading EOF for the winter SLP anomalies simulated by the HadCM3 (Fig. 2b8) and HadGEM2-CC (Fig. 2c7) are featured by a negative anomaly over the pole and Eurasia, with a maximum centered over northern Eurasia. For the HadGEM2-ES, a positive anomaly mainly occurs over the middle latitudes of North America, the northeastern Atlantic and Eurasia, whereas a negative anomaly occurs over the North Pacific, Greenland and the adjacent regions (Fig. 2c8). These results indicate that the models from Hadley Centre may have difficulties in simulating the spatial patterns of the winter AO. In particular, they all exaggerate the relationship between AO and SLP anomalies over Siberia.

The observed AO pattern consists of three activity centers as denoted by the star symbol (Fig. 2a). One is located near the pole (A1), and the other two are located in the middle latitudes of the Atlantic (A2) and the Pacific (A3). The observed A1 is characterized by a single-pole structure and centered near the Atlantic. More than half of the CMIP5 models produce an A1 shifting to the Eastern Hemisphere and/or with a dipole structure. In addition, most models dis-

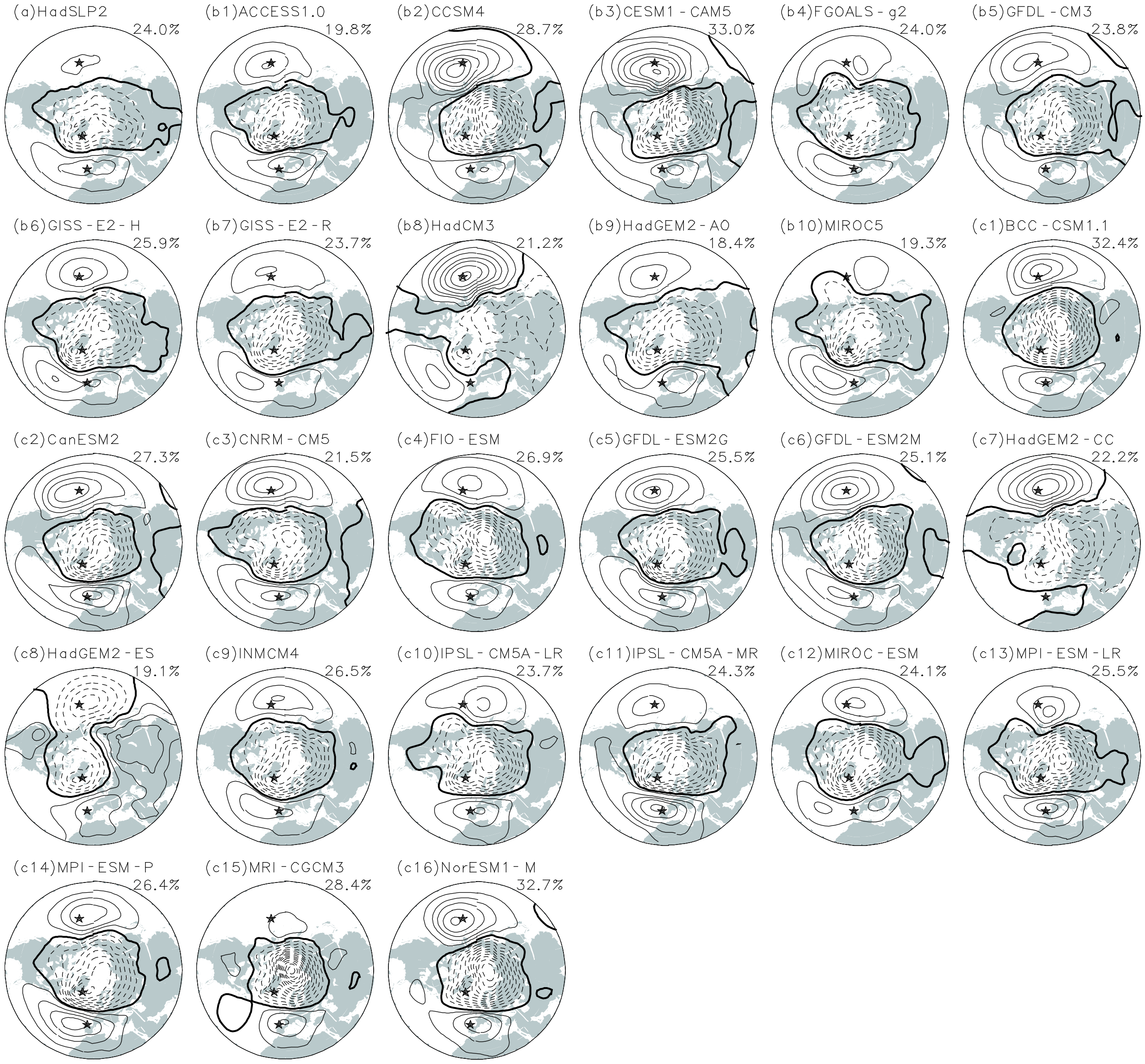

Figure 2 Regressions of SLP anomalies in winter on the AO index derived from the observation (HadSLP2) and the CMIP5 model simulations (the dashed line indicates negative values and the thick solid line is zero; the percentage of variance explained by the winter AO pattern is given at the top right-hand corner of each frame; ★ shows the three activity centers of the AO obtained from the observation)

place A2 more eastward or westward. Only five models, IPSL-CM5A-MR, MIROC5, MPI-ESM-LR, MPI-ESM-P and MRI-CGCM3, reproduce A3 with a weaker magnitude than A2, as is observed.

Almost all the models overestimate the magnitude of the AO pattern, especially the activity center in the North Pacific. To quantitatively measure the resemblance of the simulated AO pattern to the observed, the Taylor diagram [*Taylor*, 2001], which summarizes the comparison of wintertime AO pattern between the observation and the CMIP5 model simulations, is shown in Figure 3. The results indicate that the spatial correlation coefficient with the observation is above 0.80 for all the CMIP5 models, except the three models from Hadley Centre. More than half of the models have a spatial correlation coefficient with the observation of no less than 0.90. The amplitude of the AO pattern for each model is about 1.2 to 1.9 times as that of the observation, which further confirms that all models overestimate the amplitude of AO pattern.

The majority of the physical climate models reproduce an AO pattern that more resembles the observation than the Earth system models (Fig. 3). The AO is a dominant mode of the extra-tropical, low-frequency atmospheric variability, and its formation and maintenance are closely related to the atmospheric internal dynamics. Since the Earth system model incorporates a coupled carbon cycle, the reproduction may be more complicated than the physical climate model, which only consists of interactions between the ocean, land, atmosphere and sea ice. In other words, the latter is advantageous in simulating the AO pattern at the recent development in coupled models.

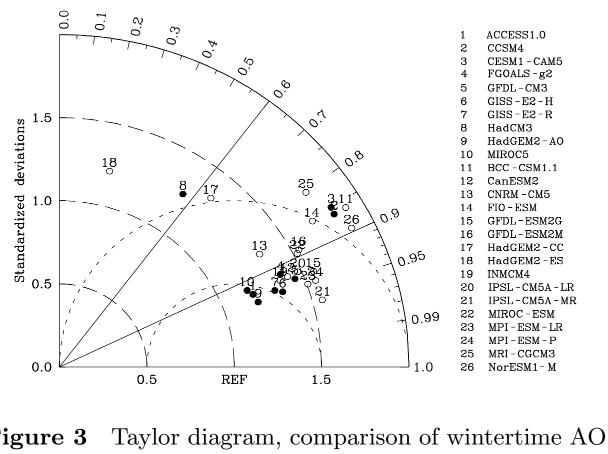

Figure 3 Taylor diagram, comparison of wintertime AO pattern between observation and CMIP5 model simulations. The radial distance from the origin indicates the standard deviation of AO pattern for each model normalized by the observed value. The azimuthal position denotes the correlation between the observed and simulated AO pattern. A solid circle indicates a physical climate system model and a hollow circle an Earth system model

3.3 *Vertical structure in the zonal-mean zonal wind field*

The AO is characterized by an equivalent barotropic structure from the surface upward into the lower stratosphere during boreal winter [*Thompson and Wallace*, 2001]. The zonal-mean zonal wind anomalies associated with the AO exhibit a meridional dipole in the mid-high latitudes of the Northern Hemisphere. Corresponding to the positive phase of the AO, easterly anomalies occur in the middle latitudes south of 45°N, with a maximum in the upper troposphere, while westerly anomalies are observed in high latitudes, amplifying with height upward into the lower stratosphere (Fig. 4a). These wind anomalies correspond to the weakened subtropical westerly jet and the strengthened polar jet [*Li and Wang*, 2003].

To evaluate the vertical structure of the AO as simulated by the CMIP5 models, Figure 4 shows the regression of zonal-mean zonal wind anomaly onto the AO index derived from the observation and the model simulations during winter. It is indicated that almost all of the CMIP5 models exhibit a meridional dipole in the zonal-mean zonal wind anomaly field associated with the AO in the mid-high latitudes of the Northern Hemisphere, as seen in observation. But the models tend to overestimate or underestimate the observed amplitude of the dipole. In addition, there are significant biases in the location of the dipole between the simulations and the observation. The mid- and high-latitude activities of the dipole are hereafter referred to as SJ and PJ, respectively. The CMIP5 models, except GISS-E2-R (Fig. 4b7), MRI-CGCM3 (Fig. 4c15) and the three models from the Hadley Centre (Fig. 4-b8, 4-c7 and 4-c8), are all able to reproduce the observed PJ amplifying and titling poleward with height. But most models tend to display the PJ more northward. Some models have difficulties in simulating the location of the wind maximum corresponding to the PJ. For example, the FGOALS-g2 (Fig. 4b4), GFDL-

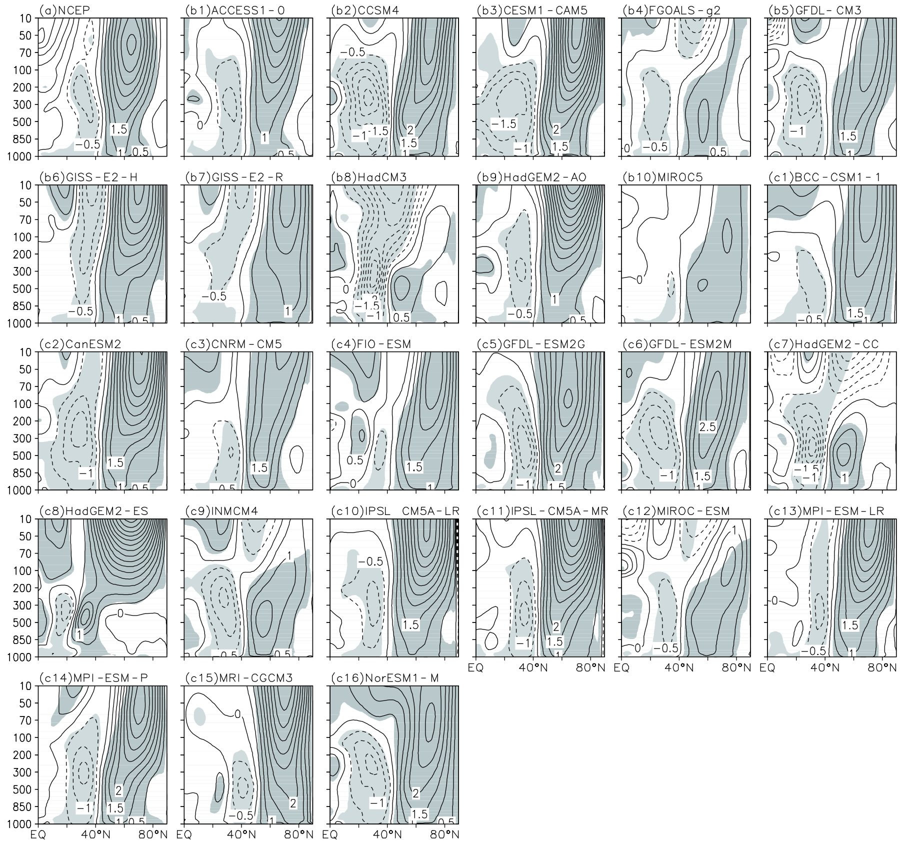

Figure 4 Regressions of the wintertime zonal-mean zonal wind anomaly (m s^{-1}) with the AO index derived from (a) the observation (NCEP) and (b, c) the CMIP5 model simulations (gray shading indicates significance at the 95% confidence level)

ESM2G (Fig. 4c5), GFDL-ESM2M (Fig. 4c6), INMCM4 (Fig. 4c9), MIROC5 (Fig. 4b10) and MIROC-ESM (Fig. 4c12) display the wind maximum of the PJ more downward to the upper or middle troposphere. The wind maximum of the SJ is centered in the troposphere in most of the model simulations, similar to the observation. However, there are some models, such as GISS-E2-H (Fig. 4b6) and GISS-E2-R (Fig. 4b7), which display the wind maximum of the SJ more upward to the lower stratosphere. In the CCSM4 (Fig. 4b2), CESM1-CAM5 (Fig. 4b3) and GFDL-CM3 (Fig. 4b5), the SJ extends more southward compared to the observation. Overall, the vertical structure of the AO is best simulated by the MPI-ESM-P than the other CMIP5 models.

4 Conclusions and discussion

The temporal variability and spatial pattern of the AO simulated in the historical experiment of 26 CMIP5 models were evaluated. The spectral analysis of monthly AO index indicates that only the HadCM3, HadGEM2-CC, and HadGEM2-ES, all from the Hadley Centre, exhibit a significant and tall peak near 1 year and two relatively small peaks near 4 and 6 months. The other 23 models exhibit no statistically significant spectral peak in the historical experiment, as similar to the observations. Also, these models are able to reproduce the AO pattern in the SLP anomaly field during winter. But the magnitudes of the AO pattern tend to be overestimated in all models. The majority of the physical climate models reproduce an AO pattern that resembles the observation better than the Earth system models. The observed zonal-mean zonal wind anomalies associated with the AO are characterized by a meridional dipole in the mid-high latitudes of the Northern Hemisphere during winter. Although almost all CMIP5 models can capture a dipole, there are significant biases in both magnitude and location of the dipole between the simulations and observation, indicating that the ability of most CMIP5 models to simulate the vertical structure of the AO needs to be improved. Considering the temporal variability and spatial structures in both horizontal and vertical directions, the MPI-ESM-P reproduces the best AO pattern in comparison of the 26 CMIP5 models and the observation.

Acknowledgements

The authors are grateful for the useful comments and suggestions of the two anonymous reviewers. We acknowledge the WCRP Working Group on Coupled Modeling, which is responsible for CMIP5, and we thank the climate modeling groups for producing and making available their model outputs. This work was supported by the National Basic Research Program of China (No. 2010CB950501 & 2010CB950404), the National Natural Science Foundation of China (No. 41205058), and the China Postdoctoral Science Foundation (No. 2012M510634).

References

Allan, R., and T. Ansell, 2006: A new globally complete monthly historical gridded mean sea level pressure dataset (HadSLP2): 1850-2004. *J. Climate*, **19**, 5816-5842.

Barnston, A. G., and R. E. Livezey, 1987: Classification, seasonality and persistence of low-frequency atmospheric circulation patterns. *Monthly Weather Review*, **115**, 1083-1126.

Gong, D.-Y., and S.-W. Wang, 2003: Influence of Arctic Oscillation on winter climate over China. *Acta Geographica Sinica* (in Chinese), **58**(4), 559-568.

Gong, D.-Y., S.-W. Wang, and J.-H. Zhu, 2001: East Asian winter monsoon and Arctic Oscillation. *Geophys. Res. Lett.*, **28**, 2073-2076.

Jü, J.-H., J.-Z. Ren, and J.-M. Lü, 2004: Effect of interdecadal variation of Arctic Oscillation on temperature increasing in North of East Asian winter. *Plateau Meteorology* (in Chinese), **23**(4), 429-434.

Kalnay, E., M. Kanamitsu, R. Kistler, et al., 1996: The NCEP/NCAR 40-year reanalysis project. *Bull. Amer. Meteor. Soc.*, **77**, 437-472.

Li, J.-P., and J. X. L. Wang, 2003: A modified zonal index and its physical sense. *Geophys. Res. Lett.*, **30**, doi:1011029P2003GL017441.

Miller, R. L., G. A. Schmidt, and D. T. Shindell, 2006: Forced annular variations in the 20th century Intergovernmental Panel on Climate Change assessment report models. *J. Geophys. Res.*, **111**, D18101.

Robertson, A. W., 2001: Influence of ocean-atmosphere interaction on the Arctic Oscillation in two general circulation models. *J. Climate*, **14**, 3240-3254.

Stoner, A. M. K., K. Hayhoe, and D. J. Wuebbles, 2009: Assessing general circulation model simulations of atmospheric teleconnection patterns. *J. Climate*, **22**, 4348-4372.

Tang, G.-L., Y. Luo, J.-B. Huang, et al., 2012: Continuation of the global warming. *Progressus Inquisitiones De Mutatione Climatis* (in Chinese), **8**(4), 235-242.

Taylor, K. E., 2001: Summarizing multiple aspects of model performance in a single diagram. *J. Geophys. Res.*, **106**, 7183-7192.

Taylor K. E., R. J. Stouffer, and G. A. Meehl, 2012: An overview of CMIP5 and the experiment design. *Bull. Amer. Meteor. Soc.*, **93**, 485-498.

Thompson, D. W. J., and J. M. Wallace, 1998: The Arctic Oscillation signature in the wintertime geopotential height and temperature fields. *Geophys. Res. Lett.*, **25**, 1297-1300.

Thompson, D. W. J., and J. M. Wallace, 2000: Annular modes in the extratropical circulation. Part I: Month-to-month variability. *J. Climate*, **13**, 1000-1016.

Thompson, D. W. J., and J. M. Wallace, 2001: Regional climate impacts of the Northern Hemisphere annular mode. *Science*, **293**, 85-89.

Wang, S.-W., Y. Luo, Z.-C. Zhao, et al., 2012: Attribution of climate warming to the causes. *Progressus Inquisitiones De Mutatione Climatis* (in Chinese), **8**(4), 308-312.

Wu, B.-Y., and J. Wang, 2002: Winter Arctic Oscillation, Siberian High and East Asian winter monsoon. *Geophys. Res. Lett.*, **29**(19), doi:10.1029/2002GL015373.

Xin, X.-G., T.-J. Zhou, and R.-C. Yu, 2008: The Arctic Oscillation in coupled climate models. *Chinese Journal of Geophysics*, **51**(2), 223-239.

Yamazaki, K., and Y. Shinya, 1999: Analysis of the Arctic Oscillation simulated by AGCM. *Journal of Meterological Society of Japan*, **77**, 1287-1298.

Zhu, X., W.-J. Dong, and Y. Guo, 2013: Comparison of simulated winter and spring Arctic Oscillation variability by CMIP5 and CMIP3 coupled models. *Advances in Climate Change Research* (in Chinese), **9**(3), 165-172.

Zhu, Y.-L., and H.-J. Wang, 2008: The Arctic and Antarctic oscillations in the IPCC AR4 coupled models. *Acta Meteorologica Sinica* (in Chinese), **66**(6), 993-1004.

ADVANCES IN ATMOSPHERIC SCIENCES, VOL. 30, NO. 4, 2013, 1173–1186

Impact of the North Atlantic Sea Surface Temperature Tripole on the East Asian Summer Monsoon

ZUO Jinqing*[1,2] (左金清), LI Weijing[2] (李维京), SUN Chenghu[2] (孙丞虎), XU Li[3], and REN Hong-Li[2] (任宏利)

[1] *Chinese Academy of Meteorological Sciences, Beijing* 100081

[2] *Laboratory for Climate Studies, National Climate Center, China Meteorological Administration, Beijing* 100081

[3] *Department of Atmospheric, Oceanic and Earth Science, George Mason University, Fairfax, Virginia* 22030, *USA*

(Received 17 June 2012; revised 16 September 2012; accepted 19 October 2012)

ABSTRACT

A strong (weak) East Asian summer monsoon (EASM) is usually concurrent with the tripole pattern of North Atlantic SST anomalies on the interannual timescale during summer, which has positive (negative) SST anomalies in the northwestern North Atlantic and negative (positive) SST anomalies in the subpolar and tropical ocean. The mechanisms responsible for this linkage are diagnosed in the present study. It is shown that a barotropic wave-train pattern occurring over the Atlantic-Eurasia region likely acts as a link between the EASM and the SST tripole during summer. This wave-train pattern is concurrent with geopotential height anomalies over the Ural Mountains, which has a substantial effect on the EASM. Diagnosis based on observations and linear dynamical model results reveals that the mechanism for maintaining the wave-train pattern involves both the anomalous diabatic heating and synoptic eddy-vorticity forcing. Since the North Atlantic SST tripole is closely coupled with the North Atlantic Oscillation (NAO), the relationships between these two factors and the EASM are also examined. It is found that the connection of the EASM with the summer SST tripole is sensitive to the meridional location of the tripole, which is characterized by large seasonal variations due to the north–south movement of the activity centers of the NAO. The SST tripole that has a strong relationship with the EASM appears to be closely coupled with the NAO in the previous spring rather than in the simultaneous summer.

Key words: EASM, North Atlantic SST tripole, diabatic heating, eddy-vorticity forcing, NAO

Citation: Zuo, J. Q., W. J. Li, C. H. Sun, L. Xu, and H.-L. Ren, 2013. Impact of the North Atlantic sea surface temperature tripole on the East Asian summer monsoon. *Adv. Atmos. Sci.*, **30**(4), 1173–1186, doi: 10.1007/s00376-012-2125-5.

1. Introduction

The East Asian summer monsoon (EASM) prevails over China, especially over Eastern China. The summer drought/flood events over this region, which usually cause a large impact on society and the economy, are closely related to EASM variations (Ding, 1992). Owing to the complex nature of the EASM, a better understanding of cause-effect and potential predictors for EASM variability is needed, and thus this issue is a hot topic in the climate research.

EASM variability is influenced by atmospheric circulation anomalies, not only over the tropical and subtropical monsoon region, but also over the middle and high latitudes of the Northern Hemisphere (Zhang and Tao, 1998; Wu and Zhang, 2011). Recent studies have demonstrated that North Atlantic SST anomalies could exert an important impact on East Asian climate variability by inducing a zonal wave-train pattern occurring over the Atlantic-Eurasia region during summer (Wu et al., 2010, 2011). In particular, a strong EASM is usually concurrent with a tripole pattern of SST anomalies in the North Atlantic on the interannual timescale (Wu et al., 2009; Zuo et al., 2012), which features positive SST anomalies in the Northwest Atlantic and negative SST anomalies in the

*Corresponding author: ZUO Jinqing, jqzuo425@126.com

subpolar and tropical ocean, and vice versa. Gu et al (2009) pointed out that this SST tripole also has an important effect on EASM rainfall on the decadal timescale. However, these studies focused mainly on the persistence of the SST tripole from spring through summer, and far too little attention has been paid to the mechanism responsible for the linkage between the tripole and the EASM. Thus, in this study we attempt to answer the question of how the summer SST tripole in the North Atlantic induces changes in atmospheric circulation and then exerts an impact on the EASM on the interannual timescale.

Previous studies have revealed that the North Atlantic Oscillation (NAO), which is believed to be a potential predictor for EASM variability on the interannual timescale (Ogi et al., 2003; Sung et al., 2006), is always followed by the SST tripole in the North Atlantic (Cayan, 1992; Deser and Timlin, 1997; Czaja and Frankignoul, 2002; Zhou et al., 2006). Owing to the strong persistence of the SST tripole from spring through summer, the tripole tends to act as a link between the spring NAO and the EASM (Wu et al., 2009). It has been indicated that the NAO is an atmospheric teleconnection pattern evident in all the seasons of the year in the Northern Hemisphere (Barnston and Livezey, 1987). Nevertheless, the interannual variability of East Asian summer climate is strongly correlated with the NAO and the associated North Atlantic SST tripole in the previous spring rather than in the simultaneous summer (Wu et al., 2009, 2010, 2011). This raises the question as to why the relationship of the EASM with the previous spring NAO is better than that with the simultaneous summer NAO. Thus, another issue to be addressed in this study is whether there are differences in the NAO-induced SST tripole between spring and summer as well as in the relationships between these two factors and the EASM on the interannual timescale.

This paper is composed of six sections. The observational data and two linear dynamic models applied in the study are described in section 2. The linkage between EASM and the North Atlantic summer SST tripole is illustrated in section 3 and the mechanisms responsible for it are explored in section 4. The relationships among the North Atlantic SST tripole, NAO and EASM are further discussed in section 5. Finally, a summary and discussion are given in section 6.

2. Data and models

2.1 *Observational data*

The daily and monthly geopotential height and zonal and meridional wind components, with a horizontal resolution of 2.5°×2.5°, were obtained from the National Centers for Environmental Prediction/National Center for Atmospheric Research (NCEP/NCAR) reanalysis (Kalnay et al., 1996). These variables are available at standard pressure levels and cover the period 1948–2011. This study also employed monthly sensible and latent heat fluxes, as well as 10-m horizontal winds, with 192 equally-spaced longitudinal grid points and 94 unequally-spaced latitudinal grid points, derived from the NCEP/NCAR reanalysis. In addition, we utilized monthly SST data from the National Oceanic and Atmospheric Administration (NOAA) for the period 1948–2011 (Smith et al., 2008). These data have a horizontal resolution of 2.0°×2.0°. The monthly mean rainfall data, with a horizontal resolution of 2.5°×2.5°, were obtained from the Climate Prediction Center (CPC) Merged Analysis of Precipitation (CMAP) (Xie and Arkin, 1997) for the period 1979–2009.

The EASM index used in the study was defined as the difference in regional-averaged 850-hPa zonal wind between the East Asian tropical monsoon trough region (5°–15°N, 90°–130°E) and the East Asian subtropical region (22.5°–32.5°N, 110°–140°E) (Wang and Fan, 1999). A high EASM index denoted a strong EASM, which was generally concurrent with drought in the Yangtze River region in China during summer, and vice versa. According to Li and Wang (2003), the NAO index was calculated based on monthly differences in normalized sea level pressure between 35°N and 65°N over the North Atlantic (80°W–30°E).

To quantitatively describe the interannual variations of the North Atlantic SST tripole that had a strong relationship with the EASM, a SST index (hereinafter referred to as TI) was constructed as the difference between regional-averaged SST anomalies in the middle North Atlantic (34°–44°N, 72°–62°W) and the sum of regional-averaged SST anomalies in the tropics (44°–56°N, 40°–24°W) and in the subpolar ocean (0°–18°N, 46°–24°W). The choice of these domains was based on the linear correlations of the EASM index with SST anomalies in the North Atlantic during summer (Zuo et al., 2012; see their Fig. 3h). During the positive (negative) phase of the SST tripole, SST anomalies were higher (lower) than normal in the Northwest Atlantic, and lower (higher) than normal in the subpolar and tropical ocean. Figure 1 displays the time series of normalized summer TI and EASM indices during the period 1979–2011. It can be seen that the EASM index had a significant in-phase relationship with the summer TI. Their correlation coefficient was 0.55, which was significant at the 95% confidence level.

Owing to the weak correlation between the EASM and the North Atlantic summer SST tripole before

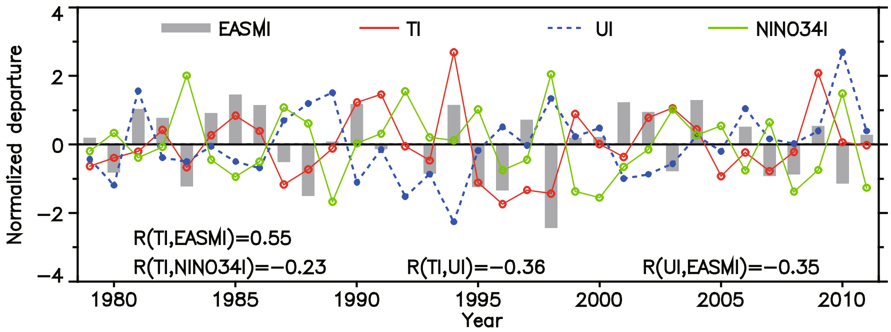

Fig. 1. Time series of the normalized summer tripole SST index (TI), EASM index (EASMI) and Ural geopotential height index (UI), and the preceding winter Nino3.4 SST index (Nino34I) for the period 1979–2011. R is the linear correlation coefficient.

the late 1970s (Zuo et al., 2012), the observational analysis in this study was performed for the period 1979–2011, expect for the moving-correlation shown in Fig. 10. Besides, the linear trends of all the time series were removed before the analysis.

2.2 *Linear dynamic models*

In this study, the role of diabatic heating in maintaining the anomalous low-frequency flow was diagnosed via a linear barotropic model. This model was a time-independent model with a horizontal resolution of T42 and followed a simple barotropic vorticity equation given as:

$$\partial_t \nabla^2 \psi' + J\left(\overline{\psi}, \nabla^2 \psi'\right) + J\left(\psi', \nabla^2 \overline{\psi} + f\right) + \nu \nabla^6 \psi' + \alpha \nabla^2 \psi' = S' , \tag{1}$$

where t denotes the time derivative; J represents a Jacobian operator; $\overline{\psi}$ and ψ' are the basic state and perturbation stream functions, respectively; f is the Coriolis parameter; and S' is the anomalous vorticity source induced by the divergent part of the circulation. The barotropic model included a linear damping term that represented the Rayleigh friction, and scale-selective biharmonic diffusion. The biharmonic diffusion coefficient v was selected to dampen the small-scale eddy in one day, while the Rayleigh friction coefficient α was set at $(10\ \mathrm{d})^{-1}$, which ensured that the system was stable at integration (Watanabe, 2004).

The linear baroclinic model employed in this study was a time-dependent model based on primitive equations. The model had a resolution of T42 in the horizontal direction and 20 sigma (σ) levels in the vertical direction. Rayleigh friction and Newtonian damping employed in the model were given as the rate of $(1\ \mathrm{d})^{-1}$ for the lower ($\sigma \leqslant 0.03$) and upper ($\sigma \geqslant 0.9$) levels, and $(30\ \mathrm{d})^{-1}$ for the other levels. The biharmonic diffusion coefficient was $2\times10^{16}\ \mathrm{m}^4\ \mathrm{s}^{-1}$. More details relating to this model can be found in Watanabe and Kimoto (2000) and Watanabe and Jin (2003). With the dissipation terms adopted, the model response took about 20 days to approach a steady state. So, the average of the last five days of a 30-day integration is analyzed in this paper.

3. The linkage between the EASM and the North Atlantic summer SST tripole

To expose the connection between the EASM and the summer SST tripole in the North Atlantic, we employed regression analysis to the summer TI and geopotential height anomalies at 300 hPa, 500 hPa and 850 hPa, respectively. The associated results are given in Fig. 2. Also included in Fig. 2a is the upper-level westerly jet stream represented by the climatological summer mean of 300-hPa zonal wind. It can be seen that a clear zonal wave-train pattern occurs over the Atlantic-Eurasia region. For convenience, this wave-train pattern will be referred to simply as NAE throughout the remainder of the paper. Note that the NAE pattern has the same phase in the lower, middle and upper troposphere, thereby showing an equivalent barotropic structure in the entire troposphere. Associated with the NAE pattern, negative height anomalies prevail over both the subpolar North Atlantic and the region around the Ural Mountains, while positive height anomalies prevail over both the northwest Atlantic and western Europe. These height anomaly centers are mainly located along the upper-level westerly jet stream. The NAE pattern seems to be induced by the North Atlantic summer SST tripole, and the mechanisms that maintain this pattern will be further explored in section 4. In addition, a meridional wave-train pattern can be seen along the East Asian Coast, which is possibly related to the diabatic heating over the tropical Northwest Pacific (Huang and Li, 1987; Nitta, 1987; Huang and Sun, 1992) and thus beyond the scope of this study.

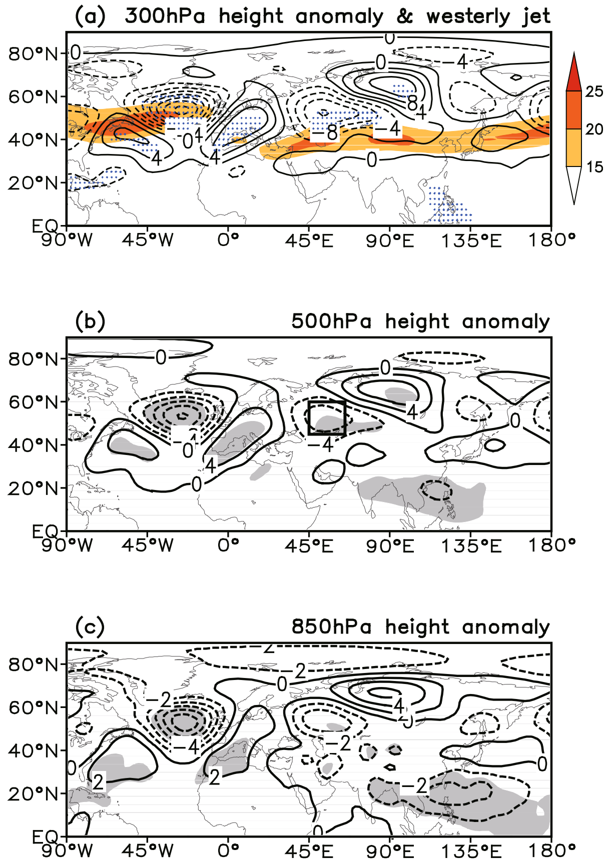

Fig. 2. Geopotential height anomalies (contour; gpm) at (a) 300 hPa, (b) 500 hPa, and (c) 850 hPa, obtained by regressing upon the tripole SST index during summer. Shading in (a) represents the climatological summer mean of 300-hPa zonal wind (m s^{-1}). Dots in (a) and shading in (b) and (c) indicate those regions that are significant at the 95% confidence level. The box in (b) denotes the domain for defining the Ural geopotential height index.

From the above analysis, the EASM and the North Atlantic summer SST tripole appear to be linked by the NAE pattern, which is concurrent with geopotential height anomalies over the region around the Ural Mountains. Many previous studies have revealed that atmospheric circulation anomalies over the Ural Mountains have a substantial effect on the EASM (Zhang and Tao, 1998; Li and Ji, 2001). A positive anomaly of seasonal-mean 500-hPa geopotential height around the Ural Mountains represents intensified blocking activity over this region, which favors an enhanced East Asian subtropical front that tends to result in a weakened EASM, and vice versa. As mentioned above, the negative (positive) geopotential height anomalies over the Ural Mountains coincide with the positive (negative) phase of the North Atlantic SST tripole during summer (Fig. 2), which agrees with the in-phase relationship between the tripole and the EASM (Fig. 1). This result indicates that the impact of the summer SST tripole on the EASM is closely linked to the Ural circulation anomalies. Wu et al. (2009) pointed out that the SST tripole could also result in circulation anomalies over the Okhotsk Sea, but our results show that the regressed geopotential height anomalies over this region are insignificant during summer (Fig. 2).

To support the role of Ural circulation anomalies in linking the EASM and the North Atlantic summer SST tripole, we plotted in Fig. 3 the correlations of summer SST anomalies in the North Atlantic with the summer Ural height index (UI) and EASM index, respectively. The UI here is defined as the regional-averaged 500-hPa geopotential height anomalies in the Ural region (45°–60°N, 45°–65°E). For the convenience of comparison, the sign of the UI has been reversed. It can be seen that the pattern of correlations between the UI and SST anomalies greatly resembles that of the correlations between the EASM index and SST anomalies, not only in shape but also in meridional location, both projecting on the positive tripole mode in the North Atlantic. In addition, the correlation coefficients of the summer UI with the summer TI and EASM index were −0.36 and −0.35, respectively, both of which were significant at the 95% confidence level. These results indicate that geopotential height anomalies around the Ural Mountains have a close relationship with the North Atlantic SST tripole during summer, which supports the conclusion that the former appears to play a key role in linking the SST tripole and the EASM on the interannual timescale.

4. Mechanism diagnostics

The results reported in section 3 suggested that the NAE pattern occurring over the Atlantic-Eurasia region appears to act as a link between the EASM and the North Atlantic summer SST tripole. In this section, the mechanisms responsible for maintaining the NAE pattern are further discussed by focusing on the diabatic heating and synoptic eddy-vorticity forcing, which are the two most important forcings among all forcings to maintain the anomalous low-frequency in middle latitudes (Branstator, 1992; Peng and Whitaker, 1999; Peng et al., 2003).

4.1 *Role of diabatic heating in maintaining the NAE pattern*

The SST anomalies initially induce changes in the local atmospheric circulation through diabatic heating and then could exert an impact on the remote atmospheric circulation by energy dispersion of Rossby

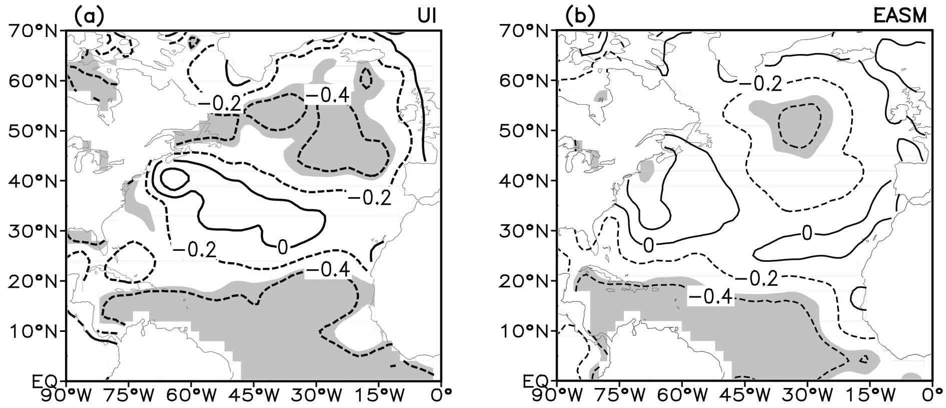

Fig. 3. Correlation coefficients between SST anomalies and (a) Ural geopotential height index (UI) and (b) EASM index during summer. Shading represents those regions that are significant at the 95% confidence level. For convenience of comparison, the sign of UI has been reversed.

waves (Trenberth et al., 1998; Peng and Whitaker, 1999; Peng et al., 2003). Hence, the role of diabatic heating associated with the North Atlantic summer SST tripole in maintaining the NAE pattern is diagnosed.

Figures 4a–c show the anomalies of SST, 500-hPa vertical velocity and precipitation, respectively, obtained by regressing upon the TI during summer. Positive (negative) values of vertical velocity denote rising (sinking) motion. Owing to the similar pattern of regressed anomalies between the positive and negative phases of the SST tripole, except for a reversal in the sign, a detailed description is only given for the positive phase as follows. It is shown that there are positive SST anomalies in the Northwest Atlantic between 30°N and 45°N, and negative SST anomalies in the tropical North Atlantic between 5°N and 15°N, as well as in the subpolar ocean between 45°N and 60°N (Fig. 4a). Anomalous descent at 500 hPa (Fig. 4b) and below-normal precipitation (Fig. 4c) are seen over the tropical North Atlantic where the SST anomalies are negative, thereby indicating a suppressed convective activity by the cold SST anomaly. To balance the anomalous descent in the troposphere, anomalous convergent flow prevails in the upper troposphere (data not shown), which further triggers an anomalous Rossby wave source (Sardeshmuhk and Hoskins, 1988) and thus tends to provide a forcing for maintaining the NAE pattern. Negative precipitation anomalies can be seen over the middle North Atlantic, which are concurrent with the positive local SST anomalies, indicating that the associated diabatic heating appears to be insignificant over this region.

As expected, anomalous cyclonic flow prevails in the upper troposphere (Fig. 2a) and anticyclonic flow in the lower troposphere (Fig. 2c) over the Caribbean Sea and the adjacent regions, which feature a Gill-type response (Gill, 1980) to the tropical North Atlantic cooling. Note that a meridional wave-train pattern of geopotential height anomalies can be seen along the North American East Coast (Fig. 2), which is connected with the NAE pattern. These results indicate that the maintenance of the NAE pattern appears to depend on the tropical North Atlantic diabatic heating.

To confirm the role of diabatic heating in maintaining the NAE pattern, in Fig. 4d we show the turbulent heat flux (the sum of sensible and latent heat flux, and hereinafter referred to as SHLE) anomalies obtained by regressing upon the TI during summer. Positive (negative) SHLE indicates heat flux out of (into) the ocean surface. The 10-m horizontal wind anomalies regressed upon the TI is also included in Fig. 4d. Negative SHLE anomalies can be seen over the Northeast Atlantic between 10°N and 30°N, which are concurrent with the negative SST anomalies and neutral surface wind anomalies over this region. This indicates that the SST plays an active role in determining SHLE anomalies in the low latitudes of the North Atlantic. On the other hand, weak and positive SHLE anomalies are found over the western subtropical North Atlantic, corresponding to the warm SST anomalies, but less precipitation and southerly anomalies are found over this region. Moreover, positive SHLE anomalies can be seen over the subpolar North Atlantic, which are concurrent with the cold SST anomalies and strengthened westerlies over this region. Therefore, it appears that the positive SHLE anomalies over the subtropical (subpolar) North Atlantic mainly result from the strengthened southerly (westerly) flows, suggesting that atmospheric circulation plays a dominant role in determining the SHLE and SST anomalies in the extratropical

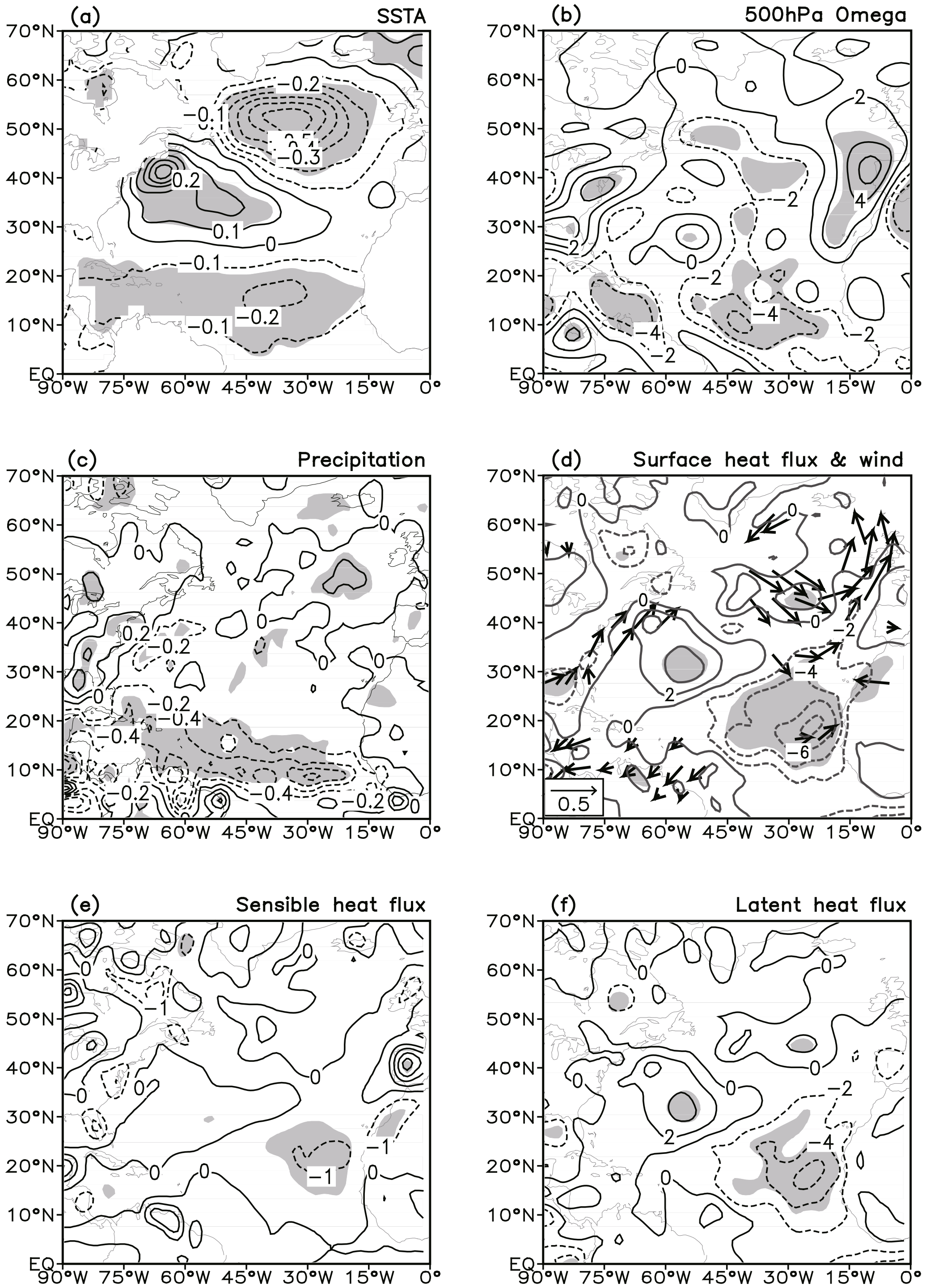

Fig. 4. (a) SST anomalies (K) obtained by regressing upon the tripole SST index during summer. Shading represents those regions that are significant at the 95% confidence level. (b) The same as in (a), but for the vertical velocity anomaly (10^{-3} Pa s^{-1}) at 500 hPa. Positive values in (b) denote rising motion. (c) The same as in (a), but for the precipitation anomaly (mm d^{-1}). (d) The same as in (a), but for the anomalies of total heat flux (sum of latent and sensible heat flux; contour; W m^{-2}) and 10-m horizontal wind vectors (vector; m s^{-1}). (e–f) The same as in (a), but for sensible and latent heat flux anomalies (W m^{-2}), respectively. A positive (negative) heat flux anomaly indicates heat flux out of (into) the ocean surface.

North Atlantic. To examine the respective contribution of sensible heat flux (SH) and latent heat flux (LE) to the SHLE, regression analysis was further applied to the summer TI and SH and LE anomalies, respectively. The results show that the SH anomalies are relatively weak over almost the whole North Atlantic (Fig. 4e), but the pattern of the LE anomalies (Fig. 4f) resembles closely that of the SHLE anomalies in the North Atlantic (Fig. 4d). Moreover, the magnitude of LE anomalies is comparable with that of SHLE anomalies. Therefore, the SHLE anomalies associated with the North Atlantic SST tripole are mainly determined by the LE anomalies during summer. These results support the importance of the role of tropical North Atlantic diabatic heating in maintaining the NAE pattern.

Further evidence for the connection of the NAE pattern with tropical North Atlantic diabatic heating is given in Fig. 5a, which shows the 500-hPa stream function anomaly and associated wave-activity flux (WAF) (Takaya and Nakamura, 2001) obtained by regressing upon the TI during summer. Associated with the NAE pattern, there are significant WAFs extended

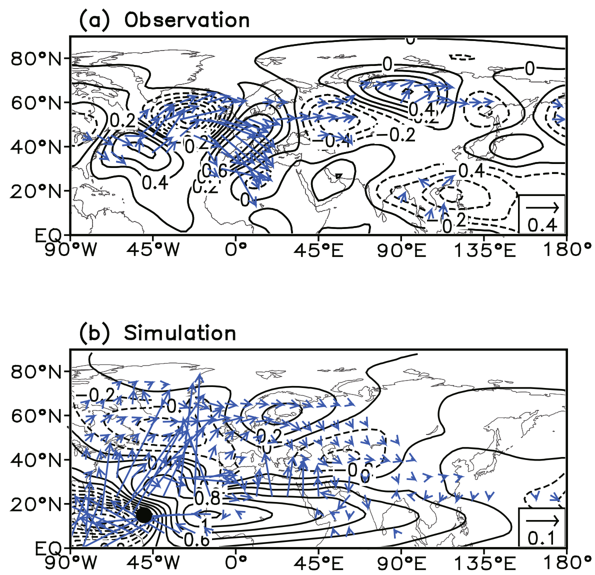

Fig. 5. (a) 500-hPa stream function anomaly (contour; 10^6 m^2 s^{-1}) and the associated wave-activity flux (vector; m^2 s^{-2}) obtained by regressing upon the tripole SST index during summer. (b) The same as in (a), but for the steady barotropic model response to the idealized vorticity forcing centered at (15°N, 50°W) (denoted by a closed circle).

northward from the middle North Atlantic to the subpolar ocean and then divided into two branches. One is southward to North Africa, and the other eastward to the region around the Ural Mountains. This suggests that tropical North Atlantic diabatic heating makes an important contribution to Atlantic–Eurasian circulation change through the NAE pattern.

Owing to the barotropic nature of the NAE pattern and its possible connection with tropical North Atlantic diabatic heating, processes that generate the height anomalies are conceivably understood in a barotropic vorticity equation (Branstator, 1983). For this purpose, an idealized experiment was conducted by using the linear barotropic model forced by the anomalous vorticity source. Based on the 500-hPa vertical velocity and precipitation anomalies shown in Figs. 4b and c, the prescribed vorticity forcing in the model was placed over the tropical North Atlantic with a maximum of 2.0×10^{-11} s^{-2} at (15°N, 50°W). The model was linearized about the climatological summer mean of the 300-hPa stream function derived from the NCEP/NCAR reanalysis. Figure 5b shows the stream function response and associated WAF to the idealized vorticity forcing. A clear wave-train pattern was found over the Atlantic-Eurasia region (Fig. 5b), which resembles the observed NAE pattern (Fig. 5a). In particular, anomalous cyclonic flows were identified over the Ural Mountains in both the model and observations, though the former shifted southward compared with the latter. These results support the importance of the role of tropical North Atlantic diabatic heating in maintaining the NAE pattern. Note that the stream function response in the model was smaller compared with the observational regression over the middle North Atlantic, but larger over the tropics. Actually, the observational regression reflected the equilibrium state among all the forcings. This implies that other factors, such as transient eddy forcing, may make an important contribution to maintaining the NAE pattern.

4.2 *Role of synoptic eddy-vorticity forcing in enhancing the NAE pattern*

In addition to diabatic heating, synoptic eddy forcing is another of the most important forcings in maintaining the anomalous low-frequency flow over the middle latitudes (Lau and Nath, 1991; Kug and Jin, 2009; Ren et al., 2009). In particular, synoptic eddy-vorticity forcing is the most important component of the eddy forcings (Branstator, 1992). Previous numerical studies have revealed that synoptic eddy-vorticity forcing is of vital importance to maintaining the atmospheric response to the North Atlantic SST anomalies during winter (Watanabe and Kimoto, 2000; Peng et al., 2003; Li, 2004; Li et al., 2007; Pan, 2007; Han et al, 2011). However, synoptic eddy forcing is sensitive to the background flow (Peng and Whitaker, 1999).

Hence, the role of synoptic eddy-vorticity forcing associated with the North Atlantic summer SST tripole in maintaining the NAE pattern is investigated.

According to the quasi-geostrophic potential vorticity equation, the synoptic eddy-vorticity feedback to the anomalous low-frequency flow could be depicted by a stream function tendency (ψ_t) satisfying the relationship as (Lau and Holopainen, 1984):

$$\nabla^2\psi_t = -\nabla\cdot\overline{\boldsymbol{V}'\zeta'}\,, \tag{2}$$

where $\boldsymbol{V}$ and ζ are the horizontal wind vector and relative vorticity, respectively. Here, the prime represents the synoptic-eddy component, and the overbar denotes a time average. To obtain the synoptic-eddy component, we applied the Lanczos filter (Duchon, 1979) to the daily zonal and meridional winds for the period ranging from two to eight days. The stream function tendency due to synoptic eddy-vorticity forcing was obtained by solving the Poisson equation.

Since synoptic eddy-vorticity forcing is highly correlated with storm-track activity, we examine both the anomalies of storm-track activity (Fig. 6a) and the eddy-induced stream function tendency at 300 hPa (Fig. 6b) obtained by regressing upon the TI during summer. The storm-track activity is represented by the root mean square of band-pass filtered (2–8 days) 500-hPa geopotential height. Also included in Figs. 6a and b are the climatological summer mean of storm-track activity and 300-hPa zonal wind, respectively. Owing to the barotropic nature of synoptic eddy-vorticity forcing and its largest effect on the low-frequency flow in the upper troposphere (Lau and Nath, 1991; Branstator, 1992), regression analysis was only applied to the 300-hPa eddy-induced stream function tendency in this study. We find that the regressed anomalies of storm-track activity show a north–south dipole straddling its mean position over the North Atlantic (Fig. 6a). During the positive phase of the North Atlantic SST tripole, the storm-track activity is enhanced on the south side and weakened in the north, which indicates a southward shift of the storm-track activity. Moreover, obvious and negative eddy-induced stream function tendency can be seen over the region near the North Atlantic upper-level westerly jet exit (Fig. 6b), which coincides with the negative geopotential height anomaly over this region (Fig. 2), thereby indicating a positive eddy-vorticity feedback. The negative eddy-induced stream function tendency also coincides with the southward shift of the storm-track activity over the North Atlantic, which indicates that the synoptic eddy-vorticity forcing is closely related to changes in the storm-track activity. An opposite sce-

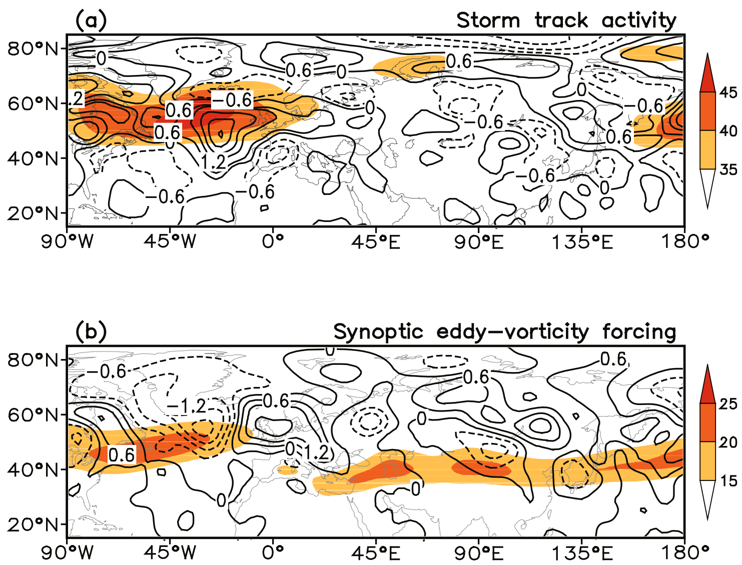

Fig. 6. (a) Anomalies of the storm-track activity (contour) obtained by regressing upon the tripole SST index during summer. The storm-track activity is defined as the root mean square of band-pass filtered 500-hPa geopotential height in the period of 2–8 days. Shading indicates the climatological summer mean of storm-track activity. Units are gpm. (b) The same as in (a), but for the stream function tendency (contour; m^2 s^{-2}) due to synoptic eddy-vorticity forcing at 300 hPa. Shading represents the climatological summer mean of zonal wind for the same layer (m s^{-1}).

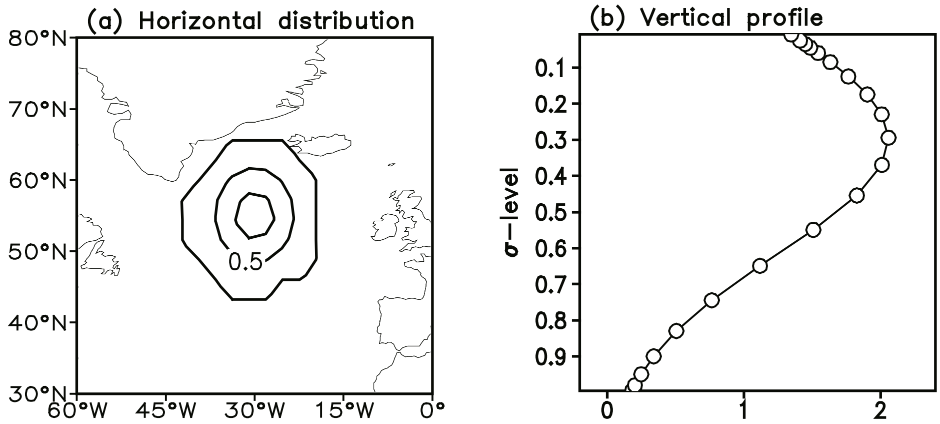

Fig. 7. (a) The vertical mean of eddy-vorticity forcing and (b) vertical profile of the forcing centered at (55°N, 30°W). Units: 10^{-11} s^{-2}.

nario can be seen for the negative phase of the North Atlantic SST tripole. There, results suggest that the synoptic eddy-vorticity flux divergence associated with the North Atlantic SST tripole appears to play an important role in maintaining the NAE pattern via a positive feedback mechanism during summer.

Linear baroclinic models are useful tools to diagnose the mechanism for maintaining the anomalous low-frequency flow by synoptic eddy forcing (Watanabe and Kimoto, 2000; Peng et al., 2003). Thus, an idealized experiment was performed by using a linear baroclinic model to confirm the role of synoptic eddy-vorticity forcing in maintaining the NAE pattern. For this experiment, the model was linearized about the summer climatology derived from the NCEP/NCAR reanalysis and forced by the synoptic eddy-vorticity flux divergence, which acted as the synoptic eddy-vorticity forcing. The horizontal distribution of depth-averaged eddy-vorticity forcing and the vertical profile of the maximum forcing in the initial state are given in Fig. 7. According to the observed eddy-induced stream function tendency (Fig. 6b), the eddy-vorticity forcing in the model was centered at σ=0.29 in the vertical direction and (55°N, 30°W) in the horizontal direction. As shown in Fig. 8, these idealized eddy-vorticity forcings applied to the baroclinic model triggered a negative stream function response right over the region where the forcings were placed, and two branches of Rossby waves to the east. One was southeastward to North Africa, and the other was eastward to East Asia, which resulted in a negative stream function response over the Ural Mountains. Note that the pattern of stream function response in the baroclinic model greatly resembled the observations shown in Fig. 5a. Therefore, the consistency between model simulation and observations is strong enough to support an active role of synoptic eddy-vorticity forcing in enhancing the NAE pattern during summer.

Experiments with an atmospheric general circulation model and a diagnostic linear baroclinic model by Li et al. (2007) suggested that the extratropical response to a tropical Atlantic SST anomaly is maintained primarily by synoptic eddy-vorticity forcing during winter. In other words, synoptic eddy-vorticity

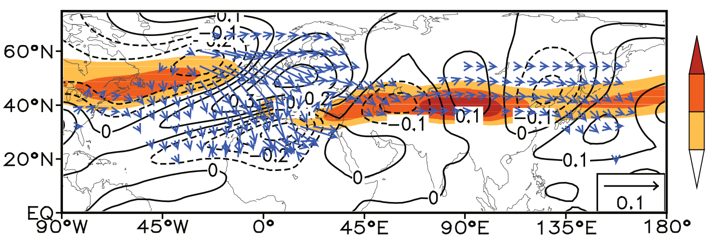

Fig. 8. Steady baroclinic model response as represented by the stream function (contour; 10^6 m^2 s^{-1}) and the associated wave-activity flux (vector; m^2 s^{-2}) at σ=0.29 to the idealized eddy-vorticity forcing shown in Fig. 7. Shading denotes the climatological summer mean of zonal wind (m s^{-1}) for the same layer.

forcing is of vital importance in maintaining the atmospheric response to the North Atlantic SST anomalies during both winter and summer.

Also of note is that the Asian response (Fig. 8) is mainly trapped in the upper-level westerly jet, whereas the observed anomalies in the NAE pattern (Fig. 2a) prevail along the poleward flank of the Asian jet. Namely, the position of the NAE pattern in Fig. 8 relative to the upper-level jet is different from that seen in observations over Asia. It has been demonstrated that two-way synoptic eddy and low-frequency (SELF) feedback plays an essential role in generating the low-frequency anomalies in the extratropics (Jin et al., 2006; Pan et al., 2006; Ren et al., 2012), but synoptic eddy forcing is just considered as an external forcing in the linear model used in this study. Therefore, a lack of two-way SELF feedback may contribute to the aforementioned difference between the model simulation and observations.

5. Relationships among the North Atlantic SST tripole, NAO and EASM

The tripole-like SST anomalies in the North Atlantic Ocean primarily result from the NAO-like dipole in the atmospheric circulation (Cayan, 1992; Deser and Timlin, 1997; Czaja and Frankignoul, 2002; Zhou et al., 2006). Given this, is the North Atlantic summer SST tripole that has a strong relationship with the EASM (referred to as the EASM-related SST tripole) coupled with the simultaneous summer NAO? To address this question, we calculated the correlation coefficients between SST anomalies in the North Atlantic and the NAO index during summer, and the results are shown in Fig. 9a. It can be seen that the correlations show a clear tripole pattern in the North Atlantic, which suggests that the SST tripole is closely coupled with the NAO during summer. A comparison of Fig. 9a and Fig. 3b reveals that the summer NAO-coupled SST tripole resembles closely the EASM-related SST tripole in shape, but the location of the former is about 5°–10° northward compared with that of the latter. The summer NAO-coupled SST tripole is mainly located in the extratropics northward of about 20°N, while the EASM-related SST tripole has significant SST anomalies in the tropics southward of about 20°N. These results imply the EASM-related SST tripole seems to have no significant relationship with the simultaneous summer NAO.

It has been indicated that the activity centers of the NAO would move northward systematically from winter to summer (Barnston and Livezey, 1987), which may lead to seasonal changes in the meridional location of the NAO-induced SST tripole in the North Atlantic. This raises the possibility that the EASM-related SST tripole may be linked to the previous spring NAO. Thus, in Fig. 9b we display the correlations between SST anomalies in the North Atlantic and the NAO index during spring. It can be seen that their correlations exhibit a tripole pattern in the North Atlantic, thereby indicating that the SST tripole is also coupled with the NAO during spring. Moreover, the NAO-coupled SST tripole in the spring is located more southward than that in the summer. The former resembles closely the EASM-related SST tripole not only in shape but also in meridional location. These results indicate that the summer SST tripole that has a strong relationship with the EASM tends to result from the NAO in the previous spring rather than in the simultaneous summer.

To further understand the relationships among the EASM, North Atlantic SST tripole and NAO on the

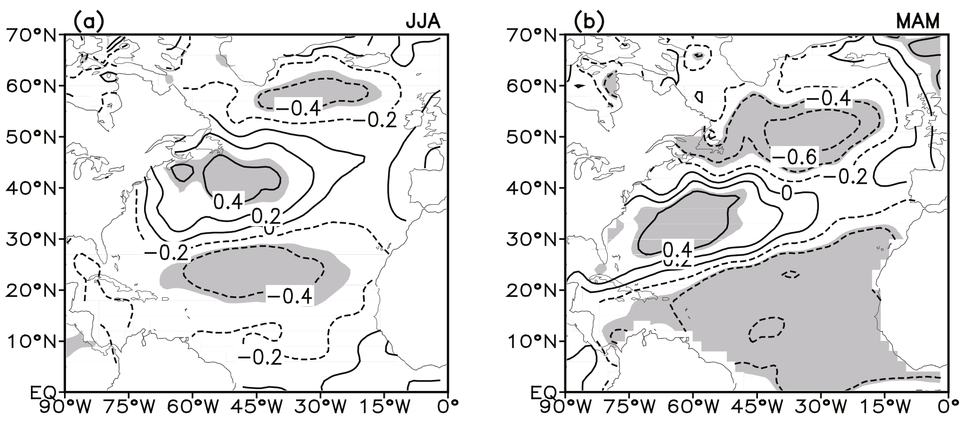

Fig. 9. Correlation coefficients between the NAO index and SST anomalies during (a) summer and (b) spring. Shading represents those regions that are significant at the 95% confidence level.

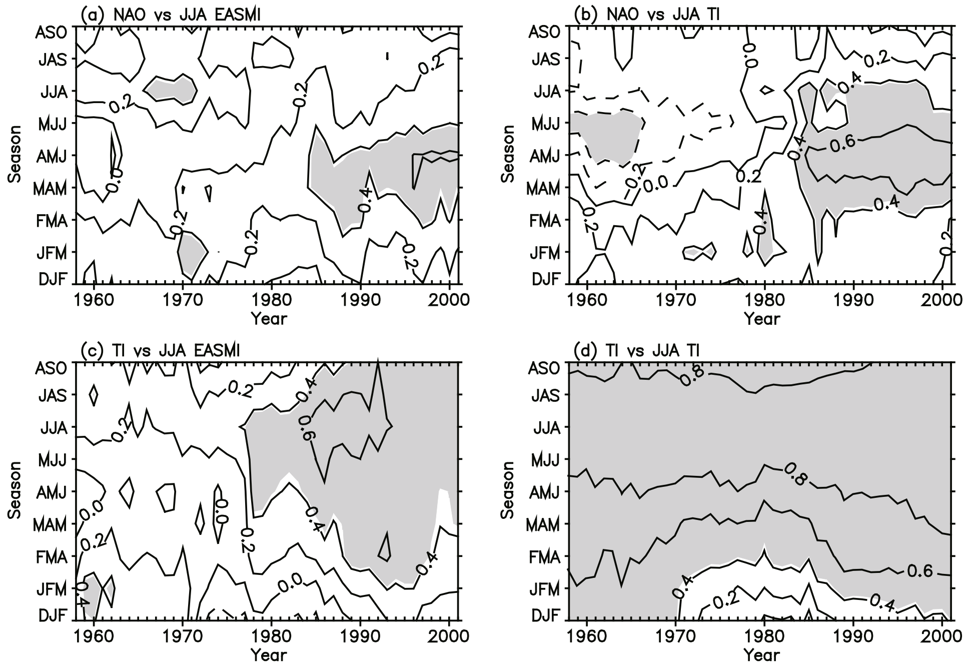

Fig. 10. Lead/lag moving-correlations between summer EASM index (EASMI) and 3-month-running-averaged NAO indices from the preceding January to the following September with a 21-yr moving window for the period 1948–2011. Shading shows significance at the 95% confidence level. (b) The same as in (a), but for the summer tripole SST index (TI). (c) The same as in (a), but for the summer EASMI and the 3-month-running-averaged TI from the preceding January to the following September. (d) The same as in (c), but for the summer TI.

interannual timescale, in Fig. 10a (Fig. 10b) we show the lead/lag moving-correlations between the summer EASM index (TI) and the 3-month-running-avaraged NAO indices from the preceding January to the following September with a 21-yr moving window for the period 1948–2011. We also calculated the lead/lag moving-correlations between the EASM index and 3-month-running-avaraged TI for the same period, as shown in Fig. 10c. Note that the TI here is to describe the interannual variations of the EASM-related SST tripole. It can be seen that the summer EASM index and TI are both correlated most closely with the previous spring NAO index, while the EASM index is linked most closely to the simultaneous summer TI, though their sliding correlations are all characterized by large decadal variations. The decadal changes in the relationships among the EASM, TI and NAO indices occur in the late 1970s, a possible mechanism for which was given in our previous study (Zuo et al., 2012). These results support the conclusion that the summer SST tripole that has a significant impact on the EASM is closely related to the NAO in the previous spring rather than in the simultaneous summer.

To briefly investigate the persistence of the North Atlantic SST tripole, the lead/lag sliding cross-autocorrelations of the summer TI were calculated (see Fig. 10d). We can see that the summer TI is correlated closely with the previous spring TI for the whole period from 1948 to 2011, which indicates the SST tripole has a relatively strong persistence from spring through summer, being in good agreement with previous work (Wu et al., 2009). The seasonal northward movement of the activity centers of the NAO tends to provide favorable conditions for the NAO-induced SST tripole to persist from spring through summer.

We can infer from the above results that the impact of the North Atlantic summer SST tripole on the EASM is sensitive to the meridional location of the tripole. In order to confirm this hypothesis, another idealized experiment was performed by using the linear barotropic model. In this experiment, the horizontal distribution of the anomalous vorticity forcing was the same as in Fig. 5b, except the center for maximum forcing shifted 10° northward and was located at (25°N, 50°W). The steady stream function response and the associated WAF to this idealized vorticity forcing are given in Fig. 11. Note that a clear wave-train pattern propagated from the subtropical North Atlantic to Western Europe, and then divided into two branches. One was northeastward to Eurasia north-

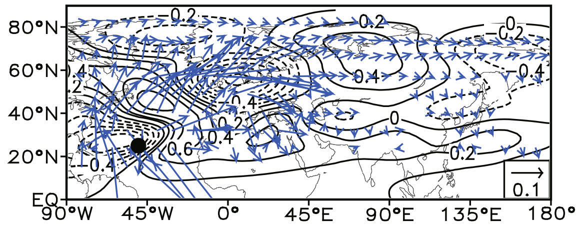

Fig. 11. The same as in Fig. 5b, but for the idealized vorticity forcing with a maximum centered at (25°N, 50°W).

ward of about 60°N, and the other southward to North Africa. There was no obvious stream function response over the Ural Mountains and East Asia. By comparing Fig. 11 with Fig. 5b, we can see that there was a significant difference in the pathways of the atmospheric wave-train response to the idealized vorticity forcing with different meridional location, supporting the hypothesis that the impact of the summer SST tripole on the EASM is sensitive to the meridional location of the tripole. Our conclusion is also supported by previous studies in which it was demonstrated that the pattern of the atmospheric response to the heating with different meridional locations may be different because the synoptic eddy-vorticity feedback depends on the position of the heating relative to the storm track (Peng and Whitaker, 1999; Li et al., 2006).

6. Summary and discussion

A strong (weak) EASM is usually concurrent with the North Atlantic summer SST tripole on the interannual timescale, which has positive (negative) SST anomalies in the Northwest Atlantic and negative (positive) SST anomalies in the subpolar and tropical ocean. In the present study, the mechanism responsible for this linkage was diagnosed by using observations for the period 1979–2011. It has been shown that the NAE pattern occurring over the Atlantic-Eurasia region appears to act as a link between the EASM and the summer SST tripole. The NAE pattern is concurrent with the geopotential height anomaly over the region around the Ural Mountains, which has a substantial effect on the EASM. Further diagnosis based on observations and a linear barotropic model revealed that the maintenance of the NAE pattern appears to depend on the diabatic heating associated with the tropical North Atlantic SST anomaly. On the other hand, the NAE pattern in turn induces a southward/northward shift of the storm-track activity over the North Atlantic, which tends to result in a positive eddy-vorticity feedback, and thus enhances the NAE pattern. Diagnosis based on a linear baroclinic model confirmed the active role of synoptic eddy-vorticity forcing in maintaining the NAE pattern.

Since the North Atlantic SST tripole mainly results from the driving of the NAO-like atmospheric forcing, relationships between these two factors and the EASM were further investigated on the interannual timescale. It was revealed that the summer SST tripole that has a strong relationship with the EASM is closely coupled with the NAO in the preceding spring rather than in the simultaneous summer, which appears to be attributable to the seasonal north–south movement of the activity centers of the NAO. The spring NAO-coupled SST tripole has pronounced SST anomalies in the tropics, while the summer NAO-coupled SST tripole is mainly confined to the extratropics due to the northward shift of the summer NAO itself. Barotropic modeling results confirmed that the type of SST tripole located in the extratropics has no significant impact on the EASM. Therefore, the relationship of the EASM with the North Atlantic summer SST tripole is sensitive to the meridional location of the tripole on the interannual timescale.

The present analysis indicates that the tropical component of the North Atlantic summer SST tripole plays the key role in influencing the EASM. On the other hand, SST changes in the tropical North Atlantic are influenced strongly not only by the NAO, but also by ENSO [Xie and Carton (2004), and references therein]. Thus, a question arises as to whether the results regarding the linkage between the North Atlantic summer SST tripole and EASM are contaminated by the ENSO signals. As illustrated by Wu et al. (2011), the relationship between the North Atlantic spring SST tripole and the preceding winter ENSO is significant in the 1980s and 1990s, but weak in the latest decade. In this study, we found that the correlation coefficient between the summer tripole SST index and the preceding winter Nino3.4 SST was only -0.23 for the period 1979–2011 (Fig. 1), which is not significant at the 90% confidence level. In addition, the NAE pattern that acts as a link between the North Atlantic summer SST tripole and EASM was still robust after removing the ENSO signals from the summer tripole SST index and the atmospheric fields based on a linear regression method using the winter-mean Nino3.4 SST index (data not shown). Therefore, it appears that the relationship between the North Atlantic summer SST tripole and EASM is independent of ENSO during the period analyzed in this study. Wu et al. (2011) suggested that the North Atlantic SST tripole can have an impact on Northeast China summer temperature, independent of ENSO, which is in agreement with our conclusions.

Previous numerical studies have suggested that

SST anomalies in the extratropical North Atlantic tend to have a considerable impact on atmospheric circulation (Peng et al., 2003; Li, 2004). This raises the possibility that extratropical SST anomalies corresponding to the North Atlantic summer SST tripole may make a contribution to the linkage between the tripole and the EASM, which is, however, hard to identify by observational diagnosis due to the dominant role of the atmosphere during the interannual ocean–atmosphere interaction processes over this region. Though the numerical simulation by Watanabe and Kimoto (2000) revealed that the mid-latitude SST anomaly corresponding to the North Atlantic SST tripole has positive feedback on the anomalous atmospheric circulation during winter, observational analysis in this study indicated that its effect appears to be relatively weak during summer. However, more studies are needed to identify the relative contribution of the tropical and extratropical SST anomalies corresponding to the North Atlantic summer SST tripole by using climate models in which the atmospheric intrinsic variability could be well reproduced.

Acknowledgements. The authors are grateful for the linear dynamic models provided by Dr. M. WATANABE and the useful comments and suggestions of the two anonymous reviewers. We also thank Dr. WU Bingyi for carefully reading an early draft of this article and offering constructive criticism. This work was jointly supported by the National Basic Research Program of China (Grant Nos. 2010CB950404, 2013CB430203, 2010CB950501 and 2012CB955901), the National Natural Science Foundation of China (Grant No. 41205058), the China Postdoctoral Science Foundation (Grant No. 2012M510634), and the National Science and Technology Support Program of China (Grant No. 2009BAC51B05).

REFERENCES

Barnston, A. G., and R. E. Livezey, 1987: Classification, seasonality and persistence of low-frequency atmospheric circulation patterns. *Mon. Wea. Rev.*, **115**, 1083–1126.

Branstator, G., 1983: Horizontal energy propagation in a barotropic atmosphere with meridional and zonal structure. *J. Atmos. Sci.*, **40**, 1689–1708.

Branstator, G., 1992: The maintenance of low-frequency atmospheric anomalies. *J. Atmos. Sci.*, **49**, 1924–1945.

Cayan, D. R., 1992: Latent and sensible heat flux anomalies over the northern oceans: Driving the sea surface temperature. *J. Phys. Oceanogr.*, **22**, 859–881.

Czaja, A., and C. Frankignoul, 2002: Observed impact of Atlantic SST anomalies on the North Atlantic oscillation. *J. Climate*, **15**, 606–623.

Deser, C., and M. Timlin, 1997: Atmosphere-ocean interaction on weekly timescales in the North Atlantic and Pacific. *J. Climate*, **10**, 393–408.

Ding, Y. H., 1992: Summer monsoon rainfalls in China. *J. Meteor. Soc. Japan.*, **70**, 373–396.

Duchon, C., 1979: Lanczos filtering in one and two dimensions. *J. Appl. Meteor.*, **18**, 1016–1022.

Gill, A. E., 1980: Some simple solutions for heat-induced tropical circulation. *Quart. J. Roy. Meteor. Soc.*, **106**, 447–462.

Gu, W., C. Y. Li, X. Wang, W. Zhou, and W. J. Li, 2009: Linkage between mei-yu precipitation and North Atlantic SST on the decadal timescale. *Adv. Atmos. Sci.*, **26**, 101–108, doi: 10.1007/s00376-009-0101-5.

Han, Z., S. Li, and M. Mu, 2011: The role of warm North Atlantic SST in the formation of positive height anomalies over the Ural Mountains during January 2008. *Adv. Atmos. Sci.*, **28**, 246–256, doi: 10.1007/s00376-010-0069-1.

Huang, R. H., and W. J. Li, 1987: Influence of the anomaly of heat source over the northwestern tropical Pacific for the subtropical high over East Asia. *Proc. Inter. Conf. on the General Circulation of East Asia*, Chengdu, China, 40–45.

Huang, R. H., and F. Y. Sun, 1992: Impacts of the tropical western Pacific on the East Asian summer monsoon. *J. Meteor. Soc. Japan.*, **70**, 243–256.

Jin, F.-F., L.-L. Pan, and M. Watanabe, 2006: Dynamics of synoptic eddy and low-frequency flow interaction. Part I: A linear closure. *J. Atmos. Sci.*, **63**, 1677–1694.

Kalnay, E., and Coauthors, 1996: The NCEP/NCAR 40–year reanalysis project. *Bull. Amer. Meteor. Soc.*, **77**, 437–472.

Kug, J.-S., and F.-F. Jin, 2009: Left-hand rule for synoptic eddy feedback on low-frequency flow. *Geophys. Res. Lett.*, **36**, L05709, doi: 10.1029/2008GL036435.

Lau, N.-C., and E. O. Holopainen, 1984: Transient eddy forcing of the time-mean flow as indentified by geopotential tendencies. *J. Atmos. Sci.*, **41**, 313–328.

Lau, N.-C., and M. J. Nath, 1991: Variability of the baroclinic and barotropic transient eddy forcing associated with monthly changes in the midlatitude storm tracks. *J. Atmos. Sci.*, **48**, 2589–2613.

Li, J., and J. X. L. Wang, 2003: A new North Atlantic Oscillation index and its variability. *Adv. Atmos. Sci.*, **20**, 661–676.

Li, S., 2004: Influence of the Northwest Atlantic SST anomaly on the circulation over the Ural Mountains. *J. Meteor. Soc. Japan*, **82**, 971–988.

Li, S., and L. Ji, 2001: Background circulation characteristics of the persistent anomalies of the summertime circulation over the Ural Mountains. *Acta Meteorologica Sinica*, **59**, 280–293. (in Chinese)

Li., S., M. P. Hoerling, S. Peng, and K. M. Weickmann, 2006: The annular response to tropical Pacific SST forcing. *J. Climate*, **19**, 1802–1819.

Li., S., W. A. Robinson, M. P. Hoerling, and K. M. Weickmann, 2007: Dynamics of the extratropical response to a tropical Atlantic SST anomaly. *J. Climate*, **20**, 560–574.

Nitta, T., 1987: Convective activities in the tropical western Pacific and their impacts on the Northern Hemisphere summer circulation. *J. Meteor. Soc. Japan.*, **65**, 165–171.

Ogi, M., Y. Tachibana, and K. Yamazaki, 2003: Impact of the wintertime North Atlantic Oscillation (NAO) on the summertime atmospheric circulation. *Geophys. Res. Lett.*, **30**, 1704, doi: 10.1029/2003GL017280.

Pan, L.-L., 2007: Synoptic eddy feedback and air–sea interaction in the North Atlantic region. *Climate Dyn.*, **29**, 647–659.

Pan, L.-L., F.-F. Jin, and M. Watanabe, 2006: Dynamics of synoptic eddy and low-frequency flow interaction. Part III: Baroclinic model results. *J. Atmos. Sci.*, **63**, 1709–1725.

Peng, S., and J. S. Whitaker, 1999: Mechanisms determining the atmospheric response to midlatitude SST anomalies. *J. Climate*, **12**, 1393–1408.

Peng, S., W. A. Robinson, and S. Li, 2003: Mechanisms for the NAO responses to the North Atlantic SST tripole. *J. Climate*, **16**, 1987–2004.

Ren, H.-L., F.-F. Jin, J.-S. Kug, J.-X. Zhao, and J. Park, 2009: A kinematic mechanism for positive feedback between synoptic eddies and NAO. *Geophys. Res. Lett.*, **36**, L11709, doi: 10.1029/2009GL037294.

Ren, H.-L., F.-F. Jin, and L. Gao, 2012: Anatomy of synoptic Eddy–NAO Interaction through eddy structure decomposition. *J. Atmos. Sci.*, **69**, 2171–2191.

Sardeshmukh, P. D., and B. J. Hoskins, 1988: The generation of global rotational flow by steady idealized tropical divergence. *J. Atmos. Sci.*, **45**, 1288–1251.

Smith, T. M., R. W. Reynolds, T. C. Peterson, and J. Lawrimore, 2008: Improvements to NOAA's historical merged land-ocean surface temperature analysis (1880–2006). *J. Climate*, **21**, 2283–2296.

Sung, M.-K., W.-T. Kwon, H.-J. Baek, K.-O. Boo, G.-H. Lim, and J.-S. Kug, 2006: A possible impact of the North Atlantic Oscillation on the East Asian summer monsoon precipitation. *Geophys. Res. Lett.*, **33**, L21713, doi: 10.1029/2006GL027253.

Takaya, K., and H. Nakamura, 2001: A formulation of a phase-independent wave-activity flux for stationary and migratory quasigeostrophic eddies on a zonally varying basic flow. *J. Atmos. Sci.*, **58**, 608–627.

Trenberth, K. E., G. W. Branstator, D. Karoly, A. Kumar, N.-C. Lau, and C. Ropelewski, 1998: Progress during TOGA in understanding and modeling global teleconnections associated with tropical sea surface temperatures. *J. Geophys. Res.*, **103**, 14291–14324.

Wang, B., and Z. Fan, 1999: Choice of South Asian summer monsoon indices. *Bull. Amer. Meteor. Soc.*, **80**, 629–638.

Watanabe, M., 2004: Asian jet waveguide and a downstream extension of the North Atlantic oscillation. *J. Climate*, **17**, 4674–4691.

Watanabe, M., and M. Kimoto, 2000: Atmosphere–ocean thermal coupling in the North Atlantic: A positive feedback. *Quart. J. Roy. Meteor. Soc.*, **126**, 3343–3369.

Watanabe, M., and F.-F. Jin, 2003: A moist linear baroclinic model: Coupled dynamical–convective response to El Niño. *J. Climate*, **16**, 1121–1139.

Wu, B. Y., and R. H. Zhang, 2011: Interannual variability of the East Asian summer monsoon and its association with the anomalous atmospheric circulation over the mid-high latitudes and external forcing. *Acta Meteorologica Sinica*, **69**, 219–233. (in Chinese)

Wu, R., S. Yang, S. Liu, L. Sun, Y. Lian, and Z. Gao, 2010: Change in the relationship between Northeast China summer temperature and ENSO. *J. Geophys. Res.*, **115**, D21107, doi: 10.1029/2010JD014422.

Wu, R., S. Yang, S. Liu, L. Sun, Y. Lian, and Z. Gao, 2011: Northeast China summer temperature and North Atlantic SST. *J. Geophys. Res.*, **116**, D16116, doi: 10.1029/2011JD015779.

Wu, Z., B. Wang, J. Li, and F.-F. Jin, 2009: An empirical seasonal prediction model of the East Asian summer monsoon using ENSO and NAO. *J. Geophys. Res.*, **114**, D18120, doi: 10.1029/2009JD011733.

Xie, P., and P. A. Arkin, 1997: Global precipitation: A 17-year monthly analysis based on gauge observations, satellite estimates, and numerical model outputs. *Bull. Amer. Meteor. Soc.*, **78**, 2539–2558.

Xie, S.-P., and J. A. Carton, 2004: Tropical Atlantic variability: Patterns, mechanisms, and impacts. *Earth Climate: The Ocean-Atmosphere Interaction*, C. Wang, S.-P. Xie, and J. A. Carton, Eds., Geophysical Monograph, 121–142.

Zhang, Q. Y., and S. Y. Tao, 1998: Influence of Asian mid-high latitude circulation on East Asian summer rainfall. *Acta Meteorologica Sinica*, **56**, 199–211. (in Chinese)

Zhou, T., R. Yu, Y. Gao, and H. Drange, 2006: Ocean-atmosphere coupled model simulation of North Atlantic interannual variability I: Local air-sea interaction. *Acta Meteorologica Sinica*, **64**, 1–17. (in Chinese)

Zuo, J. Q., W. J. Li, H. L. Ren, and L. J. Chen, 2012: Change of the relationship between spring NAO and East Asian summer monsoon and its possible mechanism. *Chinese Journal of Geophysics.*, **55**, 23–34. (in Chinese)

第9卷 第3期 2013年5月
气候变化研究进展
PROGRESSUS INQUISITIONES DE MUTATIONE CLIMATIS
Vol. 9 No. 3 May 2013

编者按：

气候模式广泛应用在气候与气候变化研究中，气候变化的预估几乎完全依赖模式的模拟。耦合模式比较计划第五阶段（CMIP5）的工作始于2008年，有一些在IPCC第四次评估报告（AR4）中提出来的问题，将通过CMIP5在IPCC第五次评估报告（AR5）中得到反映。目前有五十多个模式参加CMIP5，很多模式组已经完成模拟试验并相继公布了结果。为了让读者了解新一代全球气候模式的评估和研究结果，本刊组织了“CMIP5专栏”，评估CMIP5模式对北极涛动、北半球积雪和中国年平均气温的模拟能力，并给出对北半球积雪的预估结果，在一些研究中还对CMIP5和CMIP3模式模拟结果进行了比较。

doi:10.3969/j.issn.1673-1719.2013.03.001
左金清，李维京，任宏利. CMIP5模式对北极涛动的模拟评估 [J]. 气候变化研究进展, 2013, 9 (3): 157-164

CMIP5模式对北极涛动的模拟评估

左金清[1,2]，李维京[2]，任宏利[2]

1 中国气象科学研究院，北京 100081；2 中国气象局气候研究开放实验室／中国气象局国家气候中心，北京 100081

摘 要：基于国际耦合模式比较计划第五阶段（CMIP5）历史试验（historical）的输出结果，评估了26个耦合模式对北极涛动（AO）的模拟能力。对各模式逐月AO指数序列的功率谱分析表明，有23个模式能够模拟出AO模态无显著变化周期的特征。这些模式也能够较好地再现冬季AO在海平面气压场上的主要分布特征，但均高估了AO模态的强度。对于伴随着冬季AO位相变化而出现的中高纬度偶极型的纬向平均纬向风异常，CMIP5中只有一些模式有较好的模拟表现，大多数模式对其中心位置和强度的模拟存在明显不足。对比之下，MPI-ESM-P对AO时空特征的模拟更接近观测结果。

关键词：北极涛动；模拟评估；耦合模式；CMIP5

引 言

大量研究显示，近百年来全球平均地表温度显著升高[1]，这使得气候变化的检测和归因分析及未来预估成为了当今国际气候变化研究领域的热点话题[2]。当前，开展气候变化机理研究和气候变化情景预估，在很大程度上依赖于气候系统模式。通常来讲，人们相信若气候模式对过去和现在的气候变化

收稿日期：2012-12-11；**修回日期**：2013-01-28
资助项目：国家重点基础研究发展规划项目（2010CB950501，2010CB950404）；国家自然科学基金项目（41205058）；中国博士后科学基金项目（2012M510634）
作者简介：左金清，女，博士后，主要从事气候动力学和气候变化研究，jqzuo425@126.com

有较好的模拟能力，那么它对未来气候变化预估也具有相对高的可信度。因此，开展气候系统模式评估显得尤为关键，其中对大气低频变率支配模态的模拟是模式评估的重要方面[3]。

北极涛动（AO）被认为是北半球热带外大气低频变率的主导模态，反映了中纬度与极地间大气质量的反向变化关系[4]。由于AO具有近似纬向对称的结构，因此也被称为北半球环状模[5]。研究表明，AO对北半球大范围的地表气候异常以及风暴活动等具有重要的影响，尤其是北美、格陵兰岛、欧亚大陆和北非等区域的地表气温异常与 AO 的变率密切相关[5-6]。同时，AO也是影响东亚冬季风以及中国冬季地表气温和降水异常的重要因子[7-9]。在20世纪后20年中，冬季AO的高指数位相持续维持，加剧了包括东北亚在内的欧亚大陆的增暖现象[6,10]。由此可见，AO的位相变化能够显著地改变北半球大范围的地表气候状况，对未来气候变化具有重要指示意义。

对 AO 时空特征的模拟能力是衡量模式性能的重要指标。已有研究表明，大气环流和海气耦合模式都可以较好地模拟出 AO 模态的主要空间特征，但均模拟不出20世纪后50年冬季AO指数的上升趋势[11-12]。基于国际耦合模式比较计划第三阶段（CMIP3）历史模拟（即20世纪气候模拟，20C3M）的输出结果，许多学者研究了全球不同模式机构的海气耦合模式对AO时空结构的模拟能力[3,13-15]。他们的研究指出，几乎所有CMIP3模式都可以较好地再现AO的空间模态，但对其强度和位置以及时间变率的模拟能力仍需进一步提高。

最近的CMIP计划（即CMIP5），已于2008年9月由世界气候研究计划（WCRP）下的耦合模式工作组（WGCM）组织启动，全球近30个模式机构参与该计划。CMIP5模式将为气候变化机理研究和未来预估提供重要的数值模拟数据，相关评估结果则为政府间气候变化专门委员会（IPCC）第五次评估报告（AR5）提供重要的科学依据[16]。与前几个阶段的CMIP模式相比，大部分CMIP5模式在物理过程、耦合碳循环等方面有明显的改进。那么，这些当今国际上最先进的耦合模式对AO的时空结构的模拟能力如何？为了回答此问题，本文将全面评估26个CMIP5模式对AO的时间变率和空间结构的模拟能力。

1 模式和资料介绍

我们搜集到了26个CMIP5模式的输出结果，其基本信息见附录表1，这些模式分别来自于全球11个国家的多个模式机构。其中，有3个模式来源于中国。对于这26个CMIP5模式，大部分大气分量模式的水平分辨率为2°～3°，分辨率最高的是日本模式MRI-CGCM3（1.1°）。其中，有10个模式为不含耦合碳循环过程的物理气候系统模式，其他16个模式为包含耦合碳循环过程的地球系统模式。

本文所采用的数值模拟数据均为CMIP5历史试验（historical）的输出结果。该试验是在工业革命前控制试验（piControl）的基础上选取初始场，然后对模式进行不少于156年（1850—2005年）的积分。强迫场除了包含与观测一致的温室气体、臭氧、气溶胶和太阳常数外，还首次加入了随时间变化的土地覆盖[16]。为了便于比较，我们将所有模式输出结果都插值到了2.5°×2.5°的规则网格上。

为了与模拟结果进行比较，本文还采用了以下观测资料：1) 英国Hadley中心提供的月平均海平面气压（HadSLP2）[17]，水平分辨率为5°×5°；2) NCEP/NCAR标准等压面月平均纬向风资料[18]，水平分辨率为2.5°×2.5°。

根据前人的研究[5]，本文将AO模态定义为20°N以北逐月海平面气压（SLP）距平自然正交函数（EOF）分解的第一主模态。在进行EOF分解之前，我们对各格点数据进行了面积加权处理。EOF第一模态所对应的标准化时间系数则定义为AO指数。为了便于比较AO模态的强度，将其表示为SLP距平对AO指数的回归。在本文中，所有资料的分析时段均取为1950—2005年。由于AO的变率在冬季最显著，而且其主要活动中心存在季节性南北移动[19]，所以本文只分析了冬季（12月至次年2月）AO的空间结构特征。在对AO指数序列进行功率谱分析时，则是利用了整个研究时段中全年所有月份的数据。此外，在进行相关／回归分析之前，去除了所有序列的线性趋势。

2　模拟与观测结果的对比分析

2.1　AO的时间变率

图 1 显示了基于再分析资料和模式输出结果得到的逐月 AO 指数序列的平滑功率谱。观测结果显示，AO模态存在准半年、准一年和准三年的变化周期，但相应的谱峰都不显著（图1a）。除了Hadley中心的3个模式HadCM3（图1b8）、HadGEM2-CC（图1c7）及 HadGEM2-ES（图 1c8）外，其余所有模式中AO指数的功率谱均不存在显著的峰值。大部分模式都可以模拟出与观测相似的准半年周期振荡，不过只有不足一半的模式能够模拟出与观测类似的准一年周期振荡。在 GFDL-CM3（图 1b5）、GFDL-ESM2G（图1c5）及MPI-ESM-LR（图1c13）中，AO模态存在与观测相似的准三年周期振荡，不过GFDL-CM3的准三年周期振荡偏强。对于Hadley中心的3个模式，AO指数之间具有相似的功率谱特征，均存在非常显著的准一年变化周期，同时还存在4个月和6个月左右的次变化周期，说明这3个模式所模拟的AO模态存在很强的季节至年际变率。此外，一些模式还存在 4 个月和 8～9 个月的变化周期，以及准两年和4～5年的低频变率，这都是从观测资料中检测不到的。

观测分析揭示，在20世纪50—70年代冬季AO以负位相为主，而在 20 世纪 80 年代至 21 世纪初期则相反。最近 10 年，冬季 AO 又表现出由正位相向负位相转变的趋势，表明冬季AO具有明显的年代际变率。从观测AO的功率谱曲线上也可以看到，在低

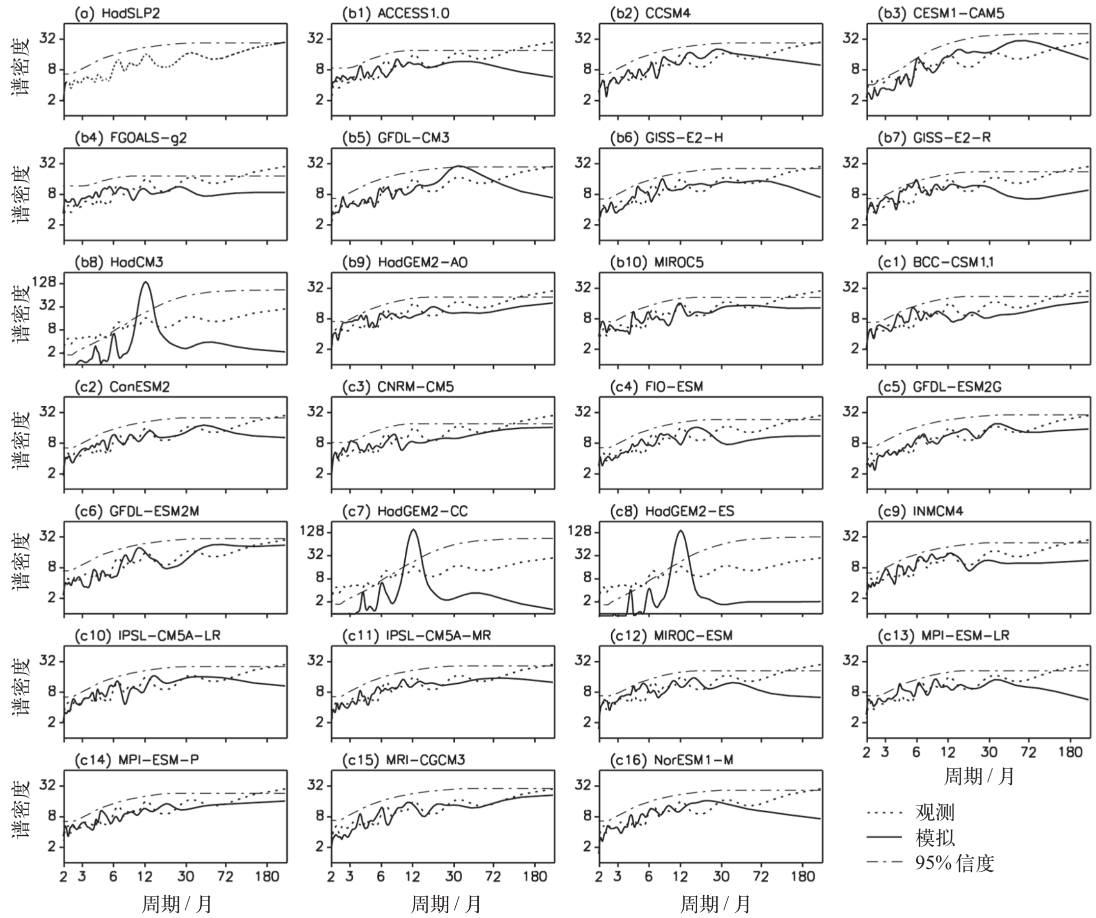

图 1　观测（HadSLP2）和 CMIP5 模式中逐月 AO 指数序列的平滑功率谱（点划线表示 95% 信度水平对应的红噪声标准谱；a 为观测；b1～b10 为物理气候系统模式；c1～c16 为地球系统模式）

Fig. 1　Smoothed power spectrum for the time series of monthly AO index derived from the observation (HadSLP2) and the CMIP5 model simulations. The solid line with dots indicates the 95% confidence limit about the red noise spectrum. b1−b10 are the physical climate system models and c1−c16 the Earth system models

频一端其谱密度具有明显的上升趋势（图1a）。对比模拟结果可知，CMIP5中有几个模式对AO的上述功率谱特征模拟得较好，这些模式包括BCC-CSM1.1（图1c1）、CNRM-CM5（图1c3）、HadGEM2-AO（图1b9）、MPI-ESM-P（图1c14）和MRI-CGCM3（图1c15）。而在近一半的模式中，AO的谱密度在低频一端存在明显的下降趋势，说明这些模式中AO的年代际变率偏弱。我们还对冬季平均的AO指数进行了功率谱分析（图略），发现它与逐月AO指数在相同频段上的功率谱特征基本一致，这进一步表明多数模式对AO年代际变率的模拟能力有待提高。此外，对比物理气候系统模式和地球系统模式对AO时间变率的模拟能力，发现这两类模式之间的差异不明显。

2.2 海平面气压场上的AO模态

为了考察CMIP5模式对冬季AO空间模态的模拟能力，图2给出了冬季AO指数与热带外北半球SLP距平的回归分布图。对比模拟与观测结果可以看到，除了Hadley中心的3个模式外，其他所有模式对冬季AO的空间模态都有相对较好的识别能力。对于模式HadCM3（图2b8）和HadGEM2-CC（图

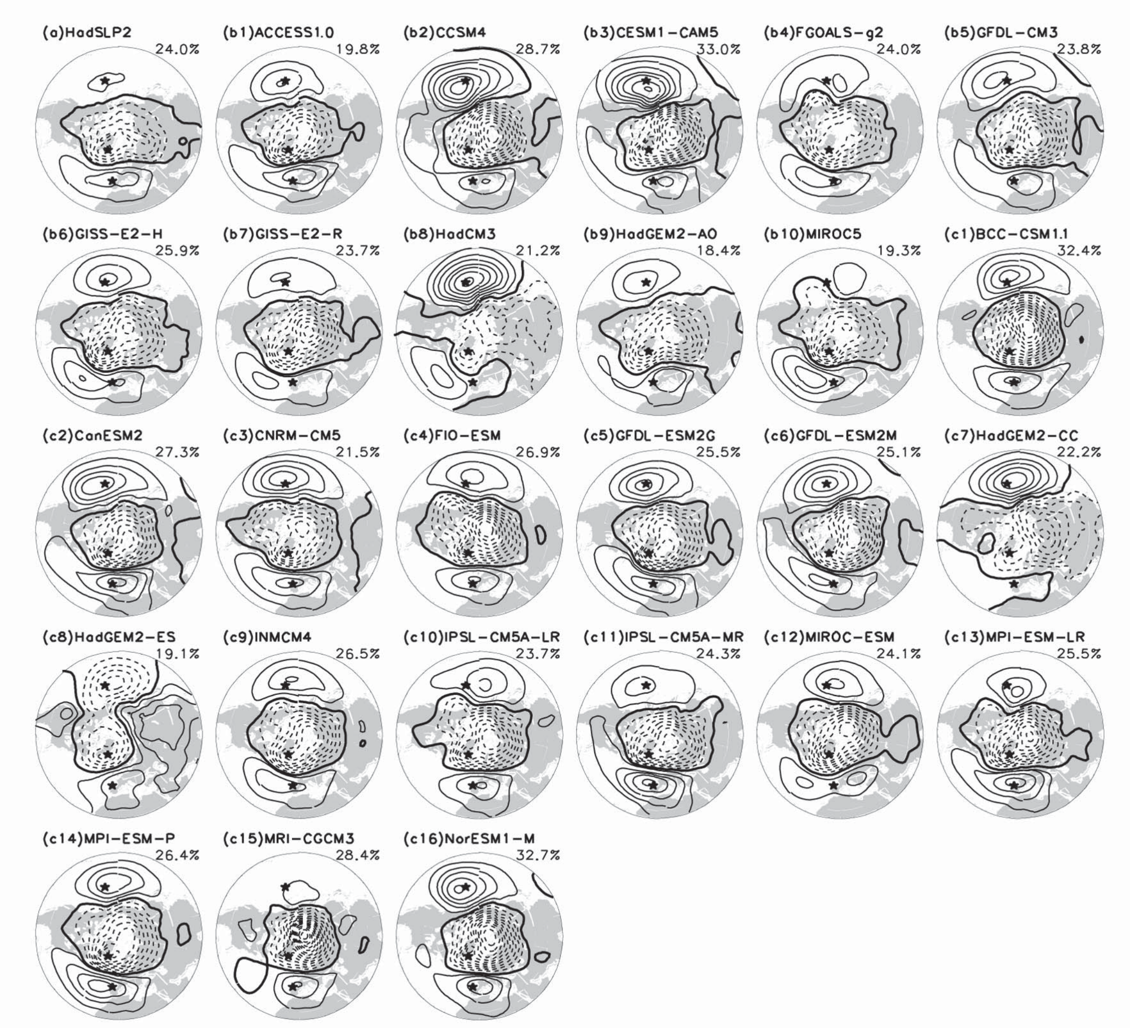

图2 观测（HadSLP2）和CMIP5模式中冬季AO指数与海平面气压距平的回归分布（等值线间隔为1，虚线表示负值，粗实线为零线；右上角数字表示冬季AO的解释方差；“★”表示根据观测结果所确定的AO 3个活动中心的位置）

Fig. 2 Regressions of the wintertime sea level pressure anomaly upon the AO index derived from the observation (HadSLP2) and the CMIP5 model simulations. The contour interval is 1. Dashed line indicates negative values and zero line is thickened. The percentage of variance explained by the winter AO pattern is given at the top right-hand corner of each pattern. “★” denotes the three active centers of the AO obtained from the observation

2c7）所模拟的热带外北半球 SLP 距平的 EOF 第一主模态，负的SLP异常主要出现在极地和欧亚大陆，而且异常中心偏向欧亚大陆北部。对于 HadGEM2-ES（图2c8），北美以及北大西洋东部至欧亚大陆的中纬度地区均为正的 SLP 距平控制，中纬度北太平洋和格陵兰岛及其邻近区域则为负的SLP距平控制。由此可见，Hadley中心的3个模式对AO空间模态的识别存在一定难度，尤其是夸大了AO与西伯利亚地区 SLP 异常之间的联系。

从图2(a) 可以看到，AO存在3个主要的活动中心，分别位于北极（记为A1）、中纬度北大西洋（A2）及北太平洋（A3）。为了能够更好地体现模式对A1～A3 的模拟能力，在图 2 中均用“★”标识了它们的中心位置。观测结果显示，A1 呈单极结构，其中心位置主要偏向北大西洋一侧。然而，在超过半数的模式中 A1主要偏向东半球，或者呈现双极结构。在大部分模式中A2的中心位置往往较观测结果偏东或偏西。还可以注意到，A3 的观测强度明显偏弱于 A2，而只有 5 个模式（IPSL-CM5A-MR、MIROC5、MPI-ESM-LR、MPI-ESM-P 和 MRI-CGCM3）模拟出了该特征。

图2的结果同时表明，几乎所有模式都存在AO强度偏强的问题，特别是在北太平洋区域该问题表现更突出。为了进一步定量评估模式对AO空间模态的模拟能力，图 3 给出了冬季 AO 模态的泰勒图[20]。结果显示，除了 Hadley 中心的 3 个模式外，模拟与观测的 AO 模态的空间相关系数都在 0.80 以上，其中相关系数超过 0.90 的模式占到了总数的一半以上。对于AO模态的强度，模拟值约为观测值的1.2～1.9 倍，这进一步证实所有模式都高估了 AO 模态的强度。

从图 3 还可以注意到，相对于地球系统模式来说，大部分物理气候系统模式所模拟的冬季AO模态的强度更接近观测结果。实际上，AO作为一种大气低频模态，它的形成和维持机制主要与大气内部动力学有关。地球系统模式由于包含了耦合碳循环过程，其物理过程更复杂。因此，目前主要考虑海、陆、气、冰相互作用过程的物理气候系统模式对AO模态的模拟可能更具优势。

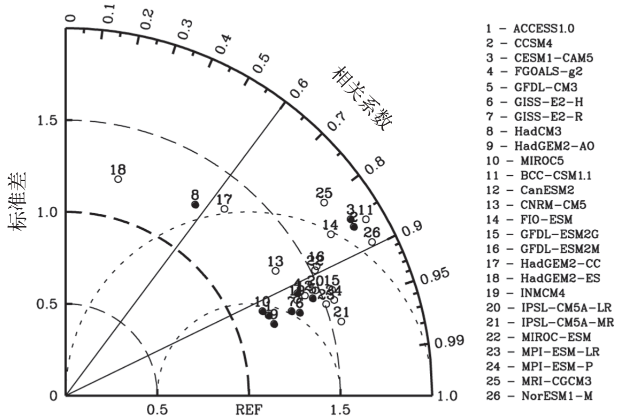

图3 冬季 AO 模态的泰勒图（半径表示 AO 模态的模拟标准差与观测的比率，与纵坐标轴的角度代表模拟与观测的空间相关系数；实心圆表示物理气候系统模式，空心圆表示地球系统模式）

Fig. 3 Taylor diagram summarizes the comparison of wintertime AO pattern between observation and CMIP5 model simulations. The radial distance from the origin indicates the standard deviation of AO pattern for each model normalized by the observed value. The azimuthal position denotes the correlation between the observed and simulated AO pattern. Solid circle indicates the physical climate system model and hollow the Earth system model

2.3　AO 的垂直结构

在冬季，AO 信号可以从近地表向上延伸至平流层底层，在纬向平均纬向风场上表现为准正压的经向偶极型[5]。当 AO 处于正位相时，45°N 以南的中纬度地区主要为东风异常控制，其极大值中心位于对流层高层；45°N以北的高纬度地区则主要为西风异常控制，其中西风异常的强度随高度的升高而增大，极大值中心出现在平流层底层（图4a）。这些环流变化，恰好反映了副热带西风急流的减弱和极地急流的增强[21]。当AO处于负位相时，上述环流模态恰好相反。

为了考察 CMIP5 模式对 AO 垂直结构的模拟能力，我们对冬季AO指数与纬向平均纬向风距平进行了回归分析（图 4）。对比模拟与观测结果可知，几乎所有模式都能够再现与冬季 AO 相关联的北半球中纬度和高纬度纬向平均纬向风异常之间的反向变化关系。不过，模式模拟的纬向风异常的强度往往偏高或偏低于观测结果，其中心位置与观测结果也普遍存在较大差异。为了描述方便，我们将与AO相

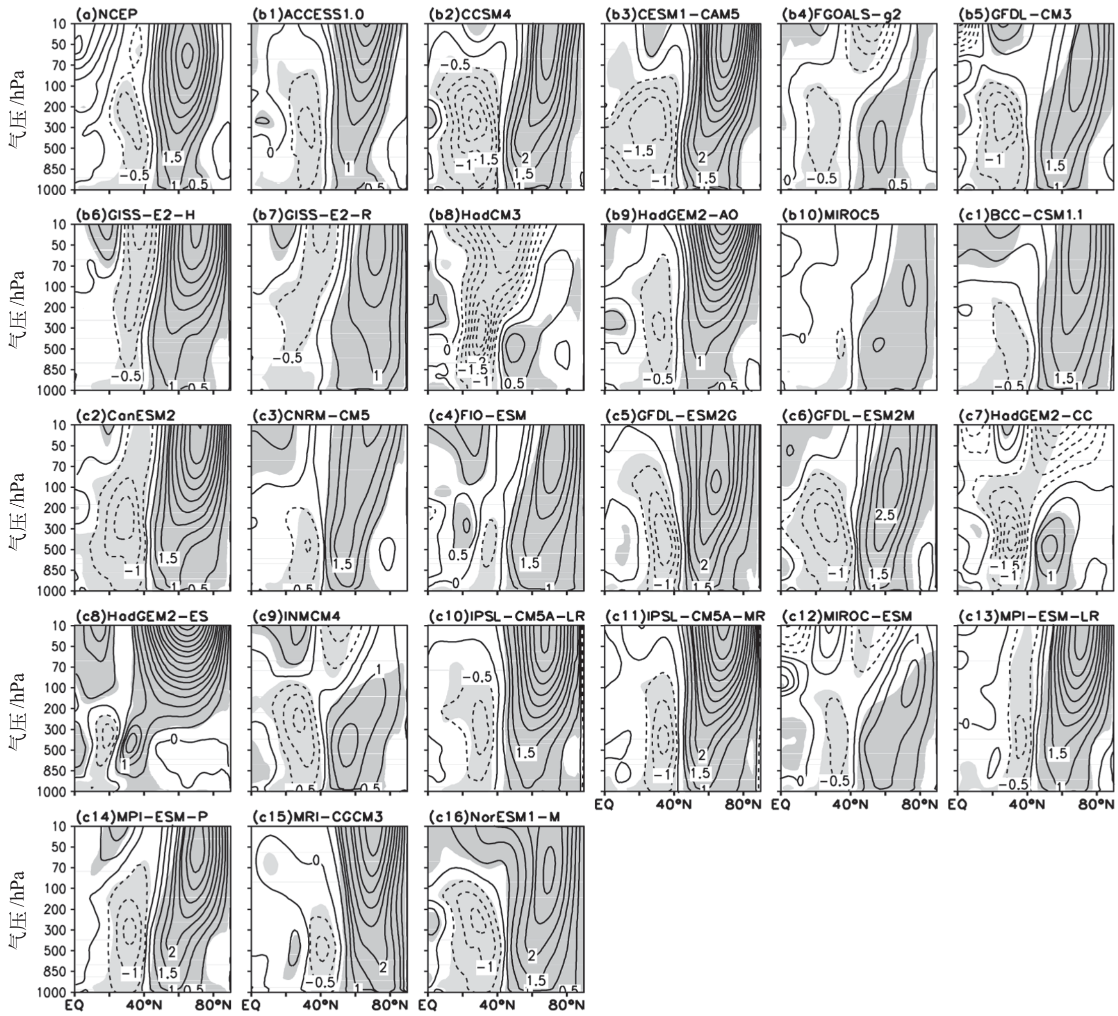

图4 观测（NCEP）和CMIP5模式中冬季AO指数与纬向平均纬向风距平（m/s）的回归分布
（阴影表示信度水平达95%的区域）

Fig. 4 Regressions of the wintertime zonal-mean zonal wind anomaly (m/s) upon the AO index derived from (a) the observation (NCEP) and (b, c) the CMIP5 model simulations. Shading indicates significance at the 95% confidence level

关联的中（高）纬度的纬向风异常中心记为SJ（PJ）。可以注意到，除了GISS-E2-R（图4b7）、MRI-CGCM3（图4c15）以及Hadley中心的3个模式（图4b8、图4c7、图4c8）外，其余模式基本上都可以较好地模拟出PJ的强度随高度升高而增大且中心轴线向极地一侧倾斜的特征。不过，模式对PJ的北边界和极值中心位置的模拟普遍偏北。还有一些模式对PJ极值中心的垂直位置的识别能力较差。例如，FGOALS-g2（图4b4）、GFDL-ESM2G（图4c5）、GFDL-ESM2M（图4c6）、INMCM4（图4c9）、MIROC5（图4b10）和MIROC-ESM（图4c12）等模式中，PJ的极值中心下移到了对流层顶层或中层。对于SJ，在大部分模式中其极值中心主要出现在对流层，这与观测结果类似。不过，在一些模式中SJ的极值中心却上移至了平流层底层，如GISS-E2-H（图4b6）和GISS-E2-R（图4b7）。对于CCSM4（图4b2）、CESM1-CAM5（图4b3）和GFDL-CM3（图4b5），SJ的南边界几乎向南扩展到了赤道附近，即其经向范围被明显扩大。相对来说，MPI-ESM-P（图4c14）对冬季AO垂直结构的模拟更接近观测结果。

3 总结与讨论

基于CMIP5历史试验的输出结果，本文系统评估了26个耦合模式对AO的时间变率和空间结构的模拟能力。对各模式逐月AO指数序列的功率谱分析

表明，只有在 Hadley 中心的 HadCM3，HadGEM2-CC 和 HadGEM2-ES 中，AO 模态存在显著的准一年周期振荡以及相对较弱的4个月和6个月左右的周期振荡。在其余的 23 个模式中，AO 均无显著的变化周期，这与观测结果相似。进一步的分析表明，这 23 个模式都能够较好地再现冬季 AO 在海平面气压距平场上的主要分布特征，但均高估了AO模态的强度。相对于地球系统模式来说，大部分物理气候系统模式所模拟的冬季 AO 模态的强度更接近观测结果。在北半球中高纬度地区，虽然大部分模式都能够模拟出伴随着冬季 AO 的位相变化出现的偶极型的纬向平均纬向风异常，但对其中心位置和强度的模拟往往与观测存在较大偏差，说明耦合模式对AO 垂直结构的模拟能力仍需进一步提高。对比之下，MPI-ESM-P 对 AO的时间变率以及水平和垂直结构的模拟更接近观测结果。■

致 谢：感谢世界气候研究计划耦合模式工作组和各模式机构为 CMIP5 试验所作的贡献，同时感谢英国 Hadley 中心和美国 NCEP/NCAR 提供的再分析资料。

参考文献

[1] 唐国利, 罗勇, 黄建斌, 等. 气候变暖在继续 [J]. 气候变化研究进展, 2012, 8 (4): 235-242

[2] 王绍武, 罗勇, 赵宗慈, 等. 气候变暖的归因研究 [J]. 气候变化研究进展, 2012, 8 (4): 308-312

[3] Stoner A M K, Hayhoe K, Wuebbles D J. Assessing general circulation model simulations of atmospheric teleconnection patterns [J]. Journal of Climate, 2009, 22: 4348-4372

[4] Thompson D W J, Wallace J M. The Arctic Oscillation signature in the wintertime geopotential height and temperature fields [J]. Geophysical Research Letters, 1998, 25: 1297-1300

[5] Thompson D W J, Wallace J M. Annular modes in the extratropical circulation. Part I : month-to-month variability [J]. Journal of Climate, 2000, 13: 1000-1016

[6] Thompson D W J, Wallace J M. Regional climate impacts of the Northern Hemisphere annular mode [J]. Science, 2001, 293: 85-89

[7] Gong D Y, Wang S W, Zhu J H. East Asian winter monsoon and Arctic Oscillation [J]. Geophysical Research Letters, 2001, 28: 2073-2076

[8] Wu B Y, Wang J. Winter Arctic Oscillation, Siberian High and East Asian winter monsoon [J]. Geophysical Research Letters, 2002, 29 (19), 1897, doi:10.1029/2002GL015373

[9] 龚道溢, 王绍武. 近百年北极涛动对中国冬季气候的影响 [J]. 地理学报, 2003, 58 (4): 559-568

[10] 琚建华, 任菊章, 吕俊梅. 北极涛动年代际变化对东亚北部冬季气温增暖的影响 [J]. 高原气象, 2004, 23 (4): 429-434

[11] Yamazaki K, Shinya Y. Analysis of the Arctic Oscillation simulated by AGCM [J]. Journal of Meterological Society of Japan, 1999, 77: 1287-1298

[12] Robertson A W. Influence of ocean-atmosphere interaction on the Arctic Oscillation in two general circulation models [J]. Journal of Climate, 2001, 14: 3240-3254

[13] Miller R L, Schmidt G A, Shindell D T. Forced annular variations in the 20th century Intergovernmental Panel on Climate Change assessment report models [J]. Journal of Geophysical Research, 2006, 111, D18101

[14] 辛晓歌, 周天军, 宇如聪. 气候系统模式对北极涛动的模拟 [J]. 地球物理学报, 2008, 51 (2): 337-351

[15] 祝亚丽, 王会军. 基于IPCC AR4耦合模式的南极涛动和北极涛动的模拟及未来变化预估 [J]. 气象学报, 2008, 66 (6): 993-1004

[16] Taylor K E, Stouffer R J, Meehl G A. An overview of CMIP5 and the experiment design [J]. Bulletin of the American Meteorological Society, 2012, 93: 485-498

[17] Allan R, Ansell T. A new globally complete monthly historical gridded mean sea level pressure dataset (HadSLP2): 1850−2004 [J]. Journal of Climate, 2006, 19: 5816-5842

[18] Kalnay E, Kanamitsu M, Kistler R, *et al*. The NCEP/NCAR 40-year reanalysis project [J]. Bulletin of the American Meteorological Society, 1996, 77: 437-472

[19] Barnston A G, Livezey R E. Classification, seasonality and persistence of low-frequency atmospheric circulation patterns [J]. Monthly Weather Review, 1987, 115: 1083-1126

[20] Taylor K E. Summarizing multiple aspects of model performance in a single diagram [J]. Journal of Geophysical Research, 2001, 106: 7183-7192

[21] Li J P, Wang J X L. A modified zonal index and its physical sense [J]. Geophysical Research Letters, 2003, 30, doi:1011029P2003GL017441

The Arctic Oscillation in the CMIP5 Models

Zuo Jinqing[1, 2], Li Weijing[2], Ren Hongli[2]

1 *Chinese Academy of Meteorological Sciences, Beijing* 100081*, China*; 2 *Laboratory for Climate Studies, National Climate Center, China Meteorological Administration, Beijing* 100081*, China*

Abstract: The temporal variability and spatial pattern of the Arctic Oscillation (AO) simulated in the historical experiment of 26 coupled climate models participating in the Coupled Model Intercomparison Project Phase 5 (CMIP5) were evaluated. Spectral analysis of the monthly AO time series indicates that 23 out of 26 of the CMIP5 models exhibit no statistically significant spectral peak in the historical experiment, as seen in the observed time series. Also, these models are able to reproduce the AO pattern in the sea level pressure anomaly field during boreal winter. But the strength of AO pattern tends to be overestimated in all the models. The zonal-mean zonal wind anomalies associated with the winter AO exhibit a dipole in latitude, which is only well reproduced by a few models. Most models show significant biases in both strength and location of the meridional dipole in the zonal-mean zonal wind anomaly filed associated with the winter AO. In considering the temporal variability as well as spatial structures in both horizontal and vertical directions, the model MPI-ESM-P reproduces an AO pattern that more resembles the observation.

Key words: Arctic Oscillation; model evaluation; coupled climate model; CMIP5

信息与动态

地球会罹患“金星综合症”吗？

2013年4月15日，美国专门研究气候变化的科学家J. Hansen在哥伦比亚大学网站(http://environmentaljusticetv.wordpress.com/2013/04/17/exaggeration-jumping-the-gun-and-the-venus-syndrome/）上发表文章，警告地球可能患“金星综合症”。4月19日英国《每日邮报》作了报导。所谓“金星综合症”是指地球大气可能演变为类似金星当前大气的状态：表面气压约为地球的90倍、气体成分主要是CO_2、表面温度约500 ℃。当然，如果地球大气转变为这种状态，那显然就不再适宜人类居住了，甚至于在远没有达到这个状态之前人类就不能生存了。地球大气怎么会变成这个样子呢？Hansen认为罪魁祸首就是燃烧化石燃料，如果不加限制，很可能会达到失控的状态。这里关键是反馈作用，即一旦气候变暖，则会影响地球系统的其他成员，这些成员的变化又反过来使变暖加剧。例如气候变暖，海水蒸发加强，大气中水汽增加，水汽也是一种重要的温室气体，因此温室效应加剧，气候进一步变暖。这一类反馈，是快速反馈，可能使原来的变暖增加2～3倍，但是还达不到失控的地步。另一种更重要的反馈是慢反馈。例如冰盖消失、甲烷水合物融化。这些反馈的作用要比快速反馈强得多，而且作用时间要长。地球的历史上就不乏这样的例子。如古新世与始新世交界的热力极大期(PETM）约发生于5500万年前，那时深海温度可能比现代高8 ℃，大气中的CO_2浓度接近4000×10^{-6}，而现在工业化以来虽然已经增加了40%，但也还不到400×10^{-6}。研究表明，PETM大气中CO_2剧增可能是海洋中甲烷水合物融化的结果。一旦失控，则只有当全部燃料都耗尽，变暖的过程才会停止，但是那时可能已经罹患了“金星综合症”。Hansen对这个患病过程作了推测：气候变暖导致对流层升高，水汽上传到高层分解，氢气逃逸到地球之外。但是，作者也指出，这个过程可能要几亿年。

因此，更现实的是关注未来几百年可能发生的变化是否会激发类似于PETM的事件。Hansen的研究表明，研究古气候敏感度及古代的暖期，即地质学上的温室期，对预估未来的气候变化有重要的意义。

北京大学 王绍武，黄建斌

附录

表 1 CMIP5 模式概况

Table 1 Information of CMIP5 climate models

模式名称	国家	水平分辨率（经纬度）	模式名称	国家	水平分辨率（经纬度）
ACCESS1.0	澳大利亚	1.875° × 1.25°	GISS-E2-H	美国	2.5° × 2.0°
ACCESS1.3	澳大利亚	1.875° × 1.25°	GISS-E2-R	美国	2.5° × 2.0°
BCC-CSM1.1	中国	2.8° × 2.8°	HadCM3	英国	3.75° × 2.5°
BNU-ESM	中国	2.8° × 2.8°	HadGEM2-AO	韩国	1.875° × 1.25°
CanESM2	加拿大	2.8° × 2.8°	HadGEM2-CC	英国	1.875° × 1.25°
CCSM4	美国	1.25° × 0.94°	HadGEM2-ES	英国	1.875° × 1.25°
CESM1-BGC	美国	1.25° × 0.94°	INM-CM4	俄罗斯	2.0° × 1.5°
CESM1-CAM5	美国	2.5° × 1.9°	IPSL-CM5A-LR	法国	3.75° × 1.875°
CESM1-FASTCHEM	美国	1.25° × 0.94°	IPSL-CM5A-MR	法国	2.5° × 1.25°
CESM1-WACCM	美国	2.5° × 1.875°	IPSL-CM5B-LR	法国	3.75° × 1.875°
CMCC-CM	意大利	0.75° × 0.75°	MIROC5	日本	1.4° × 1.4°
CNRM-CM5	法国	1.4° × 1.4°	MIROC-ESM	日本	2.8° × 2.8°
CSIRO-Mk3.6.0	澳大利亚	1.875° × 1.875°	MIROC-ESM-CHEM	日本	2.8° × 2.8°
FGOALS-g2	中国	2.8° × 2.8°	MPI-ESM-LR	德国	1.9° × 1.9°
FGOALS-s2	中国	2.8° × 1.7°	MPI-ESM-MR	德国	1.875° × 1.875°
FIO-ESM	中国	2.8° × 2.8°	MPI-ESM-P	德国	1.9° × 1.9°
GFDL-CM3	美国	2.5° × 2.0°	MRI-CGCM3	日本	1.1° × 1.1°
GFDL-ESM2G	美国	2.5° × 2.0°	NorESM1-M	挪威	2.5° × 1.875°
GFDL-ESM2M	美国	2.5° × 2.0°	NorESM1-ME	挪威	2.5° × 1.875°

表 2 CMIP3 模式概况

Table 2 Information of CMIP3 climate models

模式名称	国家	水平分辨率（经纬度）	模式名称	国家	水平分辨率（经纬度）
BCCR-BCM2.0	挪威	2.8° × 2.8°	GISS-AOM	美国	4.0° × 3.0°
CCSM3	美国	1.4° × 1.4°	GISS-EH	美国	5.0° × 4.0°
CGCM3.1-T47	加拿大	3.75° × 3.75°	GISS-ER	美国	5.0° × 4.0°
CGCM3.1-T63	加拿大	2.8° × 2.8°	INM-CM3.0	俄罗斯	5.0° × 4.0°
CNRM-CM3	法国	2.8° × 2.8°	IPSL-CM4	法国	3.75° × 2.5°
CSIRO-MK3.0	澳大利亚	1.875° × 1.875°	MIROC3.2-hires	日本	1.125° × 1.125°
ECHAM5	德国	1.875° × 1.875°	MIROC3.2-medres	日本	2.8° × 2.8°
ECHO-G	德国	3.75° × 3.75°	MRI-CGCM2.3.2	日本	2.8° × 2.8°
FGOALS-g1.0	中国	2.8° × 3.0°	PCM1	美国	2.8° × 2.8°
GFDL-CM2.0	美国	2.5° × 2.0°	UKMO-HadCM3	英国	3.75° × 2.5°
GFDL-CM2.1	美国	2.5° × 2.0°	UKMO-HadGEM1	英国	1.875° × 1.25°

论文编目索引

1. 陈丽娟，袁　媛，杨明珠，等. 2013：海温异常对东亚夏季风影响机理的研究进展. *应用气象学报*，24(5)：521-532.

2. 达朝究，冯爱霞，龚志强，宋　健. 2013：缓变下垫面对浅水方程的动力学订正. *物理学报*，62(3)：039202，2013-3.

3. 封国林，孙树鹏，赵俊虎，郑志海. 2013：基于2009年初长江中下游地区持续阴雨过程的10—30天延伸期稳定分量的提取及配置分析. *中国科学:地球科学*，43(5)：836-847.

4. 封国林，赵俊虎，支　蓉，等. 2013：动力-统计客观定量化汛期降水预测研究新进展. *应用气象学报*，24(6)：656-665.

5. 冯亚文，任国玉，刘志雨，吴吉东，张　雷. 2013：长江上游降水变化及其对径流的影响. *资源科学*，35(6)：1268-1276.

6. Ge，B.，Y. Sun，Y. Liu，H. Dong，D. Ji，Q. Jiang，J. Li，and Z. Wang. 2013：Nitrogen dioxide measurement by cavity attenuated phase shift spectroscopy (CAPS) and implications in ozone production efficiency and nitrate formation in Beijing，China. *Journal of Geophysical Research：Atmospheres*，118，1-11，doi：10.1002/jgrd.50757.

7. 龚振淞，陈丽娟. 2013：2010年西北太平洋与南海热带气旋活动异常的成因分析. *气候与环境研究*，18(3)：342-352.

8. 胡娅敏，覃志年，陈丽娟，等. 2013：基于多时间尺度的回归集成预测模型. *气象*，39(9)：1182-1189.

9. 贾小龙，陈丽娟，等. 2013：利用海气耦合模式预测的大尺度环流进行热带气旋年频数的预测试验. *热带气象学报*，29(1)：37-46.

10. 李　娇，任国玉，战云健. 2013：浅谈极端气温事件研究中阈值确定方法. *气象科技进展*，DOI:10.3969/j.issn.2095-1973.2013.05.006.

11. 李维京，李　怡，陈丽娟，赵振国. 2013：我国冬季气温与影响因子关系的年代际变化. *应用气象学报*，24(4)：385-396.

12. Liu Y，Fan K，Yan Y-P. 2013：A new statistical downscaling scheme for predicting winter precipitation in China. *Atmospheric and Oceanic Science Letters*，6：332-336，doi:10.3878/j.issn.1674-2834.13.0008.

13. 刘　颖，范　可，张　颖. 2013：基于CFS模式的中国站点夏季降水统计降尺度预测. *大气科学*，37(6)：1287-1296，doi:10.3878/j.issn.1006-9895.2012.12143.

14. 刘玉莲，任国玉，于宏敏，康恒元. 2013：我国强降雪气候特征及其变化. *应用气象学报*，24(3)：304-313.

15. 彭　杰，张　华，沈新勇. 2013：东亚地区云垂直结构的CloudSat卫星观测研究. *大气科学*，37(1)：91-100.

16. 覃志年，胡娅敏，陈丽娟. 2013：广西夏季降水的多时间尺度特征及影响因子. *应用气象学报*，24(5)：565-575.

17. Ren，Hong-Li，and Fei-Fei Jin. 2013：Recharge Oscillator Mechanisms in Two Types of ENSO. *Journal of Climate*，26(17)，6506-6523，doi:10.1175/JCLI-D-12-00601.1.

18. Ren，Hong-Li，Fei-Fei Jin，Malte F. Stuecker，Ruihuang Xie. 2013：ENSO regime change since the late

1970s as manifested by two types of ENSO. *Journal of the Meteorological Society of Japan*, 91(6): 835-842, DOI:10.2151/jmsj.2013-608.s00704-013-0894-0.

19. 沈志超，任国玉，李　娇，孙秀宝. 2013：中国东北地区冬季气温变化特征及其与大气环流异常的关系. *气象与环境学报*，29(1)：47-54.
20. Dong SI and Yihui DING. 2013: Decadal Change in the Correlation Pattern between the Tibetan Plateau Winter Snow and the East Asian Summer Precipitation during 1979—2011. *Journal of Climate*, 26: 7622-7634.
21. 苏　涛，张世轩，支　蓉，陈丽娟. 2013：江淮流域夏季降水对前冬持续时间长短的响应. *物理学报*，62(6)：DOI：10.7498/aps.62.069203.
22. 孙秀宝，任国玉，任芝花，沈志超. 2013：风场变形误差对冬季降雪测量及其趋势估算的影响. *气候与环境研究*，18(2)：178-186.
23. 孙　颖，尹　红，田沁花，等. 2013：全球和中国区域近50年气候变化检测归因研究进展. *气候变化研究进展*，9(4)：235 -245.
24. 王东阡，周　兵，孙丞虎，等. 2013：2012/2013年东亚冬季风活动特征及其可能成因分析. 气象，39(7)：930-937.
25. Wang K, Feng G, et al. 2013: Analysis of stable components in extended-range forecast for the coming 10-30 days in winter 2010 and 2011. *Chinese Physics B*, 22(12): 129202.
26. 王小玲，丁一汇. 2013：2010年夏季欧亚异常阻高演变过程及对天气气候的影响. 气象，39(9)：1089-1095.
27. 王晓娟，沈柏竹，龚志强，封国林. 2013：中国冬季区域性极端低温事件分类及其与气候指数极端性的联系. *物理学报*，62(22)：229201.
28. Zhili Wang, Hua Zhang, et al. 2013: Effect of non-spherical dust aerosol on its direct radiative forcing. *Atmospheric Research*, 120-121: 112-126.
29. Zhili Wang, Hua Zhang, et al. 2013: Radiative forcing and climate response due to the presence of black carbon in cloud droplets. *Journal of Geophysical Research*, 118 (9): 3662-3675.
30. 吴焕萍，张永强，孙家民，邵鹏程. 2013：气候信息交互显示与分析平台(CIPAS)设计与实现. *应用气象学报*，24(5)：631-640.
31. 吴　佳，高学杰. 2013：一套格点化的中国区域逐日观测资料及与其它资料的对比. *地球物理学报*，56(4)：1102-1111，doi：10.6038/cjg20130406.
32. Xie, S.-P., B. Lu(co-first author), and B. Xiang. 2013: Similar spatial patterns of climate responses to aerosol and greenhouse gas changes. *Nature Geoscience*, 6, 828-832.
33. 杨明珠，陈丽娟，宋文玲. 2013：黑潮区海温对中国北方初霜冻日期的影响研究. 气象，39(9)：1125-1132.
34. Yang, P., G. Y. Ren, W. D. Liu. 2013: Spatial and temporal characteristics of Beijing urban heat island intensity. *Journal of Applied Meteorology and Climatology*, 52: 1803-1816, DOI: 10.1175/JAMC-D-12-0125.1.
35. Qinglong You, Klaus Fraedrich, Jinzhong Min, Shichang Kang, Xiuhua Zhu, Guoyu Ren, et al. 2013: Can temperature extremes in China be calculated from reanalysis? *Global and Planetary Change*, 111 (2013)268-279.

36. Qinglong You, Yang Jiao, Houbo Lin, Jinzhong Min, Shichang Kang, Guoyu Ren, et al. 2013: Comparison of NCEP/NCAR and ERA-40 total cloud cover with surface observations over the Tibetan Plateau. *Interantional Journal of Climatology*, (2013) DOI: 10.1002/joc.3852.

37. Qinglong You, Arturo Sanchez-Lorenzo, Martin Wild, Doris Folini, Klaus Fraedrich, Guoyu Ren, et al. 2013: Decadal variation of surface solar radiation in the Tibetan Plateau from observations, reanalysis and model simulations. *Clim Dyn*, (2013) 40:2073-2086, DOI 10.1007/s00382-012-1383-3.

38. Qinglong You, Klaus Fraedrich, Guoyu Ren, et al. 2013: Variability of temperature in the Tibetan Plateau based on homogenized surface stations and reanalysis data. *Interantional Journal of Climatology*, 33: 1337-1347, DOI: 10.1002/joc.3512.

39. Qinglong You, Guoyu Ren, Klaus Fraedrich, Shichang Kanga, Yuyu Ren, et al. 2013: Winter temperature extremes in China and their possible causes. *International Jouranl of Climatology*, 33: 1444-1455, DOI: 10.1002/joc.3525.

40. Qinglong You, Klaus Fraedrich, Frank Sielmann, Jinzhong Min, Shichang Kang, Zhenming Ji, Xiuhua Zhu, Guoyu Ren. 2013: Present and projected degree days in China from observation, reanalysis and simulations. *Clim Dyn*, DOI: 10.1007/s00382-013-1960-0.

41. 于宏敏，任国玉，刘玉莲. 2013：黑龙江省大气边界层不同高度风速变化. *自然资源学报*，28(10)：1718-1730.

42. 战云健，任国玉，任玉玉，等. 2013：1951—2009 年东亚地区日降水趋势特征分析. *气候与环境研究*，18(6)：767-780，doi:10.3878/j.issn.1006-9585.

43. 张本志，任国玉，张子曰，等. 2013：北京中心商务区夏季近地面气温时空分布特征. *气象与环境学报*，29(5)：26-34.

44. Zhang, H., Jing, X. and Li, J. 2013: Application and evaluation of McICA scheme with new radiation code in BCC_AGCM 2.0.1. Geosci. *Model Development Discussions*, 6, 4933-4982.

45. ZHANG Hua, PENG Jie, JING XianWen, LI JiangNan. 2013: The features of cloud overlapping in Eastern Asia and their effect on cloud radiative forcing. *Science China Earth Sciences*, 2013, 56(5): 737-747.

46. 张　华，彭　杰，等. 2013：东亚地区云的垂直重叠特性及其对云辐射强迫的影响. *中国科学：地球科学*，43(4)：523-535.

47. Hua Zhang, Qing Yin et al. 2013: Influence of changes in solar radiation on changes of surface temperature in China. *Acta Meteorologica Sinica*, 27(1), 87-97, doi: 10.1007/s13351-013-0109-8.

48. Hua Zhang, Ruoyu Zhang, Guangyu Shi. 2013: An updated estimation of radiative forcing due to CO2 and its effect on global surface temperature change. *Advances in Atmospheric Sciences*, 30(4): 1017-1024.

49. 张　华，张若玉，何金海，等. 2013：CH_4 和 N_2O 的辐射强迫与全球增温潜能. *大气科学*，37 (3)：745-754.

50. Zhang, L., G. Y. Ren, Y. Y. Ren, A. Y. Zhang, Z. Y. Chu, Y. Q. Zhou. 2013: Effect of data homogenization on estimate of temperature trend: a case of Huairou station in Beijing Municipality. *Theor Appl Climatol*, DOI: 10.1007/s00704-013-0894-0.

51. 张世轩，封国林，赵俊虎. 2013：长江中下游地区暴雨“积成效应”. *物理学报*，62(6)：029201.

52. 赵俊虎，杨　杰，龚志强，等. 2013：欧亚中高纬阻塞高压关键区高度场动力-统计跨季度预测实验. *物理学*

报，62(9)：099206.

53. 周　晨，张　华，王志立. 2013：黑碳与非吸收性气溶胶的不同混合方式对其光学性质的影响. *光学学报*，33(8)：270-281.

54. ZHOU Wei，CHENG Yan-Jie，WANG Su-Juan，et al. 2013：Evaluation and Preprocess of Chinese Fengyun-3A Sea Surface Temperature Experimental Product for Data Assimilation. *Atmospheric and Oceanic Science Letters*，6(3)：128-132.

55. 周　巍，王东晓，俎婷婷，等. 2013：基于三层嵌套网格的珠江口冬季盐度层化的数值模拟. *海洋与湖沼*，44(3)：545-556.

56. 竺夏英，陈丽娟，李　想. 2013：2012 年冬春季高原积雪异常对亚洲夏季风的影响. 气象，39(9)：1111-1118.

57. ZUO Jin-Qing，LI Wei-Jing，REN Hong-Li. 2013：Representation of the Arctic Oscillation in the CMIP5 Models. *Advances in Climate Change Research*，4(4)：242-249.

58. Zuo Jinqing，Li Weijing，Sun Chenghu，Xu Li，and Ren Hong-Li. 2013：Impact of the North Atlantic Sea Surface Temperature Tripole on the East Asian Summer Monsoon. *Advances in Atmospheric Sciences*，30(4)：1173-1186.

59. 左金清，李维京，任宏利. 2013：CMIP5 模式对北极涛动的模拟评估. *气候变化研究进展*，39(3)：157-164.

LCS

气候研究开放实验室